The evolution of the Himalaya since the Late Miocene, as told by the history of its erosion

Sébastien Lénard

Thèse

Présentée et soutenue publiquement pour l'obtention du titre de

DOCTEUR DE L'UNIVERSITÉ DE LORRAINE

Mention : «Géosciences»

Évolution de l'Himalaya de la fin du Miocène à nos jours à partir de l'histoire de son érosion

Soutenue le 26 novembre 2019 à Nancy
Par Sébastien LÉNARD

Membres du Jury :

Rapporteurs :	**Mme Taylor Schildgen, Universität Postdam**
	M. Vincent Godard, Université d'Aix-Marseille
Examinateurs :	**Mme Pascale Huyghe, Université Grenoble I**
	M. Sébastien Carretier, Université de Toulouse
Directeur de thèse :	**M. Jérôme Lavé, Université de Lorraine**
Co-Directeur :	**M. Christian France-Lanord, CNRS**
Invités :	**M. Julien Charreau, Université de Lorraine**

CRPG-CNRS Université de Lorraine - UMR 7358
15, rue Notre-Dame des Pauvres 54501 Vandoeuvre-lès-Nancy

Thèse

submitted and publicly defended in fulfillment of the requirements for the degree of
DOCTEUR DE L'UNIVERSITÉ DE LORRAINE
in «Geosciences»

The evolution of the Himalaya since the Late Miocene, as told by the history of its erosion

Defended on the 26th of November 2019 in Nancy
By Sébastien LÉNARD

Members of the Jury :

Reviewers :	**Ms Taylor Schildgen, Universität Postdam**
	Mr Vincent Godard, Université d'Aix-Marseille
Examinateurs :	**Ms Pascale Huyghe, Université Grenoble I**
	Mr Sébastien Carretier, Université de Toulouse
Thesis Advisor :	**Mr Jérôme Lavé, Université de Lorraine**
Co-Advisor :	**Mr Christian France-Lanord, CNRS**
Invité :	**Mr Julien Charreau, Université de Lorraine**

CRPG-CNRS Université de Lorraine - UMR 7358
15, rue Notre-Dame des Pauvres 54501 Vandoeuvre-lès-Nancy
France

THESIS OUTLINE

To further investigate the debate about tectonics, climate and denudation, this thesis aims to obtain an independent temporal record of erosion rates at the orogen-scale and at low-latitudes over the the late Cenozoic time span. The Himalaya, at the convergence of the Indian and Eurasian plates, has epitomized this debate and will be the object of the present thesis, through geochemical and isotopic measurements applied on deep sea sedimentary sites drilled in the Bengal Bay (France-Lanord et al., 2016; Clemens et al., 2016) and on a new continental sedimentary section in the Valmiki Wildlife Sanctuary, National Park & Tiger Reserve, Bihar, India.

This manuscript consists of three introductory chapters (Chapters I-III), one methodological chapter (Chapter IV), two joint-authorship manuscripts that have been submitted to peer-reviewed international journals (Chapters V and VI), two drafts of future joint-authorship manuscripts (Chapters VII and VIII), a synthesis and conclusion (Chapter IX), and a synthesis in french (Chapter X). The data acquired during this thesis are compiled in tables at the end of the manuscript.

PLAN DE THESE

Pour approfondir le débat sur la tectonique, le climat et la dénudation, cette thèse vise à obtenir un enregistrement temporel indépendant des taux d'érosion à court terme à l'échelle orogénique et aux basses latitudes, sur la durée du Cénozoïque tardif. L'Himalaya, à la convergence des plaques indienne et eurasienne, a incarné ce débat et fera l'objet de la présente thèse, à travers des mesures géochimiques et isotopiques appliquées sur des sites sédimentaires forés en eau profonde dans la baie du Bengale (France-Lanord et al, 2016 ; Clemens et al, 2016) et sur une nouvelle section sédimentaire continentale dans la réserve naturelle protégée de Valmiki, dans l'Etat du Bihar en Inde.

Ce manuscrit se compose de trois chapitres d'introduction (chapitres I à III), d'un chapitre méthodologique (chapitre IV), de deux manuscrits co-écrits et soumis à des revues internationales à comité de lecture (chapitres V et VI), de deux ébauches de futurs manuscrits co-écrits (chapitres VI et VIII), d'une synthèse et conclusion (chapitre IX) et d'une synthèse en français (chapitre X). Les données acquises durant cette thèse sont compilées dans des tableaux à la fin du manuscrit.

PLEASE CITE THIS WORK AS:

Lenard, S. J.P. (2019). Évolution de l'Himalaya de la fin du Miocène à nos jours à partir de l'histoire de son érosion - The evolution of the Himalaya since the Late Miocene, as told by the history of its erosion, PhD thesis [en], Université de Lorraine, France. www.theses.fr.

ABSTRACT

An intense debate animates the Earth Sciences community about the impact of the Glaciations on mountain ranges. Mountains develop their relief from the interaction of tectonics with climate through erosion. Erosion breaks rocks in the highland, and rivers and submarine gravity flows (turbidites) transfer the waste material to sedimentary basins. Erosion results from the action of rainfall, rivers or glaciers. Studies suggest that changes in the rainfall amplitude or seasonality, and changes in the extent of glaciers have triggered a worldwide and considerable increase of erosion rates for the last millions of years. However, this hypothesis is debated because past erosion rates are estimated with indirect approaches.

Here, I focus on the Himalaya, the iconic mountain range at the convergence of the Indian and Eurasian plates. There, the highests summits and the deepest valleys on Earth grow. Landslides and glacial erosion supply one of the highest sedimentary fluxes to the oceans. To determine the past erosion rates, I measured the amount of the ^{10}Be cosmogenic isotope accumulated in the quartz sediment. These isotopes are produced at Earth's surface by the interaction of cosmic rays with matter. Isotopes gradually accumulate in rocks close to the surface, depending on the elevation and the erosion rates. The isotopic concentration in sediment gives access to the average erosion rate of the source drainage basin. To determine the source of sediment and the deposition paleoenvironment, I performed supplementary measurements on Sr-Nd and C-O isotopes.

I conducted my measurements on two sites. Site A consists in sandy turbidites sedimented on the deep sea floor of the Bengal Bay and collected by Expeditions 353 and 354 of the International Ocean Discovery Program. Site B consists in molasse sediment deposited at the front of the Himalaya, in the Siwalik Hills, within the Valmiki Wildlife Sanctuary in India. Site A integrates the erosion of the Ganga and Brahmaputra drainage basins, covering Central and Eastern Himalaya. Site B integrates the erosion of the Narayani-Gandak basin, covering Central Nepal.

My results yield an unprecedented insight in the variation of erosion in a mountain range over the last seven million years. They imply that average erosion rates have been steady since at least three million years in the Himalaya, despite the variations in sediment transfer or the locus of erosion, and despite intense late Cenozoic Glaciations.

RESUME

La communauté des sciences de la Terre est animée d'un intense débat sur l'impact des Glaciations sur les chaînes de montagnes. Les montagnes forment leur relief à partir des interactions entre la tectonique, le climat et l'érosion. L'érosion détruit les roches en altitude et les rivières et les écoulements gravitaires sous-marins (turbidites) en transfèrent les débris vers les bassins sédimentaires. L'érosion résulte de l'action des précipitations, des rivières ou des glaciers. Des études suggèrent que les changements dans l'amplitude ou la saisonnalité des précipitations et les changements dans l'étendue des glaciers ont provoqué une augmentation mondiale et considérable des taux d'érosion sur les derniers millions d'années. Cependant, cette hypothèse est débattue car les taux d'érosion passés sont estimés avec des approches indirectes.

Ici, je me concentre sur l'Himalaya, la chaîne de montagne par excellence située à la convergence des plaques indiennes et eurasiennes. C'est là que se développent les plus hauts sommets et les vallées les plus profondes de la Terre. Les glissements de terrain et l'érosion glaciaire fournissent l'un des flux sédimentaires les plus élevés aux océans. Pour déterminer les taux d'érosion passés, j'ai mesuré la quantité d'isotope cosmogénique ^{10}Be accumulée dans le sédiment de quartz. Ces isotopes sont produits à la surface de la Terre par l'interaction des rayons cosmiques avec la matière. Les isotopes s'accumulent progressivement dans les roches proches de la surface, en fonction de l'altitude et des taux d'érosion. La concentration isotopique du sédiment donne accès au taux d'érosion moyen du bassin versant à la source de celui-ci. Pour déterminer la source des sédiments et le paléoenvironnement de dépôt, j'ai effectué des mesures complémentaires sur les isotopes Sr-Nd et C-O.

J'ai réalisé mes mesures sur deux sites. Le site A est constitué de turbidites sableuses sédimentées dans les fonds marins de la baie du Bengale et recueillies par les expéditions 353 et 354 du programme scientifique IODP. Le site B est constitué de molasses déposées au front de l'Himalaya, dans les collines des Siwaliks, au sein du sanctuaire animalier de Valmiki en Inde. Le site A intègre l'érosion des bassins versants du Gange et du Brahmapoutre, couvrant l'Himalaya central et oriental. Le site B intègre l'érosion du bassin Narayani-Gandak, qui couvre le centre du Népal.

Mes résultats donnent un aperçu sans précédent de la variation de l'érosion dans une chaîne de montagnes au cours des sept derniers millions d'années. Ils impliquent que les taux d'érosion moyens sont stables depuis au moins trois millions d'années dans l'Himalaya, malgré les variations dans le transfert sédimentaire ou sur le lieu de l'érosion, et malgré les glaciations intenses de la fin du Cénozoïque.

CONTENTS

FIGURES

TABLES

RESUME ETENDU

X.1. CONTEXTE

X.1.1. Changement climate et estimation des taux d'érosion

Les décennies précédentes de recherche ont vu l'émergence d'un intense débat sur les interactions entre la tectonique et le climat au travers de la dénudation. Une question clé et sans réponse est de savoir si le changement climatique a un impact sur les taux d'érosion et affecte le développement des chaînes de montagnes indépendamment de leur configuration tectonique. Et l'un des principaux problèmes pour répondre à cette question est que les taux d'érosion passés ne peuvent être déterminés que par des approches indirectes. Un nombre significatif d'études montre une augmentation globale et considérable des taux d'érosion au cours du Cénozoïque tardif (p. ex. Zhang et al., 2001 ; Herman et al., 2013). Cette augmentation apparente est synchrone avec un changement climatique global caractérisé par une aridification et l'émergence des cycles glaciaires/interglaciaires avec les glaciations de l'hémisphère nord. Cette augmentation apparente touche plusieurs chaînes de montagnes de façon indiscriminée. Ainsi, le lien entre le changement climatique et cette augmentation apparente des taux d'érosion devrait être évident.

Mais les approches utilisées pour déterminer les taux d'érosion requièrent des hypothèses fortes qui n'ont pas été régulièrement vérifiées. Les bilans sédimentaires ou les taux d'accumulation dépendent des contraintes de datation individuelles de chaque site. Mais ces contraintes de datation sont difficiles à acquérir, en particulier dans les séries continentales grossières du Pléistocène. Dans ce cas, les travailleurs sont tentés de corréler temporellement les couches de chaque site les unes aux autres à l'aide de leurs caractéristiques sédimentaires (les faciès). Mais ces faciès sédimentaires, plutôt que de varier en fonction du climat, varient en fonction de la distance au front de propagation du gravier (Dubille et Lavé, 2015) ou en fonction de l'errance du lit de la rivière, qui sont des paramètres locaux. Les travaux de Charreau et al (2009) contredisent les résultats de Zhang et al (2001) en Asie centrale en montrant que les formations grossières du front du Tianshan sont diachrones et illustrent cette situation. Les bilans sédimentaires dépendent également de la résolution spatio-temporelle des sites de forage. Un bilan sédimentaire réalisé sur les sédiments glaciogènes déposés sur la marge norvégienne qui a été largement explorée (Dowdeswell et al., 2010) a plus de valeur qu'un bilan sédimentaire réalisé dans la baie du Bengale qui possède peu de données en eau profonde (Métivier et al., 1999 ; Clift et Gaedicke, 2002; Clemens et al., 2016; France-Lanord et al., 2016).

La thermochronométrie in situ repose sur l'hypothèse forte que le géotherme a une configuration simple et moyennée régionalement, classiquement selon une seule dimension (par exemple, Fox et al., 2014 ; Herman et al., 2013). Mais le champ thermique dans les chaînes de montagnes actives est tout sauf simple. Des variations latérales se produisent avec l'advection horizontale (Huntington et al., 2007; Herman et al., 2010a; van der Beek et al., 2010). Des variations spatiales se produisent avec le flux thermique hydrothermal (Copeland et al., 1991 ; Derry et al., 2009) et le flux d'eau souterraine provoqué par le relief de haute montagne (Whipp et Ehlers, 2007). Le géotherme peut être instable dans le temps et différent selon thermochronomètres appliqués sur le même échantillon. Le risque est de combiner des

données provenant d'échantillons distincts et de thermochronomètres distincts qui ne présentent pas la même histoire de dénudation (Schildgen et al., 2018).

X.1.2. Hypothèses associées à l'utilisation des isotopes cosmogéniques terrestres

Dans cette thèse, nous avons démontré que l'utilisation des isotopes cosmogéniques terrestres pour estimer les taux moyens d'érosion dans un bassin versant requiert des hypothèses qui pourraient être plus facilement vérifiées que pour les autres approches, du moins dans l'Himalaya. Alors que le flux cosmique est resté stable depuis 10 Ma (Leya et al., 2000), nous montrons que les fluctuations du dipôle géomagnétique influencent les taux de production cosmogénique dans une marge de 20%. L'altitude passée du bassin versant peut être estimée à l'aide des isotopes de l'oxygène et est probablement restée stable dans le centre de l'Himalaya depuis 10 Ma (Garzione et al., 2000 ; Gébelin et al., 2013). L'exposition récente des échantillons aux rayons cosmiques peut être évaluée à l'aide d'un couple d'isotopes cosmogéniques de demi-vies distinctes. Comme précédemment démontré (Lauer et Willenbring, 2010), l'exposition pendant le transfert des sédiments dans la plaine inondable peut être déterminée au moyen d'un modèle de transfert. Le recyclage affecte les concentrations des isotopes cosmogéniques parce que les échantillons ont conservé une histoire d'érosion plus ancienne. Ce recyclage peut être évalué à l'aide des éléments majeurs. La géométrie du bassin détermine l'altitude moyenne qui affecte le calcul des taux moyens de production. La stabilité de cette géométrie peut être estimée par une analyse de provenance à l'aide des isotopes du strontium et du néodyme.

X.2. RESULTATS

Dans ce contexte, l'objectif de cette thèse était d'obtenir un enregistrement temporel des taux d'érosion dans l'Himalaya, qui soit indépendant des autres méthodes. Cet objectif est atteint grâce à deux nouveaux enregistrements.

X.2.1. L'enregistrement du cône du Bengale

Le premier enregistrement consiste en une série de 28 concentrations en ^{10}Be extraites du sable quartzeux du cône du Bengale et intègre l'érosion sur des échelles de temps de 1 à 10 ka dans le bassin versant du Gange-Brahmapoutre depuis 6,2 Ma, avec une haute résolution depuis le dernier million d'années (Chapitre VI). L'acquisition de concentrations à partir de ces anciens échantillons dans les sédiments marins a été possible grâce à l'abondance de sable dans les turbidites du cône du Bengale. Pour mieux déterminer les séries temporelles, nous fournissons de nouvelles contraintes sur des nanofossiles ainsi qu'un nouveau modèle d'âge pour le site U1450 foré par l'expédition IODP 354 (chapitre V).

Nous complétons nos concentrations par une analyse de provenance basée sur les isotopes Sr-Nd mesurés sur les échantillons de sable en vrac. Cette analyse tire parti des signatures isotopiques distinctes

des sédiments du Gange et du Brahmapoutre (Galy and France-Lanord, 2001). Nous démontrons que la provenance des turbidites sableuses est affectée par la séquestration du sable dans lees plaines d'inondation ou par des systèmes turbiditiques éventuellement distincts pour le Gange et le Brahmapoutre. Les turbidites sableuses d'âge inférieur à 0,45 Ma dans les forages de l'expedition 354 proviennent uniquement du Brahmapoutre.

Le principal résultat découlant des mesures effectuées dans le cône du Bengale est l'absence d'augmentation ou de diminution des taux moyens d'érosion dans l'Himalaya central et oriental depuis 6,2 Ma, en dépit du changement climatique et en dépit de preuves géomorphologiques claires indiquant l'intensité des glaciations passées dans l'Himalaya. Les taux d'érosion moyens dans le bassin du Gange et du Brahmapoutre restent proches des valeurs modernes, à 1 mm/an.

X.2.2. L'enregistrement des sections Valmiki

Le deuxième enregistrement consiste en une série de 36 concentrations en ^{10}Be extraites du sable quartzeux des sédiments continentaux Siwalik du bassin d'avant-pays de l'Himalaya, dans la zone naturelle protégée de Valmiki, dans l'Etat du Bihar en Inde (chapitre VIII). Cette série intègre l'érosion dans le bassin de la Narayani-Gandak au Népal central de 7,4 à 1,2 Ma. L'acquisition d'un signal distinct du blanc pour de tels échantillons anciens a été possible grâce aux grandes masses de quartz que nous avons préparées pour les mesures. Nous fournissons les observations de terrain sur les nouvelles sections Valmiki, d'est en ouest, les sections Patalaia, Ganguli, Dwarda, Gonauli et Maloni Naha, la série complète ayant une épaisseur décrite d'environ 4.000 m (Chapitre VII). Nous déterminons les contraintes magnétostratigraphiques qui couvrent la période de 8,1 à 0,78 Ma. Par conséquent, les sections Valmiki font partie de la famille réduite des sections Siwalik couvrant la presque totalité du Cénozoïque tardif. Nous estimons l'initiation des plis Siwalik locaux à 0,74$\pm$0,06 Ma pour le Dwarda, Ganguli et Patalaia et à 0,3-0,4 Ma pour les Gonauli et le Maloni Naha. Ces âges sont beaucoup plus jeunes qu'ailleurs dans les collines Siwalik.

Nous complétons nos résultats par une étude paléoenvironnementale à l'aide des isotopes de l'oxygène et du carbone sur des silts en vrac, une analyse de provenance à l'aide des isotopes Sr-Nd mesurés sur les échantillons de sable en vrac, ainsi qu'une analyse de l'exposition cosmogénique récente par des mesures de concentrations en ^{36}Cl. L'étude paléoenvironnementale bénéficie de la forte teneur en carbonates secondaires de nos échantillons limoneux. Ces carbonates secondaires se composent en partie de ciment diagénétique et de carbonates pédogéniques. Le ratio δ^{13}C dans les carbonates pédogéniques varie en fonction de la domination environnementale des plantes C_3 ou C_4, les deux groupes ayant un mode d'absorption du CO_2 distincte et se développant dans des conditions climatiques distinctes. Le ratio δ^{18}O varie en fonction du volume de précipitations et de leur saisonnalité. L'analyse de provenance Sr-Nd bénéficie des signatures isotopiques distinctes des principales unités géologiques de l'Himalaya (Morin, 2015).

Les résultats de notre étude sur le $\delta^{13}C$ pourraient permettre d'établir de nouvelles contraintes temporelles précises sur la transition vers une domination des plantes C_4 dans les plaines de l'Himalaya central. Ces nouvelles contraintes montreraient que le changement se produit de manière synchrone dans l'Himalaya central et occidental (nos résultats ; Quade et Cerling, 1995 ; Vögeli et al., 2017a). De plus, ils fourniraient la première preuve jamais dévoilée d'un retour à une végétation mixte en C_3 et C_4 à l'aube des glaciations de l'hémisphère nord. Nos résultats sur le $\delta^{18}O$ détectent qu'au moins la partie inférieure des sections Valmiki est affectée par la diagenèse précoce. Pour la partie supérieure, ils montreraient une aridification et/ou une augmentation de la saisonnalité au cours de la période, en dépit des glaciations de l'hémisphère nord, et contrairement à l'Himalaya occidental (Quade et Cerling, 1995). Ces résultats impliqueraient que l'intensité de la mousson sud-asiatique a varié au Cénozoïque tardif, avec un affaiblissement initial et un renforcement partiel ultérieur à l'aube des glaciations de l'hémisphère nord. Pour être validées, ces interprétations sur les signaux du $\delta^{13}C$ et du $\delta^{18}O$ demandent une analyse pétrographique approfondie des échantillons.

Notre analyse de provenance Sr-Nd combinée à nos concentrations en ^{10}Be implique que le bassin versant de la Narayani-Gandak demeure stable de 7,4 Ma à 1,2 Ma et n'a pas capturé d'affluents au nord. Nos résultats en Sr-Nd suggèrent une relative stabilité de l'érosion dans la chaîne inférieure, couverte par le Lesser Himalaya, malgré le duplexage en cours. Ils suggèrent également une diminution initiale des taux d'érosion sur le flanc sud et les sommets plus élevés, principalement couverts par le High Himalaya Crystalline (HHC) et dans une moindre mesure par les séries téthysiennes (TSS), suivie d'une réaugmentation après 1,7 Ma. Cette variabilité peut être attribuée aux fluctuations de la mousson sud-asiatique ou aux glaciations.

Nos résultats en ^{36}Cl impliquent que l'exposition récente aux rayons cosmiques est limitée pour la majeure partie des sections Valmiki. L'extension de ce résultat aux échantillons plus anciens nécessite de nouvelles mesures.

Le principal résultat des mesures effectuées sur les sections Valmiki est l'absence d'augmentation ou de diminution des taux moyens d'érosion dans le centre du Népal depuis environ 5 Ma, en dépit du changement climatique et en dépit de preuves géomorphologiques montrant clairement l'intensité des glaciations passées dans le centre du Népal. Cette stabilité, comparée aux variations des contributions du HHC et du TSS, implique que la diminution ou l'augmentation des taux d'érosion dans la partie Haut Himalaya du bassin de la Narayani-Gandak devrait être compensée par une diminution ou une augmentation ailleurs. Les taux d'érosion moyens dans le bassin Narayani-Gandak restent proches des valeurs modernes, à 2 mm/an. Ces valeurs sont supérieures au taux d'érosion moyen du Cône du Bengale et impliquent que certains segments de l'Himalaya ont des taux d'érosion bien inférieurs à 1 mm/an.

Le résultat secondaire est l'augmentation des taux d'érosion pendant la période de 7,4 à 5 Ma. Nous soulignons que cette augmentation doit être confirmée par d'autres mesures et modélisations. Une fois confirmée, cette augmentation pourrait signifier que l'initiation du duplexage a été plus tardive dans le centre du Népal que dans l'ouest du pays et que les paysages ont mis plusieurs millions d'années à s'adapter à cette nouvelle configuration tectonique. Cela remet en question l'hypothèse selon laquelle l'Himalaya dans le centre du Népal est en état d'équilibre depuis 10 Ma, du moins jusqu'à 5 Ma, ce qui devrait avoir un impact sur les études sur l'érosion dans cette région.

Dernier point concernant l'enregistrement de Valmiki, les taux d'érosion apparents dérivés de nos concentrations en ^{10}Be présentent une forte variabilité depuis 3,2 Ma. Ceci confirme des résultats antérieurs qui montrent le poids écrasant dans les sédiments des glissements de terrain à base profonde ou des glissements de terrain affectant les crêtes des chaînes de montagnes (Puchol et al., 2014 ; Dingle et al., 2018). Nous notons toutefois que la variabilité passée est beaucoup plus grande qu'à l'époque moderne, ce qui suggère qu'aucun analogue moderne des glissements de terrain que nous pouvons détecter dans notre enregistrement n'aurait jamais existé dans l'histoire récente. Cette variabilité n'affecte pas l'évolution du taux d'érosion moyen et nos conclusions.

X.3. CONCLUSION

Nos résultats démontrent que les taux d'érosion moyens dans l'Himalaya n'ont pas augmenté depuis au moins ca. 5 Ma, en dépit d'un changement important des conditions climatiques, comme le suggèrent nos mesures isotopiques complémentaires des concentrations en ^{10}Be. Cela implique que le changement climatique ne peut à lui seul augmenter ou diminuer les taux moyens d'érosion dans l'Himalaya, et que la tectonique est le principal moteur des variations des taux d'érosion moyens. Cependant, cela ne contredit pas les variations locales des taux d'érosion selon le climat, comme le montrerait notre analyse de provenance sur les sections Valmiki ou certaines études thermochronométriques in situ (Huntington et al., 2006). Pour obtenir un taux d'érosion moyen stable dans le bassin, une augmentation locale des taux d'érosion devrait être compensée par une diminution locale des taux d'érosion ailleurs. Mais ce concept nécessite de nouvelles mesures et modélisations pour être exploré.

La question à un million de dollars se pose à présent ainsi : pouvons-nous étendre notre approche et nos conclusions à d'autres chaînes de montagnes dans le monde ? Nous avons bénéficié de l'abondance en sable, provenant du volume considérable de sédiments fournis par la chaîne himalayenne, des bonnes contraintes de datation, de la grande taille du bassin de drainage amortissant les évolutions marginales du réseau de drainage, et des différences significatives dans la signature isotopique des formations couvrant le bassin de drainage. Une telle configuration idéale n'est peut-être pas disponible ailleurs, comme le

montrent les premiers travaux de Bierman et al (2016) au large du Groenland.

Les Andes sont une autre chaîne de montagnes pour laquelle on a interprété une augmentation apparente des taux d'érosion (Herman et al., 2013 ; Herman et Brandon, 2015). Plusieurs études ont porté sur le bassin d'avant-pays des Andes au nord-ouest de l'Argentine et ont mesuré les concentrations en ^{10}Be dans des sédiments quartzeux (Val et al., 2016 ; Amidon et al., 2017 ; Pingel et al., 2019). Deux études montrent une diminution des taux d'érosion qu'elles attribuent à l'augmentation de l'aridité, produite soit par le soulèvement tectonique créant une ombre pluviométrique (Pingel et al., 2019) soit par le changement climatique du Cénozoïque tardif (Amidon et al., 2017). Cependant, ces études n'ont probablement pas la même portée que les nôtres en raison de la taille limitée des bassins versants et des incertitudes quant à un éventuel recyclage.

Une autre étude (Puchol et al., 2017) a porté sur le Tianshan, une chaîne de montagnes pour laquelle une augmentation apparente des taux d'érosion a aussi été interprétée (Zhang et al., 2001 ; Molnar, 2004). Bien que le Tianshan soit situé à 1 700 km et 15°N des sections Valmiki, dans un contexte tectonique distinct, la tendance de leurs taux d'érosion moyens semble étonnamment similaire à notre enregistrement à Valmiki, soit une augmentation des taux d'environ 8 à 3-4 Ma suivie de taux stables. Même si l'augmentation apparente initiale des taux d'érosion exige des mesures et une modélisation plus poussées pour les sections Tianshan et Valmiki, la combinaison de leur étude et de la nôtre constitue un argument de poids en défaveur d'une augmentation des taux d'érosion pendant les glaciations de l'hémisphère Nord, du moins pour les orogènes actifs.

Cet argument est encore renforcé par une étude précédente qui démontre, à l'aide de la luminescence optiquement stimulée (LSO), que les taux d'érosion sont demeurés stables au cours du dernier cycle glaciaire dans les Alpes du Sud de la Nouvelle-Zélande (Herman et al., 2010b) et sont similaires aux taux d'érosion à long terme déduits de la thermochronométrie. Mais nous notons que leurs résultats peuvent ne pas être étendus à l'ensemble du Pléistocène, en raison d'une tendance différente suggérée par les résultats obtenus à l'aide de la thermochronométrie ^{4}He/^{3}He (Shuster et al., 2011).

Nos conclusions peuvent-elles s'étendre aux orogènes éteints ? De récents résultats obtenus sur le cône turbiditique du Var, qui recueille des sédiments provenant des Alpes du sud-ouest, en Europe, suggèrent une réponse négative (Mariotti, 2020). Leurs résultats, qui s'étendent sur le dernier cycle glaciaire, montrent que les taux d'érosion ont augmenté dans le dernier maximum glaciaire. Cependant, il pourrait s'agir d'un cas exceptionnel, et malheureusement, ni notre étude ni celle de Puchol et al (2017) n'ont cette résolution pour confirmer une situation aussi exceptionnelle au dernier maximum glaciaire dans l'Himalaya ou dans le Tianshan. Par conséquent, la réponse des orogènes éteints au changement climatique nécessite une étude plus approfondie sur des échelles de temps de plusieurs millions d'années. Cette réponse peut être différente de celle des orogènes actifs, que nos résultats montrent comme étant dominés par la tectonique.

I. INTRODUCTION

I.1. EARLY WORK

Tectonics and climate operate the processes at the origin of the Earth's surface modelling and controlled the dispersion and evolution of life before the advent of human beings on Earth. The interest in the role of climate emerged in the 19th century, with the early studies about glacial erosion (Agassiz, 1840), chemical and biological weathering (Ebelmen, 1845; Branner, 1896) and the decisive evidence that CO_2 can impact the atmospheric temperatures through the greenhouse effect (Arrhenius, 1896). With the link between climate, weathering and erosion established at the turn of the 20th century (Chamberlin, 1899), geomorphologists (e.g. Davis, 1899; Penck, 1924) developed landscape evolution models mainly focused on the interactions between these factors, with a role of tectonics that remained not fully appraised and limited to the brief and occasional supply of an initial elevated topography (e.g. Dana, 1873; Suess, 1883-1908).

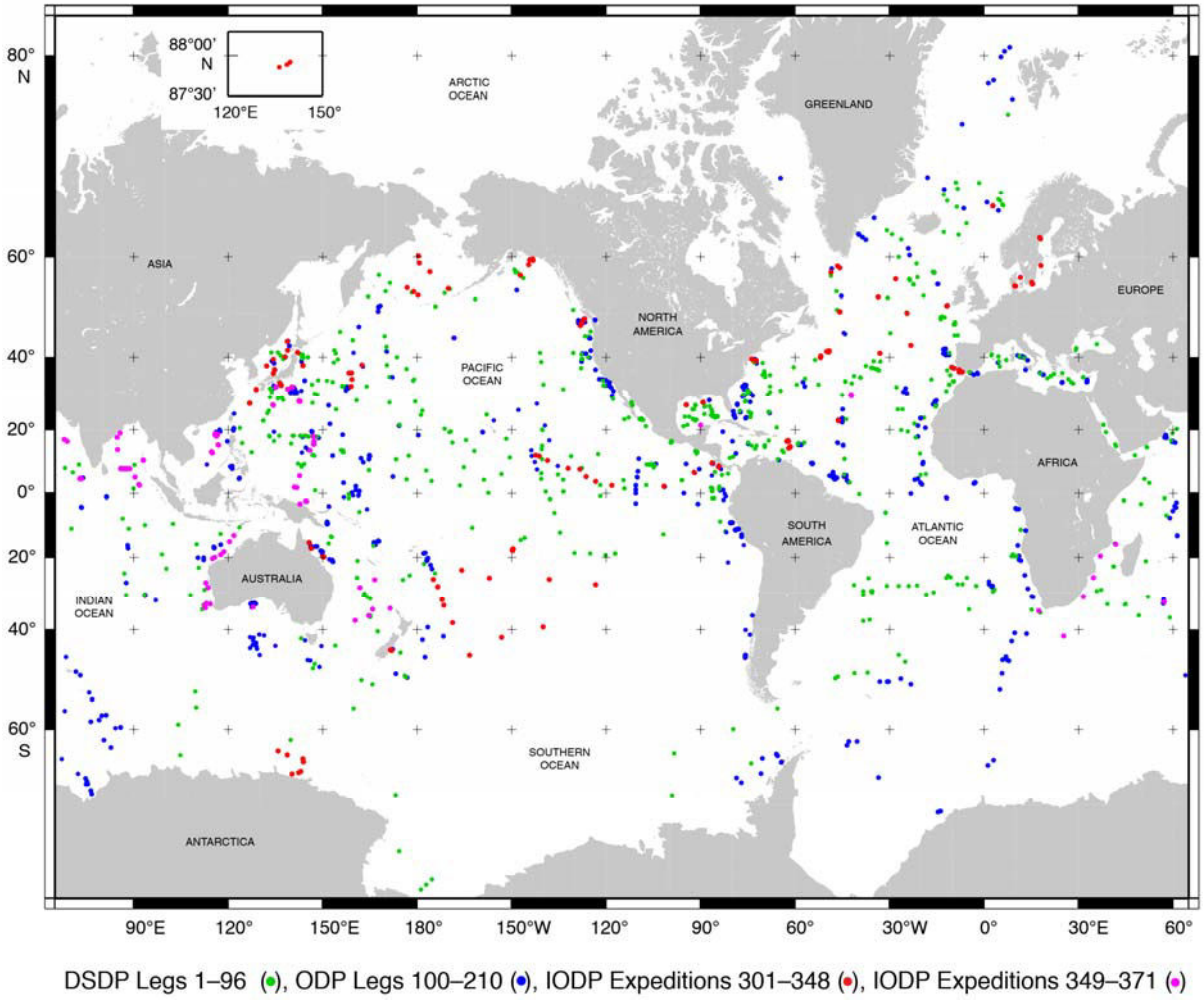

Figure I-1. DSDP, ODP, IODP worldwide drill sites.

Deep Sea Drilling Project (1968-1983), Ocean Drilling Program (1985-2003 and International Ocean Drilling.

I.2. DISCOVERIES FROM THE OCEAN FLOOR EXPLORATION

However, since the 1950s onwards, the thorough exploration of the oceans (Figure I-1) has completely reshaped the field of Earth Sciences. The exploration was performed through international expeditions, the most important being part of the Deep Sea Drilling Program, DSDP, and its successors the Ocean Drilling Project, ODP and the International Ocean Drilling Project, IODP. This work has led to a worldwide collection of geophysical surveys, drilled bedrock and sedimentary cores, geochemical and isotopic analyses. The systematic survey led rapidly to the revolutionary discovery of sea-floor spreading (e.g. Dietz, 1961), considered as a concrete evidence of the precursory hypothesis of plate tectonics by Wegener (1912). The older fixist ideas about mountain building (e.g. Dana, 1873; Suess, 1883-1908) progressively let place to the model of a planet where deep earth processes impact the Earth's surface, with continents drifting over time and tectonics interacting with erosion over long periods.

The analysis of the marine sedimentary record led to additional and fundamental discoveries. The

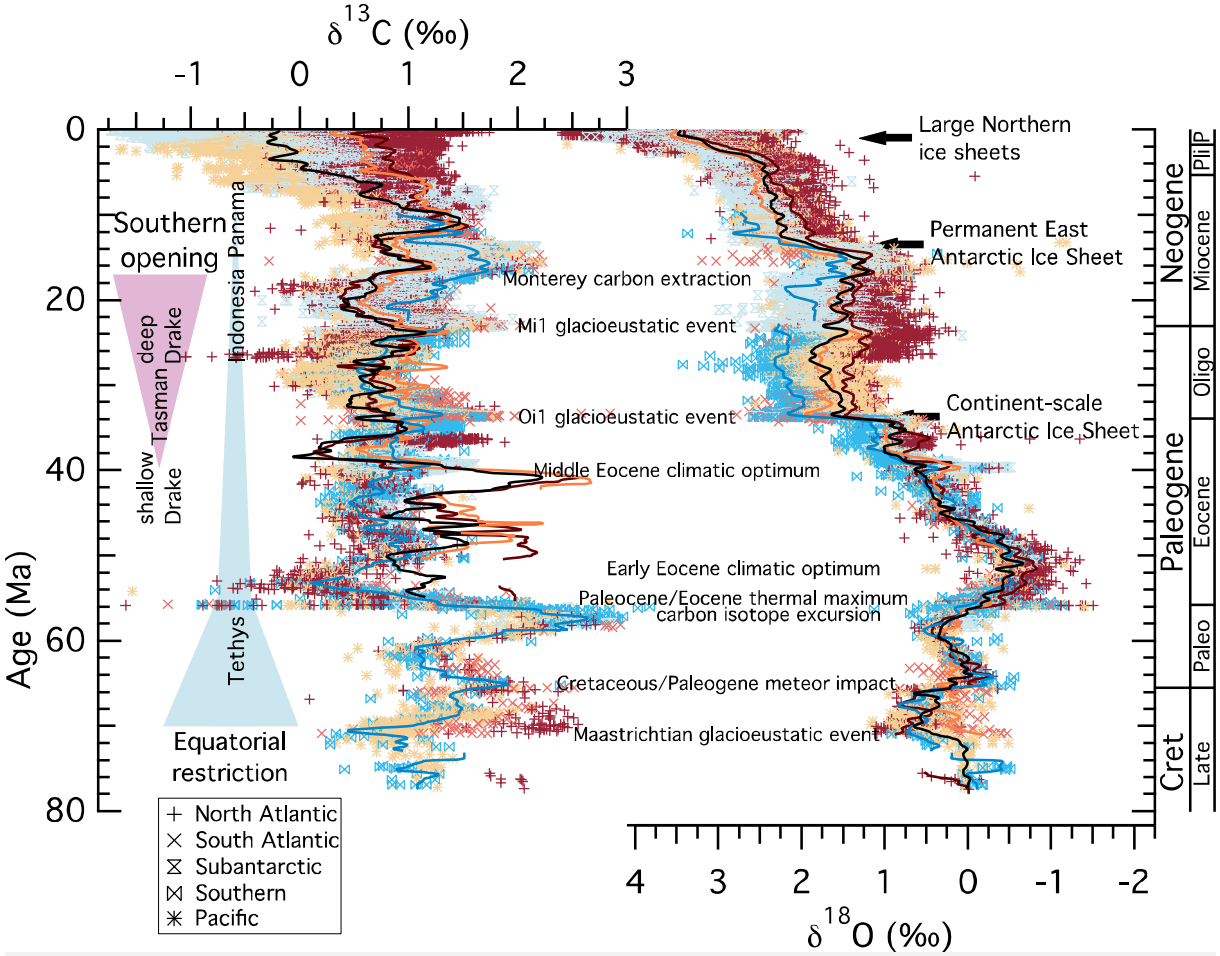

Figure I-2. Benthic foraminiferal isotopes since 80 Ma.

Global compilation of $\delta^{13}C$ and $\delta^{18}O$ extracted from benthic foraminifera, corrected to Cibicidoides-equivalent values (‰ VPDB). The global best fit trend is presented in black and separate fits for each ocean are in colours. The Indian Ocean is not included. (modified from Cramer et al., 2009).

isotopic results (Figure I-2) present unexpectedly large and global variations. The stable isotopes of O highlight that the climate of the Earth has passed through alternating phases of warming and cooling for a long time, and has been subject to a long phase of cooling since 50 Ma ($\delta^{18}O$ applied on benthic foraminifera, early studies of Shackleton et al., 1975; 1984; global compilations by Raymo and Ruddiman, 1992; Zachos et al., 2001; Hansen et al., 2008; Cramer et al., 2009; Mudelsee et al., 2014) with an acceleration in the late Cenozoic, from 8 millions of years (Ma) to modern times, and the formation of large ice-sheets in the Northern Hemisphere. In parallel, the strontium (Sr) radiogenic isotopes have similarly presented a long increasing trend since 40 Ma, which might be interpreted as an acceleration of silicate chemical weathering, or a shift in weathered sources (Koepnick et al., 1985; Richter et al., 1992), or in shift the Sr isotopic composition of the source (modern times: Edmond, 1992; Neogene times: Derry and France-Lanord, 1996). This increase in chemical weathering rates could have been triggered by a global acceleration of erosion, as suggested by compilations of detrital sediment accumulation rates since 35 Ma (Figure I-3), with a 3 to 4-fold increase for the late Cenozoic (Davies et al., 1977; Hay et al., 1988b; Olson et al., 2016).

I.3. THE "TECTONICS, CLIMATE AND DENUDATION" DEBATE

On the basis of these discoveries, Raymo and Ruddiman (1992) and Molnar and England (1990) laid the foundations for the present debate upon the interactions between tectonics, climate and denudation (review e.g. in Champagnac et al., 2014). Raymo et al. (1988), Raymo (1991) and Raymo and Ruddiman (1992a, 1992b) advanced that uplift of mountain ranges could have triggered climate cooling through the consumption of CO_2 by silicate chemical weathering, supposedly favoured by enhanced erosion due to relief increase. Their hypothesis was given even more weight with the findings that mountain uplift also favoured carbon burial (Derry and France-Lanord, 1996; France-Lanord and Derry, 1997; Galy et al., 2007), because of erosion and rapid burial in anoxic conditions.

In contrast, Molnar and England (1990) revive the hypothesis of Donnelly (1982) and dispute the premise of Raymo and Ruddiman (1992) by proposing that climate cooling was the primary driver of accelerated erosion. They advance as a cause that glacial processes should be more efficient to erode rocks than fluvial processes. Accelerated erosion would have led in turn to the uplift of mountain peaks and increase in relief. The two positions led to an explosion of studies about the potential links between climate, tectonics and erosion. The debate culminated for the late Cenozoic, with the revealed contradiction between evidences of the drop of greenhouse gases (Lüthi et al., 2008; Beerling and Royer, 2011; Foster et al., 2017), evidences for climate cooling and ice-sheet development (Zachos et al., 2001; Lisiecki and Raymo, 2005; Hansen et al., 2008), evidences of a global and substantial acceleration of erosion (Zhang et al., 2001; Herman et al., 2013), all of them apparently opposing to evidences of stable silicate chemical weathering rates (Willenbring and von Blanckenburg, 2010; Misra and Froelich, 2012).

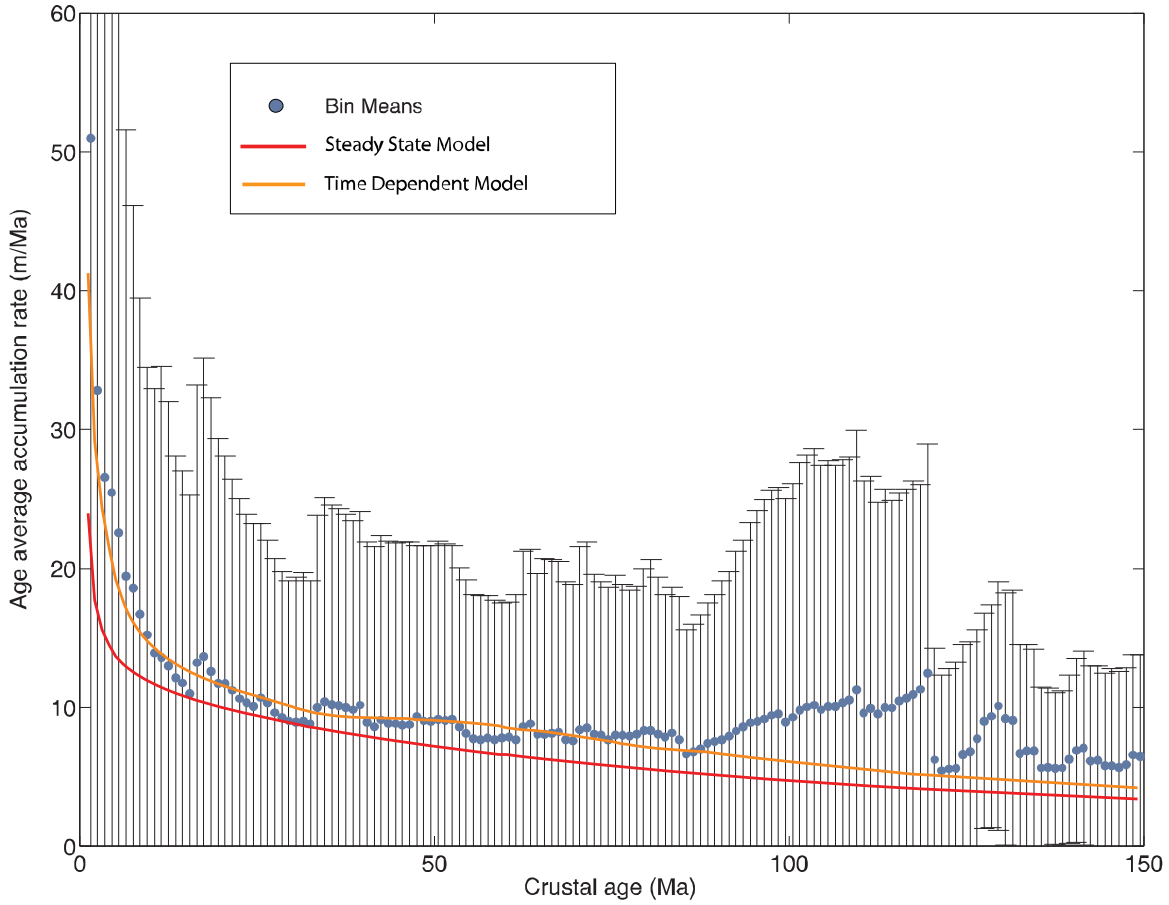

Figure I-3. Deep sea average sediment accumulation rate since 150 Ma.

Accumulation rates are presented in function of the age of the underlying oceanic crust, with 1 Myr age-bin means and standard deviations. The data are compared with two models: a steady-state accumulation model considers an accumulation rate depending on ocean crust age and uniform in time; a time-dependent model considers an accumulation rate depending on time and uniform in space (from Olson et al., 2016; including data compiled by Hay et al., 1988).

I.4. THIS THESIS

To further investigate the debate about tectonics, climate and denudation, this thesis aims to obtain an independent temporal record of short-term erosion rates at the orogen-scale and at low-latitudes over the late Cenozoic time span. The Himalaya, at the convergence of the Indian and Eurasian plates, has epitomized this debate and will be the object of the present thesis, through geochemical and isotopic measurements applied on deep sea sedimentary sites drilled in the Bengal Bay (France-Lanord et al., 2016a; Clemens et al., 2016) and on a new continental sedimentary section in the Valmiki Wildlife Sanctuary, National Park & Tiger Reserve, Bihar, India.

II. CONTEXT

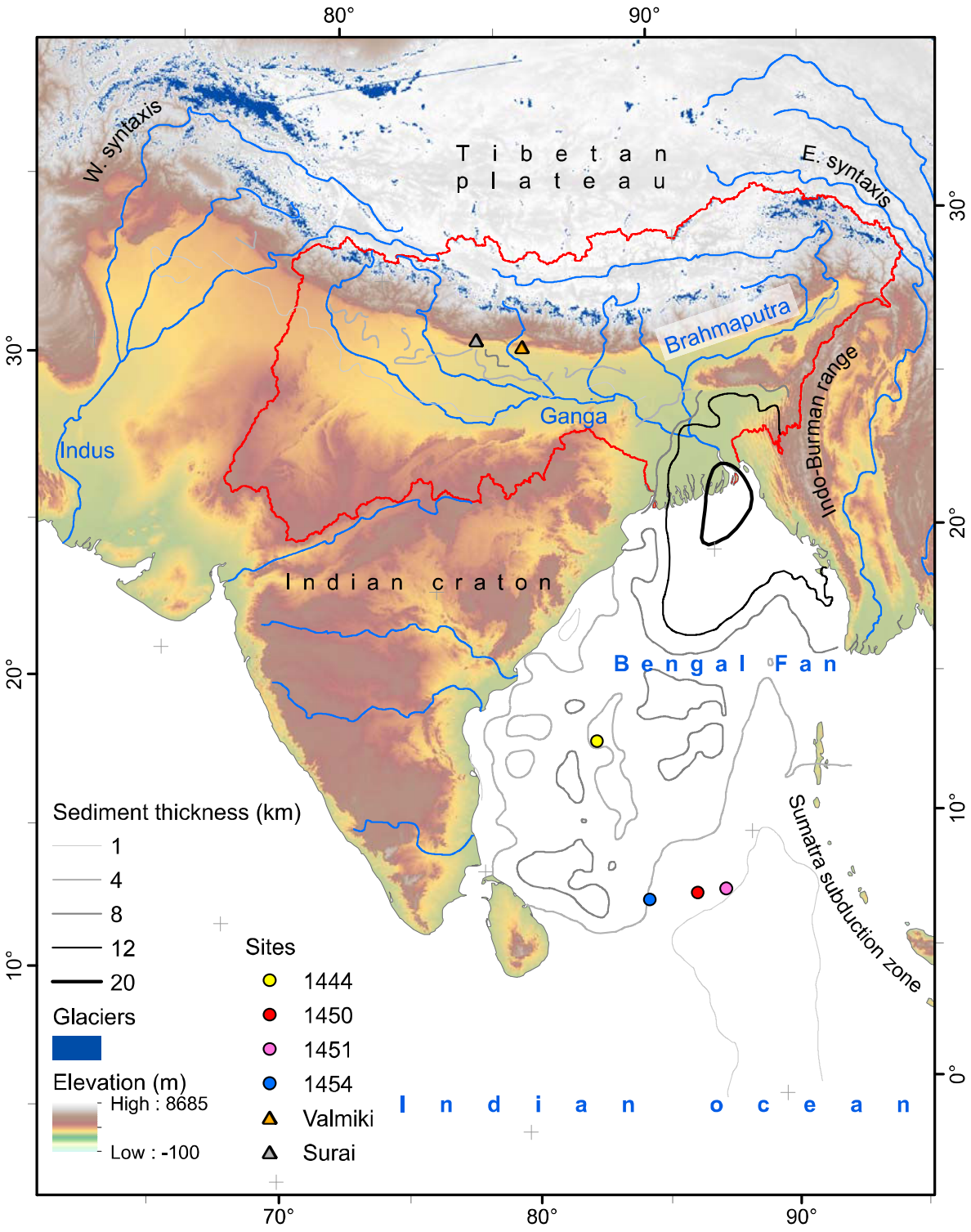
80°
90°
30°
20°
10°
0°
70°
W. syntaxis
Tibetan plateau
E. syntaxis
Brahmaputra
Ganga
Indus
Indo-Burman range
Indian craton
Bengal Fan
Sumatra subduction zone
Indian ocean
Sediment thickness (km)
1
4
8
12
20
Glaciers
Elevation (m)
High : 8685
Low : -100
Sites
1444
1450
1451
1454
Valmiki
Surai

Figure II-4. Geography of the Himalayan region.

Previous page.

The limits of the Ganga-Brahmaputra catchment are indicated in red. The Exp. 354 sites analyzed in this thesis and the new Siwalik section (Valmiki) along with a published Siwalik section (Surai) are indicated. Sediment thickness (compilation of Dasgupta et al., 2000 and Radhakrishna et al., 2010, including data of Curray et al., 1991) have poor resolution along the eastern coast of India and in the Nicobar Fan. Modern glaciers compiled in Armstrong et al., 2005; Raup et al., 2007. Asian South Lambert Conformal conic projection.

II.1. THE HIMALAYA

II.1.1. Physiographic and geological units

The Himalaya (Figure II-4-Figure II-5) is a fold-and-thrust belt that has developed since the collision at the early Cenozoic between the Indian and Eurasian plates (Patriat and Achache, 1984; Meng et al., 2012; DeCelles et al., 2014; Hu et al., 2015, 2016). The Himalaya forms an NW-SE trending 2,400 km-long and 300-400 km-wide arc, with two corners termed western and eastern syntaxes, and is classically divided in subparallel elongated physiographic and geologic units potentially homogeneous along strike (Gansser, 1964; Le Fort, 1986; syntheses of Hodges, 2000; Goscombe et al., 2006; DeCelles et al., 2016; review in Valdiya, 2015; Garzanti, 2019).

At the south of the Himalaya (Figure II-5) lies the foreland sedimentary basin, consisting in the Ganga and Brahmaputra floodplains (avg. < 120 m.a.s.l.). The floodplains extend to the Bengal delta (avg. < 20 m.a.s.l.), with the sedimentary system continuing in the Indian Ocean, through the submarine delta on the Bengal shelf to the turbiditic Bengal Fan (e.g. Curray et al., 2003). The Neogene cover of the foreland basin has been exhumed and folded at the front of the Himalaya, in the Siwalik hills (avg.

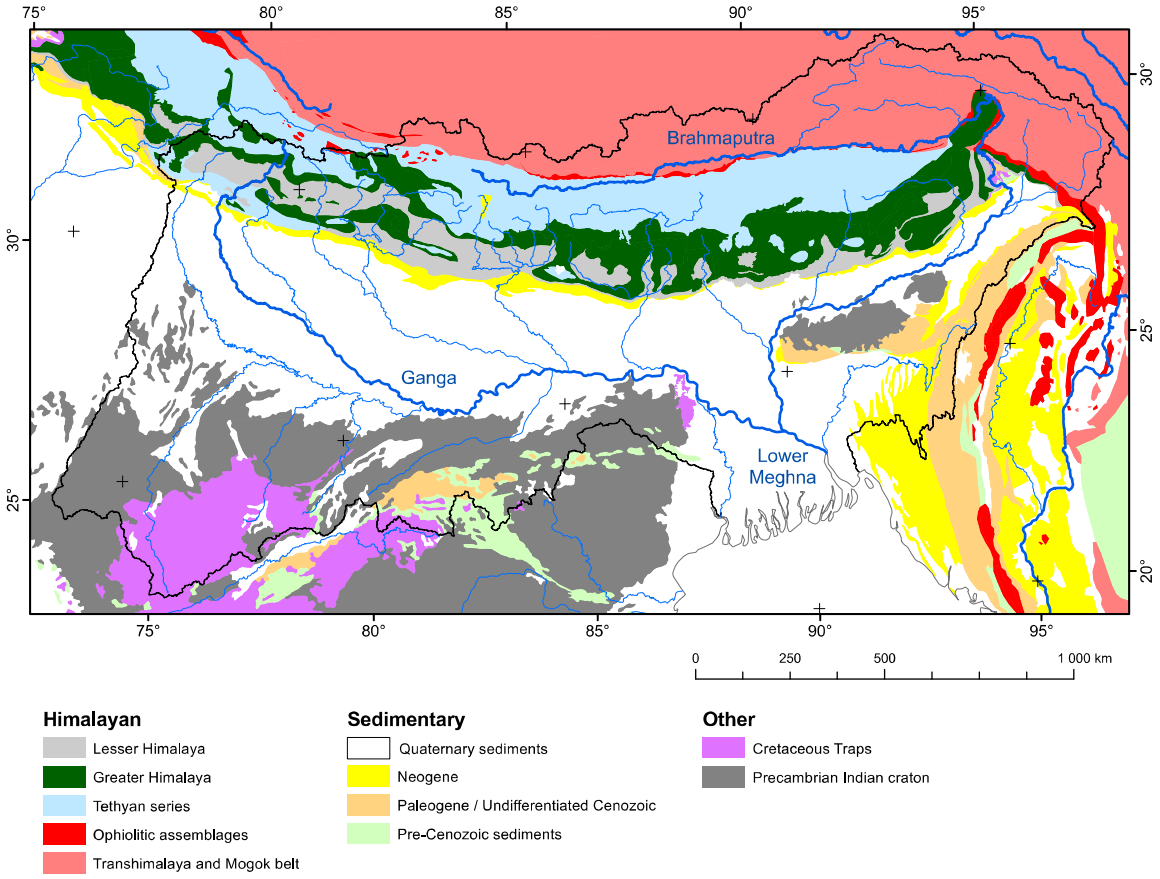

Figure II-5. Geological map of the central and eastern Himalayan region.

Asian South Lambert Conformal conic projection (map drawn from compilations Tables SII-1 and SII-2). Published complementary structural sections are provided in Figure II-9.

~500 m.a.s.l.), bound to the south by the Main Frontal Thrust (e.g. Mugnier et al., 1999; Lavé and Avouac, 2000). The Cenozoic cover of the southeastern flank of the basin has also been exhumed in the Indo-Burman fold-belt (avg. ~1,300 m.a.s.l., with high relief; e.g. Maurin and Rangin, 2009), along with Mesozoic marine sediments and ophiolitic assemblages (Mitchell, 1993; Allen et al., 2008), in the continuity of the Sunda subduction Trench. Remnants of the Cretaceous traps and Indian Precambrian craton (< 1,000 m.a.s.l.) rise at the southern limits of the Ganga floodplain and along the Brahmaputra (the Shillong or Meghalaya plateau, avg. ~1,300 m.a.s.l., and the Mikir hills).

Separated from the Siwaliks by the Main Boundary Thrust (Gansser, 1964; Meigs et al., 1995; DeCelles et al., 1998), rises the Lesser Himalaya (avg. ~2,000 m). The Lesser Himalaya consist of low- to medium-grade metasediments, mainly of Precambrian age and with an inverted metamorphic gradient, with occasional crystalline or sedimentary nappes of lithologically similar to the High Himalaya and the Tethyan unit respectively (e.g. Célérier et al., 2009; Yu et al., 2015).

Separated from the Lesser Himalaya by the Main Central Thrust (e.g., Gansser, 1964; Le Fort, 1975) rises from 3,000 m to more than 8,000 m.a.s.l. the High Himalaya, also coined Greater Himalaya, with avg. elevation > 6,000 m.a.s.l. and relief occasionally > 5,000 m. The High Himalaya consists in medium to

high-grade metasedimentary and meta-igneous rocks, with an inverted metamorphic gradient, intruded by synorogenic leucogranites (Le Fort et al., 1987).

Separated from the High Himalaya by the South Tibetan Detachment (Burg et al., 1984; Burchfiel et al., 1992; Searle et al., 1997) the Tethyan formations partly cover the north of the high range, with a relief similar to the High Himalaya, and the south of the Tibetan plateau, with avg. elevation northwards progressively decreasing to ~4,500 m. The Tethyan unit consists in the Precambrian to Eocene low-grade metasedimentary succession deposited at the north of the Indian margin, and occasionally contains granitoid intrusions or older crystalline rocks.

Separated from the Tethyan realm by the ophiolitic suture, an assemblage of sediments and ophiolitic complexes, the Transhimalayan formations extend northwards on the Tibetan plateau, and are derived from the magmatic arcs linked to the Cretaceous to Paleocene subduction of the Neotethys.

II.1.2. Precipitations and hydrography

Asia is subject to two seasonal monsoons, the South Asian monsoon and the East Asian monsoon (review in Wang, 2006; Molnar et al., 2010), which produce a contrast between dry winter and wet late spring/summer seasons. The South Asian monsoon, which includes the regional Indian monsoon, results from the cross equatorial heat transfer between the Southern Hemisphere, dominated in the region by the Indian Ocean and the Northern Hemisphere partly covered by the Asian continent. This heat transfer is partly controlled by the orographic effect of the Himalayan range (modelling of Boos and Kuang, 2010, 2013; discussion in Molnar et al., 2010).

At the time of the debate between Raymo and Molnar, Asian monsoons were supposed to have appeared or strengthened in the late Cenozoic (Quade et al., 1989) but they revealed to be as old as ca. 24 Ma (Clift et al., 2008, 2014; Clift and Webb, 2018), potentially dating back to ca. 34 Ma (Licht et al., 2014; Gupta et al., 2015) or earlier (Caves et al., 2015; Caves Rugenstein and Chamberlain, 2018).

The Himalaya receives heavy precipitations (Figure II-6), mainly (~80%) during the monsoon (Bookhagen et al., 2006a, 2006b; Bookhagen and Burbank, 2010; Anderman et al., 2011). In Nepal, precipitations according to rain gauge stations vary from 150 mm/yr to 4,700 mm/yr, with the majority of

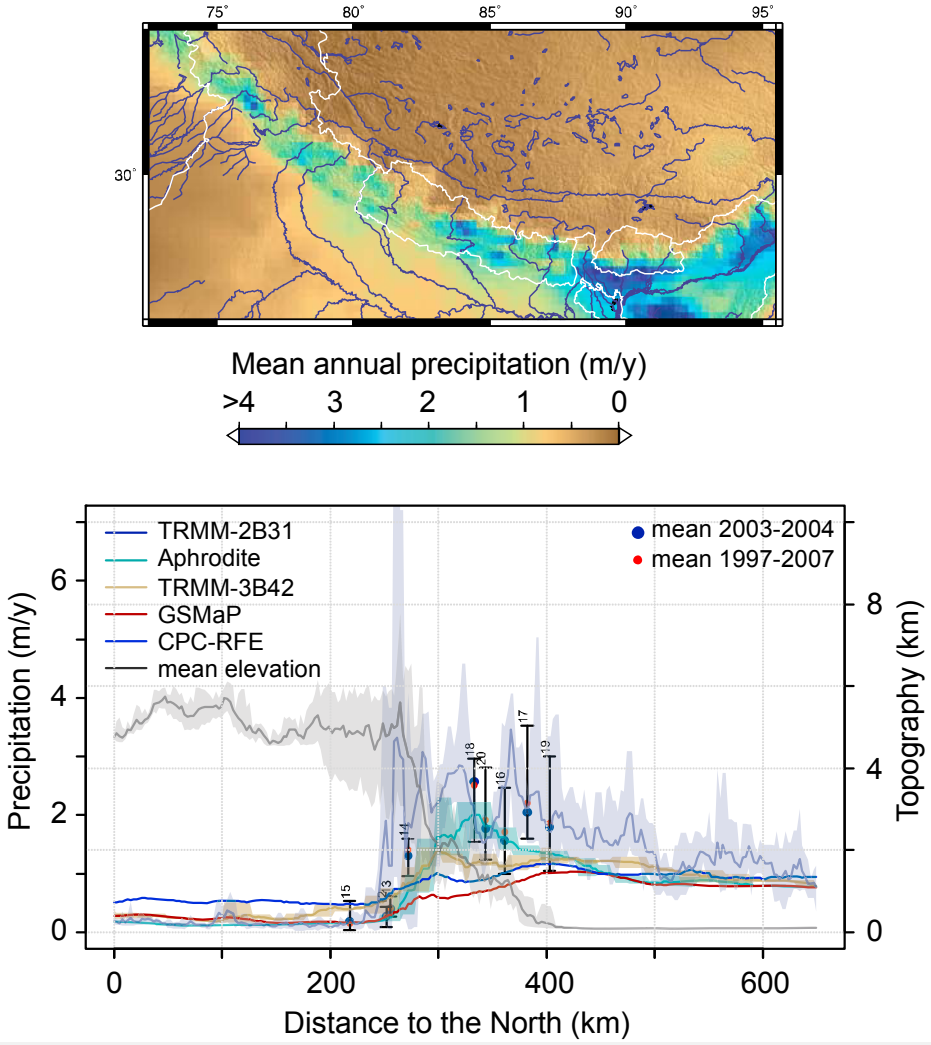

Figure II-6. Precipitations in the Himalaya.

The map is interpolated from gauge station annual data of the Aphrodite Network. The swath profile presents for central Nepal the annual precipitations interpolated from different datasets, along with topography. Minimum-maximum are represented by shaded curves. Gauged data are plotted with an error-bar corresponding to the 30 yrs maxima and minima (modified from Andermann et al., 2011).

reported stations being in valleys and receiving 1,000-2,000 mm/yr (Anderman et al., 2011). A strong contrast exists between the wet southern flank and the drier areas in the rain shadow of the higher summits, such as the Mustang area, and the Tibetan plateau (~450 mm/yr in Lhasa). Similar observations can be made for the eastern Himalaya which is probably subject to precipitations more intense than the Central Himalaya (Bookhagen et al., 2006a, 2006b).

The Himalayan hydrographic network (Figure II-4) organizes around three main rivers, from west to east, the Indus, the Ganga, and the Brahmaputra, the two latter joining into the Lower Meghna in the Bengal delta plain. Several significant transversal Himalayan tributaries join the network, among them the Karnali-Ghaghara, the Narayani-Gandak and the Arun-Kosi, as well as cratonic tributaries, the Chambal and the Son. The majority of the river discharge occurs during the monsoonal season. Marked differences

exist between the Ganga and the Brahmaputra. The rivers present distinct morphologies (meandering Ganga vs braided Brahmaputra), which characterizes a different capacity to transport sediments, indicated by the Brahmaputra discharge double of the Ganga one (GRDC, 1996, quotation of Lupker, 2011) and a floodplain 5 times smaller than the Ganga one. Suspended sediment flux present variability, but are potentially of comparable order, ~ 500 - 600 Mt/yr (1966 to 1970 measurements, RSP, 1996, quotation of Lupker, 2011).

II.1.3. Glaciations

The Himalayan glaciers (Figure II-4) presently cover ~2% of the Lower Meghna drainage basin and ~5% of the Himalayan part of the catchment (including the eastern syntaxis, Figure II-4). The Himalayan glaciers might have increased their extent to ~20% of the mountain range during the Last Glacial Maximum (Shi, 2002). The hypothesis of an extensive ice-sheet during the last 500 ka was proposed by Kuhle (e.g. Kuhle, 1995; Kuhle, 2011) but contradicted by geochronologic constraints (e.g. Lehmkuhl et al., 1998; review in Owen and Dortch, 2014). According to Owen and Dortch, 2014's review, in the central and eastern range, including the SE Tibetan plateau, maritime glaciers are dominantly fed by monsoons and have a warm-based sole, whereas in the western range, continental glaciers are fed by monsoons and rainfalls caused by westerlies and have a mix-based sole. Accumulation is favoured by frequent snow avalanches during the summer and a protecting debris cover originated from tectonics, which varies according to locations.

In their review, Owen and Dortch, 2014 exposed that the Himalaya were subject to alternate phases of increases and decreases of ice extent during the Quaternary, although there is no direct evidence before 300-400 ka. Evidences consist in the identification and dating of moraines, using ^{14}C, OSL and cosmogenic nuclides. Moraine identification is not straightforward, because of a possible confusion with landslides or rock avalanches (Hewitt, 1999). Additionally, in the central and eastern Himalaya, intense rainfall combined with tectonics rapidly erases the older moraines.

There is some debate whether glacial advances were synchronous or not across the orogen during the last glacial cycle, i.e. since 120 ka, particularly between the drier western part and the wetter central and eastern part (e.g. Owen and Dortch, 2014).

II.2. TECTONICS VIEWED BY THERMOCHRONOMETRY

The Himalayan tectonic structures were described by the early works of Gansser (1964) and Le Fort (1975).

A definition of tectonics could cover all processes of deformation and transfer of energy that affect the crustal rocks (e.g. Burbank and Anderson, 2011). At the Earth's surface, the most common type of deformation is brittle deformation, when rocks fracture and eventually slip along faults, resulting in

earthquakes, the majority of them being small, and a minority being of large magnitude (e.g. 2008s Wenchuan earthquake, Sichuan, China, moment magnitude M_w 7.9, Parker et al., 2011; 2015s Gorkha earthquake, Nepal, M_w 7.8, Elliott et al., 2016). At greater depths, because of pressure and temperature, rocks deform by sliding in a ductile way, without producing significant fractures.

II.2.1. Tectonic drivers and elevation change

Tectonics find energy from the deep Earth's mechanisms, through the coupling of mantle convection and plate motion. Plate subduction and collision form mountain ranges by elevating topography and increasing relief. In turn, topography and relief are secondary drivers for tectonics, as they redistribute crustal masses over a region and alter the stress field with gravity (e.g. Molnar and Lyon-Caen, 1988; Beaumont et al., 1992; Avouac and Burov, 1996; Willett and Pope, 2004).

At the Earth's surface, erosion and climate can load and unload the crust by large bodies of matter, and act as complementary drivers of deformation. Erosion and sedimentation, by the removal of rocks from elevated area and their accumulation in basins alter the stress field (Willett et al., 1993; Beaumont et al., 2001; Calais et al., 2010) with among others, some regional isostatic effects. Climate also impacts the state of stress by the regular redistribution of water (Bettinelli et al., 2008; Bollinger et al., 2010) and ice masses (Hampel et al., 2007; Doser and Rodriguez, 2011).

Independently of its drivers, tectonics act as the primary control of the Earth's topography. Earthquakes have a direct impact on elevation through uplift or subsidence, e.g. for the 2015s Nepalese Gorkha earthquake (Elliott et al., 2016). In parallel, earthquakes heavily fracture rocks and precondition them to their removal by co- or postseismic landslides (Molnar et al., 2007, Clarke and Burbank, 2011). Landslides may fully compensate the elevation gain of earthquakes, e.g. for the 2008s Wenchuan earthquake (Parker et al., 2011), but this question remains debated (Molnar, 2012; Densmore, 2012; modelling in Marc et al., 2016).

II.2.2. Evolution of tectonics in the Himalaya

The spatial and temporal evolution of tectonics is a major question (Burbank and Anderson, 2011), in particular for the Himalaya (e.g. review in Avouac, 2007). The Indian and Eurasian plates (Figure II-7) have converged until their collision at ca. 50 Ma, according paleomagnetic data (Patriat and Achache, 1984;

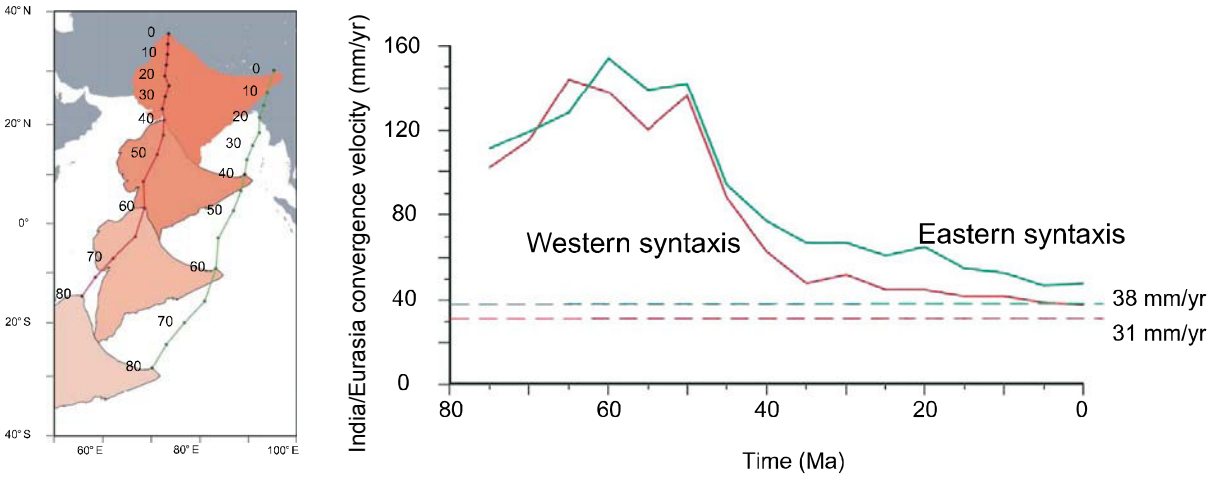

Figure II-7. Indo-Eurasian plate convergence.

The map reconstructs the northward movement of the Indian plate from geomagnetic data (Royer and Patriat, 2002). Convergence rates are computed for points attached at the Indian plate and located at the eastern and western syntaxes (Figure II-4) in modern times (modified from Avouac, 2007).

Meng et al., 2012) or potentially earlier at ca. 59 Ma, as told by sedimentary data (DeCelles et al., 2014; Hu et al., 2015, 2016). From ca. 50 to 35 Ma, the convergence has slowed down (Patriat and Achache, 1984; Meng et al., 2012), potentially because of the building of topography (Tapponier et al., 2001; Copley et al., 2010). Since 35 Ma onwards, the convergence has continued thereafter at steady rates of 4-5 cm/yr (Patriat and Achache, 1984; Meng et al., 2012), with elevations in the Himalaya and in the Tibet probably similar to present ones, as told by paleoaltimetry from stable isotopes (Garzione et al., 2000; Rowley et al., 2001; Spicer et al., 2003; Quade et al., 2011; Gébelin et al., 2013; Hoke et al., 2014), but still discussed in view of the fossil record (e.g. Deng and Ding, 2015).

The convergence between India and Asia is accommodated by crustal shortening and strike slip faulting (shown by geodetic measurements, Molnar and Tapponier, 1975; Larson et al., 1999; Tapponier et al., 2001; Zhang et al., 2004), but the contribution of each mechanism is still debated. Deformation is potentially not uniformly distributed along the orogenic wedge, as shown for instance by the gravity dataset compiled by Hetényi et al., 2016 (Figure II-8), or by thermochronometric data in Nepal (Figure II-9, van der Beek et al., 2016).

On short timescales (< 100 kyr), it is still unclear whether rates of deformation remain constant or if earthquakes happen by clusters interspersed of quiet periods. On longer timescales (> 100 kyr - 1 Myr), deformation and denudation could spatially shift its focus. With a compilation of in situ thermochronometric data, Thiede and Ehlers, 2013, showed that denudation rates differ consistently along the Himalaya and from south to north. They also show that denudation rates could have increased in some areas since 4 Ma, but they let the debate open concerning the causes of this shift (either climatic or tectonic causes).

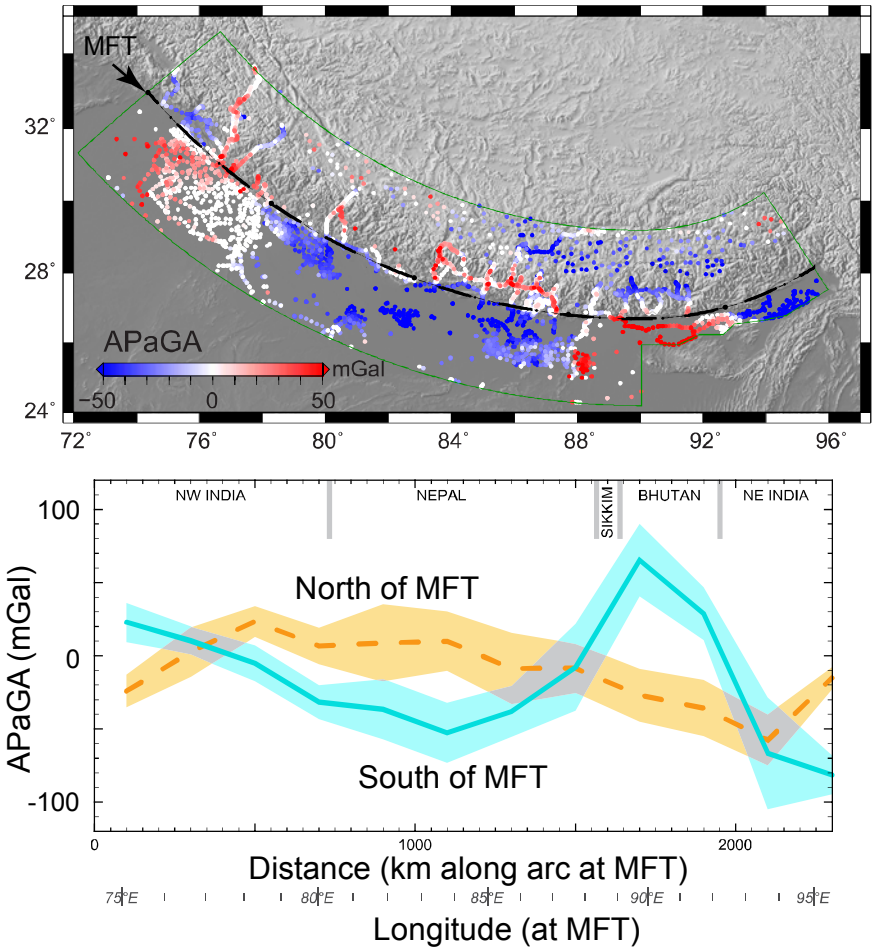

Figure II-8. Arc Parallel gravity anomalies (APaGa) along the Himalaya.

APaGa are obtained by subtracting the average arc perpendicular profile to the gravity dataset. The map presents the spatial results. The chart presents the difference of APaGa between the north and south of the Main Frontal Thrust (MFT). The data are interpreted as showing 4 segments with different plate flexure geometry (modified from Hetényi et al., 2016).

Late Cenozoic shifts in deformation patterns are possibly evidenced in the eastern Himalaya. In situ thermochronometric data show a decrease in the denudation rates in eastern Bhutan since 6 Ma (Grujic

et al., 2006). This decrease was attributed to convergence partitioning (Vernant et al., 2014; Coutand et al., 2016) into the uplift of the Shillong plateau (Najman et al., 2016), although the timing of this uplift can be debated (Biswas et al., 2007; Clark and Bilham, 2008). Conversely, an increase in denudation rates was observed in the eastern syntaxis (Figure II-10), close to the Namche Barwa, since 4 Ma, through the interpretation of in situ (Burg et al., 1997; Seward and Burg, 2008; Yang et al., 2018) and detrital thermochronometric data (Bracciali et al., 2016), in particular from the Bengal Fan (Najman et al., 2019), although the timing remains discussed (Zeitler et al., 2014). In addition, rather than an increase, a simple shift of denudation patterns could have occured, as suggested by the in-situ OSL results of King et al., 2016a, which highlight a potential northward migration of the locus of high erosion rates in the eastern

syntaxis.

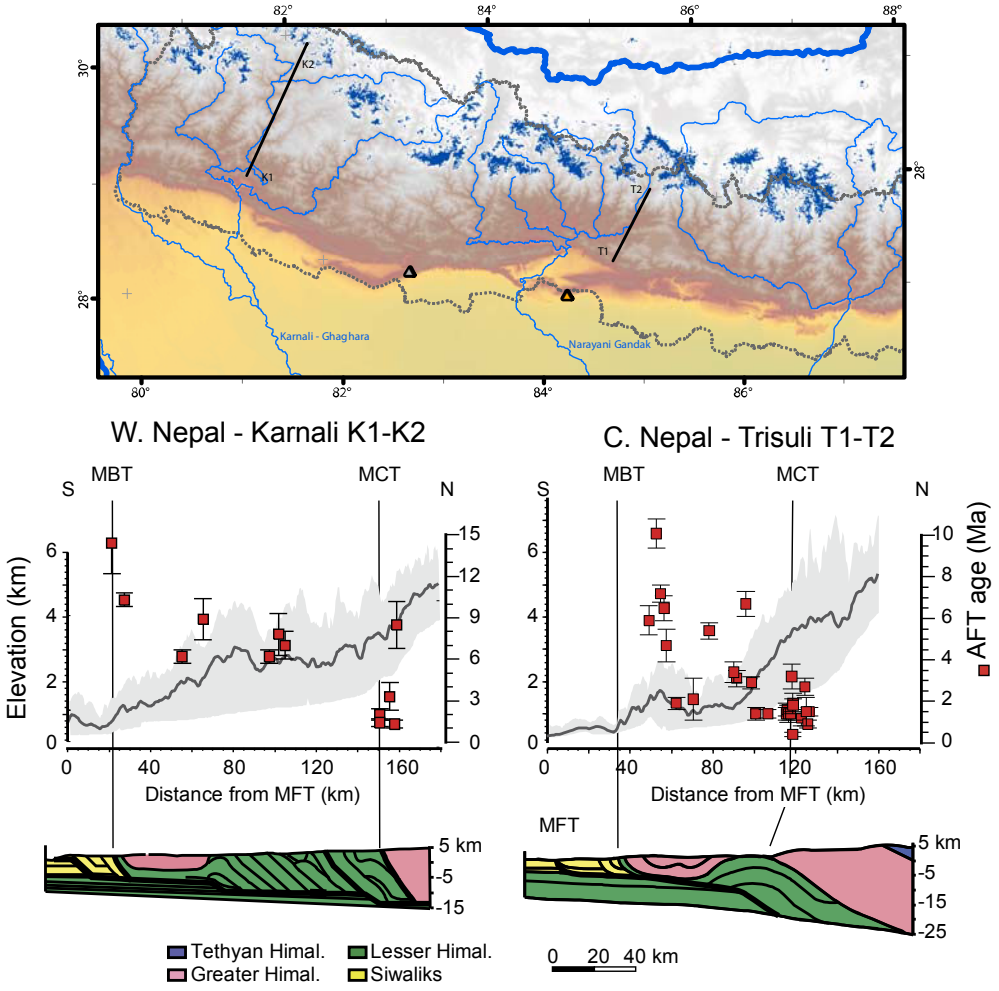

Figure II-9. In situ apatite fission tracks (AFT) different patterns in Central Himalaya.

AFT ages are presented along 2 N-S transects in Nepal.They present a distinct pattern, reflecting the mean elevation (grey curve, with minimum-maximum in the shaded area) and the corresponding structural regional cross-sections (modified from van der Beek et al., 2016;Trisuli transect data from Robert et al., 2009; structural sections from Jouanne et al., 2004).

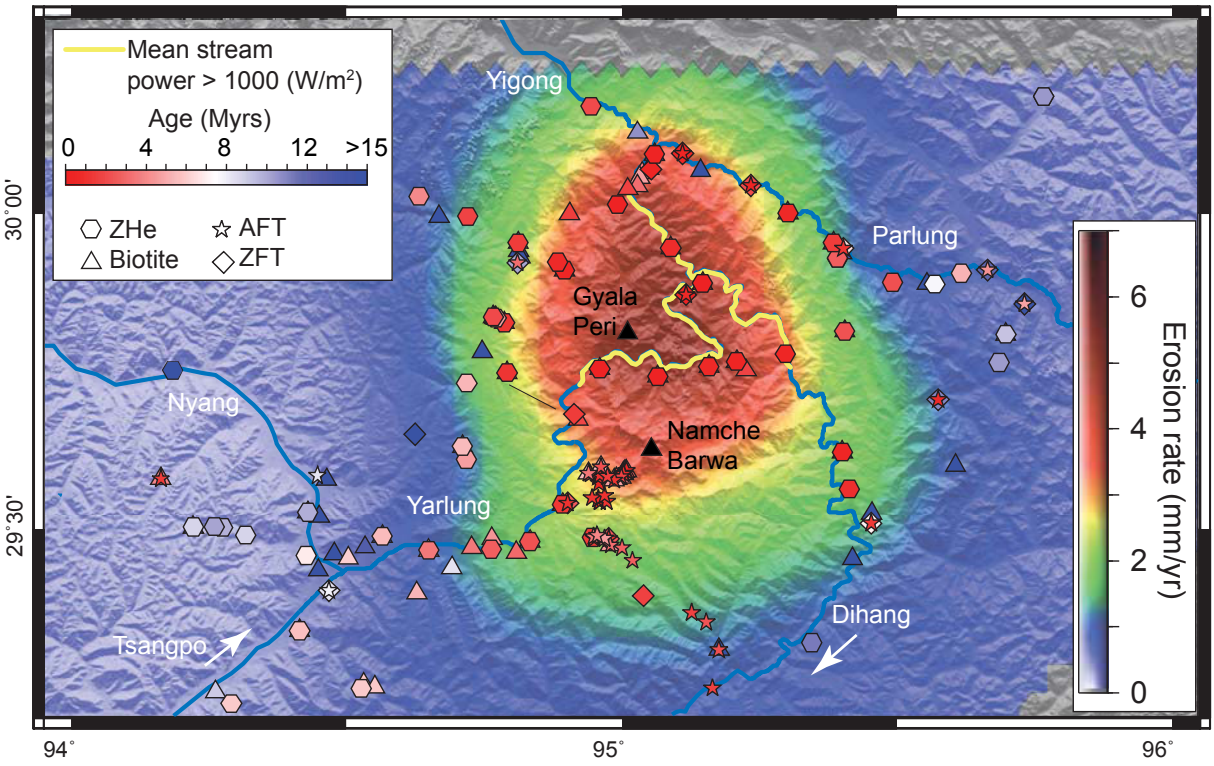

Figure II-10. In situ thermochronometry in the eastern syntaxis.

Compilation of biotite $^{40}Ar/^{39}Ar$, zircon (U-Th)/He (ZHe), zircon fission tracks (ZFT) and apatite fission tracks (AFT). The eastern syntaxis (Figure II-4) is crossed by the Tsangpo - Yarlung - Dihang that continues as the Brahmaputra in the Indian floodplain. The stream profile of the Yarlung drops of 1km in 50 km in the area of high stream power. Average erosion rates were inversed for the 2-0 Ma period using the code of Fox et al., 2014; Herman and Brandon, 2015 (modified from King et al., 2016).

II.3. CLIMATE

Regional or global climate is defined by a set of statistics on weather parameters, as temperature and precipitation. These statistics are computed over a period that makes it possible to smooth rare and extreme events (≥ 10-30 yr). Past climate is reconstructed from various proxies, stable isotopes, e.g. $\delta^{18}O$, or palynology among others, in ice or sedimentary records (e.g. review in Aitken and Stokes, 1997; Hartmann, 2016). These proxies show that the Earth's climate regularly moved between greenhouse and icehouse states (Fisher, 1982).

II.3.1. Greenhouse gases

The incoming solar radiation constitutes the primary source of heat on the Earth's surface (full review of the climatic processes in Hartmann, 2016). Secondary radiations, exchanged between the ground and the greenhouse gases maintain heat in the atmosphere (Arrhenius, 1896). The greenhouse effect is primarily caused by water vapor and clouds (~75%) and CO_2 and CH_4. However, because of naturally condensing in the Earth's conditions, water alone would not be able to maintain temperature, and only non-condensing CO_2 and CH_4 have an effective radiative forcing on the atmosphere temperature (Lacis et al., 2010).

The abundance of atmospheric CO2 is controlled by the long-term C biogeological cycle (Figure II-11, review in Kump et al., 2000 and Berner, 2004). CO2 is degassed in the atmosphere through

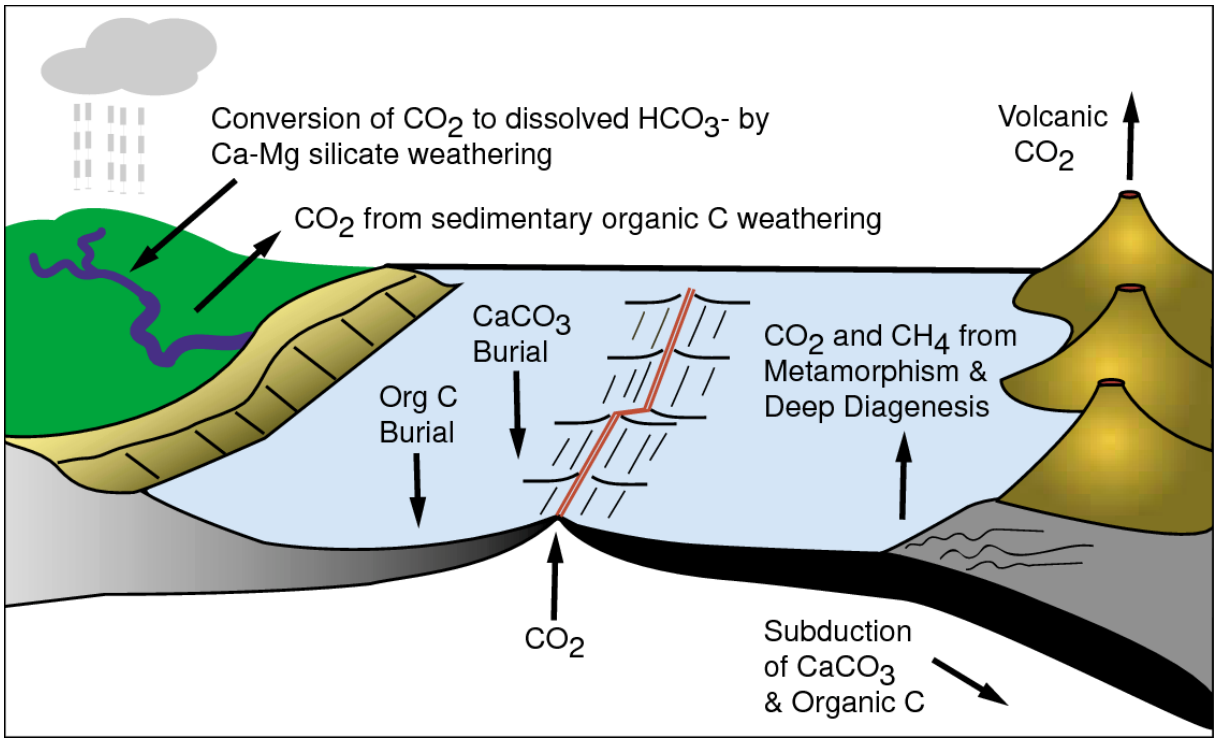

Figure II-11. Long-term carbon cycle.

(from Berner, 1999).

volcanism and metamorphism of carbonates and organic carbon in subduction zones. Conversely, CO2 is stored in the crust through chemical weathering of Ca-bearing silicate minerals (Ebelmen work in the 19th century; Walker et al., 1981; Gaillardet et al., 1999) and carbon burial (Derry and France-Lanord, 1997). CH_4 (review in Beerling et al., 2009) plays a secondary role in the greenhouse effect. CH_4 is mainly produced by the decomposition of organic matter by anaerobic bacteriae in wetlands, with minor contributions of the oceans, wildfires, termites, hydrates and volcanoes, while a minor part of CH_4 is absorbed by soils.

Positive feedbacks can enhance the drop or the rise of greenhouse gases. An expansion of ice cover increases albedo, which reflects solar radiation and subsequently enhances cooling. An expansion of permafrost at the expense of wetlands increase greenhouse gases storage and also enhances cooling. Conversely, negative feedbacks decelerate the greenhouses gases trend. Chemical weathering is favoured by high temperatures, precipitations and runoff, vegetation, and fresh rock supply (Gaillardet et al., 1999 with data from Meybeck and Ragu, 1997; discussion of the relative weight of the factors in Kump et al., 2000). As silicate chemical weathering consumes CO_2, temperatures drop, atmospheric vapour condenses, precipitations drop, vegetation declines, all this leading in turn to a deceleration of silicate weathering. Fresh rock supply is favoured by erosion and volcanism. Erosion depends on precipitations, and then, as precipitations decrease, erosion decelerates, thus limiting fresh rock supply and silicate weathering. Still erosion also depends on the volume and nature of soils, which are favoured by dry periods of low erosion rates, which ultimately make it possible an acceleration of erosion when precipitations come back (e.g. discussion in Zhang et al., 2001; Molnar, 2004). In addition, counter-intuitively, silicate weathering of volcanic rocks, such as basalts, could fully negate the increase in greenhouse gases concentrations caused by volcanism (Dessert et al., 2003). The relative importance of each of these feedbacks is still difficult to quantify, model and compare (e.g. Berner, 2004; examples of models: Geoclim model, Arndt et al., 2011; RokGeM model, Colbourn et al., 2013).

II.3.2. Heat redistribution, geography and tectonics

It appears that tectonics play a fundamental role in the long-term fluctuations of greenhouse gases (see discussion in Li et al., 2009). Tectonics control mid-ocean ridge spreading and plate subduction rates (Van Der Meer et al., 2014). As underlined by Raymo and Ruddiman, 1992, tectonics produce uplift of mountain ranges and can accelerate physical erosion because of heavy fracturing and the increased capacity of erosive agents deriving from elevation increase (e.g. review in Burbank and Anderson, 2011). However, tectonic uplift alone is not sufficient to accelerate physical erosion, and neither is the abundance of fractured rocks sufficient to accelerate chemical weathering.

Redistribution of heat and water across the planet is necessary to focus warmth and precipitations along mountain ranges and subsequently enhance physical and chemical weathering. This redistribution is performed on short timescales through the atmospheric circulation, including gases, water and particles, and "longer" timescales through the oceanic circulation (e.g. Stommel and Arons, 1959) and the water

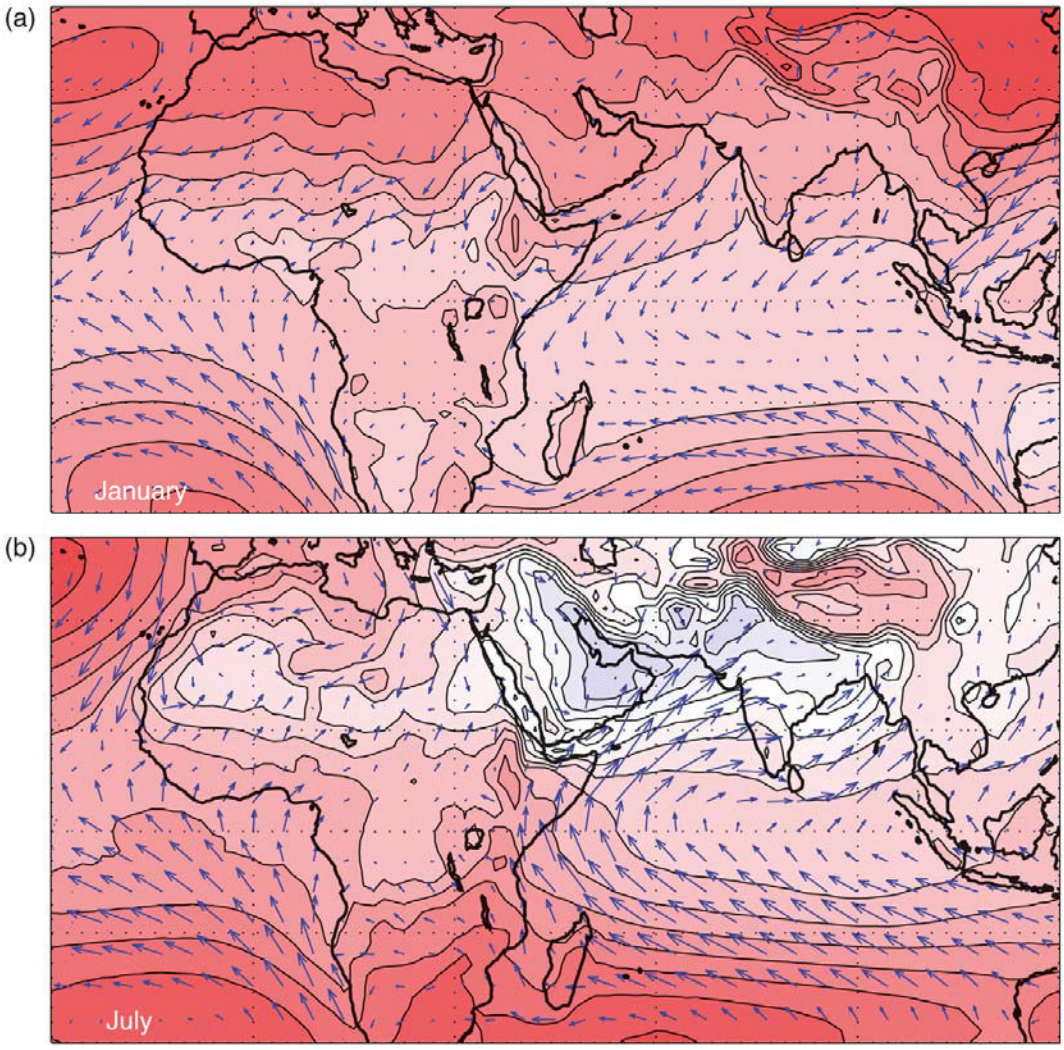

Figure II-12. Seasonal atmospheric configuration for the Afro-Asian monsoon region.

Monsoonal climates are characterized by the alternation of wet and dry seasons. The SE Asian monsoon carry precipitations along the Himalaya from June to September.

For January and July, the maps show 1000 hPa height (20m contour intervals, positive heights in red) and wind vectors (the largest: 15 m/s) for the 30°S-40°N and 30°W-120°E region in Mercator projection (from Hartmann, 2016, data from ERA Interim).

cycle, with the growth and demise of glaciers. This redistribution required the existence of passages and barriers, as well as climatically contrasted zones. This is primarily regulated by tectonics. Mountain ranges, in function of their geography (Goddéris et al., 2014), can act as orogenic barriers and concentrate precipitations in one area at the expense of another (e.g. monsoon in the Himalaya, Figure II-12, vs relative "drought" in the Tibet, Boos and Kuang, 2010, 2013). The opening of passages through continents can facilitate oceanic circulation (e.g. Panama closure, Haug and Tiedemann, 1998; Bartoli et al., 2005; Ramírez et al., 2016). The presence of separated continents, dispersed across the planet, in particular at the poles and near the tropics ensures climatically contrasted areas. This contrast is increased by a positive feedback during glaciations, as permanent cold and dry ice-sheets settle on land present at the

poles.

II.3.3. Orbital cycles

In superimposition to tectonics, the orbital oscillations of the planet, coined Milankovitch cycles, exert a secondary control on global climate, over short-timescales (Figure II-13, e.g. Hays et al., 1976; Clemens and Tiedemann, 1997; review in Zachos et al., 2001). Eccentricity characterizes the elliptical to near circular orbit around the Sun and fluctuates with periods of 100 and 400 kyr. Obliquity characterizes the tilt of planet axis relative to the ecliptic plane and fluctuates with periods of 41 kyr. Precession characterizes the wobble of the rotation axis and fluctuates with periods of 23 and 19 kyr. Obliquity and precession have a major control on seasonal contrasts between hemispheres, while eccentricity is supposed to have only a limited amplification role (Zachos et al., 2001). Sea surface temperature, deep sea temperature and CO_2 concentrations have been shown to evolve coevally according these orbital cycles (Shakun et al., 2015).

II.3.4. Global sea-level

Climate and greenhouse concentrations seem to be the 1st order control of global sea-level (van Sickel et al., 2004; Miller et al., 2005, 2011, Kominz et al., 2008; Cramer et al., 2011, with comments in Müller et al., 2008 and Cogné and Humler, 2008; Foster and Rohling, 2013; Rohling et al., 2014), with

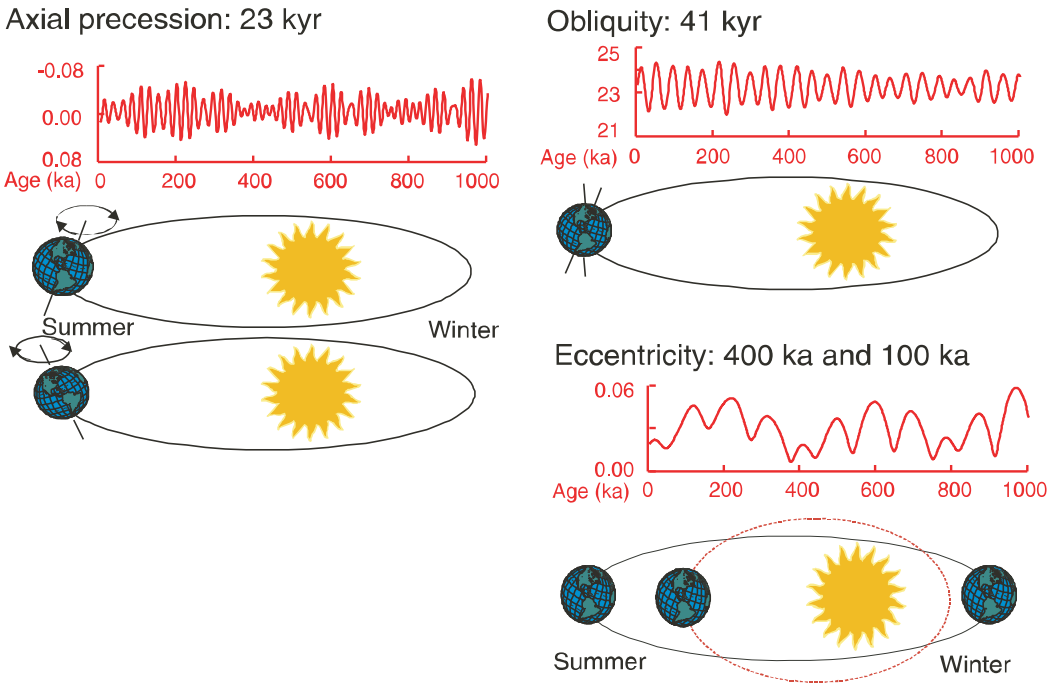

Figure II-13. Orbital cycles.

Three orbital cycles control the position of the Earth relative to the sun and the mid-term climate of its hemispheres (see text; modified from Zachos et al., 2001).

global sea-level decreasing as temperatures and CO_2 concentrations decrease (Foster and Rohling, 2013), suggesting that a strong dependence to the expansion and shrinkage of ice-sheets and glaciers, at least since 100 Ma (van Sickel et al., 2004; Miller et al., 2005, 2011).

II.3.5. Cenozoic climate change

The role of greenhouse gases is particularly highlighted in the context of the global climate cooling since 50 Ma, from evidence of the deep sea (Figure I-2, $\delta^{18}O$ benthic foraminifer data global compilations, early studies of Shackleton et al., 1975 and 1984; Raymo and Ruddiman, 1992; Zachos et al., 2001, 2008; Hansen et al., 2008; Mudelsee et al., 2014) and the sea surface (alkenone unsaturation data global compilation since 12 Ma, Herbert et al., 2016), and even potentially starting earlier (Cramer et al., 2009; Veizer and Prokoph, 2015, both latter studies with Cramer et al., 2011 and Passchier, 2018 include discussions about the limits of the proxy and these compilations). Temperatures dropped coevally with atmospheric concentrations in CO_2 (Figure II-14, Royer et al., 2004; Lüthi et al., 2008; Beerling and Royer,

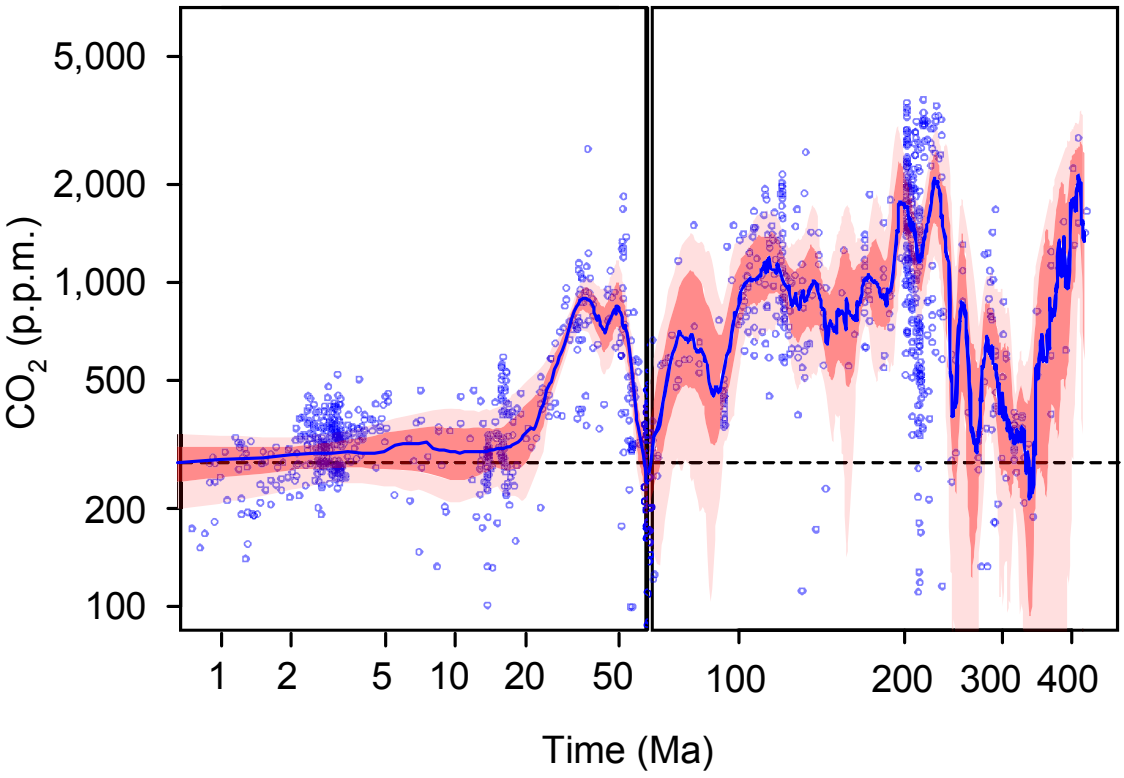

Figure II-14. Atmospheric CO_2 reconstruction for the Phanerozoic.

Blue dots show a compilation of atmospheric CO_2 sedimentary multi-proxy data along a log-time scale: leaf stomata, pedogenic carbonates $\delta^{13}C$, foraminifer $\delta^{11}B$, liverwort $\delta^{13}C$ and $\delta^{13}C$ of alkenones. The most likely LOESS fit (locally estimated scatterplot smoothing, a regression model, e.g. Chandler and Scott, 2011) is shown by the blue curve, with the 68 and 95% confidence intervals in dark and light red shaded bands. (modified from Foster et al., 2017, compilations of Foster et al., 2017).

2011; modelling by Stap et al., 2016; Foster et al., 2017; phanerozoic record from marine phytane C

isotopes, Witkowski et al., 2018), although some proxies for CO_2 require calibration improvement (e.g. the compilation of Foster et al., 2017 can show distinct trends or values depending on the proxy). CO_2 drop potentially leads to a complete compensation of the Phanerozoic increase in solar radiation (hypothesis of Walker et al., 1981; compilation and interpretation of Foster et al., 2017).

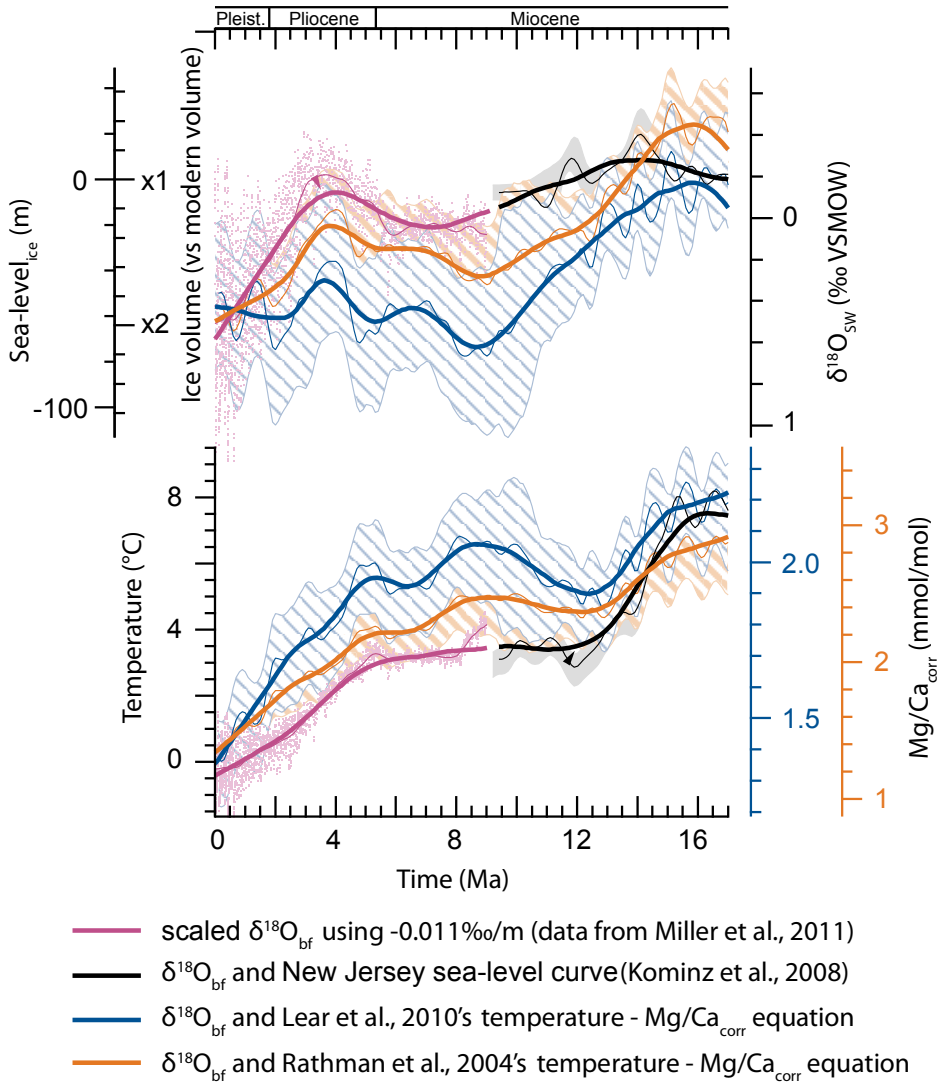

Figure II-15. Deep ocean temperature, sea-level and ice volume reconstruction since 16 Ma.

The panels present reconstructions for sea-level and equivalent ice volume, and deep sea temperature. These reconstructions are based on models combining the benthic foraminifer $\delta^{18}O_{bf}$ record with other proxies, such as the New Jersey sea-level curve or benthic foraminifer Mg/Ca data. This approach is of interest because δ^{18}Obf records both fluctuations of sea-level and fluctuations of ice-volumes, but is still debated (modified from Cramer et al., 2011, their Fig. S7; compilations of Cramer et al., 2009 and Katz et al, 2010, updated in Cramer et al., 2011).

Cenozoic global climate cooling favoured the progressive setup of ice sheets in polar areas (Arctic,

Moran et al., 2006; Antarctic, Carter et al., 2017; Greenland, Eldrett et al., 2007; modelling of De Conto et al., 2008) and also probably the setup of isolated ice-caps in elevated mountain ranges at lower latitudes (De Conto et al., 2008). Cooling also perturbed water redistribution through precipitations across the planet, with drier continents (e.g. Sahara, Schuster et al., 2006a, b; Kroepelin, 2006; Swezey, 2006; Atacama, Arancibia et al., 2006; Taklimakan, Tarim, Sun et al., 2011) but also potentially wetter areas subject to monsoons (South Asia and the Himalaya, review in Clift and Webb, 2018; early studies of Clemens et al., 1991; Prell and Kutzbach, 1992; studies of Clemens et al., 2008; Clift et al., 2008; An et al., 2011; Reuter et al., 2013; Clift et al., 2014, Licht et al., 2014; Caves Rugenstein and Chamberlain, 2018). A drier climate could have favoured grassland over woodland (Figure II-16), but the cause of the Cenozoic development of grassland remain debated (e.g. Retallack, 2001). In parallel, the drop in CO_2 could have favoured vegetation using C_4-photosynthesis, which is more efficient than the C_3-pathway (e.g. Sage, 2004), particularly at low latitudes and low elevation since 3 to 8 Ma (using $\delta^{13}C$, Quade et al., 1989; Cerling et al., 1997; Edwards et al., 2010; compilations of oceanic record by Shackleton, 1987; Zachos et al., 2001).

Global climate cooling culminates in the late Cenozoic (Figure II-15, benthic foraminifera $\delta^{18}O$ data, Shackleton et al., 1984; Lisiecki and Raymo, 2005; Shakun et al., 2015), as sea-surface temperatures potentially drop of 5 to 15°C (Figure II-17, alkenone saturation data, Herbert et al., 2016; multiproxy model of Snyder, 2016), depending on the latitude, and as atmospheric CO_2 concentrations potentially decrease of ~40 % from ~350 ppm at ca. 4 Ma (compilations of proxies in Beerling and Royer, 2011; Foster et al., 2017; Witkowski et al., 2018) to ~220 ppm for the last Ma (ice-core data, Lüthi et al., 2008; Bereiter et al., 2015). Cool conditions, with low atmospheric concentrations have settled since 2 Ma (Figure II-18). Large ice-sheets have grown and shrunk since ca. 3 Ma in areas where they are unstable in interglacial periods, such as in North America and North Europe, and the fluctuations between glacial and interglacial periods finally shift to longer 100 kyr-cycles dominated by glacial periods since ca. 0.8 Ma (e.g. Shakun et al., 2015).

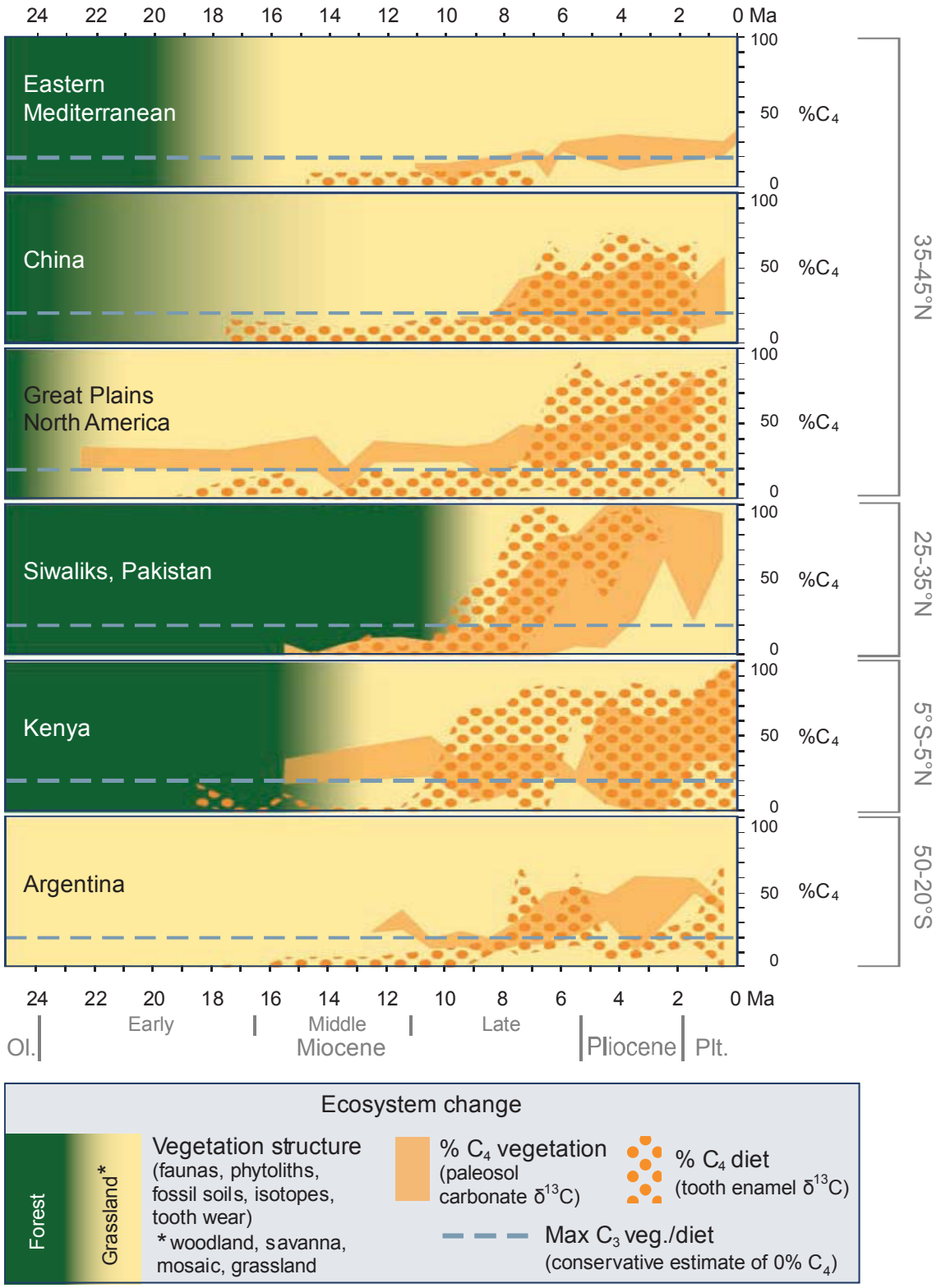

Figure II-16. Forest to grassland and C_3 to C_4 vegetation shift since 24 Ma.

For 6 regions, the evolution of forest to grassland is shown by the green-yellow transition bands. The proxies showing the expansion of C_4 plants is shown by orange shaded areas for paleosol data and dot-shaded areas for tooth enamel data (modified from Edwards et al., 2010, compilation in Edwards et al., 2010).

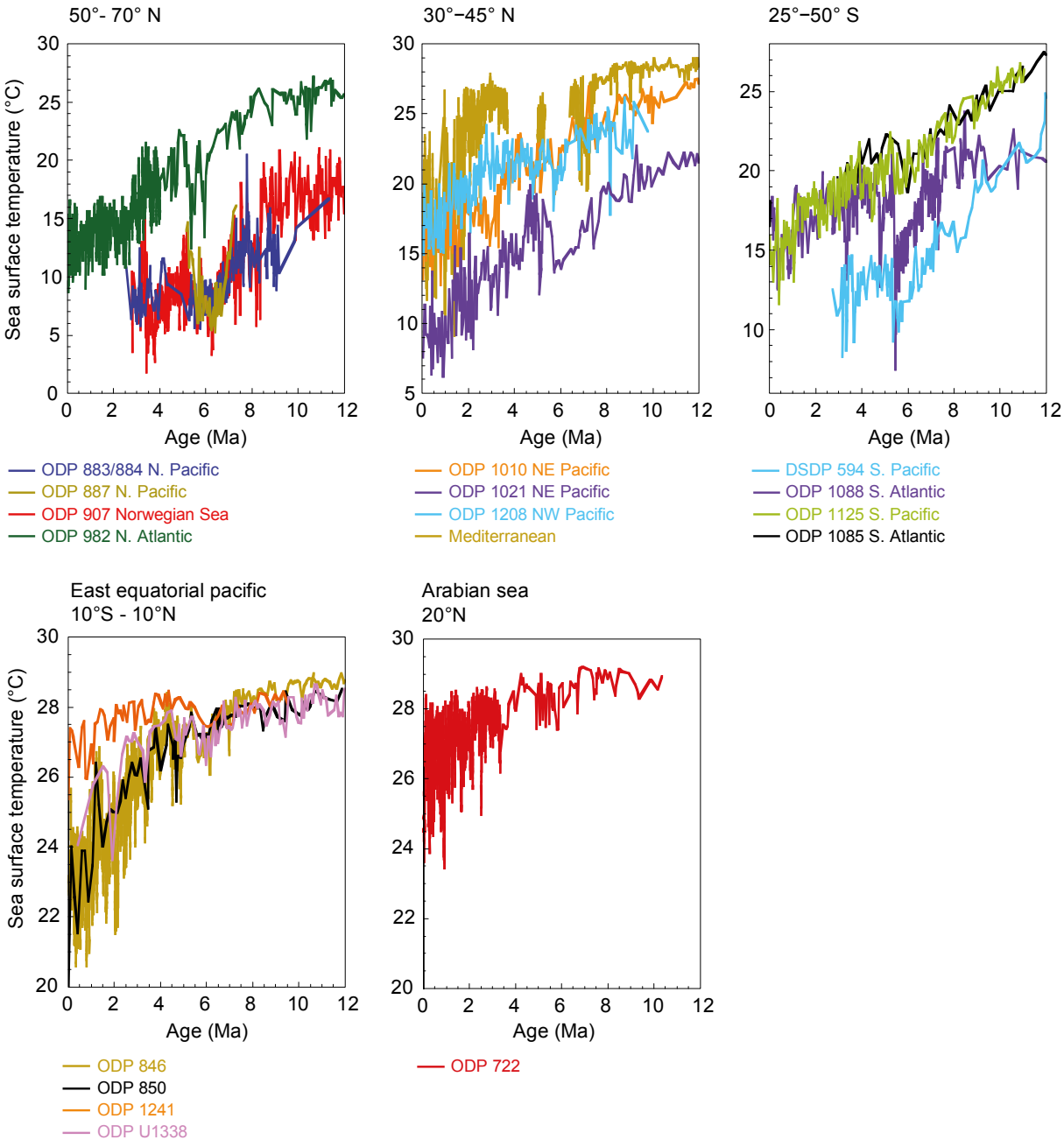

Figure II-17. Sea surface temperature by region since 12 Ma.

Each inset regroups absolute sea surface temperature curves for a set of sedimentary cores, obtained using the alkenone unsaturation method. Note the temperature scale that is different for each inset. Each region is subject to a temperature drop, even though this drop is not synchronous and it has not a uniform amplitude (modified from Herbert, 2016; compilation and new data from Herbert et al., 2016).

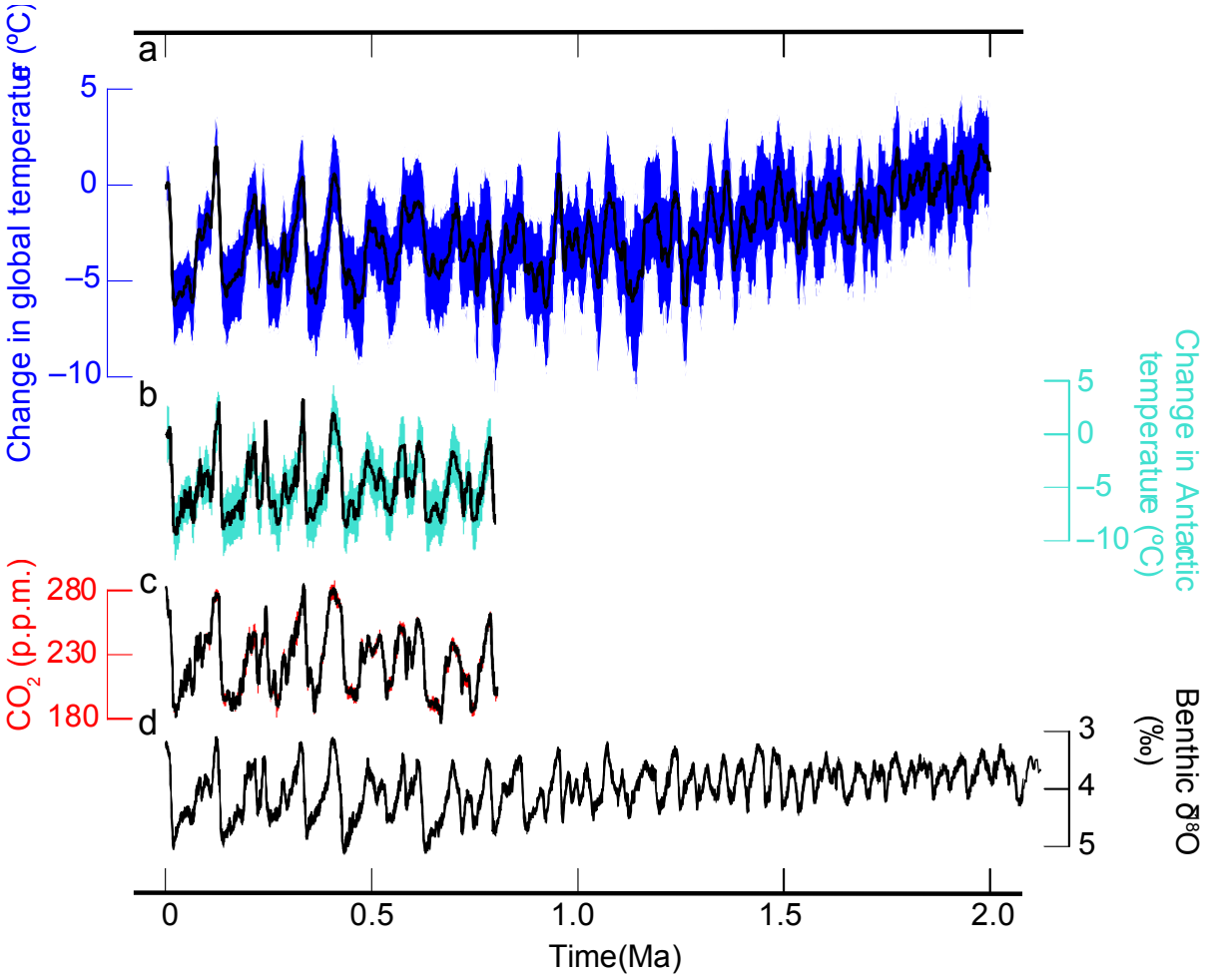

Figure II-18. Atmospheric CO_2, benthic $\delta^{18}O$ and global change in surface temperature since 2 Ma.

a. Global average surface temperature deviation from modern temperature (averaged over 0-5 ka) in blue, modelled from a compilation of sedimentary multi-proxies (Snyder, 2016).

b. Stacked reconstruction of temperature change in Antarctic, in cyan (Parrenin et al., 2013).

c. Stacked reconstruction of atmospheric CO_2 concentrations, in red (Bereiter et al., 2015).

d. Stack of benthic foraminifer $\delta^{18}O$, in grey (Lisiecki and Raymo, 2005). In all panels, the solid black lines show the median estimate and the colour shaded areas show the 95% confidence interval. (modified from Snyder, 2016).

II.4. DENUDATION

The following sub-chapters represent a synthesis of denudation processes explained in Hugget, 2011 and Harvey, 2012.

II.4.1. Mechanical and chemical processes

Denudation (Figure II-19, e.g. review in Hugget, 2011; Harvey, 2012) forms the combination of weathering and transport processes that extract and export rocks and minerals from a source to a sink, i.e. a sedimentary basin. Weathering includes mechanical and chemical processes that led to the breakdown of rocks. Until favourable transport conditions are met, the resulting material can partly remain in place as soil or regolith (Figure II-19).

Mechanical weathering develops fractures in rocks when they expand under variations of pressure, during their approach to the surface through denudation. Mechanical weathering is particularly enhanced in tectonic contexts (see above). It is also favoured in periglacial environments where water is regularly subject to freeze-thaw conditions that enable it to penetrate the fractures and expand them when frozen.

Chemical weathering is produced by the interaction of a mildly acid water with minerals and includes dissolution, hydration, reduction-oxidation, hydrolysis and chelation. This action is favoured by vegetation and in soils rich in organic matter. Rates of chemical weathering differ according minerals and weaker minerals, such as carbonates, biotites and plagioclases, are more easily weathered than stronger minerals, such as quartz. Chemical weathering is favoured in warm and wet conditions, especially in tropical regions.

Both mechanical and chemical weathering is enhanced by erosion and a regular export of the remaining material to bring at the surface unweathered rocks. However, a too frequent removal of material tends to prevent chemical weathering.

II.4.2. Erosion, transport and deposition

II.4.2.1. Slope processes

Slope processes (Figure II-20) export the weathered material downslope. Rockfall and scree processes release rocks by a simple fall and are favoured by high relief. Overland flows move weathered particles by the waterflow produced by intense rainfall on soils that are saturated in water. They are favoured in arid areas and form characteristic badland landscapes. Mass movements, from the slow soil creep and solifluction to the faster debris flow, are produced by the water content of unconsolidated material. As pore pressure increases, the material progressively deforms, reaching an abrupt release in case of debris flow. Mass movements are favoured by intense rainfall and snow or icemelt, in particular in

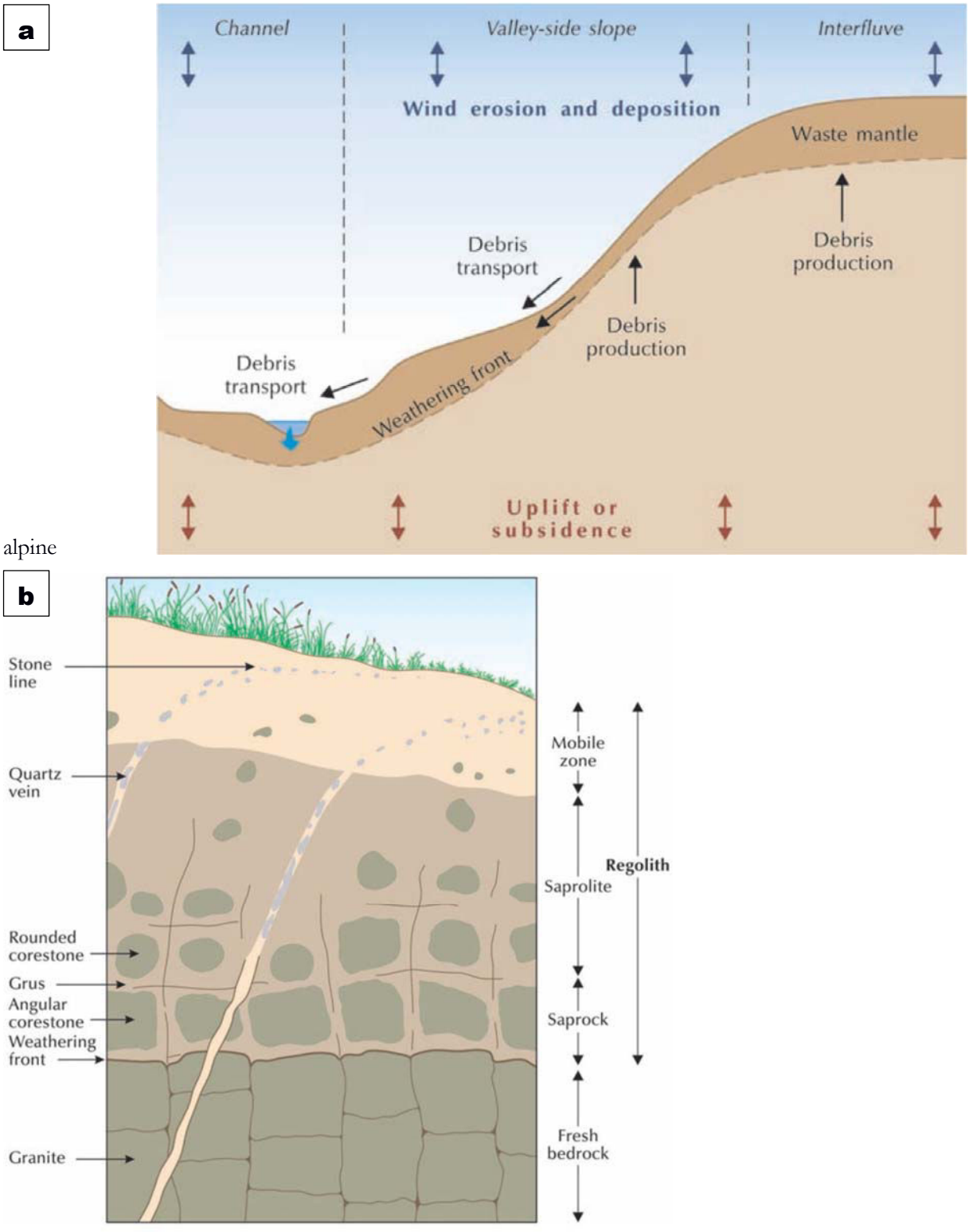

Figure II-19. Hillslope system and weathering profile.

a. hillslope sediment production system: weathered rocks can temporarily stay in the "waste mantle" or exported by erosion and debris transport to the channel.

b. typical weathering profile in granitic rocks. The weathering front separates the fresh bedrock from the regolith (from Hugget, 2011, his Fig. 2.1 and 7.3).

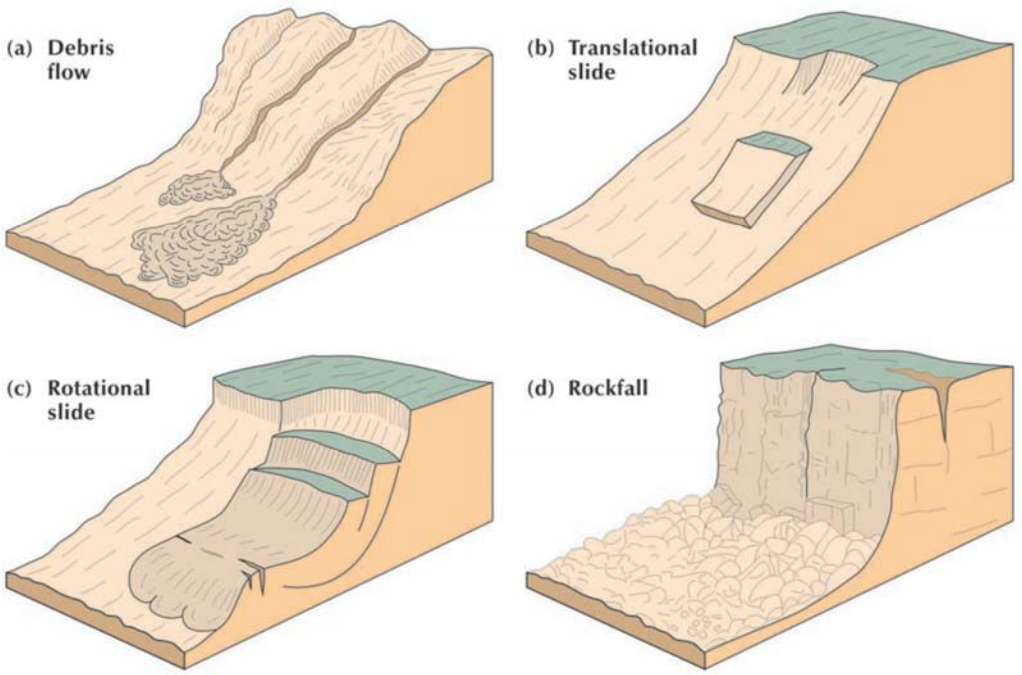

Figure II-20. Some mass movements.

(from Hugget, 2011, his Fig. 8.1).

environments. Landslides is a subgroup of mass movements as it involves the development of a failure surface on which unconsolidated material will abruptly slides downslope. Landslides are favoured by steep slopes and high pore water pressure. Then they are frequently triggered by a combination of earthquakes and intense rainfall, although they can also originate from permafrost melting.

Slope processes have an impact exceeding the area they cover. By the addition of sediments to rivers, they influence its capability to erode, transport and deposit (see below). In addition, they can occasionally move a large mass of rocks and form temporary debris-dammed lakes. These lakes are at the origin of increased river discharge and related incision and transport when dam-failures occur (Korup et al., 2010).

II.4.2.2. Fluvial incision

Rivers form the prime agent for the export of dissolved elements and undissolved sediment. Finer particles as clay and silt are transported as suspended load over large distances whereas coarser particles as gravel and cobble are transported in fits and starts as bedload. Depending on fluvial conditions, sand can be transported either as suspended load or bedload. The capacity of rivers to incise their channel, transfer and deposit sediments is formalized by the "stream power" and depends on water discharge, slope and the volume and nature of transported sediments. River incision occurs by the rolling and bouncing of bedload, and is favoured by high discharge, steep slopes and sufficiently large sediments. Additionally, incision also depends on the nature of the channel, the unconsolidated alluvial channels being more easily incised than bedrock channels. River incision is therefore enhanced in high-relief areas subject to active tectonics

and/or seasonal intense rainfalls or snowmelt.

II.4.2.3. Glacial erosion

Glaciers form a secondary export agent. Glaciers form when snow accumulation exceeds snowmelt. They move by fracturing at their interface with atmosphere and by slow flowing at depth. The base of "warm-based" glaciers (Figure II-21) can move by melt and refreeze, when atmospheric temperatures are

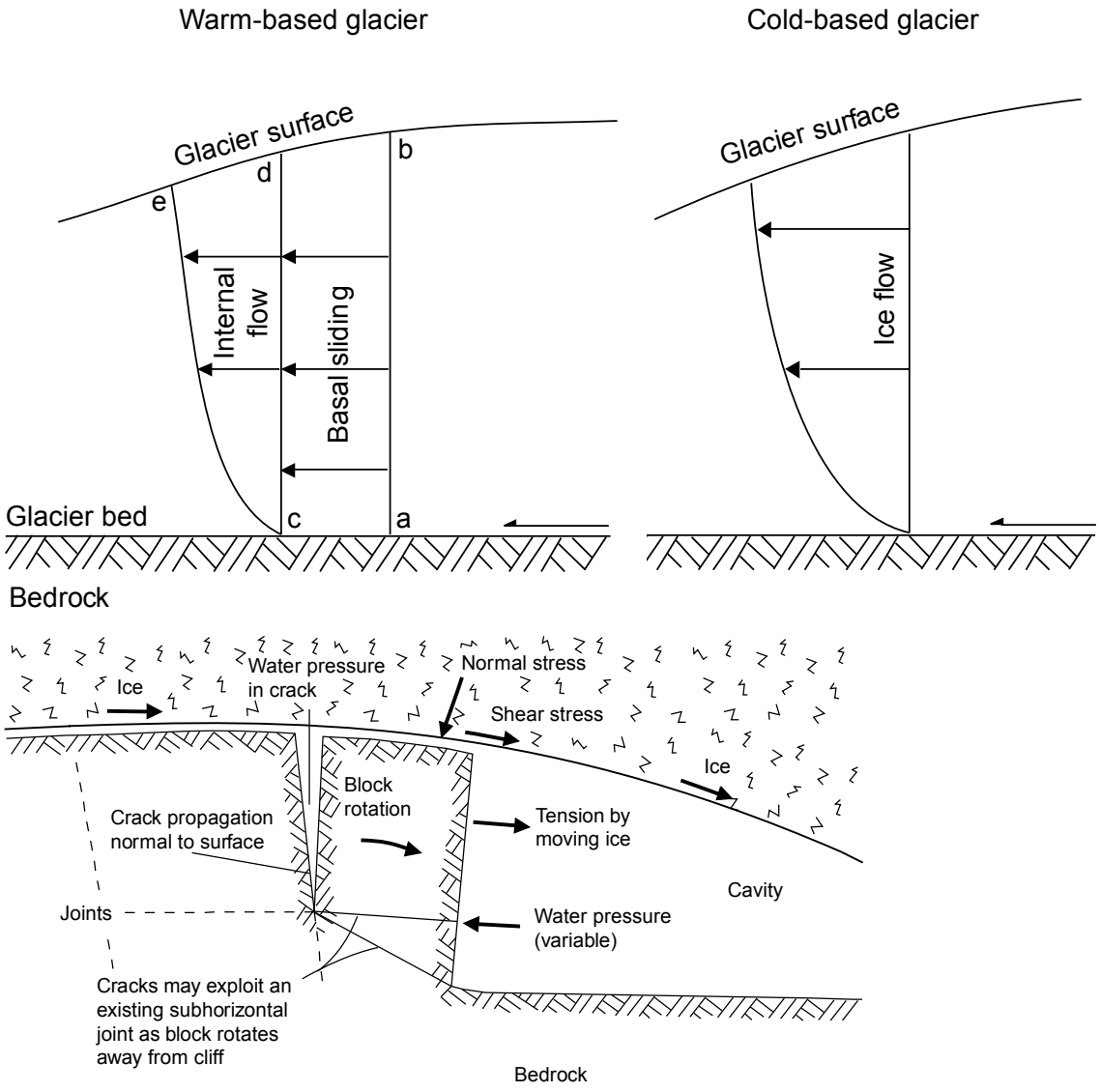

Figure II-21. Deformation of warm- and cold-based glaciers and glacial quarrying.

The upper insets present warm- and cold-based glacier deformation. The lower inset presents glacial quarrying. Transport of sediments can occur for both glaciers, but erosion by is supposed to be limited for cold-based glaciers. A glacier can shift from warm-based to cold-based regularly, and can also have different regimes depending on the part of the glaciers (modified from Bennet and Glasser, 2011, their Fig. 3.9 and 5.6).

close to zero or when the base is close to pressure melting point. Conversely, the base of "cold-based" glaciers remains frozen to the rock basal moves are limited when ice thickness is thin and atmospheric temperatures low. Glaciers transport and embed sediments originating from rockfalls and mass movements. They erode rocks either by the plucking/quarrying of rocks frozen into the bed, or by the action of subglacial meltwater, or by the abrasion by rocks embedded in ice. Therefore, the erosive capabilities of glaciers may be favoured by temperatures close to zero, an ice sufficiently thick and the availability of weathered sediments.

The impact of glaciers on the sedimentary flux far exceeds the area they cover. Seasonal snowmelt induces downstream discharge of high amplitude. As greenhouse progresses, ice melts and forms ice-dammed lakes that can cover a significant area (e.g. lake Agassiz-Ojibway in North America, Lajeunesse and St-Onge, 2008; Nicholl et al., 2012; Lajeunesse, 2012; or in the Himalaya, Montgomery et al., 2004; Scherler et al., 2014). Dam-failures then lead to glacial lake outburst floods (GLOF) that intensely temporally increase river discharge and thus incision and transport. Furthermore, as glaciers grow to form ice-caps, the topography of landscape becomes progressively hidden by the ice topography, which allow the shift of drainage divides, as it was the case during the last glacial cycles in Scandinavia (e.g. Mangerud et al., 2004; Kleman et al., 2008) and North America (e.g. Dyke et al., 2002; Hodder et al., 2016).

II.4.2.4. Complementary erosive processes

Aeolian processes produce mechanical weathering and transport in arid areas. In combination with glaciers, they are at the origin of the glacial loess deposits (e.g. Muhs et al., 2003). Coastal processes also produce erosion and transport.

II.4.3. Sedimentary flux at modern times

In modern times, the regions presenting the higher denudation rates are located at low latitudes, in particular in South Asia (Figure II-22, Milliman and Meade, 1983; Milliman and Farnworth, 2011). Except the Amazon and the Mississippi basins, these areas are all subject to active tectonics, which favour mechanical weathering and landslides. The majority of them are also subject to seasonal intense precipitations, in particular the S. Asian Monsoon. Even though the glacial sedimentary yields from Greenland and Antarctica remain difficult to measure (Andrews and Syvitski, 1994), these glacial regions appear to be globally negligible providers of sediments (Milliman and Farnworth, 2011).

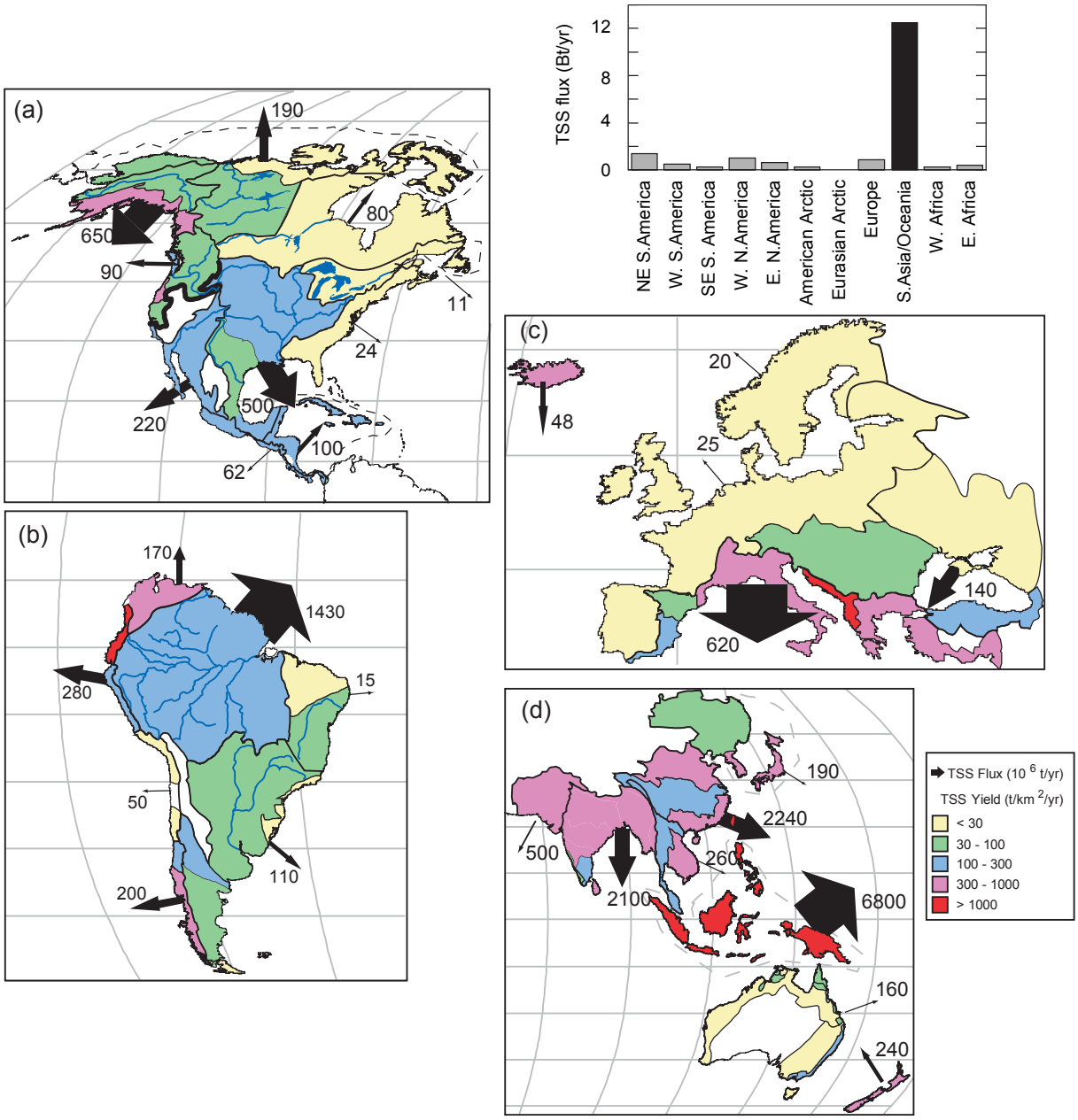

Figure II-22. Worldwide total suspended sediment (TSS) flux and calculated yield.

The upper right inset synthesizes the annual sedimentary flux for each region.The other panels show the flux with arrows and figures and the sedimentary yield by colours (modified from Milliman and Farnworth, 2011, their Fig. 2.31).

II.5. THE SEDIMENTARY RECORD

The sedimentary record is explored either from outcrops in the field or from drilled holes, with the frequent help of seismic reflection profiles. The preservation of the record decreases over time, notably because of the subduction of the oceanic floor (e.g. subduction of the Nicobar Fan into the Sunda Trench, Susilohadi et al., 2005; McNeill and Henstock, 2014) and the nature of erosion, transport and sedimentation, as explained below.

II.5.1. The stochastic nature of sediments

Sediments originate from the physical erosion from a region source and are transported through potential temporary storages to their ultimate destination, a sedimentary basin (Figure II-23). Therefore in theory, the terrigenous record should be a mirror of the eroded rocks. However, the stratigraphic record is inherently discontinuous (Sadler, 1981; Tipper, 1983), with brief periods of erosion and deposition, interrupted by long and quiet hiatuses. As discussed by Schumer and Jerolmack, 2009, over short timescales, sediment transport controls deposition, erosion, and hiatuses

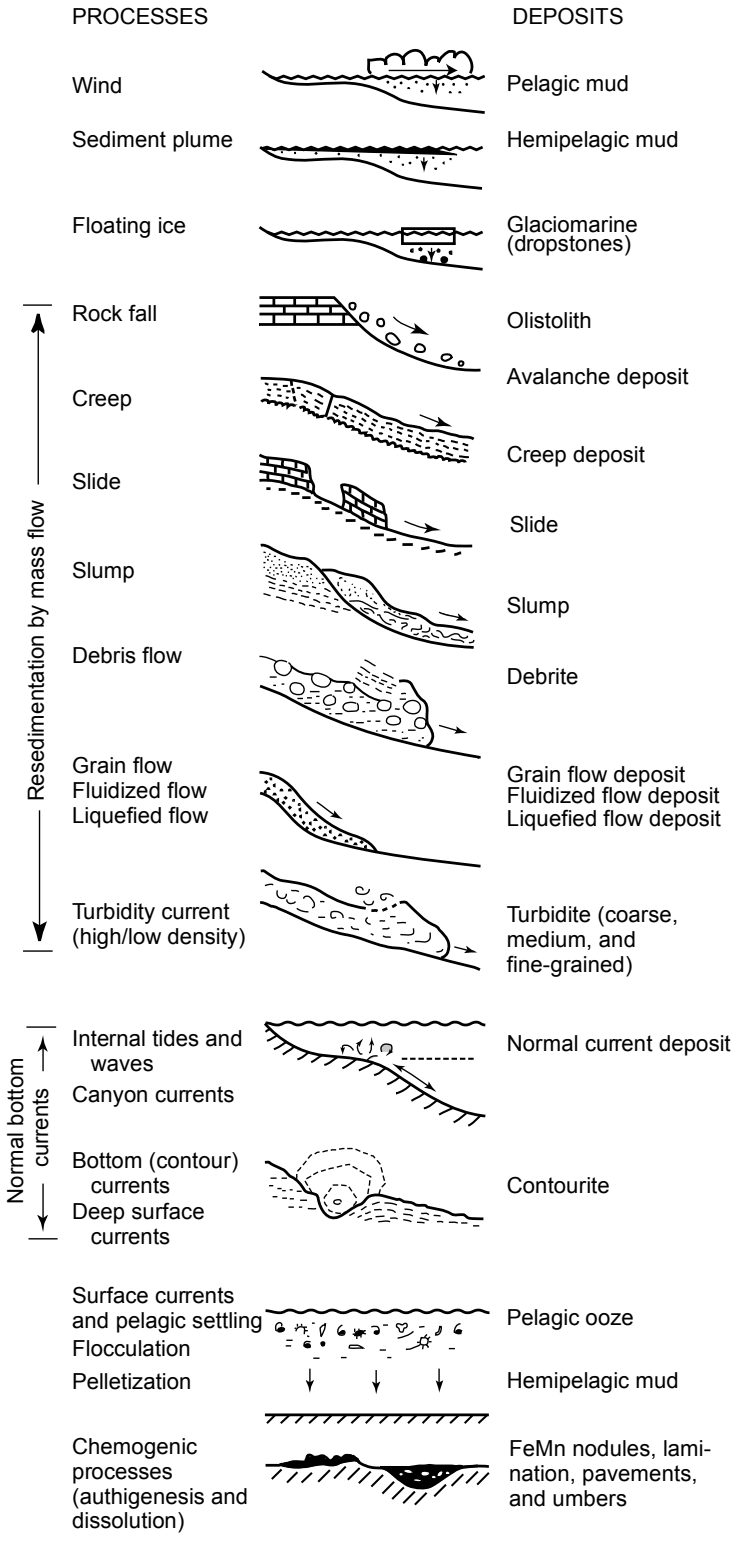

Figure II-23. Deep sea sediment transfer and deposition.

(from Boggs, 2014, his Fig. 14, p. 265, after Stow et al., 1994).

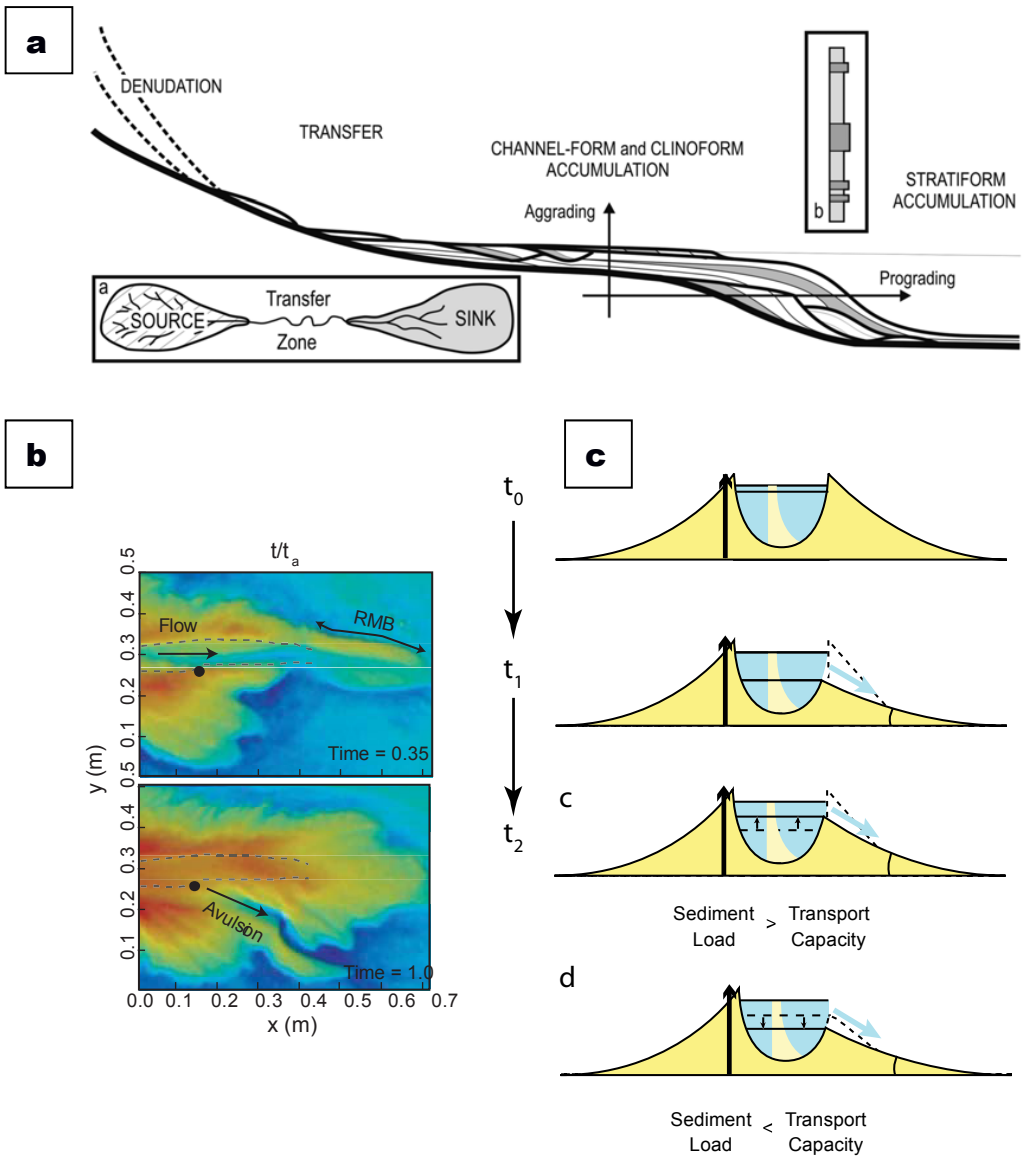

Figure II-24. Concept of avulsion.

a. Source to sink system (from Sadler and Jerolmack, 2015). The catchment is the source and the basin the sink. In a delta environment, depending on short-term (avulsions) and mid-term (accommodation, depending on sea-level and the sedimentary flux) conditions, deposition can be done vertically (aggradation) or horizontally (progradation), thus impacting local accumulation rates independently of the effective volume of sediments exported.

b. Model of a avulsing delta (from Edmonds et al., 2009). At a certain limit, deposition transit from prograding on the mouth bar (RMB) to aggradation upstream, thus increasing the overbank flows and pressure on the levees. The levees fail and the river avulses.

c. Model of a crevasse development in an alluvial channel (modified from Dalman and Weltje, 2008). At t0, the levees of the channel are stable. At t1, an event produces a failure in the levee (a crevasse). The theoretical model implies that if sediment load is sufficient, the levee progressively repairs (c), but if transport is important, the levee is progressively incised and lead to an avulsion (d).

in a sedimentary basin.

Sediment transport is driven by stochastic processes (e.g. Figure II-23), unsteady and intermittent by nature, and even under stable conditions, instantaneous deposition and erosion rates vary in time and space. Sediments can be exported by pulses rather through a continuous flux, especially in contexts with frequent landslides (e.g. Gabet et al., 2004a; Gallo and Lavé, 2014), or in arid regions subject to rare storms (e.g. Bookhagen et al., 2005). Discharge conditions also control the intermittence of bedload transport (Singh et al., 2009). Because of sediment deposition, rivers and the submarine flows tend to frequently avulse (Figure II-24), and channels and deltas tend to migrate (Jerolmack and Paola, 2007; Kim and Jerolmack, 2008; Hajek and Wolinsky, 2012).

Over longer timescales, unsteadiness and intermittence are smoothed, and deposition and erosion are controlled by the accommodation space (definition discussed in Muto and Steel, 2000), modulated by the sedimentary flux, subsidence and sea-level. Each factor does not present comparable time -scale, as subsidence varies at long timescales (0.1-1 Ma) whereas the sedimentary flux varies at short timescales and sea-level varies at mid-timescales (10-100kyr). When the sediment flux exceeds accommodation space, it spills over into another basin. The basins presenting high accumulation rates are notably subject to this phenomenon (Sommerfield, 2006). In addition, accommodation space can vary markedly across the sedimentary basin, markedly close to the edges, in case of tectonics or growth by progradation onto sediment-free areas (discussion in Molnar, 2004). Therefore the ability of sediments to locally record the full sedimentary flux is limited (Sadler, 1999), particularly in shallow platforms impacted by the sea-level fluctuations, such as continental shelves, or in contexts susceptible to rare and long hiatuses, such as the continental record.

II.5.2. The provenance topic

II.5.2.1. Recycling

Sediments can originate from recycling of sediments temporarily stored in the catchment, and in that case, they contain a second history in superimposition of the first one. Unravelling these two stories may be possible in some cases with the use of combined isotopic markers (Whitmann et al;, 2011), but it is still impossible to formulate any conclusion from sedimentary accumulation rates. This problem is acute for foreland basins exhumed at their margin by the frontal thrust of a fold and thrust belt (e.g. the Siwaliks in their later record, the upper Siwaliks, from 3-1 Ma onwards, Ojha et al., 2009; Chirouze et al., 2012; Puchol, 2013; Coutand et al., 2016).

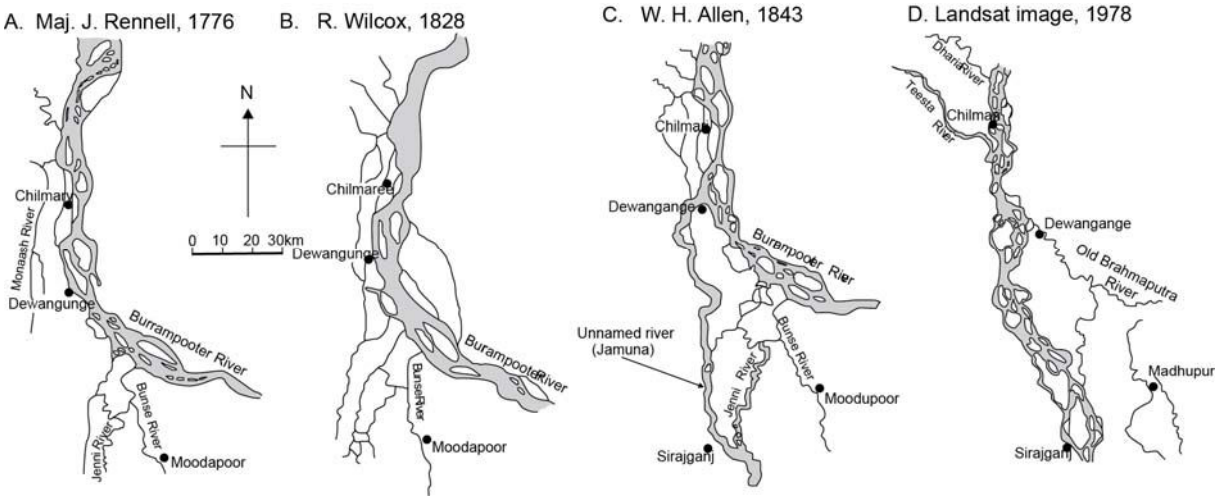

Figure II-25. Historic evolution of the Brahmaputra-Jamuna course in Bangladesh.
Compilation by Bristow, 1999 (modified from Best et al., 2007, their Fig. 19.3, p. 400).

II.5.2.2. Drainage evolution

Because of their capacity to transport sediments, river and glacial networks, along with aeolian processes in arid regions, form an essential component of the landscape modelling and the filling of sedimentary basins. The area that they drain, the catchment, can evolve in geometry and topography over time, which therefore alter the volume and the characteristics of the sediments transported to the basins. These networks dynamically evolve to equilibrium between crustal moves produced by tectonics, glaciations, and basin water filling/flushing, and topographic changes produced by erosion and sedimentation. Channels move laterally and retreat headward, and drainage divides migrate (e.g. Bishop, 1995; Willett et al., 2014). Streams can be diverted by divide breaching, either in a "bottom-up" way (Bishop, 1995), when a river actively capture a part of a neighbouring catchment (stream piracy) or in a "top-down" way when a stream join another catchment, following a diversion caused by tectonics or glaciers.

Drainage evolution is studied through the morphology of the fluvial and glacial network and the regional elevation differences (e.g. Bishop, 1995; Willett et al., 2014), in combination with mineralogic and isotopic provenance analyses and dating of the sedimentary record. The interpretation of this work is usually not straightforward, because continental sedimentary records have usually loose dating constraints and provenance signatures are not always associated to a unique source, the problem being exacerbated in case of recycling.

Although avulsions and channel migration are frequent in alluvial floodplains (e.g. shift of the course of the Brahmaputra from the 1700s, Bristow, 1999, Figure II-25, evolution of the Bengal delta over the Holocene, Allison et al., 2003; Goodbred et al., 2014), the frequency of these changes in bedrock contexts is still debated (e.g. Bishop, 1995; Willett et al., 2014). This is highlighted by the debate around

the drainage reorganisation in the Himalayan eastern syntaxis (e.g. Seeber and Gornitz, 1983; Brookfield, 1998; Clark et al., 2004; Cina et al., 2009; Chirouze et al., 2013; Robinson et al., 2014), with several studies pointing to an early connection of the Brahmaputra to the Tibetan plateau (Figure II-26, Lang and Huntington, 2014; Bracciali et al., 2015, see Bengal Fan chapter). Bishop, 1995 argues that in absence of consistent crustal moves and a significant elevation difference combined with a low divide between two catchments, drainage reorganisation is probably rare.

As illustrated in the Himalaya (e.g. Lang and Huntington, 2014; NW Himalaya in Sinclair et al., 2017), tectonics yield the primary source of crustal moves. Although of lower intensity, crustal deformation and flexure in passive margins, caused by the weight of sediments, can control the organisation of the fluvial network (e.g. Brazilian margin, Amazon, Driscoll and Karner, 1994) and Willett et al., 2014 demonstrated for the NE Atlantic margin that fluvial networks can be in disequilibrium even far from tectonic plate boundaries.

In contrast with the potentially slow evolution of fluvial networks by tectonics, glaciations probably induce frequent, rapid and large drainage modifications. The complex network of icestreams and supraglacial/subglacial rivers and lakes (e.g. Smith et al., 2015) is sensitive to minor changes in glacial thickness (Vaughan et al., 2008; Carter et al., 2013), occurring during glacial advances and retreat (Shugar et al., 2017), especially in areas of low basal relief (Carter et al., 2013). This was illustrated by the shifts of drainage divides during the last glacial cycles in Scandinavia (e.g. Mangerud et al., 2004; Kleman et al., 2008) and North America (e.g. Dyke et al., 2002; Hodder et al., 2016).

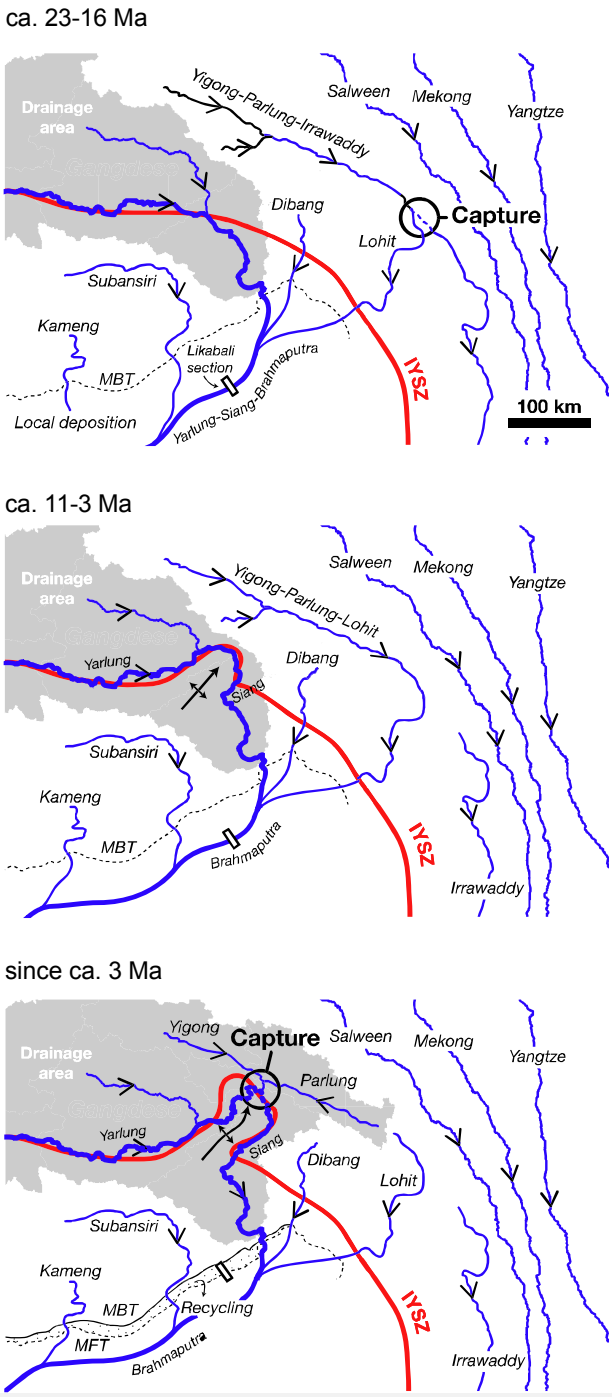

Figure II-26. Possible evolution of drainage in the Himalayan eastern syntaxis.

The course of the Yarlung-Tsangpo-Siang-Brahmaputra shifts as the deformation propagates northeastwards, resulting in drainage modification. IYSZ: Indus-Yarlung-Tsangpo suture (modified from Lang and Huntington, 2014; their data and Robinson et al., 2014's data).

II.5.3. Accumulation rates and sedimentary budgets

To a first approximation and keeping the previous topics in mind, the accumulation rate of terrigenous sediment in the stratigraphic record should be a proxy for the physical erosion rates of the land surface.

But early work (Barrell, 1917; Schuchert, 1931) observed that preservation of sediments decreased with age, notably because older sediments are recycled into young sediments (Gilluly, 1949). Consequently, sediment accumulation rates have a strong dependency on the timespan used for their averaging, with short-term rates tending to be faster than long-term rates (compilation of Saddler, 1981; Tipper, 1983). One can circumvent this dependency with the acquisition of accumulation rates measured over a constant time interval (Gardner et al., 1987). This acquisition remains delicate because dating constraints become spaced with the age of sediments. Additionally, continental clastic series are usually more challenging to date compared with marine series, because of the scarcity of biostratigraphic markers. One can also constrain the maximum time of hiatuses from the structure, geomorphology and the geometry of the deposition environment, it may be still possible to get reliable average accumulation rates if averaged on long timespans (Schumer and Jerolmack, 2009). One can also favour a 2-D approach (e.g. Sadler and Jerolmack, 2015) or source to sink sedimentary budgets, including continental and marine basins (review in Hinderer et al., 2012), instead of limiting studies to individual sites, as it is still frequently the case.

Another common topic concerns the consideration of compaction and its correction: as the sediment is buried, its interstitial porosity is progressively squeezed. Rates of compaction not only depends on mechanical processes but also on chemical processes linked to pressure dissolution (e.g. Suetnova and Vasseur, 2000), which make their assessment not simple.)

But a central issue for accumulation rate estimation and sedimentary budgets, which is not evoked by critics of this method (e.g. Sadler, 1981; Schumer and Jerolmack, 2009; Willenbring and Jerolmack, 2016), is to confirm that catchments remained stable over the period of study (e.g. Bishop 1995; Molnar, 2004), otherwise mass balance cannot be reached and variations would be misinterpreted.

II.6. LATE CENOZOIC EVOLUTION OF THE DENUDATION RECORDS

II.6.1. Accumulation rates and sedimentary budgets

II.6.1.1. The deep sea basins

With the systematic exploration of the deep sea distal basins, workers unexpectedly observed marked coeval variations in carbonaceous and terrigenous average accumulation rates (compilations of Davies et al., 1977; Hay et al., 1988a; review in Hay et al., 1988b; Molnar, 2004; reinterpretation in Olson et al., 2016). Terrigenous sediments are transported downslope from the marginal basin to the deep sea floor by turbidity currents and current transport. They can also be transferred from continents to ocean (and other continents) through aeolian transport. The deep sea records show that terrigenous accumulation rates are subject to a global increase since ca. 35 Ma (Davies et al., 1977; Hay et al., 1988a), with a 3-fold acceleration since 5 Ma (Hay et al., 1988a). A coeval and at least 2-fold increase in the Al content of sediments from individual sites corroborate these observations, at least since 15 Ma (Donnelly, 1982).

Lower accumulation rates in the past are partly caused by the higher frequency of hiatuses in the sedimentary record (Moore and Heath, 1977), but these hiatuses, which depend on the activity of the bottom water flow, present a large spatial variability in the oceans (Moore et al., 1978), as the individual accumulation rates also do (remark by Molnar, 2004). Although classically interpolated with an exponential curve (Hay et al., 1988a; Zhang et al., 2001), the global deep sea terrigenous record presents more subtle variations, with a peak around 40-50 Ma, a low at 25-35 Ma, and a relative stability at 5-20 Ma (Hay et al., 1988a).

In a recent study, Olson et al., 2016 (Figure I-3, Figure II-27) reappraise the early work of Davies et al., 1977 and Hay et al., 1988a and show that global terrigenous average accumulation rates roughly follow a steady-state accumulation model, except since 0-5 Ma. Interestingly, they present average accumulation rates for each ocean (excepted for the Arctic and Antarctic oceans), and none of the oceans presents an increase in sediment volume of amplitude similar to the global average. In particular, average accumulation has been steady since 25 Ma for the North Atlantic and since ca. 15 Ma for the Indian Ocean (Olson et al., 2016). This highlights the statistical limits of this kind of global approach, which gathers largely heterogeneous areas, with very different accumulation rates (results of Olson et al., 2016; Straume et al., 2019).

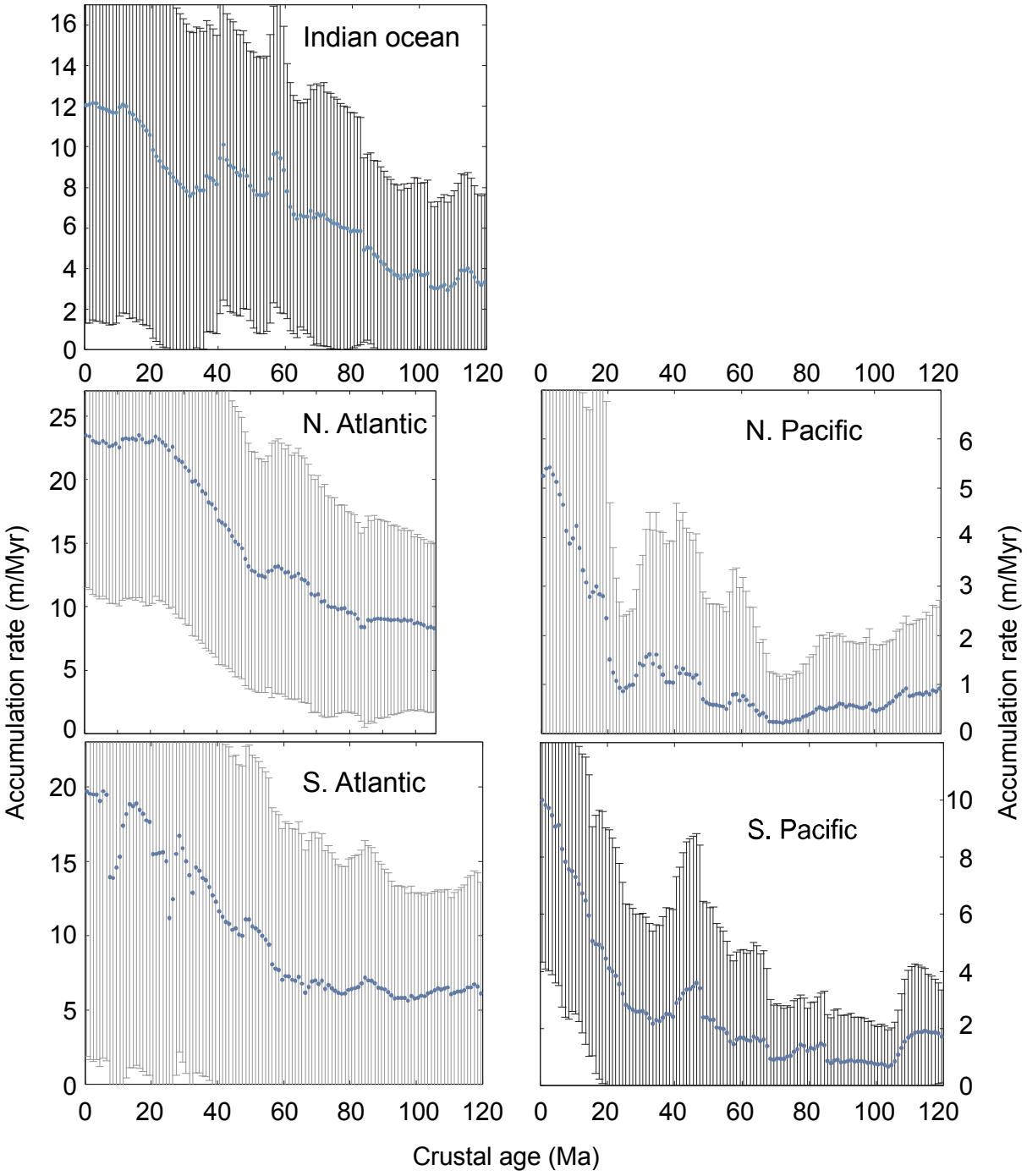

Figure II-27. Deep sea average accumulation rates by oceanic basin.

For each panel, mean accumulation rate and standard deviation are presented in function of crustal age, by 1-Myr timespan. Note the different scales for the y-axis in panels (from Olson et al., 2016; based on the early work of Hay et al., 1988; DSDP site data).

II.6.1.2. Turbiditic fans, continental margins and foreland basins

Since the 1980s, a thorough exploration of turbiditic fans, continental margins and foreland basins, including endorheic basins (Figure II-28, compilation in Zhang et al., 2001; Molnar, 2004) has completed the deep sea record and make it possible to investigate individual source-to-sink systems. Accumulation rates and sedimentary budgets (not exhaustive compilation in Table SII-3) present an impressive increase since 2-5 Ma in most areas (Zhang et al., 2001). Zhang et al., 2001 and Molnar, 2004 assert that this increase is independent from latitude. This point is critical because the low-latitude regions yield presently the majority of sedimentary flux (Milliman and Farnsworth, 2011), noting that the sedimentary flux in Greenland and Antarctica remains difficult to constrain (e.g. Andrews and Syvitski, 1994). In case that these regions have not been subject to a consistent acceleration of accumulation, the scenario of a global increase in erosion rates in the late Cenozoic should fall apart.

The work of Métivier et al., 1999; Métivier, 2002 seems to be a convincing argument for an acceleration of accumulation at low latitudes, by showing a 2- to 3-fold global increase in the accumulation rates in South Asia. Regrettably, because it is based on proprietary data (Métivier et al., 1999), this work was never fully reproduced (Clift and Gaedicke, 2002; Clift et al., 2002; Clift, 2006). Additionally, Métivier et al., 1999 acknowledge themselves the potentially "large but unquantifiable uncertainties" linked to their reconstructions, which might explain why previous workers (Curray 1994, Einsele et al. 1996) did not try to reconstruct the evolution at "high" resolution. They are chiefly based on the shelf stratigraphy (discussion in Molnar, 2004) since most of Asian Cenozoic basins have only limited deep sea drillings, rarely reaching the basement, or located on ridges or at the edges of the fans (Clift and Gaedicke, 2002). We will therefore not discuss exhaustively about the Métivier et al., 1999's study and focus on other studies.

The overall picture for low-latitudes regions is probably different than the one described in Métivier et al., 1999, as recently shown by the Expeditions 353 and 354 on the Bengal Fan (Clemens et al., 2016; France-Lanord et al., 2016) and 362 on the Nicobar Fan (McNeill et al., 2017). Several basins present an absence of increase, either in Asia (Figure II-29): the Ganga foreland basin (Métivier et al., 1999), the Gulf of Thailand basin and the Mekong delta (Clift, 2006), North Borneo basin (Hall and Nichols, 2002; Morley and Back, 2008) or in Africa: the Niger delta (Grimaud et al., 2018). Some basins (the Indus Fan, the Red River and Pearl River Basins, Clift, 2006; Andean foreland basin, Uba et al., 2007) are effectively subject to an increase, but only appear to recover from a previous decelerating phase at ca. 3 - 10 Ma. Other basins present a development linked with drainage reorganisation (Zambezi Delta, Walford et al., 2005; Amazon Fan, Dobson et al., 2001; Harris and Mix, 2002; Figueiredo et al., 2009, although this latter can be debated), a shift of their sedimentary depocenter (Angola, Congo, Lavier et al., 2001; Ferry et al., 2004) or when there are several close sources, can have an alternation of sediments from distinct sources (e.g. S. Chinese sea, with the Pearl River basin, dominated by Taiwanese sediments from 3 Ma onwards, Wan et al., 2010).

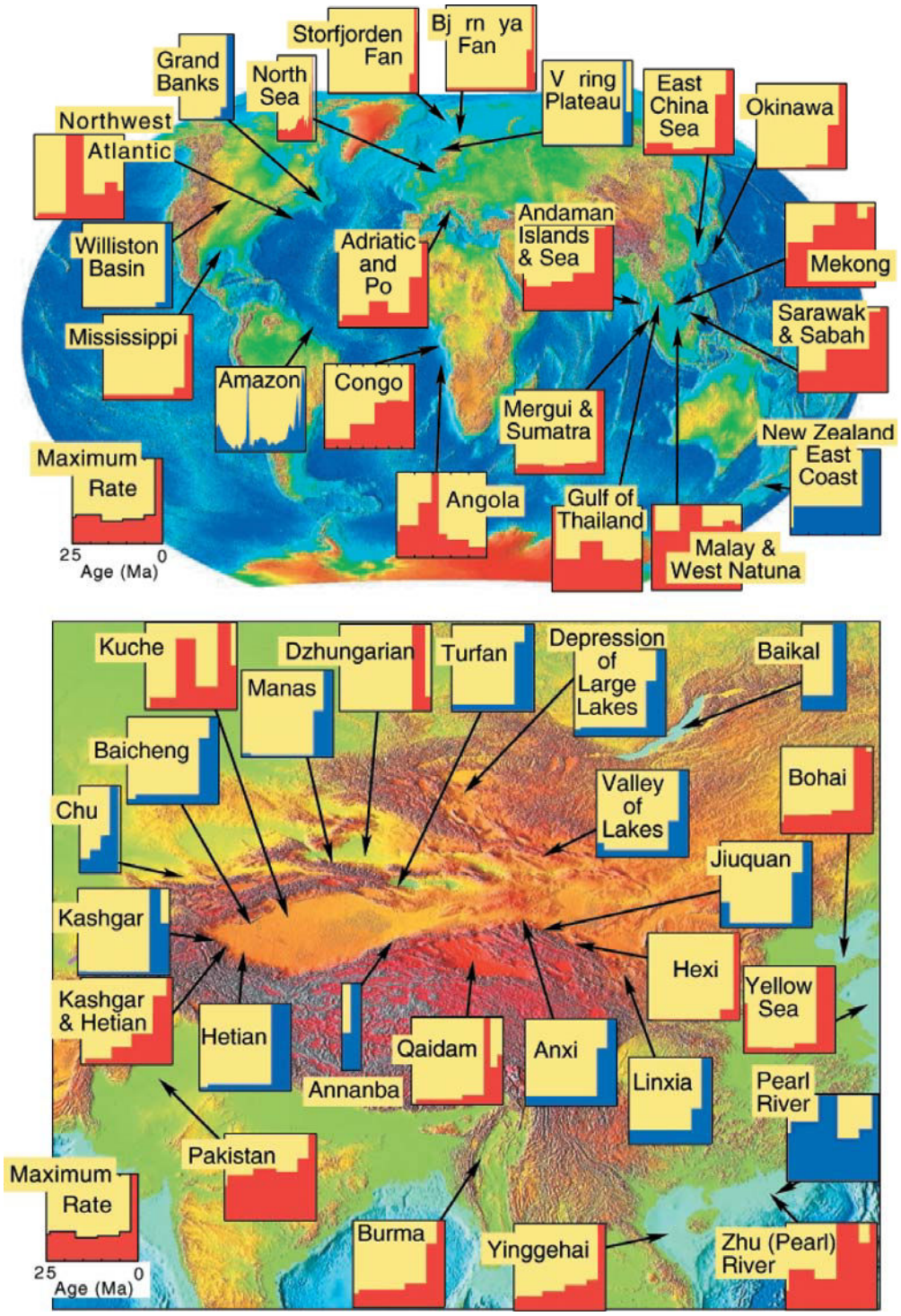

Figure II-28. Compilation of continental margin and foreland accumulation rates.

The lower panel is a focus on Asia of the upper panel. For each region is shown a chart y=accumulation rate, x=Age (Ma) with age rightwards decreasing. Red diagrams present mass accumulation rates compaction corrected, blue ones show point measurement, without compaction corrected except Pearl River. Note that several of these studies, including the Mississippi record have been amended by new data afterwards or require revisions in view of new data, in particular in NE Tibet (Charreau et al., 2009a, see text) (from Molnar, 2004; initial work by Zhang et al., 2001).

The impact of the shift in the partitioning of sediments might be illustrated with the Ganga-Brahmaputra catchment: accumulation may have decelerated in the Ganga basin (ca. 5 Ma, Métivier et al., 1999) and in the Nicobar Fan (ca. 2 Ma, McNeill et al., 2017), while accelerating in the Bengal Fan (ca. 5 Ma, Métivier et al., 1999), even though with the previous caveats and the remarks of Clift and Gaedicke, 2002, this acceleration is still unconfirmed.

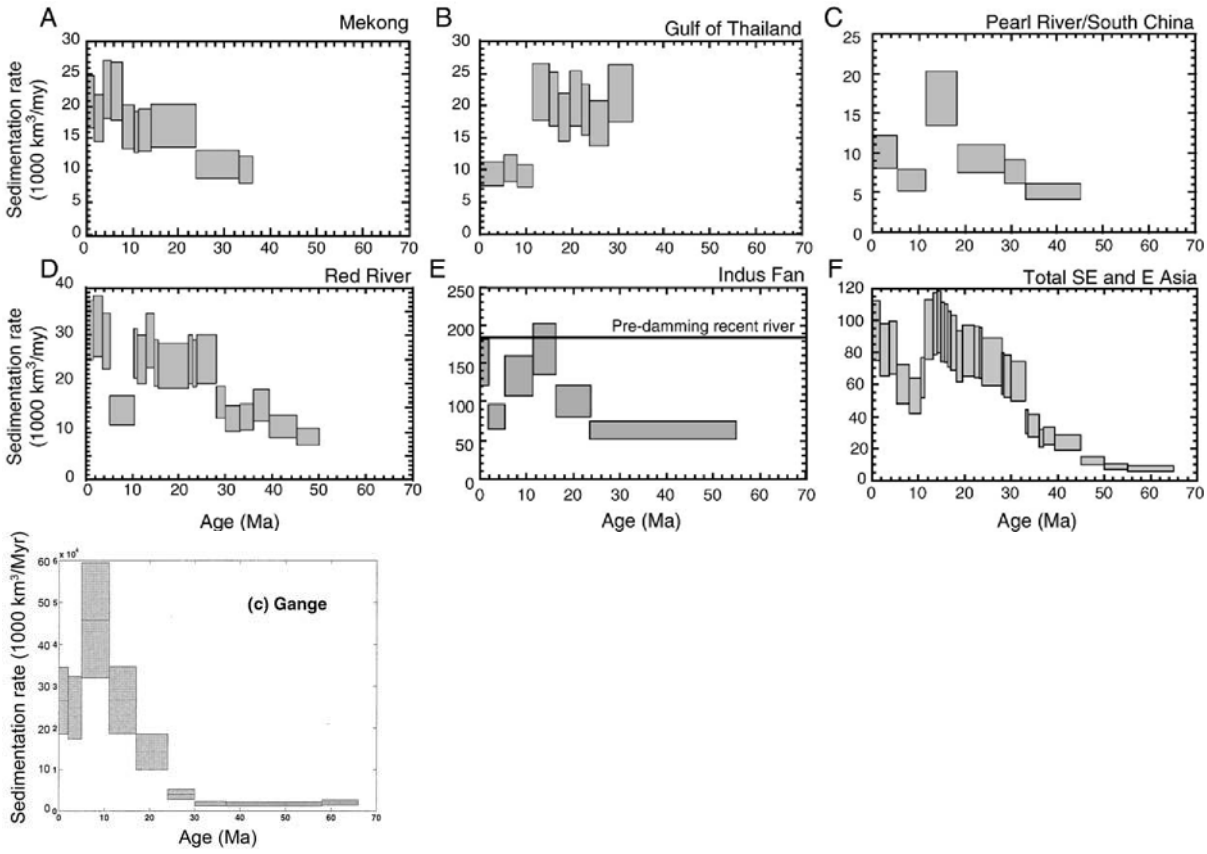

Figure II-29. Compilation of accumulation rates in Asia.

All insets present sediment budgets for Asian catchments, with y-axis as accumulation rate (1,000 km3/Myr). Note that the budget for the Pearl River includes Taiwanese sediments from 3 Ma onwards (Wan et al., 2010). (modified from Clift, 2006, excepted for the Gange inset modified from Métivier et al., 1999).

At higher latitudes, an acceleration of accumulation in the late Cenozoic is more strongly evidenced (see Table SII-3), except in Central Asia (Zhang et al., 2001) for which the timing has been evidenced to be diachronous over the region, from 15 to 0.7 Ma (Charreau et al., 2005, 2006, 2009; Lu et al., 2010). All of the studied systems include areas that were submitted to late Cenozoic glaciations (e.g. Scandinavia, Dowdeswell et al., 2010; North Sea, Anell et al., 2010; European Alps, Kuhlemann et al., 2002; New Zealand, Carter and Carter, 1996) although one of the systems, the Mississippi delta (e.g. Hay et al., 1989; Galloway et al., 2011) has a catchment that largely covers never-glaciated areas. Scandinavia, North Sea and the Mississippi deltas have been subject to regular and massive drainage reorganisations (e.g. Kuhlmann et al., 2004; Galloway et al., 2011; Komatsu et al., 2016; Carson et al., 2018) or potential post tectonic moves that may have modified depocenters (Overeem et al., 2001; Galloway et al., 2011). Even though New Zealand is located at a plate boundary, a potential impact seems limited since modern denudation and uplift appear in steady-state (Adams, 1980).

II.6.2. The seawater continental silicate chemical weathering record

II.6.2.1. The seawater $^{87}Sr/^{86}Sr$

Early workers (e.g. Raymo et al., 1988; Raymo and Ruddiman, 1992) considered the marine carbonate Sr isotopic data as a proxy for continental silicate chemical weathering. Global compilations (Figure II-30, Koepnick et al., 1985; Richter et al., 1992) present a rapid increase in the seawater $^{87}Sr/^{86}Sr$ at 40-15 Ma, followed by a slower increase from 15 Ma afterwards, which was interpreted by Raymo and Ruddiman, 1992 as an increase in silicate weathering, potentially caused by the Cenozoic Tibetan-Himalayan uplift. However, Raymo and Ruddiman, 1992 acknowledge that the proxy might not be able to represent the real amplitudes of the fluctuations of the silicate weathering flux. First, it is delicate to separate the silicate contribution of Sr from the carbonate contribution, this latter not impacting CO_2 concentrations (see discussion in Berner, 2004, p. 37, based on Blum et al., 1998 and Jacobson et al., 2003's data). Second, the variations of the ratio may be caused by variations of the isotopic ratios of the source rocks (discussion in Kump et al., 2000).

The interpretation of the marine $^{87}Sr/^{86}Sr$ as a proxy for silicate chemical weathering was strongly contested in the 1990s and several works argued that the increase of the ratio was caused by the erosion of a continental crust enriched in ^{87}Sr as the Himalayan one (Edmond, 1992, Derry and France-Lanord, 1996, Galy et al. 1999).

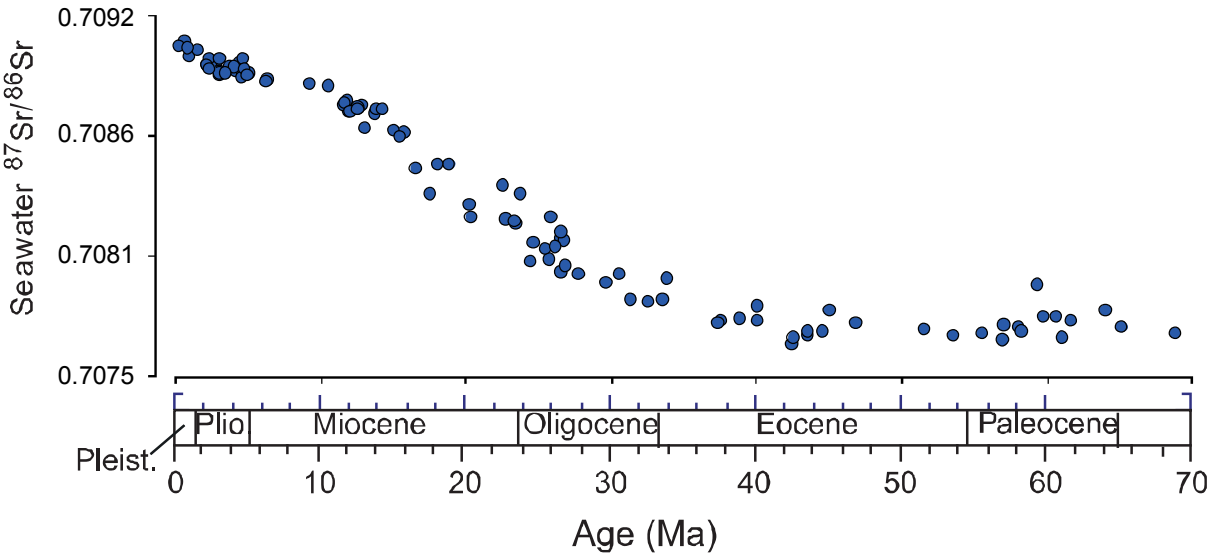

Figure II-30. Seawater $^{87}Sr/^{86}Sr$ curve since 70 Ma.

Foraminifer and nanofossil $^{87}Sr/^{86}Sr$ from DSDP cores in the Atlantic, Pacific, Indian oceans and the Caribbean Sea (data from Koepnick et al., 1985).

II.6.2.2. The seawater $^{10}Be/^{9}Be$ and $\delta^{7}Li$

Twenty years after the Raymo and Ruddiman, 1992's work, two new silicate weathering proxies, $\delta^{7}Li$ (review in Tang et al., 2007) and $^{10}Be/^{9}Be$ (Brown et al., 1992b; von Blanckenburg et al., 1996) yielded a contradictory view to this work. Misra and Froelich, 2012, complemented the work of Hathorne and James, 2006 by measuring $\delta^{7}Li$ on planktonic foraminifera tests samples from sites covering distinct periods since 70 Ma (Figure II-31). Their work confirms a global acceleration of silicate weathering, extending on a broader period, 60 to 6 Ma, with quiet and more active episodes. From 6 Ma onwards, the $\delta^{7}Li$ record (limited for this period to data of ODP site 758 in the Bengal bay), is relatively stable.

Willenbring and von Blanckenburg, 2010, compiled $^{10}Be/^{9}Be$ measurements from ocean cores and Fe-Mn crusts from the Arctic, the Atlantic and the Pacific, which cover similar periods (Figure II-32). While ^{10}Be is a cosmogenic nuclide mainly derived from the atmosphere through rain and is supposed constant over the last 10 Ma (Leya et al., 2000), ^{9}Be is derived from continents mainly through fluvial input, and is supposed to have increased if silicate weathering has accelerated over time. The method relies on the hypothesis that both isotopes homogenize at least the basin scale (early formulation in von Blanckenburg and Igel, 1999; modelling in Iger and von Blanckenburg, 2000). It was later confirmed that the homogenization was also valid at a global scale (von Blanckenburg and Bouchez, 2014; Wittmann et al., 2017) if sites were sufficiently remote from the coast (Wittmann et al., 2017). Willenbring and von Blanckenburg, 2010 interpret their compilation as showing that oceanic $^{10}Be/^{9}Be$ fluctuate in the range of modern ratios since 10 Ma, knowing that modern ratios can vary up to a factor of 2 (compilation of von

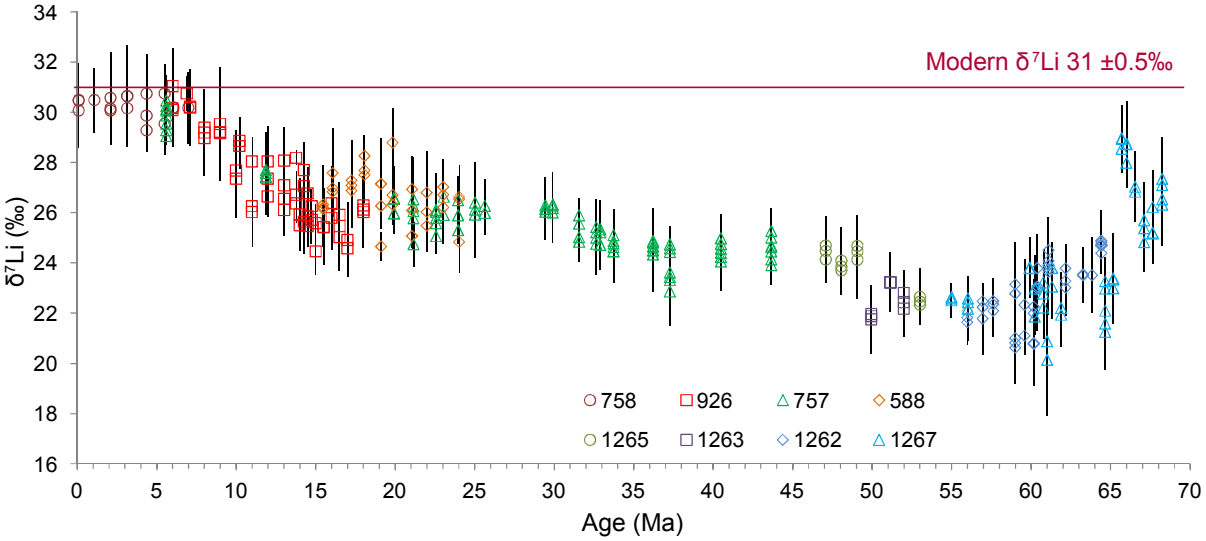

Figure II-31. Seawater δ^7Li curve since 70 Ma.

Foraminifer δ^7Li measurements from deep ocean, with 2-σ error linked to reproducibility (compilation from Misra and Froelich, 2012, including their data).

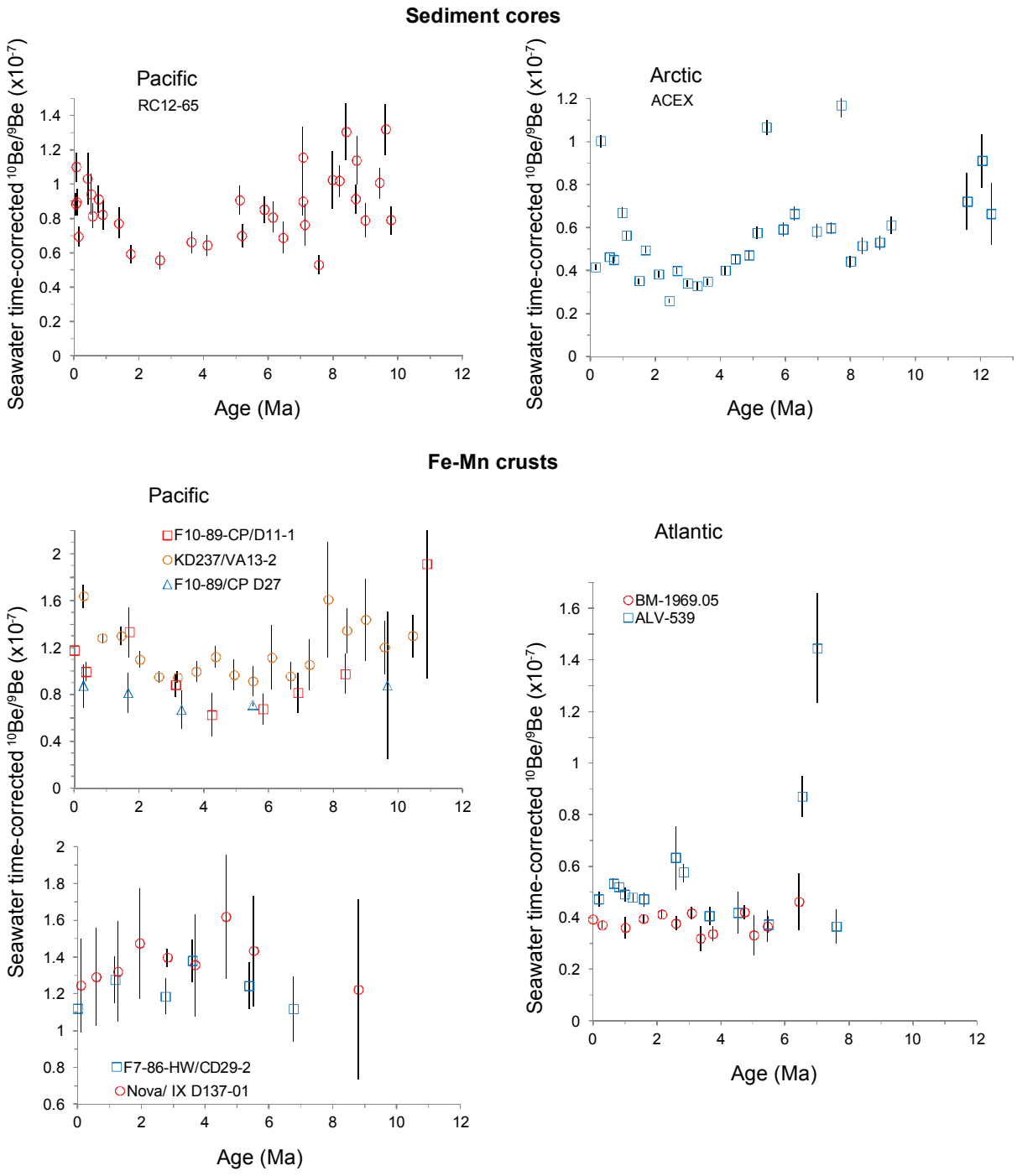

Figure II-32. Seawater ^{10}Be/^{9}Be compilation since 12 Ma.

The panels present in y-axis seawater ^{10}Be/^{9}Be corrected from decay for sediment cores and Fe-Mn crusts from the Pacific, Arctic and Atlantic. The drill sites are indicated for each panel. Data compiled by Willenbring and von Blanckenburg, 2010 (including sediment core data from Bourlès et al., 1989 and Franck et al., 2008).

Blanckenburg et al., 1996). This absence of a continuous decreasing trend appears as a compelling argument against a significant increase in silicate chemical weathering rates over the late Cenozoic. Similarly, von Blanckenburg et al., 2015 compiled data of the same proxy from high-resolution marine records covering the last 2 Ma and confirm stable average silicate weathering over the period. They also highlight that fluctuations of silicate weathering potentially do not follow a simple correlation to the variations of temperature during the Quaternary, as told by $\delta^{18}O$ on benthic foraminifera.

II.6.2.3. Consequences for the causes of the CO_2 fluctuations in the late Cenozoic

These new results suggest that the marked fluctuations of CO_2 observed during the late Cenozoic cannot be explained by global fluctuations in silicate weathering. The limited global variations of silicate weathering may originate from two causes. First, the lithology of the rocks subject to physical erosion is important. When eroded silicate rocks have a low Ca-content, silicate contribution to chemical weathering is superseded by carbonate contribution in environments subject to high physical erosion, as suggested by Berner and shown by chemical budgets using major elements, (the Himalaya, Derry and France-Lanord, 1997; Lupker et al., 2012b) and by $\delta^{44/40}Ca$ and Ca/Na (New Zealand (schists), Moore et al., 2013; Iceland (basalts), Jacobson et al., 2015). However, this observation appears debatable for glacial areas (Moore et al., 2013; Jacobson et al., 2015).

Second, as global cooling accelerated (Herbert et al., 2016), the kinetics of weathering became less favorable, as shown in India by the Indus Fan record (Clift, 2006). The importance of kinetics was highlighted in the Himalaya by West (2012) and Lupker et al. (2012b), who evidence that chemical weathering mainly occurs during the floodplain transfer, as previously suggested by Molnar and England (1990), potentially because at higher elevations, weathering kinetics are limited by temperature (Norton and von Blanckenburg, 2010), although this might be not the case in tectonically active mountains (Larsen et al., 2014). In addition, Lupker et al. (2013) show strongly different weathering flux between the Holocene and the Last Glacial Maximum, a period when weathering flux could have been reduced by 90%.

However, these apparently less favourable kinetics seem to contradict the view of stable silicate chemical weathering rates (Willenbring and von Blanckenburg, 2010; von Blanckenburg et al., 2015) and let open the suggestion that some regions may have seen an acceleration of silicate weathering whereas others, as India have witnessed a deceleration.

II.6.3. The $^{10}Be/^{9}Be$ detrital record

Cosmogenic nuclides produced in crystals, in particular ^{10}Be in quartz, can be used as a proxy for short-term denudation rates. They can either be measured in situ, i.e. on the bedrock, or in sediments, and in that case they give access to denudation rates averaged across a catchment (see 0.

Methodologic overview). This method is widely employed to obtain modern erosion rates (e.g.

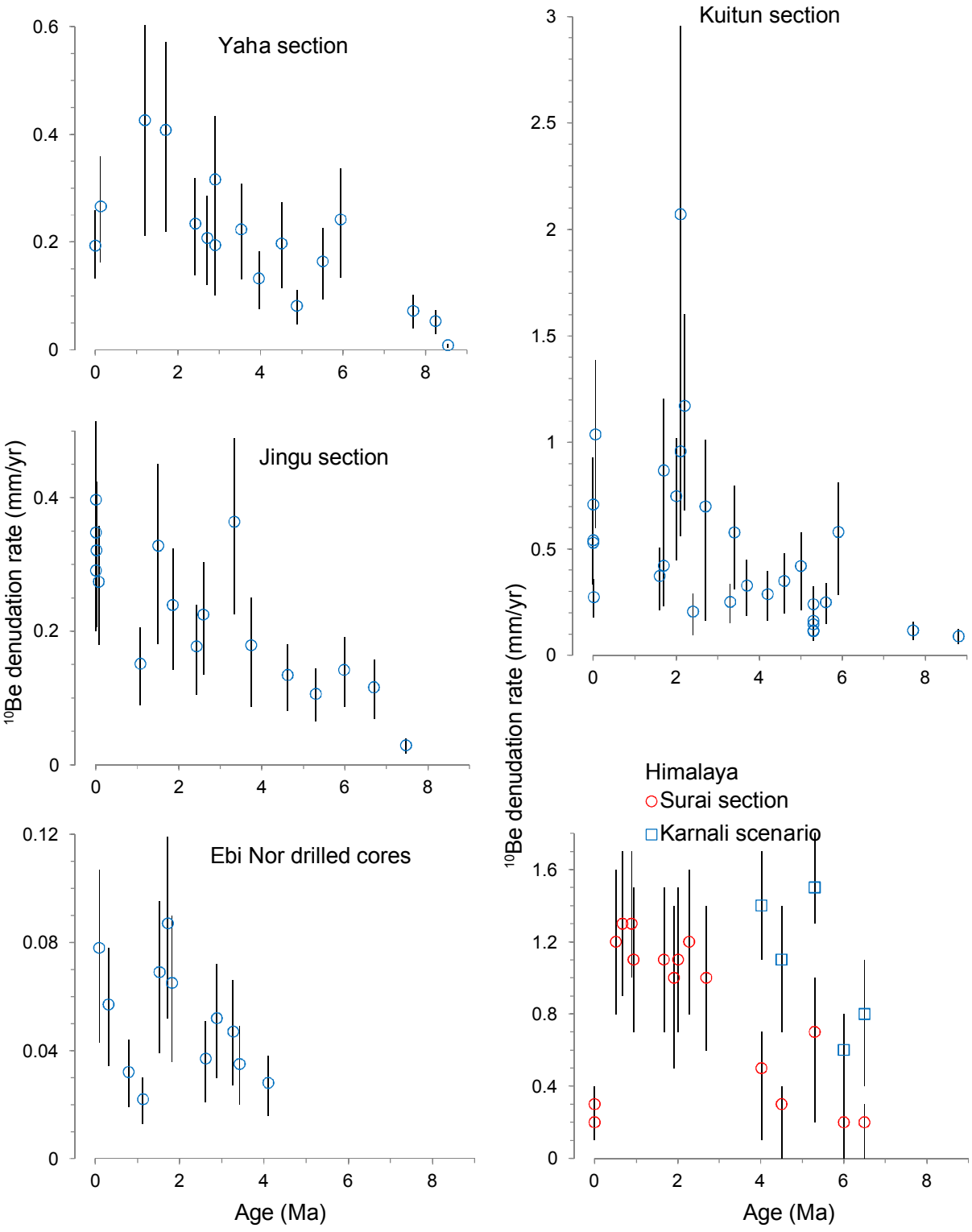

Figure II-33. ^{10}Be erosion rates in Asian foreland basins since 8 Ma.

The panels present for Tianshan, NE Tibet (Yaha, Kyutun, Jingu section and Ebi Nor cores, Puchol et al., 2017) and Himalaya (Surai section, Puchol, 2013) the ^{10}Be erosion rates in y-axis in function of ages in x-axis. For the Himalayan panel, the data are interpreted in 2 scenarios: the red dots show the rates at catchment staying stable over the period; the blue squares propose that the catchment might differ before 4 Ma (see text, Puchol, 2013).

compilation in Portenga and Bierman, 2011) but more rarely for past erosion rates, and only a limited number of studies present data covering the late Cenozoic, mainly for catchments < 5,000 km². Additionally, only a few number of studies discuss about the effect of a potential shift of provenance, recycling, or recent exposure.

At low latitudes, two studies in Central Himalaya (Figure II-33, Surai section) and in the Andes yield contradictory results. In Central Himalaya, for a small unglaciated catchment in front of the range (Surai section), Puchol, 2013 shows that erosion progressively accelerated since 6.5 Ma onwards, with a rapid shift at 3-4 Ma (3-fold increase in the rates in total). Contrastingly, modern denudation rates are similar to rates before 4 Ma. The workers acknowledge that the 3-4 Ma shift might have been caused by a change of provenance from a major Transhimalayan river to the present interfluvial river, but no provenance data sustain such a sudden shift over the period (Huyghe et al., 2001). At similar latitudes in the east of the South Central Andes, Val et al., 2016; Amidon et al., 2017; Pingel et al., 2019 show a deceleration of erosion from 7 Ma to 2 Ma, even though the rates are variable for the smaller catchments. Amidon et al., 2017 and Pingel et al., 2019 interpret this deceleration as the result of an increased aridity, but the abrupt decreases observed in some basins might have been caused by drainage reorganisation (e.g. Val et al., 2016; Pingel et al., 2013).

At high latitudes, only one study is available (offshore record, Bierman et al., 2016) and shows that E. Greenland was subject to a consistent increase in erosion rates since 7.5 Ma onwards. However, it is difficult to constrain the catchment over time, since the provenance can remain undetermined because of the fluctuations of drainage divides with ice growth or the nature of the record, the ice raft debris (IRD) deposited by icebergs.

The rest of the studies were obtained at mid latitudes. In Central Asia, Tianshan (Figure II-33), Charreau et al., 2011; Puchol et al., 2017 show an acceleration of erosion since 9 Ma onwards for 4 catchments. This acceleration seems to slow down after 3-4 Ma with an increase in the variability of denudation rates. Importantly Puchol et al., 2017 show that accumulation rates in these foreland basins, which increased in 3 of the catchments at ca. 11 Ma (Charreau et al., 2005; Charreau et al., 2006; Charreau et al., 2009b) are decorrelated from erosion rates, contrarily to the assumption of Zhang et al., 2001; Molnar, 2004.

In North America and West Europe (early compilation of Granger and Schaller, 2014), there is no global acceleration of erosion rates, even if several studies do show an acceleration (Europe: Alps, Haeuselmann et al., 2007; Meuse rivers, Schaller et al., 2004; Vltava and Guadalquivir rivers, Schaller et al., 2016; North America: Cumberland plateau: Anthony and Granger, 2007; Rocky Mountains, Refsnider et al., 2010) in particular at 0.7 - 1 Ma (Haeuselmann et al., 2007).

II.6.4. The detrital thermochronometric record

II.6.4.1. A few words about thermochronometry

Thermochronometry (review in Reiners and Brandon, 2006), also coined thermochronology, gives access to long-term denudation rates. Radioactive decay and spontaneous fission of the isotopes of certain father elements, such as U or K, produce daughters such as noble gases and damage trails in crystals, and the measurements of fathers and daughters yield apparent ages. These ages depend on the natural diffusion or annealing of daughters over time, which occur when the crystals are above a certain closure

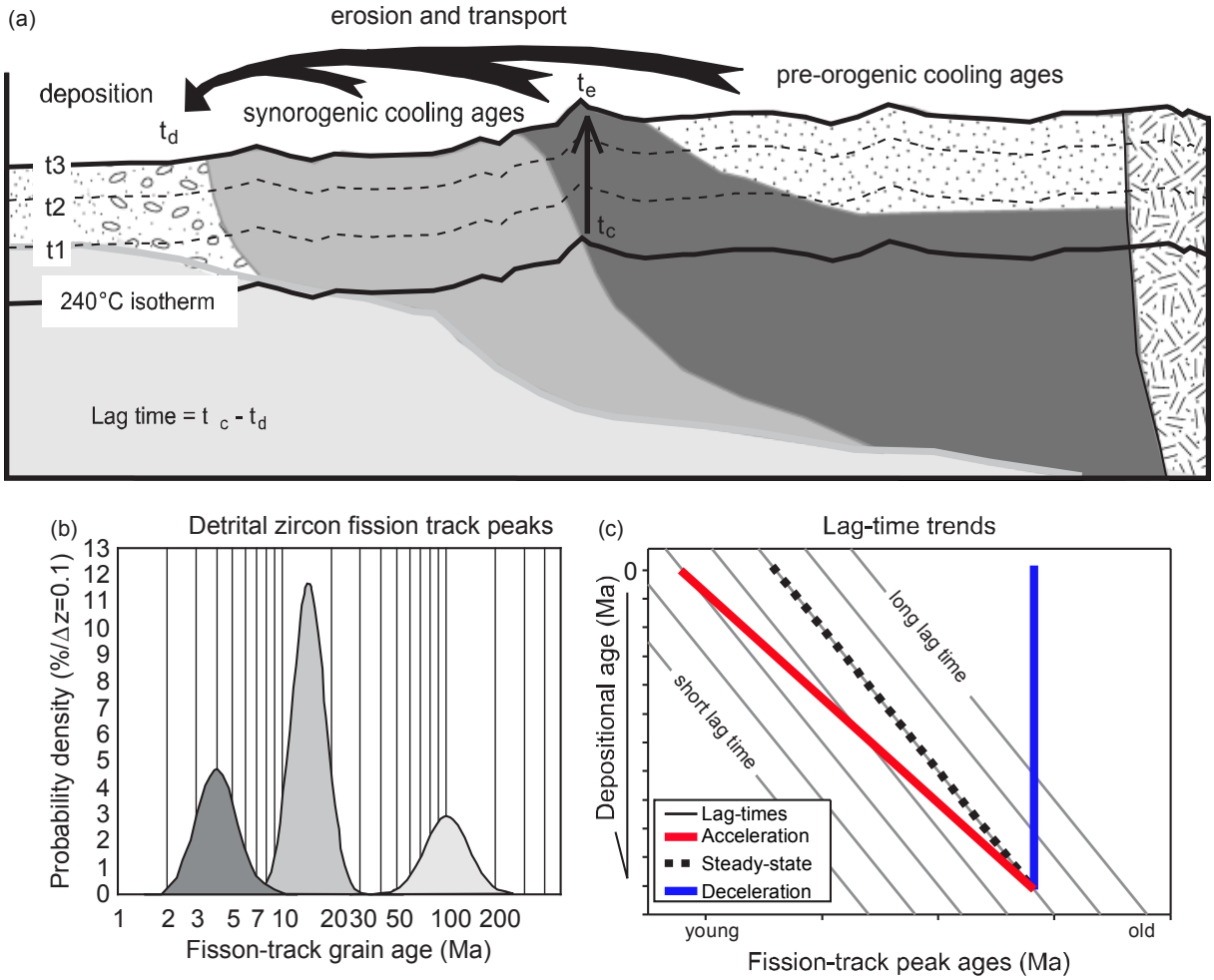

Figure II-34. Principle of detrital thermochronometry.

a. Lag-time concept for simple vertical denudation path. t_c, time of closure of the thermochronometric system; t_e, time of erosion; t_d, time of deposition.

b. Example of probability density plot, yielding best fit peaks that may be derived from the coloured areas in a.

c. Three possible lag-time trends that reflect trends in denudation (figures modified from Bernet et al., 2006).

temperature. This closure temperature depends on the isotopic system and the denudation path of the

rocks. As rocks exhume, they cool down across the Earth's temperature field and this travel can be inversely reconstructed from the thermochronometric ages, which led to long-term denudation rates.

Thermochronometry can be applied in situ, i.e. on bedrock or on sediments, and in that case is coined detrital thermochronometry. To better constrain the evolution of erosion rates, several thermochronometers can be measured. Low temperatures systems include luminescence apatite (U–Th)/He (40-60 to 120°C, Flowers et al., 2009; Gautheron et al., 2009) and the complementary method $^{4}He/^{3}He$ (20-70°C, Shuster and Farley, 2004), apatite fission track (60-120°C, Gallagher et al., 1998), zircon (U–Th)/He (140-220°C, Guenthner et al., 2013), zircon fission tracks (240-300 °C, Rahn et al., 2004). Luminescence, which includes optically stimulated luminescence (OSL) and thermoluminescence (TL) thermochronometry, complement these methods (OSL: 30-100°C, King et al., 2016b). The principle of luminescence is based on the trapping and thermal release of electrons in crystals, in reaction to in situ radiation and rock cooling (review in Herman and King, 2018). Its application is currently limited to rocks subject to erosion rates > 2-3 mm/yr, i.e. in tectonically active regions.

Conversely to $^{10}Be/^{9}Be$ which yields denudation rates averaged across a catchment, detrital thermochronology (e.g. Bernet and Spiegel, 2004) usually gives access to long-term maximum denudation rates from a catchment. The denudation rates are obtained from the lag-time (Figure II-34), i.e. the difference between the thermochronological and depositional ages of the sample (Garver et al., 1999; Bernet et al., 2001, 2006; van der Beek et al., 2006), with the assumption that transport time is negligible compared to the cooling time of minerals, and frequently employing a numerical thermal model (e.g. Brandon et al., 1998; Rahl et al., 2007; Whipp et al., 2007; Braun et al., 2012). A steady lag-time would point to steady denudation; a decrease in the lag-time would point to an acceleration of denudation, and conversely for an increase in the lag-time.

Detrital thermochronology requires several points to be taken into consideration. Sediment samples typically contain multiple age components, and the youngest component is frequently the only one considered for interpretation in lag-times. These age components are determined by inverse modelling the population of single grain ages of a sample (e.g. Brandon, 2002; brief review in Naylor et al., 2015). As demonstrated in Naylor et al., 2015 and classically overlooked in studies, the resolution of this modelling can be different along the stratigraphic record, with in particular lower resolution for older samples. In that case, the modelling can induce artificial shifts in lag-times that which prevent a correct interpretation.

Denudation rates derived from detrital thermochronometry are maximum denudation rates (e.g. van der Beek et al. 2006) and they characterize only the area that erodes the more rapidly, independently of the evolution of the location and the relative size of this area. Superimposed to this consideration, mineral fertility may be variable across the catchment (e.g. central Himalaya, Amidon et al., 2005; Alps, Malusà et al., 2017; central Europe, Glotzbach et al., 2018), and lagtimes might reflect only a limited part of the catchment. In addition, some thermochronometers are subject to hydraulic sorting (e.g. muscovite $^{40}Ar/^{39}Ar$, Gemignani et al., 2018) or abrasion during transport (e.g. apatite (U-Th)/He, Rosenkranz,

2018), which can influence the results.

For the thermochronometers sensitive to the lowest temperatures, in particular apatite fission tracks and apatite (U-Th)/He, samples may have been thermally partly reset during burial and present thermochronometric ages younger than depositional ages, thus preventing the determining of lag-times (e.g. Gavillot et al., 2018).

Furthermore, a shift in denudation involves a progressive modification of the thermal field. As explained in Rahl et al., 2007, this modification is non-linear, and time of several Myr can be required to allow the unreset rocks to be denuded and the thermal field to get back to a steady state. Therefore, the thermochronometers sensitive to the lowest temperatures present an improved ability to determine the erosion history, even though all thermochronometers produce histories with large uncertainties in case of rapid changes in denudation rates (Rahl et al., 2007). Additionally, the resolution of most thermochronometers in environments with low denudation rates (≤ 0.5 mm/yr, Rahl et al., 2007) is undoubtedly too low to detect changes that happened in the late Cenozoic.

II.6.4.2. Detrital thermochronometric data

A not exhaustive compilation of detrital thermochronometric data is presented Table SII-4. To our knowledge, no dataset in Central Himalaya (e.g. Figure II-35, van der Beek et al., 2006; Chirouze et al., 2013) and the European Alps (e.g. Glotzbach et al., 2011) indicate an acceleration of maximum denudation in the late Cenozoic. However, a Zircon fission track and white mica $^{40}Ar/^{39}Ar$ dataset from the foreland basins close to the Himalayan eastern syntaxis (Lang et al., 2016) and a zircon fission track and rutile U-Pb dataset from the Bengal Fan (Figure II-36, Najman et al., 2019) indicate an acceleration at 3-7 Ma, which has been interpreted to be linked to the Namche Barwa denudation. These results remain presently contradicted by apatite and zircon fission tracks data from the Bengal Fan that show steady denudation since 9-12 Ma (Huyghe et al., 2019).

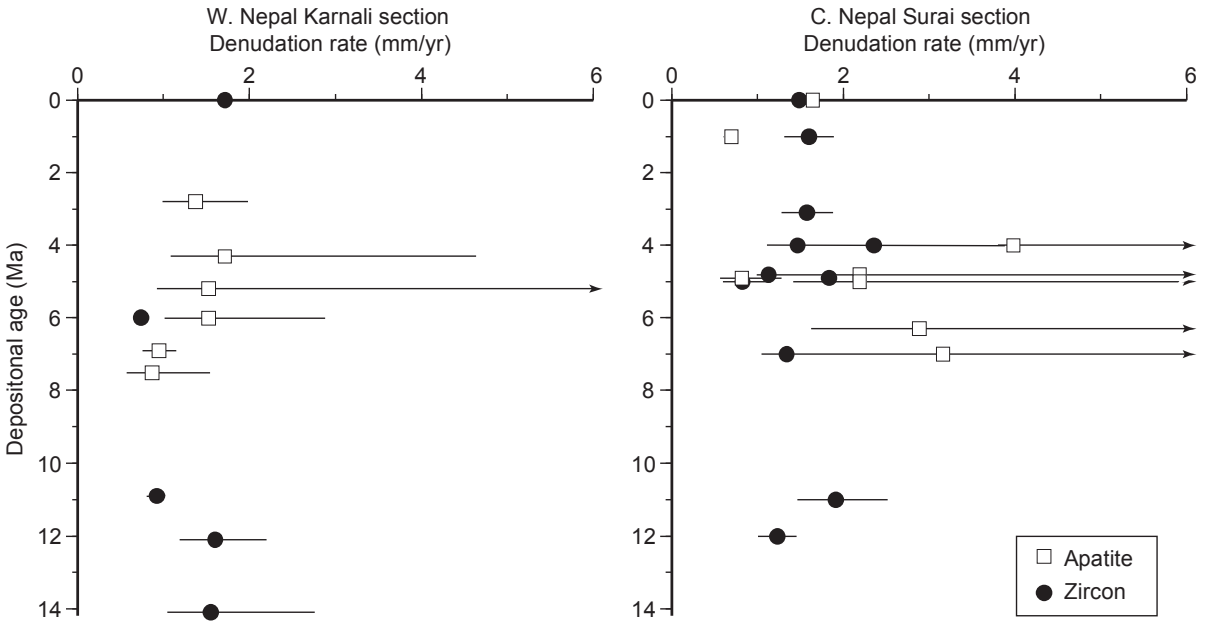

Figure II-35. Thermochronometric peak denudation rates in Central Himalaya since 14 Ma.

Zircon and apatite fission track peak denudation rates for the Karnali and Surai Siwalik sections. The rates are derived from lag-times with a modified version of the 1-D thermal model of Brandon et al., 1998. Uncertainties are computed from 2-σ uncertainties of peak or central ages (modified from van der Beek et al., 2006).

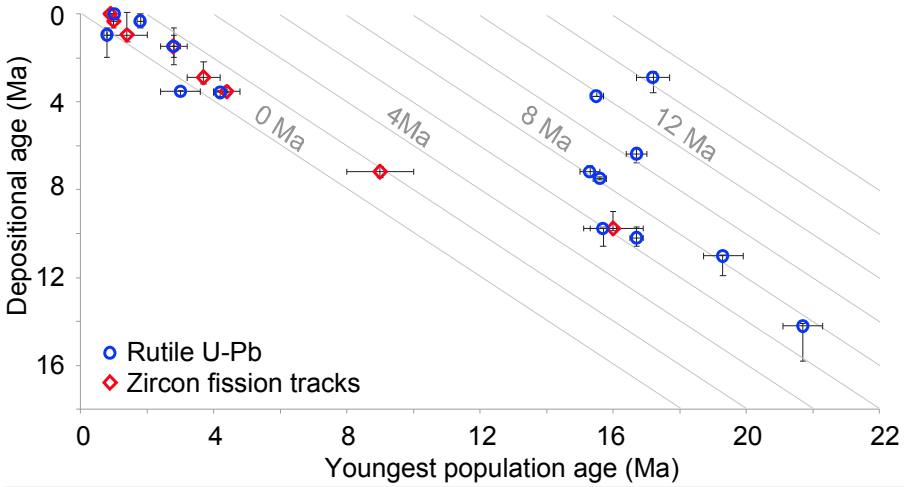

Figure II-36. Thermochronometric lag-times from the Bengal Fan Exp. 354 since 14 Ma.

Lag-times for rutile U-Pb and zircon fission tracks derived from the youngest population obtained with the algorithm of Galbraith, 2005 implemented in DensityPlotter (Vermeesch, 2012). Note that white mica $^{40}Ar/^{39}Ar$ and apatite U-Pb (Najman et al., 2019), along with apatite fission tracks (Huyghe et al., 2019) extracted from the same sites do not show this shift in lagtimes observed in rutile U-Pb at 4 Ma (modified from Najman et al., 2019).

II.6.5. The in situ thermochronometric record

While detrital methods give access to the overall denudation of a catchment, in situ methods give insight on the local evolution of denudation, which may be more easily related to determined processes of erosion. This has been the case concerning regions impacted by glaciations. Acceleration of denudation was observed using low temperature thermochronometers such as apatite (U-Th)/He and $^{3}He/^{4}He$, and sometimes apatite fission tracks. The setup of this acceleration is progressive from high latitudes to lower latitudes (Valla, 2018): ca. 30-35 Ma in Antarctica (Thomson et al., 2013) and Greenland (e.g. Bernard et al., 2017), ca. 5-7 Ma in South Andes (Patagonia, Thomson et al., 2010), ca. 1.8-2 Ma in New Zealand (Shuster et al., 2011) and in North America (British Columbia, Shuster et al., 2005), ca. 1 Ma in Western European Alps (Valla et al., 2011, 2012; but the acceleration may have initiated earlier, Vernon et al., 2008) and potentially in Central Himalaya (Huntington et al., 2006; Blythe et al., 2007), although this latter case might be unrelated to glaciations (e.g. Thiede and Ehlers, 2013).

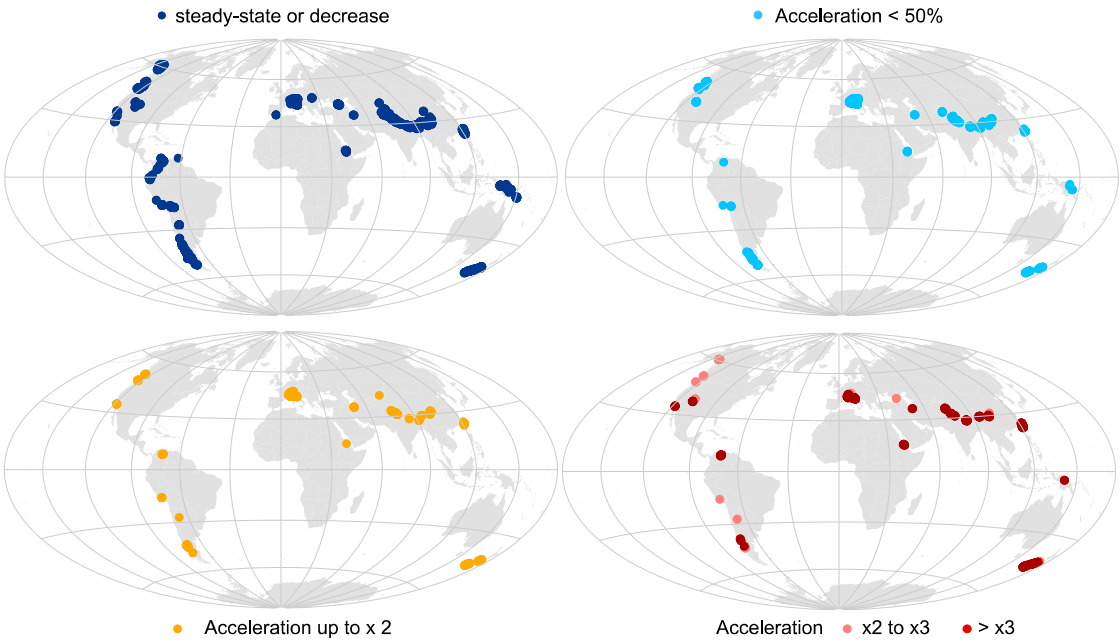

Figure II-37. Worldwide in-situ denudation rates 2-0 Myr ago vs denudation rates 6-4 Myr ago.

The panels present the results of the 1-D thermal inversion of Herman et al., 2013. Each panel presents the locations where the ratio of denudation rates 2-0 Myr ago on denudation rates 6-4 Myr ago is ≤ 1 (i.e. steady state or deceleration of denudation), and where this ratio is > 1 (i.e. acceleration), with several class values displayed. Note that the regions with enough resolution can locally present a large variation of the ratio. Herman et al., 2013 applied the code of Fox et al., 2014 to their compilation of multi-thermochronometer measurements, then spatially interpolated their results and computed a spatial resolution parameter. They compute the denudation rates by bins of 2 Myr. The panels only show their results when their resolution parameter > 0.25.

Herman et al., 2013 (Figure II-37) compiled ~18,000 thermochronometric data of various thermochronometric systems and derived worldwide denudation rates using a linear inversion method (Fox et al., 2014). This linear inversion method has been debated because it may combine samples with separate denudation histories, which may led to artificial changes in denudation rates (Schildgen et al., 2018; Herman et al., 2019). The work of Herman et al., 2013 shows that the majority of thermochronometric datasets do not have the resolution to determine whether a global acceleration in denudation occurred, because of low spatial resolution, an insufficient number of thermochronometers measured, or because of low denudation rates, which concern all not tectonically active regions. However, this work also evidences that active orogens, among them the European Alps, the Andes, the Rocky Mountains and the Himalaya have locally experienced a coeval 1- to 4-fold increase in erosion rates at ca. 2-4 Ma.

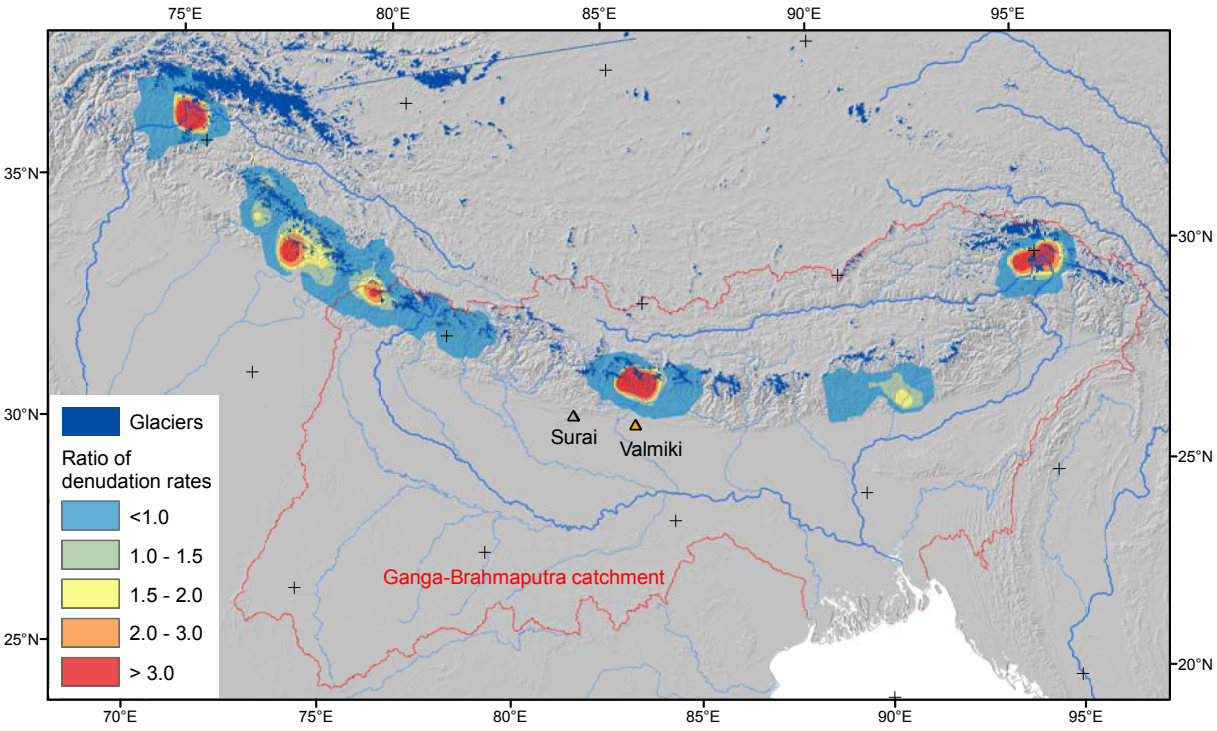

Figure II-38. In-situ denudation rates 2-0 Myr ago / denudation rates 6-4 Myr ago for the Himalaya.

Focus on the Himalaya of the results of Herman et al., 2013. We re-interpolated their denudation rates with ordinary kriging for display, excluding their areas with a limited number of data or having their resolution parameter < 0.25.

II.7. POSSIBLE CAUSES FOR AN ACCELERATION OF DENUDATION RATES

II.7.1. Have sea-level fluctuations altered export of sediments to the deep sea?

To explain the variations of sediment deposition, some workers advanced that global sea-level fluctuations may have alter the partitioning of sediments between the shelf, the slope and rise and the deep sea (Worsley and Davies, 1979; Hay, 1988a, b). This hypothesis has a link with the emergence of sequence stratigraphy (e.g. Posamentier and Vail, 1988, Vail et al., 1991) and the research about turbiditic fans (review in Bouma and Stone, 2000; e.g. Congo-Zaire fan, Savoye et al., 2009; Bengal Fan, Curray et al., 2003). Deposition on the continental margins or their erosion is driven by accommodation space, which originates from the balance between the sedimentary flux, subsidence, and sea-level. The global sea-level controls this balance at 10-100 kyr timescales (e.g. Hay et al., 1988b). A high sea-level favours deposition on the continental margin whereas a low sea-level favours incision of the shelf and produces the bypass of sediments and their export to the deep sea (Figure II-39).

The growth of ice-sheets in the Northern Hemisphere produced the late Cenozoic global drop of average sea-level (Miller et al., 2005, 2011). Coevally the sea-level variations in elevation increased (~100-140 m, Miller et al., 2005) with the variations of the shoreline position (~100 km). This would have induced both an acceleration of shelf denudation, progradation of deltas and an acceleration of accumulation in the deep sea.

However, the sediment export to the deep sea is probably not limited to periods of low-stand, contrary to the predictions of the early sequence stratigraphic models (e.g. Posamentier and Vail, 1988, Vail et al., 1991). Burgess and Hovius, 1998 show that the timespan to form a delta is longer than periods of high-stands, which suggests that deposition also occurs during high-stands, as shown during the Holocene for the Bengal Fan (Figure II-40, Bergmann, 2018, and earlier studies of Weber et al., 1997, 2003; Mitchell et al., 2003).

The sea-level fluctuations also trigger drainage reorganisation, particularly in wide continental margins, when low-stands favour large drainage basins (e.g. North Sea, Overeem et al., 2001; Barent's sea, Laberg et al., 2010). As seen above, these reorganisations have an impact on accumulation.

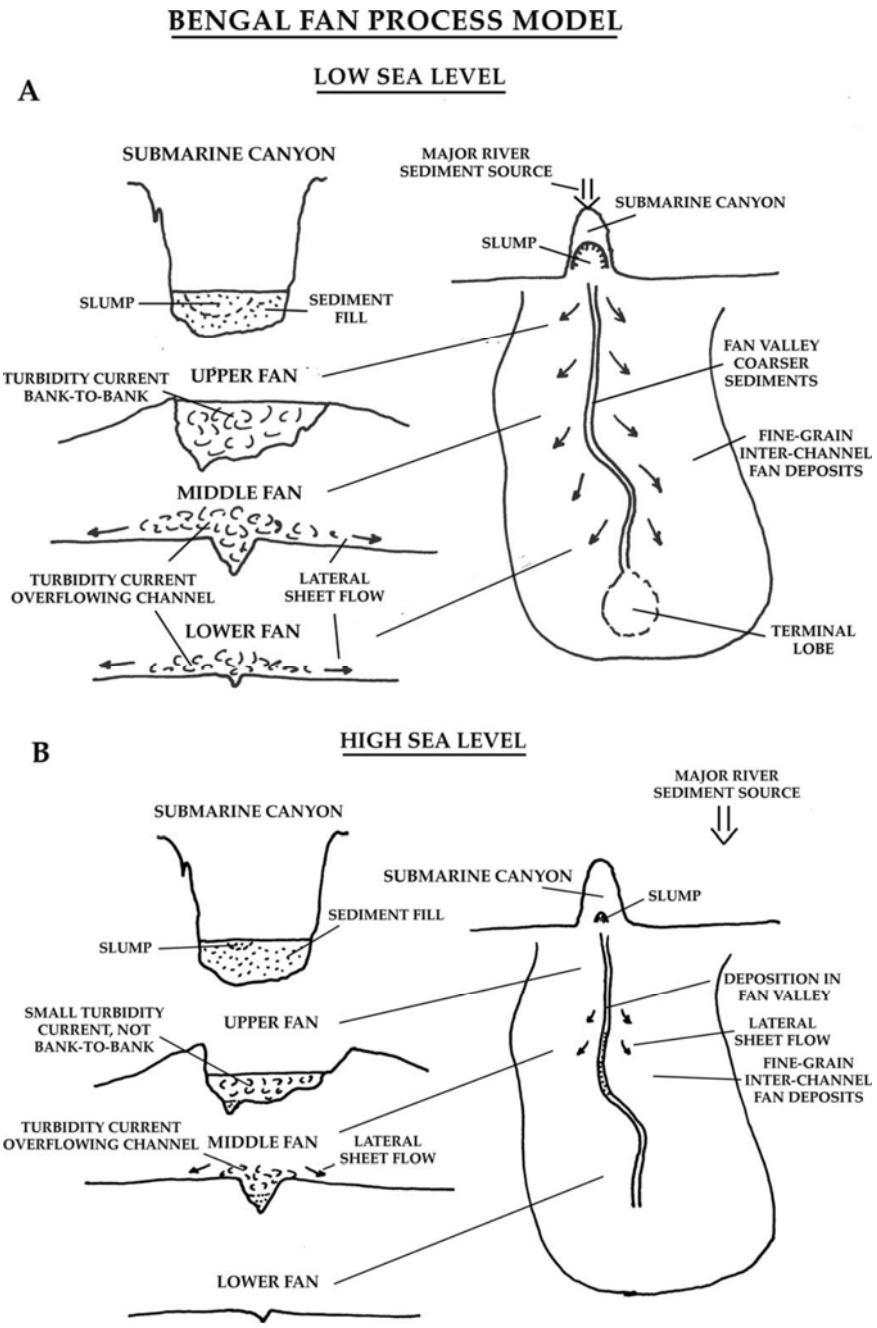

Figure II-39. Classic turbiditic deposition model fluctuating with sea-level.

In this model, a large turbiditic fan, such as the Bengal Fan, is fed mainly during low sea-level, when the submarine canyon may be directly connected to the delta. During high sea-level, only the upper part of the fan is fed (from Curray et al., 2003).

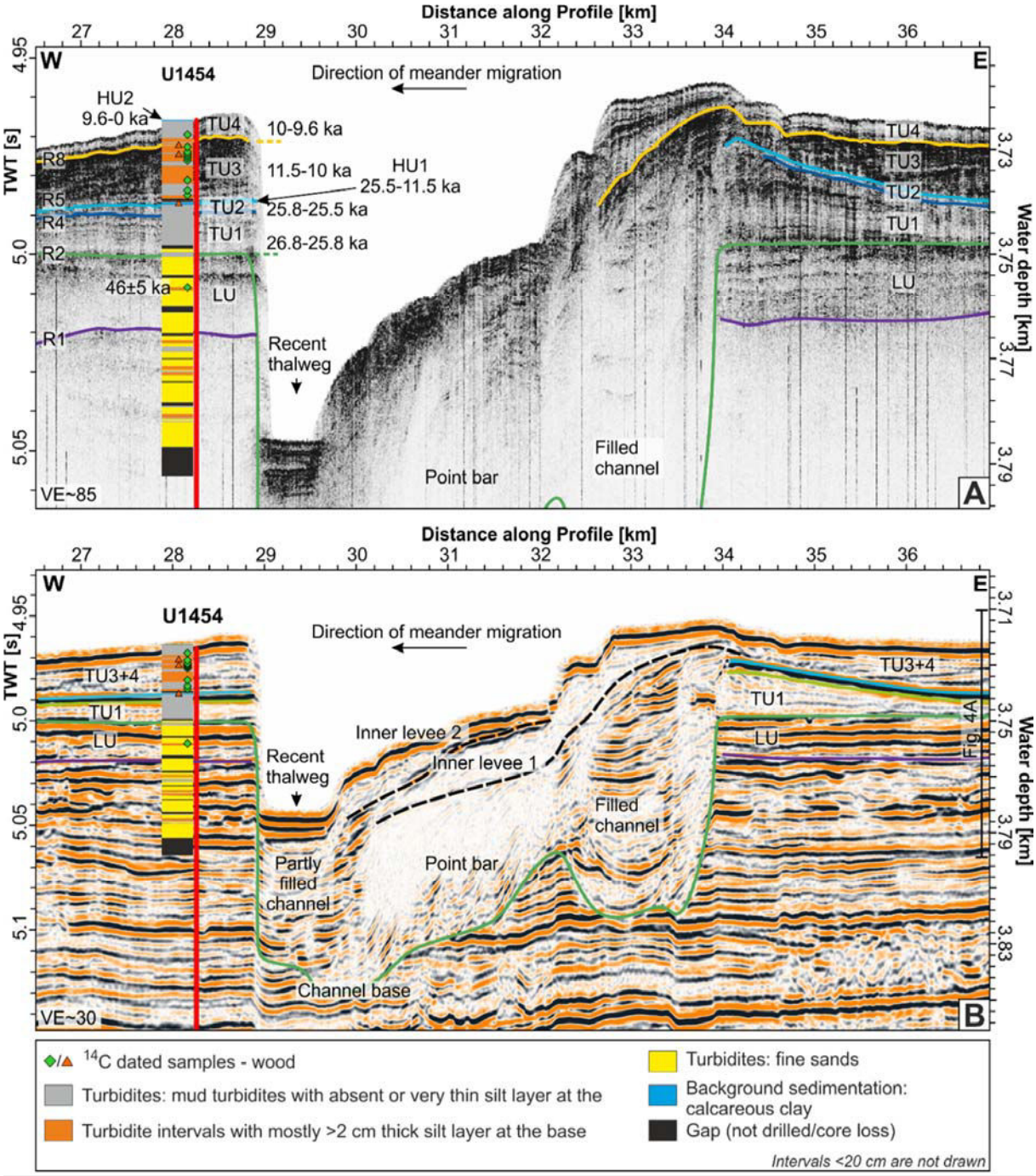

Figure II-40. Turbiditic deposition in Exp. 354 site U1454 during the Holocene sea-level rise.

A. very-high-resolution parametric sediment echosounder (Parasound) data along with the stratigraphic log of U1454 (France-Lanord et al., 2016a; location in Figure II-4) and the levee units.

B. same profile showing the high-resolution multichannel seismic (MCS) data along with the log, with a different vertical scale. Not the vertical exaggeration of the profiles. Parasound and MCS data were obtained during the cruises SO93 in 1994 and SO125 in 1997 (from Bergmann, 2018).

II.7.2. Active tectonics

To explain the global increase in the atmospheric CO_2 concentrations in absence of a change in mid-ocean ridge spreading (Sclater et al., 1981; Cogné and Humler, 2008), Raymo and Ruddiman, 1992, considered the tectonic uplift of the Himalaya and the Tibetan plateau which still was temporally poorly constrained at the end of the 20th century (e.g. Tapponier et al., 2001, see subchapter Himalaya). The modern Himalaya yields a large proportion of dissolved flux (e.g. Milliman and Farnsworth, 2011), which might suggest that relief and precipitations had a stronger control on chemical weathering than temperature (Raymo and Ruddiman, 1992), a hypothesis which remained unsustained (e.g. Willenbring and von Blanckenburg, 2010; Lupker et al., 2012a). Not only the Himalayan uplift would have caused an acceleration of physical and chemical weathering, but the combined uplift of the Tibetan plateau would have produced intense monsoonal precipitations, which would have in turn reinforce this acceleration.

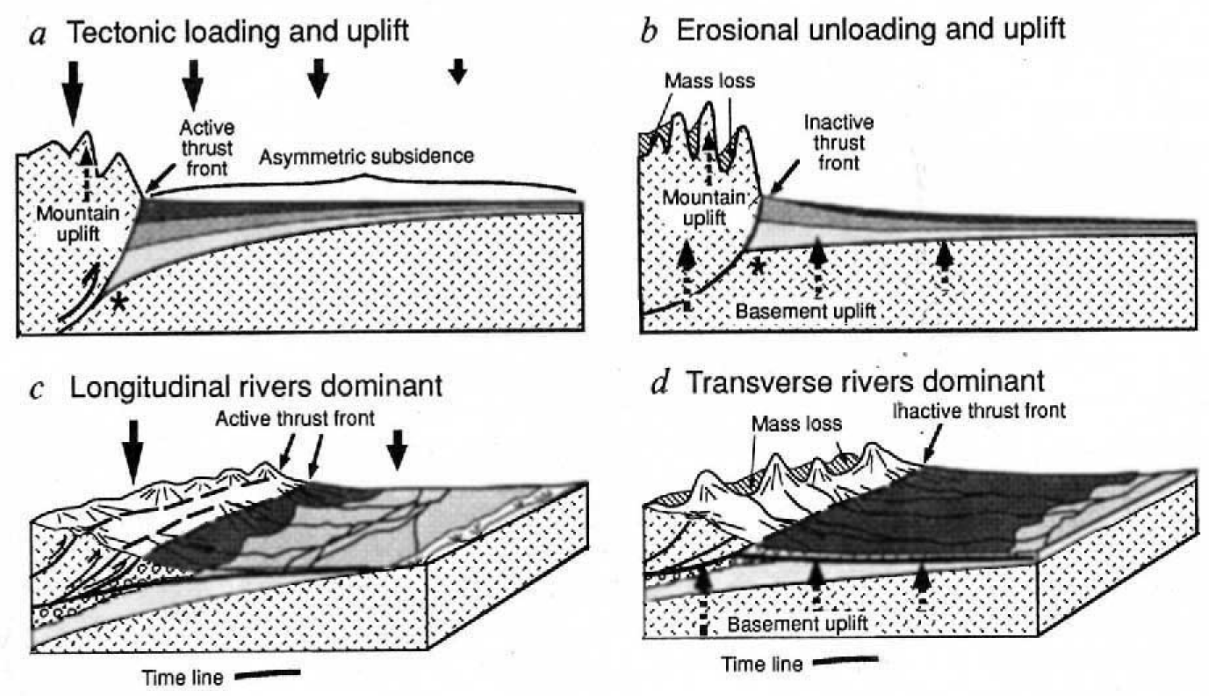

Figure II-41. Foreland deposition patterns depending on tectonic loading or erosional unloading.

a. Tectonic deformation produces regional uplift of the mountain range and asymmetric subsidence (arrows) in the foreland basin and wedge-shaped sedimentary strata thicken towards the thrust front.

b. Erosional unloading reduces the mean elevation and the crustal thickness below the mountain rang, which leads as a reaction to peaks and the foreland basin uplift (dashed arrows). New sedimentary are strata are tabular.

c. and d. This difference in uplift also produce different drainage networks, dominated by longitudinal rivers flowing close to the range for the case a., and by transverse rivers which prograde across the foreland and restrict the longitudinal rivers to the distal part. (from Burbank, 1992).

Opposing the Raymo and Ruddiman, 1992's thesis, Molnar and England, 1990 demonstrated that the paleobotanical markers point to climate change instead of increase in elevation. Similarly, the geomorphological and stratigraphic markers that point to supposedly "youthful landscapes" and that are classically used to sustain late Cenozoic mountain uplift only involve accelerated physical erosion and incision, which decrease mean elevation. Erosion produces in turn uplift of mountain ridges and peaks by isostatic rebound, which cannot fully negate the impact of erosion on mean elevation. In opposition to Raymo et al., 1988, Molnar and England, 1990 posited that climate cooling was the original driver of a potential acceleration of erosion and not the reverse, and that accelerated erosion only further degraded climate by a positive feedback.

This topic of isostatic-flexural response of mountain ridges to acceleration of denudation has also been used to explain the apparent reduction of accumulation in the Ganga Himalayan foreland basin (Figure II-41, Burbank, 1992). However, Whipple et al., 1999 show that the formation of relief linked to this process is probably limited in active tectonic mountain ranges.

Even though there is neither global tectonic uplift or any major tectonic uplift to explain a possible increase in denudation rates in the late Cenozoic, one can only observe that tectonics and climate often combine to produce ones of the regions with the highest denudation rates, such as the Himalaya, Taiwan (e.g. Dadson et al., 2003) and Borneo (Milliman and Farnworth, 2011). Shifts in tectonic patterns of different types have been evidenced for the late Cenozoic in the eastern Himalaya (e.g. Zeitler et al., 2014; Bracciali et al., 2016; King et al., 2016a; see chapter above), in New Zealand (review in Jiao et al., 2017), in Taiwan (review in Beyssac et al., 2007) and in the European Alps (e.g. Baran et al., 2014; Fox et al., 2015). All of these examples show an apparent acceleration of denudation during the late Cenozoic, but the respective roles between tectonics and climate remain delicate to disentangle (King et al., 2016a; Jiao et al., 2017).

II.7.3. A shift to dry and stormy climate?

With their thesis, Molnar and England, 1990 followed early workers who assumed that global climate change rather than tectonics was the driver of these variations of sediment accumulation in the deep sea. In their seminal paper, Davies et al., 1977 acknowledge that continental denudation in modern times is lower in arid regions such as Australia than elsewhere and advance that a potentially wetter climate in the late Cenozoic may have accelerated denudation. Even though wetter conditions, following an arid period, were effectively observed in some regions as in SW North America (Antevs, 1952; Chapin, 2008; Galloway et al., 2011), the hypothesis of a global amplification of precipitations coeval with global cooling is contradicted by the progressive expansion of grasslands over woodlands since 24 Ma (review in Retallack, 2001; compilation in Edwards et al., 2010) and the drying of Africa (review in Demenocal, 1995) and Asia (Detmann et al., 2001; review in Clift and Webb, 2018).

Molnar and England, 1990 and Molnar, 2001 advance that a stormier climate caused by the

increase in the latitudinal gradient of atmospheric temperatures could explain that erosion may have accelerated in spite of a worldwide increased aridity. They reconsider the frequent "thick deposits of conglomerates dated from the Cenozoic [which] surround steep mountain ranges", a potential evidence of a change of frequency and intensity of fluvial discharges. In areas where tectonics and ice are absent, river incision becomes the dominant process in mechanical denudation. River incision is controlled by the capacity of the river to transport bedload, which is favoured during high discharge caused by heavy storms or upstream snowmelt. In modern and late Pleistocene times, arid climates are characterized by rarer and more intense floods than wet climates (Turcotte and Green, 1993; Molnar, 2001 and Dead Sea Pleistocene lacustrine deposits, Frostick and Reid, 1989). This suggests that climate cooling and drying may have

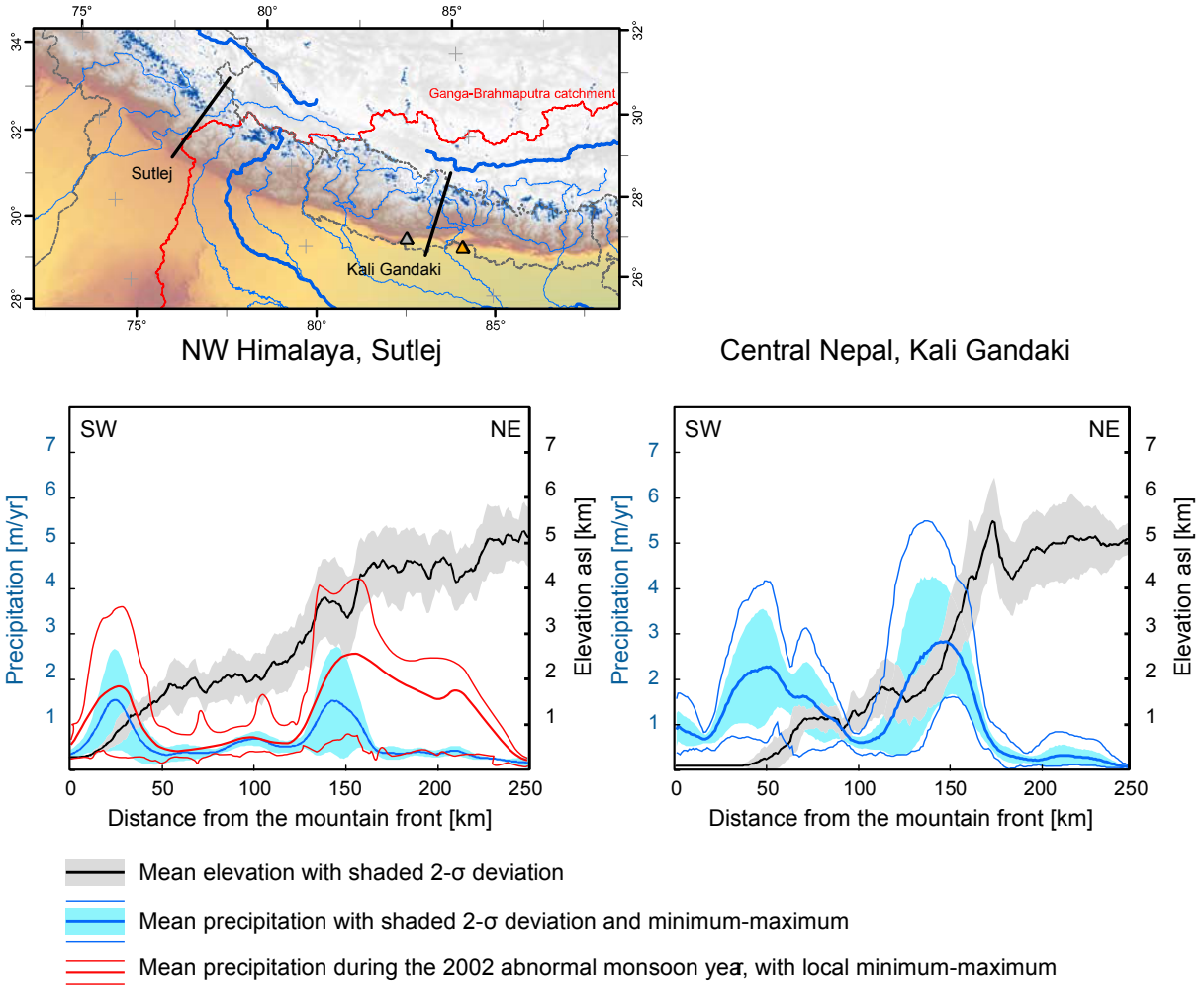

Figure II-42. Himalayan precipitation swath profiles with the effect of abnormal monsoon years.

The precipitation profiles are centered along 2 transversal Himalayan valleys, and derived from passive microwave data (1992-2001) acquired from the Special Sensor Microwave/
Imager (SSM/I) of the polar-orbiting Defense Meteorological Satellite Program (DMSP). (modified from Bookhagen et al., 2005).

increased the intensity and the frequency of rare floods, and thus increased erosion rates, despite a decrease in average discharge (Molnar and England, 1990; Molnar, 2001).

It should be noted that the hypothesis of a higher capacity of fluvial transport of sediments is compatible with the sea-level cause hypothesis, and would have enhanced the effects of lowstands with large volumes of sediments exported to the deep sea.

However, this hypothesis that a drier climate favours erosion is not sustained by the sedimentary record of continental margins, for which accumulation decelerate during the drier episodes at ca. 5-10 Ma (NW Gulf of Mexico, Hay et al., 1989; Galloway et al., 2011; Indus Fan and Pearl River mouth basin, Clift et al., 2002; Clift, 2006; Red River, Clift, 2006; Indo-Gangetic floodplain, Métivier et al., 1999). Additionally, the modern global sedimentary load is not dominated by arid regions, such as Australia, but by South Asia (compilation in Milliman and Farnsworth, 2011, p. 28 and p. 43), characterized by the combination of active tectonics and a warm and wet climate.

II.7.4. A shift to variable climate?

In contrast with Davies et al., 1977, Donnelly, 1982 advances that climatic conditions by themselves, either wet or glacial/periglacial conditions, cannot have such a large and global impact on denudation rates. With an analogy with erosion processes in Australia (Douglas, 1967), his thesis posits that the increase in the climatic variability during the late Cenozoic effectively favoured an acceleration of denudation.

Zhang et al., 2001 and Molnar, 2004 further developed this theory by contending that a potential absence of a steady state between relief evolution and denudation might lead to an acceleration of denudation in the late Cenozoic. They observe that the deep sea $\delta^{18}O$ record (Figure I-2, Figure II-18, e.g. Zachos et al., 2001; Lisiecki and Raymo, 2005; Cramer et al., 2009) presents a progressive increase in the peak to peak variations, from 0.5‰ at 4 Ma to 2‰ at ca. 1 Ma, through the start of glaciations in the Northern Hemisphere at ca. 2.6 Ma (Shackleton et al., 1975).

In addition to the deep sea $\delta^{18}O$ record, Zhang et al., 2001 also observe the aeolian sedimentary record in North China, consisting in loess interlayered by paleosols (Porter et al., 1992; review in Zhang et al., 2001 and Muhs et al., 2003). They advance that both records show a switch from a stable climate to a climate rapidly evolving from dry and cold to wet and warm extreme conditions, i.e. icehouse to greenhouse, and reversely. According to them, greenhouse might precondition bedrock by periglacial fractures, landslides or soil production. Icehouse in turn might favour transport either by glaciers or by stormy floods. Because the landscape response time to a change in denudation is too long (~0.5-2.5 Myr, Whipple, 2001) compared to the length of orbital cycles (see above, Figure II-13, eccentricity: 100 and 400 kyr, obliquity: 41 kyr, precession: 19 and 23 kyr), this switch might prevent any steady state between relief evolution and denudation, and thus lead to an acceleration of denudation.

This thesis appears appealing because it suggests that glacial erosion is not the main driver of the acceleration of denudation. This could explain why accumulation rates do not increase coevally with climate cooling from 15 Ma onwards ($\delta^{18}O$ curve of Zachos et al., 2001) and why accumulation rates remain low at 25-35 Ma, despite a cool period characterized by the setup of the Antarctic ice-sheet and the related initiation of bottom cold water currents in the Southern Hemisphere.

However, the very foundations of this thesis can be debated. When they write "the change from a virtually unchanging climate to one that has been changing rapidly, as dictated by Milankovitch forcing", Zhang et al., 2001 implicitly suggest that the deep sea $\delta^{18}O$ variations increase in frequency over time, i.e. from an almost null frequency to a high frequency, which is incorrect (Figure II-18, Zachos et al., 2001; Cramer et al., 2009). They are based on 19-23 kyr precession cycles in the early Cenozoic and shift to 40 kyr obliquity cycles at ca. 33 Ma, coeval with the setup of the Antarctic ice-sheet. Furthermore they are dominated by 100 kyr eccentricity since 0.7-0.8 Ma (Liesiecki and Raymo, 2005). In addition, from 33 Ma onwards, the $\delta^{18}O$ record is dominantly impacted by the volume of ice-sheets and thus the increase in amplitude does not necessarily imply an increase in amplitude of temperatures. The compilation of sea surface temperatures by Herbert et al., 2016 shows that an increase in the amplitude of temperatures effectively occurs regionally, but not globally. Although some areas such as North China (Porter et al., 1992; review in Zhang et al., 2001 and Muhs et al., 2003) and Scandinavia (e.g. Hjelstuen et al.,1999; Rise et al., 2005; Dowdeswell et al., 2010) were subject to extreme variations, others, such as Borneo (Hall and Nichols, 2002; Morley and Back, 2008), appear to have been subject to steady climatic conditions over the late Cenozoic.

II.7.5. Enhanced glacial erosion?

Even though early workers (Molnar and England, 1990; Zhang et al., 2001) raised the possibility that glaciations produced an acceleration of erosion, the thesis that glacial erosion had a severe impact on worldwide mountain ranges was only developed since the paper of Herman et al., 2013. In tectonically active mountain ranges, fluvial and glacial erosion rates can reach similar values (Hallet et al., 1996; Koppes et al., 2012), probably because tectonics already supply a consistent volume of fractured rocks. But it is not systematically the case (e.g. Montgomery, 2002). In general, glacial erosion (Figure II-21), produced by quarrying and abrasion, presents spatially highly variable rates and depends on the ice-sliding velocity (e.g. compilation of Hallet et al., 1996; Central Nepal, Godard et al., 2012). The velocity is controlled by snow accumulation, which increases with precipitation and steep relief, as shown for the Franz Josef Glacier, New Zealand (Figure II-43, Herman et al., 2015). As demonstrated in Herman et al., 2015, the control of snow accumulation and slope on velocity and the control of velocity on erosion are non-linear. This means that in areas of fast sliding (i.e. mainly in glacial valleys), a minor change in climate or relief delivers a substantial impact on erosion rates.

The impact of glacial erosion goes beyond glacial valleys. Using numerical modelling, Steer et al.,

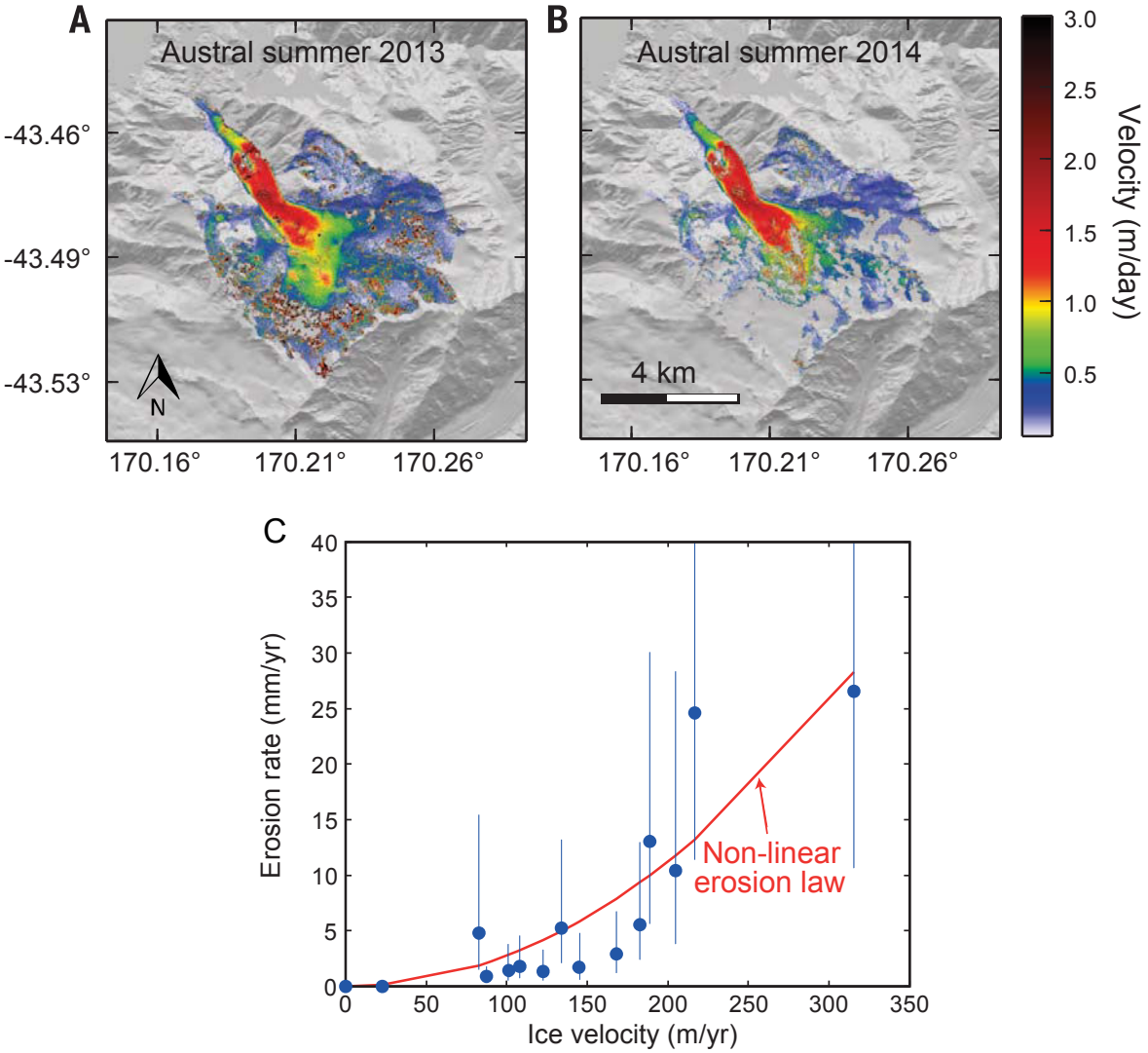

Figure II-43. Distribution of glacial surface velocity and link with erosion, Franz Josef Glacier, New Zealand Southern Alps.

a. and b. Average 3-D surface velocity reconstructed from the measurement of the 3-D displacement of the glacier surface using Worldview stereo images, integrated over 10 (a) and 12 (b) respectively, with 1-σ uncertainty of ⊠0.007 m/day.

c. Erosion rates computed from the suspended load measured with a gauge downstream the glacier terminus from nov, 2013 to apr. 2014, with the (verified) assumption that the volume of sediments stored in the glacier is constant. Erosion rates and velocities integrated on a 1-km bin size. Error bars originate from the temporal variability of the suspended load (modified from Herman et al., 2015).

2012; Pedersen et al., 2014; Egholm et al., 2017 showed that the elevated plateaux at high latitudes were the product of glacial erosion rather than preserved remnants of a preglacial topography, as classically presumed. As proposed by Egholm et al., 2017, glacial erosion may increase or decrease relief in function of "the wavelength of the underlying topography". In addition, glacial erosion has the ability to limit mountain elevation and shape relief above snowline, through the so-called "glacial buzzsaw", evidenced in

North West Himalaya by Brozović et al., 1997. The timing of this buzzsaw can be debated, as Sternai et al., 2013 suggest with numeric modelling calibrated on the Alps that the buzzsaw may occur only lately in glaciations, after the headward propagation of glacial erosion. The impact of glacial erosion is not limited to the region above snowline, as the glaciers also modify the hypsometry below the snowline (Egholm et al., 2009), hence causing a side effect on fluvial incision even during the interglacial period (potential cause of the results of Herman et al., 2010b in New Zealand).

Even though glacial erosion rates were probably important in mountain ranges in the late Cenozoic, there is an open debate about the evolution of glacial erosion at the timescale of several million years. Numerical modelling (Figure II-44, Pedersen and Egholm, 2013) and geomorphologic studies (Alps, Norton et al., 2010) show that early glaciations precondition topography so that the following glaciations expand more rapidly and colonize more easily previously unglaciated areas with minimal climate forcing (e.g. glacial valleys below snowline)). With this thesis, we would expect that as cooling deepens and glaciations extend, glacial erosion rates should increase. However, compilations of short-term and long-term erosion rates (Koppes et al., 2012), along with thermochronometric studies (Tochilin et al., 2012; Christeleit et al., 2017) suggest that the acceleration effect of glaciations on erosion vanishes after several Myr.

The whole reasoning about the acceleration of erosion caused by glaciations may be not valid for tectonically active and wet regions located at low latitudes, in particular in South Asia. Temperatures decrease has been limited compared to mid and high latitudes. Even though glaciations were extensive in the last glacial cycles (e.g. Owen and Dortch, 2014), tectonics combined with the monsoonal climate might rapidly correct during the interglacial period the modification of the hypsometry realised during the glacial period, thus limiting the preconditioning effect that favours large extension of ice-sheets and glacial erosion.

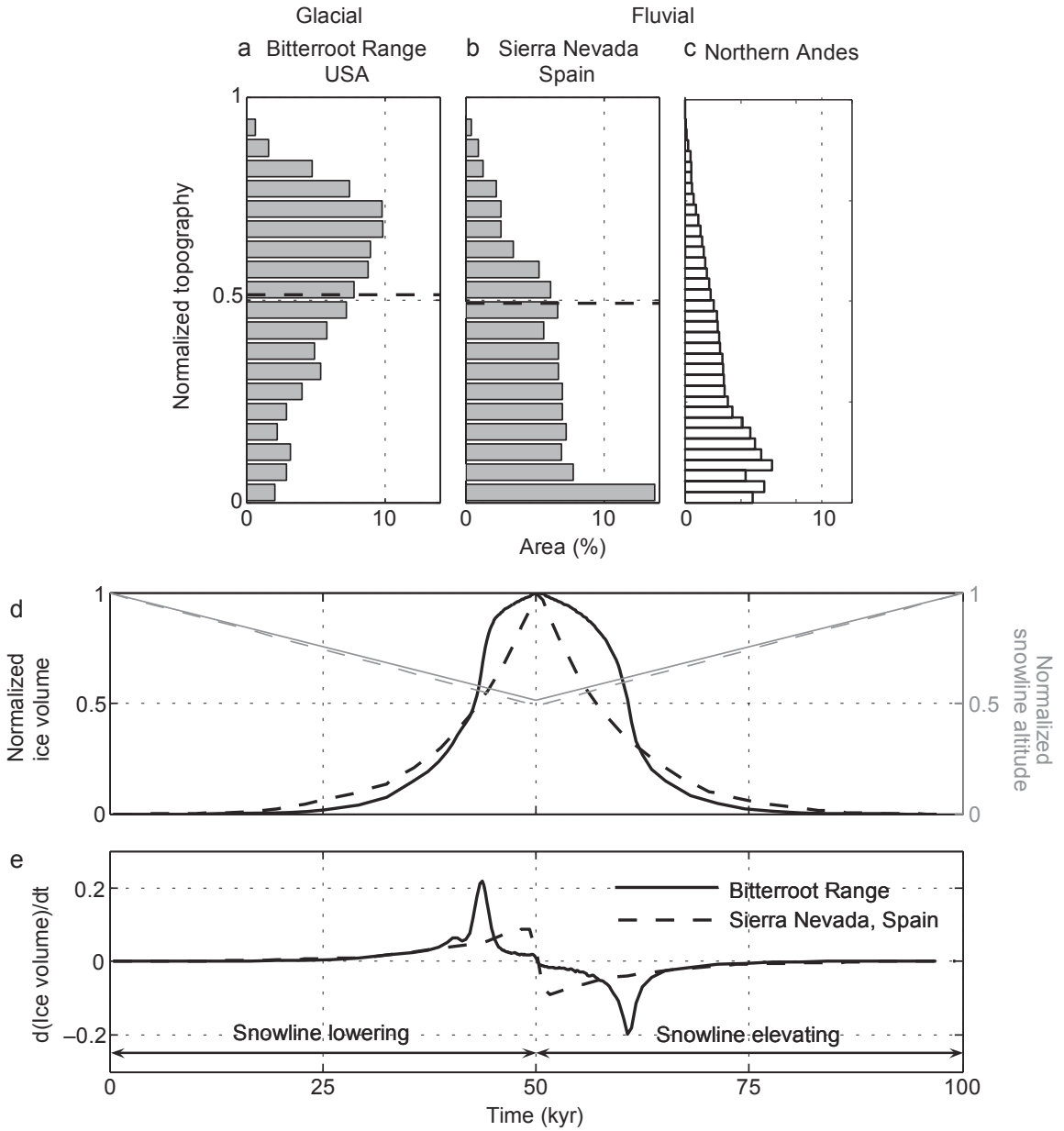

Figure II-44. Ice volumes preconditioned by topography during glaciations, as shown by numerical modelling.

a.(Bear creek catchment, 46.4°N 114.4°W), b. (Aldeire catchment, 37.1°N 3.1°W), c (9°N71°W) represent modern hypsometric distributions of glacial and fluvial landscapes, normalized to the local base level. Dashed lines show the minimum level of the snowline at 50 kyr. The hypsometry varies in function of the past glaciations.

d. Time evolution of the ice volume (solid and dashed black curves) and snowline altitude (solid and dashed grey curves) for the a. and b. landscapes. The ice volume grows faster for the glacial landscape a. than for the fluvial landscape b., despite a similar evolution in snowline altitude.

e. Time evolution of the rate of ice volume fluctuation for the a. and b. landscapes. (insets a., b., d., e. modified from Pedesen et al., 2013 and inset c. modified from Egholm et al., 2009).

II.8. TABLES

In Tables attached to the manuscript

Table SII-1. Compilation of geological map references.

Table SII-2. Compilation of bedrock Sr-Nd isotopic measurements.

Table SII-3. Compilation of accumulation rate and sedimentary budgets.

Table SII-4. Compilation of detrital thermochronometry studies.

Table SII-5. Compilation of ^{10}Be paleoerosion studies.

III. AIM OF THE THESIS

III.1. SYNTHESIS OF THE TOPIC

The previous decades of research have demonstrated interactions between tectonic, climate and denudation, but have not yielded a global and marked evidence of an acceleration of denudation coeval with the late Cenozoic climate change.

III.1.1. Tectonics

Over the late Cenozoic, active tectonics do not have undergone substantial global change (Cogné and Humler, 2008) but tectonic patterns have evolved locally even though some mechanisms are still unclear presently. In the Central and Eastern Himalaya, the changes probably consist in the focus of denudation on the eastern syntaxis at ca. 4-10 Ma (e.g. Seward and Burg, 2008) apparently at the expense of western Bhutan (e.g. Grujic et al., 2006). The question of a tectonic change in Central Himalaya remains open since in situ (e.g. Huntington et al., 2006; compilation and reinterpretation in Thiede and Ehlers, 2013) and detrital (e.g. van der Beek et al., 2006) thermochronometry do not converge. The Bengal delta may have coevally been impacted by the rise of the Shillong plateau at ca. 10 Ma (e.g. Clark and Bilham, 2008) or later at ca. 2-3 Ma (e.g. Najman et al., 2016), followed by its later abutment by the Indo-Burman wedge after 2 Ma (Maurin and Rangin, 2009). The Himalayan distal turbiditic system was impacted by the Sunda subduction, which probably cuts the Himalayan supply of the Nicobar Fan at ca. 2 Ma (McNeill et al., 2017) and lets the Bengal Fan the main distal system.

III.1.2. Climate

The late Cenozoic global climate cooling is neither synchronous nor homogeneous across the planet. Cooling starts at ca. 10-6 Ma at the high latitudes (and possibly earlier in the Southern Hemisphere) and progressively expands to reach the lower latitudes at ca. 4-2 Ma (Herbert et al., 2016). The amplitude of cooling is larger in high- than in low-latitudes (Herbert et al., 2016), thus increasing the latitudinal temperature gradient over time. This cooling was associated with the early formation of ice-caps or even ice-sheets at high latitudes (Christeleit et al., 2017; Biermann et al., 2017). Without evidence of early glaciations at low latitudes (e.g. Owen and Dortch, 2014) and considering the global benthic $\delta^{18}O$ record (Zachos et al., 2001; Hansen et al., 2008), ice caps might develop only after 2.8 Ma at lower latitudes. Along with the orbital fluctuations of temperatures and of ice-sheet growth and demise (Zachos et al., 2001), the amplitude of sea-level fluctuations progressively increases from 30-40 m before 6.4 Ma to > 100 m since 0.8 Ma (Miller et al., 2005).

The possible impact of the late Cenozoic cooling on aridity is not clear, since the Cenozoic as a whole is subject to an increased aridity which begins with the expansion of grasses at 24-10 Ma (Edwards et al., 2010) and continues with the probable formation of deserts at 9-5 Ma (Schuster et al., 2006; Arancibia et al., 2006). The expansion of C_4 plants, more adapted to low CO_2 atmospheric concentrations, is potentially linked to multiple causes (Edwards et al., 2010). Even though a coeval decrease and

stabilisation of atmospheric CO_2 concentrations can now be evidenced (compilation of Foster et al., 2017 and data of Lüthi et al., 2008), the origin of the late Cenozoic cooling remains unknown.

In the Himalaya, even though the Indus region potentially underwent a reduction of weathering since 8-10 Ma (Clift et al., 2008), the record of the Bengal Fan at 8°N point to a stable low weathering regime in the Central and Eastern region (France-Lanord et al., 2019), which probably indicates that monsoonal conditions remain stable over the period.

III.1.3. Chemical denudation

Global silicate chemical weathering rates seems to have been subject only to limited 2-σ variations below 40% since 10 Ma according the seawater $^{10}Be/^{9}Be$ record (Willenbring and von Blanckenburg, 2010) but only 6 Ma according the seawater $\delta^{7}Li$ record (Misra and Froelich, 2012). These limited variations seem at odds with the previous significant increase in chemical weathering rates at 6-15 Ma (Misra and Froelich, 2012), despite global cooling and increased aridity (Zachos et al., 2001; Edwards et al., 2010). The places where these past variations occur are undetermined, but might not concern some tropical and tectonically active regions such as the Himalayan region (Clift et al., 2008; France-Lanord et al., 2019). This stability of silicate chemical weathering rates might imply that global erosion rates remained also stable in the late Cenozoic. However, the relationship between silicate weathering and erosion are not linear (e.g. Lupker et al., 2012b; Moore et al., 2013; discussion in Norton and Schlunegger, 2017) and it appears that silicate weathering rates may have decreased during glacial periods even in tectonic areas (Himalaya, Lupker et al., 2013).

III.1.4. Physical denudation

III.1.4.1. Sediment accumulation rates

A global acceleration of erosion remains presently unevidenced by sediment accumulation rates, or their more evolved version, the sedimentary budgets. Because of the statistical approach, the deep sea record can present an artificial global increase in accumulation rates which is not seen when focussing each oceanic basin (Hay et al., 1988; Olson et al., 2016). Accumulation rates and sedimentary budgets are impacted by the capacity of tectonics and glaciations to shift drainage divides (e.g. Kuhlmann et al., 2004; Lang and Huntington, 2014) and may be not reliable when not including a provenance study, or a geomorphologic study on the continent (e.g. Grimaud et al., 2018). They are also impacted by incorrect dating of formations, as shown for Central Asia (Zhang et al., 2001; Charreau et al., 2009a). For the Central and Eastern Himalaya, despite previous attempts (Métivier et al., 1999), a sedimentary budget is almost impossible to resolve presently because only a limited number of drilled cores are available at the core of the turbiditic Bengal Fan (Exp. 354, France-Lanord et al., 2016a) and Nicobar Fan (Exp. 362, McNeill et al., 2016). In addition, the Himalayan sedimentary basins were impacted by tectonics in the late Cenozoic (see above).

III.1.4.2. Detrital thermochronometry

The limited number of detrital thermochronometric studies do not suggest an acceleration of erosion in mountain ranges in the late Cenozoic (e.g. van der Beek et al., 2006; Glotzbach et al., 2011; Huyghe et al., 2019). Only two studies have been realised at the orogen-scale (Central and West Himalaya, Bengal Fan at 8°N, Najman et al., 2019; Huyghe et al., 2019) but they yield divergent results. The present methodology (see e.g. Braun et al., 2018) only detect the variation of erosion of the places denuding the fastest and cannot check without a provenance study if these places move, change of extent and if erosion rates change in areas eroding more slowly (e.g. Najman et al., 2019, who interpret their results as the shift of Himalayan fast denudation to the eastern syntaxis in the late Cenozoic).

III.1.4.3. Detrital cosmogenic nuclides

In contrast with detrital thermochronometry, detrital cosmogenic nuclides, such as $^{10}Be/^{9}Be$ (e.g. Schaller et al., 2004) yield erosion rates averaged across a catchment on short-timescales. Although no study has been realised at the orogen-scale, published studies give relevant yet divergent results. Greenland (ODP sites 987 and 918, Bierman et al., 2016), Central Asia (Tianshan foreland basin, Puchol et al., 2017) and Central Himalaya (Siwalik foreland basin, Surai section, Puchol, 2013) show an acceleration of erosion from 9-6 to 3-4 Ma, followed by a stabilisation since 3-4 Ma along with a high variability in some regions (ODP 918, Tianshan, Surai section). Conversely, East Central Andes (NW Argentina, Val et al., 2016; Amidon et al., 2017; Pingel et al., 2019) show a deceleration of erosion since 7-4 Ma to 2 Ma, with no available data for the 2-0 Ma period (except modern ones). Against these results, one can raise the rarely discussed problem of a shift of drainage basins and provenance (e.g. Puchol, 2013, but the problem concerns all the studies), recycling, or recent exposure (except the marine record of Bierman et al., 2016). However, these studies reinforce the idea that global climate cooling did not have comparable effects across the Earth's surface.

III.1.4.4. In situ thermochronometry

Even though in situ thermochronometry can only yield local erosion rates, this approach makes it possible to determine which surface processes might have accelerate erosion in the late Cenozoic. A set of studies demonstrated a late Cenozoic acceleration of erosion in glaciated tectonically active mountain ranges, with an early phase at 10-5 Ma in South Andes, followed by a deceleration (Thomson et al., 2010; Christeleit et al., 2017), an acceleration phase at 1.8-2 to 0 Ma in the Northern Rocky Mountains (Shuster et al., 2005) and in the Southern Alps, New Zealand (Shuster et al., 2011) and more recently at 1-0 Ma in the Western European Alps (Valla et al., 2011, 2012, 2016) and in Central Himalaya (Huntington et al., 2006), although the effective start is less constrained in this area (between 2.5 and 0.9, Huntington et al., 2006). Herman et al., 2013 assemble a worldwide compilation > 17,000 thermochronometric data and realise a 1-D inversion to obtain an evolution of denudation rates across the Earth. A recent debate has arisen concerning the justification of this inversion (Schildgen et al., 2018; Herman et al., 2019) but it does

not appear to challenge the two main results of their study. First, thermochronometry do not have the resolution to detect a late Cenozoic change in erosion in places subject to low erosion rates, included in some tectonically active regions. This concerns the majority of places on Earth. Second, they show that a majority of places where an acceleration of erosion is detected are in tectonic glaciated mountain ranges, whatever the latitude.

Herman et al., 2013 interpret their results as pointing to a global acceleration of erosion in mountain ranges caused by glaciations. However, complementary thermochronometric studies (King et al., 2016a; Jiao et al., 2017) highlight the difficulty to disentangle the role of tectonics and climate in a change of erosion rates in regions of high erosion rates. In addition, other thermochronometric data suggest that the potential acceleration was probably not coeval worldwide and rather followed a latitudinal progression (Valla, 2018). Herman et al., 2013 acknowledge that their approach does not have resolution on locations where tectonics are absent, and in particular the places which were/are subject to the largest extent of glaciations, i.e. the Arctic and Antarctic regions, where thermochronometric data suggest an early acceleration at 30-20 Ma (Tochilin et al., 2012; Thomson et al., 2013; Bernard et al., 2017). Notably, the phase of acceleration of erosion caused by glaciations may lead after several Myr to a slowing of the acceleration and stable erosion rates, as observed in Antarctica since 20-10 Ma (Tochilin et al., 2012), locally in the South Andes since 5 Ma (Christeleit et al., 2017) and potentially in the Southern Alps of New Zealand since 0.1-1 Ma (Herman et al., 2010b; Jiao et al., 2017).

III.2. AIM OF THE THESIS

The aim of this thesis is to obtain an independent temporal record of erosion rates that covers the scale of an orogen located at low-latitudes for the late Cenozoic. This record would make it possible to further investigate the topics developed in the following.

III.2.1. A record of erosion at an orogenic scale

From the synthesis above, it emerges that orogens have a central place in the debate about the relationship between climate change and erosion. Their erosion rates are sufficiently high to make it possible to detect variations. Tectonics favour physical erosion of rocks and erosion processes are only limited by climatic variations. However, tectonics also appear as a drawback since disentangling the tectonic and climatic roles remains a challenge. Further understanding on the relationship between tectonics, climate change and erosion requires a temporal record (1) that aggregates erosion rates at the orogen-scale, (2) that contrary to sediment budgets is independent of transport processes, and (3) which signal is not subject to interferences of the areas with the highest erosion rates, as detrital thermochronometry is.

Such a record still does not exist. Although evidence of accelerated erosion in the late Cenozoic is available for several orogens, this evidence remains limited to the parts of an orogen that exhume the

fastest and we still do not know if this acceleration was compensated by a slowdown in the rest of the orogen. This prevents further understanding of the orogenic response and deformation to climate change.

III.2.2. A new erosion record for South Asia

The acquisition of an erosion record for South Asia is necessary to constrain the potential impact of the global increase in sediment export on carbon burial and atmospheric CO_2 consumption. South Asia is the locus of tectonically active mountain ranges and high precipitations. In modern times, as it was probably the case over the late Cenozoic, the global sedimentary flux is dominated by South Asia. Even if erosion may have accelerated elsewhere, an absence of acceleration of erosion in this region would imply that the increase in sediment export may have only been limited and carbon burial probably had a limited impact on the atmospheric CO_2 variations of the late Cenozoic.

III.2.3. A check on erosion patterns and increased variability at low latitudes

A new erosion record will make it possible to further investigate the spatial and temporal patterns of the change of erosion rates during climate cooling.

In situ thermochronometric datasets and detrital $^{10}Be/^{9}Be$ datasets show that climate cooling can induce a change in erosion rates (e.g. Shuster et al., 2005; Schaller et al., 2004). This change can be an acceleration, as occurred during the glacial carving of formerly unglaciated valleys. Erosion may have accelerated in glaciated areas because of the possible ability of glaciations to precondition landscapes and favour a larger extent of ice in the following glaciations (Pedersen and Egholm, 2013). However, this preconditioning may have been limited at low latitudes when precipitations and active tectonics rapidly change landscapes during interglacial periods. Without the ability to rapidly cover unglaciated areas, it is uncertain that erosion would have accelerated.

Periglacial areas have been probably of larger extent than glacial areas during the late Cenozoic. There is still no clear status for an acceleration of erosion in these areas. In situ thermochronometry does not have much information to provide (e.g. Herman et al., 2013). Detrital $^{10}Be/^{9}Be$ datasets diverge, some indicating an acceleration, others indicating a deceleration (e.g. Granger et al., 2001; Puchol et al., 2017; see also Delunel et al., 2010). The conditions to enhanced periglacial erosion require sufficient water, rocks sufficiently fractured and an area that is sufficiently large and subject to subfreezing temperatures. Low latitude regions, with high precipitations and active tectonics fit to the two first conditions but not particularly to the third one, because of their high relief. This would raise the question if periglacial processes were sufficient at these latitudes to accelerate erosion.

It is also delicate to obtain a status on areas that were not subject to glacial and periglacial processes, which form a large part of the low-latitude orogens. Late Cenozoic cooling is supposed to have increased aridity, which already increased since the Miocene (e.g. Edwards et al., 2010). It is uncertain that

this late increase would have occurred in South Asia (e.g. Vögeli et al., 2017a) and if it was sufficient to impact erosion rates.

Last, in places subject to an acceleration of erosion, this acceleration seems temporary and lead to a new equilibrium with steady average erosion rates (Puchol et al., 2017). Detrital $^{10}Be/^{9}Be$ also shows that this acceleration seems to lead to a higher variability of erosion rates. However, it is uncertain that this phenomenon be limited to glacial and periglacial areas or could be generalized.

III.3. DEVELOPED APPROACH

III.3.1. Sedimentary archives

I consider for this thesis two sedimentary archives, a distal archive at the orogen-scale and a proximal archive at a scale of a large Himalayan catchment. The comparison of these two distinct and complementart scales should yield relevant information.

III.3.1.1. Bengal Fan Exp. 353 - 354

The first archive is analysed from a set of sand samples from turbidites of the Bengal Fan. The samples were collected during IODP Exp. 354 (France-Lanord et al., 2016a) and 353 (Clemens et al., 2016). Exp. 354 followed an acquisition of high-resolution seismic data along 4 E-W profiles in the Bengal Fan (Spiess et al., 1998; Schwenk and Spiess, 2009). These profiles revealed numerous channel-levees systems (Schwenk and Spiess, 2009; Bergmann, 2018) along with unchannelled deposits (Bergmann, 2018). The Bengal Fan has been probably fed even during sea-level rises and high stands (Weber et al., 1997; 2003; Michels et al., 2003). To take into account the spatial depocenter variability, Exp. 354 drilled an E-W transect of 7 sites at 8°N (France-Lanord et al., 2016a). Exp. 353 drilled a complementary site at 16°N (Clemens et al., 2016). The continuity of this site with the sites of Exp. 354 are evidence by ^{14}C dating constraints by Hein et al. (2017). The retrieved cores consist of turbiditic unconsolidated sand and silt interlayered by hemipelagic intervals. All sites were dated by biostratigraphy, magnetostratigraphy and occasionally tephrostratigraphy (France-Lanord et al., 2016a; Blum et al., 2018). An age-model covering the last Ma and using high-resolution multichannel seismic data was recently realised for the Exp. 354 sites (Reilly, 2018). These data were also analysed by Bergmann, 2018, who described the migration of the channel deposits during the late Pleistocene. Her results show a return of turbiditic sedimentation at 8°N since ca. 0.5 Ma, after an abandonment caused by the migration of the depocentre. Additionally, they suggest that deposition might be independent of global sea-level variations (p.99).

Detrital Zircon U-Pb provenance data (Blum et al., 2018) show that sediments chiefly derive from the Himalaya with a potential variation of the proportion of Ganga and Brahmaputra sediments. Detrital thermochronometric data do not converge to a unique evolution, as rutile U-Pb and some zircon fission tracks (Najman et al., 2019) show a shift to higher maximum erosion rates at 7-5 Ma linked to the eastern

syntaxis (Namche Barwa) and white mica $^{40}Ar/^{39}Ar$, apatite U-Pb and some zircon fission tracks (Najman et al., 2019) point to stable maximum erosion rates.

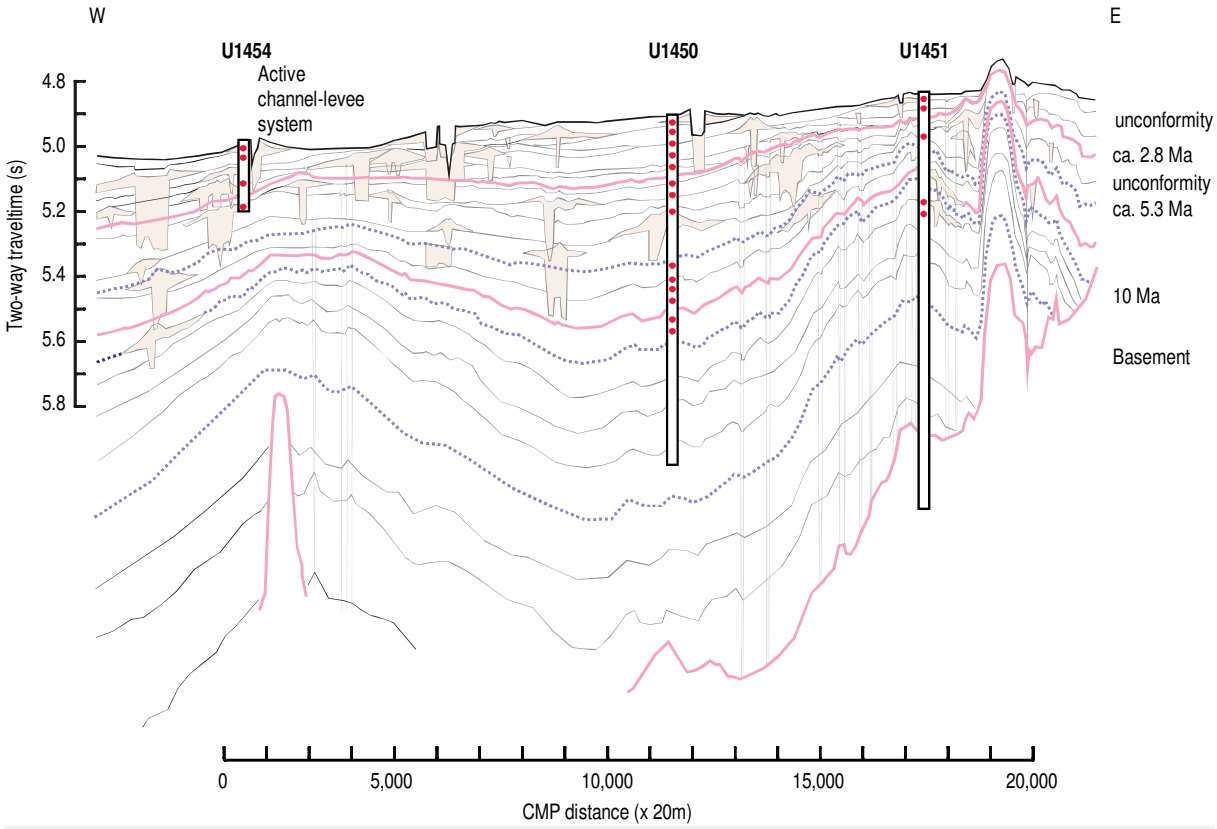

Figure III-45. Sampling in the Bengal Fan

The three selected Holes for sampling are indicated on an interpreted seismic profile of the Bengal Fan at 8°N, Expedition 354 (Schwenk and Spiess, 2009; France-Lanord et al., 2016). Note that the other holes of the Expedition are not indicated. A fourth Hole was selected from Expedition 353 at 16°N. The map of the Holes is in Chapter VI. The Holes are rich in sand, as shown in the stratigraphic log Chapter V, which makes possible ^{10}Be measurements in quartz.

III.3.1.2. Siwalik sections in the Valmiki Wildlife Sanctuary, Bihar, India

The second archive is analysed from a previously unstudied group of Siwalik sections in the Valmiki Wildlife Sanctuary, National Park & Tiger Reserve, Bihar, North India. The sections are located in the front of the Himalayan range and consist of sediments from the Indo-Gangetic foreland basin that has been exhumed since 1-3 Ma in the Siwalik folds. The sections presently outcrop along several rivers incising the Siwalik Hills. The sections are close to the outlet of the Nepalese Narayani river. The Narayani catchment includes the massifs of the Annapurnas, the Dhaulagiri, the Manaslu, the Ganesh and the Langtang. The Narayani flows into India under the name of Gandak. The paleo-Gandak alluvial fan has been studied by Morin, 2015. Three drilled cores cover the last 20 ka and potentially up to the last 100-50 ka. ^{10}Be denudation rates present a range of variations of 50-80% and were possibly lower than modern

rates during the last glacial period. No important shift of provenance neither in chemical weathering is observed.

Several other Siwalik sections have been already described, dated and investigated, in particular the Surai section located at this West of the Valmiki sections, for which ^{10}Be denudation rates (Puchol, 2013), detrital zircon and apatite fission tracks (Bernet et al., 2006; van der Beek et al., 2006) and Sr-Nd isotopic provenance data are available. With the advisors of this thesis, I made the choice to focus on new Siwalik sections for several reasons.

The archives should record the sediments of a Himalayan catchment rather than an interfluvial catchment (such as the thoroughly investigated Surai section), so as to obtain erosion rates averaged on a full N-S Himalayan transect, from the Tibetan plateau to the frontal thrust. The Narayani catchment has been probably the most studied Himalayan catchment in Central and Eastern Himalaya, in particular by the CNRS workers since the opening of Nepal in 1951 (e.g. Bordet et al., 1967; Le Fort, 1975). The lithology and the isotopic signature of the formations are well constrained (e.g. Morin, 2015). The catchment yields a consistent part of the Himalayan sedimentary flux (Lupker et al., 2012a, 2017). The Narayani catchment also presents the advantage that it was potentially unimpacted by a shift in tectonic dynamics in the late Cenozoic, contrary to catchments in the Eastern Himalaya (e.g. Grujic et al., 2006; Seward and Burg, 2008). Last, the Siwalik fold limb at the Valmiki national park is potentially younger (i.e. < 1 Ma, Jérôme Lavé pers. comm.) than elsewhere in the Siwaliks (ca. 2-4 Ma). This might ensure that the major part of the record is unaffected by recycling.

III.3.2. Methodology

To obtain denudation rates averaged at the catchment scale, I measure in situ ^{10}Be concentrations contained in fine sand quartz, which is almost ubiquitous in the Himalaya, and derive apparent ^{10}Be denudation rates. ^{10}Be is a radioactive cosmogenic nuclide produced in matter by the cosmic rays. When rocks are exhumed to the Earth's surface, their crystals get progressively enriched in cosmogenic nuclides, at a rate which depends on denudation rates and the geographical location and elevation of rocks.

Deriving denudation rates from ^{10}Be concentrations require complementary dating constraints. For the Bengal Fan samples, I used the published and unpublished biostratigraphic and magnetostratigraphic constraints, along with an age model using high-resolution seismic data. I established a new age model for the part of the U1450 site older than 1.2 Ma. For the Siwalik samples, Julien Charreau established the magnetostratigraphic age model.

Interpreting these apparent ^{10}Be denudation rates into a story of erosion of the catchment requires several considerations. The provenance of sediments may have shifted over time, either by the capture or loss of subcatchments or by the displacement of the outlet of the river at the front of the range or by the reconfiguration of the fluvial network, in the alluvial plain and delta. When catchments have contrasted elevations as for the Narayani and the Ganga-Brahmaputra, this shift of provenance impacts the ^{10}Be

concentrations, even though denudation remains stable. Here, exploiting the fact that the Himalaya consists in subparallel E-W formations of different isotopic signatures, I perform a provenance study with the measurement of Sr and Nd isotopes in the bulk silicates of the samples.

The Siwaliks may consist of recycled sediments in their upper part. These sediments combine two denudation histories that are delicate to disentangle. The systematic measurement of ^{26}Al, another cosmogenic nuclide might have helped to better constrain these histories, but I have not managed to obtain ^{26}Al results coherent with ^{10}Be results (in Appendix). I detect recycled sediments using the major elements, with a strong depletion in Na and Al as indicated in the modern Siwalik river sediment.

Transport time may have also impacted ^{10}Be concentrations. Again, this contribution could have been constrained by the measurement of ^{26}Al in combination with ^{10}Be. However, transport has been shown to be rapid in the Himalaya, at least for sand (Lupker et al., 2011; 2012a).

Last, recent exposure to cosmic rays, during the Siwalik denudation, may have also impacted ^{10}Be concentrations. We performed ^{36}Cl measurements, ^{36}Cl being a cosmogenic nuclide of half-life shorter than ^{10}Be, on a limited number of samples to check this exposure.

IV. METHODOLOGIC OVERVIEW

Cosmogenic nuclides such as ^{10}Be are produced through the interactions between the cosmic flux and matter at the Earth's surface. The "meteoric" production, in the atmosphere, dominates the "in-situ" production, in minerals. The method described below consists in measuring the concentration of in-situ nuclides in the minerals. When applied to rocks and with the knowledge of cosmogenic production rates, this concentration gives access to local denudation rates. The method also gives access to basin-scale denudation rates when applied to river sediments (Figure IV-46, Brown et al., 1995; Granger et al., 1996). The use of in-situ ^{10}Be has become common to study modern erosion rates (presently more than 200 studies, live updated compilation in https://earth.uow.edu.au/, Codilean et al., 2018) and paleo-erosion rates (28 studies, table T05, methodologic review in Dosseto and Schaller, 2016).

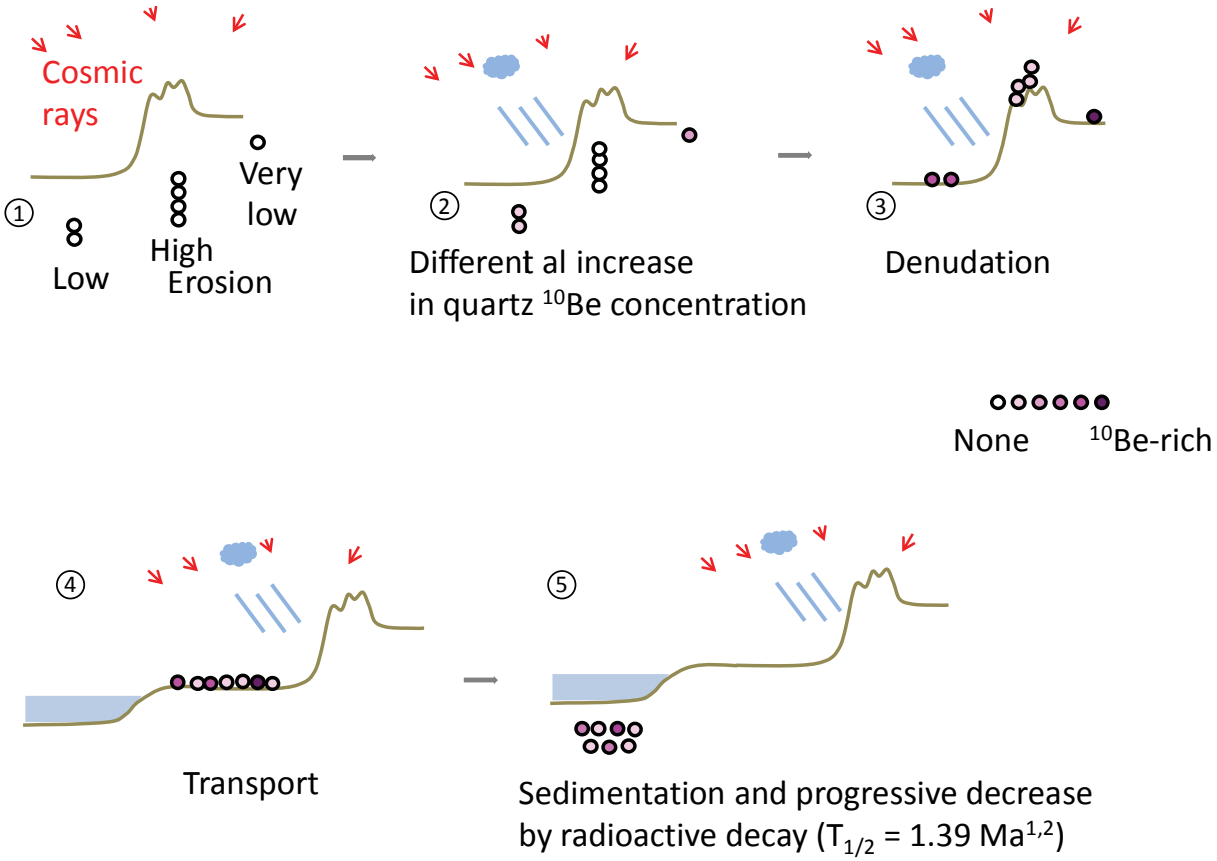

Figure IV-46. Source to sink evolution of ^{10}Be concentrations in Himalayan rocks and sediments.

A catchment consisting of a slowly eroding high plateau, rapidly eroding mountain range and slowly eroding low elevated area is considered. As denudation progress, minerals (quartz) get impacted by cosmic rays and produce in situ ^{10}Be. ^{10}Be concentrations differ according denudation rates and elevation. When minerals reach the surface, they are extracted and transported by rivers to their sink, a sedimentary basin. After burial, ^{10}Be production stop and ^{10}Be begin to decay (information in Lupker et al., 2012a; Puchol et al., 2017; half-life from Chmeleff et al.,2010; Korschinek et al., 2010).

^{10}Be is commonly used to measure denudation rates because all production pathways are cosmogenic and the ^{9}Be stable isotope is commonly unfound in nature. This allows fixing the ^{10}Be/^{9}Be at the dissolution with a carrier of a known concentration, and limiting the uncertainties for ^{9}Be measurements. Quartz is a ubiquitous mineral, and meteoric ^{10}Be is easily removed from minerals.

The following synthesizes the approach to determine the necessary production rates to derive denudation rates from ^{10}Be concentrations. A production rate is the quantity of a certain cosmogenic nuclide produced in a certain mineral during a given time. The production rates vary in function of the target nuclei and/or the cosmogenic nuclide species, the type of cosmic particles, and the intensity (i.e. abundance of particles) and energy spectrum of the secondary cosmic flux, which both evolve spatially and temporally (Lal and Peters, 1967; review in Dunai, 2010).

IV.1. THE COSMIC FLUX AND ITS QUANTIFICATION

IV.1.1. The neutron cosmic flux

The primary cosmic flux mainly consists of low to high-energy protons (~90%) and in less proportion α-particles. The flux originates from the galaxy, and is supposed to have been stable over the last 10 Ma, according to measurements from meteorites (Vogt et al., 1990; Leya et al., 2000). When approaching the Earth, the flux is partially deflected against the geomagnetic field (Lal and Peters, 1967) and only a portion of the flux penetrates the atmosphere downwards to the surface (Lal and Peters, 1967). The initiation of a nuclear cascade through interactions with matter (Figure IV-47, Serber, 1947) converts the flux in a secondary flux composed of high-energy/fast neutrons and muons. Because of their strong interactions with matter (Simpson and Fagot, 1953; Simpson et al., 1953; Lal, 1988), nuclear reactions caused by neutrons dominate in the atmosphere down to several meters below surface, before being overwhelmed by nuclear reactions caused by muons down to depths of several kms (Lal and Peters, 1967).

The geomagnetic field regulates the abundance and energy of cosmic protons that can penetrate the atmosphere, according to the spatial location of the incident particles and the temporal evolution of the geomagnetic field. The geomagnetic field is typically approximated as a virtual axial dipole (Acton et al., 1996) over a millennial timescale, but have complementary components over shorter timescales. Classically, the intensity and energy of the cosmic flux are considered to decrease towards lower latitudes while above 60° the variation is negligible (Shea et al., 1965; Lal and Peters 1967; Lal, 1991). However, the spatial variations of the geomagnetic field do not fit exactly latitudes. Another criterion, the effective vertical cutoff rigidity R_c, also written as P (Figure IV-48, Elsasser et al., 1956; Shea et al., 1965; discussion in Lifton et al., 2008) is considered. The rigidity of a particle corresponds to its momentum per charge and

is a function of its energy. Only the particles with a rigidity > the local R_c pass through the atmosphere. R_c is computed numerically. The cosmic flux also depends temporally on the intensity and orientation of the geomagnetic dipole (Dunai, 2001; Pigati and Lifton, 2004; Lifton, 2016; discussion in Nishiizumi et al., 1989), which fluctuated over the last million yrs in a ±30% margin (Valet and Meynadier, 1993; Carcaillet et al., 2004; Muscheler et al., 2005; Ménabréaz et al., 2014).

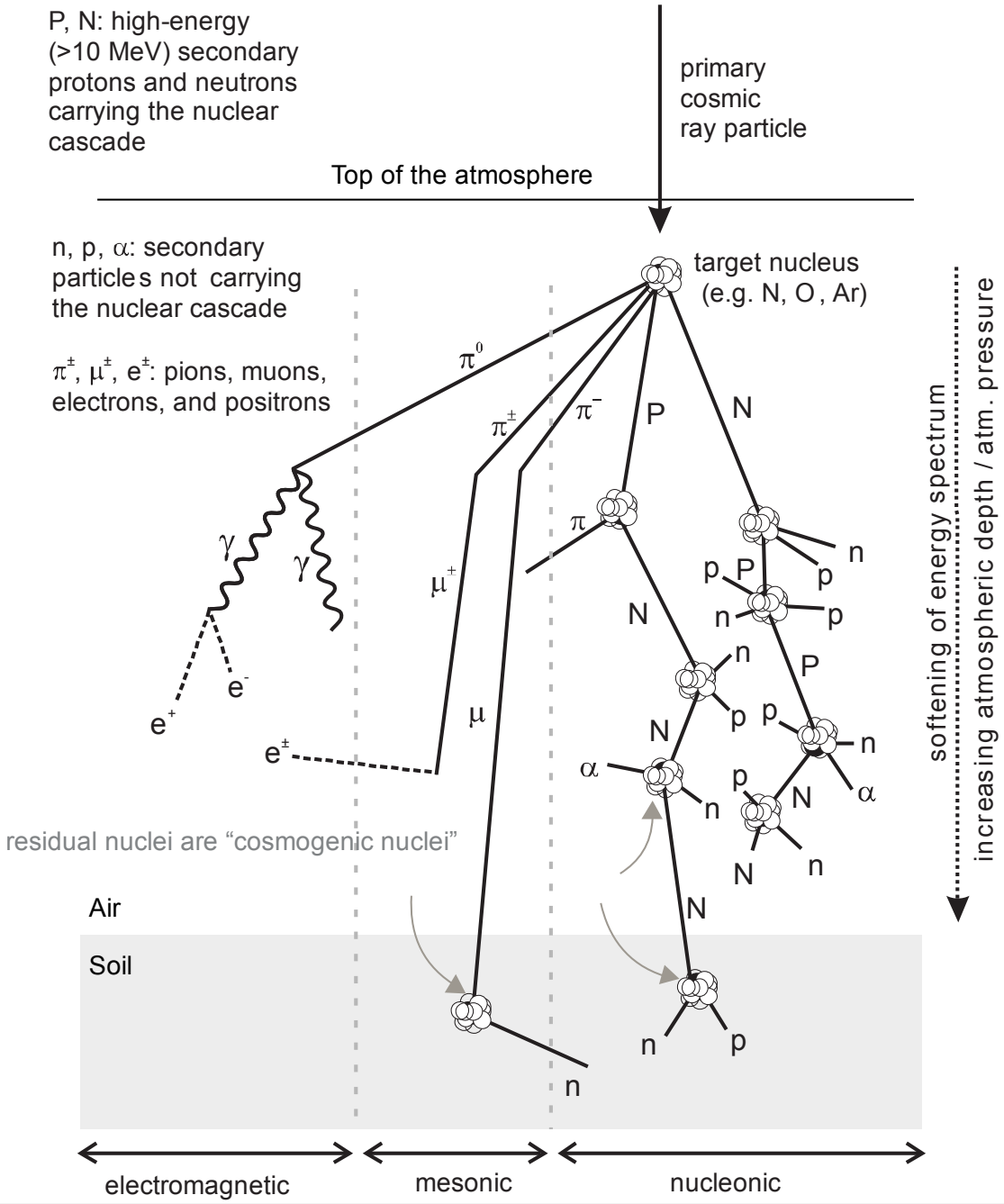

Figure IV-47. Cosmic nuclear cascade.

Nuclear reactions produce cosmogenic nuclides and secondary particles. The production is dominated by meteoric nuclides produced in the atmosphere and a small proportion is produced in situ in the rocks (modified from Dunai and Lifton, 2014 and Gosse and Phillips, 2001).

Once the cosmic high-energy protons penetrate the atmosphere, they are converted into high-energy neutrons through spallation. Spallation is the most frequent nuclear reaction in the atmosphere and consists in the off-sputtering of particles of lower energy through collision with atomic nuclei, such as O and N. From the top atmosphere to the subsurface, the intensity of the neutron flux is related to its energy spectrum (Simpson and Fagot, 1953; Simpson et al., 1953; Lal and Peters, 1967). As neutrons move downwards, they gradually loose energy through spallation (Lal and Peters, 1967; Masarik and Beer, 1999, 2009). In parallel, the overall abundance of neutrons gradually decreases through a reaction complementary to spallation, known as the thermal neutron capture (Liu et al., 1994, 1995; Phillips et al., 2001). Thermal neutrons are slow/low-energy neutrons which are naturally absorbed by atoms. Close to ground-level and in the first cms below surface, neutrons are majoritarily thermal neutrons and are absorbed in a few meters below surface (Liu et al., 1994, 1995; Phillips et al., 2001).

The neutron flux approximately decreases according to an exponential law inversely correlated to the mass length (Lal and Peters, 1967; Lal, 1988; discussion in Dunai, 2000), as formulated in Gosse and Phillips, 2001:

$$\Phi_f(Z) = \Phi_f(0) \times \exp\left(-\frac{Z}{\Lambda_f}\right)$$

with Φ_f: intensity of the flux, Z: the vertical mass length or vertical cumulative length, and Λ_f: a parameter known as effective attenuation length, attenuation coefficient, e-folding length or absorption free mean path (Figure IV-48). The mass length Z (in g.cm^{-2}) is the product of the path length of the flux through the medium and the density of the traversed medium. When the medium is the atmosphere, the mass length is coined the atmospheric depth and is a function of the local pressure, which itself is a function of elevation. The attenuation length Λ_f is a linear function of the length required to stop the particle and therefore only depends on the velocity/energy of the particle. Hence, the attenuation length evolves spatially: the length increases with the cutoff rigidity R_c (i.e. roughly decreases with the latitude) and decreases with atmospheric depth (increases with elevation) (Brown et al., 1992a; Dunai, 2000; Gosse and Phillips, 2001; Sato et al., 2008; Marrero et al., 2016). Attenuation lengths in the atmosphere are in the 120-160 g.cm^{-2} range (compilation in Dunai, 2000; Gosse and Phillips, 2001). In the subsurface, attenuation lengths are longer, in the 150-190 g.cm^{-2} range (compilation in Gosse and Phillips, 2001; computation by Sato et al., 2008 and Marrero et al., 2016).

The flux of thermal neutrons punctually diverges from this exponential law as it is anomalously depleted in the first 10's of cms below surface. This depletion is caused by the diffusion of thermal neutrons out of the surface and their trapping by nitrogen, which is abundant in atmosphere (Liu et al., 1994, 1995; Phillips et al., 2001). Water content in subsurface tends to limit this diffusion (Phillips et al., 2001).

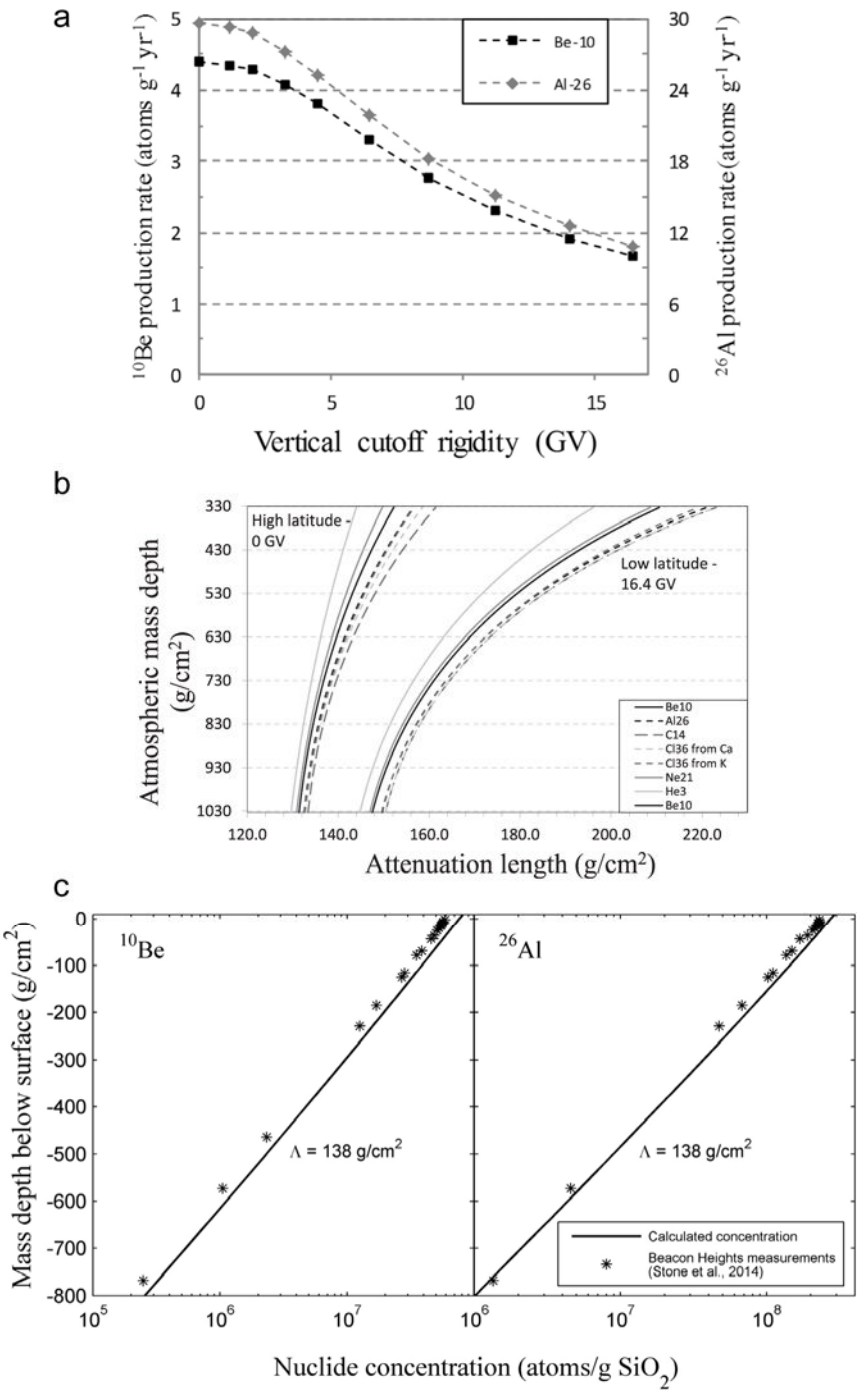

Figure IV-48. Cosmogenic nuclide production, vertical cutoff rigidity and mass depth.

a. The vertical cutoff rigidity (the geomagnetic latitude) controls the reflection of the cosmic flux at the top of the atmosphere. A higher rigidity (at low latitude) decrease production rates.

b. The 2 sets of curves correspond to 2 different rigidities and present the variation of attenuation length, a proxy for the rate of decrease in production rates, versus the atmospheric mass depth, i.e. the elevation.

c. The 2 insets present soil vertical profile measurements and model of nuclide concentrations (logarithmic scale) versus the depth. (modified from Argento et al., 2015).

IV.1.2. The muon cosmic flux

Muons are tertiary charged products resulting from spallations by protons in the top atmosphere. Muons interact weakly with matter (Lal and Peters, 1967; review in Charalambus, 1971; Fabryka-Martin, 1988; Stone et al., 1998; Heisinger et al., 2002a, 2002b; Braucher et al., 2003, 2011, 2013; Balco, 2017). Muons are roughly as abundant as neutrons at ground-level and dominate cosmic particles a few meters below surface (Lal, 1988, review in Fabryka-Martin, 1988; Stone et al., 1998; Gosse and Phillips, 2001). At a depth of 1,000g.cm^{-2}, ~300-400 m, fast muons overwhelm other particles (Lal and Peters, 1967; Heisinger et al., 2002a; Braucher et al., 2013). Muons penetrate several kilometers in the deep subsurface (Lal and Peters, 1967; Heisinger et al., 2002a; Braucher et al., 2013). Muons gradually loose energy through γ-radiations at the origin of photodisintegration reactions. Slow negative muons, coined as stopping negative muons, are subject to muon capture by atoms, while positive muons capture electrons to form a pseudo-isotope of H. Muon nuclear reactions are dominated by negative muon captures in the first meters of the subsurface and photodisintegration at greater depths (review in Balco, 2017). Negative muon captures and photodisintegration reactions produce neutrons that are themselves subject to spallation and thermal neutron capture.

At ground-level, the flux of muons depends only marginally on the geomagnetic field (review in Stone et al., 1998) but the atmospheric depth, i.e. the elevation has an influence on the flux. According to physical laws (Heisinger et al., 2002a, b; discussion in Balco, 2017; Charreau et al., 2019), the muon flux does not evolve similarly than the neutron and in particular does not follow an exponential law or a combination of exponential laws. Indeed, as the abundance of muons progressively decreases in the depths, the flux get concentrated in high-energy muons (discussion in Balco, 2017). As a result, muons have an attenuation length which increases with depth, and determining the flux intensity requires advanced computing of an integral.

IV.1.3. Quantification of the cosmic flux

The quantification of the cosmic flux makes it possible to determine the cosmogenic production rates for a place of study. The cosmic flux is quantified through complementary approaches: irradiation experiments (Lal and Peters, 1967), geological calibration (Fuse and Anders, 1969; Nishiizumi et al., 1989), or numeric simulation based on physical laws (Masarik and Reedy, 1995). Irradiation experiments are a way to assess the variations of modern cosmic flux, through the measurement of nuclear reactions using photographic emulsions (Powell et al., 1959), neutron detectors (Simpson, 1951) and neutron monitors (Hatton, 1971). Photographic emulsions record the tracks generated by the charged products of nuclear reactions while neutron detectors and monitors count the neutrons produced. Monitors are an evolved version of detectors, that sample fixed portions of the energetic spectrum of neutrons. In that way, neutron monitors present an energy bias known as the multiplicity effect (Hatton, 1971; Lifton et al., 2014), which tends to overestimate the high-energy portion of the spectrum (discussion in Lifton et al., 2014). This overestimation requires a difficult correction to determine.

Geological calibration (Nishiizumi et al., 1989; review in Gosse and Phillips, 2001; Balco et al., 2008; discussion in Martin et al., 2017) consists in measuring the concentration of cosmogenic nuclides of a subaerial surface which age was measured independently by another method. The history of the surface should be simple and the surface must have been stable for the period, without erosion and shielding from cosmic rays by cliffs or ice. Radiocarbon is classically used as an independent dating method. Calibrated data are reported to sea level and high latitude (SLHL) and are frequently updated, at least for the most common cosmogenic nuclides (Martin et al., 2017, through the ICE-D database).

Numerical simulations (Masarik and Reedy, 1995) use models to simulate physical processes such as the particle interactions and transport.

IV.2. COMPUTATION OF DENUDATION RATES

IV.2.1. Determination of production rates

In practice, geological calibration forms presently the basis for the neutron production rate determination, at least for ^{10}Be and ^{26}Al (Phillips et al., 2016; Martin et al., 2017; Charreau et al., 2019). When available, workers select data calibrated close to the study location. However, because of the difficulty to get an independent dating constraint, calibrated sites are not available on all continents, for instance in Asia, and in that case, an average of calibrated production rates on Earth is considered. For ^{10}Be, the calibration dataset remains limited (Figure IV-49, ~20 sites reviewed for ^{10}Be spallation, Martin et al., 2017; only a few sites for muonic reactions, Braucher et al., 2011).

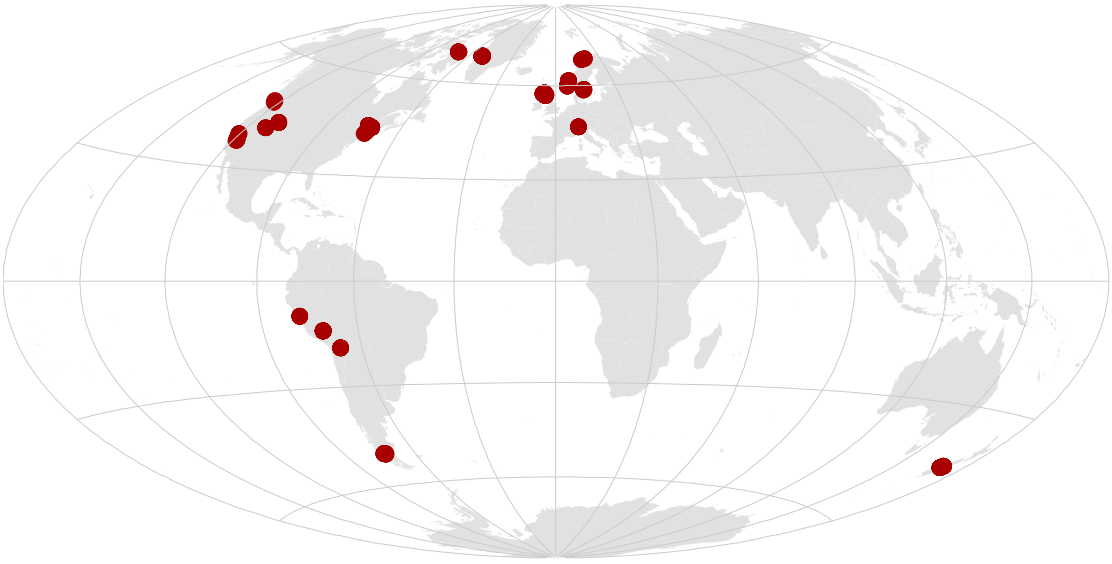

Figure IV-49. ^{10}Be geological calibration site map.

Data retrieved from the ICE-D database June, 2019 (http://calibration.ice-d.org/; Martin et al., 2017).

In contrast, the determination of the muon production rate is still debated (Balco et al., 2008;

Phillips et al., 2016; Balco, 2017; Martin et al., 2017; Charreau et al., 2019), with experimental measurements (Heisinger et al., 2002a, 2002b) overpredicting empirical production rates (Braucher et al., 2003, 2011, 2013; Kim and Englert, 2004). Braucher et al. (2013) assume that the 2 discrete energies (for so-called fast and slow muons) selected for these experiments may not represent the natural muon energy spectrum. Charreau et al. (2019) performed a benchmark of muon computations for several catchments, according 2 methods, either with a constant muon attenuation length or with an attenuation length varying with denudation rate. This second method requires iterative computation, which is computer-time consuming. They found out that the first method gave similar or better results than the second one.

The determination of production rates requires translating the SLHL calibrated data to the area of study using a scaling model (Lal, 1991, Stone, 2000; review in Dunai, 2010; Phillips et al., 2016; CronusCalc code of Marrero et al., 2016; CREp code of Martin et al., 2017 and Basinga code of Charreau et al., 2019). To determine the overall production rate of a catchment, a recent approach consists in computing cell by cell production rates with a digital elevation model (DEM) (e.g. Godard et al., 2012; Lupker et al., 2012a; Basinga code of Charreau et al., 2019).

IV.2.2. Scaling models

The scaling models (Figure IV-50) are elaborated using irradiation experimental data and numerical simulations. The original time-independent model of Lal (1991), later modified by Stone (2000) and Balco et al. (2008), is still largely used in studies. The model, called "Lm", has only 2 input parameters, the geographic latitude, replaced by the cut-off rigidity in Balco et al., 2008, and the atmospheric pressure. The relatively time-efficient algorithm usually makes reliable predictions on the number of nuclear reactions.

However, the model does not include the temporal variations of the geomagnetic field, which effect can be consistent for slowly eroding areas (Lifton, 2016; Martin et al., 2017). Other models were developed using the neutron monitor data (Lifton et al., 2005, 2008; Dunai, 2000, 2001; Desilets and Zreda, 2003; Desilets et al., 2006), but because of the multiplicity effect of neutron monitors, these models do not have predictions at the level of the Lal-Stone model. A new approach based on numerical simulations of physical processes was developed separately by Lifton et al. (2014), with the work of Sato et al. (2008), and by Argento et al. (2015a, 2015b).

The main challenges for scaling models remain presently computing time and reliable predictions.

The use of "Lm" and "LSD" (Lifton et al., 2014) models for catchment production rate scaling was thoroughly benchmarked by Charreau et al. (2019), through the use of the Basinga code. According to their results, differences on production rates are negligible, except for catchments of high latitude and high elevation or low latitude and low elevation, 20-30% difference, as previously shown by Phillips et al. (2016). The impact on denudation rates is insignificant for the majority of catchments, except when denudation rates are very low (<10% difference, Charreau et al., 2019). Therefore the "Lm" model, which has a rather rough approach compare with the "LSD" model, which better represents physical processes,

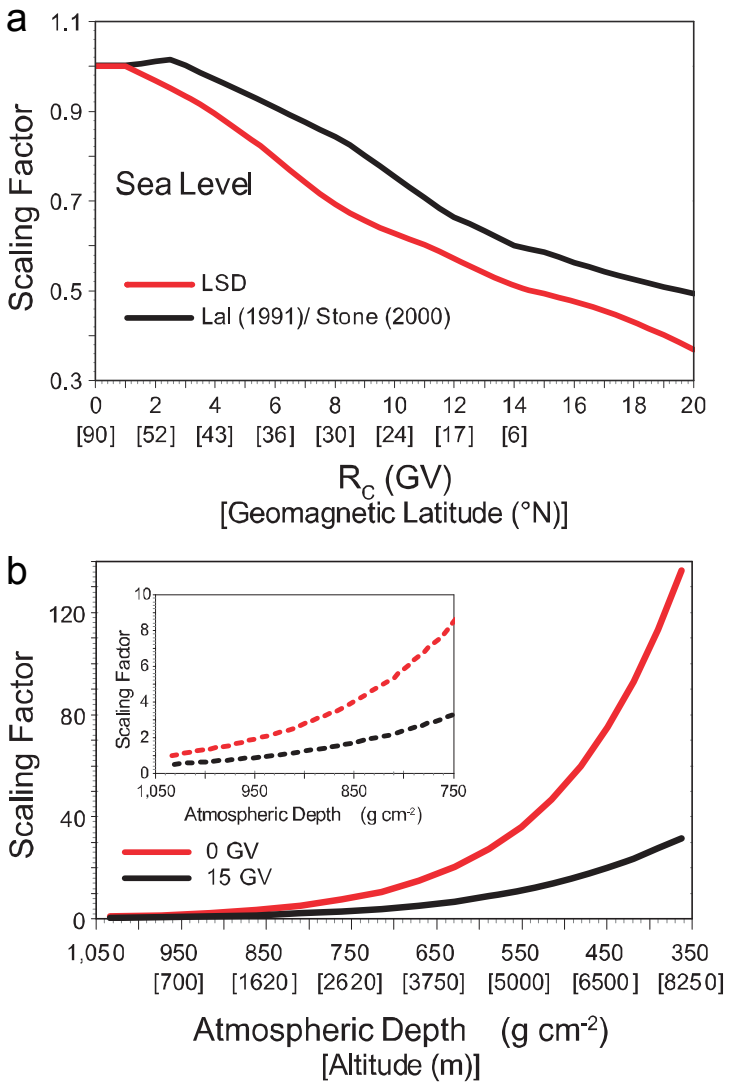

Figure IV-50. Cosmic flux scaling models.

a. Scaling factor versus the cutoff rigidity R_c, computed according to the model of Lal(1991)-Stone(2000) and the model of Lifton et al. (2014) (LSD).

b. Scaling factor versus the atmospheric depth (i.e. elevation), computed with the 2 models. The inset focus on elevations below 2,600 m (modified from Dunai and Lifton, 2014).

still appears at its advantage.

IV.2.3. Analytical computation of quartz in situ ^{10}Be denudation rates

The following description synthesizes the approach of Lal (1991), with the help of reviews in Martin et al. (2017) and in the Basinga code, Charreau et al. (2019). It is supposed that the computation is realized on areas containing quartz.

At any location of the Earth, the impacts of the particles i (neutrons and muons) with matter produce cosmogenic nuclides according different pathways. The rates of production, P_i depends on the pathway and are normalized to sea level high latitude $P_{i,SLHL}$ (see above). Local production rates $P_i(L,h,t)$ are formulated as below:

$$P_i(L,h,t) = P_{i,SLHL} \times S_i(L,h,t)$$

and are obtained by computing local scaling factors $S_i(L,h,t)$ using a model. These factors depend on the latitude L, the atmospheric pressure h (at sea-level, ≈1030 g.cm^{-2}), and time t. The latest codes (Marrero et al., 2016; Martin et al., 2017; Charreau et al., 2019) replace L by the cut-off rigidity R_c, which depends on the magnetic moment (Elsasser et al., 1956), which itself depends on t.

The exponential attenuation of the cosmic flux leads to the expression of the production rate $P_i(x,t)$ of in situ nuclides in subsurface minerals as a function of the depth $x(t)$ and time t, for the cosmic particle i:

$$P_i(x,t) = P_i(0) \times e^{-\frac{\rho}{\Lambda_i}x(t)} \quad (1)$$

where $P(0)$: production rate at the surface, ρ: density of rocks and Λ_i: attenuation length of the particle. It should be note that this function is theoretically not valid for all pathways. As explained below and in Charreau et al. (2019), even though muons have attenuation lengths varying with depth, the approximation of their attenuation length to a constant induce only negligible variations for catchments having erosion rates sufficiently high (i.e. > 0.01 - 0.001 mm/yr).

For radioactive nuclides of disintegration constant λ, such as ^{10}Be, the concentration $N(x,t)$ is given by:

$$\frac{dN(x,t)}{dt} = -N(x,t)\lambda + \sum_i P_i(x,t) \quad (2)$$

The depth $x(t)$ is linked to erosion $\varepsilon(t)$ this way:

$$x(t) = \int_0^t \varepsilon(t)dt + \varepsilon_0 \quad (3)$$

Two key assumptions have to be made to analytically resolve this equation: (a) the erosion rate should stay steady over the period of accumulation $\varepsilon(t) = \varepsilon_0$, and (b) the secular equilibrium should have been attained $t \gg \lambda + \max\left(\frac{\rho}{\Lambda_i}\right)$. If these assumptions are valid, the concentration of nuclides in

minerals at the surface can be approximated as:

$$N(0,t) = N(0,t=0) \times e^{-\lambda t} + \sum_i P_i(0)\left(\lambda + \frac{\rho\varepsilon_0}{\Lambda_i}\right)^{-1} \quad (4)$$

and in the case of steady-state erosion:

$$N(0,t) = \sum_i P_i(0)\left(\lambda + \frac{\rho\varepsilon_0}{\Lambda_i}\right)^{-1} \quad (5)$$

which leads, by neglecting λ to the equation:

$$\varepsilon_0 = \rho \times \sum_i \frac{P_i(0) \times \Lambda_i}{N(0,t)} \quad (6)$$

IV.2.4. Topographic and glacial shielding

The computation above requires some correction when rocks are partly or fully shielded from cosmic rays, either by topography (Lal, 1991; Gosse and Phillips, 2001; Dunne et al., 1999; Codilean, 2006) or by ice cover (Wittmann et al., 2007; Godard et al., 2012; Guillon et al., 2015). Topographic shielding can be caused by relief or local slope and is assumed consistent in steep areas (corrections up to 20%, Norton and Vanacker, 2009). However, Dibiase, 2018 suggests through a simple model that the present corrections (Codilean, 2006) overestimate the effect of shielding, because they do not properly take into account the effect of oblique pathways on slopes, which increase the attenuation length at depth, counterbalancing the effect of topographic shielding. Dibiase, 2018 proposes that these corrections should be limited to areas with very steep slopes, with heterogeneous quartz distribution, but the topic probably requires further investigation.

Shielding also occurs for areas covered by ice (Wittmann et al., 2007; Godard et al., 2012; Guillon et al., 2015). For ^{10}Be and ^{26}Al, ice cover is usually considered as enough thick to fully shield the cosmic rays (Wittmann et al., 2007), leading to null production rates. Nevertheless, it has been shown that sediments transferred by glaciers often include supra-glacial sediments with not null concentrations (Godard et al., 2012; Guillon et al., 2015). In addition, muon production still continues at great depths.

It has been shown that snow cover could also produce shielding, although of less importance (5-10% impact of production rates, Schildgen et al., 2005; Scherler et al., 2014).

As for muon production, it appears that shielding corrections probably require further work to fully reproduce the natural processes. In addition, these corrections assume a certain permanence of relief and ice cover, and are therefore delicate to apply for production rates of the past.

IV.3. LIMITS OF THE ^{10}BE METHOD

The following synthesizes the potential limits of the ^{10}Be method to precisely determine denudation rates of a catchment. Several of these limits are systematically overlooked in studies, giving the false feeling that erosion rates are given with low uncertainties, when in fact they are potentially underestimated.

IV.3.1. Analytic measurements

The concentrations of radioactive cosmogenic nuclides are measured with an accelerator mass spectrometer (e.g. Arnold et al., 2010) and analytical uncertainties are now usually below 5% for the majority of studies (compilation in https://earth.uow.edu.au/, Codilean et al., 2018). However, this is not the case for studies with past samples, which contain low concentrations because of radioactivity and potentially because of high erosion rates. The problem probably originates from the preparation of the samples and the separation of cosmogenic nuclides. The classic approach is to extract Be from large quantities of quartz for old samples. This approach was of limited success for our studies, with the majority of our samples having ^{26}Al below detection level and ^{10}Be having still high uncertainties for some samples. Large quantities of quartz also increase the natural ^{9}Be concentration, which can interfere with the ^{9}Be volume added as a carrier. In addition, no systematic study of potential impacts of these larger quartz quantities on the steps of separation was ever performed.

According observations performed by A. Mariotti (pers. comm.) after the measurements performed in this work, one can improve consistently the yields of the Be and Al extraction by checking the pH with an electronic device instead of a pH paper.

IV.3.2. Reproducibility

Given our results on replicates (up to 30% of difference), without systematic bias related to grain sizes (size < 500 µm) as previously observed by Lupker et al. (2012a, 2017) for the Himalaya, one can argue than reproducibility is not as good as expected and increase uncertainties. This potentially means that the Be extraction has an impact on concentrations, speculatively during the quartz dissolution and evaporation of the solution. This topic of reproducibility needs further investigation, to determine if is limited on certain areas of the Earth, or to some laboratories, or is more general.

IV.3.3. ^{10}Be production rates, geography of the catchment, provenance and recycling

^{10}Be production rates are delicate to determine spatially and temporally. We saw above that only a limited number of calibration sites existed. Calibrated data close to the study make it possible to reduce the inherent uncertainties of the scaling model. There is presently no available calibrated data anywhere in Asia, which prevent to validate the scaling models in this continent.

Quartz fertility may impact ^{10}Be production rates at the catchment scale. No study has been performed to validate the simplification of a complete absence of quartz in basaltic and calcareous lithologies, which often contain either small acid intrusions (rhyolites) or a siliceous component (either detrital or recrystallisation following diagenesis).

Production rates are also delicate to determine for the past. The computing codes take into account the temporal variability of the magnetic field for modern production rates, but there is presently no similar code for past production rates.

In addition, one hypothesizes that the geography of the catchment remains stable in the past, i.e. with a constant topography and extent. This is debatable, especially in tectonic and glacial contexts, where subcatchments can be captured or disconnected. This can be discussed when a complementary provenance study, for instance using Sr-Nd isotopes, is available. The basis of a provenance study lays on the fact that geological formations in a catchment can have distinct isotopic signatures, which can be found out in the mixed sediment. We can then follow if certain formations yielded more sediment, which may induce a shift of the geography, or a shift in the location of high erosion rates.

One of the potentially biggest problem found in detrital studies, and sometimes overlooked, is that the catchment changed completely (example proposed in Puchol, 2013). In active ranges, this can occur in particular in the foreland basin, which boundary is progressively exhumed by the frontal thrust. This implies that a the recent part of the record might be recycled from older sediments, thus making it impossible to reconstruct erosion rates for this period.

Finally, the present shielding corrections for topography and ice/snow cover probably do not represent all natural processes and require further investigation, in particular in mountainous areas.

IV.3.4. Steady-state landscape

To analytically solve the equation of the denudation rates, the assumption of a steady-state landscape is made (Lal, 1991). This induces that denudation rates were constant during the accumulation of cosmogenic nuclides in the rocks, in the subsurface. Lal (1991) proposes to systematically measure two cosmogenic nuclides having a distinct half-life to check this hypothesis, but it is not systematically possible. Complex histories, with pulses of erosion, because of climate change or tectonics, interspersed with quiet periods, induce an unsteady state.

In tectonic areas with high erosion rates, like in the Himalaya, concentrations are integrated over periods < 1,000-5,000 yrs, which may be too short a time to integrate two different histories. But the question remains for the areas surrounding the Himalaya, the Indian craton and the Tibetan plateau, which supply sediment to the Ganga and the Brahmaputra.

IV.3.5. Impact of stochastic events

Landslides represent the dominant factor of erosion in active tectonic ranges (Hovius et al., 1997; Khudi catchment in central Nepal: Gallo and Lavé, 2014; Puchol et al., 2014). Contrary to fluvial incision or glacial abrasion, landslides extract rocks of contrasted concentrations (Figure IV-51, Puchol et al., 2014): rocks originating from depths with low to null cosmogenic nuclide concentration and rocks originating from ridges with high concentration. Landslides can also trigger consistent variations between concentrations for different grain-sizes, in particular between gravel and sand (Puchol et al., 2014). Puchol et al. (2014) put into question the validity of the Lal (1991)'s equation to determine erosion rates in such contexts, since instantaneous erosion rates can substantially differ from long term erosion rates. They particularly contradict the threshold in area proposed by Niemi et al. (2005) and Yanites et al. (2009) which allows considering that the variations caused by landslides are smoothed.

Lupker et al. (2017) propose an abrasion model (Figure IV-52) to simulate the evolution of concentrations in sediments along the Brahmaputra, downstream the Namche Barwa, location of frequent and large landslides. They show that abrasion could homogenize concentrations after a distance of 50-150 km.

Since major landslides occur locally at a frequency of 5,000 - 10,000 yrs (Puchol et al., 2014), one

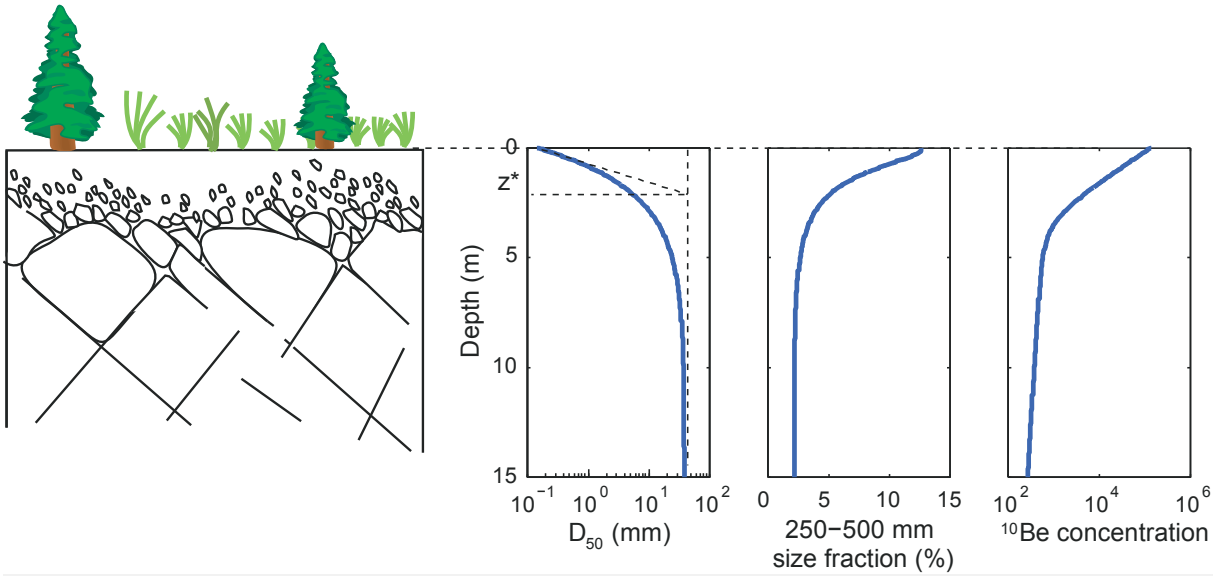

Figure IV-51. Evolution with depth of grain size and ^{10}Be concentration.

Model of the median grain size (D50), the 250-500 µm fraction and the ^{10}Be concentration profile following collapse from the rim of the landslide (from Puchol et al., 2014).

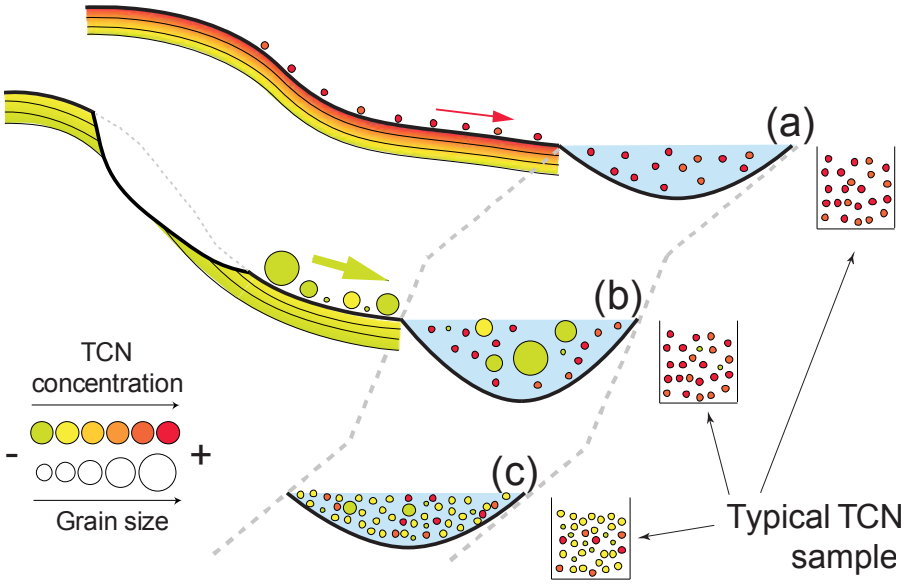

Figure IV-52. Evolution of the sediment ^{10}Be signal in the Tsangpo-Brahmaputra.

a. Transfer to the river of concentrated sediments from the slowly eroding Tibetan plateau

b. Transfer of coarse sediments, poor in ^{10}Be, from the rapidly eroding and landslide prone eastern syntaxis

c. Grain abrasion and homogenizing of the ^{10}Be signal (from Lupker et al., 2017).

can only suppose that for large catchments as the Ganga or the Brahmaputra, the stochastic effect of local landslides is smoothed over the very large area of the catchments. However, after a course of > 800 km in the floodplain, the large variations of concentrations of the Brahmaputra and the Lower Meghna at their outlets, might put into question this hypothesis even for large systems.

IV.3.6. Exposure during transport to sink or recent exposure

Post-erosion exposure (Figure IV-53) leads to an underestimation of denudation rates, because cosmogenic nuclides accumulate in sediment located at a place different from the location of denudation. As previously said, complex histories question the validity of the Lal (1991) to determine denudation rates. They can be detected through the combined measurement of several cosmogenic nuclides (Lal, 1991; Wittmann et al., 2009).

The assessment of transport time can be realized with dating measurements or modelling (Lupker et al., 2012a). This assessment in modern times and in the past is difficult because of potential different behaviours for grains of different sediment size and possibly different river capacity to transport sediments in the past. Burial time is potentially easier to determine by dating stratigraphy.

Recent exposure occurs for continental outcrops and depends on river incision rates. Workers

often assume that collecting samples at the bottom of a cliff allow to make recent exposure negligible, but this hypothesis remains to be more thoroughly checked through a model (like Dibiase, 2018).

IV.3.7. Dating

Dating constraints have an impact on paleodenudation rates, in particular for old samples. This impact is limited when several dating methods are applied, which is not possible in all detrital contexts. Dating uncertainties are complex to determine, and in our view often underestimated. For instance, Lallier et al., 2013 proposed a code to correlate automatically magnetostratigraphic columns. This code allows checking the impact on boundary conditions on the age model, which in our view introduce uncertainties which cannot presently properly assessed. In addition, ages are often determined by computing average accumulation rates from the dating constraints. This sometimes leads to extrapolate accumulation rates to periods lacking dating constraints. Because detrital feeding is not continuous, with periods of incision, deposit, or absence of activity, this can introduce biases which are usually not included in the computation of uncertainties.

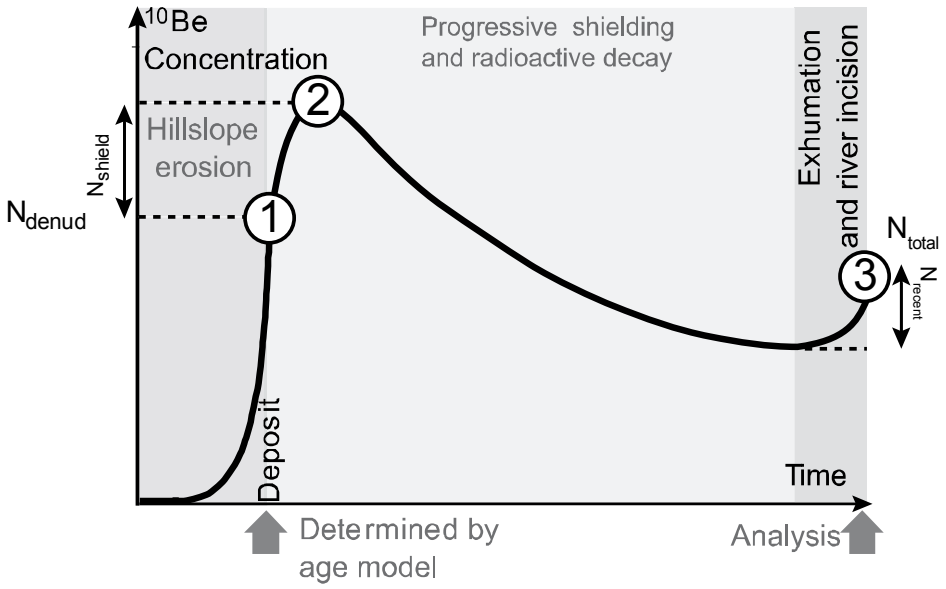

Figure IV-53. Evolution of ^{10}Be from rock denudation to sediment burial and later denudation phase.

When minerals reach the surface (1), their concentration (Ndenud) depends on local ^{10}Be production rates and denudation rates. Minerals are then transported and deposited. They get progressively shielded from cosmic rays during their burial (2). Then the concentration decreases over time because of radio-active decay. At last, minerals may be subject to a later phase of denudation (3) and reexposure to cosmic rays. (from Puchol et al., 2017).

V. DATA REPORT: CALCAREOUS NANNOFOSSILS AND LITHOLOGIC CONSTRAINTS ON THE AGE MODEL OF IODP SITE U1450

Sebastien J.P. Lenard[1*§], Jarrett Cruz[2], Christian France-Lanord[1], Jérôme Lavé[1], Brendan T. Reilly[3]

[1]CRPG, Université de Lorraine, 15 rue Notre Dame des Pauvres, 54500 Vandœuvre-lès-Nancy, France

[2]Department of Earth, Ocean and Atmospheric Science, Florida State University, Tallahassee, Florida, USA

[3]College of Earth, Ocean, and Atmospheric Sciences, Oregon State University, Corvallis, Oregon, 97331, USA

*Correspondence to: sebastien.lenard@gmail.com

§ now at IC2MP, HydrASA, Université de Poitiers, 4 rue Michel Brunet, 86000 Poitiers, France

V.1. ABSTRACT

International Ocean Discovery Program (IODP) Expedition 354 Site U1450 was drilled at the center of a transect of seven sites across the Bengal Fan at 8°N where long-term accumulation rate are the highest. Site U1450 primarily consists of sandy and silty-sandy turbidites deposited at a rate above 20 cm/ky. During periods when depocenter shifted away from Site U1450, calcareous clay hemipelagic sediment was deposited at lower accumulation rate around 1-2 cm/ky. The dating of the Lower Pleistocene and Pliocene sequences is hindered by the scarcity of microfossil in turbidites and the restriction of paleomagnetic data to the upper 190 m. This report presents the identification of new calcareous nannofossils collected from hemipelagic and turbiditic intervals between 218 and 687 m CSF-A. These data are consolidated in a statistical age model that is constrained with ranges of plausible accumulation rates for the distinct lithologies. The age probability model ranges from 1.2 to 7.3 Ma for depths from 175.8 to 812.0 m CSF-A. Depending on constraints, 2-σ uncertainties are around ±0.2 and 0.4 Ma.

V.2. INTRODUCTION

The Bengal Fan forms a record of the past erosion of the Himalaya at the orogen-scale and has been explored through a 320 km E-W transect of 7 sites cored by the International Ocean Discovery Program (IODP) Expedition 354 at 8°N (France-Lanord et al., 2016a). The fan sediments dominantly consist of turbidites that derive from the northern Bay of Bengal shelf and are the product of the Himalayan erosion conveyed by the Brahmaputra and Ganga rivers. At 8°N, Neogene fan sediments have a thickness larger than two kilometers and represent an archive of the past erosion and environment of the Himalayan orogen (Galy et al. 2010; Blum et al., 2018; Najman et al., 2019). While parameters such as provenance, erosion rate, vegetation and precipitation can be derived from turbidite mineralogical, chemical and isotopic compositions, the interpretation of the record is highly dependent on the determination of deposition age at each site. The accumulation of turbidites in the fan is discontinuous as the depocenter migrates from east to west and vice versa, depending on the course of the primary channel of transport (Schwenk and Spiess 2009; France-Lanord et al., 2016a). Turbidites are sediments delicate to date as microfossils are scarce and occasionally recycled. Therefore, age determination chiefly relies on the carbonate-rich hemipelagic horizons accumulated during periods of absence of turbiditic deposition. There, paleo-magnetic, biostratigraphic and sediment lightness allow refining the age model of the transect (Weber and Reilly, 2016). Furthermore, Reilly (2018) refined the age model of the Pleistocene transect through a statistical approach using direct age constraints combined to lithological constraints on accumulation rates and seismic stratigraphy correlations. In the Miocene-Pliocene part of the record, age determination is more difficult as there are no or rare paleo-magnetic constraints because of non-oriented coring.

Site U1450 (France-Lanord et al., 2016b) is located in the axial part of the transect and has been delicate to date as it was the locus of a high accumulation of thick sandy interlevee deposits and, compared to Site U1451, limited hemipelagic intervals during the Pliocene and Early Pleistocene. This led to the accumulation of more than 400 m of sand-rich turbidites over a period of less than 3 My. This corresponds to an average accumulation rate of 15 cm/ky over this period (France-Lanord et al. 2016b). Based on new biostratigraphic data, Blum et al. (2018) reported even higher accumulation rate around 38 cm/ky between 335 and 605 m CSF-A (core depth below seafloor) and 2.9 and 3.6 Ma. However, the presence of more than 50 m of hemipelagic sediment deposited during this depth interval suggests that this interval should correspond to a longer age span. Assuming an accumulation rate in the order of 1-2 cm/ky for hemipelagic sediment implies 2 to 5 Mys that is incompatible with the proposed 0.7 My duration of the interval. A refined age model for Site U1450 requires complementing biostratigraphic datums and accounting for lithological constraints on accumulation rates. This report presents (1) new calcareous nannofossil datums between 218 and 687 m CSF-A, and (2) an age model taking into account available biostratigraphic data and lithostratigraphic constraints on accumulation rates.

V.3. MATERIAL AND METHODS

V.3.1. Calcareous Nannofossils

Standard smear-slide techniques were utilized for biostratigraphic examination. To process a sample, sediment is placed into a cup with water and mixed. A drop of the sediment-water solution is then added to the cover slip. The cover slip is dried on a hot plate, then a mixture of jet dry and water is added to the cover slip. The sediment is then evenly spread across the coverslip using a toothpick. The coverslip is then placed back on a hot plate to remove excess moisture. After drying, the cover slip is mounted using a labelled glass microscope slide with Norland optical adhesive (Number 61). The slide is then placed back onto the hot plate for the glue to spread evenly under the cover slip. The slide is then placed under a UV light bulb until the adhesive has cured and hardened.

Samples were examined using a Zeiss Axiostar+ light microscope. The microscope is equipped with oil immersion lenses with magnifications of 40x, 63x and 100x. They are capable of viewing samples under brightfield phase contrast and cross-polarized light. They are also equipped with a trinocular head and imaging equipment for documentation of marker species.

Samples were analyzed for the presence or absence of marker species. Background taxa were also recorded as present or absent using estimates of abundances. The standard nannofossil zonation of Martini (1971), Bukry (1973), and Okada and Bukry (1980) were utilized evaluate nannofossil age datums. These zonal schemes have been correlated with the Gradstein et al. (2012) geological timescale and a published study by Denne et al. (2005), referenced under the ABX acronym.

V.3.2. Age model

The age model is constructed using a Monte-Carlo approach. Following Reilly (2018), the approach consists in predicting the potential age models by the cross-checking of random age models with observed constraints. These random models are produced by making an initial assumption on the probability distribution of accumulation rates. In Bayesian statistics, this assumption is coined the prior distribution or "prior". The core log is divided into intervals that are classified according to their lithology. For each interval, a random set of individual accumulation rates is drawn following realistic ranges of accumulation rates depending on the lithology. These constraints are "the prior" in the Monte-Carlo approach. The sets of interval individual accumulation rates are then assembled to form a set of random accumulation rate temporal series. Then the set of random temporal paths is constructed using an initial time constraint. The random temporal paths are subsequently cross-checked with the available age datums and all paths not respecting these constraints are rejected. The approach is iterated until a statistically sufficient number of solutions is found.

Here for Site U1450, the split intervals correspond to the core units. The intervals are classified as turbiditic, hemipelagic, or undetermined units, based on the lithostratigraphic log in France-Lanord et al., 2016b. Each first (FO), first common (FCO) and last occurrence (LO) dating marker of Table SV-1-Table SV-2 is associated to the closest interval above the depth of the marker. An uncertainty of ±0.01 Ma is affected to each marker. An initial age of 1.185 Ma for the 175.9 m CSF-A depth is determined by the position of the top of the C1r.3r (middle Matuyama) polarity zone of the 2012 Geologic Timescale (France-Lanord et al., 2016b; Gradstein et al., 2012). The following "prior" is selected for accumulation rates: (1) a uniform distribution in the 10-230 cm/ky for turbiditic intervals (2) a uniform distribution in the 1-5 cm/ky range for hemipelagic intervals. These ranges were selected from the average accumulation rates of all seven Expedition 354 sites computed in Reilly (2018) for the 0-1.2 Ma period. For intervals below 474.7 m CSF-A, core recovery was lower, which generates more uncertainty in the lithology. To let the model accept solutions with accumulation rates diverging from the range affected to each lithology, we apply a bimodal distribution. The first mode is the uniform distribution previously selected, weighed by a factor of 0.7 and the second mode is a uniform distribution in the 5-35 cm/ky, weighed by a factor of 0.3. As a consequence, it allows turbiditic intervals to present accumulation rates lower than average and hemipelagic intervals to present accumulation rates higher than average.

Numerical sampling of accumulation rates includes a compaction term with separate laws for turbiditic and hemipelagic intervals (Baldwin & Butler, 1985). This compaction correction is applied to the prior accumulation rates given above in function of the sampling depth, considering that the reference rates were defined at a mean depth of 100 m (Reilly, 2018). Numerical sampling was performed million times over the 175.6-811.9 m CSF-A depth range until that 10,000 paths respect the micropaleontological constraints were obtained.

V.4. RESULTS

V.4.1. Calcareous Nannofossils identifications

For this study we prepared and observed 125 new samples (Table SV-3). Key nannofossils identifications are presented Figure V-54 and Table SV-1. Due to the nature of sampling at this site, the analyses of Top events (Last Occurrence) are mainly utilized. Without continuous sampling to trace abundance shifts it is difficult to assign First Occurrence events. 18 events are presented in sample depths from 218 to 687 m. The first event Scyphosphaera pulcherrima is assigned "Within" to signify the sample is older than 1.03 but younger than 1.6 Ma, likely below the actual Top of this zone. The remaining 17 events are marked with Top, this signifies the first observation considered to be in situ of the marker species. Due to the nature of the study site, its significant turbidite activity and rarity of some marker species, the events likely do not signify the true top. This is considered in the range of error mentioned previously. Another important factor that needs to be considered when assigning an absolute age is the diachronous characteristic of nannoplankton. The ABX age values assigned are from a study of Gulf of Mexico nannofossil events, therefore ages may differ from Indian Ocean events.

Figure V-54. Nannofossil Markers in plain and polarized light.

Next page.

1 Amaurolithus primus, 2 Amaurolithus tricorniculatus, 3 Calcidiscus macintyrei, 4 Ceratolithus acutus, 5 Ceratolithus rugosus, 6 Discoaster asymmetricus, 7 Discoaster brouweri, 8 Discoaster pentaradiatus, 9 Discoaster quinqueramus, 10 Discoaster tamalis, 11 Discoaster triradiatus, 12 Nicklithus amplificus, 13 Reticulofenestra pseudoumbilicus, 14 Triquetrorhabdulus rugosus.

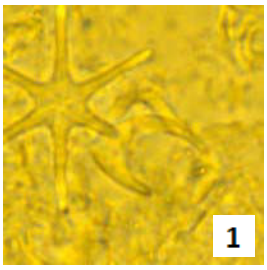

Amaurolithus primus

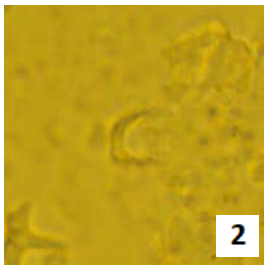

Amaurolithus tricorniculatus

Calcidiscus macintyrei

Ceratolithus acutus

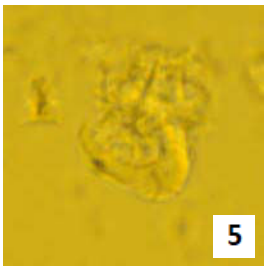

Ceratolithus rugosus

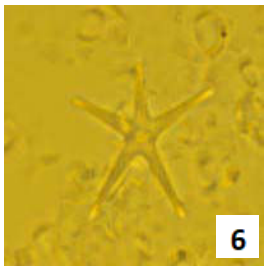

Discoaster asymmetricus

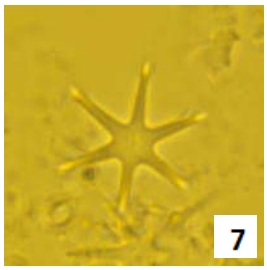

Discoaster brouweri

Discoaster pentaradiatus

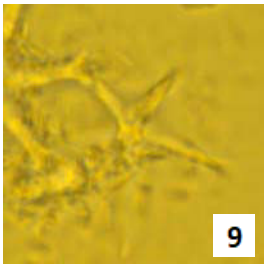

Discoaster quinqueramus

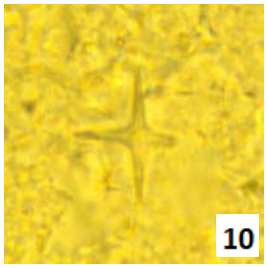

Discoaster tamalis

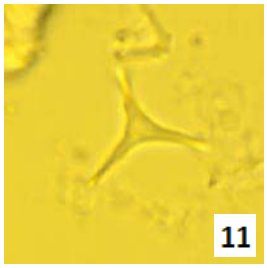

Discoaster triradiatus

Nicklithus amplificus

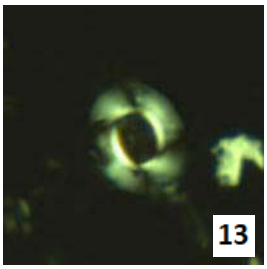

Reticulofenestra pseudoumbilicus

Triquetrorhabdulus rugosus

V.4.2. Age Model

The computed age model with its uncertainties is presented in Figure V-55 and Table SV-4. All solutions respect the constraints given by our new calcareous nannofossil datums (Table SV-1) and the published biostratigraphic datums (Table SV-2, France-Lanord et al., 2016b; Blum et al., 2018). Two-sigma uncertainties vary between ±0.2 and 0.4 Ma depending on the configuration of age and lithological constraints.

The younger boundary of the age envelope is constrained by 24 last occurrence (LO) or last common occurrence (LCO) datums, and the oldest boundary is constrained by first 4 occurrence (FO) datums only. The model is better constrained in the central interval, 390-700 m CSF-A corresponding to 2.9-6.7 Ma. One couple of LO-FO datums at ~700 mm CSF-A strongly control the age model. Because of the limited number of FO datums, the prior distribution of accumulation rates exerts a control complementary to the LO datums on the age model.

The age model displays a stepwise shape reflecting the alternation of short and thick sand and silt turbidites with long and thin hemipelagic episodes. The accumulation rate prior distribution that was selected for the model is compatible with the datums. As expected, the predicted turbiditic accumulation rates are fully controlled by the "prior" and therefore are only indicative. They do not diverge from 110±100 cm/ky for the 175-475 m CSF-A interval and only occasionally diverge from 65^{+135}_{-60} cm/ky for the 475-805 m CSF-A interval. Contrary to the turbiditic intervals, the hemipelagic intervals present predicted accumulation rates that seem independent of the "prior", with on average $2.0^{+2.0}_{-1.2}$ cm/ky for the 175-475 m CSF-A interval. Predicted values are slightly higher for the 475-630 m CSF-A interval, at $2.8^{+23.9}_{-1.8}$ cm/ky and higher for the 657-800 m CSF-A interval at $8.0^{+22.0}_{-6.4}$ cm/ky.

Figure V-55. Age model of Site U1450.

Next page.

Reconstructed in this study, with the 0-175.9 m CSF-A part from Reilly (2018). For clarity, the cores of Hole U1450B that overlap the cores of Hole U1450A are not indicated. The lithostratigraphic log is from France-Lanord et al. (2016b).

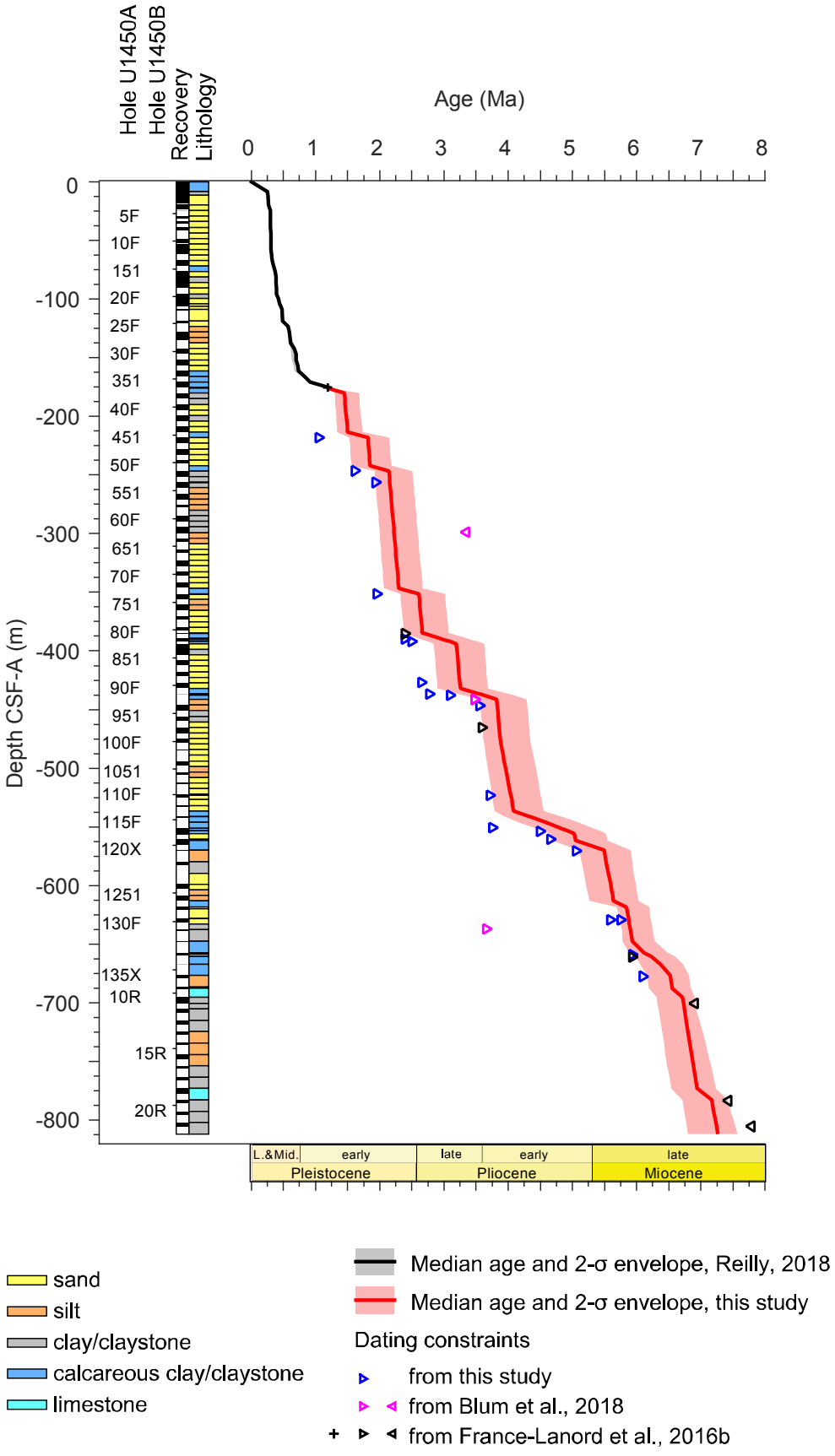
Hole U1450A
Hole U1450B
Recovery
Lithology
Age (Ma)
0
1
2
3
4
5
6
7
8
Depth CSF-A (m)
0
-100
-200
-300
-400
-500
-600
-700
-800
5F
10F
151
20F
25F
30F
351
40F
451
50F
551
60F
651
70F
751
80F
851
90F
951
100F
1051
110F
115F
120X
1251
130F
135X
10R
15R
20R
L.&Mid.
early
late
early
late
Pleistocene
Pliocene
Miocene
sand
silt
clay/claystone
calcareous clay/claystone
limestone
Median age and 2-σ envelope, Reilly, 2018
Median age and 2-σ envelope, this study
Dating constraints
from this study
from Blum et al., 2018
from France-Lanord et al., 2016b

Acknowledgements

The samples were provided by IODP. The staff of IODP Kochi Core Center are thanked for their assistance for sample collection in February 2019. Funding was provided by a Université de Lorraine-CRPG PhD fellowship and a Université de Poitiers A.T.E.R. of S.L. and ANR Himal Fan project.

Author contributions

C.F.L. designed the study. J.C. performed the nannofossil observations. S.L. and J.L. performed the computing for the age model. B.R. supplied the part of the age model younger than 1.2 Ma. S.L. J.C., C.F.L. and J.L. interpreted the results and wrote the manuscript.

V.5. TABLES

In Tables attached to this manuscript.

Table SV-1. Biostratigraphy of samples from Site 1450A.

Table SV-2. Published age datums considered for the age model of the site U1450.

Table SV-3. List of observed samples.

Table SV-4. Predicted age model of the site U1450.

VI. STEADY EROSION OF THE HIMALAYA DURING THE LATE CENOZOIC CLIMATE CHANGE

Sebastien J.P. Lenard*[1§], Jérôme Lavé[1], Christian France-Lanord[1], ASTER Team[2†]

[1]CRPG, Université de Lorraine, UMR 7358, 15 rue Notre Dame des Pauvres, 54500 Vandœuvre-lès-Nancy, France

[2]Université Aix-Marseille, CNRS-IRD-Collège de France, UM 34 CEREGE, Technopôle de l'Environnement Arbois-Méditerranée, BP80, 13545 Aix-en-Provence, France

*Correspondence to: sebastien.lenard@gmail.com

§now at IC2MP, HydrASA, Université de Poitiers, 4 rue Michel Brunet, 86000 Poitiers, France

†Georges Aumaître, Didier L Bourlès, Karim Keddadouche.

INTRODUCTORY PARAGRAPH

The onset of the Northern Hemisphere Glaciations with prevailing glacial-interglacial cycles is suggested having triggered a global increase in continental erosion rates during the late Cenozoic. However, the effect of the climate variability on erosion rates is not sustained by all proxies and has sparked an intense debate on the potential biases of the approaches. Here, we measured the concentrations of the cosmogenic nuclide ^{10}Be contained in the detrital quartz deposited over the last 6 Ma in the Bengal Fan to quantify how the Himalayan erosion responded to this climate transition. The ^{10}Be concentrations are partially controlled by the distinct contributions of the Ganga and Brahmaputra drainage basins, which can be accounted for by the Sr and Nd isotopic compositions of the sediment. Despite changes in the sediment source, the reconstructed paleoerosion rates have remained stable for the last 6 Ma and do not reveal any visible impact of the late Cenozoic climate change on the erosion of the Himalaya.

VI.1. INTRODUCTION

In mountain ranges, a substantial increase in physical and chemical erosion rates has been attributed to an amplified climate variability and repeated glaciations during the late Cenozoic (Kuhlemann et al., 2002; Thiede and Ehlers, 2013; Herman et al., 2013; Zhang et al., 2001; Molnar, 2004; Pedersen and Egholm, 2013). However, the hypothesis of a long-term climate forcing of erosion rates is at odds with global proxies such as the seawater ^{10}Be/^{9}Be, which suggests steady chemical weathering and erosion rates over the same time span (Willenbring and von Blanckenburg, 2010). These contradictions have fostered a debate on the biases affecting the respective proxies for erosion rates (Schumer and Jerolmack, 2009; Moore et al., 2013; Norton and Schlunegger, 2017; Schildgen et al., 2018) and contributing to this debate requires new, independent approaches.

In this study, we quantified the paleoerosion rates of the Himalaya since the late Miocene with the measurement of cosmogenic nuclides accumulated in terrigenous sediment (Brown et al., 1995; Granger et al., 2001; Schaller et al., 2002; Bierman et al., 2016; Puchol et al., 2017). The Himalaya were subject to a variation of the glacial cover between less than 5% in modern times (GLIMS Database, Raup et al., 2007) and up to 20% in the Last Glacial Maximum (Shi, 2002), and to an increased variability of the precipitations of the Indian Summer Monsoon (An et al., 2011) during the late Cenozoic. Therefore, the Himalaya represent a key location to explore the interactions between erosion and climate during this time span.

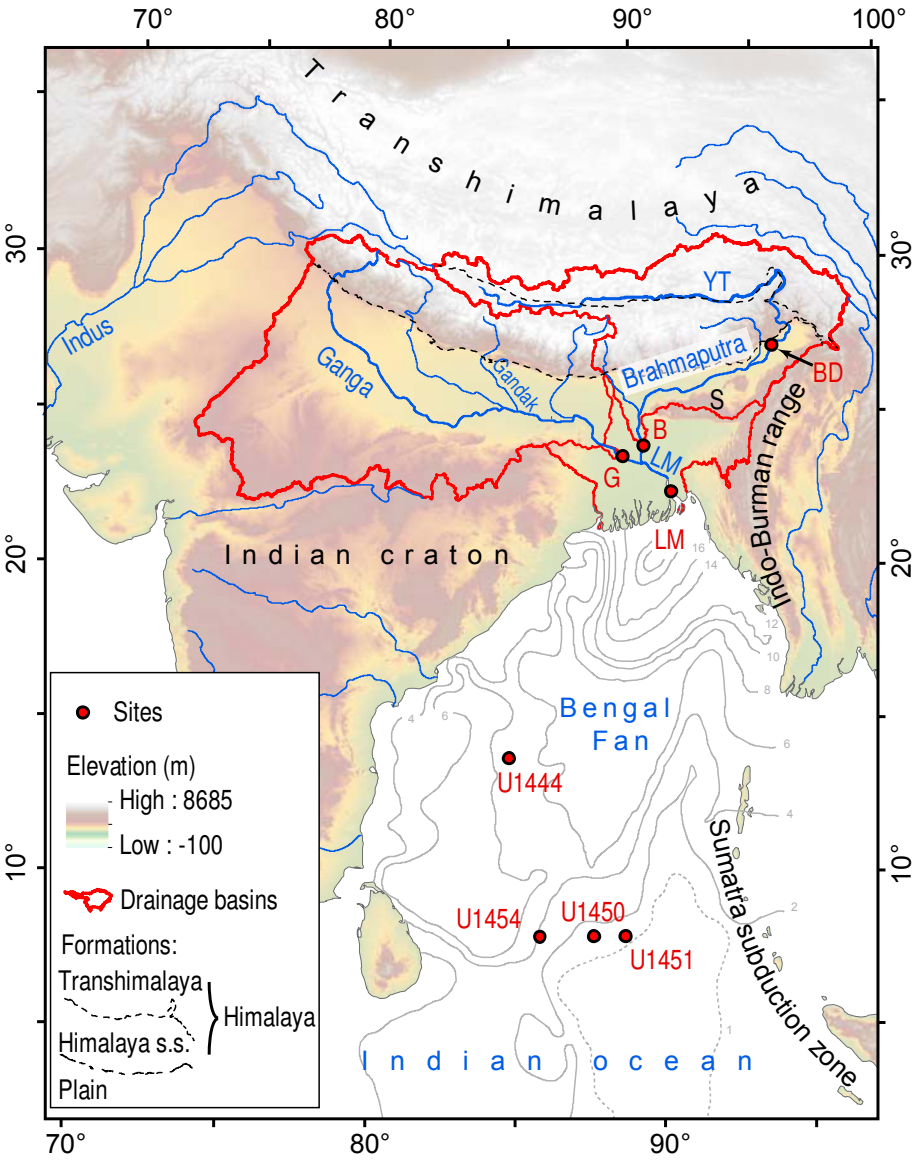

Figure VI-56. Setting of the Bengal Fan.

Geographical map of the Himalaya and the Bengal Bay. The Bengal Fan IODP Sites and the sampling sites of modern river sand, G: Ganga at Harding Bridge, B: Brahmaputra at Sirajganj/Jamuna Bridge, Bangladesh, BD: upstream Brahmaputra at Dibrugarh, close to the range outlet, LM: Lower Meghna are indicated. The basins of the rivers are contoured in red. They include the Himalaya, which is divided with dashed black lines into the Transhimalaya and the Himalaya stricto sensu (s.s.). The Bengal Fan is represented by the marine isopachs in km (Curray, 1991; Radhakrishna et al., 2010). Several geographical features are indicated, among them the Lower Meghna River (LM), the Yarlung-Tsangpo River (YT), the Shillong Plateau (S).

VI.2. APPROACH FOR EROSION RATE QUANTIFICATION

The sediment eroded from the Central and Eastern Himalaya is conveyed by the Ganga and the Brahmaputra rivers respectively, and after their confluence, by the Lower Meghna river to the Bengal Shelf, and dispersed across the Bengal Fan by a 3000 km-long turbiditic system (Curray et al., 2003; Schwenk and Spiess, 2009) (Figure II-8). Samples were obtained by the drilling of the Bengal Fan by the International Ocean Discovery Program (IODP) Expeditions 353 and 354 at latitudes of 16°N and 8°N respectively (Clemens et al., 2016; France-Lanord et al., 2016a) and by the sampling of the Lower Meghna modern sand.

These drillings returned an unprecedented record of Himalayan erosion, including sand-rich turbidites suitable for in situ ^{10}Be cosmogenic nuclide measurements in the quartz fine sand fraction. The ^{10}Be concentrations were corrected for radioactive decay using the sediment deposition age (Clemens et al., 2016; France-Lanord et al., 2016a; Reilly, 2018; this thesis, Chapter V), and interpreted in terms of average paleoerosion rates for the whole Central and Eastern Himalayan arc. Because the modern river sediment of the Ganga and Brahmaputra exhibit distinct Sr and Nd isotopic compositions in their bulk silicate fraction (Galy and France-Lanord, 2001; Singh and France-Lanord, 2002; Singh et al., 2008; Lupker et al., 2012a, 2017), the measurement of isotopic compositions in the Bengal fan samples provides additional constraints to identify the relative contributions of the Central and Eastern Himalaya over time.

VI.3. ^{10}BE CONCENTRATIONS

Four drill sites of the Bengal Fan were selected to limit the effect of turbiditic sedimentation gaps caused by the migration of the turbiditic channels (France-Lanord et al., 2016a; Reilly, 2018; this thesis, Chapter V). The ^{10}Be concentrations reflect erosion rates across the source basin of the sandy sediment of the Bengal Fan. They average the signal of several million grains of quartz eroded over ~1 ka on mountain hillslopes, even if the signal can be damped over periods of 1-10 ka during the sediment transfer through the floodplain (Lupker et al., 2012a). Here, the ^{10}Be corrected concentrations, i.e. paleoconcentrations, for the Bengal Fan reach on average $31\pm11 \times 10^3$ atom/g over the last 6.2 Ma, with fluctuations between 12×10^3 and 64×10^3 atom/g (Figure VI-57b, Table SVI-1 column AE). The ^{10}Be concentrations measured in the modern sand of the Lower Meghna present a similar average value at $38\pm8 \times 10^3$ atom/g within uncertainties, but a lower dispersion compared to the Bengal Fan paleoconcentrations with values ranging between 29×10^3 and 50×10^3 atom/g.

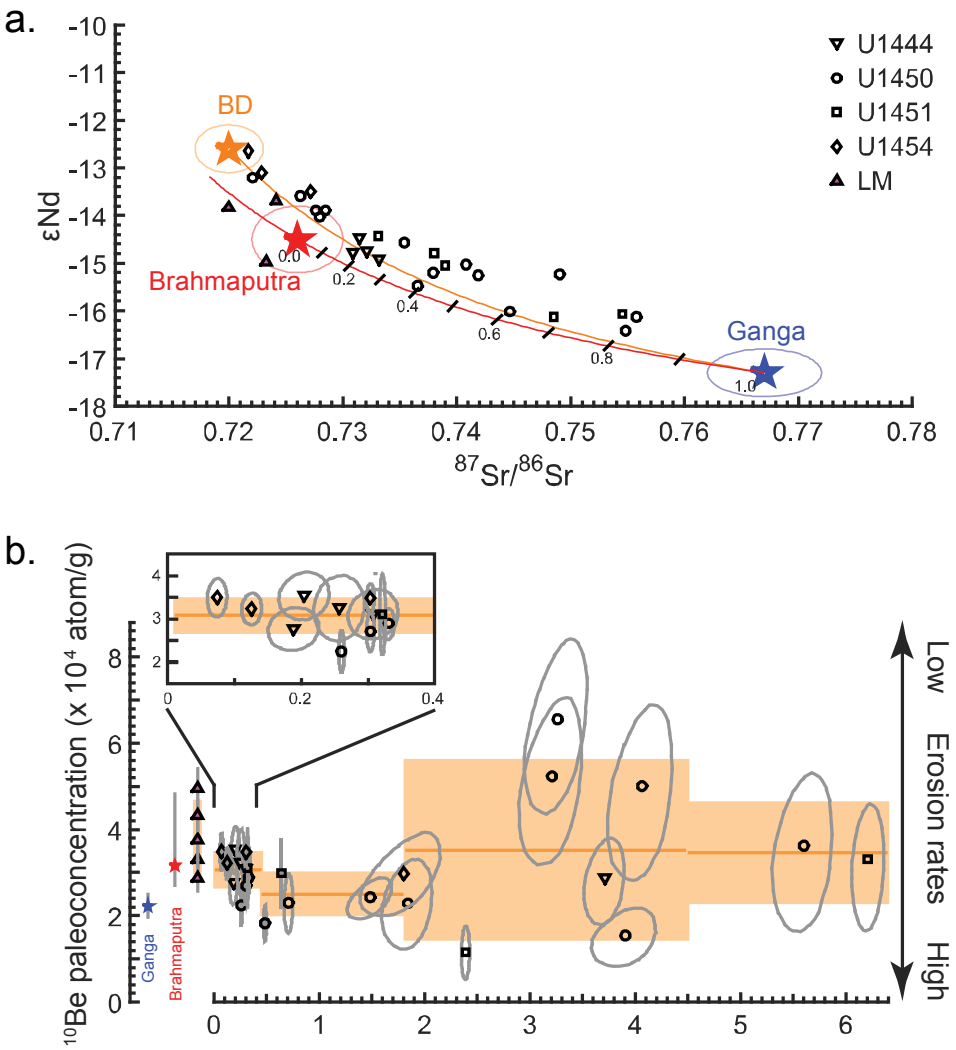

Figure VI-57. ^{10}Be and Sr-Nd isotopic results.

a. Sr-Nd isotopic composition results. The results for the Bengal Fan and the Lower Meghna sand plot along a mixing trend between the Ganga and the Brahmaputra sand, with the fraction fG indicated and with distinct symbols for the four IODP Sites and the Lower Meghna (LM). The trend with the Brahmaputra at Dibrugarh (BD, Figure II-8) is also indicated.

b. Evolution of the ^{10}Be paleoconcentrations in the Bengal Fan and concentrations in the Lower Meghna sand, with an inset focusing on the 0 - 0.4 Ma time span. The ^{10}Be concentrations are inversely correlated to erosion rates. The 1-σ uncertainty is represented by ellipses surrounding the dots. The concentrations of the Ganga (Lupker et al., 2012a) and the Brahmaputra (Lupker et al., 2017) are indicated for comparison. We selected intervals with homogeneous Sr-Nd isotopic composition and computed the average and standard deviations of the paleoconcentrations, which are represented by orange bars and rectangular areas respectively.

The Bengal Fan paleoconcentrations do not follow a long-term decreasing trend that would indicate a long-term increase in erosion rates. We observe that before ca. 4.5 Ma (2 values) and after 1.8 Ma (17 values), the paleoconcentrations are close to the average value of 31±11x10^3 atom/g. For these periods, the dispersion is smaller than the one observed on the modern sand of the Brahmaputra (Lupker et al., 2017) and the Lower Meghna (Figure VI-57b). In contrast, the 4.5-1.8 Ma period (7 values) is affected by the largest dispersion.

VI.4. APPARENT EROSION RATES

From our ^{10}Be paleoconcentrations C, we derived the apparent Himalayan mean erosion rates $\bar{e}$ using the simplified equation (Supplementary Information 4 and 8):

$$\bar{e} = \frac{\Lambda}{\rho}\frac{\bar{P}}{C} \quad (1)$$

with $\bar{P}$ the mean production rate of the modern Himalayan part of the basin (Figure II-8), Λ the nucleon attenuation length and ρ the crustal rock density. The use of this equation is permitted under three verified conditions (Supplementary Information): (A) the temporal variability of the cosmogenic nuclide production rate, caused by Earth magnetic dipole variations, has remained within the range of uncertainties of the ^{10}Be concentrations; (B) the geography and elevation of the contributing area, i.e. the Himalayan part of the Ganga and Brahmaputra basins, have remained stable; (C) the exposure of the sediment to cosmic rays during the transfer through the floodplain has a negligible impact on the ^{10}Be concentrations.

The so-derived paleoerosion rates (Table SVI-1 column AH) are found similar on average to the modern value of ~1 mm/y derived from the concentrations of the Ganga and Brahmaputra (Lupker et al., 2012a, 2017). Nevertheless, before any further interpretation of this apparent erosion stability, a fourth condition must be verified in the case of the Ganga and the Brahmaputra: the sediment of these two large Himalayan rivers has to be mixed in proportion of their erosional fluxes downstream to the drilling sites in the Bengal Fan. This latter condition is further examined with our provenance analyses.

VI.5. SR-ND ISOTOPES

The ^{87}Sr/^{86}Sr and εNd values for the Bengal Fan present an organized trend, with covariations from respectively 0.721 and -12.6 to 0.756 and -16.2 (Figure VI-57a, Table SVI-1 columns AL, AO). This trend suggests that the Bengal Fan sand originates from a simple binary mixing. Compared with the compositions of the modern Brahmaputra and Ganga river sediment, the low εNd / high ^{87}Sr/^{86}Sr endmember tends towards the composition of the Ganga in Bangladesh (Singh et al., 2008), corresponding to the erosion of the formations of the Himalaya s.s. (sensu stricto, Figure II-8) (Lesser Himalaya, High Himalaya Crystalline and Tethyan Sedimentary Series). The high εNd / low ^{87}Sr/^{86}Sr

endmember overlaps the composition of the Brahmaputra in Bangladesh (Galy and France-Lanord, 2001; Singh and France-Lanord, 2002) and reaches the composition of the Brahmaputra sampled upstream close to the mountain range outlet (BD pole on Figure VI-57a, Singh and France-Lanord, 2002). The composition of the Brahmaputra sediment reflects a mixing between the Himalaya s.s., the Transhimalaya and the mantle-derived formations drained by the Yarlung-Tsangpo and the Eastern tributaries of the Brahmaputra (Singh and France-Lanord, 2002).

The modern bedload Sr-Nd isotopic composition of the Lower Meghna (Figure VI-57a) is similar to that of the Brahmaputra and suggests an absence of a Ganga sand contribution. This is further confirmed by the Sr concentration of the bulk sediment (Figure VI-62b) showing that the sandy bedload composition of the Lower Meghna overlaps with the composition of the Brahmaputra sediment, whereas the suspended load composition corresponds to a mixing between the Ganga and the Brahmaputra sediment. This implies a sharp difference in sand sequestration and export between the Ganga and the Brahmaputra floodplains in modern times, with most of the Ganga sand sequestered in the Ganga floodplain as demonstrated by the geochemical and granulometric budgets developed in the Supplementary Information.

We derived the proportion of the Bengal Fan and Lower Meghna sediment issued from the Ganga basin, called fraction f_G, from a projection on a Ganga-Brahmaputra mixing trend and obtained values ranging from 75% to -40% (Figure VI-58a, Table SVI-1 column AQ). The negative fractions correspond to compositions with a lower contribution of the Himalaya s.s. than the one observed in the modern Brahmaputra in Bangladesh. While the provenance appears to be independent from the Site position, f_G displays a clear decrease since 0.45 Ma.

If the sediments of the Ganga and the Brahmaputra are fully exported to the Bengal Fan, the variations of f_G reflect changes in erosion rates either in the Ganga basin or in the Brahmaputra basin. Alternatively, the variations of f_G reflect changes in sand sequestration in the floodplains of both rivers or changes in the system routing sediments from both rivers to turbidites. In that case, extreme compositions are explained by the sequestration of most of the Ganga sand as in modern times, or by distinct outlets and distinct turbiditic systems for the Ganga and Brahmaputra (Curray et al., 2003; Contreras-Rosales et al., 2016; Blum et al., 2018), resulting in cores that recorded turbidites derived from the Brahmaputra. The computation of paleoerosion rates should include these alternative conditions.

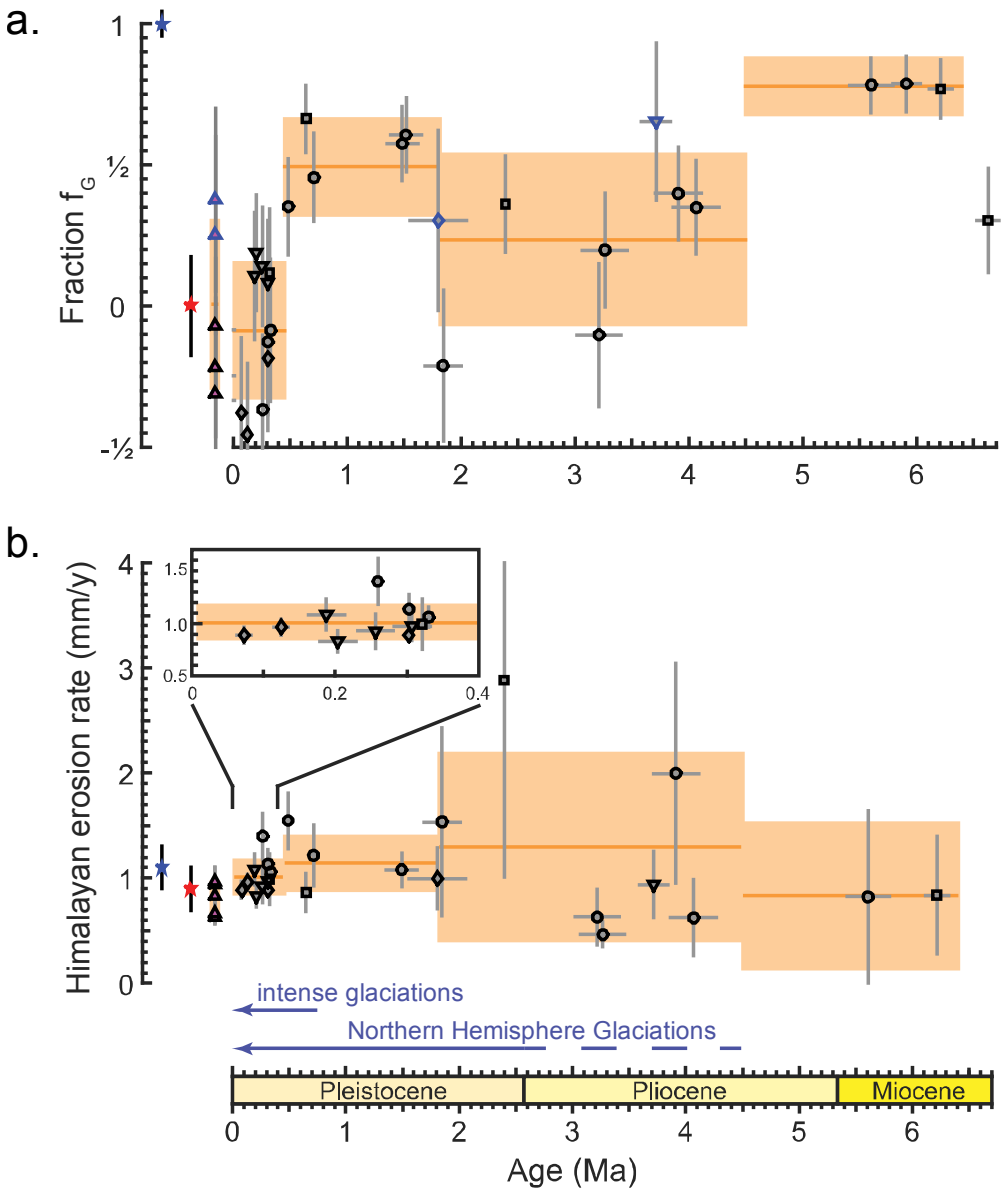

Figure VI-58. Fraction f_G and erosion rates.

a. Fraction f_G of the Bengal Fan and Lower Meghna sand issued from the Ganga basin as a function of time. The black-contoured dots are computed from Sr-Nd isotopes and the blue-contoured dots are computed from the Sr concentration. The average f_G and the deviation are indicated as in b. Three samples measured for Sr-Nd isotopes were not measured for ^{10}Be concentrations. A chart presenting the ^{10}Be paleoconcentrations as a function of f_G is also available (Figure VI-63).

b. Himalayan erosion rates in the case of a regional climate forcing of erosion, determined on the Himalayan s.s. and the Transhimalayan part of the basin, with an inset similar to b. The average erosion rate and the deviation are indicated as in b.

VI.6. TEST OF THE CLIMATE FORCING HYPOTHESIS

To explore how this variable export of the Ganga and Brahmaputra sand impacts our preliminary conclusions on the stability of the Himalayan erosion rates during the late Cenozoic, we developed a test for the climate forcing hypothesis (detailed computation in Supplementary Information). The mixing of two end-members with ^{10}Be concentrations C_G and C_B yields a final concentration C that is a function of f_G as shown below (the indices G and B indicating the Ganga and Brahmaputra respectively):

$$C = f_G \times C_G + (1 - f_G) \times C_B \quad (2)$$

At steady state, C_G and C_B depend on the undetermined mean erosion rates e_G and e_B of each drainage basin.

In case of sequestration in the floodplains or distinct turbiditic systems, the equation (2) cannot be simplified, and the mean Himalayan erosion rate remains undetermined. This indetermination can be waived under the assumption that most Himalayan landscapes respond similarly to a global climate forcing (Zhang et al., 2001). In that case, we can test the simplified configuration for which e_G and e_B co-vary over time. The mean Himalayan erosion rate $\bar{e}(t)$ is then determined from the modern mean erosion rate $\bar{e}_0$ through $\bar{e}(t) = K(t) \times \bar{e}_0$

with the regional climatic amplification factor of erosion relative to modern conditions $K(t) = \left(f_G(t) \times C_{G,0} + \left(1 - f_G(t)\right) \times C_{B,0}\right)/C(t)$, and with $C_{G,0}$ and $C_{B,0}$ the modern ^{10}Be concentrations in the sand of each river.

The resulting mean Himalayan erosion rate displays a signal (Figure VI-58b, Table SVI-1 column AV) similar to that of the paleoconcentration, i.e. a constant mean erosion rate over the last 6.2 Ma, between 0.8 and 1.3 mm/y, close to the modern values of ~1 mm/y. Although some scenarios more complex than this uniform climate forcing hypothesis would be worth developing with additional constraints, this demonstrates that despite the variable mixing of the Ganga and Brahmaputra sand, the primary conclusion of our data on the absence of an increase in erosion rates seems robust.

VI.7. IMPLICATIONS

Our results suggest that the climate forcing of erosion is weak in the Himalaya, as argued on a global scale by (Willenbring and von Blanckenburg, 2010). The marked increase in local erosion rates documented by in situ thermochronometry in the Himalaya (Huntington et al., 2006; Herman et al., 2013; Yang et al., 2018) is not reflected by an increase in the mean erosion rates reconstructed using cosmogenic nuclide concentrations in the Bengal Fan. This may imply that available thermochronometric data in the Himalaya are only of local tectonic or geomorphologic significance and do not reflect the average erosion of the Central and Eastern Himalaya as cosmogenic nuclides applied on sediment do.

In mountain ranges, the extension of ice during the late Cenozoic climate cooling likely produced an increase in erosion rates (Herman et al., 2013; Pedersen and Egholm, 2013) or at least an increase in the variability of the erosion rates as shown by several ^{10}Be records (Schaller et al., 2004; Haeuselmann et al., 2007; Puchol et al., 2017). In the High Himalaya, prominent glacially-shaped valleys attest for the intensity of glacial erosion. However, our results do not indicate any significant increase in erosion rates since 6.2 Ma, and they even point to a slight decrease since 0.45 Ma. The amplitude of the variations in the ^{10}Be erosion rates is paradoxically lower during the intensification of the Northern Hemisphere Glaciations (since ~0.8 Ma) than during the previous period, even if this might partly arise from buffering effects caused by glacio-eustatic variations and temporary sediment storage in the delta, as shown since 11 ka (Goodbred and Kuehl, 2000). In any case, our results suggest that glacial erosion had no manifest impact on the global volume of the sediment exported from the Central and Eastern Himalaya.

In absence of a clear climate control on Himalayan erosion, the large fluctuations of paleoconcentrations and provenances documented in this study between 1.8 and 4.5 Ma (Figure VI-57-Figure VI-58) could reflect transient responses to regional changes in tectonics. Such changes are documented during that period for the Eastern Syntaxis (Burg et al., 1997; Zeitler et al., 2014; Yang et al., 2018) and in the foreland sedimentary basin with the rise of the Shillong Plateau (Najman et al., 2016) and the development of the Indo-Burman wedge (Maurin and Rangin, 2009). Further studies with an approach similar to ours applied in the Himalayan foreland basin should help in specifying those possible tectonic imprints.

VI.8. METHODS

The samples were selected from the sand sediment of four sites drilled in the Bengal Bay during the IODP Expeditions 353 and 354 (Figure II-8, Table SVI-1) (Clemens et al., 2016; France-Lanord et al., 2016a). The $^{10}Be/^{9}Be$ ratios were measured at the ASTER national Accelerator Mass Spectrometer facility (CEREGE, Aix-en-Provence, France) (Arnold et al., 2010; Braucher et al., 2015) and the Sr-Nd isotopes were measured at CRPG-CNRS-UL (Nancy, France) (Hein et al., 2017). The samples were prepared and decontaminated from the atmospheric ^{10}Be contribution at CRPG-CNRS-UL (Nancy, France) following standard procedures (Brown et al., 1991; Lupker et al., 2012a, 2017; Hein et al., 2017; Puchol et al., 2017). The ^{10}Be paleoconcentrations were computed (Puchol et al., 2017) assuming that they reflect, to the first order, the mean concentration at the outlet of the Himalayan range, i.e. accounting only for radioactive decay and neglecting any additional ^{10}Be production during the sediment transfer in the foreland basins, and any recent exposure since the Bengal Fan sediment are lying below a >2,000 m water column. The fraction f_G was computed from the modern Ganga and Brahmaputra sediment isotopic signatures, under the assumption that these compositions have remained stable since 7 Ma. The full formulation of f_G and the regional climatic amplification factor of erosion relative to modern conditions $K(t)$, along with the paleoerosion rates is developed in the Supplementary Information.

Acknowledgments

The samples were provided by IODP. The staff of IODP Kochi Core Center are acknowledged for their assistance for sample collection, and the teams of CRPG, SARM and CEREGE for their assistance in sample preparation and measurements. The ^{10}Be measurements were performed at the ASTER AMS national facility (CEREGE, Aix en Provence) which is supported by the INSU/CNRS, the ANR through the "Projets thématiques d'excellence" program for the "Equipements d'excellence" ASTER-CEREGE action and IRD. Funding was provided by a Université de Lorraine-CRPG PhD fellowship and a Université de Poitiers A.T.E.R. of S.L. and ANR Himal Fan project.

Author contributions

C.F.L. and J.L. designed the study. S.L. and T.A. performed the measurements. J.L. and S.L. performed the computations. S.L., J.L. and C.F.L. interpreted the results and wrote the manuscript.

VI.9. EXTENDED METHODS

VI.9.1. Material

The sample locations are presented in Figure II-8 and complementary information is in Table SVI-1.

The IODP Expedition 354 drilled a transect of seven holes extending from the late Pleistocene to the Miocene at 8°N (Figure II-8) (France-Lanord et al., 2016a). The cores consist of sand and silt turbidites interbedded with hemipelagic calcareous clay. Another hole drilled during Expedition 353 also provides a turbiditic record in the northwestern Bay of Bengal at 16°N (Clemens et al., 2016). The abundance in nano/microfossils and the presence of clayey material appropriate for paleomagnetic dating contributed to yield dating constraints over the full period up to recent times (Clemens et al., 2016; France-Lanord et al., 2016a; Reilly, 2018, this thesis, Chapter V).

The abundance in quartz-rich sand in the turbidites makes possible the application of in-situ-produced ^{10}Be measurement. We selected 28 samples from the inter-levee and sand lobe turbidites from 4 drilled sites: U1450, U1451 and U1454 at 8°N, and U1444 at 14°N (Figure II-8). Overall, the samples cover the 0.07 - 6.6 Ma range, with a higher density in the 0.07 - 0.7 Ma range. We also selected five modern bedload samples from the Lower Meghna representing the modern export of the Ganga and Brahmaputra to the Bay of Bengal. All Bengal Fan and modern samples are unconsolidated sediment. The majority of samples are rich in the coarse fraction (> 125 μm).

VI.9.2. ^{10}Be/^{9}Be preparation and measurements

The ^{10}Be/^{9}Be information and results are presented in Figure VI-59, and in Table SVI-1.

The samples were prepared and decontaminated from the atmospheric ^{10}Be contribution at CRPG-CNRS-UL (Nancy, France) following standard procedures (Brown et al., 1991; Lupker et al., 2012a, 2017; Puchol et al., 2017). The measurement of the ^{10}Be/^{9}Be ratios for a selected granulometric fraction (125-250 μm except for four samples, Table SVI-1) was performed at the ASTER national Accelerator Mass Spectrometer facility (CEREGE, Aix-en-Provence, France) (Arnold et al., 2010), with a normalization to the in-house standard STD-11, using an assigned ^{10}Be/^{9}Be ratio of (1.191 ± 0.013) x 10^{-11} (Braucher et al., 2015).

We used a sufficient amount of quartz (i.e. > 100 g, Table SVI-1) to lower analytical uncertainties for the older samples. A 75-250 μm fraction was selected for the four samples with little coarse material > 125 μm. The mean difference in ^{10}Be concentrations between the 75-125, 125-250 and 75-250 μm fractions (duplicate analyses on five samples) reaches 17% and therefore indicate that the granulometry of the analyzed fraction plays a minor role in the dispersion of data (Figure VI-60).

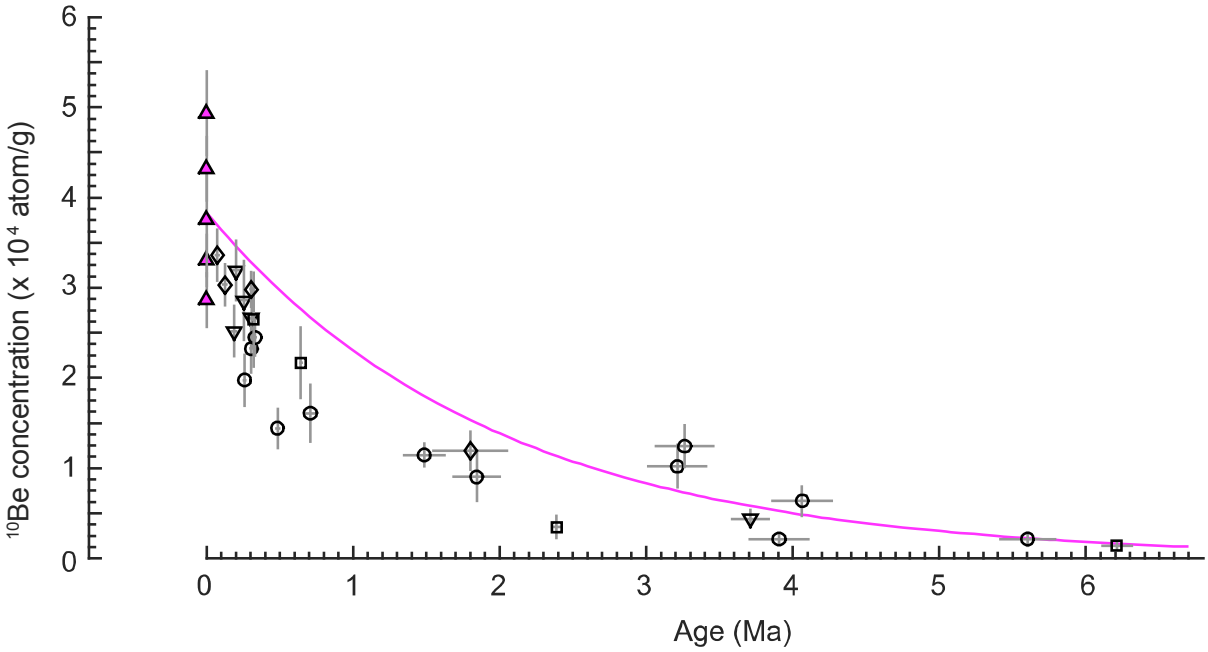

Figure VI-59. ^{10}Be concentration results.

The theoretical radioactive correction curve from the average ^{10}Be concentration of the Lower Meghna is indicated. Same symbols as Figure VI-57.

In addition, we performed a check on a potential natural ^{9}Be content in the quartz that could interfere with the ^{9}Be content of the carrier (see discussion in Lupker et al., 2017). After evaporation and dissolution of the residue in HCl, an aliquot was collected for ^{9}Be measurement using ICP-MS at CRPG, Nancy. We found ^{9}Be concentrations of the same order as the ^{9}Be concentrations predicted from the added mass of the carrier, which confirms that the natural ^{9}Be content is negligible in the analyzed samples.

VI.9.3. ^{10}Be paleoconcentrations

The ^{10}Be paleoconcentrations and erosion rates results are presented in Figure VI-57b and in Table SVI-1.

As the Bengal Fan samples have been shielded from cosmic rays since deposition, the ^{10}Be concentrations (Figure VI-59) are only corrected for radioactive decay using a ^{10}Be half-life of $1.387\pm0.012\times10^{6}$ y (Korschinek et al., 2010; Chmeleff et al., 2010) to obtain ^{10}Be paleoconcentrations (Figure VI-57b, Table SVI-1). These paleoconcentrations integrate the initial ^{10}Be signal acquired during erosion and the possible additional exposure to cosmic rays during sediment transport to the Bay of Bengal. They are inversely correlated to erosion rates. In the modern system, the exposure during sediment transfer represents less than 10-15% of the initial signal in the Ganga plain (Lupker et al., 2011, 2012a) and is within the concentration analytical uncertainties of this study. In the following, we assume that the ^{10}Be paleoconcentrations reflect to the first order the mean concentration at the outlet of the

Himalayan range, i.e. accounting only for radioactive decay and neglecting any additional ^{10}Be production during the sediment transfer in the foreland basins, and any recent exposure since the Bengal Fan sediment are lying below a >2000 m water column. The role of the sediment sequestration is discussed further.

In Figure VI-57-Figure VI-58, we selected intervals with homogeneous Sr-Nd isotopic composition and computed the average and standard deviations of the paleoconcentrations. The influence of the selected intervals on the average values remains limited (Figure VI-61).

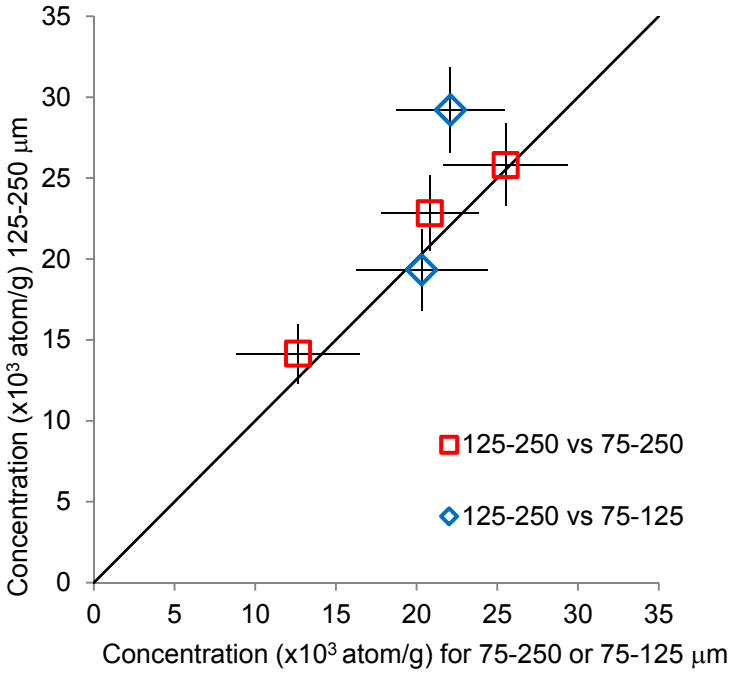

Figure VI-60. Grain size influence on the ^{10}Be concentration.

Despite a limited set of analysis in two different size fractions (75-125 µm) and (125-250 µm) (Table SVI-1-Table SVI-2), the grain size does not have a major influence on ^{10}Be concentration. One sample (U1444A-7H) displays a larger value for the coarsest fraction and might be explained by a larger proportion of Brahmaputra coarse sediment in this fraction (modern ^{10}Be concentrations of the Ganga and Brahmaputra sand in Table SVI-6). The overall agreement between the (75-250 µm) and (125-250 µm) fractions makes it possible to plot and discuss on the same graphs the data issued from these two size fractions.

Figure VI-61. Influence of the averaging interval.

Next page.

One might prefer dividing the period of study according to different averaging intervals than the ones we selected (Figure VI-57-Figure VI-58). For instance, one could merge the 4.5-3.5 Ma interval with the 6.5-4.5 Ma interval. This new division does not alter the evolution of the mean ^{10}Be paleoconcentration (a.), the mean f_G (b.) and the mean paleoerosion rate (c.), and associated conclusions.

a.

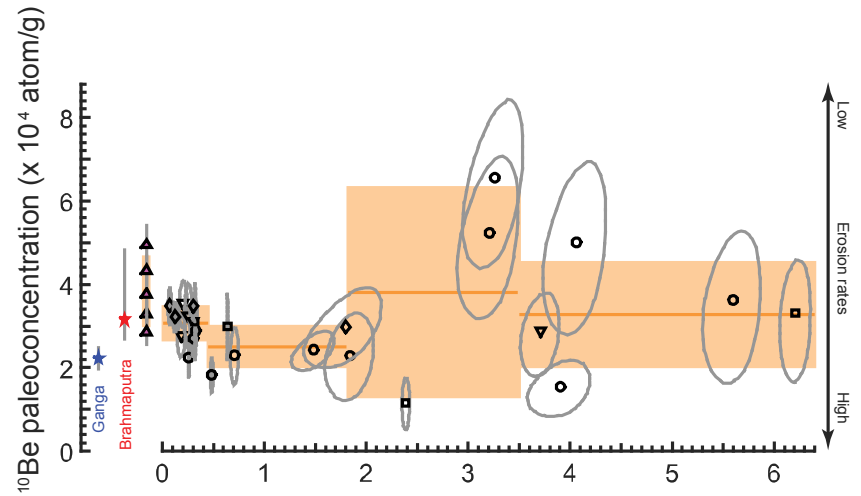
^{10}Be paleoconcentration (x 10^4 atom/g)
0
2
4
6
8
Ganga
Brahmaputra
0
1
2
3
4
5
6
Low
Erosion rates
High

b.

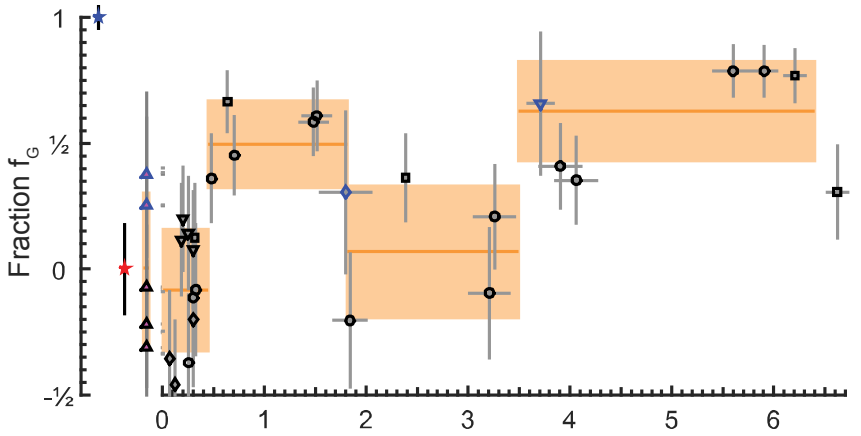
Fraction f_G
1
½
0
-½
0
1
2
3
4
5
6

c.

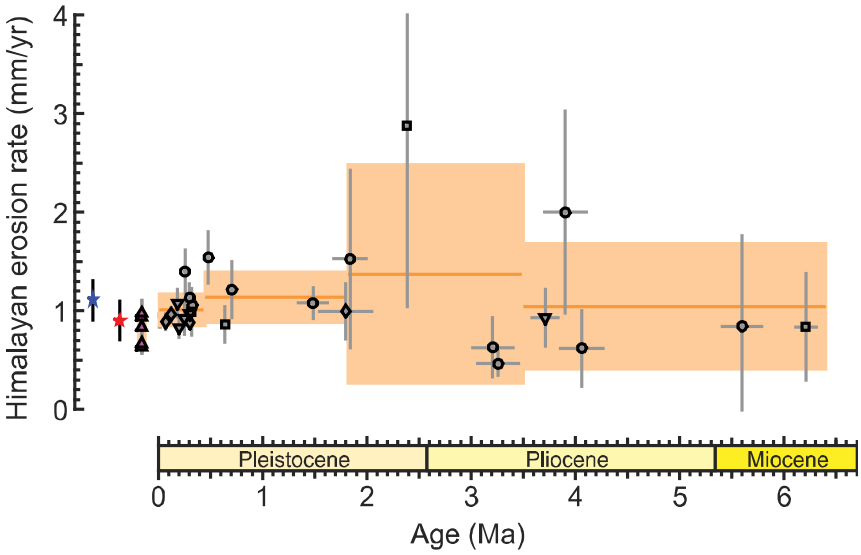
Himalayan erosion rate (mm/yr)
0
1
2
3
4
Pleistocene
Pliocene
Miocene
0
1
2
3
4
5
6
Age (Ma)

VI.9.4. Production rates and erosion rates

The apparent mean erosion rates $\bar{e}$ over the whole basin is computed using the simplified equation (e.g. Brown et al., 1995):

$$\bar{e} = \frac{\Lambda}{\rho}\frac{\bar{P}}{C} \qquad (1)$$

with $\bar{P}$ the mean production rate of the modern Himalayan part of the basin (Figure II-8), Λ the nucleon attenuation length and ρ the crustal rock density. The use of this equation is permitted under three conditions: (A) the temporal variability of the cosmogenic nuclide production rate, caused by Earth magnetic dipole variations, has remained within the range of the ^{10}Be concentration uncertainties; (B) the geography and elevation of the contributing area, i.e. the Himalayan part of the Ganga and Brahmaputra basins, have remained stable; (C) the exposure of the sediment to cosmic rays during the sediment transfer through the floodplain has a negligible impact on the ^{10}Be concentrations.

Because the average cosmogenic nuclide production rate has remained in a range of -10% to 30% of the modern value (Figure VI-65), Condition A is fulfilled since ca. 4 Ma. Condition B is verified since the late Miocene, given the provenance analyses within foreland folded sediment series in Central Himalaya (Huyghe et al., 2001; Robinson et al., 2001) and Eastern Himalaya (Chirouze et al., 2013; Bracciali et al., 2016), and given the paleoaltimetry along northern Himalaya (Gébelin et al., 2013; Garzione et al., 2000). Condition C is verified because the ^{10}Be concentration increase by less than 20% during sediment transfer within the Ganga foreland basin (Lupker et al., 2012a).

The ^{10}Be production rates were computed using Basinga (Charreau et al., 2019) with the Lal-Stone scaling model (Lal, 1991; Stone, 2000; modified by Charreau et al., 2019). Basinga considers three pathways: neutrons, slow muons and fast muons, with constant attenuation lengths. We set the sea level high latitude production rate at 4.18 atom/g (Martin et al., 2017), with factors of 0.9886, 0.0027 and 0.0087 for the neutron, slow and fast muonic contributions respectively (Braucher et al., 2011). We took into account the glacial cover with the GLIMS database (Raup et al., 2007) but we did not include topographic shielding, following the suggestion of Dibiase (2018). We also did not include paleomagnetic variations.

The drainage basins of the Ganga, Brahmaputra and Lower Meghna were delimited by removing the plains covered by Quaternary deposits (approximate elevation lower than 200 m) and the quartz-lacking areas (the Cretaceous basaltic formations overlying the Indian Craton). For the production rates limited to the Himalayan part of the basins (Figure II-8), we also removed the southern sub-basins covering the Indian Craton, the Shillong Plateau and the Indo-Burman Range (see Lupker et al., 2012a). The sediment flux of the southern sub-basins is limited to ~1% of the Himalayan derived flux, based on ^{10}Be measurements in rivers draining these sub-basins (Lupker et al., 2012a, 2017; Rosenkranz et al., 2018).

Consequently, we approximated the Himalayan erosion as follows:

$$\bar{e}_H = \frac{A_T \times \bar{e}_T \pm A_S \times \bar{e}_S}{A_H} \cong \frac{A_T}{A_H} \times \bar{e}_T \ ,$$

with $\bar{e}$ and A the mean erosion rates and areas of the full basin (T), the Himalayan part of the basin (H) and the southern sub-basins (S).

The areas, production rates and erosion rates of the basins are summarized in Table SVI-6.

VI.9.5. Sr-Nd isotopic measurements on bulk silicate samples

The Sr-Nd isotopic results are presented in Figure VI-57a and in Table SVI-1.

The samples were prepared and measured for Sr-Nd isotopes at CRPG-CNRS-UL (Nancy, France) after acetic acid leaching (Hein et al., 2017). Bulk aliquots of the samples were collected before ^{10}Be sample preparation and rinsed with milli-Q water to reduce sea salt contributions. They were then powdered and leached with 10% acetic acid (Galy et al., 1996) and prepared to obtain a silicate residue. $^{87}Sr/^{86}Sr$ was measured on this residue using a Triton Plus(TM) multi-collector thermal ionization mass spectrometer with NBS-987 as a standard and quality control. $^{143}Nd/^{144}Nd$ was measured using a Neptune plus multi-collector inductively coupled plasma mass spectrometer. $^{143}Nd/^{144}Nd$ was first normalized to $^{146}Nd/^{144}Nd = 0.7219$ using an exponential law and then to the JNdi-1 following a pseudo-standard sample-bracketing method (one standard for each 4–5 samples, Yang et al., 2017).

VI.9.6. Computation of the fraction f_G

The results for the fraction f_G are presented in Figure VI-58a and Table SVI-1.

The sediment of the Bengal Fan and the Lower Meghna is expected to reflect a mixing between Ganga and Brahmaputra sediment. Since the two rivers drain lithologies with a distinct isotopic signature (Galy and France-Lanord, 2001), their sediment also present a distinct signature (Table SVI-6) (Galy and France-Lanord, 2001; Singh and France-Lanord, 2002; Singh et al., 2008; Goodbred et al., 2014). Based on the results from the late Cenozoic foreland sediment in Central Himalaya (Huyghe et al., 2001, 2005; Robinson et al., 2001) and Eastern Himalaya (Chirouze et al., 2013; Bracciali et al., 2016), we assume that the Ganga and Brahmaputra poles have remained stable since 7 Ma. Therefore, the sediment of the Bengal Fan is presumed to follow a mixing trend between these two poles.

The fraction f_G of Bengal Fan or Lower Meghna sand issued from the Ganga basin can be determined applying an equation similar to (1) either on the Nd or Sr isotopes. For instance, for Sr:

$$\left[^{87}Sr\right] = f_G \times \left[^{87}Sr\right]_G + (1 - f_G) \times \left[^{87}Sr\right]_B$$

and $\left[^{86}Sr\right] = f_G \times \left[^{86}Sr\right]_G + (1 - f_G) \times \left[^{86}Sr\right]_B$

The combination of both equations leads to (Morin, 2015, p. 319):

$$\frac{^{87}Sr}{^{86}Sr} = \frac{f_G \times [Sr]_G \times \frac{^{87}Sr}{^{86}Sr}_G + (1 - f_G) \times [Sr]_B \times \frac{^{87}Sr}{^{86}Sr}_B}{f_G \times [Sr]_G + (1 - f_G) \times [Sr]_B}$$

and similarly for Nd:

$$\varepsilon_{Nd} = \frac{f_G \times [Nd]_G \times \varepsilon_{Nd}G + (1 - f_G) \times [Nd]_B \times \varepsilon_{Nd}B}{f_G \times [Nd]_G + (1 - f_G) \times [Nd]_B}$$

Because the inversion of f_G is overdetermined by the two mixing equations on $^{87}Sr/^{86}Sr$ and εNd, we compute the probability density function of f_G for each sample according to Tarantola (2005):

$$pdf = \iint exp\left(\left(\frac{\frac{^{87}Sr}{^{86}Sr}_{predicted} - \frac{^{87}Sr}{^{86}Sr}_{observed}}{\sigma_{\frac{^{87}Sr}{^{86}Sr}}}\right)^2 - \left(\frac{\varepsilon_{Nd_{predicted}} - \varepsilon_{Nd_{observed}}}{\sigma_{\varepsilon_{Nd}}}\right)^2\right) h_G h_B dx_G dx_B$$

with $\sigma_{\frac{^{87}Sr}{^{86}Sr}}$ and $\sigma_{\varepsilon_{Nd}}$ the mean uncertainties on the isotopic signatures of the Ganga and Brahmaputra poles (Table SVI-6), and h_G and h_B the multivariate density function of each pole. The above expression does not account for the analytic uncertainties on the sample measurements (Table SVI-1), which are negligible compared to the uncertainties of each pole.

Then, for each sample, the mean and 1-σ uncertainty on f_G was computed from its respective pdf.

Figure VI-62. Estimate of f_G based on the Sr concentration.

Next page.

a. Calibration of the f_G obtained using Sr concentration versus the f_G obtained using Sr-Nd isotopic data, for the Bengal Fan and Lower Meghna samples having both measurements. Thanks to the distinct Sr concentrations of the Ganga and Brahmaputra sediment (Table SVI-6), this calibration makes it possible to derive a fraction f_G for samples having a Sr concentration measurement without a Sr-Nd isotopic measurement.

b. Sr concentration as a function of Al/Si, a proxy for granulometry (Lupker et al., 2011), for the Ganga, Brahmaputra and Lower Meghna bulk sediment, dataset in Table SVI-5 (this study; Lupker et al., 2013). The coarser fraction, i.e. the sandy bedload, of the Lower Meghna sediment overlaps with the composition of Brahmaputra sediment whereas the finer fraction, i.e. the suspended load, corresponds to a mixing of sediment between the Ganga and the Brahmaputra sediment.

a.

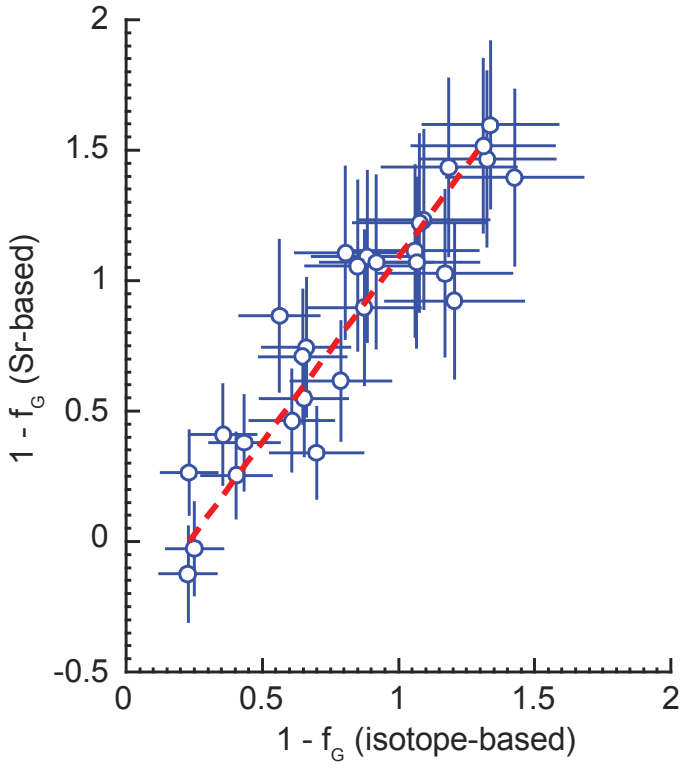
2
1.5
1
0.5
0
-0.5
0
0.5
1
1.5
2
1 - f_G (Sr-based)
1 - f_G (isotope-based)

b.

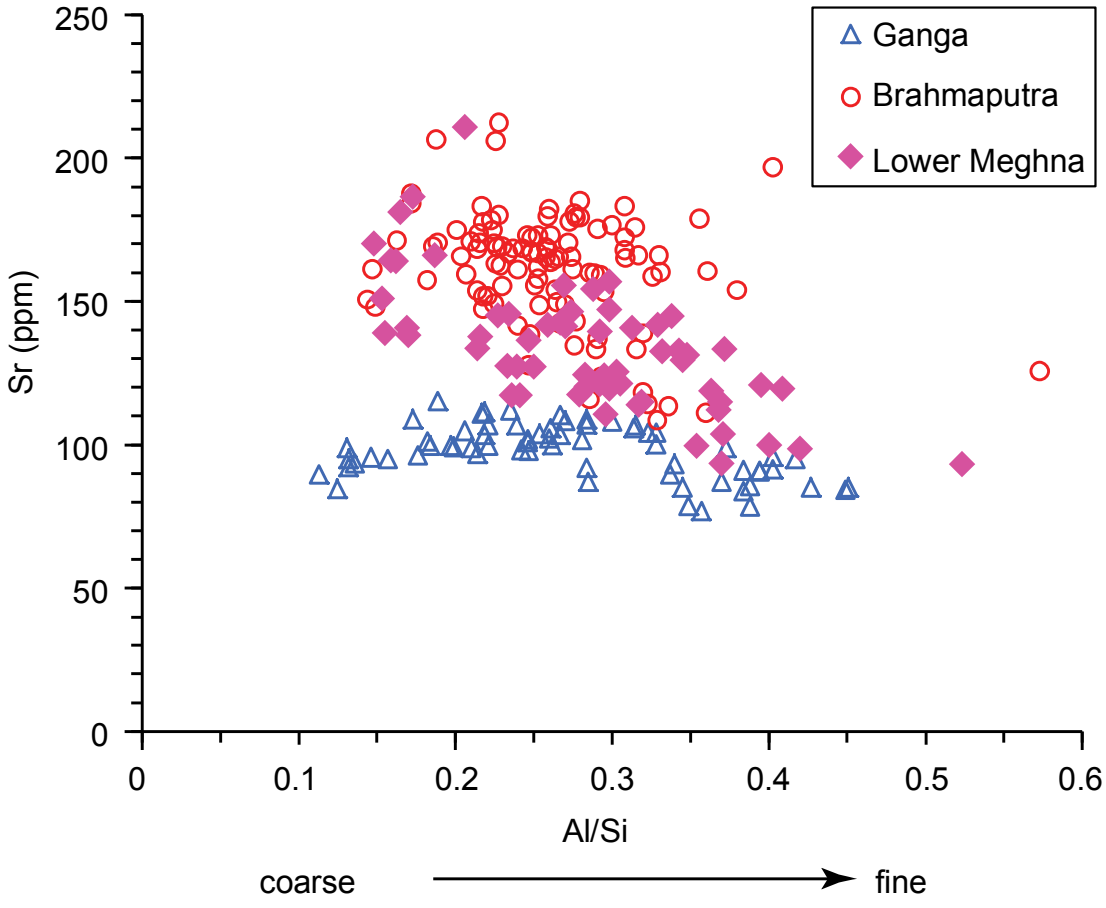
Ganga
Brahmaputra
Lower Meghna
250
200
150
100
50
0
0
0.1
0.2
0.3
0.4
0.5
0.6
Sr (ppm)
Al/Si
coarse
fine

For a few samples, isotopic measurements were not performed. In that case, the marked difference of the Sr concentration between the Ganga and Brahmaputra sediment and the resulting close relationship between the Sr concentration and $^{87}Sr/^{86}Sr$ (Goodbred et al., 2014) are used as a proxy to estimate f_G (Figure VI-62).

Negative values of f_G:

Each main Himalayan formation, from north to south, the Transhimalaya, the Tethyan Sedimentary Series, the High Himalaya Crystalline and the Lesser Himalaya, has a distinct Sr-Nd isotopic signature, as shown in the Figure 10 of Hein et al. (2017). The Brahmaputra sediment at Dibrugarh (BD location in Figure II-8), close to the range outlet, presents a signature enriched in Transhimalayan formations and mantle-derived formations drained by the Yarlung-Tsangpo and the Eastern tributaries of the Brahmaputra. This signature is progressively diluted downstream with the aggregation of the other rivers draining solely Himalayan s.s. formations and reaches values closer to the Brahmaputra at Jamuna Bridge (B location in Figure II-8). The late Pleistocene samples with f_G values below 0-20% likely reflect situations for which only the Brahmaputra was at the origin of the recorded turbidites. We assume that extreme events could lead to direct pulses of sediment from the range outlet to Bangladesh, without minimum dilution by Himalayan s.s. tributaries. Alternatively, this may reflect erosion conditions that favour strongly the erosion of the Transhimalaya compared to the Himalaya s.s..

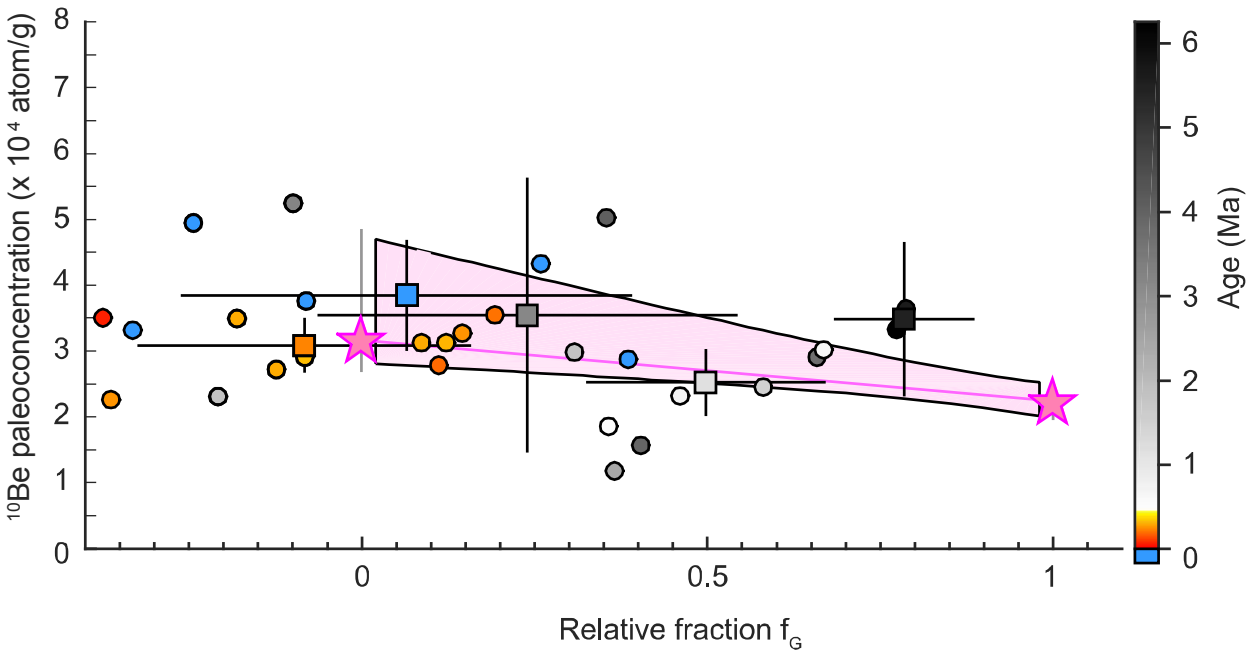

Figure VI-63. ^{10}Be paleoconcentration vs f_G.

The chart shows the distribution of ^{10}Be paleoconcentrations of the Bengal Fan and the Lower Meghna sand as a function of (1) the fraction f_G of the Bengal Fan and Lower Meghna sand issued from the Ganga basin (on the x-axis) and (2) the age of sand (in color, blue for the Lower Meghna sand, red to yellow for the Bengal Fan sand younger than 0.5 Ma and white to black for the older sand). Each sample is represented by a small dot of color. Uncertainties are not presented for clarity and are visible in Figure VI-57b. The average for each interval defined in Figure VI-57-Figure VI-58 is displayed by square dots with 1-σ uncertainty bars. The modern Ganga (G) and Brahmaputra (B) poles are shown by pink stars. The zone of potential values obtained by a mixing of modern Ganga and Brahmaputra sand is shown by the pink polygon. Despite some scattering at ca. 2-4 Ma, the values averaged over the intervals seem independent from the fraction of Ganga sand and appear stable.

VI.9.7. Modern geochemical and granulometric budgets in the Ganga

The combination of a geochemical budget with a granulometric budget makes it possible to assess the overall sequestered flux of Ganga sediment in the Ganga floodplain and highlight the preferential sequestration of the sand fraction. Here, these budgets are focused on the Narayani-Gandak to Ganga system, the Gandak being a tributary of the Ganga (Figure II-8).

Geochemical budget:

Following Lupker et al. (2011), we compared the sediment content in the immobile elements (i.e. for which the dissolution flux can be neglected) Al and Fe at the mountain range outlet and the plain

outlet, and budgeted the sequestration flux by considering the same elements in the sediment deposited in the plain (Figure VI-64a). Here, the geochemical signature of Himalayan rivers at the range outlet is estimated from data acquired in the Narayani-Gandak at the Himalayan front during the 2010s monsoon (Morin et al., 2018), and integrated over time and channel cross-section, following the methods of Lupker et al. (2011). The signature of the plain outlet was estimated by Lupker et al. (2011) for the Ganga at Harding Bridge (Figure II-8). The signature of the sediment deposited in the plain is defined from ~80 samples of sediment of the Gandak Fan drilled cores (Morin, 2015), which correspond to sediment deposition since ca. 50 ka, and from ~30 samples of Siwalik sandstone deposited by the Narayani-Gandak system since the late Miocene (this thesis, Chapter VII).

While our assessment of the geochemical signatures for the range outlet and the deposited sediment (Figure VI-64a) falls within the error bars of the poles approximated by Lupker et al. (2011) (their Figure 15), we obtain sediment budget values significantly higher: ~30% (instead of their ~10%) of the sediment issued from the range (~165 Mt/y) would be sequestered in the Ganga plain.

Granulometric budget:

Discrete granulometric measurements have been conducted for variable depth and discharge values in the Narayani (Morin et al., 2018) and the Ganga (Lupker et al., 2011). Through adequate interpolation (see above respective references for the methods), we performed integrations over time and channel cross-sections and provide the average grain size distribution of the whole sediment transported by each river (Figure VI-64b). The coarse sediment fraction (> 125 μm) represents ~40% of the sediment exported by the Narayani at the range outlet. Contrastingly, the coarse fraction represents only ~20% of the sediment transported by the Ganga at Harding Bridge, i.e. the plain outlet.

Figure VI-64. Modern geochemical and granulometric budgets in the Ganga plain.

Next page.

a. Geochemical budget: Fe/Si vs Al/Si distribution of sediment in the Ganga plain. The geochemical poles for the (1) plain outlet, the (2) range outlet and the (3) plain deposits are represented by color-filled stars surrounded by border-colored 1-σ uncertainty envelopes. While the (1) plain outlet was previously assessed from (1) data of the Ganga at Harding Bridge (Lupker et al., 2011), we estimated the other poles (Extended Methods) with (2) data from the Narayani-Gandak at the Himalayan front (Morin et al., 2018) and (3) data from the Gandak megafan (Morin, 2015) and from a new Siwalik section (this thesis, Chapter VII). For comparison, the shaded black stars and envelopes represent the previous approximations of Lupker et al. (2011) for these poles.

b. Granulometric budget: cumulative distribution of grain size (logarithmic scale) for the Ganga and Narayani measured at variable depth and discharge values. The granulometric fraction favoured for 10Be measurements in this study (125-250 μm) is indicated.

a.

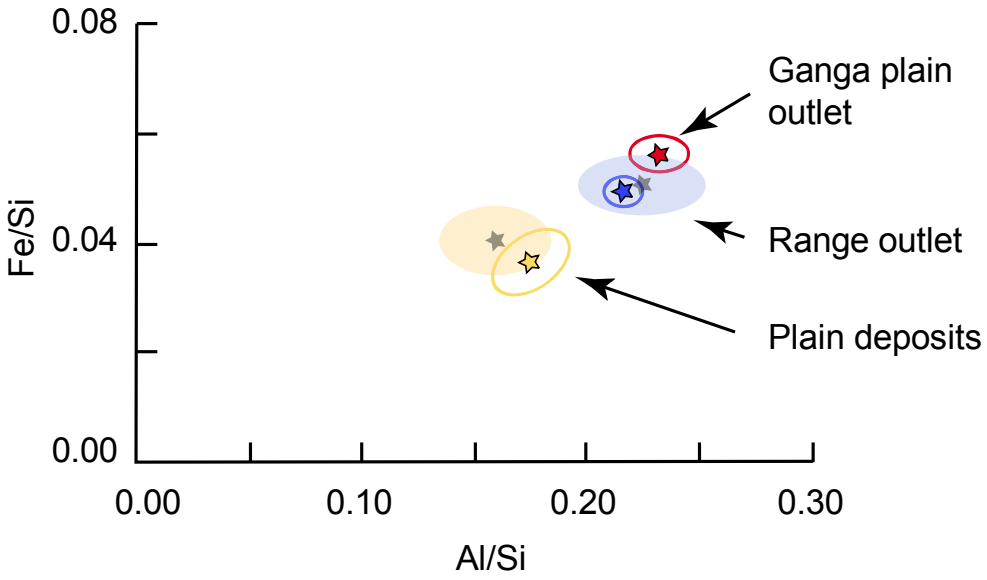
0.08
0.04
0.00
Fe/Si
0.00
0.10
0.20
0.30
Al/Si
Ganga plain outlet
Range outlet
Plain deposits

b.

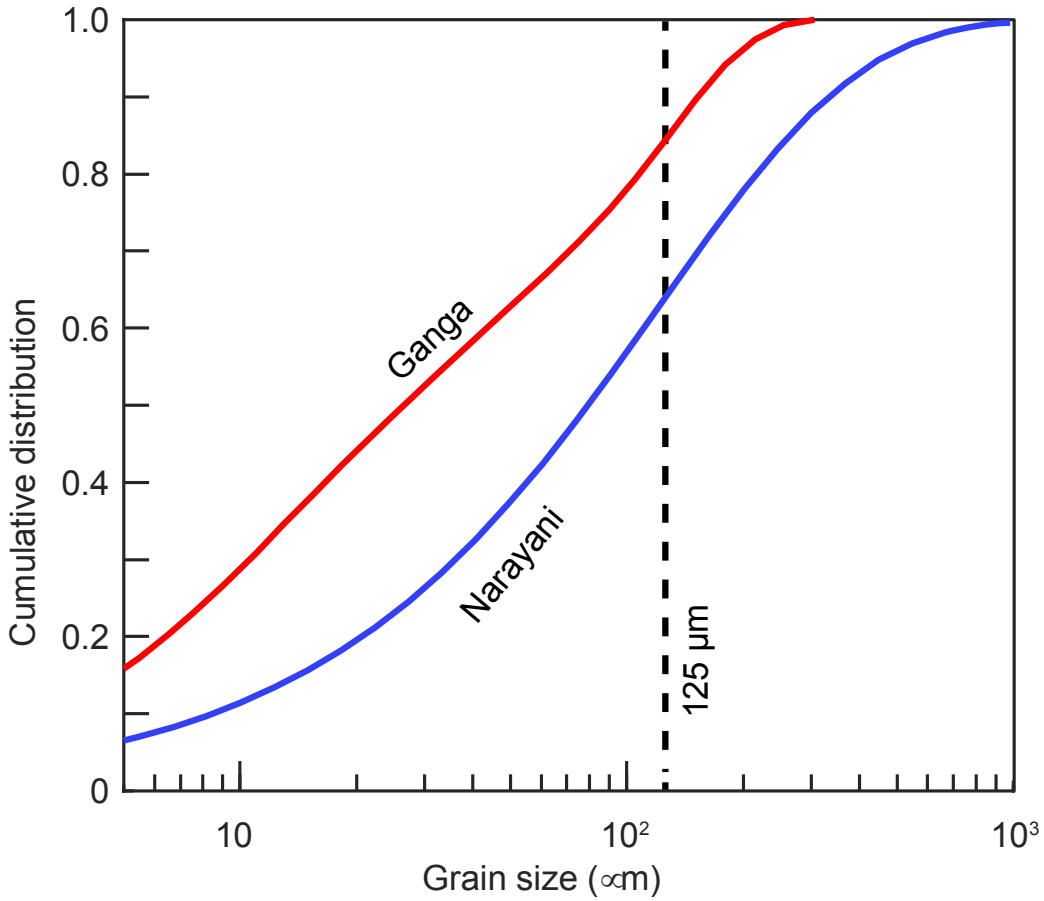
1.0
0.8
0.6
0.4
0.2
0
Cumulative distribution
Ganga
Narayani
125 µm
10
10²
10³
Grain size (∝m)

By the addition of the higher sequestration than previously estimated and the preferential sequestration of the coarse fraction, we estimate that ~60% of the coarse fraction (>125 μm) of the sediment issued from the central Himalaya is deposited in the Ganga plain, and therefore does not reach the confluence with the Brahmaputra. This could explain that bedload with a Ganga isotopic signature is absent in the lower Meghna bedload sediment.

Because of a lack of data, we cannot perform similar geochemical and granulometric budgets for the Brahmaputra plain. Nevertheless, we assume that the sequestration of sand is more limited in the Brahmaputra plain because the Brahmaputra plain has little accommodation space (Figure II-8, e.g. Hetényi et al., 2016). In that case, the Brahmaputra sand would dilute the Ganga sand, an effect reinforced by the fact that the Brahmaputra has a sediment load 1.75 to 2 times higher than the Ganga according to the measured fluxes of suspended load (Delft Hydraulics and Danish Hydraulics Institute, 1996; Lupker et al., 2011) or ^{10}Be derived erosional fluxes (Lupker et al., 2012a, 2017).

This configuration of the Brahmaputra plain might have been different before the rise of the Shillong Plateau (Najman et al., 2016) and the growth of the Indo-Burman wedge (Maurin and Rangin, 2009), which might have favoured a higher sequestration of the coarse fraction in the Brahmaputra plain than in modern times.

VI.9.8. Test of the climate forcing hypothesis

The results of the test are presented in Figure VI-58b and in Table SVI-1.

In case of a variable mixing in the foreland plain (differential sequestration) or in the shelf (separate turbiditic systems), the ^{10}Be concentration of the sandy fraction of the Lower Meghna river or the concentration of the Bengal Fan turbidites can be written from a mixing perspective: $C = f_G \times C_G + (1 - f_G) \times C_B$ with C_G and C_B the ^{10}Be concentrations of the Ganga and Brahmaputra sand respectively. At steady state, these concentrations depend on the mean erosion rates in the basins of these rivers according to:

$C_G = \sum_{i=1,3} \frac{\Lambda_i \times P_{G,i}}{\rho \times e_G}$ and $C_B = \sum_{i=1,3} \frac{\Lambda_i \times P_{B,i}}{\rho \times e_B}$, with Λ_i the attenuation lengths of nucleons or muons, ρ the density of eroded rocks, $P_{G,i}$ and $P_{B,i}$ the mean nucleogenic and muogenic cosmogenic nuclide production rates in the respective drainage basins, and e_G and e_B the mean erosion rates in the basins (e.g. Puchol et al., 2017). It follows:

$$C = \sum_{i=1,3} \frac{\Lambda_i}{\rho} \times \left(f_G \times \frac{P_{G,i}}{e_G} + (1 - f_G) \times \frac{P_{B,i}}{e_B} \right) \quad \text{(S1)}.$$

If the Ganga and Brahmaputra sediments are fully exported to the Bengal Fan, the proportion $f_G = \frac{A_G \times e_G}{A_B \times e_B + A_G \times e_G}$, A_G and A_B being the areas of the basins, and the above equation simplifies to the classical equation $C = \frac{1}{\bar{e}} \times \sum_{i=1,3} \frac{\Lambda_i \times \bar{P_i}}{\rho}$ with $\bar{P_i}$ and $\bar{e}$ the mean nucleogenic and muogenic production

and erosion rates over the whole basin of the Lower Meghna. Otherwise, the expression (S1) cannot be simplified and leads to the indetermination of the mean erosion rate.

To overcome the indetermination, we chose to test a scenario in which all the Himalayan landscapes would similarly respond to a regional forcing (Zhang et al., 2001), i.e. in which e_G and e_B co-vary:

$e_G(t) = K(t) \times e_{G,0}$ and $\varepsilon_B(t) = K(t) \times e_{B,0}$, with $e_{G,0}$ and $e_{B,0}$ the modern erosion rates of the Ganga and Brahmaputra basins respectively and $K(t)$ the regional amplification factor.

In that case, assuming that the temporal variability of the production rates remains negligible over the period of study (further section, Figure VI-65), the mean erosion rate of the Lower Meghna basin can be derived from equation (S1) through

$$\bar{e}(t) = K(t) \times \bar{e}_0 = K(t) \times \frac{A_G \times e_{G,0} + A_B \times e_{B,0}}{A_G + A_B}, \quad \text{(S2)}$$

with $K(t) = \frac{1}{C(t)} \times \sum_{i=1,3} \frac{\Lambda_i}{\rho} \times \left(f_G(t) \times \frac{P_{G,i}}{e_{G,0}} + \left(1 - f_G(t)\right) \times \frac{P_{B,i}}{e_{B,0}} \right)$

in other terms $K(t) = f_G(t) \times \frac{C_{G,0}}{C(t)} + \left(1 - f_G(t)\right) \times \frac{C_{B,0}}{C(t)}$ (S3)

and $\bar{e}_0$ the mean modern erosion rate of the Lower Meghna basin.

These equations are also valid when we restrict the Lower Meghna basin to the Himalayan s.s. and Transhimalayan part to determine the Himalayan erosion rate, as proposed by Lupker et al. (2012a) and (2017).

However, these equations are difficult to verify when $f_G < 0$. In that case, we should expect the ^{10}Be concentration of the mixing to be larger than the concentration of the Brahmaputra before the confluence at 31x10^3 atom/g. Since the ^{10}Be concentration of the Brahmaputra in Dibrugarh (Figure II-8) is poorly defined, as well as the concentrations of the Himalayan tributaries of the Brahmaputra that display variable values between 8 and 41x10^3 atom/g (Lupker et al., 2017), we chose to consider f_G=0 in (S3) for those cases (i.e. for six samples of the Bengal Fan in the time span 0.5-0 Ma and for two older samples, and for three samples of the Lower Meghna).

VI.9.9. Temporal variability of cosmogenic nuclide production rates

The cosmogenic nuclide production rates depend on the solar activity, stable over the last 10 Ma (Leya et al., 2000), and the intensity of Earth's magnetic field (Lifton, 2016). We explored the impact of the temporal variations of Earth's magnetic dipole intensity on production and erosion rates in Figure VI-65. Using different databases of dipole paleointensity, the continuous Muscheler et al.'s (2005) database from 0 to 60 ka, the SINT2000 continuous database (Valet et al., 2005) from 60 to 2000 ka, and the PINT lava flow discrete database (Biggin et al., 2010), having a low resolution for the record older than 4 Ma, we

computed the 10Be production rate normalized to modern values as a function of time, for a basin with a hypsometry close to the Himalayan s.s. and Transhimalayan part of the Ganga-Brahmaputra basin, at a mid-latitude of 28°N, and according to the magnetic correction in the Lal-Stone model (Lal, 1991; Stone, 2000). Since 2 or 4.5 Ma, the nucleogenic production rate displays significant variations (Figure VI-65) and a 10% higher average than in modern times, with a standard deviation of ~15-17%, which remains in the uncertainties of our ^{10}Be results.

Remarkably, the extreme variations in production rates (Figure VI-65) could explain the apparent paleoerosion rate variations up to a factor of two, even in absence of effective acceleration of erosion.

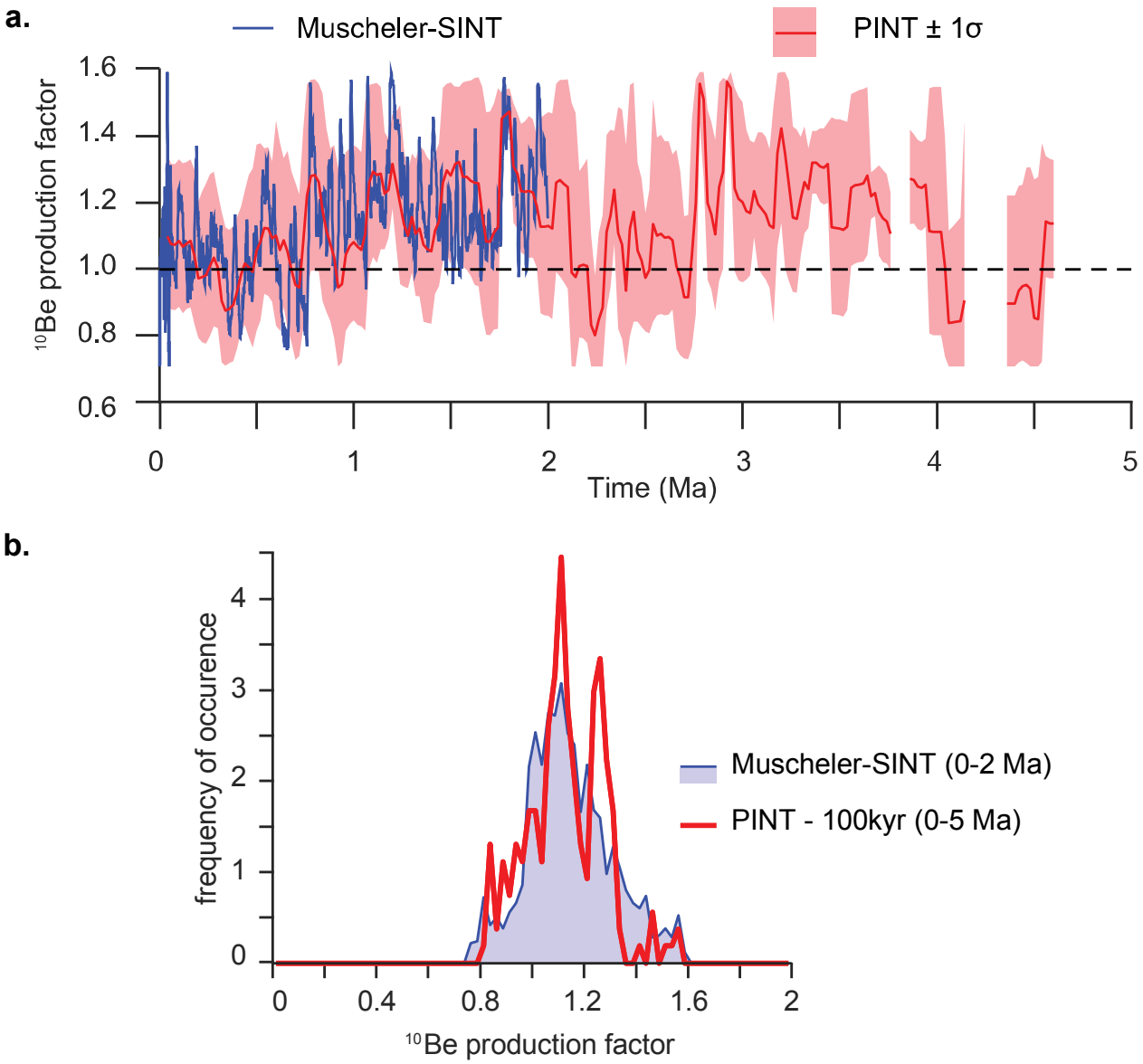

Figure VI-65. Effect of the variations of the geomagnetic dipole on the ^{10}Be production rate.

a. ^{10}Be production rate normalized to modern values as a function of time, for a basin of Himalayan hypsometry at a latitude of 28°N. Two dipole temporal databases are explored: (1) the continuous Muscheler-SINT sediment database (Muscheler et al., 2005; Valet et al., 2005) and (2) the discrete PINT lava flow database (Biggin et al., 2010). A 100 ka-long averaging sliding window is applied to the PINT record to buffer the data dispersion and fill the data voids. The resulting curve with the 1-σ uncertainty envelope is presented.

b. ^{10}Be normalized production rate distribution for the two databases. Despite distinct periods (0-2 Ma vs 0-5 Ma) and resolution (0.5 ka vs ~50 ka), the distribution for both databases is similar for low frequency (period > 100 ka) signal variations.

VI.10. TABLES

In Tables attached to this manuscript.

Table SVI-1. Sample information, dating, ^{10}Be and Sr-Nd isotopic results.

Table SVI-2. ^{10}Be duplicate results.

Table SVI-3. ^{10}Be blanks

Table SVI-4. Major and trace element results.

Table SVI-5. Chemical analyses of river sediment.

Table SVI-6. Sr-Nd and ^{10}Be data from river sediment used for the f_G and K(t) computation.

VII. THE VALMIKI SECTIONS: A NEW SEDIMENTARY RECORD OF THE CENTRAL HIMALAYA (DRAFT)

VII.1. INTRODUCTION

VII.1.1. The South Asian Monsoon during the late Cenozoic

Mountain ranges develop from the interaction of tectonics and climate through erosion (Beaumont et al., 2001; Whipple, 2009). This is illustrated by the breathtaking relief of the Himalaya. There, at the convergence of the Indian and Eurasian plates, the action of the South Asian Monsoon (SA Monsoon) and the late Cenozoic Glaciations have modeled the relief of the mountain range. The SA Monsoon is defined by the seasonal alternation of surface winds. Summer south westerlies bring warm and moist air from the Indian Ocean towards the front of the Himalaya where precipitations fall. Winter north easterlies produce dry to arid conditions, particularly in Central and Western Himalaya (Bookhagen and Burbank, 2010; Andermann et al., 2011). The SA Monsoon is favoured by the elevation of the Himalayan range, which insulate the warm and moist air from the cold and dry air of Central Asia (Boos and Kuang, 2010; Molnar et al., 2010).

Since the early work of Quade et al. (1989), Kroon et al. (1991) and Prell et al. (1992), we know that the amplitude and frequency of the monsoonal precipitations evolved over long timescales during the last eight million years. The past SA monsoon has been investigated by indirect approaches applied on fossils, paleosoils or organic matter. Such material is available in the deep sea sediment as in the Arabian Sea or in the Bengal Bay and in the continental sediment deposited in the Himalayan foreland basin and later exhumed in the Siwalik Hills. A significant dataset points to an increased seasonality of precipitations at ca. 8-7 Ma. The shift in the abundance of marine siliceous and calcareous nanofossils in the Arabian Sea was interpreted as the consequence of a shift in the marine upwelling caused by an intensification of the surface winds (Kroon et al. 991; Prell et al., 1992). The shift in oxygen and carbon isotopes in pedogenic carbonates and fossils of the Siwaliks show the expansion and prevalence of C_4 plants that are more adapted to aridity than C3 plants (Quade et al., 1989; Quade and Cerling, 1995; Quade et al., 1995; Cerling et al., 1997). Weathering proxies as clay mineralogy or major elements point to increased weathering linked to a potential amplification of the precipitation seasonality (Derry and France-Lanord, 1996; Huyghe et al., 2005, 2011) or major elements (Clift et al., 2008).

However, supplementary data put in question the hypothesis of an evolution of the SA Monsoon in the late Cenozoic and the spatial and temporal pattern of this evolution remains controversial (Dettman et al., 2001; Ghosh et al., 2004; Sanyal et al., 2004, 2005, 2010; Behrensmeyer et al., 2007a, b; Huang et al., 2007; Rodriguez et al., 2014; France-Lanord et al., 2016a; Ghosh et al., 2017; Vögeli et al., 2017a, b; Ghosh et al., 2018). Using O isotopes on fossil freshwater shells, Dettman et al. (2001) demonstrate that, even if the yearly amplitude of precipitations may have decreased, the frequency of precipitations remains steady on average over the period, in contradiction to the interpretation of previous studies (Quade and Cerling, 1995; Quade et al., 1995). Using C isotopes on bulk organic matter, Vögeli et al. (2017a) goes farther: the yearly amount of monsoonal precipitations would have remained steady in the Eastern Himalaya, preventing the prevalence of the C4 plants, contrary to Western Himalaya (Quade and Cerling,

1995; Vögeli et al., 2017a). And the final blow is struck by the results of the Expedition 354 in the Bengal Fan at 8°N (France-Lanord et al., 2016a), which clay mineralogy does not show increased weathering at 8-7 Ma, contrary to the results at 1°S (Derry and France-Lanord, 1996).

To overcome these contradictions, a C-O record on pedogenic carbonates from the Surai Section in Central Himalaya could help to make a comparison and understand this difference (Harrison et al., 1993; Quade et al., 1995; Ojha et al., 2000; Ojha et al., 2009). But this comparison is difficult because data are variable after 6 Ma and lack of temporal resolution (Quade et al., 1995). To add to the confusion, neither Western nor Central Himalaya is dominated by C4 plants in modern times (Still et al., 2003). Therefore, these irreconcilable contradictions require obtaining a new, high-resolution record in Central Himalaya to check the potential variability of the SA Monsoon evolution through the late Cenozoic.

VII.1.2. Approach

Here, we unveil a new Siwalik group of sections located in the Valmiki Wildlife Sanctuary, Bihar, India. The Valmiki Sections form an almost continuous series of molasses thick of ~4,000 m. They record the deposits of the Narayani-Gandak river, which outlet sits ~50 km west of the sections and ~160 km west of the Surai Section. The Narayani-Gandak form the major river draining Central Nepal and is the prime tributary of the Ganga.

Dating constraints were provided for the deepest ~3,600 m series, corresponding to the 8.2 - 0.7 Ma time span, using paleomagnetic analyses and stochastic magnetostratigraphic correlations (Lallier et al., 2013). The geometry and age of the Siwalik folds at this location were determined. The formations were analyzed with field observations. Granulometry, weathering and a potential recycling were estimated using major and trace elements. We measured the O and C stable isotopes on the fine silts and selected the samples richer in carbonates than the Narayani sand. Therefore, the signal we measured partly originates from detrital carbonates but also from pedogenic carbonates. The variation of this signal makes it possible to explore the local variations of proportions between C3 and C4 plants and the local variations of precipitations.

VII.2. CONTEXT

VII.2.1. Geology, physiography and precipitation distribution

The Himalayan range is characterized by several distinct physiographic units. From North to South: the topography displays low to moderate relief along the high elevation southern Tibetan Plateau, then relief and elevation increase southward and culminate in the High Himalaya (HH), elevation and relief drop suddenly in Central Nepal to reach the hilly landscapes of the Lesser Himalaya (LH), finally the topography reachs its lowest elevation in the frontal relief of the Siwalik Hills, just north of the Ganga Plain.

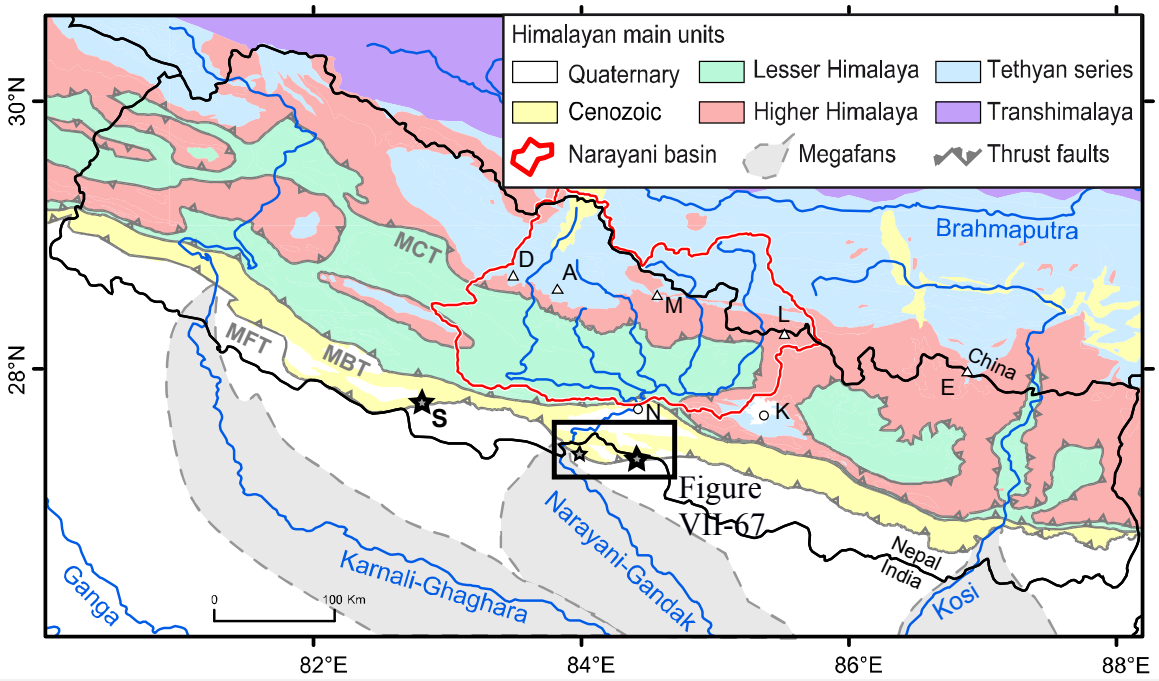

Figure VII-66. Lithologic map of Central Himalaya.

The main Himalayan units and main thrusts are delimited: MFT (Maint Frontal Thrust), MBT (Main Boundary Thrust) and MCT (Main Central Thrust). The Quaternary alluvial megafans are underlined , along with several geographic features, among them the drainage basin of the Narayani in red, the Nepalese boundaries in black, cities: K: Kathmandu; N: Narayanghat, and summits: A: Annapurnas; D: Daulaghiri; E: Everest; L: Langtang; M: Manaslu. A frame precise the location of the Valmiki Sections and the Surai Section (S) is also indicated. For clarity, the tributaries of the Karnali and the Kosi are not indicated (geological map compiled by the Department of Mines and Geology, Kathmandu, 1994)

The geology roughly follows the physiography. The Himalaya is divided into four subparallel main lithologic units (Figure VII-66, Gansser, 1964; Le Fort, 1975, 1986; Hodges, 2000) from north to south: the Tethyan sedimentary series (TSS) consisting in medium to low-grade detrital and carbonate metasediments; the High Himalaya Crystalline (HHC) consisting in high-grade crystalline metamorphic units; the Lesser Himalaya (LH), consisting in low- to medium grade metasediments; the Siwalik series, which consist in exhumed synorogenic sediment and extend southwards in the Ganga plain.

The Himalaya in Central Nepal is characterized by a large south to north variation in precipitations. In the Ganga Plain, annual rainfall range between 1 and 1.5 m/y. A sharp increase is observed in the Siwaliks Hills and the Mahabarat (Bookhagen and Burbank, 2010). The precipitations drop when arriving in the LH to 1.5-2 m/y, before rising along the southern flank of the high Himalayan peaks with 2 to 5 m/y monsoonal precipitations (Burbank et al., 2003; Andermann et al., 2011). Finally, as one penetrates northwards in the precipitation shadow behind the higher summits, precipitations become rarer (<0.4 m/y).

VII.2.2. The Siwalik molasses

The north of the foreland basin has been exhumed in the Siwalik Hills along successive fold and thrust belts at the front of the Himalaya. In Central Himalaya, the Siwalik Hills present a low elevation (< 1,000 m) with a sharp relief. Himalayan rivers as well as local rivers have deeply incised the Siwalik uplifting folds and exposed kilometric and continuous sections as old as ca. 15 Ma (Gautam and Fujiwara, 2000). The molasses form a sedimentary succession thicker than 6 km (Dasgupta et al., 2000), with accumulation rates at ~0.3-0.5 mm/y (Appel et al., 1991; Harrison et al., 1993).

The Cenozoic synorogenic continental deposits of the Siwalik molasses present sedimentary facies similar to the modern facies of the Indian foreland basin. The Siwalik molasses are divided into three units (e.g. Quade et al., 1995; DeCelles et al., 1998): the Lower Siwaliks (fine-grained sandstone, mudstone and clays), the Middle Siwaliks (medium to coarse sandstone alternating with occasional clay and mudstone layers) and Upper Siwaliks (conglomeratic alluvial fans and gravely braided river deposits). These changes of facies point to changes in fluvial styles: first from a meandering to a deep braided system at ca. 10-6 Ma, then to a shallow braided system at ca. 6.5 Ma and finally to a gravelly braided system after ca. 3.0–2.5 Ma (Nakayama and Ulak, 1999; Huyghe et al., 2005). As indicated by $\delta^{13}C$ in paleosoil carbonates, the deposition environment shifted at ca. 7-4 Ma from a C_3-dominated to a potentially C_4-dominated vegetation, probably indicating more arid or seasonal conditions (Quade et al., 1995; Ojha et al., 2009). But as previously noted, Quade et al. (1995)'s dataset lack resolution.

The change of fluvial styles has classically been interpreted as resulting from the facies evolution caused by the southward migration of the mountain wedge during the Himalayan orogeny. The Himalayan foreland basin has developed by flexural subsidence along the thrust belt, so that the mountain wedge migration produces a southward migration of the sediment pinch out in the southern part of the basin. In

Central Himalaya, this migration has reached between 15 ± 5 mm/y (Lyon-Caen and Molnar, 1985) and 19 ± 5 mm/y since ca. 15 Ma (Mugnier and Huyghe, 2006). This range of values is consistent with the shortening rates determined by geodetic measurements (Bettinelli et al., 2006), the Holocene slip rate on the Main Himalayan Thrust (MHT) (Lavé and Avouac, 2000), or the average shortening rates since ca. 15 Ma (Avouac, 2015; Mugnier et al., 2004).

Therefore, the facies have been deposited diachronously along the Himalaya and transversely to the foreland basin and probably only describe the lithostratigraphic variations associated to the migration of the thrust wedge (Lyon-Caen and Molnar, 1985; Quade et al., 1995; Ojha et al., 2009) and the gravel front (Dubille and Lavé, 2015).

The molasses are of fluvial or lacustrine origin. As indicated by paleocurrent analyses, they were deposited by southward-flowing rivers in Central Himalaya (Tokuoka et al., 1990; DeCelles et al., 1998) and derive from sediment eroded in one of the major Himalayan drainage basins, e.g. the Karnali-Ghaghara or the Narayani-Gandak, or in a smaller basin of the Lesser Himalaya, e.g. the western Rapti (Charreau et al., in prep.). The biostratigraphic constraints of the Siwaliks are limited but not absent, particularly in the Surai (Corvinus and Rimal, 2001). Since the 1980s, magnetostratigraphic studies have significantly improved the age models of the Siwalik sections (e.g. Appel et al., 1991; Harrison et al., 1993; Ojha et al., 2009; Charreau et al., in prep.) but in most cases, no dating constraints are available in the Pleistocene, which mainly consist of coarse sediment in the available Siwalik sections.

VII.2.3. The Narayani-Gandak drainage basin

The Himalayan drainage network is organized in several N-S transverse rivers which originate in the south Tibet or in the northern flank of the range and join into a few major rivers in the Lesser Himalaya (Figure VII-66). These chief rivers deposit sediment in alluvial megafans (fan areas of 10^4-10^5 km^2, DeCelles et al., 1998; Gupta, 1997) in the foreland basin. Smaller rivers draining only the Siwalik and the Lesser Himalaya alternate with the trans-Himalayan rivers and deposit smaller interfans (DeCelles et al., 1998; Gupta, 1997; Wells and Dorr, 1987).

The Narayani-Gandak drainage basin covers Central Nepal and is drained at the west by the Kali Gandaki and the Marsyandi, which drain the Annapurna range, and at the east by the Buri Gandaki and the Trisuli. The Narayani initiates at the confluence of the Kali Gandaki and the Trisuli and after cutting the Siwaliks, becomes the Gandak in the Indian plain. The Gandak is a braided river wide of one to six kilometers that deposits sediment along an alluvial megafan. After a southeastward course of ~230 km, the Gandak join the Ganga in its floodplain.

In its central part, south of the Annapurnas, the drainage basin is characterized by the largest rainfall amount up to 5 m/y (Andermann et al., 2011). At this location, it also presents considerable relief (7,500 m over a 30 km distance). As one penetrates northwards in the precipitation shadow behind the higher summits of the Annapurnas or the Manaslu, precipitations become rarer (< 0.4 m/y).

VII.3. MATERIAL AND METHODS

VII.3.1. Description of the Valmiki Sections

The Valmiki Sections consist in two sets of sections exposed along local rivers in the Outer Siwalik Hills: the CR sections are in the southern flank of the South West Churia Range (CR) close to Gobardhana and the VR sections are in the Valmiki Nagar Range (VR) close to Gonauli and Valmiki Nagar (Figure VII-67). They are located in the Valmiki Wildlife Sanctuary, National Park & Tiger Reserve, at the NW of the Bihar State in India close to the Nepalese boundary and at ~50 km (CR sections) and ~20 km (VR sections) eastwards from the Narayani-Gandak dam. Because of the relatively isolated location, the sections have not been previously studied.

In this region, the Siwalik sediments are folded into a series of several folds, including the CR and the VR folds, of elevation ranging from 250 m to 700 m on the hanging wall of the Main Frontal Thrust. North to this relief, a piggy-back basin called the Chitwan Dun has developed.

The CR area includes from west to east the Dwarda, the Ganguli and the Patalaia Rivers. The VR area includes from west to east the Maloni Naha and the Gonauli Rivers. In both areas, the rivers drain the southernmost limb of the Siwalik anticlines into the Indian floodplain. Contrastingly, the VR rivers, which is limited in elevation (250 m) only expose limited and discontinuous sections.

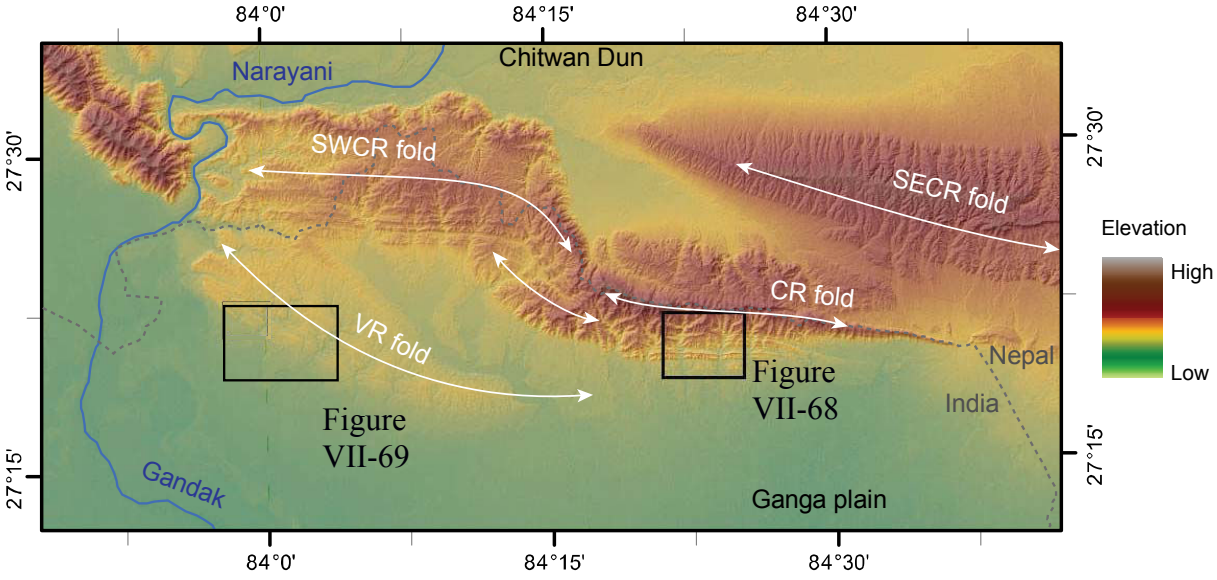

Figure VII-67. Topographic map of the Outer Siwalik Hills.

The folds are represented, along with the Narayani river and the locations of the CR (Churia Range) and VR (Valmiki Range) Sections (Local Siwalik range names from Divyardashini and Singh, 2019).

VII.3.2. Material

The new magnetostratigraphic sections were obtained by sampling across the southern limb of the South West Churia Range (CR) during two field trips in 2012 and 2016 (Figure VII-67). To increase the length of sampling, in particular for the upper/younger part of the stratigraphic column, we had to complement the main Dwarda Section by the Ganguli and the Patalaia Sections, two small sections located a few kilometers further east (Figure VII-68). The regularity of the bedding dip and the ability to follow between the three segments a similar topographic expression of a few indurated layers, make it possible to precisely match the relative position of the three stratigraphic sub-sections.

Because of the modern configuration of the Chitwan Dun (Figure VII-67), our preliminary observations in the sedimentary logs of the Dwarda and the Ganguli Sections (and also the Surai Section, Charreau et al., in prep) suggested a potential shift of the provenance in the upper part of the sedimentary record. In complement, during a third trip in 2017, we sampled a few individual samples along the southern limb of the Valmiki Nagar Range (VR) which is much closer to the modern range outlet of the Narayani-Gandak (Figure VII-67). For these samples, we assume a similar sedimentation rate as in the CR Sections to estimate the sample stratigraphic ages.

In both folds (CR and VR), we collected clayey to fine sand samples for paleomagnetism and stable isotope measurements. We also collected medium to coarse sand samples for geochemical measurements and future cosmogenic nuclide measurements (which results are presented in this thesis, Chapter VIII).

VII.3.3. Magnetostratigraphy and stochastic correlation dating

A total of 382 samples collected in the Dwarda, the Ganguli and the Patalaia sections were measured for paleomagnetic analyses and 185 samples yielded stable results (Table SVII-1). We sampled only the finer silty to sandy horizons by drilling, except for a few samples extracted by hand with Polyvinyl chloride (PVC) cubes. Bedding attitude, sun correction and GPS coordinates were measured at each sampling location. The thickness between two successive sites was taped when possible and if not, estimated from the GPS coordinates. In parallel, we logged down the stratigraphic succession and measured strikes and dips along the sections. All sampling sites were stratigraphically replaced according to the stratigraphic depth estimated during logging. This depth was recalculated with the tape measurements, the strike and dips of the strata and the GPS coordinates. The start of the sections was placed at ~100 m below the Ganga plain. The samples from the VR sections have been attributed depths by translating the series and the geometry of the fold of the CR area.

To isolate the characteristic and primary magnetic remanence directions, the samples were demagnetized using an alternating field and 10 to 12 steps, in the paleomagnetism laboratory of the Institut du Globe de Paris. The remanences at each step were measured using a three-axis DC Squid in the same laboratory. We established the magnetic polarity sequence of the three sections by selecting magnetic intervals based on a minimum of two successive horizons possessing the same polarity. Samples were not

assigned a polarity if they possessed transitional directions (i.e., directions that fall outside our 60° criteria. The magnetostratigraphic column was then correlated to the reference scale of Ogg (2012) to establish the depositional ages of the sections. To better address the ambiguities and uncertainties related to the correlations, we used a numerical method based on the Dynamic Time Warping algorithm and automatically calculated 10,000 of reasonably likely correlations. In this approach the correlations are computed in order to minimize the local variation of the accumulation rate (Lallier et al., 2013).

VII.3.4. Major and trace element measurements

Major element data trace sediment sorting since Al/Si and Fe/Si ratios in the Himalayan system are related to grain size (Lupker et al., 2012b). Because Na and K are mobile elements, the K/Si or Na/Si can be used to characterize the apparent weathering intensity (Galy and France-Lanord, 2001; Lupker et al., 2011). The covariation of major and trace elements can also be used to determine the provenance of sediment, since the main Himalayan units (the TSS, HHC and LH) are characterized by distinct geochemical signatures. But because of the mobility of certain elements, this approach should be considered to be complementary of an isotopic approach not included in this study.

Major and trace element measurements were performed at SARM (Vandoeuvre-les-Nancy, France) on a fraction of powdered aliquots of fine sandy samples after LiBO2 fusion (Carignan et al., 2001), using ICP-OES iCap6500 for major element and Sc concentrations, and ICP-MS iCapQ for trace elements (Table SVII-3).

VII.3.5. Stable isotope measurements

Since the carbon in the soil carbonate (i.e. pedogenic carbonate) forms in isotopic equilibrium with local soil CO_2, which is determined by the local plant cover, the carbon isotopes in pedogenic carbonates yield information on the local paleovegetation (e.g. Cerling, 1984; Quade et al., 1989). C_3 and C_4 plants have different $^{13}C/^{12}C$ ratios because of their different photosynthetic pathways for carbon sequestration (e.g. O'Leary, 1981; review in Sage et al., 2018). C_3 plants include almost all trees and grasses favoured by cool and wet conditions and present $\delta^{13}C$ composition in the 35-20 ‰ range (O'Leary, 1981). C_4 plants mainly consist in grasses favoured by warmth and the alternation of drought and seasonal/monsoonal precipitation, and average at ~-13 ‰. The isotopic composition of soil organic matter and soil CO_2 is then related to the proportion of C_3:C_4 plants in the local vegetation. Gaseous diffusion and exchange increase $\delta^{13}C$ of ~15 ‰ in pedogenic carbonate with respect to soil CO_2 (Cerling et al., 1989), which means that $\delta^{13}C$ in pedogenic carbonate would have values ~ -12 ‰ when formed under a C_3 vegetation, and +2 ‰ when formed under a C_4 vegetation.

The measurements on C and O isotopes were performed on the drilled samples used for magnetostratigraphy, which have a clayey to fine sand composition. Carbonates in these samples have a detrital and a secondary pedogenic component. Since the proportion of detrital carbonates in the modern

Narayani sediment amounts to 10-20 %, we assume that this proportion is similar in our samples. Practically, the proportion is probably lower because the detrital carbonates are easily weathered compared to the indurated pedogenic carbonates. We therefore considered the samples having a proportion of carbonates higher than 20 % to effectively trace the $\delta^{13}C$ signature of pedogenic carbonates.

Oxygen isotopes in soil carbonates are considered to be correlated with the seasonality of precipitations, i.e. the alternation between wet and dry seasons and to be inversely correlated to the amount of precipitations (Quade and Cerling, 1995). The isotopic value partly depends on the degree of water evaporation in the soil. Evaporation fractionates the oxygen isotopes and enrich the $\delta^{18}O$ ratio of the residual soil water and of the soil carbonates formed in presence of this water. Precipitations focused in the summer would therefore increase the $\delta^{18}O$ whereas less seasonal precipitations, i.e. an increase in winter precipitations relatively to summer precipitations would have the opposite effect. But the $\delta^{18}O$ in soil carbonates is also determined by temperature and by the value of meteoric water, which can bias the proxy (Quade and Cerling, 1995). An increase in soil temperature would probably not have a major effect, but in depth, diagenesis could modify the ratio in a larger extent than for $\delta^{13}C$ (Quade et al., 1995). An increase in the temperature of the local air masses would increase the $\delta^{18}O$ of precipitations and of soil carbonates. This effect may be offset by the gradual depletion of $\delta^{18}O$ of the seasonal precipitations caused by the moisture cooling and the related reduction of evaporation. The intepretation of $\delta^{18}O$ is difficult because the time of the formation of the soil carbonate during the season remains undetermined. The $\delta^{18}O$ of precipitation changes by 8-10‰ from dry to wet season (Gajurel et al. 2006). Then there is a potential for a large bias. Since there are no real good data on the condition of cristallisation of these carbonates, their interpretation remain hampered by uncertainties.

Carbon and oxygen isotopic compositions of calcite were measured using an auto sampler Gasbench coupled with a Thermo Scientific MAT253 isotope ratio mass spectrometer (IRMS) at CRPG-CNRS-UL (Vandoeuvre-les-Nancy, France). For each sample, an aliquot between 250 and 300 µg of carbonate was reacted with 2 mL of supersaturated orthophosphoric acid at 70°C for at least 5 h under a He atmosphere. The carbon and oxygen isotopic compositions of the produced CO_2 were then measured with a Thermo Scientific MAT253 continuous flow isotope ratio mass spectrometer. Values are quoted in the delta notation in % relative toV-PeeDeeBelemnite (V-PDB) for carbon and to V-SMOW for oxygen. All sample measurements were adjusted to the internal reference calibrated on the international standards IAEA CO-1, IAEA CO-8 and NBS 19. The results are presented Table SVII-4.

Along with the 211 drilled samples, we also measured the stable isotopes for a set of coarser samples used for ^{10}Be measurements. The results (Table SVII-3) are compared with available data on modern river sand and kankars in the Gandak Fan (Morin, 2015).

VII.4. RESULTS

VII.4.1. Description of the Valmiki Sections

The cumulated thickness of the CR sections amounts to ~3,850 m, with the Dwarda section exposing a continuous section thick of ~3,500 m and the other sections, which overlap at the top of the Dwarda section, exposing ~380 m (the Ganguli) and ~210 m (the Patalaia).

For their major part, the CR series consist in south-dipping beds with an inclination of 55-65°. Along the southern part (< ~210-250 m) bedding flattens down to 30° over a distance of 400 m (Figure VII-68). Bedding in the northern part (>2,600 m) also flattens down to 25°, but more gradually and accompanied by a counterclokwise rotation of the bedding strike (from South dipping toward SE dipping). No stratigraphic duplication, major unconformities or faults were identified.

VII.4.2. The frontal Churia (CR) fold

The determination of the geometry and age of the fold (Figure VII-68) was performed using our dip measurements in the southern limb of the fold, from the front of the fold up to close to the fold axis, combined with satellite imagery (available in Google Earth©).

While the CR ridge culminates at ~500 m above the Ganga plain, the sections show 4,000 m of exhumed rocks, which attests to the deep exhumation of the range. The CR fold develops over a width of 12 km as an anticline with a steep south frontal limb of 61± 5°. The geometry and possible asymmetry of the fold are difficult to assess because of the lack of published data and visible strata in satellite imagery. Therefore, finite shortening remains undetermined. The absence of a frontal tectonic scarp underlines that the MFT does not reach surface at this location and alluvial terraces at the fold front 10 km east of the Ganguli display bedding-parallel shear zones. These two observations suggest that the CR fold might correspond to a fault propagation fold.

VII.4.3. The Valmiki Nagar (VR) fold

The determination of the geometry and age of the fold (Figure VII-69) was performed using our limited dip measurements in the southern limb of the fold, from the front of the fold up the fold axis, combined with satellite imagery (available in Google Earth©).

Despite deep erosion, the VR ridge culminates at 60-100 m above the plain, with 25-50 m of local relief, which points to a low-scale tectonic uplift. The VR fold develops over 9.5 km as an asymmetric anticline with a 75° steep south frontal limb and a gentler northern limb. Finite shortening is assessed to be of ~750 m for the southern limb and likely > 1.5 km for the total fold. Although a detachment fold is not to be excluded, the VR fold is more probably a fault propagation fold.

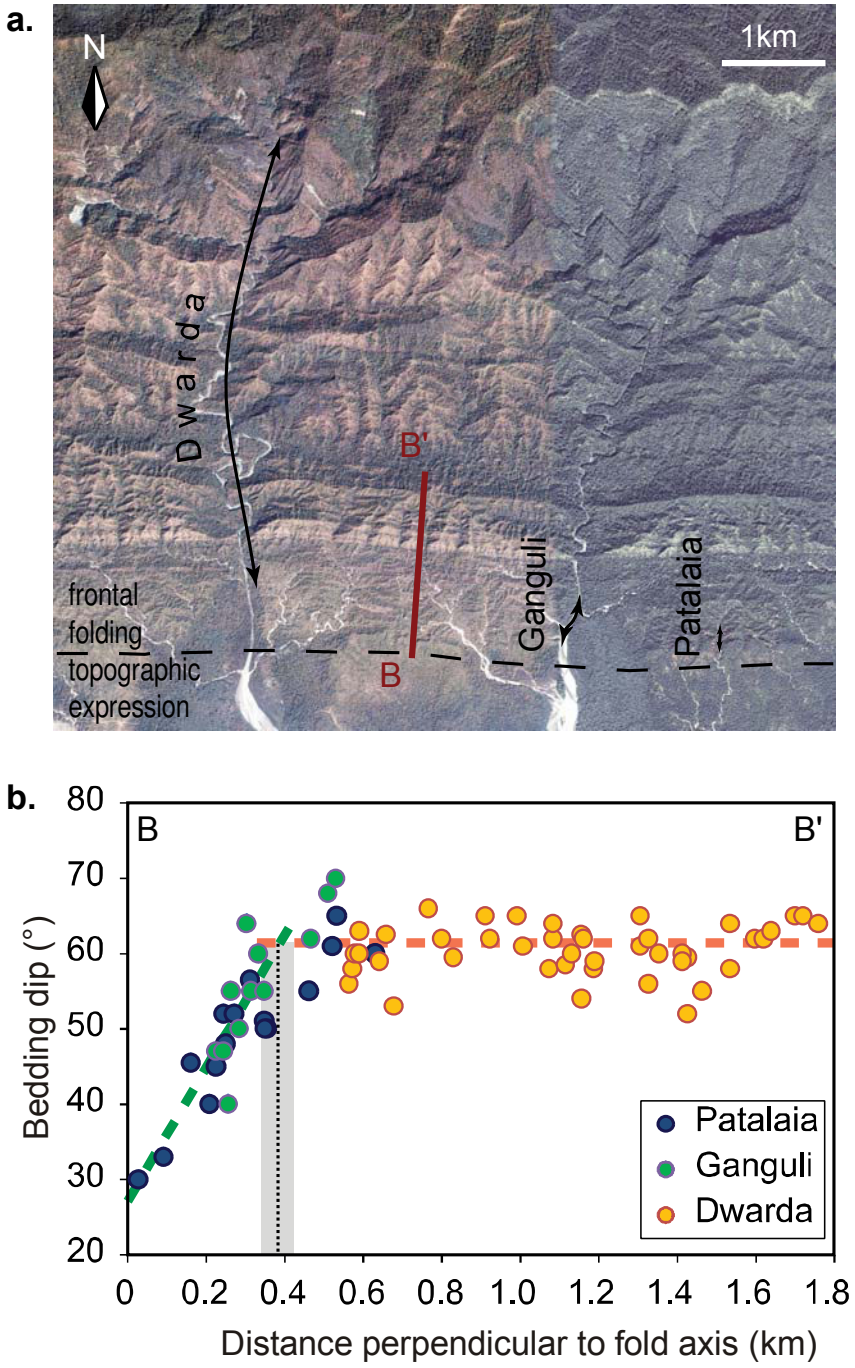

Figure VII-68. Southwest Churia Range Sections (CR).

a. The Dwarda, Ganguli and Patalaia Sections are presented with a background satellite image (Google Earth©). The location of the transect BB' is indicated.

b. Projection of the dip-measurements for the three sections on the BB' transect.

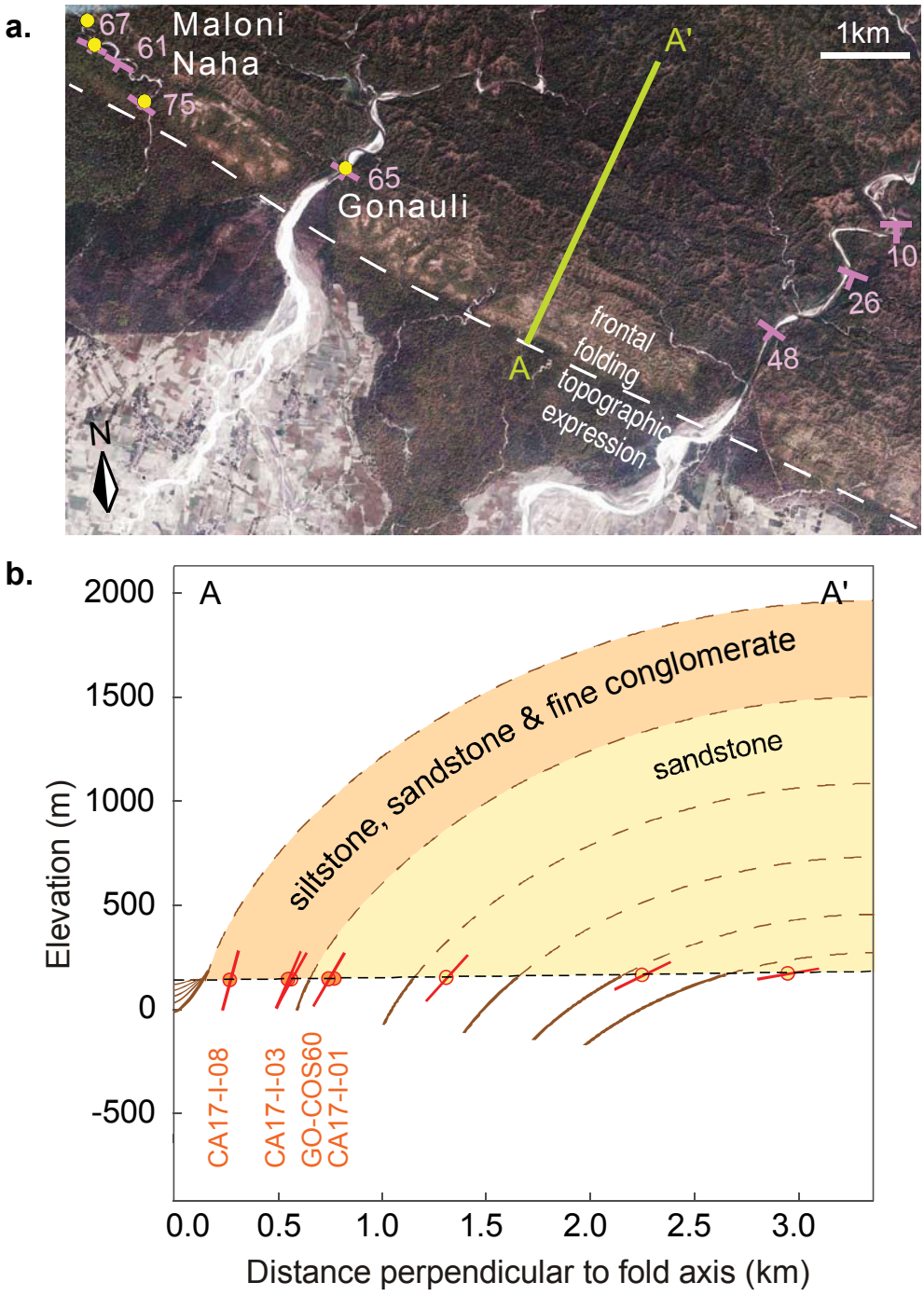

Figure VII-69. Valmiki Nagar Range Sections (VR).

a. The locations of the discontinuous Gonauli and Maloni Naha Sections are represented by dots where samples were collected, with a background satellite image (Google Earth©). The location of the transect AA' is indicated.

b. Projection of the dip-measurements and the samples for the three sections on the AA' transect.

VII.4.4. Paleomagnetic dating

The paleomagnetic results and the magnetostratigraphic correlation are presented in Figure VII-70 and in Table SVII-1-Table SVII-2.

Remark: this section requires further development.

Figure VII-70. Sedimentary log and magnetostratigraphic correlation.

Next page.

a. Sedimentary logs of the CR Sections (c: clay, s: silt, S: sand, f: fine sand, m: medium sand, c: coarse sand, G: gravel, P: pebble). Location of the CR Sections is indicated in Figure VII-67-Figure VII-68. The discontinuous VR Sections are not represented for clarity.

b. Stratigraphic position of the silty and sandy samples for geochemical and isotopic measurements (Table SVII-1-Table SVII-3). Only the samples having yielded results are indicated. The sandy samples are coloured whether they are from the Dwarda (red) and the Ganguli (blue), or from the VR Sections (green). No sample from the Patalaia has geochemical or isotopic measurements.

c. Paleomagnetism declination and inclination (Table SVII-1).

d. Magnetostratigraphic correlation results using the algorithm of Lallier et al. (2013). Magnetic intervals were selected based on a minimum of two successive horizons possessing the same polarity. Samples were not assigned a polarity if they possessed transitional directions. The best fit age model is indicated by the red curve (resulting ages for the samples in Table SVII-1-Table SVII-3.

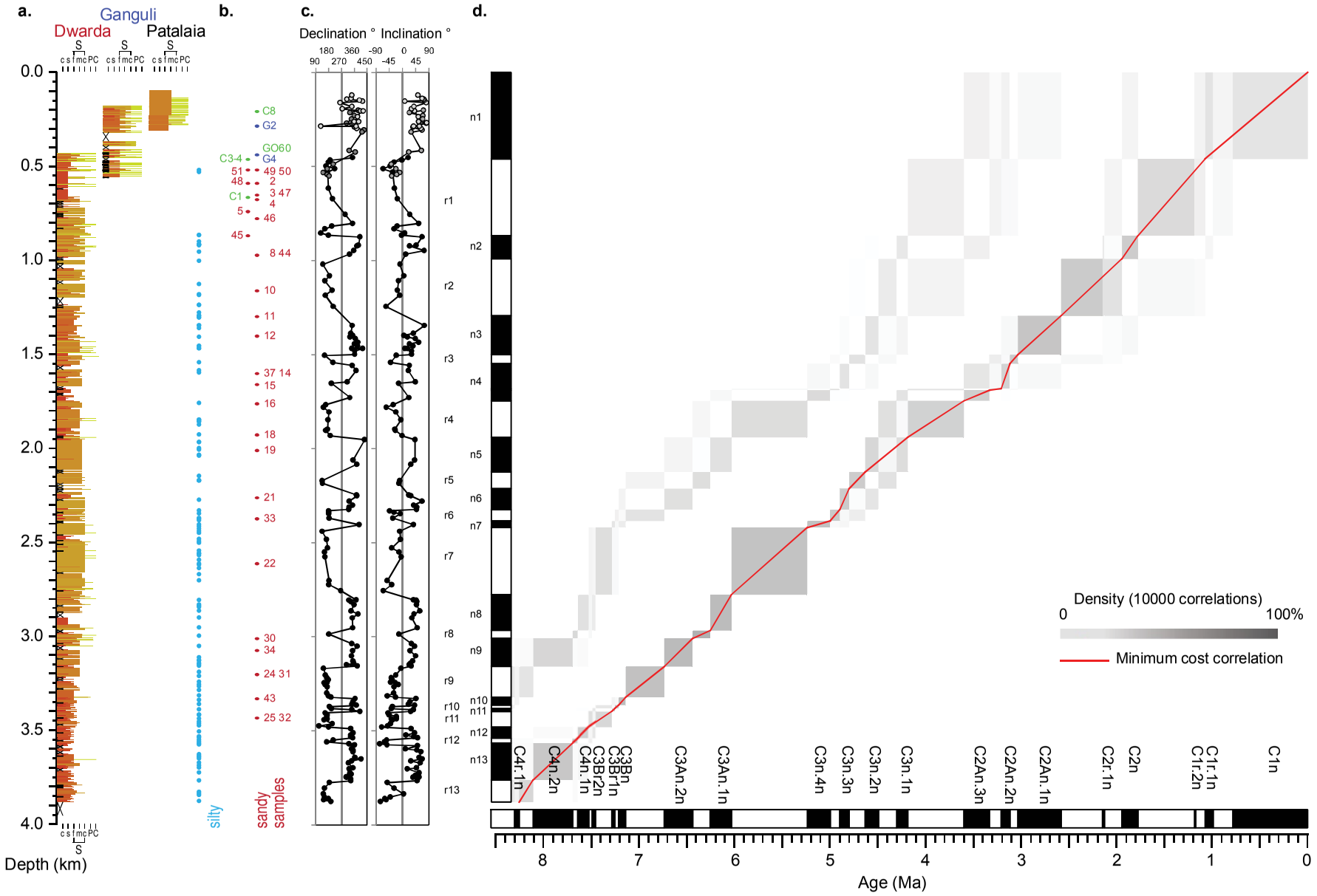
a.
Ganguli
Dwarda
Patalaia
S
c s f mc PC
0.0
0.5
1.0
1.5
2.0
2.5
3.0
3.5
4.0
Depth (km)
silty
b.
C8
G2
GO60
C3-4
G4
51
49 50
48
2
C1
3 47
4
5
46
45
8 44
10
11
12
37 14
15
16
18
19
21
33
22
30
34
24 31
43
25 32
sandy samples
c.
Declination °
Inclination °
180 360 -90 0 90
90 270 450 -45 45
d.
n1
n2
n3
n4
n5
n6
n7
n8
n9
n10
n11
n12
n13
r1
r2
r3
r4
r5
r6
r7
r8
r9
r10
r11
r12
r13
C4r.1n
C4n.2n
C4n.1n
C3Br2n
C3Bn
C3Br1n
C3An.2n
C3An.1n
C3n.4n
C3n.3n
C3n.2n
C3n.1n
C2An.3n
C2An.2n
C2An.1n
C2r.1n
C2n
C1r.1n
C1r.2n
C1n
Density (10000 correlations)
0
100%
Minimum cost correlation
8
7
6
5
4
3
2
1
0
Age (Ma)

VII.4.5. Sedimentology

The series can be divided into five facies (Figure VII-70a).

From 3,950 to 3,470 m (8.2 to 7.5 Ma), the series are dominated by metric fine sand - silty beds fining upwards, with rare clay and few paleosoils. Several massive and decametric fine- to medium sandstone bodies intercalate in the series. They present rare cross-bedding and contain few thin pebble or mud ball thin beds and occasional silt lenses.

From 3,470 to 2,880 m (7.5 to 6.1 Ma), the series gradually become dominated by massive and plurimetric to decametric fine- to medium sandstone bodies similar to the previous group. The transition is not regular, and thin fine sand - silty beds fining upwards occur even in the top of this group. Several centimetric coarse to gravelly beds with an erosional base intercalate in the bodies close to the top of the group.

From 2,880 to 1,930 m (6.1 to 4.2 Ma), the series present almost continuous and pluridecametric massive medium- to coarse sandstone bodies having a "salt and pepper" type. Close to the top of the group thinner beds of decimetric to plurimetric thickness occur but massive bodies are still present. These bodies present occasional cross-bedding, lenses of silt and occasional indurated calcareous nodules. They regularly incorporate mud balls, either isolatedly or in metric pebbly beds. Metric fining-up thin beds and clayey beds are very rare. At ~2,723 m, a neat 3-D cross-bedding yields a flowing direction of N160 to N200.

From 1,930 to 670 m (4.2 to 1.4 Ma), the series are dominated by plurimetric to decametric massive medium- to coarse "salt and pepper" sandstone bodies, which can occasionally be with fine grain size or gravelly/pebbly, and which often display cross-bedding and more rarely, coarser lenses. In the lower part of the group, several metric fine sand - silty beds fining upwards and some metric to rarely decametric silty/clayey horizons are present. All over the 1,930 - 670 m group, metric beds with mud balls or gravels/pebbles, intraformational conglomerates (puddingstones) and channel lag deposits occasionally intercalate with other layers.

From 670 to 100 m (< 1.4 Ma), the three sections differ. The Dwarda (up to 430 m) is dominated by massive yellow-grey unconsolidated siltstone, intercalated by metric pebbly beds. The lower part of the Ganguli has several gaps, but can be described as dominated by decametric sets of pebbly beds intercalated with massive silty to fine sand. The upper part of the Ganguli is dominated by metric gravelly to pebbly beds intercalated with massive silty to medium sand occasionally containing fine gravelly lenses. The Patalaia is dominated by massive yellow to red silty to fine sand, occasionally containing gravelly lenses, and discontinuously intercalated by pebbly beds, made of finer and somehow more angular clasts than the conglomerates observed along the Dwarda. Over the three sections, conglomerates represent 20 to 40% of the strata in the 670 - 100 m group.

VII.4.6. Age estimate of the frontal Churia (CR) fold

Crustal shortening in this area is shared by a second anticline (SECR) at the north of the CR fold, both having a similar topography and relief (Figure VII-67). Given that the relief ratio between both structures is close to 1 (with lateral variations) and that uplift rates correlate to relief or elevation in the Siwaliks (Hurtrez et al., 1999), shortening should be roughly distributed equally between the CR and the SECR. With a total shortening on the MFT close to 20 mm/y over the Holocene (Lavé and Avouac, 2000), we assess that the CR fold accommodates ≈10 mm/y of shortening. By hypothesizing fault ramp at 30°, the common value for thrust faults which has been generally verified in the Siwaliks, uplift rate in the CR range should be at ≈5 mm/y. This rough assessment is of an order of magnitude similar to the uplift rate of an alluvial terrace at the fold front close to the Ganguli. This terrace, with an elevation of 25 m, presents a 2 m weathering front of orange color. Using the approach developed in Lavé and Avouac (2000) we estimated that the age of the terrace is ca. 10 ka, giving an uplift rate ≈ 2.5 mm/y.

The initiation age of the CR folding is determined by the observation of the syn-folding sediments. The compilation of the dips obtained along the Ganguli and the Patalaia sections shows a gradual decrease from 61° to 30°. The shift starts at 385±35 m from the front, close to the G25 sample (≈317 m depth), which indicates a start of the CR folding at ≈0.74±0.06 Ma.

Our results imply that the samples of the Ganguli and the Patalaia above 317 m, including Ggcos1 and Ggcos2, originate from recycled sediment.

VII.4.7. Age estimate of the Valmiki Nagar (VR) fold

Crustal shortening in this area is shared by a second anticline (SWCR) at the north of the VR fold (Figure VII-67). This anticline is deeply eroded and present a relief and topography higher than the VR fold by a factor three to four (ridge elevation: 250-320 m above the plain, local relief: 100-200 m), which points to an intermediate-scale tectonic uplift. Using the same approach as for the CR fold, we assess that the uplift of the SWCR fold is three to four times higher than the uplift of the VR fold. Therefore, the SWCR fold accommodates three to four times more shortening, which implies that the VR fold accommodates ≈4-5 mm/y of shortening.

Given this rate and the amount of finite shortening, we deduct that the VR fold initiation age should roughly be at ca. 0.3 - 0.4 Ma. With a 0.5 mm/y average sedimentation rate, this corresponds to a stratum 150 to 200 m below surface. This value is consistent with a maximal thickness of 250 m, based on the location of Site A at ~260 m from the front and on a dip of strata of 75° like in A.

Our results imply that one sample of the VR sections (Ca17i08) has probably a recycled origin.

VII.4.8. Major and trace elements

The major element results for our sandy samples divide the sections into three periods (Figure VII-71, Table SVII-3). From 7.4 to ca. 2-2.5 Ma, the Al/Si ratio, a proxy for grain size (Lupker et al., 2012b), stays in the range of the modern Narayani sand, with a small decrease from ≈0.16 to ≈0.14. The Na/Si, a proxy for chemical weathering (Lupker et al., 2012b), is steady at lower values than the Narayani, ≈0.03, with more variable and higher values before 6 Ma. The Na/Si ratio presents subtle variations of a ≈2 My period, with lows at ca. 3 and 5 Ma. Other ratios, Fe/Si, Mg/Si, K/Si (which is also a proxy for chemical weathering) and Ti/Si present a decreasing trend, and Fe/Si presents second-order variations similar to Na/Si. from ca. 2-2.5 to 1.2 Ma, the Al/Si increases to ≈0.17, with more variable values after 1.5 Ma. Na/Si follows the same pattern, with three samples higher than ≈ 0.05. Other majors, Fe/Si, K/Si and Ti/Si also present more variable and higher values whereas Mg/Si continues to decrease. After 1.2 Ma, all ratios suddenly drop. Al/Si reaches ≈0.08 and Na/Si is below 0.01, values which characterize the local Siwalik rivers.

The trace element results (Table SVII-3) chiefly reflect the same trends as the major elements, although with a variable amplitude and including for some of them the second-order variations (Figure VII-71). This is particularly the case for some alkali metals (Rb, Cs), alkaline earth metals (Sr which traces chemical weathering of carbonates, Ba), metals (Co, Cr, Ga, Nb, Ni, Sc, V, W, Zn) and some rare earth elements (notably Eu).

Figure VII-71. Major and trace element results from medium to coarse sand.

Next page.

Major elements normalized to Si, following Lupker et al. (2012b). Trace elements normalized to the Upper Continental Crust (UC) (Taylor and McLennan). The Valmiki samples are presented in black circles except the two samples younger that the initiation ages of the folds, which are in red. References are presented for comparison: the values of the Narayani sand (N, in blue), the Gandak Megafan sand and silt (GR, in magenta), the Rapti in the Chitwan Dun (in yellow), with the averages of the TSS, HHC and LH (Morin, 2015). For clarity, the y-axis is cut at the top, which prevents the display of the upper values of the references. The results are available in Table SVII-3.

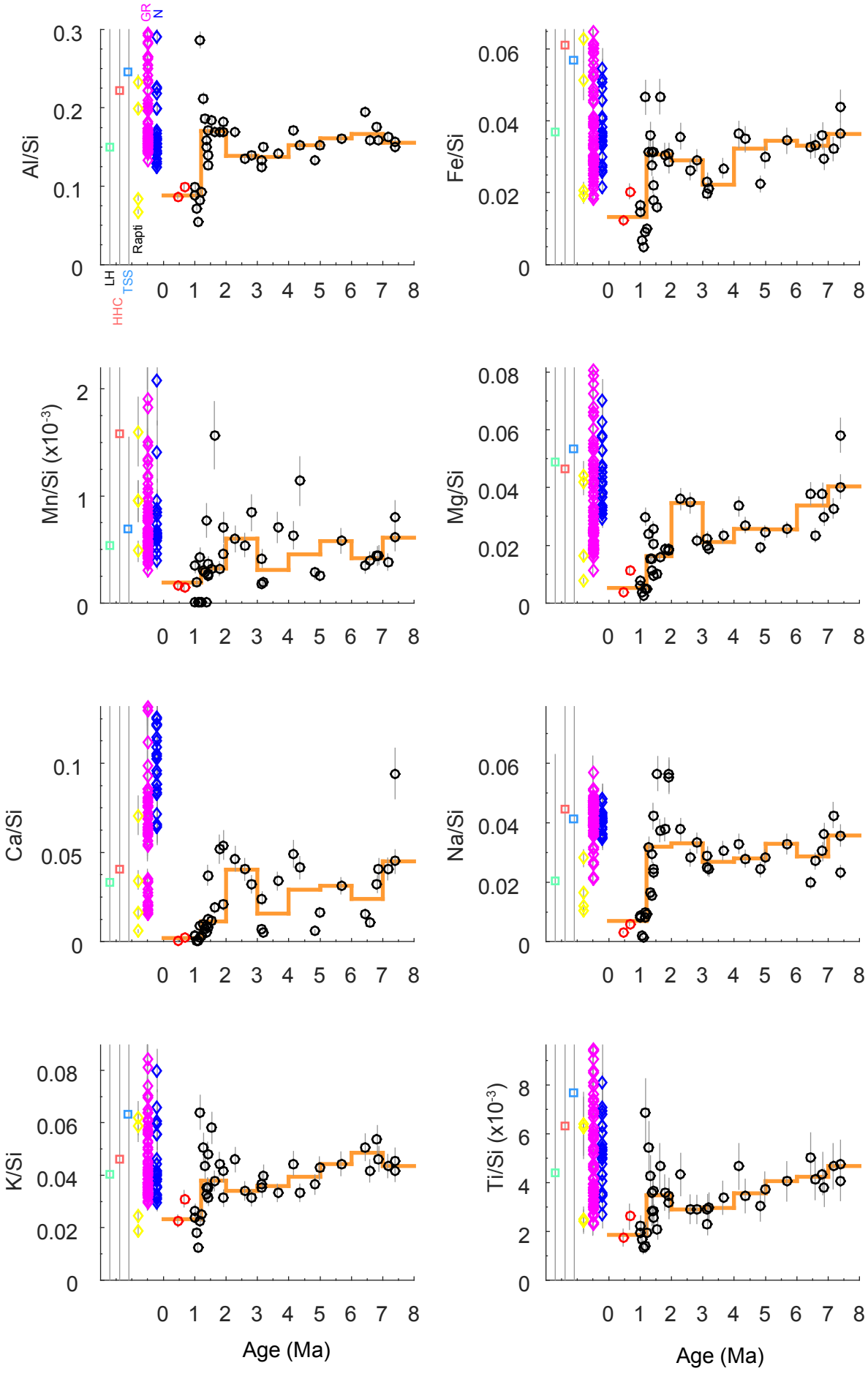
Al/Si
Fe/Si
Mn/Si (x10-3)
Mg/Si
Ca/Si
Na/Si
K/Si
Ti/Si (x10-3)
Age (Ma)
Age (Ma)
LH
HHC
TSS
Rapti
GR
N

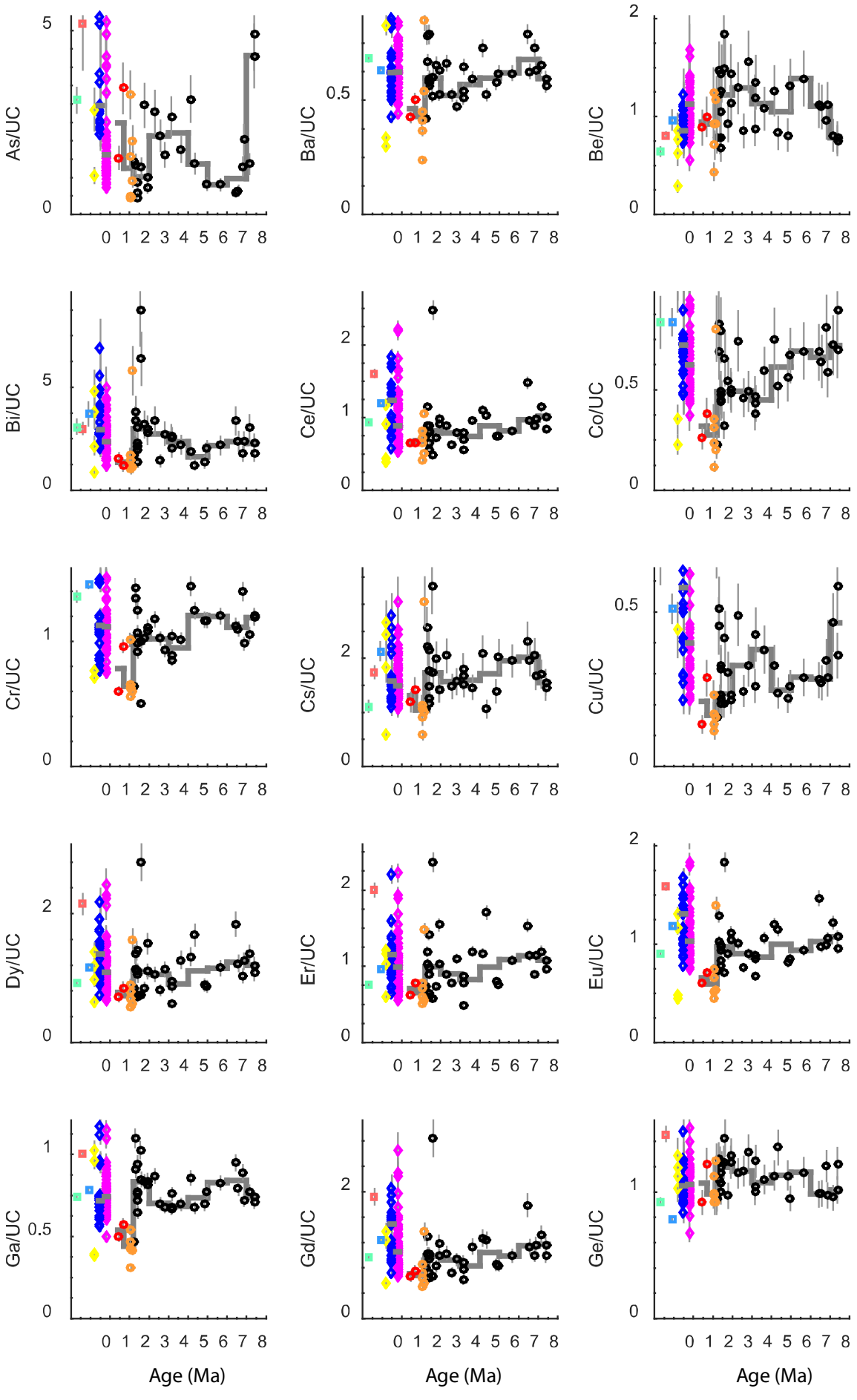
As/UC
Ba/UC
Be/UC
Bi/UC
Ce/UC
Co/UC
Cr/UC
Cs/UC
Cu/UC
Dy/UC
Er/UC
Eu/UC
Ga/UC
Gd/UC
Ge/UC
0 1 2 3 4 5 6 7 8
Age (Ma)

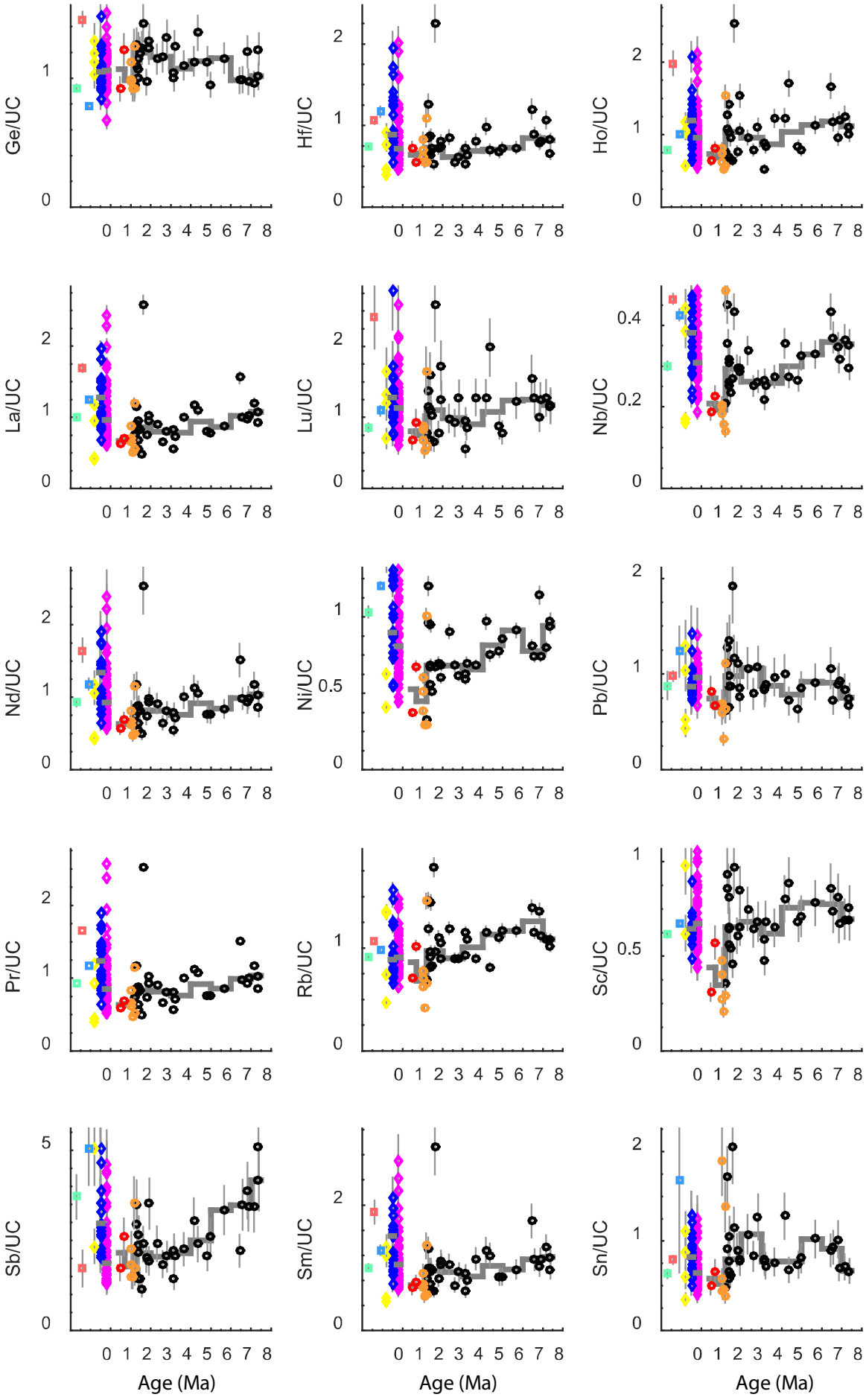
Ge/UC
Hf/UC
Ho/UC
La/UC
Lu/UC
Nb/UC
Nd/UC
Ni/UC
Pb/UC
Pr/UC
Rb/UC
Sc/UC
Sb/UC
Sm/UC
Sn/UC
Age (Ma)
Age (Ma)
Age (Ma)

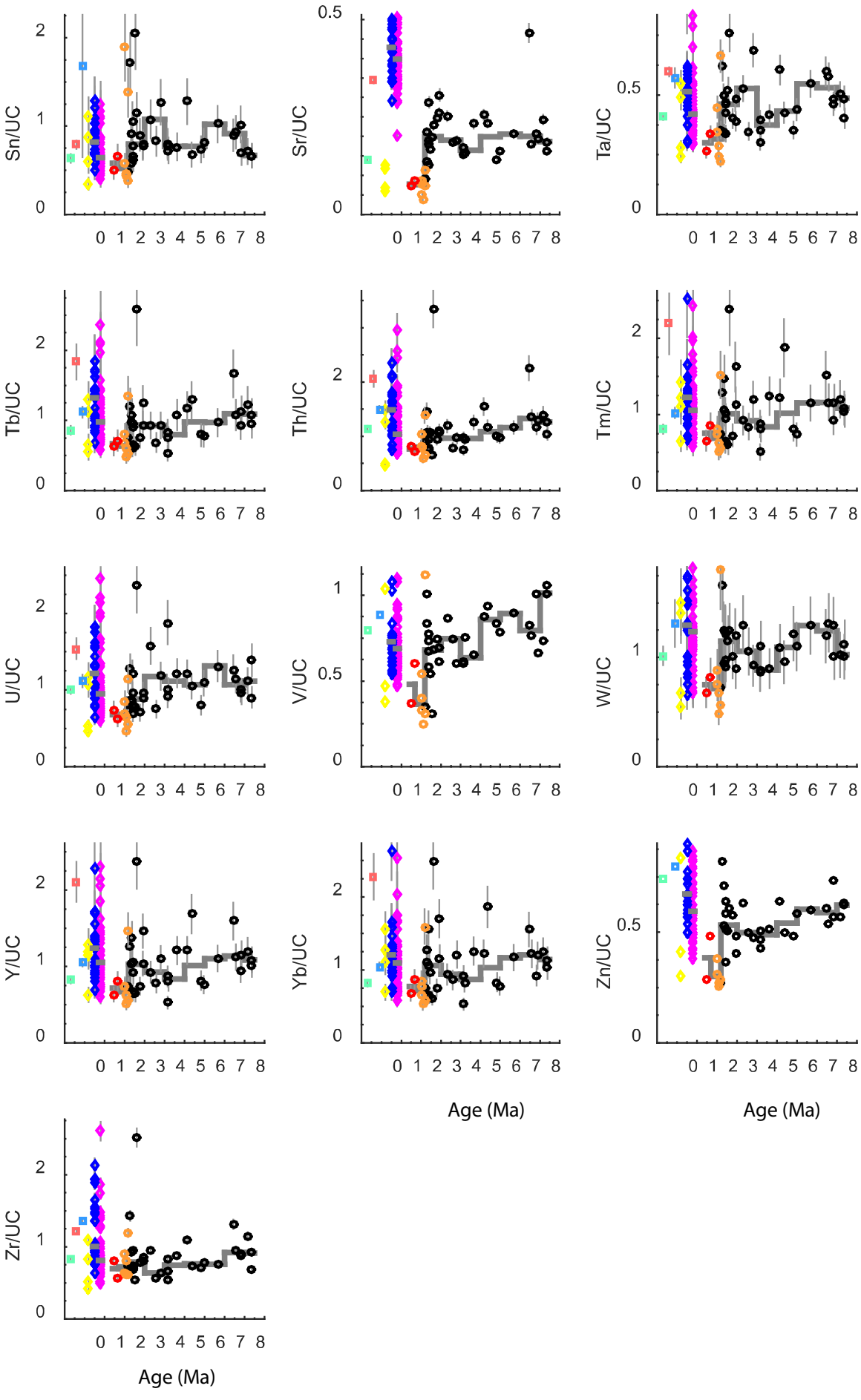
Sn/UC
Sr/UC
Ta/UC
Tb/UC
Th/UC
Tm/UC
U/UC
V/UC
W/UC
Y/UC
Yb/UC
Zn/UC
Zr/UC
Age (Ma)
Age (Ma)
Age (Ma)

VII.4.9. C and O isotopes

The sandy samples (Table SVII-3) present a low carbonate content of ~3±3 %, with the samples above -750 m (< 1.6 Ma) and also several samples below completely depleted in carbonates. For the samples still having carbonates (> 1%), $\delta^{13}C$ has stable values at ~2 ‰ and $\delta^{18}O$ increases of two units above 1,700 m (< 3.6 Ma) from stable values at ~14 ‰. Even if the carbonate content is lower than for the modern Narayani at 10-20%, weathering was limited and did not remove completely the carbonates, except in the upper part. The isotopic compositions are similar to the ones of the Himalayan rivers (Lupker et al., 2012b) and compatible with the isotopic signature of Himalayan rocks (Galy et al., 1999).

Figure VII-72. $\delta^{13}C$ results and comparison with other Siwalik sections.

Next page.

a. Our results on bulk carbonates from the Valmiki Sections. Only the results from clayey to fine sand are presented (Table SVII-4). The results are compared with available data measured on pedogenic carbonates from the Surai Section (~160 km west of the Valmiki Sections, Quade et al., 1995). Note that the ages of the Surai samples have not been updated with the new available age model (Charreau et al., in prep.). Data measured on pedogenic kankars (pink diamonds) from the Gandak Megafan, along with data measured on bulk carbonates on the Narayani sediment (blue diamonds) are also presented for comparison (Morin, 2015; unpublished data from C. France-Lanord and T. Rigaudier). The $\delta^{13}C$ signatures of a mix dominated by 100% of C4 plants or by 100% of C3 plants are indicated by black lines (Quade et al., 1995). The range of values from Himalayan rocks is indicated by the grey-shaded area (Galy et al., 1999).

b. Available $\delta^{13}C$ data measured on pedogenic carbonates in Western Himalayan sections, in Northern India (Vögeli et al., 2017a).

c. Available $\delta^{13}C$ data measured on pedogenic carbonates in Western Himalayan sections, in Pakistan (Quade et al., 1989; Quade and Cerling, 1995). Note that the ages are the same than the ones used in Quade and Cerling (1995) .

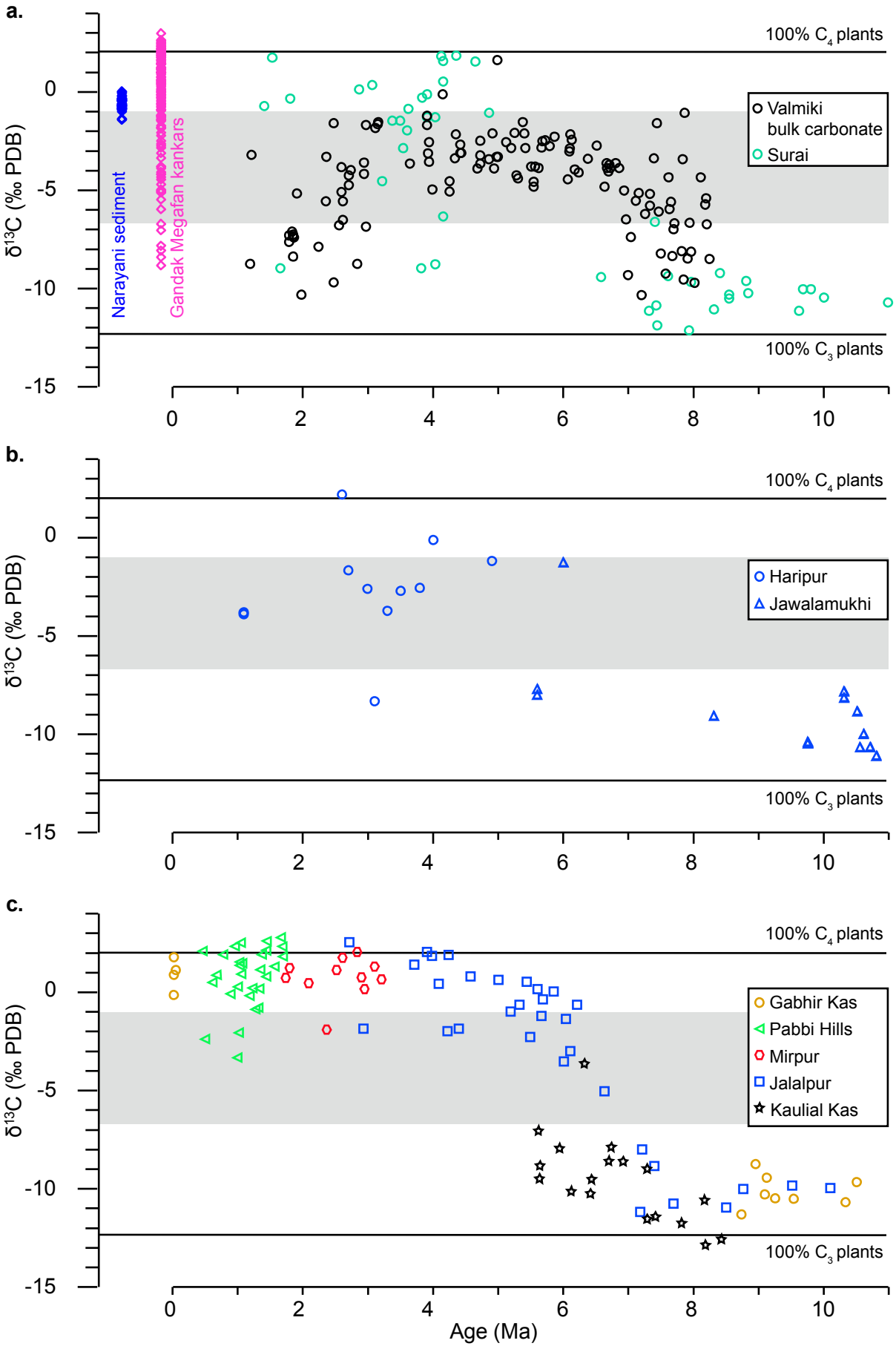
a.
100% C4 plants
100% C3 plants
δ13C (‰ PDB)
Narayani sediment
Gandak Megafan kankars
Valmiki bulk carbonate
Surai
b.
Haripur
Jawalamukhi
c.
Gabhir Kas
Pabbi Hills
Mirpur
Jalalpur
Kaulial Kas
Age (Ma)

The silty samples (Table SVII-4) present a high carbonate content of 25±14 %, except in the upper part of the record (< 650 m / 1.4 Ma) and 126 samples out of 182 have a content higher than the detrital content of the modern Narayani (i.e. > 20 %). These 126 samples are enriched in secondary carbonates. These secondary carbonates may be composed of post-burial diagenetic cement or syn-deposition pedogenic carbonates. As developed in the Methods, one can assume that the evolution of our isotopic values reflect the evolution of the signature of the diagenetic cement and/or pedogenic carbonates and not the detrital carbonates. For reference, the modern Narayani sediment, which contains exclusively detrital carbonates, has a $\delta^{13}C$ of ~ -1‰ (Morin, 2015; unpublished data from C. France-Lanord and T. Rigaudier). For these samples, the $\delta^{13}C$ evolution is divided into three phases (Figure VII-72). Below 3,250 m (8.2 - 6.9 Ma), the $\delta^{13}C$ display variable values in the ~ -3 - -9 ‰ range; in the 3,250 - 1,540 m interval (6.9 - 3.1 Ma), the $\delta^{13}C$ values are restricted in the ~ -2 - -5 ‰ range; in the 1,540 - 520 m interval (3.1 - 1.1 Ma), the $\delta^{13}C$ has again variable values in in the ~ -3 - -9 ‰ range.

Contrastingly, the $\delta^{18}O$ show a clear and gradual increase over the full period from ~ -10 - -18 ‰ to ~ -4 - -12 ‰ (Figure VII-73).

The high carbonate content of the silty samples confirms that weathering was limited for the majority of the record, except in its youngest part (< 1.4 Ma), and therefore preserves the soil carbonate isotopic signature.

Figure VII-73. $\delta^{18}O$ results and comparison with other Siwalik sections.

Next page.

a. Similarly to Figure VII-72, our results on bulk carbonates from the Valmiki Sections. Only the results from clayey to fine sand are presented (Table SVII-4). Ou results are compared with available data measured on pedogenic carbonates for the Surai Section and the kankars of the Gandak Megafan or on bulk carbonates of the Narayani sand (Quade et al., 1995; Morin, 2015; unpublished data from C. France-Lanord and T. Rigaudier). The range of the $\delta^{18}O$ values of modern precipitations at this latitude and elevation are indicated by a light-blue-shaded area (Bowen and Wilkinson, 2002).

b. Available $\delta^{18}O$ data measured on pedogenic carbonates in Western Himalayan sections, in Northern India (Vögeli et al., 2017a).

c. Available $\delta^{18}O$ data measured on pedogenic carbonates in Western Himalayan sections, in Pakistan (Quade et al., 1989; Quade and Cerling, 1995).

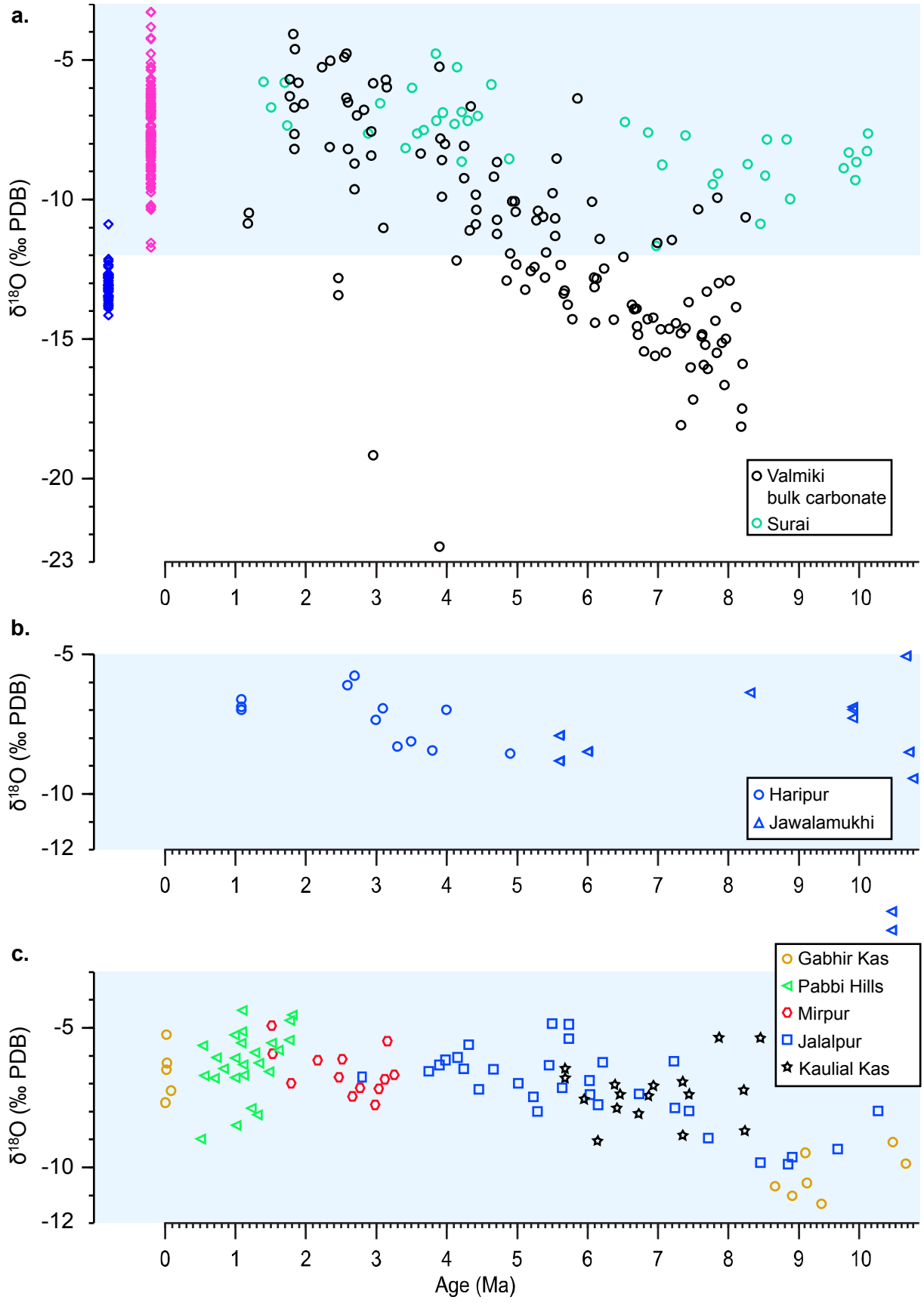
a.
δ18O (‰ PDB)
-5
-10
-15
-20
-23
0
1
2
3
4
5
6
7
8
9
10
Valmiki
bulk carbonate
Surai
b.
δ18O (‰ PDB)
-5
-10
-12
Haripur
Jawalamukhi
c.
δ18O (‰ PDB)
-5
-10
-12
Gabhir Kas
Pabbi Hills
Mirpur
Jalalpur
Kaulial Kas
Age (Ma)

VII.5. DISCUSSION

VII.5.1. Fluvial style evolution

The CR sedimentary facies dominantly characterize an active wide braided alluvial system, with occurrence of high flood conditions (presence of mud balls) and are related to the Middle Siwalik group. The facies associated to a meandering system (overbank deposits) are mainly restricted to the lower part (> 3,470 m - ca. 7.5 Ma), but make occasional appearances in the other parts. The facies of the upper part (< 670 m - ca. 1.4 Ma) characterize an environment closer to the gravel front of the main river (Dubille and Lavé, 2015) and/or may indicate the input of local rivers (this latter assumption requiring further validation).

The facies of the upper part marks a contrast with other Siwalik sections (e.g. the Surai Section, Corvinus and Rimal, 2001; the Haripur Section, Thomas et al., 2002). Conglomeratic beds are present but they are not continuous. Therefore, following the definition of (Quade et al., 1995), we propose that the upper part of the described series do not present the facies of the Upper Siwalik group stricto sensu and should be considered to be the continuation of the Middle Siwalik group.

VII.5.2. Recycling

The period younger than 1.2 Ma is marked by quartz-dominated sand (low Al/Si), which potentially point to successive weathering episodes. This SiO_2 enrichment may derive from recycling sands from the Siwaliks, as shown in modern Siwalik river sediment and also by the samples determined as recycled by the geometry of the CR and VR folds (Ca17i08 and Ggcos2). The recycling hypothesis is sustained by the depletion of Na and other elements, which points to advanced chemical weathering. Therefore, the age of 1.2 Ma might be the turning point when the Narayani channel did not reoccupy the CR location to deposit sand. This shift was sudden and probably linked to the regional development of the Siwalik ranges which may have impacted the course of the Narayani (e.g. the model described in Figure 17 in Divyadarshini and Singh, 2019, which detail is however not supported by our data).

To our knowledge, the only other Siwalik Section for which a recycling investigation has been performed is the Surai Section (Charreau et al., in prep.), which show recycling starting at ca. 3.5 Ma. This might indicate that the Valmiki Section is one of the rare Siwalik Sections that record the original Himalayan erosion signal until the middle Pleistocene. But further work is required to determine recycling in other Siwalik Sections, which more generally has an incidence on the interpretation of previous results in provenance (e.g. Huyghe et al., 2001; Robinson et al., 2001) or erosion (Bernet et al., 2006; van der Beek et al., 2006).

VII.5.3. Detection of a shift of provenance?

Before 2.3 Ma, the coeval evolution in sands of elements with Al/Si suggests that granulometry controls the elemental content. The small decrease in Al/Si before 2.3 Ma fits well with the increase in grain size related to the progression of the gravel front (Dubille and Lavé, 2015). But this explanation does not explain the shift at ca 2-2.5 Ma.

A shift of provenance may have affected the elemental composition. The geochemical signature of the HHC, and in particular of leucogranites (Morin, 2015) is enriched in the majority of elements (other than Si) compared to the TSS and the LH. Then, the coeval increase in these elements at ca. 2-2.5 Ma may be caused by the relative increase in the contribution of the HHC compared to the contribution of the TSS and LH in our samples.

This evolution may be realized by a shift of the focus of erosion. This has been proposed for the Pleistocene with amplified glacial erosion on the High Himalayan peaks, therefore mostly eroding the HHC and the TSS units (Herman et al., 2013; Thiede and Ehlers, 2013).

VII.5.4. Evolution of precipitations

The following interpretation is based on the possibility that the signal we observe partly represents the signal of the pedogenic carbonates. However this signal probably includes the signal of diagenetic cements, which requires further petrographic investigation.

Our $\delta^{18}O$ record initiates the trend with an average of ~-16‰, which is a value unseen in modern conditions at these latitudes and elevation. Additionally, the initial values are distinct from the ~-10.5‰ average in Western Himalaya and the ~-9‰ average in the Surai Section at 8 Ma (Quade and Cerling, 1995; Quade et al., 1995). In contrast, the average of all sections at ca. 1 Ma is close to ~-6‰. Values below -11‰ are unseen in modern precipitations at this latitude (Bowen and Wilkinson, 2002). Therefore, it is probable that the $\delta^{18}O$ signal older than 5.5 Ma has been depleted by early diagenesis, at similar depths (> 2,500 m) that what has been observed from clays in the Karnali Section, Western Nepal (Huyghe et al., 2005). However, reaching values of ~-16‰ only with early diagenesis requires that original values were already very low.

From 5.5 Ma (until 1.7Ma, the end of the record), our $\delta^{18}O$ record in pedogenic carbonates presents a clear increasing trend until 1.7 Ma. This trend points to a gradual decrease in precipitations and/or an amplifed rainfall seasonality in the Central Himalaya. Even though a regional shift in the $\delta^{18}O$ of the meteoric precipitations caused by the late Cenozoic global climate change cannot be excluded, its impact should have remained limited (Quade and Cerling, 1995).

Our results confirm the clay mineralogy dataset in Central Himalaya (Huyghe et al., 2005, 2011) but not the O isotopic dataset on freshwater bivalves and mammal teeth (Dettman et al., 2001). We note that the record of Dettman et al. (2001) has a limited resolution and maybe do not display the full variability of the $\delta^{18}O$ signal as studies in pedogenic carbonates. This would require further analyses which may have been prevented by the rarity of the fossil record in the Siwaliks.

VII.5.5. Late Miocene shift to C4-dominated vegetation

Similar preliminary remark than for the previous section.

Contrary to the $\delta^{18}O$ signal, early diagenesis has a limited impact on the $\delta^{13}C$ signal (Quade and Cerling, 1995; Quade et al., 1995). We note additionally that the record is in the spectrum of values for pedogenic carbonates.

While the previous studies (Harrison et al., 1993; Quade et al., 1995; Ojha et al., 2000; Ojha et al., 2009) yielded limited constraints on the timing and the pattern of the shift to the C_4 plant prevalence in the Ganga plain during the late Miocene, we show that the shift occurred suddenly at ca. 6.9 Ma, after a 6-9 - 8.2 Ma period of competition between the C_3 and C_4 pathways, even though we cannot define the start of this transition in the Ganga plain.

Our results might confirm the synchronicity at ca. 7 Ma predicted by Quade et al. (1995) between Western and Central Himalaya (for Pakistan: Quade et al., 1989; Quade and Cerling, 1995; Barry et al., 2002; note that results for northern India (Ghosh et al., 2004; Ghosh et al., 2018), even if they show the prevalence of C_4 plants in the Pliocene, contradict each other about the timing and the pattern of the shift). But they are in contradiction with the results of Vögeli et al. (2017a) for Eastern Himalaya.

VII.5.6. Late Pliocene shift back to mixed vegetation

Similar preliminary remark than for the previous sections.

Until ca. 4 Ma, the $\delta^{18}O$ increasing trends are similar in the Western (Quade and Cerling, 1995) and Central Himalayan plains. In contrast, they diverge after ca. 4 Ma, with an increasing trend of $\delta^{18}O$ in Central Himalaya compared to steady values in Western Himalaya.

As told by the $\delta^{13}C$ signal, the vegetation shifts back to a competition between the C_3 and C_4 pathways after 3.1 Ma. Such a shift back has never been observed, in particularly in Western Himalaya, where the C_4 pathway dominates until the late Pleistocene (Quade and Cerling, 1995).

To explore the causes of the shifts of the C_3 - C_4 pathway competition, we can refer to the late Pleistocene to Holocene records. In the Bengal Fan, the $\delta^{13}C$ on organic matter shifted to lower values during the early Holocene (Galy et al., 2008; Hein et al., 2017). This shift is confirmed by the $\delta^{13}C$ on kankars in the Narayani-Gandak Fan (unpublished data from Morin, France-Lanord and Rigaudier), which also shows a shift back to higher $\delta^{13}C$ in the late Holocene.

The early to mid-Holocene in South Asia is characterized by warm and moist/wet conditions with strengthened monsoonal conditions (Goodbred and Kuel, 2000; Herzschuh, 2006) while the late Holocene is cooler and drier. Thus, two not-exclusive hypotheses could explain the Holocene $\delta^{13}C$ variations: either the increase in precipitations benefits to the C_3 plant production or the focus of heavy precipitations during the summer, the growth period for C_4 plants, would reduce soil evaporation and the high water soil content would limit the development of C_4 plants.

Therefore, the full $\delta^{13}C$ Himalayan dataset suggests that the competition between C_3 and C_4 pathways is controlled by the strength of the SA Monsoon. Given the $\delta^{13}C$ and $\delta^{18}O$ record of our samples and the Holocene analog, we propose the following scenario. The late Cenozoic climate change in the Ganga plain initially produces a sudden weakening of the SA Monsoon, with a rapid decrease in precipitations in Western and Central Himalaya, which has favoured the prevalence of C_4 plants after 6.9 Ma. The weakening is not so strong since the SA Monsoon still bring precipitations in Eastern Himalaya to prevent precipitations in competition monsoonal winds become too weak to bring precipitations to Central and Western Himalaya, but strong enough to bring precipitations to Eastern Himalaya. In other words, and contrary to the Arabian Sea record (Kroon et al., 1991; Prell et al., 1992; Clift et al., 2008) and to previous interpretations in the Siwaliks (Quade and Cerling, 1995; Quade et al., 1995), this suggests a weakening of the SA Monsoon at 6.9 Ma.

In a second phase starting at 3-4 Ma, the SA Monsoon regains enough strength to bring back precipitations in Central Himalaya, but not in Western Himalaya, and resets the competition between C_3 and C_4 plants. The hypothesis of an overall strengthening of the Asian Monsoons has been suggested from the Northern South China Sea record (Wan et al., 2007; Clift et al., 2014).

These observations highlight that despite a drop of temperatures of probably uniform amplitude during the late Cenozoic, climate change had a sharply different impact across the Himalaya.

VII.6. CONCLUSION

In this work, we presented the new and promising Valmiki group of Siwalik sections located in the Valmiki Wildlife Sanctuary, Bihar, India. These series, thick of ⊠4,000 m cover almost the full late Cenozoic, from 8.2 to ca. 0.7-04 Ma. Until 1.2 Ma, the Valmiki Sections form an original and chiefly unrecycled record of erosion in the drainage basin of the Narayani-Gandak in Central Nepal, the major tributary of the Ganga. The Valmiki Sections have particularly good dating constraints for the 8.2 - 0.8 Ma time span. These series make it possible to perform a deep investigation of the links between erosion and the late Cenozoic Climate Change.

The new Valmiki Sections also form a paleoenvironmental record of the Ganga plain, as demonstrated here. We demonstrate for the first time that the prevalence of C4 plants can shift as fast as it has appeared, as shown at ca. 3.2 and 6.9 Ma respectively. This prevalence is intimately related to the strength of the SA Monsoon, but unexpectedly in contradiction with the previous works (Quade et al., 1989; Quade et al., 1995; Vögeli et al., 2017a). The late Cenozoic climate change produced such changes in the atmospheric circulation that the SA Monsoon was subject to a major loss of strength followed only by a partial recovery at the start of the Northern Hemisphere Glaciations. It remains to be seen if these changes had any impact on the erosion and development of the Himalaya.

Acknowledgments

The Bihar State Forest Department is acknowledged for authorization for working and sampling in the Valmiki Wildlife Sanctuary, National Park & Tiger Reserve. V. Jain and R. Sinha are warmly acknowledged for their assistance in getting these authorizations. The teams of CRPG and SARM, along with Master students from the ENSG are thanked for their assistance in sample preparation and measurements. The field and analytic works were funded by the ANR Calimero, ANR Himal Fan projects and an INSU Syster project. S. Lenard PhD funding was provided by a Université de Lorraine-CRPG 3-year PhD fellowship and a Université de Poitiers 1-year A.T.E.R..

Author contributions

Potential co-authors:

Sebastien J.P. Lenard*[1], Jérôme Lavé[1], Julien Charreau[1], Christian France-Lanord[1], Thomas Rigaudier[1], Ananta Gajurel[2], Rahul Kumar Kaushal[3], Raphaël Pik[1]

[1]CRPG, Université de Lorraine, 15 rue Notre Dame des Pauvres, 54500 Vandœuvre-lès-Nancy, France

[2]Department of Geology, Tribhuvan University, Kathmandu, Nepal

[3]Indian Institute of Technology Gandhinagar (IITGN), Gandhinagar, Gujarat, 382355, India

J.L., C.F.L. and J.C. designed the study. J.C., J.L., S.L., A.G., R.K., R.P. and C.F.L. collected the samples. A.G. and J.L. log the sedimentary facies. J.C. and S.L performed the paleomagnetic measurements. J.C. reconstructed the magnetostratigraphic timescale. S.L., O.L. and T.R. performed the oxygen and carbon isotopic measurements. J.L. performed the structural analysis. SL., J.L., J.C. and C.F.L. interpreted the results and wrote the manuscript.

VII.7. TABLES

In Tables attached to this manuscript.

Table SVII-1. Paleomagnetism results.

Table SVII-2. Clayey to fine sand sample information, magnetostratigraphic correlation results.

Table SVII-3. Medium to coarse sandy samples information, oxygen-carbon isotope, major and trace elements results.

Table SVII-4. Clayey to fine sand bulk carbonate oxygen - carbon isotopic results.

VIII. LATE CENOZOIC EVOLUTION OF EROSION RATES IN THE NARAYANI-GANDAK BASIN, CENTRAL HIMALAYA (DRAFT)

VIII.1. INTRODUCTION

VIII.1.1. Has climate forced erosion rates in the late Cenozoic?

The late Cenozoic is characterized by a global and considerable shift of climatic conditions. From ca. 8 Ma onward, the planet experiences a gradual drop of temperatures that culminates by the settlement of large ice-sheets in the Northern Hemisphere at ca. 2.6 Ma, with an intensification of glaciations after ca. 0.8 Ma (Lisiecki and Raymo, 2005; Cramer et al., 2011; Herbert et al., 2016). The late Cenozoic is also a period of large variations in the precipitation pattern. Several regions on Earth, and particularly in Asia, see a decline in precipitations and an increasing contrast between wet and dry seasons (Quade et al., 1989; Caves Rugenstein and Chamberlain, 2018). With the onset of glacial-interglacial cycles at ca. 2.6-4.5 Ma, climate becomes unstable and long, cold, dry, and stormy periods alternate with wet and warm periods (Cerling et al., 1997; Edwards et al., 2010).

The late Cenozoic climate change should have triggered global changes in erosion patterns. In mid-latitude mountain ranges, glacial and periglacial erosional processes particularly developed (Zhang et al., 2001). However, the question whether such a shift in climate triggers a shift in erosion rates remains one of the major unanswered questions in geomorphology (Molnar and England, 1990; Zhang et al., 2001; Molnar, 2004; Willenbring and von Blanckenburg, 2010; Herman et al., 2013; Schildgen et al., 2018). The majority of the studies that show a substantial increase in erosion rates (i.e. by a factor of several units) during the last millions of years (e.g. Zhang et al., 2001; Molnar, 2004; Herman et al., 2013) have later been contradicted. The approaches they use, either sediment accumulation rates, thermochronometry or terrestrial cosmogenic nuclides (TCN), has a distinct resolution and distinct biases (Rahl et al., 2007; Charreau et al., 2009a; Schumer and Jerolmack, 2009; Willenbring and von Blanckenburg, 2010; Naylor et al., 2015; Schildgen et al., 2018; this thesis). When the results of each proxy are compared over a regional scale, they reveal inconsistencies, as it has been recently demonstrated for the Himalaya (this thesis, Chapter VI).

VIII.1.2. Approach

The investigation of the late Cenozoic erosion of mountain ranges has benefited from a recent approach based on the "fossil" TCN content in sedimentary archives. To obtain paleoerosion rates, this approach can be developed in the sediment of the foreland basin or further downstream in offshore deposits. In the case of the Himalaya, the Bengal Fan represents the distal part of the erosion and deposition system. Such record provides average erosion rates over a large scale of the range, i.e. over a wide area drained by the Ganga and Brahmaputra Rivers (this thesis, Chapter VI). But this record cannot supply a detailed view of the lateral variations in erosion along the Himalayan Arc.

The continental sediment record of the foreland basin preserved in front of the Himalaya in the Siwalik Hills is therefore fully complementary to the distal record. Still, having such a detrital record with strong dating constraints remains a challenge. In the Himalaya, most sections have been dated by

magnetostratigraphy, but few of these sections provide dating constraints up to the late Pleistocene. Indeed, conglomeratic facies dominate the upper part of the sections and these facies are unsuitable for paleomagnetism measurements. In Nepal, the Surai Section is the only section with constraints as young as ca. 1.2 - 1.8 Ma (Appel et al., 1991; Charreau et al., in prep.). The Surai Section is located between the outlets of two major transverse Himalayan rivers and may have recorded a shift of provenance at ~3-4 Ma, from transverse Himalayan river material to sediment from frontal rivers draining the southern part of the Himalaya or the Siwaliks Hills (Charreau et al., in prep.).

Investigating the erosion of the Himalaya in the late Cenozoic therefore requires two conditions: sedimentary sections with silty or sandy facies included in the upper part of the sections and with sediment having a steady provenance from the High Himalaya. The first condition is satisfied by selecting a Siwalik fold sufficiently far from the Main Boundary Thrust (farther than 15-20 km, Figure VIII-74), i.e. beyond the gravel-sand transition observed in the Himalayan rivers (Dubille et Lavé, 2015; Dingle et al., 2017). The second condition is fulfilled by selecting a location in front of the outlet of a large and transverse Himalayan river and assuming it was stable through time. The folds developed south of the Chitwan Dun, the largest piggy-back basin in Nepal, and in the axis of the Narayani/Gandak outlet (Figure VIII-74-Figure VIII-75), represent one of the targets that fulfill both conditions in Nepal. Because detailed sedimentologic, structural or magnetostratigraphic studies of this area are absent, we had to conduct a completely new study and to document a new dedicated section (this thesis, Chapter VII).

Here, we develop an approach which may provide new directions for the debate about the interactions between tectonics, climate, and erosion. The individual biases of the proxies are overcome by their combination for the investigation of erosion rates with a focus on a limited region having a known paleoenvironmental record. We chose to explore the past erosion patterns in the Narayani-Gandak drainage basin in the Himalaya. This basin covers Central Nepal and is the prime contributor of sediment for the Ganga (Lupker et al., 2012a). Central Nepal has been extensively investigated in terms of erosion, tectonics, climate, and paleoenvironment (e.g. Quade et al., 1995; Lavé and Avouac, 2000; Bernet et al., 2006; van der Beek et al., 2006; Huntington et al., 2006; Robert et al., 2009; Andermann et al., 2011; Herman et al., 2013; Lupker et al., 2012a; Godard et al., 2012, 2014; Morin, 2015; Charreau et al., in prep.; this thesis, Chapter VII).

We based our investigation on the Valmiki Sections in the Siwalik Hills, ~50 km east of the range outlet of the Narayani (this thesis, Chapter VII.). The Siwaliks form the exhumed part of the foreland Himalayan basin at the front of the range. Contrary to other Siwalik sections, the Valmiki Sections consist in an original record of a major Himalayan basin that covers a time span from the late Miocene to the middle Pleistocene (8.2 - 1.2 Ma). To determine the paleoerosion rates of the basin, we measured the ^{10}Be concentrations in the quartz sand fraction (Puchol et al., 2017). These concentrations were corrected from the recent exposure contribution using a simple model. We validated this model by measuring ^{36}Cl in the feldspar fraction of the samples (Schimmelpfennig et al., 2009) and taking advantage of the half-life of ^{36}Cl

shorter than the one of ^{10}Be. We corrected the resulting concentrations for radioactive decay and deduct the ^{10}Be contribution associated with sediment transport using a transfer model (Lauer and Willenbring, 2010). The apparent ^{10}Be paleoerosion rates of the Narayani basin were finally reconstructed.

To further explore the past erosion patterns, we traced the provenance of the eroded rocks by measuring Sr-Nd isotopes and taking advantage of the distinct isotopic signatures of the Himalayan lithologic units (Galy and France-Lanord, 2001; Morin, 2015).

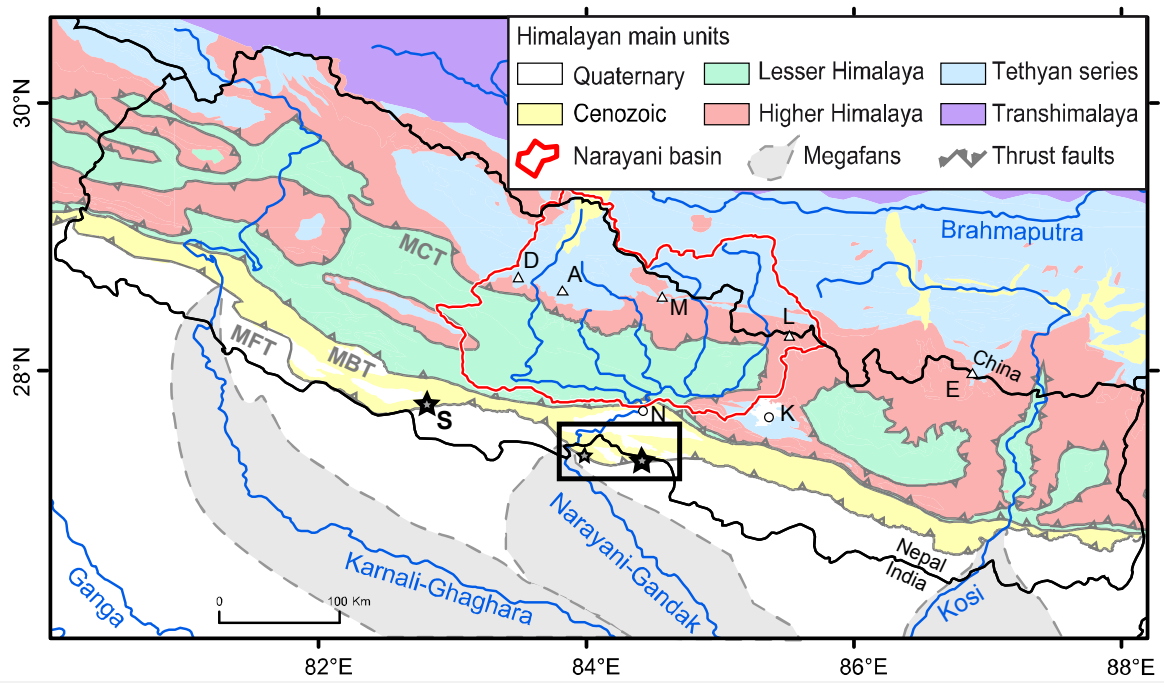

Figure VIII-74. Lithologic map of Central Himalaya.

The main Himalayan units and main thrusts are delimited: MFT (Maint Frontal Thrust), MBT (Main Boundary Thrust) and MCT (Main Central Thrust). The Quaternary alluvial megafans are underlined, along with several geographic features, among them the drainage basin of the Narayani in red, the Nepalese boundaries in black, cities: K: Kathmandu; N: Narayanghat, and summits: A: Annapurnas; D: Daulaghiri; E: Everest; L: Langtang; M: Manaslu. A frame precise the location of the Valmiki Sections and the Surai Section (S) is also indicated. For clarity, the tributaries of the Karnali and the Kosi are not indicated (geological map compiled by the Department of Mines and Geology, Kathmandu, 1994)

VIII.2. GEOLOGICAL CONTEXT OF THE CENTRAL HIMALAYA

VIII.2.1. Structure and lithology

In its central part, the Himalayan fold and thrust belt is structured along four majors WNW-ESE-oriented faults , from north to south: the Southern Tibetan Detachment (STD), the Main Central Thrust (MCT), the Main Boundary Thrust (MBT) and the Main Frontal Thrust (MFT) at the southern limit of the Himalaya (Gansser, 1964; Burg et al., 1984; Le Fort, 1986; Hodges, 2000). The MCT, MBT and MFT are north dipping. At depth, they are assumed to join at the interface between the Indian Plate and the underthrust Asian Plate, and form the Main Himalayan Thrust (MHT) (Schelling and Arita, 1991; Pandey et al., 1995; Lavé and Avouac, 2001; Elliott et al., 2016), which was imaged by seismology in Central Nepal (Nábelek et al., 2009).

Lithologically, the Himalaya is divided into subparallel units (Figure 1, Gansser, 1964; Le Fort, 1975, 1986; Hodges, 2000) that are described in the following from north to south. South of the Tibetan plateau, the Tethyan sedimentary series (TSS) consist in medium to low-grade detrital and carbonate metasediments of Paleozoic to Mesozoic age. The STD separates these series from the High Himalaya Crystalline (HHC) that consists in high-grade crystalline metamorphic units. The two units are intruded by Miocene leucogranites. The HHC overthrusts the Lesser Himalaya (LH) along the MCT, with an inverted metamorphic sequence. The LH consists in low- to medium grade metasediments of Precambrian age and, excepted in Central Nepal, several subsisting klippes of lithology similar to the HHC overlain by a Tethyan sedimentary component. The front of the Himalaya is bound by the MBT and the MFT and consist in exhumed synorogenic sediments, the Siwalik series, which extend in the Ganga plain southwards from the MFT.

VIII.2.2. Long-term structural evolution

Since at least ca. 15 Ma (Kohn et al., 2004), the Himalaya has exhumed with brittle deformation, with passive passive transport over the MHT and thin skinned tectonics. Duplexes developed in the LH after ca. 10 Ma (Schelling and Arita, 1991; DeCelles et al., 2001; Huyghe et al., 2001; Robinson et al., 2003; Herman et al., 2010a; Robinson and McQuarrie, 2012) and propagated southwards of the MCT, with the gradual activation of thrusts intervening between the MCT and the front of the range (Le Fort, 1975) and finally activated the MBT at ca. 5 Ma (DeCelles et al., 1998, 2001, with an earlier estimate at ca. 11 Ma by Meigs et al., 1995) and the MFT at ca. 2.4-1.8 Ma (in Western Nepal, Mugnier et al., 1999, 2004).

The activity along the MCT is considered having ceased at ca. 15 Ma (e.g. DeCelles et al., 2001). In view of some thermochronometric and thermobarometric data, a group of workers proposed a reactivation of the MCT in the late Cenozoic, with an out-of-sequence thrusting (Harrison et al., 1997; Catlos et al., 2001; Hodges et al., 2004; Wobus et al., 2003, 2005). Modelling studies (Whipp et al., 2007; Robert et al., 2009; Herman et al., 2010a) showed that this was not necessary to explain the data, which, by the way, have not been confirmed by other datasets (Blythe et al., 2007; Nadin and Martin, 2012).

Additionally, the recent 2015 Gorkha earthquake has not shown any displacement on the MCT (Elliott et al., 2016, contradicted by Whipple et al., 2016).

Complementary information on the E-W geometry of the MHT.

Topographic, geodetic and thermochronometric show that the geometry of the MHT is probably not uniform along the range and particularly in Nepal (Berger et al., 2004; Harvey et al., 2015; van der Beek et al., 2016). In Central and Eastern Nepal, the MHT is characterized by a major mid-crustal ramp (Schelling and Arita, 1991; Pandey et al., 1995; Lavé and Avouac, 2001) below the MCT and the nearby physiographic transition from an average topography (~1,000 - 2,000 m) with mild relief in the south to the high range (~5,000 - 6,000 m) with steep relief in north. This ramp is assumed to sustain rock uplift and denudation in the High Himalaya (Lavé and Avouac, 2001). By the focus of orographic precipitations on relief (precipitations up to 5 m/y in the flank of the Annapurnas, Andermann et al., 2011), long-term denudation rates reach 2-5 mm/y values in the High Himalaya (Lavé and Avouac, 2001; Blythe et al., 2007; Herman et al., 2010a), with a possible increase in denudation rates in the late Cenozoic (Copeland et al., 2015), compared to 0.5-1.2 mm/y in the Lesser Himalaya (Herman et al., 2010a). Contrastingly, in Western Nepal, the mid-crustal ramp is absent (Berger et al., 2004; Harvey et al., 2015), the physiographic transition is more progressive, with the high topography and the MCT shifted northwards, and apparent denudation rates are lower by a factor two (van der Beek et al., 2016), with a possible decrease during the Late Cenozoic (Copeland et al., 2015). Using modelling, Mercier et al. (2017) has advanced that the lateral variations of the MHT and in the isolation of klippes were linked to the asynchronous evolution of the cycle of ramp formation along the range, which could be caused by differences in rheology between the Himalayan lithologic units. In their model, the life-time of a mid-crustal ramp would be between 2 and 5 Ma.

VIII.2.3. The Narayani-Gandak drainage basin

The Himalayan drainage network is organized in several transverse rivers which originate in the north of the range and join into a few major rivers in the Lesser Himalaya (DeCelles et al., 1998; Gupta, 1997). These chief rivers deposit sediment in alluvial megafans (fan areas of 10^4-10^5 km^2, DeCelles et al., 1998; Gupta, 1997) in the foreland basin. Smaller rivers draining only the Siwalik and the Lesser Himalaya alternate with the Himalayan rivers and deposit smaller interfans (DeCelles et al., 1998; Gupta, 1997; Wells and Dorr, 1987).

The Narayani-Gandak drainage basin covers Central Nepal and is drained at the west by the Kali Gandaki and the Marsyandi, which drain the Annapurna range, and at the east by the Buri Gandaki and the Trisuli. The Narayani initiates at the confluence of the Kali Gandaki and the Trisuli and after cutting the Siwaliks, becomes the Gandak in the Indian plain. The Gandak is a braided river wide of one to six km that deposits sediment in an alluvial megafan. After a southeastward course of ~230 km, the Gandak join

the Ganga in its floodplain.

The Narayani-Gandak is the prime contributor of discharge (~ 50 km^3/y; DHM, 2003; DHM/FFS, 2004) and sediment (~150 Mt/y ; Morin et al., 2018) to the Ganga. The modern erosion rates are higher than for the other sub-basins of the Ganga network (Andermann et al., 2012; Lupker et al., 2012a; although this can be discussed in view of the data on the Karnali of Ojha et al. (submitted)). The average erosion rate amounts to $1.6^{+0.35}_{-0.2}$ mm/y according to suspended sediment flux (Andermann et al., 2012; Morin et al., 2018) and at 1.7 ± 0.4 mm/y according to in situ ^{10}Be concentrations in the quartz fraction of bedload sediment (Lupker et al., 2012a).

As elsewhere in the Himalayan front, Central Nepal is subject to the South Asian Monsoon (SA Monsoon). The SA Monsoon produces the alternation of a warm and moist summer with heavy precipitations and a dry to arid winter, particularly in Central and Western Himalaya (Bookhagen and Burbank, 2010; Andermann et al., 2011). From south to north of the Himalaya, a precipitation gradient exists and influences erosion rates. The southern flank of the high Himalayan peaks along the physiographic transition presents 1-2 m/y monsoonal precipitations (Andermann et al., 2011), up to 5 m/y at the south of the Annapurnas. It also presents considerable relief (5,000 m over a 100 km distance) and ~2-3 mm/y erosion rates (Vance et al., 2003; Andermann et al., 2012; Godard et al., 2012, 2014; Lupker et al., 2012a). In contrast, the middle elevation and relief area at the south of these high peaks presents ~0.1-1 mm/y erosion rates, with the same amount of precipitations (Wobus et al., 2005; Andermann et al., 2012; Godard et al., 2012, 2014). As one penetrates northwards in the precipitation shadow behind the higher summits, precipitations become rarer (< 0.4 m/y) (Burbank et al., 2003), erosion rates decrease (< 0.2-0.4 mm/y) (Gabet et al., 2008) and relief loses amplitude (< 1,000 m).

The TSS, HHC and LH occupy 34%, 24% and 42% respectively of the total area of the drainage basin (outlet at Narayanghat). The southern Himalayan flank is covered by ~70% of HHC and ~30% of TSS. The southern area is covered by the LH and the northern area by the TSS. As told by Sr-Nd isotopes, the sediment of the modern Narayani is roughly approximated by a mix of ~50% of TSS, ~20% of HHC and ~30% of LH (data and methodology of Morin, 2015).

Erosion in Central Nepal chiefly results from the landsliding activity derived from the combination of high relief and intense monsoonal precipitations (Gabet et al., 2004a,b; Gallo and Lavé, 2014; Morin et al., 2018; Marc et al., 2019). With a glacial cover of ~9% of the basin in modern times (Raup et al., 2007), distributed for 40% in the HHC and 60% in the TSS, the modern glacial erosive flux is assumed to be comparatively negligible (Morin, 2015).

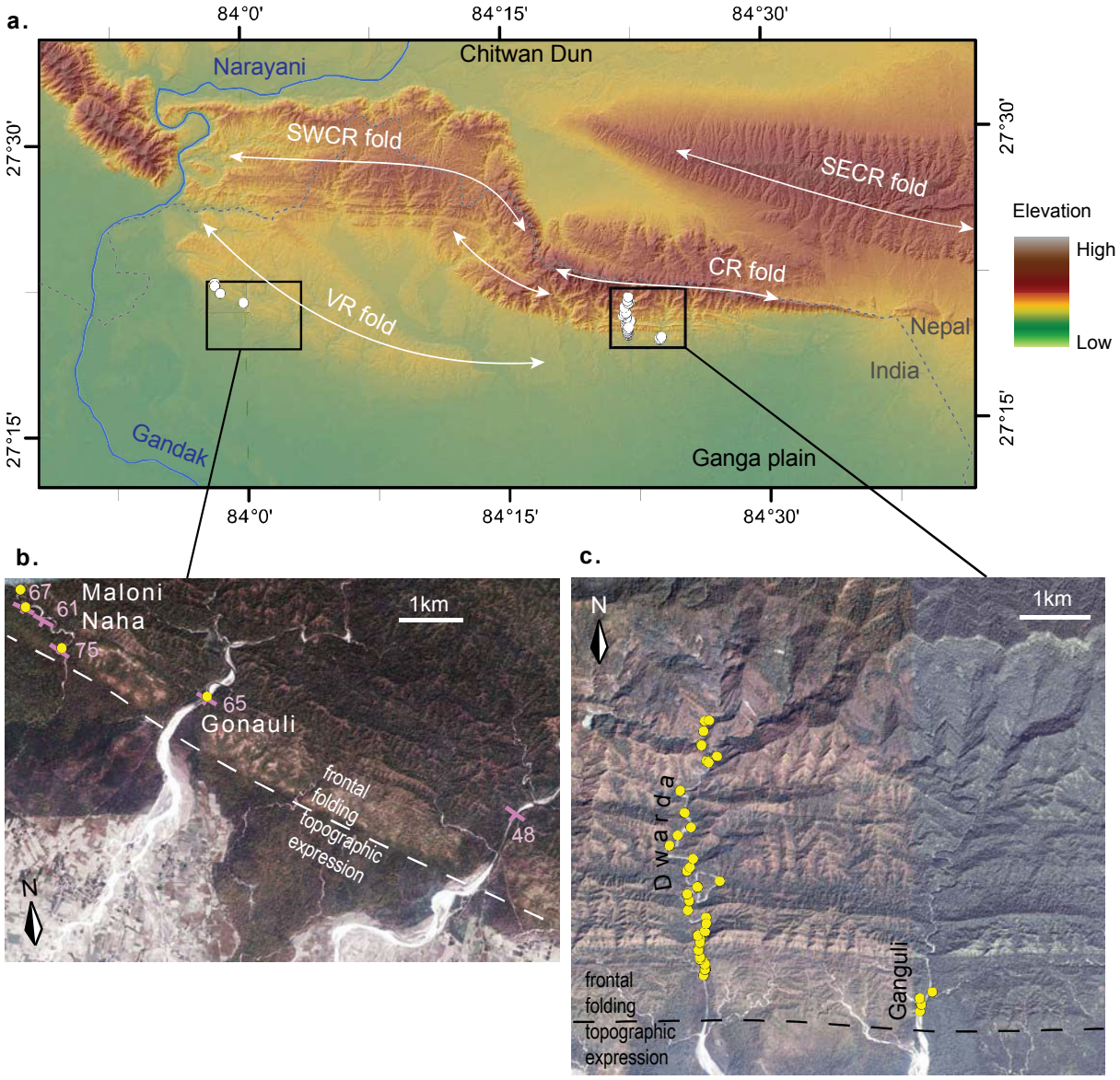

Figure VIII-75. Valmiki Sections in the Outer Siwalik Hills.

a. Topographic map of the Outer Siwalik Hills. The folds are represented, along with the Narayani - Gandakl river, and the frames indicate the locations of the West Churia Sections (CR) and the Valmiki Nagar Sections (VR).

b. Sample map of the VR Sections, the Gonauli and the Maloni Naha. Dips from this thesis, Chapter VII.

c. Sample map of the CR Sections, the Dwarda and the Ganguli. Background satellite images provided by Google Earth©

VIII.2.4. The Valmiki Sections

The Valmiki Sections consist in molasse series thick of >4,000 m exposed along local rivers in the Outer Siwalik Hills on the hanging wall of the MFT (this thesis, Chapter VII). They are located in the Valmiki Wildlife Sanctuary, National Park & Tiger Reserve, at the NW of the Bihar State in India close to the Nepalese boundary and at ~50 km eastwards from the Narayani-Gandak dam. The sections are from east to west: the Patalaia, the Ganguli, the Dwarda, which is the largest section, the Gonauli and the Maloni Naha. The sections have magnetostratigraphic dating constraints over the 8.2-0.8 Ma time span. They record the erosion in the Narayani-Gandak basin, except for the upper part (0.4-1.2 Ma) consisting in recycled sediment (This thesis, Chapter VII). The Valmiki Sections present facies of the Middle Siwalik and chiefly consist in thick fine-to-coarse sandy bodies, with occasional silty fining up layers and become more silty with ⊠40% of pebbly beds in the upper part (< 1.4 Ma).

Figure VIII-76. Magnetostratigraphic log and position of samples.

Next page.

a. Sedimentary logs of the CR Sections (c: clay, s: silt, S: sand, f: fine sand, m: medium sand, c: coarse sand, G: gravel, P: pebble). The discontinuous VR Sections are not represented for clarity (this thesis, Chapter VII).

b. Stratigraphic position of the sandy samples measured for Sr-Nd isotopes and ^{10}Be content. Samples without a ^{10}Be measurement are indicated by a star. Only the samples having yielded results are indicated. The samples are coloured whether they are from the Dwarda (red) and the Ganguli (blue), or from the VR Sections (green). The names of the samples were abbreviated. No sample from the Patalaia has isotopic measurements.

c. Magnetostratigraphic correlation, using the timescale of Gradstein et al. (2012) (this thesis, Chapter VII).

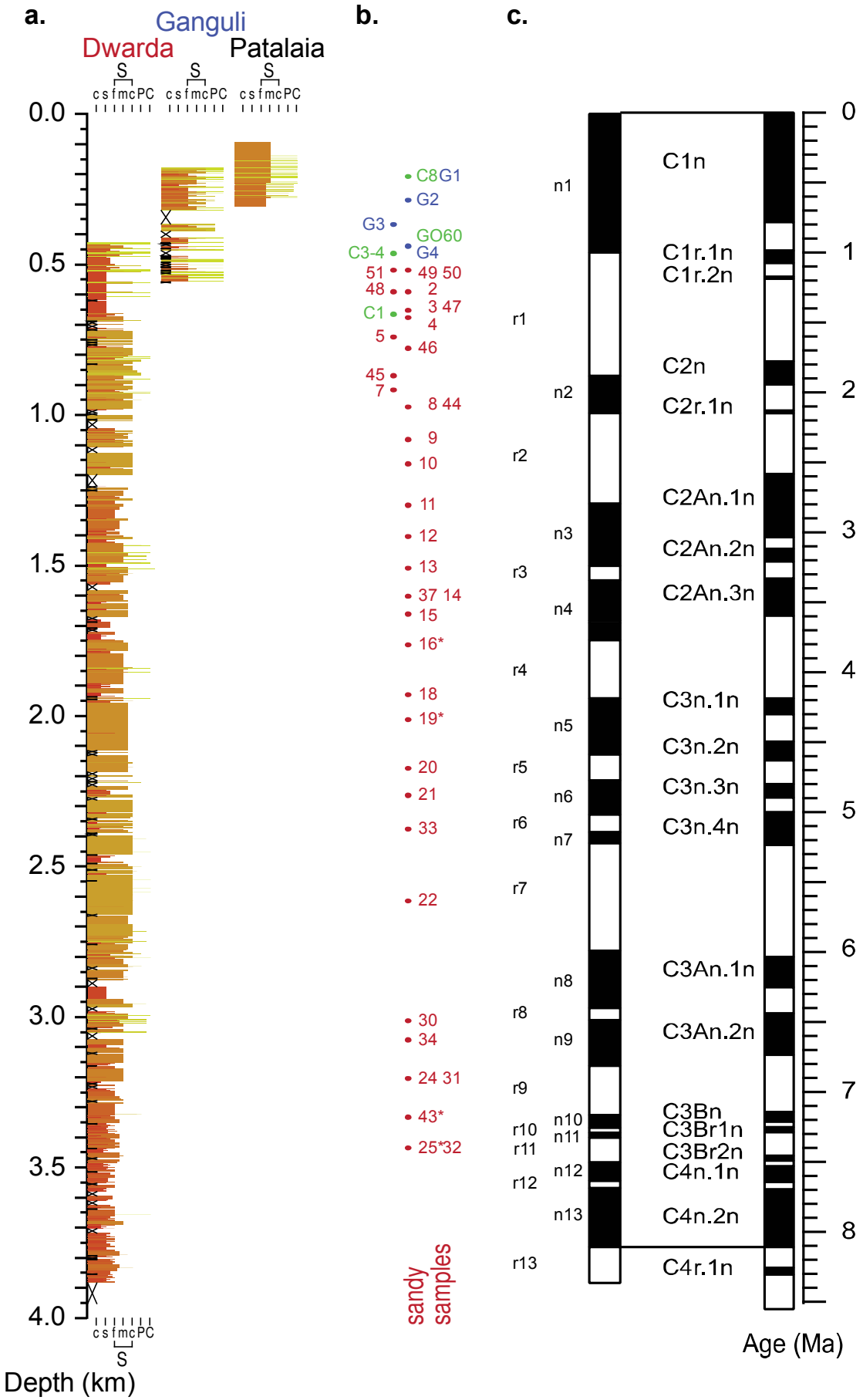
a.
Ganguli
Dwarda
Patalaia
S
c s f m c PC
0.0
0.5
1.0
1.5
2.0
2.5
3.0
3.5
4.0
Depth (km)
b.
C8 G1
G2
G3
GO60
C3-4
G4
51
49 50
48
2
C1
3 47
4
5
46
45
7
8 44
9
10
11
12
13
37 14
15
16*
18
19*
20
21
33
22
30
34
24 31
43*
25*32
sandy samples
c.
n1
C1n
C1r.1n
C1r.2n
r1
C2n
n2
C2r.1n
r2
C2An.1n
n3
C2An.2n
r3
C2An.3n
n4
r4
C3n.1n
n5
C3n.2n
r5
C3n.3n
n6
r6
C3n.4n
n7
r7
C3An.1n
n8
r8
C3An.2n
n9
r9
C3Bn
n10
r10
C3Br1n
n11
r11
C3Br2n
n12
C4n.1n
r12
n13
C4n.2n
r13
C4r.1n
0
1
2
3
4
5
6
7
8
Age (Ma)

VIII.3. MATERIAL AND METHODS

VIII.3.1. Material

We collected coarse to medium size sandy samples for cosmogenic nuclide and Sr-Nd isotope measurements during three field trips: in 2012 and 2016 for the Ganguli, the Dwarda and the Gonauli samples, and in 2017 for the Maloni Naha samples. sections of the South East Churia Range (CR), i.e. the Patalaia, the Ganguli and the Dwarda sections. The sections are fully described in the Chapter VII of this thesis, who also provided dating constraints, C-O and major and trace element measurements.

VIII.3.2. Sr-Nd isotopic composition measurements

Our approach is based on the comparison of isotopic and chemical composition of past sediment with the analog modern river sediment. This approach provides information to decipher the reworking of weathered sediment and identify potential changes in the rock sources. In the Himalaya, Sr and Nd isotopic and major element analyses in past foreland sediment provide a tool to reconstruct the evolution of the rock sources through time (Huyghe et al., 2001; Mandal et al., 2019; Robinson et al., 2001; Szulc et al., 2006).

In complement to the numerous studies that have constrained the isotopic signatures of the Himalayan units (Deniel et al., 1987; France-Lanord et al., 1993; Parrish and Hodges, 1996; Robinson et al., 2001), Morin (2015) analyzed the sediment of selected rivers draining specific lithologies, which integrate the isotopic signature of the main units. Those results provide a synthesis on the isotopic signature of the three main geological units in Central Nepal, i.e. the HHC, TSS and LH. A low εNd between -20 and -26 and a high $^{87}Sr/^{86}Sr$ ratio characterize the LH. In contrast, the HHC and TSS have a less negative εNd between -14 and -17 and their $^{87}Sr/^{86}Sr$ ratio are ~0.76 for HHC and ~0.72 for TSS.

The samples were prepared and measured for Sr-Nd isotopes at CRPG-CNRS-UL (Vandoeuvre-les-Nancy, France) after acetic acid leaching (Hein et al., 2017). Bulk aliquots of the samples were collected before the ^{10}Be sample preparation and rinsed with milli-Q water to reduce sea salt contributions. They were then powdered and leached with 10% acetic acid (Galy et al., 1996) and prepared to obtain a silicate residue. $^{87}Sr/^{86}Sr$ was measured on the residue using a Triton Plus(TM) multi-collector thermal ionization mass spectrometer with NBS-987 as a standard and quality control. $^{143}Nd/^{144}Nd$ was measured using a Neptune plus multi-collector inductively coupled plasma mass spectrometer. $^{143}Nd/^{144}Nd$ was first normalized to $^{146}Nd/^{144}Nd = 0.7219$ using an exponential law and then to the JNdi-1 following a pseudo-standard sample-bracketing method (one standard for each 4–5 samples, Yang et al., 2017). 143Nd/144Nd values are reported as εNd(0), using CHU(0) = 0.512638 (Goldstein et al., 1984).

Our results (Figure VIII-78, Table SVIII-1 columns AW-BB) are compared with data from the modern Narayani sediment (Singh et al., 2008; Morin, 2015) and from cores in the late Pleistocene Gandak Fan (Morin, 2015).

VIII.3.3. Lithological fraction computing

We followed the approach described in Morin (2015, p. 319) to compute the fractions of TSS, HHC and LH in the sediment. Considering 1, 2 and 3 the different lithologies and f_i their respective fractions, the concentration C of each isotope in the ternary mixing is defined by the equation:

$$C = \sum_i f_i \times C_i \qquad (1)$$

Because the range in isotopic compositions of Sr or Nd is small, ^{86}Sr and ^{144}Nd are close to a constant fraction of total [Sr] and [Nd] respectively. After combination of the respective equations for each member of the coupled isotopes (^{86}Sr and ^{87}Sr, or ^{144}Nd and ^{143}Nd), and arranging a linear relationship with respect to f_1, f_2, f_3, the following equation is obtained for the two couples of isotopes, $^{87}Sr/^{86}Sr$ or $^{143}Nd/^{144}Nd$:

$$\sum_i f_i \times C_i \times (R - R_i) = 0 \qquad (2)$$

with R the isotopic ratio measured in the sediment, and R_i the isotopic ratio of each lithologic unit. We resolved the set of equations with a Monte-Carlo simulation using 10,000 iterations.

The ratios and concentrations used for each unit were set from the averages obtained by Morin (2015). We propagated the analytical uncertainties of our isotopic measurements to examine the relative evolution of the respective fractions.

The lithological fractions presented here (Figure VIII-79, Table SVIII-1 columns BC-BH) do not take into account the carbonate contribution, accounting for ~40% of the effective contribution of the TSS to the Narayani modern sand.

VIII.3.4. $^{10}Be/^{9}Be$ measurements

A total of 39 samples of fine to medium consolidated or unconsolidated sandstone were prepared for analyses of ^{10}Be concentrations. To limit the potential contamination by a recent exposure to cosmic rays, the majority of sampling locations were selected in fresh exposure at the bottom of cliffs of several meters presently incised by the Siwalik rivers. Assuming that the ^{10}Be concentrations in samples were probably low because of potentially high erosion rates (> 1 mm/y), we sampled unusually large masses of sand (1 to 5 kg) to extract a sufficient amount of quartz and a measurable amount of ^{10}Be.

All samples except four were prepared at CRPG-CNRS-UL (Vandoeuvre-les-Nancy, France) for ^{10}Be measurements following the CEREGE (Aix-en-Provence, France) procedure, which is similar to the one used for other studies (Lupker et al., 2012a, 2017; Puchol et al., 2017; Charreau et al., in prep.; This

thesis, Chapter VI), and using a sufficient amount of quartz (i.e. > 100 g, representing 10^8 to 10^{10} grains of quartz) to lower analytical uncertainties for older samples. Four samples were similarly prepared at CEREGE (Aix-Marseille, France). This study focused on fractions in the 125-250 µm or 140-280 µm range of grain sizes, except for two samples. For these samples, the 250-500 µm fraction was selected either because the 125-250 µm was too small (DWCOS22) or because sample purification failed (DWCOS11). Each sample was sieved under water and then underwent magnetic separation and sodium polytungstate density separation. The feldspar fraction was separated from the quartz fraction for ^{36}Cl measurements on five samples using flotation. The quartz fraction then underwent repeated selective leaching in H_2SiF_6 and HCl to get quartz-enriched samples. For each sample, the quartz fraction was inserted in one Nalgen© bottle, except for samples of quartz mass > 260 g which were inserted in two or three bottles. Meteoric ^{10}Be was removed by 3 sequential HF etchings in stochiometric proportions to dissolve 30 wt% of the quartz in each bottle (Brown et al., 1991). The remaining mass of quartz was measured (Table SVIII-1 columns K-L).

A small mass of a ^9Be carrier of known concentration was added to the quartz which was subsequently dissolved in HF. For the samples with two or three bottles, the carrier was added into one bottle only. For eight samples, the carrier was taken from an industrial solution having $\left[{}^9Be_{carrier} \right]$ = 1,000 ppm and $\left({}^{10}Be/\ {}^9Be \right)_{carrier}$ = 1.4±0.3x10^{-15} . To measure old samples with low ^{10}Be concentrations, the carrier was made in-house from phenakite minerals. The carrier presents $\left[{}^9Be_{carrier} \right]$ = 2,020±83 ppm and $\left({}^{10}Be/\ {}^9Be \right)_{carrier}$ = 4±2x10^{-16}, except for the four samples prepared at CEREGE for which the carrier presents $\left[{}^9Be_{carrier} \right]$ = 3,025 ppm and $\left({}^{10}Be/\ {}^9Be \right)_{carrier}$ = 1.4±0.3x10^{-15}. The dissolved solutions were evaporated in Evapoclean© 150 ml tubes at 110 °C (during several days for the oldest samples). The residue was dissolved in HCl and purified on two successive columns per sample by anion exchange, cation exchange, alkaline precipitation, and oxidation. We note that the columns have been previously calibrated for 30-50 g of quartz by CEREGE and have not recalibrated for the large masses of quartz we used, which probably induced a low-quality purification for the oldest samples and affected the precision of our measurements. Finally, the solution was precipitated as $Be(OH)_2$ and dehydrated to BeO at 1,000 °C.

The $\left({}^{10}Be/\ {}^9Be \right)_{quartz}$ measurements on the BeO target were performed at the ASTER national Accelerator Mass Spectrometer facility (CEREGE, Aix-en-Provence, France) (Arnold et al., 2010), with a normalization to the in-house standard STD-11, using an assigned $^{10}Be/^9Be$ ratio of (1.191 ± 0.013) x 10^{-11} (Braucher et al., 2015). Ten procedural blanks were separated and measured using a similar procedure, obtaining an average $\left({}^{10}Be/\ {}^9Be \right)_{blank}$ = 10^{-14} for the industrial carrier and 3x10^{-15} for the in-house carrier. Our results are presented in Table SVIII-1 columns S-Z.

VIII.3.5. ^{10}Be concentration determination

We performed a check on potential natural ^{9}Be content in the quartz that could interfere with the ^{9}Be content of the carrier (see discussion in Lupker et al., 2017). After evaporation and redissolution in HCl, an aliquot was collected for ^{9}Be measurement using ICP-MS at CRPG-CNRS-UL (Vandoeuvre-les-Nancy, France). As in a previous study (This thesis, Chapter VI), we expected that the measured concentrations be slightly lower than the predicted concentrations (Table SVIII-1 columns M-R), because of the potential loss of Be after addition of the ^{9}Be carrier, during dissolution and evaporation. However, for the majority of samples we found ^{9}Be concentrations 0-60% higher than the ^{9}Be concentrations predicted from the added mass of the carrier, with levels > 100% for some samples with a large mass. This might suggest that natural ^{9}Be content is not negligible for the Valmiki samples, as for the Bhutanese river sand (Portenga et al., 2015). For the computation of ^{10}Be concentrations (Table SVIII-1 columns AA-AD), we conservatively considered the higher ^{9}Be content from the predicted and measured contents. For the samples without ^{9}Be measurements, we applied an 1-σ uncertainty of 25% on the ^{9}Be concentration.

The quartz ^{10}Be concentration in at/g was computed using:

$$\left[{}^{10}Be\right]_{quartz} = \left(\left(\frac{{}^{10}Be}{{}^{9}Be}\right)_{quartz} - \left(\frac{{}^{10}Be}{{}^{9}Be}\right)_{blank}\right) \times \left[\,{}^{9}Be_{carrier}\right] \times m_{\,{}^{9}Be_{carrier}} \times \frac{1}{m_{quartz}} \qquad (3)$$

and uncertainties were propagated using standard statistical formulas:

$dz = \sqrt{dx^2 + dy^2}$ for $z = x + y$ and $\frac{dz}{z} = \sqrt{\left(\frac{dx}{x}\right)^2 + \left(\frac{dy}{y}\right)^2}$ for $z = x \times y$ (e.g. Taylor, 1996).

We performed duplicate analyses on two samples only. We found an average difference of 42% between duplicates and took the average concentration for further interpretation of these samples.

Our results (Figure VIII-81-Figure VIII-82, Table VIII-1 columns AC-AD (before plain exposure and recent exposure corrections, and AO-AR) are compared with published ^{10}Be data obtained from modern sands of the Narayani, 125-250 µm fractions collected at Narayanghat, Nepal (Lupker et al., 2012a) and late Pleistocene sand from the Gandak megafan, 125-400 µm fractions collected from 3 drilled cores at 50-100 km east of Bettiah, Bihar, India (Morin, 2015). The data were obtained with similar procedures than ours, within the same facilities.

VIII.3.6. ^{36}Cl measurements and ^{10}Be recent exposure contribution

The recent exposure of the outcrops to cosmic rays affects the original ^{10}Be concentrations and requires a correction. Relying on the rapid decay of the ^{36}Cl that limits the inherited ^{36}Cl paleoconcetrations, we estimate the recent exposure by measuring the ^{36}Cl content of the feldspar of our samples.

The feldspar fraction of five samples was prepared for ^{36}Cl extraction at CEREGE following the protocol of Schimmelpfennig et al. (2011). The samples were washed with mQ and etched in limited amounts of a HF (40%)/ HNO_3(10%) mixture (volume ratio 1:2) to dissolve ~10% of the mass. An aliquot of 1 g was then taken for chemical composition analysis at SARM (Vandoeuvre-les-Nancy, France). Approximately 1.9 mg of chloride in the form of a chloride carrier (OakRidge National Laboratory), enriched in ^{35}Cl (99.9%), was added to the samples and the samples were dissolved with an excess amount of the HF/HNO_3 mixture. The supernatant was separated by centrifuging from the fluoric cake formed during the dissolution reaction. AgCl was precipitated by adding $AgNO_3$, redissolved in dilute NH_4OH, and $Ba(NO_3)_2$ was added to precipitate BaSO4/$BaCO_3$, in order to reduce the isobaric interference of ^{36}S during the ^{36}Cl AMS measurements. The AgCl was again precipitated with HNO_3 and collected by centrifuging. The AgCl precipitates were rinsed and dried.

The $^{35}Cl/^{36}Cl$ and $^{36}Cl/^{37}Cl$ were measured from isotope dilution AMS measurements at ASTER-CEREGE, normalized to a ^{36}Cl standard prepared by K. Nishiizumi (Sharma et al., 1990), assuming a natural $^{35}Cl/^{37}Cl$ ratio of 3.127. The results are presented in Table SVIII-7.

Complementary geochemical measurements were performed in the feldspar fractions by SARM (Vandoeuvre-les-Nancy, France). The results are presented in Table SVIII-6.

Simple model (Table SVIII-9):

We used a simple computation to assess this contribution (Table SVIII-9) and compared the results with the contribution estimated from ^{36}Cl (Table SVIII-8).

We computed the radiogenic contribution, i.e. the ^{36}Cl production through the ^{35}Cl capture of thermal and epithermal neutrons, by hypothesizing that the samples were fully water saturated and that sandstone porosity can be approximated (Dubille, 2008) by the law of Baldwin and Butler (1985) as a function of depth, with a rock density of 2.7 g/cm^3.

We obtained a porosity varying from ~40% for the younger samples to ~20% for the older ones. We computed the estimate for the recent exposure contribution for an incision rate of 5±2 mm/y and a shielding factor of $0.65^{+0.10}_{-0.20}$. This contribution amounts to 200 - 1,500 atom/g, which represents ~10-20% of the measured concentrations for the younger samples and ~30-40% for the older ones.

Contribution computed from the ^{36}Cl measurements (Table SVIII-8):

We computed the ^{10}Be concentration caused by recent exposure the following way. By the input of ^{36}Cl and chemical data in the Chronus calculator (Marrero et al., 2016), we obtained the ^{36}Cl cosmogenic and radiogenic contributions. At the time of writing, the calculator does not take into account erosion rates for this computation. The radiogenic contribution is > 70-90% for our samples, which are rich in Cl and might be overestimated for the samples presenting negative cosmogenic contributions. Based on the ^{10}Be and ^{36}Cl decay constants, and using the production rates given by the Chronus calculator, we first

estimate the residual (inherited) ^{36}Cl paleoconcentration, then we subtract it to the cosmogenic component to obtain the component related to the recent exposure. Then, we computed the ^{36}Cl production rates at the elevation of the sections (200 m) using the Chronus calculator (unfortunately, we were not able to take into account an erosion rate of 5 mm/y), and we derived the ^{36}Cl/^{10}Be production rate at this elevation. Not taking into account erosion induces an underestimated muonic contribution which impacts the final results.

We finally obtained the recent exposure contribution to the ^{10}Be concentrations, ranging from 0 to 1200 atom/g, which validates our model.

These results are presented with the simple model in Figure VIII-80 and the results are reported for our samples in Table SVIII-1 columns AE-AK.

VIII.3.7. ^{10}Be floodplain exposure contribution

Exposure during sediment transport and burial affects the original ^{10}Be concentrations and also requires a correction. To assess the ^{10}Be contribution during floodplain transfer and final burial, we used the steady state and sediment mass-balance-based model of Lauer and Willenbring (2010). In this model, sediment is carried into the floodplain with an initial concentration $C_c(0)$. While moving downstream, a fraction of sediment is deposited throughout reservoirs in the floodplain and replaced with material previously stored in these reservoirs. Each reservoir is assumed to be well-mixed off.

At a distance x measured down the channel axis from the range outlet, the equation (6) in Lauer and Willenbring (2010) yields the average ^{10}Be concentration in floodplain sediment $C_f(x)$ as a function of the ^{10}Be concentration in river sediment $C_c(x)$:

$$C_f = \frac{1}{(\frac{1}{t_{ex}} + \frac{1}{t_{agg}} + \lambda)} \left(\frac{C_c(0)}{t_{prod}} + \left(\frac{1}{t_{ex}} + \frac{1}{t_{agg}} \right) C_c \right) \qquad (4)$$

with t_{prod} the time to accumulate a mass of ^{10}Be in the floodplain sediment if sediment concentration amounts to $C_c(0)$; t_{ex} the time to rework by lateral exchange the mass stored in the floodplain; t_{agg} the time to transfer the mass stored in the floodplain to another location; λ the ^{10}Be decay constant.

We added to this model the deep muonic production once the sediment is buried below the depth of re-erosion H, i.e. below the depth of the active channel at bankful discharge. The following equation provides the mean concentration gain $\Delta C(x)$:

$$\Delta C(x) \cong C_f(x) - C_0(x) + \sum_{j=1,3} \frac{P_j \Lambda_j}{\sigma \rho} e^{-\frac{H\rho}{\Lambda_j}} \qquad (5)$$

with σ the mean aggradation rate in the floodplain; P_j the production rates and Λ_j the attenuation

lengths of the nucleogenic or muonic contributions; ρ the density. This equation is valid if we neglect the radioactive decay in the initial equation (valid as long as $\frac{\sigma\rho}{\Lambda_j} \gg \lambda$) .

The paleoposition x of the samples was estimated with their deposition ages, based on a southward migration rate of the range outlet of 15±5 mm/y (Lyon-Caen and Molnar, 1985).

The geomorphologic parameters for the Narayani river used as input parameters in the model are reported in Table SVIII-4. The parameters are derived from published studies or from our own measurements. The sediment aggradation rate was derived from our magnetostratigraphic results and the channel lateral migration rate and sinuosity were estimated using the channel location observed over two decades of satellite imagery, available on Google Earth©.

The computation of the floodplain exposure contribution was performed under several assumptions that do not impact the order of magnitude of our results: the active floodplain depth, aggradation rate, sinuosity and channel lateral migration rate were considered spatially uniform from the range outlet to the floodplain outlet (Lauer and Willenbring, 2010; Lupker et al., 2012a) and downstream sediment fining is also omitted.

The results of the contribution of the floodplain exposure are presented Table SVIII-5 and reported for our samples in Table SVIII-1 columns AL-AM.

VIII.3.8. Determination of paleoerosion rates

The recent exposure contribution was subtracted to the measured ^{10}Be concentrations and the resulting concentrations were corrected for radioactive decay using a ^{10}Be half-life of 1.387±0.012×10^6 y (Korschinek et al., 2010; Chmeleff et al., 2010) to obtain ^{10}Be paleoconcentrations. These paleoconcentrations were corrected from the floodplain transfer contribution.

We derived the average paleoerosion rates $\bar{e}$ in the Narayani basin using the equation (e.g. Puchol et al., 2017):

$$\bar{e} = \sum_{i=1,3} \frac{\Lambda_i \times P_i}{\rho \times C} \qquad (6)$$

with Λ_i the attenuation lengths of nucleons or muons, ρ the density of eroded rocks, P_i the mean nucleogenic and muogenic cosmogenic nuclide average production rates in the basin. The use of this equation is permitted under the assumptions that the temporal cosmogenic nuclide production rate variability remains within the range of the ^{10}Be concentration uncertainties (This thesis, Chapter VI), that the geography of the Narayani basin and the sediment provenance have remained similar since 8 Ma, and that ^{10}Be concentrations are not partly inherited from a previous history of erosion and sedimentation (i.e. by recycling). The paleoerosion rates uncertainties were propagated using a Monte-Carlo approach.

The ^{10}Be production rates were computed using Basinga (Charreau et al., 2019) with the Lal-Stone

scaling model (Lal, 1991; Stone, 2000; modified by Charreau et al., 2019). We set the sea level high latitude (SLHL) production rate at 4.18 atom/g (Martin et al., 2017), with factors of 0.9886, 0.0027 and 0.0087 for the SLHL neutron, slow and fast muonic contributions respectively (Braucher et al., 2011). We took into account the glacial cover with the GLIMS database (Raup et al., 2007) but we did not include topographic shielding, following the suggestion of Dibiase, (2018). We also did not include paleomagnetic variations. The Narayani drainage basin was determined by a range outlet located close to the Main Boundary Thrust (MBT, Figure VIII-74) at Narayanghat and therefore does not include the Siwalik units.

Our paleoerosion rates (Figure VIII-82, Table VIII-1 columns AS-AU) are compared with the erosion rates recomputed from the concentrations of the Narayani river sediment (Lupker et al., 2012a) and of the late Pleistocene Gandak Fan (Morin, 2015).

VIII.4. RESULTS

VIII.4.1. Sr-Nd isotopes and lithologic fractions

Our sandy samples (Figure VIII-78-Figure VIII-77, Table SVIII-1 columns AW-BB) present $^{87}Sr/^{86}Sr$ at ~0.766±0.012 and εNd at ~-17.7±0.8, with a distribution in the upper range of the values for the modern Narayani. Their evolution is divided into two periods. From 7.4 to ca. 1.7 Ma, the $^{87}Sr/^{86}Sr$ decreases from 0.775 to 0.76, with apparent fluctuations with a ~2 My period. The εNd decrease coevally from -17.4 to -18.5, with values presenting a large dispersion. Isotopic trends shift from ca. 1.7 Ma to 0.465 Ma and the $^{87}Sr/^{86}Sr$ and εNd increase to 0.770 and -17.4 respectively, with again a large dispersion for εNd.

Since both isotopic ratios are not affected by the same biases (Garçon et al., 2014), the covariation of their mean trend implies shifts of provenance over the period. When plotted one against another (Figure VIII-77), the ratios are consistent with a ternary mixing between the three Himalayan units and show a dominance of the TSS and HHC components compared to the LH. The values are slightly higher than the values for the modern Narayani and for the Gandak Megafan (Singh et al., 2008; Morin, 2015). This points to a lower contribution of the TSS in the mix of our samples compared to the late Pleistocene and modern times. Our older (> 4 Ma) and younger samples (< 2 Ma) seem closer to the HHC than the intermediate samples.

The inversion of our results through a ternary mixing model highlight the evolution of the respective contribution of each unit (Figure VIII-79, Table SVIII-1 columns BC-BH). The contributions of the HHC and TSS combined (HHC+TSS) and of the LH vary around stable averages of 74 and 26% respectively. The contribution of the HHC+TSS appears higher before 1.7 Ma than afterwards, and conversely for the LH. Subtle variations of a ~2 My period are also observed with a higher contribution of the LH at ca. 5 and 3 Ma. When the contribution of the HHC is separated from the TSS, we observe a decreasing HHC contribution from 7.4 to 1.7 Ma followed by an increase after 1.7 Ma, and conversely for the TSS contribution.

Figure VIII-77. Sr-Nd results.

Next page.

a. The $^{87}Sr/^{86}Sr$ values of the Valmiki Sections are indicated by black dots and are compared with the values of the Narayani and the late Pleistocene Gandak Megafan (Morin, 2015). Some Valmiki samples are considered recycled (because of the age of the folds) or probably recycled (because of major elements) (this thesis, Chapter VII). These samples are indicated by red and orange dots respectively. The grey curve represents the median of values for each time bin. The three poles HHC, TSS and LH are indicated (Morin, 2015).

b. The εNd values of the Valmiki Sections are represented using the same colours as in **a.**

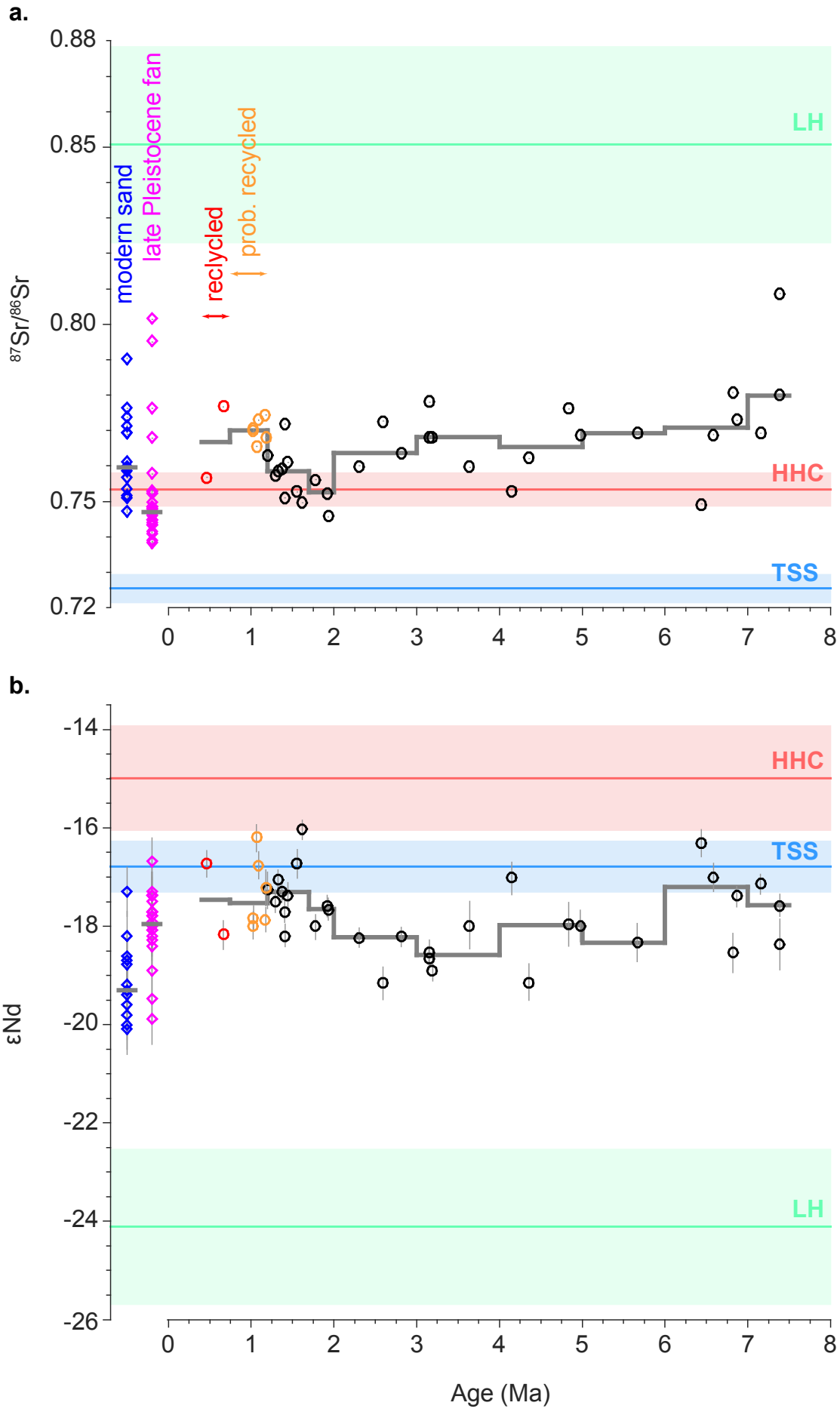
a.
0.88
0.85
0.80
0.75
0.72
$^{87}Sr/^{86}Sr$
modern sand
late Pleistocene fan
reclycled
prob. recycled
LH
HHC
TSS
0
1
2
3
4
5
6
7
8
b.
-14
-16
-18
-20
-22
-24
-26
εNd
HHC
TSS
LH
0
1
2
3
4
5
6
7
8
Age (Ma)

The relative first-order stability of the contribution of the HHC+TSS and of the LH suggests that the Narayani drainage remains stable over time, with only limited modifications. We will check this assertion after presenting the ^{10}Be results.

The respective variations of the HHC compared to the TSS contribution, along with the second-order variations reflect the variations of major and trace elements, at least before 1.2 Ma, ie. before the probable shift in the Valmiki Sections from an Himalayan source to recycled sediment (this thesis, Chapter VII).

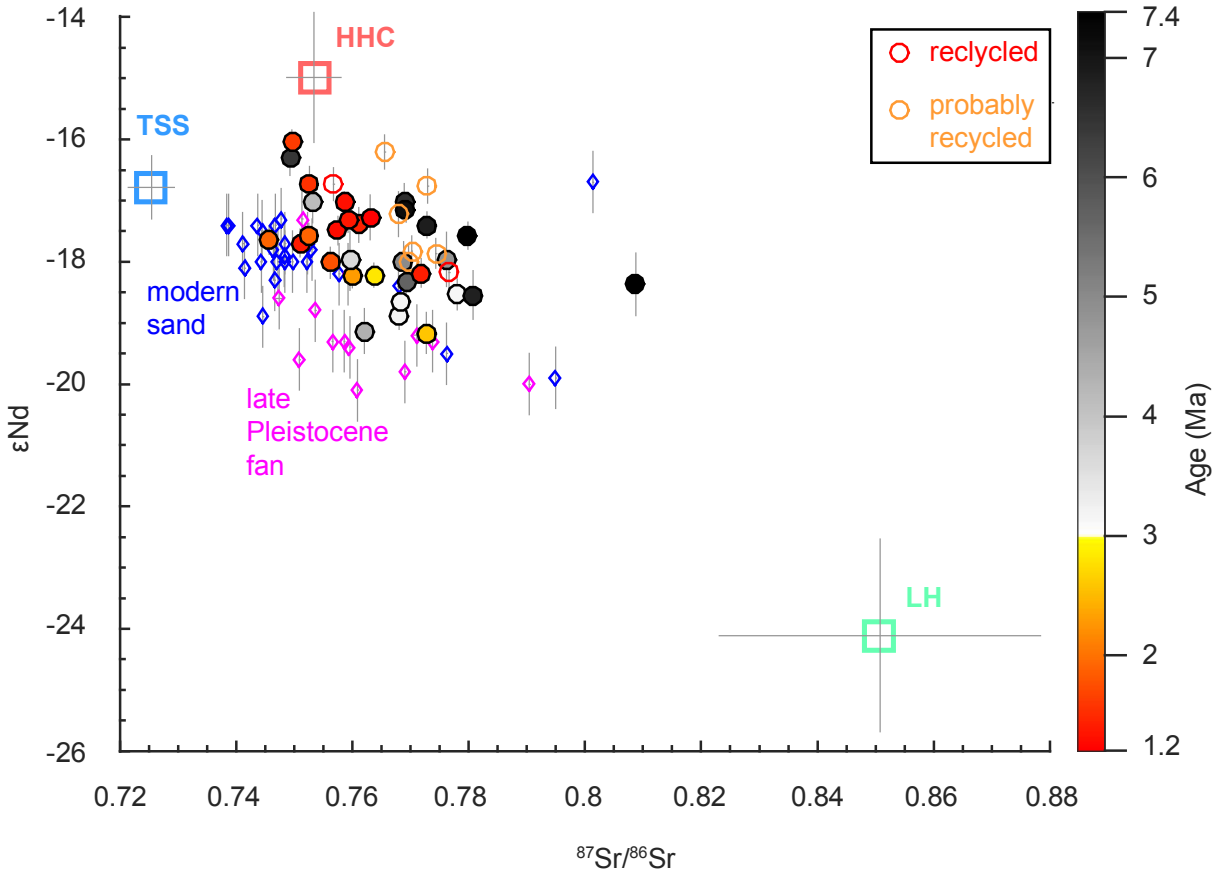

Figure VIII-78. Sr-Nd isotopic results plotted one against another.

Our results are plotted using the age-dependent colour scale. The values of the Narayani and the late Pleistocene Gandak Megafan are indicated for comparison (Morin, 2015). The three poles HHC, TSS and LH are also indicated (Morin, 2015).

Figure VIII-79. Lithologic fractions in a ternary mix.

Next page.

Our HHC, TSS, HHC and LH fractions (**a.**, **b.**, and **c.** respectively) derived from a ternary mix between the average poles yielded by Morin, 2015 and with the input of our Sr-Nd results, are presented. The grey curve represents the median of values for each time bin. For comparison, the values of the modern Narayani sand and the late Pleistocene Gandak Megafan are indicated (Morin, 2015)

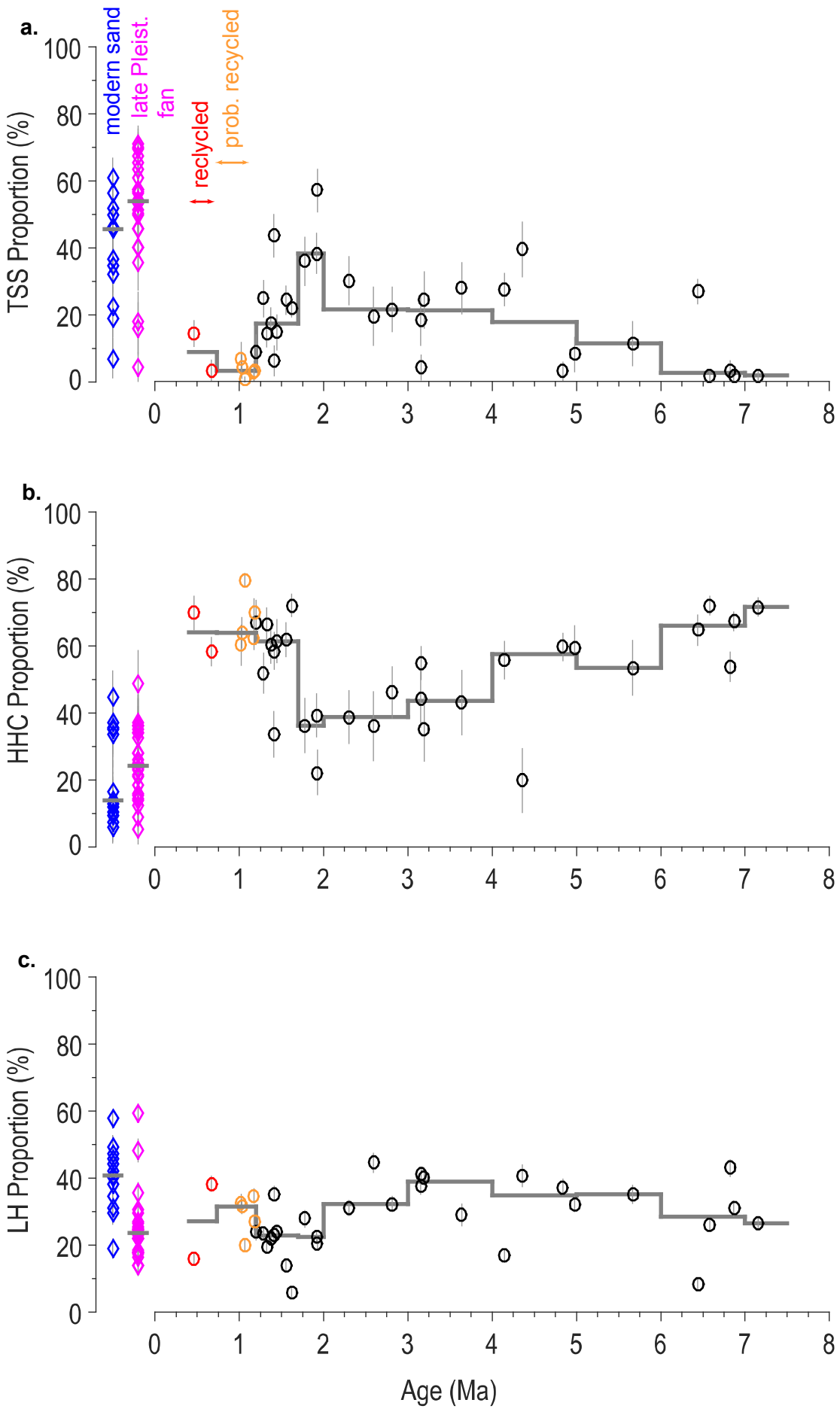
a.
b.
c.
modern sand
late Pleist. fan
recycled
prob. recycled
TSS Proportion (%)
HHC Proportion (%)
LH Proportion (%)
Age (Ma)
0
20
40
60
80
100
0
1
2
3
4
5
6
7
8

VIII.4.2. ^{36}Cl measurements and recent exposure contribution

We used a simple model to assess the recent exposure contribution and compared the results with the contribution estimated from ^{36}Cl (Figure VIII-80, Tables VIII-6-9). We computed the estimate for the recent exposure contribution for an incision rate of 5±2 mm/y and a shielding factor of $0.65^{+0.10}_{-0.20}$. This contribution amounts to 200 - 1,500 atom/g, which represents ⊠10-20% of the measured concentrations for the younger samples and ⊠30-40% for the older ones. The radiogenic contribution is > 70-90% for our samples, which are rich in Cl and might be overestimated for the samples presenting negative cosmogenic contributions. We use this recent exposure model to correct the ^{10}Be paleoconcentrations of the full set of samples.

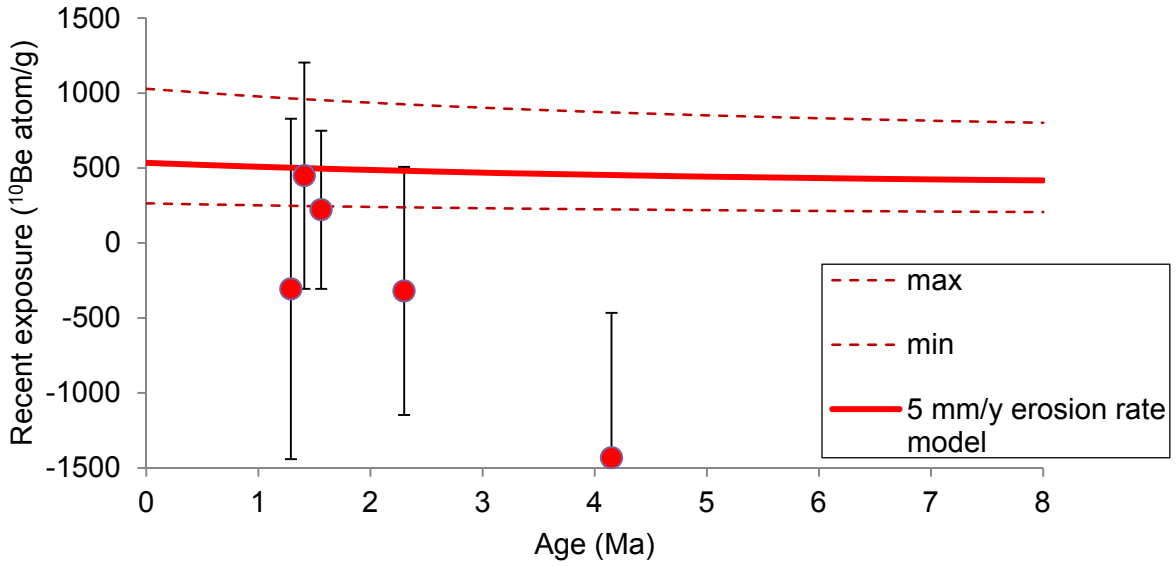

Figure VIII-80. Recent exposure computed using the ^{36}Cl measurements or the model.
The ^{10}Be contribution by recent exposure and assessed from the ^{36}Cl measurements is indicated by red dots. Note that no sample older than ca. 4 Ma has ^{36}Cl measurements. The ^{10}Be contribution assessed using the model is indicated by the red curve.

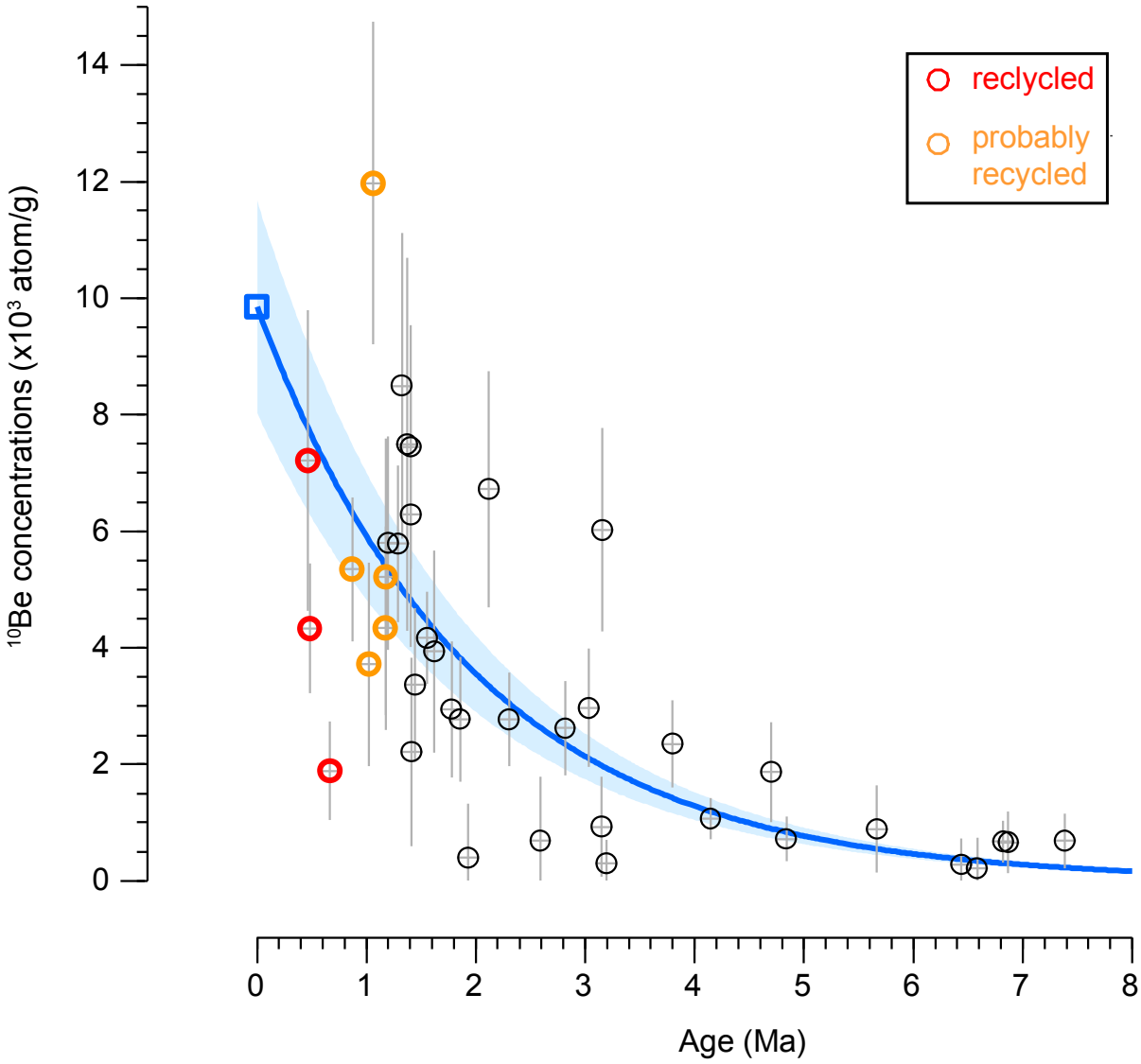

Figure VIII-81. ^{10}Be concentration results.

Our ^{10}Be concentrations from the Valmiki Sections are indicated by black dots. The recycled or probably recycled samples are indicated by red and orange dots. The presented concentrations include the floodplain exposure and recent exposure corrections. The theorical concentration derived from the average modern Narayani ^{10}Be concentration (Lupker et al., 2012a) and corrected from radioactive decay is indicated by the blue curve and the blue-shaded area represents 1-σ uncertainties.

VIII.4.3. ^{10}Be paleoconcentrations

The ^{10}Be concentrations are presented in Figure VIII-81 (also Table VIII-1 columns AC-AP). The derived ^{10}Be paleoconcentrations (Figure VIII-82, Table VIII-1 columns AQ-AR) present an average of $7.8 \pm 6.0 \times 10^3$ atom/g, slightly lower than the modern Narayani average and lower than the Gandak Megafan average (the paleoconcentrations are inversely correlated to paleoerosion rates).

The ^{10}Be paleoconcentrations overlap the concentrations of the Narayani and the Gandak Megafan but present a much larger dispersion. The average paleoconcentration initially decreases by a factor three to four before ca. 5 Ma. After ca. 5 Ma, the average paleoconcentrations remain stable, but individual samples present a large dispersion. The paleoconcentrations do not present organized second-order variations, as would have been expected from an impact of glacial-interglacial cycles.

VIII.4.4. Evolution of the drainage basin

Converting the paleoconcentrations into erosion rates requires validating that the Narayani drainage basin remains stable since 7.4 Ma. We saw that the relative contribution of the HHC compared to the TSS varies significantly (Figure VIII-79).

Under the assumption of steady erosion rates and uplift for each unit (Herman et al., 2010), the variations of the TSS/HHC contributions can be explained by the variation of their area in the drainage basin. Given the geometry of the TTS and HHC units, we can only consider that the Narayani network captured or lose TSS-dominated sub-basins occupying a significant area. But southward paleo-current analyses in the Kali Gandakhi past sediment does not favour this hypothesis (Adhikari and Wagreich, 2011). Since these sub-basins are at a higher elevation than the average elevation of the Narayani basin, a capture should trigger an increase in ^{10}Be production rates and a loss should trigger their decrease. But our ^{10}Be paleoconcentration results initially decrease and then become steady on average (Figure VIII-82).

Figure VIII-82. ^{10}Be paleoconcentration and erosion rates.

Next page.

a. The paleoconcentration results of the Valmiki Sections are presented, with the same colour codes as in Figure VIII-77. The grey curve represents the median of values for each time bin. The part of the curve before 5 Ma is dashed, because of the potential biases described in the discussion. The values of the modern Narayani sand and of the late Pleistocene Gandak Megafan are indicated for comparison (Lupker et al., 2012a; Morin, 2015).

b. Past erosion rates (paleoerosion rates) derived from our ^{10}Be paleoconcentrations and using the Narayani drainage basin. The grey curve represents the median of values for each time bin.

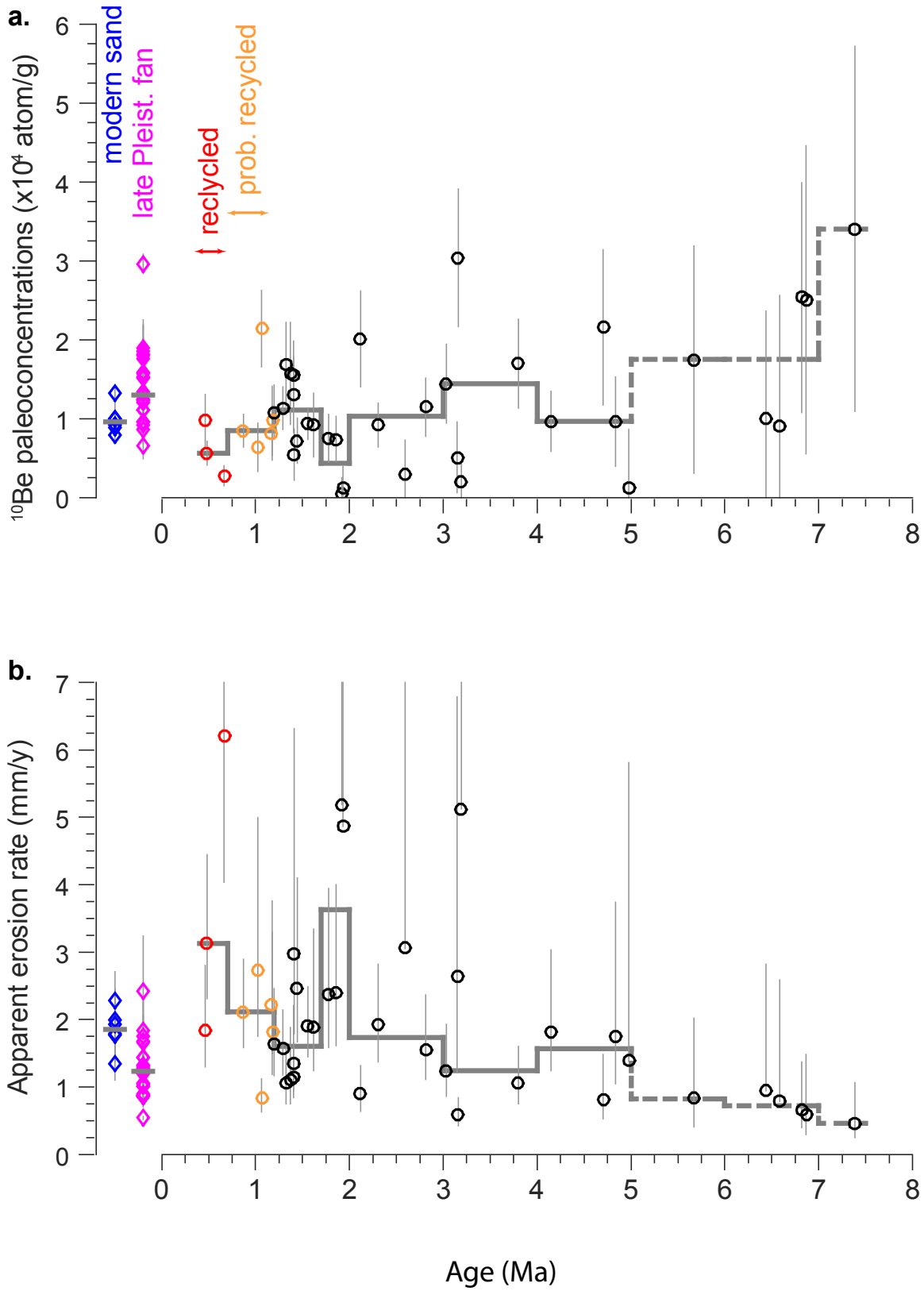
a.
modern sand
late Pleist. fan
reclycled
prob. recycled
^{10}Be paleoconcentrations (x10^4 atom/g)
0
1
2
3
4
5
6
b.
Apparent erosion rate (mm/y)
0
1
2
3
4
5
6
7
0
1
2
3
4
5
6
7
8
Age (Ma)

In the case of captures of TSS sub-basins with steady erosion rates of each unit, the initial decrease of the ^{10}Be paleoconcentrations requires a considerable increase of erosion rates to compensate the increase of the ^{10}Be production rates in this scenario. The following stability of ^{10}Be paleoconcentrations also requires that erosion rates continue to increase to compensate the increase of ^{10}Be production rates. These requirements are incompatible with the assumption of steady erosion rates of each unit.

Alternatively, local erosion rates might have gradually increased in the TSS and/or decrease in the HHC. Since the HHC and TSS-dominated areas are subject to similar ^{10}Be production rates, this does not have an impact on the overall ^{10}Be production rate of the basin. Consequently, this may not have a disproportionate impact on ^{10}Be paleoconcentrations as the first scenario has.

Therefore, we assume that the combination of our Sr-Nd isotope and ^{10}Be concentrations imply that the Narayani basin has remained stable from 7.4 Ma to 1.2 Ma (start of recycling of our sections, this thesis, Chapter VII).

VIII.4.5. Erosion rates

Our apparent paleoerosion rates of the Narayani basin (Figure VIII-82, Table VIII-1 columns AS-AU) average at 2±3 mm/y over the 7.4 - 1.2 Ma time span. This average is close to the modern values from the Narayani river sand and higher than the late Pleistocene paleoerosion rates from the Gandak Megafan (Lupker et al., 2012a; Morin, 2015; see also Godard et al., 2014). The erosion rates average the signal of several million grains of quartz eroded over ~1 ka on mountain hillslopes. This signal is partly damped over 1-10 ka time spans during the sediment transfer through the floodplain (Lupker et al., 2012a). These erosion rates are valid under the verified assumptions that the cosmogenic nuclide production rate varies within the range of the ^{10}Be concentration uncertainties (this thesis, Chapter VI), that the geography of the Narayani basin has remained similar since 7.4 Ma, and that ^{10}Be concentrations are not partly inherited from a previous history of erosion and sedimentation (i.e. by recycling).

The erosion rates reflect the evolution of ^{10}Be paleoconcentrations, with lower values and less dispersion before ca. 5 Ma than afterwards. An increase in the average erosion rate from ⊠0.6 mm/y to ⊠2 mm/y is observed before ca. 5 Ma, but afterwards, erosion rates remain steady on average at ⊠2 mm/y.

VIII.5. DISCUSSION

VIII.5.1. Biased ^{10}Be concentrations for old samples?

The potential biases related to ^{10}Be concentrations of old samples is often an overlooked topic (e.g. this thesis, Chapter VI).

While the preparation protocol we used was calibrated for small quantities of quartz, we had to dissolve large quantities of quartz to obtain a signal for ^{10}Be measurements. This approach was successful since our measured ^{10}Be/^{9}Be ratios are for all samples but one higher than three times the blank. But these large quantities induced a limited purification of the ^{10}Be target and thus an increase in uncertainties.

The addition of the ^{9}Be carrier make it possible to fix the ^{10}Be/^{9}Be ratio before dissolution and evaporation. However, this works only for samples having a negligible amount of natural ^{9}Be, which was not the case for our old samples (Table VIII-1 columns QR). We measured the ^{9}Be content after evaporation and redissolution. But a loss of ^{9}Be during evaporation and redissolution, although not very likely, might have occurred and would induce an artificially decreased ^{10}Be concentration.

These old samples present the low ^{10}Be concentrations (Table VIII-1 columns AA-AP) caused by radioactive decay. The correction for recent exposure is associated with large uncertainties (this thesis, Subchapter VIII.3), and its underestimation would induce a disproportionate overestimation of the concentrations.

Similarly, the correction for exposure during transport and burial of sediment may have an impact, although probably a smaller one. Two phenomenons could lead to an underestimation of exposure for the sediment deposited far from the range outlet. Channel dynamics may be different and lower lateral migration rates may affect the older samples because of their distance. The 125-250 µm fraction ratio between the river and the floodplain sediment may be higher upstream than downstream. Both phenomenons lead to a less efficient exchange between the river and the floodplain and a longer exposure to cosmic rays in the floodplain before the final deep burial of the sediments.

To fully assess the reality of the observed decreased paleoconcentrations in this study and in Puchol et al. (2017) work, all these potential biases require a further investigation that goes beyond this study. In absence of further tests, we chose to keep the oldest samples for our interpretation.

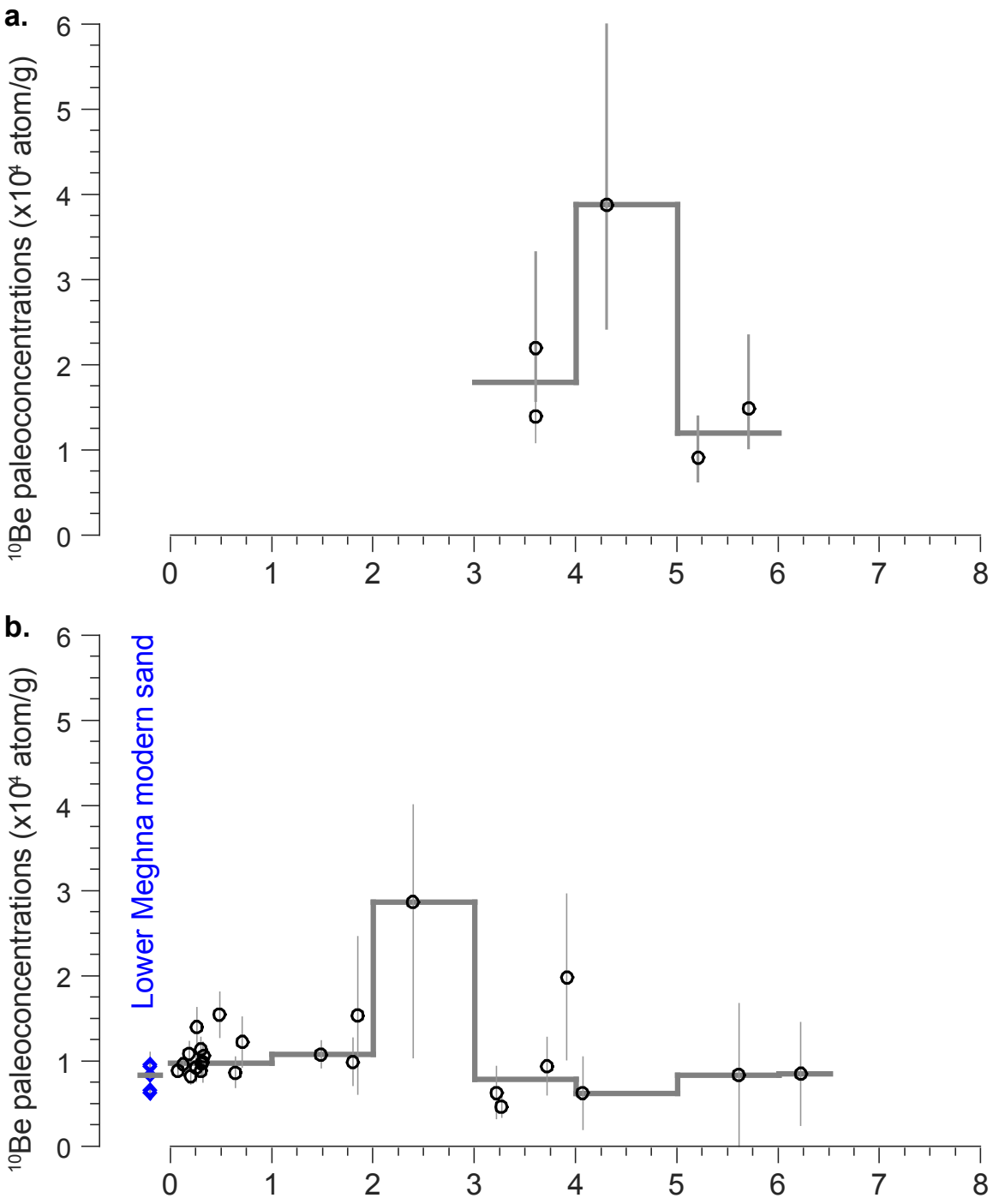

Figure VIII-83. Complementary Himalayan ^{10}Be erosion rates.

a. Erosion rates obtained from the Surai Section, at ~160 km west of the Narayani Section (Charreau et al., in prep.). These rates integrate erosion in a basin similar to the Narayani basin.

b. Erosion rates obtained from turbidites of the Bengal Fan (this thesis, Chapter VI). These rates integrate erosion in the Ganga and Brahmaputra basin (Central and Eastern Himalaya). The grey curve represents the median of values for each time bin.

VIII.5.2. Variability of apparent erosion rates

Our ^{10}Be apparent erosion rates present more variability than for the modern record, in particular after ca. 4 Ma (Figure VIII-82). Such high variability is not observed for the Narayani basin, either in modern sediment (samples that cover the last decade, Lupker et al., 2012a) or in the Late Pleistocene Gandak Fan (samples ≥50 ka, Morin, 2015). Large basins are assumed to smooth out stochastic processes such as landslides (Niemi et al., 2005; Yanites et al., 2009; West et al., 2014). However, measurements performed in river sand (Lupker et al., 2012a) or in fluvial terrace material (Dingle et al., 2018) of other large Himalayan rivers (the Karnali-Ghaghara or the Kosi) demonstrate that large and transverse Himalayan rivers may also produce short-term variations of the ^{10}Be signal by a factor three.

VIII.5.3. Comparison with other ^{10}Be datasets

After ca. 5 Ma, the erosion rates in the Narayani basin are similar to the Himalayan ^{10}Be erosion rates recorded in the Surai section (Figure VIII-83), which average at 2±1 mm/y from 5.7 to 3.6 Ma (Puchol, 2013; Charreau et al., in prep.). Our erosion rates are however higher than the ^{10}Be erosion rates recorded in the Bengal Fan (Figure VIII-83), the latter presenting a steady average at 1.0±0.3 mm/y since ca. 6.2 Ma (This thesis, Chapter VI). This implies that Central Nepal has been a major erosion hotspot in the Himalaya since at least ca. 3.2-3.8 Ma compared to other areas, as in modern times (Godard et al., 2012; Godard et al., 2014).

Figure VIII-84. Local Himalayan erosion rates derived from in situ thermochronometry.

Next page.

a. Erosion rates obtained from a compilation of in situ thermochronometric data and inverted using Fox et al. (2014) 1-D thermal code (data and inversion from Herman et al., 2013). The yellow curve indicates the average erosion rate for 2-Ma time bin and the grey-shaded area represents the standard deviation.

b., c., d., e. presents the average erosion rates and standard deviations for distinct sets of erosion rates. We artificially group each local erosion rate obtained by Herman et al. (2013) according the following sets: rates > 2 mm/y, between 1 and 2 mm/y, between 0.5 and 1 mm/y, and rates < 0.5 mm/y. Each group presents a distinct evolution (coloured curve: average rate, grey-shaded: standard deviation.

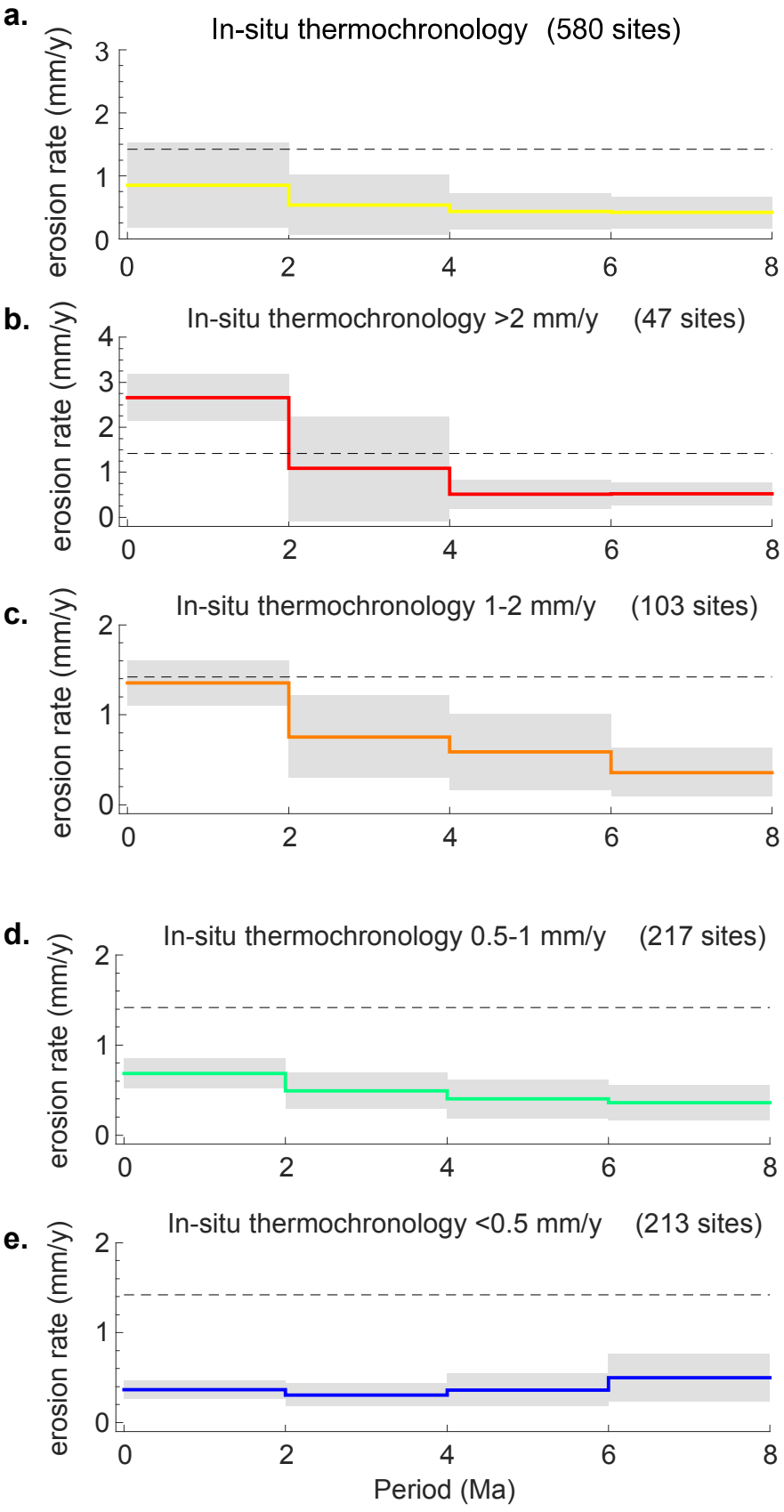
a.
In-situ thermochronology (580 sites)
b.
In-situ thermochronology >2 mm/y (47 sites)
c.
In-situ thermochronology 1-2 mm/y (103 sites)
d.
In-situ thermochronology 0.5-1 mm/y (217 sites)
e.
In-situ thermochronology <0.5 mm/y (213 sites)
erosion rate (mm/y)
Period (Ma)

VIII.5.4. Comparison with detrital thermochronometry

Our short term erosion rates are also close to the long-term erosion rates derived from detrital thermochronometry in the Karnali and Surai section, even if they do not integrate the same Himalayan basin (van der Beek et al., 2006; Naylor et al., 2015).

VIII.5.5. Comparison with in situ thermochronometry

Our erosion rates (Figure VIII-82) are also of the same order as the local erosion rates reconstructed from in situ thermochronometry in the Himalaya (Figure VIII-84, Herman et al., 2013). In detail, some thermochronometric studies present a similar average (Gautam and Koshimizu, 1991; Blythe et al., 2007; Robert et al., 2009; Herman et al., 2010a, 2013; Thiede and Ehlers, 2013; van der Beek et al., 2016) whereas others present a higher average (Nadin and Martin, 2012; Arita and Ganzawa, 1997).

Our results do not sustain a significant increase in the erosion rates (i.e. x 2 to x 5) in Central Nepal since 3 Ma and contradict the models obtained from thermochronometric data for this time span (Huntington et al., 2006; Blythe et al., 2007; Herman et al., 2013; Thiede and Ehlers, 2013). Consequently, our ^{10}Be results confirm the results obtained previously from the Bengal Fan for this period (Figure VIII-83, this thesis, Chapter VI).

However, our average ^{10}Be signal evolves differently from the signal of the Bengal Fan before ca 3.2 - 3.8 Ma (this thesis, Chapter VI). Our signal implies increased erosion rates by a factor four in Central Nepal during the 7 to ca. 3.2 - 3.8 Ma time span. This again contradicts Herman et al. (2013)'s and Thiede and Ehlers (2013)'s models which do not predict such an early increase. It also contradicts Herman et al. (2010a)'s model which predicted a rapid increase in the erosion rates at ca. 10 Ma lasting just one million year and associated to the initiation of the midcrustal duplex (p. 24 of their work).

VIII.5.6. Possible causes of the difference between ^{10}Be and in situ thermochronometry

As previously noted, erosion rates can be measured only by indirect approaches which have distinct resolution and distinct biases. The erosion rates estimated from ^{10}Be represent erosion rates averaged throughout the drainage basin of the Narayani whereas the rates from in situ thermochronometry estimate local erosion rates. However, the method used by Herman et al. (2013) and detailed in Fox et al. (2014) is assumed to overcome this limitation. One possibility is that the number of thermochronometric data is too limited to obtain reliable results. This is particularly the case for the areas covered by the LH and the TSS, which are poor in minerals fitting to low-temperature thermochronometric measurements. One can imagine a scenario where the HHC sees increased erosion rates whereas the other units see a decrease, which shall result in an average stability. However, they obtain average erosion rates for the 0-4 Ma time span lower than ours for the same time span, which suggests that they take into account low-eroding areas and that resolution may be not the source of the difference.

^{10}Be quantifies the span from the time when rock was impacted the first time by cosmic rays to the time when it was impacted the last. The ^{10}Be concentrations are affected by the geomagnetic field, the elevation of the basin, the locus of erosion (high elevation or low elevation), and erosion rates. The variation of the geomagnetic field has not induced variations larger than our uncertainties (this thesis, Chapter VI). Elevation in Central Himalaya is likely stable over the period (Garzione et al., 2000; Gébelin et al., 2013). Our Sr-Nd data show that the basin changed only marginally, thus without a large variation of mean elevation. Therefore, we can assume that the average of our ^{10}Be concentrations can be simply converted in erosion rates.

In situ thermochronometry quantifies cooling rates and dates the age of the passage of the rock through an isotherm which depends on the thermochronometer and on the cooling history. The conversion of the cooling rates into denudation/erosion rates requires a thermal model, which often simplified to a 1-D model (e.g. Fox et al. (2014)'s model) and does not take into account lateral advection nor horizontal transport (Huntington et al., 2007; Herman et al., 2010a; van der Beek et al., 2010). In Central Nepal, both the hydrothermal heat flow (Copeland et al., 1991; Derry et al., 2009) and the groundwater flow driven by the high mountain relief (Whipp and Ehlers, 2007) might also impact local geotherms and make partly inadequate a simplified model exclusively based on heat diffusion. Obtaining a series of erosion rates from in situ thermochronometry is possible by combining measurements using thermochronometers sensitive to distinct closure temperatures and/or combining measurements on samples with distinct elevation (i.e. elevation profile). As demonstrated by Schildgen et al. (2018), this combination of samples requires that they have undergone the same erosional history, which may be not usual.

This description of both approaches suggests that ^{10}Be is rather straightforward compared to in situ thermochronometry. The issues raised by in situ thermochronometry are illustrated by the sharply different results in terms of timing of an increase in erosion between Herman et al. (2010a) and (2013), caused by differences in the size of the dataset and in the thermal model. The fact that the three studies (this work; Herman et al., 2010a, 2013) detect increased erosion rates in Central Nepal suggests that despite all the issues raised by in situ thermochronometry, its results can partly be reproduced by 10Be. However, the difference of several millions of years between the studies probably points to the raw imprecision of the thermal model.

VIII.6. IMPLICATIONS

VIII.6.1. The late Cenozoic climate change in Central Himalaya

Previous studies demonstrated that the late Cenozoic global climate change deeply impacted the Himalayan range. Using oxygen and carbon isotopic measurements on the Valmiki Sections and other available results (Quade and Cerling, 1995; Quade et al., 1995; Vögeli et al., 2017a), this thesis, Chapter VII suggested that the South Asian Monsoon (SA Monsoon) weakens at 6.9 Ma and brings limited precipitations to Central and Western Himalaya afterwards. But this situation may have shifted at ca. 3.2 Ma with a strengthening of the SA Monsoon which brings back significant precipitations in Central Himalaya.

> Our Sr-Nd isotopic results seem to reflect this evolution of the Monsoon on erosion. A strong monsoon impacts the amount of precipitations received by the southern flank of the Himalaya, dominantly covered by the HHC. Then, the focus of precipitations seems to increase the erosion of the HHC at the expense of the TSS, as seen from ca. 7-8 Ma onwards and after ca. 1.7 Ma. Conversely, a weak monsoon brings less precipitation to the Himalayan flank and seems to produce the rebalance of erosion between the HHC and the TSS. This reasoning appears counterintuitive, because a weakening of the monsoon also reduces the amount of precipitations in the TSS, which are located further north.

Alternatively, the shift of sources at ca. 1.7 Ma may be explained by an expansion of glaciers and a related global amplification of extensive glaciations (Shi, 2002) that could have induced a consistent increase in the erosion rates (Vance et al., 2003; Huntington et al., 2006). But the timing and intensity of the late Cenozoic Glaciations remains poorly determined in the Himalaya. Few clues are available about ice expansion before ca. 0.3-0.4 Ma (Owen and Dortch, 2014) and even before the last glacial cycle for the Central Himalaya (Finkel et al., 2003; Zech et al., 2009). The drop of temperatures in the late Cenozoic might be limited at these latitudes compared to higher latitudes (Herbert et al., 2016). The intensity of glaciations during the Last Glacial Maximum has been underlined, with an extent of glacial cover up to 20% of the Himalaya compared to 5% in modern times (9% in the Narayani basin) (Shi, 2002; Raup et al., 2007), but could be debated for the Central Himalaya in view of available data (Duncan et al., 1998; Fort, 2000; Zech, 2003; Pratt-Sitaula et al., 2011). One of the major problems is that many geomorphologic features have been considered early as moraines while they were remnants of debris flows or rock avalanches (Hewitt, 1999). Additionally, it seems unclear why the HHC would be more affected than the TSS, except if the development of glaciers has been facilitated by higher precipitations in the southern flank than in the northern area.

However, in absence of a non climatic cause to explain the variations of HHC and TSS proportions, we assume that our Sr-Nd results are compatible with a local increase of erosion caused by glaciations.

VIII.6.2. The late Cenozoic climate change and erosion rates

Our ^{10}Be data from the Valmiki Sections demonstrate for the first time that average erosion rates do not increase in Central Nepal during the Northern Hemisphere Glaciations. This contrasts with the indirect evidence we provide from our Sr-Nd isotopic measurements and available data (This thesis, Chapter VII) that extensive glaciers likely settle and grow in the High Himalaya at ca. 1.7 Ma. These glaciers either produced increased erosion rates in the HHC, as previously advanced by the interpretation of in situ thermochronometric data (Herman et al., 2013; Thiede and Ehlers, 2013, using among others the data of Huntington et al., 2006) or induced a decrease in the erosion rates elsewhere. Whatever the case, the main impact of our results is that for an orogen presumed in tectonic steady-state such as the Himalaya (DeCelles et al., 2001; Lyon-Caen and Molnar, 1985), a local increase in the erosion rates induces a decrease elsewhere in the orogen. A possible explanation is that the impacted rocks may have not yet reached the surface (Naylor et al., 2015; Willenbring and Jerolmack, 2016).

Since climate does not have an impact on average erosion rates in the Narayani basin after ca. 5 Ma, and because erosion rates as recorded in the Bengal Fan are steady on average since 6.2 Ma (this thesis, Chapter VI), we can doubt that climate has an impact for the ca. 5 - 7.4 Ma time span. If we follow our results for the first period and our discussion about the late Cenozoic climate change in Central Himalaya, a decrease in precipitations would have decreased erosion rates in the HHC and triggered increased erosion rates. But this balancing mechanism probably works only if the range is in tectonic steady state. Therefore, if the biases we listed for old samples are contradicted by further measurements and refining of the various corrections, our ^{10}Be results imply that Central Nepal was not in tectonic steady state at ca. 5 - 7.4 Ma.

Contrary to Western Nepal (Robinson et al., 2001, 2003; Huyghe et al., 2001; Robinson and McQuarrie, 2012) or to Eastern Nepal (Schelling and Arita, 1991), the LH duplex would have initiated later in Central Nepal. Our low erosion rates at 7 Ma (0.5 mm/y) may contradict Herman et al. (2010a)'s model which obtains a ca. 10 Ma initiation age of the duplex in Central Nepal and a steady state reached in one million year. Our results, if confirmed, may yield the evidence that the Himalayan range in Central Nepal took several millions of years to reach steady state between tectonic uplift and erosion after the initiation of the duplex. These results may partly confirm the $^{40}Ar/^{39}Ar$ results of Copeland et al. (2015) who advanced that erosion rates increased since 10 Ma in Central Nepal but not in Western Nepal. The steady state in Central Nepal might have been paradoxically reached when Central Himalaya began to receive more precipitations and when glaciers began to settle and grow there.

These results for the 5 - 7.4 Ma time span, if confirmed, might also imply that the mean elevation of the Narayani-Gandak was lower at 7.4 Ma than at 5 Ma. As a consequence, the production rates and erosion rates would be lower at 7.4 Ma than what has been computed, and the amplitude of the increase in erosion rates would be lower than what we obtained. One could argue that this hypothesis is contradicted by the $\delta^{18}O$ data of the Thakhola Graben, in the northern area (Garzione et al., 2010). They based their $\delta^{18}O$ elevation gradient using Quade et al. (1995)'s data at low elevation in the Surai Section. However, this dataset has not sufficient resolution over the 7 - 1 Ma time span, compared to the new $\delta^{18}O$ record of the Valmiki Sections (this thesis, Chapter VII). This contradiction therefore requires further investigation using a model combining Garzione et al. (2000)'s data and the data of the Valmiki Sections.

VIII.7. CONCLUSION

In this work, we measured the ^{10}Be concentrations and Sr-Nd isotopic ratios on the erosion record of the drainage basin of the Narayani-Gandak, the Valmiki Sections. Our results cover the 8.2 - 1.2 Ma time span (7.4 - 1.2 Ma for erosion rates) and demonstrate that Central Nepal was not subject to increased average erosion rates during the Northern Hemisphere Glaciations. This absence of increase occurs in spite of the probable increase in the erosion rates in the High Himalaya, associated to amplified monsoonal precipitations and, to a lesser extent, amplified glacial erosion. Our results imply that the Himalaya in Central Nepal was in steady state between tectonic uplift and erosion during this period.

But, if our ^{10}Be results are confirmed for the older samples, this assumption of steady state was probably not the case before ca. 5 Ma. From 7.4 to ca. 5 Ma, average erosion rates would have increased by a factor of four. This suggests that the LH duplex was still in early development during this period in Central Nepal.

Our contribution supplies a new and full dataset. By the comparison with the extensive previous work on erosion, this dataset makes it possible to have deeper insight on the past erosion in Central Nepal and yield a significant advance to better understand the subtle links between climate, tectonics and erosion in active mountain ranges.

Acknowledgments

The Bihar State Forest Department is acknowledged for authorization for working and sampling in the Valmiki Wildlife Sanctuary, National Park & Tiger Reserve. V. Jain and R. Sinha are warmly acknowledged for their assistance in getting these authorizations. The teams of CRPG and SARM, along with The teams of CRPG, SARM and CEREGE are thanked for their assistance in sample preparation and measurements. The ^{10}Be measurements were performed at the ASTER AMS national facility (CEREGE, Aix en Provence) which is supported by the INSU/CNRS, the ANR through the "Projets thématiques d'excellence" program for the "Equipements d'excellence" ASTER-CEREGE action and IRD. The field and analytic works were funded by the ANR Calimero, ANR Himal Fan projects and an INSU Syster project. S. Lenard PhD funding was provided by a Université de Lorraine-CRPG 3-year PhD fellowship and a Université de Poitiers 1-year A.T.E.R..

Author contributions

Potential co-authors:

Sebastien J.P. Lenard*[1], Jérôme Lavé[1], Christian France-Lanord[1], Julien Charreau[1], Catherine Zimmermann[1], Aymeric Schumacher[1], Rahul Kumar Kaushal[2], Ananta Gajurel[3], Raphaël Pik[1], ASTER Team[4†]

[1]CRPG, Université de Lorraine, 15 rue Notre Dame des Pauvres, 54500 Vandœuvre-lès-Nancy, France

[2]Indian Institute of Technology Gandhinagar (IITGN), Gandhinagar, Gujarat, 382355, India

[3]Department of Geology, Tribhuvan University, Kathmandu, Nepal

[4]Université Aix-Marseille, CNRS-IRD-Collège de France, UM 34 CEREGE, Technopôle de l'Environnement Arbois-Méditerranée, BP80, 13545 Aix-en-Provence, France

[†]Georges Aumaître, Didier L Bourlès, Karim Keddadouche, Laetitia Leanni

J.L., C.F.L. and J.C. designed the study. J.C., J.L., S.L., C.F.L., A.G., R.K. and R.P. collected the samples. S.L., A.T., C.Z., A.S. performed the measurements. J.L., J.C. and S.L. performed the computations. SL., J.L. and C.F.L. interpreted the results and wrote the manuscript.

VIII.8. TABLES

In Tables attached to this manuscript.

Table SVIII-1. Sample information, dating, ^{10}Be, Sr-Nd isotopic results.

Table SVIII-2. ^{10}Be results for duplicate samples.

Table SVIII-3. ^{10}Be blanks.

Table SVIII-4. Parameters used for the flood plain transfer model.

Table SVIII-5. ^{10}Be contribution in the flood plain calculated using the transfer flood plain model for the Narayani river.

Table SVIII-6. Major and trace elements results on the feldspar fraction.

Table SVIII-7. Feldspar fraction ^{36}Cl results.

Table SVIII-8. Recent exposure computation with ^{36}Cl results.

Table SVIII-9. Recent exposure model.

IX. SYNTHESIS

IX.1. CONTEXT

IX.1.1. Climate change and erosion rate estimates

The previous decades of research have seen an intense debate about the interactions between tectonics and climate through denudation. One key and unanswered question is whether climate change impacts erosion rates and affects the development of mountain ranges independently of their tectonic pattern. And one key issue to answer this question is that past erosion rates can only be determined through indirect approaches. A significant number of studies shows an apparent global and considerable increase in erosion rates in the Late Cenozoic (e.g. Zhang et al., 2001; Herman et al., 2013). This apparent increase is coeval with a global climate change characterized by an increase in aridity and the rise of glacial/interglacial cycles along with the Northern Hemisphere Glaciations. This apparent increase affects several mountain ranges indiscriminately. Thus, the link between climate change and this apparent increase in erosion rates should be obvious.

The approaches used to determine erosion rates require strong assumptions, which have been regularly unverified. Sediment budgets or accumulation rates depend on the individual dating constraints of each site. These dating constraints are difficult to obtain, particularly in the coarse Pleistocene continental series. In that case, workers are tempted to temporally correlate the layers of each site with each other by using their sedimentary characteristics (facies). But these sedimentary facies, rather than varying in function of climate, vary as a function of the distance to the gravel front (Dubille and Lavé, 2015) or of the wandering of the river channel, which are local parameters. This was illustrated by the work of Charreau et al. (2009) who contradicting the results of Zhang et al. (2001) in Central Asia by showing that the coarse formations at the front of the Tianshan are diachronous. Sedimentary budgets also depend on the spatio-temporal resolution of drill sites. A sedimentary budget performed on the glaciogenic sediments deposited on the extensively explored Norwegian margin (Dowdeswell et al., 2010) has more value than a sedimentary budget performed in the Bengal Bay which has few data in the deep sea (Métivier et al., 1999; Clift and Gaedicke, 2002; Clemens et al., 2016; France-Lanord et al., 2016).

In situ thermochronometry depend on the strong assumption that the geotherm has a simple configuration averaged regionally, classically in one dimension (e.g. Fox et al., 2014; Herman et al., 2013). But the thermal field in active mountain ranges is all but simple. Lateral variations occur with horizontal advection (Huntington et al., 2007; Herman et al., 2010b; van der Beek et al., 2010). Spatial variations occur with the hydrothermal heat flow (Copeland et al., 1991; Derry et al., 2009) and the groundwater flow driven by the high mountain relief (Whipp and Ehlers, 2007). The geotherm can be unsteady through time and different for distinct thermochronometers applied on the same sample. The risk is to combine data from distinct samples and distinct thermochronometers which do not tell the same history of denudation (Schildgen et al., 2018).

IX.1.2. Assumptions associated to the use of terretrial cosmogenic nuclides

In this thesis, we demonstrated that the use of terrestrial cosmogenic nuclides to estimate average erosion rates in a drainage basin requires assumptions that could be more easily verified compared to other approaches, at least in the Himalaya. While the cosmic flux has remained steady since 10 Ma (Leya et al., 2000), we show that the geomagnetic dipole fluctuations influence the cosmogenic production rates within a ⊠20% margin. The past elevation of the drainage basin may be estimated using oxygen isotopes and has probably remained steady in Central Himalaya for the last 10 Ma (Garzione et al., 2000; Gébelin et al., 2013). Recent exposure of samples to cosmic rays can be assessed using a couple of cosmogenic nuclides of distinct half-lives. As shown before (Lauer and Willenbring, 2010), exposure during the transfer of sediment through the floodplain can be determined through a transfer model. Recycling affects cosmogenic nuclide concentrations because the samples have kept an older erosional history. Recycling can be assessed using major elements. The geometry of the basin determines the mean elevation which affects the computation of the mean production rates. The stability of this geometry can be estimated with a provenance analysis using strontium and neodymium isotopes.

IX.2. RESULTS

In this context, the aim of this thesis was to obtain an independent temporal record of erosion rates in the Himalaya. This aim is achieved thanks to two new records.

IX.2.1. The Bengal Fan record

The first record consists in a series of 28 ^{10}Be concentrations extracted from the quartz sand of the deep sea Bengal Fan and integrates erosion over 1-10 ka timescales in the Ganga-Brahmaputra drainage basin since 6.2 Ma, with a high resolution for the last million year (Chapter VI). The acquisition of concentrations from such old samples in marine sediment was possible thanks to the abundance of sand in the Bengal Fan turbidites. To better determine the temporal series, we provide new nanofossil constraints along with a new age model for Expedition 354 U1450 Drill Site (Chapter V).

We supplement our concentrations with a provenance analysis based on Sr-Nd isotopes measured on the bulk sandy samples. This analysis takes advantage of the distinct isotopic signatures of the Ganga and the Brahmaputra sediment (Galy and France-Lanord, 2001). We demonstrate that the provenance of the sandy turbidites is affected by floodplain sequestration or possible distinct turbiditic systems for the Ganga and the Brahmaputra. The sandy turbidites younger than 0.45 Ma in the Expedition 354 drill sites originate only from the Brahmaputra.

The key result deriving from the measurements in the Bengal Fan is the absence of increase or

decrease in the average erosion rates in the Central and Eastern Himalaya since 6.2 Ma, despite climate change and despite clear geomorphologic evidence in the Himalaya for past intense glaciations. The average erosion rates in the Ganga and Brahmaputra basin remains close to modern values, at ≈1 mm/y.

IX.2.2. The Valmiki Section record

The second record consists in a series of 36 ^{10}Be concentrations extracted from the quartz sand of the foreland basin continental Siwalik sediment located in the Valmiki Wildlife Sanctuary, National Park & Tiger Reserve, Bihar, India (Chapter VIII). This series integrates erosion in the Narayani-Gandak basin in Central Nepal from 7.4 to 1.2 Ma. The acquisition of a signal distinct from the blank for such old samples was possible thanks to the large mass of quartz we prepared for measurements. We provide the field observations of the new Valmiki Sections, from east to west, the Patalaia, the Ganguli, the Dwarda, the Gonauli and the Maloni Naha Sections, the full series having a described thickness of ≈4,000 m (Chapter VII). We determine magnetostratigraphic constraints that cover the 8.1 - 0.78 Ma time span. Hence, the Valmiki Sections are part of a very limited set of the Siwalik Sections covering the almost full late Cenozoic. We estimate the initiation of the local Siwalik folds at ≈0.74±0.06 Ma for the Dwarda, Ganguli and Patalaia and at ≈0.3-0.4 Ma for the Gonauli and the Maloni Naha. These ages are significantly younger than elsewhere in the Siwalik Hills.

We supplement our results with a paleoenvironmental study based on oxygen and carbon isotopes on bulk silts, with a provenance analysis based on on Sr-Nd isotopes applied on the bulk sandy samples, along with an analysis of recent cosmogenic exposure with ^{36}Cl measurements. The paleoenvironmental study benefits from the high secondary carbonate content of our silty samples. These secondary carbonates partly consist in diagenetic cement and partly in pedogenic carbonates. The $\delta^{13}C$ ratio in pedogenic carbonates varies as a function of the environmental prevalence of C_3 or C_4 plants, both groups having a distinct pathway to absorb CO_2 and growing under distinct climatic conditions. The $\delta^{18}O$ ratio varies as a function of the amount of precipitations and seasonality. The Sr-Nd provenance analysis takes advantage of the distinct isotopic signatures of the main Himalayan units (Morin, 2015).

Our $\delta^{13}C$ results may yield new and precise timing constraints on the shift to a prevalence of C4 plants in the plains of Central Himalaya. These new constraints may evidence that the shift occur synchronously in the Central and Western Himalaya (our results; Quade and Cerling, 1995; Vögeli et al., 2017a). Additionally, they may yield the first evidence ever found of a shift back to a mix of C_3 and C_4 vegetation at the dawn of the Northern Hemisphere Glaciations. Our $\delta^{18}O$ results detect that at least the lower part of the Valmiki Sections is impacted by early diagenesis, as previously observed for the Surai Section (Sanyal et al., 2005). For the upper part, they might show an increase in aridity and/or seasonality over the period, in spite of the initiation of the Northern Hemisphere Glaciations and in contrast with Western Himalaya (Quade and Cerling, 1995). These results might imply that the South Asian Monsoon varied in intensity during the late Cenozoic, with an initial weakening and a later partial restrengthening at the dawn of the Northern Hemisphere Glaciations. To be validated, these interpretations on the $\delta^{13}C$ and $\delta^{18}O$ signals require further petrographic observations of the samples.

Our Sr-Nd provenance analysis combined with our ^{10}Be concentrations imply that the Narayani-Gandak drainage basin remains stable from 7.4 Ma to 1.2 Ma with only marginal modifications. Our Sr-Nd results suggest a relative stability of erosion in the lower mountain range, covered by the Lesser Himalaya, despite the ongoing duplexing. They also suggest an initial decrease in erosion rates in the southern flank and the higher summits, mainly covered by the High Himalaya Crystalline (HHC) and to a lesser extent by the Tethyan Series (TSS), followed by a recover after 1.7 Ma. This variability might be attributed to the fluctuations of the South Asian Monsoon or to the Glaciations.

Our ^{36}Cl results imply that recent exposure to cosmic rays is limited for the major part of the Valmiki Sections. Extending this implication to the older samples requires new measurements.

The key result deriving from the measurements in the Valmiki Sections is the absence of increase or decrease in the average erosion rates in Central Nepal since ca. 5 Ma, despite climate change and despite clear geomorphologic evidence in Central Nepal for past intense glaciations. This stability, compared to the variations of the contributions of the HHC and the TSS, implies that the decrease or increase in erosion rates in the High Himalayan part of the Narayani-Gandak basin should be compensated by a decrease or an increase elsewhere. The average erosion rates in the Narayani-Gandak basin remains close to modern values, at ⊠2 mm/y. These values are higher than the Bengal Fan average erosion rate and imply that some Himalayan segments have erosion rates much lower than 1 mm/y.

The secondary result is the increase in erosion rates during the 7.4 - 5 Ma time span. We underline that this increase need to be confirmed by further measurements and modelling. When confirmed, this increase may imply that the initiation of duplexing was later in Central Nepal than in Western Nepal and that landscapes took several millions of years to adapt to the new tectonic configuration. This questions the assumption that the Himalaya in Central Nepal has been in steady state since 10 Ma, at least until 5 Ma, which should have an impact on erosional studies in this region.

As the last point about the Valmiki record, the apparent erosion rates derived from our ^{10}Be concentrations display a high variability since 3.2 Ma. This confirms previous results that show the overwhelming weight in sediment of deep-seated landslides or landslides affecting the ridges of mountain ranges (Puchol et al., 2014; Dingle et al., 2018). We note however that the past variability is much higher than in modern times, suggesting that no modern analog of the landslides we may detect in our record would have existed in recent history. This variability does not affect the evolution of the average erosion rate and our conclusions.

IX.3. CONCLUSION

Our results demonstrate that average erosion rates in the Himalaya have not increased since at least ca. 5 Ma, despite a large change of climatic conditions, as suggested by our isotopic record in addition to the ^{10}Be concentrations. This implies that climate change alone cannot increase or decrease average erosion rates in the Himalaya, and that tectonics is the main driver for the fluctuations of average erosion rates. However, this does not contradict local variations of erosion rates depending on climate, as possibly shown by our provenance analysis on the Valmiki Sections, or by some in situ thermochronometric studies (Huntington et al., 2006). To obtain a steady average erosion rate in the basin, a local increase in erosion rates should be compensated by a local decrease in erosion rates elsewhere. But this concept requires further measurements and modelling to be explored.

The one-million-dollar question now is: can we extend our approach and conclusions to other mountain ranges in the world? We took advantage of the abundance of sand, originated from the considerable volume of sediment provided by the Himalayan range, the good dating constraints, the large size of the drainage basin buffering the marginal changes of drainage network, and the significant differences in the isotopic signature of the formations covering the drainage basin. Such an ideal configuration may not be available elsewhere, as shown by the early work of Bierman et al. (2016) offshore Greenland.

The Andes is another mountain range where an apparent increase in erosion rates has been interpreted (Herman et al., 2013; Herman and Brandon, 2015). Several studies investigated the Andes foreland basin in Northwestern Argentina measuring ^{10}Be in quartz sediment (Val et al., 2016; Amidon et

al., 2017; Pingel et al., 2019). Two studies show a decrease in erosion rates that they attribute to the increasing aridity, either linked to the range uplift creating a rain shadow (Pingel et al., 2019) or to the late Cenozoic climate change (Amidon et al., 2017). However, these studies might not bear the same significance as ours because of the limited size of the drainage basins and uncertainties about a potential recycling.

Another study (Puchol et al., 2017) investigated the Tianshan, a mountain range where an apparent increase in erosion rates has also been interpreted (Zhang et al., 2001; Molnar, 2004). Even though the Tianshan is at 1,700 km and ~15° N of the Valmiki Sections, in a distinct tectonic context, the trend of their average erosion rates appear roughly similar to our Valmiki record, i.e. an increase in rates from ca. 8 to 3-4 Ma followed by stable rates. Even though the early apparent increase in erosion rates require further measurements and modelling for the Tianshan Sections and the Valmiki Sections, the combination of their study and ours forms a strong argument against an increase in erosion rates during the Northern Hemisphere Glaciations, at least in active orogens.

This argument is further reinforced by an earlier study that demonstrates, using Optically Stimulated Luminescence (OSL), that erosion rates remained steady during the last glacial cycle in the Southern Alps of New Zealand (Herman et al., 2010b) and are similar to the long-term erosion rates derived from thermochronometry. But we note that their results may not be extended to the full Pleistocene, because of a different trend shown by results obtained by using $^{4}He/^{3}He$ thermochronometry (Shuster et al., 2011).

Do our conclusions extend to extinct orogens? Recent results from the Var Submarine Fan, which collects sediment from the Southwestern Alps in Europe suggests a negative answer (Mariotti, 2020). Their results, extending over the last glacial cycle demonstrate that erosion rates increased in the Last Glacial Maximum. However, this might be an exceptional case, and unfortunately, neither our study nor the study of Puchol et al. (2017)'s has this resolution to confirm such an exceptional situation at the Last Glacial Maximum in the Himalaya or in the Tianshan. Therefore, the response of extinct orogens to climate change requires further investigation on timescales of millions of years. This response may be different that the response of active orogens, which our results show as dominated by tectonics.

X. SYNTHESE

X.1. CONTEXTE

X.1.1. Changement climate et estimation des taux d'érosion

Les décennies précédentes de recherche ont vu l'émergence d'un intense débat sur les interactions entre la tectonique et le climat au travers de la dénudation. Une question clé et sans réponse est de savoir si le changement climatique a un impact sur les taux d'érosion et affecte le développement des chaînes de montagnes indépendamment de leur configuration tectonique. Et l'un des principaux problèmes pour répondre à cette question est que les taux d'érosion passés ne peuvent être déterminés que par des approches indirectes. Un nombre significatif d'études montre une augmentation globale et considérable des taux d'érosion au cours du Cénozoïque tardif (p. ex. Zhang et al., 2001 ; Herman et al., 2013). Cette augmentation apparente est synchrone avec un changement climatique global caractérisé par une aridification et l'émergence des cycles glaciaires/interglaciaires avec les glaciations de l'hémisphère nord. Cette augmentation apparente touche plusieurs chaînes de montagnes de façon indiscriminée. Ainsi, le lien entre le changement climatique et cette augmentation apparente des taux d'érosion devrait être évident.

Mais les approches utilisées pour déterminer les taux d'érosion requièrent des hypothèses fortes qui n'ont pas été régulièrement vérifiées. Les bilans sédimentaires ou les taux d'accumulation dépendent des contraintes de datation individuelles de chaque site. Mais ces contraintes de datation sont difficiles à acquérir, en particulier dans les séries continentales grossières du Pléistocène. Dans ce cas, les travailleurs sont tentés de corréler temporellement les couches de chaque site les unes aux autres à l'aide de leurs caractéristiques sédimentaires (les faciès). Mais ces faciès sédimentaires, plutôt que de varier en fonction du climat, varient en fonction de la distance au front de propagation du gravier (Dubille et Lavé, 2015) ou en fonction de l'errance du lit de la rivière, qui sont des paramètres locaux. Les travaux de Charreau et al (2009) contredisent les résultats de Zhang et al (2001) en Asie centrale en montrant que les formations grossières du front du Tianshan sont diachrones et illustrent cette situation. Les bilans sédimentaires dépendent également de la résolution spatio-temporelle des sites de forage. Un bilan sédimentaire réalisé sur les sédiments glaciogènes déposés sur la marge norvégienne qui a été largement explorée (Dowdeswell et al., 2010) a plus de valeur qu'un bilan sédimentaire réalisé dans la baie du Bengale qui possède peu de données en eau profonde (Métivier et al., 1999 ; Clift et Gaedicke, 2002; Clemens et al., 2016; France-Lanord et al., 2016).

La thermochronométrie in situ repose sur l'hypothèse forte que le géotherme a une configuration simple et moyennée régionalement, classiquement selon une seule dimension (par exemple, Fox et al., 2014 ; Herman et al., 2013). Mais le champ thermique dans les chaînes de montagnes actives est tout sauf simple. Des variations latérales se produisent avec l'advection horizontale (Huntington et al., 2007; Herman et al., 2010a; van der Beek et al., 2010). Des variations spatiales se produisent avec le flux thermique hydrothermal (Copeland et al., 1991 ; Derry et al., 2009) et le flux d'eau souterraine provoqué par le relief de haute montagne (Whipp et Ehlers, 2007). Le géotherme peut être instable dans le temps et différent selon thermochronomètres appliqués sur le même échantillon. Le risque est de combiner des

données provenant d'échantillons distincts et de thermochronomètres distincts qui ne présentent pas la même histoire de dénudation (Schildgen et al., 2018).

X.1.2. Hypothèses associées à l'utilisation des isotopes cosmogéniques terrestres

Dans cette thèse, nous avons démontré que l'utilisation des isotopes cosmogéniques terrestres pour estimer les taux moyens d'érosion dans un bassin versant requiert des hypothèses qui pourraient être plus facilement vérifiées que pour les autres approches, du moins dans l'Himalaya. Alors que le flux cosmique est resté stable depuis 10 Ma (Leya et al., 2000), nous montrons que les fluctuations du dipôle géomagnétique influencent les taux de production cosmogénique dans une marge de 20%. L'altitude passée du bassin versant peut être estimée à l'aide des isotopes de l'oxygène et est probablement restée stable dans le centre de l'Himalaya depuis 10 Ma (Garzione et al., 2000 ; Gébelin et al., 2013). L'exposition récente des échantillons aux rayons cosmiques peut être évaluée à l'aide d'un couple d'isotopes cosmogéniques de demi-vies distinctes. Comme précédemment démontré (Lauer et Willenbring, 2010), l'exposition pendant le transfert des sédiments dans la plaine inondable peut être déterminée au moyen d'un modèle de transfert. Le recyclage affecte les concentrations des isotopes cosmogéniques parce que les échantillons ont conservé une histoire d'érosion plus ancienne. Ce recyclage peut être évalué à l'aide des éléments majeurs. La géométrie du bassin détermine l'altitude moyenne qui affecte le calcul des taux moyens de production. La stabilité de cette géométrie peut être estimée par une analyse de provenance à l'aide des isotopes du strontium et du néodyme.

X.2. RESULTATS

Dans ce contexte, l'objectif de cette thèse était d'obtenir un enregistrement temporel des taux d'érosion dans l'Himalaya, qui soit indépendant des autres méthodes. Cet objectif est atteint grâce à deux nouveaux enregistrements.

X.2.1. L'enregistrement du cône du Bengale

Le premier enregistrement consiste en une série de 28 concentrations en ^{10}Be extraites du sable quartzeux du cône du Bengale et intègre l'érosion sur des échelles de temps de 1 à 10 ka dans le bassin versant du Gange-Brahmapoutre depuis 6,2 Ma, avec une haute résolution depuis le dernier million d'années (Chapitre VI). L'acquisition de concentrations à partir de ces anciens échantillons dans les sédiments marins a été possible grâce à l'abondance de sable dans les turbidites du cône du Bengale. Pour mieux déterminer les séries temporelles, nous fournissons de nouvelles contraintes sur des nanofossiles ainsi qu'un nouveau modèle d'âge pour le site U1450 foré par l'expédition IODP 354 (chapitre V).

Nous complétons nos concentrations par une analyse de provenance basée sur les isotopes Sr-Nd mesurés sur les échantillons de sable en vrac. Cette analyse tire parti des signatures isotopiques distinctes

des sédiments du Gange et du Brahmapoutre (Galy and France-Lanord, 2001). Nous démontrons que la provenance des turbidites sableuses est affectée par la séquestration du sable dans lees plaines d'inondation ou par des systèmes turbiditiques éventuellement distincts pour le Gange et le Brahmapoutre. Les turbidites sableuses d'âge inférieur à 0,45 Ma dans les forages de l'expedition 354 proviennent uniquement du Brahmapoutre.

Le principal résultat découlant des mesures effectuées dans le cône du Bengale est l'absence d'augmentation ou de diminution des taux moyens d'érosion dans l'Himalaya central et oriental depuis 6,2 Ma, en dépit du changement climatique et en dépit de preuves géomorphologiques claires indiquant l'intensité des glaciations passées dans l'Himalaya. Les taux d'érosion moyens dans le bassin du Gange et du Brahmapoutre restent proches des valeurs modernes, à 1 mm/an.

X.2.2. L'enregistrement des sections Valmiki

Le deuxième enregistrement consiste en une série de 36 concentrations en ^{10}Be extraites du sable quartzeux des sédiments continentaux Siwalik du bassin d'avant-pays de l'Himalaya, dans la zone naturelle protégée de Valmiki, dans l'Etat du Bihar en Inde (chapitre VIII). Cette série intègre l'érosion dans le bassin de la Narayani-Gandak au Népal central de 7,4 à 1,2 Ma. L'acquisition d'un signal distinct du blanc pour de tels échantillons anciens a été possible grâce aux grandes masses de quartz que nous avons préparées pour les mesures. Nous fournissons les observations de terrain sur les nouvelles sections Valmiki, d'est en ouest, les sections Patalaia, Ganguli, Dwarda, Gonauli et Maloni Naha, la série complète ayant une épaisseur décrite d'environ 4.000 m (Chapitre VII). Nous déterminons les contraintes magnétostratigraphiques qui couvrent la période de 8,1 à 0,78 Ma. Par conséquent, les sections Valmiki font partie de la famille réduite des sections Siwalik couvrant la presque totalité du Cénozoïque tardif. Nous estimons l'initiation des plis Siwalik locaux à 0,74$\pm$0,06 Ma pour le Dwarda, Ganguli et Patalaia et à 0,3-0,4 Ma pour les Gonauli et le Maloni Naha. Ces âges sont beaucoup plus jeunes qu'ailleurs dans les collines Siwalik.

Nous complétons nos résultats par une étude paléoenvironnementale à l'aide des isotopes de l'oxygène et du carbone sur des silts en vrac, une analyse de provenance à l'aide des isotopes Sr-Nd mesurés sur les échantillons de sable en vrac, ainsi qu'une analyse de l'exposition cosmogénique récente par des mesures de concentrations en ^{36}Cl. L'étude paléoenvironnementale bénéficie de la forte teneur en carbonates secondaires de nos échantillons limoneux. Ces carbonates secondaires se composent en partie de ciment diagénétique et de carbonates pédogéniques. Le ratio δ^{13}C dans les carbonates pédogéniques varie en fonction de la domination environnementale des plantes C_3 ou C_4, les deux groupes ayant un mode d'absorption du CO_2 distincte et se développant dans des conditions climatiques distinctes. Le ratio δ^{18}O varie en fonction du volume de précipitations et de leur saisonnalité. L'analyse de provenance Sr-Nd bénéficie des signatures isotopiques distinctes des principales unités géologiques de l'Himalaya (Morin, 2015).

Les résultats de notre étude sur le $\delta^{13}C$ pourraient permettre d'établir de nouvelles contraintes temporelles précises sur la transition vers une domination des plantes C_4 dans les plaines de l'Himalaya central. Ces nouvelles contraintes montreraient que le changement se produit de manière synchrone dans l'Himalaya central et occidental (nos résultats ; Quade et Cerling, 1995 ; Vögeli et al., 2017a). De plus, ils fourniraient la première preuve jamais dévoilée d'un retour à une végétation mixte en C_3 et C_4 à l'aube des glaciations de l'hémisphère nord. Nos résultats sur le $\delta^{18}O$ détectent qu'au moins la partie inférieure des sections Valmiki est affectée par la diagenèse précoce. Pour la partie supérieure, ils montreraient une aridification et/ou une augmentation de la saisonnalité au cours de la période, en dépit des glaciations de l'hémisphère nord, et contrairement à l'Himalaya occidental (Quade et Cerling, 1995). Ces résultats impliqueraient que l'intensité de la mousson sud-asiatique a varié au Cénozoïque tardif, avec un affaiblissement initial et un renforcement partiel ultérieur à l'aube des glaciations de l'hémisphère nord. Pour être validées, ces interprétations sur les signaux du $\delta^{13}C$ et du $\delta^{18}O$ demandent une analyse pétrographique approfondie des échantillons.

Notre analyse de provenance Sr-Nd combinée à nos concentrations en ^{10}Be implique que le bassin versant de la Narayani-Gandak demeure stable de 7,4 Ma à 1,2 Ma et n'a pas capturé d'affluents au nord. Nos résultats en Sr-Nd suggèrent une relative stabilité de l'érosion dans la chaîne inférieure, couverte par le Lesser Himalaya, malgré le duplexage en cours. Ils suggèrent également une diminution initiale des taux d'érosion sur le flanc sud et les sommets plus élevés, principalement couverts par le High Himalaya Crystalline (HHC) et dans une moindre mesure par les séries téthysiennes (TSS), suivie d'une réaugmentation après 1,7 Ma. Cette variabilité peut être attribuée aux fluctuations de la mousson sud-asiatique ou aux glaciations.

Nos résultats en ^{36}Cl impliquent que l'exposition récente aux rayons cosmiques est limitée pour la majeure partie des sections Valmiki. L'extension de ce résultat aux échantillons plus anciens nécessite de nouvelles mesures.

Le principal résultat des mesures effectuées sur les sections Valmiki est l'absence d'augmentation ou de diminution des taux moyens d'érosion dans le centre du Népal depuis environ 5 Ma, en dépit du changement climatique et en dépit de preuves géomorphologiques montrant clairement l'intensité des glaciations passées dans le centre du Népal. Cette stabilité, comparée aux variations des contributions du HHC et du TSS, implique que la diminution ou l'augmentation des taux d'érosion dans la partie Haut Himalaya du bassin de la Narayani-Gandak devrait être compensée par une diminution ou une augmentation ailleurs. Les taux d'érosion moyens dans le bassin Narayani-Gandak restent proches des valeurs modernes, à 2 mm/an. Ces valeurs sont supérieures au taux d'érosion moyen du Cône du Bengale et impliquent que certains segments de l'Himalaya ont des taux d'érosion bien inférieurs à 1 mm/an.

Le résultat secondaire est l'augmentation des taux d'érosion pendant la période de 7,4 à 5 Ma. Nous soulignons que cette augmentation doit être confirmée par d'autres mesures et modélisations. Une fois confirmée, cette augmentation pourrait signifier que l'initiation du duplexage a été plus tardive dans le centre du Népal que dans l'ouest du pays et que les paysages ont mis plusieurs millions d'années à s'adapter à cette nouvelle configuration tectonique. Cela remet en question l'hypothèse selon laquelle l'Himalaya dans le centre du Népal est en état d'équilibre depuis 10 Ma, du moins jusqu'à 5 Ma, ce qui devrait avoir un impact sur les études sur l'érosion dans cette région.

Dernier point concernant l'enregistrement de Valmiki, les taux d'érosion apparents dérivés de nos concentrations en ^{10}Be présentent une forte variabilité depuis 3,2 Ma. Ceci confirme des résultats antérieurs qui montrent le poids écrasant dans les sédiments des glissements de terrain à base profonde ou des glissements de terrain affectant les crêtes des chaînes de montagnes (Puchol et al., 2014 ; Dingle et al., 2018). Nous notons toutefois que la variabilité passée est beaucoup plus grande qu'à l'époque moderne, ce qui suggère qu'aucun analogue moderne des glissements de terrain que nous pouvons détecter dans notre enregistrement n'aurait jamais existé dans l'histoire récente. Cette variabilité n'affecte pas l'évolution du taux d'érosion moyen et nos conclusions.

X.3. CONCLUSION

Nos résultats démontrent que les taux d'érosion moyens dans l'Himalaya n'ont pas augmenté depuis au moins ca. 5 Ma, en dépit d'un changement important des conditions climatiques, comme le suggèrent nos mesures isotopiques complémentaires des concentrations en ^{10}Be. Cela implique que le changement climatique ne peut à lui seul augmenter ou diminuer les taux moyens d'érosion dans l'Himalaya, et que la tectonique est le principal moteur des variations des taux d'érosion moyens. Cependant, cela ne contredit pas les variations locales des taux d'érosion selon le climat, comme le montrerait notre analyse de provenance sur les sections Valmiki ou certaines études thermochronométriques in situ (Huntington et al., 2006). Pour obtenir un taux d'érosion moyen stable dans le bassin, une augmentation locale des taux d'érosion devrait être compensée par une diminution locale des taux d'érosion ailleurs. Mais ce concept nécessite de nouvelles mesures et modélisations pour être exploré.

La question à un million de dollars se pose à présent ainsi : pouvons-nous étendre notre approche et nos conclusions à d'autres chaînes de montagnes dans le monde ? Nous avons bénéficié de l'abondance en sable, provenant du volume considérable de sédiments fournis par la chaîne himalayenne, des bonnes contraintes de datation, de la grande taille du bassin de drainage amortissant les évolutions marginales du réseau de drainage, et des différences significatives dans la signature isotopique des formations couvrant le bassin de drainage. Une telle configuration idéale n'est peut-être pas disponible ailleurs, comme le

montrent les premiers travaux de Bierman et al (2016) au large du Groenland.

Les Andes sont une autre chaîne de montagnes pour laquelle on a interprété une augmentation apparente des taux d'érosion (Herman et al., 2013 ; Herman et Brandon, 2015). Plusieurs études ont porté sur le bassin d'avant-pays des Andes au nord-ouest de l'Argentine et ont mesuré les concentrations en ^{10}Be dans des sédiments quartzeux (Val et al., 2016 ; Amidon et al., 2017 ; Pingel et al., 2019). Deux études montrent une diminution des taux d'érosion qu'elles attribuent à l'augmentation de l'aridité, produite soit par le soulèvement tectonique créant une ombre pluviométrique (Pingel et al., 2019) soit par le changement climatique du Cénozoïque tardif (Amidon et al., 2017). Cependant, ces études n'ont probablement pas la même portée que les nôtres en raison de la taille limitée des bassins versants et des incertitudes quant à un éventuel recyclage.

Une autre étude (Puchol et al., 2017) a porté sur le Tianshan, une chaîne de montagnes pour laquelle une augmentation apparente des taux d'érosion a aussi été interprétée (Zhang et al., 2001 ; Molnar, 2004). Bien que le Tianshan soit situé à 1 700 km et 15°N des sections Valmiki, dans un contexte tectonique distinct, la tendance de leurs taux d'érosion moyens semble étonnamment similaire à notre enregistrement à Valmiki, soit une augmentation des taux d'environ 8 à 3-4 Ma suivie de taux stables. Même si l'augmentation apparente initiale des taux d'érosion exige des mesures et une modélisation plus poussées pour les sections Tianshan et Valmiki, la combinaison de leur étude et de la nôtre constitue un argument de poids en défaveur d'une augmentation des taux d'érosion pendant les glaciations de l'hémisphère Nord, du moins pour les orogènes actifs.

Cet argument est encore renforcé par une étude précédente qui démontre, à l'aide de la luminescence optiquement stimulée (LSO), que les taux d'érosion sont demeurés stables au cours du dernier cycle glaciaire dans les Alpes du Sud de la Nouvelle-Zélande (Herman et al., 2010b) et sont similaires aux taux d'érosion à long terme déduits de la thermochronométrie. Mais nous notons que leurs résultats peuvent ne pas être étendus à l'ensemble du Pléistocène, en raison d'une tendance différente suggérée par les résultats obtenus à l'aide de la thermochronométrie ^{4}He/^{3}He (Shuster et al., 2011).

Nos conclusions peuvent-elles s'étendre aux orogènes éteints ? De récents résultats obtenus sur le cône turbiditique du Var, qui recueille des sédiments provenant des Alpes du sud-ouest, en Europe, suggèrent une réponse négative (Mariotti, 2020). Leurs résultats, qui s'étendent sur le dernier cycle glaciaire, montrent que les taux d'érosion ont augmenté dans le dernier maximum glaciaire. Cependant, il pourrait s'agir d'un cas exceptionnel, et malheureusement, ni notre étude ni celle de Puchol et al (2017) n'ont cette résolution pour confirmer une situation aussi exceptionnelle au dernier maximum glaciaire dans l'Himalaya ou dans le Tianshan. Par conséquent, la réponse des orogènes éteints au changement climatique nécessite une étude plus approfondie sur des échelles de temps de plusieurs millions d'années. Cette réponse peut être différente de celle des orogènes actifs, que nos résultats montrent comme étant dominés par la tectonique.

BIBLIOGRAPHY

Acton, G.D., Petronotis, K.E., Cape, C.D., Ilg, S.R., Gordon, R.G., Bryan, P.C., 1996. A test of the geocentric axial dipole hypothesis from an analysis of the skewness of the central marine magnetic anomaly. Earth and Planetary Science Letters 144, 337 – 346. https://doi.org/10.1016/S0012-821X(96)00168-9

Adams, J., 1980. Contemporary uplift and erosion of the Southern Alps, New Zealand. Geological Society of America Bulletin 91, 1 – 114. https://doi.org/10.1130/gsab-p2-91-1

Adhikari, B.R., Wagreich, M., 2011. Provenance evolution of collapse graben fill in the Himalaya—The Miocene to Quaternary Thakkhola-Mustang Graben (Nepal). Sedimentary Geology 233, 1 – 14. https://doi.org/10.1016/j.sedgeo.2010.09.021

Agassiz, L., 1840. Etudes sur les glaciers. Jent et Gassmann. https://doi.org/10.1017/CBO9781139235877

Aitken, M.J., Stokes, S., 1997. Climatostratigraphy, in: Taylor, R.E., Aitken, M.J. (Eds.), Chronometric Dating in Archaeology. Springer US, Boston, MA, pp. 1 – 30. https://doi.org/10.1007/978-1-4757-9694-0_1

Allen, R., Najman, Y., Carter, A., Barfod, D., Bickle, M.J., Chapman, H.J., Garzanti, E., Vezzoli, G., Ando, S., Parrish, R.R., 2008. Provenance of the Tertiary sedimentary rocks of the Indo-Burman Ranges, Burma (Myanmar): Burman arc or Himalayan-derived? Journal of the Geological Society 165, 1045 – 1057. https://doi.org/10.1144/0016-76492007-143

Amidon, W.H., Burbank, D.W., Gehrels, G.E., 2005. U – Pb zircon ages as a sediment mixing tracer in the Nepal Himalaya. Earth and Planetary Science Letters 235, 244 – 260. https://doi.org/10.1016/j.epsl.2005.03.019

Amidon, W.H., Fisher, G.B., Burbank, D.W., Ciccioli, P.L., Alonso, R.N., Gorin, A.L., Silverhart, P.H., Kylander-Clark, A.R.C., Christoffersen, M.S., 2017. Mio-Pliocene aridity in the south-central Andes associated with Southern Hemisphere cold periods. Proceedings of the National Academy of Sciences 114, 6474 – 6479. https://doi.org/10.1073/pnas.1700327114

An, Z., Clemens, S.C., Shen, J., Qiang, X., Jin, Z., Sun, Y., Prell, W.L., Luo, J., Wang, S., Xu, H., Cai, Y., Zhou, W., Liu, X., Liu, W., Shi, Z., Yan, L., Xiao, X., Chang, H., Wu, F., Ai, L., Lu, F., 2011. Glacial-Interglacial Indian Summer Monsoon Dynamics. Science 333, 719 – 723. https://doi.org/10.1126/science.1203752

Andermann, C., Bonnet, S., Gloaguen, R., 2011. Evaluation of precipitation data sets along the Himalayan front. Geochemistry, Geophysics, Geosystems 12. https://doi.org/10.1029/2011gc003513

Andermann, C., Crave, A., Gloaguen, R., Davy, P., Bonnet, S., 2012. Connecting source and transport: Suspended sediments in the Nepal Himalayas. Earth and Planetary Science Letters 351 – 352, 158 – 170. https://doi.org/10.1016/j.epsl.2012.06.059

Andrews, J.T., Syvitski, J.P.M., 1994. Sediment fluxes along high latitude glaciated continental margins: Northeast Canada and Eastern Greenland. Material Fluxes on the Surface of the Earth 99 – 115.

Anell, I., Thybo, H., Stratford, W., 2010. Relating Cenozoic North Sea sediments to topography in southern Norway: The interplay between tectonics and climate. Earth and Planetary Science Letters 300, 19 – 32. https://doi.org/10.1016/j.epsl.2010.09.009

Antevs, E., 1952. Cenozoic climates of the Great Basin. Geologische Rundschau 40, 94 – 108. https://doi.org/10.1007/bf01803218

Anthony, D.M., Granger, D.E., 2007. A new chronology for the age of Appalachian erosional surfaces determined by cosmogenic nuclides in cave sediments. Earth Surface Processes and Landforms 32, 874 – 887. https://doi.org/10.1002/esp.1446

Appel, E., Rösler, W., Corvinus, G., 1991. Magnetostratigraphy of the Miocene-Pleistocene Surai Khola Siwaliks in West Nepal. Geophysical Journal International 105, 191 – 198. https://doi.org/10.1111/j.1365-246X.1991.tb03455.x

Arancibia, G., Matthews, S.J., de Arce, C.P., 2006. K – Ar and 40Ar/39Ar geochronology of supergene processes in the Atacama Desert, Northern Chile: tectonic and climatic relations. Journal of the Geological Society 163, 107 – 118. https://doi.org/10.1144/0016-764904-161

Argento, D.C., Stone, J.O., Reedy, R.C., O'Brien, K., 2015. Physics-based modeling of cosmogenic nuclides part I – Radiation

transport methods and new insights. Quaternary Geochronology 26, 29 – 43. https://doi.org/10.1016/j.quageo.2014.09.004

Argento, D.C., Stone, J.O., Reedy, R.C., O'Brien, K., 2015. Physics-based modeling of cosmogenic nuclides part II – Key aspects of in-situ cosmogenic nuclide production. Quaternary Geochronology 26, 44 – 55. https://doi.org/10.1016/j.quageo.2014.09.005

Arita, K., Ganzawa, Y., 1997. Thrust tectonics and uplift process of the Nepal Himalaya revealed from fission-track ages. Journal of Geography (Chigaku Zasshi) 106, 156 – 167. https://doi.org/10.5026/jgeography.106.156

Armstrong, R., Raup, B., Khalsa, S.J.S., Barry, R., Kargel, J., Helm, C., Kieffer, H., 2005. GLIMS glacier database. National Snow and Ice Data Center, Boulder, Colorado, USA.

Arndt, S., Regnier, P., Goddéris, Y., Donnadieu, Y., 2011. GEOCLIM reloaded (v 1.0): a new coupled earth system model for past climate change, Geosci. Model Dev., 4, 451 – 481, doi: 10.5194. Geoscientific Model Development 4, 451 – 481. https://doi.org/10.5194/gmd-4-451-2011

Arnold, M., Merchel, S., Bourlès, D.L., Braucher, R., Benedetti, L., Finkel, R.C., Aumaître, G., Gottdang, A., Klein, M., 2010. The French accelerator mass spectrometry facility ASTER: Improved performance and developments. Nuclear Instruments and Methods in Physics Research Section B: Beam Interactions with Materials and Atoms 268, 1954 – 1959. https://doi.org/10.1016/j.nimb.2010.02.107

Arrhenius, S., 1896. On the influence of carbonic acid in the air upon the temperature of the ground. The London, Edinburgh, and Dublin Philosophical Magazine and Journal of Science 41, 237 – 276. https://doi.org/10.1080/14786449608620846

Avouac, J.P., Burov, E.B., 1996. Erosion as a driving mechanism of intracontinental mountain growth. Journal of Geophysical Research: Solid Earth 101, 17747 – 17769. https://doi.org/10.1029/96JB01344

Avouac, J.-P., 2007. Dynamic processes in extensional and compressional settings-mountain building: from earthquakes to geological deformation, in: Schubert, G. (Ed.), Treatise on Geophysics, 6. pp. 377 – 439. https://doi.org/10.1016/b978-044452748-6.00112-7

Avouac, J.-P., 2015. Mountain Building: From earthquakes to geological deformation, in: Treatise on Geophysics. pp. 381 – 432. https://doi.org/10.1016/b978-0-444-53802-4.00120-2

Balco, G., Stone, J.O., Lifton, N.A., Dunai, T.J., 2008. A complete and easily accessible means of calculating surface exposure ages or erosion rates from 10Be and 26Al measurements. Quaternary Geochronology, Prospects for the New Frontiers of earth and Environmental Sciences 3, 174 – 195. https://doi.org/10.1016/j.quageo.2007.12.001

Balco, G., 2017. Production rate calculations for cosmic-ray-muon-produced 10 Be and 26 Al benchmarked against geological calibration data. Quaternary Geochronology 39, 150 – 173. https://doi.org/10.1016/j.quageo.2017.02.001

Baldwin, B., Butler, C.O., 1985. Compaction Curves. AAPG Bulletin 69, 622-626.

Baran, R., Friedrich, A.M., Schlunegger, F., 2014. The late Miocene to Holocene erosion pattern of the Alpine foreland basin reflects Eurasian slab unloading beneath the western Alps rather than global climate change. Lithosphere 6, 124 – 131. https://doi.org/10.1130/L307.1

Barrell, J., 1917. Rhythms and the measurements of geologic time. Geological Society of America Bulletin 28, 745 – 904. https://doi.org/10.1130/GSAB-28-745

Barry, J.C., Morgan, M.E., Flynn, L.J., Pilbeam, D., Behrensmeyer, A.K., Raza, S.M., Khan, I.A., Badgley, C., Hicks, J., Kelley, J., 2002. Faunal and environmental change in the late Miocene Siwaliks of northern Pakistan. Paleobiology 28, 1 – 71. https://doi.org/10.1666/0094-8373(2002)28[1:FAECIT]2.0.CO;2

Bartoli, G., Sarnthein, M., Weinelt, M., Erlenkeuser, H., Garbe-Schönberg, D., Lea, D.W., 2005. Final closure of Panama and the onset of northern hemisphere glaciation. Earth and Planetary Science Letters 237, 33 – 44. https://doi.org/10.1016/j.epsl.2005.06.020

Beaumont, C., Fullsack, P., Hamilton, J., 1992. Erosional control of active compressional orogens, in: McClay, K.R. (Ed.), Thrust Tectonics. Springer Netherlands, Dordrecht, pp. 1 – 18. https://doi.org/10.1007/978-94-011-3066-0_1

Beaumont, C., Jamieson, R.A., Nguyen, M.H., Lee, B., 2001. Himalayan tectonics explained by extrusion of a low-viscosity crustal channel coupled to focused surface denudation. Nature 414, 738 – 742. https://doi.org/10.1038/414738a

Beerling, D.J., Royer, D.L., 2011. Convergent Cenozoic CO2 history. Nature Geosci 4, 418 – 420. https://doi.org/10.1038/ngeo1186

Beerling, D., Berner, R.A., Mackenzie, F.T., Harfoot, M.B., Pyle, J.A., 2009. Methane and the CH4 related greenhouse effect over the past 400 million years. American Journal of Science 309, 97 – 113. https://doi.org/10.2475/02.2009.01

Bennett, M.M., Glasser, N.F., 2011. Glacial geology: ice sheets and landforms. John Wiley & Sons.

Bereiter, B., Eggleston, S., Schmitt, J., Nehrbass-Ahles, C., Stocker, T.F., Fischer, H., Kipfstuhl, S., Chappellaz, J., 2015. Revision of the EPICA Dome C CO2 record from 800 to 600 kyr before present. Geophysical Research Letters 42, 542 – 549. https://doi.org/10.1002/2014GL061957

Behrensmeyer, A.K., Quade, J., Cerling, T.E., Kappelman, J., Khan, I.A., Copeland, P., Roe, L., Hicks, J., Stubblefield, P., Willis, B.J., 2007. The structure and rate of late Miocene expansion of C4 plants: Evidence from lateral variation in stable isotopes in paleosols of the Siwalik Group, northern Pakistan. Geological Society of America Bulletin 119, 1486 – 1505. https://doi.org/10.1130/b26064.1

Behrensmeyer, A.K., Quade, J., Cerling, T.E., Kappelman, J., Khan, I.A., Copeland, P., Roe, L., Hicks, J., Stubblefield, P., Willis, B.J., Latorre, C., 2007. Evidence from lateral variation in stable isotopes in paleosols of the Siwalik Group, northern Pakistan. Geological Society of America Bulletin 119, 1486 – 1505. https://doi.org/10.1130/B26064.1

Berger, A., Jouanne, F., Hassani, R., Mugnier, J.L., 2004. Modelling the spatial distribution of present-day deformation in Nepal: how cylindrical is the Main Himalayan Thrust in Nepal? Geophysical Journal International 156, 94 – 114. https://doi.org/10.1111/j.1365-246X.2004.02038.x

Bergmann, F., 2018. The Bengal Fan on different temporal and spatial scales. Integrating seismoacoustic and IODP Expedition 354 data to examine internal and external controls on depositional processes. Bremen University, Bremen, Germany. https://www.marum.de/Binaries/Binary17731/PhD-Defence-Bergmann-Fenna.pdf

Bernard, S., Daval, D., Ackerer, P., Pont, S., Meibom, A., 2017. Burial-induced oxygen-isotope re-equilibration of fossil foraminifera explains ocean paleotemperature paradoxes. Nature Communications 8, 1134. https://doi.org/10.1038/s41467-017-01225-9

Berner, R.A., Caldeira, K., 1997. The need for mass balance and feedback in the geochemical carbon cycle. Geology 25, 955 – 956. https://doi.org/10.1130/0091-7613(1997)025<0955:tnfmba>2.3.co;2

Berner, R.A., 1999. A new look at the long-term carbon cycle. GSA Today 9, 1 – 6.

Berner, R.A., 2004. The phanerozoic carbon cycle: CO_2 and O_2. Oxford University Press, Oxford ; New York.

Bernet, M., Spiegel, C., 2004. Introduction: Detrital thermochronology, in: Bernet, M., Spiegel, C. (Eds.), Detrital Thermochronology - Provenance Analysis, Exhumation, and Landscape Evolution of Mountain Belts. Geological Society of America Special Paper 378, Boulder, Colorado, pp. 1 – 6. https://doi.org/10.1130/0-8137-2378-7.1

Bernet, M., Zattin, M., Garver, J.I., Brandon, M.T., Vance, J.A., 2001. Steady-state exhumation of the European Alps. Geology 29, 35 – 38. https://doi.org/10.1130/0091-7613(2001)029<0035:sseote>2.0.co;2

Bernet, M., van der Beek, P., Pik, R., Huyghe, P., Mugnier, J.-L., Labrin, E., Szulc, A., 2006. Miocene to Recent exhumation of the central Himalaya determined from combined detrital zircon fission-track and U/Pb analysis of Siwalik sediments, western Nepal. Basin Research 18, 393 – 412. https://doi.org/10.1111/j.1365-2117.2006.00303.x

Best, J.L., Ashworth, P.J., Sarker, M.H., Roden, J.E., 2007. The Brahmaputra-Jamuna River, Bangladesh, in: Gupta, A. (Ed.), Large Rivers: Geomorphology and Management. pp. 395 – 430. https://doi.org/10.1002/9780470723722.ch19

Bettinelli, P., Avouac, J.-P., Flouzat, M., Jouanne, F., Bollinger, L., Willis, P., Chitrakar, G.R., 2006. Plate motion of India and interseismic strain in the Nepal Himalaya from GPS and DORIS measurements. Journal of Geodesy

80, 567 – 589. https://doi.org/10.1007/s00190-006-0030-3

Bettinelli, P., Avouac, J.-P., Flouzat, M., Bollinger, L., Ramillien, G., Rajaure, S., Sapkota, S., 2008. Seasonal variations of seismicity and geodetic strain in the Himalaya induced by surface hydrology. Earth and Planetary Science Letters 266, 332 – 344. https://doi.org/10.1016/j.epsl.2007.11.021

Beyssac, O., Simoes, M., Avouac, J.P., Farley, K.A., Chen, Y.-G., Chan, Y.-C., Goffé, B., 2007. Late Cenozoic metamorphic evolution and exhumation of Taiwan. Tectonics 26, TC6001. https://doi.org/10.1029/2006TC002064

Bierman, P.R., Shakun, J.D., Corbett, L.B., Zimmerman, S.R., Rood, D.H., 2016. A persistent and dynamic East Greenland Ice Sheet over the past 7.5 million years. Nature 540, 256 – 260. https://doi.org/10.1038/nature20147

Biggin, A.J., McCormack, A., Roberts, A., 2010. Paleointensity database updated and upgraded. Eos, Transactions American Geophysical Union 91, 15. https://doi.org/10.1029/2010eo020003

Bishop, P., 1995. Drainage rearrangement by river capture, beheading and diversion. Progress in Physical Geography: Earth and Environment 19, 449 – 473. https://doi.org/10.1177/030913339501900402

Biswas, S., Coutand, I., Grujic, D., Hager, C., Stöckli, D., Grasemann, B., 2007. Exhumation and uplift of the Shillong plateau and its influence on the eastern Himalayas: New constraints from apatite and zircon (U-Th-[Sm])/He and apatite fission track analyses: UPLIFT OF THE SHILLONG PLATEAU. Tectonics 26, n/a-n/a. https://doi.org/10.1029/2007TC002125

Blum, J.D., Gazis, C.A., Jacobson, A.D., Page Chamberlain, C., 1998. Carbonate versus silicate weathering in the Raikhot watershed within the High Himalayan Crystalline Series. Geology 26, 411 – 414. https://doi.org/10.1130/0091-7613(1998)026<0411:cvswit>2.3.co;2

Blum, M., Rogers, K., Gleason, J., Najman, Y., Cruz, J., Fox, L., 2018. Allogenic and Autogenic Signals in the Stratigraphic Record of the Deep-Sea Bengal Fan. Scientific Reports 8. https://doi.org/10.1038/s41598-018-25819-5

Blythe, A.E., Burbank, D.W., Carter, A., Schmidt, K., Putkonen, J., 2007. Plio-Quaternary exhumation history of the central Nepalese Himalaya: 1. Apatite and zircon fission track and apatite [U-Th]/He analyses: CENTRAL NEPAL PLIO-QUATERNARY EXHUMATION. Tectonics 26, n/a-n/a. https://doi.org/10.1029/2006TC001990

Boggs, S., 2014. Principles of sedimentology and stratigraphy, 5th ed. Pearson, Harlow.

Bollinger, L., Nicolas, M., Marin, S., 2010. Hydrological triggering of the seismicity around a salt diapir in Castellane, France. Earth and Planetary Science Letters 290, 20 – 29. https://doi.org/10.1016/j.epsl.2009.11.051

Bookhagen, B., Burbank, D.W., 2006. Topography, relief, and TRMM-derived rainfall variations along the Himalaya. Geophysical Research Letters 33. https://doi.org/10.1029/2006GL026037

Bookhagen, B., Burbank, D.W., 2006. Correction to "Topography, relief, and TRMM-derived rainfall variations along the Himalaya." Geophysical Research Letters 33. https://doi.org/10.1029/2006gl026944

Bookhagen, B., Burbank, D.W., 2010. Toward a complete Himalayan hydrological budget: Spatiotemporal distribution of snowmelt and rainfall and their impact on river discharge. Journal of Geophysical Research 115. https://doi.org/10.1029/2009JF001426

Bookhagen, B., Thiede, R.C., Strecker, M.R., 2005. Abnormal monsoon years and their control on erosion and sediment flux in the high, arid northwest Himalaya. Earth and Planetary Science Letters 231, 131 – 146. https://doi.org/10.1016/j.epsl.2004.11.014

Boos, W.R., Kuang, Z., 2010. Dominant control of the South Asian monsoon by orographic insulation versus plateau heating. Nature 463, 218 – 222. https://doi.org/10.1038/nature08707

Boos, W.R., Kuang, Z., 2013. Sensitivity of the South Asian monsoon to elevated and non-elevated heating. Scientific Reports 3. https://doi.org/10.1038/srep01192

Bordet, P., Colchen, M., Lefort, P., Mouterde, R., Remy, M., 1967. Donnees nouvelles sur la geologie de la Thakkhola (Himalaya du Nepal). Bulletin de la Société Géologique de France S7-IX, 883 – 896. https://doi.org/10.2113/gssgfbull.S7-IX.6.883

Bouma, A.H., Stone, C.G., 2000. Fine-grained turbidite systems. AAPG Memoir 72.

Bourles, D., Raisbeck, G.M., Yiou, F., 1989. 10Be and 9Be in marine sediments and their potential for dating. Geochimica et Cosmochimica Acta 53, 443 – 452. https://doi.org/10.1016/0016-7037(89)90395-5

Bowen, G.J., Wilkinson, B., 2002. Spatial distribution of δ 18O in meteoric precipitation. Geology 30, 315 – 318. https://doi.org/10.1130/0091-7613(2002)030<0315:sdooim>2.0.co;2

Bracciali, L., Najman, Y., Parrish, R.R., Akhter, S.H., Millar, I., 2015. The Brahmaputra tale of tectonics and erosion: Early Miocene river capture in the Eastern Himalaya. Earth and Planetary Science Letters 415, 25 – 37. https://doi.org/10.1016/j.epsl.2015.01.022

Bracciali, L., Parrish, R.R., Najman, Y., Smye, A., Carter, A., Wijbrans, J.R., 2016. Plio-Pleistocene exhumation of the eastern Himalayan syntaxis and its domal 'pop-up'. Earth-Science Reviews 160, 350 – 385. https://doi.org/10.1016/j.earscirev.2016.07.010

Brandon, M.T., Roden-Tice, M.K., Garver, J.I., 1998. Late Cenozoic exhumation of the Cascadia accretionary wedge in the Olympic Mountains, northwest Washington State. Geological Society of America Bulletin 110, 985 – 1009. https://doi.org/10.1130/0016-7606(1998)110<0985:lceotc>2.3.co;2

Brandon, M.T., 2002. Decomposition of mixed grain age distributions using Binomfit. On track 24, 13 – 18.

Branner, J.C., 1897. Bacteria and the Decomposition of Rocks. American Journal of Science 3, 438. https://doi.org/10.2475/ajs.s4-3.18.438

Braucher, R., Brown, E.T., Bourlès, D.L., Colin, F., 2003. In situ produced 10Be measurements at great depths: implications for production rates by fast muons. Earth and Planetary Science Letters 211, 251 – 258. https://doi.org/10.1016/S0012-821X(03)00205-X

Braucher, R., Merchel, S., Borgomano, J., Bourlès, D.L., 2011. Production of cosmogenic radionuclides at great depth: A multi element approach. Earth and Planetary Science Letters 309, 1 – 9. https://doi.org/10.1016/j.epsl.2011.06.036

Braucher, R., Bourlès, D., Merchel, S., Romani, J.V., Fernadez-Mosquera, D., Marti, K., Leanni, L., Chauvet, F., Arnold, M., Aumaître, G., 2013. Determination of muon attenuation lengths in depth profiles from in situ produced cosmogenic nuclides. Nuclear Instruments and Methods in Physics Research Section B: Beam Interactions with Materials and Atoms 294, 484 – 490. https://doi.org/10.1016/j.nimb.2012.05.023

Braucher, R., Guillou, V., Bourlès, D.L., Arnold, M., Aumaître, G., Keddadouche, K., Nottoli, E., 2015. Preparation of ASTER in-house 10Be/9Be standard solutions. Nuclear Instruments and Methods in Physics Research Section B: Beam Interactions with Materials and Atoms 361, 335 – 340. https://doi.org/10.1016/j.nimb.2015.06.012

Braun, J., van der Beek, P., Valla, P., Robert, X., Herman, F., Glotzbach, C., Pedersen, V., Perry, C., Simon-Labric, T., Prigent, C., 2012. Quantifying rates of landscape evolution and tectonic processes by thermochronology and numerical modeling of crustal heat transport using PECUBE. Tectonophysics 524 – 525, 1 – 28. https://doi.org/10.1016/j.tecto.2011.12.035

Braun, J., Gemignani, L., Van Der Beek, P., 2018. Extracting information on the spatial variability in erosion rate stored in detrital cooling age distributions in river sands. Earth Surface Dynamics 6, 257. https://doi.org/10.5194/esurf-6-257-2018

Bristow, C.S., 1999. Gradual Avulsion, River Metamorphosis and Reworking by Underfit Streams: a Modern Example from the Brahmaputra River in Bangladesh and a Possible Ancient Example in the Spanish Pyrenees, in: Smith, N.D., Rogers, J. (Eds.), Fluvial Sedimentology VI. Blackwell Publishing Ltd., Oxford, UK, pp. 221 – 230. https://doi.org/10.1002/9781444304213.ch17

Brookfield, M.E., 1998. The evolution of the great river systems of southern Asia during the Cenozoic India-Asia collision: rivers draining southwards. Geomorphology 22, 285 – 312. https://doi.org/10.1016/S0169-555X(97)00082-2

Brown, E.T., Edmond, J.M., Raisbeck, G.M., Yiou, F., Kurz, M.D., Brook, E.J., 1991. Examination of surface exposure ages of Antarctic moraines using in situ produced 10Be and 26Al. Geochimica et Cosmochimica Acta 55, 2269 – 2283. https://doi.org/10.1016/0016-7037(91)90103-C

Brown, E.T., Brook, E.J., Raisbeck, G.M., Yiou, F., Kurz, M.D., 1992. Effective attenuation

lengths of cosmic rays producing 10Be AND 26Al in quartz: Implications for exposure age dating. Geophys. Res. Lett. 19, 369 – 372. https://doi.org/10.1029/92GL00266

Brown, E.T., Measures, C.I., Edmond, J.M., Bourlès, D.L., Raisbeck, G.M., Yiou, F., 1992. Continental inputs of beryllium to the oceans. Earth and planetary science letters 114, 101 – 111. https://doi.org/10.1016/0012-821x(92)90154-n

Brown, E.T., Stallard, R.F., Larsen, M.C., Raisbeck, G.M., Yiou, F., 1995. Denudation rates determined from the accumulation of in situ-produced 10Be in the luquillo experimental forest, Puerto Rico. Earth and Planetary Science Letters 129, 193 – 202. https://doi.org/10.1016/0012-821X(94)00249-X

Brozović, N., Burbank, D.W., Meigs, A.J., 1997. Climatic Limits on Landscape Development in the Northwestern Himalaya. Science 276, 571 – 574. https://doi.org/10.1126/science.276.5312.571

Bukry, D., 1973. Low-latitude coccolith biostratigraphic zonation. Initial Reports of the Deep Sea Drilling Project, 15 685-703.

Burbank, D.W., Anderson, R.S., 2011. Tectonic Geomorphology. John Wiley & Sons, Ltd, Chichester, UK. https://doi.org/10.1002/9781444345063

Burbank, D.W., 1992. Causes of recent Himalayan uplift deduced from deposited patterns in the Ganges basin. Nature 357, 680 – 683. https://doi.org/10.1038/357680a0

Burchfiel, B.C., Chen, Zhiliang, Hodges, Kip V., Liu, Yuping, Royden, Leigh H., Deng, Changrong, Xu, Jiene, 1992. The South Tibetan detachment system, Himalayan orogen: Extension contemporaneous with and parallel to shortening in a collision mountain belt., in: The South Tibetan Detachment System, Himalayan Orogen: Extension Contemporaneous with and Parallel to Shortening in a Collision Mountain Belt. Geological Society of America Special Paper 269, pp. 1 – 41. https://doi.org/10.1130/spe269-p1

Burg, J.P., Brunel, M., Gapais, D., Chen, G.M., Liu, G.H., 1984. Deformation of leucogranites of the crystalline Main Central Sheet in southern Tibet (China). Journal of Structural Geology 6, 535 – 542. https://doi.org/10.1016/0191-8141(84)90063-4

Burg, J.-P., Davy, P., Nievergelt, P., Oberli, F., Seward, D., Diao, Z., Meier, M., 1997. Exhumation during crustal folding in the Namche-Barwa syntaxis. Terra Nova 9, 53 – 56. https://doi.org/10.1111/j.1365-3121.1997.tb00001.x

Burgess, P.M., Hovius, N., 1998. Rates of delta progradation during highstands: consequences for timing of deposition in deep-marine systems. Journal of the Geological Society 155, 217 – 222. https://doi.org/10.1144/gsjgs.155.2.0217

Calais, E., Freed, A.M., Van Arsdale, R., Stein, S., 2010. Triggering of New Madrid seismicity by late-Pleistocene erosion. Nature 466, 608 – 612. https://doi.org/10.1038/nature09258

Carcaillet, J.T., Bourlès, D.L., Thouveny, N., 2004. Geomagnetic dipole moment and 10Be production rate intercalibration from authigenic 10Be/9Be for the last 1.3 Ma. Geochemistry, Geophysics, Geosystems 5, n/a-n/a. https://doi.org/10.1029/2003GC000641

Carignan, J., Hild, P., Mevelle, G., Morel, J., Yeghicheyan, D., 2001. Routine Analyses of Trace Elements in Geological Samples using Flow Injection and Low Pressure On-Line Liquid Chromatography Coupled to ICP-MS: A Study of Geochemical Reference Materials BR, DR-N, UB-N, AN-G and GH. Geostandards Newsletter 25, 187 – 198. https://doi.org/10.1111/j.1751-908X.2001.tb00595.x

Carson, E.C., Rawling III, J.E., Attig, J.W., Bates, B.R., 2018. Late Cenozoic evolution of the upper Mississippi River, stream piracy, and reorganization of North American Mid-Continent drainage systems. GSA Today 28. https://doi.org/10.1130/GSATG355A.1

Carter, R.M., Carter, L., 1996. The abyssal bounty fan and lower Bounty Channel: evolution of a rifted-margin sedimentary system. Marine Geology 130, 181 – 202. https://doi.org/10.1016/0025-3227(95)00139-5

Carter, S.P., Fricker, H.A., Siegfried, M.R., 2013. Evidence of rapid subglacial water piracy under Whillans Ice Stream, West Antarctica. Journal of Glaciology 59, 1147 – 1162. https://doi.org/10.3189/2013jog13j085

Carter, A., Riley, T.R., Hillenbrand, C.-D., Rittner, M., 2017. Widespread Antarctic glaciation during the Late Eocene. Earth and Planetary

Science Letters 458, 49 – 57. https://doi.org/10.1016/j.epsl.2016.10.045

Catlos, E.J., Harrison, T.M., Kohn, M.J., Grove, M., Ryerson, F.J., Manning, C.E., Upreti, B.N., 2001. Geochronologic and thermobarometric constraints on the evolution of the Main Central Thrust, central Nepal Himalaya. J. Geophys. Res. 106, 16177 – 16204. https://doi.org/10.1029/2000JB900375

Caves, J.K., Winnick, M.J., Graham, S.A., Sjostrom, D.J., Mulch, A., Chamberlain, C.P., 2015. Role of the westerlies in Central Asia climate over the Cenozoic. Earth and Planetary Science Letters 428, 33 – 43. https://doi.org/10.1016/j.epsl.2015.07.023

Caves Rugenstein, J.K., Chamberlain, C.P., 2018. The evolution of hydroclimate in Asia over the Cenozoic: A stable-isotope perspective. Earth-Science Reviews 185, 1129 – 1156. https://doi.org/10.1016/j.earscirev.2018.09.003

Célérier, J., Harrison, T.M., Webb, A.A.G., Yin, A., 2009. The Kumaun and Garwhal Lesser Himalaya, India: Part 1. Structure and stratigraphyThe Kumaun and Garwhal Lesser Himalaya: Structure and stratigraphy. Geological Society of America Bulletin 121, 1262 – 1280. https://doi.org/10.1130/b26344.1

Cerling, T.E., Quade, J., Wang, Y., Bowman, J.R., 1989. Carbon isotopes in soils and palaeosols as ecology and palaeoecology indicators. Nature 341, 138 – 139. https://doi.org/10.1038/341138a0

Cerling, T.E., Harris, J.M., MacFadden, B.J., Leakey, M.G., Quade, J., Eisenmann, V., Ehleringer, J.R., 1997. Global vegetation change through the Miocene/Pliocene boundary. Nature 389, 153 – 158. https://doi.org/10.1038/38229

Cerling, T.E., 1984. The stable isotopic composition of modern soil carbonate and its relationship to climate. Earth and Planetary Science Letters 71, 229 – 240. https://doi.org/10.1016/0012-821X(84)90089-X

Chamberlin, T.C., 1899. An attempt to frame a working hypothesis of the cause of glacial periods on an atmospheric basis. The Journal of Geology 7, 545 – 584. https://doi.org/10.1086/608449

Champagnac, J.-D., Valla, P.G., Herman, F., 2014. Late-Cenozoic relief evolution under evolving climate: A review. Tectonophysics 614, 44 – 65. https://doi.org/10.1016/j.tecto.2013.11.037

Chandler, R., Scott, M., 2011. Statistical Methods for Trend Detection and Analysis in the Environmental Sciences, Wiley. ed, Statistics in practice.

Chapin, C.E., 2008. Interplay of oceanographic and paleoclimate events with tectonism during middle to late Miocene sedimentation across the southwestern USA. Geosphere 4, 976 – 991. https://doi.org/10.1130/GES00171.1

Charalambus, S., 1971. Nuclear transmutation by negative stopped muons and the activity induced by the cosmic-ray muons. Nuclear Physics A 166, 145 – 161. https://doi.org/10.1016/0375-9474(71)90419-2

Charreau, J., Chen, Y., Gilder, S., Dominguez, S., Avouac, J.-P., Sen, S., Sun, D., Li, Y., Wang, W.-M., 2005. Magnetostratigraphy and rock magnetism of the Neogene Kuitun He section (northwest China): implications for Late Cenozoic uplift of the Tianshan mountains. Earth and Planetary Science Letters 230, 177 – 192. https://doi.org/10.1016/j.epsl.2004.11.002

Charreau, J., Gilder, S., Chen, Y., Dominguez, S., Avouac, J.-P., Sen, S., Jolivet, M., Li, Y., Wang, W., 2006. Magnetostratigraphy of the Yaha section, Tarim Basin (China): 11 Ma acceleration in erosion and uplift of the Tian Shan mountains. Geology 34, 181 – 184. https://doi.org/10.1130/G22106.1

Charreau, J., Gumiaux, C., Avouac, J.-P., Augier, R., Chen, Y., Barrier, L., Gilder, S., Dominguez, S., Charles, N., Wang, Q., 2009. The Neogene Xiyu Formation, a diachronous prograding gravel wedge at front of the Tianshan: Climatic and tectonic implications. Earth and Planetary Science Letters 287, 298 – 310. https://doi.org/10.1016/j.epsl.2009.07.035

Charreau, J., Chen, Y., Gilder, S., Barrier, L., Dominguez, S., Augier, R., Sen, S., Avouac, J.-P., Gallaud, A., Graveleau, F., Wang, Q., 2009. Neogene uplift of the Tian Shan Mountains observed in the magnetic record of the Jingou River section (northwest China). Tectonics 28. https://doi.org/10.1029/2007TC002137

Charreau, J., Blard, P.-H., Puchol, N., Avouac, J.-P., Lallier-Vergès, E., Bourlès, D., Braucher, R., Gallaud, A., Finkel, R., Jolivet, M., Chen, Y., Roy, P., 2011. Paleo-erosion rates in Central Asia since 9Ma: A transient increase at the onset of Quaternary glaciations? Earth and

Planetary Science Letters 304, 85 – 92. https://doi.org/10.1016/j.epsl.2011.01.018

Charreau, J., Blard, P.-H., Zumaque, J., Martin, L.C.P., Delobel, T., Szafran, L., 2019. Basinga: A cell-by-cell GIS toolbox for computing basin average scaling factors, cosmogenic production rates and denudation rates. Earth Surface Processes and Landforms. https://doi.org/10.1002/esp.4649

Charreau, J., Lavé, J., France-Lanord, C., Blard, P.-H., Pik, R., Puchol, N., Gajurel, A.P., ASTER Team, in prep. A high resolution, 6 Myr record of paleodenudation rates in Central Himalayas inferred from cosmogenic nuclides in the Surai Khola section.

Chirouze, F., Dupont-Nivet, G., Huyghe, P., Beek, P. van der, Chakraborti, T., Bernet, M., Erens, V., 2012. Magnetostratigraphy of the Neogene Siwalik Group in the far eastern Himalaya: Kameng section, Arunachal Pradesh, India. Journal of Asian Earth Sciences 44, 117 – 135. https://doi.org/10.1016/j.jseaes.2011.05.016

Chirouze, F., Huyghe, P., van der Beek, P., Chauvel, C., Chakraborty, T., Dupont-Nivet, G., Bernet, M., 2013. Tectonics, exhumation, and drainage evolution of the eastern Himalaya since 13 Ma from detrital geochemistry and thermochronology, Kameng River Section, Arunachal Pradesh. Geological Society of America Bulletin 125, 523 – 538. https://doi.org/10.1130/B30697.1

Chmeleff, J., von Blanckenburg, F., Kossert, K., Jakob, D., 2010. Determination of the 10Be half-life by multicollector ICP-MS and liquid scintillation counting. Nuclear Instruments and Methods in Physics Research Section B: Beam Interactions with Materials and Atoms 268, 192 – 199. https://doi.org/10.1016/j.nimb.2009.09.012

Christeleit, E.C., Brandon, M.T., Shuster, D.L., 2017. Miocene development of alpine glacial relief in the Patagonian Andes, as revealed by low-temperature thermochronometry. Earth and Planetary Science Letters 460, 152 – 163. https://doi.org/10.1016/j.epsl.2016.12.019

Cina, S.E., Yin, A., Grove, M., Dubey, C.S., Shukla, D.P., Lovera, O.M., Kelty, T.K., Gehrels, G.E., Foster, D.A., 2009. Gangdese arc detritus within the eastern Himalayan Neogene foreland basin: Implications for the Neogene evolution of the Yalu – Brahmaputra River system. Earth and Planetary Science Letters 285, 150 – 162. https://doi.org/10.1016/j.epsl.2009.06.005

Clark, M., Bilham, R., 2008. Miocene rise of the Shillong Plateau and the beginning of the end for the Eastern Himalaya. Earth and Planetary Science Letters 269, 337 – 351. https://doi.org/10.1016/j.epsl.2008.01.045

Clark, M.K., Schoenbohm, L.M., Royden, L.H., Whipple, K.X., Burchfiel, B.C., Zhang, X., Tang, W., Wang, E., Chen, L., 2004. Surface uplift, tectonics, and erosion of eastern Tibet from large-scale drainage patterns. Tectonics 23, n/a-n/a. https://doi.org/10.1029/2002tc001402

Clarke, B.A., Burbank, D.W., 2011. Quantifying bedrock-fracture patterns within the shallow subsurface: Implications for rock mass strength, bedrock landslides, and erodibility. Journal of Geophysical Research: Earth Surface 116. https://doi.org/10.1029/2011JF001987

Clemens, S.C., Tiedemann, R., 1997. Eccentricity forcing of Pliocene – early Pleistocene climate revealed in a marine oxygen-isotope record. Nature 385, 801. https://doi.org/10.1038/385801a0

Clemens, S., Prell, W., Murray, D., Shimmield, G., Weedon, G., 1991. Forcing mechanisms of the Indian Ocean monsoon. Nature 353, 720 – 725. https://doi.org/10.1038/353720a0

Clemens, S.C., Prell, W.L., Sun, Y., Liu, Z., Chen, G., 2008. Southern Hemisphere forcing of Pliocene δ18O and the evolution of Indo-Asian monsoons. Paleoceanography 23, PA4210. https://doi.org/10.1029/2008PA001638

Clemens, S.C., Kuhnt, W., LeVay, L.J., Anand, P., Ando, T., Bartol, M., Bolton, C.T., Ding, X., Gariboldi, K., Giosan, L., Hathorne, E.C., Huang, Y., Jaiswal, P., Kim, S., Kirkpatrick, J.B., Littler, K., Marino, G., Martinez, P., Naik, D., Peketi, A., Phillips, S.C., Robinson, M.M., Romero, O.E., Sagar, N., Taladay, K.B., Taylor, S.N., Thirumalai, K., Uramoto, G., Usui, Y., Wang, J., Yamamoto, M.,, Zhou, L., 2016. Expedition 353 summary, in: Clemens, S.C., Kuhnt, W., LeVay, L.J., the Expedition 353 Scientists (Eds.), Indian Monsoon Rainfall. Proceedings of the International Ocean Discovery Program, 353, pp. 1 – 32. https://doi.org/10.14379/iodp.proc.353.101.2016

Clift, P., Gaedicke, C., 2002. Accelerated mass flux to the Arabian Sea during the middle to late Miocene. Geology 30, 207. https://doi.org/10.1130/0091-7613(2002)030<0207:AMFTTA>2.0.CO;2

Clift, P.D., Webb, A.A.G., 2018. A history of the Asian monsoon and its interactions with solid Earth tectonics in Cenozoic South Asia, in: Treloar, P. J., Searle, M. P. (Eds.), Himalayan Tectonics: A Modern Synthesis. Geological Society, London, Special Publications, 483, p. SP483.1. https://doi.org/10.1144/SP483.1

Clift, P., Gaedicke, C., Edwards, R., Lee, J.I., Hildebrand, P., Amjad, S., White, R.S., Schlü ter, H.-U., 2002. The stratigraphic evolution of the Indus Fan and the history of sedimentation in the Arabian Sea. Marine Geophysical Researches 23, 223 − 245. https://doi.org/10.1023/A:1023627123093

Clift, P.D., Hodges, K.V., Heslop, D., Hannigan, R., Van Long, H., Calves, G., 2008. Correlation of Himalayan exhumation rates and Asian monsoon intensity. Nature Geoscience 1, 875 − 880. https://doi.org/10.1038/ngeo351

Clift, P.D., Wan, S., Blusztajn, J., 2014. Reconstructing chemical weathering, physical erosion and monsoon intensity since 25 Ma in the northern South China Sea: A review of competing proxies. Earth-Science Reviews 130, 86 − 102. https://doi.org/10.1016/j.earscirev.2014.01.002

Clift, P.D., 2006. Controls on the erosion of Cenozoic Asia and the flux of clastic sediment to the ocean. Earth and Planetary Science Letters 241, 571 − 580. https://doi.org/10.1016/j.epsl.2005.11.028

Codilean, A., Munack, H., Cohen, T., Saktura, W., Gray, A., Mudd, S., 2018. OCTOPUS: An open cosmogenic isotope and luminescence database. Faculty of Science, Medicine and Health - Papers: Part B 2123 − 2139. https://doi.org/10.5194/essd-10-2123-2018

Codilean, A.T., 2006. Calculation of the cosmogenic nuclide production topographic shielding scaling factor for large areas using DEMs. Earth Surface Processes and Landforms 31, 785 − 794. https://doi.org/10.1002/esp.1336

Cogné, J.-P., Humler, E., 2004. Temporal variation of oceanic spreading and crustal production rates during the last 180 My. Earth and Planetary Science Letters 227, 427 − 439. https://doi.org/10.1016/j.epsl.2004.09.002

Colbourn, G., Ridgwell, A., Lenton, T.M., 2013. The rock geochemical model (RokGeM) v0. 9. Geoscientific Model Development 6, 1543 − 1573. https://doi.org/10.5194/gmd-6-1543-2013

Contreras-Rosales, L.A., Schefuß, E., Meyer, V., Palamenghi, L., Lückge, A., Jennerjahn, T.C., 2016. Origin and fate of sedimentary organic matter in the northern Bay of Bengal during the last 18ka. Global and Planetary Change 146, 53 − 66. https://doi.org/10.1016/j.gloplacha.2016.09.008

Copeland, P., Bertrand, G., France-Lanord, C., Sundell, K., 2015. 40Ar/39Ar ages of muscovites from modern Himalayan rivers: Himalayan evolution and the relative contribution of tectonics and climate. Geosphere GES01154.1. https://doi.org/10.1130/GES01154.1

Copley, A., Avouac, J.-P., Royer, J.-Y., 2010. India-Asia collision and the Cenozoic slowdown of the Indian plate: Implications for the forces driving plate motions. J. Geophys. Res. 115, B03410. https://doi.org/10.1029/2009JB006634

Corvinus, G., Rimal, L.N., 2001. Biostratigraphy and geology of the neogene Siwalik group of the Surai Khola and Rato Khola areas in Nepal. Palaeogeography, Palaeoclimatology, Palaeoecology 165, 251 − 279. https://doi.org/10.1016/S0031-0182(00)00163-2

Coutand, I., Barrier, L., Govin, G., Grujic, D., Hoorn, C., Dupont-Nivet, G., Najman, Y., 2016. Late Miocene-Pleistocene evolution of India-Eurasia convergence partitioning between the Bhutan Himalaya and the Shillong Plateau: New evidences from foreland basin deposits along the Dungsam Chu section, eastern Bhutan. Tectonics 35, 2963 − 2994. https://doi.org/10.1002/2016TC004258

Cramer, B.S., Toggweiler, J.R., Wright, J.D., Katz, M.E., Miller, K.G., 2009. Ocean overturning since the Late Cretaceous: Inferences from a new benthic foraminiferal isotope compilation. Paleoceanography 24, PA4216. https://doi.org/10.1029/2008pa001683

Cramer, B.S., Miller, K.G., Barrett, P.J., Wright, J.D., 2011. Late Cretaceous − Neogene trends in deep ocean temperature and continental ice volume: Reconciling records of benthic foraminiferal geochemistry (δ 18O and Mg/Ca) with sea level history. Journal of Geophysical Research: Oceans 116, C12023. https://doi.org/10.1029/2011JC007255

Curray, J.R., Emmel, F.J., Moore, D.G., 2003. The Bengal Fan: morphology, geometry, stratigraphy, history and processes. Marine and Petroleum Geology 19, 1191 − 1223.

https://doi.org/10.1016/S0264-8172(03)00035-7

Curray, J.R., 1991. Possible greenschist metamorphism at the base of a 22-km sedimentary section, Bay of Bengal. Geology 19, 1097 – 1100. https://doi.org/10.1130/0091-7613(1991)019<1097:PGMATB>2.3.CO;2

Curray, J.R., 1994. Sediment volume and mass beneath the Bay of Bengal. Earth and Planetary Science Letters 125, 371 – 383. https://doi.org/10.1016/0012-821X(94)90227-5

Dadson, S.J., Hovius, N., Chen, H., Dade, W.B., Hsieh, M.-L., Willett, S.D., Hu, J.-C., Horng, M.-J., Chen, M.-C., Stark, C.P., Lague, D., Lin, J.-C., 2003. Links between erosion, runoff variability and seismicity in the Taiwan orogen. Nature 426, 648 – 651. https://doi.org/10.1038/nature02150

Dana, J.D., 1873. On some Results of the Earth's Contraction from cooling, including a discussion of the Origin of Mountains, and the nature of the Earth's Interior. American Journal of Science and Arts 5, 423.

Dasgupta, S., Narula, P.L., Acharyya, S.K., Banerjee, J., 2000. Seismotectonic atlas of India and its environs. Geological Survey of India.

Davies, T.A., Hay, W.W., Southam, J.R., Worsley, T.R., 1977. Estimates of Cenozoic Oceanic Sedimentation Rates. Science 197, 53 – 55. https://doi.org/10.1126/science.197.4298.53

Davis, W.M., 1899. The Geographical Cycle. The Geographical Journal 14, 481 – 504. https://doi.org/10.2307/1774538

DeCelles, P.G., Gehrels, G.E., Quade, J., Ojha, T.P., Kapp, P.A., Upreti, B.N., 1998. Neogene foreland basin deposits, erosional unroofing, and the kinematic history of the Himalayan fold-thrust belt, western Nepal. Geological Society of America Bulletin 110, 2 – 21. https://doi.org/10.1130/0016-7606(1998)110<0002:NFBDEU>2.3.CO;2

DeCelles, P.G., Robinson, D.M., Quade, J., Ojha, T.P., Garzione, C.N., Copeland, P., Upreti, B.N., 2001. Stratigraphy, structure, and tectonic evolution of the Himalayan fold-thrust belt in western Nepal. Tectonics 20, 487 – 509. https://doi.org/10.1029/2000TC001226

DeCelles, P.G., Kapp, P., Gehrels, G.E., Ding, L., 2014. Paleocene-Eocene foreland basin evolution in the Himalaya of southern Tibet and Nepal: Implications for the age of initial India-Asia collision. Tectonics 33, 2014TC003522. https://doi.org/10.1002/2014TC003522

DeCelles, P.G., Carrapa, B., Gehrels, G.E., Chakraborty, T., Ghosh, P., 2016. Along-strike continuity of structure, stratigraphy, and kinematic history in the Himalayan thrust belt: The view from Northeastern India. Tectonics 35, 2995 – 3027. https://doi.org/10.1002/2016tc004298

DeConto, R.M., Pollard, D., Wilson, P.A., Pälike, H., Lear, C.H., Pagani, M., 2008. Thresholds for Cenozoic bipolar glaciation. Nature 455, 652 – 656. https://doi.org/10.1038/nature07337

Delft Hydraulics and Danish Hydraulics Institute, River Survey Project, Flood Action Plan 24, Water Resour. Plann. Org., Dhaka., 1996.

Delunel, R., van der Beek, P.A., Carcaillet, J., Bourlès, D.L., Valla, P.G., 2010. Frost-cracking control on catchment denudation rates: Insights from in situ produced 10Be concentrations in stream sediments (Ecrins – Pelvoux massif, French Western Alps). Earth and Planetary Science Letters 293, 72 – 83. https://doi.org/10.1016/j.epsl.2010.02.020

Demenocal, P.B., 1995. Plio-pleistocene African climate. Science 53 – 59. https://doi.org/10.1126/science.270.5233.53

Deng, T., Ding, L., 2015. Paleoaltimetry reconstructions of the Tibetan Plateau: progress and contradictions. Natl Sci Rev 2, 417 – 437. https://doi.org/10.1093/nsr/nwv062

Deniel, C., Vidal, P., Fernandez, A., Le Fort, P., Peucat, J.-J., 1987. Isotopic study of the Manaslu granite (Himalaya, Nepal): inferences on the age and source of Himalayan leucogranites. Contributions to Mineralogy and Petrology 96, 78 – 92. https://doi.org/10.1007/BF00375529

Denne, R., Callender, A, and Nault, M. 2005. Applied Biostratigraphix Gulf of Mexico Biostratigraphic Chart Neogene Calcareous Nannofossils, Houston TX. https://www.data.boem.gov/Paleo/Files/biochart.pdf

Densmore, A.L., Parker, R.N., Rosser, N.J., de Michele, M., Yong, L., Runqiu, H., Whadcoat, S., Petley, D.N., 2012. Reply to "Isostasy can't be ignored." Nature Geoscience 5, 83 – 84. https://doi.org/10.1038/ngeo1385

Derry, L.A., France-Lanord, C., 1997. Himalayan Weathering and Erosion Fluxes: Climate and Tectonic Controls, in: Ruddiman, W.F. (Ed.), Tectonic Uplift and Climate Change. Springer US, Boston, MA, pp. 289 – 312. https://doi.org/10.1007/978-1-4615-5935-1_12

Derry, L.A., France-Lanord, C., 1996. Neogene growth of the sedimentary organic carbon reservoir. Paleoceanography 11, 267 – 275. https://doi.org/10.1029/95PA03839

Desilets, D., Zreda, M., 2003. Spatial and temporal distribution of secondary cosmic-ray nucleon intensities and applications to in situ cosmogenic dating. Earth and Planetary Science Letters 206, 21 – 42. https://doi.org/10.1016/S0012-821X(02)01088-9

Desilets, D., Zreda, M., Prabu, T., 2006. Extended scaling factors for in situ cosmogenic nuclides: New measurements at low latitude. Earth and Planetary Science Letters 246, 265 – 276. https://doi.org/10.1016/j.epsl.2006.03.051

Dessert, C., Dupré, B., Gaillardet, J., François, L.M., Allegre, C.J., 2003. Basalt weathering laws and the impact of basalt weathering on the global carbon cycle. Chemical Geology 202, 257 – 273. https://doi.org/10.1016/j.chemgeo.2002.10.001

Dettman, D.L., Kohn, M.J., Quade, J., Ryerson, F.J., Ojha, T.P., Hamidullah, S., 2001. Seasonal stable isotope evidence for a strong Asian monsoon throughout the past 10.7 m.y. Geology 29, 31 – 34. https://doi.org/10.1130/0091-7613(2001)029<0031:SSIEFA>2.0.CO;2

DHM, 2003. Suspended Sediment Concentration Records. Department of Hydrology and Meteorology, His Majesty's Government, Kathmandu, Nepal

DHM/FFS, 2004. Hydrological Data (2002 – 2003). Department of Hydrologyand Meteorology, Flood Forecasting Section, Kathmandu, Nepal

DiBiase, R.A., 2018. Short Communication: Increasing vertical attenuation length of cosmogenic nuclide production on steep slopes negates topographic shielding corrections for catchment erosion rates. Earth Surface Dynamics Discussions 1 – 17. https://doi.org/10.5194/esurf-2018-48

Dietz, R.S., 1961. Continent and ocean basin evolution by spreading of the sea floor. Nature 190, 854 – 857. https://doi.org/10.1038/190854a0

Dingle, E.H., Attal, M., Sinclair, H.D., 2017. Abrasion-set limits on Himalayan gravel flux. Nature 544, 471 – 474. https://doi.org/10.1038/nature22039

Dingle, E.H., Sinclair, H.D., Attal, M., Rodés, Á., Singh, V., 2018. Temporal variability in detrital 10Be concentrations in a large Himalayan catchment. Earth Surface Dynamics 6, 611 – 635. https://doi.org/10.5194/esurf-6-611-2018

Divyadarshini, A., Singh, V., 2019. Investigating topographic metrics to decipher structural model and morphotectonic evolution of the Frontal Siwalik Ranges, Central Himalaya, Nepal. Geomorphology 337, 31 – 52. https://doi.org/10.1016/j.geomorph.2019.03.028

Dobson, D.M., Dickens, G.R., Rea, D.K., 2001. Terrigenous sediment on Ceara Rise: a Cenozoic record of South American orogeny and erosion. Palaeogeography, Palaeoclimatology, Palaeoecology 165, 215 – 229. https://doi.org/10.1016/s0031-0182(00)00161-9

Donnelly, T.W., 1982. Worldwide continental denudation and climatic deterioration during the late Tertiary: Evidence from deep-sea sediments. Geology 10, 451 – 454. https://doi.org/10.1130/0091-7613(1982)10<451:WCDACD>2.0.CO;2

Doser, D.I., Rodriguez, H., 2011. A seismotectonic study of the Southeastern Alaska Region. Tectonophysics 497, 105 – 113. https://doi.org/10.1016/j.tecto.2010.10.019

Dosseto, A., Schaller, M., 2016. The erosion response to Quaternary climate change quantified using uranium isotopes and in situ-produced cosmogenic nuclides. Earth-Science Reviews 155, 60 – 81. https://doi.org/10.1016/j.earscirev.2016.01.015

Douglas, I., 1967. Man, vegetation and the sediment yields of rivers. Nature 215, 925 – 928. https://doi.org/10.1038/215925a0

Dowdeswell, J.A., Ottesen, D., Rise, L., 2010. Rates of sediment delivery from the Fennoscandian Ice Sheet through an ice age. Geology 38, 3 – 6. https://doi.org/10.1130/G25523.1

Driscoll, N.W., Karner, G.D., 1994. Flexural deformation due to Amazon Fan loading: A feedback mechanism affecting sediment delivery to margins. Geology 22, 1015 –

1018. https://doi.org/10.1130/0091-7613(1994)022<1015:fddtaf>2.3.co;2

Dunai, T.J., Lifton, N.A., 2014. The Nuts and Bolts of Cosmogenic Nuclide Production. Elements 10, 347 – 350. https://doi.org/10.2113/gselements.10.5.347

Dunai, T.J., 2000. Scaling factors for production rates of in situ produced cosmogenic nuclides: a critical reevaluation. Earth and Planetary Science Letters 176, 157 – 169. https://doi.org/10.1016/S0012-821X(99)00310-6

Dunai, T.J., 2001. Influence of secular variation of the geomagnetic field on production rates of in situ produced cosmogenic nuclides. Earth and Planetary Science Letters 193, 197 – 212. https://doi.org/10.1016/S0012-821X(01)00503-9

Dunai, T.J., 2010. Cosmogenic nuclides principles, concepts and applications in the earth surface sciences. Cambridge University Press, Cambridge; New York. https://doi.org/10.1017/CBO9780511804519

Dunne, J., Elmore, D., Muzikar, P., 1999. Scaling factors for the rates of production of cosmogenic nuclides for geometric shielding and attenuation at depth on sloped surfaces. Geomorphology 27, 3 – 11. https://doi.org/10.1016/s0169-555x(98)00086-5

Dyke, A.S., Andrews, J.T., Clark, P.U., England, J.H., Miller, G.H., Shaw, J., Veillette, J.J., 2002. The Laurentide and Innuitian ice sheets during the last glacial maximum. Quaternary Science Reviews 21, 9 – 31. https://doi.org/10.1016/s0277-3791(01)00095-6

Ebelmen, J.-J., 1845. Sur les produits de la décomposition des espèces minérales de la famille des silicates. Annales des Mines 7, 66.

Edmond, J.M., 1992. Himalayan Tectonics, Weathering Processes, and the Strontium Isotope Record in Marine Limestones. Science 258, 1594 – 1597. https://doi.org/10.1126/science.258.5088.1594

Edwards, E.J., Osborne, C.P., Stromberg, C.A.E., Smith, S.A., C4 Grasses Consortium, Bond, W.J., Christin, P.A., Cousins, A.B., Duvall, M.R., Fox, D.L., Freckleton, R.P., Ghannoum, O., Hartwell, J., Huang, Y., Janis, C.M., Keeley, J.E., Kellogg, E.A., Knapp, A.K., Leakey, A.D.B., Nelson, D.M., Saarela, J.M., Sage, R.F., Sala, O.E., Salamin, N., Still, C.J., Tipple, B., 2010. The Origins of C4 Grasslands: Integrating Evolutionary and Ecosystem Science. Science 328, 587 – 591. https://doi.org/10.1126/science.1177216

Egholm, D.L., Nielsen, S.B., Pedersen, V.K., Lesemann, J.-E., 2009. Glacial effects limiting mountain height. Nature 460, 884 – 887. https://doi.org/10.1038/nature08263

Egholm, D.L., Jansen, J.D., Brædstrup, C.F., Pedersen, V.K., Andersen, J.L., Ugelvig, S.V., Larsen, N.K., Knudsen, M.F., 2017. Formation of plateau landscapes on glaciated continental margins. Nature Geoscience 10, ngeo2980. https://doi.org/10.1038/ngeo2980

Einsele, G., Ratschbacher, L., Wetzel, A., 1996. The Himalaya-Bengal Fan denudation-accumulation system during the past 20 Ma. the Journal of Geology 104, 163 – 184. https://doi.org/10.1086/629812

Eldrett, J.S., Harding, I.C., Wilson, P.A., Butler, E., Roberts, A.P., 2007. Continental ice in Greenland during the Eocene and Oligocene. Nature 446, 176 – 179. https://doi.org/10.1038/nature05591

Elliott, J.R., Jolivet, R., González, P.J., Avouac, J.-P., Hollingsworth, J., Searle, M.P., Stevens, V.L., 2016. Himalayan megathrust geometry and relation to topography revealed by the Gorkha earthquake. Nature Geoscience 9, 174 – 180. https://doi.org/10.1038/ngeo2623

Elsasser, W., Ney, E.P., Winckler, J.R., 1956. Cosmic-ray intensity and geomagnetism. Nature 178, 1226. https://doi.org/10.1038/1781226a0

Fabryka-Martin, J.T., 1988. Production of radionuclides in the earth and their hydrogeologic significance, with emphasis on chlorine-36 and iodine-129. The University of Arizona.

Ferry, J.-N., Babonneau, N., Mulder, T., Parize, O., Raillard, S., 2004. Morphogenesis of Congo submarine canyon and valley: implications about the theories of the canyons formation. Geodinamica Acta 17, 241 – 251. https://doi.org/10.3166/ga.17.241-251

Figueiredo, J., Hoorn, C., Van der Ven, P., Soares, E., 2009. Late Miocene onset of the Amazon River and the Amazon deep-sea fan: Evidence from the Foz do Amazonas Basin. Geology 37, 619 – 622. https://doi.org/10.1130/G25567A.1

Fisher, A.G., 1982. Long-term climatic oscillations recorded in stratigraphy, in: Climate in Earth

History. Washington, DC: National Academy of Sciences, pp. 97 – 104.

Flowers, R.M., Ketcham, R.A., Shuster, D.L., Farley, K.A., 2009. Apatite (U – Th)/He thermochronometry using a radiation damage accumulation and annealing model. Geochimica et Cosmochimica Acta 73, 2347 – 2365. https://doi.org/10.1016/j.gca.2009.01.015

Foster, G.L., Rohling, E.J., 2013. Relationship between sea level and climate forcing by CO2 on geological timescales. Proceedings of the National Academy of Sciences 110, 1209 – 1214. https://doi.org/10.1073/pnas.1216073110

Foster, G.L., Royer, D.L., Lunt, D.J., 2017. Future climate forcing potentially without precedent in the last 420 million years. Nature Communications 8, 14845. https://doi.org/10.1038/ncomms14845

Fox, M., Herman, F., Willett, S.D., May, D.A., 2014. A linear inversion method to infer exhumation rates in space and time from thermochronometric data. Earth Surface Dynamics 2, 47 – 65. https://doi.org/10.5194/esurf-2-47-2014

Fox, M., Herman, F., Kissling, E., Willett, S.D., 2015. Rapid exhumation in the Western Alps driven by slab detachment and glacial erosion. Geology 43, 379 – 382. https://doi.org/10.1130/G36411.1

France-Lanord, C., Derry, L.A., 1997. Organic carbon burial forcing of the carbon cycle from Himalayan erosion. Nature 390, 65 – 67. https://doi.org/10.1038/36324

France-Lanord, C., Derry, L., Michard, A., 1993. Evolution of the Himalaya since Miocene time: isotopic and sedimentological evidence from the Bengal Fan. Geological Society, London, Special Publications 74, 603 – 621. https://doi.org/10.1144/GSL.SP.1993.074.01.40

France-Lanord, C., Spiess, V., Klaus, A., Schwenk, T., , Adhikari, R.R., Adhikari, S.K., Bahk, J.-J., Baxter, A.T., Cruz, J.W., Das, S.K., Dekens, P., Duleba, W., Fox, L.R., Galy, A., Galy, V., Ge, J., Gleason, J.D., Gyawali, B.R., Huyghe, P., Jia, G., Lantzsch, H., Manoj, M.C., Martos Martin, Y., Meynadier, L., Najman, Y.M.R., Nakajima, A., Ponton, C., Reilly, B.T., Rogers, K.G., Savian, J.F., Schwenk, T., Selkin, P.A., Weber, M.E., Williams, T., and Yoshida, K., 2016b. Site U1450. In France-Lanord, C., Spiess, V., Klaus, A., Schwenk, T., and the Expedition 354 Scientists, 2016a. Bengal Fan. Proceedings of the International Ocean Discovery Program, 354: College Station, TX (International Ocean Discovery Program). http://dx.doi.org/10.14379/iodp.proc.354.2016

France-Lanord, C., Spiess, V., Klaus, A., Adhikari, R.R., Adhikari, S.K., Bahk, J.-J., Baxter, A.T., Cruz, J.W., Das, S.K., Dekens, P., Duleba, W., Fox, L.R., Galy, A., Galy, V., Ge, J., Gleason, J.D., Gyawali, B.R., Huyghe, P., Jia, G., Lantzsch, H., Manoj, M.C., Martos Martin, Y., Meynadier, L., Najman, Y.M.R., Nakajima, A., Ponton, C., Reilly, B.T., Rogers, K.G., Savian, J.F., Schwenk, T., Selkin, P.A., Weber, M.E., Williams, T., and Yoshida, K., 2016b. Site U1450. In France-Lanord, C., Spiess, V., Klaus, A., Schwenk, T., and the Expedition 354 Scientists, Bengal Fan. Proceedings of the International Ocean Discovery Program, 354: College Station, TX (International Ocean Discovery Program). http://dx.doi.org/10.14379/iodp.proc.354.104.2016

France-Lanord, C., Galy, A., Huyghe, P., Rigaudier, T., 2019. Neogene Himalayan erosion regime and climate recorded in the Bengal Fan at 8°N (IODP Exp. 354), in: Geophysical Research Abstracts. Presented at the EGU, pp. EGU2019-14627. https://meetingorganizer.copernicus.org/EGU2019/EGU2019-14627.pdf

Frank, M., Backman, J., Jakobsson, M., Moran, K., O'Regan, M., King, J., Haley, B.A., Kubik, P.W., Garbe-Schönberg, D., 2008. Beryllium isotopes in central Arctic Ocean sediments over the past 12.3 million years: Stratigraphic and paleoclimatic implications. Paleoceanography and Paleoclimatology 23. https://doi.org/10.1029/2007PA001478

Frostick, L.E., Reid, I. a. N., 1989. Climatic versus tectonic controls of fan sequences: lessons from the Dead Sea, Israel. Journal of the Geological Society 146, 527 – 538. https://doi.org/10.1144/gsjgs.146.3.0527

Fuse, K., Anders, E., 1969. Aluminum-26 in meteorites. Geochimica et Cosmochimica Acta 33, 653 – 670. https://doi.org/10.1016/0016-7037(69)90113-6

Gabet, E.J., Burbank, D.W., Putkonen, J.K., Pratt-Sitaula, B.A., Ojha, T., 2004. Rainfall thresholds for landsliding in the Himalayas of Nepal. Geomorphology 63, 131 – 143. https://doi.org/10.1016/j.geomorph.2004.03.011

Gabet, E.J., Pratt-Sitaula, B.A., Burbank, D.W., 2004. Climatic controls on hillslope angle and relief in the Himalayas. Geol 32, 629. https://doi.org/10.1130/G20641.1

Gabet, E., Burbank, D., Prattsitaula, B., Putkonen, J., Bookhagen, B., 2008. Modern erosion rates in the High Himalayas of Nepal. Earth and Planetary Science Letters 267, 482 – 494. https://doi.org/10.1016/j.epsl.2007.11.059

Gajurel, A.P., France-Lanord, C., Huyghe, P., Guilmette, C., Gurung, D., 2006. C and O isotope compositions of modern fresh-water mollusc shells and river waters from the Himalaya and Ganga plain. Chemical Geology 233, 156 – 183. https://doi.org/10.1016/j.chemgeo.2006.03.002

Gaillardet, J., Dupré, B., Louvat, P., Allegre, C.J., 1999. Global silicate weathering and CO2 consumption rates deduced from the chemistry of large rivers. Chemical geology 159, 3 – 30. https://doi.org/10.1016/s0009-2541(99)00031-5

Galbraith, R.F., 2005. Statistics for fission track analysis. Chapman and Hall/CRC.

Gallagher, K., Brown, R., Johnson, C., 1998. Fission track analysis and its applications to geological problems. Annual Review of Earth and Planetary Sciences 26, 519 – 572. https://doi.org/10.1146/annurev.earth.26.1.519

Gallo, F., Lavé, J., 2014. Evolution of a large landslide in the High Himalaya of central Nepal during the last half-century. Geomorphology 223, 20 – 32. https://doi.org/10.1016/j.geomorph.2014.06.021

Galloway, W.E., Whiteaker, T.L., Ganey-Curry, P., 2011. History of Cenozoic North American drainage basin evolution, sediment yield, and accumulation in the Gulf of Mexico basin. Geosphere 7, 938 – 973. https://doi.org/10.1130/GES00647.1

Galy, A., France-Lanord, C., 2001. Higher erosion rates in the Himalaya: Geochemical constraints on riverine fluxes. Geology 29, 23. https://doi.org/10.1130/0091-7613(2001)029<0023:HERITH>2.0.CO;2

Galy, A., France-Lanord, C., Derry, L.A., 1996. The Late Oligocene-Early Miocene Himalayan belt Constraints deduced from isotopic compositions of Early Miocene turbidites in the Bengal Fan. Tectonophysics 260, 109 – 118. https://doi.org/10.1016/0040-1951(96)00079-0

Galy, A., France-Lanord, C., Derry, L.A., 1999. The strontium isotopic budget of Himalayan rivers in Nepal and Bangladesh. Geochimica et Cosmochimica Acta 63, 1905 – 1925. https://doi.org/10.1016/s0016-7037(99)00081-2

Galy, V., France-Lanord, C., Beyssac, O., Faure, P., Kudrass, H., Palhol, F., 2007. Efficient organic carbon burial in the Bengal fan sustained by the Himalayan erosional system. Nature 450, 407 – 410. https://doi.org/10.1038/nature06273

Galy, V., François, L., France-Lanord, C., Faure, P., Kudrass, H., Palhol, F., Singh, S.K., 2008. C4 plants decline in the Himalayan basin since the Last Glacial Maximum. Quaternary Science Reviews 27, 1396 – 1409. https://doi.org/10.1016/j.quascirev.2008.04.005

Galy, V., France-Lanord, C., Peucker-Ehrenbrink, B., Huyghe, P., 2010. Sr-Nd-Os evidence for a stable erosion regime in the Himalaya during the past 12Myr. Earth and Planetary Science Letters 290, 474-480. https://doi.org/10.1016/j.epsl.2010.01.004

Gansser, A., 1964. Geology of the Himalayas. Wiley-Interscience, New York.

Garçon, M., Chauvel, C., France-Lanord, C., Limonta, M., Garzanti, E., 2014. Which minerals control the Nd – Hf – Sr – Pb isotopic compositions of river sediments? Chemical Geology 364, 42 – 55. https://doi.org/10.1016/j.chemgeo.2013.11.018

Gardner, T.W., Jorgensen, D.W., Shuman, C., Lemieux, C.R., 1987. Geomorphic and tectonic process rates: Effects of measured time interval. Geology 15, 259 – 261. https://doi.org/10.1016/0198-0254(87)90162-2

Garver, J.I., Brandon, M.T., Roden-Tice, M., Kamp, P.J.J., 1999. Exhumation history of orogenic highlands determined by detrital fission-track thermochronology, in: Ring, U., Brandon, M. T., Lister, G. S., Willett, S. D. (Eds.), Geological Society, London, Special Publications, 154, pp. 283 – 304. https://doi.org/10.1144/GSL.SP.1999.154.01.13

Garzanti, E., 2019. The Himalayan Foreland Basin from collision onset to the present: a sedimentary – petrology perspective, in: Treloar, P. J., Searle, M. P. (Eds.), Himalayan Tectonics: A Synthesis. Geological Society, London, Special

Publications, 483, p. SP483.17. https://doi.org/10.1144/SP483.17

Garzione, C.N., Dettman, D.L., Quade, J., DeCelles, P.G., Butler, R.F., 2000. High times on the Tibetan Plateau: Paleoelevation of the Thakkhola graben, Nepal. Geology 28, 339 – 342. https://doi.org/10.1130/0091-7613(2000)028<0339:htottp>2.3.co;2

Garzione, C.N., DeCelles, P.G., Hodkinson, D.G., Ojha, T.P., Upreti, B.N., 2003. East-west extension and Miocene environmental change in the southern Tibetan plateau: Thakkhola graben, central Nepal. GSA Bulletin 115, 3 – 20. https://doi.org/10.1130/0016-7606(2003)115<0003:EWEAME>2.0.CO;2

Gautam, P., Fujiwara, Y., 2000. Magnetic polarity stratigraphy of Siwalik Group sediments of Karnali River section in western Nepal. Geophysical Journal International 142, 812 – 824. https://doi.org/10.1046/j.1365-246x.2000.00185.x

Gautam, P., Koshimizu, S., 1991. Zircon and apatite fission-track dating of the Ampipal alkaline massif, the Nepal Lesser Himalaya. Journal of Nepal Geological Society 7, 1 – 8.

Gautheron, C., Tassan-Got, L., Barbarand, J., Pagel, M., 2009. Effect of alpha-damage annealing on apatite (U – Th)/He thermochronology. Chemical Geology 266, 157 – 170. https://doi.org/10.1016/j.chemgeo.2009.06.001

Gavillot, Y., Meigs, A.J., Sousa, F.J., Stockli, D., Yule, D., Malik, M., 2018. Late Cenozoic Foreland-to-Hinterland Low-Temperature Exhumation History of the Kashmir Himalaya. Tectonics 37, 3041 – 3068. https://doi.org/10.1029/2017TC004668

Gébelin, A., Mulch, A., Teyssier, C., Jessup, M.J., Law, R.D., Brunel, M., 2013. The Miocene elevation of Mount Everest. Geology 41, 799 – 802. https://doi.org/10.1130/G34331.1

Gemignani, L., van der Beek, P.A., Braun, J., Najman, Y., Bernet, M., Garzanti, E., Wijbrans, J.R., 2018. Downstream evolution of the thermochronologic age signal in the Brahmaputra catchment (eastern Himalaya): Implications for the detrital record of erosion. Earth and Planetary Science Letters 499, 48 – 61. https://doi.org/10.1016/j.epsl.2018.07.019

Ghosh, P., Padia, J.T., Mohindra, R., 2004. Stable isotopic studies of palaeosol sediment from Upper Siwalik of Himachal Himalaya: evidence for high monsoonal intensity during late Miocene? Palaeogeography, Palaeoclimatology, Palaeoecology 206, 103 – 114. https://doi.org/10.1016/j.palaeo.2004.01.014

Ghosh, S., Sanyal, P., Kumar, R., 2017. Evolution of C4 plants and controlling factors: Insight from n-alkane isotopic values of NW Indian Siwalik paleosols. Organic Geochemistry 110, 110 – 121. https://doi.org/10.1016/j.orggeochem.2017.04.009

Ghosh, S., Sanyal, P., Sangode, S.J., Nanda, A.C., 2018. Substrate control of C4 plant abundance in the Himalayan foreland: A study based on inter-basinal records from Plio-Pleistocene Siwalik Group sediments. Palaeogeography, Palaeoclimatology, Palaeoecology 511, 341 – 351. https://doi.org/10.1016/j.palaeo.2018.08.019

Gilluly, J., 1949. Distribution of mountain building in geologic time. Geological Society of America Bulletin 60, 561 – 590. https://doi.org/10.1130/0016-7606(1949)60[561:dombig]2.0.co;2

Glotzbach, C., Bernet, M., Van Der Beek, P., 2011. Detrital thermochronology records changing source areas and steady exhumation in the Western European Alps. Geology 39, 239 – 242. https://doi.org/10.1130/G31757.1

Glotzbach, C., Busschers, F.S., Winsemann, J., 2018. Detrital thermochronology of Rhine, Elbe and Meuse river sediment (Central Europe): implications for provenance, erosion and mineral fertility. International Journal of Earth Sciences 107, 459 – 479. https://doi.org/10.1007/s00531-017-1502-9

Godard, V., Burbank, D.W., Bourlès, D.L., Bookhagen, B., Braucher, R., Fisher, G.B., 2012. Impact of glacial erosion on 10Be concentrations in fluvial sediments of the Marsyandi catchment, central Nepal. J. Geophys. Res. 117, F03013. https://doi.org/10.1029/2011JF002230

Godard, V., Bourles, D.L., Spinabella, F., Burbank, D.W., Bookhagen, B., Fisher, G.B., Moulin, A., Leanni, L., 2014. Dominance of tectonics over climate in Himalayan denudation. Geology 42, 243 – 246. https://doi.org/10.1130/G35342.1

Goddéris, Y., Donnadieu, Y., Le Hir, G., Lefebvre, V., Nardin, E., 2014. The role of palaeogeography in the Phanerozoic history of atmospheric CO2 and climate. Earth-

Science Reviews 128, 122 – 138. https://doi.org/10.1016/j.earscirev.2013.11.004

Goldstein, S.L., O'nions, R.K., Hamilton, P.J., 1984. A Sm-Nd isotopic study of atmospheric dusts and particulates from major river systems. Earth and planetary Science letters 70, 221 – 236. https://doi.org/10.1016/0012-821x(84)90007-4

Goodbred, S.L., Kuehl, S.A., 2000. The significance of large sediment supply, active tectonism, and eustasy on margin sequence development: Late Quaternary stratigraphy and evolution of the Ganges – Brahmaputra delta. Sedimentary Geology 133, 227 – 248. https://doi.org/10.1016/S0037-0738(00)00041-5

Goodbred, S.L., Kuehl, S.A., 2000. Enormous Ganges-Brahmaputra sediment discharge during strengthened early Holocene monsoon. Geology 28, 1083. https://doi.org/10.1130/0091-7613(2000)28<1083:EGSDDS>2.0.CO;2

Goodbred, S.L., Paolo, P.M., Ullah, M.S., Pate, R.D., Khan, S.R., Kuehl, S.A., Singh, S.K., Rahaman, W., 2014. Piecing together the Ganges-Brahmaputra-Meghna River delta: Use of sediment provenance to reconstruct the history and interaction of multiple fluvial systems during Holocene delta evolution. Geological Society of America Bulletin 126, 1495 – 1510. https://doi.org/10.1130/B30965.1

Goscombe, B., Gray, D., Hand, M., 2006. Crustal architecture of the Himalayan metamorphic front in eastern Nepal. Gondwana Research 10, 232 – 255. https://doi.org/10.1016/j.gr.2006.05.003

Gosse, J.C., Phillips, F.M., 2001. Terrestrial in situ cosmogenic nuclides: theory and application. Quaternary Science Reviews 20, 1475 – 1560. https://doi.org/10.1016/S0277-3791(00)00171-2

Gradstein, F.M., Ogg, J., Schmitz, M., Ogg, G. (Eds.), 2012. The Geologic Time Scale 2012, 1st ed. ed. Elsevier.

Granger, D.E., Schaller, M., 2014. Cosmogenic Nuclides and Erosion at the Watershed Scale. Elements 10, 369 – 373. https://doi.org/10.2113/gselements.10.5.369

Granger, D.E., Kirchner, J.W., Finkel, R., 1996. Spatially Averaged Long-Term Erosion Rates Measured from in Situ-Produced Cosmogenic Nuclides in Alluvial Sediment. The Journal of Geology 104, 249 – 257. https://doi.org/10.1086/629823

Granger, D.E., Fabel, D., Palmer, A.N., 2001. Pliocene-Pleistocene incision of the Green River, Kentucky, determined from radioactive decay of cosmogenic 26Al and 10Be in Mammoth Cave sediments. Geological Society of America Bulletin 113, 825 – 836. https://doi.org/10.1130/0016-7606(2001)113<0825:PPIOTG>2.0.CO;2

GRDC, 1996. Freshwater Flux from the Continents into the World Oceans based on the Data of the Global Runoff Data Base. Global Runoff Data Center

Grimaud, J.-L., Rouby, D., Chardon, D., Beauvais, A., 2018. Cenozoic sediment budget of West Africa and the Niger delta. Basin Research 30, 169 – 186. https://doi.org/10.1111/bre.12248

Grujic, D., Coutand, I., Bookhagen, B., Bonnet, S., Blythe, A., Duncan, C., 2006. Climatic forcing of erosion, landscape, and tectonics in the Bhutan Himalayas. Geology 34, 801. https://doi.org/10.1130/G22648.1

Guenthner, W.R., Reiners, P.W., Ketcham, R.A., Nasdala, L., Giester, G., 2013. Helium diffusion in natural zircon: Radiation damage, anisotropy, and the interpretation of zircon (U-Th)/He thermochronology. American Journal of Science 313, 145 – 198. https://doi.org/10.2475/03.2013.01

Guillon, H., Mugnier, J.-L., Buoncristiani, J.-F., Carcaillet, J., Godon, C., Prud'homme, C., Beek, P. van der, Vassallo, R., 2015. Improved discrimination of subglacial and periglacial erosion using 10Be concentration measurements in subglacial and supraglacial sediment load of the Bossons glacier (Mont Blanc massif, France). Earth Surface Processes and Landforms 40, 1202 – 1215. https://doi.org/10.1002/esp.3713

Gupta, A.K., Yuvaraja, A., Prakasam, M., Clemens, S.C., Velu, A., 2015. Evolution of the South Asian monsoon wind system since the late Middle Miocene. Palaeogeography, Palaeoclimatology, Palaeoecology 438, 160 – 167. https://doi.org/10.1016/j.palaeo.2015.08.006

Gupta, S., 1997. Himalayan drainage patterns and the origin of fluvial megafans in the Ganges foreland basin. Geology 25, 11 – 14. https://doi.org/10.1130/0091-7613(1997)025<0011:hdpato>2.3.co;2

Haeuselmann, P., Granger, D.E., Jeannin, P.-Y., Lauritzen, S.-E., 2007. Abrupt glacial valley

incision at 0.8 Ma dated from cave deposits in Switzerland. Geology 35, 143. https://doi.org/10.1130/G23094A

Hajek, E.A., Wolinsky, M.A., 2012. Simplified process modeling of river avulsion and alluvial architecture: connecting models and field data. Sedimentary Geology 257, 1 – 30. https://doi.org/10.1016/j.sedgeo.2011.09.005

Hall, R., Nichols, G., 2002. Cenozoic sedimentation and tectonics in Borneo: climatic influences on orogenesis, in: Jones, S. J., Frostick, L. (Eds.), Sediment Flux to Basins: Causes, Controls and Consequences. Geological Society, London, Special Publications, 191, pp. 5 – 22. https://doi.org/10.1144/gsl.sp.2002.191.01.02

Hallet, B., Hunter, L., Bogen, J., 1996. Rates of erosion and sediment evacuation by glaciers: A review of field data and their implications. Global and Planetary Change, Impact of Glaciations on Basin Evolution: Data and Models from the Norwegian Margin and Adjacent Areas 12, 213 – 235. https://doi.org/10.1016/0921-8181(95)00021-6

Hampel, A., Hetzel, R., Densmore, A.L., 2007. Postglacial slip-rate increase on the Teton normal fault, northern Basin and Range Province, caused by melting of the Yellowstone ice cap and deglaciation of the Teton Range? Geology 35, 1107 – 1110. https://doi.org/10.1130/G24093A.1

Hansen, J., Sato, M., Kharecha, P., Beerling, D., Berner, R., Masson-Delmotte, V., Pagani, M., Raymo, M., Royer, D.L., Zachos, J.C., 2008. Target atmospheric CO2: Where should humanity aim? The Open Atmospheric Science Journal 2, 217 – 231. https://doi.org/10.2174/1874282300802010217

Harris, S.E., Mix, A.C., 2002. Climate and tectonic influences on continental erosion of tropical South America, 0 – 13 Ma. Geology 30, 447 – 450. https://doi.org/10.1130/0091-7613(2002)030<0447:catioc>2.0.co;2

Harrison, T.M., Copeland, P., Hall, S.A., Quade, J., Burner, S., Ojha, T.P., Kidd, W.S.F., 1993. Isotopic preservation of Himalayan/Tibetan uplift, denudation, and climatic histories of two molasse deposits. The Journal of Geology 101, 157 – 175. https://doi.org/10.1086/648214

Harrison, T.M., Ryerson, F.J., Le Fort, P., Yin, A., Lovera, O.M., Catlos, E.J., 1997. A late Miocene-Pliocene origin for the central Himalayan inverted metamorphism. Earth and Planetary Science Letters 146, E1 – E7. https://doi.org/10.1016/s0012-821x(96)00215-4

Hartmann, D.L., 2016. Global Physical Climatology, 2nd ed. Elsevier Science. https://doi.org/10.1016/c2009-0-00030-0

Harvey, J.E., Burbank, D.W., Bookhagen, B., 2015. Along-strike changes in Himalayan thrust geometry: Topographic and tectonic discontinuities in western Nepal. Lithosphere 7, 511 – 518. https://doi.org/10.1130/L444.1

Harvey, A., 2012. Introducing Geomorphology. Dunedin.

Hathorne, E.C., James, R.H., 2006. Temporal record of lithium in seawater: A tracer for silicate weathering? Earth and Planetary Science Letters 246, 393 – 406. https://doi.org/10.1016/j.epsl.2006.04.020

Hatton, C.J., 1971. The neutron monitor. Progress in Elementary Particle and Cosmic Rays Physics, vol. X. North-Holland, Amsterdam.

Haug, G.H., Tiedemann, R., 1998. Effect of the formation of the Isthmus of Panama on Atlantic Ocean thermohaline circulation. Nature 393, 673 – 676. https://doi.org/10.1038/31447

Hay, W.W., Sloan, J.L., Wold, C.N., 1988. Mass/age distribution and composition of sediments on the ocean floor and the global rate of sediment subduction. J. Geophys. Res. 93, 14933 – 14940. https://doi.org/10.1029/JB093iB12p14933

Hay, W.W., Rosol, M.J., Sloan II, J.L., Jory, D.E., 1988. Plate tectonic control of global patterns of detrital and carbonate sedimentation. Developments in Sedimentology 42, 1 – 34. https://doi.org/10.1016/s0070-4571(08)70163-8

Hay, W.W., Shaw, C.A., Wold, C.N., 1989. Mass-balanced paleogeographic reconstructions. Geologische Rundschau 78, 207 – 242. https://doi.org/10.1007/BF01988362

Hays, J.D., Imbrie, J., Shackleton, N.J., 1976. Variations in the Earth's orbit: pacemaker of the ice ages. Science 194, 1121 – 1132. https://doi.org/10.1126/science.194.4270.1121

Hein, C.J., Galy, V., Galy, A., France-Lanord, C., Kudrass, H., Schwenk, T., 2017. Post-glacial climate forcing of surface processes in the Ganges – Brahmaputra river basin and

implications for carbon sequestration. Earth and Planetary Science Letters 478, 89 – 101. https://doi.org/10.1016/j.epsl.2017.08.013

Heisinger, B., Lal, D., Jull, A.J.T., Kubik, P., Ivy-Ochs, S., Neumaier, S., Knie, K., Lazarev, V., Nolte, E., 2002. Production of selected cosmogenic radionuclides by muons: 1. Fast muons. Earth and Planetary Science Letters 200, 345 – 355. https://doi.org/10.1016/S0012-821X(02)00640-4

Heisinger, B., Lal, D., Jull, A.J.T., Kubik, P., Ivy-Ochs, S., Knie, K., Nolte, E., 2002. Production of selected cosmogenic radionuclides by muons: 2. Capture of negative muons. Earth and Planetary Science Letters 200, 357 – 369. https://doi.org/10.1016/S0012-821X(02)00641-6

Herbert, T.D., Lawrence, K.T., Tzanova, A., Peterson, L.C., Caballero-Gill, R., Kelly, C.S., 2016. Late Miocene global cooling and the rise of modern ecosystems. Nature Geoscience 9, 843 – 847. https://doi.org/10.1038/ngeo2813

Herman, F., Brandon, M., 2015. Mid-latitude glacial erosion hotspot related to equatorial shifts in southern Westerlies. Geology 43, 987 – 990. https://doi.org/10.1130/G37008.1

Herman, F., King, G.E., 2018. Luminescence Thermochronometry: Investigating the Link between Mountain Erosion, Tectonics and Climate. Elements: An International Magazine of Mineralogy, Geochemistry, and Petrology 14, 33 – 38. https://doi.org/10.2138/gselements.14.1.33

Herman, F., Copeland, P., Avouac, J.-P., Bollinger, L., Mahéo, G., Le Fort, P., Rai, S., Foster, D., P êcher, A., Stüwe, K., Henry, P., 2010. Exhumation, crustal deformation, and thermal structure of the Nepal Himalaya derived from the inversion of thermochronological and thermobarometric data and modeling of the topography. J. Geophys. Res. 115, B06407. https://doi.org/10.1029/2008JB006126

Herman, F., Rhodes, E.J., Braun, J., Heiniger, L., 2010. Uniform erosion rates and relief amplitude during glacial cycles in the Southern Alps of New Zealand, as revealed from OSL-thermochronology. Earth and Planetary Science Letters 297, 183 – 189. https://doi.org/10.1016/j.epsl.2010.06.019

Herman, F., Seward, D., Valla, P.G., Carter, A., Kohn, B., Willett, S.D., Ehlers, T.A., 2013. Worldwide acceleration of mountain erosion under a cooling climate. Nature 504, 423 – 426. https://doi.org/10.1038/nature12877

Herman, F., Beyssac, O., Brughelli, M., Lane, S.N., Leprince, S., Adatte, T., Lin, J.Y., Avouac, J.-P., Cox, S.C., 2015. Erosion by an Alpine glacier. Science 350, 193 – 195. https://doi.org/10.1126/science.aab2386

Herman, F., Willett, S., Matt, F., Yang, R., Stalder, N., Todd, E., 2019. Does spatial averaging of thermochronometric data contain a bias towards acceleration?, in: Geophysical Research Abstracts. Presented at the EGU, Vienna, pp. EGU2019-16043. https://meetingorganizer.copernicus.org/EGU2019/EGU2019-16043-1.pdf

Herzschuh, U., 2006. Palaeo-moisture evolution in monsoonal Central Asia during the last 50,000 years. Quaternary Science Reviews 25, 163 – 178. https://doi.org/10.1016/j.quascirev.2005.02.006

Hetényi, G., Cattin, R., Berthet, T., Le Moigne, N., Chophel, J., Lechmann, S., Hammer, P., Drukpa, D., Sapkota, S.N., Gautier, S., 2016. Segmentation of the Himalayas as revealed by arc-parallel gravity anomalies. Scientific reports 6, 33866. https://doi.org/10.1038/srep33866

Hewitt, K., 1999. Quaternary moraines vs catastrophic rock avalanches in the Karakoram Himalaya, northern Pakistan. Quaternary Research 51, 220 – 237. https://doi.org/10.1006/qres.1999.2033

Hinderer, M., 2012. From gullies to mountain belts: A review of sediment budgets at various scales. Sedimentary Geology 280, 21 – 59. https://doi.org/10.1016/j.sedgeo.2012.03.009

Hjelstuen, B.O., Eldholm, O., Skogseid, J., 1999. Cenozoic evolution of the northern Vøring margin. Geological Society of America Bulletin 111, 1792 – 1807. https://doi.org/10.1130/0016-7606(1999)111<1792:CEOTNV>2.3.CO;2

Hodder, T.J., Ross, M., Menzies, J., 2016. Sedimentary record of ice divide migration and ice streams in the Keewatin core region of the Laurentide Ice Sheet. Sedimentary Geology, Ancient ice streams and their megalineated beds 338, 97 – 114. https://doi.org/10.1016/j.sedgeo.2016.01.001

Hodges, K.V., Wobus, C., Ruhl, K., Schildgen, T., Whipple, K., 2004. Quaternary deformation, river steepening, and heavy precipitation at

the front of the Higher Himalayan ranges. Earth and Planetary Science Letters 220, 379 – 389. https://doi.org/10.1016/S0012-821X(04)00063-9

Hodges, K.V., 2000. Tectonics of the Himalaya and southern Tibet from two perspectives. Geological Society of America Bulletin 112, 324 – 350. https://doi.org/10.1130/0016-7606(2000)112<0324:tothas>2.3.co;2

Hovius, N., Stark, C.P., Allen, P.A., 1997. Sediment flux from a mountain belt derived by landslide mapping. Geology 25, 231 – 234. https://doi.org/10.1130/0091-7613(1997)025<0231:SFFAMB>2.3.CO;2

Hu, X., Garzanti, E., Moore, T., Raffi, I., 2015. Direct stratigraphic dating of India-Asia collision onset at the Selandian (middle Paleocene, 59 ± 1 Ma). Geology G36872.1. https://doi.org/10.1130/G36872.1

Hu, X., Garzanti, E., Wang, J., Huang, W., An, W., Webb, A., 2016. The timing of India-Asia collision onset – Facts, theories, controversies. Earth-Science Reviews 160, 264 – 299. https://doi.org/10.1016/j.earscirev.2016.07.014

Huang, Y., Clemens, S.C., Liu, W., Wang, Y., Prell, W.L., 2007. Large-scale hydrological change drove the late Miocene C4 plant expansion in the Himalayan foreland and Arabian Peninsula. Geol 35, 531. https://doi.org/10.1130/G23666A.1

Huggett, R.J., 2011. Fundamentals of geomorphology, 3rd ed, Routledge fundamentals of physical geography series. Routledge, London.

Huntington, K.W., Blythe, A.E., Hodges, K.V., 2006. Climate change and Late Pliocene acceleration of erosion in the Himalaya. Earth and Planetary Science Letters 252, 107 – 118. https://doi.org/10.1016/j.epsl.2006.09.031

Hurtrez, J.-E., Lucazeau, F., Lavé, J., Avouac, J.-P., 1999. Investigation of the relationships between basin morphology, tectonic uplift, and denudation from the study of an active fold belt in the Siwalik Hills, central Nepal. Journal of Geophysical Research: Solid Earth 104, 12779 – 12796. https://doi.org/10.1029/1998JB900098

Huyghe, P., Galy, A., Mugnier, J.-L., France-Lanord, C., 2001. Propagation of the thrust system and erosion in the Lesser Himalaya: Geochemical and sedimentological evidence. Geology 29, 1007. https://doi.org/10.1130/0091-7613(2001)029<1007:POTTSA>2.0.CO;2

Huyghe, P., Mugnier, J.L., Gajurel, A.P., Delcaillau, B., 2005. Tectonic and climatic control of the changes in the sedimentary record of the Karnali River section (Siwaliks of western Nepal). The Island Arc 14, 311 – 327. https://doi.org/10.1111/j.1440-1738.2005.00500.x

Huyghe, P., Guilbaud, R., Bernet, M., Galy, A., Gajurel, A.P., 2011. Significance of the clay mineral distribution in fluvial sediments of the Neogene to Recent Himalayan Foreland Basin (west-central Nepal). Basin Research 23, 332 – 345. https://doi.org/10.1111/j.1365-2117.2010.00485.x

Huyghe, P., Rosenkranz, R., Bernet, M., Pik, R., Galy, A., Naylor, M., France-Lanord, C., Mugnier, J.-L., 2019. Persistent fast Himalayan exhumation since 12 Ma recorded by Apatite and Zircon Fission Track Dating from the Bengal Fan (IODP 354), in: Geophysical Research Abstracts. Presented at the EGU, Vienne, pp. EGU2019-18374. https://meetingorganizer.copernicus.org/EGU2019/EGU2019-18374.pdf

Igel, H., von Blanckenburg, F., 2000. Lateral mixing and advection of reactive isotopetracers in ocean basins: Numerical modeling. Geochemistry, geophysics, geosystems 1. https://doi.org/10.1029/1999gc000003

Iverson, R.M., 2000. Landslide triggering by rain infiltration. Water Resour. Res. 36, 1897 – 1910. https://doi.org/10.1029/2000WR900090

Jacobson, A.D., Blum, J.D., Chamberlain, C.P., Craw, D., Koons, P.O., 2003. Climatic and tectonic controls on chemical weathering in the New Zealand Southern Alps. Geochimica et Cosmochimica Acta 67, 29 – 46. https://doi.org/10.1016/s0016-7037(02)01053-0

Jacobson, A.D., Andrews, M.G., Lehn, G.O., Holmden, C., 2015. Silicate versus carbonate weathering in Iceland: New insights from Ca isotopes. Earth and Planetary Science Letters 416, 132 – 142. https://doi.org/10.1016/j.epsl.2015.01.030

Jerolmack, D.J., Paola, C., 2007. Complexity in a cellular model of river avulsion. Geomorphology 91, 259 – 270. https://doi.org/10.1016/j.geomorph.2007.04.022

Jiao, R., Herman, F., Seward, D., 2017. Late Cenozoic exhumation model of New Zealand: Impacts from tectonics and climate. Earth-science reviews 166, 286 – 298.

https://doi.org/10.1016/j.earscirev.2017.01.003

Jouanne, F., Mugnier, J.-L., Gamond, J.F., Le Fort, P., Pandey, M.R., Bollinger, L., Flouzat, M., Avouac, J.P., 2004. Current shortening across the Himalayas of Nepal. Geophysical Journal International 157, 1 – 14. https://doi.org/10.1111/j.1365-246X.2004.02180.x

Katz, M.E., Cramer, B.S., Franzese, A., Hönisch, B., Miller, K.G., Rosenthal, Y., Wright, J.D., 2010. Traditional and emerging geochemical proxies in foraminifera. The Journal of Foraminiferal Research 40, 165 – 192. https://doi.org/10.2113/gsjfr.40.2.165

Hoke, G.D., Liu-Zeng, J., Hren, M.T., Wissink, G.K., Garzione, C.N., 2014. Stable isotopes reveal high southeast Tibetan Plateau margin since the Paleogene. Earth and Planetary Science Letters 394, 270 – 278. https://doi.org/10.1016/j.epsl.2014.03.007

Kim, K.J., Englert, P.A.J., 2004. Profiles of in situ 10Be and 26Al at great depths at the Macraes Flat, East Otago, New Zealand. Earth and Planetary Science Letters 223, 113 – 126. https://doi.org/10.1016/j.epsl.2004.04.006

Kim, W., Jerolmack, D.J., 2008. The pulse of calm fan deltas. The Journal of Geology 116, 315 – 330. https://doi.org/10.1086/588830

Kim, D.E., Seong, Y.B., Choi, K.H., Yu, B.Y., 2017. Role of debris flow on the change of 10Be concentration in rapidly eroding watersheds: a case study on the Seti River, central Nepal. J. Mt. Sci. 14, 716 – 730. https://doi.org/10.1007/s11629-016-4282-y

King, G.E., Herman, F., Guralnik, B., 2016. Northward migration of the eastern Himalayan syntaxis revealed by OSL thermochronometry. Science 353, 800 – 804. https://doi.org/10.1126/science.aaf2637

King, G.E., Guralnik, B., Valla, P.G., Herman, F., 2016. Trapped-charge thermochronometry and thermometry: A status review. Chemical Geology 446, 3 – 17. https://doi.org/10.1016/j.chemgeo.2016.08.023

Kleman, J., Stroeven, A.P., Lundqvist, J., 2008. Patterns of Quaternary ice sheet erosion and deposition in Fennoscandia and a theoretical framework for explanation. Geomorphology, Glacial Landscape Evolution - Implications for Glacial Processes, Patterns and Reconstructions 97, 73 – 90. https://doi.org/10.1016/j.geomorph.2007.02.049

Koepnick, R.B., Burke, W.H., Denison, R.E., Hetherington, E.A., Nelson, H.F., Otto, J.B., Waite, L.E., 1985. Construction of the seawater 87Sr86Sr curve for the cenozoic and cretaceous: Supporting data. Chemical Geology: Isotope Geoscience section 58, 55 – 81. https://doi.org/10.1016/0168-9622(85)90027-2

Kohn, M.J., Wieland, M.S., Parkinson, C.D., Upreti, B.N., 2004. Miocene faulting at plate tectonic velocity in the Himalaya of central Nepal. Earth and Planetary Science Letters 228, 299 – 310. https://doi.org/10.1016/j.epsl.2004.10.007

Komatsu, G., Baker, V.R., Arzhannikov, S.G., Gallagher, R., Arzhannikova, A.V., Murana, A., Oguchi, T., 2016. Catastrophic flooding, palaeolakes, and late Quaternary drainage reorganization in northern Eurasia. International Geology Review 58, 1693 – 1722. https://doi.org/10.1080/00206814.2015.1048314

Kominz, M.A., Browning, J.V., Miller, K.G., Sugarman, P.J., Mizintseva, S., Scotese, C.R., 2008. Late Cretaceous to Miocene sea-level estimates from the New Jersey and Delaware coastal plain coreholes: An error analysis. Basin Research 20, 211 – 226. https://doi.org/10.1111/j.1365-2117.2008.00354.x

Koppes, M., Hallet, B., Rignot, E., Mouginot, J., Wellner, J.S., Boldt, K., 2015. Observed latitudinal variations in erosion as a function of glacier dynamics. Nature 526, 100 – 103. https://doi.org/10.1038/nature15385

Korschinek, G., Bergmaier, A., Faestermann, T., Gerstmann, U.C., Knie, K., Rugel, G., Wallner, A., Dillmann, I., Dollinger, G., von Gostomski, Ch.L., Kossert, K., Maiti, M., Poutivtsev, M., Remmert, A., 2010. A new value for the half-life of 10Be by Heavy-Ion Elastic Recoil Detection and liquid scintillation counting. Nuclear Instruments and Methods in Physics Research Section B: Beam Interactions with Materials and Atoms 268, 187 – 191. https://doi.org/10.1016/j.nimb.2009.09.020

Korup, O., Montgomery, D.R., Hewitt, K., 2010. Glacier and landslide feedbacks to topographic relief in the Himalayan syntaxes. Proceedings of the National Academy of Sciences 107, 5317 – 5322. https://doi.org/10.1073/pnas.0907531107

Kroepelin, S., 2006. Revisiting the age of the Sahara desert. Science 312, 1138 – 1139.

https://doi.org/10.1126/science.312.5777.1138b

Kroon, D., Thineke, S., Troelstra, S.R., 1991. Onset of monsoonal related upwelling in the western arabian sea as revealed by planktonic foraminifers, in: Proceedings of the Ocean Drilling Program, Scientific Results, 117. Prell, W. L., Niitsuma, N., et al. https://doi.org/10.2973/odp.proc.sr.117.126.1991

Kuhle, M., 1995. Glacial isostatic uplift of Tibet as a consequence of a former ice sheet. GeoJournal 37, 431 – 449. https://doi.org/10.1007/bf00806933

Kuhle, M., 2011. The High Glacial (Last Ice Age and Last Glacial Maximum) Ice Cover of High and Central Asia, with a Critical Review of Some Recent OSL and TCN Dates, in: Ehlers, J., Gibbard, P.L., Hughes, P.D. (Eds.), Developments in Quaternary Sciences, Quaternary Glaciations - Extent and Chronology. Elsevier, pp. 943 – 965. https://doi.org/10.1016/B978-0-444-53447-7.00068-4

Kuhlemann, J., Frisch, W., Székely, B., Dunkl, I., Kazmér, M., 2002. Post-collisional sediment budget history of the Alps: tectonic versus climatic control. International Journal of Earth Sciences 91, 818 – 837. https://doi.org/10.1007/s00531-002-0266-y

Kuhlmann, G., de Boer, P.L., Pedersen, R.B., Wong, T.E., 2004. Provenance of Pliocene sediments and paleoenvironmental changes in the southern North Sea region using Samarium – Neodymium (Sm/Nd) provenance ages and clay mineralogy. Sedimentary Geology, Quantitative Provenance Analysis of Sediments 171, 205 – 226. https://doi.org/10.1016/j.sedgeo.2004.05.016

Kump, L.R., Brantley, S.L., Arthur, M.A., 2000. Chemical weathering, atmospheric CO2, and climate. Annual Review of Earth and Planetary Sciences 28, 611 – 667. https://doi.org/10.1146/annurev.earth.28.1.611

Laberg, J.S., Andreassen, K., Knies, J., Vorren, T.O., Winsborrow, M., 2010. Late Pliocene – Pleistocene development of the Barents Sea Ice Sheet. Geology 38, 107 – 110. https://doi.org/10.1130/G30193.1

Lacis, A.A., Schmidt, G.A., Rind, D., Ruedy, R.A., 2010. Atmospheric CO2: Principal control knob governing Earth's temperature. Science 330, 356 – 359. https://doi.org/10.1126/science.1190653

Lajeunesse, P., St-Onge, G., 2008. The subglacial origin of the Lake Agassiz – Ojibway final outburst flood. Nature Geoscience 1, 184. https://doi.org/10.1038/ngeo130

Lal, D., Peters, B., 1967. Cosmic ray produced radioactivity on the Earth, in: Sitte, K. (Ed.), Kosmische Strahlung II/Cosmic Rays II. Handbuch der Physik / Encyclopedia of Physics, vol 9 / 46 / 2. Springer, Berlin, Heidelberg, pp. 551 – 612. https://doi.org/10.1007/978-3-642-46079-1_7

Lal, D., 1988. In situ-produced cosmogenic isotopes in terrestrial rocks. Annual Review of Earth and Planetary Sciences 16, 355 – 388. https://doi.org/10.1146/annurev.ea.16.050188.002035

Lal, D., 1991. Cosmic ray labeling of erosion surfaces: in situ nuclide production rates and erosion models. Earth and Planetary Science Letters 104, 424 – 439. https://doi.org/10.1016/0012-821X(91)90220-C

Lallier, F., Antoine, C., Charreau, J., Caumon, G., Ruiu, J., 2013. Management of ambiguities in magnetostratigraphic correlation. Earth and Planetary Science Letters 371 – 372, 26 – 36. https://doi.org/10.1016/j.epsl.2013.04.019

Lang, K.A., Huntington, K.W., 2014. Antecedence of the Yarlung – Siang – Brahmaputra River, eastern Himalaya. Earth and Planetary Science Letters 397, 145 – 158. https://doi.org/10.1016/j.epsl.2014.04.026

Lang, K.A., Huntington, K.W., Burmester, R., Housen, B., 2016. Rapid exhumation of the eastern Himalayan syntaxis since the late Miocene. Geological Society of America Bulletin 128, 1403 – 1422. https://doi.org/10.1130/B31419.1

Larsen, I.J., Almond, P.C., Eger, A., Stone, J.O., Montgomery, D.R., Malcolm, B., 2014. Rapid soil production and weathering in the Southern Alps, New Zealand. Science 343, 637 – 640. https://doi.org/10.1126/science.1244908

Larson, K.M., Bürgmann, R., Bilham, R., Freymueller, J.T., 1999. Kinematics of the India-Eurasia collision zone from GPS measurements. Journal of Geophysical Research: Solid Earth 104, 1077 – 1093. https://doi.org/10.1029/1998jb900043

Lauer, J., Willenbring, J., 2010. Steady state reach-scale theory for radioactive tracer concentration in a simple channel/floodplain system. Journal of Geophysical Research: Earth Surface 115. https://doi.org/10.1029/2009jf001480

Lavé, J., Avouac, J.P., 2000. Active folding of fluvial terraces across the Siwaliks Hills, Himalayas of central Nepal. J. Geophys. Res. 105, 5735 – 5770. https://doi.org/10.1029/1999JB900292

Lavé, J., Avouac, J.P., 2001. Fluvial incision and tectonic uplift across the Himalayas of central Nepal. J. Geophys. Res. 106, 26561 – 26591. https://doi.org/10.1029/2001JB000359

Lavier, L.L., Steckler, M.S., Brigaud, F., 2001. Climatic and tectonic control on the Cenozoic evolution of the West African margin. Marine Geology 178, 63 – 80. https://doi.org/10.1016/S0025-3227(01)00175-X

Le Fort, P., Cuney, M., Deniel, C., France-Lanord, C., Sheppard, S.M.F., Upreti, B.N., Vidal, P., 1987. Crustal generation of the Himalayan leucogranites. Tectonophysics, Deep Seated Processes in Collision Zones 134, 39 – 57. https://doi.org/10.1016/0040-1951(87)90248-4

Le Fort, P., 1975. Himalayas: the collided range. Present knowledge of the continental arc. American Journal of Science 275, 1 – 44.

Le Fort, P., 1986. Metamorphism and magmatism during the Himalayan collision, in: Coward, M. P., Ries, A. C. (Eds.), Collision Tectonics. Geological Society, London, Special Publication 19, pp. 159 – 172. https://doi.org/10.1144/GSL.SP.1986.019.01.08

Lear, C.H., Mawbey, E.M., Rosenthal, Y., 2010. Cenozoic benthic foraminiferal Mg/Ca and Li/Ca records: Toward unlocking temperatures and saturation states. Paleoceanography 25, PA4215. https://doi.org/10.1029/2009PA001880

Lehmkuhl, F., Owen, L.A., Derbyshire, E., 1998. Late Quaternary glacial history of northeast Tibet. Quaternary Proceedings 6, 121 – 142.

Lajeunesse, P., 2012. Palaeoclimate: A history of outbursts. Nature Geosci 5, 846 – 847. https://doi.org/10.1038/ngeo1651

Leya, I., Lange, H.-J., Neumann, S., Wieler, R., Michel, R., 2000. The production of cosmogenic nuclides in stony meteoroids by galactic cosmic-ray particles. Meteoritics & Planetary Science 35, 259 – 286. https://doi.org/10.1111/j.1945-5100.2000.tb01775.x

Li, G., Ji, J., Chen, J., Kemp, D.B., 2009. Evolution of the Cenozoic carbon cycle: The roles of tectonics and CO2 fertilization. Global Biogeochemical Cycles 23, GB1009. https://doi.org/10.1029/2008GB003220

Licht, A., van Cappelle, M., Abels, H.A., Ladant, J.-B., Trabucho-Alexandre, J., France-Lanord, C., Donnadieu, Y., Vandenberghe, J., Rigaudier, T., Lécuyer, C., Terry Jr, D., Adriaens, R., Boura, A., Guo, Z., Soe, A.N., Quade, J., Dupont-Nivet, G., Jaeger, J.-J., 2014. Asian monsoons in a late Eocene greenhouse world. Nature 513, 501 – 506. https://doi.org/10.1038/nature13704

Lifton, N.A., Bieber, J.W., Clem, J.M., Duldig, M.L., Evenson, P., Humble, J.E., Pyle, R., 2005. Addressing solar modulation and long-term uncertainties in scaling secondary cosmic rays for in situ cosmogenic nuclide applications. Earth and Planetary Science Letters 239, 140 – 161. https://doi.org/10.1016/j.epsl.2005.07.001

Lifton, N., Smart, D.F., Shea, M.A., 2008. Scaling time-integrated in situ cosmogenic nuclide production rates using a continuous geomagnetic model. Earth and Planetary Science Letters 268, 190 – 201. https://doi.org/10.1016/j.epsl.2008.01.021

Lifton, N., Sato, T., Dunai, T.J., 2014. Scaling in situ cosmogenic nuclide production rates using analytical approximations to atmospheric cosmic-ray fluxes. Earth and Planetary Science Letters 386, 149 – 160. https://doi.org/10.1016/j.epsl.2013.10.052

Lifton, N., 2016. Implications of two Holocene time-dependent geomagnetic models for cosmogenic nuclide production rate scaling. Earth and Planetary Science Letters 433, 257 – 268. https://doi.org/10.1016/j.epsl.2015.11.006

Lisiecki, L.E., Raymo, M.E., 2005. A Pliocene-Pleistocene stack of 57 globally distributed benthic δ18O records. Paleoceanography 20, PA1003. https://doi.org/10.1029/2004PA001071

Liu, B., Phillips, F.M., Fabryka-Martin, J.T., Fowler, M.M., Stone, W.D., 1994. Cosmogenic 36Cl accumulation in unstable landforms: 1. Effects of the thermal neutron distribution. Water Resources Research 30, 3115 – 3125. https://doi.org/10.1029/94wr00761

Liu, B., Phillips, F.M., Fabryka - Martin, J.T., Fowler, M.M., Stone, W.D., 1995. Correction to

"Cosmogenic 36Cl Accumulation in Unstable Landforms: 1. Effects of the Thermal Neutron Distribution" by B. Liu, F. M. Phillips, J. T. Fabryka-Martin, M. M. Fowler, and W. D. Stone. Water Resources Research 31, 1159 – 1159. https://doi.org/10.1029/95WR00080

Lu, H., Burbank, D.W., Li, Y., Liu, Y., 2010. Late Cenozoic structural and stratigraphic evolution of the northern Chinese Tian Shan foreland. Basin Research 22, 249 – 269. https://doi.org/10.1111/j.1365-2117.2009.00412.x

Lupker, M., France-Lanord, C., Lavé, J., Bouchez, J., Galy, V., Métivier, F., Gaillardet, J., Lartiges, B., Mugnier, J.-L., 2011. A Rouse-based method to integrate the chemical composition of river sediments: Application to the Ganga basin. Journal of Geophysical Research 116. https://doi.org/10.1029/2010JF001947

Lupker, M., Blard, P.-H., Lavé, J., France-Lanord, C., Leanni, L., Puchol, N., Charreau, J., Bourlès, D., 2012. 10Be-derived Himalayan denudation rates and sediment budgets in the Ganga basin. Earth and Planetary Science Letters 333 – 334, 146 – 156. https://doi.org/10.1016/j.epsl.2012.04.020

Lupker, M., France-Lanord, C., Galy, V., Lavé, J., Gaillardet, J., Gajurel, A.P., Guilmette, C., Rahman, M., Singh, S.K., Sinha, R., 2012. Predominant floodplain over mountain weathering of Himalayan sediments (Ganga basin). Geochimica et Cosmochimica Acta 84, 410 – 432. https://doi.org/10.1016/j.gca.2012.02.001

Lupker, M., France-Lanord, C., Galy, V., Lavé, J., Kudrass, H., 2013. Increasing chemical weathering in the Himalayan system since the Last Glacial Maximum. Earth and Planetary Science Letters 365, 243 – 252. https://doi.org/10.1016/j.epsl.2013.01.038

Lupker, M., Lavé, J., France-Lanord, C., Christl, M., Bourlès, D., Carcaillet, J., Maden, C., Wieler, R., Rahman, M., Bezbaruah, D., Xiaohan, L., 2017. 10Be systematics in the Tsangpo-Brahmaputra catchment: the cosmogenic nuclide legacy of the eastern Himalayan syntaxis. Earth Surface Dynamics 5, 429 – 449. https://doi.org/10.5194/esurf-5-429-2017

Lüthi, D., Le Floch, M., Bereiter, B., Blunier, T., Barnola, J.-M., Siegenthaler, U., Raynaud, D., Jouzel, J., Fischer, H., Kawamura, K., Stocker, T.F., 2008. High-resolution carbon dioxide concentration record 650,000 – 800,000 years before present. Nature 453, 379 – 382. https://doi.org/10.1038/nature06949

Lyon-Caen, H., Molnar, P., 1985. Gravity anomalies, flexure of the Indian Plate, and the structure, support and evolution of the Himalaya and Ganga Basin. Tectonics 4, 513 – 538. https://doi.org/10.1029/TC004i006p00513

Malusà, M.G., Wang, J., Garzanti, E., Liu, Z.-C., Villa, I.M., Wittmann, H., 2017. Trace-element and Nd-isotope systematics in detrital apatite of the Po river catchment: implications for provenance discrimination and the lag-time approach to detrital thermochronology. Lithos 290, 48 – 59. https://doi.org/10.1016/j.lithos.2017.08.006

Mandal, S.K., Scherler, D., Romer, R.L., Burg, J.-P., Guillong, M., Schleicher, A.M., 2019. Multiproxy Isotopic and Geochemical Analysis of the Siwalik Sediments in NW India: Implication for the Late Cenozoic Tectonic Evolution of the Himalaya. Tectonics 38, 120 – 143.

Mangerud, J., Jakobsson, M., Alexanderson, H., Astakhov, V., Clarke, G.K., Henriksen, M., Hjort, C., Krinner, G., Lunkka, J.-P., Möller, P., 2004. Ice-dammed lakes and rerouting of the drainage of northern Eurasia during the Last Glaciation. Quaternary Science Reviews 23, 1313 – 1332. https://doi.org/10.1016/j.quascirev.2003.12.009

Marc, O., Hovius, N., Meunier, P., 2016. The mass balance of earthquakes and earthquake sequences. Geophysical Research Letters 43, 3708 – 3716. https://doi.org/10.1002/2016GL068333

Mariotti, A., 2020. Impact du dernier cycle glaciaire-interglaciaire sur la dénudation dans les Alpes du Sud. Université de Lorraine.

Marrero, S.M., Phillips, F.M., Borchers, B., Lifton, N., Aumer, R., Balco, G., 2016. Cosmogenic nuclide systematics and the CRONUScalc program. Quaternary Geochronology 31, 160 – 187. https://doi.org/10.1016/j.quageo.2015.09.005

Martin, L.C.P., Blard, P.-H., Balco, G., Lavé, J., Delunel, R., Lifton, N., Laurent, V., 2017. The CREp program and the ICE-D production rate calibration database: A fully parameterizable and updated online tool to compute cosmic-ray exposure ages. Quaternary Geochronology 38, 25 – 49.

https://doi.org/10.1016/j.quageo.2016.11.006

Martini, E., 1971. Standard Tertiary and Quaternary calcareous nannoplankton zonation, in: Proc. II Planktonic Conference, Roma 1970, Roma, Tecnoscienza. pp. 739-785.

Masarik, J., Beer, J., 1999. Simulation of particle fluxes and cosmogenic nuclide production in the Earth's atmosphere. Journal of Geophysical Research: Atmospheres 104, 12099 – 12111. https://doi.org/10.1029/1998jd200091

Masarik, J., Beer, J., 2009. An updated simulation of particle fluxes and cosmogenic nuclide production in the Earth's atmosphere. Journal of Geophysical Research: Atmospheres 114. https://doi.org/10.1029/2008jd010557

Masarik, J., Reedy, R.C., 1995. Terrestrial cosmogenic-nuclide production systematics calculated from numerical simulations. Earth and Planetary Science Letters 136, 381 – 395. https://doi.org/doi.org/10.1016/0012-821x(95)00169-d

Maurin, T., Rangin, C., 2009. Structure and kinematics of the Indo-Burmese Wedge: Recent and fast growth of the outer wedge. Tectonics 28, n/a-n/a. https://doi.org/10.1029/2008TC002276

Maurin, T., Rangin, C., 2009. Structure and kinematics of the Indo-Burmese Wedge: Recent and fast growth of the outer wedge. Tectonics 28, TC2010. https://doi.org/10.1029/2008TC002276

McNeill, L.C., Henstock, T.J., 2014. Forearc structure and morphology along the Sumatra-Andaman subduction zone. Tectonics 33, 112 – 134. https://doi.org/10.1002/2012TC003264

McNeill, L.C., Dugan, B., Backman, J., Pickering, K.T., Pouderoux, H.F.A., Henstock, T.J., Petronotis, K.E., Carter, A., Chemale, F., Milliken, K.L., Kutterolf, S., Mukoyoshi, H., Chen, W., Kachovich, S., Mitchison, F.L., Bourlange, S., Colson, T.A., Frederik, M.C.G., Guèrin, G., Hamahashi, M., House, B.M., Hüpers, A., Jeppson, T.N., Kenigsberg, A.R., Kuranaga, M., Nair, N., Owari, S., Shan, Y., Song, I., Torres, M.E., Vannucchi, P., Vrolijk, P.J., Yang, T., Zhao, X., Thomas, E., 2017. Understanding Himalayan erosion and the significance of the Nicobar Fan. Earth and Planetary Science Letters 475, 134 – 142. https://doi.org/10.1016/j.epsl.2017.07.019

Meigs, A.J., Burbank, D.W., Beck, R.A., 1995. Middle-late Miocene (> 10 Ma) formation of the Main Boundary thrust in the western Himalaya. Geology 23, 423 – 426. https://doi.org/10.1130/0091-7613(1995)023<0423:mlmmfo>2.3.co;2

Ménabréaz, L., Thouveny, N., Bourlès, D.L., Vidal, L., 2014. The geomagnetic dipole moment variation between 250 and 800 ka BP reconstructed from the authigenic 10Be/9Be signature in West Equatorial Pacific sediments. Earth and Planetary Science Letters 385, 190 – 205. https://doi.org/10.1016/j.epsl.2013.10.037

Meng, J., Wang, C., Zhao, X., Coe, R., Li, Y., Finn, D., 2012. India-Asia collision was at 24 N and 50 Ma: palaeomagnetic proof from southernmost Asia. Scientific reports 2, 925. https://doi.org/10.1038/srep00925

Métivier, F., Gaudemer, Y., Tapponnier, P., Klein, M., 1999. Mass accumulation rates in Asia during the Cenozoic. Geophys. J. Int. 137, 280 – 318. https://doi.org/10.1046/j.1365-246X.1999.00802.x

Métivier, F., 2002. On the use of sedimentation rates in deciphering global change. Geophysical Research Letters 29, 41-1-41 – 4. https://doi.org/10.1029/2002GL015261

Meybeck, M., Ragu, A., 1997. River discharges to the oceans: an assessment of suspended solids, major ions and nutrients. UNEP.

Michels, K.H., Suckow, A., Breitzke, M., Kudrass, H.R., Kottke, B., 2003. Sediment transport in the shelf canyon "Swatch of No Ground" (Bay of Bengal). Deep Sea Research Part II: Topical Studies in Oceanography 50, 1003 – 1022. https://doi.org/10.1016/S0967-0645(02)00617-3

Miller, K.G., Kominz, M.A., Browning, J.V., Wright, J.D., Mountain, G.S., Katz, M.E., Sugarman, P.J., Cramer, B.S., Christie-Blick, N., Pekar, S.F., 2005. The Phanerozoic Record of Global Sea-Level Change. Science 310, 1293 – 1298. https://doi.org/10.1126/science.1116412

Miller, K., Mountain, G., Wright, J., Browning, J., 2011. A 180-Million-Year Record of Sea Level and Ice Volume Variations from Continental Margin and Deep-Sea Isotopic Records. Oceanography 24, 40 – 53. https://doi.org/10.5670/oceanog.2011.26

Milliman, J.D., Farnsworth, K.L., 2011. River discharge to the coastal ocean: a global synthesis. Cambridge University Press.

Milliman, J.D., Meade, R.H., 1983. World-Wide Delivery of River Sediment to the Oceans. The Journal of Geology 91, 1 – 21. https://doi.org/10.1086/628741

Misra, S., Froelich, P.N., 2012. Lithium Isotope History of Cenozoic Seawater: Changes in Silicate Weathering and Reverse Weathering. Science 335, 818 – 823. https://doi.org/10.1126/science.1214697

Mitchell, A.H.G., 1993. Cretaceous – Cenozoic tectonic events in the western Myanmar (Burma) – Assam region. Journal of the Geological Society 150, 1089 – 1102. https://doi.org/10.1144/gsjgs.150.6.1089

Molnar, P., England, P., 1990. Late Cenozoic uplift of mountain ranges and global climate change: chicken or egg? Nature 346, 29 – 34. https://doi.org/10.1038/346029a0

Molnar, P., Lyon-Caen, H., 1988. Some simple physical aspects of the support, structure, and evolution of mountain belts, in: Geological Society of America Special Papers. Geological Society of America, pp. 179 – 208. https://doi.org/10.1130/SPE218-p179

Molnar, P., Tapponnier, P., 1975. Cenozoic tectonics of Asia: effects of a continental collision. science 189, 419 – 426. https://doi.org/10.1126/science.189.4201.419

Molnar, P., Anderson, R.S., Anderson, S.P., 2007. Tectonics, fracturing of rock, and erosion. Journal of Geophysical Research: Earth Surface 112. https://doi.org/10.1029/2005JF000433

Molnar, P., Boos, W.R., Battisti, D.S., 2010. Orographic Controls on Climate and Paleoclimate of Asia: Thermal and Mechanical Roles for the Tibetan Plateau. Annual Review of Earth and Planetary Sciences 38, 77 – 102. https://doi.org/10.1146/annurev-earth-040809-152456

Molnar, P., 2001. Climate change, flooding in arid environments, and erosion rates. Geology 29, 1071 – 1074. https://doi.org/10.1130/0091-7613(2001)029<1071:CCFIAE>2.0.CO;2

Molnar, P., 2004. Late Cenozoic increase in accumulation rates of terrestrial sediment: how might climate change have affected erosion rates? Annual Review of Earth and Planetary Sciences 32, 67 – 89. https://doi.org/10.1146/annurev.earth.32.091003.143456

Molnar, P., 2012. Isostasy can't be ignored. Nature Geoscience 5, 83. https://doi.org/10.1038/ngeo1383

Montgomery, D.R., Hallet, B., Yuping, L., Finnegan, N., Anders, A., Gillespie, A., Greenberg, H.M., 2004. Evidence for Holocene megafloods down the tsangpo River gorge, Southeastern Tibet. Quaternary Research 62, 201 – 207. https://doi.org/10.1016/j.yqres.2004.06.008

Montgomery, D.R., 2002. Valley formation by fluvial and glacial erosion. Geology 30, 1047 – 1050. https://doi.org/10.1130/0091-7613(2002)030<1047:VFBFAG>2.0.CO;2

Moore Jr, T.C., Heath, G.R., 1977. Survival of deep-sea sedimentary sections. Earth and Planetary Science Letters 37, 71 – 80. https://doi.org/10.1016/0012-821x(77)90147-9

Moore Jr, T.C., Van Andel, T.H., Sancetta, C., Pisias, N., 1978. Cenozoic hiatuses in pelagic sediments. Micropaleontology 113 – 138. https://doi.org/10.2307/1485246

Moore, J., Jacobson, A.D., Holmden, C., Craw, D., 2013. Tracking the relationship between mountain uplift, silicate weathering, and long-term CO2 consumption with Ca isotopes: Southern Alps, New Zealand. Chemical Geology 341, 110 – 127. https://doi.org/10.1016/j.chemgeo.2013.01.005

Moran, K., Backman, J., Brinkhuis, H., Clemens, S.C., Cronin, T., Dickens, G.R., Eynaud, F., Gattacceca, J., Jakobsson, M., Jordan, R.W., Kaminski, M., King, J., Koc, N., Krylov, A., Martinez, N., Matthiessen, J., McInroy, D., Moore, T.C., Onodera, J., O'Regan, M., Pälike, H., Rea, B., Rio, D., Sakamoto, T., Smith, D.C., Stein, R., St John, K., Suto, I., Suzuki, N., Takahashi, K., Watanabe, M., Yamamoto, M., Farrell, J., Frank, M., Kubik, P., Jokat, W., Kristoffersen, Y., 2006. The Cenozoic palaeoenvironment of the Arctic Ocean. Nature 441, 601 – 605. https://doi.org/10.1038/nature04800

Morin, G.P., Lavé, J., France-Lanord, C., Rigaudier, T., Gajurel, A.P., Sinha, R., 2018. Annual Sediment Transport Dynamics in the Narayani Basin, Central Nepal: Assessing the Impacts of Erosion Processes in the Annual Sediment Budget. Journal of Geophysical Research: Earth Surface 123, 2341 – 2376. https://doi.org/10.1029/2017JF004460

Morin, G., 2015. L'Érosion Et L'Alteration Et Leur Évolution Depuis Le Tardi-Pleistocene : Analyse Des Processus D'Érosion A Partir De Sediments De Riviere Actuels Et Passes Au Nepal Central. Université de Lorraine, Nancy, France. https://www.theses.fr/193281864

Morley, C.K., Back, S., 2008. Estimating hinterland exhumation from late orogenic basin volume, NW Borneo. Journal of the Geological Society 165, 353 – 366. https://doi.org/10.1144/0016-76492007-067

Mudelsee, M., Bickert, T., Lear, C.H., Lohmann, G., 2014. Cenozoic climate changes: A review based on time series analysis of marine benthic δ 18O records. Rev. Geophys. 52, 333 – 374. https://doi.org/10.1002/2013RG000440

Mugnier, J.-L., Huyghe, P., 2006. Ganges basin geometry records a pre-15 Ma isostatic rebound of Himalaya. Geology 34, 445 – 448. https://doi.org/10.1130/g22089.1

Mugnier, J.L., Leturmy, P., Mascle, G., Huyghe, P., Chalaron, E., Vidal, G., Husson, L., Delcaillau, B., 1999. The Siwaliks of western Nepal: I. Geometry and kinematics. Journal of Asian Earth Sciences 17, 629 – 642. https://doi.org/10.1016/s1367-9120(99)00038-3

Mugnier, J.-L., Huyghe, P., Leturmy, P., Jouanne, F., 2004. Episodicity and rates of thrust-sheet motion in the Himalayas (western Nepal), in: Thrust Tectonics and Hydrocarbon Systems, AAPG Memoir. K. R. McClay. http://archives.datapages.com/data/specpubs/memoir82/CHAPTER6/CHAPTER6.HTM

Muhs, D.R., Bettis, E.A., 2003. Quaternary loess-paleosol sequences as examples of climate-driven sedimentary extremes, in: Chan, M.A., Archer, A.W. (Eds.), Extreme Depositional Environments: Mega End Members in Geologic Time. Geological Society of America Special Paper 370, Boulder, Colorado, pp. 53 – 74. https://doi.org/10.1130/0-8137-2370-1.53

Müller, R.D., Sdrolias, M., Gaina, C., Steinberger, B., Heine, C., 2008. Long-Term Sea-Level Fluctuations Driven by Ocean Basin Dynamics. Science 319, 1357 – 1362. https://doi.org/10.1126/science.1151540

Muscheler, R., Beer, J., Kubik, P.W., Synal, H.-A., 2005. Geomagnetic field intensity during the last 60,000 years based on 10Be and 36Cl from the Summit ice cores and 14C. Quaternary Science Reviews 24, 1849 – 1860. https://doi.org/10.1016/j.quascirev.2005.01.012

Muto, T., Steel, R.J., 2000. The accommodation concept in sequence stratigraphy: some dimensional problems and possible redefinition. Sedimentary Geology 130, 1 – 10. https://doi.org/10.1016/s0037-0738(99)00107-4

Nábelek, J., Hetényi, G., Vergne, J., Sapkota, S., Kafle, B., Jiang, M., Su, H., Chen, J., Huang, B.-S., Team, t. H.-C., 2009. Underplating in the Himalaya-Tibet Collision Zone Revealed by the Hi-CLIMB Experiment. Science 325, 1371 – 1374. https://doi.org/10.1126/science.1167719

Nadin, E.S., Martin, A.J., 2012. Apatite thermochronometry within a knickzone near the Higher Himalaya front, central Nepal: No resolvable fault motion in the past one million years. Tectonics 31, n/a-n/a. https://doi.org/10.1029/2011TC003000

Najman, Y., Bracciali, L., Parrish, R.R., Chisty, E., Copley, A., 2016. Evolving strain partitioning in the Eastern Himalaya: The growth of the Shillong Plateau. Earth and Planetary Science Letters 433, 1 – 9. https://doi.org/10.1016/j.epsl.2015.10.017

Najman, Y., Mark, C., Barfod, D.N., Carter, A., Parrish, R., Chew, D., Gemignani, L., 2019. Spatial and temporal trends in exhumation of the Eastern Himalaya and syntaxis as determined from a multitechnique detrital thermochronological study of the Bengal Fan. Geological Society of America Bulletin. https://doi.org/10.1130/B35031.1

Nakayama, K., Ulak, P.D., 1999. Evolution of fluvial style in the Siwalik Group in the foothills of the Nepal Himalaya. Sedimentary Geology 125, 205 – 224. https://doi.org/10.1016/S0037-0738(99)00012-3

Naylor, M., Sinclair, H.D., Bernet, M., van der Beek, P., Kirstein, L.A., 2015. Bias in detrital fission track grain-age populations: Implications for reconstructing changing erosion rates. Earth and Planetary Science Letters 422, 94 – 104. https://doi.org/10.1016/j.epsl.2015.04.020

Nicholl, J.A., Hodell, D.A., Naafs, B.D.A., Hillaire-Marcel, C., Channell, J.E., Romero, O.E., 2012. A Laurentide outburst flooding event during the last interglacial period. Nature Geoscience 5, 901. https://doi.org/10.1038/NGEO1622

Niemi, N.A., Oskin, M., Burbank, D.W., Heimsath, A.M., Gabet, E.J., 2005. Effects of bedrock landslides on cosmogenically determined erosion rates. Earth and Planetary Science Letters 237, 480 − 498. https://doi.org/10.1016/j.epsl.2005.07.009

Nishiizumi, K., Winterer, E.L., Kohl, C.P., Klein, J., Middleton, R., Lal, D., Arnold, J.R., 1989. Cosmic ray production rates of 10Be and 26Al in quartz from glacially polished rocks. J. Geophys. Res. 94, 17907 − 17915. https://doi.org/10.1029/JB094iB12p17907

Norton, K.P., Schlunegger, F., 2017. Lack of a weathering signal with increased Cenozoic erosion? Terra Nova 29, 265 − 272. https://doi.org/10.1111/ter.12278

Norton, K.P., Vanacker, V., 2009. Effects of terrain smoothing on topographic shielding correction factors for cosmogenic nuclide-derived estimates of basin-averaged denudation rates. Earth Surface Processes and Landforms 34, 145 − 154. https://doi.org/10.1002/esp.1700

Norton, K.P., von Blanckenburg, F., 2010. Silicate weathering of soil-mantled slopes in an active Alpine landscape. Geochimica et Cosmochimica Acta 74, 5243 − 5258. https://doi.org/10.1016/j.gca.2010.06.019

Norton, K.P., Abbühl, L.M., Schlunegger, F., 2010. Glacial conditioning as an erosional driving force in the Central Alps. Geology 38, 655 − 658. https://doi.org/10.1130/G31102.1

Ogg, J.G., 2012. Geomagnetic Polarity Time Scale, in: Gradstein, F.M. (Ed.), The Geological Time Scale.

Ojha, T.P., Butler, R.F., Quade, J., DeCelles, P.G., Richards, D., Upreti, B.N., 2000. Magnetic polarity stratigraphy of the Neogene Siwalik Group at Khutia Khola, far western Nepal. GSA Bulletin 112, 424 − 434. https://doi.org/10.1130/0016-7606(2000)112<424:MPSOTN>2.0.CO;2

Ojha, T.P., Butler, R.F., DeCelles, P.G., Quade, J., 2009. Magnetic polarity stratigraphy of the Neogene foreland basin deposits of Nepal. Basin Research 21, 61 − 90. https://doi.org/10.1111/j.1365-2117.2008.00374.x

Ojha, L., Ferrier, K.L., Tank Ojha, T., 2019. Millennial-scale denudation rates in the Himalaya of Far Western Nepal. Earth Surface Dynamics Discussion. https://doi.org/10.5194/esurf-2019-7

Okada, H., Bukry, D., 1980. Supplementary modification and introduction of code numbers to the low-latitude coccolith biostratigraphic zonation (Bukry, 1973; 1975). Marine Micropaleontology 5, 321-325. https://doi.org/10.1016/0377-8398(80)90016-X

O'Leary, M.H., 1981. Carbon isotope fractionation in plants. Phytochemistry 20, 553 − 567. https://doi.org/10.1016/0031-9422(81)85134-5

Olson, P., Reynolds, E., Hinnov, L., Goswami, A., 2016. Variation of ocean sediment thickness with crustal age. Geochemistry, Geophysics, Geosystems 17, 1349 − 1369. https://doi.org/10.1002/2015GC006143

Overeem, I., Weltje, G.J., Bishop-Kay, C., Kroonenberg, S.B., 2001. The Late Cenozoic Eridanos delta system in the Southern North Sea Basin: a climate signal in sediment supply? Basin Research 13, 293 − 312. https://doi.org/10.1046/j.1365-2117.2001.00151.x

Owen, L.A., Dortch, J.M., 2014. Nature and timing of Quaternary glaciation in the Himalayan − Tibetan orogen. Quaternary Science Reviews 88, 14 − 54. https://doi.org/10.1016/j.quascirev.2013.11.016

Parker, R.N., Densmore, A.L., Rosser, N.J., de Michele, M., Li, Y., Huang, R., Whadcoat, S., Petley, D.N., 2011. Mass wasting triggered by the 2008 Wenchuan earthquake is greater than orogenic growth. Nature Geoscience 4, 449 − 452. https://doi.org/10.1038/ngeo1154

Parrenin, F., Masson-Delmotte, V., Köhler, P., Raynaud, D., Paillard, D., Schwander, J., Barbante, C., Landais, A., Wegner, A., Jouzel, J., 2013. Synchronous change of atmospheric CO2 and Antarctic temperature during the last deglacial warming. Science 339, 1060 − 1063. https://doi.org/10.1126/science.1226368

Parrish, R.R., Hodges, V., 1996. Isotopic constraints on the age and provenance of the Lesser and Greater Himalayan sequences, Nepalese Himalaya. Geological Society of America Bulletin 108, 904 − 911. https://doi.org/10.1130/0016-7606(1996)108<0904:ICOTAA>2.3.CO;2

Passchier, S., 2018. Ice sheets and climate: the marine geological record, in: Menzies, J., van der Meer, J. J.M. (Eds.), Past Glacial Environments. pp. 565 − 584.

https://doi.org/10.1016/B978-0-08-100524-8.00017-8

Patriat, P., Achache, J., 1984. India − Eurasia collision chronology has implications for crustal shortening and driving mechanism of plates. Nature 311, 615 − 621. https://doi.org/10.1038/311615a0

Pedersen, V.K., Egholm, D.L., 2013. Glaciations in response to climate variations preconditioned by evolving topography. Nature 493, 206 − 210. https://doi.org/10.1038/nature11786

Pedersen, V.K., Huismans, R.S., Herman, F., Egholm, D.L., 2014. Controls of initial topography on temporal and spatial patterns of glacial erosion. Geomorphology 223, 96 − 116. https://doi.org/10.1016/j.geomorph.2014.06.028

Penck, W., 1924. Morphological analysis of landforms. Translated by Hella Czeck and KC Boswell, 1953. St. Martin's Press, New York, New York, USA.

Phillips, F.M., Stone, W.D., Fabryka-Martin, J.T., 2001. An improved approach to calculating low-energy cosmic-ray neutron fluxes near the landratmosphere interface 13. https://doi.org/10.1016/s0009-2541(00)00329-6

Phillips, F.M., Argento, D.C., Balco, G., Caffee, M.W., Clem, J., Dunai, T.J., Finkel, R., Goehring, B., Gosse, J.C., Hudson, A.M., others, 2016. The CRONUS-Earth project: a synthesis. Quaternary Geochronology 31, 119 − 154. https://doi.org/10.1016/j.quaint.2012.08.1175

Pigati, J.S., Lifton, N.A., 2004. Geomagnetic effects on time-integrated cosmogenic nuclide production with emphasis on in situ 14C and 10Be. Earth and Planetary Science Letters 226, 193 − 205. https://doi.org/10.1016/j.epsl.2004.07.031

Pingel, H., Strecker, M.R., Alonso, R.N., Schmitt, A.K., 2013. Neotectonic basin and landscape evolution in the Eastern Cordillera of NW Argentina, Humahuaca Basin (~ 24 S). Basin Research 25, 554 − 573. https://doi.org/10.1111/bre.12016

Pingel, H., Schildgen, T., Strecker, M.R., Wittmann, H., 2019. Pliocene − Pleistocene orographic control on denudation in northwest Argentina. Geology 47, 359 − 362. https://doi.org/10.1130/G45800.1

Portenga, E.W., Bierman, P.R., 2011. Understanding Earth's eroding surface with 10Be. GSA Today 21, 4 − 10. https://doi.org/10.1130/G111A.1

Portenga, E.W., Bierman, P.R., Duncan, C., Corbett, L.B., Kehrwald, N.M., Rood, D.H., 2015. Erosion rates of the Bhutanese Himalaya determined using in situ-produced 10Be. Geomorphology 233, 112 − 126. https://doi.org/10.1016/j.geomorph.2014.09.027

Porter, S.C., Zhisheng, A., Hongbo, Z., 1992. Cyclic Quaternary alluviation and terracing in a nonglaciated drainage basin on the north flank of the Qinling Shan, central China. Quaternary Research 38, 157 − 169. https://doi.org/10.1016/0033-5894(92)90053-l

Posamentier, H.W., Vail, P.R., 1988. Eustatic controls on clastic deposition II—sequence and systems tract models, in: Wilgus, C. K., Hastings, B. S., Kendall, C. G. S. C., Posamentier, H. W., Ross, C. A., Van Wagoner, J. C. (Eds.), Sea-Level Changes: An Integrated Approach. SEPM special publication, 42.

Powell, C.F., Fowler, P.H., Perkins, D.H., 1959. The study of elementary particles by the photographic method: an account of the principal techniques and discoveries illustrated by an atlas of photomicrographs. Pergamon, London.

Pratt, B., Burbank, D.W., Heimsath, A., Ojha, T., 2002. Impulsive alluviation during early Holocene strengthened monsoons, central Nepal Himalaya. Geology 30, 911. https://doi.org/10.1130/0091-7613(2002)030<0911:IADEHS>2.0.CO;2

Prell, W.L., Kutzbach, J.E., 1992. Sensitivity of the Indian monsoon to forcing parameters and implications for its evolution. Nature 360, 647 − 652. https://doi.org/10.1038/360647a0

Prell, W.L., Murray, D.W., Clemens, S.C., Anderson, D.M., 1992. Evolution and variability of the Indian Ocean summer monsoon: evidence from the western Arabian Sea drilling program, in: Duncan, R.A., D.K. Rea, R.B. Kidd, U. von Rad, J.K. Weissel (Eds.), Synthesis of Results from Scientific Drilling in the Indian Ocean. pp. 447 − 469. https://doi.org/10.1029/gm070p0447

Puchol, N., Lavé, J., Lupker, M., Blard, P.-H., Gallo, F., France-Lanord, C., 2014. Grain-size dependent concentration of cosmogenic 10Be and erosion dynamics in a landslide-dominated Himalayan watershed. Geomorphology 224, 55 − 68.

https://doi.org/10.1016/j.geomorph.2014.06.019

Puchol, N., Charreau, J., Blard, P.-H., Lavé, J., Dominguez, S., Pik, R., Saint-Carlier, D., ASTER Team, 2017. Limited impact of Quaternary glaciations on denudation rates in Central Asia. Geological Society of America Bulletin 129 (3 – 4), 479 – 499. https://doi.org/10.1130/B31475.1

Puchol, N., 2013. Détermination des paléo-taux d'érosion par l'utilisation des isotopes cosmogéniques. Cas de la transition Pliocène-Pleistocène. Université de Nancy, INPL, Lorraine, Nancy. https://tel.archives-ouvertes.fr/tel-00958150

Quade, J., Cerling, T.E., 1995. Expansion of C4 grasses in the Late Miocene of Northern Pakistan: evidence from stable isotopes in paleosols. Palaeogeography, Palaeoclimatology, Palaeoecology, Long Records of Continental Ecosystems: Paleogene of Wyoming-Montana and Neogene of Pakistan 115, 91 – 116. https://doi.org/10.1016/0031-0182(94)00108-K

Quade, J., Cerling, T.E., Bowman, J.R., 1989. Development of Asian monsoon revealed by marked ecological shift during the latest Miocene in northern Pakistan. Nature 342, 163 – 166. https://doi.org/10.1038/342163a0

Quade, J., Cater, J.M., Ojha, T.P., Adam, J., Harrison, T.M., 1995. Late Miocene environmental change in Nepal and the northern Indian subcontinent: Stable isotopic evidence from paleosols. Geological Society of America Bulletin 107, 1381 – 1397. https://doi.org/10.1130/0016-7606(1995)107<1381:lmecin>2.3.co;2

Quade, J., Breecker, D.O., Daeron, M., Eiler, J., 2011. The paleoaltimetry of Tibet: An isotopic perspective. American Journal of Science 311, 77 – 115. https://doi.org/10.2475/02.2011.01

Radhakrishna, M., Subrahmanyam, C., Damodharan, T., 2010. Thin oceanic crust below Bay of Bengal inferred from 3-D gravity interpretation. Tectonophysics 493, 93 – 105. https://doi.org/10.1016/j.tecto.2010.07.004

Rahl, J., Ehlers, T., Vanderpluijm, B., 2007. Quantifying transient erosion of orogens with detrital thermochronology from syntectonic basin deposits. Earth and Planetary Science Letters 256, 147 – 161. https://doi.org/10.1016/j.epsl.2007.01.020

Rahn, M.K., Brandon, M.T., Batt, G.E., Garver, J.I., 2004. A zero-damage model for fission-track annealing in zircon. American Mineralogist 89, 473 – 484. https://doi.org/10.2138/am-2004-0401

Ramírez, D.A., Foster, D.A., Min, K., Montes, C., Cardona, A., Sadove, G., 2016. Exhumation of the Panama basement complex and basins: Implications for the closure of the Central American seaway: EXHUMATION OF PANAMA COMPLEX AND BASINS. Geochemistry, Geophysics, Geosystems 17, 1758 – 1777. https://doi.org/10.1002/2016GC006289

Rathmann, S., Hess, S., Kuhnert, H., Mulitza, S., 2004. Mg/Ca ratios of the benthic foraminifera Oridorsalis umbonatus obtained by laser ablation from core top sediments: Relationship to bottom water temperature. Geochemistry, Geophysics, Geosystems 5. https://doi.org/10.1029/2004GC000808

Raup, B., Racoviteanu, A., Khalsa, S.J.S., Helm, C., Armstrong, R., Arnaud, Y., 2007. The GLIMS geospatial glacier database: A new tool for studying glacier change. Global and Planetary Change, Climate Change Impacts on Mountain Glaciers and Permafrost 56, 101 – 110. https://doi.org/10.1016/j.gloplacha.2006.07.018

Raymo, M.E., Ruddiman, W.F., 1992. Tectonic forcing of late Cenozoic climate. Nature 359, 117 – 122. https://doi.org/10.1038/359117a0

Raymo, M.E., Ruddiman, W.F., 1992. Resp. Tectonic forcing of late Cenozoic climate. Nature 359, 117 – 122.

Raymo, M.E., Ruddiman, W.F., Froelich, P.N., 1988. Influence of late Cenozoic mountain building on ocean geochemical cycles. Geology 16, 649 – 653. https://doi.org/10.1130/0091-7613(1988)016<0649:iolcmb>2.3.co;2

Raymo, M.E., 1991. Geochemical evidence supporting TC Chamberlin's theory of glaciation. Geology 19, 344 – 347. https://doi.org/10.1130/0091-7613(1991)019<0344:gestcc>2.3.co;2

Refsnider, K.A., 2010. Dramatic increase in late Cenozoic alpine erosion rates recorded by cave sediment in the southern Rocky Mountains. Earth and Planetary Science Letters 297, 505 – 511. https://doi.org/10.1016/j.epsl.2010.07.002

Reilly, B.T. (2018). Deciphering Quaternary geomagnetic, glacial, and depositional

histories using paleomagnetism in tandem with other chronostratigraphic and sedimentological approaches. Corvallis, Or.: Oregon State University.

Reilly, B.T., 2018. Deciphering Quaternary Geomagnetic, Glacial, and Depositional Histories Using Paleomagnetism in Tandem with Other Chronostratigraphic and Sedimentological Approaches, phD Thesis. Oregon State University

Reilly, B.T., 2018. Deciphering Quaternary geomagnetic, glacial, and depositional histories using paleomagnetism in tandem with other chronostratigraphic and sedimentological approaches. Corvallis, Or.: Oregon State University.

Reiners, P.W., Brandon, M.T., 2006. Using Thermochronology to Understand Orogenic Erosion. Annual Review of Earth and Planetary Sciences 34, 419 – 466. https://doi.org/10.1146/annurev.earth.34.031405.125202

Retallack, G.J., 2001. Cenozoic Expansion of Grasslands and Climatic Cooling. The Journal of Geology 109, 407 – 426. https://doi.org/10.1086/320791

Reuter, M., Kern, A.K., Harzhauser, M., Kroh, A., Piller, W.E., 2013. Global warming and South Indian monsoon rainfall—lessons from the Mid-Miocene. Gondwana Research 23, 1172 – 1177. https://doi.org/10.1016/j.gr.2012.07.015

Richter, F.M., Rowley, D.B., DePaolo, D.J., 1992. Sr isotope evolution of seawater: the role of tectonics. Earth and Planetary Science Letters 109, 11 – 23. https://doi.org/10.1016/0012-821X(92)90070-C

Rise, L., Ottesen, D., Berg, K., Lundin, E., 2005. Large-scale development of the mid-Norwegian margin during the last 3 million years. Marine and Petroleum Geology 22, 33 – 44. https://doi.org/10.1016/j.marpetgeo.2004.10.010

Robert, X., van der Beek, P., Braun, J., Perry, C., Dubille, M., Mugnier, J.-L., 2009. Assessing Quaternary reactivation of the Main Central thrust zone (central Nepal Himalaya): New thermochronologic data and numerical modeling. Geology 37, 731 – 734. https://doi.org/10.1130/G25736A.1

Robert, X., van der Beek, P., Braun, J., Perry, C., Mugnier, J.-L., 2011. Control of detachment geometry on lateral variations in exhumation rates in the Himalaya: Insights from low-temperature thermochronology and numerical modeling. Journal of Geophysical Research 116. https://doi.org/10.1029/2010JB007893

Robinson, D.M., McQuarrie, N., 2012. Pulsed deformation and variable slip rates within the central Himalayan thrust belt. Lithosphere 4, 449 – 464. https://doi.org/10.1130/L204.1

Robinson, D.M., DeCelles, P.G., Patchett, P.J., Garzione, C.N., 2001. The kinematic evolution of the Nepalese Himalaya interpreted from Nd isotopes. Earth and Planetary Science Letters 192, 507 – 521. https://doi.org/10.1016/S0012-821X(01)00451-4

Robinson, D.M., DeCelles, P.G., Garzione, C.N., Pearson, O.N., Harrison, T.M., Catlos, E.J., 2003. Kinematic model for the Main Central thrust in Nepal 4. https://doi.org/10.1130/0091-7613(2003)031<0359:kmftmc>2.0.co;2

Robinson, R.A.J., Brezina, C.A., Parrish, R.R., Horstwood, M.S.A., Nay Win Oo, Bird, M.I., Myint Thein, Walters, A.S., Oliver, G.J.H., Khin Zaw, 2014. Large rivers and orogens: The evolution of the Yarlung Tsangpo – Irrawaddy system and the eastern Himalayan syntaxis. Gondwana Research 26, 112 – 121. https://doi.org/10.1016/j.gr.2013.07.002

Rodriguez, M., Chamot-Rooke, N., Huchon, P., Fournier, M., Delescluse, M., 2014. The Owen Ridge uplift in the Arabian Sea: implications for the sedimentary record of Indian monsoon in late Miocene. Earth and Planetary Science Letters 394, 1 – 12. https://doi.org/10.1016/j.epsl.2014.03.011

Rohling, E.J., Foster, G.L., Grant, K.M., Marino, G., Roberts, A.P., Tamisiea, M.E., Williams, F., 2014. Sea-level and deep-sea-temperature variability over the past 5.3 million years. Nature 508, 477 – 482. https://doi.org/10.1038/nature13230

Rosenkranz, R., Schildgen, T., Wittmann, H., Spiegel, C., 2018. Coupling erosion and topographic development in the rainiest place on Earth: Reconstructing the Shillong Plateau uplift history with in-situ cosmogenic 10 Be. Earth and Planetary Science Letters 483, 39 – 51. https://doi.org/10.1016/j.epsl.2017.11.047

Rosenkranz, R.V., 2018. Understanding Geodynamic Processes from Sediments: Detrital Thermochronology and Cosmogenic Nuclide Analyses from the Himalayas (PhD Thesis). Universität Bremen.

https://elib.suub.uni-bremen.de/peid/D00106587.html

Rowley, D.B., Pierrehumbert, R.T., Currie, B.S., 2001. A new approach to stable isotope-based paleoaltimetry: implications for paleoaltimetry and paleohypsometry of the High Himalaya since the Late Miocene. Earth and Planetary Science Letters 188, 253 – 268. https://doi.org/10.1016/s0012-821x(01)00324-7

Royer, J.Y., Patriat, P., 2002. L'inde part a la derive, in: Avouac, J.-P., De Wever, P. (Eds.), Himalaya-Tibet, Le Choc Des Continents. pp. 25 – 31.

Royer, D.L., Berner, R.A., Montañez, I.P., Tabor, N.J., Beerling, D.J., 2004. CO2 as a primary driver of Phanerozoic climate. GSA Today 14, 4. https://doi.org/10.1130/1052-5173(2004)014<4:CAAPDO>2.0.CO;2

RSP, 1996. River Survey Project, Flood Action Plan final report. Delft Hydraulics and DHI

Sadler, P.M., Jerolmack, D.J., 2015. Scaling laws for aggradation, denudation and progradation rates: the case for time-scale invariance at sediment sources and sinks, in: Smith, D. G., Bailey, R. J., Burgess, P. M., Fraser, A. J. (Eds.), Strata and Time: Probing the Gaps in Our Understanding. Geological Society, London, Special Publications, 404, pp. 69 – 88. https://doi.org/10.1144/SP404.7

Sadler, P.M., 1981. Sediment accumulation rates and the completeness of stratigraphic sections. The Journal of Geology 89, 569 – 584. https://doi.org/10.1086/628623

Sadler, P.M., 1999. The influence of hiatuses on sediment accumulation rates, in: GeoResearch Forum.

Sage, R.F., Monson, R.K., Ehleringer, J.R., Adachi, S., Pearcy, R.W., 2018. Some like it hot: the physiological ecology of C4 plant evolution. Oecologia 187, 941 – 966. https://doi.org/10.1007/s00442-018-4191-6

Sage, R.F., 2004. The evolution of C4 photosynthesis. New Phytologist 161, 341 – 370. https://doi.org/10.1111/j.1469-8137.2004.00974.x

Sanyal, P., Bhattacharya, S.K., Kumar, R., Ghosh, S.K., Sangode, S.J., 2004. Mio – Pliocene monsoonal record from Himalayan foreland basin (Indian Siwalik) and its relation to vegetational change. Palaeogeography, Palaeoclimatology, Palaeoecology 205, 23 – 41. https://doi.org/10.1016/j.palaeo.2003.11.013

Sanyal, P., Bhattacharya, S.K., Prasad, M., 2005. Chemical diagenesis of Siwalik sandstone: Isotopic and mineralogical proxies from Surai Khola section, Nepal. Sedimentary Geology 180, 57 – 74. https://doi.org/10.1016/j.sedgeo.2005.06.005

Sanyal, P., Sarkar, A., Bhattacharya, S.K., Kumar, R., Ghosh, S.K., Agrawal, S., 2010. Intensification of monsoon, microclimate and asynchronous C4 appearance: Isotopic evidence from the Indian Siwalik sediments. Palaeogeography, Palaeoclimatology, Palaeoecology 296, 165 – 173. https://doi.org/10.1016/j.palaeo.2010.07.003

Sato, T., Yasuda, H., Niita, K., Endo, A., Sihver, L., 2008. Development of PARMA: PHITS-based analytical radiation model in the atmosphere. Radiation research 170, 244 – 259. https://doi.org/10.1667/rr1094.1

Savoye, B., Babonneau, N., Dennielou, B., Bez, M., 2009. Geological overview of the Angola – Congo margin, the Congo deep-sea fan and its submarine valleys. Deep Sea Research Part II: Topical Studies in Oceanography 56, 2169 – 2182. https://doi.org/10.1016/j.dsr2.2009.04.001

Schaller, M., Von Blanckenburg, F., Veldkamp, A., Tebbens, L.A., Hovius, N., Kubik, P.W., 2002. A 30 000 yr record of erosion rates from cosmogenic 10 Be in Middle European river terraces. Earth and Planetary Science Letters 204, 307 – 320. https://doi.org/10.1016/s0012-821x(02)00951-2

Schaller, M., Blanckenburg, F. von, Hovius, N., Veldkamp, A., van den Berg, M.W., Kubik, P.W., 2004. Paleoerosion Rates from Cosmogenic 10Be in a 1.3 Ma Terrace Sequence: Response of the River Meuse to Changes in Climate and Rock Uplift. The Journal of Geology 112, 127 – 144. https://doi.org/10.1086/381654

Schaller, M., Ehlers, T.A., Stor, T., Torrent, J., Lobato, L., Christl, M., Vockenhuber, C., 2016. Spatial and temporal variations in denudation rates derived from cosmogenic nuclides in four European fluvial terrace sequences. Geomorphology 274, 180 – 192. https://doi.org/10.1016/j.geomorph.2016.08.018

Schelling, D., Arita, K., 1991. Thrust tectonics, crustal shortening, and the structure of the far-

eastern Nepal Himalaya. Tectonics 10, 851 – 862. https://doi.org/10.1029/91TC01011

Scherler, D., Bookhagen, B., Strecker, M.R., 2014. Tectonic control on 10Be-derived erosion rates in the Garhwal Himalaya, India. Journal of Geophysical Research: Earth Surface 119, 83 – 105. https://doi.org/10.1002/2013JF002955

Schildgen, T.F., Phillips, W.M., Purves, R.S., 2005. Simulation of snow shielding corrections for cosmogenic nuclide surface exposure studies. Geomorphology 64, 67 – 85. https://doi.org/10.1016/j.geomorph.2004.05.003

Schildgen, T.F., van der Beek, P.A., Sinclair, H.D., Thiede, R.C., 2018. Spatial correlation bias in late-Cenozoic erosion histories derived from thermochronology. Nature 559, 89 – 93. https://doi.org/10.1038/s41586-018-0260-6

Schimmelpfennig, I., 2009. Cosmogenic Cl-36 in Ca and K rich minerals: analytical developments, production rate calibrations and cross calibration with He-3 and Ne-21. Université d'Aix-Marseille. https://tel.archives-ouvertes.fr/tel-00468337

Schimmelpfennig, I., Benedetti, L., Finkel, R., Pik, R., Blard, P.-H., Bourlès, D., Burnard, P., Williams, A., 2009. Sources of in-situ 36Cl in basaltic rocks. Implications for calibration of production rates. Quaternary Geochronology, Advances in Cosmogenic Isotope Research from CRONUS-EU 4, 441 – 461. https://doi.org/10.1016/j.quageo.2009.06.003

Schimmelpfennig, I., Williams, A., Pik, R., Burnard, P., Niedermann, S., Finkel, R., Schneider, B., Benedetti, L., 2011. Inter-comparison of cosmogenic in-situ 3He, 21Ne and 36Cl at low latitude along an altitude transect on the SE slope of Kilimanjaro volcano (3° S, Tanzania). Quaternary Geochronology 6, 425 – 436. https://doi.org/10.1016/j.quageo.2011.05.002

Schuchert, C., 1931. Geochronology, or the Age of the Earth on the Basis of Sediments and Life. Bulletin 80 (Washington) Physics of the Earth 4, 10 – 64.

Schumer, R., Jerolmack, D.J., 2009. Real and apparent changes in sediment deposition rates through time. Journal of Geophysical Research: Earth Surface 114, F00A06. https://doi.org/10.1029/2009JF001266

Schuster, M., Duringer, P., Ghienne, J.-F., Vignaud, P., Mackaye, H.T., Likius, A., Brunet, M., 2006. The age of the Sahara desert. Science 311, 821 – 821. https://doi.org/10.1126/science.1120161

Schuster, M., Duringer, P., Ghienne, J.-F., Vignaud, P., Mackaye, H.T., Likius, A., Brunet, M., 2006. Resp. Revisiting the age of the Sahara desert. Science 312, 1138 – 1139.

Schwenk, T., Spiess, V., 2009. Architecture and stratigraphy of the Bengal Fan as response to tectonic and climate revealed from high-resolution seismic data, in: Kneller, B.C., Martinsen, O.J., McCaffrey, B. (Eds.), External Controls on Deep-Water Depositional Systems. SEPM special publication 92, Tulsa, Okla, pp. 107 – 131. https://doi.org/10.2110/sepmsp.092.107

Sclater, J.G., Parsons, B., Jaupart, C., 1981. Oceans and continents: similarities and differences in the mechanisms of heat loss. Journal of Geophysical Research: Solid Earth 86, 11535 – 11552. https://doi.org/10.1029/jb086ib12p11535

Searle, M.P., Parrish, R.R., Hodges, K.V., Hurford, A., Ayres, M.W., Whitehouse, M.J., 1997. Shisha Pangma Leucogranite, South Tibetan Himalaya: Field Relations, Geochemistry, Age, Origin, and Emplacement. The Journal of Geology 105, 295 – 318. https://doi.org/10.1086/515924

Seeber, L., Gornitz, V., 1983. River profiles along the Himalayan arc as indicators of active tectonics. Tectonophysics 92, 335 – 367. https://doi.org/10.1016/0040-1951(83)90201-9

Serber, R., 1947. The Production of High Energy Neutrons by Stripping. Phys. Rev. 72, 1008 – 1016. https://doi.org/10.1103/PhysRev.72.1008

Seward, D., Burg, J.-P., 2008. Growth of the Namche Barwa Syntaxis and associated evolution of the Tsangpo Gorge: Constraints from structural and thermochronological data. Tectonophysics 451, 282 – 289. https://doi.org/10.1016/j.tecto.2007.11.057

Shackleton, N.J., Kennett, J.P., 1975. Late Cenozoic oxygen and carbon isotopic changes at DSDP Site 284: Implications for glacial history of the Northern Hemisphere and Antarctica, in: Initial Reports of the Deep Sea Drilling Project, 29. Kennett J.P., Houtz R.E., Andrews P.B. et al., pp. 801 – 807. https://doi.org/10.2973/dsdp.proc.29.120.1975

Shackleton, N.J., Backman, J., Zimmerman, H. t, Kent, D.V., Hall, M.A., Roberts, D.G., Schnitker, D., Baldauf, J.G., Desprairies, A., Homrighausen, R., 1984. Oxygen isotope calibration of the onset of ice-rafting and history of glaciation in the North Atlantic region. Nature 307, 620 – 623. https://doi.org/10.1038/307620a0

Shackleton, N.J., 1987. The carbon isotope record of the Cenozoic, in: Brooks, J., Fleet, A. J. (Eds.), Marine Petroleum Source Rocks. Geological Society of London Special Publications 26, pp. 427 – 438. https://doi.org/10.1144/GSL.SP.1987.026.01.27

Shakun, J.D., Lea, D.W., Lisiecki, L.E., Raymo, M.E., 2015. An 800-kyr record of global surface ocean δ18O and implications for ice volume-temperature coupling. Earth and Planetary Science Letters 426, 58 – 68. https://doi.org/10.1016/j.epsl.2015.05.042

Sharma, P., Kubik, P.W., Fehn, U., Gove, H.E., Nishiizumi, K., Elmore, D., 1990. Development of 36Cl standards for AMS. Nuclear Instruments and Methods in Physics Research Section B: Beam Interactions with Materials and Atoms 52, 410 – 415. https://doi.org/10.1016/0168-583X(90)90447-3

Shea, M.A., Smart, D.F., McCracken, K.G., 1965. A study of vertical cutoff rigidities using sixth degree simulations of the geomagnetic field. Journal of Geophysical Research 70, 4117 – 4130. https://doi.org/10.1029/JZ070i017p04117

Shi, Y., 2002. Characteristics of late Quaternary monsoonal glaciation on the Tibetan Plateau and in East Asia. Quaternary International 97 – 98, 79 – 91. https://doi.org/10.1016/S1040-6182(02)00053-8

Shugar, D.H., Clague, J.J., Best, J.L., Schoof, C., Willis, M.J., Copland, L., Roe, G.H., 2017. River piracy and drainage basin reorganization led by climate-driven glacier retreat. Nature Geoscience 10, 370 – 375. https://doi.org/10.1038/ngeo2932

Shuster, D.L., Farley, K.A., 2004. 4He/3He thermochronometry. Earth and Planetary Science Letters 217, 1 – 17. https://doi.org/10.1016/S0012-821X(03)00595-8

Shuster, D.L., Ehlers, T.A., Rusmore, M.E., Farley, K.A., 2005. Rapid Glacial Erosion at 1.8 Ma Revealed by 4He/3He Thermochronometry. Science 310, 1668 – 1670. https://doi.org/10.1126/science.1118519

Shuster, D.L., Cuffey, K.M., Sanders, J.W., Balco, G., 2011. Thermochronometry Reveals Headward Propagation of Erosion in an Alpine Landscape. Science 332, 84 – 88. https://doi.org/10.1126/science.1198401

Van Sickel, W.A., Kominz, M.A., Miller, K.G., Browning, J.V., 2004. Late Cretaceous and Cenozoic sea-level estimates: backstripping analysis of borehole data, onshore New Jersey. Basin Research 16, 451 – 465. https://doi.org/10.1111/j.1365-2117.2004.00242.x

Simpson, J.A., Fagot, W.C., 1953. Properties of the Low Energy Nucleonic Component at Large Atmospheric Depths. Phys. Rev. 90, 1068 – 1072. https://doi.org/10.1103/PhysRev.90.1068

Simpson, J.A., Fonger, W., Treiman, S.B., 1953. Cosmic radiation intensity-time variations and their origin. I. Neutron intensity variation method and meteorological factors. Physical Review 90, 934. https://doi.org/10.1103/PhysRev.90.934

Simpson, J.A., 1951. Neutrons Produced in the Atmosphere by the Cosmic Radiations. Physical Review 83, 1175 – 1188. https://doi.org/10.1103/physrev.83.1175

Sinclair, H.D., Mudd, S.M., Dingle, E., Hobley, D.E.J., Robinson, R., Walcott, R., 2017. Squeezing river catchments through tectonics: Shortening and erosion across the Indus Valley, NW Himalaya. Geological Society of America Bulletin 129, 203 – 217. https://doi.org/10.1130/B31435.1

Singh, S.K., France-Lanord, C., 2002. Tracing the distribution of erosion in the Brahmaputra watershed from isotopic compositions of stream sediments. Earth and Planetary Science Letters 202, 645 – 662. https://doi.org/10.1016/S0012-821X(02)00822-1

Singh, S.K., Rai, S.K., Krishnaswami, S., 2008. Sr and Nd isotopes in river sediments from the Ganga Basin: Sediment provenance and spatial variability in physical erosion. Journal of Geophysical Research 113. https://doi.org/10.1029/2007JF000909

Singh, A., Fienberg, K., Jerolmack, D.J., Marr, J., Foufoula-Georgiou, E., 2009. Experimental evidence for statistical scaling and intermittency in sediment transport rates. Journal of Geophysical Research: Earth Surface 114, F1025. https://doi.org/10.1029/2007JF000963

Smith, L.C., Chu, V.W., Yang, K., Gleason, C.J., Pitcher, L.H., Rennermalm, A.K., Legleiter, C.J., Behar, A.E., Overstreet, B.T., Moustafa, S.E., 2015. Efficient meltwater drainage through supraglacial streams and rivers on the southwest Greenland ice sheet. Proceedings of the National Academy of Sciences 112, 1001 – 1006. https://doi.org/10.1073/pnas.1413024112

Snyder, C.W., 2016. Evolution of global temperature over the past two million years. Nature 538, 226. https://doi.org/10.1038/nature19798

Sommerfield, C.K., 2006. On sediment accumulation rates and stratigraphic completeness: Lessons from Holocene ocean margins. Continental Shelf Research 26, 2225 – 2240. https://doi.org/10.1016/j.csr.2006.07.015

Spicer, R.A., Harris, N.B., Widdowson, M., Herman, A.B., Guo, S., Valdes, P.J., Wolfe, J.A., Kelley, S.P., 2003. Constant elevation of southern Tibet over the past 15 million years. Nature 421, 622 – 624. https://doi.org/10.1038/nature01356

Stap, L.B., de Boer, B., Ziegler, M., Bintanja, R., Lourens, L.J., van de Wal, R.S.W., 2016. CO2 over the past 5 million years: Continuous simulation and new δ 11B-based proxy data. Earth and Planetary Science Letters 439, 1 – 10. https://doi.org/10.1016/j.epsl.2016.01.022

Steer, P., Huismans, R.S., Valla, P.G., Gac, S., Herman, F., 2012. Bimodal Plio – Quaternary glacial erosion of fjords and low-relief surfaces in Scandinavia. Nature Geoscience 5, 635 – 639. https://doi.org/10.1038/ngeo1549

Sternai, P., Herman, F., Valla, P.G., Champagnac, J.-D., 2013. Spatial and temporal variations of glacial erosion in the Rhône valley (Swiss Alps): Insights from numerical modeling. Earth and Planetary Science Letters 368, 119 – 131. https://doi.org/10.1016/j.epsl.2013.02.039

Still, C.J., Berry, J.A., Collatz, G.J., DeFries, R.S., 2003. Global distribution of C3 and C4 vegetation: Carbon cycle implications: C 4 PLANTS AND CARBON CYCLE. Global Biogeochemical Cycles 17, 6-1-6 – 14. https://doi.org/10.1029/2001GB001807

Stommel, H., Arons, A.B., 1959. On the abyssal circulation of the world ocean—II. An idealized model of the circulation pattern and amplitude in oceanic basins. Deep Sea Research (1953) 6, 217 – 233. https://doi.org/10.1016/0146-6313(59)90075-9

Stone, J.O.H., Evans, J.M., Fifield, L.K., Allan, G.L., Cresswell, R.G., 1998. Cosmogenic chlorine-36 production in calcite by muons. Geochimica et Cosmochimica Acta 62, 433 – 454. https://doi.org/10.1016/s0016-7037(97)00369-4

Stone, J.O., 2000. Air pressure and cosmogenic isotope production. Journal of Geophysical Research: Solid Earth 105, 23753 – 23759. https://doi.org/10.1029/2000JB900181

Stow, D.A.V., 1994. Deep sea processes of sediment transport and deposition. Sediment transport and depositional processes. 257 – 291.

Straume, E.O., Gaina, C., Medvedev, S., Hochmuth, K., Gohl, K., Whittaker, J.M., Abdul Fattah, R., Doornenbal, J.C., Hopper, J.R., 2019. GlobSed: Updated Total Sediment Thickness in the World's Oceans. Geochemistry, Geophysics, Geosystems 20, 1756 – 1772. https://doi.org/10.1029/2018GC008115

Suess, E., 1883-1909. Der Antlitz der Erde, 5 vols. F. Tempsky. Prague and Vienna.

Suetnova, E., Vasseur, G., 2000. 1-D modelling rock compaction in sedimentary basins using a visco-elastic rheology. Earth and Planetary Science Letters 178, 373 – 383. https://doi.org/10.1016/s0012-821x(00)00074-1

Sun, D., Bloemendal, J., Yi, Z., Zhu, Y., Wang, X., Zhang, Yuebao, Li, Z., Wang, F., Han, F., Zhang, Yan, 2011. Palaeomagnetic and palaeoenvironmental study of two parallel sections of late Cenozoic strata in the central Taklimakan Desert: Implications for the desertification of the Tarim Basin. Palaeogeography, Palaeoclimatology, Palaeoecology 300, 1 – 10. https://doi.org/10.1016/j.palaeo.2010.11.015

Susilohadi, S., Gaedicke, C., Ehrhardt, A., 2005. Neogene structures and sedimentation history along the Sunda forearc basins off southwest Sumatra and southwest Java. Marine Geology 219, 133 – 154. https://doi.org/10.1016/j.margeo.2005.05.001

Swezey, C. S., 2006. Revisiting the age of the Sahara desert. Science 312, 1138 – 1139.

Szulc, A.G., Najman, Y., Sinclair, H.D., Pringle, M., Bickle, M., Chapman, H., Garzanti, E., And ò, S., Huyghe, P., Mugnier, J.-L., Ojha, T., DeCelles, P., 2006. Tectonic evolution of the Himalaya constrained by detrital 40Ar-39Ar, Sm-Nd and petrographic data from

the Siwalik foreland basin succession, SW Nepal: Tectonic evolution of the Himalaya. Basin Research 18, 375 − 391. https://doi.org/10.1111/j.1365-2117.2006.00307.x

Tang, Y.-J., Zhang, H.-F., Ying, J.-F., 2007. Review of the lithium isotope system as a geochemical tracer. International Geology Review 49, 374 − 388. https://doi.org/10.2747/0020-6814.49.4.374

Tapponnier, P., Zhiqin, X., Roger, F., Meyer, B., Arnaud, N., Wittlinger, G., Jingsui, Y., 2001. Oblique stepwise rise and growth of the Tibet Plateau. Science 294, 1671 − 1677. https://doi.org/10.1126/science.105978

Tarantola, A., 2005. Inverse problem theory and methods for model parameter estimation. Society of Industrial and Applied Mathematics.

Taylor, S.R., McLennan, S.M., 1995. The geochemical evolution of the continental crust. Rev. Geophys. 33, 241 − 265. https://doi.org/10.1029/95RG00262

Taylor, J.R., 1996. An Introduction to Error Analysis: The Study of Uncertainties in Physical Measurements, 2nd edition. ed. University Science Books, Sausalito, Calif.

Thiede, R.C., Ehlers, T.A., 2013. Large spatial and temporal variations in Himalayan denudation. Earth and Planetary Science Letters 371 − 372, 278 − 293. https://doi.org/10.1016/j.epsl.2013.03.004

Thomas, J.V., Parkash, B., Mohindra, R., 2002. Lithofacies and palaeosol analysis of the Middle and Upper Siwalik Groups (Plio − Pleistocene), Haripur-Kolar section, Himachal Pradesh, India. Sedimentary Geology 150, 343 − 366. https://doi.org/10.1016/S0037-0738(01)00203-2

Thomson, S.N., Brandon, M.T., Tomkin, J.H., Reiners, P.W., Vásquez, C., Wilson, N.J., 2010. Glaciation as a destructive and constructive control on mountain building. Nature 467, 313 − 317. https://doi.org/10.1038/nature09365

Thomson, S.N., Reiners, P.W., Hemming, S.R., Gehrels, G.E., 2013. The contribution of glacial erosion to shaping the hidden landscape of East Antarctica. Nature Geoscience 6, 203 − 207. https://doi.org/10.1038/ngeo1722

Tipper, J.C., 1983. Rates of sedimentation, and stratigraphical completeness. Nature 302, 696 − 698. https://doi.org/10.1038/302696a0

Tochilin, C.J., Reiners, P.W., Thomson, S.N., Gehrels, G.E., Hemming, S.R., Pierce, E.L., 2012. Erosional history of the Prydz Bay sector of East Antarctica from detrital apatite and zircon geo- and thermochronology multidating. Geochemistry, Geophysics, Geosystems 13, Q11015. https://doi.org/10.1029/2012GC004364

Tokuoka, T., Takayasu, K., Hisatomi, K., 1990. Stratigraphy and Geologic structures of the Churia (Siwalik) Group in the Tinau Khola-Binai Khola Area, West Central Nepal. Memoirs of the Faculty of Science, Shimane University 71 − 88.

Torres, M.A., West, A.J., Li, G., 2014. Sulphide oxidation and carbonate dissolution as a source of CO2 over geological timescales. Nature 507, 346 − 349. https://doi.org/10.1038/nature13030

Torres, M.A., West, A.J., Clark, K.E., Paris, G., Bouchez, J., Ponton, C., Feakins, S.J., Galy, V., Adkins, J.F., 2016. The acid and alkalinity budgets of weathering in the Andes − Amazon system: Insights into the erosional control of global biogeochemical cycles. Earth and Planetary Science Letters 450, 381 − 391. https://doi.org/10.1016/j.epsl.2016.06.012

Turcotte, D.L., Greene, L., 1993. A scale-invariant approach to flood-frequency analysis. Stochastic Hydrol Hydraul 7, 33 − 40. https://doi.org/10.1007/BF01581565

Uba, C.E., Strecker, M.R., Schmitt, A.K., 2007. Increased sediment accumulation rates and climatic forcing in the central Andes during the late Miocene. Geology 35, 979. https://doi.org/10.1130/G224025A.1

Vail, P.R., 1991. The stratigraphic signatures of tectonics, eustacy and sedimentology-an overview. Cycles and events in stratigraphy 617 − 659.

Val, P., Hoke, G.D., Fosdick, J.C., Wittmann, H., 2016. Reconciling tectonic shortening, sedimentation and spatial patterns of erosion from 10Be paleo-erosion rates in the Argentine Precordillera. Earth and Planetary Science Letters 450, 173 − 185. https://doi.org/10.1016/j.epsl.2016.06.015

Valdiya, K.S., 2015. The making of India: geodynamic evolution. Springer. https://doi.org/10.1007/978-3-319-25029-8

Valet, J.-P., Meynadier, L., 1993. Geomagnetic field intensity and reversals during the past four

million years. Nature 366, 234. https://doi.org/10.1038/366234a0

Valet, J.-P., Meynadier, L., Guyodo, Y., 2005. Geomagnetic dipole strength and reversal rate over the past two million years. Nature 435, 802 – 805. https://doi.org/10.1038/nature03674

Valla, P.G., Shuster, D.L., van der Beek, P.A., 2011. Significant increase in relief of the European Alps during mid-Pleistocene glaciations. Nature Geoscience 4, 688 – 692. https://doi.org/10.1038/ngeo1242

Valla, P.G., van der Beek, P.A., Shuster, D.L., Braun, J., Herman, F., Tassan-Got, L., Gautheron, C., 2012. Late Neogene exhumation and relief development of the Aar and Aiguilles Rouges massifs (Swiss Alps) from low-temperature thermochronology modeling and 4He/3He thermochronometry. J. Geophys. Res. 117, F01004. https://doi.org/10.1029/2011JF002043

Valla, P.G., Rahn, M., Shuster, D.L., van der Beek, P.A., 2016. Multi-phase late-Neogene exhumation history of the Aar massif, Swiss central Alps. Terra Nova 28, 383 – 393. https://doi.org/10.1111/ter.12231

Valla, P., 2018. Late Cenozoic climate cooling, mountain erosion and relief evolution, in: Thermo2018 Abstracts. Presented at the Thermo2018.

van der Beek, P., Robert, X., Mugnier, J.-L., Bernet, M., Huyghe, P., Labrin, E., 2006. Late Miocene – recent exhumation of the central Himalaya and recycling in the foreland basin assessed by apatite fission-track thermochronology of Siwalik sediments, Nepal. Basin Research 18, 413 – 434. https://doi.org/10.1111/j.1365-2117.2006.00305.x

van der Beek, P.A., Valla, P.G., Herman, F., Braun, J., Persano, C., Dobson, K.J., Labrin, E., 2010. Inversion of thermochronological age – elevation profiles to extract independent estimates of denudation and relief history — II: Application to the French Western Alps. Earth and Planetary Science Letters 296, 9 – 22. https://doi.org/10.1016/j.epsl.2010.04.032

van der Beek, P., Litty, C., Baudin, M., Mercier, J., Robert, X., Hardwick, E., 2016. Contrasting tectonically driven exhumation and incision patterns, western versus central Nepal Himalaya. Geology 44, 327 – 330. https://doi.org/10.1130/G37579.1

Van Der Meer, D.G., Zeebe, R.E., van Hinsbergen, D.J., Sluijs, A., Spakman, W., Torsvik, T.H., 2014. Plate tectonic controls on atmospheric CO2 levels since the Triassic. Proceedings of the National Academy of Sciences 111, 4380 – 4385. https://doi.org/10.1073/pnas.1315657111

Vance, D., Bickle, M., Ivy-Ochs, S., Kubik, P.W., 2003. Erosion and exhumation in the Himalaya from cosmogenic isotope inventories of river sediments. Earth and Planetary Science Letters 206, 273 – 288. https://doi.org/10.1016/S0012-821X(02)01102-0

Vaughan, D.G., Corr, H.F., Smith, A.M., Pritchard, H.D., Shepherd, A., 2008. Flow-switching and water piracy between Rutford ice stream and Carlson inlet, West Antarctica. Journal of Glaciology 54, 41 – 48. https://doi.org/10.3189/002214308784409125

Veizer, J., Prokoph, A., 2015. Temperatures and oxygen isotopic composition of Phanerozoic oceans. Earth-Science Reviews 146, 92 – 104. https://doi.org/10.1016/j.earscirev.2015.03.008

Vermeesch, P., 2012. On the visualisation of detrital age distributions. Chemical Geology 312 – 313, 190 – 194. https://doi.org/10.1016/j.chemgeo.2012.04.021

Vernant, P., Bilham, R., Szeliga, W., Drupka, D., Kalita, S., Bhattacharyya, A.K., Gaur, V.K., Pelgay, P., Cattin, R., Berthet, T., 2014. Clockwise rotation of the Brahmaputra Valley relative to India: Tectonic convergence in the eastern Himalaya, Naga Hills, and Shillong Plateau: New GPS velocity field Bhutan. Journal of Geophysical Research: Solid Earth 119, 6558 – 6571. https://doi.org/10.1002/2014JB011196

Vernon, A.J., Van Der Beek, P.A., Sinclair, H.D., Rahn, M.K., 2008. Increase in late Neogene denudation of the European Alps confirmed by analysis of a fission-track thermochronology database. Earth and Planetary Science Letters 270, 316 – 329. https://doi.org/10.1016/j.epsl.2008.03.053

Vögeli, N., Najman, Y., van der Beek, P., Huyghe, P., Wynn, P.M., Govin, G., van der Veen, I., Sachse, D., 2017. Lateral variations in vegetation in the Himalaya since the Miocene and implications for climate evolution. Earth and Planetary Science Letters 471, 1 – 9. https://doi.org/10.1016/j.epsl.2017.04.037

Vögeli, N., van der Beek, P., Huyghe, P., Najman, Y., 2017. Weathering in the Himalaya, an East-West Comparison: Indications from Major Elements and Clay Mineralogy. The Journal of Geology 125, 515 – 529. https://doi.org/10.1086/692652

Vogt, S., Herzog, G.F., Reedy, R.C., 1990. Cosmogenic nuclides in extraterrestrial materials. Reviews of Geophysics 28, 253. https://doi.org/10.1029/RG028i003p00253

von Blanckenburg, F., Bouchez, J., 2014. River fluxes to the sea from the ocean's 10Be/9Be ratio. Earth and Planetary Science Letters 387, 34 – 43. https://doi.org/10.1016/j.epsl.2013.11.004

von Blanckenburg, F., Igel, H., 1999. Lateral mixing and advection of reactive isotope tracers in ocean basins: observations and mechanisms. Earth and planetary science letters 169, 113 – 128. https://doi.org/10.1016/s0012-821x(99)00070-9

von Blanckenburg, F., O'nions, R.K., Belshaw, N.S., Gibb, A., Hein, J.R., 1996. Global distribution of beryllium isotopes in deep ocean water as derived from Fe / Mn crusts. Earth and Planetary Science Letters 141, 213 – 226. https://doi.org/10.1016/0012-821x(96)00059-3

von Blanckenburg, F., Bouchez, J., Ibarra, D.E., Maher, K., 2015. Stable runoff and weathering fluxes into the oceans over Quaternary climate cycles. Nature Geoscience 8, 538 – 542. https://doi.org/10.1038/ngeo2452

Walford, H.L., White, N.J., Sydow, J.C., 2005. Solid sediment load history of the Zambezi Delta. Earth and Planetary Science Letters 238, 49 – 63. https://doi.org/10.1016/j.epsl.2005.07.014

Walker, J.C.G., Hays, P.B., Kasting, J.F., 1981. A negative feedback mechanism for the long-term stabilization of Earth's surface temperature. Journal of Geophysical Research: Oceans 86, 9776 – 9782. https://doi.org/10.1029/JC086iC10p09776

Wan, S., Li, A., Clift, P.D., Stuut, J.-B.W., 2007. Development of the East Asian monsoon: Mineralogical and sedimentologic records in the northern South China Sea since 20 Ma. Palaeogeography, Palaeoclimatology, Palaeoecology 254, 561 – 582. https://doi.org/10.1016/j.palaeo.2007.07.009

Wan, S., Li, A., Clift, P.D., Wu, S., Xu, K., Li, T., 2010. Increased contribution of terrigenous supply from Taiwan to the northern South China Sea since 3 Ma. Marine Geology 278, 115 – 121. https://doi.org/10.1016/j.margeo.2010.09.008

Wang, B., 2006. The Asian Monsoon, Springer. ed. https://doi.org/10.1007/3-540-37722-0

Weber, M.E., Reilly, B.T., 2018. Hemipelagic and turbiditic deposits constrain lower Bengal Fan depositional history through Pleistocene climate, monsoon, and sea level transitions. Quaternary Science Reviews 199, 159-173. https://doi.org/10.1016/j.quascirev.2018.09.027

Weber, M.E., Wiedicke, M.H., Kudrass, H.R., Hü bscher, C., Erlenkeuser, H., 1997. Active growth of the Bengal Fan during sea-level rise and highstand. Geology 25, 315 – 318. https://doi.org/10.1130/0091-7613(1997)025<0315:AGOTBF>2.3.CO;2

Weber, M.E., Wiedicke-Hombach, M., Kudrass, H.R., Erlenkeuser, H., 2003. Bengal Fan sediment transport activity and response to climate forcing inferred from sediment physical properties. Sedimentary Geology, Sedimentary Geology of the Bengal Basin, Bangladesh, in relation to the Asia-Greater India collision and the evolution of the eastern Bay of Bengal 155, 361 – 381. https://doi.org/10.1016/S0037-0738(02)00187-2

Wegener, A., 1912. Die entstehung der kontinente. Geologische Rundschau 3, 276 – 292.

Wells, N.A., Dorr, J.A., 1987. Shifting of the Kosi river, northern India. Geology 15, 204 – 207. https://doi.org/10.1130/0091-7613(1987)15<204:sotkrn>2.0.co;2

West, A.J., Hetzel, R., Li, G., Jin, Z., Zhang, F., Hilton, R.G., Densmore, A.L., 2014. Dilution of 10Be in detrital quartz by earthquake-induced landslides: Implications for determining denudation rates and potential to provide insights into landslide sediment dynamics. Earth and Planetary Science Letters 396, 143 – 153. https://doi.org/10.1016/j.epsl.2014.03.058

Whipp, D.M., Ehlers, T.A., 2007. Influence of groundwater flow on thermochronometer-derived exhumation rates in the central Nepalese Himalaya. Geol 35, 851. https://doi.org/10.1130/G23788A.1

Whipp, D.M., Ehlers, T.A., Blythe, A.E., Huntington, K.W., Hodges, K.V., Burbank, D.W., 2007. Plio-Quaternary exhumation history of the central Nepalese Himalaya: 2. Thermokinematic and thermochronometer

age prediction model. Tectonics 26, n/a-n/a. https://doi.org/10.1029/2006TC001991

Whipple, K.X., Kirby, E., Brocklehurst, S.H., 1999. Geomorphic limits to climate-induced increases in topographic relief. Nature 401, 39 – 43. https://doi.org/10.1038/43375

Whipple, K.X., 2001. Fluvial Landscape Response Time: How Plausible Is Steady-State Denudation? Am J Sci 301, 313 – 325. https://doi.org/10.2475/ajs.301.4-5.313

Whipple, K.X., 2009. The influence of climate on the tectonic evolution of mountain belts. Nature Geoscience 2, 97 – 104. https://doi.org/10.1038/ngeo413

Willenbring, J.K., Jerolmack, D.J., 2016. The null hypothesis: globally steady rates of erosion, weathering fluxes and shelf sediment accumulation during Late Cenozoic mountain uplift and glaciation. Terra Nova 28, 11 – 18. https://doi.org/10.1111/ter.12185

Willenbring, J.K., von Blanckenburg, F., 2010. Long-term stability of global erosion rates and weathering during late-Cenozoic cooling. Nature 465, 211 – 214. https://doi.org/10.1038/nature09044

Willett, S.D., Pope, D.C., 2004. Thermo-Mechanical Models of Convergent Orogenesis: Thermal and Rheologic Dependence of Crustal Deformation, in: Karner, G.D., Taylor, B., Driscoll, N.W., Kohlstedt, D.L. (Eds.), Rheology and Deformation of the Lithosphere at Continental Margins. Columbia University Press, New York Chichester, West Sussex. https://doi.org/10.7312/karn12738-008

Willett, S., Beaumont, C., Fullsack, P., 1993. Mechanical model for the tectonics of doubly vergent compressional orogens. Geology 21, 371 – 374. https://doi.org/10.1130/0091-7613(1993)021<0371:MMFTTO>2.3.CO;2

Willett, S.D., McCoy, S.W., Perron, J.T., Goren, L., Chen, C.-Y., 2014. Dynamic reorganization of river basins. Science 343, 1248765. https://doi.org/10.1126/science.1248765

Witkowski, C.R., Weijers, J.W.H., Blais, B., Schouten, S., Damsté, J.S.S., 2018. Molecular fossils from phytoplankton reveal secular PCO2 trend over the Phanerozoic. Science Advances 4, eaat4556. https://doi.org/10.1126/sciadv.aat4556

Wittmann, H., von Blanckenburg, F., Kruesmann, T., Norton, K.P., Kubik, P.W., 2007. Relation between rock uplift and denudation from cosmogenic nuclides in river sediment in the Central Alps of Switzerland. Journal of Geophysical Research: Earth Surface 112. https://doi.org/10.1029/2006jf000729

Wittmann, H., von Blanckenburg, F., Guyot, J.L., Maurice, L., Kubik, P.W., 2009. From source to sink: Preserving the cosmogenic 10Be-derived denudation rate signal of the Bolivian Andes in sediment of the Beni and Mamoré foreland basins. Earth and Planetary Science Letters 288, 463 – 474. https://doi.org/10.1016/j.epsl.2009.10.008

Wittmann, H., von Blanckenburg, F., Maurice, L., Guyot, J.L., Kubik, P.W., 2011. Recycling of Amazon floodplain sediment quantified by cosmogenic 26Al and 10Be. Geology 39, 467 – 470. https://doi.org/10.1130/G31829.1

Wittmann, H., von Blanckenburg, F., Mohtadi, M., Christl, M., Bernhardt, A., 2017. The competition between coastal trace metal fluxes and oceanic mixing from the 10Be/9Be ratio: Implications for sedimentary records. Geophysical Research Letters 44, 8443 – 8452. https://doi.org/10.1002/2017GL074259

Wobus, C.W., Hodges, K.V., Whipple, K.X., 2003. Has focused denudation sustained active thrusting at the Himalayan topographic front? Geology 31, 861 – 864. https://doi.org/10.1130/g19730.1

Wobus, C., Heimsath, A., Whipple, K., Hodges, K., 2005. Active out-of-sequence thrust faulting in the central Nepalese Himalaya. Nature 434, 1008 – 1011. https://doi.org/10.1038/nature03499

Worsley, T.R., Davies, T.A., 1979. Sea-level fluctuations and deep-sea sedimentation rates. Science 203, 455 – 456. https://doi.org/10.1126/science.203.4379.455

Yang, Y., Galy, A., Fang, X., Yang, R., Zhang, W., Zan, J., 2017. Eolian dust forcing of river chemistry on the northeastern Tibetan Plateau since 8 Ma. Earth and Planetary Science Letters 464, 200 – 210. https://doi.org/10.1016/j.epsl.2017.02.009

Yang, R., Herman, F., Fellin, M.G., Maden, C., 2018. Exhumation and topographic evolution of the Namche Barwa Syntaxis, eastern Himalaya. Tectonophysics 722, 43 – 52. https://doi.org/10.1016/j.tecto.2017.10.026

Yanites, B.J., Tucker, G.E., Anderson, R.S., 2009. Numerical and analytical models of cosmogenic radionuclide dynamics in landslide - dominated drainage basins.

Journal of Geophysical Research: Earth Surface 114. https://doi.org/10.1029/2008JF001088

Yu, H., Webb, A.A.G., He, D., 2015. Extrusion vs. duplexing models of Himalayan mountain building 1: Discovery of the Pabbar thrust confirms duplex-dominated growth of the northwestern Indian Himalaya since Mid-Miocene. Tectonics 34, 313 – 333. https://doi.org/10.1002/2014tc003589

Zachos, J., Pagani, M., Sloan, L., Thomas, E., Billups, K., 2001. Trends, Rhythms, and Aberrations in Global Climate 65 Ma to Present. Science 292, 686 – 693. https://doi.org/10.1126/science.1059412

Zachos, J.C., Dickens, G.R., Zeebe, R.E., 2008. An early Cenozoic perspective on greenhouse warming and carbon-cycle dynamics. Nature 451, 279 – 283. https://doi.org/10.1038/nature06588

Zeitler, P.K., Meltzer, A.S., Brown, L., Kidd, W.S., Lim, C., Enkelmann, E., 2014. Tectonics and topographic evolution of Namche Barwa and the easternmost Lhasa block, Tibet, in: Nie, J., Horton, B.K., Hoke, G.D. (Eds.), Toward an Improved Understanding of Uplift Mechanisms and the Elevation History of the Tibetan Plateau. Geological Society of America Special Paper 507, pp. SPE507 – 02. https://doi.org/10.1130/2014.2507(02)

Zhang, P.Z., Molnar, P., Downs, W.R., 2001. Increased sedimentation rates and grain sizes 2 – 4 Myr ago due to the influence of climate change on erosion rates. Nature 410, 891 – 897. https://doi.org/10.1038/35073504

Zhang, P.-Z., Shen, Z., Wang, M., Gan, W., Bü rgmann, R., Molnar, P., Wang, Q., Niu, Z., Sun, J., Wu, J., 2004. Continuous deformation of the Tibetan Plateau from global positioning system data. Geology 32, 809 – 812. https://doi.org/10.1130/g20554.1

TABLES

Table SII-1. Compilation of geological map references.

Table SII-1 (…/…)

Authors	Reference
Acharyya et al., 2007	Acharyya, S.K., 2007. Evolution of the Himalayan Paleogene foreland basin, influence of its litho-packet on the formation of thrust-related domes and windows in the Eastern Himalayas – A review. Journal of Asian Earth Sciences 31, 1–17. https://doi.org/10.1016/j.jseaes.2007.03.007
Acharyya and Saha, 2018	Acharyya, S.K., Saha, P., 2018. Himalayan Paleogene Foreland Basin, its collision induced early volcanic history and failed rift initiation. Journal of Asian Earth Sciences, Emergence and Evolution of Himalayan Foreland Basin 162, 3–12. https://doi.org/10.1016/j.jseaes.2018.04.031
Bhargava 1995	Bhargava, O.N., 1995. The Bhutan Himalaya, a geological account. Geological Survey of India.
Bhattacharyya and Mitra, 2009	Bhattacharyya, K., Mitra, G., 2009. A new kinematic evolutionary model for the growth of a duplex — an example from the Rangit duplex, Sikkim Himalaya, India. Gondwana Research 16, 697–715. https://doi.org/10.1016/j.gr.2009.07.006
Burg et al., 1998	Burg, J.-P., Nievergelt, P., Oberli, F., Seward, D., Davy, P., Maurin, J.-C., Diao, Z., Meier, M., 1998. The Namche Barwa syntaxis: evidence for exhumation related to compressional crustal folding. Journal of Asian Earth Sciences 16, 239–252. https://doi.org/10.1016/S0743-9547(98)00002-6
Célérier et al., 2009 and refs therein	Célérier, J., Harrison, T.M., Webb, A.A.G., Yin, A., 2009. The Kumaun and Garwhal Lesser Himalaya, India: Part 1. Structure and stratigraphyThe Kumaun and Garwhal Lesser Himalaya: Structure and stratigraphy. Geological Society of America Bulletin 121, 1262–1280. https://doi.org/10.1130/b26344.1
Clark and Bilham, 2008	Clark, M., Bilham, R., 2008. Miocene rise of the Shillong Plateau and the beginning of the end for the Eastern Himalaya. Earth and Planetary Science Letters 269, 337–351. https://doi.org/10.1016/j.epsl.2008.01.045
Cottle et al., 2015	Cottle, J.M., Searle, M.P., Jessup, M.J., Crowley, J.L., Law, R.D., 2015. Rongbuk re-visited: Geochronology of leucogranites in the footwall of the South Tibetan Detachment System, Everest Region, Southern Tibet. Lithos 227, 94–106. https://doi.org/10.1016/j.lithos.2015.03.019
Ding et al., 2005	Ding, L., Kapp, P., Wan, X., 2005. Paleocene–Eocene record of ophiolite obduction and initial India-Asia collision, south central Tibet. Tectonics 24. https://doi.org/10.1029/2004TC001729
Dithal, 2015	Dhital, M.R., 2015. Geology of the Nepal Himalaya: regional perspective of the classic collided orogen. Springer International Publishing, Cham. https://doi.org/10.1007/978-3-319-02496-7
Gardiner et al., 2014	Gardiner, N.J., Robb, L.J., Searle, M.P., 2014. The metallogenic provinces of Myanmar. Applied Earth Science 123, 25–38. https://doi.org/10.1179/1743275814Y.0000000049
Geng et al., 2003	Geng, Q., Pan, G., Zheng, L., Chen, Z., Sun, Z., Ou, C., Dong, H., Wang, X.,, Li, S., Lou, X., and Fu, H., and 14 unnamed others, 2003. Geologic map of Motou area: Chengdu, China.
Ghose and Kent, 2003	Ghose, N.C., Kent, R.W., 2003. The Rajmahal basalts: a review of their geology, composition and petrogenesis. Memoirs-Geological Society of India 167–196.
Goscombe and Hand, 2000	Goscombe, B., Hand, M., 2000. Contrasting P–T Paths in the Eastern Himalaya, Nepal: Inverted Isograds in a Paired Metamorphic Mountain Belt. J Petrology 41, 1673–1719. https://doi.org/10.1093/petrology/41.12.1673
Goscombe et al., 2006	Goscombe, B., Gray, D., Hand, M., 2006. Crustal architecture of the Himalayan metamorphic front in eastern Nepal. Gondwana Research 10, 232–255. https://doi.org/10.1016/j.gr.2006.05.003
Greenwood et al., 2016	Greenwood, L.V., Argles, T.W., Parrish, R.R., Harris, N.B.W., Warren, C., 2016. The geology and tectonics of central Bhutan. Journal of the Geological Society 173, 352–369. https://doi.org/10.1144/jgs2015-031
Grujic et al., 2002	Grujic, D., Hollister, L.S., Parrish, R.R., 2002. Himalayan metamorphic sequence as an orogenic channel: insight from Bhutan. Earth and Planetary Science Letters 198, 177–191.
Grujic et al., 2011.	Grujic, D., Warren, C.J., Wooden, J.L., 2011. Rapid synconvergent exhumation of Miocene-aged lower orogenic crust in the eastern Himalaya. Lithosphere 3, 346–366. https://doi.org/10.1130/l154.1
Indian Geol. Survey - Nagaland map, 1995	
Indian Geol. Survey - Kashmir map, 1995	
Indian Geol. Survey - Manipur map, 1995	
Jessup et al., 2008a	Jessup, M.J., Cottle, J.M., Searle, M.P., Law, R.D., Newell, D.L., Tracy, R.J., Waters, D.J., 2008. P–T–t–D paths of Everest Series schist, Nepal. Journal of Metamorphic Geology 26, 717–739.
Jessup et al., 2008b	Jessup, M.J., Newell, D.L., Cottle, J.M., Berger, A.L., Spotila, J.A., 2008. Orogen-parallel extension and exhumation enhanced by denudation in the trans-Himalayan Arun River gorge, Ama Drime Massif, Tibet-Nepal. Geology 36, 587–590.
Jiang et al., 2017	Jiang, H., Li, W.-Q., Jiang, S.-Y., Wang, H., Wei, X.-P., 2017. Geochronological, geochemical and Sr-Nd-Hf isotopic constraints on the petrogenesis of Late Cretaceous A-type granites from the Sibumasu Block, Southern Myanmar, SE Asia. Lithos 268–271. https://doi.org/10.1016/j.lithos.2016.11.005

Table SII-1 (…/…)

Authors	Reference
Kali et al., 2010	Kali, E., Leloup, P.H., Arnaud, N., Mahéo, G., Liu, D., Boutonnet, E., Van der Woerd, J., Liu, X., Liu-Zeng, J., Li, H., 2010. Exhumation history of the deepest central Himalayan rocks, Ama Drime range: Key pressure-temperature-deformation-time constraints on orogenic models. Tectonics 29.
Kellett et al., 2009	Kellett, D.A., Grujic, D., Erdmann, S., 2009. Miocene structural reorganization of the South Tibetan detachment, eastern Himalaya: Implications for continental collision. Lithosphere 1, 259–281.
Kellett 2010	Kellett, D.A., Grujic, D., Warren, C., Cottle, J., Jamieson, R., Tenzin, T., 2010. Metamorphic history of a syn-convergent orogen-parallel detachment: The South Tibetan detachment system, Bhutan Himalaya. Journal of Metamorphic Geology 28, 785–808.
Liu et al., 2017	Liu, Z.-C., Wu, F.-Y., Qiu, Z.-L., Wang, J.-G., Liu, X.-C., Ji, W.-Q., Liu, C.-Z., 2017. Leucogranite geochronological constraints on the termination of the South Tibetan Detachment in eastern Himalaya. Tectonophysics 721, 106–122. https://doi.org/10.1016/j.tecto.2017.08.019
Long et al., 2011	Long, S., McQuarrie, N., Tobgay, T., Grujic, D., 2011. Geometry and crustal shortening of the Himalayan fold-thrust belt, eastern and central Bhutan. GSA Bulletin 123, 1427–1447.
Mandal et al., 2019	Mandal, S.K., Scherler, D., Romer, R.L., Burg, J.-P., Guillong, M., Schleicher, A.M., 2019. Multiproxy Isotopic and Geochemical Analysis of the Siwalik Sediments in NW India: Implication for the Late Cenozoic Tectonic Evolution of the Himalaya. Tectonics 38, 120–143.
Miller et al., 1999	Miller, C., Schuster, R., Klötzli, U., Frank, W., Purtscheller, F., 1999. Post-Collisional Potassic and Ultrapotassic Magmatism in SW Tibet: Geochemical and Sr–Nd–Pb–O Isotopic Constraints for Mantle Source Characteristics and Petrogenesis. J Petrology 40, 1399–1424. https://doi.org/10.1093/petroj/40.9.1399
Chinese Geological Survey, Tibet map, 1983	
Morin, 2015	Morin, G., 2015. L'Érosion Et L'Alteration Et Leur Évolution Depuis Le Tardi-Pleistocene : Analyse Des Processus D'Érosion A Partir De Sediments De Riviere Actuels Et Passes Au Nepal Central. Université de Lorraine, Nancy, France.
Mukherjee, 2015.	Mukherjee, S., 2015. A review on out-of-sequence deformation in the Himalaya. Geological Society, London, Special Publications 412, 67–109.
Myanmar Geol. Survey, 2013	
Searle et al., 2007	Searle, M.P., Stephenson, B., Walker, J., Walker, C., 2007. Restoration of the Western Himalaya: implications for metamorphic protoliths, thrust and normal faulting, and channel flow models. Episodes 30, 242.
Strong et al., 2019	Strong, C.M., Attal, M., Mudd, S.M., Sinclair, H.D., 2019. Lithological control on the geomorphic evolution of the Shillong Plateau in Northeast India. Geomorphology 330, 133–150. https://doi.org/10.1016/j.geomorph.2019.01.016
Upreti et Lefort, 1999, et refs therein	Upreti, B.N., Le Fort, P., 1999. Lesser Himalayan crystalline nappes of Nepal: Problems of their origin, in: Special Paper 328: Himalaya and Tibet: Mountain Roots to Mountain Tops. Geological Society of America, pp. 225–238. https://doi.org/10.1130/0-8137-2328-0.225
Wan 2005	
Webb et al., 2011	Webb, A.A.G., Schmitt, A.K., He, D., Weigand, E.L., 2011. Structural and geochronological evidence for the leading edge of the Greater Himalayan Crystalline complex in the central Nepal Himalaya. Earth and Planetary Science Letters 304, 483–495. https://doi.org/10.1016/j.epsl.2011.02.024
Xu et al., 2010	Xu, W.-C., Zhang, H.-F., Parrish, R., Harris, N., Guo, L., Yuan, H.-L., 2010. Timing of granulite-facies metamorphism in the eastern Himalayan syntaxis and its tectonic implications. Tectonophysics 485, 231–244. https://doi.org/10.1016/j.tecto.2009.12.023
Yin et al., 2010	Yin, A., Dubey, C.S., Kelty, T.K., Webb, A.A.G., Harrison, T.M., Chou, C.Y., Celerier, J., 2010. Geologic correlation of the Himalayan orogen and Indian craton: Part 2. Structural geology, geochronology, and tectonic evolution of the Eastern Himalaya. Geological Society of America Bulletin 122, 360–395. https://doi.org/10.1130/B26461.1
Yu et al., 2015	Yu, H., Webb, A.A.G., He, D., 2015. Extrusion vs. duplexing models of Himalayan mountain building 1: Discovery of the Pabbar thrust confirms duplex-dominated growth of the northwestern Indian Himalaya since Mid-Miocene. Tectonics 34, 313–333. https://doi.org/10.1002/2014tc003589
Zeitler et al. 2014	Zeitler, P.K., Meltzer, A.S., Brown, L., Kidd, W.S., Lim, C., Enkelmann, E., 2014. Tectonics and topographic evolution of Namche Barwa and the easternmost Lhasa block, Tibet, in: Nie, J., Horton, B.K., Hoke, G.D. (Eds.), Toward an Improved Understanding of Uplift Mechanisms and the Elevation History of the Tibetan Plateau. Geological Society of America Special Paper 507, pp. SPE507–02. https://doi.org/10.1130/2014.2507(02)
Zeng et al. ,2009	Zeng, L., Liu, J., Gao, L., Xie, K., Wen, L., 2009. Early Oligocene anatexis in the Yardoi gneiss dome, southern Tibet and geological implications. Chin. Sci. Bull. 54, 104. https://doi.org/10.1007/s11434-008-0362-x

Table SII-1 (…/…)

Authors	Reference
Zhang et al., 2007	Zhang, J.J., 2007. A review on the extensional structures in the northern Himalaya and southern Tibet. Geological Bulletin of China 26, 639–649.

Table SII-2. Compilation of bedrock Sr-Nd isotopic measurements.

Not exhaustive. Check comment for dubious datasets. LH: Lesser Himalaya, HHC: High Himalaya Crystalline, TSS: Tethyan Sedimentary Series. BL: bedload, SL: suspended load, W.R.: whole rock

Table SII-2 (…/…)

	Ech.#	Region	River	Locality	Formation	Category	Type	Rock type	North	East	Date	Rb Sil	Sr Sil	87Rb/86Sr	87Sr/86Sr S	2s.d.	Sm Sil	Nd Sil	147Sm/144Nd
TSS	NAG 22	C. Nepal	Marsyandi	source	TSS	TSS	BL		28.786	83.964	28/11/1995	218	93.6		0.7219		10.1	64.3	
TSS	MAR-50	C. Nepal	Marsyandi	Temang	TSS	TSS	BL		28.53	84.316					0.7315				
TSS	MAR-45	C. Nepal	Naar k.	RG	TSS	TSS	BL		28.561	84.257					0.722066				
TSS	MO 501	C. Nepal	Kali	Tukuche	TSS	TSS	SL		28.703	83.635	26/07/1998	172.5	156.5		0.723111			30.3	
TSS	NAG 33	C. Nepal	Kali	Koketani	TSS	TSS	BL		28.647	83.594	02/12/1995	136.7	95.8		0.729111		6.8	38.4	
TSS	NAG 36	C. Nepal	Kali	Kopchepani	TSS	TSS	BL		28.647	83.594	02/12/1995	223.7	153.2		0.724852		6.7	38.5	
TSS	LO2	C. Nepal	Kali	Kagbeni	mixed TSS basin		BL		28.841	83.784	16/05/1993	159.3	95.9		0.73196		5.3	30	
TSS	NAG 20	C. Nepal	Kali	Kagbeni	mixed TSS basin		BL		28.841	83.784	25/11/1993	157	96		0.731627		3.6	19.3	
TSS	NAG 25	C. Nepal	Kali	Jomoson	mixed TSS basin		BL		28.785	83.734	01/12/1995	248	162.4		0.722487		8.5	47.5	
TSS	MO 504	C. Nepal	Yamkim	outlet	TSS	TSS	SL		28.711	83.641	26/07/1998		56.3		0.7594			29.5	
TSS	MO 516	C. Nepal	Kali		mixed TSS basin		SL		83.636	28.558	27/07/1998		195.9		0.72198			34.9	
TSS	NAG 38	C. Nepal	Kali	Dana	mixed TSS basin		BL		28.558	83.636	03/12/1995	157	135		0.730227		5.9	32.2	
TSS	NAG 42	C. Nepal	Kali	Tatopani	mixed TSS basin		BL		28.496	83.654	05/12/1995	153.2	142.9		0.729763		5.2	28.9	
TSS	MAR-52	C. Nepal	Dudh k.	Darapani	mixed TSS basin		BL		28.535	84.366					0.731861				
TSS	MAR-57	C. Nepal	Marsyandi	Tal depot de terasse pour tester la variabilité t	mixed TSS basin		BL		28.465	84.373					0.729856				
TSS	MAR-55	C. Nepal	Marsyandi	Tal	mixed TSS basin		BL		28.467	84.373					0.731092				
TSS	HF 10	C. Nepal	Seti		mixed TSS basin		BL					128.6	47.3		0.737782		3.8	22.3	
HHC	MO 50	C. Nepal	Chepe	Vallon	HHC	HHC	BL				06/05/1997				0.753712				
HHC	MAR-26	C. Nepal	Chepe		HHC	HHC	BL		28.112	84.427					0.754397				
HHC	KN 101	C. Nepal	Likhu		HHC	HHC	BL		27.891	85.249		301.9	106.4		0.750994		6.1	31.7	
HHC	KN 83	C. Nepal	Tadi		HHC	HHC	BL		27.891	85.249	06/05/1997	117	131		0.75086			29.5	
HHC	CA11215C	C. Nepal	Khudi k. N	Branche Nord	HHC	HHC	Sand/Gravels		28.318	84.356	14/11/2011				0.755024	0.00001			
HHC	CA10112A	C. Nepal	Khudi k. W	Branch W	HHC	HHC	Bank		28.365	84.305	15/11/2010				0.757583	8E-06			
HHC	SKD71	C. Nepal	Khudi k.	Khudi	HHC	HHC	SL		28.306	84.33	23/08/2010				0.762701	1.1E-05			
HHC	CA11212A	C. Nepal	Khudi	Nord W basin	HHC	HHC	Sand/Gravels		28.405	84.263	10/11/2011				0.748403	1.1E-05			
HHC	CA10113	C. Nepal	Khudi basin	HHC Trib	HHC	HHC	Bank		28.365	84.305	15/11/2010				0.756553	7E-06			
HHC	CA954	C. Nepal	Khudi basin	Landslide	HHC	HHC	Bank		28.372	84.294	11/11/2009				0.761857	7E-06			
HHC	GA 32	C. Nepal	Mailung	Paigutang	mixed HHC basin		Bank		28.222	85.188	06/10/1999	127.4			0.754785				
HHC	CA10116	C. Nepal	Khudi k.	Khudi Power house	mixed HHC basin		Bank		28.288	84.345	16/11/2010				0.761467	1.1E-05			
HHC	CA11111	C. Nepal	Khudi k.	Khudi Power house	mixed HHC basin		SL		28.289	84.345	29/07/2011				0.762997	1.7E-05			
HHC	B106	C. Nepal	6.1		0.8 HHC bedrock	HHC	W.R.								0.76506				
HHC	B114	C. Nepal	3		0.8 HHC bedrock	HHC	W.R.								0.75794				
HHC	NL43	C. Nepal	3.9		0.7 HHC bedrock	HHC	W.R.								0.747452				
HHC	NL58	C. Nepal	3.1		0.7 HHC bedrock	HHC	W.R.								0.745126				
HHC	NL59	C. Nepal	1.1		0.7 HHC bedrock	HHC	W.R.								0.733112				
HHC	NL74	C. Nepal	2		0.7 HHC bedrock	HHC	W.R.								0.733546				
HHC	NL75	C. Nepal	5.5		0.8 HHC bedrock	HHC	W.R.								0.75495				
HHC	NL76	C. Nepal	1.4		0.7 HHC bedrock	HHC	W.R.								0.733218				
HHC	NL85	C. Nepal	2		0.7 HHC bedrock	HHC	W.R.								0.745317				
HHC	NL93	C. Nepal	0.4		0.7 HHC bedrock	HHC	W.R.								0.734352				
HHC	NL420	C. Nepal	19.2		0.8 HHC bedrock	HHC	W.R.								0.806501				
LH	NAG 4	C. Nepal	Bijaipur	Kundahar	LH	LH	BL		28.245	84	11/11/1995	106.8	44.8		0.879796		5.4	30.1	
LH	MO 112	C. Nepal	Isul k.	Bhuri G.	LH	LH	BL		28.048	84.808	12/05/1997				0.874814				
LH	MO 102	C. Nepal	Marsel k.	Darondi	LH	LH	BL		28.041	84.669	11/05/1997		48.9		0.840096				
LH	MO 109	C. Nepal	Mati k.	Bhuri G.	LH	LH	BL		28.045	84.806	12/05/1997		50.2		0.853771				
LH	MO 207	C. Nepal	Andi	Kali Gandaki	LH	LH	BL		28.043	83.79	18/05/1997				0.892148				
LH	GA 99	C. Nepal	Mailung	landslide	LH	LH	Bank		28.148	85.199	11/10/1999		74.8		0.822903			31.6	
LH	GA 112	C. Nepal	Mailung	Camp	LH	LH	Bank		28.082	85.207	12/10/1999		62.2		0.855181			30.1	
LH	MAR28	C. Nepal	Paudi k.	RG	LH	LH	BL		28.123	84.408					0.824				
LH	MAR64	C. Nepal	Ngadi Khola	RG	LH	LH	BL		28.31	84.404					0.814				
LH	GA 50	C. Nepal	Mailung Col		LH	LH	bedrock Bank		28.218	85.181	08/10/1999		19.8		0.885761			32.7	
LH	AP 346	C. Nepal		Manaslu section	LH Kuncha pelites	LH	W.R.					252	21	38.07	1.6809		8.08	44	
LH	AP 385	C. Nepal		Manaslu section	LH Kuncha pelites	LH	W.R.					236	63	13.48	1.0301		6.58	36.6	
TSS	NA 178	C. Nepal		Manaslu section	TSS Jurassic schist		W.R.										3.99	20.33	
TSS	NA 181	C. Nepal		Manaslu section	TSS Cretaceous (volcaniclastic)		W.R.										12.61	58.97	
HHC	DK 43	C. Nepal		Manaslu	Leucogranite		W.R.						8		0.77822	12			
HHC	DK 45	C. Nepal		Manaslu	Leucogranite	HHC granite	W.R.						4.5		0.83248	26			
HHC	DK 46	C. Nepal		Manaslu	Leucogranite		W.R.						6.5		0.78704	15			

Table SII-2 (…/…)

Ech.#	Region	River	Locality	Formation	Category	Type	Rock type	North	East	Date	Rb Sil	Sr Sil	87Rb/86Sr	87Sr/86Sr S	2s.d.	Sm Sil	Nd Sil	147Sm/144Nd
HHCDK 47	C. Nepal		Manaslu	Leucogranite		W.R.						12		0.76864	19			
HHCDK 48	C. Nepal		Manaslu	Leucogranite		W.R.						10		0.77713	12			
HHCDK 49	C. Nepal		Manaslu	Leucogranite		W.R.						6.5		0.79503	27			
HHCDK 50	C. Nepal		Manaslu	Leucogranite		W.R.						5		0.80201	11			
HHCDK 51	C. Nepal		Manaslu	Leucogranite		W.R.						66		0.75147	13			
HHCDK 52	C. Nepal		Manaslu	Leucogranite	HHC granite	W.R.						82.5		0.74967	9		4.3	
HHCDK 53	C. Nepal		Manaslu	Leucogranite		W.R.						146.5		0.74416	12			
HHCDK 54	C. Nepal		Manaslu	Leucogranite	HHC granite	W.R.						216		0.74328	19		13.7	
HHCDK 54	C. Nepal		Manaslu	Leucogranite	HHC granite	W.R.						216		0.74328	19		11.7	
HHCDK 55a	C. Nepal		Manaslu	Leucogranite	HHC granite	W.R.						204		0.74292	8		11.8	
HHCDK 55b	C. Nepal		Manaslu	Leucogranite		W.R.						72		0.74428	12			
HHCDK 56	C. Nepal		Manaslu	Leucogranite		W.R.						104		0.74476	12			
HHCDK 57	C. Nepal		Manaslu	Leucogranite		W.R.						4.5		0.80125	9			
HHCDK 58	C. Nepal		Manaslu	Leucogranite	HHC granite	W.R.						4		0.77126	18			
HHCDK 59	C. Nepal		Manaslu	Leucogranite	HHC granite	W.R.						65		0.74554	14		4.3	
HHCU 464	C. Nepal		Manaslu	Leucogranite		W.R.						53.5		0.76458	8			
HHCU 464	C. Nepal		Manaslu	Leucogranite		W.R.						54		0.76389	12			
HHCU 464	C. Nepal		Manaslu	Leucogranite		Muscovite						5		0.98037	9			
HHCU 464	C. Nepal		Manaslu	Leucogranite		Apatite						81		0.75998	8			
HHCU 464	C. Nepal		Manaslu	Leucogranite		Apatite						79		0.75995	10			
HHCU 464	C. Nepal		Manaslu	Leucogranite		K Feldspar						146		0.7662	5			
HHCU 464	C. Nepal		Manaslu	Leucogranite		K Feldspar						105.5		0.76652	5			
HHCU 476	C. Nepal		Manaslu	Leucogranite		W.R.						44.2		0.76477				
HHCU 476	C. Nepal		Manaslu	Leucogranite		Muscovite						10.2		0.84969				
HHCU 476	C. Nepal		Manaslu	Leucogranite		Muscovite						10.8		0.85424				
HHCX 12	C. Nepal		Manaslu	Leucogranite		W.R.						52		0.76385				
HHCX 12	C. Nepal		Manaslu	Leucogranite		Muscovite						10		0.8171	10			
HHCX 12	C. Nepal		Manaslu	Leucogranite		Muscovite						10		0.81487	8			
HHCDK 157	C. Nepal		Manaslu	Leucogranite		W.R.						71.5		0.75525	8			
HHCDK 157	C. Nepal		Manaslu	Leucogranite		Muscovite						3		1.2094	18			
HHCDK 195	C. Nepal		Manaslu	Leucogranite		W.R.						135.5		0.74357	12			
HHCDK 195	C. Nepal		Manaslu	Leucogranite		W.R.						127		0.74355	9			
HHCDK 195	C. Nepal		Manaslu	Leucogranite		Muscovite						19.5		0.76484	8			
HHCDK 195	C. Nepal		Manaslu	Leucogranite		Biotite						17		0.76641	10			
HHCD 22	C. Nepal		Manaslu	Leucogranite	HHC granite	W.R.						131		0.74275	27			
HHCD 22	C. Nepal		Manaslu	Leucogranite		Muscovite						11		0.78023	4			
HHCD 22	C. Nepal		Manaslu	Leucogranite		Muscovite						12		0.77709	9			
HHCDK 65	C. Nepal		Manaslu	Leucogranite		W.R.						49.5		0.76053	7			
HHCDK 67	C. Nepal		Manaslu	Leucogranite		W.R.						83		0.74343	7			
HHCDK 72	C. Nepal		Manaslu	Leucogranite		W.R.						100		0.74519	4			
HHCDK 98	C. Nepal		Manaslu	Leucogranite		W.R.						64		0.75415	3			
HHCDK 102	C. Nepal		Manaslu	Leucogranite		W.R.						61		0.75589	10			
HHCDK 111	C. Nepal		Manaslu	Leucogranite		W.R.						56		0.75794	7			
HHCDK 112	C. Nepal		Manaslu	Leucogranite		W.R.						53		0.75055	11			
HHCDK 116	C. Nepal		Manaslu	Leucogranite		W.R.						54		0.75407	3			
HHCDK 136	C. Nepal		Manaslu	Leucogranite		W.R.						54		0.75257	5			
HHCDK 138	C. Nepal		Manaslu	Leucogranite		W.R.						55.5		0.7518	12			
HHCDK 139	C. Nepal		Manaslu	Leucogranite		W.R.						65.5		0.7469	4			
HHCDK 140	C. Nepal		Manaslu	Leucogranite		W.R.						58.5		0.74872	5			
HHCDK 141	C. Nepal		Manaslu	Leucogranite		W.R.						65.5		0.75162	10			
HHCDK 151	C. Nepal		Manaslu	Leucogranite		W.R.						70.5		0.75347	8			
HHCDK 151	C. Nepal		Manaslu	Leucogranite		W.R.						70.5		0.75317				
HHCDK 152	C. Nepal		Manaslu	Leucogranite		W.R.						25.5		0.76741	11			
HHCDK 157	C. Nepal		Manaslu	Leucogranite		W.R.						71.5		0.75525	8			
HHCDK 160	C. Nepal		Manaslu	Leucogranite		W.R.						66		0.75571	4			
HHCDK 161	C. Nepal		Manaslu	Leucogranite		W.R.						72.5		0.75563	3			
HHCDK 162	C. Nepal		Manaslu	Leucogranite		W.R.						43.5		0.76173	4			
HHCDK 167	C. Nepal		Manaslu	Leucogranite		W.R.						63		0.76498	4			
HHCDK 180	C. Nepal		Manaslu	Leucogranite		W.R.						107		0.7439	7			
HHCDK 185	C. Nepal		Manaslu	Leucogranite		W.R.						111		0.74938	5			
HHCDK 186	C. Nepal		Manaslu	Leucogranite		W.R.						103.5		0.7495	9			
HHCDK 188	C. Nepal		Manaslu	Leucogranite		W.R.						87.5		0.74885	6			
HHCDK 191	C. Nepal		Manaslu	Leucogranite		W.R.						69		0.75269	3			
HHCDK 195	C. Nepal		Manaslu	Leucogranite		W.R.						135		0.74359	5			
HHCDK 211	C. Nepal		Manaslu	Leucogranite		W.R.						78		0.74533	6			
HHCDK 213	C. Nepal		Manaslu	Leucogranite		W.R.						63.5		0.76337	9			
HHCDK 214	C. Nepal		Manaslu	Leucogranite		W.R.						54		0.76126	4			
HHCDK 217	C. Nepal		Manaslu	Leucogranite		W.R.						48.5		0.74851	6			
HHCDK 220	C. Nepal		Manaslu	Leucogranite		W.R.						60		0.74633	9			
HHCDK 237	C. Nepal		Manaslu	Leucogranite	HHC granite	W.R.						46.5		0.76792	10			
HHCDK 240	C. Nepal		Manaslu	Leucogranite		W.R.						68		0.74735	11			

Table SII-2 (…/…)

Ech.#	Region	River	Locality	Formation	Category	Type	Rock type	North	East	Date	Rb Sil	Sr Sil	87Rb/86Sr	87Sr/86Sr S	2s.d.	Sm Sil	Nd Sil	147Sm/144Nd
HHCDK 242	C. Nepal		Manaslu	Leucogranite		W.R.						99.5		0.74608	11			
HHCDK 247	C. Nepal		Manaslu	Leucogranite		W.R.						56		0.76625	5			
HHCDK 268	C. Nepal		Manaslu	Leucogranite		W.R.						82.5		0.75231	6			
HHCD 22	C. Nepal		Manaslu	Leucogranite		W.R.						5.56		0.74275	27			
HHCD 14	C. Nepal		Manaslu	Leucogranite		W.R.						7.29		0.74562	6			
HHCD 37	C. Nepal		Manaslu	Leucogranite	HHC granite	W.R.						13.28		0.74444	11			
HHCD 45	C. Nepal		Manaslu	Leucogranite	HHC granite	W.R.						14.7		0.75478				
HHCDK 200	C. Nepal		Manaslu Sect. 1	Leucogranite	HHC granite	W.R.						108.5		0.74711	9		11.6	
HHCDK 202	C. Nepal		Manaslu Sect. 1	Leucogranite		W.R.						106		0.74865	8			
HHCDK 203	C. Nepal		Manaslu Sect. 1	Leucogranite		W.R.						105		0.749	7			
HHCDK 204	C. Nepal		Manaslu Sect. 1	Leucogranite		W.R.						105		0.74873	8			
HHCDK 205	C. Nepal		Manaslu Sect. 1	Leucogranite		W.R.						107.5		0.74887	8			
HHCDK 206	C. Nepal		Manaslu Sect. 1	Leucogranite		W.R.						106.5		0.74868	4			
HHCDK 207	C. Nepal		Manaslu Sect. 1	Leucogranite	HHC granite	W.R.						104.5		0.74895	7		13.4	
HHCDK 207	C. Nepal		Manaslu Sect. 1	Leucogranite	HHC granite	W.R.						104.5		0.74895	7		13.4	
HHCDK 208	C. Nepal		Manaslu Sect. 1	Leucogranite	HHC granite	W.R.						108.5		0.74819	20		15.4	
HHCDK 208	C. Nepal		Manaslu Sect. 1	Leucogranite	HHC granite	W.R.						108.5		0.74819	20		15.4	
HHCDK 209	C. Nepal		Manaslu Sect. 1	Leucogranite	HHC granite	W.R.						102		0.75061	8		13	
HHCDK 210	C. Nepal		Manaslu Sect. 1	Leucogranite		W.R.						109		0.74781	9			
HHCDK 244	C. Nepal		Manaslu Sect. 1	Leucogranite		W.R.						111.8		0.74857	15			
HHCDK 168	C. Nepal		Manaslu Sect. 2	Leucogranite	HHC granite	W.R.						39.5		0.77162	9		7	
HHCDK 168	C. Nepal		Manaslu Sect. 2	Leucogranite	HHC granite	W.R.						39.5		0.77162	9		7	
HHCDK 169	C. Nepal		Manaslu Sect. 2	Leucogranite		W.R.						40		0.77081	22			
HHCDK 170	C. Nepal		Manaslu Sect. 2	Leucogranite		W.R.						42.5		0.76817	10			
HHCDK 171	C. Nepal		Manaslu Sect. 2	Leucogranite		W.R.						71		0.76479	6			
HHCDK 172	C. Nepal		Manaslu Sect. 2	Leucogranite	HHC granite	W.R.						63.5		0.7651	8		6.7	
HHCDK 173	C. Nepal		Manaslu Sect. 2	Leucogranite		W.R.						52		0.76592	8			
HHCDK 174a	C. Nepal		Manaslu Sect. 2	Leucogranite	HHC granite	W.R.						63		0.75957	35			
HHCDK 175	C. Nepal		Manaslu Sect. 2	Leucogranite	HHC granite	W.R.						54.5		0.76522	17		10.7	
HHCNL 219 (1)	C. Nepal		Manaslu Sect. 4	granite dyke	HHC granite	W.R.						104		0.74841	5			
HHCNL 222 (2)	C. Nepal		Manaslu Sect. 4	granite dyke		W.R.						39.5		0.76961	10			
HHCNL 223 (2)	C. Nepal		Manaslu Sect. 4	granite dyke		W.R.						39		0.77031	9			
HHCNL 224 (2)	C. Nepal		Manaslu Sect. 4	granite dyke	HHC granite	W.R.						54.5		0.76949	9		6.2	
HHCNL 225 (2)	C. Nepal		Manaslu Sect. 4	granite dyke	HHC granite	W.R.						26.5		0.76776	9		2.4	
HHCNL 226 (3)	C. Nepal		Manaslu Sect. 4	granite dyke		W.R.						37		0.7707	8			
HHCNL 227 (3)	C. Nepal		Manaslu Sect. 4	granite dyke	HHC granite	W.R.						22.5		0.78163	9		2.2	
HHCNL 206	C. Nepal		Manaslu Sect. 5	Leucogranite	HHC granite	W.R.						77		0.74204	4		4.6	
HHCNL 207	C. Nepal		Manaslu Sect. 5	Leucogranite	HHC granite	W.R.						71.5		0.75136	9		4.9	
HHCNL 208	C. Nepal		Manaslu Sect. 5	Leucogranite	HHC granite	W.R.						36		0.75917	8		2.3	
HHCNL 234	C. Nepal		Manaslu	Leucogranite		W.R.											6.5	
HHCU 862	C. Nepal		Manaslu	Leucogranite		W.R.												
HHCNL 43a	C. Nepal		Manaslu	Fl Gneiss	HHC	W.R.						157.5		0.74745	4		39.6	
HHCNL 58a	C. Nepal		Manaslu	Fl Gneiss	HHC	W.R.						132.5		0.74513	8		35.8	
HHCNL 59a	C. Nepal		Manaslu	Fl Gneiss	HHC	W.R.						267		0.73311	4		39.9	
HHCNL 74	C. Nepal		Manaslu	Fl Gneiss	HHC	W.R.						220		0.73355	11		37.7	
HHCNL 75	C. Nepal		Manaslu	Fl Gneiss	HHC	W.R.						48.5		0.75495	6		22.9	
HHCNL 76	C. Nepal		Manaslu	Fl Gneiss	HHC	W.R.						249.5		0.73322	10		30.2	
HHCNL 81	C. Nepal		Manaslu	Fl Gneiss		W.R.						156.5		0.74596	7			
HHCNL 85	C. Nepal		Manaslu	Fl Gneiss	HHC	W.R.						163		0.74532	6		24.2	
HHCNL 86	C. Nepal		Manaslu	Fl Gneiss		W.R.						181.5		0.73799	8			
HHCNL 93	C. Nepal		Manaslu	Fl Gneiss	HHC	W.R.						269.5		0.73435	6		20.1	
HHCNL 100	C. Nepal		Manaslu	Fl Gneiss		W.R.						210.5		0.73113	6			
HHCNL 100	C. Nepal		Manaslu	Fl Gneiss		W.R.						210.5		0.73114	5			
HHCNL 172	C. Nepal		Manaslu	Fl Gneiss		W.R.						225.5		0.72899	5			
HHCNL 499	C. Nepal		Manaslu	Fl Gneiss		W.R.						104		0.74425	7			
HHCNL 512	C. Nepal		Manaslu	Fl Gneiss		W.R.						90.5		0.74872	8			
HHCβ 106a	C. Nepal		Manaslu	Fl Gneiss	HHC	W.R.					193	92	6.08	0.76506			25.3	
HHCβ 114a	C. Nepal		Manaslu	Fl Gneiss	HHC	W.R.					71.1	68.2	3.02	0.75794			25.5	
HHCβ 114a	C. Nepal		Manaslu	Fl Gneiss	HHC	W.R.					71.8	69.9	2.98	0.75743			25.5	
HHCU 48	C. Nepal		Manaslu	Fl Gneiss	HHC	W.R.					163	172	2.75	0.75037				
LH AP9*	C. Nepal		Manaslu section	LH		W.R.					143	11	40.08	1.5098				
LH AP440*	C. Nepal		Manaslu section	LH		W.R.					98	83	3.48	0.83318				
LH AP 524*	C. Nepal		Manaslu section	LH		W.R.					321	76	12.52	0.96411				
LH AP 825*	C. Nepal		Manaslu section	LH		W.R.					123	74	4.82	0.82573				
LH AP 874*	C. Nepal		Manaslu section	LH		W.R.					366	56	19.58	1.01761				
LH AP 888*	C. Nepal		Manaslu section	LH		W.R.					126	44	8.48	0.89964				

Table SII-2 (…/…)

Ech.#	Region	River	Locality	Formation	Category	Type	Rock type	North	East	Date	Rb Sil	Sr Sil	87Rb/86Sr	87Sr/86Sr S	2s.d.	Sm Sil	Nd Sil	147Sm/144Nd
LH NL1*	C. Nepal		Manaslu section	LH		W.R.					114	19	17.79	0.93696				
LH NL3f	C. Nepal		Manaslu section	LH		W.R.					1	7	7.66	0.86772				
LH NL4t	C. Nepal		Manaslu section	LH		W.R.					288	55	15.32	0.93943				
HHCNL 428t	C. Nepal		Manaslu section	FII		W.R.					190	231	2.39	0.734586				
HHCNL 623t	C. Nepal		Manaslu section	FII		W.R.					5	772	0.018	0.714109				
HHCD77*	C. Nepal		Manaslu section	FIII		W.R.					327	104	9.08	0.78959				
HHCD94*	C. Nepal		Manaslu section	FIII		W.R.					391	62	18.13	0.83959				
HHCM84*	C. Nepal		Manaslu section	FIII		W.R.					343	43	23.1	0.88141				
HHCNA 116|	C. Nepal		Manaslu section	FIII		W.R.					270	66	11.91	0.80357				
HHCNA 155*	C. Nepal		Manaslu section	FIII		W.R.					209	78	7.782	0.77686				
HHCNA 156*	C. Nepal		Manaslu section	FIII		W.R.					300	62	13.97	0.81281				
HHCNA 216*	C. Nepal		Manaslu section	FIII		W.R.					377	21	51.55	1.06315				
HHCNA 218*	C. Nepal		Manaslu section	FIII		W.R.					252	67	10.85	0.7902				
HHCNL 478t	C. Nepal		Manaslu section	FIII		W.R.					296	44	19.63	0.88366				
HHCT200*	C. Nepal		Manaslu section	FIII		W.R.					399	161	7.17	0.75552				
HHCU203t	C. Nepal		Manaslu section	FIII		W.R.					185	113	4.76	0.76802				
HHCU284*	C. Nepal		Manaslu section	FIII		W.R.					280	61	13.22	0.80069				
HHCU308*	C. Nepal		Manaslu section	FIII		W.R.					340	56	17.6	0.83973				
HHCU725*	C. Nepal		Manaslu section	FIII		W.R.					257	74	10.13	0.78487				
HHCU925*	C. Nepal		Manaslu section	FIII		W.R.					289	83	10.1	0.79627				
HHCU277	C. Nepal		Manaslu	Leucogranite		W.R.	Rb and Sr bulk											
HHCN 67	C. Nepal		Manaslu	Leucogranite		W.R.												
HHCM 102	C. Nepal		Manaslu	FI		W.R.					170	35.3	13.93	0.78067				
HHCM 114	C. Nepal		Manaslu	FI		W.R.					182	58.3	2.75	0.76189				
HHCL 12	C. Nepal		Manaslu	FI		W.R.					126	67.8	5.37	0.77409				
HHCM 108	C. Nepal		Manaslu	FI		W.R.					163	140	3.38	0.7647				
HHCU 124	C. Nepal		Manaslu	FI		W.R.					181	199	2.63	0.73959				
HHCM 107	C. Nepal		Manaslu	FI		W.R.					50.6	190	0.77	0.73962				
TSS 87 28				TSS Cretaceous	TSS	W.R.					42	61	1.9	0.71266		9.1	45.5	
TSS 87 32				TSS Trias	TSS	W.R.					19	45	1.19	0.70899		3.6	18.6	
TSS LA 194	W. Himalaya		Indus	TSS Indus margin		W.R.					11	299	0.1	0.70981		5.9	33.2	
TSS LA 158	W. Himalaya		Indus	TSS Indus margin		W.R.					96	50	5.29	0.72903		5	23.2	
TSS 25 1	W. Himalaya		Ladakh	TSS Suture Ladak		W.R.					7	662	0.03	0.70762		1.6	6.4	
TSS 89 1	W. Himalaya		Ladakh	TSS Suture Ladak		W.R.					44	258	0.47	0.70606		3	13.9	
TSS 1TBkag	C. Nepal			Chukh Fm		W.R.	sandstone									16.5	84.95	0.1174
TSS 2TBpha	C. Nepal			Dogger Fm		W.R.	shale									4.75	33.22	0.0864
TSS 3TBjom	C. Nepal			Jomson Fm		W.R.	shale									9.05	53.17	0.1028
TSS 4TBSya	C. Nepal			Tilicho Fm		W.R.	phyllite									10.35	63.38	0.0987
TSS 5TBMar	C. Nepal			Tilichio Fm		W.R.	phyllite									11.8	64.5	0.1105
TSS DD-31	W. Nepal			Melmura Fm		W.R.	shale									5.84	29.59	0.1193
TSS DD-33	W. Nepal			Melmura Fm		W.R.	shale									6.71	35.99	0.1128
HHCAG-106	E. Nepal			Formation I		W.R.	paragneiss									6.48	35.16	0.1113
HHCAG-109	E. Nepal			Formation I		W.R.	paragneiss									6.97	38.69	0.1089
HHC9TBkal	C. Nepal			Formation III		W.R.	orthogneiss									7.08	27.92	0.1533
HHC12TBgh	C. Nepal			Formation I		W.R.	paragneiss									7.26	37.85	0.116
HHC13TBru	C. Nepal			Formation II		W.R.	paragneiss									8.36	41.77	0.1209
HHCAG-105	E. Nepal			Formation I		W.R.	paragneiss									2.17	8.85	0.1483
HHCDDG-98	W. Nepa	Greater Himalayan klippen		C-O granite, DT		W.R.	granite									6.02	26.6	0.1369
HHCDD-40	W. Nepa	Greater Himalayan klippen		Kalikot Schist, Dt		W.R.	schist									3.88	18.74	0.125
LH K1-99	C. Nepal			Benighat Fm		W.R.	shale									3.97	29.93	0.0801
LH SR-37	W. Nepal			Benighat Fm		W.R.	shale									3.83	20	0.1159
LH SR-35	W. Nepal			Benighat Fm		W.R.	shale									5.05	27.79	0.1098
LH DD-58	W. Nepal			Benighat Fm		W.R.	shale									7.37	42.22	0.1055
LH 23TBtu	C. Nepal			Syangia Fm		W.R.	shale									5.82	33.15	0.1062
LH 23TBSe	C. Nepal			Syangia Fm		W.R.	phyllite									6.23	37.03	0.1016
LH CH-1	W. Nepal			Galyang Fm		W.R.	phyllite									3.04	16.16	0.1138
LH DD-15	W. Nepal			Galyang Fm		W.R.	phyllite									10.1	52.32	0.1167
LH 22TBPu	C. Nepal			Galyang Fm		W.R.	shale									7.36	37.77	0.1177

Table SII-2 (…/…)

	Ech.#	Region	River	Locality	Formation	Category	Type	Rock type	North	East	Date	Rb Sil	Sr Sil	87Rb/86Sr	87Sr/86Sr S	2s.d.	Sm Sil	Nd Sil	147Sm/144Nd
LH	24TBLi	C. Nepal			Galyang Fm		W.R.	phyllite									10.98	65.18	0.1018
LH	K3-99	C. Nepal			Galyang Fm		W.R.	shale									3.57	18.42	0.117
LH	DD-52	W. Nepal			Sangram Fm		W.R.	shale									9.31	49.94	0.1127
LH	20TBSl	C. Nepal			Sangram Fm		W.R.	shale									8.72	47.63	0.1107
LH	18TBBra	C. Nepal			Ranimata Fm		W.R.	shale									6.7	38.76	0.1044
LH	K2-99	C. Nepal			Ranimata Fm		W.R.	phyllite									6.62	34.82	0.1148
LH	AG-103	E. Nepal			Ranimata Fm		W.R.	phyllite									6.75	35.31	0.1155
LH	AG-104	E. Nepal			Ranimata Fm		W.R.	phyllite									3.9	21.22	0.1112
LH	SR-30	W. Nepal			Ulleri		W.R.	gneiss									5.26	25.11	0.1266
LH	AG-111	E. Nepal			Ulleri		W.R.	gneiss									4.82	21.96	0.1327
LH	AG-112	E. Nepal			Ulleri		W.R.	gneiss									5.15	25.72	0.121
THB	K89G185			I	Tibetan lava		W.R.												
THB	K89G186			I	Tibetan lava		W.R.												
THB	K89G191			I	Tibetan lava		W.R.												
THB	K89G192			I	Tibetan lava		W.R.												
THB	K89G193			I	Tibetan lava		W.R.												
THB	K89G197			I	Tibetan lava		W.R.												
THB	K89G200			I	Tibetan lava		W.R.												
THB	KP23-1			II	Tibetan lava		W.R.												
THB	KP23-3			II	Tibetan lava		W.R.												
THB	KP24-1			III	Tibetan lava		W.R.												
THB	KP12-2			IV	Tibetan lava		W.R.												
THB	KP12-5			IV	Tibetan lava		W.R.												
THB	KP12-7			IV	Tibetan lava		W.R.												
THB	K705			IV	Tibetan lava		W.R.												
THB	K708			IV	Tibetan lava		W.R.												
THB	K713			IV	Tibetan lava		W.R.												
THB	K716			IV	Tibetan lava		W.R.												
THB	K718			IV	Tibetan lava		W.R.												
THB	K720			IV	Tibetan lava		W.R.												
THB	K723			IV	Tibetan lava		W.R.												
THB	K731			IV	Tibetan lava		W.R.												
THB	K732			IV	Tibetan lava		W.R.												
THB	K738			IV	Tibetan lava		W.R.												
THB	KP12-4			IV	Tibetan lava		W.R.												
THB	KP10-3	N. Lhasa Plutonic belt		V	Tibetan lava		W.R.								0.70896				
THB	KP10-6	N. Lhasa Plutonic belt		V	Tibetan lava		W.R.								0.70792				
THB	BG121			VI	Tibetan lava		W.R.												
THB	BG124			VI	Tibetan lava		W.R.												
THB	KP35-10			VII	Tibetan lava		W.R.												
THB	BB94-2	N. Lhasa Plutonic belt		VIII	Tibetan lava		W.R.								0.70823				
THB	BB104	N. Lhasa Plutonic belt		VIII	Tibetan lava		W.R.								0.70798				
THB	K9006			VII	Tibetan lava		W.R.												
THB	K9007			VII	Tibetan lava		W.R.												
THB	K9008			VII	Tibetan lava		W.R.												
THB	K9016			VII	Tibetan lava		W.R.												
THB	K9018			VII	Tibetan lava		W.R.												
THB	K9021			VII	Tibetan lava		W.R.												
THB	K9026			VII	Tibetan lava		W.R.												
THB	K9028			VII	Tibetan lava		W.R.												
THB	K9031			VII	Tibetan lava		W.R.												
THB	K9032			VII	Tibetan lava		W.R.												
THB	K9038			VII	Tibetan lava		W.R.												
THB	K9024	N. Lhasa Plutonic belt		IX	Tibetan lava		W.R.								0.708374				
THB	K9027	N. Lhasa Plutonic belt		V-IX	Tibetan lava		W.R.								0.708189				
THB	K9001			VII	Tibetan lava		W.R.												
THB	K9041			VII	Tibetan lava		W.R.												
THB	COUL311	S. Tibet Lhassa Gang		XI	Tibetan lava	Gangdese belt	W.R.								0.70797				
THB	COUL326	S. Tibet Lhassa Gang		XI	Tibetan lava	Gangdese belt	W.R.								0.7059				
THB	COUL328	S. Tibet Lhassa Gang		XI	Tibetan lava	Gangdese belt	W.R.								0.70641				
THB	COUL338	S. Tibet Lhassa Gang		XI	Tibetan lava	Gangdese belt	W.R.								0.70493				
THB	COUL339	S. Tibet Lhassa Gang		XI	Tibetan lava	Gangdese belt	W.R.								0.7048				
THB	K89G159	S. Tibet Karakorum		X	Tibetan lava		W.R.								0.71481				
THB	K89G162	S. Tibet Karakorum		X	Tibetan lava		W.R.								0.71552				
THB	K89G163	S. Tibet Karakorum		X	Tibetan lava		W.R.												

Table SII-2 (…/…)

Ech.#	Region	River	Locality	Formation	Category	Type	Rock type	North	East	Date	Rb Sil	Sr Sil	87Rb/86Sr	87Sr/86Sr S	2s.d.	Sm Sil	Nd Sil	147Sm/144Nd
THB ET103A	F.E. Transhimalaya		Along Parlung	Azhagong batholith	E. Transhimala	W.R.	Deformed granite				770	145	3.39	0.717494		5.54	33.4	0.1
THB ET104B	F.E. Transhimalaya		Along Parlung	Azhagong batholith	E. Transhimala	W.R.	Granite				176	105	4.86	0.716762		2.53		0.109
THB ET105A	F.E. Transhimalaya		Along Parlung	Azhagong batholith	E. Transhimala	W.R.	Granite				161	163	2.86	0.715423		2.9		0.114
THB ET105B	F.E. Transhimalaya		Along Parlung	Azhagong batholith	E. Transhimala	W.R.	Granite				240	94.2	7.38	0.714782		4.4	21.9	0.121
THB ET107A	F.E. Transhimalaya		Along Parlung	Azhagong batholith	E. Transhimala	W.R.	Granite				330	63.9	14.9	0.741119		10.1	52.5	0.116
THB ET117A	F.E. Transhimalaya		Along Parlung	Azhagong batholith	E. Transhimala	W.R.	Granite				177	229	2.24	0.713866		4.2	2.2	0.12
THB ET120A	F.E. Transhimalaya		Along Parlung	Azhagong batholith	E. Transhimala	W.R.	Granite				204	230	2.57	0.706863		2.57	10.95	0.809
THB ET122A	F.E. Transhimalaya		Along Parlung	Azhagong batholith	E. Transhimala	W.R.	Granodiorite				91.8	723	0.367	0.711866		0.71	31.9	0.125
THB ET125A	F.E. Transhimalaya		Along Parlung	Azhagong batholith	E. Transhimala	W.R.	Deformed granite				181	195	2.69	0.722641		6.92	37.3	0.112
THB ET105G	F.E. Transhimalaya		Along Parlung	Azhagong enclaves	E. Transhimala	W.R.	Enclave				58.8	220	0.774	0.706562		4.83	20.9	0.14
THB ET119A	F.E. Transhimalaya		Along Parlung	Azhagong enclaves		W.R.	Enclave				139	694	0.58	0.706447				
THB ET120C	F.E. Transhimalaya		Along Parlung	Azhagong enclaves	E. Transhimala	W.R.	Enclave				55.7	546	0.295	0.706237		5.71	27.1	0.127
THB ET120D	F.E. Transhimalaya		Along Parlung	Azhagong enclaves	E. Transhimala	W.R.	Enclave				31.1	425	0.212	0.706173		8.27	33.8	0.148
THB ET120E	F.E. Transhimalaya		Along Parlung	Azhagong enclaves	E. Transhimala	W.R.	Enclave				50.2	273	0.532	0.706092		4.11	17.1	0.145
THB ET106A2	F.E. Transhimalaya		NE. Of Parlung	Demulha batholith	High alkali E. Tı	W.R.	Granite				491	6.46	120	0.977088		8.22	25.1	0.198
THB ET219B2	F.E. Transhimalaya		NE. Of Parlung	Demulha batholith	High alkali E. Tı	W.R.	Granite				644	8.9	210	0.974909		10.6	36.6	0.175
THB ET220B	F.E. Transhimalaya		NE. Of Parlung	Demulha batholith	High alkali E. Tı	W.R.	Granite				713	11.5	180	0.949798		11.8	49.8	0.143
THB ET221B	F.E. Transhimalaya		NE. Of Parlung	Demulha batholith	High alkali E. Tı	W.R.	Granite				675	9.57	204	0.955354		12.6	52.3	0.146
THB ET222B	F.E. Transhimalaya		NE. Of Parlung	Demulha batholith	High alkali E. Tı	W.R.	Granite				658	9.15	208	0.960528		13.5	54.7	0.149
THB ET113A	F.E. Transhimalaya		S. of Parlung	Chayu batholith	E. Transhimala	W.R.	Granite				226	214	3.06	0.716425		9.38	46.1	0.123
THB ET115F1	F.E. Transhimalaya		S. of Parlung	Chayu batholith	E. Transhimala	W.R.	Granite				396	69.7	16.4	0.749173		7.05	41.3	0.103
THB ET116B	F.E. Transhimalaya		S. of Parlung	Chayu batholith	E. Transhimala	W.R.	Granite				345	81.5	12.2	0.750538		5.04	22.2	0.137
THB ET203B	F.E. Transhimalaya		S. of Parlung	Chayu batholith	E. Transhimala	W.R.	Granite				207	221	2.71	0.707888		5.8	27	0.13
THB ET203D	F.E. Transhimalaya		S. of Parlung	Chayu batholith	E. Transhimala	W.R.	Granite				221	156	4.1	0.707959		7.47	35.8	0.126
THB 73–73	F.E. Transhimalaya		S. of Parlung	Chayu batholith	E. Transhimala	W.R.	Granite				385	129	8.68	0.760712		5.61	23.7	0.143
THB RAW11	F.E. Transhimalaya		Center of Parlung	Ranwu volcanic rocks	E. Transhimala	W.R.	Andesite				89.4	185	1.4	0.708774		6.41	30.7	0.126
THB RAW12	F.E. Transhimalaya		Center of Parlung	Ranwu volcanic rocks	E. Transhimala	W.R.	Basaltic_andesite				96.8	146	1.92	0.709886		6.59	30.9	0.129
THB RAW13	F.E. Transhimalaya		Center of Parlung	Ranwu volcanic rocks	E. Transhimala	W.R.	Andesite				124	108	3.31	0.712819		8.61	41.3	0.126
THB RAW15	F.E. Transhimalaya		Center of Parlung	Ranwu volcanic rocks	E. Transhimala	W.R.	Basaltic_andesite				30.7	319	0.278	0.706806		6.19	29.1	0.128
THB RAW17	F.E. Transhimalaya		Center of Parlung	Ranwu volcanic rocks	E. Transhimala	W.R.	Dacite				157	64.3	7.08	0.717157		4.46	22.4	0.12
THB RAW20	F.E. Transhimalaya		Center of Parlung	Ranwu volcanic rocks	E. Transhimala	W.R.	Basaltic_andesite				56.6	279	0.588	0.707451		6.76	31.5	0.13
THB RAW22	F.E. Transhimalaya		Center of Parlung	Ranwu volcanic rocks	E. Transhimala	W.R.	Basaltic_andesite				134	265	1.46	0.707820		10.3	48.7	0.127
THB RAW24	F.E. Transhimalaya		Center of Parlung	Ranwu volcanic rocks	E. Transhimala	W.R.	Basaltic_andesite				95.6	273	1.02	0.707072		8.51	41	0.125
THB RAW25	F.E. Transhimalaya		Center of Parlung	Ranwu volcanic rocks	E. Transhimala	W.R.	Basalt				91	223	1.18	0.707405		5.67	26.6	0.129
THB RAW26	F.E. Transhimalaya		Center of Parlung	Ranwu volcanic rocks	E. Transhimala	W.R.	Basaltic_andesite				57.6	290	0.575	0.706797		5.8	27.3	0.129
THB RAW29	F.E. Transhimalaya		Center of Parlung	Ranwu volcanic rocks	E. Transhimala	W.R.	Basaltic_andesite				77.5	293	0.765	0.706974		5.84	28.1	0.126
THB RAW30	F.E. Transhimalaya		Center of Parlung	Ranwu volcanic rocks	E. Transhimala	W.R.	Basalt				69.3	243	0.827	0.707362		7.18	32.2	0.135
	Locality																	
THB T212	S.E. Tibe	S.E. of Lhasa	Langxian	Gangdese batholith	Gangdese belt	W.R.	Granite adak	29.00° N	93.31° E		90.3	622		0.705239		3.03	16.8	
THB T027	S.E. Tibe	S.E. of Lhasa	Langxian	Gangdese batholith	Gangdese belt	W.R.	Granite adak	29.00° N	93.32° E		41.3	622		0.70472		2.51	14.41	
THB T213	S.E. Tibe	S.E. of Lhasa	Langxian	Gangdese batholith	Gangdese belt	W.R.	Granite adak	29.04° N	93.34° E		45.1	688		0.704591		2.68	13.92	
THB T215	S.E. Tibe	S.E. of Lhasa	Langxian	Gangdese batholith	Gangdese belt	W.R.	Granite adak	29.10° N	93.41° E		54.5	757		0.7047		2.09	14.53	
THB T026	S.E. Tibe	S.E. of Lhasa	Langxian	Gangdese batholith	Gangdese belt	W.R.	Granite adak	29.12° N	93.44° E		53.3	626		0.704693		2.61	17.61	
THB T216A	S.E. Tibe	S.E. of Lhasa	Lilong	Gangdese batholith	Gangdese belt	W.R.	Granite adak	29.17° N	93.61° E		35.9	768.0		0.7		2.2	14.4	
THB T217	S.E. Tibe	S.E. of Lhasa	Lilong	Gangdese batholith	Gangdese belt	W.R.	Granite adak	29.14° N	93.64° E		49.9	780		0.704655		2.17	13.25	
THB T024	S.E. Tibe	S.E. of Lhasa	Lilong	Gangdese batholith	Gangdese belt	W.R.	Granite adak	29.14° N	93.75° E		40.9	738		0.704562		1.62	10.23	
THB T218B	S.E. Tibe	S.E. of Lhasa	Lilong	Gangdese batholith	Gangdese belt	W.R.	Granite adak	29.14° N	93.75° E		42.6	719		0.704581		1.63	9.44	
THB CY1-01	F.E. Transhimalaya		Zayu	NE. Gangdese	E. Transhimala	W.R.	Granite				203	144	4.0862	0.72546	1.4E-05	8.21	47.8	0.1037
CY1-02	F.E. Transhimalaya		Zayu	NE. Gangdese		W.R.	Granite				275	108				11.2	59	
CY1-02R	F.E. Transhimalaya		Zayu	NE. Gangdese		W.R.	Granite				269	109				10.2	52.1	
CY1-1	F.E. Transhimalaya		Zayu	NE. Gangdese	E. Transhimala	W.R.	Granite				248	101	7.0855	0.730375	1.2E-05	9.86	43.8	0.1361
CY2-1	F.E. Transhimalaya		Zayu	NE. Gangdese		W.R.	Granite				203	58.5				6.42	33.7	
CY3-1	F.E. Transhimalaya		Zayu	NE. Gangdese	E. Transhimala	W.R.	Granite				312	51.7	17.4673	0.744253	0.00001	10.6	55.8	0.1153
CY4-1	F.E. Transhimalaya		Zayu	NE. Gangdese	E. Transhimala	W.R.	Granite				191	77.7	7.1293	0.729346	1.4E-05	7.43	44.9	0.1001
CY6-1	F.E. Transhimalaya		Zayu	NE. Gangdese	E. Transhimala	W.R.	Granite				189	73.3	7.4785	0.730475	1.1E-05	6.43	37.6	0.1033

Linzizong successions:

B – Basalt, BA – Basaltic andesite, A – Andesite, D – Dacite, R – Rhyolite.

Table SII-2 (…/…)

Ech.#	Region	River	Locality	Formation	Category	Type	Rock type	North	East	Date	Rb Sil	Sr Sil	87Rb/86Sr	87Sr/86Sr S	2s.d.	Sm Sil	Nd Sil	147Sm/144Nd
T233C	S. Tibet	1. Dianzhong	Formation	Linzigong volcanics	Linzigong lava	W.R.	B				19.1	962	0.057	0.70485	19	9.1	44.1	0.125
T238B	S. Tibet	1. Dianzhong	Formation	Linzigong volcanics	Linzigong lava	W.R.	BA				5.2	638	0.023	0.705082	13	4.7	21.2	0.132
T239	S. Tibet	1. Dianzhong	Formation	Linzigong volcanics	Linzigong lava	W.R.	A				31.1	527	0.171	0.706282	14	4.2	20.2	0.127
T136B	S. Tibet	1. Dianzhong	Formation	Linzigong volcanics	Linzigong lava	W.R.	R				242	53.3	13.17	0.739981	12	58.8	142	0.251
T134	S. Tibet	1. Dianzhong	Formation	Linzigong volcanics	Linzigong lava	W.R.	R				206	443	1.348	0.713115	14	11.7	64.5	0.109
T136A	S. Tibet	1. Dianzhong	Formation	Linzigong volcanics	Linzigong lava	W.R.	R				275	46.5	17.11	0.737603	15	17.1	101	0.103
T234C	S. Tibet	2. Nianbo	Formation	Linzigong volcanics	Linzigong lava	W.R.	D				46.5	1120	0.12	0.705179	15	6.2	35.2	0.107
T235B	S. Tibet	2. Nianbo	Formation	Linzigong volcanics	Linzigong lava	W.R.	R				116	108	3.088	0.708966	27	7.3	39.2	0.112
T042D	S. Tibet	3. Pana For	a. Calc-alkaline suite	Linzigong volcanics	Linzigong lava	W.R.	B				29.6	487	0.176	0.703779	17	4.6	20.9	0.132
T006B2	S. Tibet	3. Pana For	a. Calc-alkaline suite	Linzigong volcanics	Linzigong lava	W.R.	B				41	473	0.251	0.707243	13	4.6	20.9	0.133
T116A	S. Tibet	3. Pana For	a. Calc-alkaline suite	Linzigong volcanics	Linzigong lava	W.R.	B				73	327	0.647	0.708556	11	7.3	32.3	0.138
T083C	S. Tibet	3. Pana For	a. Calc-alkaline suite	Linzigong volcanics	Linzigong lava	W.R.	B				85.9	294	0.846	0.705341	12	5.7	24.7	0.139
T047	S. Tibet	3. Pana For	a. Calc-alkaline suite	Linzigong volcanics	Linzigong lava	W.R.	B				120	445	0.783	0.705841	18	5.8	27.6	0.127
T006B1	S. Tibet	3. Pana For	a. Calc-alkaline suite	Linzigong volcanics	Linzigong lava	W.R.	BA				36.1	409	0.256	0.705951	16	4.1	19.9	0.124
T056B	S. Tibet	3. Pana For	a. Calc-alkaline suite	Linzigong volcanics	Linzigong lava	W.R.	BA				12	266	0.131	0.706038	11	3.6	15.7	0.139
T049B	S. Tibet	3. Pana For	a. Calc-alkaline suite	Linzigong volcanics	Linzigong lava	W.R.	BA				70.3	643	0.317	0.706418	11	4.7	25.5	0.112
T054A	S. Tibet	3. Pana For	a. Calc-alkaline suite	Linzigong volcanics	Linzigong lava	W.R.	BA				33.6	557	0.174	0.705779	14	5.5	23.8	0.139
T062B	S. Tibet	3. Pana For	a. Calc-alkaline suite	Linzigong volcanics	Linzigong lava	W.R.	A				83.8	404	0.6	0.705532	12	6.6	32.1	0.124
T063	S. Tibet	3. Pana For	a. Calc-alkaline suite	Linzigong volcanics	Linzigong lava	W.R.	A				83.1	667	0.361	0.705562	13	4.7	22.8	0.124
T055A	S. Tibet	3. Pana For	a. Calc-alkaline suite	Linzigong volcanics	Linzigong lava	W.R.	A				17.5	417	0.121	0.705156	12	4.5	21	0.131
T040A	S. Tibet	3. Pana For	a. Calc-alkaline suite	Linzigong volcanics	Linzigong lava	W.R.	D				110	453	0.704	0.70597	13	5.4	27.5	0.118
T038F	S. Tibet	3. Pana For	a. Calc-alkaline suite	Linzigong volcanics	Linzigong lava	W.R.	D				248	65.4	10.99	0.715798	22	6	31	0.117
T051C	S. Tibet	3. Pana For	a. Calc-alkaline suite	Linzigong volcanics	Linzigong lava	W.R.	R				170	178	2.754	0.70736	7	3.3	19.2	0.105
T065B	S. Tibet	3. Pana For	a. Calc-alkaline suite	Linzigong volcanics	Linzigong lava	W.R.	R				183	131	4.046	0.707747	18	5.5	30.7	0.109
T036D	S. Tibet	3. Pana For	b. Low-K suite	Linzigong volcanics	Linzigong lava	W.R.	B				19.7	746	0.076	0.704302	15	3	12.6	0.147
T041H	S. Tibet	3. Pana For	b. Low-K suite	Linzigong volcanics	Linzigong lava	W.R.	B				10.8	926	0.034	0.704054	14	3.2	13	0.146
T041F	S. Tibet	3. Pana For	b. Low-K suite	Linzigong volcanics	Linzigong lava	W.R.	BA				21.3	703	0.088	0.704031	14	2.9	12.1	0.142
T034A	S. Tibet	3. Pana For	b. Low-K suite	Linzigong volcanics	Linzigong lava	W.R.	A				10.1	280	0.104	0.703814	10	2.9	11.7	0.151
ST055C	S. Tibet	3. Pana For	c. Shoshonitic suite	Linzigong volcanics	Linzigong lava	W.R.	BA				160	1066	0.434	0.70648	13	8.2	41.3	0.12
ST061A	S. Tibet	3. Pana For	c. Shoshonitic suite	Linzigong volcanics	Linzigong lava	W.R.	BA				392	393	2.886	0.708851	8	10.3	46.7	0.133
ST057A	S. Tibet	3. Pana For	c. Shoshonitic suite	Linzigong volcanics	Linzigong lava	W.R.	A				252	805	0.905	0.708656	19	8.6	46.6	0.112
ST059A	S. Tibet	3. Pana For	c. Shoshonitic suite	Linzigong volcanics	Linzigong lava	W.R.	D				120	130	4.907	0.708236	12	8	43.7	0.11
ST053	S. Tibet	3. Pana For	c. Shoshonitic suite	Linzigong volcanics	Linzigong lava	W.R.	D				321	641	1.448	0.708107	16	9.1	52.8	0.104
ST062	S. Tibet	3. Pana For	c. Shoshonitic suite	Linzigong volcanics	Linzigong lava	W.R.	D				454	350	3.758	0.709576	18	11.4	68.3	0.101
ST060C	S. Tibet	3. Pana For	c. Shoshonitic suite	Linzigong volcanics	Linzigong lava	W.R.	D				426	378	3.259	0.70887	17	10.7	62.1	0.104
ST055A	S. Tibet	3. Pana For	c. Shoshonitic suite	Linzigong volcanics	Linzigong lava	W.R.	R				416	160	7.523	0.717727	15	9.8	57.9	0.102
T155	S. Tibet	3. Pana For	d. High-REE suite	Linzigong volcanics	Linzigong lava	W.R.	R				203	393	1.499	0.706855	12	7.9	43.3	0.11
T082B	S. Tibet	3. Pana For	d. High-REE suite	Linzigong volcanics	Linzigong lava	W.R.	R				115	153	2.181	0.707916	14	3.2	20.4	0.094
T103	S. Tibet	3. Pana For	d. High-REE suite	Lizigong volcanics		W.R.	R				307	61.8	14.39	X	X	10.1	55.6	0.109
ST058	S. Tibet	3. Pana For	e. Evolved suite	Linzigong volcanics	Linzigong lava	W.R.	D				325	578	1.628	0.754776	36	8.6	49.8	0.104
T065A	S. Tibet	3. Pana For	e. Evolved suite	Linzigong volcanics	Linzigong lava	W.R.	R				131	108	3.5	0.760054	11	5.5	29.1	0.113
T072A	S. Tibet	Northern Province:		Linzigong volcanics	Linzigong lava	W.R.	B				120	330	1.052	0.713173	9	7	38.8	0.109
T129A	S. Tibet	Northern Province:		Linzigong volcanics	Linzigong lava	W.R.	BA				107	276	1.124	0.727732	8	4	17.5	0.139
T072E	S. Tibet	Northern Province:		Linzigong volcanics	Linzigong lava	W.R.	A				50.7	371	0.396	0.712857	13	5.5	28.5	0.116
T131A	S. Tibet	Northern Province:		Linzigong volcanics	Linzigong lava	W.R.	R				15	143	0.303	0.713131	60	6.4	34	0.113
T169A	S. Tibet	Northern Province:		Lizigong volcanics		W.R.	R				431	33.7	37.06	X	X	8.4	43.7	0.116
T079B	S. Tibet	Sangri Group:		Linzigong volcanics	Linzigong lava	W.R.	B				139	620	0.649	0.705626	13	5.2	22.2	0.142
ET021B	S. Tibet	Sangri Group:		Linzigong volcanics	Linzigong lava	W.R.	B				10.3	341	0.087	0.704563	13	2.4	9.3	0.155
ST119A	S. Tibet	Sangri Group:		Linzigong volcanics	Linzigong lava	W.R.	B				2.2	520	0.012	0.703481	6	4.7	20.7	0.138
ST122	S. Tibet	Sangri Group:		Linzigong volcanics	Linzigong lava	W.R.	B				1.1	482	0.007	0.703776	7	5.2	25.6	0.124
ST101B	S. Tibet	Sangri Group:		Linzigong volcanics	Linzigong lava	W.R.	A				24.9	607	0.119	0.704472	11	4	21.7	0.113
ST102B	S. Tibet	Sangri Group:		Linzigong volcanics	Linzigong lava	W.R.	A				50.3	367	0.396	0.704574	15	3.1	14.3	0.133
ET021C	S. Tibet	Sangri Group:		Linzigong volcanics	Linzigong lava	W.R.	A				65.7	333	0.572	0.704639	15	3.8	17	0.135
ET022A	S. Tibet	Sangri Group:		Linzigong volcanics	Linzigong lava	W.R.	R				75.9	195	1.125	0.707115	15	2.2	12	0.109
ET024	S. Tibet	Sangri Group:		Linzigong volcanics	Linzigong lava	W.R.	R				92.2	225	1.188	0.707376	13	2.2	13.1	0.104
THB T358	S.E. Tibe	TGP	W. of Lhasa	PG granodiorite, NM granite and their associated porph	Gangdese belt	W.R.	TGP = Tinggongporphyry; PG = Pagu granodio				145	673	0.4	0.7057	3	3.88	24.6	0.098
THB T379	S.E. Tibe	PG	W. of Lhasa	PG granodiorite, NM granite and their associated porph	Gangdese belt	W.R.					153	766	0.581	0.70633	5	4.37	27	0.098
THB T380	S.E. Tibe	PG	W. of Lhasa	PG granodiorite, NM granite and their associated porph	Gangdese belt	W.R.					158	814	0.564	0.70612	3	3.58	21	0.103
THB T381	S.E. Tibe	PG	W. of Lhasa	PG granodiorite, NM granite and their associated porph	Gangdese belt	W.R.					162	724	0.651	0.70611	3	4	23.8	0.102
THB T399	S.E. Tibe	NMP	W. of Lhasa	PG granodiorite, NM granite and their associated porph	Gangdese belt	W.R.					204	713	0.829	0.70693	3	4.48	26.3	0.103
THB T400	S.E. Tibe	NMP	W. of Lhasa	PG granodiorite, NM granite and their associated porph	Gangdese belt	W.R.					187	683	0.795	0.70699	3	5.11	30	0.103
THB T401	S.E. Tibe	NM	W. of Lhasa	PG granodiorite, NM granite and their associated porph	Gangdese belt	W.R.					187.0	583.0	0.93	0.70835	3	4.0	24.5	0.098
THB T403	S.E. Tibe	NM	W. of Lhasa	PG granodiorite, NM granite and their associated porph	Gangdese belt	W.R.					372	628	1.716	0.70677	3	4.55	25.7	0.107

Table SII-2 (…/…)

Ech.#	Region	River	Locality	Formation	Category	Type	Rock type	North	East	Date	Rb SiI	Sr SiI	87Rb/86Sr	87Sr/86Sr S	2s.d.	Sm SiI	Nd SiI	147Sm/144Nd
THB T404	S.E. Tibe	NM	W. of Lhasa	PG granodiorite, NM granite and their associated porph	Gangdese belt	W.R.					270	582	1.343	0.70784	3	4.8	29	0.1
THB T604	S.E. Tibe	MG	Eastern syntaxis	Mafic granulite from eastern Himalayan syntaxis	Gangdese belt	W.R.							0.236	0.70734	7			0.187
THB T605	S.E. Tibe	MG	Eastern syntaxis	Mafic granulite from eastern Himalayan syntaxis	Gangdese belt	W.R.							0.29	0.70587	6			0.184
THB T606	S.E. Tibe	MG	Eastern syntaxis	Mafic granulite from eastern Himalayan syntaxis	Gangdese belt	W.R.							0.202	0.7078	5			0.185
THB T607	S.E. Tibe	MG	Eastern syntaxis	Mafic granulite from eastern Himalayan syntaxis	Gangdese belt	W.R.							1.497	0.71114	4			0.184
THB T608	S.E. Tibe	MG	Eastern syntaxis	Mafic granulite from eastern Himalayan syntaxis	Gangdese belt	W.R.							0.276	0.70913	4			0.176
THB 09NDS-11	S.E. Tibet		Lhasa	Nuri intrusive rocks	Gangdese belt	W.R.	Granite porphyry				57.1	535	0.3093	0.706387		2.53	15.8	0.0971
THB 09NDZ-12	S.E. Tibet		Lhasa	Nuri intrusive rocks	Gangdese belt	W.R.	Granite porphyry				33.9	778	0.1261	0.7063		2.82	17.6	0.0973
THB 09NDZ-15	S.E. Tibet		Lhasa	Nuri intrusive rocks	Gangdese belt	W.R.	Granodiorite				282	433	1.885	0.707606		4.41	31.2	0.0856
THB 09NDZ-19	S.E. Tibet		Lhasa	Nuri intrusive rocks	Gangdese belt	W.R.	Felsophyre				82	282	0.8424	0.707072		2.88	19.3	0.0902
THB 09NDS-17	S.E. Tibet		Lhasa	Nuri intrusive rocks	Gangdese belt	W.R.	Quartz diorite porphyrite				134	715	0.544	0.705164		4.64	27.2	0.1033
THB 08ND-4	S.E. Tibet		Lhasa	Nuri intrusive rocks	Gangdese belt	W.R.	Quartz diorite (southern)				89.2	702	0.3678	0.704553		3.05	17.2	0.1073
THB 09nds-2	S.E. Tibet		Lhasa	Nuri intrusive rocks	Gangdese belt	W.R.	Monzogranite				156	310	1.451	0.705445		4.78	25.8	0.1122
THB 08ND-15	S.E. Tibet		Lhasa	Nuri intrusive rocks		W.R.	Quartz diorite (northern)											
TSS SXI (12)-2	S.E. Tibet		S. Lhasa, S. Yarlung Tsangpo	Sangxiu Fm	TSS volcanics	W.R.	Felsic volc.				110.7	126.9	2.53	0.726431	14	12.71	68.15	0.1128
TSS SXI (9)-1	S.E. Tibet		S. Lhasa, S. Yarlung Tsangpo	Sangxiu Fm	TSS volcanics	W.R.	Felsic volc.				128.9	129.7	2.883	0.729021	13	13.25	70.27	0.114
TSS SXI (8)-3	S.E. Tibet		S. Lhasa, S. Yarlung Tsangpo	Sangxiu Fm	TSS volcanics	W.R.	Felsic volc.				121.9	73.78	4.793	0.731036	13	13.64	72.77	0.1134
TSS SXI (1)-2	S.E. Tibet		S. Lhasa, S. Yarlung Tsangpo	Sangxiu Fm	TSS volcanics	W.R.	massive basalt				8.49	387.6	0.0634	0.710024	25	9.46	42.36	0.1351
TSS SXI (1)-1	S.E. Tibet		S. Lhasa, S. Yarlung Tsangpo	Sangxiu Fm	TSS volcanics	W.R.	massive basalt				1.07	753.4	0.0041	0.709135	7	9.28	41.42	0.1355
TSS SXII (1)-1	S.E. Tibet		S. Lhasa, S. Yarlung Tsangpo	Sangxiu Fm	TSS volcanics	W.R.	massive basalt				11.1	196.1	0.1639	0.70768	13	10.27	45.45	0.1366
TSS SXII (9)-3	S.E. Tibet		S. Lhasa, S. Yarlung Tsangpo	Sangxiu Fm	TSS volcanics	W.R.	pillow basalt				1.63	273.7	0.0173	0.707788	17	9.94	42.64	0.141
THB SXI(2)-1	S.E. Tibet		S. Lhasa, S. Yarlung Tsangpo	Sangxiu Fm		W.R.	massive basalt									10.01	45.97	0.1317
THB SXI(1)-1-(2	S.E. Tibet		S. Lhasa, S. Yarlung Tsangpo	Sangxiu Fm		W.R.	massive basalt									9.81	43.8	0.1354
THB Pyroxene i	S.E. Tibet		S. Lhasa, S. Yarlung Tsangpo	Sangxiu Fm		W.R.	massive basalt									9.96	44.17	0.1363
THB YZS-1	S.E. Tibet		S.W. Lhasa, Xigaze	Yarlung Tsanpo suture	Yarlung Tsangb	W.R.	ophiolites				5.53	118.9	0.1344	0.70418		1.515	4.005	0.2287
THB YZS-2	S.E. Tibet		S.W. Lhasa, Xigaze	Yarlung Tsanpo suture	Yarlung Tsangb	W.R.	ophiolites				4.14	105.8	0.1132	0.70428		2.274	6.246	0.22
THB YZS-3	S.E. Tibet		S.W. Lhasa, Xigaze	Yarlung Tsanpo suture	Yarlung Tsangb	W.R.	ophiolites				11.2	130.9	0.2485	0.70446		1.603	4.224	0.2294
THB YZS-6	S.E. Tibet		S.W. Lhasa, Xigaze	Yarlung Tsanpo suture	Yarlung Tsangb	W.R.	ophiolites				4.07	130.3	0.0905	0.7041		3.173	9.214	0.2082
THB YZS-7	S.E. Tibet		S.W. Lhasa, Xigaze	Yarlung Tsanpo suture	Yarlung Tsangb	W.R.	ophiolites				6.56	109.5	0.1734	0.70421		2.793	7.922	0.2131
THB YZS-11	S.E. Tibet		S.W. Lhasa, Xigaze	Yarlung Tsanpo suture	Yarlung Tsangb	W.R.	ophiolites				7.66	116.3	0.1904	0.70425		2.846	8.16	0.2148
TSS 0319-02	S.E. Tibet		S.E. Lhasa	Yardoi gneiss dome	TSS	W.R.	Gt-Bi-gneiss				229.3	39.11	17.393	0.96378	14	4.67	22.45	0.1259
TSS 0319-03	S.E. Tibet		S.E. Lhasa	Yardoi gneiss dome	TSS	W.R.	Gt-Bi-gneiss				280.3	40.19	20.534	0.884871	15	4.91	25.37	0.1171
TSS 0319-07	S.E. Tibet		S.E. Lhasa	Yardoi gneiss dome	TSS	W.R.	Gt-Bi-gneiss				383.4	24.97	45.183	0.880607	14	2.79	12.76	0.1322
TSS 0321-021	S.E. Tibet		S.E. Lhasa	Yardoi gneiss dome	TSS	W.R.	Gt-Mus gneiss				183.3	6.91	78.634	0.961299	15	6.1	30.51	0.1209
TSS 0321-12	S.E. Tibet		S.E. Lhasa	Yardoi gneiss dome	TSS	W.R.	Gt-Bi-gneiss				156.7	7.11	65.249	0.93649	14	3.48	16.93	0.1243
TSS 0321-011	S.E. Tibet		S.E. Lhasa	Yardoi gneiss dome	TSS	W.R.	Gt-graphite gneiss				182.5	86.8	6.091	0.722345	16	6.95	36.75	0.1144
TSS 0321-08	S.E. Tibet		S.E. Lhasa	Yardoi gneiss dome	TSS	W.R.	Gt amphibolite				1.89	236.2	0.0232	0.712084	16	9.6	36.52	0.1589
TSS 0321-09	S.E. Tibet		S.E. Lhasa	Yardoi gneiss dome	TSS	W.R.	Gt amphibolite				2.41	246.2	0.0283	0.712669	14	9.66	36.65	0.1593
TSS 0321-031	S.E. Tibet		S.E. Lhasa	Yardoi gneiss dome	TSS granite	W.R.	leucogranite				64.24	155.5	1.198	0.718102	14	1.24	5.08	0.1481
TSS 0321-041	S.E. Tibet		S.E. Lhasa	Yardoi gneiss dome	TSS granite	W.R.	leucogranite				73.93	177.3	1.208	0.71916	17	1.26	4.45	0.1709
TSS 0323-02	S.E. Tibet		S.E. Lhasa	Yardoi gneiss dome	TSS granite	W.R.	leucogranite				244.2	288.7	2.45	0.717262	14	0.99	3.17	0.1897
TSS 0322-01	S.E. Tibet		S.E. Lhasa	Yardoi gneiss dome	TSS granite	W.R.	leucogranite				278	105	7.672	0.719373	11	3.64	10.5	0.2097
TSS 0322-04	S.E. Tibet		S.E. Lhasa	Yardoi gneiss dome	TSS granite	W.R.	leucogranite				273.2	88.85	8.907	0.719471	19	1.77	5.29	0.2027
TSS 0323-01	S.E. Tibet		S.E. Lhasa	Yardoi gneiss dome	TSS granite	W.R.	leucogranite				174.7	163.4	3.095	0.714873	13	1.85	6.45	0.1733
TSS 0323-03	S.E. Tibet		S.E. Lhasa	Yardoi gneiss dome	TSS granite	W.R.	leucogranite				178.3	157.1	3.286	0.715995	15	1.31	4.49	0.1763
TSS 0323-04	S.E. Tibet		S.E. Lhasa	Yardoi gneiss dome	TSS granite	W.R.	leucogranite				193.9	140.5	3.998	0.71628	18	1.32	4.29	0.186
TSS 0321-07	S.E. Tibet		S.E. Lhasa	Yardoi gneiss dome	TSS granite	W.R.	leucogranite				55.01	213.3	0.747	0.719715	20	0.85	3.54	0.1452
TSS 0319-06	S.E. Tibet		S.E. Lhasa	Yardoi gneiss dome	TSS granite	W.R.	leucogranite				182.1	300.4	1.755	0.716362	14	3.61	18.17	0.1202

Table SII-2 (…/…)

Ech.#	Region	River	Locality	Formation	Category	Type	Rock type	North	East	Date	Rb Sil	Sr Sil	87Rb/86Sr	87Sr/86Sr S	2s.d.	Sm Sil	Nd Sil	147Sm/144Nd
THB CHP1	S.C. Tibe	W. Lhasa (in	Tangra Yumco-Xuruco graben	Chazi felsic ultrapotassic lavas	K-rich Transhim	W.R.					893	704	3.781	0.720692	12	22.8	128	0.01104
THB CHP3	S.C. Tibe	W. Lhasa (in	Tangra Yumco-Xuruco graben	Chazi felsic ultrapotassic lavas	K-rich Transhim	W.R.					720	685	3.133	0.720806	11	21.1	124	0.01055
THB CHP4	S.C. Tibe	W. Lhasa (in	Tangra Yumco-Xuruco graben	Chazi felsic ultrapotassic lavas	K-rich Transhim	W.R.					751	731	3.063	0.720856	13	22.6	129	0.01086
THB CHP6	S.C. Tibe	W. Lhasa (in	Tangra Yumco-Xuruco graben	Chazi felsic ultrapotassic lavas	K-rich Transhim	W.R.					721	688	3.124	0.720617	10	22.7	131	0.01074
THB CHP7	S.C. Tibe	W. Lhasa (in	Tangra Yumco-Xuruco graben	Chazi felsic ultrapotassic lavas	K-rich Transhim	W.R.					709	607	3.482	0.720817	12	19.3	112	0.01068
THB CHP8	S.C. Tibe	W. Lhasa (in	Tangra Yumco-Xuruco graben	Chazi felsic ultrapotassic lavas	K-rich Transhim	W.R.					751	682	3.283	0.72077	13	21.9	128	0.01061
THB CHP10	S.C. Tibe	W. Lhasa (in	Tangra Yumco-Xuruco graben	Chazi felsic ultrapotassic lavas	K-rich Transhim	W.R.					713	676	3.144	0.72072	13	21.3	124	0.01065
THB CHP12	S.C. Tibe	W. Lhasa (in	Tangra Yumco-Xuruco graben	Chazi felsic ultrapotassic lavas	K-rich Transhim	W.R.					685	692	2.951	0.720608	14	20.6	120	0.01064
THB CHP13	S.C. Tibe	W. Lhasa (in	Tangra Yumco-Xuruco graben	Chazi felsic ultrapotassic lavas	K-rich Transhim	W.R.					772	701	3.283	0.720679	12	23.1	131	0.01093
THB CHP15	S.C. Tibe	W. Lhasa (in	Tangra Yumco-Xuruco graben	Chazi felsic ultrapotassic lavas	K-rich Transhim	W.R.					563	513	3.272	0.727212	13	21.1	117	0.01118
THB CHP17	S.C. Tibe	W. Lhasa (in	Tangra Yumco-Xuruco graben	Chazi felsic ultrapotassic lavas	K-rich Transhim	W.R.					568	537	3.153	0.728115	13	20.9	116	0.01117
THB CHP18	S.C. Tibe	W. Lhasa (in	Tangra Yumco-Xuruco graben	Chazi felsic ultrapotassic lavas	K-rich Transhim	W.R.					562	561	2.986	0.728712	12	22.3	122	0.01133
THB SRD08-05	S.E. Tibe	E. Lhasa	N. Gangdese	Sharang granitoids	Gangdese belt	W.R.	Quartz monzonite				151.01	567.28	0.7704	0.706185	14	1.89	36.9	0.0311
THB SRD08-10	S.E. Tibe	E. Lhasa	N. Gangdese	Sharang granitoids	Gangdese belt	W.R.	Quartz diorite				76.99	756.96	0.2943	0.70613	13	5.9	28.9	0.1233
THB SRD-6	S.E. Tibe	E. Lhasa	N. Gangdese	Sharang granitoids	Gangdese belt	W.R.	Granite				204.03	224.5	2.6308	0.709077	14	6.3	35.5	0.1073
THB SRZK0905	S.E. Tibe	E. Lhasa	N. Gangdese	Sharang granitoids	Gangdese belt	W.R.	Prophyritic granite				283.91	118.81	6.9192	0.71132	12	5.37	31.8	0.102
THB SRZK0205	S.E. Tibe	E. Lhasa	N. Gangdese	Sharang granitoids	Gangdese belt	W.R.	Granite porphyry				214.72	395.96	1.5696	0.707406	11	4.03	22.8	0.1071
THB SRZK0107	S.E. Tibe	E. Lhasa	N. Gangdese	Sharang granitoids	Gangdese belt	W.R.	Granite porphyry				185.1	235.1	2.2788	0.708328	11	3.62	20.4	0.1076
THB SRZK0107	S.E. Tibe	E. Lhasa	N. Gangdese	Sharang granitoids	Gangdese belt	W.R.	Granite porphyry				188.6	284.9	1.9167	0.707964	10	4.97	28.5	0.1054
THB SRZK003-	S.E. Tibe	E. Lhasa	N. Gangdese	Sharang granitoids	Gangdese belt	W.R.	Granite porphyry				190.3	232.3	2.3707	0.708573	12	5.12	28.7	0.1082
THB SRZK0704	S.E. Tibe	E. Lhasa	N. Gangdese	Sharang granitoids	Gangdese belt	W.R.	Dacite porphyry				255.1	153.74	4.8057	0.71363	14	9.83	59.4	0.1
THB SRZK0905	S.E. Tibe	E. Lhasa	N. Gangdese	Sharang granitoids	Gangdese belt	W.R.	Granodiorite porphyry				330.8	200.5	4.7761	0.708128	11	3.02	19.7	0.0929
THB SRZK0304	S.E. Tibe	E. Lhasa	N. Gangdese	Sharang granitoids	Gangdese belt	W.R.	Granodiorite porphyry				487.55	214.64	6.5749	0.70785	11	3.78	23.7	0.0967
THB SRD08-01	S.E. Tibe	E. Lhasa	N. Gangdese	Sharang granitoids	Gangdese belt	W.R.	Lamporphyre				274.2	800.9	0.9914	0.712778	10	10.44	62.4	0.1013
THB SRD08-02	S.E. Tibe	E. Lhasa	N. Gangdese	Sharang granitoids	Gangdese belt	W.R.	Lamporphyre				247.13	731.15	0.9788	0.712655	14	8.84	56.5	0.0946
THB TI/10	S. Tibet	W. Lhasa		Mibale ultrapotassic lava	K-rich Transhim	W.R.					790	1421		0.719154	12	31.2	218.7	
THB TI/11	S. Tibet	W. Lhasa		Mibale ultrapotassic lava	K-rich Transhim	W.R.					550	1564		0.718477	12	31	217.1	
THB TI/18	S. Tibet	W. Lhasa		Mibale ultrapotassic lava	K-rich Transhim	W.R.					576	1196		0.719612	17	32	196.1	
THB TI/13	S. Tibet	W. Lhasa		Mibale ultrapotassic lava	K-rich Transhim	W.R.					391.0	1633.0		0.716764	11	24.6	168.6	
THB TI/03	S. Tibet	W. Lhasa		Mibale ultrapotassic lava	K-rich Transhim	W.R.					611	1260		0.719945	18	28.2	182.8	
THB TI/08	S. Tibet	W. Lhasa		Mibale ultrapotassic lava	K-rich Transhim	W.R.					598	1207		0.719518	9	30.8	189.6	
THB TI/17	S. Tibet	W. Lhasa		Mibale ultrapotassic lava	K-rich Transhim	W.R.					939	1004		0.72658	12	42.7	241.3	
THB TI/06	S. Tibet	W. Lhasa		Mibale ultrapotassic lava	K-rich Transhim	W.R.					441	1371		0.719806	20	22.9	185.6	
THB TI/59	S. Tibet	W. Lhasa		Mibale ultrapotassic lava	K-rich Transhim	W.R.					442	930		0.71824	19	21.8	165.4	
THB CHZ-1	S. Tibet	W. Lhasa		Chazi ultrapotassic lava	K-rich Transhim	W.R.					880	810		0.736476	12	46.4	244	
THB CHZ-2	S. Tibet	W. Lhasa		Chazi ultrapotassic lava		W.R.					702	798				45.7	247	
THB CHZ-3	S. Tibet	W. Lhasa		Chazi ultrapotassic lava		W.R.					784	704				42.9	231	
THB CHZ-4	S. Tibet	W. Lhasa		Chazi ultrapotassic lava		W.R.					712	660				36.8	199	
THB CHZ-5	S. Tibet	W. Lhasa		Chazi ultrapotassic lava	K-rich Transhim	W.R.					781.0	739.0		0.730948	12	40.6	215.0	
THB CHZ-6	S. Tibet	W. Lhasa		Chazi ultrapotassic lava		W.R.					785	688				40.4	221	
THB CHZ-7	S. Tibet	W. Lhasa		Chazi ultrapotassic lava		W.R.					871	844				45	236	
THB CHZ-8	S. Tibet	W. Lhasa		Chazi ultrapotassic lava	K-rich Transhim	W.R.					564	1072		0.731065	12	43.7	234	
THB CHZ-9	S. Tibet	W. Lhasa		Chazi ultrapotassic lava		W.R.					538	911				47.5	247	
THB CHZ-10	S. Tibet	W. Lhasa		Chazi ultrapotassic lava	K-rich Transhim	W.R.					529	861		0.736455	13	45.7	243	
THB CHZ-11	S. Tibet	W. Lhasa		Chazi ultrapotassic lava		W.R.					811	855				45.1	237	
THB CHZ-12	S. Tibet	W. Lhasa		Chazi ultrapotassic lava	K-rich Transhim	W.R.					795	790		0.736385	12	48	254	
																	Nd weird …	
THB 99T53	S. Tibet	W. Lhasa	Tangra Yumco graben	Wenbu potassic lava	K-rich Transhim	W.R.					380	1442	0.7628	0.72216	2	27.5	206.6	0.08056
THB 99T56	S. Tibet	W. Lhasa	Tangra Yumco graben	Wenbu potassic lava	K-rich Transhim	W.R.					504	1155	1.261	0.72218	1	33.9	253.5	0.08091
THB 99T57	S. Tibet	W. Lhasa	Tangra Yumco graben	Wenbu potassic lava	K-rich Transhim	W.R.					333	1847	1.282	0.72438	2	36.4	253.5	0.07813
THB 99T60	S. Tibet	W. Lhasa	Tangra Yumco graben	Wenbu potassic lava	K-rich Transhim	W.R.					497	1122	0.521	0.71845	3	27.1	210	0.08677
THB 99T62	S. Tibet	W. Lhasa	Tangra Yumco graben	Wenbu potassic lava	K-rich Transhim	W.R.					470	1513	0.8982	0.72052	2	28.7	208.9	0.08294
THB 99T132	S. Tibet	W. Lhasa	Xurruco graben	Chazi potassic lava	K-rich Transhim	W.R.					799	1593	1.451	0.72036	2	31.8	159.9	0.1201
THB 99T134	S. Tibet	W. Lhasa	Xurruco graben	Chazi potassic lava	K-rich Transhim	W.R.					266	593	1.296	0.71843	2	12.9	79.1	0.09859
THB 99T145	S. Tibet	W. Lhasa	Xurruco graben	Chazi potassic lava	K-rich Transhim	W.R.					600	794	2.183	0.7182	2	17.4	98.2	0.107
THB 99T152	S. Tibet	W. Lhasa	Xurruco graben	Chazi potassic lava	K-rich Transhim	W.R.					834	872	2.765	0.71983	1	22.2	120.1	0.1116
THB 99T154	S. Tibet	W. Lhasa	Xurruco graben	Chazi potassic lava	K-rich Transhim	W.R.					317	1260	0.7267	0.71666	1	23.3	129.1	0.1092

Table SII-2 (…/…)

Ech.#	Region	River	Locality	Formation	Category	Type	Rock type	North	East	Date	Rb Sil	Sr Sil	87Rb/86Sr	87Sr/86Sr S	2s.d.	Sm Sil	Nd Sil	147Sm/144Nd
THB JPT3	S. Tibet	W. Lhasa		Namling potassic lava	K-rich Transhim	W.R.	andesite				116.2	802.9	0.42	0.706694	25c	5.3	31.1	0.1
THB JPT5.2	S. Tibet	W. Lhasa		Namling potassic lava	K-rich Transhim	W.R.	dacite				206.2	206.2	1.26	0.706945	8b	4.7	30	0.09
THB JPT8	S. Tibet	W. Lhasa		Namling potassic lava	K-rich Transhim	W.R.	rhyolite				314.6	314.6	5.75	0.711373	25c	1.6	11.4	0.08
			Lithology (PVR : potassic, UPVR : ultra potassic)															
THB DJC1302	S.C. Tibe	N. of Saga S	Adakite	Dajia Co	Linzigong lava	W.R.	trachyte	29°50.298	85°45.988'		134	880		0.707263	0.00001	4.81	27.2	
THB DJC1303	S.C. Tibe	N. of Saga S	Adakite	Dajia Co		W.R.	trachyte	29°53.828	5°44.547'		125	898				4.53	26.1	
THB DJC1304	S.C. Tibe	N. of Saga S	Adakite	Dajia Co		W.R.	trachyte	29°50.298	85°45.988'		119	873				4.68	26	
THB DJC1305	S.C. Tibe	N. of Saga S	Adakite	Dajia Co		W.R.	trachyte	29°50.298	85°45.988'		123	855				3.96	22.1	
THB DJC1306	S.C. Tibe	N. of Saga S	Adakite	Dajia Co	Linzigong lava	W.R.	trachyte	29°50.298	85°45.988'		123	988		0.70725	1.2E-05	4.62	27.2	
THB DJC1307	S.C. Tibe	N. of Saga S	Adakite	Dajia Co	Linzigong lava	W.R.	trachyte	29°50.298	85°45.988'		123	1002		0.707417	1.4E-05	5.09	28.9	
THB DJC1308	S.C. Tibe	N. of Saga S	Adakite	Dajia Co	Linzigong lava	W.R.	trachyte	29°50.298	85°45.988'		121	941		0.707391	1.4E-05	4.72	25.9	
THB DJC1309	S.C. Tibe	N. of Saga S	Adakite	Dajia Co	Linzigong lava	W.R.	trachyte	29°50.298	85°45.988'		117	990		0.707358	1.3E-05	4.32	24.5	
THB DJC1310	S.C. Tibe	N. of Saga S	Adakite	Dajia Co		W.R.	trachyte	29°50.298	85°45.988'		123	884				4.88	26.7	
THB DJC1311	S.C. Tibe	N. of Saga S	Adakite	Dajia Co		W.R.	trachyte	29°50.298	85°45.988'		123	985				4.65	26.5	
THB DJC1312	S.C. Tibe	N. of Saga S	Adakite	Dajia Co		W.R.	trachyte	29°50.298	85°45.988'									
THB DJC1313	S.C. Tibe	N. of Saga S	Adakite	Dajia Co	Linzigong lava	W.R.	trachyte	29°50.298	85°45.988'		122	903		0.707278	1.3E-05	4.7	26	
THB DJC1314	S.C. Tibe	N. of Saga S	Adakite	Dajia Co		W.R.	trachyte	29°50.298	85°45.988'		85.4	991				4.56	25.6	
THB DJC1315	S.C. Tibe	N. of Saga S	Adakite	Dajia Co	Linzigong lava	W.R.	trachyte	29°50.198	85°46.037'		55.6	1039		0.706916	1.2E-05	4.6	25.5	
THB YY1101	S.E. Tibe	W. Lhasa	PVR	Yangying	Linzigong lava	W.R.	trachyte	29°43.319	0°22.321'		286	1324		0.71217	7E-06	16.1	105	
THB YY1102	S.E. Tibe	W. Lhasa	PVR	Yangying	Linzigong lava	W.R.	trachyte	29°43.319	0°22.302'		263	1260		0.71214	1.8E-05	15.3	100	
THB YY1105	S.E. Tibe	W. Lhasa	PVR	Yangying		W.R.	trachyte	29°43.229	0°22.161'		267	1182				13.2	86.2	
THB YY1106	S.E. Tibe	W. Lhasa	PVR	Yangying	Linzigong lava	W.R.	trachyte	29°43.209	0°22.079'		321	1283		0.712216	1.1E-05	15.5	100	
THB YY1108	S.E. Tibe	W. Lhasa	PVR	Yangying		W.R.	trachyte	29°43.139	0°22.026'		319	1268				14.9	96.8	
THB YY1111	S.E. Tibe	W. Lhasa	PVR	Yangying	Linzigong lava	W.R.	trachyte	29°43.109	0°21.990'		272	1294		0.712476	2.5E-05	15.8	101	
THB CZ1301	S.C. Tibe	N. of Saga S	PVR	Chazi	K-rich Transhim	W.R.	trachyte	29°50.778	6°44.803'		642	714		0.720771	0.00001	19.5	110	
THB CZ1302	S.C. Tibe	N. of Saga S	PVR	Chazi	K-rich Transhim	W.R.	trachyte	29°50.778	6°44.748'		593	836		0.719659	1.1E-05	16.3	94.6	
THB CZ1303	S.C. Tibe	N. of Saga S	PVR	Chazi	K-rich Transhim	W.R.	trachyte	29°50.778	6°44.693'		758	720		0.720539	8E-06	21.7	118	
THB CZ1304	S.C. Tibe	N. of Saga S	PVR	Chazi		W.R.	trachyte	29°50.808	6°44.800'		624	719				18.1	104	
THB CZ1305	S.C. Tibe	N. of Saga S	UPVR	Chazi		W.R.	trachydacite	29°50.808	6°44.800'		686	523				20.1	108	
THB CZ1306	S.C. Tibe	N. of Saga S	UPVR	Chazi	K-rich Transhim	W.R.	trachyte	29°55.118	6°42.112'		466	663		0.724798	9E-06	16.2	89.8	
THB CZ1307	S.C. Tibe	N. of Saga S	UPVR	Chazi	K-rich Transhim	W.R.	trachyte	29°55.128	6°42.103'		460	618		0.724383	0.00001	15.2	83.8	
THB CZ1308	S.C. Tibe	N. of Saga S	UPVR	Chazi		W.R.	trachyte	29°55.128	6°42.103'		464	628				16.2	88	
THB CZ1309	S.C. Tibe	N. of Saga S	UPVR	Chazi	K-rich Transhim	W.R.	trachyte	29°55.108	6°42.105'		469	651		0.724757	9E-06	16.4	88.2	
THB CZ1310	S.C. Tibe	N. of Saga S	PVR	Chazi	K-rich Transhim	W.R.	trachyte	29°55.328	6°41.695'		440	634		0.723	0.00001	12.8	69.2	
THB CZ1311	S.C. Tibe	N. of Saga S	UPVR	Chazi	K-rich Transhim	W.R.	trachyte	29°55.278	6°41.707'		433	609		0.723353	0.00001	12.8	70.5	
THB YR1101	W. Tibet	Xungba	PVR	Yare		W.R.	trachydacite	31°56.108	1°07.476'		437	142		0.727566	1.6E-05	11.9	76.6	
THB YR1102	W. Tibet	Xungba	PVR	Yare		W.R.	trachydacite	31°56.088	1°07.425'		413	229				12.4	80.1	
THB YR1103	W. Tibet	Xungba	PVR	Yare		W.R.	trachydacite	31°56.088	1°07.425'		392	282		0.725098	1.2E-05	12.2	78	
THB YR1104	W. Tibet	Xungba	PVR	Yare		W.R.	rhyolite	31°56.088	1°07.425'		409	285				13	83.5	
THB YR1105	W. Tibet	Xungba	PVR	Yare		W.R.	trachydacite	31°56.088	1°07.425'		416	230		0.723609	7E-06	12.1	79.7	
THB YR1106	W. Tibet	Xungba	PVR	Yare		W.R.	trachyte	31°54.308	1°10.199'		393	480		0.736849	1.1E-05	9.9	61.5	
THB YR1107	W. Tibet	Xungba	PVR	Yare		W.R.	trachyte	31°54.308	1°10.199'		378	399				10.7	68.9	
THB YR1108	W. Tibet	Xungba	PVR	Yare		W.R.	trachyte	31°54.308	1°10.199'		401	381		0.732684	1.4E-05	11.1	70.2	
THB YR1109	W. Tibet	Xungba	PVR	Yare		W.R.	trachydacite	31°54.308	1°10.199'		388	326		0.730714	8E-06	10.1	64.5	
THB YR1111	W. Tibet	Xungba	PVR	Yare		W.R.	trachyte	31°54.308	1°10.199'		387	406		0.731571	1.5E-05	10.5	67	
THB YR1112	W. Tibet	Xungba	PVR	Yare		W.R.	trachyte	31°54.308	1°10.199'		424	395				11.5	74.8	
THB YR1113	W. Tibet	Xungba	PVR	Yare		W.R.	trachydacite	31°54.308	1°10.199'		382	389		0.729528	7E-06	10.1	66.6	
THB YR1114	W. Tibet	Xungba	PVR	Yare		W.R.	trachyte	31°54.308	1°10.199'		380	343		0.731207	1.3E-05	10.7	66.2	
THB YR1115	W. Tibet	Xungba	PVR	Yare		W.R.	trachyte	31°54.308	1°10.199'		404	382				10.8	70	
THB YR1116	W. Tibet	Xungba	PVR	Yare		W.R.	trachyte	31°54.308	1°10.199'		406	433				11.5	72	
THB YR1117	W. Tibet	Xungba	PVR	Yare		W.R.	trachyte	31°54.308	1°10.199'		398	400				10.5	66	
THB YR1118	W. Tibet	Xungba	PVR	Yare		W.R.	trachyandesi	31°54.308	1°10.199'		157	1393		0.707932	1.9E-05	11.2	61.4	
THB ZB1101	W. Tibet	N. Maiga	PVR	Zabuye		W.R.	trachyandesi	31°22.338	4°23.459'		499	1427		0.711192	1.5E-05	16.1	83.4	
THB ZB1103	W. Tibet	N. Maiga	PVR	Zabuye		W.R.	trachyte	31°22.338	4°23.459'		440	1435				14.4	76.1	
THB ZB1104	W. Tibet	N. Maiga	PVR	Zabuye		W.R.	trachyandesi	31°22.348	4°23.442'		501	1356		0.711194	1.4E-05	16	81.2	
THB ZB1105	W. Tibet	N. Maiga	PVR	Zabuye		W.R.	trachyandesi	31°22.348	4°23.442'		464	1367				15.4	78.9	
THB ZB1107	W. Tibet	N. Maiga	PVR	Zabuye		W.R.	trachyandesi	31°22.348	4°23.442'		416	1537				14.1	72.8	
THB ZB1110	W. Tibet	N. Maiga	PVR	Zabuye		W.R.	trachyte	31°22.668	4°23.527'		406	1408		0.710519	1.2E-05	14.6	77.3	
THB 10SR-08	S.E. Tibe	S.E. Lhasa		Bima Fm Sangri	S. Lhasa terran	W.R.	Dacite				20.8	296	0.2035	0.706039	4	4.27	22.1	0.1168
THB 10SR-13	S.E. Tibe	S.E. Lhasa		Bima Fm Sangri	S. Lhasa terran	W.R.	Andesite				26.8	342	0.227	0.705403	6	3.13	13.9	0.1358

Table SII-2 (…/…)

Ech.#	Region	River	Locality	Formation	Category	Type	Rock type	North	East	Date	Rb SiI	Sr SiI	87Rb/86Sr	87Sr/86Sr S	2s.d.	Sm SiI	Nd SiI	147Sm/144Nd
THB 10SR-48	S.E. Tibe	S.E. Lhasa		Bima Fm Sangri	S. Lhasa terran	W.R.	Andesite				72.6	329	0.6383	0.704906	4	5.27	29.5	0.1078
THB 10SR-27	S.E. Tibe	S.E. Lhasa		Bima Fm Sangri	S. Lhasa terran	W.R.	Group I Basalt				2.31	278	0.024	0.704191	6	3.14	10.8	0.1768
THB 10SR-32	S.E. Tibe	S.E. Lhasa		Bima Fm Sangri	S. Lhasa terran	W.R.	Group I Basalt				0.55	435	0.0037	0.70411	5	2.78	9.87	0.1704
THB 10SR-39	S.E. Tibe	S.E. Lhasa		Bima Fm Sangri	S. Lhasa terran	W.R.	Group I Basalt				3.35	741	0.0131	0.70402	6	2.92	11.1	0.1586
THB 10SR-28	S.E. Tibe	S.E. Lhasa		Bima Fm Sangri	S. Lhasa terran	W.R.	Group II Basalt				1.65	275	0.0174	0.705074	6	5.14	22.9	0.1356
THB 10SR-33	S.E. Tibe	S.E. Lhasa		Bima Fm Sangri	S. Lhasa terran	W.R.	Group II Basalt				5.29	578	0.0264	0.704609	5	4.64	19.1	0.1469
THB 10SR-41	S.E. Tibe	S.E. Lhasa		Bima Fm Sangri	S. Lhasa terran	W.R.	Group II Basalt				11	500	0.0634	0.70415	6	2.58	9.38	0.1665
THB 10SR-43	S.E. Tibe	S.E. Lhasa		Bima Fm Sangri	S. Lhasa terran	W.R.	Group II Basalt				6.29	614	0.0296	0.704164	4	3.1	12.3	0.153
THB 10SR-23	S.E. Tibe	S.E. Lhasa		Bima Fm Sangri	S. Lhasa terran	W.R.	Volcanic tuff				35.9	500	0.2078	0.705515	5	11.2	52.3	0.1291
TSS D1614	S.E. Tibe	S. Lhasa	close STDS	Laguila Fm intrusion Comei	LIP	TSS volcanics	W.R.	granodiorite			149.55	242.57	1.7865	0.72372	5	12.73	67.01	0.1148
TSS D1616	S.E. Tibe	S. Lhasa	close STDS	Laguila Fm intrusion Comei	LIP	TSS volcanics	W.R.	Quartz monzonite			42.91	918.93	1.0728	0.71906	8	6.58	25.27	0.1197
TSS D1617	S.E. Tibe	S. Lhasa	close STDS	Laguila Fm intrusion Comei	LIP	TSS volcanics	W.R.	Gabbro			43.83	679.22	0.1351	0.70667	4	8.43	33.3	0.1574
TSS D1618-2	S.E. Tibe	S. Lhasa	close STDS	Laguila Fm intrusion Comei	LIP	TSS volcanics	W.R.	Gabbro			23.78	624.16	0.1867	0.70637	5	7.61	30.78	0.1529
TSS D1619	S.E. Tibe	S. Lhasa	close STDS	Laguila Fm intrusion Comei	LIP	TSS volcanics	W.R.	Gabbro			36.24	733.03	0.1102	0.7061	4	7	27.38	0.1495
TSS D1620	S.E. Tibe	S. Lhasa	close STDS	Laguila Fm intrusion Comei	LIP	TSS volcanics	W.R.	Gabbro			33.09	558.9	0.143	0.70579	7	9.63	39.09	0.1545
TSS D1631-1	S.E. Tibe	S. Lhasa	close STDS	Laguila Fm intrusion Comei	LIP	TSS volcanics	W.R.	Diabase			26.57	686.81	0.1713	0.70589	4	6.7	26.54	0.1489
TSS D1631-2	S.E. Tibe	S. Lhasa	close STDS	Laguila Fm intrusion Comei	LIP	TSS volcanics	W.R.	Diabase			30.97	671.98	0.1119	0.70559	6	8.48	34.46	0.1525
TSS D1631-3	S.E. Tibe	S. Lhasa	close STDS	Laguila Fm intrusion Comei	LIP	TSS volcanics	W.R.	Diabase			31.1	671	0.1333	0.70689	7	8.56	34.7	0.1487
HHC J-G4	S. Tibet	28.5N	85.2E	High Himalaya leucogranite	Gyirong Leucogranite	HHC granite	W.R.	Tourmaline granite			568.42	37.81		0.805152	11	0.66	2.73	
HHC J-G7	S. Tibet	28.5N	85.2E	High Himalaya leucogranite	Gyirong Leucogranite	HHC granite	W.R.	Tourmaline granite			321.71	41.35		0.764437	13	1.15	3.91	
HHC J-G16	S. Tibet	28.5N	85.2E	High Himalaya leucogranite	Gyirong Leucogranite	HHC granite	W.R.	Tourmaline granite			452.2	68.33		0.789032	13	1.13	3.97	
HHC J-G2	S. Tibet	28.5N	85.2E	High Himalaya leucogranite	Gyirong Leucogranite	HHC granite	W.R.	Tourmaline granite			510.17	34.71		0.796708	9	1.18	4.34	
HHC NL-12	S. Tibet	28.4N	86.5E	High Himalaya leucogranite	Nyalam Leucogranite	HHC granite	W.R.	Tourmaline granite			381.32	27.09		0.761095	16	1.58	5.56	
HHC NL-25	S. Tibet	28.4N	86.5E	High Himalaya leucogranite	Nyalam Leucogranite	HHC granite	W.R.	Tourmaline granite			479.52	77.11		0.776032	13	0.96	3.11	
HHC NL-36	S. Tibet	28.4N	86.5E	High Himalaya leucogranite	Nyalam Leucogranite	HHC granite	W.R.	Tourmaline granite			472.65	98.79		0.755964	12	1.75	5.83	
HHC NL-03	S. Tibet	28.4N	86.5E	High Himalaya leucogranite	Nyalam Leucogranite	HHC granite	W.R.	Tourmaline granite			656.61	112.18		0.772143	17	1.03	3.66	
HHC NL-31	S. Tibet	28.4N	86.5E	High Himalaya leucogranite	Nyalam Leucogranite	HHC granite	W.R.	Tourmaline granite			320.16	39.74		0.767136	19	1.46	5.21	
HHC N-702	S. Tibet	28.4N	86.5E	High Himalaya leucogranite	Nyalam Leucogranite	HHC granite	W.R.	2 mica granite			268.17	108.41		0.748326	14	3.54	14.26	
HHC NL-07	S. Tibet	28.4N	86.5E	High Himalaya leucogranite	Nyalam Leucogranite	HHC granite	W.R.	2 mica granite			218.69	89.02		0.741938	11	3.23	11.08	
HHC DZ-15	S. Tibet	28.4N	87.7E	High Himalaya leucogranite	Dinggye Leucogranite	HHC granite	W.R.	2 mica granite			95.86	57.28		0.776943	7	1.97	6.12	
HHC DG-2	S. Tibet	28.4N	87.7E	High Himalaya leucogranite	Dinggye Leucogranite	HHC granite	W.R.	2 mica granite			102.37	44.43		0.797401	12	1.72	5.44	
HHC DG-08	S. Tibet	28.4N	87.7E	High Himalaya leucogranite	Dinggye Leucogranite	HHC granite	W.R.	Tourmaline granite			325.9	59.58		0.783094	8	1.35	4.46	
HHC DG-24	S. Tibet	28.4N	87.7E	High Himalaya leucogranite	Dinggye Leucogranite	HHC granite	W.R.	Tourmaline granite			416.36	53.74		0.802116	10	0.74	3.25	
HHC GP-05	S. Tibet	27.5N	89E	High Himalaya leucogranite	Gaowu Leucogranite	HHC granite	W.R.	2 mica granite			281.27	76.8		0.770283	9	2.27	6.91	
HHC GP-09	S. Tibet	27.5N	89E	High Himalaya leucogranite	Gaowu Leucogranite	HHC granite	W.R.	2 mica granite			349.14	89.37		0.788309	13	2.54	8.43	
HHC GU-8	S. Tibet	27.5N	89E	High Himalaya leucogranite	Gaowu Leucogranite	HHC granite	W.R.	2 mica granite			212.71	138.09		0.733469	12	2.62	7.69	
HHC GG-2	S. Tibet	27.5N	89E	High Himalaya leucogranite	Gaowu Leucogranite	HHC granite	W.R.	2 mica granite			294.55	126.74		0.757376	16	4.14	15.07	
HHC GF-6	S. Tibet	27.5N	89E	High Himalaya leucogranite	Gaowu Leucogranite	HHC granite	W.R.	Tourmaline granite			446.9	118.05		0.768546	14	1.01	4.03	
HHC GZ-7	S. Tibet	27.5N	89E	High Himalaya leucogranite	Gaowu Leucogranite	HHC granite	W.R.	Tourmaline granite			269.52	23.71		0.794827	10	1.13	3.89	
TSS LG-17	S. Lhasa	28.3N	91.0E	Tethyan Himalaya leucogranite	Luozha Leucogranite	TSS granite	W.R.	2 mica granite			223.14	106.7		0.744316	13	3.81	12.78	
TSS LG-02	S. Lhasa	28.3N	91.0E	Tethyan Himalaya leucogranite	Luozha Leucogranite	TSS granite	W.R.	2 mica granite			169.37	145.67		0.749258	17	6.15	28.48	
TSS LG-29	S. Lhasa	28.3N	91.0E	Tethyan Himalaya leucogranite	Luozha Leucogranite	TSS granite	W.R.	2 mica granite			186.42	134.58		0.746031	16	5.93	23.16	
TSS LG-06	S. Lhasa	28.3N	91.0E	Tethyan Himalaya leucogranite	Luozha Leucogranite	TSS granite	W.R.	2 mica granite			204.69	74.72		0.725625	12	3.05	12.45	
TSS ZF-31	S. Lhasa	29N	90E	Tethyan Himalaya leucogranite	Quzhen Leucogranite	TSS granite	W.R.	2 mica granite			289.44	116.52		0.768905	11	4.63	22.57	
TSS ZF-26	S. Lhasa	29N	90E	Tethyan Himalaya leucogranite	Quzhen Leucogranite	TSS granite	W.R.	2 mica granite			327.58	67.85		0.729351	9	3.59	18.23	
TSS ZF-18	S. Lhasa	29N	90E	Tethyan Himalaya leucogranite	Quzhen Leucogranite	TSS granite	W.R.	2 mica granite			335.8	116.72		0.736713	10	3.11	15.76	
TSS ZF-38	S. Lhasa	29N	90E	Tethyan Himalaya leucogranite	Quzhen Leucogranite	TSS granite	W.R.	Tourmaline granite			362.11	109.46		0.741164	15	4.15	20.35	
TSS JK3/05	S. Tibet	Sakya		Tethyan Himalaya leucogranite	Kuday granite	TSS granite	W.R.	Leucogranites			136.4	165.2	2.379854	0.763193	0.00001	2.88	14.01	
TSS JK3/08	S. Tibet	Sakya		Tethyan Himalaya leucogranite	Kuday granite		W.R.	Leucogranites			191.7	140				2.49	9.35	
TSS JK3/12a	S. Tibet	Sakya		Tethyan Himalaya leucogranite	Kuday granite		W.R.	Leucogranites			261.2	96.61				2.47	9.22	
TSS JK3/13b	S. Tibet	Sakya		Tethyan Himalaya leucogranite	Kuday granite		W.R.	Leucogranites			137.3	60.46				1.71	3.86	
TSS TO3/29x	S. Tibet	Sakya		Tethyan Himalaya leucogranite	Lijun granite		W.R.	Leucogranites			113.9	28.57				3.04	10.6	
TSS TO3/31ix	S. Tibet	Sakya		Tethyan Himalaya leucogranite	Lijun granite		W.R.	Leucogranites			15.1	28.41				1.81	4.86	
TSS TO3/33x	S. Tibet	Sakya		Tethyan Himalaya leucogranite	Lijun granite	TSS granite	W.R.	Leucogranites			243.1	52.4	13.43815	0.813269	3E-06	5.99	24.07	
TSS JK4/07a	S. Tibet	Sakya		Tethyan Himalaya leucogranite	Wing granite	TSS granite	W.R.	Leucogranites			219.3	62.4	10.14899	0.782417	3E-06	7.22	31.87	
TSS JK4/08	S. Tibet	Sakya		Tethyan Himalaya leucogranite	Kua granite		W.R.	Leucogranites			355.6	97.7	10.49434	0.766507	1.7E-05	5.38	23.45	
TSS JK4/09a	S. Tibet	Sakya		Tethyan Himalaya leucogranite	Kua granite		W.R.	Leucogranites			80.92	103				3.01	9.76	
TSS JK4/09b	S. Tibet	Sakya		Tethyan Himalaya leucogranite	Kua granite		W.R.	Leucogranites			71.49	210.4				3.92	19.35	
TSS JK3/25	S. Tibet	Sakya		Tethyan Himalaya leucogranite	Kouwo granite		W.R.	Leucogranites			186.6	174.8				4.45	20.67	
TSS TO3/25i	S. Tibet	Sakya		Tethyan Himalaya leucogranite	Mabja granite	TSS granite	W.R.	Leucogranites			353.8	70.3	14.67104	0.878522	1.3E-05	3.63	15	

Table SII-2 (…/…)

Ech.#	Region	River	Locality	Formation	Category	Type	Rock type	North	East	Date	Rb SiI	Sr SiI	87Rb/86Sr	87Sr/86Sr S	2s.d.	Sm SiI	Nd SiI	147Sm/144Nd
TSS JK4/11b	S. Tibet	Sakya	Tethyan Himalaya leucogranite	Donggong granite		W.R.	Leucogranites				230	50.9				6.33	28.59	
TSS JK4/12a	S. Tibet	Sakya	Tethyan Himalaya leucogranite	Donggong granite		W.R.	Leucogranites				171.4	187.2				4.79	22.32	
TSS JK4/12b	S. Tibet	Sakya	Tethyan Himalaya leucogranite	Donggong granite		W.R.	Leucogranites				234.1	12.68				0.54	1.4	
TSS JK4/13g	S. Tibet	Sakya	Tethyan Himalaya leucogranite	Gomdre granite	TSS granite	W.R.	Leucogranites				171.3	183.8	2.680178	0.740012	1.1E-05	5.33	25.69	
TSS T71	S. Tibet	Sakya	Tethyan Himalaya gneiss	Kangmar gneiss	TSS	W.R.	bt Gneiss				159	43	10.78	0.77277	0.00001	3.65	16.3	0.135
TSS T72	S. Tibet	Sakya	Tethyan Himalaya gneiss	Kangmar gneiss	TSS	W.R.	bt Gneiss				141	34	11.91	0.77305	0.00002	2.94	12.5	0.142
TSS T97-61	S. Tibet	Sakya	Tethyan Himalaya gneiss	Kangmar gneiss	TSS	W.R.	bt Gneiss				144	86	4.84	0.77305	0.00002	4.59	23.1	0.12
TSS T136	S. Tibet	Sakya	Tethyan Himalaya gneiss	Kangmar gneiss	TSS	W.R.	bt Gneiss				173	44	11.31	0.78009	0.00001	3.3	15.3	0.13
TSS T100	S. Tibet	Sakya	Tethyan Himalaya granite	Kuday granite	TSS granite	W.R.	bt-mu Gr+gt				156	61	7.33	0.76605	0.00003	1.34	4.9	0.167
TSS T101	S. Tibet	Sakya	Tethyan Himalaya granite	Kuday granite	TSS granite	W.R.	bt-mu Gr+gt				180	60	8.64	0.77149	0.00002	1.85	6.9	0.162
TSS T104	S. Tibet	Sakya	Tethyan Himalaya granite	Kuday granite	TSS granite	W.R.	bt-mu Gr+gt				119	41	8.38	0.78518	0.00004	1.08	3.8	0.173
TSS T105	S. Tibet	Sakya	Tethyan Himalaya granite	Kuday granite	TSS granite	W.R.	bt-mu Gr+gt				145	70	6.03	0.78308	0.00002	1.72	5.7	0.183
TSS T110	S. Tibet	Sakya	Tethyan Himalaya granite	Kouwu Kouwo granite	TSS granite	W.R.	bt-mu Gr				41	64	1.84	0.73848	0.00001	2.73	12.2	0.135
TSS T111	S. Tibet	Sakya	Tethyan Himalaya granite	Kouwu Kouwo granite	TSS granite	W.R.	bt-mu Gr				87	123	2.04	0.73843	0.00001	3.35	14.9	0.136
TSS T113	S. Tibet	Sakya	Tethyan Himalaya granite	Kouwu Kouwo granite	TSS granite	W.R.	bt-mu Gr				66	131	1.44	0.7377	0.00001	5.05	23.3	0.131
TSS T114	S. Tibet	Sakya	Tethyan Himalaya granite	Kouwu Kouwo granite	TSS granite	W.R.	bt-mu Gr				70	139	1.45	0.73732	0.00001	4.4	20.1	0.132
TSS T117	S. Tibet	Sakya	Tethyan Himalaya granite	Mabja granite		W.R.	mu-bt Gr+and				276	33				1.96	7.8	
TSS T118	S. Tibet	Sakya	Tethyan Himalaya granite	Mabja granite	TSS granite	W.R.	bt-mu Gr+tm				257	36	20.82	0.85328	0.00003	1.76	7.4	0.144
TSS T120	S. Tibet	Sakya	Tethyan Himalaya granite	Mabja granite	TSS granite	W.R.	bt-mu Gr+tm				297	26	32.94	0.8532	0.00001	1.25	5.1	0.149
TSS T121	S. Tibet	Sakya	Tethyan Himalaya granite	Mabja granite	TSS granite	W.R.	bt-mu Gr+tm, ky				321	30	31.17	0.85474	0.00001	2.33	9.2	0.153
TSS T73	S. Tibet	Sakya	Tethyan Himalaya granite	Lhagoi Kangri granite	TSS granite	W.R.	bt Gr+sill				227	68	9.64	0.74063	0.00002	1.84	8.1	0.137
TSS T74	S. Tibet	Sakya	Tethyan Himalaya granite	Lhagoi Kangri granite	TSS granite	W.R.	bt-mu Gr+sill				216	58	10.62	0.74066	0.00002	1.95	8.6	0.137
TSS T75	S. Tibet	Sakya	Tethyan Himalaya leucogranite	Lhagoi Kangri granite	TSS granite	W.R.	bt-mu Gr+sill				137	104	3.79	0.74128	0.00002	3.83	17.4	0.133
TSS T76	S. Tibet	Sakya	Tethyan Himalaya leucogranite	Dingge leucogranite	TSS granite	W.R.	mu-bt Gr				238	21	31.94	0.77956	0.00002	1.25	3.8	0.201
TSS T77	S. Tibet	Sakya	Tethyan Himalaya leucogranite	Dingge leucogranite	TSS granite	W.R.	mu Gr+tm				302	12	73.4	0.77106	0.00002	0.59	1.7	0.209
TSS T78a	S. Tibet	Sakya	Tethyan Himalaya leucogranite	Dingge leucogranite		W.R.	mu-bt Gr				277	17				1.82	5.5	0.201
TSS T97-26	S. Tibet	Sakya	Tethyan Himalaya leucogranite	Yaddon leucogranite	TSS granite	W.R.	mu-bt Gr+tm				256	72	10.29	0.77294	0.00001	2.28	9.6	0.145
TSS T97-57	S. Tibet	Sakya	Tethyan Himalaya leucogranite	Yaddon leucogranite	TSS granite	W.R.	mu-bt Gr				309	36	24.72	0.76081	0.00002	1.02	3.8	0.162
TSS T107	S. Tibet	Sakya	Tethyan metasediments	Kuday metasediments	TSS	W.R.	mu-bt-gt migmatite				126	152	2.39	0.74846	0.00001	8.81	45.5	0.117
TSS T125	S. Tibet	Sakya	Tethyan metasediments	Kangmar schists	TSS	W.R.	mu-bt schist				207	85	7.07	0.79031	0.00001	7.97	40.1	0.12
TSS T129	S. Tibet	Sakya	Tethyan metasediments	Kangmar schists		W.R.	bt-mu schist				131	32				5.57	25.7	
TSS T135	S. Tibet	Sakya	Tethyan metasediments	Kangmar schists	TSS	W.R.	bt-mu-st-gt schist				127	57	6.41	0.77871	0.00001	7.25	37.3	0.118
TSS T137	S. Tibet	Sakya	Tethyan metasediments	Kangmar schists	TSS	W.R.	bt-mu-gt-st schist				114	49	6.65	0.77034	0.00001	5.3	26.5	0.121
THB L-72	E. Aruna	Lohit riv		Lohit batholith		W.R.	Diorite	28°20′32	97°10′41″		8.86	113.78	0.208	0.704671	0.0002			
THB L-45	E. Aruna	Lohit riv		Lohit batholith		W.R.	Diorite	28°02′14	96°56′55″		174.98	120.61	5.683	0.703876	0.0003			
THB L-70	E. Aruna	Lohit riv		Lohit batholith		W.R.	Granodiorite	28°18′20	97°06′25″		121.09	314.04	1.116	0.707093	0.0003			
THB L-71	E. Aruna	Lohit riv		Lohit batholith		W.R.	Granodiorite	28°19′43	97°08′48″		53.94	346.44	0.4503	0.704698	0.0002			
THB L-69	E. Aruna	Lohit riv		Lohit batholith		W.R.	Granite	28°15′44	97°01′38″		66.08	89.149	1.6795	0.714987	0.0001			
THB D-62	E. Aruna	Dibang riv		Lohit batholith		W.R.	Diorite	28°50′78	96°50′48″		104.55	201.49	1.5009	0.705863	0.0002			
THB D-63	E. Aruna	Dibang riv		Lohit batholith		W.R.	Granite	28°50′77	96°50′45″		113.2	139.9	2.34072	0.706152	0.0002			
THB D-69	E. Aruna	Dibang riv		Lohit batholith		W.R.	Granodiorite	28°50′78	96°50′50″		108.29	411.82	0.76061	0.705601	0.0003			
THB 07TB33a-1	S. Lhasa, N. Suture			Kelu intrusive rock	Gangdese belt	W.R.	Q-monzonite				91.4	716	0.369	0.704298	1.3E-05	5.05	29.2	0.105
THB 07TB33a-2	S. Lhasa, N. Suture			Kelu intrusive rock	Gangdese belt	W.R.	Diorite				41.3	937	0.128	0.704147	0.00001	4.03	21.9	0.111
THB 07TB33b-2	S. Lhasa, N. Suture			Kelu intrusive rock	Gangdese belt	W.R.	Q-monzonite				87.1	735	0.343	0.704272	1.7E-05	5.24	30.4	0.104
THB 07TB33d	S. Lhasa, N. Suture			Kelu intrusive rock	Gangdese belt	W.R.	Diorite				20.2	745	0.0785	0.704224	1.7E-05	2	12.4	0.122
THB 07TB33e	S. Lhasa, N. Suture			Kelu intrusive rock	Gangdese belt	W.R.	Q-monzonite				82.4	762	0.313	0.704273	1.7E-05	4.84	28.2	0.104
TSS 11SN16-1	S. Lhasa, S. of Suture			Comei granite	TSS granite	W.R.	Granite porphyry				77.4	68.1	3.29	0.730404	6	12.6	67.6	0.113
TSS 11SN17-1	S. Lhasa, S. of Suture			Comei granite	TSS granite	W.R.	Granite porphyry				371	200	5.38	0.736446	6	29.3	162	0.11
TSS 11SN18-2	S. Lhasa, S. of Suture			Comei granite	TSS granite	W.R.	Granite porphyry				178	113	4.57	0.735865	5	13.3	72.6	0.111
TSS 11SN19-2	S. Lhasa, S. of Suture			Comei granite	TSS granite	W.R.	Granite porphyry				182	112	4.72	0.735519	6	13.6	75.9	0.109
TSS 11SN20-2	S. Lhasa, S. of Suture			Comei granite	TSS granite	W.R.	Granite porphyry				166	94.3	5.1	0.735452	6	13.1	71.7	0.111
TSS 09TB116-1	S. Lhasa, S. of Suture			Comei granite	TSS granite	W.R.	Granite porphyry				169	131	3.74	0.736342	16	14.1	76.6	0.112
TSS 09TB116-4	S. Lhasa, S. of Suture			Comei granite	TSS granite	W.R.	Granite porphyry				169	136	3.62	0.736694	13	15.2	80.8	0.114
TSS 09TB116-5	S. Lhasa, S. of Suture			Comei granite	TSS granite	W.R.	Granite porphyry				160	134	3.46	0.735685	15	13	71.8	0.11

Table SII-2 (…/…)

Ech.#	Region	River	Locality	Formation	Category	Type	Rock type	North	East	Date	Rb Sil	Sr Sil	87Rb/86Sr	87Sr/86Sr S	2s.d.	Sm Sil	Nd Sil	147Sm/144Nd
THB S31	SW. Tibe	Chaxiezangbu				sediments	Coordinates,	N30°08′	E83°19′					0.719185	15			
THB S32	SW. Tibe	Shiquan River				sediments		N32°30′	E80°06′					0.716324	9			
THB S33	SW. Tibe	Niyangqu River				sediments		N29°28′	E94°25′					0.719489	8			
THB S34	S. Tibet	Lhasa River				sediments		N29°23′	E90°53′					0.714446	11			
THB S35	Lhasa	Xiangqu River				sediments		N29°31′	E89°05′					0.715149	9			
THB S36	Lhasa	Geerzangbu				sediments		N32°27′	E80°10′					0.71222	11			
THB S37	Lhasa	Yarlung zangbu				sediments		N29°19′	E89°06′					0.713761	8			
THB S38	Lhasa	Yarlung zangbu				sediments		N29°20′	E90°16′					0.712849	9			
THB S39	before E	Yarlung zangbu				sediments		N29°19′	E94°20′					0.713521	9			
THB T1	Lhasa	Sand				sediments		N29°23′	E90°49′					0.714176	12			
THB T2	Lhasa	Sand				sediments		N29°27′	E90°55′					0.711504	12			
Hima S40		Xiangquan River				sediments		N31°30′	E79°48′					0.732	10			
THB T849	E. Namc	East syntaxis	E. Lhasa terrane granites	Bolonggong#3 Granite	E. Transhimalay	W.R.	epidote-bearing granodiorite				188	563	0.966	0.720927	6E-06	5.68	39.2	0.0877
THB T850	E. Namc	East syntaxis	E. Lhasa terrane granites	Bolonggong#3 Granite	E. Transhimalay	W.R.	epidote-bearing granodiorite				190.0	541.0	1.016	0.721176	6E-06	5.1	29.1	0.1049
THB T1047	E. Namc	East syntaxis	E. Lhasa terrane granites	Bolonggong#2 Granite	E. Transhimalay	W.R.	Foliated granite				173	342	1.467	0.72061	6E-06	5.91	37.4	0.0956
THB T1066	E. Namc	East syntaxis	E. Lhasa terrane granites	Bolonggong#4 Granite	E. Transhimalay	W.R.	porphyritic granite				163	412	1.147	0.717421	6E-06	6.49	49.6	0.0792
THB T1067	E. Namc	East syntaxis	E. Lhasa terrane granites	Bolonggong#4 Granite	E. Transhimalay	W.R.	porphyritic granite				162	439	1.07	0.717396	7E-06	8.05	56.7	0.0857
THB T847	E. Namc	East syntaxis	E. Lhasa terrane granites	Bolonggong#4 Granite	E. Transhimalay	W.R.	porphyritic granite				148	483	0.891	0.711953	5E-06	7.39	43.8	0.102
THB T1034	E. Namc	East syntaxis	E. Lhasa terrane granites	Bolonggong#1 Granite	E. Transhimalay	W.R.	porphyritic granite				145	917	0.459	0.706997	6E-06	5.81	43.4	0.081
THB T1035	E. Namc	East syntaxis	E. Lhasa terrane granites	Bolonggong#1 Granite	E. Transhimalay	W.R.	porphyritic granite				131.0	1057.0	0.358	0.7064	6E-06	7.7	51.3	0.091
THB T830	E. Namc	East syntaxis	E. Lhasa terrane granites	52K Granite	E. Transhimalay	W.R.	granite				162	372	1.263	0.707276	4E-06	2.45	25.6	0.0579
THB T831	E. Namc	East syntaxis	E. Lhasa terrane granites	52K Granite	E. Transhimalay	W.R.	granite				153	259	1.706	0.710117	5E-06	5.29	30.7	0.1042
THB T1010	E. Namc	East syntaxis	E. Lhasa terrane granites	Meiri Granite	E. Transhimalay	W.R.	granitoids				75	450	0.485	0.707481	6E-06	3.68	17.2	0.1293
THB T1014	E. Namc	East syntaxis	E. Lhasa terrane granites	Meiri Granite	E. Transhimalay	W.R.	granitoids				69	261	0.768	0.706188	4E-06	3.96	21.2	0.1129
THB T1015	E. Namc	East syntaxis	E. Lhasa terrane granites	Meiri Granite	E. Transhimalay	W.R.	granitoids				66	279	0.683	0.706615	5E-06	3.57	21.7	0.0996
THB T691	E. Namc	East syntaxis	E. Lhasa terrane granites	Beibeng Granite	E. Transhimalay	W.R.	biotite granite				150	208	2.084	0.707048	4E-06	7.93	50.3	0.0953
THB T979	E. Namc	East syntaxis	E. Lhasa terrane granites	Beibeng Granite	E. Transhimalay	W.R.	biotite granite				119	38	0.888	0.710589	5E-06	6.32	35.7	0.1071
HHC 502068	C. Nepal	Annapurna	Modi Khola	Formation I		W.R.	paragneiss	28.428	83.826							6.96	35.38	0.1189
HHC 502069	C. Nepal	Annapurna	Modi Khola	Formation I		W.R.	metasandstc	28.427	83.8							3.85	20.23	0.115
HHC 502070	C. Nepal	Annapurna	Modi Khola	Formation I		W.R.	schist	28.419	83.82							6.39	33.01	0.117
HHC 502071	C. Nepal	Annapurna	Modi Khola	Formation I		W.R.	schist	28.417	83.821							7.1	36.52	0.1176
HHC 502072	C. Nepal	Annapurna	Modi Khola	Formation I		W.R.	psammitic s	28.415	83.817									
502073	C. Nepal	Annapurna	Modi Khola	Lower foreland basin		W.R.	quartzite	28.414	83.814									
LH 502075	C. Nepal	Annapurna	Modi Khola	Kuncha		W.R.	psammitic pl	28.412	83.807							1.71	8.32	0.1244
HHC 502104	C. Nepal	Annapurna	Seti Nadi	Formation I		W.R.	paragneiss	28.38	83.972							5.94	29.63	0.1213
HHC 502105A	C. Nepal	Annapurna	Seti Nadi	Formation I		W.R.	paragneiss	28.377	83.97							6.79	34.09	0.1203
HHC 502105B	C. Nepal	Annapurna	Seti Nadi	Formation I		W.R.	schist	28.377	83.97							7.3	37.89	0.1164
HHC 502106	C. Nepal	Annapurna	Seti Nadi	Formation I		W.R.	schist	28.373	83.969							5.74	28.86	0.1203
HHC 502107	C. Nepal	Annapurna	Seti Nadi	Formation I		W.R.	quartzite	28.369	83.967									
LH 502108	C. Nepal	Annapurna	Seti Nadi	Kuncha		W.R.	phyllite	28.362	83.961							6.58	35.16	0.1131
LH 502097	C. Nepal	Annapurna	Seti Nadi	Kuncha		W.R.	graphitic phy	28.347	83.962							4.63	25.98	0.1077
HHC 502128	C. Nepal	Annapurna	Madi Nadi	Formation I		W.R.	paragneiss	28.315	84.092							7.93	41.3	0.1161
HHC 502129	C. Nepal	Annapurna	Madi Nadi	Formation I		W.R.	paragneiss	28.31	84.094							7.06	35.95	0.1188
HHC 502133	C. Nepal	Annapurna	Madi Nadi	Formation I		W.R.	schist	28.307	84.092							5.99	29.84	0.1214
HHC 502132	C. Nepal	Annapurna	Madi Nadi	Formation I		W.R.	psammitic s	28.306	84.09							5.93	29.91	0.1199
LH 502130	C. Nepal	Annapurna	Madi Nadi	post-Kuncha Nawakot		W.R.	graphitic phy	28.301	84.093							5.45	29	0.1136
LH 502134	C. Nepal	Annapurna	Madi Nadi	post-Kuncha Nawakot		W.R.	phyllitic quar	28.299	84.092									
LH 502131	C. Nepal	Annapurna	Madi Nadi	post-Kuncha Nawakot		W.R.	graphitic phy	28.295	84.093							2.87	15.34	0.113
LH 502136	C. Nepal	Annapurna	Madi Nadi	post-Kuncha Nawakot		W.R.	phyllite	28.285	84.091							3.8	21.94	0.1044
HHC 502152	C. Nepal	Annapurna	Nayu Ridge	Formation I		W.R.	paragneiss	28.306	84.302							5.73	28.85	0.12
HHC 502149	C. Nepal	Annapurna	Nayu Ridge	Formation I		W.R.	paragneiss	28.304	84.301							7.21	36.33	0.12
HHC 502148	C. Nepal	Annapurna	Nayu Ridge	Formation I		W.R.	graphitic sch	28.304	84.302							8.4	43.6	0.1165
HHC 502147	C. Nepal	Annapurna	Nayu Ridge	Formation I		W.R.	graphitic sch	28.3	84.302							7.3	37.84	0.1166
LH 502146	C. Nepal	Annapurna	Nayu Ridge	Kuncha		W.R.	phyllite	28.293	84.304							5.74	32.08	0.1077
LH 602002	C. Nepal	Annapurna	Nayu Ridge	Kuncha		W.R.	phyllite	28.269	84.313							7.53	40.92	0.1112
HHC 402086	C. Nepal	Annapurna	Marsyangdi Nadi	Formation I		W.R.	paragneiss	28.348	84.403							6.04	30.81	0.1184
HHC 402088	C. Nepal	Annapurna	Marsyangdi Nadi	Formation I		W.R.	paragneiss	28.345	84.398							8.88	46.04	0.1166
HHC 402090	C. Nepal	Annapurna	Marsyangdi Nadi	Formation I		W.R.	paragneiss	28.341	84.398							5.22	28.01	0.1127
HHC 402092A	C. Nepal	Annapurna	Marsyangdi Nadi	Formation I		W.R.	quartzite	28.338	84.399							1.59	8.5	0.1131
HHC 402092B	C. Nepal	Annapurna	Marsyangdi Nadi	Formation I		W.R.	graphitic sch	28.338	84.399							5.08	26.2	0.1172

Table SII-2 (…/…)

	Ech.#	Region	River	Locality	Formation	Category	Type	Rock type	North	East	Date	Rb Sil	Sr Sil	87Rb/86Sr	87Sr/86Sr S	2s.d.	Sm Sil	Nd Sil	147Sm/144Nd
LH	402093	C. Nepal	Annapurna	Marsyangdi Nadi	Kuncha		W.R.	schist	28.334	84.4							4.94	28.95	0.1032
LH	402097	C. Nepal	Annapurna	Marsyangdi Nadi	Kuncha		W.R.	phyllite	28.315	84.401							6.61	37.52	0.1065
TSS	D6344-B1	S. Lhasa	Tethyan clos	28.5N 92E	Cuonadong granitic gneiss	TSS	W.R.					330	64	14.9213	0.830656	1.7E-05	8.66	44	0.119
TSS	D6344-B7	S. Lhasa	Tethyan clos	28.5N 92E	Cuonadong granitic gneiss	TSS	W.R.					377	64.9	16.8048	0.841679	1.4E-05	10.1	53.2	0.114
TSS	D1542-B2	S. Lhasa	Tethyan clos	28.5N 92E	Cuonadong granitic gneiss	TSS	W.R.					489	65.4	21.6344	0.877716	1.4E-05	8.08	45.9	0.106
TSS	D1536-B2	S. Lhasa	Tethyan clos	28.5N 92E	Cuonadong granitic gneiss	TSS	W.R.					374	63.6	17.0303	0.843617	1.7E-05	9.25	46.7	0.120
TSS	D6304-B2	S. Lhasa	Tethyan clos	28.5N 92E	Cuonadong granitic gneiss	TSS	W.R.					319	65.5	14.1127	0.823222	1.7E-05	10.3	53.4	0.116
TSS	D6304-B3	S. Lhasa	Tethyan clos	28.5N 92E	Cuonadong granitic gneiss	TSS	W.R.					345	63.3	15.7879	0.835659	1.3E-05	7.81	41	0.115
HHC	22D	C. Nepal			Manaslu granite	HHC granite	W.R.							5.98	0.74332	40			0.141
HHC	A404	C. Nepal			Palung granite	HHC granite	W.R.							37.8	0.82131	50			
HHC	132	C. Nepal			Makalu granite		W.R.												0.121
	HB68	Ladakh		granodiorite	Ladakh		W.R.							0.17	0.705	1			0.108
	HB74			diorite	Ladakh		W.R.							0.352	0.7048	1			0.617
					Yangying potassic volcanic rocks														
THB	YY-07	W. Lhas	29.5N 90.5E	Pujiemu		K-rich Transhim	W.R.	trachyte				275	1262	0.6293	0.712153	1.1E-05	14.6	99.4	0.0889
THB	YY-08	W. Lhas	29.5N 90.5E	Qialagai	Yangying potassic volcanic rocks	K-rich Transhim	W.R.	trachyte				350	1333	0.7607	0.712093	0.00001	16.2	110	0.089
THB	YY-10	W. Lhas	29.5N 90.5E	Pujiemu	Yangying potassic volcanic rocks	K-rich Transhim	W.R.	trachyte				306	1317	0.6724	0.712146	1.3E-05	15	103	0.0884
THB	YY-12	W. Lhas	29.5N 90.5E	Pujiemu	Yangying potassic volcanic rocks	K-rich Transhim	W.R.	trachyte				289	1289	0.6487	0.712189	1.1E-05	14	96.3	0.0876
TSS	LKZ-1	S. Lhasa	29N 90E		Langkazi leucogranite	TSS granite	W.R.					170	249	1.977	0.730955	12	3.58	17	0.127301
TSS	LKZ-2	S. Lhasa	29N 90E		Langkazi leucogranite	TSS granite	W.R.					176	249	2.046	0.726953	15	4.59	21.9	0.126697
TSS	LKZ-3	S. Lhasa	29N 90E		Langkazi leucogranite	TSS granite	W.R.					182	258	2.041	0.726967	15	4.71	22.9	0.124332
TSS	LKZ-4	S. Lhasa	29N 90E		Langkazi leucogranite	TSS granite	W.R.					185	272	1.97	0.72715	16	6.38	31.7	0.121663
TSS	LKZ-5	S. Lhasa	29N 90E		Langkazi leucogranite	TSS granite	W.R.					177	367	1.395	0.716426	15	3.83	18.5	0.125148
TSS	LKZ-10	S. Lhasa	29N 90E		Langkazi leucogranite		W.R.												
TSS	LKZ-6	S. Lhasa	29N 90E		Langkazi leucogranite	TSS granite	W.R.					175	382	1.327	0.716782	15	4.16	20.8	0.1209
TSS	LKZ-8	S. Lhasa	29N 90E		Langkazi diorite enclave	TSS granite	W.R.					262	655	1.157	0.714415	13	12.4	66	0.113573
TSS	LKZ-12	S. Lhasa	29N 90E		Langkazi diorite enclave	TSS granite	W.R.					186	679	0.791	0.709741	20	5.63	26.9	0.126754
TSS	LKZ-13	S. Lhasa	29N 90E		Langkazi diorite enclave	TSS granite	W.R.					269	666	1.169	0.70941	16	6.51	25.4	0.154933
TSS	LKZ-15-1	S. Lhasa	29N 90E		Langkazi diorite enclave	TSS granite	W.R.					210	737	0.825	0.709377	13	5.28	25.1	0.127162
TSS	LKZ-15-2	S. Lhasa	29N 90E		Langkazi diorite enclave	TSS granite	W.R.					199	709	0.812	0.709409	17	5.44	27	0.121796
TSS	LKZ-16	S. Lhasa	29N 90E		Langkazi diorite enclave	TSS granite	W.R.					317	840	1.093	0.71385	14	12.2	73.2	0.10075
TSS	LKZ-17	S. Lhasa	29N 90E		Langkazi diorite enclave	TSS granite	W.R.					315	592	1.541	0.710628	17	5.21	24.1	0.130682
TSS	LKZ-19	S. Lhasa	29N 90E		Langkazi diorite enclave	TSS granite	W.R.					297	775	1.108	0.708667	14	6.33	24.9	0.153674
TSS	09FW115	S.W. Lha	30N 90E		Ramba dome	TSS granite	W.R.	porphyritic two-mica granite gneiss dykes				149	300	1.44	0.717417	22	2.94	14	0.1272
TSS	12FW111	S.W. Lha	30N 90E		Ramba dome	TSS granite	W.R.	porphyritic two-mica granite gneiss dykes				141	223	1.828	0.717975	21	4.43	21.6	0.1241
TSS	12FW112	S.W. Lha	30N 90E		Ramba dome	TSS granite	W.R.	porphyritic two-mica granite gneiss dykes				209	696	0.869	0.708604	20	2.77	15.1	0.1111
TSS	09FW116	S.W. Lha	30N 90E		Ramba dome	TSS granite	W.R.	2 mica granite pluton				299	141	6.163	0.73218	20	3.9	16.9	0.1396
TSS	09FW118	S.W. Lha	30N 90E		Ramba dome	TSS granite	W.R.	2 mica granite pluton				427	99.1	12.51	0.740026	25	3.95	19.2	0.1245
TSS	09FW120	S.W. Lha	30N 90E		Ramba dome	TSS granite	W.R.	2 mica granite pluton				337	134	7.29	0.742221	13	4.87	23.6	0.1247
TSS	09FW121	S.W. Lha	30N 90E		Ramba dome	TSS granite	W.R.	2 mica granite pluton				331	130	7.368	0.739637	15	4.33	21.7	0.1205
TSS	12FW115	S.W. Lha	30N 90E		Ramba dome	TSS granite	W.R.	2 mica granite pluton				364	126	8.376	0.736043	23	4.28	21.2	0.122
TSS	12FW116	S.W. Lha	30N 90E		Ramba dome	TSS granite	W.R.	2 mica granite pluton				332	155	6.228	0.73837	25	5.19	25.9	0.121
TSS	09FW114	S.W. Lha	30N 90E		Ramba dome	TSS granite	W.R.	garnet-bearing granite dykes				476	19	72.64	0.730147	20	0.65	1.7	0.2321
TSS	09FW119	S.W. Lha	30N 90E		Ramba dome	TSS granite	W.R.	garnet-bearing granite dykes				365	92.2	11.472	0.714106	17	0.76	2.02	0.2282
TSS	12FW103	S.W. Lha	30N 90E		Ramba dome	TSS granite	W.R.	garnet-bearing granite dykes				408	8.29	142.893	0.732946	20	0.29	0.84	0.2125
TSS	12FW104	S.W. Lha	30N 90E		Ramba dome	TSS granite	W.R.	garnet-bearing granite dykes				400	20.5	56.548	0.72561	17	0.18	0.56	0.1918
TSS	12FW105	S.W. Lha	30N 90E		Ramba dome	TSS granite	W.R.	garnet-bearing granite dykes				231	23.4	28.644	0.72546	17	0.34	1.12	0.1813
TSS	12FW106	S.W. Lha	30N 90E		Ramba dome	TSS granite	W.R.	garnet-bearing granite dykes				549	19.5	81.507	0.732044	20	0.49	1.51	0.1963
TSS	12FW109	S.W. Lha	30N 90E		Ramba dome	TSS granite	W.R.	garnet-bearing granite dykes				580	16.4	102.573	0.731359	17	0.78	2.19	0.2151
TSS	12FW101	S.W. Lha	30N 90E		Ramba dome hosting rock	TSS	W.R.	Metasedimentary-garnet–saturolite two-mica schist						2.614	0.714083	25			0.1208
TSS	12FW107	S.W. Lha	30N 90E		Ramba dome hosting rock	TSS	W.R.	Metasedimetary-garnet–amphibolite quartz schist						0.327	0.713873	13			0.1155
TSS	12FW102	S.W. Lha	30N 90E		Ramba dome hosting rock	TSS	W.R.	Metabasite–amphibole plagiogneiss						0.144	0.70752	14			0.1691

Table SII-2 (…/…)

Ech.#	Region	River	Locality	Formation	Category	Type	Rock type	North	East	Date	Rb Sil	Sr Sil	87Rb/86Sr	87Sr/86Sr S	2s.d.	Sm Sil	Nd Sil	147Sm/144Nd
TSS 12FW108	S.W. Lha	30N	90E	Ramba dome hosting rock	TSS	W.R.	Metabasite–amphibole plagiogneiss						0.068	0.70623	26			0.1685
TSS 12FW110	S.W. Lha	30N	90E	Ramba dome hosting rock	TSS	W.R.	Metabasite–amphibole plagiogneiss						2.332	0.712158	17			0.1723
TSS 12FW113	S.W. Lha	30N	90E	Ramba dome hosting rock	TSS	W.R.	Metabasite–amphibole plagiogneiss						0.241	0.709596	18			0.17
TSS 12FW114	S.W. Lha	30N	90E	Ramba dome hosting rock	TSS	W.R.	Metabasite–amphibolite						0.606	0.708479	17			0.167
TSS JK3/15	S.W. Lha	28.5N	88.5E	Sakya dome	Kuday dykes	TSS volcanics	W.R.	Latite			84	1595	0.15	0.7077	7E-06	7.78	45.51	0.103
TSS JK3/17	S.W. Lha	28.5N	88.5E	Sakya dome	Kuday dykes	TSS volcanics	W.R.	Latite			74	1572	0.13	0.70784	7E-06	7.61	44.33	0.104
TSS TO3/14i	S.W. Lha	28.5N	88.5E	Sakya dome	Kuday dykes	TSS volcanics	W.R.	Dacite			133	1269	0.3	0.70789	6E-06	7.78	52.58	0.089
TSS SD51	S.W. Lha	28.5N	88.5E	Sakya dome	Kuday dykes	TSS volcanics	W.R.	Dacite			75	1672	0.13	0.70784	1.1E-05	7.11	44.77	0.096
TSS JK3/16	S.W. Lha	28.5N	88.5E	Sakya dome	Kuday dykes	TSS volcanics	W.R.	Dacite			97	885	0.31	0.70714	1.1E-05	3.82	20.55	0.113
TSS T108	S.W. Lha	28.5N	88.5E	Sakya dome	Kuday dykes	TSS volcanics	W.R.	Dacite			59	1458	0.12	0.71059	8E-06	5.7	35.72	0.096
TSS SD50	S.W. Lha	28.5N	88.5E	Sakya dome	Kuday dykes	TSS volcanics	W.R.	Rhyolite			93	676	0.39	0.70731	1.1E-05	2.89	13.98	0.125
TSS T109	S.W. Lha	28.5N	88.5E	Sakya dome	Kuday dykes	TSS volcanics	W.R.	Rhyolite or microgranite ?			40	366	0.31	0.7076	0.00002	2.18	10.12	0.13
TSS G40	S.W. Lha	28.5N	88.5E	Sakya dome	Nyainqentanglha gneisses	TSS	W.R.	Gneiss			299	210	4.07	0.70903	1.1E-05	8.23	58.36	0.085
TSS G38E	S.W. Lha	28.5N	88.5E	Sakya dome	Nyainqentanglha gneisses	TSS	W.R.	Gneiss			237	360	1.71	0.70921	1.2E-05	8.7	63.12	0.084
TSS T0659-3	S. Tibet	29N	85.5E	Malashan gneiss dome	Paiku pluton in Malashan gneiss dome	TSS granite	W.R.	Tourmaline leucogranite			369	38.9	27.414	0.763382	13	3.36	0.94	0.169
TSS T0659-4	S. Tibet	29N	85.5E	Malashan gneiss dome	Paiku pluton in Malashan gneiss dome	TSS granite	W.R.	Tourmaline leucogranite			338	38.1	25.638	0.761717	13	3.37	0.98	0.176
TSS T0659-6	S. Tibet	29N	85.5E	Malashan gneiss dome	Paiku pluton in Malashan gneiss dome	TSS granite	W.R.	Tourmaline leucogranite			348	37.3	26.963	0.7602	16	4.12	1.19	0.175
TSS T0659-11	S. Tibet	29N	85.5E	Malashan gneiss dome	Paiku pluton in Malashan gneiss dome	TSS granite	W.R.	Two-mica granite			327	70.9	13.329	0.732263	14	7.29	2.11	0.175
TSS T0659-12	S. Tibet	29N	85.5E	Malashan gneiss dome	Paiku pluton in Malashan gneiss dome	TSS granite	W.R.	Two-mica granite			292	119	7.091	0.747446	16	5.42	1.5	0.167
TSS T0659-13	S. Tibet	29N	85.5E	Malashan gneiss dome	Paiku pluton in Malashan gneiss dome	TSS granite	W.R.	Two-mica granite			349	75.6	13.341	0.747321	17	6.16	1.89	0.186
TSS T0659-14	S. Tibet	29N	85.5E	Malashan gneiss dome	Paiku pluton in Malashan gneiss dome	TSS granite	W.R.	Two-mica granite			333	63.5	15.155	0.748351	21	6.85	1.9	0.168
TSS T0474-1	S.E. Lha	29N	92E	Yardoi gneiss dome	Yardoi gneiss dome	TSS granite	W.R.	Two-mica granite			114	373	0.8833	0.715565	14	4.32	21.5	0.1214
TSS T0474-2	S.E. Lha	29N	92E	Yardoi gneiss dome	Yardoi gneiss dome	TSS granite	W.R.	Two-mica granite			110	398	0.7987	0.714672	15	4.43	22.7	0.1179
TSS T0474-3	S.E. Lha	29N	92E	Yardoi gneiss dome	Yardoi gneiss dome	TSS granite	W.R.	Two-mica granite			158	317	1.4404	0.716349	12	4.52	23	0.1187
TSS T0686-1	S.E. Lha	29N	92E	Yardoi gneiss dome	Yardoi gneiss dome		W.R.	Two-mica granite			192	337				4.34	20.7	
TSS T0686-2	S.E. Lha	29N	92E	Yardoi gneiss dome	Yardoi gneiss dome		W.R.	Two-mica granite			185	324				3.87	18.9	
TSS T0686-3	S.E. Lha	29N	92E	Yardoi gneiss dome	Yardoi gneiss dome		W.R.	Two-mica granite			192	311				5.19	24.9	
TSS T391	S.E. Lha	29N	92E	Yardoi gneiss dome	Dala	TSS granite	W.R.	Two-mica granite			175	388	1.4404	0.712092	14	4.35	22	0.1194
TSS T0391-1	S.E. Lha	29N	92E	Yardoi gneiss dome	Dala	TSS granite	W.R.	Two-mica granite			156	374	1.3035	0.712044	16	3.31	15.4	0.1298
TSS T0391-2	S.E. Lha	29N	92E	Yardoi gneiss dome	Dala	TSS granite	W.R.	Two-mica granite			153	341	1.2055	0.718918	24	3.8	16.9	0.1358
TSS T0391-3	S.E. Lha	29N	92E	Yardoi gneiss dome	Dala	TSS granite	W.R.	Two-mica granite			149	361	1.2967	0.715153	15	3.33	15.8	0.1273
TSS T0685-1	S.E. Lha	29N	92E	Yardoi gneiss dome	Dala		W.R.	Two-mica granite			136	388				5.01	25.8	
TSS T0685-2	S.E. Lha	29N	92E	Yardoi gneiss dome	Dala		W.R.	Two-mica granite			156	355				4.46	22.4	
TSS T0684-1	S.E. Lha	29N	92E	Yardoi gneiss dome	Ridang	TSS granite	W.R.	Subvolcanic porphyritic leucogranite			241	34.9	19.9567	0.729162	12	1.05	3.57	0.1779
TSS T0684-2	S.E. Lha	29N	92E	Yardoi gneiss dome	Ridang	TSS granite	W.R.	Subvolcanic porphyritic leucogranite			212	78.6	7.7949	0.720797	14	1.21	3.52	0.208
TSS T0684-3	S.E. Lha	29N	92E	Yardoi gneiss dome	Ridang	TSS granite	W.R.	Subvolcanic porphyritic leucogranite			196	40.8	13.8833	0.724812	15	0.91	2.79	0.1973
TSS T0684-4	S.E. Lha	29N	92E	Yardoi gneiss dome	Ridang	TSS granite	W.R.	Subvolcanic porphyritic leucogranite			202	47	12.4209	0.723606	14	1.11	4.21	0.1595
TSS T0684-5	S.E. Lha	29N	92E	Yardoi gneiss dome	Ridang	TSS granite	W.R.	Subvolcanic porphyritic leucogranite			196	62	9.1361	0.722347	15	1.17	3.46	0.2046
TSS T0684-6	S.E. Lha	29N	92E	Yardoi gneiss dome	Ridang	TSS granite	W.R.	Subvolcanic porphyritic leucogranite			275	44.4	17.8998	0.729088	24	0.89	2.69	0.2002
TSS T0684-7	S.E. Lha	29N	92E	Yardoi gneiss dome	Ridang	TSS granite	W.R.	Subvolcanic porphyritic leucogranite			160	27.2	17	0.726391	16	0.61	1.76	0.2097
TSS T0471-1	S.E. Lha	29N	92E	Yardoi gneiss dome	Yardoi gneiss dome	TSS granite	W.R.	Leucogranite			103	38.5	7.7317	0.7205	15	2.87	4.23	0.4105
TSS T0471-2	S.E. Lha	29N	92E	Yardoi gneiss dome	Yardoi gneiss dome	TSS granite	W.R.	Leucogranite			107	45.1	6.8565	0.715486	15	0.81	2.52	0.1945
TSS T0471-3	S.E. Lha	29N	92E	Yardoi gneiss dome	Yardoi gneiss dome	TSS granite	W.R.	Leucogranite			130	55.7	6.7451	0.71536	15	1.63	6.48	0.1522
TSS T0471-4	S.E. Lha	29N	92E	Yardoi gneiss dome	Yardoi gneiss dome	TSS granite	W.R.	Leucogranite			104	106	2.8355	0.715106	14	0.78	3.17	0.1489
TSS T0471-5	S.E. Lha	29N	92E	Yardoi gneiss dome	Yardoi gneiss dome	TSS granite	W.R.	Leucogranite			126	90.2	4.037	0.715393	15	0.82	3.27	0.1517
HHC 602008	E. Himal	92E		Arunachal leucogranites	TSS granite	W.R.	Leucogranite				279.4	190.5	4.294	0.824754	1.3E-05	10.6	46	0.1398
HHC 602009	E. Himal	92E		Arunachal leucogranites	TSS granite	W.R.	Leucogranite				169.5	108	4.5826	0.799797	1.7E-05	7.2	32.9	0.133
HHC 602010	E. Himal	92E		Arunachal leucogranites	TSS granite	W.R.	Leucogranite				99.1	66.3	4.3621	0.804067	1.4E-05	3.2	12.8	0.151
TSS T263	E. Himal	92E		Tsona leucogranites	TSS granite	W.R.	Leucogranite				408.9	64.2	18.547	0.764508	2.4E-05	4.6	17.2	0.1612
TSS T264	E. Himal	92E		Tsona leucogranites	TSS granite	W.R.	Leucogranite				436	36.7	34.5645	0.766703	1.3E-05	3.6	12.1	0.1779
TSS T265	E. Himal	92E		Tsona leucogranites	TSS granite	W.R.	Leucogranite				289.6	43.4	19.4479	0.782315	1.6E-05	3	9.8	0.1877
HHC 602005	E. Himal	92E		Arunachal crystalline	HHC	W.R.	Pelite				69.8	40.7	5.0497	0.876757	1.6E-05	5.5	27.5	0.1212
HHC 602011	E. Himal	92E		Arunachal crystalline	HHC	W.R.	Metagranite				343.5	11.9	91.5567	1.709545	2.3E-05	11.6	66	0.1067
HHC 602012	E. Himal	92E		Arunachal crystalline	HHC	W.R.	Orthogneiss				149.4	134.4	3.2308	0.752523	1.2E-05	3.4	13.7	0.1485
TSS 405008	E. Himal	92E	Dala igneous complex	Dala granitoids	TSS granite	W.R.	Granodiorite				125.4	340.2	7.859	0.718534	1.5E-05	4.5	22.5	0.1207
TSS 405011	E. Himal	92E	Dala igneous complex	Dala granitoids	TSS granite	W.R.	Granodiorite				124.3	336.1	7.833	0.718602	1.6E-05	3.9	19.2	0.1217
TSS 405013	E. Himal	92E	Dala igneous complex	Dala granitoids	TSS granite	W.R.	Granodiorite				144.7	280.7	5.6192	0.717773	1.7E-05	4.2	20.1	0.1248
TSS 410007	E. Himal	92E	Dala igneous complex	Dala granitoids	TSS granite	W.R.	Monzodiorite				122.7	478.6	11.2989	0.717999	2.1E-05	5.7	29.4	0.1177
TSS 410008	E. Himal	92E	Dala igneous complex	Dala granitoids	TSS granite	W.R.	Granodiorite				116.2	348.3	8.6757	0.71858	8E-06	6.1	29.9	0.1229

Table SII-2 (…/…)

	Ech.#	Region	River	Locality	Formation	Category	Type	Rock type	North	East	Date	Rb SII	Sr SII	87Rb/86Sr	87Sr/86Sr S	2s.d.	Sm SII	Nd SII	147Sm/144Nd
TSS	410009	E. Himal	92E	Dala igneous complex	Dala granitoids	TSS granite	W.R.	Granodiorite				121.1	344.3	8.2361	0.718523	1.2E-05	5.8	31.4	0.1118
TSS	410010	E. Himal	92E	Dala igneous complex	Dala granitoids	TSS granite	W.R.	Granodiorite				90.5	425.8	13.6286	0.717663	2.9E-05	6.8	35.8	0.1142
TSS	410012	E. Himal	92E	Dala igneous complex	Dala granitoids	TSS granite	W.R.	Granodiorite				113.3	548.3	14.0162	0.716476	0.00001	1.8	8.5	0.1258
TSS	310019	E. Himal	92E	Yala-Xiangbo dome and igneous complex	Yala-Xiangbo leucogranites	TSS granite	W.R.	Leucogranite				151.5	128.5	2.4565	0.715531	1.8E-05	2.5	10.4	0.1426
TSS	310021	E. Himal	92E	Yala-Xiangbo dome and igneous complex	Yala-Xiangbo leucogranites	TSS granite	W.R.	Leucogranite				630.2	74.9	0.3472	0.808553	1.7E-05	3	8.5	0.2138
TSS	310037	E. Himal	92E	Yala-Xiangbo dome and igneous complex	Yala-Xiangbo leucogranites	TSS granite	W.R.	Leucogranite				400.3	128.3	0.9284	0.715601	1.2E-05	1.1	4.1	0.1567
TSS	310038	E. Himal	92E	Yala-Xiangbo dome and igneous complex	Yala-Xiangbo leucogranites	TSS granite	W.R.	Leucogranite				274.9	29.6	0.312	0.729187	2.1E-05	1.7	4.6	0.223
TSS	310008	E. Himal	92E	Yala-Xiangbo dome and igneous complex	Yala-Xiangbo pelites	TSS	W.R.	Pelite				240.5	152.9	1.842	0.718011	1.6E-05	7.8	44.8	0.105
TSS	310013	E. Himal	92E	Yala-Xiangbo dome and igneous complex	Yala-Xiangbo pelites	TSS	W.R.	Pelite				144.3	174.5	3.5038	0.719065	1.2E-05	5.1	26.7	0.1154
TSS	310015	E. Himal	92E	Yala-Xiangbo dome and igneous complex	Yala-Xiangbo pelites	TSS	W.R.	Pelite				151.7	202.2	3.8598	0.716368	1.6E-05	4.8	23.8	0.1213
TSS	310029	E. Himal	92E	Yala-Xiangbo dome and igneous complex	Yala-Xiangbo pelites	TSS	W.R.	Pelite				275.4	237.4	2.4966	0.715313	1.6E-05	6.4	34.2	0.1135
TSS	310034	E. Himal	92E	Yala-Xiangbo dome and igneous complex	Yala-Xiangbo pelites	TSS	W.R.	Pelite				222.2	55.1	0.7279	0.845424	1.9E-05	4.8	25.4	0.1154
TSS	310039	E. Himal	92E	Yala-Xiangbo dome and igneous complex	Yala-Xiangbo pelites	TSS	W.R.	Pelite				275.4	111.1	1.1691	0.718509	1.3E-05	5.5	30.9	0.1074
TSS	310014	E. Himal	92E		Tethyan mafic	TSS	W.R.	Mafic				0.6	297.9	1436.8	0.708029	1.4E-05	3	9.9	0.1808
THB	QC4	N. Lhasa	30N	90E	Nyainqentanglha Shan crystalline complex	Transhimalaya	W.R.	two-mica-granite				335	37.4	26.03	0.75283		2.3	7.5	
THB	BD-7-00	N. Lhasa	30N	90E	Nyainqentanglha Shan crystalline complex	Transhimalaya	W.R.	none				236.0	336.0	53.18	0.71493		3.9	25.8	
THB	BD-8-00	N. Lhasa	30N	90E	Nyainqentanglha Shan crystalline complex	Transhimalaya	W.R.	none				190	97	3.91	0.71369		3.06	18	
THB	QC5	N. Lhasa	30N	90E	Nyainqentanglha Shan crystalline complex	Transhimalaya	W.R.	two-mica-granite				599	115	15.09	0.72379		2.4	9	
THB	99-5-11-2	N. Lhasa	30N	90E	Nyainqentanglha Shan crystalline complex		W.R.	granite				326.67	121.48	6.38	0.7099		5.61	28.96	
THB	99-5-9-3	N. Lhasa	30N	90E	Nyainqentanglha Shan crystalline complex	Transhimalaya	W.R.	mylonite-gneiss				318.62	235.71	2.85	0.70757		3.58	19.17	
THB	QC2	N. Lhasa	30N	90E	Nyainqentanglha Shan crystalline complex	Transhimalaya	W.R.	biotite-granite				331	122	7.85	0.71431		16.2	98.5	
THB	QC14	N. Lhasa	30N	90E	Nyainqentanglha Shan crystalline complex	Transhimalaya	W.R.	two-mica-granite				435	290	4.34	0.70791		6.3	49.3	
THB	ND-4-00	N. Lhasa	30N	90E	Nyainqentanglha Shan crystalline complex		W.R.	garnet-two-mica-granite				427.52	381.68	37.18	0.70444		3.6	33.62	
THB	BD-3-00	N. Lhasa	30N	90E	Nyainqentanglha Shan crystalline complex	Transhimalaya	W.R.	none				444	144	14.69	0.71597		7.15	41.2	
THB	QC17	N. Lhasa	30N	90E	Nyainqentanglha Shan crystalline complex	Transhimalaya	W.R.	granite				392	106	10.7	0.71155		5.5	25.9	
THB	QC18	N. Lhasa	30N	90E	Nyainqentanglha Shan crystalline complex	Transhimalaya	W.R.	biotite-granite				335.0	113.0	8.58	0.71125		4.6	21.8	
THB	QC19	N. Lhasa	30N	90E	Nyainqentanglha Shan crystalline complex	Transhimalaya	W.R.	biotite-granite				409	56.6	20.92	0.71305		5.3	20.6	
THB	99-5-4-2	N. Lhasa	30N	90E	Nyainqentanglha Shan crystalline complex		W.R.	biotite-granite				272.01	402.42	12.47	0.71303		9.58	59.81	
THB	ND-3-00	N. Lhasa	30N	90E	Nyainqentanglha Shan crystalline complex		W.R.	granite				244	334				8.1	44.9	
THB	99-5-2-1a	N. Lhasa	30N	90E	Nyainqentanglha Shan crystalline complex	Transhimalaya	W.R.	granite						5.67	0.71143				
THB	ND-15-00	N. Lhasa	30N	90E	Nyainqentanglha Shan crystalline complex		W.R.	none				278	334				5.71	31.9	
THB	99-5-5-4d	N. Lhasa	30N	90E	Nyainqentanglha Shan crystalline complex	Transhimalaya	W.R.	none				203	168	3.5	0.70906		4.9	27.8	
THB	ND-14-00b	N. Lhasa	30N	90E	Nyainqentanglha Shan crystalline complex		W.R.	granite				218	281				2.81	11.7	
THB	99-5-9-4a	N. Lhasa	30N	90E	Nyainqentanglha Shan crystalline complex	Transhimalaya	W.R.	orthogneiss				164	73	6.51	0.72415		4.25	20.5	
THB	99-5-7-2a	N. Lhasa	30N	90E	Nyainqentanglha Shan crystalline complex		W.R.	granite				266	20	38.58	0.73617		7.45	20.5	
THB	ND-22-00	N. Lhasa	30N	90E	Nyainqentanglha Shan crystalline complex		W.R.	none				221	57				6.99	27.1	
THB	99-5-11-1a	N. Lhasa	30N	90E	Nyainqentanglha Shan crystalline complex	Transhimalaya	W.R.	biotite-granite				352	517	1.97	0.70964		4.46	29.5	
THB	99-5-7-3b	N. Lhasa	30N	90E	Nyainqentanglha Shan crystalline complex	Transhimalaya	W.R.	granite				210	134	4.54	0.71164		4.08	24.2	
THB	99-7-26-1b	N. Lhasa	30N	90E	Nyainqentanglha Shan crystalline complex		W.R.	two-mica-granite				415.0	62.0	19.48	0.77006		3.4	14.4	
THB	QC3b	N. Lhasa	30N	90E	Nyainqentanglha Shan crystalline complex	Transhimalaya	W.R.	orthogneiss						3.79	0.76973				
THB	QC7	N. Lhasa	30N	90E	Nyainqentanglha Shan crystalline complex	Transhimalaya	W.R.	biotite-granite						7.55	0.70958				
THB	QC8	N. Lhasa	30N	90E	Nyainqentanglha Shan crystalline complex	Transhimalaya	W.R.	granodiorite						5.53	0.71398				
THB	QC11a	N. Lhasa	30N	90E	Nyainqentanglha Shan crystalline complex	Transhimalaya	W.R.	granulite						3.99	0.72691				
THB	QC12b-a	N. Lhasa	30N	90E	Nyainqentanglha Shan crystalline complex	Transhimalaya	W.R.	orthogneiss						10.36	0.71106				
THB	99-5-5-4c	N. Lhasa	30N	90E	Nyainqentanglha Shan crystalline complex		W.R.	none						3.07	0.70916				
THB	99-7-27-3c	N. Lhasa	30N	90E	Nyainqentanglha Shan crystalline complex		W.R.	dike						10.92	0.72107				
LH o	NBH-22	Bhutan			Paro formation		W.R.	Schist									6.62	24.86	
LH o	BU07-73	Bhutan			Paro formation		W.R.	Quartzite									2.282	8.165	
LH o	BU07-75	Bhutan			Paro formation		W.R.	Quartzite									7.552	28.97	
LH o	BU07-76	Bhutan			Paro formation		W.R.	Quartzite									1.014	5.283	
LH o	BU07-77	Bhutan			Paro formation		W.R.	Quartzite									0.848	3.235	
LH o	BU07-83	Bhutan			Paro formation		W.R.	Orthogneiss									4.492	17.027	
HHC	BKS-2A	N. Kathn	Bhote Koshi				W.R.	Garnetiferou	27.973	85.963							7.8417	40.9026	
HHC	BKS-2B	N. Kathn	Bhote Koshi				W.R.	Psammitic a	27.971	85.961							7.0621	36.2985	
HHC	BKS-3	N. Kathn	Bhote Koshi				W.R.	Garnet–kyan	27.971	85.96							10.0598	53.0707	
HHC	BKS-4	N. Kathn	Bhote Koshi				W.R.	Garnetiferou	27.97	85.96							9.2288	49.1331	
HHC	BKS-23	N. Kathn	Bhote Koshi				W.R.	Kyanite–garr	27.969	85.959							7.7469	38.2112	
HHC	BKS-22	N. Kathn	Bhote Koshi				W.R.	Micaceous q	27.969	85.959							4.6708	23.2022	
LH	BKS-10	N. Kathn	Bhote Koshi				W.R.	Garnetiferou	27.966	85.958							6.102	33.675	
LH	BKS-9	N. Kathn	Bhote Koshi				W.R.	Garnetiferou	27.962	85.956							5.83	31.117	

Table SII-2 (…/…)

Ech.#	Region	River	Locality	Formation	Category	Type	Rock type	North	East	Date	Rb Sil	Sr Sil	87Rb/86Sr	87Sr/86Sr S	2s.d.	Sm Sil	Nd Sil	147Sm/144Nd
LH 51x	Sikkim	North Sikkim	Gangtok-Mangan waterwheel			W.R.	garnet-staur	N27	25.159	E88 37.530						29.18	5.43	0.112024
LH 53	Sikkim	North Sikkim	Rang Rang			W.R.	garnet schist	N27	27.958	E88 31.473						49.98	8.871	0.10685
HHC 57	Sikkim	North Sikkim	Myang			W.R.	garnet fibroli	N27	31.642	E88 36.396						38.56	7.687	0.12001
LH 59a	Sikkim	North Sikkim	Singhik			W.R.	garnet-staur	N27	30.956	E88 33.454						31.07	5.789	0.112165
HHC 64a	Sikkim	North Sikkim	Toong			W.R.	sillimanite m	N27	33.637	E88 39.152						46.48	8.818	0.114209
HHC 66	Sikkim	North Sikkim	Chungthang-Lachung			W.R.	garnet gneis	N27	37.233	E88 39.729						39.97	7.802	0.117508
LH 94	Sikkim	North Sikkim	Sangkalang			W.R.	garnet mica	N27	31.965	E88 30.591						55.03	9.828	0.107513
LH 97	Sikkim	North Sikkim	Mangan petrol pump			W.R.	mica schist	N27	29.534	E88 31.686						41.12	7.305	0.106946
LH 82	Sikkim	Kalimpong h	Pedong			W.R.	garnet mica	N27	07.153	E88 35.209						36.71	6.699	0.109856
HHC 106	Sikkim	Kalimpong h	Rishop			W.R.	garnet mica	N27	06.357	E88 38.734						42.6	8.381	0.118436
LH 123	Sikkim	Kalimpong h	Neora valley			W.R.	fibrolite mica	N27	06.170	E88 40.405						43.24	8.217	0.114399
LH 147	Sikkim	Kalimpong h	Lava road			W.R.	kyanite-fibrol	N27	01.742	E88 42.062						37.36	7.244	0.116726
LH 149	Sikkim	Kalimpong h	Lava road			W.R.	chlorite-mus	N27	00.124	E88 41.876						38.31	7.192	0.113014
HHC 156	Sikkim	Kalimpong h	Lolaygoan			W.R.	garnet mica	N27	04.290	E88 36.886						32.32	6.182	0.115147
LH 159	Sikkim	Kalimpong h	Lolaygoan			W.R.	fibrolite mica	N27	01.117	E88 33.829						38.33	7.282	0.114369
HHC 214x	Sikkim	West Sikkim	Yoksom			W.R.	garnet-kyani	N27	21.362	E88 13.237						49.6	9.486	0.115133
LH 246a	Sikkim	West Sikkim	Dentam			W.R.	sillimanite m	N27	16.456	E88 10.333						53.43	9.852	0.111003
HHC 267	Sikkim	West Sikkim	Kabur			W.R.	garnet-2nd s	N27	15.512	E88 09.255						36.8	7.117	0.116425
LH 275	Sikkim	West Sikkim	Pelling			W.R.	garnet fibroli	N27	18.308	E88 12.495						50.81	9.461	0.112095
HHC 278	Sikkim	West Sikkim	Pelling			W.R.	garnet-staur	N27	18.015	E88 13.286						47.13	9.431	0.120464
HHC BH-220	NW Bhu	Proche TSS	Masang Kang			W.R.					0.34	14				0.06	0.1	
HHC BH-274	NW Bhu	Proche TSS	Masang Kang			W.R.					8	6						
HHC BH-175A	NW Bhu	Proche TSS	Masang Kang			W.R.					5.38	132				4.48	13.94	
HHC BH-254	NW Bhu	Proche TSS	Masang Kang			W.R.					103	106				4.21	12.49	
HHC BH-256	NW Bhu	Proche TSS	Masang Kang			W.R.					23.14	68				2.39	7.84	
HHC BH-203	NW Bhu	Proche TSS	Masang Kang			W.R.					22.93	55				3.17	11.68	
HHC BH-217A	NW Bhu	Proche TSS	Masang Kang			W.R.					109.05	50				8.69	35.84	0.141523
HHC BH-219	NW Bhu	Proche TSS	Masang Kang			W.R.					5.35	39				1.87	6.91	0.158144
HHC BH-245	NW Bhu	Proche TSS	Masang Kang			W.R.					35.22	125				28.78	64	
HHC BH-246	NW Bhu	Proche TSS	Masang Kang			W.R.					42.62	429				2.58	9.36	
HHC BH-249	NW Bhu	Proche TSS	Masang Kang			W.R.					51	101					21	
HHC BH-252	NW Bhu	Proche TSS	Masang Kang			W.R.					84	173					14	
HHC BH-253	NW Bhu	Proche TSS	Masang Kang			W.R.					45.63	237				3.71	16.62	
HHC BH-255	NW Bhu	Proche TSS	Masang Kang			W.R.					10	107					17	
HHC BH-257	NW Bhu	Proche TSS	Masang Kang			W.R.					47.55	103				3.06	13.18	
HHC BH-266	NW Bhu	Proche TSS	Masang Kang			W.R.					45	81					14	
HHC BH-292	NW Bhu	Proche TSS	Masang Kang			W.R.					10	88					11	0.172029
HHC BH-268	NW Bhu	Proche TSS	Masang Kang			W.R.					68.37	48				12.56	55.48	
TSS CN1341	S.E. Lhasa			Cuonadong gneiss dome	TSS granite	W.R.	leucogranite				516.3	30.01	49.77	0.72762	1.9E-05	2.39	6.47	0.2248
TSS CN1341-1	S.E. Lhasa			Cuonadong gneiss dome	TSS granite	W.R.	leucogranite				522.3	30.11	50.18	0.746102	1.3E-05	2.26	6.16	0.2233
TSS CN1353	S.E. Lhasa			Cuonadong gneiss dome	TSS granite	W.R.	leucogranite				365.7	66.81	15.83	0.73087	0.00001	1.52	5.13	0.1803
TSS CN1353-1	S.E. Lhasa			Cuonadong gneiss dome	TSS granite	W.R.	leucogranite				354.9	66.02	15.55	0.730832	1.3E-05	1.26	4.07	0.188
TSS CN1354	S.E. Lhasa			Cuonadong gneiss dome	TSS granite	W.R.	leucogranite				317.6	91.23	10.07	0.727906	9E-06	3.01	10.82	0.1695
TSS T0832-GN	S. Tibet	86°E		Xiaru dome	TSS	W.R.	granitic gneiss				585	71.1	23.78	0.85541	15	1.95	7.39	0.16
TSS T0832-GN	S. Tibet	86°E		Xiaru dome		W.R.	granitic gneiss				851	52.6				5.72	22.6	
TSS T0832-GN	S. Tibet	86°E		Xiaru dome	TSS	W.R.	granitic gneiss				587	53.8	31.53	0.894211	15	4.3	17.3	0.15
TSS T0832-GN	S. Tibet	86°E		Xiaru dome	TSS	W.R.	granitic gneiss				567	79.8	20.53	0.835204	15	1.87	6.75	0.17
TSS T0832-GN	S. Tibet	86°E		Xiaru dome		W.R.	granitic gneiss				468	84.1	16.08	0.803396	15	3.97	13	0.19
TSS T0832-GN	S. Tibet	86°E		Xiaru dome		W.R.	granitic gneiss				563	45.8				3.8	14.7	
TSS T0832-GN	S. Tibet	86°E		Xiaru dome	TSS	W.R.	granitic gneiss				780	69	32.67	0.888121	14	1.74	6.38	0.17
TSS T0833-1	S. Tibet	86°E		Xiaru dome		W.R.	granitic gneiss				526	98.4				2.17	8.68	
TSS T0833-2	S. Tibet	86°E		Xiaru dome		W.R.	granitic gneiss				19.1	20.7				2.05	6.72	
TSS T0833-3	S. Tibet	86°E		Xiaru dome		W.R.	granitic gneiss				71.2	27.3				3.38	15.5	
TSS T0833-4	S. Tibet	86°E		Xiaru dome		W.R.	granitic gneiss				11.4	20.3				3.62	13.1	
TSS T0833-5	S. Tibet	86°E		Xiaru dome		W.R.	granitic gneiss				140	37.5				3.15	14.4	
TSS T0833-6	S. Tibet	86°E		Xiaru dome		W.R.	granitic gneiss				250	63.9				1.99	7.01	
TSS T0833-7	S. Tibet	86°E		Xiaru dome		W.R.	granitic gneiss				433	77.6				1.99	7.41	
TSS T0834-LG-	S. Tibet	86°E		Xiaru dome	TSS	W.R.	granitic gneiss				781	30.4	54.51	0.990181	15	3.44	10.7	0.16
TSS T0834-LG-	S. Tibet	86°E		Xiaru dome	TSS	W.R.	granitic gneiss				540	23.2	43.13	0.944275	18	2.59	8.22	0.16
TSS T0834-LG-	S. Tibet	86°E		Xiaru dome	TSS	W.R.	granitic gneiss				589	22	44.57	0.9589	15	3.28	10.6	0.16

Table SII-2 (…/…)

Ech.#	Region	River	Locality	Formation	Category	Type	Rock type	North	East	Date	Rb SiI	Sr SiI	87Rb/86Sr	87Sr/86Sr S	2s.d.	Sm SiI	Nd SiI	147Sm/144Nd
TSS T0834-LG-	S. Tibet	86°E		Xiaru dome	TSS	W.R.	granitic gneiss				595	20.6	54.63	1.043264	14	3.17	10.5	0.19
TSS T0834-LG-	S. Tibet	86°E		Xiaru dome	TSS	W.R.	granitic gneiss				674	21.8	38.44	0.953378	14	3.36	11.7	0.16
TSS T0834-GN	S. Tibet	86°E		Xiaru dome		W.R.	granitic gneiss				696	36.9				4.23	15.9	
TSS T0834-GN	S. Tibet	86°E		Xiaru dome		W.R.	granitic gneiss				694	46.5				4.6	17.4	
TSS T0834-GN	S. Tibet	86°E		Xiaru dome		W.R.	granitic gneiss				674	43.7				3.97	14.7	
TSS T0834-GN	S. Tibet	86°E		Xiaru dome		W.R.	granitic gneiss				690	36.5				1.77	5.68	
TSS T0834-GN	S. Tibet	86°E		Xiaru dome		W.R.	granitic gneiss				649	48.8				3.36	12.6	
TSS T0835-LG1	S. Tibet	86°E		Xiaru dome		W.R.	granitic gneiss				733	19.2				1.53	3.14	
TSS T0835-LG2	S. Tibet	86°E		Xiaru dome	TSS	W.R.	granitic gneiss				665	27.7	69.38	1.172756	15	3.02	11.1	0.16
TSS T0835-LG3	S. Tibet	86°E		Xiaru dome	TSS	W.R.	granitic gneiss				777	35.6	63.08	1.081933	14	4.51	19.1	0.14
TSS T0835-LG4	S. Tibet	86°E		Xiaru dome	TSS	W.R.	granitic gneiss				613	30.4	58.28	1.112372	16	2.28	8.45	0.16
TSS T0835-LG5	S. Tibet	86°E		Xiaru dome	TSS	W.R.	granitic gneiss				658	30.4	62.55	1.05725	20	3	10.9	0.17
TSS T0835-LG6	S. Tibet	86°E		Xiaru dome		W.R.	granitic gneiss				647	16.9				0.72	1.66	
TSS T0839-LG1	S. Tibet	86°E		Xiaru dome	TSS	W.R.	granitic gneiss				604	44.6	39.14	0.98783	15	3.02	12.2	0.15
TSS T0839-LG2	S. Tibet	86°E		Xiaru dome	TSS	W.R.	granitic gneiss				554	43.6	36.72	0.986412	15	3.17	12.4	0.16
TSS T0839-LG3	S. Tibet	86°E		Xiaru dome	TSS	W.R.	granitic gneiss				593	42.1	40.71	1.002769	15	2.61	10.5	0.15
TSS T0777-A1	S. Tibet		88°E	Lhagoi Kangri dome	TSS	W.R.	granitic gneiss				178	153	3.37	0.737192	8	3.29	14	0.14
TSS T0777-A2	S. Tibet		88°E	Lhagoi Kangri dome	TSS	W.R.	granitic gneiss				191	171	3.23	0.736636	8	3.67	16	0.14
TSS T0777-A3	S. Tibet		88°E	Lhagoi Kangri dome	TSS	W.R.	granitic gneiss				186	151	3.56	0.737548	16	3.47	14.3	0.15
TSS T0777-A4	S. Tibet		88°E	Lhagoi Kangri dome	TSS	W.R.	granitic gneiss				243	118	5.96	0.738734	12	2.82	11.3	0.15
TSS T0777-A5	S. Tibet		88°E	Lhagoi Kangri dome	TSS	W.R.	granitic gneiss				184	166	3.21	0.74188	12	4.68	22	0.13
TSS T0777-B1	S. Tibet		88°E	Lhagoi Kangri dome		W.R.	granitic gneiss				212	45.9				2.08	6.02	
TSS T0777-B2	S. Tibet		88°E	Lhagoi Kangri dome		W.R.	granitic gneiss				230	49				1.79	4.86	
TSS T0777-C1	S. Tibet		88°E	Lhagoi Kangri dome	TSS	W.R.	granitic gneiss				192	145	3.83	0.741996	16	4.59	20.5	0.14
TSS T0777-C2	S. Tibet		88°E	Lhagoi Kangri dome	TSS	W.R.	granitic gneiss				264	85.6	8.92	0.745986	12	3.84	14.8	0.16
TSS T0777-C3	S. Tibet		88°E	Lhagoi Kangri dome	TSS	W.R.	granitic gneiss				185	132	4.06	0.743093	20	4.17	19.8	0.13
TSS T0777-C4	S. Tibet		88°E	Lhagoi Kangri dome	TSS	W.R.	granitic gneiss				166	172	2.79	0.739012	15	5.23	24	0.13
TSS T0777-C5	S. Tibet		88°E	Lhagoi Kangri dome	TSS	W.R.	granitic gneiss				240	97.1	7.15	0.744359	22	3.11	11.3	0.17
TSS T0526-LG-	S. Tibet		90°E	Kangmar dome		W.R.	granitic gneiss				303	61.8				1.69	6.26	
TSS T0526-LG-	S. Tibet		90°E	Kangmar dome		W.R.	granitic gneiss				382	68.3				2.26	7.51	
TSS T0526-LG-	S. Tibet		90°E	Kangmar dome		W.R.	granitic gneiss				330	28.1				2	6.41	
TSS T0526-LG-	S. Tibet		90°E	Kangmar dome		W.R.	granitic gneiss				332	28.2				2.49	8.06	
TSS T0526-LG-	S. Tibet		90°E	Kangmar dome		W.R.	granitic gneiss				206	50.3				3.89	17.6	
TSS T0526-LG-	S. Tibet		90°E	Kangmar dome		W.R.	granitic gneiss				212	50.3				3.25	14.2	
TSS T0527-LG-	S. Tibet		90°E	Kangmar dome		W.R.	granitic gneiss				288	56.9				2.22	7.58	
TSS T0527-LG-	S. Tibet		90°E	Kangmar dome		W.R.	granitic gneiss				305	61.2				1.2	4.23	
TSS T0527-LG-	S. Tibet		90°E	Kangmar dome		W.R.	granitic gneiss				302	33.6				2.42	7.88	
TSS T0527-LG-	S. Tibet		90°E	Kangmar dome		W.R.	granitic gneiss				291	63.2				4.46	21.8	
TSS T0527-LG-	S. Tibet		90°E	Kangmar dome		W.R.	granitic gneiss				322	25.1				2.04	6.11	
TSS T0527-LG-	S. Tibet		90°E	Kangmar dome		W.R.	granitic gneiss				351	31.1				2.1	7	
TSS T0898-1	S. Tibet		88°E	Mabja dome		W.R.	granitic gneiss				333	83.1				10.6	43.8	
TSS T0898-2	S. Tibet		88°E	Mabja dome		W.R.	granitic gneiss				252	74.2				6.49	28.7	
TSS T0898-3	S. Tibet		88°E	Mabja dome		W.R.	granitic gneiss				189	72.7				8.96	43.3	
TSS T0898-4	S. Tibet		88°E	Mabja dome		W.R.	granitic gneiss				320	86.5				9.6	46.6	
HHC T0812-A-1	N.E. Ner	Close to TSS	86°E	Gyirong	HHC	W.R.	granitic gneiss				213	71.3	8.63	0.781718	20	6.6	30.4	0.13
HHC T0812-A-2	N.E. Ner	Close to TSS	86°E	Gyirong	HHC	W.R.	granitic gneiss				273	86.6	9.11	0.780233	18	7.49	33.8	0.13
HHC T0812-A-3	N.E. Ner	Close to TSS	86°E	Gyirong	HHC	W.R.	granitic gneiss				251	79.5	9.12	0.779024	14	7.91	36	0.13
HHC T0812-A-4	N.E. Ner	Close to TSS	86°E	Gyirong	HHC	W.R.	granitic gneiss				351	97.6	10.39	0.778114	15	5.68	25.2	0.14
HHC T0812-B-1	N.E. Ner	Close to TSS	86°E	Gyirong	HHC	W.R.	granitic gneiss				219	82	7.72	0.785905	16	5.61	23.8	0.14
HHC T0812-B-2	N.E. Ner	Close to TSS	86°E	Gyirong	HHC	W.R.	granitic gneiss				241	68	10.24	0.790804	15	6.46	27.8	0.14
HHC T0812-B-3	N.E. Ner	Close to TSS	86°E	Gyirong	HHC	W.R.	granitic gneiss				249	86.2	8.35	0.786131	14	6.47	30	0.13
HHC T0814--1	N.E. Ner	Close to TSS	86°E	Gyirong	HHC	W.R.	granitic gneiss				224	80.4	8.05	0.772889	14	10.6	47.8	0.13
HHC T0814--2	N.E. Ner	Close to TSS	86°E	Gyirong	HHC	W.R.	granitic gneiss				243	78.3	8.97	0.771145	13	9.48	43.4	0.13
HHC T0814--3	N.E. Ner	Close to TSS	86°E	Gyirong		W.R.	granitic gneiss				213	77.6				10.6	47.5	
HHC T0814--4	N.E. Ner	Close to TSS	86°E	Gyirong		W.R.	granitic gneiss				242	98.9				11.9	54.6	
HHC T0814--5	N.E. Ner	Close to TSS	86°E	Gyirong	HHC	W.R.	granitic gneiss				219	74.6	8.48	0.761903	16	5.13	20	0.16
HHC T0814--6	N.E. Ner	Close to TSS	86°E	Gyirong	HHC	W.R.	granitic gneiss				218	56.6	11.13	0.787114	14	2.94	9.93	0.18
HHC ZC10-04	N.E. Ner	Close to TSS	86°E	Gyirong		W.R.	granitic gneiss				266	90.1				5.59	27.1	
HHC ZC10-06	N.E. Ner	Close to TSS	86°E	Gyirong		W.R.	granitic gneiss				304	79.4				6.84	30.4	
HHC ZC10-07	N.E. Ner	Close to TSS	86°E	Gyirong		W.R.	granitic gneiss				319	84.8				6.13	28.6	
HHC T0512-2	Bhutan		90°E	Yadong		W.R.	granitic gneiss				228	56				4.06	20.8	
HHC T0512-3	Bhutan		90°E	Yadong		W.R.	granitic gneiss				274	31				2.41	10.9	
HHC T0512-6	Bhutan		90°E	Yadong		W.R.	granitic gneiss				312	18				2.92	7.84	
HHC T0252-1	E. syntaxis			Namche Barwa	HHC	W.R.	granitic gneiss				278	108	7.5	0.785768	12	8.56	44.1	0.12
HHC T0252-2	E. syntaxis			Namche Barwa	HHC	W.R.	granitic gneiss				263	100	7.67	0.788657	13	5.23	24.4	0.13
HHC T0252-12-	E. syntaxis			Namche Barwa	HHC	W.R.	granitic gneiss				129	319	1.17	0.72404	11	6.42	32.7	0.12
HHC T0252-12-	E. syntaxis			Namche Barwa	HHC	W.R.	granitic gneiss				132	325	1.18	0.724118	12	6.49	30.5	0.13
HHC T0252-12-	E. syntaxis			Namche Barwa	HHC	W.R.	granitic gneiss				120	313	1.11	0.724072	9	5.94	27.9	0.13
T0748						W.R.	granitic gneiss				419	116				7.95	49	

Table SII-2 (…/…)

Ech.#	Region	River	Locality	Formation	Category	Type	Rock type	North	East	Date	Rb Sil	Sr Sil	87Rb/86Sr	87Sr/86Sr S	2s.d.	Sm Sil	Nd Sil	147Sm/144Nd
TSS T0646-2	S. Tibet	29°N	86°E	Malashan gneiss dome	TSS granite	W.R.	Two-mica granites				194	192	2.9201	0.745158	22	3.65	16.8	0.1314
TSS T0646-1	S. Tibet	29°N	86°E	Malashan gneiss dome	TSS granite	W.R.	Two-mica granites				172	148	3.3586	0.745316	14	3.24	14.9	0.1316
TSS T0646-3	S. Tibet	29°N	86°E	Malashan gneiss dome	TSS granite	W.R.	Two-mica granites				171	146	3.3849	0.746425	16	5.27	24.8	0.1286
TSS T0646-4	S. Tibet	29°N	86°E	Malashan gneiss dome	TSS granite	W.R.	Two-mica granites				182	166	3.1686	0.745396	14	3.58	17.7	0.1224
TSS T0646-5	S. Tibet	29°N	86°E	Malashan gneiss dome	TSS granite	W.R.	Two-mica granites				181	150	3.4873	0.746377	14	3.46	15.8	0.1325
TSS T0647-1	S. Tibet	29°N	86°E	Malashan gneiss dome	TSS granite	W.R.	Two-mica granites				184	168	3.1652	0.745724	12	3.88	17.6	0.1334
TSS T0647-2	S. Tibet	29°N	86°E	Malashan gneiss dome	TSS granite	W.R.	Two-mica granites				175	156	3.242	0.74592	12	4.2	19.5	0.1303
TSS T0647-3	S. Tibet	29°N	86°E	Malashan gneiss dome	TSS granite	W.R.	Two-mica granites				196	162	3.4965	0.74593	22	3.64	16.5	0.1335
TSS T0658	S. Tibet	29°N	86°E	Malashan gneiss dome	TSS granite	W.R.	Two-mica granites				205	162	3.6571	0.749062	15	3.81	16.6	0.1389
TSS T0661-1A	S. Tibet	29°N	86°E	Malashan gneiss dome	TSS granite	W.R.	Two-mica granites				187	172	3.142	0.743283	13	3.74	15.3	0.1479
TSS T0661-2A	S. Tibet	29°N	86°E	Malashan gneiss dome	TSS granite	W.R.	Two-mica granites				172	193	2.5755	0.742167	13	4.08	18.4	0.1342
TSS T0661-3A	S. Tibet	29°N	86°E	Malashan gneiss dome	TSS granite	W.R.	Two-mica granites				176	180	2.8258	0.74061	15	3.84	17.2	0.1351
TSS T0661-4	S. Tibet	29°N	86°E	Malashan gneiss dome	TSS granite	W.R.	Two-mica granites				185	180	2.9703	0.739806	17	3.76	17.4	0.1307
TSS TMLS-09A	S. Tibet	29°N	86°E	Malashan gneiss dome	TSS granite	W.R.	Two-mica granites				203	187	3.1373	0.749162	18	4.27	20.3	0.1273
TSS TMLS-09B	S. Tibet	29°N	86°E	Malashan gneiss dome	TSS granite	W.R.	Two-mica granites				203	173	3.3912	0.748864	11	4.69	21.8	0.1302
TSS T0659-3	S. Tibet	29°N	86°E	Malashan gneiss dome	TSS granite	W.R.	Leucogranites				369	38.9	27.4141	0.763382	13	0.94	3.36	0.1693
TSS T0659-4	S. Tibet	29°N	86°E	Malashan gneiss dome	TSS granite	W.R.	Leucogranites				338	38.1	25.6383	0.761717	13	0.98	3.37	0.1759
TSS T0659-6	S. Tibet	29°N	86°E	Malashan gneiss dome	TSS granite	W.R.	Leucogranites				348	37.3	26.963	0.7602	16	1.19	4.12	0.1747
TSS T0659-11	S. Tibet	29°N	86°E	Malashan gneiss dome	TSS granite	W.R.	Leucogranites				327	70.9	13.3291	0.732263	14	2.11	7.29	0.1751
TSS T0659-12	S. Tibet	29°N	86°E	Malashan gneiss dome	TSS granite	W.R.	Leucogranites				292	119	7.0914	0.747446	16	1.5	5.42	0.1674
TSS T0659-13	S. Tibet	29°N	86°E	Malashan gneiss dome	TSS granite	W.R.	Leucogranites				349	75.6	13.3414	0.747321	17	1.89	6.16	0.1856
TSS T0659-14	S. Tibet	29°N	86°E	Malashan gneiss dome	TSS granite	W.R.	Leucogranites				333	63.5	15.1554	0.748351	21	1.9	6.85	0.1678
TSS T0647-4	S. Tibet	29°N	86°E	Malashan gneiss dome	TSS	W.R.	Graphite-bearing schists				40.1	798	0.1452	0.708424	15	2.84	15.1	0.1138
TSS T0647-5	S. Tibet	29°N	86°E	Malashan gneiss dome	TSS	W.R.	Graphite-bearing schists				49.6	794	0.1805	0.708496	15	3.18	18.1	0.1063
LH/H GMH 1	N.W. Ne	30.5°N	82°E	Gurla Mandhata metamorphic core complex		W.R.	schist				177.9	83.3	6.207584	0.756428	10	5.7295	41.623	0.083204
LH/H GMH 2	N.W. Ne	30.5°N	82°E	Gurla Mandhata metamorphic core complex		W.R.	gneiss				212.3	154	4.004667	0.749965	18	4.9638	29.427	0.10196
LH/H GMH 3	N.W. Ne	30.5°N	82°E	Gurla Mandhata metamorphic core complex		W.R.	gneiss				219.2	69.6	9.155453	0.757327	10	2.9721	29.017	0.061912
LH GMH 4	N.W. Ne	30.5°N	82°E	Gurla Mandhata metamorphic core complex	LH	W.R.	migmatite (L)				198.3	147.9	3.953733	0.905126	10	3.4786	12.722	0.16528
LH GMH 5	N.W. Ne	30.5°N	82°E	Gurla Mandhata metamorphic core complex	LH	W.R.	migmatite (L)				433.1	25.7	50.0705	0.983977	18	1.9202	10.607	0.10943
LH GMH 6	N.W. Ne	30.5°N	82°E	Gurla Mandhata metamorphic core complex	LH	W.R.	migmatite (M)				175.1	149.2	3.42965	0.81149	10	1.5545	10.723	0.087627
LH GMH 7	N.W. Ne	30.5°N	82°E	Gurla Mandhata metamorphic core complex	LH	W.R.	migmatite (M)				251.5	182.5	4.023178	0.801073	14	3.5288	30.85	0.069142
LH/H GMH 8	N.W. Ne	30.5°N	82°E	Gurla Mandhata metamorphic core complex		W.R.	granite sill				288.2	63.8	13.13539	0.760196	10	5.3513	14.236	0.22721
LH GMH 9	N.W. Ne	30.5°N	82°E	Gurla Mandhata metamorphic core complex	LH	W.R.	granite sill				340.2	25	40.07249	0.890723	10	4.4079	29.488	0.090355
HHC HE 5	Far-east	HHC	Kangchenjunga Migmatite	Formation I		W.R.	Sil–Grt–Bt banded gneiss									20.23	4.03	0.1203
HHC HE13	Far-east	HHC	Mahabharat Crystallines	Formation I		W.R.	Sil–Grt–Bt banded gneiss									13.97	3.16	0.1369
HHC HE14	Far-east	HHC	Mahabharat Crystallines	Formation I		W.R.	Grt–Bt migmatitic gneiss				Ms					32.35	6.74	0.1261
HHC HE17	Far-east	HHC	Junbesi Paragneiss	Formation I		W.R.	Ky–Grt–Bt–Ms gneiss									28.42	6.37	0.1355
HHC HE18	Far-east	HHC	Junbesi Paragneiss	Formation I		W.R.	Ky–Grt–Bt–Ms gneiss									24.73	5.35	0.1309
HHC HE24	Far-east	HHC	Junbesi Paragneiss	Formation I		W.R.	Grt–Bt banded gneiss									18.73	4.13	0.1332
HHC HE25	Far-east	HHC	Kangchenjunga Migmatite	Formation I		W.R.	Bt banded augen gneiss									34	7.46	0.1327
HHC HE26	Far-east	HHC	Kangchenjunga Migmatite	Formation I		W.R.	Sil–Grt–Crd–Bt migmatitic gneiss									11.22	2.46	0.1326
HHC HE32	Far-east	HHC	Kangchenjunga Migmatite	Formation I		W.R.	Sil–Crd–Grt–Bt migmatitic gneiss									57.99	9.95	0.1037
HHC HE68	Far-east	HHC	Junbesi Paragneiss	Formation I		W.R.	Ky–St–Grt–Bt–Ms–Chl gneiss									28.69	6.01	0.1266
HHC HE71	Far-east	HHC	Junbesi Paragneiss	Formation I		W.R.	Sil–Ky–Grt–Bt gneiss									29.17	5.66	0.1167
HHC HE76	Far-east	HHC	Kangchenjunga Migmatite	Formation I		W.R.	Sil–Grt–Bt–Chl migmatite									45.49	8.77	0.1166
HHC HE77	Far-east	HHC	Junbesi Paragneiss	Formation I		W.R.	Grt–Ms–Bt gneiss									30.26	5.92	0.1183
LH/H ME11	Far-east	MCTZ	Sun Kosi Phyllite	MCT zone		W.R.	Bt–Ms schist									24.89	5.48	0.1332
LH/H ME12	Far-east	MCTZ	Sun Kosi Phyllite	MCT zone		W.R.	Grt–St–Bt–Ms schist									67.81	13	0.1159
LH/H ME15	Far-east	MCTZ	Khare Phyllite	MCT zone		W.R.	Ms–Chl phyllite									40.2	8.07	0.1213
LH/H ME16	Far-east	MCTZ	Sisne Khola Augen Gneiss	MCT zone		W.R.	Ms–Bt augen gneiss									20.95	4.64	0.1338
LH ME19	Far-east	MCTZ	Khare Phyllite	MCT zone		W.R.	Ep–Ms–Bt–Chl gneiss				Ms and Bt, Chl replacing Grt					46.03	9.05	0.1188
LH ME22	Far-east	MCTZ	Khare Phyllite	MCT zone		W.R.	Ms–Chl phyllite									32.65	5.72	0.1059
LH ME23	Far-east	MCTZ	Khare Phyllite	MCT zone		W.R.	Ep–Ms–Bt mylonitic schist									27.71	6.08	0.1325
LH ME75	Far-east	MCTZ	Sisne Khola Augen Gneiss	MCT zone		W.R.	Ms–Bt gneiss									44.27	8.7	0.1188
LH ME76	Far-east	MCTZ	Khare Phyllite	MCT zone		W.R.	Ms–Bt siliceous schist									n.d.	n.d.	n.d.
LH LE20	Far-east	LLHS	Taplejung Group	Nawakot Group		W.R.	Chl–Se phyllite									25.34	4.73	0.1128
LH LE21	Far-east	LLHS	Taplejung Group	Nawakot Group		W.R.	Chl–Se siliceous phyllite									11.7	2.28	0.1179
LH LE28	Far-east	LLHS	Taplejung Group	Nawakot Group		W.R.	Chl–Se phyllite									43.5	7.98	0.1109
LH LE78	Far-east	LLHS	Taplejung Group	Nawakot Group		W.R.	Chl–Se schist									64.81	11.99	0.1119
LH LE79	Far-east	LLHS	Taplejung Group	Nawakot Group		W.R.	Ms–Bt schist									34.72	7.05	0.1228
LH LE10	Far-east	ULHS	Taplejung Group	Nawakot Group		W.R.	Chl–Se phyllite									37.9	7.95	0.1268
HHC HC46	Central N	HHC	Himalayan gneisses	Formation I		W.R.	Bt migmatitic gneiss									33.33	6.92	0.1256
HHC HC47	Central N	HHC	Himalayan gneisses	Formation I		W.R.	Grt–Bt gneiss									28.22	6.18	0.1324

Table SII-2 (…/…)

	Ech.#	Region	River	Locality	Formation	Category	Type	Rock type	North	East	Date	Rb Sil	Sr Sil	87Rb/86Sr	87Sr/86Sr S	2s.d.	Sm Sil	Nd Sil	147Sm/144Nd
LH	MC49	Central H	MCTZ	MCT zone	MCT zone		W.R.	Gr-rich black phyllite									29.69	5.12	0.1042
LH	MC69	Central H	MCTZ	MCT zone	MCT zone		W.R.	Ms white quartzite									9.06	1.94	0.1293
LH	MC74	Central H	MCTZ	MCT zone	MCT zone		W.R.	Chl–Se phyllitic schist									36.79	6.75	0.111
LH	LC50	Central H	LLHS	Nawakot Group	Kuncha		W.R.	Bt–Ms phyllite									24.81	4.36	0.1062
LH	LC70	Central H	LLHS	Nawakot Group	Fagfog Quartzite		W.R.	Pale-green quartzite									13.96	2.38	0.103
LH	LC71	Central H	LLHS	Nawakot Group	Fagfog Quartzite		W.R.	Chl–Bt–Ms phyllite									35.37	6.72	0.1149
LH	LC72	Central H	LLHS	Nawakot Group	Kuncha		W.R.	Bt–Ms phyllite									25.16	4.65	0.1118
LH	LC73	Central H	LLHS	Nawakot Group	Kuncha		W.R.	Bt–Ms phyllite									29.2	5.48	0.1135
LH	LC53	Central H	ULHS	Nawakot Group	Nourpul		W.R.	Ms siliceous sandstone									10.37	1.9	0.1108
LH	LC54	Central H	ULHS	Nawakot Group	Benighat Slates		W.R.	Black phyllite									35.78	7	0.1182
LH	LC55	Central H	ULHS	Nawakot Group	Nourpul		W.R.	Chl–Se phyllite									25.75	4.62	0.1084
LH	LC56	Central H	ULHS	Nawakot Group	Benighat Slates		W.R.	Black phyllite									34.4	6.11	0.1074
LH	LC57	Central H	ULHS	Nawakot Group	Benighat Slates		W.R.	Phyllitic slate									23.16	4.99	0.1303
HHC	HW8	Western	HHC	Himalayan gneisses	Formation I		W.R.	Grt–Ms–Bt gneiss									30.51	6.7	0.1327
HHC	HW9	Western	HHC	Himalayan gneisses	Formation I		W.R.	Ky–Grt–Ms–Bt gneiss									29.62	5.86	0.1197
HHC	HW36	Western	HHC	Himalayan gneisses	Formation I		W.R.	Grt–Bt gneiss									29.04	5.95	0.1239
LH	MW7	Western	MCTZ	MCT zone	MCT zone		W.R.	Grt–Bt banded gneiss									35.24	6.93	0.1188
LH/H	MW35	Western	MCTZ	MCT zone	MCT zone		W.R.	Grt–Bt–Ms phyllitic schist									47.12	9.46	0.1213
LH	MW38	Western	MCTZ	MCT zone	MCT zone		W.R.	Ep–Ms–Bt mylonitic gneiss									38.44	7.5	0.1179
LH	MW61	Western	MCTZ	MCT zone	MCT zone		W.R.	Chl–Se phyllite									41.38	7.84	0.1145
LH	LW4	Western	LLHS	Quartzose Sandstone Fm.	Kuncha Fm		W.R.	Chl–Se phyllite									17.72	3.68	0.1256
LH	LW5	Western	LLHS	Phyllite Fm.	Dandagaon Phyllites		W.R.	Bt–Ms–gr black phyllite									30.42	6.92	0.1209
LH	LW62	Western	LLHS	Quartzite Fm.	Fagfog Quartzite		W.R.	White quartzite									5.89	1.15	0.1181
LH	LW64	Western	LLHS	Quartzite Fm.	Fagfog Quartzite		W.R.	Calcareous white quartzite									1.51	0.32	0.1276
LH	LW65	Western	LLHS	Phyllite Fm.	Dandagaon Phyllites		W.R.	Bt–Ms–Gr black phyllite									27.53	4.96	0.1088
LH	LW68	Western	LLHS	Quartzite Fm.	Fagfog Quartzite		W.R.	White quartzite									4.2	0.77	0.1105
LH	LW39	Western	ULHS	Laminated Slate Fm.	Benighat Slates Grayish slate		W.R.	Spotted loess									31.53	5.62	0.1077
LH	LW40	Western	ULHS	Laminated Slate Fm.	Benighat Slates		W.R.	Black slate									16.81	2.82	0.1013
LH	LW43	Western	ULHS	Lower Variegated Rock Fm.	Benighat Slates?		W.R.	Brick-colored sandstone									22.93	4.63	0.1221
LH	LW63	Western	ULHS	Lower Variegated Rock Fm.	Benighat Slates?		W.R.	Calcareous grey quartzite									n.d.	n.d.	n.d.
TSS	AY06-29-0	S. Lhasa			Langjiexue Group		W.R.	coarse-gd ss	28°58.27	91°39.571'E							5.21	28.99	0.1087
TSS	AY06-29-0	S. Lhasa			Langjiexue Group		W.R.	siltstone	28°58.27	91°39.571'E							7.96	45.06	0.1068
TSS	AY06-29-0	S. Lhasa			Langjiexue Group		W.R.	fine-grained	28°56.99	91°38.927'E							8.89	50.53	0.1063
TSS	AY07-03-0	S. Lhasa			Langjiexue Group		W.R.	meta-greywa	29°05.56	90°23.602'E							6.31	30.96	0.1232
TSS	AY07-01-0	S. Lhasa			Lhakang Formation		W.R.	slate	28°15.60	91°13.699'E							4.83	27.23	0.1072
TSS	AY07-01-0	S. Lhasa			Lhakang Formation		W.R.	meta-pelite	28°10.40	91°14.165'E							6.95	44.37	0.0947
TSS	AY07-01-0	S. Lhasa			Lhakang Formation		W.R.	quartz arenit	28°10.40	91°14.165'E							6.63	35.57	0.1128
TSS	AY07-02-0	S. Lhasa			Lhakang Formation		W.R.	phyllite	28°07.27	91°05.805'E							7.81	46.06	0.1025
TSS	AY07-02-0	S. Lhasa			Lhakang Formation		W.R.	sandy phyllit	28°13.14	91°00.510'E							6.26	33.64	0.1125
TSS	AY07-02-0	S. Lhasa			Lhakang Formation		W.R.	phyllite	28°13.14	91°00.510'E							10.94	61.92	0.1068
HHC	B45	Bhutan			HHS (N. of Kakhtang thrust)	HHC	W.R.	Bt gneiss	27° 35.0	91° 29.89'		133	123	3.13	0.75348	0.00002	5.85	28.02	0.126
HHC	B87	Bhutan			HHS (N. of Kakhtang thrust)	HHC	W.R.	Bt gneiss	27° 29.8	89° 21.25'		164	182	2.61	0.74394	0.00001	8.84	45.81	0.117
HHC	Bh3	Bhutan			HHS (N. of Kakhtang thrust)		W.R.	Bt-sill gneiss	27° 51.9	89° 43.55'		77	60				4.75	23.11	0.124
HHC	B39	Bhutan			HHS (S. of Kakhtang thrust)	HHC	W.R.	Ky schist	27° 20.3	91° 32.76'		227	37	17.68	0.83617	0.00002	9.08	45.69	0.12
HHC	B41	Bhutan			HHS (S. of Kakhtang thrust)	HHC	W.R.	Bt gneiss	27° 25.9	91° 34.18'		182	118	4.47	0.77531	0.00003	10.15	50.69	0.121
HHC	B50	Bhutan			HHS (S. of Kakhtang thrust)	HHC	W.R.	Sill schist	27° 20.8	91° 37.08'		163	45	10.46	0.77506	0.00002	7.74	37.9	0.124
HHC	B51	Bhutan			HHS (S. of Kakhtang thrust)	HHC	W.R.	Mica schist	27° 20.8	91° 37.62'		92	15	17.8	0.83681	0.00001	6.1	30.25	0.122
HHC	B68	Bhutan			HHS (S. of Kakhtang thrust)	HHC	W.R.	Bt gneiss	27° 14.2	91° 33.12'		166	102	4.71	0.76448	0.00002	6.69	31.6	0.128
HHC	B71b	Bhutan			HHS (S. of Kakhtang thrust)	HHC	W.R.	Quartzite	27° 17.8	91° 28.48'		77	17	13.08	0.92056	0.00002	2.39	11.78	0.122
HHC	B81	Bhutan			HHS (S. of Kakhtang thrust)	HHC	W.R.	Gnt phyllite	27° 27.4	90° 22.07'		283	38	21.4	0.80052	0.00001	9.65	47.12	0.124
HHC	B83	Bhutan			HHS (S. of Kakhtang thrust)	HHC	W.R.	Gnt schist	27° 30.9	90° 17.74'		247	166	4.31	0.72775	0.00001	13.77	67.7	0.123
HHC	B85b	Bhutan			HHS (S. of Kakhtang thrust)	HHC	W.R.	Gnt schist	27° 23.4	89° 35.24'		144	40	10.32	0.78961	0.00002	8.24	41.68	0.119
HHC	B88b	Bhutan			HHS (S. of Kakhtang thrust)	HHC	W.R.	Gnt schist	27° 18.8	89° 32.92'		163	157	3.01	0.75981	0.00001	8.21	40.42	0.123
HHC	Bh6	Bhutan			HHS (S. of Kakhtang thrust)		W.R.	Bt gneiss	27° 37.7	89° 49.23'		268	69				3.94	19	0.125
HHC	Bh10b	Bhutan			HHS (S. of Kakhtang thrust)		W.R.	Gnt schist	27° 18.8	89° 32.74'		114	140				6.34	30.65	0.122
HHC	Bh12	Bhutan			HHS (S. of Kakhtang thrust)		W.R.	Gnt schist	26° 55.0	89° 28.45'		153	159				6.61	32.18	0.124
LH	B29a	Bhutan			Daling-Shumar Formation	LH	W.R.	Quartzite	27° 16.3	91° 14.87'		198	53	10.87	0.91818	0.00002	1.05	6.23	0.102
LH	B29b	Bhutan			Daling-Shumar Formation	LH	W.R.	Phyllite	27° 16.3	91° 14.87'		42	10	12.07	0.88034	0.00001	5.68	31.93	0.107
LH	B36a	Bhutan			Daling-Shumar Formation	LH	W.R.	Phyllite	27° 15.9	91° 23.82'		220.0	43.0	14.92	0.97145	0.00002	13.1	74.3	0.1
LH	B75	Bhutan			Daling-Shumar Formation	LH	W.R.	Quartzite	27° 16.1	91° 23.74'		33	4	24.85	1.05902	0.00004	1.68	9.21	0.11
LH	Bh13	Bhutan			Daling-Shumar Formation		W.R.	Phyllite	26° 54.0	89° 27.00'		232	82				7.54	49.24	0.092
LH	LT-4	C. Nepal		Langtang			W.R.										4.83	26.36	0.1108
LH	LT-6	C. Nepal		Langtang			W.R.										5.79	31.96	0.1096

Table SII-2 (…/…)

	Ech.#	Region	River	Locality	Formation	Category	Type	Rock type	North	East	Date	Rb Sil	Sr Sil	87Rb/86Sr	87Sr/86Sr S	2s.d.	Sm Sil	Nd Sil	147Sm/144Nd
LH	LT-7	C. Nepal		Langtang			W.R.										10.08	54.75	0.1113
LH	LT-10	C. Nepal		Langtang			W.R.										7.01	38.68	0.1095
LH	LT-18	C. Nepal		Langtang			W.R.										8.14	43.34	0.1085
LH	LT-19	C. Nepal		Langtang			W.R.										6.75	38.13	0.107
LH/H	LT-20	C. Nepal		Langtang	Syabru Bensi augen gneiss		W.R.	augen gneiss									2.21	10.51	0.1273
LH/H	LT-33	C. Nepal		Langtang	Syabru gneiss		W.R.	nonmigmatitic, kyanitebearing pelitic gneiss									7.59	39.01	0.1177
LH/H	LT-34	C. Nepal		Langtang	Syabru gneiss		W.R.	nonmigmatitic, kyanitebearing pelitic gneiss									2.26	11.87	0.1153
HHC	LT-21	C. Nepal		Langtang	Gosainkund gneiss		W.R.	gneiss									6.77	34.99	0.1169
HHC	LT-22	C. Nepal		Langtang	Gosainkund gneiss		W.R.	gneiss									8.96	45.54	0.119
HHC	LT-24	C. Nepal		Langtang	Gosainkund gneiss		W.R.	gneiss									8.35	43.54	0.1159
HHC	LT-29	C. Nepal		Langtang	Gosainkund gneiss		W.R.	gneiss									5.7	30.53	0.11
THB	12PD01-1	N. Lhasa		Pangduo, E. Linzizong shoshonitic volcanic rocks	Pana formation	Linzigong lava	W.R.	Basalt				92.3	1305	0.2041	0.705197	1.3E-05	10.6	50.4	0.1272
THB	12PD05-1	N. Lhasa		Pangduo, E. Linzizong shoshonitic volcanic rocks	Pana formation	Linzigong lava	W.R.	Basaltic andesite				104	526	0.5728	0.706662	7E-06	7.38	35.7	0.1251
THB	12PD05-2	N. Lhasa		Pangduo, E. Linzizong shoshonitic volcanic rocks	Pana formation		W.R.	Basaltic andesite				151	1008				7.54	36.3	
THB	12PD05-3	N. Lhasa		Pangduo, E. Linzizong shoshonitic volcanic rocks	Pana formation	Linzigong lava	W.R.	Basaltic andesite				157	940	0.4826	0.70644	1.1E-05	7.33	36	0.1232
THB	12PD05-4	N. Lhasa		Pangduo, E. Linzizong shoshonitic volcanic rocks	Pana formation	Linzigong lava	W.R.	Basaltic andesite				133	963	0.3971	0.706448	1.3E-05	7.6	36.9	0.1247
THB	12PD02-1	N. Lhasa		Pangduo, E. Linzizong shoshonitic volcanic rocks	Pana formation	Linzigong lava	W.R.	Dacite				338	482	2.025	0.708328	1.1E-05	7.96	45.2	0.1066
THB	12PD03-1	N. Lhasa		Pangduo, E. Linzizong shoshonitic volcanic rocks	Pana formation		W.R.	Dacite				359	496				9.67	56.5	
THB	12PD04-1	N. Lhasa		Pangduo, E. Linzizong shoshonitic volcanic rocks	Pana formation		W.R.	Dacite				352	475				8.14	45.5	
THB	12PD06-1	N. Lhasa		Pangduo, E. Linzizong shoshonitic volcanic rocks	Pana formation	Linzigong lava	W.R.	Dacite				410	249	4.7497	0.709955	1.1E-05	8.66	48.8	0.1074
THB	12PD07-1	N. Lhasa		Pangduo, E. Linzizong shoshonitic volcanic rocks	Pana formation	Linzigong lava	W.R.	Dacite				340	587	1.6731	0.70757	1.2E-05	8.19	45.4	0.1091
THB	12PD08-1	N. Lhasa		Pangduo, E. Linzizong shoshonitic volcanic rocks	Pana formation		W.R.	Dacite				327	547				7.77	43.9	
THB	12PD09-1	N. Lhasa		Pangduo, E. Gangdese belt	Nuoco formation ?	Transhimalaya	W.R.	Sandstone				233	165	4.0736	0.743454	1.4E-05	6.28	33.1	0.1048
THB	12PD11-1	N. Lhasa		Pangduo, E. Gangdese belt	Nuoco formation ?	Transhimalaya	W.R.	Sandstone				195	270	2.0843	0.728382	1.2E-05	7.1	36.3	0.1185
THB	CM10-04-(	N.W. Lhasa			Mibale	K-rich Transhim	W.R.	Ultrapotassic trachyte to trachyandesite				753.9	838.8	2.6	0.719233	14	20.13	138.1	0.09
THB	CM10-04-(	N.W. Lhasa			Mibale	K-rich Transhim	W.R.	Ultrapotassic trachyte to trachyandesite				604.1	984.5	1.8	0.719124	19	18.53	128.6	0.09
THB	CM10-04-1	N.W. Lhasa			Mibale	K-rich Transhim	W.R.	Ultrapotassic trachyte to trachyandesite				504.3	999.8	1.5	0.71961	10	14.62	82.07	0.11
THB	CM10-04-1	N.W. Lhasa			Mibale	K-rich Transhim	W.R.	Ultrapotassic trachyte to trachyandesite				1335.1	556.1	7	0.722064	13	9.09	60.5	0.09
THB	CM10-04-2	N.W. Lhasa			Mibale	K-rich Transhim	W.R.	Ultrapotassic trachyte to trachyandesite				403	786.2	1.5	0.720573	10	10.94	80.05	0.08
THB	CM10-04-2	N.W. Lhasa			Mibale	K-rich Transhim	W.R.	Ultrapotassic trachyte to trachyandesite				450.8	997.4	1.3	0.720746	14	10.79	78.32	0.08
THB	CQQ4-04-(	N.W. Lhasa			Maiga	K-rich Transhim	W.R.	Ultrapotassic trachyandesite				368.8	1167.2	0.9	0.722189	12	26.83	127.9	0.13
THB	CQQ4-04-(	N.W. Lhasa			Maiga	K-rich Transhim	W.R.	Ultrapotassic trachyandesite				327.1	1165.7	0.8	0.722129	13	22.7	100.8	0.14
THB	DJB98-11	S.W. Tib		31°N 80°E	Dajiweng	Yarlung Tsangbo suture	Yarlung Tsangb	W.R.	Ophiolites			4.06	1425	0.0083	0.70824		5.15	20.95	0.1486
THB	L	S.W. Tib		31°N 80°E	Dajiweng	Yarlung Tsangbo suture	Yarlung Tsangb	W.R.	Ophiolites			9.29	504.8	0.0533	0.70692		2.193	7.338	0.1807
THB	DJB98-18	S.W. Tib		31°N 80°E	Dajiweng	Yarlung Tsangbo suture	Yarlung Tsangb	W.R.	Ophiolites			1.59	611.3	0.0075	0.70461		1.237	3.677	0.2033
THB	DJB98-20	S.W. Tib		31°N 80°E	Dajiweng	Yarlung Tsangbo suture	Yarlung Tsangb	W.R.	Ophiolites			4.71	369.2	0.0369	0.70403		7.359	35.1	0.1268
THB	BAR98-1 (	S.W. Tib		31°N 80°E	Bar	Yarlung Tsangbo suture	Yarlung Tsangb	W.R.	Ophiolites			5.9	218.7	0.078	0.70413		3.292	9.096	0.2188
THB	BAR98-3 (	S.W. Tib		31°N 80°E	Bar	Yarlung Tsangbo suture	Yarlung Tsangb	W.R.	Ophiolites			69.4	448.1	0.4481	0.70485		1.966	5.38	0.2208
THB	BAR98-6	S.W. Tib		31°N 80°E	Bar	Yarlung Tsangbo suture	Yarlung Tsangb	W.R.	Ophiolites			7.37	147.7	0.1442	0.70443		7.33	34.42	0.1287
THB	DQ98-9 G	S.W. Tib		30°N 83°E	Dangqiong	Yarlung Tsangbo suture	Yarlung Tsangb	W.R.	Ophiolites			0.182	191.2	0.0028	0.70321		3.143	8.239	0.2306
THB	DQ98-12 (	S.W. Tib		30°N 83°E	Dangqiong	Yarlung Tsangbo suture	Yarlung Tsangb	W.R.	Ophiolites			0.294	137	0.0062	0.70307		3.017	8.123	0.2245
THB	DQ98-14 [	S.W. Tib		30°N 83°E	Dangqiong	Yarlung Tsangbo suture	Yarlung Tsangb	W.R.	Ophiolites			0.4	204.6	0.0056	0.70295		6.068	16.91	0.2169
THB	XL98-10 D	S. Tibet		29°N 89°E	Xialu	Yarlung Tsangbo suture	Yarlung Tsangb	W.R.	Ophiolites			2.11	166.3	0.0366	0.70345		2.705	8.011	0.2041
THB	DZ98-1 G	S. Tibet		29°N 89°E	Dazhuqu Dazhuka	Yarlung Tsangbo suture	Yarlung Tsangb	W.R.	Ophiolites			0.728	180.7	0.0117	0.70356		2.446	6.66	0.222
THB	DZ98-12 D	S. Tibet		29°N 89°E	Dazhuqu Dazhuka	Yarlung Tsangbo suture	Yarlung Tsangb	W.R.	Ophiolites			0.301	128	0.0068	0.70451		2.677	7.654	0.2114
THB	L	S. Tibet		29°N 89°E	Dazhuqu Dazhuka	Yarlung Tsangbo suture	Yarlung Tsangb	W.R.	Ophiolites			0.359	169.7	0.0061	0.7044		2.162	5.595	0.2355
THB	DZ98-19	S. Tibet		29°N 89°E	Dazhuqu Dazhuka	Yarlung Tsangbo suture	Yarlung Tsangb	W.R.	Ophiolites			1.82	158.1	0.0333	0.70433		2.896	8.642	0.2026
THB	LC98-3	S.E. Tib		29°N 92°E	Langceling	Yarlung Tsangbo suture	Yarlung Tsangb	W.R.	Ophiolites			3.35	98.84	0.098	0.70472		1.706	4.639	0.2223
THB	LC98-4	S.E. Tib		29°N 92°E	Langceling	Yarlung Tsangbo suture	Yarlung Tsangb	W.R.	Ophiolites			10.3	130	0.2291	0.70485		1.477	3.534	0.2525
THB	LC98-6	S.E. Tib		29°N 92°E	Langceling	Yarlung Tsangbo suture	Yarlung Tsangb	W.R.	Ophiolites			5.22	82.2	0.1836	0.70483		1.023	2.413	0.2561
THB	LB98-1 G	S.E. Tib		29°N 92°E	Luobusha	Yarlung Tsangbo suture	Yarlung Tsangb	W.R.	Ophiolites			13.1	294	0.1287	0.70621		3.86	10.94	0.2134
THB	L	S.E. Tib		29°N 92°E	Luobusha	Yarlung Tsangbo suture	Yarlung Tsangb	W.R.	Ophiolites			17	340.3	0.1328	0.7061		4.707	13.46	0.2114
THB	LB98-3 G	S.E. Tib		29°N 92°E	Luobusha	Yarlung Tsangbo suture	Yarlung Tsangb	W.R.	Ophiolites			0.897	118.8	0.0218	0.703		2.047	5.732	0.2159
THB	19	S.E. Lhasa			Sangri pluton	Transhimalayar	W.R.					144	807	0.407	0.706398	7E-06	6.07	41	0.0939
THB	110	E. Synta	W. Namche Barwa		Dangru pluton / Dongru	Transhimalayar	W.R.					117	415	0.769	0.706865	7E-06	2.52	14	0.113232
THB	109A	E. Synta	W. Namche Barwa		Dangru pluton / Dongru	Transhimalayar	W.R.					118	366	0.848	0.707921	4.9E-05	3.06	17	0.106808
THB	109B	E. Synta	W. Namche Barwa		Dangru pluton / Dongru		W.R.					129	418				3.15	18	
THB	111A	E. Synta	W. Namche Barwa		Dangru pluton / Dongru	Transhimalayar	W.R.					97	512	0.525	0.707403	0.00001	3.46	21	0.104461

Table SII-2 (…/…)

Ech.#	Region	River	Locality	Formation	Category	Type	Rock type	North	East	Date	Rb Sil	Sr Sil	87Rb/86Sr	87Sr/86Sr S	2s.d.	Sm Sil	Nd Sil	147Sm/144Nd
THB 111B	E. Synta	W. Namche	Barwa	Dangru pluton / Dongru	Transhimalayar	W.R.					80	512	0.447	0.706927	1.1E-05	2.93	18	0.10849
THB 14	E. Synta	W. Namche	Barwa	Linzhi pluton / Nyingchi		W.R.					114	935				7.87	50	
THB 119A	E. Synta	W. Namche	Barwa	Linzhi pluton / Nyingchi	Transhimalayar	W.R.					96	980	0.248	0.706279	8E-06	5.12	37	0.091869
THB 119B	E. Synta	W. Namche	Barwa	Linzhi pluton / Nyingchi		W.R.					106	848				5.13	35	
THB 119C	E. Synta	W. Namche	Barwa	Linzhi pluton / Nyingchi	Transhimalayar	W.R.					107	976	0.273	0.707024	1.6E-05	5.28	39	0.085206
THB 119D	E. Synta	W. Namche	Barwa	Linzhi pluton / Nyingchi		W.R.					118	905				4.76	33	
THB 120A	E. Synta	W. Namche	Barwa	Linzhi pluton / Nyingchi	Transhimalayar	W.R.					97	785	0.324	0.70745	1.3E-05	6.08	38	0.115409
THB 120B	E. Synta	W. Namche	Barwa	Linzhi pluton / Nyingchi		W.R.					108	834				6.67	42	
THB 120E	E. Synta	W. Namche	Barwa	Linzhi pluton / Nyingchi		W.R.					101	808				8.23	71	
THB 138A	E. Synta	E. Namche E	Close Dibang	Lengduo pluton	E. Transhimala	W.R.					184	750	0.641	0.707537	8E-06	3.08	18	0.102882
THB 138B	E. Synta	E. Namche E	Close Dibang	Lengduo pluton	E. Transhimala	W.R.					229	581	1.028	0.710662	1.1E-05	6.73	43	0.097812
THB 138D	E. Synta	E. Namche E	Close Dibang	Lengduo pluton		W.R.					219	578				14.44	181	
THB 140A	E. Synta	E. Namche E	Close Dibang	Damu pluton	E. Transhimala	W.R.					200	582	0.849	0.707686	1.1E-05	4.98	29	
THB 140B	E. Synta	E. Namche E	Close Dibang	Damu pluton	E. Transhimala	W.R.					163	509	0.825	0.707945	3.3E-05	7.98	113	
THB 140C	E. Synta	E. Namche E	Close Dibang	Damu pluton		W.R.					55	812				3.73	22	
HHC ZB06-80M	E. Synta	W. Namche	Barwa	Zhibai fm	HHC	W.R.	pelitic migmatite				128	44.5	8.4071	0.809799	13	7.03	35.4	0.1201
HHC ZB06-66M	E. Synta	W. Namche	Barwa	Pai fm	HHC	W.R.	pelitic migmatite				276	50.7	15.8668	0.78399	16	5.81	27.8	0.1264
HHC ZB06-35M	E. Synta	W. Namche	Barwa	Pai fm	HHC	W.R.	pelitic migmatite				183	296	1.7949	0.742286	13	7.03	39	0.1091
HHC ZB09-18M	E. Synta	W. Namche	Barwa	Zhibai fm	HHC	W.R.	pelitic migmatite				209	111	5.4604	0.76686	10	7.77	35.8	0.1312
HHC ZB06-80L	E. Synta	W. Namche	Barwa	Zhibai fm	HHC	W.R.	pelitic migmatite				8	129	0.1809	0.790428	13	4.29	23.4	0.1109
HHC ZB06-66L	E. Synta	W. Namche	Barwa	Pai fm	HHC	W.R.	pelitic migmatite				122	78.5	4.5297	0.784105	16	1.79	9.95	0.1088
HHC ZB06-35L	E. Synta	W. Namche	Barwa	Pai fm	HHC	W.R.	pelitic migmatite				22.9	324	0.2051	0.74073	15	1.47	7.82	0.1136
HHC ZB09-18L1	E. Synta	W. Namche	Barwa	Zhibai fm	HHC	W.R.	pelitic migmatite				80.5	397	0.588	0.765146	11	1.75	6.73	0.1573
HHC ZB09-18L2	E. Synta	W. Namche	Barwa	Zhibai fm	HHC	W.R.	pelitic migmatite				62.3	311	0.5809	0.764965	13	2.02	9.72	0.1257
THB DY-7	W. Lhas	30-31°N	86.3	1 Garwa	K-rich Transhim	W.R.	potassic lava							0.712847	11			
THB DC2	W. Lhas	30-31°N	86.3	1 Garwa	K-rich Transhim	W.R.	potassic lava							0.718046	14			
THB D509	W. Lhas	30-31°N	86.3	1 Garwa	K-rich Transhim	W.R.	potassic lava							0.716054	10			
THB DG43	W. Lhas	30-31°N	86.3	1 Garwa	K-rich Transhim	W.R.	potassic lava							0.714758	9			
THB YE51	W. Lhas	30-31°N	86.3	2 Yaqian	K-rich Transhim	W.R.	potassic lava							0.718364	13			
THB YC08	W. Lhas	30-31°N	86.3	2 Yaqian	K-rich Transhim	W.R.	potassic lava							0.718469	12			
THB YG13	W. Lhas	30-31°N	86.3	2 Yaqian	K-rich Transhim	W.R.	potassic lava							0.717351	11			
THB YF12	W. Lhas	30-31°N	86.3	2 Yaqian	K-rich Transhim	W.R.	potassic lava							0.719673	14			
THB YA32	W. Lhas	30-31°N	86.3	2 Yaqian	K-rich Transhim	W.R.	potassic lava							0.719041	13			
THB MH78	W. Lhas	30-31°N	86.3	3 Mibale	K-rich Transhim	W.R.	potassic lava							0.719877	13			
THB MH69	W. Lhas	30-31°N	86.3	3 Mibale	K-rich Transhim	W.R.	potassic lava							0.721486	10			
THB MG-3	W. Lhas	30-31°N	86.3	3 Mibale	K-rich Transhim	W.R.	potassic lava							0.719649	11			
THB MY1	W. Lhas	30-31°N	86.3	3 Mibale	K-rich Transhim	W.R.	potassic lava							0.722672	12			
THB MK09	W. Lhas	30-31°N	86.3	3 Mibale	K-rich Transhim	W.R.	potassic lava							0.720948	10			
THB MR21	W. Lhas	30-31°N	86.3	3 Mibale	K-rich Transhim	W.R.	potassic lava							0.725133	10			
THB MA75	W. Lhas	30-31°N	86.3	3 Mibale	K-rich Transhim	W.R.	potassic lava							0.720861	12			
THB MX5	W. Lhas	30-31°N	86.3	3 Mibale	K-rich Transhim	W.R.	potassic lava							0.718768	13			
THB 2003T534	W. Lhas	30-31°N	86.3	4 Yiqian	K-rich Transhim	W.R.	potassic lava							0.71991	10			
THB 2003T536	W. Lhas	30-31°N	86.3	4 Yiqian	K-rich Transhim	W.R.	potassic lava							0.72066	10			
THB 2003T539	W. Lhas	30-31°N	86.3	4 Yiqian	K-rich Transhim	W.R.	potassic lava							0.72093	10			
THB G8	W. Lhas	30-31°N	86.3	5 Chazi	K-rich Transhim	W.R.	potassic lava							0.729418	10			
THB C10	W. Lhas	30-31°N	86.3	5 Chazi	K-rich Transhim	W.R.	potassic lava							0.735896	12			
THB CV5	W. Lhas	30-31°N	86.3	5 Chazi	K-rich Transhim	W.R.	potassic lava							0.733316	16			
THB C76	W. Lhas	30-31°N	86.3	5 Chazi	K-rich Transhim	W.R.	potassic lava							0.730484	11			
THB CH4	W. Lhas	30-31°N	86.3	5 Chazi	K-rich Transhim	W.R.	potassic lava							0.733043	12			
THB CH7	W. Lhas	30-31°N	86.3	5 Chazi	K-rich Transhim	W.R.	potassic lava							0.726819	12			
THB C03	W. Lhas	30-31°N	86.3	5 Chazi	K-rich Transhim	W.R.	potassic lava							0.723169	15			
THB CX38	W. Lhas	30-31°N	86.3	5 Chazi	K-rich Transhim	W.R.	potassic lava							0.721648	13			
THB C25	W. Lhas	30-31°N	86.3	5 Chazi	K-rich Transhim	W.R.	potassic lava							0.736552	11			
THB ZF09	S.W. Tib	33°N	80°E	1 Shiquanhe	Transhimalayar	W.R.	adakite	33.5	80.2			135	819	0.708124	9	5.47	26.9	
THB GUO62	S.W. Tib	32°N	82°E	2 Gegar	Transhimalayar	W.R.	adakite	31.5	81.8			167	490	0.707423	13	4.09	17.2	
THB GUO51	S.W. Tib	32°N	82°E	2 Gegar	Transhimalayar	W.R.	adakite	31.5	81.8			188	689	0.709188	11	3.55	18.4	
THB GUO48	S. Tibet	30°N	85°E	3 Daggyai	Transhimalayar	W.R.	adakite	29.6	85.6			88.3	1024	0.706812	10	5.02	25.4	
THB GUO37	W. Lhas	30°N	90°E	4 Xigaze	Transhimalayar	W.R.	adakite	29.3	88.8			92.8	1133	0.706639	11	3.77	19.2	
THB G09	W. Lhas	30°N	90°E	5 Wuyu	Transhimalayar	W.R.	adakite	29.4	89.4			252	785	0.706004	16	3.21	20.7	
THB ZFG17	W. Lhas	30°N	90°E	6 Majiang	Transhimalayar	W.R.	adakite	29.7	89.9			188	889	0.704807	10	3.64	19.3	
THB G006	S. Lhasa	30°N	92°E	7 Nanmu	Transhimalayar	W.R.	adakite	29.5	90.9			158	317	0.704911	15	1.24	6.22	
THB G019	E. Lhasa	30°N	93°E	8 Jiama	Transhimalayar	W.R.	adakite	29.8	91.8			369	448	0.708114	11	3	20.8	

Table SII-2 (…/…)

Ech.#	Region	River	Locality	Formation	Category	Type	Rock type	North	East	Date	Rb SII	Sr SII	87Rb/86Sr	87Sr/86Sr S	2s.d.	Sm SII	Nd SII	147Sm/144Nd
THB G016	E. Lhasa	30°N	93°E	8 Jiama	Transhimalayar	W.R.	adakite	29.8	91.8			401	422	0.707937	14	3.15	23.4	
THB G025	E. Synta	30°N	95°E	9 Linzhi / Nyingchi pluton	Transhimalayar	W.R.	adakite	29.6	94.6			84.2	1003	0.705516	12	4.14	26.5	
TSS T0837-1	S.W. Lh	29°N	86°E	Xiaru leucogranite	TSS granite	W.R.	tourmaline-bearing leucogranite				657	36.5	53.99	1.083722	1.9E-05	3.48	12.1	0.174
TSS T0837-2	S.W. Lh	29°N	86°E	Xiaru leucogranite	TSS granite	W.R.	tourmaline-bearing leucogranite				712	36.8	58.07	1.088746	2.3E-05	3.53	13.3	0.161
TSS T0837-3	S.W. Lh	29°N	86°E	Xiaru leucogranite	TSS granite	W.R.	tourmaline-bearing leucogranite				693	42	49.3	1.041412	1.5E-05	3.32	11.6	0.173
TSS T0837-4	S.W. Lh	29°N	86°E	Xiaru leucogranite	TSS granite	W.R.	tourmaline-bearing leucogranite				558	82.2	19.91	0.848154	1.3E-05	6.22	29	0.13
TSS T0659-T-1	S.W. Lh	28.°N	85°E	Paiku leucogranite		W.R.	tourmaline-bearing leucogranite				459	32.4				0.79	2.02	
TSS T0659-T-2	S.W. Lh	28.°N	85°E	Paiku leucogranite		W.R.	tourmaline-bearing leucogranite				488	10.8				1.51	4.06	
TSS LZH1101a	S.E. Lha	28.5°N	91°E	Lhozag granite	TSS granite	W.R.	Tg				430	72	17.8085	0.730355	9E-06	2.71	9.1	0.1798
TSS LZH1102a	S.E. Lha	28.5°N	91°E	Lhozag granite		W.R.	Tg				280	63.5				2.23	5.56	
TSS LZH1103a	S.E. Lha	28.5°N	91°E	Lhozag granite	TSS granite	W.R.	Tg				350	67.9	15.3662	0.73109	6E-06	3.7	11.8	0.1901
TSS LZH1107a	S.E. Lha	28.5°N	91°E	Lhozag granite	TSS granite	W.R.	Tg				385	70.6	16.2554	0.731431	5E-06	2.96	10.1	0.1763
TSS LZH1111a	S.E. Lha	28.5°N	91°E	Lhozag granite		W.R.	Tg				350	71.3				2.73	9.17	
TSS LZH1113a	S.E. Lha	28.5°N	91°E	Lhozag granite		W.R.	Tg				410	83.9				3.77	13	
TSS LZH1114	S.E. Lha	28.5°N	91°E	Lhozag granite	TSS granite	W.R.	2mg				237	111	6.3538	0.763556	6E-06	2.52	8.53	0.1788
TSS LZH1115	S.E. Lha	28.5°N	91°E	Lhozag granite	TSS granite	W.R.	2mg				487	63.1	23.0395	0.745409	7E-06	4.32	15.7	0.1662
TSS LZH1116	S.E. Lha	28.5°N	91°E	Lhozag granite		W.R.	2mg				459	12.4				2.23	6.61	
TSS LZH1125	S.E. Lha	28.5°N	91°E	Lhozag granite		W.R.	2mg				267	207				4.05	19.6	
TSS LZH1126	S.E. Lha	28.5°N	91°E	Lhozag granite	TSS granite	W.R.	2mg				221	212	3.10851	0.739152	7E-06	4.25	20	0.1288
TSS LZH1127	S.E. Lha	28.5°N	91°E	Lhozag granite		W.R.	2mg				273	165				4.04	17.7	
TSS LZH1128	S.E. Lha	28.5°N	91°E	Lhozag granite	TSS granite	W.R.	2mg				354	107	9.8323	0.728101	9E-06	4.52	18	0.1522
TSS LZH1129	S.E. Lha	28.5°N	91°E	Lhozag granite		W.R.	2mg				365	84.4				4.23	16	
TSS LZH1130	S.E. Lha	28.5°N	91°E	Lhozag granite		W.R.	2mg				245	262				4.91	23.6	
TSS LZH1131	S.E. Lha	28.5°N	91°E	Lhozag granite	TSS granite	W.R.	2mg				452	35.5	38.0091	0.763744	7E-06	3.89	13.5	0.1741
TSS LZH1133	S.E. Lha	28.5°N	91°E	Lhozag granite		W.R.	2mg				400	59.4				2.67	9.38	
TSS T0319-06	S.E. Lhasa		Yardoi	Yardoi gneiss dome	TSS granite	W.R.	Two-mica granite				188.1	334.6	1.6238	0.716362	14	3.61	18.17	0.1202
TSS T0319-07	S.E. Lhasa		Yardoi	Yardoi gneiss dome	TSS granite	W.R.	Two-mica granite				244.2	318.7	2.2144	0.717262	14	5.16	25.1	0.1233
TSS T0319-08	S.E. Lhasa		Yardoi	Yardoi gneiss dome	TSS granite	W.R.	Two-mica granite				155.1	315.3	1.4207	0.719715	20	6.98	35.1	0.1193
TSS T0320-06	S.E. Lhasa		Yardoi	Yardoi gneiss dome	TSS granite	W.R.	Two-mica granite				25.9	1322	0.0566	0.711977	18	1.16	4.6	0.1522
TSS T0317-01	S.E. Lhasa		Yardoi	Dala pluton	TSS granite	W.R.	Two-mica granite				176.6	344	1.4836	0.7185	16	4.43	22.07	0.1214
TSS T0317-02	S.E. Lhasa		Yardoi	Dala pluton	TSS granite	W.R.	Two-mica granite				159.9	405.2	1.1405	0.718617	15	4.56	22.78	0.1211
TSS T0317-03	S.E. Lhasa		Yardoi	Dala pluton	TSS granite	W.R.	Two-mica granite				162.8	412.3	1.1411	0.718494	15	4.48	22.77	0.1189
TSS T0317-04	S.E. Lhasa		Yardoi	Dala pluton	TSS granite	W.R.	Two-mica granite				148.5	378.9	1.1327	0.718526	14	4.39	21.65	0.1227
TSS T0317-05	S.E. Lhasa		Yardoi	Dala pluton	TSS granite	W.R.	Two-mica granite				149.6	376.3	1.1489	0.71844	16	4.41	22.17	0.1202
TSS T0317-06	S.E. Lhasa		Yardoi	Dala pluton	TSS granite	W.R.	Two-mica granite				165.7	403.1	1.188	0.718532	15	4.59	23.31	0.1191
TSS T0389-4	S.E. Lhasa		Yardoi	Quedang	TSS granite	W.R.	Two-mica granite				213.2	246.6	2.4986	0.717158	12	4.19	20.75	0.1221
TSS T0389-5	S.E. Lhasa		Yardoi	Quedang	TSS granite	W.R.	Two-mica granite				195.5	346.5	1.6306	0.71605	15	3.96	19.75	0.1211
TSS T0389-6	S.E. Lhasa		Yardoi	Quedang	TSS granite	W.R.	Two-mica granite				176	323.3	1.5733	0.717009	18	3.88	18.95	0.124
TSS T0389-7	S.E. Lhasa		Yardoi	Quedang	TSS granite	W.R.	Two-mica granite				186.8	295.7	1.8257	0.716942	15	4.14	21.13	0.1005
TSS T0389-8	S.E. Lhasa		Yardoi	Quedang	TSS granite	W.R.	Two-mica granite				179.1	300.4	1.723	0.716621	21	3.51	16.98	0.1399
TSS T0389-9	S.E. Lhasa		Yardoi	Quedang	TSS granite	W.R.	Two-mica granite				183.8	319.5	1.6625	0.716946	15	3.93	19.37	0.1002
TSS T0389-11	S.E. Lhasa		Yardoi	Quedang	TSS granite	W.R.	Two-mica granite				170.5	298.7	1.6496	0.717176	13	3.21	15.06	0.1289
TSS T0389-12	S.E. Lhasa		Yardoi	Quedang	TSS granite	W.R.	Two-mica granite				152.3	310.1	1.4194	0.717117	14	2.99	14.26	0.127
TSS T0389-17	S.E. Lhasa		Yardoi	Yardoi gneiss dome	TSS	W.R.	Amphibolite				126.8	79.3	4.638	0.736184	11	9.54	51.82	0.1114
TSS T0321-08	S.E. Lhasa		Yardoi	Yardoi gneiss dome	TSS	W.R.	Amphibolite				1.89	236.2	0.0232	0.712084	16	9.6	36.52	0.1589
TSS T0321-09	S.E. Lhasa		Yardoi	Yardoi gneiss dome	TSS	W.R.	Amphibolite				2.41	246.2	0.0283	0.712669	14	9.66	36.65	0.1593
TSS T0394-10	S.E. Lhasa		Yardoi	Yardoi gneiss dome	TSS	W.R.	Amphibolite				425	428	2.8697	0.714429	12	7.82	34.46	0.1372
TSS T0394-21	S.E. Lhasa		Yardoi	Yardoi gneiss dome	TSS	W.R.	Amphibolite				8.98	160.2	0.1623	0.711551	13	10.14	58.94	0.104
TSS T0394-1	S.E. Lhasa		Yardoi	Yardoi gneiss dome	TSS	W.R.	Amphibolite				27.88	186.2	0.3772	0.714183	13	6.23	28.8	0.1308
TSS T0394-6	S.E. Lhasa		Yardoi	Yardoi gneiss dome	TSS	W.R.	Amphibolite				39.09	176.7	0.5254	0.711257	14	3.99	19.04	0.1268
TSS T0394-8	S.E. Lhasa		Yardoi	Yardoi gneiss dome	TSS	W.R.	Amphibolite				7.71	83.3	0.2758	0.714926	12	4.2	21.07	0.1205
TSS T0392-0	S.E. Lhasa		Yardoi	Yardoi gneiss dome	TSS	W.R.	Augen Gneiss				258.5	19.5	38.815	0.853244	14	4.75	23.48	0.1224
TSS T0392-1	S.E. Lhasa		Yardoi	Yardoi gneiss dome	TSS	W.R.	Augen Gneiss				278.9	14.8	56.149	0.99585	15	5.62	25.79	0.1319
TSS T0392-3	S.E. Lhasa		Yardoi	Yardoi gneiss dome	TSS	W.R.	Augen Gneiss				345.8	21.3	48.397	0.998985	15	8.22	38.64	0.1287
TSS T0395-01	S.E. Lhasa		Yardoi	Yardoi gneiss dome	TSS	W.R.	Augen Gneiss				464.6	2.9	491.06	1.4603	4	3.87	10.53	0.2221
TSS T0395-03	S.E. Lhasa		Yardoi	Yardoi gneiss dome	TSS	W.R.	Augen Gneiss				429.2	12.6	98.4435	1.26313	4	4.49	13.93	0.1949
THB Lz9915	close to	Linzigong vo	Linzhou	Pana	Linzigong lava	W.R.					148.2	360.4	1.19	0.705718	9	5.188	29.14	0.1077
THB Lz9914	close to	Linzigong vo	Linzhou	Pana	Linzigong lava	W.R.					183.2	184.9	2.868	0.707123	25	2.271	12.88	0.1067
THB L1087–2	close to	Linzigong vo	Linzhou	Pana	Linzigong lava	W.R.					177.53	188.4	2.721	0.707431	15	2.741	15.871	0.1044

Table SII-2 (…/…)

Ech.#	Region	River	Locality	Formation	Category	Type	Rock type	North	East	Date	Rb Sil	Sr Sil	87Rb/86Sr	87Sr/86Sr S	2s.d.	Sm Sil	Nd Sil	147Sm/144Nd
THB Lz991	close to	Linzigong vo	Linzhou	Nianbo	Linzigong lava	W.R.					147.6	92.3	4.625	0.710485	13	5.802	30.4	0.1154
THB Lz993	close to	Linzigong vo	Linzhou	Nianbo	Linzigong lava	W.R.					165.4	97.06	4.936	0.711575	18	4.683	26.19	0.1082
THB LZ998	close to	Linzigong vo	Linzhou	Nianbo	Linzigong lava	W.R.					92.91	57.51	4.678	0.711971	10	2.833	14.38	0.1192
THB Lz9913	close to	Linzigong vo	Linzhou	Dianzhong	Linzigong lava	W.R.					35.66	486.5	0.212	0.705176	11	4.514	20.6	0.1325
THB Lz9930	close to	Linzigong vo	Linzhou	Dianzhong	Linzigong lava	W.R.					52.44	390.1	0.3891	0.705671	12	3.945	18.61	0.1282
THB Lz9924	close to	Linzigong vo	Linzhou	Dianzhong	Linzigong lava	W.R.					65.58	355.7	0.5336	0.705883	13	4.273	21.46	0.1204
THB Lz9922	close to	Linzigong vo	Linzhou	mafic dike	Linzigong lava	W.R.					21.02	1100	0.05533	0.705002	11	9.593	47.73	0.1216
THB 09TB21-2	S.E. Lha	29.2°N 94°E	W. Nyingchi, on Yarlung Tsangpo	Milin granitoids	Gangdese belt	W.R.	Diorite				30.5	479	0.1844	0.704579	12	2.79	12.6	0.1342
THB 09TB22	S.E. Lha	29.2°N 94°E	W. Nyingchi, on Yarlung Tsangpo	Milin granitoids	Gangdese belt	W.R.	Diorite				21.7	551	0.1138	0.704521	12	2.44	10.5	0.141
THB 09TB38-1	S.E. Lha	29.2°N 94°E	W. Nyingchi, on Yarlung Tsangpo	Milin granitoids	Gangdese belt	W.R.	Diorite				25.8	498	0.1495	0.704561	12	3.92	19	0.1246
THB 09TB39	S.E. Lha	29.2°N 94°E	W. Nyingchi, on Yarlung Tsangpo	Milin granitoids	Gangdese belt	W.R.	Diorite				22.7	592	0.1108	0.70443	11	2.76	13.2	0.127
THB 09TB41-3	S.E. Lha	29.2°N 94°E	W. Nyingchi, on Yarlung Tsangpo	Milin granitoids	Gangdese belt	W.R.	Diorite				14.2	571	0.072	0.704427	11	3.3	15.7	0.1269
THB 09TB45-3	S.E. Lha	29.2°N 94°E	W. Nyingchi, on Yarlung Tsangpo	Milin granitoids	Gangdese belt	W.R.	Diorite				21.3	516	0.1191	0.704448	11	3.45	14.4	0.1444
THB 09TB46-2	S.E. Lha	29.2°N 94°E	W. Nyingchi, on Yarlung Tsangpo	Milin granitoids	Gangdese belt	W.R.	Diorite				37.1	509	0.2109	0.704496	12	3.23	15.1	0.1294
THB 09TB47-1	S.E. Lha	29.2°N 94°E	W. Nyingchi, on Yarlung Tsangpo	Milin granitoids	Gangdese belt	W.R.	Diorite				3.05	907	0.0097	0.704231	14	1.43	6.95	0.1241
THB 09TB47-3	S.E. Lha	29.2°N 94°E	W. Nyingchi, on Yarlung Tsangpo	Milin granitoids	Gangdese belt	W.R.	Diorite				28	468	0.173	0.704451	12	3.35	15.4	0.1316
THB 09TB50	S.E. Lha	29.2°N 94°E	W. Nyingchi, on Yarlung Tsangpo	Milin granitoids	Gangdese belt	W.R.	Diorite				41.6	480	0.2501	0.704564	14	2.78	12.8	0.1307
THB 09TB51-2	S.E. Lha	29.2°N 94°E	W. Nyingchi, on Yarlung Tsangpo	Milin granitoids	Gangdese belt	W.R.	Diorite				17.5	560	0.0904	0.704346	14	2.12	10.6	0.1203
THB 09TB36	S.E. Lha	29.2°N 94°E	W. Nyingchi, on Yarlung Tsangpo	Milin granitoids	Gangdese belt	W.R.	Granodiorite				35.2	511	0.1992	0.704668	14	2.84	14.4	0.1194
THB 09TB38-2	S.E. Lha	29.2°N 94°E	W. Nyingchi, on Yarlung Tsangpo	Milin granitoids	Gangdese belt	W.R.	Granodiorite				29.2	517	0.1632	0.704559	13	2.55	12.8	0.1201
THB 09TB41-1	S.E. Lha	29.2°N 94°E	W. Nyingchi, on Yarlung Tsangpo	Milin granitoids	Gangdese belt	W.R.	Granodiorite				21	598	0.1017	0.704411	10	2.03	10.5	0.1168
THB 09TB45-1	S.E. Lha	29.2°N 94°E	W. Nyingchi, on Yarlung Tsangpo	Milin granitoids	Gangdese belt	W.R.	Granodiorite				38.8	380	0.2954	0.704592	12	2.01	10	0.1214
THB 09TB45-2	S.E. Lha	29.2°N 94°E	W. Nyingchi, on Yarlung Tsangpo	Milin granitoids	Gangdese belt	W.R.	Granodiorite				46.4	387	0.3472	0.704645	11	2.02	10.6	0.1157
THB 09TB48-1	S.E. Lha	29.2°N 94°E	W. Nyingchi, on Yarlung Tsangpo	Milin granitoids	Gangdese belt	W.R.	Granodiorite				29.5	495	0.1727	0.704475	13	2	10	0.1203
THB 09TB68	S.E. Lhasa		I	Zhenga dorite-gabbro suite	Gangdese belt	W.R.	Amphibole gabbro				15.4	566	0.0789	0.704393	15	1.3	5.29	0.1483
THB 09TB72-1	S.E. Lhasa		I	Zhenga dorite-gabbro suite	Gangdese belt	W.R.	Amphibole gabbro				16.2	493	0.095	0.704934	14	1.36	5.1	0.1609
THB 09TB73	S.E. Lhasa		I	Zhenga dorite-gabbro suite	Gangdese belt	W.R.	Amphibole gabbro				16.3	510	0.0925	0.704467	14	1.48	5.88	0.1526
THB 09TB76	S.E. Lhasa		I	Zhenga dorite-gabbro suite	Gangdese belt	W.R.	Amphibole gabbro				7.45	798	0.027	0.704663	13	1.84	7.11	0.1562
THB 09TB79	S.E. Lhasa		I	Zhenga dorite-gabbro suite	Gangdese belt	W.R.	Amphibole gabbro				15.7	852	0.0533	0.704516	14	1.57	6.16	0.1539
THB 09TB67-1	S.E. Lhasa		II	Zhenga dorite-gabbro suite	Gangdese belt	W.R.	Amphibole gabbro				33.1	532	0.18	0.705024	17	3.05	13.5	0.1366
THB 09TB69	S.E. Lhasa		II	Zhenga dorite-gabbro suite	Gangdese belt	W.R.	Amphibole gabbro				30.1	861	0.1009	0.70469	14	4.1	19.8	0.1252
THB 09TB71	S.E. Lhasa		II	Zhenga dorite-gabbro suite	Gangdese belt	W.R.	Amphibole gabbro				29.9	439	0.1968	0.70504	17	2.98	10.5	0.1721
THB 09TB78-1a	S.E. Lhasa			Zhenga dorite-gabbro suite	Gangdese belt	W.R.	Amphibole gabbro				76.6	589	0.3758	0.7074	11	3.17	12.6	0.1527
THB 09TB78-2	S.E. Lhasa			Zhenga dorite-gabbro suite	Gangdese belt	W.R.	Diorite				171	130	3.8242	0.756998	6	6.96	32	0.1316
THB 09TB21-1	S.E. Lha	29.2°N 94°E	W. Nyingchi, on Yarlung Tsangpo	Milin intrusive suite	Gangdese belt	W.R.	Norite				3.22	551	0.0169	0.704384	10	1.68	6.59	0.1545
THB 09TB30-1	S.E. Lha	29.2°N 94°E	W. Nyingchi, on Yarlung Tsangpo	Milin intrusive suite	Gangdese belt	W.R.	Norite				1.48	84.4	0.0507	0.70445	13	1.21	4.25	0.1715
THB 09TB30-3	S.E. Lha	29.2°N 94°E	W. Nyingchi, on Yarlung Tsangpo	Milin intrusive suite	Gangdese belt	W.R.	Norite				1.58	803	0.0057	0.704337	11	1.54	5.22	0.1782
THB 09TB32	S.E. Lha	29.2°N 94°E	W. Nyingchi, on Yarlung Tsangpo	Milin intrusive suite	Gangdese belt	W.R.	Norite				3.26	421	0.0224	0.704267	12	0.979	3.7	0.1602
THB 09TB41-2	S.E. Lha	29.2°N 94°E	W. Nyingchi, on Yarlung Tsangpo	Milin intrusive suite	Gangdese belt	W.R.	Norite				1.68	544	0.0089	0.704241	15	1.45	5.13	0.1705
THB 09TB44-5	S.E. Lha	29.2°N 94°E	W. Nyingchi, on Yarlung Tsangpo	Milin intrusive suite	Gangdese belt	W.R.	Norite				4	803	0.0144	0.704648	10	0.786	2.75	0.173
THB 09TB49-2	S.E. Lha	29.2°N 94°E	W. Nyingchi, on Yarlung Tsangpo	Milin intrusive suite	Gangdese belt	W.R.	Norite				6.51	640	0.0294	0.704327	11	3.75	17.1	0.1326
THB 09TB30-2	S.E. Lha	29.2°N 94°E	W. Nyingchi, on Yarlung Tsangpo	Milin intrusive suite	Gangdese belt	W.R.	Hornblendite				1.67	270	0.0179	0.704352	12	2.2	7.91	0.1678
THB 09TB35-3	S.E. Lha	29.2°N 94°E	W. Nyingchi, on Yarlung Tsangpo	Milin intrusive suite	Gangdese belt	W.R.	Hornblendite				3.26	127	0.0743	0.704495	22	1.75	5.93	0.1787
THB 09TB42-2	S.E. Lha	29.2°N 94°E	W. Nyingchi, on Yarlung Tsangpo	Milin intrusive suite	Gangdese belt	W.R.	Hornblendite				1.5	72	0.0601	0.704402	13	1.42	4.94	0.1734
THB 09TB43-1	S.E. Lha	29.2°N 94°E	W. Nyingchi, on Yarlung Tsangpo	Milin intrusive suite	Gangdese belt	W.R.	Hornblendite				1.94	89.2	0.0628	0.704486	10	2.79	9.98	0.1688
THB 09TB43-2	S.E. Lha	29.2°N 94°E	W. Nyingchi, on Yarlung Tsangpo	Milin intrusive suite	Gangdese belt	W.R.	Hornblendite				2	75.2	0.0768	0.70445	13	1.81	6.68	0.1638
THB 09TB44-3	S.E. Lha	29.2°N 94°E	W. Nyingchi, on Yarlung Tsangpo	Milin intrusive suite	Gangdese belt	W.R.	Hornblendite				3.25	219	0.0428	0.704621	12	4.07	12.3	0.2009
THB 09TB61	S.E. Lhasa			Quguosha gabbros	Gangdese belt	W.R.	amphibole gabbro						0.0994	0.705768	5			0.1121
THB 11SR10-6	S.E. Lhasa			Quguosha gabbros	Gangdese belt	W.R.	amphibole gabbro						0.0681	0.705822	6			0.1269
THB 11SR10-7	S.E. Lhasa			Quguosha gabbros		W.R.	amphibole gabbro						0.0436	0.705803	6			0.1201
THB 09TB63	S.E. Lhasa			Quguosha gabbros	Gangdese belt	W.R.	amphibole gabbro						0.0981	0.705752	6			0.1075
THB 09TB64	S.E. Lhasa			Quguosha gabbros	Gangdese belt	W.R.	amphibole gabbro						0.3693	0.70576	7			0.1124
THB 11SR10-1	S.E. Lhasa			Quguosha gabbros	Gangdese belt	W.R.	amphibole gabbro						0.2045	0.705789	5			0.1034
THB 11SR10-4	S.E. Lhasa			Quguosha gabbros	Gangdese belt	W.R.	amphibole gabbro						0.7447	0.705933	5			0.1301

Table SII-2 (…/…)

Ech.#	Region	River	Locality	Formation	Category	Type	Rock type	North	East	Date	Rb Sil	Sr Sil	87Rb/86Sr	87Sr/86Sr S	2s.d.	Sm Sil	Nd Sil	147Sm/144Nd
THB T0548	Nyingchi			E. Gangdese batholith	Gangdese belt		gabbro				45.9	930	0.1428	0.705637	1.3E-05	10.9	48.1	0.137
THB T0878-1	Nyingchi			E. Gangdese batholith	Gangdese belt		gabbro				41.7	800	0.1506	0.705683	1.1E-05	9.5	36.8	0.1562
THB T0878-2	Nyingchi			E. Gangdese batholith	Gangdese belt		gabbro				31.7	856	0.107	0.705705	1.4E-05	9	33	0.1654
THB T0878-3	Nyingchi			E. Gangdese batholith	Gangdese belt		gabbro				113	844	0.3869	0.706055	1.5E-05	9.7	47.4	0.1238
THB T0878-4	Nyingchi			E. Gangdese batholith	Gangdese belt		gabbro				40.6	776	0.1512	0.705754	1.5E-05	12.5	53.5	0.1412
THB T0878-5	Nyingchi			E. Gangdese batholith	Gangdese belt		gabbro				32.7	1116	0.0847	0.705537	1.5E-05	8.9	37.7	0.1425
THB T0878-6	Nyingchi			E. Gangdese batholith	Gangdese belt		gabbro				25.2	1288	0.0565	0.705592	7E-06	5.4	22.4	0.1449
THB T0289	N.E. Lhasa			E. Gangdese batholith	Gangdese belt		basaltic dyke				28.8	430	0.1938	0.705469	1.4E-05	3.5	16.3	0.1312
THB T0580-D2-	Nyingchi			E. Gangdese batholith	Gangdese belt		basaltic dyke				27.8	808	0.0994	0.706371	1.2E-05	10.5	58	0.1094
THB T0580-D2-	Nyingchi			E. Gangdese batholith	Gangdese belt		basaltic dyke				45.7	830	0.1591	0.706069	9E-06	8.5	35.6	0.1447
THB T0580-D2-	Nyingchi			E. Gangdese batholith	Gangdese belt		basaltic dyke				49.5	738	0.1938	0.706088	1.4E-05	9.2	49.6	0.1121
THB T0580-D1-	Nyingchi			E. Gangdese batholith	Gangdese belt		basaltic dyke				36.6	404	0.2618	0.705913	1.2E-05	16.4	105	0.0944
THB T0580-D1-	Nyingchi			E. Gangdese batholith	Gangdese belt		basaltic dyke				36.1	321	0.325	0.706022	1.4E-05	14.2	87	0.0987
THB T0580-D1-	Nyingchi			E. Gangdese batholith	Gangdese belt		basaltic dyke				33.4	371	0.2602	0.705967	1.2E-05	14.6	94.2	0.0937
THB T0580-14-	Nyingchi			E. Gangdese batholith	Gangdese belt		mafic enclave				54.4	722	0.2178	0.705972	7E-06	10.4	41.7	0.1508
THB T0580-14-	Nyingchi			E. Gangdese batholith	Gangdese belt		dioritic enclave				51.9	701	0.214	0.705992	1.4E-05	10.6	49.3	0.13
THB T0580-14-(	Nyingchi			E. Gangdese batholith	Gangdese belt		mafic enclave				113	1448	0.2255	0.706373	6E-06	19.5	114	0.1034
THB T0580-14-(	Nyingchi			E. Gangdese batholith	Gangdese belt		mafic enclave				86.2	521	0.4782	0.706519	1.4E-05	7.4	28	0.1589
THB T0580-14-(	Nyingchi			E. Gangdese batholith	Gangdese belt		mafic enclave				111	1588	0.202	0.706258	1.4E-05	17.6	99.4	0.107
THB T0580-14-(	Nyingchi			E. Gangdese batholith	Gangdese belt		mafic enclave				47.8	1054	0.1311	0.705896	1.5E-05	11.9	62.7	0.1147
THB T0934-13	Nyingchi			E. Gangdese batholith	Gangdese belt		mafic enclave				137	366	1.0831	0.708454	1.2E-05	2.4	10.1	0.1437
THB T0934-14-	Nyingchi			E. Gangdese batholith	Gangdese belt		mafic enclave				63.5	1544	0.119	0.705544	0.00001	8.4	48	0.1059
THB T0594-B1	Lhasa			C. Gangdese batholith	Gangdese belt		gabbro				6.8	670	0.0293	0.703998	1.1E-05	3	13.3	0.1377
THB T0594-B2	Lhasa			C. Gangdese batholith	Gangdese belt		gabbro				6.6	669	0.0286	0.703938	1.5E-05	2.9	12.9	0.1368
THB T0594-B3	Lhasa			C. Gangdese batholith	Gangdese belt		gabbro				6	641	0.0271	0.703876	1.2E-05	3.6	15.3	0.1426
THB T0594-B4	Lhasa			C. Gangdese batholith	Gangdese belt		gabbro				4.3	656	0.019	0.703897	1.3E-05	5.3	21.3	0.151
THB T0594-B5	Lhasa			C. Gangdese batholith	Gangdese belt		gabbro				6.1	731	0.0241	0.703841	1.4E-05	3.9	15.9	0.1483
THB T1031-NR	S.W. Lhasa			C. Gangdese batholith	Gangdese belt		norite				21.3	844	0.073	0.704306	1.3E-05	4	18	0.135
THB T1031-NR:	S.W. Lhasa			C. Gangdese batholith	Gangdese belt		norite				17.1	724	0.0683	0.704256	1.3E-05	4	17.4	0.1397
THB T1031-NR:	S.W. Lhasa			C. Gangdese batholith	Gangdese belt		norite				32.3	897	0.1041	0.704297	1.5E-05	3.5	16.2	0.1314
THB T1031-NR-	S.W. Lhasa			C. Gangdese batholith	Gangdese belt		norite				64.3	769	0.2418	0.704367	1.3E-05	3.5	14.5	0.1468
THB T1031-NR!	S.W. Lhasa			C. Gangdese batholith	Gangdese belt		norite				8.4	848	0.0286	0.704205	1.2E-05	3.4	15.4	0.1343
THB T1033-NR	S.W. Lhasa			C. Gangdese batholith	Gangdese belt		gabbro				24.9	699	0.103	0.704308	1.1E-05	4.4	19.5	0.1373
THB T1033-NR:	S.W. Lhasa			C. Gangdese batholith	Gangdese belt		gabbro				21.3	778	0.0792	0.704226	1.1E-05	4.1	17.3	0.1447
THB T1034-GR	S.W. Lhasa			C. Gangdese batholith	Gangdese belt		gabbro				52	979	0.1536	0.704009	1.7E-05	7.1	32	0.1334
THB T1034-GR	S.W. Lhasa			C. Gangdese batholith	Gangdese belt		gabbro				42.7	913	0.1353	0.703986	1.3E-05	7.6	32.9	0.1391
THB T1034-GR	S.W. Lhasa			C. Gangdese batholith	Gangdese belt		gabbro				65.8	1186	0.1604	0.704003	1.2E-05	7.6	32.8	0.1408
THB T1034-GR	S.W. Lhasa			C. Gangdese batholith	Gangdese belt		gabbro				45.2	1114	0.1173	0.70393	9E-06	6.6	28.4	0.1407
THB T1034-GR	S.W. Lhasa			C. Gangdese batholith	Gangdese belt		gabbro				52	982	0.1531	0.704006	0.00001	6.1	25.7	0.1428
HHC DK89	C. Nepal		Larkya phase	Manaslu granite			2M				311	87	10.35	n.d.				
HHC U315	C. Nepal		Larkya phase	Manaslu granite	HHC granite		2M				393	51.4	22.2	0.759326		2.41	7.91	0.1848
HHC XG43	C. Nepal		Larkya phase	Manaslu granite			T				438	47	25.63	0.773818				
HHC XG46	C. Nepal		Larkya phase	Manaslu granite			2MT				306	47	22.14	0.771027				
HHC XG56	C. Nepal		Larkya phase	Manaslu granite	HHC granite		2M				433	41.6	30.27	0.76509		1.86	5.76	0.1967
HHC XG102	C. Nepal		Larkya phase	Manaslu granite	HHC granite		2M				470	44.7	30.55	0.761066		2.37	7.67	0.1856
HHC XG270	C. Nepal		Larkya phase	Manaslu granite			2M				349	65	15.55	0.760331				
HHC XP130	C. Nepal		Larkya phase	Manaslu granite	HHC granite		2M				369	49.8	21.52	0.752333		1.69	5.85	0.174
HHC DK203	C. Nepal		Bimtang phase	Manaslu granite			2M				303	105	8.38	0.748998				
HHC DK208	C. Nepal		Bimtang phase	Manaslu granite	HHC granite		2M				316	109	8.44	0.748189		4	15.4	0.159
HHC XG162	C. Nepal		Bimtang phase	Manaslu granite			2M				114	114	2.9	0.746491				
HHC XL24	C. Nepal		Bimtang phase	Manaslu granite			2MT				276	83	9.63	0.744458				
HHC SKG8	E. Nepal			Langtang granite			Granites				115.6	250.6	6.3	0.75394				
HHC SKG9	E. Nepal			Langtang granite			Granites				331.2	85.3	0.75	0.76201				
HHC SKG12	E. Nepal			Langtang granite	HHC granite		Granites				120.9	194.7	4.68	0.75322		2.71	9.677	0.169
HHC SKG13	E. Nepal			Langtang granite			Granites				41.9	214.4	14.87	0.74971				
HHC SKG15	E. Nepal			Langtang granite	HHC granite		Granites				159	251	4.58	0.73724		4.107	16.09	0.154
HHC SKG3	E. Nepal			Langtang granite			Granites				67.4	244	1051	0.74515				
HHC SKG4	E. Nepal			Langtang granite			Granites				83	291	1018	0.74579				
HHC KG211	E. Nepal			Langtang granite			Granites				58	269	13.48	0.75342				
HHC KG208	E. Nepal			Langtang granite	HHC granite		Granites				127	236	5.4	0.75781		3.148	15.19	0.125
HHC KG210	E. Nepal			Langtang granite			Granites				66	221	9.73	0.74969				
HHC KG214	E. Nepal			Langtang granite	HHC granite		Granites				144	227	4.58	0.75711		4.296	16.92	0.153
HHC KG215	E. Nepal			Langtang granite			Granites				64	244	11.08	0.75106				

Table SII-2 (…/…)

Ech.#	Region	River	Locality	Formation	Category	Type	Rock type	North	East	Date	Rb Sil	Sr Sil	87Rb/86Sr	87Sr/86Sr S	2s.d.	Sm Sil	Nd Sil	147Sm/144Nd
HHC SLM1	E. Nepal			Langtang metamorphic			Migmatites				54.4	258.2	13.89	0.82545				
HHC LM201	E. Nepal			Langtang metamorphic			Migmatites				31	109	1025	0.7835				
HHC SKM2	E. Nepal			Langtang metamorphic			Migmatites				34.9	99.3	8.31	0.80355				
HHC SKM3	E. Nepal			Langtang metamorphic			Migmatites				35	153	12.78	0.81429				
HHC LM207	E. Nepal			Langtang metamorphic	HHC		Migmatites				24	146	17.81	0.83052		5.653	28.8	0.119
HHC LM209	E. Nepal			Langtang metamorphic			Migmatites				46	246	15.66	0.83156				
HHC LM211	E. Nepal			Langtang metamorphic			Migmatites				45	299	19.54	0.87698				
HHC SM201	E. Nepal			Langtang metamorphic			Schists				120	206	4.99	0.75768				
HHC SM203	E. Nepal			Langtang metamorphic			Schists				180	307	4.96	0.75043				
HHC SM202	E. Nepal			Langtang metamorphic	HHC		Schists				132	138	3.04	0.75294		6.38	29.29	0.132
HHC SM206	E. Nepal			Langtang metamorphic	HHC		Schists				91	112	3.58	0.75263		n/d	n/d	0.130*
HHC SSM6	E. Nepal			Langtang metamorphic	HHC		Schists				111.3	197	515	0.76231		7.81	38.07	0.124
HHC RM201	E. Nepal			Langtang metamorphic			Schists				150	139	2.69	0.76075				
HHC SNM2	E. Nepal			Langtang metamorphic			Augen gneiss				131.4	234.7	5.2	0.76609				
HHC NM203	E. Nepal			Langtang metamorphic			Augen gneiss				79	239	8.81	0.77203				
THB LKA-01	Lhasa			Dazi volcanics	Transhimalayan lava		basaltic andesite				23.5	554		0.704528	12	3.79	16.8	
THB LKA-02	Lhasa			Dazi volcanics			basaltic andesite				21.1	677				3.75	16.3	
THB LKA-03	Lhasa			Dazi volcanics			basaltic andesite				47.2	514				3.71	16.6	
THB LKA-04	Lhasa			Dazi volcanics	Transhimalayan lava		basalt				0.736	171		0.706168	12	3.46	13.4	
THB LKA-05	Lhasa			Dazi volcanics	Transhimalayan lava		basalt				0.267	177		0.705815	10	3.05	11.8	
THB LKA-06	Lhasa			Dazi volcanics			alt.				264	364				2.61	9.64	
THB LKA-07	Lhasa			Dazi volcanics	Transhimalayan lava		alt.				200	291		0.706888	10	2.6	9.62	
THB LKA-08	Lhasa			Dazi volcanics			alt.				313	201				2.52	9.34	
THB LKA-09	Lhasa			Dazi volcanics			alt.				320	200				2.99	11.6	
THB LKA-11	Lhasa			Dazi volcanics	Transhimalayan lava		alt.				218	290		0.707244	11	3.33	13.8	
THB LKA-12	Lhasa			Dazi volcanics	Transhimalayan lava		alt.				257	132		0.707807	14	2.8	8.48	
THB LKA-13	Lhasa			Dazi volcanics	Transhimalayan lava		alt.				175	290		0.706414	11	2.89	11.2	
THB LKA-14	Lhasa			Dazi volcanics	Transhimalayan lava		basalt				18.5	315		0.705745	13	2.2	8.13	
THB LKA-15	Lhasa			Dazi volcanics	Transhimalayan lava		basalt				33.1	129.0		0.706101	13	2.2	8.2	
THB LKA-16	Lhasa			Dazi volcanics	Transhimalayan lava		basalt				42.6	290		0.70591	14	2.96	11.4	
THB LKA-17	Lhasa			Dazi volcanics	Transhimalayan lava		alt.				270	413		0.706421	13	2.56	9.53	
THB LKA-19	Lhasa			Dazi volcanics			alt.				419	298				2.74	10.2	
THB L012	Lhasa			Dazi volcanics	Transhimalayan lava									0.707951	13			
THB L014	Lhasa			Dazi volcanics	Transhimalayan lava									0.707718	12			
THB T993	E. syntax	S.E. Namche	on Siang	Motuo	E. Transhimalayan batholiths		Hb-gabbro				15	1015	0.041765	0.706654	4E-06	4.63	22.4	0.125187
THB T998	E. syntax	S.E. Namche	on Siang	Motuo			Hb-gabbro				7	1137				8.77	37.3	
THB T1000	E. syntax	S.E. Namche	on Siang	Motuo	E. Transhimalayan batholiths		Gabbro–diorite				37	1047	0.102274	0.707713	5E-06	2.52	14.5	0.104971
THB T1008	E. syntax	S.E. Namche	on Siang	Motuo	E. Transhimalayan batholiths		Hb-gabbro				11	782	0.039414	0.706862	6E-06	8.18	31.3	0.157815
THB T1009	E. syntax	S.E. Namche	on Siang	Motuo			Hb-gabbro				50	663				6.35	22.7	
THB T1016	E. syntax	S.E. Namche	on Siang	Motuo	E. Transhimalayan batholiths		Gabbro–diorite				127	709	0.521171	0.708538	7E-06	4.93	21.6	0.138186
THB T1017	E. syntax	S.E. Namche	on Siang	Motuo	E. Transhimalayan batholiths		Hb-gabbro				87	728	0.346836	0.708877	4E-06	6.66	30.9	0.130175
THB T1220	E. syntax	N.E. Namche	barwa, close Dibang	52K	E. Transhimalayan batholiths		Bi-gabbro				68	845	0.232077	0.706638	4E-06	8.12	38.8	0.126634
THB T1222	E. syntax	N.E. Namche	barwa, close Dibang	52K			Bi-gabbro				75	886				10.62	62.4	
THB T1224	E. syntax	N.E. Namche	barwa, close Dibang	52K	E. Transhimalayan batholiths		Diorite				122	671	0.52912	0.707225	4E-06	7.79	40	0.117659
THB T699	E. syntax	S.E. Namche	on Siang	Damu	E. Transhimalayan batholiths		quartz–monzonite intruded by two-mica granite				74.7	932		0.708733	4E-06	6.08	39.1	
THB T700	E. syntax	S.E. Namche	on Siang	Damu	E. Transhimalayan batholiths		quartz–monzonite intruded by two-mica granite				102	813		0.707209	6E-06	8.59	57	
THB T1019	E. syntax	S.E. Namche	on Siang	Damu			quartz–monzonite intruded by two-mica granite				106	986				8.05	58.1	
THB T1020	E. syntax	S.E. Namche	on Siang	Damu			quartz–monzonite intruded by two-mica granite				226	653				6.65	48.6	
THB T829	E. syntax	N.E. Namche	barwa, close Dibang	52 K	E. Transhimalayan batholiths		biotite granite and porphyritic quartz–monzonite				175	588		0.707657	4E-06	5.81	37.1	
THB T836	E. syntax	N.E. Namche	barwa, close Dibang	52 K	E. Transhimalayan batholiths		biotite granite and porphyritic quartz–monzonite				148	543		0.707632	9E-06	4.3	26.8	
THB T1223	E. syntax	N.E. Namche	barwa, close Dibang	52 K			biotite granite and porphyritic quartz–monzonite				130	651				9.3	53	
THB T1225	E. syntax	N.E. Namche	barwa, close Dibang	52 K			biotite granite and porphyritic quartz–monzonite				145	534				6.46	39	
THB T1226	E. syntax	N.E. Namche	barwa, close Dibang	52 K			biotite granite and porphyritic quartz–monzonite				149	577				6.67	42.2	
THB BD01	E. Lhasa		S. Gangdese	Yeba fm	Gangdese belt						0.5	442	0.0038	0.704339	12	4.4	19.3	0.1406
THB BD21	E. Lhasa		S. Gangdese	Yeba fm	Gangdese belt						9	459	0.0404	0.704455	12	3.4	14.8	0.1471

Table SII-2 (…/…)

Ech.#	Region	River	Locality	Formation	Category	Type	Rock type	North	East	Date	Rb Sil	Sr Sil	87Rb/86Sr	87Sr/86Sr S	2s.d.	Sm Sil	Nd Sil	147Sm/144Nd
THB DZ13-1	E. Lhasa		S. Gangdese	Yeba fm	Gangdese belt						0.8	474	0.0044	0.70455	11	3.4	14	0.1516
THB DZ07-2	E. Lhasa		S. Gangdese	Yeba fm	Gangdese belt						50.2	397	0.3657	0.705956	11	2.2	9	0.1551
THB BD04	E. Lhasa		S. Gangdese	Yeba fm	Gangdese belt						6.5	538	0.0244	0.704881	14	4.5	19.2	0.1411
THB BD13	E. Lhasa		S. Gangdese	Yeba fm	Gangdese belt						6.2	515	0.0377	0.704618	13	3.7	15.5	0.1472
THB BD16	E. Lhasa		S. Gangdese	Yeba fm	Gangdese belt						3.8	831	0.008	0.704334	10	3.6	15.5	0.1434
THB YB5-2	E. Lhasa		S. Gangdese	Yeba fm	Gangdese belt						2.5	365	0.0121	0.704553	13	3.3	14.7	0.1491
THB YB5-3	E. Lhasa		S. Gangdese	Yeba fm	Gangdese belt						0.5	343	0.0056	0.704289	15	3.9	17.4	0.1457
THB DZ09-1	E. Lhasa		S. Gangdese	Yeba fm	Gangdese belt						7.1	213	0.0722	0.705249	14	3.7	15.5	0.1412
THB DZ11-1	E. Lhasa		S. Gangdese	Yeba fm	Gangdese belt						81.6	516	0.3406	0.707272	9	3.5	14.8	0.1416
THB BD19	E. Lhasa		S. Gangdese	Yeba fm	Gangdese belt						0.8	556	0.0059	0.704843	9	4.9	21.2	0.1388
THB YB5-1	E. Lhasa		S. Gangdese	Yeba fm	Gangdese belt						48.3	679	0.1285	0.704958	10	5	23	0.1406
THB DZ01-2	E. Lhasa		S. Gangdese	Yeba fm	Gangdese belt		Dacite				26	445	0.1732	0.704811	13	5.3	24.6	0.1303
THB DZ02-1	E. Lhasa		S. Gangdese	Yeba fm			Dacite				80.9	248	0.717	0.705833	12	4.7	23.6	
THB DZ03-1	E. Lhasa		S. Gangdese	Yeba fm	Gangdese belt		Dacite				149	149	2.4112	0.709351	12	4.1	20.5	0.1156
THB DZ03-2	E. Lhasa		S. Gangdese	Yeba fm	Gangdese belt		Dacite				68.4	400	0.4621	0.705466	12	3.9	18.2	0.128
THB DZ05-1	E. Lhasa		S. Gangdese	Yeba fm	Gangdese belt		Dacite				80.2	305	0.7963	0.706303	12	3.5	17.6	0.1209
THB DZ07-4	E. Lhasa		S. Gangdese	Yeba fm	Gangdese belt		Dacite				113	198	1.8614	0.708627	12	4	20.4	0.1205
THB T519	E. Synta	W. Namche	Nyingchi	Bayi granite	Transhimalaya granite		2 mica Gr				94.6	326	0.842	0.706755	3E-06	12.8	2.32	0.1099
THB T520	E. Synta	W. Namche	Nyingchi	Bayi granite	Transhimalaya granite		2 mica Gr				105.3	356	0.859	0.706746	3E-06	12.9	2.46	0.1149
THB T521	E. Synta	W. Namche	Nyingchi	Bayi granite	Transhimalaya granite		2 mica Gr				117.8	306	1.115	0.706903	3E-06	12.8	2.39	0.1128
THB T522	E. Synta	W. Namche	Nyingchi	Bayi granite	Transhimalaya granite		2 mica Gr				115.3	286	1.171	0.706874	4E-06	12.6	2.44	0.1174
THB T523	E. Synta	W. Namche	Nyingchi	Bayi granite	Transhimalaya granite		2 mica Gr				115.1	287	1.162	0.706894	3E-06	12.6	2.52	0.1208
THB T524	E. Synta	W. Namche	Nyingchi	Bayi granite	Transhimalaya granite		2 mica Gr				67.4	477	0.41	0.706694	7E-06	17.6	2.75	0.0944
THB T634	E. Synta	W. Namche	Nyingchi	Lunan granodiorite	Transhimalaya granite		2 mica Gd				75.3	716	0.305	0.706058	4E-06	30.1	4.57	0.0919
THB T636	E. Synta	W. Namche	Nyingchi	Lunan granodiorite	Transhimalaya granite		2 mica Gd				92.8	748	0.36	0.707156	3E-06	33.5	5.73	0.1033
THB T637	E. Synta	W. Namche	Nyingchi	Lunan granodiorite	Transhimalaya granite		2 mica Gr				64.2	509	0.366	0.706122	3E-06	51.3	6.77	0.0797
THB T638	E. Synta	W. Namche	Nyingchi	Lunan granodiorite	Transhimalaya granite		2 mica Gd				83.9	816	0.291	0.706282	4E-06	17	3	0.1096
THB T529	E. Synta	W. Namche	Nyingchi	Confluence granite	Transhimalaya granite		Bt Gr				106.6	304	1.015	0.707299	3E-06	26.4	4.75	0.1088
THB T525	E. Synta	W. Namche	Nyingchi	Nyingchi gneiss	Transhimalaya								5.01	0.731138	3E-06			0.1119
THB T527	E. Synta	W. Namche	Nyingchi	Nyingchi gneiss	Transhimalaya								0.595	0.713515	3E-06			0.1046
THB T528	E. Synta	W. Namche	Nyingchi	Nyingchi gneiss	Transhimalaya								2.189	0.734012	3E-06			0.1174
HHC T600	E. Synta	W. Namche	Nyingchi	Zhibai gneiss	HHC								7.37	0.77102	5E-06			0.1182
HHC T602	E. Synta	W. Namche	Nyingchi	Zhibai gneiss	HHC								2.193	0.75298	0.00001			0.1243
HHC T603	E. Synta	W. Namche	Nyingchi	Zhibai gneiss	HHC								6.231	0.7638	1.6E-05			0.1205
HHC T617	E. Synta	W. Namche	Nyingchi	Zhibai gneiss	HHC								6.995	0.80988	1.3E-05			0.1176
HHC T618	E. Synta	W. Namche	Nyingchi	Zhibai gneiss	HHC								11.274	0.79822	5E-06			0.1078
HHC T611	E. Synta	W. Namche	Nyingchi	Duoxiongla migmatite	HHC								12.023	0.99018	9E-06			0.1169
HHC T612	E. Synta	W. Namche	Nyingchi	Duoxiongla migmatite	HHC								5.122	0.84919	1.2E-05			0.1022
HHC T613	E. Synta	W. Namche	Nyingchi	Duoxiongla migmatite	HHC								3.818	0.80611	7E-06			0.1196
HHC T614	E. Synta	W. Namche	Nyingchi	Duoxiongla migmatite	HHC								1.678	0.74643	4E-06			0.1222
HHC T616	E. Synta	W. Namche	Nyingchi	Duoxiongla migmatite	HHC								5.354	0.83374	7E-06			0.1224
THB T684	E. Synta	S.E. Namche	Barwa	Beibeng granite	E. Transhimalayan batholiths		two-mica granite				84	411	0.59	0.706734	6E-06	3.79	23.66	0.0969
THB T686	E. Synta	S.E. Namche	Barwa	Beibeng granite	E. Transhimalayan batholiths		two-mica granite				82	492	0.48	0.706656	5E-06	1.85	10.2	0.1093
THB T690	E. Synta	S.E. Namche	Barwa	Beibeng granite	E. Transhimalayan batholiths		two-mica granite				81	471	0.498	0.706108	6E-06	2.57	13.87	0.1119
THB T692	E. Synta	S.E. Namche	Barwa	Beibeng granite	E. Transhimalayan batholiths		two-mica granite				112	460	0.708	0.706474	4E-06	1.6	9.93	0.0972
THB T697	E. Synta	S.E. Namche	Barwa	Damu granite	E. Transhimalayan batholiths		two-mica granite				137	218	0.315	0.70658	5E-06	3.73	23.15	0.0794
THB T698	E. Synta	S.E. Namche	Barwa	Damu granite	E. Transhimalayan batholiths		two-mica granite				168	344	1.419	0.706827	4E-06	5.19	36.06	0.087
THB T1018	E. Synta	S.E. Namche	Barwa	Damu granite	E. Transhimalayan batholiths		two-mica granite				119	176	1.967	0.721502	7E-06	6.44	35.24	0.1105
THB T866	E. Synta	N.E. Namche	Barwa	Bomi granite	E. Transhimalayan batholiths		foliated granite				108	668	0.468	0.712603	6E-06	3.16	16.23	0.1177
THB T1037	E. Synta	E. Namche	Barwa	Bolonggong granite	E. Transhimalayan batholiths		two-mica granite				125	424	0.853	0.70719	5E-06	1.82	9.75	0.1128
THB T1038	E. Synta	E. Namche	Barwa	Bolonggong granite	E. Transhimalayan batholiths		two-mica granite				102	496	0.594	0.706287	5E-06	2.33	13.07	0.1076
THB T1041	E. Synta	E. Namche	Barwa	Bolonggong granite	E. Transhimalayan batholiths		two-mica granite				126	473	0.774	0.708319	5E-06	3.42	18.83	0.1097
THB T1043	E. Synta	E. Namche	Barwa	Bolonggong granite	E. Transhimalayan batholiths		two-mica granite				102	457	0.644	0.706681	4E-06	4.86	29.31	0.1003
THB T1059	E. Synta	E. Namche	Barwa	Bolonggong granite	E. Transhimalayan batholiths		two-mica granite				117	381	0.889	0.706876	5E-06	3.91	23.12	0.1022
THB T1061	E. Synta	E. Namche	Barwa	Bolonggong granite	E. Transhimalayan batholiths		two-mica granite				121	403	0.868	0.706425	4E-06	4.01	21.48	0.1129
TSS/ T856	E. Syntaxis			Bomi Group (metam)	Transhimalaya		garnet–biotite–plagioclase gneiss						4.252	0.748429	5E-06			0.1041
TSS/ T865	E. Syntaxis			Bomi Group (metam)	Transhimalaya		garnet–biotite–plagioclase gneiss						4.318	0.740547	5E-06			0.1155
TSS/ T867	E. Syntaxis			Bomi Group (metam)	Transhimalaya		garnet–biotite–plagioclase gneiss						2.061	0.733837	7E-06			0.1113
TSS/ T837	E. Syntaxis			Bomi Group (metam)	Transhimalaya		amphibolite						0.824	0.721199	6E-06			0.1014
HHC 111920	E. Synta	W. Namche	Qiangna	Dongjiu S.	HHC		Two-mica schist							0.939088	9			
HHC 112101	E. Synta	W. Namche	Laiguo	Laiguo S.	HHC		Epidote biotiteschist				333	134	1.17	0.711662	9	9.96	44.83	0.1349
HHC 112102	E. Synta	W. Namche	Barwa, on Yarlung Tsangbo	Laiguo S.	HHC		Muscovite quartziteschist				31	35	3.27	0.751085	10	1.1	5.93	0.1126
HHC 112104	E. Synta	W. Namche	Barwa, on Yarlung Tsangbo	Laiguo S.	HHC		Muscovitemylonite							1.060312	10			

Table SII-2 (…/…)

	Ech.#	Region	River	Locality	Formation	Category	Type	Rock type	North	East	Date	Rb Sil	Sr Sil	87Rb/86Sr	87Sr/86Sr S	2s.d.	Sm Sil	Nd Sil	147Sm/144Nd
HHC	112107	E. Synta	W. Namche	Laiguo section	Laiguo S.	HHC		Biotite gneiss							0.880905	9			
HHC	112108	E. Synta	W. Namche	Barwa, on Yarlung Tsangbo	Laiguo S.	HHC		Augen biotitegneiss							1.098777	10			
HHC	112113	E. Synta	W. Namche	Barwa, on Yarlung Tsangbo	Pei S.	HHC		Augen sillimanitebiotite gneiss				171	211	3.59	0.746684	10	9.74	66.35	0.0891
HHC	112115	E. Synta	W. Namche	Barwa, on Yarlung Tsangbo	Pei S.	HHC		Sillimanite biotitegneiss				186	140	2.19	0.732574	10	4.17	30.83	0.0821
HHC	112120	E. Synta	W. Namche	Barwa, on Yarlung Tsangbo	Pei S.	HHC		Sillimanite biotitegneiss				33	213	19.24	0.90654	10	12.21	63.28	0.1171
HHC	112125	E. Synta	W. Namche	Barwa, on Yarlung Tsangbo	Namche Barwa S.	HHC		Garnet sillimanitebiotite gneiss							0.883291	10			
HHC	112201	E. Synta	W. Namche	Baga	Namche Barwa S.	HHC		Garnet biotitegneiss							0.958788	9			
HHC	112202	E. Synta	W. Namche	Barwa, on Yarlung Tsangbo	Namche Barwa S.	HHC		Garnet sillimanite gneiss							1.172496	11			
HHC	112203	E. Synta	W. Namche	Barwa, on Yarlung Tsangbo	Namche Barwa S.	HHC		Garnet sillimanite gneiss							0.87613	10			
HHC	112204	E. Synta	W. Namche	Barwa, on Yarlung Tsangbo	Namche Barwa S.	HHC		Garnet sillimanite gneiss				264	119	1.31	0.723834	10	10.01	55.36	0.1098
HHC	112301	E. Synta	W. Namche	S. Baga	Pei S.	HHC		Biotite gneiss				65	110	4.91	0.763553	8	6.56	33.08	0.1204
HHC	112302	E. Synta	W. Namche	Barwa, on Yarlung Tsangbo	Pei S.	HHC		Sillimanite biotite gneiss							1.121539	11			
HHC	112303	E. Synta	W. Namche	Barwa, on Yarlung Tsangbo	Pei S.	HHC		Sillimanite biotite gneiss				313	18	0.16	0.706741	9	4.36	13.87	0.1909
HHC	112402	E. Synta	W. Namche	W. Luxia	Dongjiu S.	HHC		Two-mica quartziteschist				49	71	4.2	0.74611	10	3.49	17.57	0.1206
HHC	112404	E. Synta	W. Namche	E. Deyiang	Pei S.	HHC		Garnet sillimanitegneiss				99	219	6.42	0.799306	9	9.68	50.8	0.1157
HHC	112601	E. Synta	W. Namche	S. Layue	Namche Barwa S.	HHC		Garnet sillimanitemigmatite				66	180	7.9	0.804812	9	8.53	45.37	0.1141
LH	KR38	Garhwal	Chandpur	30.2°N 79-80°E	Outer LH			Shale						11.22	0.82303				0.1176
LH	KR40	Garhwal	Chandpur	30.2°N 79-80°E	Outer LH			Sst						5.8	0.77091				0.1109
LH	KR41	Garhwal	Chandpur	30.2°N 79-80°E	Outer LH			Shale						10.01	0.80036				0.128
LH	KR44	Garhwal	Chandpur	30.2°N 79-80°E	Outer LH			Shale						10.07	0.81505				0.1212
LH	KR50	Garhwal	Chandpur	30.2°N 79-80°E	Outer LH			Shale						5.13	0.74993				0.1252
LH	KR146	Garhwal	Chandpur	30.2°N 79-80°E	Outer LH			Shale						14.31	0.7993				0.1157
LH	KR1	Garhwal	Deoban	30.2°N 79-80°E	Inner LH			Calc-sil						1.89	0.73309				0.1073
LH	KR4	Garhwal	Deoban	30.2°N 79-80°E	Inner LH			Carb						0.88	0.74123				0.1145
LH	KR85	Garhwal	Berinag	30.2°N 79-80°E	Inner LH			Phyllite						0.58	0.73292				0.1336
LH	KR102	Garhwal	Deoban	30.2°N 79-80°E	Inner LH			Calc-sil						9.72	0.93085				0.1152
LH	KR106	Garhwal	Berinag	30.2°N 79-80°E	Inner LH			Qtz-schist						43.39	1.17645				0.1144
LH	KR132	Garhwal	Berinag	30.2°N 79-80°E	Inner LH			Phyllite						0.12	0.71582				0.1336
LH?	KR52	Garhwal	Ramgarh	30.2°N 79-80°E	Ramgarh group			Schist						7.64	0.92238				0.1223
LH?	KR57	Garhwal	Ramgarh	30.2°N 79-80°E	Ramgarh group			Schist						80.04	0.93				0.1128
LH?	KR82	Garhwal	Munsiari	30.2°N 79-80°E	Munsiari goup			Gneiss						3.8	0.82451				0.1231
LH?	KR113	Garhwal	Munsiari	30.2°N 79-80°E	Munsiari goup			Gneiss						44.45	1.047				0.12
LH?	KR122	Garhwal	Munsiari	30.2°N 79-80°E	Munsiari goup			Qtzite						1.07	0.73692				0.1064
LH?	KR124	Garhwal	Munsiari	30.2°N 79-80°E	Munsiari goup			Gneiss						6.65	0.92049				0.1101
LH?	KR126	Garhwal	Munsiari	30.2°N 79-80°E	Munsiari goup			Gneiss						4.05	0.87794				0.1192
LH?	KR128	Garhwal	Munsiari	30.2°N 79-80°E	Munsiari goup			Gneiss						11.56	0.98043				0.1139
LH?	KR130	Garhwal	Munsiari	30.2°N 79-80°E	Munsiari goup			Gneiss						4.45	0.8294				0.1246
LH?	KR134	Garhwal	Munsiari	30.2°N 79-80°E	Munsiari goup			Gneiss						6.94	1.04368				0.1361
HHC	C42/97	Garhwal	uncertain	30.2°N 79-80°E	Vaikrita thrust			Schist						9.54	0.77685				0.1346
HHC	C4B	Garhwal	Vaikrita	30.2°N 79-80°E	Vaikrita group			Schist						3.07	0.7488				0.1199
HHC	C7	Garhwal	Vaikrita	30.2°N 79-80°E	Vaikrita group			Schist						6.41	0.77797				0.117
HHC	C200	Garhwal	Vaikrita	30.2°N 79-80°E	Vaikrita group			Qtzite						1.79	0.75782				0.116
HHC	C230	Garhwal	Vaikrita	30.2°N 79-80°E	Vaikrita group			Granite						6.66	0.7844				0.1612
HHC	C235	Garhwal	Vaikrita	30.2°N 79-80°E	Vaikrita group			Qtzite						10.51	0.79023				0.1133
HHC	C34/97	Garhwal	Vaikrita	30.2°N 79-80°E	Vaikrita group			Qtzite						1.85	0.74143				0.113
HHC	KR116	Garhwal	Vaikrita	30.2°N 79-80°E	Vaikrita group			Gneiss						8.49	0.75149				0.1293
HHC	KR118	Garhwal	Vaikrita	30.2°N 79-80°E	Vaikrita group			Gneiss						2.35	0.74513				0.121
HHC	KR120	Garhwal	Vaikrita	30.2°N 79-80°E	Vaikrita group			Gneiss						32.57	0.90621				0.147
HHC	KR143	Garhwal	Vaikrita	30.2°N 79-80°E	Vaikrita group			Qtzite						2.68	0.76172				0.1112
TSS	C29/97	Garhwal	TSS	30.2°N 79-80°E	TSS			Shale						27.7	0.77229				0.1213

Table SII-2. Compilation of bedrock Sr-Nd isotopic measurements.
Not exhaustive. Check comment for dubious datasets. LH: Lesser Himalaya, HHC: High Himalaya Crystalline, TSS: Tethyan Sedimentary Se
Table SII-2 (…/…)

	Ech.#	Region	River	Locality	Formation	144Nd/142Nd	2s.d.	eNd(0)	Reference	Commer	Full reference
											Morin, G., 2015. L'Érosion Et L'Alteration Et Leur Évolution Depuis Le Tardi-Pleistocene : Analyse Des Processus D'Érosion A Partir De Sediments De Riviere Actuels Et Passes Au Nepal Central. Université de Lorraine, Nancy, France.
TSS	NAG 22	C. Nepal	Marsyandi	source	TSS	0.51179		-16.6	Morin, 2015		
TSS	MAR-50	C. Nepal	Marsyandi	Temang	TSS	0.51175		-17.3	Morin, 2015		
TSS	MAR-45	C. Nepal	Naar k.	RG	TSS	0.511807		-16.2	Morin, 2015		
TSS	MO 501	C. Nepal	Kali	Tukuche	TSS	0.511749		-17.2	Morin, 2015		
TSS	NAG 33	C. Nepal	Kali	Koketani	TSS	0.511758		-17.2	Morin, 2015		
TSS	NAG 36	C. Nepal	Kali	Kopchepani	TSS	0.51181		-16.2	Morin, 2015		
TSS	LO2	C. Nepal	Kali	Kagbeni	mixed TSS basin	0.511837		-15.6	Morin, 2015		
TSS	NAG 20	C. Nepal	Kali	Kagbeni	mixed TSS basin	0.511928		-13.8	Morin, 2015		
TSS	NAG 25	C. Nepal	Kali	Jomoson	mixed TSS basin	0.511898		-14.4	Morin, 2015		
TSS	MO 504	C. Nepal	Yamkim	outlet	TSS	0.51166		-18.9	Morin, 2015		
TSS	MO 516	C. Nepal	Kali		mixed TSS basin	0.511816		-15.9	Morin, 2015		
TSS	NAG 38	C. Nepal	Kali	Dana	mixed TSS basin	0.511823		-15.9	Morin, 2015		
TSS	NAG 42	C. Nepal	Kali	Tatopani	mixed TSS basin	0.511775		-16.8	Morin, 2015		
TSS	MAR-52	C. Nepal	Dudh k.	Darapani	mixed TSS basin	0.511712		-18.1	Morin, 2015		
TSS	MAR-57	C. Nepal	Marsyandi	Tal depot de terasse pour tester la variabilité t	mixed TSS basin	0.511782		-16.7	Morin, 2015		
TSS	MAR-55	C. Nepal	Marsyandi	Tal	mixed TSS basin	0.511726		-17.8	Morin, 2015		
TSS	HF 10	C. Nepal	Seti		mixed TSS basin	0.511748		-17.4	Morin, 2015		
HHC	MO 50	C. Nepal	Chepe	Vallon	HHC			-12.4	Morin, 2015		
HHC	MAR-26	C. Nepal	Chepe		HHC	0.511824		-15.9	Morin, 2015		
HHC	KN 101	C. Nepal	Likhu		HHC	0.511812		-16.1	Morin, 2015		
HHC	KN 83	C. Nepal	Tadi		HHC	0.511838		-15.6	Morin, 2015		
HHC	CA11215C	C. Nepal	Khudi k. N	Branche Nord	HHC	0.511867		-15.0	Morin, 2015		
HHC	CA10112A	C. Nepal	Khudi k. W	Branch W	HHC	0.511893		-14.5	Morin, 2015		
HHC	SKD71	C. Nepal	Khudi k.	Khudi	HHC	0.511894		-14.5	Morin, 2015		
HHC	CA11212A	C. Nepal	Khudi	Nord W basin	HHC	0.511835		-15.7	Morin, 2015		
HHC	CA10113	C. Nepal	Khudi basin	HHC Trib	HHC	0.511862		-15.1	Morin, 2015		
HHC	CA954	C. Nepal	Khudi basin	Landslide	HHC	0.51188		-14.8	Morin, 2015		
HHC	GA 32	C. Nepal	Mailung	Paigutang	mixed HHC basin	0.511686		-18.6	Morin, 2015		
HHC	CA10116	C. Nepal	Khudi k.	Khudi Power house	mixed HHC basin	0.511871		-15.0	Morin, 2015		
HHC	CA11111	C. Nepal	Khudi k.	Khudi Power house	mixed HHC basin	0.511857		-15.2	Morin, 2015		
HHC	B106	C. Nepal	6.1		0.8 HHC bedrock			-14.3	Morin, 2015		
HHC	B114	C. Nepal	3		0.8 HHC bedrock			-13.9	Morin, 2015		
HHC	NL43	C. Nepal	3.9		0.7 HHC bedrock			-16.2	Morin, 2015		
HHC	NL58	C. Nepal	3.1		0.7 HHC bedrock			-14.0	Morin, 2015		
HHC	NL59	C. Nepal	1.1		0.7 HHC bedrock			-15.1	Morin, 2015		
HHC	NL74	C. Nepal	2		0.7 HHC bedrock			-15.5	Morin, 2015		
HHC	NL75	C. Nepal	5.5		0.8 HHC bedrock			-16.8	Morin, 2015		
HHC	NL76	C. Nepal	1.4		0.7 HHC bedrock			-15.3	Morin, 2015		
HHC	NL85	C. Nepal	2		0.7 HHC bedrock			-18.2	Morin, 2015		
HHC	NL93	C. Nepal	0.4		0.7 HHC bedrock			-18.0	Morin, 2015		
HHC	NL420	C. Nepal	19.2		0.8 HHC bedrock			-15.5	Morin, 2015		
LH	NAG 4	C. Nepal	Bijaipur	Kundahar	LH	0.511349		-25.1	Morin, 2015		
LH	MO 112	C. Nepal	Isul k.	Bhuri G.	LH	0.511324		-25.6	Morin, 2015		
LH	MO 102	C. Nepal	Marsel k.	Darondi	LH			-23.8	Morin, 2015		
LH	MO 109	C. Nepal	Mati k.	Bhuri G.	LH			-20.7	Morin, 2015		
LH	MO 207	C. Nepal	Andi	Kali Gandaki	LH	0.511319		-25.7	Morin, 2015		
LH	GA 99	C. Nepal	Mailung	landslide	LH	0.511452		-23.0	Morin, 2015		
LH	GA 112	C. Nepal	Mailung	Camp	LH	0.511343		-25.1	Morin, 2015		
LH	MAR28	C. Nepal	Paudi k.	RG	LH	0.511392		-24.3	Morin, 2015		
LH	MAR64	C. Nepal	Ngadi Khola	RG	LH	0.511423		-23.7	Morin, 2015		
LH	GA 50	C. Nepal	Mailung Col		LH	0.511587		-20.4	Morin, 2015		
											Bouquillon, A., France-Lanord, C., Michard, A., Tiercelin, J.-J., 1990. Sedimentology and Isotopic Chemistry of the Bengal Fan Sediments: The Denudation of the Himalaya, in: Cochran, J.R., Stow, D.A.V., et al. (Eds.), Distal Bengal Fan. Proceedings of the Ocean Drilling Program, Scientific Results, Vol. 116, pp. 43–58.
LH	AP 346	C. Nepal		Manaslu section	LH Kuncha pelites	0.511397	28	-24.2	Vidal unpub., in Franc		https://doi.org/doi:10.2973/odp.proc.sr.116.117.1990
											France-Lanord, C., Le Fort, P., 1988. Crustal melting and granite genesis during the Himalayan collision orogenesis. Transactions of the Royal Society of Edinburgh: Earth Sciences 79, 183–195.
LH	AP 385	C. Nepal		Manaslu section	LH Kuncha pelites	0.511331	25	-25.5	Vidal unpub., in Franc		https://doi.org/10.1017/S0263593300014206
TSS	NA 178	C. Nepal		Manaslu section	TSS Jurassic schist	0.511795	28	-16.4	Bouquillon et al., 1990		
TSS	NA 181	C. Nepal		Manaslu section	TSS Cretaceous (volcaniclastic)	0.512405	28	-4.5	Bouquillon et al., 1990		
											Deniel, C., Vidal, P., Fernandez, A., Le Fort, P., Peucat, J.-J., 1987. Isotopic study of the Manaslu granite (Himalaya, Nepal): inferences on the age and source of Himalayan leucogranites. Contributions to
HHC	DK 43	C. Nepal		Manaslu	Leucogranite				Deniel et al., Sr-Nd bu		Mineralogy and Petrology 96, 78–92. https://doi.org/10.1007/BF00375529
HHC	DK 45	C. Nepal		Manaslu	Leucogranite	0.511827	36	-15.8	Deniel et al., 1987		
HHC	DK 46	C. Nepal		Manaslu	Leucogranite				Deniel et al., 1987		

Table SII-2 (…/…)

Ech.#	Region	River	Locality	Formation	144Nd/142Nd	2s.d.	eNd(0)	Reference	Commer	Full reference
HHCDK 47	C. Nepal		Manaslu	Leucogranite				Deniel et al., 1987		
HHCDK 48	C. Nepal		Manaslu	Leucogranite				Deniel et al., 1987		
HHCDK 49	C. Nepal		Manaslu	Leucogranite				Deniel et al., 1987		
HHCDK 50	C. Nepal		Manaslu	Leucogranite				Deniel et al., 1987		
HHCDK 51	C. Nepal		Manaslu	Leucogranite				Deniel et al., 1987		
HHCDK 52	C. Nepal		Manaslu	Leucogranite	0.511817	24	-16.0	Deniel et al., 1987		
HHCDK 53	C. Nepal		Manaslu	Leucogranite				Deniel et al., 1987		
HHCDK 54	C. Nepal		Manaslu	Leucogranite	0.51188	30	-14.8	Deniel et al., 1987; Vidal et al., 1984		
HHCDK 54	C. Nepal		Manaslu	Leucogranite	0.511849	34	-15.4	Deniel et al., 1987		
HHCDK 55a	C. Nepal		Manaslu	Leucogranite	0.511818	21	-16.0	Deniel et al., 1987		
HHCDK 55b	C. Nepal		Manaslu	Leucogranite				Deniel et al., 1987		
HHCDK 56	C. Nepal		Manaslu	Leucogranite				Deniel et al., 1987		
HHCDK 57	C. Nepal		Manaslu	Leucogranite				Deniel et al., 1987		
HHCDK 58	C. Nepal		Manaslu	Leucogranite	0.511897	12	-14.5	Deniel et al., 1987		
HHCDK 59	C. Nepal		Manaslu	Leucogranite	0.511819	35	-16.0	Deniel et al., 1987		
HHCU 464	C. Nepal		Manaslu	Leucogranite				Deniel et al., 1987		
HHCU 464	C. Nepal		Manaslu	Leucogranite				Deniel et al., 1987		
HHCU 464	C. Nepal		Manaslu	Leucogranite				Deniel et al., 1987		
HHCU 464	C. Nepal		Manaslu	Leucogranite				Deniel et al., 1987		
HHCU 464	C. Nepal		Manaslu	Leucogranite				Deniel et al., 1987		
HHCU 464	C. Nepal		Manaslu	Leucogranite				Deniel et al., 1987		
HHCU 464	C. Nepal		Manaslu	Leucogranite				Deniel et al., 1987		
HHCU 476	C. Nepal		Manaslu	Leucogranite				Vidal et al., 1982		
HHCU 476	C. Nepal		Manaslu	Leucogranite				Vidal et al., 1982		
HHCU 476	C. Nepal		Manaslu	Leucogranite				Vidal et al., 1982		
HHCX 12	C. Nepal		Manaslu	Leucogranite				Vidal et al., 1982		
HHCX 12	C. Nepal		Manaslu	Leucogranite				Deniel et al., 1987		
HHCX 12	C. Nepal		Manaslu	Leucogranite				Deniel et al., 1987		
HHCDK 157	C. Nepal		Manaslu	Leucogranite				Deniel et al., 1987		
HHCDK 157	C. Nepal		Manaslu	Leucogranite				Deniel et al., 1987		
HHCDK 195	C. Nepal		Manaslu	Leucogranite				Deniel et al., 1987		
HHCDK 195	C. Nepal		Manaslu	Leucogranite				Deniel et al., 1987		
HHCDK 195	C. Nepal		Manaslu	Leucogranite				Deniel et al., 1987		
HHCDK 195	C. Nepal		Manaslu	Leucogranite				Deniel et al., 1987		
HHCD 22	C. Nepal		Manaslu	Leucogranite	0.51184	2	-15.6	Deniel et al., 1987; Vidal et al., 1984		
HHCD 22	C. Nepal		Manaslu	Leucogranite				Deniel et al., 1987		
HHCD 22	C. Nepal		Manaslu	Leucogranite				Deniel et al., 1987		
HHCDK 65	C. Nepal		Manaslu	Leucogranite				Deniel et al., 1987		
HHCDK 67	C. Nepal		Manaslu	Leucogranite				Deniel et al., 1987		
HHCDK 72	C. Nepal		Manaslu	Leucogranite				Deniel et al., 1987		
HHCDK 98	C. Nepal		Manaslu	Leucogranite				Deniel et al., 1987		
HHCDK 102	C. Nepal		Manaslu	Leucogranite				Deniel et al., 1987		
HHCDK 111	C. Nepal		Manaslu	Leucogranite				Deniel et al., 1987		
HHCDK 112	C. Nepal		Manaslu	Leucogranite				Deniel et al., 1987		
HHCDK 116	C. Nepal		Manaslu	Leucogranite				Deniel et al., 1987		
HHCDK 136	C. Nepal		Manaslu	Leucogranite				Deniel et al., 1987		
HHCDK 138	C. Nepal		Manaslu	Leucogranite				Deniel et al., 1987		
HHCDK 139	C. Nepal		Manaslu	Leucogranite				Deniel et al., 1987		
HHCDK 140	C. Nepal		Manaslu	Leucogranite				Deniel et al., 1987		
HHCDK 141	C. Nepal		Manaslu	Leucogranite				Deniel et al., 1987		
HHCDK 151	C. Nepal		Manaslu	Leucogranite				Deniel et al., 1987		
HHCDK 151	C. Nepal		Manaslu	Leucogranite				Deniel et al., 1987		
HHCDK 152	C. Nepal		Manaslu	Leucogranite				Deniel et al., 1987		
HHCDK 157	C. Nepal		Manaslu	Leucogranite				Deniel et al., 1987		
HHCDK 160	C. Nepal		Manaslu	Leucogranite				Deniel et al., 1987		
HHCDK 161	C. Nepal		Manaslu	Leucogranite				Deniel et al., 1987		
HHCDK 162	C. Nepal		Manaslu	Leucogranite				Deniel et al., 1987		
HHCDK 167	C. Nepal		Manaslu	Leucogranite				Deniel et al., 1987		
HHCDK 180	C. Nepal		Manaslu	Leucogranite				Deniel et al., 1987		
HHCDK 185	C. Nepal		Manaslu	Leucogranite				Deniel et al., 1987		
HHCDK 186	C. Nepal		Manaslu	Leucogranite				Deniel et al., 1987		
HHCDK 188	C. Nepal		Manaslu	Leucogranite				Deniel et al., 1987		
HHCDK 191	C. Nepal		Manaslu	Leucogranite				Deniel et al., 1987		
HHCDK 195	C. Nepal		Manaslu	Leucogranite				Deniel et al., 1987		
HHCDK 211	C. Nepal		Manaslu	Leucogranite				Deniel et al., 1987		
HHCDK 213	C. Nepal		Manaslu	Leucogranite				Deniel et al., 1987		
HHCDK 214	C. Nepal		Manaslu	Leucogranite				Deniel et al., 1987		
HHCDK 217	C. Nepal		Manaslu	Leucogranite				Deniel et al., 1987		
HHCDK 220	C. Nepal		Manaslu	Leucogranite				Deniel et al., 1987		
HHCDK 237	C. Nepal		Manaslu	Leucogranite	0.511981	21	-12.8	Deniel et al., 1987		
HHCDK 240	C. Nepal		Manaslu	Leucogranite				Deniel et al., 1987		

Table SII-2 (…/…)

Ech.#	Region	River	Locality	Formation	144Nd/142Nd	2s.d.	eNd(0)	Reference	Commer	Full reference
HHCDK 242	C. Nepal		Manaslu	Leucogranite				Deniel et al., 1987		
HHCDK 247	C. Nepal		Manaslu	Leucogranite				Deniel et al., 1987		
HHCDK 268	C. Nepal		Manaslu	Leucogranite				Deniel et al., 1987		
HHCD 22	C. Nepal		Manaslu	Leucogranite				Deniel et al., 1987		
HHCD 14	C. Nepal		Manaslu	Leucogranite				Deniel et al., 1987		
HHCD 37	C. Nepal		Manaslu	Leucogranite	0.511819	15	-16.0	Deniel et al., 1987		
HHCD 45	C. Nepal		Manaslu	Leucogranite	0.5119	2	-14.4	Deniel et al., 1987; Vidal et al., 1984		
HHCDK 200	C. Nepal		Manaslu Sect. 1	Leucogranite	0.51189	40	-14.6	Deniel et al., 1987		
HHCDK 202	C. Nepal		Manaslu Sect. 1	Leucogranite				Deniel et al., 1987		
HHCDK 203	C. Nepal		Manaslu Sect. 1	Leucogranite				Deniel et al., 1987		
HHCDK 204	C. Nepal		Manaslu Sect. 1	Leucogranite				Deniel et al., 1987		
HHCDK 205	C. Nepal		Manaslu Sect. 1	Leucogranite				Deniel et al., 1987		
HHCDK 206	C. Nepal		Manaslu Sect. 1	Leucogranite				Deniel et al., 1987		
HHCDK 207	C. Nepal		Manaslu Sect. 1	Leucogranite	0.511852	40	-15.3	Deniel et al., 1987		
HHCDK 207	C. Nepal		Manaslu Sect. 1	Leucogranite	0.51188	10	-14.8	Deniel et al., 1987		
HHCDK 208	C. Nepal		Manaslu Sect. 1	Leucogranite	0.511909	40	-14.2	Deniel et al., 1987		
HHCDK 208	C. Nepal		Manaslu Sect. 1	Leucogranite	0.51188	10	-14.8	Deniel et al., 1987		
HHCDK 209	C. Nepal		Manaslu Sect. 1	Leucogranite	0.511972	37	-13.0	Deniel et al., 1987		
HHCDK 210	C. Nepal		Manaslu Sect. 1	Leucogranite				Deniel et al., 1987		
HHCDK 244	C. Nepal		Manaslu Sect. 1	Leucogranite				Deniel et al., 1987		
HHCDK 168	C. Nepal		Manaslu Sect. 2	Leucogranite	0.511961	43	-13.2	Deniel et al., 1987		
HHCDK 168	C. Nepal		Manaslu Sect. 2	Leucogranite	0.511968	51	-13.1	Deniel et al., 1987		
HHCDK 169	C. Nepal		Manaslu Sect. 2	Leucogranite				Deniel et al., 1987		
HHCDK 170	C. Nepal		Manaslu Sect. 2	Leucogranite				Deniel et al., 1987		
HHCDK 171	C. Nepal		Manaslu Sect. 2	Leucogranite				Deniel et al., 1987		
HHCDK 172	C. Nepal		Manaslu Sect. 2	Leucogranite	0.511948	17	-13.5	Deniel et al., 1987		
HHCDK 173	C. Nepal		Manaslu Sect. 2	Leucogranite				Deniel et al., 1987		
HHCDK 174a	C. Nepal		Manaslu Sect. 2	Leucogranite	0.511889	17	-14.6	Deniel et al., 1987		
HHCDK 175	C. Nepal		Manaslu Sect. 2	Leucogranite	0.511932	21	-13.8	Deniel et al., 1987		
HHCNL 219 (1)	C. Nepal		Manaslu Sect. 4	granite dyke	0.511875	10	-14.9	Deniel et al., 1987		
HHCNL 222 (2)	C. Nepal		Manaslu Sect. 4	granite dyke				Deniel et al., 1987		
HHCNL 223 (2)	C. Nepal		Manaslu Sect. 4	granite dyke				Deniel et al., 1987		
HHCNL 224 (2)	C. Nepal		Manaslu Sect. 4	granite dyke	0.511922	10	-14.0	Deniel et al., 1987		
HHCNL 225 (2)	C. Nepal		Manaslu Sect. 4	granite dyke	0.511936	16	-13.7	Deniel et al., 1987		
HHCNL 226 (3)	C. Nepal		Manaslu Sect. 4	granite dyke				Deniel et al., 1987		
HHCNL 227 (3)	C. Nepal		Manaslu Sect. 4	granite dyke	0.511909	15	-14.2	Deniel et al., 1987		
HHCNL 206	C. Nepal		Manaslu Sect. 5	Leucogranite	0.511829	11	-15.8	Deniel et al., 1987		
HHCNL 207	C. Nepal		Manaslu Sect. 5	Leucogranite	0.511887	17	-14.6	Deniel et al., 1987		
HHCNL 208	C. Nepal		Manaslu Sect. 5	Leucogranite	0.511907	12	-14.3	Deniel et al., 1987		
HHCNL 234	C. Nepal		Manaslu	Leucogranite	0.511873	18	-14.9	Deniel et al., 1987		
HHCU 862	C. Nepal		Manaslu	Leucogranite	0.511838	9	-15.6	Deniel et al., 1987		
HHCNL 43a	C. Nepal		Manaslu	FI Gneiss	0.51181	14	-16.2	Deniel et al., 1987		
HHCNL 58a	C. Nepal		Manaslu	FI Gneiss	0.511918	17	-14.0	Deniel et al., 1987		
HHCNL 59a	C. Nepal		Manaslu	FI Gneiss	0.511866	15	-15.1	Deniel et al., 1987		
HHCNL 74	C. Nepal		Manaslu	FI Gneiss	0.511844	8	-15.5	Deniel et al., 1987		
HHCNL 75	C. Nepal		Manaslu	FI Gneiss	0.511777	18	-16.8	Deniel et al., 1987		
HHCNL 76	C. Nepal		Manaslu	FI Gneiss	0.511852	21	-15.3	Deniel et al., 1987		
HHCNL 81	C. Nepal		Manaslu	FI Gneiss				Deniel et al., 1987		
HHCNL 85	C. Nepal		Manaslu	FI Gneiss	0.511706	19	-18.2	Deniel et al., 1987		
HHCNL 86	C. Nepal		Manaslu	FI Gneiss				Deniel et al., 1987		
HHCNL 93	C. Nepal		Manaslu	FI Gneiss	0.511713	21	-18.0	Deniel et al., 1987		
HHCNL 100	C. Nepal		Manaslu	FI Gneiss				Deniel et al., 1987		
HHCNL 100	C. Nepal		Manaslu	FI Gneiss				Deniel et al., 1987		
HHCNL 172	C. Nepal		Manaslu	FI Gneiss				Deniel et al., 1987		
HHCNL 499	C. Nepal		Manaslu	FI Gneiss				Deniel et al., 1987		
HHCNL 512	C. Nepal		Manaslu	FI Gneiss				Deniel et al., 1987		
										Vidal, Ph., Cocherie, A., Le Fort, P., 1982. Geochemical investigations of the origin of the Manaslu leucogranite (Himalaya, Nepal). Geochimica et Cosmochimica Acta 46, 2279–2292.
HHCβ 106a	C. Nepal		Manaslu	FI Gneiss	0.511903	18	-14.3	Vidal et al., 1982; Deni		https://doi.org/10.1016/0016-7037(82)90201-0
HHCβ 114a	C. Nepal		Manaslu	FI Gneiss	0.511905	14	-14.3	Vidal et al., 1982; Deniel et al., 1987		
HHCβ 114a	C. Nepal		Manaslu	FI Gneiss	0.511945	11	-13.5	Vidal et al., 1982; Deniel et al., 1987		
HHCU 48	C. Nepal		Manaslu	FI Gneiss	0.511817	24	-16.0	Vidal et al., 1982; Deniel et al., 1987		
										France-Lanord, C., Le Fort, P., 1988. Crustal melting and granite genesis during the Himalayan collision orogenesis. Transactions of the Royal Society of Edinburgh: Earth Sciences 79, 183–195.
LH AP9*	C. Nepal		Manaslu section	LH				Vidal unpub., in Franc		https://doi.org/10.1017/S0263593300014206
LH AP440*	C. Nepal		Manaslu section	LH				Vidal unpub., in France-Lanord and Le Fort, 1988		
LH AP 524*	C. Nepal		Manaslu section	LH				Vidal unpub., in France-Lanord and Le Fort, 1988		
LH AP 825*	C. Nepal		Manaslu section	LH				Vidal unpub., in France-Lanord and Le Fort, 1988		
LH AP 874*	C. Nepal		Manaslu section	LH				Vidal unpub., in France-Lanord and Le Fort, 1988		
LH AP 888*	C. Nepal		Manaslu section	LH				Vidal unpub., in France-Lanord and Le Fort, 1988		

Table SII-2 (…/…)

	Ech.#	Region	River	Locality	Formation	144Nd/142Nd	2s.d.	eNd(0)	Reference	Commer	Full reference
LH	NL1*	C. Nepal		Manaslu section	LH				Vidal unpub., in France-Lanord and Le Fort, 1988		
LH	NL3f	C. Nepal		Manaslu section	LH				Deniel, 1985, , in France-Lanord and Le Fort, 1988		
LH	NL4t	C. Nepal		Manaslu section	LH				Deniel, 1985, , in France-Lanord and Le Fort, 1988		
HHC	NL 428t	C. Nepal		Manaslu section	FII				Deniel, 1985, , in France-Lanord and Le Fort, 1988		
HHC	NL 623t	C. Nepal		Manaslu section	FII				Deniel, 1985, , in France-Lanord and Le Fort, 1988		
HHC	D77*	C. Nepal		Manaslu section	FIII				Vidal, in Le Fort et al., 1986, in France-Lanord and Le Fort, 1988		
HHC	D94*	C. Nepal		Manaslu section	FIII				Vidal, in Le Fort et al., 1986, in France-Lanord and Le Fort, 1988		
HHC	M84*	C. Nepal		Manaslu section	FIII				Vidal, in Le Fort et al., 1986, in France-Lanord and Le Fort, 1988		
HHC	NA 116|	C. Nepal		Manaslu section	FIII				Vidal, in Le Fort et al., 1986, in France-Lanord and Le Fort, 1988		
HHC	NA 155*	C. Nepal		Manaslu section	FIII				Vidal, in Le Fort et al., 1986, in France-Lanord and Le Fort, 1988		
HHC	NA 156*	C. Nepal		Manaslu section	FIII				Vidal, in Le Fort et al., 1986, in France-Lanord and Le Fort, 1988		
HHC	NA 216*	C. Nepal		Manaslu section	FIII				Vidal, in Le Fort et al., 1986, in France-Lanord and Le Fort, 1988		
HHC	NA 218*	C. Nepal		Manaslu section	FIII				Vidal, in Le Fort et al., 1986, in France-Lanord and Le Fort, 1988		
HHC	NL 478t	C. Nepal		Manaslu section	FIII				Deniel, 1985, , in France-Lanord and Le Fort, 1988		
HHC	T200*	C. Nepal		Manaslu section	FIII				Vidal, in Le Fort et al., 1986, in France-Lanord and Le Fort, 1988		
HHC	U203t	C. Nepal		Manaslu section	FIII				Deniel, 1985, , in France-Lanord and Le Fort, 1988		
HHC	U284*	C. Nepal		Manaslu section	FIII				Vidal, in Le Fort et al., 1986, in France-Lanord and Le Fort, 1988		
HHC	U308*	C. Nepal		Manaslu section	FIII				Vidal, in Le Fort et al., 1986, in France-Lanord and Le Fort, 1988		
HHC	U725*	C. Nepal		Manaslu section	FIII				Vidal, in Le Fort et al., 1986, in France-Lanord and Le Fort, 1988		
HHC	U925*	C. Nepal		Manaslu section	FIII				Vidal, in Le Fort et al., 1986, in France-Lanord and Le Fort, 1988		
HHC	U277	C. Nepal		Manaslu	Leucogranite	0.51197	3	-13.0	Vidal et al., 1984		Vidal, Ph., Bernard-Griffiths, J., Cocherie, A., Le Fort, P., Peucat, J.J., Sheppard, S.M.F., 1984. Geochemical comparison between Himalayan and Hercynian leucogranites. Physics of the Earth and Planetary Interiors 35, 179–190. https://doi.org/10.1016/0031-9201(84)90041-4
HHC	N 67	C. Nepal		Manaslu	Leucogranite	0.51176	9	-17.1	Vidal et al., 1984		
HHC	M 102	C. Nepal		Manaslu	FI				Vidal et al., 1982		Vidal, Ph., Cocherie, A., Le Fort, P., 1982. Geochemical investigations of the origin of the Manaslu leucogranite (Himalaya, Nepal). Geochimica et Cosmochimica Acta 46, 2279–2292. https://doi.org/10.1016/0016-7037(82)90201-0
HHC	M 114	C. Nepal		Manaslu	FI				Vidal et al., 1982		
HHC	L 12	C. Nepal		Manaslu	FI				Vidal et al., 1982		
HHC	M 108	C. Nepal		Manaslu	FI				Vidal et al., 1982		
HHC	U 124	C. Nepal		Manaslu	FI				Vidal et al., 1982		
HHC	M 107	C. Nepal		Manaslu	FI				Vidal et al., 1982		
TSS	87 28				TSS Cretaceous	0.512093	13	-10.6	France-Lanord et al., 1		France-Lanord, C., Derry, L., Michard, A., 1993. Evolution of the Himalaya since Miocene time: isotopic and sedimentological evidence from the Bengal Fan. Geological Society, London, Special Publications 74, 603–621. https://doi.org/10.1144/GSL.SP.1993.074.01.40
TSS	87 32				TSS Trias	0.511824	17	-15.9	France-Lanord et al., 1993		
TSS	LA 194	W. Himalaya		Indus	TSS Indus margin	0.511883	9	-14.7	France-Lanord et al., 1993		
TSS	LA 158	W. Himalaya		Indus	TSS Indus margin	0.512046	37	-11.5	France-Lanord et al., 1993		
TSS	25 1	W. Himalaya		Ladakh	TSS Suture Ladak	0.512313	34	-6.3	France-Lanord et al., 1993		
TSS	89 1	W. Himalaya		Ladakh	TSS Suture Ladak	0.51258	24	-1.1	France-Lanord et al., 1993		
TSS	1TBkag	C. Nepal			Chukh Fm	0.512322	31	-6.2	Robinson et al., 2001		Robinson, D.M., DeCelles, P.G., Patchett, P.J., Garzione, C.N., 2001. The kinematic evolution of the Nepalese Himalaya interpreted from Nd isotopes. Earth and Planetary Science Letters 192, 507–521. https://doi.org/10.1016/S0012-821X(01)00451-4
TSS	2TBpha	C. Nepal			Dogger Fm	0.511805	15	-16.2	Robinson et al., 2001		
TSS	3TBjom	C. Nepal			Jomson Fm	0.511673	12	-18.8	Robinson et al., 2001		
TSS	4TBSya	C. Nepal			Tilicho Fm	0.511671	9	-18.9	Robinson et al., 2001		
TSS	5TBMar	C. Nepal			Tilichio Fm	0.51175	11	-17.3	Robinson et al., 2001		
TSS	DD-31	W. Nepal			Melmura Fm	0.511734	7	-17.6	Robinson et al., 2001		
TSS	DD-33	W. Nepal			Melmura Fm	0.51161	9	-20.1	Robinson et al., 2001		
HHC	AG-106	E. Nepal			Formation I	0.511619	10	-19.9	Robinson et al., 2001		
HHC	AG-109	E. Nepal			Formation I	0.511714	14	-18.0	Robinson et al., 2001		
HHC	9TBkal	C. Nepal			Formation III	0.512137	30	-9.8	Robinson et al., 2001		
HHC	12TBgh	C. Nepal			Formation I	0.511814	13	-16.1	Robinson et al., 2001		
HHC	13TBru	C. Nepal			Formation II	0.511946	14	-13.5	Robinson et al., 2001		
HHC	AG-105	E. Nepal			Formation I	0.511836	14	-15.6	Robinson et al., 2001		
HHC	DDG-98	W. Nepa		Greater Himalayan klippen	C-O granite, DT	0.512034	15	-11.8	Robinson et al., 2001		
HHC	DD-40	W. Nepa		Greater Himalayan klippen	Kalikot Schist, Dt	0.512248	7	-7.6	Robinson et al., 2001		
LH	K1-99	C. Nepal			Benighat Fm	0.511343	14	-25.3	Robinson et al., 2001		
LH	SR-37	W. Nepal			Benighat Fm	0.51163	12	-19.7	Robinson et al., 2001		
LH	SR-35	W. Nepal			Benighat Fm	0.511575	11	-20.7	Robinson et al., 2001		
LH	DD-58	W. Nepal			Benighat Fm	0.51143	11	-23.6	Robinson et al., 2001		
LH	23TBtu	C. Nepal			Syangia Fm	0.51163	26	-19.7	Robinson et al., 2001		
LH	23TBSe	C. Nepal			Syangia Fm	0.511339	11	-25.3	Robinson et al., 2001		
LH	CH-1	W. Nepal			Galyang Fm	0.51146	15	-23.0	Robinson et al., 2001		
LH	DD-15	W. Nepal			Galyang Fm	0.511741	25	-17.5	Robinson et al., 2001		
LH	22TBPu	C. Nepal			Galyang Fm	0.511711	13	-18.1	Robinson et al., 2001		

Table SII-2 (…/…)

	Ech.#	Region	River	Locality	Formation	144Nd/142Nd	2s.d.	eNd(0)	Reference	Commer	Full reference
LH	24TBLi	C. Nepal			Galyang Fm	0.511521	11	-21.8	Robinson et al., 2001		
LH	K3-99	C. Nepal			Galyang Fm	0.511557	9	-21.1	Robinson et al., 2001		
LH	DD-52	W. Nepal			Sangram Fm	0.511822	12	-15.9	Robinson et al., 2001		
LH	20TBSI	C. Nepal			Sangram Fm	0.511444	8	-23.3	Robinson et al., 2001		
LH	18TBBra	C. Nepal			Ranimata Fm	0.511333	42	-25.5	Robinson et al., 2001		
LH	K2-99	C. Nepal			Ranimata Fm	0.511369	15	-24.8	Robinson et al., 2001		
LH	AG-103	E. Nepal			Ranimata Fm	0.511518	10	-21.8	Robinson et al., 2001		
LH	AG-104	E. Nepal			Ranimata Fm	0.51137	12	-24.7	Robinson et al., 2001		
LH	SR-30	W. Nepal			Ulleri	0.511647	8	-19.3	Robinson et al., 2001		
LH	AG-111	E. Nepal			Ulleri	0.511652	14	-19.2	Robinson et al., 2001		
LH	AG-112	E. Nepal			Ulleri	0.511571	11	-20.8	Robinson et al., 2001		
THB	K89G185			I	Tibetan lava				Turner et al., 1996		Turner, S., Arnaud, N., Liu, J., Rogers, N., Hawkesworth, C., Harris, N., Kelley, S., Van Calsteren, P., Deng, W., 1996. Post-collision, Shoshonitic Volcanism on the Tibetan Plateau: Implications for Convective Thinning of the Lithosphere and the Source of Ocean Island Basalts. Journal of Petrology 37, 45–71. https://doi.org/10.1093/petrology/37.1.45
THB	K89G186			I	Tibetan lava				Turner et al., 1996		
THB	K89G191			I	Tibetan lava				Turner et al., 1996		
THB	K89G192			I	Tibetan lava				Turner et al., 1996		
THB	K89G193			I	Tibetan lava				Turner et al., 1996		
THB	K89G197			I	Tibetan lava				Turner et al., 1996		
THB	K89G200			I	Tibetan lava				Turner et al., 1996		
THB	KP23-1			II	Tibetan lava				Turner et al., 1996		
THB	KP23-3			II	Tibetan lava				Turner et al., 1996		
THB	KP24-1			III	Tibetan lava				Turner et al., 1996		
THB	KP12-2			IV	Tibetan lava				Turner et al., 1996		
THB	KP12-5			IV	Tibetan lava				Turner et al., 1996		
THB	KP12-7			IV	Tibetan lava				Turner et al., 1996		
THB	K705			IV	Tibetan lava				Turner et al., 1996		
THB	K708			IV	Tibetan lava				Turner et al., 1996		
THB	K713			IV	Tibetan lava				Turner et al., 1996		
THB	K716			IV	Tibetan lava				Turner et al., 1996		
THB	K718			IV	Tibetan lava				Turner et al., 1996		
THB	K720			IV	Tibetan lava				Turner et al., 1996		
THB	K723			IV	Tibetan lava				Turner et al., 1996		
THB	K731			IV	Tibetan lava				Turner et al., 1996		
THB	K732			IV	Tibetan lava				Turner et al., 1996		
THB	K738			IV	Tibetan lava				Turner et al., 1996		
THB	KP12-4			IV	Tibetan lava				Turner et al., 1996		
THB	KP10-3	N. Lhasa Plutonic belt		V	Tibetan lava	0.512248		-7.6	Turner et al., 1996		
THB	KP10-6	N. Lhasa Plutonic belt		V	Tibetan lava	0.512323		-6.1	Turner et al., 1996		
THB	BG121			VI	Tibetan lava				Turner et al., 1996		
THB	BG124			VI	Tibetan lava				Turner et al., 1996		
THB	KP35-10			VII	Tibetan lava				Turner et al., 1996		
THB	BB94-2	N. Lhasa Plutonic belt		VIII	Tibetan lava	0.512318		-6.2	Turner et al., 1996		
THB	BB104	N. Lhasa Plutonic belt		VIII	Tibetan lava	0.512331		-6.0	Turner et al., 1996		
THB	K9006			VII	Tibetan lava				Turner et al., 1996		
THB	K9007			VII	Tibetan lava				Turner et al., 1996		
THB	K9008			VII	Tibetan lava				Turner et al., 1996		
THB	K9016			VII	Tibetan lava				Turner et al., 1996		
THB	K9018			VII	Tibetan lava				Turner et al., 1996		
THB	K9021			VII	Tibetan lava				Turner et al., 1996		
THB	K9026			VII	Tibetan lava				Turner et al., 1996		
THB	K9028			VII	Tibetan lava				Turner et al., 1996		
THB	K9031			VII	Tibetan lava				Turner et al., 1996		
THB	K9032			VII	Tibetan lava				Turner et al., 1996		
THB	K9038			VII	Tibetan lava				Turner et al., 1996		
THB	K9024	N. Lhasa Plutonic belt		IX	Tibetan lava	0.512324		-6.1	Turner et al., 1996		
THB	K9027	N. Lhasa Plutonic belt		V-IX	Tibetan lava	0.512333		-5.9	Turner et al., 1996		
THB	K9001			VII	Tibetan lava				Turner et al., 1996		
THB	K9041			VII	Tibetan lava				Turner et al., 1996		
THB	COUL311	S. Tibet Lhassa Gang		XI	Tibetan lava	0.51265		0.2	Turner et al., 1996		
THB	COUL326	S. Tibet Lhassa Gang		XI	Tibetan lava	0.51248		-3.1	Turner et al., 1996		
THB	COUL328	S. Tibet Lhassa Gang		XI	Tibetan lava	0.51247		-3.3	Turner et al., 1996		
THB	COUL338	S. Tibet Lhassa Gang		XI	Tibetan lava	0.5127		1.2	Turner et al., 1996		
THB	COUL339	S. Tibet Lhassa Gang		XI	Tibetan lava	0.51271		1.4	Turner et al., 1996		
THB	K89G159	S. Tibet Karakorum		X	Tibetan lava	0.51207		-11.1	Turner et al., 1996		
THB	K89G162	S. Tibet Karakorum		X	Tibetan lava	0.51203		-11.9	Turner et al., 1996		
THB	K89G163	S. Tibet Karakorum		X	Tibetan lava	0.51204		-11.7	Turner et al., 1996		

Table SII-2 (…/…)

Ech.#	Region	River	Locality	Formation	144Nd/142Nd	2s.d.	eNd(0)	Reference	Commer	Full reference
										Lin, I.-J., Chung, S.-L., Chu, C.-H., Lee, H.-Y., Gallet, S., Wu, G., Ji, J., Zhang, Y., 2012. Geochemical and Sr–Nd isotopic characteristics of Cretaceous to Paleocene granitoids and volcanic rocks, SE Tibet: petrogenesis and tectonic implications. Journal of Asian Earth Sciences 53, 131–150.
THB ET103A	F.E. Transhimalaya		Along Parlung	Azhagong batholith	0.51202		-12.1	Lin et al., 2012		
THB ET104B	F.E. Transhimalaya		Along Parlung	Azhagong batholith	0.512207		-8.4	Lin et al., 2012		
THB ET105A	F.E. Transhimalaya		Along Parlung	Azhagong batholith	0.512171		-9.1	Lin et al., 2012		
THB ET105B	F.E. Transhimalaya		Along Parlung	Azhagong batholith	0.512202		-8.5	Lin et al., 2012		
THB ET107A	F.E. Transhimalaya		Along Parlung	Azhagong batholith	0.512265		-7.3	Lin et al., 2012		
THB ET117A	F.E. Transhimalaya		Along Parlung	Azhagong batholith	0.512215		-8.3	Lin et al., 2012		
THB ET120A	F.E. Transhimalaya		Along Parlung	Azhagong batholith	0.512376		-5.1	Lin et al., 2012		
THB ET122A	F.E. Transhimalaya		Along Parlung	Azhagong batholith	0.512404		-4.6	Lin et al., 2012		
THB ET125A	F.E. Transhimalaya		Along Parlung	Azhagong batholith	0.511925		-13.9	Lin et al., 2012		
THB ET105G	F.E. Transhimalaya		Along Parlung	Azhagong enclaves	0.512372		-5.2	Lin et al., 2012		
THB ET119A	F.E. Transhimalaya		Along Parlung	Azhagong enclaves				Lin et al., 2012		
THB ET120C	F.E. Transhimalaya		Along Parlung	Azhagong enclaves	0.512454		-3.6	Lin et al., 2012		
THB ET120D	F.E. Transhimalaya		Along Parlung	Azhagong enclaves	0.512514		-2.4	Lin et al., 2012		
THB ET120E	F.E. Transhimalaya		Along Parlung	Azhagong enclaves	0.51246		-3.5	Lin et al., 2012		
THB ET106A2	F.E. Transhimalaya		NE. Of Parlung	Demulha batholith	0.512091		-10.7	Lin et al., 2012		
THB ET219B2	F.E. Transhimalaya		NE. Of Parlung	Demulha batholith	0.512038		-11.7	Lin et al., 2012		
THB ET220B	F.E. Transhimalaya		NE. Of Parlung	Demulha batholith	0.512049		-11.5	Lin et al., 2012		
THB ET221B	F.E. Transhimalaya		NE. Of Parlung	Demulha batholith	0.512047		-11.5	Lin et al., 2012		
THB ET222B	F.E. Transhimalaya		NE. Of Parlung	Demulha batholith	0.512054		-11.4	Lin et al., 2012		
THB ET113A	F.E. Transhimalaya		S. of Parlung	Chayu batholith	0.51207		-11.1	Lin et al., 2012		
THB ET115F1	F.E. Transhimalaya		S. of Parlung	Chayu batholith	0.512069		-11.1	Lin et al., 2012		
THB ET116B	F.E. Transhimalaya		S. of Parlung	Chayu batholith	0.512184		-8.9	Lin et al., 2012		
THB ET203B	F.E. Transhimalaya		S. of Parlung	Chayu batholith	0.512533		-2.0	Lin et al., 2012		
THB ET203D	F.E. Transhimalaya		S. of Parlung	Chayu batholith	0.512521		-2.3	Lin et al., 2012		
THB 73–73	F.E. Transhimalaya		S. of Parlung	Chayu batholith	0.511944		-13.5	Lin et al., 2012		
THB RAW11	F.E. Transhimalaya		Center of Parlung	Ranwu volcanic rocks	0.512557		-1.6	Lin et al., 2012		
THB RAW12	F.E. Transhimalaya		Center of Parlung	Ranwu volcanic rocks	0.512583		-1.1	Lin et al., 2012		
THB RAW13	F.E. Transhimalaya		Center of Parlung	Ranwu volcanic rocks	0.512399		-4.7	Lin et al., 2012		
THB RAW15	F.E. Transhimalaya		Center of Parlung	Ranwu volcanic rocks	0.512607		-0.6	Lin et al., 2012		
THB RAW17	F.E. Transhimalaya		Center of Parlung	Ranwu volcanic rocks	0.512269		-7.2	Lin et al., 2012		
THB RAW20	F.E. Transhimalaya		Center of Parlung	Ranwu volcanic rocks	0.512588		-1.0	Lin et al., 2012		
THB RAW22	F.E. Transhimalaya		Center of Parlung	Ranwu volcanic rocks	0.512578		-1.2	Lin et al., 2012		
THB RAW24	F.E. Transhimalaya		Center of Parlung	Ranwu volcanic rocks	0.51267		0.6	Lin et al., 2012		
THB RAW25	F.E. Transhimalaya		Center of Parlung	Ranwu volcanic rocks	0.512738		2.0	Lin et al., 2012		
THB RAW26	F.E. Transhimalaya		Center of Parlung	Ranwu volcanic rocks	0.512582		-1.1	Lin et al., 2012		
THB RAW29	F.E. Transhimalaya		Center of Parlung	Ranwu volcanic rocks	0.512577		-1.2	Lin et al., 2012		
THB RAW30	F.E. Transhimalaya		Center of Parlung	Ranwu volcanic rocks	0.512597		-0.8	Lin et al., 2012		
	Locality									
										Wen, D.-R., Chung, S.-L., Song, B., Iizuka, Y., Yang, H.-J., Ji, J., Liu, D., Gallet, S., 2008. Late Cretaceous Gangdese intrusions of adakitic geochemical characteristics, SE Tibet: petrogenesis and tectonic implications. Lithos 105, 1–11.
THB T212	S.E. Tibe	S.E. of Lhas	Langxian	Gangdese batholith	0.512637		0.0	Wen et al., 2008		
THB T027	S.E. Tibe	S.E. of Lhas	Langxian	Gangdese batholith	0.512699		1.2	Wen et al., 2008		
THB T213	S.E. Tibe	S.E. of Lhas	Langxian	Gangdese batholith	0.512748		2.1	Wen et al., 2008		
THB T215	S.E. Tibe	S.E. of Lhas	Langxian	Gangdese batholith	0.512664		0.5	Wen et al., 2008		
THB T026	S.E. Tibe	S.E. of Lhas	Langxian	Gangdese batholith	0.512747		2.1	Wen et al., 2008		
THB T216A	S.E. Tibe	S.E. of Lhas	Lilong	Gangdese batholith	0.5		1.3	Wen et al., 2008		
THB T217	S.E. Tibe	S.E. of Lhas	Lilong	Gangdese batholith	0.512673		0.7	Wen et al., 2008		
THB T024	S.E. Tibe	S.E. of Lhas	Lilong	Gangdese batholith	0.512702		1.2	Wen et al., 2008		
THB T218B	S.E. Tibe	S.E. of Lhas	Lilong	Gangdese batholith	0.512709		1.4	Wen et al., 2008		
										Zhu, D., Mo, X., Wang, L., Zhao, Z., Niu, Y., Zhou, C., Yang, Y., 2009. Petrogenesis of highly fractionated I-type granites in the Zayu area of eastern Gangdese, Tibet: Constraints from zircon U-Pb geochronology, geochemistry and Sr-Nd-Hf isotopes. Sci. China Ser. D-Earth Sci. 52, 1223–1239. https://doi.org/10.1007/s11430-009-0132-x
THB CY1-01	F.E. Transhimalaya		Zayu	NE. Gangdese	0.511999	5E-06	-12.5	Zhu et al., 2009		
CY1-02	F.E. Transhimalaya		Zayu	NE. Gangdese						
CY1-02R	F.E. Transhimalaya		Zayu	NE. Gangdese						
CY1-1	F.E. Transhimalaya		Zayu	NE. Gangdese	0.512115	8E-06	-10.2	Zhu et al., 2009		
CY2-1	F.E. Transhimalaya		Zayu	NE. Gangdese						
CY3-1	F.E. Transhimalaya		Zayu	NE. Gangdese	0.512177	6E-06	-9.0	Zhu et al., 2009		
CY4-1	F.E. Transhimalaya		Zayu	NE. Gangdese	0.512081	5E-06	-10.9	Zhu et al., 2009		
CY6-1	F.E. Transhimalaya		Zayu	NE. Gangdese	0.512072	8E-06	-11.0	Zhu et al., 2009		
	Linzizong successions:									

Table SII-2 (…/…)

Ech.#	Region	River	Locality	Formation	144Nd/142Nd	2s.d.	eNd(0)	Reference	Commer	Full reference
										Lee, H.-Y., Chung, S.-L., Ji, J., Qian, Q., Gallet, S., Lo, C.-H., Lee, T.-Y., Zhang, Q., 2012. Geochemical and Sr–Nd isotopic constraints on the genesis of the Cenozoic Linzizong volcanic successions, southern Tibet. Journal of Asian Earth Sciences, The Tibetan Orogenic Evolution: Pre- to Post-Collisional Geologic Records 53, 96–114. https://doi.org/10.1016/j.jseaes.2011.08.019
T233C	S. Tibet	1. Dianzhong	Formation	Linzigong volcanics	0.512778	6	2.7	Lee et al., 2012		
T238B	S. Tibet	1. Dianzhong	Formation	Linzigong volcanics	0.512636	4	0.0	Lee et al., 2012		
T239	S. Tibet	1. Dianzhong	Formation	Linzigong volcanics	0.512489	3	-2.9	Lee et al., 2012		
T136B	S. Tibet	1. Dianzhong	Formation	Linzigong volcanics	0.511994	3	-12.6	Lee et al., 2012		
T134	S. Tibet	1. Dianzhong	Formation	Linzigong volcanics	0.51203	4	-11.9	Lee et al., 2012		
T136A	S. Tibet	1. Dianzhong	Formation	Linzigong volcanics	0.512009	11	-12.3	Lee et al., 2012		
T234C	S. Tibet	2. Nianbo	Formation	Linzigong volcanics	0.512667	6	0.6	Lee et al., 2012		
T235B	S. Tibet	2. Nianbo	Formation	Linzigong volcanics	0.512563	7	-1.5	Lee et al., 2012		
T042D	S. Tibet	3. Pana For	a. Calc-alkaline suite	Linzigong volcanics	0.512814	4	3.4	Lee et al., 2012		
T006B2	S. Tibet	3. Pana For	a. Calc-alkaline suite	Linzigong volcanics	0.512399	11	-4.7	Lee et al., 2012		
T116A	S. Tibet	3. Pana For	a. Calc-alkaline suite	Linzigong volcanics	0.512522	2	-2.3	Lee et al., 2012		
T083C	S. Tibet	3. Pana For	a. Calc-alkaline suite	Linzigong volcanics	0.512626	15	-0.2	Lee et al., 2012		
T047	S. Tibet	3. Pana For	a. Calc-alkaline suite	Linzigong volcanics	0.512635	13	-0.1	Lee et al., 2012		
T006B1	S. Tibet	3. Pana For	a. Calc-alkaline suite	Linzigong volcanics	0.512558	3	-1.6	Lee et al., 2012		
T056B	S. Tibet	3. Pana For	a. Calc-alkaline suite	Linzigong volcanics	0.512662	9	0.5	Lee et al., 2012		
T049B	S. Tibet	3. Pana For	a. Calc-alkaline suite	Linzigong volcanics	0.51253	10	-2.1	Lee et al., 2012		
T054A	S. Tibet	3. Pana For	a. Calc-alkaline suite	Linzigong volcanics	0.512556	12	-1.6	Lee et al., 2012		
T062B	S. Tibet	3. Pana For	a. Calc-alkaline suite	Linzigong volcanics	0.512587	12	-1.0	Lee et al., 2012		
T063	S. Tibet	3. Pana For	a. Calc-alkaline suite	Linzigong volcanics	0.512582	6	-1.1	Lee et al., 2012		
T055A	S. Tibet	3. Pana For	a. Calc-alkaline suite	Linzigong volcanics	0.512651	3	0.3	Lee et al., 2012		
T040A	S. Tibet	3. Pana For	a. Calc-alkaline suite	Linzigong volcanics	0.51256	15	-1.5	Lee et al., 2012		
T038F	S. Tibet	3. Pana For	a. Calc-alkaline suite	Linzigong volcanics	0.512362	3	-5.4	Lee et al., 2012		
T051C	S. Tibet	3. Pana For	a. Calc-alkaline suite	Linzigong volcanics	0.512529	5	-2.1	Lee et al., 2012		
T065B	S. Tibet	3. Pana For	a. Calc-alkaline suite	Linzigong volcanics	0.512638	12	0.0	Lee et al., 2012		
T036D	S. Tibet	3. Pana For	b. Low-K suite	Linzigong volcanics	0.512799	12	3.1	Lee et al., 2012		
T041H	S. Tibet	3. Pana For	b. Low-K suite	Linzigong volcanics	0.512829	11	3.7	Lee et al., 2012		
T041F	S. Tibet	3. Pana For	b. Low-K suite	Linzigong volcanics	0.5128	13	3.2	Lee et al., 2012		
T034A	S. Tibet	3. Pana For	b. Low-K suite	Linzigong volcanics	0.512925	5	5.6	Lee et al., 2012		
ST055C	S. Tibet	3. Pana For	c. Shoshonitic suite	Linzigong volcanics	0.512472	1	-3.2	Lee et al., 2012		
ST061A	S. Tibet	3. Pana For	c. Shoshonitic suite	Linzigong volcanics	0.512339	6	-5.8	Lee et al., 2012		
ST057A	S. Tibet	3. Pana For	c. Shoshonitic suite	Linzigong volcanics	0.512361	3	-5.4	Lee et al., 2012		
ST059A	S. Tibet	3. Pana For	c. Shoshonitic suite	Linzigong volcanics	0.512647	20	0.2	Lee et al., 2012		
ST053	S. Tibet	3. Pana For	c. Shoshonitic suite	Linzigong volcanics	0.512317	7	-6.3	Lee et al., 2012		
ST062	S. Tibet	3. Pana For	c. Shoshonitic suite	Linzigong volcanics	0.512294	3	-6.7	Lee et al., 2012		
ST060C	S. Tibet	3. Pana For	c. Shoshonitic suite	Linzigong volcanics	0.512373	10	-5.2	Lee et al., 2012		
ST055A	S. Tibet	3. Pana For	c. Shoshonitic suite	Linzigong volcanics	0.512324	10	-6.1	Lee et al., 2012		
T155	S. Tibet	3. Pana For	d. High-REE suite	Linzigong volcanics	0.512475	2	-3.2	Lee et al., 2012		
T082B	S. Tibet	3. Pana For	d. High-REE suite	Linzigong volcanics	0.512454	13	-3.6	Lee et al., 2012		
T103	S. Tibet	3. Pana For	d. High-REE suite	Lizigong volcanics	0.512448	6	-3.7	Lee et al., 2012		
ST058	S. Tibet	3. Pana For	e. Evolved suite	Linzigong volcanics	0.511676	5	-18.8	Lee et al., 2012		
T065A	S. Tibet	3. Pana For	e. Evolved suite	Linzigong volcanics	0.511908	8	-14.2	Lee et al., 2012		
T072A	S. Tibet	Northern Province:		Linzigong volcanics	0.512082	5	-10.8	Lee et al., 2012		
T129A	S. Tibet	Northern Province:		Linzigong volcanics	0.512269	5	-7.2	Lee et al., 2012		
T072E	S. Tibet	Northern Province:		Linzigong volcanics	0.511985	12	-12.7	Lee et al., 2012		
T131A	S. Tibet	Northern Province:		Linzigong volcanics	0.512193	8	-8.7	Lee et al., 2012		
T169A	S. Tibet	Northern Province:		Lizigong volcanics	0.512225	10	-8.1	Lee et al., 2012		
T079B	S. Tibet	Sangri Group:		Linzigong volcanics	0.512616	12	-0.4	Lee et al., 2012		
ET021B	S. Tibet	Sangri Group:		Linzigong volcanics	0.512672	12	0.7	Lee et al., 2012		
ST119A	S. Tibet	Sangri Group:		Linzigong volcanics	0.512961	10	6.3	Lee et al., 2012		
ST122	S. Tibet	Sangri Group:		Linzigong volcanics	0.512889	7	4.9	Lee et al., 2012		
ST101B	S. Tibet	Sangri Group:		Linzigong volcanics	0.512725	3	1.7	Lee et al., 2012		
ST102B	S. Tibet	Sangri Group:		Linzigong volcanics	0.512796	5	3.1	Lee et al., 2012		
ET021C	S. Tibet	Sangri Group:		Linzigong volcanics	0.512737	15	1.9	Lee et al., 2012		
ET022A	S. Tibet	Sangri Group:		Linzigong volcanics	0.51263	12	-0.2	Lee et al., 2012		
ET024	S. Tibet	Sangri Group:		Linzigong volcanics	0.512495	10	-2.8	Lee et al., 2012		
										Xu, W.-C., Zhang, H.-F., Guo, L., Yuan, H.-L., 2010. Miocene high Sr/Y magmatism, south Tibet: Product of partial melting of subducted Indian continental crust and its tectonic implication. Lithos 114, 293–306. https://doi.org/10.1016/j.lithos.2009.09.005
THB T358	S.E. Tibe	TGP	W. of Lhasa	PG granodiorite, NM granite and their associated porph	0.512505	3	-2.6	Xu et al., 2010		
THB T379	S.E. Tibe	PG	W. of Lhasa	PG granodiorite, NM granite and their associated porph	0.512424	3	-4.2	Xu et al., 2010		
THB T380	S.E. Tibe	PG	W. of Lhasa	PG granodiorite, NM granite and their associated porph	0.512436	2	-3.9	Xu et al., 2010		
THB T381	S.E. Tibe	PG	W. of Lhasa	PG granodiorite, NM granite and their associated porph	0.512449	2	-3.7	Xu et al., 2010		
THB T399	S.E. Tibe	NMP	W. of Lhasa	PG granodiorite, NM granite and their associated porph	0.51233	2	-6.0	Xu et al., 2010		
THB T400	S.E. Tibe	NMP	W. of Lhasa	PG granodiorite, NM granite and their associated porph	0.512347	2	-5.7	Xu et al., 2010		
THB T401	S.E. Tibe	NM	W. of Lhasa	PG granodiorite, NM granite and their associated porph	0.512215	2	-8.3	Xu et al., 2010		
THB T403	S.E. Tibe	NM	W. of Lhasa	PG granodiorite, NM granite and their associated porph	0.512363	2	-5.4	Xu et al., 2010		

Table SII-2 (…/…)

Ech.#	Region	River	Locality	Formation	144Nd/142Nd	2s.d.	eNd(0)	Reference	Commer	Full reference
THB T404	S.E. Tibe	NM	W. of Lhasa	PG granodiorite, NM granite and their associated porph	0.512251	1	-7.5	Xu et al., 2010		
THB T604	S.E. Tibe	MG	Eastern syntaxis	Mafic granulite from eastern Himalayan syntaxis	0.512743	1	2.0	Xu et al., 2010		
THB T605	S.E. Tibe	MG	Eastern syntaxis	Mafic granulite from eastern Himalayan syntaxis	0.512769	1	2.6	Xu et al., 2010		
THB T606	S.E. Tibe	MG	Eastern syntaxis	Mafic granulite from eastern Himalayan syntaxis	0.512803	1	3.2	Xu et al., 2010		
THB T607	S.E. Tibe	MG	Eastern syntaxis	Mafic granulite from eastern Himalayan syntaxis	0.512584	1	-1.1	Xu et al., 2010		
THB T608	S.E. Tibe	MG	Eastern syntaxis	Mafic granulite from eastern Himalayan syntaxis	0.512672	2	0.7	Xu et al., 2010		
THB 09NDS-11	S.E. Tibet		Lhasa	Nuri intrusive rocks	0.512526		-2.2	Chen et al., 2015		Chen, L., Qin, K.-Z., Li, G.-M., Li, J.-X., Xiao, B., Zhao, J.-X., Fan, X., 2015. Zircon U–Pb ages, geochemistry, and Sr–Nd–Pb–Hf isotopes of the Nuri intrusive rocks in the Gangdese area, southern Tibet: Constraints on timing, petrogenesis, and tectonic transformation. Lithos 212–215, 379–396. https://doi.org/10.1016/j.lithos.2014.11.014
THB 09NDZ-12	S.E. Tibet		Lhasa	Nuri intrusive rocks	0.512526		-2.2	Chen et al., 2015		
THB 09NDZ-15	S.E. Tibet		Lhasa	Nuri intrusive rocks	0.512403		-4.6	Chen et al., 2015		
THB 09NDZ-19	S.E. Tibet		Lhasa	Nuri intrusive rocks	0.512751		2.2	Chen et al., 2015		
THB 09NDS-17	S.E. Tibet		Lhasa	Nuri intrusive rocks	0.512742		2.0	Chen et al., 2015		
THB 08ND-4	S.E. Tibet		Lhasa	Nuri intrusive rocks	0.512762		2.4	Chen et al., 2015		
THB 09nds-2	S.E. Tibet		Lhasa	Nuri intrusive rocks	0.512793		3.0	Chen et al., 2015		
THB 08ND-15	S.E. Tibet		Lhasa	Nuri intrusive rocks						
TSS SXI (12)-2	S.E. Tibet		S. Lhasa, S. Yarlung Tsangpo	Sangxiu Fm	0.511896	9	-14.5	Zhu et al., 2007; Zhu e		Zhu, D., Pan, G., Mo, X., Liao, Z., Jiang, X., Wang, L., Zhao, Z., 2007. Petrogenesis of volcanic rocks in the Sangxiu Formation, central segment of Tethyan Himalaya: A probable example of plume–lithosphere interaction. Journal of Asian Earth Sciences, The 19th Himalaya-Karakoram-Tibet Workshop (HKT19) held at Niseko, Hokkaido, Japan, 10–13 July 2004 29, 320–335. https://doi.org/10.1016/j.jseaes.2005.12.004
TSS SXI (9)-1	S.E. Tibet		S. Lhasa, S. Yarlung Tsangpo	Sangxiu Fm	0.51188	7	-14.8	Zhu et al., 2007; Zhu et al., 2005		
TSS SXI (8)-3	S.E. Tibet		S. Lhasa, S. Yarlung Tsangpo	Sangxiu Fm	0.511892	7	-14.6	Zhu et al., 2007; Zhu et al., 2005		
TSS SXI (1)-2	S.E. Tibet		S. Lhasa, S. Yarlung Tsangpo	Sangxiu Fm	0.512587	6	-1.0	Zhu et al., 2007; Zhu et al., 2005		
TSS SXI (1)-1	S.E. Tibet		S. Lhasa, S. Yarlung Tsangpo	Sangxiu Fm	0.512497	11	-2.8	Zhu et al., 2007		
TSS SXII (1)-1	S.E. Tibet		S. Lhasa, S. Yarlung Tsangpo	Sangxiu Fm	0.512688	7	1.0	Zhu et al., 2007; Zhu et al., 2005		
TSS SXII (9)-3	S.E. Tibet		S. Lhasa, S. Yarlung Tsangpo	Sangxiu Fm	0.512619	10	-0.4	Zhu et al., 2007		
THB SXI(2)-1	S.E. Tibet		S. Lhasa, S. Yarlung Tsangpo	Sangxiu Fm	0.512552	12	-1.7	Zhu et al., 2007; Zhu et al., 2005		
THB SXI(1)-1-(2	S.E. Tibet		S. Lhasa, S. Yarlung Tsangpo	Sangxiu Fm	0.512556	12	-1.6	Zhu et al., 2007; Zhu et al., 2005		
THB Pyroxene i	S.E. Tibet		S. Lhasa, S. Yarlung Tsangpo	Sangxiu Fm	0.512527	8	-2.2	Zhu et al., 2007; Zhu et al., 2005		
THB YZS-1	S.E. Tibet		S.W. Lhasa, Xigaze	Yarlung Tsanpo suture	0.513095		8.9	Mahoney et al., 1998		Mahoney, J.J., Frei, R., Tejada, M.L.G., Mo, X.X., Leat, P.T., Nägler, T.F., 1998. Tracing the Indian Ocean mantle domain through time: isotopic results from old West Indian, East Tethyan, and South Pacific seafloor. Journal of Petrology 39, 1285–1306.
THB YZS-2	S.E. Tibet		S.W. Lhasa, Xigaze	Yarlung Tsanpo suture	0.513075		8.5	Mahoney et al., 1998		
THB YZS-3	S.E. Tibet		S.W. Lhasa, Xigaze	Yarlung Tsanpo suture	0.513098		9.0	Mahoney et al., 1998		
THB YZS-6	S.E. Tibet		S.W. Lhasa, Xigaze	Yarlung Tsanpo suture	0.513059		8.2	Mahoney et al., 1998		
THB YZS-7	S.E. Tibet		S.W. Lhasa, Xigaze	Yarlung Tsanpo suture	0.513066		8.3	Mahoney et al., 1998		
THB YZS-11	S.E. Tibet		S.W. Lhasa, Xigaze	Yarlung Tsanpo suture	0.513075		8.5	Mahoney et al., 1998		
TSS 0319-02	S.E. Tibet		S.E. Lhasa	Yardoi gneiss dome	0.511906	7.0	-14.3	Zeng et al., 2009		Zeng, L., Liu, J., Gao, L., Xie, K., Wen, L., 2009. Early Oligocene anatexis in the Yardoi gneiss dome, southern Tibet and geological implications. Chin. Sci. Bull. 54, 104. https://doi.org/10.1007/s11434-008-0362-x
TSS 0319-03	S.E. Tibet		S.E. Lhasa	Yardoi gneiss dome	0.511767	10.0	-17.0	Zeng et al., 2009		
TSS 0319-07	S.E. Tibet		S.E. Lhasa	Yardoi gneiss dome	0.512044	12.0	-11.6	Zeng et al., 2009		
TSS 0321-021	S.E. Tibet		S.E. Lhasa	Yardoi gneiss dome	0.5	10	-15.7	Zeng et al., 2009		
TSS 0321-12	S.E. Tibet		S.E. Lhasa	Yardoi gneiss dome	0.51183	6.0	-15.8	Zeng et al., 2009		
TSS 0321-011	S.E. Tibet		S.E. Lhasa	Yardoi gneiss dome	0.512266	6.0	-7.3	Zeng et al., 2009		
TSS 0321-08	S.E. Tibet		S.E. Lhasa	Yardoi gneiss dome	0.5	10	-4.7	Zeng et al., 2009		
TSS 0321-09	S.E. Tibet		S.E. Lhasa	Yardoi gneiss dome	0.5	9	-4.5	Zeng et al., 2009		
TSS 0321-031	S.E. Tibet		S.E. Lhasa	Yardoi gneiss dome	0.512032	10.0	-11.8	Zeng et al., 2009		
TSS 0321-041	S.E. Tibet		S.E. Lhasa	Yardoi gneiss dome	0.512097	5.0	-10.6	Zeng et al., 2009		
TSS 0323-02	S.E. Tibet		S.E. Lhasa	Yardoi gneiss dome	0.511936	14.0	-13.7	Zeng et al., 2009		
TSS 0322-01	S.E. Tibet		S.E. Lhasa	Yardoi gneiss dome	0.512107	12.0	-10.4	Zeng et al., 2009		
TSS 0322-04	S.E. Tibet		S.E. Lhasa	Yardoi gneiss dome	0.512105	5.0	-10.4	Zeng et al., 2009		
TSS 0323-01	S.E. Tibet		S.E. Lhasa	Yardoi gneiss dome	0.512166	8.0	-9.2	Zeng et al., 2009		
TSS 0323-03	S.E. Tibet		S.E. Lhasa	Yardoi gneiss dome	0.512175	14.0	-9.0	Zeng et al., 2009		
TSS 0323-04	S.E. Tibet		S.E. Lhasa	Yardoi gneiss dome	0.51216	14.0	-9.3	Zeng et al., 2009		
TSS 0321-07	S.E. Tibet		S.E. Lhasa	Yardoi gneiss dome	0.512116	10.0	-10.2	Zeng et al., 2009		
TSS 0319-06	S.E. Tibet		S.E. Lhasa	Yardoi gneiss dome	0.512033	10.0	-11.8	Zeng et al., 2009		

Table SII-2 (…/…)

Ech.#	Region	River	Locality	Formation	144Nd/142Nd	2s.d.	eNd(0)	Reference	Commer	Full reference
										Gao, Y., Wei, R., Ma, P., Hou, Z., Yang, Z., 2009. Post-collisional ultrapotassic volcanism in the Tangra Yumco-Xuruco graben, south Tibet: Constraints from geochemistry and Sr–Nd–Pb isotope. Lithos 110, 129–139. https://doi.org/10.1016/j.lithos.2008.12.005
THB CHP1	S.C. Tibe	W. Lhasa (in	Tangra Yumco-Xuruco graben	Chazi felsic ultrapotassic lavas	0.511973	13	-13.0	Gao et al., 2009		
THB CHP3	S.C. Tibe	W. Lhasa (in	Tangra Yumco-Xuruco graben	Chazi felsic ultrapotassic lavas	0.511956	11	-13.3	Gao et al., 2009		
THB CHP4	S.C. Tibe	W. Lhasa (in	Tangra Yumco-Xuruco graben	Chazi felsic ultrapotassic lavas	0.511962	13	-13.2	Gao et al., 2009		
THB CHP6	S.C. Tibe	W. Lhasa (in	Tangra Yumco-Xuruco graben	Chazi felsic ultrapotassic lavas	0.51195	11	-13.4	Gao et al., 2009		
THB CHP7	S.C. Tibe	W. Lhasa (in	Tangra Yumco-Xuruco graben	Chazi felsic ultrapotassic lavas	0.511953	13	-13.4	Gao et al., 2009		
THB CHP8	S.C. Tibe	W. Lhasa (in	Tangra Yumco-Xuruco graben	Chazi felsic ultrapotassic lavas	0.511963	11	-13.2	Gao et al., 2009		
THB CHP10	S.C. Tibe	W. Lhasa (in	Tangra Yumco-Xuruco graben	Chazi felsic ultrapotassic lavas	0.511945	11	-13.5	Gao et al., 2009		
THB CHP12	S.C. Tibe	W. Lhasa (in	Tangra Yumco-Xuruco graben	Chazi felsic ultrapotassic lavas	0.51196	12	-13.2	Gao et al., 2009		
THB CHP13	S.C. Tibe	W. Lhasa (in	Tangra Yumco-Xuruco graben	Chazi felsic ultrapotassic lavas	0.511963	11	-13.2	Gao et al., 2009		
THB CHP15	S.C. Tibe	W. Lhasa (in	Tangra Yumco-Xuruco graben	Chazi felsic ultrapotassic lavas	0.511912	10	-14.2	Gao et al., 2009		
THB CHP17	S.C. Tibe	W. Lhasa (in	Tangra Yumco-Xuruco graben	Chazi felsic ultrapotassic lavas	0.511923	10	-13.9	Gao et al., 2009		
THB CHP18	S.C. Tibe	W. Lhasa (in	Tangra Yumco-Xuruco graben	Chazi felsic ultrapotassic lavas	0.511931	13	-13.8	Gao et al., 2009		
										Zhao, J., Qin, K., Li, G., Li, J., Xiao, B., Chen, L., 2012. Geochemistry and Petrogenesis of Granitoids at Sharang Eocene Porphyry Mo Deposit in the Main-Stage of India-Asia Continental Collision, Northern Gangdese, Tibet. Resource Geology 62, 84–98. https://doi.org/10.1111/j.1751-3928.2011.00181.x
THB SRD08-05	S.E. Tibe	E. Lhasa	N. Gangdese	Sharang granitoids	0.51248	11	-3.1	Zhao et al., 2012		
THB SRD08-10	S.E. Tibe	E. Lhasa	N. Gangdese	Sharang granitoids	0.512581	12	-1.1	Zhao et al., 2012		
THB SRD-6	S.E. Tibe	E. Lhasa	N. Gangdese	Sharang granitoids	0.512429	13	-4.1	Zhao et al., 2012		
THB SRZK0905	S.E. Tibe	E. Lhasa	N. Gangdese	Sharang granitoids	0.512405	12	-4.5	Zhao et al., 2012		
THB SRZK0205	S.E. Tibe	E. Lhasa	N. Gangdese	Sharang granitoids	0.512434	13	-4.0	Zhao et al., 2012		
THB SRZK0107	S.E. Tibe	E. Lhasa	N. Gangdese	Sharang granitoids	0.512382	12	-5.0	Zhao et al., 2012		
THB SRZK0107	S.E. Tibe	E. Lhasa	N. Gangdese	Sharang granitoids	0.512399	11	-4.7	Zhao et al., 2012		
THB SRZK003-	S.E. Tibe	E. Lhasa	N. Gangdese	Sharang granitoids	0.512372	11	-5.2	Zhao et al., 2012		
THB SRZK0704	S.E. Tibe	E. Lhasa	N. Gangdese	Sharang granitoids	0.512225	10	-8.1	Zhao et al., 2012		
THB SRZK0905	S.E. Tibe	E. Lhasa	N. Gangdese	Sharang granitoids	0.512464	11	-3.4	Zhao et al., 2012		
THB SRZK0304	S.E. Tibe	E. Lhasa	N. Gangdese	Sharang granitoids	0.512577	12	-1.2	Zhao et al., 2012		
THB SRD08-01	S.E. Tibe	E. Lhasa	N. Gangdese	Sharang granitoids	0.512257	12	-7.4	Zhao et al., 2012		
THB SRD08-02	S.E. Tibe	E. Lhasa	N. Gangdese	Sharang granitoids	0.51243	13	-4.1	Zhao et al., 2012		
										Gao, Y., Hou, Z., Kamber, B.S., Wei, R., Meng, X., Zhao, R., 2007. Lamproitic rocks from a continental collision zone: evidence for recycling of subducted Tethyan oceanic sediments in the mantle beneath southern Tibet. Journal of Petrology 48, 729–752.
THB TI/10	S. Tibet	W. Lhasa		Mibale ultrapotassic lava	0.511956	12	-13.3	Gao et al., 2(	Nd proba	
THB TI/11	S. Tibet	W. Lhasa		Mibale ultrapotassic lava	0.511946	13	-13.5	Gao et al., 2007		
THB TI/18	S. Tibet	W. Lhasa		Mibale ultrapotassic lava	0.511817	12	-16.0	Gao et al., 2007		
THB TI/13	S. Tibet	W. Lhasa		Mibale ultrapotassic lava	0.511979	12	-12.9	Gao et al., 2007		
THB TI/03	S. Tibet	W. Lhasa		Mibale ultrapotassic lava	0.511959	9	-13.2	Gao et al., 2007		
THB TI/08	S. Tibet	W. Lhasa		Mibale ultrapotassic lava	0.51188	13	-14.8	Gao et al., 2007		
THB TI/17	S. Tibet	W. Lhasa		Mibale ultrapotassic lava	0.511832	12	-15.7	Gao et al., 2007		
THB TI/06	S. Tibet	W. Lhasa		Mibale ultrapotassic lava	0.511943	9	-13.6	Gao et al., 2007		
THB TI/59	S. Tibet	W. Lhasa		Mibale ultrapotassic lava	0.511963	9	-13.2	Gao et al., 2007		
THB CHZ-1	S. Tibet	W. Lhasa		Chazi ultrapotassic lava	0.511876	11	-14.9	Gao et al., 2007		
THB CHZ-2	S. Tibet	W. Lhasa		Chazi ultrapotassic lava				Gao et al., 2007		
THB CHZ-3	S. Tibet	W. Lhasa		Chazi ultrapotassic lava				Gao et al., 2007		
THB CHZ-4	S. Tibet	W. Lhasa		Chazi ultrapotassic lava				Gao et al., 2007		
THB CHZ-5	S. Tibet	W. Lhasa		Chazi ultrapotassic lava	0.511866	12	-15.1	Gao et al., 2007		
THB CHZ-6	S. Tibet	W. Lhasa		Chazi ultrapotassic lava				Gao et al., 2007		
THB CHZ-7	S. Tibet	W. Lhasa		Chazi ultrapotassic lava				Gao et al., 2007		
THB CHZ-8	S. Tibet	W. Lhasa		Chazi ultrapotassic lava	0.511867	12	-15.0	Gao et al., 2007		
THB CHZ-9	S. Tibet	W. Lhasa		Chazi ultrapotassic lava				Gao et al., 2007		
THB CHZ-10	S. Tibet	W. Lhasa		Chazi ultrapotassic lava	0.511865	11	-15.1	Gao et al., 2007		
THB CHZ-11	S. Tibet	W. Lhasa		Chazi ultrapotassic lava				Gao et al., 2007		
THB CHZ-12	S. Tibet	W. Lhasa		Chazi ultrapotassic lava	0.511856	11	-15.3	Gao et al., 2007		
										Ding, L., Kapp, P., Zhong, D., Deng, W., 2003. Cenozoic volcanism in Tibet: evidence for a transition from oceanic to continental subduction. Journal of Petrology 44, 1833–1865.
THB 99T53	S. Tibet	W. Lhasa	Tangra Yumco graben	Wenbu potassic lava	0.511883	8	-14.7	Ding et al., 2003		
THB 99T56	S. Tibet	W. Lhasa	Tangra Yumco graben	Wenbu potassic lava	0.511888	8	-14.6	Ding et al., 2003		
THB 99T57	S. Tibet	W. Lhasa	Tangra Yumco graben	Wenbu potassic lava	0.511875	8	-14.9	Ding et al., 2003		
THB 99T60	S. Tibet	W. Lhasa	Tangra Yumco graben	Wenbu potassic lava	0.511893	7	-14.5	Ding et al., 2003		
THB 99T62	S. Tibet	W. Lhasa	Tangra Yumco graben	Wenbu potassic lava	0.511893	10	-14.5	Ding et al., 2003		
THB 99T132	S. Tibet	W. Lhasa	Xurruco graben	Chazi potassic lava	0.511985	7	-12.7	Ding et al., 2003		
THB 99T134	S. Tibet	W. Lhasa	Xurruco graben	Chazi potassic lava	0.512021	10	-12.0	Ding et al., 2003		
THB 99T145	S. Tibet	W. Lhasa	Xurruco graben	Chazi potassic lava	0.511996	8	-12.5	Ding et al., 2003		
THB 99T152	S. Tibet	W. Lhasa	Xurruco graben	Chazi potassic lava	0.511906	7	-14.3	Ding et al., 2003		
THB 99T154	S. Tibet	W. Lhasa	Xurruco graben	Chazi potassic lava	0.511946	6	-13.5	Ding et al., 2003		

Table SII-2 (…/…)

Ech.#	Region	River	Locality	Formation	144Nd/142Nd	2s.d.	eNd(0)	Reference	Commer	Full reference
										Williams, H.M., Turner, S.P., Pearce, J.A., Kelley, S.P., Harris, N.B.W., 2004. Nature of the Source Regions for Post-collisional, Potassic Magmatism in Southern and Northern Tibet from Geochemical Variations and Inverse Trace Element Modelling. J Petrology 45, 555–607. https://doi.org/10.1093/petrology/egg094
THB JPT3	S. Tibet	W. Lhasa		Namling potassic lava	0.512357	4e	-5.5	Williams et al. 2004		
THB JPT5.2	S. Tibet	W. Lhasa		Namling potassic lava	0.512307	4e	-6.5	Williams et al. 2004		
THB JPT8	S. Tibet	W. Lhasa		Namling potassic lava	0.512028	4e	-11.9	Williams et al. 2004		
			Lithology (PVR : potassic, UPVR : ultra potassic)							
										Liu, D., Zhao, Z., DePaolo, D.J., Zhu, D.-C., Meng, F.-Y., Shi, Q., Wang, Q., 2017. Potassic volcanic rocks and adakitic intrusions in southern Tibet: Insights into mantle–crust interaction and mass transfer from Indian plate. Lithos 268–271, 48–64. https://doi.org/10.1016/j.lithos.2016.10.034
THB DJC1302	S.C. Tibe	N. of Saga S	Adakite	Dajia Co	0.512312	7E-06	-6.4	Liu et al., 2017		
THB DJC1303	S.C. Tibe	N. of Saga S	Adakite	Dajia Co				Liu et al., 2017		
THB DJC1304	S.C. Tibe	N. of Saga S	Adakite	Dajia Co				Liu et al., 2017		
THB DJC1305	S.C. Tibe	N. of Saga S	Adakite	Dajia Co				Liu et al., 2017		
THB DJC1306	S.C. Tibe	N. of Saga S	Adakite	Dajia Co	0.512313	6E-06	-6.3	Liu et al., 2017		
THB DJC1307	S.C. Tibe	N. of Saga S	Adakite	Dajia Co	0.512308	7E-06	-6.4	Liu et al., 2017		
THB DJC1308	S.C. Tibe	N. of Saga S	Adakite	Dajia Co	0.512311	6E-06	-6.4	Liu et al., 2017		
THB DJC1309	S.C. Tibe	N. of Saga S	Adakite	Dajia Co	0.512313	6E-06	-6.3	Liu et al., 2017		
THB DJC1310	S.C. Tibe	N. of Saga S	Adakite	Dajia Co				Liu et al., 2017		
THB DJC1311	S.C. Tibe	N. of Saga S	Adakite	Dajia Co				Liu et al., 2017		
THB DJC1312	S.C. Tibe	N. of Saga S	Adakite	Dajia Co				Liu et al., 2017		
THB DJC1313	S.C. Tibe	N. of Saga S	Adakite	Dajia Co	0.512307	6E-06	-6.5	Liu et al., 2017		
THB DJC1314	S.C. Tibe	N. of Saga S	Adakite	Dajia Co				Liu et al., 2017		
THB DJC1315	S.C. Tibe	N. of Saga S	Adakite	Dajia Co	0.512361	6E-06	-5.4	Liu et al., 2017		
THB YY1101	S.E. Tibe	W. Lhasa	PVR	Yangying	0.512188	6E-06	-8.8	Liu et al., 2017		
THB YY1102	S.E. Tibe	W. Lhasa	PVR	Yangying	0.512195	6E-06	-8.6	Liu et al., 2017		
THB YY1105	S.E. Tibe	W. Lhasa	PVR	Yangying				Liu et al., 2017		
THB YY1106	S.E. Tibe	W. Lhasa	PVR	Yangying	0.512183	6E-06	-8.9	Liu et al., 2017		
THB YY1108	S.E. Tibe	W. Lhasa	PVR	Yangying				Liu et al., 2017		
THB YY1111	S.E. Tibe	W. Lhasa	PVR	Yangying	0.512187	7E-06	-8.8	Liu et al., 2017		
THB CZ1301	S.C. Tibe	N. of Saga S	PVR	Chazi	0.51197	6E-06	-13.0	Liu et al., 2017		
THB CZ1302	S.C. Tibe	N. of Saga S	PVR	Chazi	0.51199	6E-06	-12.6	Liu et al., 2017		
THB CZ1303	S.C. Tibe	N. of Saga S	PVR	Chazi	0.511939	7E-06	-13.6	Liu et al., 2017		
THB CZ1304	S.C. Tibe	N. of Saga S	PVR	Chazi				Liu et al., 2017		
THB CZ1305	S.C. Tibe	N. of Saga S	UPVR	Chazi				Liu et al., 2017		
THB CZ1306	S.C. Tibe	N. of Saga S	UPVR	Chazi	0.511967	7E-06	-13.1	Liu et al., 2017		
THB CZ1307	S.C. Tibe	N. of Saga S	UPVR	Chazi	0.51197	5E-06	-13.0	Liu et al., 2017		
THB CZ1308	S.C. Tibe	N. of Saga S	UPVR	Chazi				Liu et al., 2017		
THB CZ1309	S.C. Tibe	N. of Saga S	UPVR	Chazi	0.511972	6E-06	-13.0	Liu et al., 2017		
THB CZ1310	S.C. Tibe	N. of Saga S	PVR	Chazi	0.512	6E-06	-12.4	Liu et al., 2017		
THB CZ1311	S.C. Tibe	N. of Saga S	UPVR	Chazi	0.511996	6E-06	-12.5	Liu et al., 2017		
THB YR1101	W. Tibet	Xungba	PVR	Yare	0.511969	7E-06	-13.1	Liu et al., 2017		
THB YR1102	W. Tibet	Xungba	PVR	Yare				Liu et al., 2017		
THB YR1103	W. Tibet	Xungba	PVR	Yare	0.511968	7E-06	-13.1	Liu et al., 2017		
THB YR1104	W. Tibet	Xungba	PVR	Yare				Liu et al., 2017		
THB YR1105	W. Tibet	Xungba	PVR	Yare	0.511959	6E-06	-13.2	Liu et al., 2017		
THB YR1106	W. Tibet	Xungba	PVR	Yare	0.511945	7E-06	-13.5	Liu et al., 2017		
THB YR1107	W. Tibet	Xungba	PVR	Yare				Liu et al., 2017		
THB YR1108	W. Tibet	Xungba	PVR	Yare	0.511979	6E-06	-12.9	Liu et al., 2017		
THB YR1109	W. Tibet	Xungba	PVR	Yare	0.511972	6E-06	-13.0	Liu et al., 2017		
THB YR1111	W. Tibet	Xungba	PVR	Yare	0.511979	6E-06	-12.9	Liu et al., 2017		
THB YR1112	W. Tibet	Xungba	PVR	Yare				Liu et al., 2017		
THB YR1113	W. Tibet	Xungba	PVR	Yare	0.511967	6E-06	-13.1	Liu et al., 2017		
THB YR1114	W. Tibet	Xungba	PVR	Yare	0.511984	6E-06	-12.8	Liu et al., 2017		
THB YR1115	W. Tibet	Xungba	PVR	Yare				Liu et al., 2017		
THB YR1116	W. Tibet	Xungba	PVR	Yare				Liu et al., 2017		
THB YR1117	W. Tibet	Xungba	PVR	Yare	0.511976	7E-06	-12.9	Liu et al., 2017		
THB YR1118	W. Tibet	Xungba	PVR	Yare	0.512387	6E-06	-4.9	Liu et al., 2017		
THB ZB1101	W. Tibet	N. Maiga	PVR	Zabuye	0.512169	6E-06	-9.1	Liu et al., 2017		
THB ZB1103	W. Tibet	N. Maiga	PVR	Zabuye				Liu et al., 2017		
THB ZB1104	W. Tibet	N. Maiga	PVR	Zabuye	0.512166	7E-06	-9.2	Liu et al., 2017		
THB ZB1105	W. Tibet	N. Maiga	PVR	Zabuye				Liu et al., 2017		
THB ZB1107	W. Tibet	N. Maiga	PVR	Zabuye				Liu et al., 2017		
THB ZB1110	W. Tibet	N. Maiga	PVR	Zabuye	0.512207	6E-06	-8.4	Liu et al., 2017		
										Kang, Z.-Q., Xu, J.-F., Wilde, S.A., Feng, Z.-H., Chen, J.-L., Wang, B.-D., Fu, W.-C., Pan, H.-B., 2014. Geochronology and geochemistry of the Sangri Group Volcanic Rocks, Southern Lhasa Terrane: Implications for the early subduction history of the Neo-Tethys and Gangdese Magmatic Arc. Lithos 200–201, 157–168. https://doi.org/10.1016/j.lithos.2014.04.019
THB 10SR-08	S.E. Tibe	S.E. Lhasa		Bima Fm Sangri	0.512702	7	1.2	Kang et al., 2014		
THB 10SR-13	S.E. Tibe	S.E. Lhasa		Bima Fm Sangri	0.512791	10	3.0	Kang et al., 2014		

Table SII-2 (…/…)

Ech.#	Region	River	Locality	Formation	144Nd/142Nd	2s.d.	eNd(0)	Reference	Commer	Full reference
THB 10SR-48	S.E. Tibe	S.E. Lhasa		Bima Fm Sangri	0.512876	6	4.6	Kang et al., 2014		
THB 10SR-27	S.E. Tibe	S.E. Lhasa		Bima Fm Sangri	0.512967	8	6.4	Kang et al., 2014		
THB 10SR-32	S.E. Tibe	S.E. Lhasa		Bima Fm Sangri	0.512965	9	6.4	Kang et al., 2014		
THB 10SR-39	S.E. Tibe	S.E. Lhasa		Bima Fm Sangri	0.512945	9	6.0	Kang et al., 2014		
THB 10SR-28	S.E. Tibe	S.E. Lhasa		Bima Fm Sangri	0.512836	6	3.9	Kang et al., 2014		
THB 10SR-33	S.E. Tibe	S.E. Lhasa		Bima Fm Sangri	0.512811	7	3.4	Kang et al., 2014		
THB 10SR-41	S.E. Tibe	S.E. Lhasa		Bima Fm Sangri	0.512876	10	4.6	Kang et al., 2014		
THB 10SR-43	S.E. Tibe	S.E. Lhasa		Bima Fm Sangri	0.512876	8	4.6	Kang et al., 2014		
THB 10SR-23	S.E. Tibe	S.E. Lhasa		Bima Fm Sangri	0.51286	8	4.3	Kang et al., 2014		
TSS D1614	S.E. Tibe	S. Lhasa	close STDS	Laguila Fm intrusion Comei LIP	0.511972	5	-13.0	Liu et al., 2015		Liu, Z., Zhou, Q., Lai, Y., Qing, C., Li, Y., Wu, J., Xia, X., 2015. Petrogenesis of the Early Cretaceous Laguila bimodal intrusive rocks from the Tethyan Himalaya: Implications for the break-up of Eastern Gondwana. Lithos 236–237, 190–202. https://doi.org/10.1016/j.lithos.2015.09.006
TSS D1616	S.E. Tibe	S. Lhasa	close STDS	Laguila Fm intrusion Comei LIP	0.512058	6	-11.3	Liu et al., 2015		
TSS D1617	S.E. Tibe	S. Lhasa	close STDS	Laguila Fm intrusion Comei LIP	0.512756	4	2.3	Liu et al., 2015		
TSS D1618-2	S.E. Tibe	S. Lhasa	close STDS	Laguila Fm intrusion Comei LIP	0.512681	3	0.8	Liu et al., 2015		
TSS D1619	S.E. Tibe	S. Lhasa	close STDS	Laguila Fm intrusion Comei LIP	0.512727	6	1.7	Liu et al., 2015		
TSS D1620	S.E. Tibe	S. Lhasa	close STDS	Laguila Fm intrusion Comei LIP	0.512753	3	2.2	Liu et al., 2015		
TSS D1631-1	S.E. Tibe	S. Lhasa	close STDS	Laguila Fm intrusion Comei LIP	0.512727	6	1.7	Liu et al., 2015		
TSS D1631-2	S.E. Tibe	S. Lhasa	close STDS	Laguila Fm intrusion Comei LIP	0.512719	6	1.6	Liu et al., 2015		
TSS D1631-3	S.E. Tibe	S. Lhasa	close STDS	Laguila Fm intrusion Comei LIP	0.512709	6	1.4	Liu et al., 2015		
HHC J-G4	S. Tibet	28.5N 85.2E	High Himalaya leucogranite	Gyirong Leucogranite	0.511775	6	-16.8	Guo and Wilson, 2012		Guo, Z., Wilson, M., 2012. The Himalayan leucogranites: constraints on the nature of their crustal source region and geodynamic setting. Gondwana Research 22, 360–376.
HHC J-G7	S. Tibet	28.5N 85.2E	High Himalaya leucogranite	Gyirong Leucogranite	0.511813	10	-16.1	Guo and Wilson, 2012		
HHC J-G16	S. Tibet	28.5N 85.2E	High Himalaya leucogranite	Gyirong Leucogranite	0.511728	5	-17.8	Guo and Wilson, 2012		
HHC J-G2	S. Tibet	28.5N 85.2E	High Himalaya leucogranite	Gyirong Leucogranite	0.511712	8	-18.1	Guo and Wilson, 2012		
HHC NL-12	S. Tibet	28.4N 86.5E	High Himalaya leucogranite	Nyalam Leucogranite	0.511717	8	-18.0	Guo and Wilson, 2012		
HHC NL-25	S. Tibet	28.4N 86.5E	High Himalaya leucogranite	Nyalam Leucogranite	0.511718	6	-17.9	Guo and Wilson, 2012		
HHC NL-36	S. Tibet	28.4N 86.5E	High Himalaya leucogranite	Nyalam Leucogranite	0.511776	11	-16.8	Guo and Wilson, 2012		
HHC NL-03	S. Tibet	28.4N 86.5E	High Himalaya leucogranite	Nyalam Leucogranite	0.511749	9	-17.3	Guo and Wilson, 2012		
HHC NL-31	S. Tibet	28.4N 86.5E	High Himalaya leucogranite	Nyalam Leucogranite	0.511854	7	-15.3	Guo and Wilson, 2012		
HHC N-702	S. Tibet	28.4N 86.5E	High Himalaya leucogranite	Nyalam Leucogranite	0.511842	9	-15.5	Guo and Wilson, 2012		
HHC NL-07	S. Tibet	28.4N 86.5E	High Himalaya leucogranite	Nyalam Leucogranite	0.511819	12	-16.0	Guo and Wilson, 2012		
HHC DZ-15	S. Tibet	28.4N 87.7E	High Himalaya leucogranite	Dinggye Leucogranite	0.511801	10	-16.3	Guo and Wilson, 2012		
HHC DG-2	S. Tibet	28.4N 87.7E	High Himalaya leucogranite	Dinggye Leucogranite	0.511838	13	-15.6	Guo and Wilson, 2012		
HHC DG-08	S. Tibet	28.4N 87.7E	High Himalaya leucogranite	Dinggye Leucogranite	0.511772	10	-16.9	Guo and Wilson, 2012		
HHC DG-24	S. Tibet	28.4N 87.7E	High Himalaya leucogranite	Dinggye Leucogranite	0.511805	8	-16.2	Guo and Wilson, 2012		
HHC GP-05	S. Tibet	27.5N 89E	High Himalaya leucogranite	Gaowu Leucogranite	0.511889	9	-14.6	Guo and Wilson, 2012		
HHC GP-09	S. Tibet	27.5N 89E	High Himalaya leucogranite	Gaowu Leucogranite	0.511857	12	-15.2	Guo and Wilson, 2012		
HHC GU-8	S. Tibet	27.5N 89E	High Himalaya leucogranite	Gaowu Leucogranite	0.511792	7	-16.5	Guo and Wilson, 2012		
HHC GG-2	S. Tibet	27.5N 89E	High Himalaya leucogranite	Gaowu Leucogranite	0.511809	6	-16.2	Guo and Wilson, 2012		
HHC GF-6	S. Tibet	27.5N 89E	High Himalaya leucogranite	Gaowu Leucogranite	0.511872	8	-14.9	Guo and Wilson, 2012		
HHC GZ-7	S. Tibet	27.5N 89E	High Himalaya leucogranite	Gaowu Leucogranite	0.511828	9	-15.8	Guo and Wilson, 2012		
TSS LG-17	S. Lhasa	28.3N 91.0E	Tethyan Himalaya leucogranite	Luozha Leucogranite	0.511791	7	-16.5	Guo and Wilson, 2012		
TSS LG-02	S. Lhasa	28.3N 91.0E	Tethyan Himalaya leucogranite	Luozha Leucogranite	0.511806	7	-16.2	Guo and Wilson, 2012		
TSS LG-29	S. Lhasa	28.3N 91.0E	Tethyan Himalaya leucogranite	Luozha Leucogranite	0.511774	8	-16.9	Guo and Wilson, 2012		
TSS LG-06	S. Lhasa	28.3N 91.0E	Tethyan Himalaya leucogranite	Luozha Leucogranite	0.511849	9	-15.4	Guo and Wilson, 2012		
TSS ZF-31	S. Lhasa	29N 90E	Tethyan Himalaya leucogranite	Quzhen Leucogranite	0.511904	9	-14.3	Guo and Wilson, 2012		
TSS ZF-26	S. Lhasa	29N 90E	Tethyan Himalaya leucogranite	Quzhen Leucogranite	0.511917	7	-14.1	Guo and Wilson, 2012		
TSS ZF-18	S. Lhasa	29N 90E	Tethyan Himalaya leucogranite	Quzhen Leucogranite	0.511878	6	-14.8	Guo and Wilson, 2012		
TSS ZF-38	S. Lhasa	29N 90E	Tethyan Himalaya leucogranite	Quzhen Leucogranite	0.511762	8	-17.1	Guo and Wilson, 2012		
TSS JK3/05	S. Tibet	Sakya	Tethyan Himalaya leucogranite	Kuday granite	0.511947	4E-06	-13.5	King et al., 2011		King, J., Harris, N., Argles, T., Parrish, R., Zhang, H., 2011. Contribution of crustal anatexis to the tectonic evolution of Indian crust beneath southern Tibet. GSA Bulletin 123, 218–239. https://doi.org/10.1130/B30085.1
TSS JK3/08	S. Tibet	Sakya	Tethyan Himalaya leucogranite	Kuday granite				King et al., 2011		
TSS JK3/12a	S. Tibet	Sakya	Tethyan Himalaya leucogranite	Kuday granite				King et al., 2011		
TSS JK3/13b	S. Tibet	Sakya	Tethyan Himalaya leucogranite	Kuday granite				King et al., 2011		
TSS TO3/29x	S. Tibet	Sakya	Tethyan Himalaya leucogranite	Lijun granite				King et al., 2011		
TSS TO3/31ix	S. Tibet	Sakya	Tethyan Himalaya leucogranite	Lijun granite				King et al., 2011		
TSS TO3/33x	S. Tibet	Sakya	Tethyan Himalaya leucogranite	Lijun granite	0.512247	4E-06	-7.6	King et al., 2011		
TSS JK4/07a	S. Tibet	Sakya	Tethyan Himalaya leucogranite	Wing granite	0.512143	2E-06	-9.7	King et al., 2011		
TSS JK4/08	S. Tibet	Sakya	Tethyan Himalaya leucogranite	Kua granite				King et al., 2011		
TSS JK4/09a	S. Tibet	Sakya	Tethyan Himalaya leucogranite	Kua granite				King et al., 2011		
TSS JK4/09b	S. Tibet	Sakya	Tethyan Himalaya leucogranite	Kua granite				King et al., 2011		
TSS JK3/25	S. Tibet	Sakya	Tethyan Himalaya leucogranite	Kouwo granite				King et al., 2011		
TSS TO3/25i	S. Tibet	Sakya	Tethyan Himalaya leucogranite	Mabja granite	0.511623	4E-06	-19.8	King et al., 2011		

Table SII-2 (…/…)

Ech.#	Region	River	Locality	Formation	144Nd/142Nd	2s.d.	eNd(0)	Reference	Commer	Full reference
TSS JK4/11b	S. Tibet	Sakya	Tethyan Himalaya leucogranite	Donggong granite				King et al., 2011		
TSS JK4/12a	S. Tibet	Sakya	Tethyan Himalaya leucogranite	Donggong granite				King et al., 2011		
TSS JK4/12b	S. Tibet	Sakya	Tethyan Himalaya leucogranite	Donggong granite				King et al., 2011		
TSS JK4/13g	S. Tibet	Sakya	Tethyan Himalaya leucogranite	Gomdre granite	0.51193	4E-06	-13.8	King et al., 2011		
TSS T71	S. Tibet	Sakya	Tethyan Himalaya gneiss	Kangmar gneiss	0.512039	1E-05	-11.7	Zhang et al., 2004		Zhang, H., Harris, N., Parrish, R., Kelley, S., Zhang, L., Rogers, N., Argles, T., King, J., 2004. Causes and consequences of protracted melting of the mid-crust exposed in the North Himalayan antiform. Earth and Planetary Science Letters 228, 195–212.
TSS T72	S. Tibet	Sakya	Tethyan Himalaya gneiss	Kangmar gneiss	0.512093	9E-06	-10.6	Zhang et al., 2004		
TSS T97-61	S. Tibet	Sakya	Tethyan Himalaya gneiss	Kangmar gneiss	0.512065	7E-06	-11.2	Zhang et al., 2004		
TSS T136	S. Tibet	Sakya	Tethyan Himalaya gneiss	Kangmar gneiss	0.512007	7E-06	-12.3	Zhang et al., 2004		
TSS T100	S. Tibet	Sakya	Tethyan Himalaya granite	Kuday granite	0.511932	1E-05	-13.8	Zhang et al., 2004		
TSS T101	S. Tibet	Sakya	Tethyan Himalaya granite	Kuday granite	0.511951	9E-06	-13.4	Zhang et al., 2004		
TSS T104	S. Tibet	Sakya	Tethyan Himalaya granite	Kuday granite	0.511927	8E-06	-13.9	Zhang et al., 2004		
TSS T105	S. Tibet	Sakya	Tethyan Himalaya granite	Kuday granite	0.511968	9E-06	-13.1	Zhang et al., 2004		
TSS T110	S. Tibet	Sakya	Tethyan Himalaya granite	Kouwu Kouwo granite	0.511934	9E-06	-13.7	Zhang et al., 2004		
TSS T111	S. Tibet	Sakya	Tethyan Himalaya granite	Kouwu Kouwo granite	0.51191	######	-14.2	Zhang et al., 2004		
TSS T113	S. Tibet	Sakya	Tethyan Himalaya granite	Kouwu Kouwo granite	0.511944	2E-05	-13.5	Zhang et al., 2004		
TSS T114	S. Tibet	Sakya	Tethyan Himalaya granite	Kouwu Kouwo granite	0.511951	8E-06	-13.4	Zhang et al., 2004		
TSS T117	S. Tibet	Sakya	Tethyan Himalaya granite	Mabja granite				Zhang et al., 2004		
TSS T118	S. Tibet	Sakya	Tethyan Himalaya granite	Mabja granite	0.511647	1E-05	-19.3	Zhang et al., 2004		
TSS T120	S. Tibet	Sakya	Tethyan Himalaya granite	Mabja granite	0.511697	9E-06	-18.4	Zhang et al., 2004		
TSS T121	S. Tibet	Sakya	Tethyan Himalaya granite	Mabja granite	0.511662	1E-05	-19.0	Zhang et al., 2004		
TSS T73	S. Tibet	Sakya	Tethyan Himalaya granite	Lhagoi Kangri granite	0.51191	8E-06	-14.2	Zhang et al., 2004		
TSS T74	S. Tibet	Sakya	Tethyan Himalaya granite	Lhagoi Kangri granite	0.511995	1E-05	-12.5	Zhang et al., 2004		
TSS T75	S. Tibet	Sakya	Tethyan Himalaya leucogranite	Lhagoi Kangri granite	0.511937	8E-06	-13.7	Zhang et al., 2004		
TSS T76	S. Tibet	Sakya	Tethyan Himalaya leucogranite	Dingge leucogranite	0.512021	1E-05	-12.0	Zhang et al., 2004		
TSS T77	S. Tibet	Sakya	Tethyan Himalaya leucogranite	Dingge leucogranite	0.511876	9E-06	-14.9	Zhang et al., 2004		
TSS T78a	S. Tibet	Sakya	Tethyan Himalaya leucogranite	Dingge leucogranite	0.511842	1E-05	-15.5	Zhang et al., 2004		
TSS T97-26	S. Tibet	Sakya	Tethyan Himalaya leucogranite	Yaddon leucogranite	0.511797	8E-06	-16.4	Zhang et al., 2004		
TSS T97-57	S. Tibet	Sakya	Tethyan Himalaya leucogranite	Yaddon leucogranite	0.511889	9E-06	-14.6	Zhang et al., 2004		
TSS T107	S. Tibet	Sakya	Tethyan metasediments	Kuday metasediments	0.511726	7E-06	-17.8	Zhang et al., 2004		
TSS T125	S. Tibet	Sakya	Tethyan metasediments	Kangmar schists	0.511806	7E-06	-16.2	Zhang et al., 2004		
TSS T129	S. Tibet	Sakya	Tethyan metasediments	Kangmar schists				Zhang et al., 2004		
TSS T135	S. Tibet	Sakya	Tethyan metasediments	Kangmar schists	0.511877	5E-06	-14.8	Zhang et al., 2004		
TSS T137	S. Tibet	Sakya	Tethyan metasediments	Kangmar schists	0.51189	8E-06	-14.6	Zhang et al., 2004		
THB L-72	E. Aruna	Lohit riv		Lohit batholith				Goswami, 2013		Goswami, T.K., 2013. Subduction related magmatism: Constrains from the REE pattern in the Lohit Batholith, Arunachal Pradesh, India. Geosciences 3, 128–141.
THB L-45	E. Aruna	Lohit riv		Lohit batholith				Goswami, 2013		
THB L-70	E. Aruna	Lohit riv		Lohit batholith				Goswami, 2013		
THB L-71	E. Aruna	Lohit riv		Lohit batholith				Goswami, 2013		
THB L-69	E. Aruna	Lohit riv		Lohit batholith				Goswami, 2013		
THB D-62	E. Aruna	Dibang riv		Lohit batholith				Goswami, 2013		
THB D-63	E. Aruna	Dibang riv		Lohit batholith				Goswami, 2013		
THB D-69	E. Aruna	Dibang riv		Lohit batholith				Goswami, 2013		
THB 07TB33a-1	S. Lhasa, N. Suture			Kelu intrusive rock	0.512753	1E-05	2.2	Jiang et al., 2012		Jiang, Z.-Q., Wang, Q., Li, Z.-X., Wyman, D.A., Tang, G.-J., Jia, X.-H., Yang, Y.-H., 2012. Late Cretaceous (ca. 90Ma) adakitic intrusive rocks in the Kelu area, Gangdese Belt (southern Tibet): Slab melting and implications for Cu–Au mineralization. Journal of Asian Earth Sciences, The Tibetan Orogenic Evolution: Pre- to Post-Collisional Geologic Records 53, 67–81. https://doi.org/10.1016/j.jseaes.2012.02.010
THB 07TB33a-2	S. Lhasa, N. Suture			Kelu intrusive rock	0.51274	1E-05	2.0	Jiang et al., 2012		
THB 07TB33b-2	S. Lhasa, N. Suture			Kelu intrusive rock	0.512768	9E-06	2.5	Jiang et al., 2012		
THB 07TB33d	S. Lhasa, N. Suture			Kelu intrusive rock	0.512816	9E-06	3.5	Jiang et al., 2012		
THB 07TB33e	S. Lhasa, N. Suture			Kelu intrusive rock	0.512778	1E-05	2.7	Jiang et al., 2012		
TSS 11SN16-1	S. Lhasa, S. of Suture			Comei granite	0.511917	3	-14.1	Ma et al., 2018		Ma, L., Kerr, A.C., Wang, Q., Jiang, Z.-Q., Hu, W.-L., 2018. Early Cretaceous (~140Ma) aluminous A-type granites in the Tethyan Himalaya, Tibet: Products of crust-mantle interaction during lithospheric extension. Lithos 300–301, 212–226. https://doi.org/10.1016/j.lithos.2017.11.023
TSS 11SN17-1	S. Lhasa, S. of Suture			Comei granite	0.511904	3	-14.3	Ma et al., 2018		
TSS 11SN18-2	S. Lhasa, S. of Suture			Comei granite	0.511906	3	-14.3	Ma et al., 2018		
TSS 11SN19-2	S. Lhasa, S. of Suture			Comei granite	0.51191	4	-14.2	Ma et al., 2018		
TSS 11SN20-2	S. Lhasa, S. of Suture			Comei granite	0.511905	3	-14.3	Ma et al., 2018		
TSS 09TB116-1	S. Lhasa, S. of Suture			Comei granite	0.51193	8	-13.8	Ma et al., 2018		
TSS 09TB116-4	S. Lhasa, S. of Suture			Comei granite	0.511936	9	-13.7	Ma et al., 2018		
TSS 09TB116-5	S. Lhasa, S. of Suture			Comei granite	0.511943	8	-13.6	Ma et al., 2018		

Table SII-2 (…/…)

Ech.#	Region	River	Locality	Formation	144Nd/142Nd	2s.d.	eNd(0)	Reference	Commer	Full reference
THB S31	SW. Tibe	Chaxiezangbu			0.512189	5	-8.8	Wu et al., 2010		Wu, W., Xu, S., Yang, J., Yin, H., Lu, H., Zhang, K., 2010. Isotopic characteristics of river sediments on the Tibetan Plateau. Chemical Geology 269, 406–413.
THB S32	SW. Tibe	Shiquan River			0.512262	4	-7.3	Wu et al., 2010		
THB S33	SW. Tibe	Niyangqu River			0.512186	11	-8.8	Wu et al., 2010		
THB S34	S. Tibet	Lhasa River			0.512357	11	-5.5	Wu et al., 2010		
THB S35	Lhasa	Xiangqu River			0.512275	6	-7.1	Wu et al., 2010		
THB S36	Lhasa	Geerzangbu			0.512443	5	-3.8	Wu et al., 2010		
THB S37	Lhasa	Yarlung zangbu			0.512303	6	-6.5	Wu et al., 2010		
THB S38	Lhasa	Yarlung zangbu			0.512237	5	-7.8	Wu et al., 2010		
THB S39	before E	Yarlung zangbu			0.512319	10	-6.2	Wu et al., 2010		
THB T1	Lhasa	Sand			0.512248	8	-7.6	Wu et al., 2010		
THB T2	Lhasa	Sand			0.512338	4	-5.9	Wu et al., 2010		
Hima S40		Xiangquan River			0.511958	7	-13.3	Wu et al., 2010		
THB T849	E. Namc	East syntaxis	E. Lhasa terrane granites	Bolonggong#3 Granite	0.511732	4E-06	-17.7	Pan et al., 2014		Pan, F.-B., Zhang, H.-F., Xu, W.-C., Guo, L., Wang, S., Luo, B., 2014. U–Pb zircon chronology, geochemical and Sr–Nd isotopic composition of Mesozoic–Cenozoic granitoids in the SE Lhasa terrane: Petrogenesis and tectonic implications. Lithos 192–195, 142–157. https://doi.org/10.1016/j.lithos.2014.02.005
THB T850	E. Namc	East syntaxis	E. Lhasa terrane granites	Bolonggong#3 Granite	0.511751	4E-06	-17.3	Pan et al., 2014		
THB T1047	E. Namc	East syntaxis	E. Lhasa terrane granites	Bolonggong#2 Granite	0.511856	7E-06	-15.3	Pan et al., 2014		
THB T1066	E. Namc	East syntaxis	E. Lhasa terrane granites	Bolonggong#4 Granite	0.511834	6E-06	-15.7	Pan et al., 2014		
THB T1067	E. Namc	East syntaxis	E. Lhasa terrane granites	Bolonggong#4 Granite	0.511897	4E-06	-14.5	Pan et al., 2014		
THB T847	E. Namc	East syntaxis	E. Lhasa terrane granites	Bolonggong#4 Granite	0.512118	2E-06	-10.1	Pan et al., 2014		
THB T1034	E. Namc	East syntaxis	E. Lhasa terrane granites	Bolonggong#1 Granite	0.51242	4E-06	-4.3	Pan et al., 2014		
THB T1035	E. Namc	East syntaxis	E. Lhasa terrane granites	Bolonggong#1 Granite	0.512566	4E-06	-1.4	Pan et al., 2014		
THB T830	E. Namc	East syntaxis	E. Lhasa terrane granites	52K Granite	0.512456	4E-06	-3.6	Pan et al., 2014		
THB T831	E. Namc	East syntaxis	E. Lhasa terrane granites	52K Granite	0.512473	5E-06	-3.2	Pan et al., 2014		
THB T1010	E. Namc	East syntaxis	E. Lhasa terrane granites	Meiri Granite	0.512511	8E-06	-2.5	Pan et al., 2014		
THB T1014	E. Namc	East syntaxis	E. Lhasa terrane granites	Meiri Granite	0.512764	9E-06	2.5	Pan et al., 2014		
THB T1015	E. Namc	East syntaxis	E. Lhasa terrane granites	Meiri Granite	0.51259	7E-06	-0.9	Pan et al., 2014		
THB T691	E. Namc	East syntaxis	E. Lhasa terrane granites	Beibeng Granite	0.512685	4E-06	0.9	Pan et al., 2014		
THB T979	E. Namc	East syntaxis	E. Lhasa terrane granites	Beibeng Granite	0.512452	4E-06	-3.6	Pan et al., 2014		
HHC 502068	C. Nepal	Annapurna	Modi Khola	Formation I	0.511877	6	-14.8	Martin et al., 2005		Martin, A.J., DeCelles, P.G., Gehrels, G.E., Patchett, P.J., Isachsen, C., 2005. Isotopic and structural constraints on the location of the Main Central thrust in the Annapurna Range, central Nepal Himalaya. GSA Bulletin 117, 926–944. https://doi.org/10.1130/B25646.1
HHC 502069	C. Nepal	Annapurna	Modi Khola	Formation I	0.511737	6	-17.6	Martin et al., 2005		
HHC 502070	C. Nepal	Annapurna	Modi Khola	Formation I	0.511843	8	-15.5	Martin et al., 2005		
HHC 502071	C. Nepal	Annapurna	Modi Khola	Formation I	0.511779	6	-16.8	Martin et al., 2005		
HHC 502072	C. Nepal	Annapurna	Modi Khola	Formation I				Martin et al., 2005		
502073	C. Nepal	Annapurna	Modi Khola	Lower foreland basin				Martin et al., 2005		
LH 502075	C. Nepal	Annapurna	Modi Khola	Kuncha	0.511592	5	-20.4	Martin et al., 2005		
HHC 502104	C. Nepal	Annapurna	Seti Nadi	Formation I	0.511935	8	-13.7	Martin et al., 2005		
HHC 502105A	C. Nepal	Annapurna	Seti Nadi	Formation I	0.511897	5	-14.5	Martin et al., 2005		
HHC 502105B	C. Nepal	Annapurna	Seti Nadi	Formation I	0.511783	6	-16.7	Martin et al., 2005		
HHC 502106	C. Nepal	Annapurna	Seti Nadi	Formation I	0.51195	6	-13.4	Martin et al., 2005		
HHC 502107	C. Nepal	Annapurna	Seti Nadi	Formation I				Martin et al., 2005		
LH 502108	C. Nepal	Annapurna	Seti Nadi	Kuncha	0.511548	6	-21.3	Martin et al., 2005		
LH 502097	C. Nepal	Annapurna	Seti Nadi	Kuncha	0.511428	7	-23.6	Martin et al., 2005		
HHC 502128	C. Nepal	Annapurna	Madi Nadi	Formation I	0.511804	5	-16.3	Martin et al., 2005		
HHC 502129	C. Nepal	Annapurna	Madi Nadi	Formation I	0.511868	6	-15.0	Martin et al., 2005		
HHC 502133	C. Nepal	Annapurna	Madi Nadi	Formation I	0.511933	6	-13.8	Martin et al., 2005		
HHC 502132	C. Nepal	Annapurna	Madi Nadi	Formation I	0.511908	6	-14.2	Martin et al., 2005		
LH 502130	C. Nepal	Annapurna	Madi Nadi	post-Kuncha Nawakot	0.511616	6	-19.9	Martin et al., 2005		
LH 502134	C. Nepal	Annapurna	Madi Nadi	post-Kuncha Nawakot				Martin et al., 2005		
LH 502131	C. Nepal	Annapurna	Madi Nadi	post-Kuncha Nawakot	0.511568	7	-20.9	Martin et al., 2005		
LH 502136	C. Nepal	Annapurna	Madi Nadi	post-Kuncha Nawakot	0.511477	6	-22.6	Martin et al., 2005		
HHC 502152	C. Nepal	Annapurna	Nayu Ridge	Formation I	0.511903	6	-14.3	Martin et al., 2005		
HHC 502149	C. Nepal	Annapurna	Nayu Ridge	Formation I	0.511922	7	-14.0	Martin et al., 2005		
HHC 502148	C. Nepal	Annapurna	Nayu Ridge	Formation I	0.511818	7	-16.0	Martin et al., 2005		
HHC 502147	C. Nepal	Annapurna	Nayu Ridge	Formation I	0.511741	7	-17.5	Martin et al., 2005		
LH 502146	C. Nepal	Annapurna	Nayu Ridge	Kuncha	0.51144	7	-23.4	Martin et al., 2005		
LH 602002	C. Nepal	Annapurna	Nayu Ridge	Kuncha	0.511462	6	-22.9	Martin et al., 2005		
HHC 402086	C. Nepal	Annapurna	Marsyangdi Nadi	Formation I	0.511928	7	-13.8	Martin et al., 2005		
HHC 402088	C. Nepal	Annapurna	Marsyangdi Nadi	Formation I	0.51179	5	-16.5	Martin et al., 2005		
HHC 402090	C. Nepal	Annapurna	Marsyangdi Nadi	Formation I	0.511671	7	-18.9	Martin et al., 2005		
HHC 402092A	C. Nepal	Annapurna	Marsyangdi Nadi	Formation I	0.511691	6	-18.5	Martin et al., 2005		
HHC 402092B	C. Nepal	Annapurna	Marsyangdi Nadi	Formation I	0.511753	7	-17.3	Martin et al., 2005		

Table SII-2 (…/…)

	Ech.#	Region	River	Locality	Formation	144Nd/142Nd	2s.d.	eNd(0)	Reference	Commer	Full reference
LH	402093	C. Nepal	Annapurna	Marsyangdi Nadi	Kuncha	0.511449	6	-23.2	Martin et al., 2005		
LH	402097	C. Nepal	Annapurna	Marsyangdi Nadi	Kuncha	0.511384	6	-24.5	Martin et al., 2005		
											Zhang, L.K., Li, G.M., Santosh, M., Cao, H.W., Dong, S.L., Zhang, Z., Fu, J.G., Xia, X.B., Huang, Y., Liang, W., Zhang, S.T., 2018. Cambrian magmatism in the Tethys Himalaya and implications for the evolution of the Proto-Tethys along the northern Gondwana margin: A case study and overview. Geological Journal. https://doi.org/10.1002/gj.3311
TSS	D6344-B1	S. Lhasa	Tethyan clos	28.5N 92E	Cuonadong granitic gneiss	0.511964	1E-05	-13.1	Zhang et al., 2018		
TSS	D6344-B7	S. Lhasa	Tethyan clos	28.5N 92E	Cuonadong granitic gneiss	0.511915	1E-05	-14.1	Zhang et al., 2018		
TSS	D1542-B2	S. Lhasa	Tethyan clos	28.5N 92E	Cuonadong granitic gneiss	0.511889	7E-06	-14.6	Zhang et al., 2018		
TSS	D1536-B2	S. Lhasa	Tethyan clos	28.5N 92E	Cuonadong granitic gneiss	0.512015	1E-05	-12.2	Zhang et al., 2018		
TSS	D6304-B2	S. Lhasa	Tethyan clos	28.5N 92E	Cuonadong granitic gneiss	0.511968	1E-05	-13.1	Zhang et al., 2018		
TSS	D6304-B3	S. Lhasa	Tethyan clos	28.5N 92E	Cuonadong granitic gneiss	0.51192	9E-06	-14.0	Zhang et al., 2018		
											Allègre, C.J., Othman, D.B., 1980. Nd–Sr isotopic relationship in granitoid rocks and continental crust
HHC	22D	C. Nepal			Manaslu granite	0.51183	7	-15.8	Hamet and Allègre, 19		development: a chemical approach to orogenesis. Nature 286, 335.
HHC	A404	C. Nepal			Palung granite	0.51197	4	-13.0	Hamet and Allègre, 1976; Allègre and Othman, 1980		
HHC	132	C. Nepal			Makalu granite	0.51211	10	-10.3	Allègre and Othman, 1980		
	HB68	Ladakh		granodiorite	Ladakh	0.51256	3	-1.5	Hamet and Allègre, 1976; Allègre and Othman, 1980		
	HB74			diorite	Ladakh	0.51273	3	1.8	Hamet and Allègre, 1976; Allègre and Othman, 1980		
					Yangying potassic volcanic rocks						Zhang, L., Guo, Z., Zhang, M., Cheng, Z., Sun, Y., 2017. Post-collisional potassic magmatism in the eastern Lhasa terrane, South Tibet: Products of partial melting of mélanges in a continental subduction channel. Gondwana Research, Tectonic evolution and dynamics of the Tibetan Plateau 41, 9–28. https://doi.org/10.1016/j.gr.2015.11.007
THB	YY-07	W. Lhas	29.5N 90.5E	Pujiemu		0.512121	6E-06	-10.1	Zhang et al., 2017		
THB	YY-08	W. Lhas	29.5N 90.5E	Qialagai	Yangying potassic volcanic rocks	0.512134	9E-06	-9.8	Zhang et al., 2017		
THB	YY-10	W. Lhas	29.5N 90.5E	Pujiemu	Yangying potassic volcanic rocks	0.512148	7E-06	-9.6	Zhang et al., 2017		
THB	YY-12	W. Lhas	29.5N 90.5E	Pujiemu	Yangying potassic volcanic rocks	0.512138	7E-06	-9.8	Zhang et al., 2017		
											Zheng, Y., Hou, Z., Fu, Q., Zhu, D.-C., Liang, W., Xu, P., 2016. Mantle inputs to Himalayan anatexis: Insights from petrogenesis of the Miocene Langkazi leucogranite and its dioritic enclaves. Lithos 264, 125–140. https://doi.org/10.1016/j.lithos.2016.08.019
TSS	LKZ-1	S. Lhasa	29N 90E		Langkazi leucogranite	0.511987	10	-12.7	Zheng et al., 2016		
TSS	LKZ-2	S. Lhasa	29N 90E		Langkazi leucogranite	0.512012	10	-12.2	Zheng et al., 2016		
TSS	LKZ-3	S. Lhasa	29N 90E		Langkazi leucogranite	0.51201	8	-12.3	Zheng et al., 2016		
TSS	LKZ-4	S. Lhasa	29N 90E		Langkazi leucogranite	0.512012	8	-12.2	Zheng et al., 2016		
TSS	LKZ-5	S. Lhasa	29N 90E		Langkazi leucogranite	0.512104	8	-10.4	Zheng et al., 2016		
TSS	LKZ-10	S. Lhasa	29N 90E		Langkazi leucogranite				Zheng et al., 2016		
TSS	LKZ-6	S. Lhasa	29N 90E		Langkazi leucogranite	0.512087	5	-10.7	Zheng et al., 2016		
TSS	LKZ-8	S. Lhasa	29N 90E		Langkazi diorite enclave	0.512208	7	-8.4	Zheng et al., 2016		
TSS	LKZ-12	S. Lhasa	29N 90E		Langkazi diorite enclave	0.512292	10	-6.7	Zheng et al., 2016		
TSS	LKZ-13	S. Lhasa	29N 90E		Langkazi diorite enclave	0.512262	10	-7.3	Zheng et al., 2016		
TSS	LKZ-15-1	S. Lhasa	29N 90E		Langkazi diorite enclave	0.512301	5	-6.6	Zheng et al., 2016		
TSS	LKZ-15-2	S. Lhasa	29N 90E		Langkazi diorite enclave	0.512318	10	-6.2	Zheng et al., 2016		
TSS	LKZ-16	S. Lhasa	29N 90E		Langkazi diorite enclave	0.512189	10	-8.8	Zheng et al., 2016		
TSS	LKZ-17	S. Lhasa	29N 90E		Langkazi diorite enclave	0.512259	10	-7.4	Zheng et al., 2016		
TSS	LKZ-19	S. Lhasa	29N 90E		Langkazi diorite enclave	0.51225	10	-7.6	Zheng et al., 2016		
											Liu, Z.-C., Wu, F.-Y., Ji, W.-Q., Wang, J.-G., Liu, C.-Z., 2014. Petrogenesis of the Ramba leucogranite in the Tethyan Himalaya and constraints on the channel flow model. Lithos 208–209, 118–136. https://doi.org/10.1016/j.lithos.2014.08.022
TSS	09FW115	S.W. Lha	30N 90E		Ramba dome	0.511978	7	-12.9	Liu et al., 2014		
TSS	12FW111	S.W. Lha	30N 90E		Ramba dome	0.512001	18	-12.4	Liu et al., 2014		
TSS	12FW112	S.W. Lha	30N 90E		Ramba dome	0.512301	20	-6.6	Liu et al., 2014		
TSS	09FW116	S.W. Lha	30N 90E		Ramba dome	0.511941	14	-13.6	Liu et al., 2014		
TSS	09FW118	S.W. Lha	30N 90E		Ramba dome	0.511881	5	-14.8	Liu et al., 2014		
TSS	09FW120	S.W. Lha	30N 90E		Ramba dome	0.511859	5	-15.2	Liu et al., 2014		
TSS	09FW121	S.W. Lha	30N 90E		Ramba dome	0.511878	11	-14.8	Liu et al., 2014		
TSS	12FW115	S.W. Lha	30N 90E		Ramba dome	0.511899	12	-14.4	Liu et al., 2014		
TSS	12FW116	S.W. Lha	30N 90E		Ramba dome	0.511895	14	-14.5	Liu et al., 2014		
TSS	09FW114	S.W. Lha	30N 90E		Ramba dome	0.511993	9	-12.6	Liu et al., 2014		
TSS	09FW119	S.W. Lha	30N 90E		Ramba dome	0.512024	8	-12.0	Liu et al., 2014		
TSS	12FW103	S.W. Lha	30N 90E		Ramba dome	0.511957	26	-13.3	Liu et al., 2014		
TSS	12FW104	S.W. Lha	30N 90E		Ramba dome	0.512064	44	-11.2	Liu et al., 2014		
TSS	12FW105	S.W. Lha	30N 90E		Ramba dome	0.512	24	-12.4	Liu et al., 2014		
TSS	12FW106	S.W. Lha	30N 90E		Ramba dome	0.511977	28	-12.9	Liu et al., 2014		
TSS	12FW109	S.W. Lha	30N 90E		Ramba dome	0.511998	50	-12.5	Liu et al., 2014		
TSS	12FW101	S.W. Lha	30N 90E		Ramba dome hosting rock	0.512346	9	-5.7	Liu et al., 2014		
TSS	12FW107	S.W. Lha	30N 90E		Ramba dome hosting rock	0.512308	15	-6.4	Liu et al., 2014		
TSS	12FW102	S.W. Lha	30N 90E		Ramba dome hosting rock	0.512927	21	5.6	Liu et al., 2014		

Table SII-2 (…/…)

Ech.#	Region	River	Locality	Formation	144Nd/142Nd	2s.d.	eNd(0)	Reference	Commer	Full reference
TSS 12FW108	S.W. Lha	30N 90E		Ramba dome hosting rock	0.512945	15	6.0	Liu et al., 2014		
TSS 12FW110	S.W. Lha	30N 90E		Ramba dome hosting rock	0.512663	15	0.5	Liu et al., 2014		
TSS 12FW113	S.W. Lha	30N 90E		Ramba dome hosting rock	0.512907	12	5.2	Liu et al., 2014		
TSS 12FW114	S.W. Lha	30N 90E		Ramba dome hosting rock	0.512667	24	0.6	Liu et al., 2014		
										King, J., Harris, N., Argles, T., Parrish, R., Charlier, B., Sherlock, S., Zhang, H.F., 2007. First field evidence of southward ductile flow of Asian crust beneath southern Tibet. Geology 35, 727–730. https://doi.org/10.1130/G23630A.1
TSS JK3/15	S.W. Lha	28.5N 88.5E	Sakya dome	Kuday dykes	0.512425	3E-06	-4.2	King et al., 2007		
TSS JK3/17	S.W. Lha	28.5N 88.5E	Sakya dome	Kuday dykes	0.512407	9E-06	-4.5	King et al., 2007		
TSS TO3/14i	S.W. Lha	28.5N 88.5E	Sakya dome	Kuday dykes	0.512309	4E-06	-6.4	King et al., 2007		
TSS SD51	S.W. Lha	28.5N 88.5E	Sakya dome	Kuday dykes	0.512313	4E-06	-6.3	King et al., 2007		
TSS JK3/16	S.W. Lha	28.5N 88.5E	Sakya dome	Kuday dykes	0.512329	3E-06	-6.0	King et al., 2007		
TSS T108	S.W. Lha	28.5N 88.5E	Sakya dome	Kuday dykes	0.512263	1E-05	-7.3	King et al., 2007		
TSS SD50	S.W. Lha	28.5N 88.5E	Sakya dome	Kuday dykes	0.512405	1E-05	-4.5	King et al., 2007		
TSS T109	S.W. Lha	28.5N 88.5E	Sakya dome	Kuday dykes	0.512229	8E-06	-8.0	King et al., 2007		
TSS G40	S.W. Lha	28.5N 88.5E	Sakya dome	Nyainqentanglha gneisses	0.512298	4E-06	-6.6	King et al., 2007		
TSS G38E	S.W. Lha	28.5N 88.5E	Sakya dome	Nyainqentanglha gneisses	0.512288	4E-06	-6.8	King et al., 2007		
										Gao, L., Zeng, L., Hou, K., Guo, C., Tang, S., Xie, K., Hu, G., Wang, L., 2013. Episodic crustal anatexis and the formation of Paiku composite leucogranitic pluton in the Malashan Gneiss Dome, Southern Tibet. Chinese Science Bulletin 58, 3546–3563.
TSS T0659-3	S. Tibet	29N 85.5E	Malashan gneiss dome	Paiku pluton in Malashan gneiss dome	0.511956	5	-13.3	Gao et al., 2013		
TSS T0659-4	S. Tibet	29N 85.5E	Malashan gneiss dome	Paiku pluton in Malashan gneiss dome	0.511968	5	-13.1	Gao et al., 2013		
TSS T0659-6	S. Tibet	29N 85.5E	Malashan gneiss dome	Paiku pluton in Malashan gneiss dome	0.511952	13	-13.4	Gao et al., 2013		
TSS T0659-11	S. Tibet	29N 85.5E	Malashan gneiss dome	Paiku pluton in Malashan gneiss dome	0.511946	11	-13.5	Gao et al., 2013		
TSS T0659-12	S. Tibet	29N 85.5E	Malashan gneiss dome	Paiku pluton in Malashan gneiss dome	0.511946	10	-13.5	Gao et al., 2013		
TSS T0659-13	S. Tibet	29N 85.5E	Malashan gneiss dome	Paiku pluton in Malashan gneiss dome	0.511925	8	-13.9	Gao et al., 2013		
TSS T0659-14	S. Tibet	29N 85.5E	Malashan gneiss dome	Paiku pluton in Malashan gneiss dome	0.511926	7	-13.9	Gao et al., 2013		
										Zeng, L., Gao, L.-E., Tang, S., Hou, K., Guo, C., Hu, G., 2015. Eocene magmatism in the Tethyan Himalaya, southern Tibet. Geological Society, London, Special Publications 412, 287–316. https://doi.org/10.1144/SP412.8
TSS T0474-1	S.E. Lha	29N 92E	Yardoi gneiss dome	Yardoi gneiss dome	0.512062	10	-11.2	Zeng et al., 2015		
TSS T0474-2	S.E. Lha	29N 92E	Yardoi gneiss dome	Yardoi gneiss dome	0.512037	11	-11.7	Zeng et al., 2015		
TSS T0474-3	S.E. Lha	29N 92E	Yardoi gneiss dome	Yardoi gneiss dome	0.511938	10	-13.7	Zeng et al., 2015		
TSS T0686-1	S.E. Lha	29N 92E	Yardoi gneiss dome	Yardoi gneiss dome				Zeng et al., 2015		
TSS T0686-2	S.E. Lha	29N 92E	Yardoi gneiss dome	Yardoi gneiss dome				Zeng et al., 2015		
TSS T0686-3	S.E. Lha	29N 92E	Yardoi gneiss dome	Yardoi gneiss dome				Zeng et al., 2015		
TSS T391	S.E. Lha	29N 92E	Yardoi gneiss dome	Dala	0.51195	8	-13.4	Zeng et al., 2015		
TSS T0391-1	S.E. Lha	29N 92E	Yardoi gneiss dome	Dala	0.511957	9	-13.3	Zeng et al., 2015		
TSS T0391-2	S.E. Lha	29N 92E	Yardoi gneiss dome	Dala	0.512131	12	-9.9	Zeng et al., 2015		
TSS T0391-3	S.E. Lha	29N 92E	Yardoi gneiss dome	Dala	0.511948	6	-13.5	Zeng et al., 2015		
TSS T0685-1	S.E. Lha	29N 92E	Yardoi gneiss dome	Dala				Zeng et al., 2015		
TSS T0685-2	S.E. Lha	29N 92E	Yardoi gneiss dome	Dala				Zeng et al., 2015		
TSS T0684-1	S.E. Lha	29N 92E	Yardoi gneiss dome	Ridang	0.511938	10	-13.7	Zeng et al., 2015		
TSS T0684-2	S.E. Lha	29N 92E	Yardoi gneiss dome	Ridang	0.511962	10	-13.2	Zeng et al., 2015		
TSS T0684-3	S.E. Lha	29N 92E	Yardoi gneiss dome	Ridang	0.511948	6	-13.5	Zeng et al., 2015		
TSS T0684-4	S.E. Lha	29N 92E	Yardoi gneiss dome	Ridang	0.51195	8	-13.4	Zeng et al., 2015		
TSS T0684-5	S.E. Lha	29N 92E	Yardoi gneiss dome	Ridang	0.511937	11	-13.7	Zeng et al., 2015		
TSS T0684-6	S.E. Lha	29N 92E	Yardoi gneiss dome	Ridang	0.511931	12	-13.8	Zeng et al., 2015		
TSS T0684-7	S.E. Lha	29N 92E	Yardoi gneiss dome	Ridang	0.511957	9	-13.3	Zeng et al., 2015		
TSS T0471-1	S.E. Lha	29N 92E	Yardoi gneiss dome	Yardoi gneiss dome	0.512059	8	-11.3	Zeng et al., 2015		
TSS T0471-2	S.E. Lha	29N 92E	Yardoi gneiss dome	Yardoi gneiss dome	0.512136	7	-9.8	Zeng et al., 2015		
TSS T0471-3	S.E. Lha	29N 92E	Yardoi gneiss dome	Yardoi gneiss dome	0.512092	9	-10.7	Zeng et al., 2015		
TSS T0471-4	S.E. Lha	29N 92E	Yardoi gneiss dome	Yardoi gneiss dome	0.512102	6	-10.5	Zeng et al., 2015		
TSS T0471-5	S.E. Lha	29N 92E	Yardoi gneiss dome	Yardoi gneiss dome	0.512065	5	-11.2	Zeng et al., 2015		
										Aikman, A.B., Harrison, T.M., Hermann, J., 2012. The origin of Eo- and Neo-himalayan granitoids, Eastern Tibet. Journal of Asian Earth Sciences 58, 143–157. https://doi.org/10.1016/j.jseaes.2012.05.018
HHC 602008	E. Himal	92E		Arunachal leucogranites	0.51188	1E-05	-14.8	Aikman et al., 2012		
HHC 602009	E. Himal	92E		Arunachal leucogranites	0.511856	9E-06	-15.3	Aikman et al., 2012		
HHC 602010	E. Himal	92E		Arunachal leucogranites	0.511861	1E-05	-15.2	Aikman et al., 2012		
TSS T263	E. Himal	92E		Tsona leucogranites	0.51196	9E-06	-13.2	Aikman et al., 2012		
TSS T264	E. Himal	92E		Tsona leucogranites	0.511972	9E-06	-13.0	Aikman et al., 2012		
TSS T265	E. Himal	92E		Tsona leucogranites	0.511918	1E-05	-14.0	Aikman et al., 2012		
HHC 602005	E. Himal	92E		Arunachal crystalline	0.511785	7E-06	-16.6	Aikman et al., 2012		
HHC 602011	E. Himal	92E		Arunachal crystalline	0.511861	2E-05	-15.2	Aikman et al., 2012		
HHC 602012	E. Himal	92E		Arunachal crystalline	0.512013	2E-05	-12.2	Aikman et al., 2012		
TSS 405008	E. Himal	92E	Dala igneous complex	Dala granitoids	0.511998	8E-06	-12.5	Aikman et al., 2012		
TSS 405011	E. Himal	92E	Dala igneous complex	Dala granitoids	0.511971	8E-06	-13.0	Aikman et al., 2012		
TSS 405013	E. Himal	92E	Dala igneous complex	Dala granitoids	0.51209	8E-06	-10.7	Aikman et al., 2012		
TSS 410007	E. Himal	92E	Dala igneous complex	Dala granitoids	0.511957	1E-05	-13.3	Aikman et al., 2012		
TSS 410008	E. Himal	92E	Dala igneous complex	Dala granitoids	0.511934	1E-05	-13.7	Aikman et al., 2012		

Table SII-2 (…/…)

	Ech.#	Region	River	Locality	Formation	144Nd/142Nd	2s.d.	eNd(0)	Reference	Commer	Full reference
TSS	410009	E. Himal	92E	Dala igneous complex	Dala granitoids	0.511934	1E-05	-13.7	Aikman et al., 2012		
TSS	410010	E. Himal	92E	Dala igneous complex	Dala granitoids	0.511958	1E-05	-13.3	Aikman et al., 2012		
TSS	410012	E. Himal	92E	Dala igneous complex	Dala granitoids	0.512059	4E-06	-11.3	Aikman et al., 2012		
TSS	310019	E. Himal	92E	Yala-Xiangbo dome and igneous complex	Yala-Xiangbo leucogranites	0.512066	7E-06	-11.2	Aikman et al., 2012		
TSS	310021	E. Himal	92E	Yala-Xiangbo dome and igneous complex	Yala-Xiangbo leucogranites	0.512228	6E-06	-8.0	Aikman et al., 2012		
TSS	310037	E. Himal	92E	Yala-Xiangbo dome and igneous complex	Yala-Xiangbo leucogranites	0.512117	1E-05	-10.2	Aikman et al., 2012		
TSS	310038	E. Himal	92E	Yala-Xiangbo dome and igneous complex	Yala-Xiangbo leucogranites	0.511985	0.0001	-12.7	Aikman et al., 2012		
TSS	310008	E. Himal	92E	Yala-Xiangbo dome and igneous complex	Yala-Xiangbo pelites	0.512291	7E-06	-6.8	Aikman et al., 2012		
TSS	310013	E. Himal	92E	Yala-Xiangbo dome and igneous complex	Yala-Xiangbo pelites	0.512201	7E-06	-8.5	Aikman et al., 2012		
TSS	310015	E. Himal	92E	Yala-Xiangbo dome and igneous complex	Yala-Xiangbo pelites	0.512294	5E-06	-6.7	Aikman et al., 2012		
TSS	310029	E. Himal	92E	Yala-Xiangbo dome and igneous complex	Yala-Xiangbo pelites	0.512281	9E-06	-7.0	Aikman et al., 2012		
TSS	310034	E. Himal	92E	Yala-Xiangbo dome and igneous complex	Yala-Xiangbo pelites	0.511981	8E-06	-12.8	Aikman et al., 2012		
TSS	310039	E. Himal	92E	Yala-Xiangbo dome and igneous complex	Yala-Xiangbo pelites	0.512145	8E-06	-9.6	Aikman et al., 2012		
TSS	310014	E. Himal	92E		Tethyan mafic	0.512935	5E-06	5.8	Aikman et al., 2012		
THB	QC4	N. Lhasa	30N	90E	Nyainqentanglha Shan crystalline complex	0.51225		-7.6	Kapp et al., 2005		Kapp, J.L.D., Harrison, T.M., Kapp, P., Grove, M., Lovera, O.M., Lin, D., 2005. Nyainqentanglha Shan: A window into the tectonic, thermal, and geochemical evolution of the Lhasa block, southern Tibet. Journal of Geophysical Research: Solid Earth 110. https://doi.org/10.1029/2004JB003330
THB	BD-7-00	N. Lhasa	30N	90E	Nyainqentanglha Shan crystalline complex	0.512278		-7.0	Kapp et al., 2005		
THB	BD-8-00	N. Lhasa	30N	90E	Nyainqentanglha Shan crystalline complex	0.512208		-8.4	Kapp et al., 2005		
THB	QC5	N. Lhasa	30N	90E	Nyainqentanglha Shan crystalline complex	0.51203		-11.9	Kapp et al., 2005		
THB	99-5-11-2	N. Lhasa	30N	90E	Nyainqentanglha Shan crystalline complex				Kapp et al., 2005		
THB	99-5-9-3	N. Lhasa	30N	90E	Nyainqentanglha Shan crystalline complex	0.512411		-4.4	Kapp et al., 2005		
THB	QC2	N. Lhasa	30N	90E	Nyainqentanglha Shan crystalline complex	0.51226		-7.4	Kapp et al., 2005		
THB	QC14	N. Lhasa	30N	90E	Nyainqentanglha Shan crystalline complex	0.51237		-5.2	Kapp et al., 2005		
THB	ND-4-00	N. Lhasa	30N	90E	Nyainqentanglha Shan crystalline complex				Kapp et al., 2005		
THB	BD-3-00	N. Lhasa	30N	90E	Nyainqentanglha Shan crystalline complex	0.512278		-7.0	Kapp et al., 2005		
THB	QC17	N. Lhasa	30N	90E	Nyainqentanglha Shan crystalline complex	0.51232		-6.2	Kapp et al., 2005		
THB	QC18	N. Lhasa	30N	90E	Nyainqentanglha Shan crystalline complex	0.51225		-7.6	Kapp et al., 2005		
THB	QC19	N. Lhasa	30N	90E	Nyainqentanglha Shan crystalline complex	0.51231		-6.4	Kapp et al., 2005		
THB	99-5-4-2	N. Lhasa	30N	90E	Nyainqentanglha Shan crystalline complex				Kapp et al., 2005		
THB	ND-3-00	N. Lhasa	30N	90E	Nyainqentanglha Shan crystalline complex				Kapp et al., 2005		
THB	99-5-2-1a	N. Lhasa	30N	90E	Nyainqentanglha Shan crystalline complex	0.512426		-4.1	Kapp et al., 2005		
THB	ND-15-00	N. Lhasa	30N	90E	Nyainqentanglha Shan crystalline complex				Kapp et al., 2005		
THB	99-5-5-4d	N. Lhasa	30N	90E	Nyainqentanglha Shan crystalline complex	0.512454		-3.6	Kapp et al., 2005		
THB	ND-14-00b	N. Lhasa	30N	90E	Nyainqentanglha Shan crystalline complex				Kapp et al., 2005		
THB	99-5-9-4a	N. Lhasa	30N	90E	Nyainqentanglha Shan crystalline complex	0.512044		-11.6	Kapp et al., 2005		
THB	99-5-7-2a	N. Lhasa	30N	90E	Nyainqentanglha Shan crystalline complex				Kapp et al., 2005		
THB	ND-22-00	N. Lhasa	30N	90E	Nyainqentanglha Shan crystalline complex				Kapp et al., 2005		
THB	99-5-11-1a	N. Lhasa	30N	90E	Nyainqentanglha Shan crystalline complex	0.512344		-5.7	Kapp et al., 2005		
THB	99-5-7-3b	N. Lhasa	30N	90E	Nyainqentanglha Shan crystalline complex	0.512241		-7.7	Kapp et al., 2005		
THB	99-7-26-1b	N. Lhasa	30N	90E	Nyainqentanglha Shan crystalline complex				Kapp et al., 2005		
THB	QC3b	N. Lhasa	30N	90E	Nyainqentanglha Shan crystalline complex	0.51165		-19.3	Kapp et al., 2005		
THB	QC7	N. Lhasa	30N	90E	Nyainqentanglha Shan crystalline complex	0.51226		-7.4	Kapp et al., 2005		
THB	QC8	N. Lhasa	30N	90E	Nyainqentanglha Shan crystalline complex	0.51231		-6.4	Kapp et al., 2005		
THB	QC11a	N. Lhasa	30N	90E	Nyainqentanglha Shan crystalline complex	0.51186		-15.2	Kapp et al., 2005		
THB	QC12b-a	N. Lhasa	30N	90E	Nyainqentanglha Shan crystalline complex	0.51225		-7.6	Kapp et al., 2005		
THB	99-5-5-4c	N. Lhasa	30N	90E	Nyainqentanglha Shan crystalline complex				Kapp et al., 2005		
THB	99-7-27-3c	N. Lhasa	30N	90E	Nyainqentanglha Shan crystalline complex				Kapp et al., 2005		
LH o	NBH-22	Bhutan			Paro formation	0.511995	0.0016	-12.5	Tobgay et al., 2010		Tobgay, T., Long, S., McQuarrie, N., Ducea, M.N., Gehrels, G., 2010. Using isotopic and chronologic data to fingerprint strata: Challenges and benefits of variable sources to tectonic interpretations, the Paro Formation, Bhutan Himalaya. Tectonics 29.
LH o	BU07-73	Bhutan			Paro formation	0.511545	0.001	-21.3	Tobgay et al., 2010		
LH o	BU07-75	Bhutan			Paro formation	0.511677	0.0009	-18.7	Tobgay et al., 2010		
LH o	BU07-76	Bhutan			Paro formation	0.511402	0.0009	-24.1	Tobgay et al., 2010		
LH o	BU07-77	Bhutan			Paro formation	0.511382	0.0008	-24.5	Tobgay et al., 2010		
LH o	BU07-83	Bhutan			Paro formation	0.511978	0.0008	-12.9	Tobgay et al., 2010		
HHC	BKS-2A	N. Kathn	Bhote Koshi			0.511674	9E-06	-18.8	Khanal et al., 2015		Khanal, S., Robinson, D.M., Mandal, S., Simkhada, P., 2015. Structural, geochronological and geochemical evidence for two distinct thrust sheets in the 'Main Central thrust zone', the Main Central thrust and Ramgarh–Munsiari thrust: implications for upper crustal shortening in central Nepal. Geological Society, London, Special Publications 412, 221–245.
HHC	BKS-2B	N. Kathn	Bhote Koshi			0.511889	1E-05	-14.6	Khanal et al., 2015		
HHC	BKS-3	N. Kathn	Bhote Koshi			0.511703	9E-06	-18.2	Khanal et al., 2015		
HHC	BKS-4	N. Kathn	Bhote Koshi			0.511701	1E-05	-18.3	Khanal et al., 2015		
HHC	BKS-23	N. Kathn	Bhote Koshi			0.511968	9E-06	-13.1	Khanal et al., 2015		
HHC	BKS-22	N. Kathn	Bhote Koshi			0.511902	1E-05	-14.4	Khanal et al., 2015		
LH	BKS-10	N. Kathn	Bhote Koshi			0.511429	1E-05	-23.6	Khanal et al., 2015		
LH	BKS-9	N. Kathn	Bhote Koshi			0.511357	1E-05	-25.0	Khanal et al., 2015		

Table SII-2 (…/…)

	Ech.#	Region	River	Locality	Formation	144Nd/142Nd	2s.d.	eNd(0)	Reference	Commer	Full reference
											Mottram, C.M., Argles, T.W., Harris, N.B.W., Parrish, R.R., Horstwood, M.S.A., Warren, C.J., Gupta, S., 2014. Tectonic interleaving along the Main Central Thrust, Sikkim Himalaya. Journal of the Geological
LH	51x	Sikkim	North Sikkim	Gangtok-Mangan waterwheel		0.511375	0.0001	-24.6	Mottram et al., 2014		Society 171, 255–268. https://doi.org/10.1144/jgs2013-064
LH	53	Sikkim	North Sikkim	Rang Rang		0.511281	5E-05	-26.5	Mottram et al., 2014		
HHC	57	Sikkim	North Sikkim	Myang		0.511731	4E-05	-17.7	Mottram et al., 2014		
LH	59a	Sikkim	North Sikkim	Singhik		0.511388	7E-05	-24.4	Mottram et al., 2014		
HHC	64a	Sikkim	North Sikkim	Toong		0.511735	5E-05	-17.6	Mottram et al., 2014		
HHC	66	Sikkim	North Sikkim	Chungthang-Lachung		0.512017	6E-05	-12.1	Mottram et al., 2014		
LH	94	Sikkim	North Sikkim	Sangkalang		0.511219	4E-05	-27.7	Mottram et al., 2014		
LH	97	Sikkim	North Sikkim	Mangan petrol pump		0.51126	7E-05	-26.9	Mottram et al., 2014		
LH	82	Sikkim	Kalimpong h	Pedong		0.511368	7E-05	-24.8	Mottram et al., 2014		
HHC	106	Sikkim	Kalimpong h	Rishop		0.511739	4E-05	-17.5	Mottram et al., 2014		
LH	123	Sikkim	Kalimpong h	Neora valley		0.511391	5E-05	-24.3	Mottram et al., 2014		
LH	147	Sikkim	Kalimpong h	Lava road		0.511381	6E-05	-24.5	Mottram et al., 2014		
LH	149	Sikkim	Kalimpong h	Lava road		0.511374	6E-05	-24.7	Mottram et al., 2014		
HHC	156	Sikkim	Kalimpong h	Lolaygoan		0.511702	0.0001	-18.3	Mottram et al., 2014		
LH	159	Sikkim	Kalimpong h	Lolaygoan		0.511386	6E-05	-24.4	Mottram et al., 2014		
HHC	214x	Sikkim	West Sikkim	Yoksom		0.511699	7E-05	-18.3	Mottram et al., 2014		
LH	246a	Sikkim	West Sikkim	Dentam		0.511395	4E-05	-24.2	Mottram et al., 2014		
HHC	267	Sikkim	West Sikkim	Kabur		0.511698	9E-05	-18.3	Mottram et al., 2014		
LH	275	Sikkim	West Sikkim	Pelling		0.511438	9E-05	-23.4	Mottram et al., 2014		
HHC	278	Sikkim	West Sikkim	Pelling		0.511836	5E-05	-15.6	Mottram et al., 2014		
											Chakungal, J., Dostal, J., Grujic, D., Duchêne, S., Ghalley, K.S., 2010. Provenance of the Greater Himalayan sequence: Evidence from mafic granulites and amphibolites in NW Bhutan. Tectonophysics 480, 198–212.
HHC	BH-220	NW Bhu	Proche TSS	Masang Kang					Chakungal et al., 2010		https://doi.org/10.1016/j.tecto.2009.10.014
HHC	BH-274	NW Bhu	Proche TSS	Masang Kang					Chakungal et al., 2010		
HHC	BH-175A	NW Bhu	Proche TSS	Masang Kang					Chakungal et al., 2010		
HHC	BH-254	NW Bhu	Proche TSS	Masang Kang					Chakungal et al., 2010		
HHC	BH-256	NW Bhu	Proche TSS	Masang Kang					Chakungal et al., 2010		
HHC	BH-203	NW Bhu	Proche TSS	Masang Kang					Chakungal et al., 2010		
HHC	BH-217A	NW Bhu	Proche TSS	Masang Kang		0.511836		-15.6	Chakungal et al., 2010		
HHC	BH-219	NW Bhu	Proche TSS	Masang Kang		0.512625		-0.3	Chakungal et al., 2010		
HHC	BH-245	NW Bhu	Proche TSS	Masang Kang					Chakungal et al., 2010		
HHC	BH-246	NW Bhu	Proche TSS	Masang Kang					Chakungal et al., 2010		
HHC	BH-249	NW Bhu	Proche TSS	Masang Kang					Chakungal et al., 2010		
HHC	BH-252	NW Bhu	Proche TSS	Masang Kang					Chakungal et al., 2010		
HHC	BH-253	NW Bhu	Proche TSS	Masang Kang					Chakungal et al., 2010		
HHC	BH-255	NW Bhu	Proche TSS	Masang Kang					Chakungal et al., 2010		
HHC	BH-257	NW Bhu	Proche TSS	Masang Kang					Chakungal et al., 2010		
HHC	BH-266	NW Bhu	Proche TSS	Masang Kang					Chakungal et al., 2010		
HHC	BH-292	NW Bhu	Proche TSS	Masang Kang		0.512521		-2.3	Chakungal et al., 2010		
HHC	BH-268	NW Bhu	Proche TSS	Masang Kang					Chakungal et al., 2010		
											Xie, J., Qiu, H., Bai, X., Zhang, W., Wang, Q., Xia, X., 2018. Geochronological and geochemical constraints on the Cuonadong leucogranite, eastern Himalaya. Acta Geochim 37, 347–359.
TSS	CN1341	S.E. Lhasa			Cuonadong gneiss dome	0.512028	4E-06	-11.9	Xie et al., 2018		https://doi.org/10.1007/s11631-018-0273-8
TSS	CN1341-1	S.E. Lhasa			Cuonadong gneiss dome	0.512021	6E-06	-12.0	Xie et al., 2018		
TSS	CN1353	S.E. Lhasa			Cuonadong gneiss dome	0.511996	7E-06	-12.5	Xie et al., 2018		
TSS	CN1353-1	S.E. Lhasa			Cuonadong gneiss dome	0.512001	5E-06	-12.4	Xie et al., 2018		
TSS	CN1354	S.E. Lhasa			Cuonadong gneiss dome	0.51204	4E-06	-11.7	Xie et al., 2018		
											Gao, L.-E., Zeng, L., Hu, G., Wang, Y., Wang, Q., Guo, C., Hou, K., 2019. Early Paleozoic magmatism along the northern margin of East Gondwana. Lithos 334–335, 25–41. https://doi.org/10.1016/j.lithos.2019.03.007
TSS	T0832-GN	S. Tibet	86°E		Xiaru dome	0.512023	10	-12.0	Gao et al., 2019		
TSS	T0832-GN	S. Tibet	86°E		Xiaru dome				Gao et al., 2019		
TSS	T0832-GN	S. Tibet	86°E		Xiaru dome	0.512006	6	-12.3	Gao et al., 2019		
TSS	T0832-GN	S. Tibet	86°E		Xiaru dome	0.512037	10	-11.7	Gao et al., 2019		
TSS	T0832-GN	S. Tibet	86°E		Xiaru dome	0.512029	9		Gao et al., 2019		
TSS	T0832-GN	S. Tibet	86°E		Xiaru dome				Gao et al., 2019		
TSS	T0832-GN	S. Tibet	86°E		Xiaru dome	0.512011	10	-12.2	Gao et al., 2019		
TSS	T0833-1	S. Tibet	86°E		Xiaru dome				Gao et al., 2019		
TSS	T0833-2	S. Tibet	86°E		Xiaru dome				Gao et al., 2019		
TSS	T0833-3	S. Tibet	86°E		Xiaru dome				Gao et al., 2019		
TSS	T0833-4	S. Tibet	86°E		Xiaru dome				Gao et al., 2019		
TSS	T0833-5	S. Tibet	86°E		Xiaru dome				Gao et al., 2019		
TSS	T0833-6	S. Tibet	86°E		Xiaru dome				Gao et al., 2019		
TSS	T0833-7	S. Tibet	86°E		Xiaru dome				Gao et al., 2019		
TSS	T0834-LG-	S. Tibet	86°E		Xiaru dome	0.512036	8	-11.7	Gao et al., 2019		
TSS	T0834-LG-	S. Tibet	86°E		Xiaru dome	0.512032	9	-11.8	Gao et al., 2019		
TSS	T0834-LG-	S. Tibet	86°E		Xiaru dome	0.512035	5	-11.8	Gao et al., 2019		

Table SII-2 (…/…)

Ech.#	Region	River	Locality	Formation	144Nd/142Nd	2s.d.	eNd(0)	Reference	Commer	Full reference
TSS T0834-LG-	S. Tibet	86°E		Xiaru dome	0.512152	12	-9.5	Gao et al., 2019		
TSS T0834-LG-	S. Tibet	86°E		Xiaru dome	0.512041	13	-11.6	Gao et al., 2019		
TSS T0834-GN	S. Tibet	86°E		Xiaru dome				Gao et al., 2019		
TSS T0834-GN	S. Tibet	86°E		Xiaru dome				Gao et al., 2019		
TSS T0834-GN	S. Tibet	86°E		Xiaru dome				Gao et al., 2019		
TSS T0834-GN	S. Tibet	86°E		Xiaru dome				Gao et al., 2019		
TSS T0834-GN	S. Tibet	86°E		Xiaru dome				Gao et al., 2019		
TSS T0835-LG1	S. Tibet	86°E		Xiaru dome				Gao et al., 2019		
TSS T0835-LG2	S. Tibet	86°E		Xiaru dome	0.512107	12	-10.4	Gao et al., 2019		
TSS T0835-LG3	S. Tibet	86°E		Xiaru dome	0.512006	5	-12.3	Gao et al., 2019		
TSS T0835-LG4	S. Tibet	86°E		Xiaru dome	0.512094	5	-10.6	Gao et al., 2019		
TSS T0835-LG5	S. Tibet	86°E		Xiaru dome	0.512105	7	-10.4	Gao et al., 2019		
TSS T0835-LG6	S. Tibet	86°E		Xiaru dome				Gao et al., 2019		
TSS T0839-LG1	S. Tibet	86°E		Xiaru dome	0.512053	11	-11.4	Gao et al., 2019		
TSS T0839-LG2	S. Tibet	86°E		Xiaru dome	0.512055	11	-11.4	Gao et al., 2019		
TSS T0839-LG3	S. Tibet	86°E		Xiaru dome	0.512062	6	-11.2	Gao et al., 2019		
TSS T0777-A1	S. Tibet		88°E	Lhagoi Kangri dome	0.511946		-13.5	Gao et al., 2019		
TSS T0777-A2	S. Tibet		88°E	Lhagoi Kangri dome	0.51199		-12.6	Gao et al., 2019		
TSS T0777-A3	S. Tibet		88°E	Lhagoi Kangri dome	0.511996		-12.5	Gao et al., 2019		
TSS T0777-A4	S. Tibet		88°E	Lhagoi Kangri dome	0.51193		-13.8	Gao et al., 2019		
TSS T0777-A5	S. Tibet		88°E	Lhagoi Kangri dome	0.511926	10	-13.9	Gao et al., 2019		
TSS T0777-B1	S. Tibet		88°E	Lhagoi Kangri dome				Gao et al., 2019		
TSS T0777-B2	S. Tibet		88°E	Lhagoi Kangri dome				Gao et al., 2019		
TSS T0777-C1	S. Tibet		88°E	Lhagoi Kangri dome	0.511923	14	-13.9	Gao et al., 2019		
TSS T0777-C2	S. Tibet		88°E	Lhagoi Kangri dome	0.511948	8	-13.5	Gao et al., 2019		
TSS T0777-C3	S. Tibet		88°E	Lhagoi Kangri dome	0.511909	9	-14.2	Gao et al., 2019		
TSS T0777-C4	S. Tibet		88°E	Lhagoi Kangri dome	0.511933	6	-13.8	Gao et al., 2019		
TSS T0777-C5	S. Tibet		88°E	Lhagoi Kangri dome	0.511941	6	-13.6	Gao et al., 2019		
TSS T0526-LG-	S. Tibet		90°E	Kangmar dome				Gao et al., 2019		
TSS T0526-LG-	S. Tibet		90°E	Kangmar dome				Gao et al., 2019		
TSS T0526-LG-	S. Tibet		90°E	Kangmar dome				Gao et al., 2019		
TSS T0526-LG-	S. Tibet		90°E	Kangmar dome				Gao et al., 2019		
TSS T0526-LG-	S. Tibet		90°E	Kangmar dome				Gao et al., 2019		
TSS T0526-LG-	S. Tibet		90°E	Kangmar dome				Gao et al., 2019		
TSS T0527-LG-	S. Tibet		90°E	Kangmar dome				Gao et al., 2019		
TSS T0527-LG-	S. Tibet		90°E	Kangmar dome				Gao et al., 2019		
TSS T0527-LG-	S. Tibet		90°E	Kangmar dome				Gao et al., 2019		
TSS T0527-LG-	S. Tibet		90°E	Kangmar dome				Gao et al., 2019		
TSS T0527-LG-	S. Tibet		90°E	Kangmar dome				Gao et al., 2019		
TSS T0527-LG-	S. Tibet		90°E	Kangmar dome				Gao et al., 2019		
TSS T0898-1	S. Tibet		88°E	Mabja dome				Gao et al., 2019		
TSS T0898-2	S. Tibet		88°E	Mabja dome				Gao et al., 2019		
TSS T0898-3	S. Tibet		88°E	Mabja dome				Gao et al., 2019		
TSS T0898-4	S. Tibet		88°E	Mabja dome				Gao et al., 2019		
HHC T0812-A-1	N.E. Ner	Close to TSS	86°E	Gyirong	0.511941	13	-13.6	Gao et al., 2019		
HHC T0812-A-2	N.E. Ner	Close to TSS	86°E	Gyirong	0.511943	9	-13.6	Gao et al., 2019		
HHC T0812-A-3	N.E. Ner	Close to TSS	86°E	Gyirong	0.511956	11	-13.3	Gao et al., 2019		
HHC T0812-A-4	N.E. Ner	Close to TSS	86°E	Gyirong	0.51194	6	-13.6	Gao et al., 2019		
HHC T0812-B-1	N.E. Ner	Close to TSS	86°E	Gyirong	0.511972	8	-13.0	Gao et al., 2019		
HHC T0812-B-2	N.E. Ner	Close to TSS	86°E	Gyirong	0.511968	5	-13.1	Gao et al., 2019		
HHC T0812-B-3	N.E. Ner	Close to TSS	86°E	Gyirong	0.511948	9	-13.5	Gao et al., 2019		
HHC T0814--1	N.E. Ner	Close to TSS	86°E	Gyirong	0.511955	15	-13.3	Gao et al., 2019		
HHC T0814--2	N.E. Ner	Close to TSS	86°E	Gyirong	0.51195	8	-13.4	Gao et al., 2019		
HHC T0814--3	N.E. Ner	Close to TSS	86°E	Gyirong				Gao et al., 2019		
HHC T0814--4	N.E. Ner	Close to TSS	86°E	Gyirong				Gao et al., 2019		
HHC T0814--5	N.E. Ner	Close to TSS	86°E	Gyirong	0.511991	12	-12.6	Gao et al., 2019		
HHC T0814--6	N.E. Ner	Close to TSS	86°E	Gyirong	0.511999	8	-12.5	Gao et al., 2019		
HHC ZC10-04	N.E. Ner	Close to TSS	86°E	Gyirong				Gao et al., 2019		
HHC ZC10-06	N.E. Ner	Close to TSS	86°E	Gyirong				Gao et al., 2019		
HHC ZC10-07	N.E. Ner	Close to TSS	86°E	Gyirong				Gao et al., 2019		
HHC T0512-2	Bhutan		90°E	Yadong				Gao et al., 2019		
HHC T0512-3	Bhutan		90°E	Yadong				Gao et al., 2019		
HHC T0512-6	Bhutan		90°E	Yadong				Gao et al., 2019		
HHC T0252-1	E. syntaxis			Namche Barwa	0.511954	10	-13.3	Gao et al., 2019		
HHC T0252-2	E. syntaxis			Namche Barwa	0.511982	10	-12.8	Gao et al., 2019		
HHC T0252-12-	E. syntaxis			Namche Barwa	0.511988	12	-12.7	Gao et al., 2019		
HHC T0252-12-	E. syntaxis			Namche Barwa	0.511997	11	-12.5	Gao et al., 2019		
HHC T0252-12-	E. syntaxis			Namche Barwa	0.512005	11	-12.3	Gao et al., 2019		
T0748								Gao et al., 2019		

Table SII-2 (…/…)

Ech.#	Region	River	Locality	Formation	144Nd/142Nd	2s.d.	eNd(0)	Reference	Commer	Full reference
										Gao, L.-E., Zeng, L., 2014. Fluxed melting of metapelite and the formation of Miocene high-CaO two-mica granites in the Malashan gneiss dome, southern Tibet. Geochimica et Cosmochimica Acta 130, 136–155. https://doi.org/10.1016/j.gca.2014.01.003
TSS T0646-2	S. Tibet	29°N 86°E		Malashan gneiss dome	0.51191	9	-14.2	Gao and Zeng, 2014		
TSS T0646-1	S. Tibet	29°N 86°E		Malashan gneiss dome	0.511921	9	-14.0	Gao and Zeng, 2014		
TSS T0646-3	S. Tibet	29°N 86°E		Malashan gneiss dome	0.511893	11	-14.5	Gao and Zeng, 2014		
TSS T0646-4	S. Tibet	29°N 86°E		Malashan gneiss dome	0.511893	8	-14.5	Gao and Zeng, 2014		
TSS T0646-5	S. Tibet	29°N 86°E		Malashan gneiss dome	0.511891	13	-14.6	Gao and Zeng, 2014		
TSS T0647-1	S. Tibet	29°N 86°E		Malashan gneiss dome	0.511928	12	-13.8	Gao and Zeng, 2014		
TSS T0647-2	S. Tibet	29°N 86°E		Malashan gneiss dome	0.511905	6	-14.3	Gao and Zeng, 2014		
TSS T0647-3	S. Tibet	29°N 86°E		Malashan gneiss dome	0.511893	12	-14.5	Gao and Zeng, 2014		
TSS T0658	S. Tibet	29°N 86°E		Malashan gneiss dome	0.511929	12	-13.8	Gao and Zeng, 2014		
TSS T0661-1A	S. Tibet	29°N 86°E		Malashan gneiss dome	0.511909	12	-14.2	Gao and Zeng, 2014		
TSS T0661-2A	S. Tibet	29°N 86°E		Malashan gneiss dome	0.511907	5	-14.3	Gao and Zeng, 2014		
TSS T0661-3A	S. Tibet	29°N 86°E		Malashan gneiss dome	0.51193	6	-13.8	Gao and Zeng, 2014		
TSS T0661-4	S. Tibet	29°N 86°E		Malashan gneiss dome	0.511923	5	-13.9	Gao and Zeng, 2014		
TSS TMLS-09A	S. Tibet	29°N 86°E		Malashan gneiss dome	0.511924	10	-13.9	Gao and Zeng, 2014		
TSS TMLS-09B	S. Tibet	29°N 86°E		Malashan gneiss dome	0.511927	10	-13.9	Gao and Zeng, 2014		
TSS T0659-3	S. Tibet	29°N 86°E		Malashan gneiss dome	0.511956	5	-13.3	Gao and Zeng, 2014		
TSS T0659-4	S. Tibet	29°N 86°E		Malashan gneiss dome	0.511968	5	-13.1	Gao and Zeng, 2014		
TSS T0659-6	S. Tibet	29°N 86°E		Malashan gneiss dome	0.511952	13	-13.4	Gao and Zeng, 2014		
TSS T0659-11	S. Tibet	29°N 86°E		Malashan gneiss dome	0.511946	11	-13.5	Gao and Zeng, 2014		
TSS T0659-12	S. Tibet	29°N 86°E		Malashan gneiss dome	0.511946	10	-13.5	Gao and Zeng, 2014		
TSS T0659-13	S. Tibet	29°N 86°E		Malashan gneiss dome	0.511925	8	-13.9	Gao and Zeng, 2014		
TSS T0659-14	S. Tibet	29°N 86°E		Malashan gneiss dome	0.511926	7	-13.9	Gao and Zeng, 2014		
TSS T0647-4	S. Tibet	29°N 86°E		Malashan gneiss dome	0.511946	14	-13.5	Gao and Zeng, 2014		
TSS T0647-5	S. Tibet	29°N 86°E		Malashan gneiss dome	0.511907	6	-14.3	Gao and Zeng, 2014		
										Murphy, M.A., 2007. Isotopic characteristics of the Gurla Mandhata metamorphic core complex: Implications for the architecture of the Himalayan orogen. Geology 35, 983–986.
LH/H GMH 1	N.W. Ne	30.5°N 82°E		Gurla Mandhata metamorphic core complex	0.512102	11	-10.5	Murphy, 2007		
LH/H GMH 2	N.W. Ne	30.5°N 82°E		Gurla Mandhata metamorphic core complex	0.511738	13	-17.6	Murphy, 2007		
LH/H GMH 3	N.W. Ne	30.5°N 82°E		Gurla Mandhata metamorphic core complex	0.5119	11	-14.4	Murphy, 2007		
LH GMH 4	N.W. Ne	30.5°N 82°E		Gurla Mandhata metamorphic core complex	0.511467	12	-22.8	Murphy, 2007		
LH GMH 5	N.W. Ne	30.5°N 82°E		Gurla Mandhata metamorphic core complex	0.511546	26	-21.3	Murphy, 2007		
LH GMH 6	N.W. Ne	30.5°N 82°E		Gurla Mandhata metamorphic core complex	0.511457	17	-23.0	Murphy, 2007		
LH GMH 7	N.W. Ne	30.5°N 82°E		Gurla Mandhata metamorphic core complex	0.51144	14	-23.4	Murphy, 2007		
LH/H GMH 8	N.W. Ne	30.5°N 82°E		Gurla Mandhata metamorphic core complex	0.511922	12	-14.0	Murphy, 2007		
LH GMH 9	N.W. Ne	30.5°N 82°E		Gurla Mandhata metamorphic core complex	0.511546	24	-21.3	Murphy, 2007		
										Imayama, T., Arita, K., 2008. Nd isotopic data reveal the material and tectonic nature of the Main Central Thrust zone in Nepal Himalaya. Tectonophysics, Asia out of Tethys: Geochronologic, Tectonic and Sedimentary Records 451, 265–281. https://doi.org/10.1016/j.tecto.2007.11.051
HHC HE 5	Far-east	HHC	Kangchenjunga Migmatite	Formation I	0.511967	1E-05	-13.1	Imayama and Arita, 2(		
HHC HE13	Far-east	HHC	Mahabharat Crystallines	Formation I	0.511708	3E-05	-18.1	Imayama and Arita, 2008		
HHC HE14	Far-east	HHC	Mahabharat Crystallines	Formation I	0.511872	1E-05	-14.9	Imayama and Arita, 2008		
HHC HE17	Far-east	HHC	Junbesi Paragneiss	Formation I	0.511741	2E-05	-17.5	Imayama and Arita, 2008		
HHC HE18	Far-east	HHC	Junbesi Paragneiss	Formation I	0.511798	1E-05	-16.4	Imayama and Arita, 2008		
HHC HE24	Far-east	HHC	Junbesi Paragneiss	Formation I	0.511714	1E-05	-18.0	Imayama and Arita, 2008		
HHC HE25	Far-east	HHC	Kangchenjunga Migmatite	Formation I	0.512123	1E-05	-10.0	Imayama and Arita, 2008		
HHC HE26	Far-east	HHC	Kangchenjunga Migmatite	Formation I	0.511808	1E-05	-16.2	Imayama and Arita, 2008		
HHC HE32	Far-east	HHC	Kangchenjunga Migmatite	Formation I	0.51172	1E-05	-17.9	Imayama and Arita, 2008		
HHC HE68	Far-east	HHC	Junbesi Paragneiss	Formation I	0.511802	8E-06	-16.3	Imayama and Arita, 2008		
HHC HE71	Far-east	HHC	Junbesi Paragneiss	Formation I	0.511724	1E-05	-17.8	Imayama and Arita, 2008		
HHC HE76	Far-east	HHC	Kangchenjunga Migmatite	Formation I	0.511831	1E-05	-15.7	Imayama and Arita, 2008		
HHC HE77	Far-east	HHC	Junbesi Paragneiss	Formation I	0.511713	2E-05	-18.0	Imayama and Arita, 2008		
LH/H ME11	Far-east	MCTZ	Sun Kosi Phyllite	MCT zone	0.5116	2E-05	-20.2	Imayama and Arita, 2008		
LH/H ME12	Far-east	MCTZ	Sun Kosi Phyllite	MCT zone	0.511688	2E-05	-18.5	Imayama and Arita, 2008		
LH/H ME15	Far-east	MCTZ	Khare Phyllite	MCT zone	0.511513	1E-05	-21.9	Imayama and Arita, 2008		
LH/H ME16	Far-east	MCTZ	Sisne Khola Augen Gneiss	MCT zone	0.51163	1E-05	-19.7	Imayama and Arita, 2008		
LH ME19	Far-east	MCTZ	Khare Phyllite	MCT zone	0.511444	1E-05	-23.3	Imayama and Arita, 2008		
LH ME22	Far-east	MCTZ	Khare Phyllite	MCT zone	0.511293	2E-05	-26.2	Imayama and Arita, 2008		
LH ME23	Far-east	MCTZ	Khare Phyllite	MCT zone	0.511502	1E-05	-22.2	Imayama and Arita, 2008		
LH ME75	Far-east	MCTZ	Sisne Khola Augen Gneiss	MCT zone	0.511327	3E-05	-25.6	Imayama and Arita, 2008		
LH ME76	Far-east	MCTZ	Khare Phyllite	MCT zone	0.511478	2E-05	-22.6	Imayama and Arita, 2008		
LH LE20	Far-east	LLHS	Taplejung Group	Nawakot Group	0.511259	3E-05	-26.9	Imayama and Arita, 2008		
LH LE21	Far-east	LLHS	Taplejung Group	Nawakot Group	0.511334	1E-05	-25.4	Imayama and Arita, 2008		
LH LE28	Far-east	LLHS	Taplejung Group	Nawakot Group	0.511275	1E-05	-26.6	Imayama and Arita, 2008		
LH LE78	Far-east	LLHS	Taplejung Group	Nawakot Group	0.511322	1E-05	-25.7	Imayama and Arita, 2008		
LH LE79	Far-east	LLHS	Taplejung Group	Nawakot Group	0.511512	1E-05	-22.0	Imayama and Arita, 2008		
LH LE10	Far-east	ULHS	Taplejung Group	Nawakot Group	0.511757	2E-05	-17.2	Imayama and Arita, 2008		
HHC HC46	Central I	HHC	Himalayan gneisses	Formation I	0.511928	2E-05	-13.8	Imayama and Arita, 2008		
HHC HC47	Central I	HHC	Himalayan gneisses	Formation I	0.511766	2E-05	-17.0	Imayama and Arita, 2008		

Table SII-2 (…/…)

	Ech.#	Region	River	Locality	Formation	144Nd/142Nd	2s.d.	eNd(0)	Reference	Commer	Full reference
LH	MC49	Central H	MCTZ	MCT zone	MCT zone	0.511312	3E-05	-25.9	Imayama and Arita, 2008		
LH	MC69	Central H	MCTZ	MCT zone	MCT zone	0.51142	2E-05	-23.8	Imayama and Arita, 2008		
LH	MC74	Central H	MCTZ	MCT zone	MCT zone	0.511296	3E-05	-26.2	Imayama and Arita, 2008		
LH	LC50	Central H	LLHS	Nawakot Group	Kuncha	0.511328	1E-05	-25.6	Imayama and Arita, 2008		
LH	LC70	Central H	LLHS	Nawakot Group	Fagfog Quartzite	0.511357	1E-05	-25.0	Imayama and Arita, 2008		
LH	LC71	Central H	LLHS	Nawakot Group	Fagfog Quartzite	0.511342	1E-05	-25.3	Imayama and Arita, 2008		
LH	LC72	Central H	LLHS	Nawakot Group	Kuncha	0.51134	2E-05	-25.3	Imayama and Arita, 2008		
LH	LC73	Central H	LLHS	Nawakot Group	Kuncha	0.51134	1E-05	-25.3	Imayama and Arita, 2008		
LH	LC53	Central H	ULHS	Nawakot Group	Nourpul	0.511439	1E-05	-23.4	Imayama and Arita, 2008		
LH	LC54	Central H	ULHS	Nawakot Group	Benighat Slates	0.511619	1E-05	-19.9	Imayama and Arita, 2008		
LH	LC55	Central H	ULHS	Nawakot Group	Nourpul	0.511518	2E-05	-21.8	Imayama and Arita, 2008		
LH	LC56	Central H	ULHS	Nawakot Group	Benighat Slates	0.511515	2E-05	-21.9	Imayama and Arita, 2008		
LH	LC57	Central H	ULHS	Nawakot Group	Benighat Slates	0.511614	1E-05	-20.0	Imayama and Arita, 2008		
HHC	HW8	Western	HHC	Himalayan gneisses	Formation I	0.511756	5E-05	-17.2	Imayama and Arita, 2008		
HHC	HW9	Western	HHC	Himalayan gneisses	Formation I	0.511733	1E-05	-17.7	Imayama and Arita, 2008		
HHC	HW36	Western	HHC	Himalayan gneisses	Formation I	0.511898	1E-05	-14.4	Imayama and Arita, 2008		
LH	MW7	Western	MCTZ	MCT zone	MCT zone	0.511379	2E-05	-24.6	Imayama and Arita, 2008		
LH/H	MW35	Western	MCTZ	MCT zone	MCT zone	0.512005	1E-05	-12.3	Imayama and Arita, 2008		
LH	MW38	Western	MCTZ	MCT zone	MCT zone	0.511419	1E-05	-23.8	Imayama and Arita, 2008		
LH	MW61	Western	MCTZ	MCT zone	MCT zone	0.511348	2E-05	-25.2	Imayama and Arita, 2008		
LH	LW4	Western	LLHS	Quartzose Sandstone Fm.	Kuncha Fm	0.511313	2E-05	-25.8	Imayama and Arita, 2008		
LH	LW5	Western	LLHS	Phyllite Fm.	Dandagaon Phyllites	0.511342	1E-05	-25.3	Imayama and Arita, 2008		
LH	LW62	Western	LLHS	Quartzite Fm.	Fagfog Quartzite	0.511263	2E-05	-26.8	Imayama and Arita, 2008		
LH	LW64	Western	LLHS	Quartzite Fm.	Fagfog Quartzite	0.511348	3E-05	-25.2	Imayama and Arita, 2008		
LH	LW65	Western	LLHS	Phyllite Fm.	Dandagaon Phyllites	0.511306	1E-05	-26.0	Imayama and Arita, 2008		
LH	LW68	Western	LLHS	Quartzite Fm.	Fagfog Quartzite	0.511364	2E-05	-24.9	Imayama and Arita, 2008		
LH	LW39	Western	ULHS	Laminated Slate Fm.	Benighat Slates Grayish slate	0.511374	1E-05	-24.7	Imayama and Arita, 2008		
LH	LW40	Western	ULHS	Laminated Slate Fm.	Benighat Slates	0.51142	1E-05	-23.8	Imayama and Arita, 2008		
LH	LW43	Western	ULHS	Lower Variegated Rock Fm.	Benighat Slates?	0.511838	1E-05	-15.6	Imayama and Arita, 2008		
LH	LW63	Western	ULHS	Lower Variegated Rock Fm.	Benighat Slates?	0.511262	3E-05	-26.8	Imayama and Arita, 2008		
TSS	AY06-29-0	S. Lhasa			Langjiexue Group	0.512196	13	-8.6	Dai et al., 2008		Dai, J., Yin, A., Liu, W., Wang, C., 2008. Nd isotopic compositions of the Tethyan Himalayan Sequence in southeastern Tibet. Sci. China Ser. D-Earth Sci. 51, 1306–1316. https://doi.org/10.1007/s11430-008-0103-7
TSS	AY06-29-0	S. Lhasa			Langjiexue Group	0.51222	14	-8.2	Dai et al., 2008		
TSS	AY06-29-0	S. Lhasa			Langjiexue Group	0.512138	14	-9.8	Dai et al., 2008		
TSS	AY07-03-0	S. Lhasa			Langjiexue Group	0.51236	13	-5.4	Dai et al., 2008		
TSS	AY07-01-0	S. Lhasa			Lhakang Formation	0.511775	12	-16.8	Dai et al., 2008		
TSS	AY07-01-0	S. Lhasa			Lhakang Formation	0.51177	10	-16.9	Dai et al., 2008		
TSS	AY07-01-0	S. Lhasa			Lhakang Formation	0.511742	14	-17.5	Dai et al., 2008		
TSS	AY07-02-0	S. Lhasa			Lhakang Formation	0.51223	12	-8.0	Dai et al., 2008		
TSS	AY07-02-0	S. Lhasa			Lhakang Formation	0.511715	13	-18.0	Dai et al., 2008		
TSS	AY07-02-0	S. Lhasa			Lhakang Formation	0.51178	14	-16.7	Dai et al., 2008		
HHC	B45	Bhutan			HHS (N. of Kakhtang thrust)	0.511884	6E-06	-14.7	Richards et al., 2006		Richards, A., Parrish, R., Harris, N., Argles, T., Zhang, L., 2006. Correlation of lithotectonic units across the eastern Himalaya, Bhutan. Geology 34, 341–344.
HHC	B87	Bhutan			HHS (N. of Kakhtang thrust)	0.51178	2E-05	-16.7	Richards et al., 2006		
HHC	Bh3	Bhutan			HHS (N. of Kakhtang thrust)	0.512015	3E-06	-12.2	Richards et al., 2006		
HHC	B39	Bhutan			HHS (S. of Kakhtang thrust)	0.511795	9E-06	-16.4	Richards et al., 2006		
HHC	B41	Bhutan			HHS (S. of Kakhtang thrust)	0.511867	5E-06	-15.0	Richards et al., 2006		
HHC	B50	Bhutan			HHS (S. of Kakhtang thrust)	0.511873	8E-06	-14.9	Richards et al., 2006		
HHC	B51	Bhutan			HHS (S. of Kakhtang thrust)	0.511803	6E-06	-16.3	Richards et al., 2006		
HHC	B68	Bhutan			HHS (S. of Kakhtang thrust)	0.511877	7E-06	-14.8	Richards et al., 2006		
HHC	B71b	Bhutan			HHS (S. of Kakhtang thrust)	0.511738	2E-06	-17.6	Richards et al., 2006		
HHC	B81	Bhutan			HHS (S. of Kakhtang thrust)	0.511932	3E-06	-13.8	Richards et al., 2006		
HHC	B83	Bhutan			HHS (S. of Kakhtang thrust)	0.512017	4E-06	-12.1	Richards et al., 2006		
HHC	B85b	Bhutan			HHS (S. of Kakhtang thrust)	0.511801	6E-06	-16.3	Richards et al., 2006		
HHC	B88b	Bhutan			HHS (S. of Kakhtang thrust)	0.511908	1E-05	-14.2	Richards et al., 2006		
HHC	Bh6	Bhutan			HHS (S. of Kakhtang thrust)	0.511875	2E-06	-14.9	Richards et al., 2006		
HHC	Bh10b	Bhutan			HHS (S. of Kakhtang thrust)	0.511773	3E-06	-16.9	Richards et al., 2006		
HHC	Bh12	Bhutan			HHS (S. of Kakhtang thrust)	0.511789	3E-06	-16.6	Richards et al., 2006		
LH	B29a	Bhutan			Daling-Shumar Formation	0.511253	8E-06	-27.0	Richards et al., 2006		
LH	B29b	Bhutan			Daling-Shumar Formation	0.511274	5E-06	-26.6	Richards et al., 2006		
LH	B36a	Bhutan			Daling-Shumar Formation	0.5	0.0	-27.3	Richards et al., 2006		
LH	B75	Bhutan			Daling-Shumar Formation	0.511312	7E-06	-25.9	Richards et al., 2006		
LH	Bh13	Bhutan			Daling-Shumar Formation	0.510984	1E-06	-32.3	Richards et al., 2006		
LH	LT-4	C. Nepal		Langtang		0.511356	10	-25.0	Parrish and Hodges, 1		Parrish, R.R., Hodges, V., 1996. Isotopic constraints on the age and provenance of the Lesser and Greater Himalayan sequences, Nepalese Himalaya. Geological Society of America Bulletin 108, 904–911. https://doi.org/10.1130/0016-7606(1996)108<0904:ICOTAA>2.3.CO;2
LH	LT-6	C. Nepal		Langtang		0.511348	14	-25.2	Parrish and Hodges, 1996		

Table SII-2 (…/…)

	Ech.#	Region	River	Locality	Formation	144Nd/142Nd	2s.d.	eNd(0)	Reference	Commer	Full reference
LH	LT-7	C. Nepal		Langtang		0.511429	14	-23.6	Parrish and Hodges, 1996		
LH	LT-10	C. Nepal		Langtang		0.51133	6	-25.5	Parrish and Hodges, 1996		
LH	LT-18	C. Nepal		Langtang		0.511296	29	-26.2	Parrish and Hodges, 1996		
LH	LT-19	C. Nepal		Langtang		0.511423	7	-23.7	Parrish and Hodges, 1996		
LH/H	LT-20	C. Nepal		Langtang	Syabru Bensi augen gneiss	0.511532	7	-21.6	Parrish and Hodges, 1996		
LH/H	LT-33	C. Nepal		Langtang	Syabru gneiss	0.511805	13	-16.2	Parrish and Hodges, 1996		
LH/H	LT-34	C. Nepal		Langtang	Syabru gneiss	0.511741	11	-17.5	Parrish and Hodges, 1996		
HHC	LT-21	C. Nepal		Langtang	Gosainkund gneiss	0.511826	15	-15.8	Parrish and Hodges, 1996		
HHC	LT-22	C. Nepal		Langtang	Gosainkund gneiss	0.511878	14	-14.8	Parrish and Hodges, 1996		
HHC	LT-24	C. Nepal		Langtang	Gosainkund gneiss	0.511816	12	-16.0	Parrish and Hodges, 1996		
HHC	LT-29	C. Nepal		Langtang	Gosainkund gneiss	0.511691	8	-18.5	Parrish and Hodges, 1996		
											Liu, A.-L., Wang, Q., Zhu, D.-C., Zhao, Z.-D., Liu, S.-A., Wang, R., Dai, J.-G., Zheng, Y.-C., Zhang, L.-L., 2018. Origin of the ca. 50 Ma Linzizong shoshonitic volcanic rocks in the eastern Gangdese arc, southern Tibet. Lithos 304–307, 374–387. https://doi.org/10.1016/j.lithos.2018.02.017
THB	12PD01-1	N. Lhasa	Pangduo, E.	Linzizong shoshonitic volcanic rocks	Pana formation	0.512703	1E-05	1.3	Liu et al., 2018		
THB	12PD05-1	N. Lhasa	Pangduo, E.	Linzizong shoshonitic volcanic rocks	Pana formation	0.512447	1E-05	-3.7	Liu et al., 2018		
THB	12PD05-2	N. Lhasa	Pangduo, E.	Linzizong shoshonitic volcanic rocks	Pana formation				Liu et al., 2018		
THB	12PD05-3	N. Lhasa	Pangduo, E.	Linzizong shoshonitic volcanic rocks	Pana formation	0.512446	9E-06	-3.7	Liu et al., 2018		
THB	12PD05-4	N. Lhasa	Pangduo, E.	Linzizong shoshonitic volcanic rocks	Pana formation	0.512435	1E-05	-4.0	Liu et al., 2018		
THB	12PD02-1	N. Lhasa	Pangduo, E.	Linzizong shoshonitic volcanic rocks	Pana formation	0.512308	1E-05	-6.4	Liu et al., 2018		
THB	12PD03-1	N. Lhasa	Pangduo, E.	Linzizong shoshonitic volcanic rocks	Pana formation				Liu et al., 2018		
THB	12PD04-1	N. Lhasa	Pangduo, E.	Linzizong shoshonitic volcanic rocks	Pana formation				Liu et al., 2018		
THB	12PD06-1	N. Lhasa	Pangduo, E.	Linzizong shoshonitic volcanic rocks	Pana formation	0.5123	1E-05	-6.6	Liu et al., 2018		
THB	12PD07-1	N. Lhasa	Pangduo, E.	Linzizong shoshonitic volcanic rocks	Pana formation	0.512343	1E-05	-5.8	Liu et al., 2018		
THB	12PD08-1	N. Lhasa	Pangduo, E.	Linzizong shoshonitic volcanic rocks	Pana formation				Liu et al., 2018		
THB	12PD09-1	N. Lhasa	Pangduo, E.	Gangdese belt	Nuoco formation ?	0.5115952	9E-06	-20.3	Liu et al., 2018		
THB	12PD11-1	N. Lhasa	Pangduo, E.	Gangdese belt	Nuoco formation ?	0.511627	9E-06	-19.7	Liu et al., 2018		
											Huang, F., Chen, J.-L., Xu, J.-F., Wang, B.-D., Li, J., 2015. Os–Nd–Sr isotopes in Miocene ultrapotassic rocks of southern Tibet: Partial melting of a pyroxenite-bearing lithospheric mantle? Geochimica et Cosmochimica Acta 163, 279–298. https://doi.org/10.1016/j.gca.2015.04.053
THB	CM10-04-(	N.W. Lhasa			Mibale	0.511958	7	-13.3	Huang et al., 2015		
THB	CM10-04-(	N.W. Lhasa			Mibale	0.511952	5	-13.4	Huang et al., 2015		
THB	CM10-04-1	N.W. Lhasa			Mibale	0.511927	6	-13.9	Huang et al., 2015		
THB	CM10-04-1	N.W. Lhasa			Mibale	0.511894	6	-14.5	Huang et al., 2015		
THB	CM10-04-2	N.W. Lhasa			Mibale	0.511927	6	-13.9	Huang et al., 2015		
THB	CM10-04-2	N.W. Lhasa			Mibale	0.512	7	-12.4	Huang et al., 2015		
THB	CQQ4-04-(	N.W. Lhasa			Maiga	0.511801	7	-16.3	Huang et al., 2015		
THB	CQQ4-04-(	N.W. Lhasa			Maiga	0.511835	7	-15.7	Huang et al., 2015		
											Zhang, S.-Q., Mahoney, J.J., Mo, X.-X., Ghazi, A.M., Milani, L., Crawford, A.J., Guo, T.-Y., Zhao, Z.-D., 2005. Evidence for a Widespread Tethyan Upper Mantle with Indian-Ocean-Type Isotopic Characteristics. J Petrology 46, 829–858. https://doi.org/10.1093/petrology/egi002
THB	DJB98-11	S.W. Tib	31°N	80°E	Dajiweng	Yarlung Tsangbo suture	0.5128		3.2	Zhang et al., 2005	
THB	L	S.W. Tib	31°N	80°E	Dajiweng	Yarlung Tsangbo suture	0.512835		3.8	Zhang et al., 2005	
THB	DJB98-18	S.W. Tib	31°N	80°E	Dajiweng	Yarlung Tsangbo suture	0.513049		8.0	Zhang et al., 2005	
THB	DJB98-20	S.W. Tib	31°N	80°E	Dajiweng	Yarlung Tsangbo suture	0.512801		3.2	Zhang et al., 2005	
THB	BAR98-1 (	S.W. Tib	31°N	80°E	Bar	Yarlung Tsangbo suture	0.513109		9.2	Zhang et al., 2005	
THB	BAR98-3 (	S.W. Tib	31°N	80°E	Bar	Yarlung Tsangbo suture	0.513107		9.1	Zhang et al., 2005	
THB	BAR98-6	S.W. Tib	31°N	80°E	Bar	Yarlung Tsangbo suture	0.512751		2.2	Zhang et al., 2005	
THB	DQ98-9 G	S.W. Tib	30°N	83°E	Dangqiong	Yarlung Tsangbo suture	0.513114		9.3	Zhang et al., 2005	
THB	DQ98-12 (	S.W. Tib	30°N	83°E	Dangqiong	Yarlung Tsangbo suture	0.513114		9.3	Zhang et al., 2005	
THB	DQ98-14 [	S.W. Tib	30°N	83°E	Dangqiong	Yarlung Tsangbo suture	0.513111		9.2	Zhang et al., 2005	
THB	XL98-10 D	S. Tibet	29°N	89°E	Xialu	Yarlung Tsangbo suture	0.513083		8.7	Zhang et al., 2005	
THB	DZ98-1 G	S. Tibet	29°N	89°E	Dazhuqu Dazhuka	Yarlung Tsangbo suture	0.513118		9.4	Zhang et al., 2005	
THB	DZ98-12 D	S. Tibet	29°N	89°E	Dazhuqu Dazhuka	Yarlung Tsangbo suture	0.513108		9.2	Zhang et al., 2005	
THB	L	S. Tibet	29°N	89°E	Dazhuqu Dazhuka	Yarlung Tsangbo suture	0.513118		9.4	Zhang et al., 2005	
THB	DZ98-19	S. Tibet	29°N	89°E	Dazhuqu Dazhuka	Yarlung Tsangbo suture	0.51308		8.6	Zhang et al., 2005	
THB	LC98-3	S.E. Tibe	29°N	92°E	Langceling	Yarlung Tsangbo suture	0.513109		9.2	Zhang et al., 2005	
THB	LC98-4	S.E. Tibe	29°N	92°E	Langceling	Yarlung Tsangbo suture	0.513133		9.7	Zhang et al., 2005	
THB	LC98-6	S.E. Tibe	29°N	92°E	Langceling	Yarlung Tsangbo suture	0.513136		9.7	Zhang et al., 2005	
THB	LB98-1 G	S.E. Tibe	29°N	92°E	Luobusha	Yarlung Tsangbo suture	0.513071		8.4	Zhang et al., 2005	
THB	L	S.E. Tibe	29°N	92°E	Luobusha	Yarlung Tsangbo suture	0.513079		8.6	Zhang et al., 2005	
THB	LB98-3 G	S.E. Tibe	29°N	92°E	Luobusha	Yarlung Tsangbo suture	0.513086		8.7	Zhang et al., 2005	
											Zhang, L.-Y., Ducea, M.N., Ding, L., Pullen, A., Kapp, P., Hoffman, D., 2014. Southern Tibetan Oligocene–Miocene adakites: A record of Indian slab tearing. Lithos 210–211, 209–223. https://doi.org/10.1016/j.lithos.2014.09.029
THB	19	S.E. Lhasa			Sangri pluton	0.51257	2E-05	-1.3	Zhang et al., 2014		
THB	110	E. Synta	W. Namche Barwa		Dangru pluton / Dongru	0.512439	1E-05	-3.9	Zhang et al., 2014		
THB	109A	E. Synta	W. Namche Barwa		Dangru pluton / Dongru	0.512439	6E-06	-3.9	Zhang et al., 2014		
THB	109B	E. Synta	W. Namche Barwa		Dangru pluton / Dongru				Zhang et al., 2014		
THB	111A	E. Synta	W. Namche Barwa		Dangru pluton / Dongru	0.5124	9E-06	-4.6	Zhang et al., 2014		

Table SII-2 (…/…)

Ech.#	Region	River	Locality	Formation	144Nd/142Nd	2s.d.	eNd(0)	Reference	Commer	Full reference
THB 111B	E. Synta	W. Namche	Barwa	Dangru pluton / Dongru	0.512427	1E-05	-4.1	Zhang et al., 2014		
THB 14	E. Synta	W. Namche	Barwa	Linzhi pluton / Nyingchi				Zhang et al., 2014		
THB 119A	E. Synta	W. Namche	Barwa	Linzhi pluton / Nyingchi	0.512443	1E-05	-3.8	Zhang et al., 2014		
THB 119B	E. Synta	W. Namche	Barwa	Linzhi pluton / Nyingchi				Zhang et al., 2014		
THB 119C	E. Synta	W. Namche	Barwa	Linzhi pluton / Nyingchi	0.512462	5E-06	-3.4	Zhang et al., 2014		
THB 119D	E. Synta	W. Namche	Barwa	Linzhi pluton / Nyingchi				Zhang et al., 2014		
THB 120A	E. Synta	W. Namche	Barwa	Linzhi pluton / Nyingchi	0.5124	2E-05	-4.6	Zhang et al., 2014		
THB 120B	E. Synta	W. Namche	Barwa	Linzhi pluton / Nyingchi				Zhang et al., 2014		
THB 120E	E. Synta	W. Namche	Barwa	Linzhi pluton / Nyingchi				Zhang et al., 2014		
THB 138A	E. Synta	E. Namche E	Close Dibang	Lengduo pluton	0.512445	7E-06	-3.8	Zhang et al., 2014		
THB 138B	E. Synta	E. Namche E	Close Dibang	Lengduo pluton	0.512065	1E-05	-11.2	Zhang et al., 2014		
THB 138D	E. Synta	E. Namche E	Close Dibang	Lengduo pluton				Zhang et al., 2014		
THB 140A	E. Synta	E. Namche E	Close Dibang	Damu pluton	0.512441	3E-05	-3.8	Zhang et al., 2014		
THB 140B	E. Synta	E. Namche E	Close Dibang	Damu pluton	0.512426	3E-05	-4.1	Zhang et al., 2014		
THB 140C	E. Synta	E. Namche E	Close Dibang	Damu pluton				Zhang et al., 2014		
										Zeng, L., Gao, L.-E., Dong, C., Tang, S., 2012. High-pressure melting of metapelite and the formation of Ca-rich granitic melts in the Namche Barwa Massif, southern Tibet. Gondwana Research 21, 138–151. https://doi.org/10.1016/j.gr.2011.07.023
HHCZB06-80M	E. Synta	W. Namche	Barwa	Zhibai fm	0.511761	10	-17.1	Zeng et al., 2012		
HHCZB06-66M	E. Synta	W. Namche	Barwa	Pai fm	0.511962	7	-13.2	Zeng et al., 2012		
HHCZB06-35M	E. Synta	W. Namche	Barwa	Pai fm	0.511778	5	-16.8	Zeng et al., 2012		
HHCZB09-18M	E. Synta	W. Namche	Barwa	Zhibai fm	0.511835	10	-15.7	Zeng et al., 2012		
HHCZB06-80L	E. Synta	W. Namche	Barwa	Zhibai fm	0.512267	15	-7.2	Zeng et al., 2012		
HHCZB06-66L	E. Synta	W. Namche	Barwa	Pai fm	0.511952	8	-13.4	Zeng et al., 2012		
HHCZB06-35L	E. Synta	W. Namche	Barwa	Pai fm	0.511537	8	-21.5	Zeng et al., 2012		
HHCZB09-18L1	E. Synta	W. Namche	Barwa	Zhibai fm	0.511846	9	-15.4	Zeng et al., 2012		
HHCZB09-18L2	E. Synta	W. Namche	Barwa	Zhibai fm	0.511819	11	-16.0	Zeng et al., 2012		
										Guo, Z., Wilson, M., Zhang, M., Cheng, Z., Zhang, L., 2013. Post-collisional, K-rich mafic magmatism in south Tibet: constraints on Indian slab-to-wedge transport processes and plateau uplift. Contrib Mineral Petrol 165, 1311–1340. https://doi.org/10.1007/s00410-013-0860-y
THB DY-7	W. Lhas	30-31°N	86.3	1 Garwa	0.512056	7	-11.4	Guo et al., 2013		
THB DC2	W. Lhas	30-31°N	86.3	1 Garwa	0.511965	9	-13.1	Guo et al., 2013		
THB D509	W. Lhas	30-31°N	86.3	1 Garwa	0.512026	7	-11.9	Guo et al., 2013		
THB DG43	W. Lhas	30-31°N	86.3	1 Garwa	0.511941	7	-13.6	Guo et al., 2013		
THB YE51	W. Lhas	30-31°N	86.3	2 Yaqian	0.511913	8	-14.1	Guo et al., 2013		
THB YC08	W. Lhas	30-31°N	86.3	2 Yaqian	0.511917	6	-14.1	Guo et al., 2013		
THB YG13	W. Lhas	30-31°N	86.3	2 Yaqian	0.511936	11	-13.7	Guo et al., 2013		
THB YF12	W. Lhas	30-31°N	86.3	2 Yaqian	0.511983	8	-12.8	Guo et al., 2013		
THB YA32	W. Lhas	30-31°N	86.3	2 Yaqian	0.511964	8	-13.1	Guo et al., 2013		
THB MH78	W. Lhas	30-31°N	86.3	3 Mibale	0.511926	7	-13.9	Guo et al., 2013		
THB MH69	W. Lhas	30-31°N	86.3	3 Mibale	0.511992	6	-12.6	Guo et al., 2013		
THB MG-3	W. Lhas	30-31°N	86.3	3 Mibale	0.511961	8	-13.2	Guo et al., 2013		
THB MY1	W. Lhas	30-31°N	86.3	3 Mibale	0.511934	7	-13.7	Guo et al., 2013		
THB MK09	W. Lhas	30-31°N	86.3	3 Mibale	0.511926	10	-13.9	Guo et al., 2013		
THB MR21	W. Lhas	30-31°N	86.3	3 Mibale	0.511854	6	-15.3	Guo et al., 2013		
THB MA75	W. Lhas	30-31°N	86.3	3 Mibale	0.511847	12	-15.4	Guo et al., 2013		
THB MX5	W. Lhas	30-31°N	86.3	3 Mibale	0.511928	8	-13.8	Guo et al., 2013		
THB 2003T534	W. Lhas	30-31°N	86.3	4 Yiqian	0.511844	1	-15.5	Ding et al., 2006, in Guo et al., 2013		
THB 2003T536	W. Lhas	30-31°N	86.3	4 Yiqian	0.511822	1	-15.9	Ding et al., 2006, in Guo et al., 2013		
THB 2003T539	W. Lhas	30-31°N	86.3	4 Yiqian	0.511815	1	-16.1	Ding et al., 2006, in Guo et al., 2013		
THB G8	W. Lhas	30-31°N	86.3	5 Chazi	0.511856	10	-15.3	Guo et al., 2013		
THB C10	W. Lhas	30-31°N	86.3	5 Chazi	0.511874	9	-14.9	Guo et al., 2013		
THB CV5	W. Lhas	30-31°N	86.3	5 Chazi	0.511852	13	-15.3	Guo et al., 2013		
THB C76	W. Lhas	30-31°N	86.3	5 Chazi	0.511793	7	-16.5	Guo et al., 2013		
THB CH4	W. Lhas	30-31°N	86.3	5 Chazi	0.511924	6	-13.9	Guo et al., 2013		
THB CH7	W. Lhas	30-31°N	86.3	5 Chazi	0.511828	9	-15.8	Guo et al., 2013		
THB C03	W. Lhas	30-31°N	86.3	5 Chazi	0.511894	8	-14.5	Guo et al., 2013		
THB CX38	W. Lhas	30-31°N	86.3	5 Chazi	0.511887	10	-14.6	Guo et al., 2013		
THB C25	W. Lhas	30-31°N	86.3	5 Chazi	0.511826	9	-15.8	Guo et al., 2013		
										Guo, Z., Wilson, M., Liu, J., 2007. Post-collisional adakites in south Tibet: Products of partial melting of subduction-modified lower crust. Lithos, The Origin, Evolution and Present State of Continental Lithosphere 96, 205–224. https://doi.org/10.1016/j.lithos.2006.09.011
THB ZF09	S.W. Tib	33°N	80°E	1 Shiquanhe	0.512237	11	-7.8	Guo et al., 2007		
THB GUO62	S.W. Tib	32°N	82°E	2 Gegar	0.512354	10	-5.5	Guo et al., 2007		
THB GUO51	S.W. Tib	32°N	82°E	2 Gegar	0.512249	8	-7.6	Guo et al., 2007		
THB GUO48	S. Tibet	30°N	85°E	3 Daggyai	0.512147	13	-9.6	Guo et al., 2007		
THB GUO37	W. Lhas	30°N	90°E	4 Xigaze	0.512506	7	-2.6	Guo et al., 2007		
THB G09	W. Lhas	30°N	90°E	5 Wuyu	0.512588	9	-1.0	Guo et al., 2007		
THB ZFG17	W. Lhas	30°N	90°E	6 Majiang	0.512798	6	3.1	Guo et al., 2007		
THB G006	S. Lhasa	30°N	92°E	7 Nanmu	0.512604	10	-0.7	Guo et al., 2007		
THB G019	E. Lhasa	30°N	93°E	8 Jiama	0.512544	7	-1.8	Guo et al., 2007		

Table SII-2 (…/…)

Ech.#	Region	River	Locality	Formation	144Nd/142Nd	2s.d.	eNd(0)	Reference	Commer	Full reference
THB G016	E. Lhasa	30°N 93°E	8	Jiama	0.512511	8	-2.5	Guo et al., 2007		
THB G025	E. Synta	30°N 95°E	9	Linzhi / Nyingchi pluton	0.512508	8	-2.5	Guo et al., 2007		
TSS T0837-1	S.W. Lh	29°N 86°E		Xiaru leucogranite	0.512087	9E-06	-10.7	Gao et al., 2016		
TSS T0837-2	S.W. Lh	29°N 86°E		Xiaru leucogranite	0.512079	9E-06	-10.9	Gao et al., 2016		
TSS T0837-3	S.W. Lh	29°N 86°E		Xiaru leucogranite	0.512074	1E-05	-11.0	Gao et al., 2016		
TSS T0837-4	S.W. Lh	29°N 86°E		Xiaru leucogranite	0.511928	1E-05	-13.8	Gao et al., 2016		
TSS T0659-T-1	S.W. Lh	28.°N 85°E		Paiku leucogranite				Gao et al., 2016		
TSS T0659-T-2	S.W. Lh	28.°N 85°E		Paiku leucogranite				Gao et al., 2016		
TSS LZH1101a	S.E. Lha	28.5°N 91°E		Lhozag granite	0.511977	5E-06	-12.9	Huang et al., 2017		Huang, C., Zhao, Z., Li, G., Zhu, D.-C., Liu, D., Shi, Q., 2017. Leucogranites in Lhozag, southern Tibet: Implications for the tectonic evolution of the eastern Himalaya. Lithos 294–295, 246–262. https://doi.org/10.1016/j.lithos.2017.09.014
TSS LZH1102a	S.E. Lha	28.5°N 91°E		Lhozag granite				Huang et al., 2017		
TSS LZH1103a	S.E. Lha	28.5°N 91°E		Lhozag granite	0.511951	4E-06	-13.4	Huang et al., 2017		
TSS LZH1107a	S.E. Lha	28.5°N 91°E		Lhozag granite	0.51195	2E-06	-13.4	Huang et al., 2017		
TSS LZH1111a	S.E. Lha	28.5°N 91°E		Lhozag granite				Huang et al., 2017		
TSS LZH1113a	S.E. Lha	28.5°N 91°E		Lhozag granite				Huang et al., 2017		
TSS LZH1114	S.E. Lha	28.5°N 91°E		Lhozag granite	0.511998	4E-06	-12.5	Huang et al., 2017		
TSS LZH1115	S.E. Lha	28.5°N 91°E		Lhozag granite	0.511944	3E-06	-13.5	Huang et al., 2017		
TSS LZH1116	S.E. Lha	28.5°N 91°E		Lhozag granite				Huang et al., 2017		
TSS LZH1125	S.E. Lha	28.5°N 91°E		Lhozag granite				Huang et al., 2017		
TSS LZH1126	S.E. Lha	28.5°N 91°E		Lhozag granite	0.512016	3E-06	-12.1	Huang et al., 2017		
TSS LZH1127	S.E. Lha	28.5°N 91°E		Lhozag granite				Huang et al., 2017		
TSS LZH1128	S.E. Lha	28.5°N 91°E		Lhozag granite	0.511922	3E-06	-14.0	Huang et al., 2017		
TSS LZH1129	S.E. Lha	28.5°N 91°E		Lhozag granite				Huang et al., 2017		
TSS LZH1130	S.E. Lha	28.5°N 91°E		Lhozag granite				Huang et al., 2017		
TSS LZH1131	S.E. Lha	28.5°N 91°E		Lhozag granite	0.511944	4E-06	-13.5	Huang et al., 2017		
TSS LZH1133	S.E. Lha	28.5°N 91°E		Lhozag granite				Huang et al., 2017		
TSS T0319-06	S.E. Lhasa		Yardoi	Yardoi gneiss dome	0.512033	10	-11.8	Zeng et al., 2011		Zeng, L., Gao, L.-E., Xie, K., Liu-Zeng, J., 2011. Mid-Eocene high Sr/Y granites in the Northern Himalayan Gneiss Domes: Melting thickened lower continental crust. Earth and Planetary Science Letters 303, 251–266. https://doi.org/10.1016/j.epsl.2011.01.005
TSS T0319-07	S.E. Lhasa		Yardoi	Yardoi gneiss dome	0.511936	14	-13.7	Zeng et al., 2011		
TSS T0319-08	S.E. Lhasa		Yardoi	Yardoi gneiss dome	0.512116	10	-10.2	Zeng et al., 2011		
TSS T0320-06	S.E. Lhasa		Yardoi	Yardoi gneiss dome	0.51186	9	-15.2	Zeng et al., 2011		
TSS T0317-01	S.E. Lhasa		Yardoi	Dala pluton	0.511984	5	-12.8	Zeng et al., 2011		
TSS T0317-02	S.E. Lhasa		Yardoi	Dala pluton	0.512147	10	-9.6	Zeng et al., 2011		
TSS T0317-03	S.E. Lhasa		Yardoi	Dala pluton	0.51199	10	-12.6	Zeng et al., 2011		
TSS T0317-04	S.E. Lhasa		Yardoi	Dala pluton	0.511983	10	-12.8	Zeng et al., 2011		
TSS T0317-05	S.E. Lhasa		Yardoi	Dala pluton	0.511987	6	-12.7	Zeng et al., 2011		
TSS T0317-06	S.E. Lhasa		Yardoi	Dala pluton	0.511993	5	-12.6	Zeng et al., 2011		
TSS T0389-4	S.E. Lhasa		Yardoi	Quedang	0.512042	10	-11.6	Zeng et al., 2011		
TSS T0389-5	S.E. Lhasa		Yardoi	Quedang	0.512101	8	-10.5	Zeng et al., 2011		
TSS T0389-6	S.E. Lhasa		Yardoi	Quedang	0.512049	9	-11.5	Zeng et al., 2011		
TSS T0389-7	S.E. Lhasa		Yardoi	Quedang	0.512056	10	-11.4	Zeng et al., 2011		
TSS T0389-8	S.E. Lhasa		Yardoi	Quedang	0.512053	7	-11.4	Zeng et al., 2011		
TSS T0389-9	S.E. Lhasa		Yardoi	Quedang	0.51205	10	-11.5	Zeng et al., 2011		
TSS T0389-11	S.E. Lhasa		Yardoi	Quedang	0.512054	6	-11.4	Zeng et al., 2011		
TSS T0389-12	S.E. Lhasa		Yardoi	Quedang	0.512045	11	-11.6	Zeng et al., 2011		
TSS T0389-17	S.E. Lhasa		Yardoi	Yardoi gneiss dome	0.511812	11	-16.1	Zeng et al., 2011		
TSS T0321-08	S.E. Lhasa		Yardoi	Yardoi gneiss dome	0.512396	10	-4.7	Zeng et al., 2011		
TSS T0321-09	S.E. Lhasa		Yardoi	Yardoi gneiss dome	0.512406	9	-4.5	Zeng et al., 2011		
TSS T0394-10	S.E. Lhasa		Yardoi	Yardoi gneiss dome	0.512705	8	1.3	Zeng et al., 2011		
TSS T0394-21	S.E. Lhasa		Yardoi	Yardoi gneiss dome	0.512708	8	1.4	Zeng et al., 2011		
TSS T0394-1	S.E. Lhasa		Yardoi	Yardoi gneiss dome	0.512294	7	-6.7	Zeng et al., 2011		
TSS T0394-6	S.E. Lhasa		Yardoi	Yardoi gneiss dome	0.512004	6	-12.4	Zeng et al., 2011		
TSS T0394-8	S.E. Lhasa		Yardoi	Yardoi gneiss dome	0.512224	5	-8.1	Zeng et al., 2011		
TSS T0392-0	S.E. Lhasa		Yardoi	Yardoi gneiss dome	0.511832	5	-15.7	Zeng et al., 2011		
TSS T0392-1	S.E. Lhasa		Yardoi	Yardoi gneiss dome	0.51202	7	-12.1	Zeng et al., 2011		
TSS T0392-3	S.E. Lhasa		Yardoi	Yardoi gneiss dome	0.51203	8	-11.9	Zeng et al., 2011		
TSS T0395-01	S.E. Lhasa		Yardoi	Yardoi gneiss dome	0.512262	15	-7.3	Zeng et al., 2011		
TSS T0395-03	S.E. Lhasa		Yardoi	Yardoi gneiss dome	0.512118	5	-10.1	Zeng et al., 2011		
THB Lz9915	close to	Linzigong vo	Linzhou	Pana	0.512665	11	0.5	Mo et al., 2007		Mo, X., Hou, Z., Niu, Y., Dong, G., Qu, X., Zhao, Z., Yang, Z., 2007. Mantle contributions to crustal thickening during continental collision: Evidence from Cenozoic igneous rocks in southern Tibet. Lithos, The Origin, Evolution and Present State of Continental Lithosphere 96, 225–242. https://doi.org/10.1016/j.lithos.2006.10.005
THB Lz9914	close to	Linzigong vo	Linzhou	Pana	0.512651	5	0.3	Mo et al., 2007		
THB L1087–2	close to	Linzigong vo	Linzhou	Pana	0.512889	9	4.9	Mo et al., 2007		

Table SII-2 (…/…)

Ech.#	Region	River	Locality	Formation	144Nd/142Nd	2s.d.	eNd(0)	Reference	Commer	Full reference
THB Lz991	close to	Linzigong vo	Linzhou	Nianbo	0.512633	9	-0.1	Mo et al., 2007		
THB Lz993	close to	Linzigong vo	Linzhou	Nianbo	0.512626	13	-0.2	Mo et al., 2007		
THB LZ998	close to	Linzigong vo	Linzhou	Nianbo	0.512407	7	-4.5	Mo et al., 2007		
THB Lz9913	close to	Linzigong vo	Linzhou	Dianzhong	0.512628	17	-0.2	Mo et al., 2007		
THB Lz9930	close to	Linzigong vo	Linzhou	Dianzhong	0.512582	16	-1.1	Mo et al., 2007		
THB Lz9924	close to	Linzigong vo	Linzhou	Dianzhong	0.512583	10	-1.1	Mo et al., 2007		
THB Lz9922	close to	Linzigong vo	Linzhou	mafic dike	0.512777	10	2.7	Mo et al., 2007		
THB 09TB21-2	S.E. Lha	29.2°N 94°E	W. Nyingchi, on Yarlung Tsangpo	Milin granitoids	0.512788	6	2.9	Ma et al., 2013		Ma, L., Wang, Q., Wyman, D.A., Li, Z.-X., Jiang, Z.-Q., Yang, J.-H., Gou, G.-N., Guo, H.-F., 2013. Late Cretaceous (100–89Ma) magnesian charnockites with adakitic affinities in the Milin area, eastern Gangdese: Partial melting of subducted oceanic crust and implications for crustal growth in southern Tibet. Lithos 175–176, 315–332. https://doi.org/10.1016/j.lithos.2013.04.006
THB 09TB22	S.E. Lha	29.2°N 94°E	W. Nyingchi, on Yarlung Tsangpo	Milin granitoids	0.512786	6	2.9	Ma et al., 2013		
THB 09TB38-1	S.E. Lha	29.2°N 94°E	W. Nyingchi, on Yarlung Tsangpo	Milin granitoids	0.51275	6	2.2	Ma et al., 2013		
THB 09TB39	S.E. Lha	29.2°N 94°E	W. Nyingchi, on Yarlung Tsangpo	Milin granitoids	0.512737	6	1.9	Ma et al., 2013		
THB 09TB41-3	S.E. Lha	29.2°N 94°E	W. Nyingchi, on Yarlung Tsangpo	Milin granitoids	0.512754	7	2.3	Ma et al., 2013		
THB 09TB45-3	S.E. Lha	29.2°N 94°E	W. Nyingchi, on Yarlung Tsangpo	Milin granitoids	0.512797	6	3.1	Ma et al., 2013		
THB 09TB46-2	S.E. Lha	29.2°N 94°E	W. Nyingchi, on Yarlung Tsangpo	Milin granitoids	0.51276	6	2.4	Ma et al., 2013		
THB 09TB47-1	S.E. Lha	29.2°N 94°E	W. Nyingchi, on Yarlung Tsangpo	Milin granitoids	0.512768	8	2.5	Ma et al., 2013		
THB 09TB47-3	S.E. Lha	29.2°N 94°E	W. Nyingchi, on Yarlung Tsangpo	Milin granitoids	0.512775	5	2.7	Ma et al., 2013		
THB 09TB50	S.E. Lha	29.2°N 94°E	W. Nyingchi, on Yarlung Tsangpo	Milin granitoids	0.512767	7	2.5	Ma et al., 2013		
THB 09TB51-2	S.E. Lha	29.2°N 94°E	W. Nyingchi, on Yarlung Tsangpo	Milin granitoids	0.512781	13	2.8	Ma et al., 2013		
THB 09TB36	S.E. Lha	29.2°N 94°E	W. Nyingchi, on Yarlung Tsangpo	Milin granitoids	0.512714	6	1.5	Ma et al., 2013		
THB 09TB38-2	S.E. Lha	29.2°N 94°E	W. Nyingchi, on Yarlung Tsangpo	Milin granitoids	0.512738	6	2.0	Ma et al., 2013		
THB 09TB41-1	S.E. Lha	29.2°N 94°E	W. Nyingchi, on Yarlung Tsangpo	Milin granitoids	0.512738	7	2.0	Ma et al., 2013		
THB 09TB45-1	S.E. Lha	29.2°N 94°E	W. Nyingchi, on Yarlung Tsangpo	Milin granitoids	0.512794	7	3.0	Ma et al., 2013		
THB 09TB45-2	S.E. Lha	29.2°N 94°E	W. Nyingchi, on Yarlung Tsangpo	Milin granitoids	0.512796	7	3.1	Ma et al., 2013		
THB 09TB48-1	S.E. Lha	29.2°N 94°E	W. Nyingchi, on Yarlung Tsangpo	Milin granitoids	0.51279	7	3.0	Ma et al., 2013		
THB 09TB68	S.E. Lhasa		I	Zhenga dorite-gabbro suite	0.51272	8	1.6	Ma et al., 2013b		Ma, L., Wang, Q., Wyman, D.A., Jiang, Z.-Q., Yang, J.-H., Li, Q.-L., Gou, G.-N., Guo, H.-F., 2013. Late Cretaceous crustal growth in the Gangdese area, southern Tibet: Petrological and Sr–Nd–Hf–O isotopic evidence from Zhengga diorite–gabbro. Chemical Geology 349–350, 54–70. https://doi.org/10.1016/j.chemgeo.2013.04.005
THB 09TB72-1	S.E. Lhasa		I	Zhenga dorite-gabbro suite	0.512706	8	1.3	Ma et al., 2013b		
THB 09TB73	S.E. Lhasa		I	Zhenga dorite-gabbro suite	0.512805	10	3.3	Ma et al., 2013b		
THB 09TB76	S.E. Lhasa		I	Zhenga dorite-gabbro suite	0.512795	10	3.1	Ma et al., 2013b		
THB 09TB79	S.E. Lhasa		I	Zhenga dorite-gabbro suite	0.512824	7	3.6	Ma et al., 2013b		
THB 09TB67-1	S.E. Lhasa		II	Zhenga dorite-gabbro suite	0.51259	8	-0.9	Ma et al., 2013b		
THB 09TB69	S.E. Lhasa		II	Zhenga dorite-gabbro suite	0.512698	7	1.2	Ma et al., 2013b		
THB 09TB71	S.E. Lhasa		II	Zhenga dorite-gabbro suite	0.512665	10	0.5	Ma et al., 2013b		
THB 09TB78-1a	S.E. Lhasa			Zhenga dorite-gabbro suite	0.512326	9	-6.1	Ma et al., 2013b		
THB 09TB78-2	S.E. Lhasa			Zhenga dorite-gabbro suite	0.512057	3	-11.3	Ma et al., 2013b		
THB 09TB21-1	S.E. Lha	29.2°N 94°E	W. Nyingchi, on Yarlung Tsangpo	Milin intrusive suite	0.512794	9	3.0	Ma et al., 2013c		Ma, L., Wang, Q., Li, Z.-X., Wyman, D.A., Jiang, Z.-Q., Yang, J.-H., Gou, G.-N., Guo, H.-F., 2013. Early Late Cretaceous (ca. 93Ma) norites and hornblendites in the Milin area, eastern Gangdese: Lithosphere–asthenosphere interaction during slab roll-back and an insight into early Late Cretaceous (ca. 100–80Ma) magmatic "flare-up" in southern Lhasa (Tibet). Lithos 172–173, 17–30. https://doi.org/10.1016/j.lithos.2013.03.007
THB 09TB30-1	S.E. Lha	29.2°N 94°E	W. Nyingchi, on Yarlung Tsangpo	Milin intrusive suite	0.512784	9	2.8	Ma et al., 2013c		
THB 09TB30-3	S.E. Lha	29.2°N 94°E	W. Nyingchi, on Yarlung Tsangpo	Milin intrusive suite	0.512775	11	2.7	Ma et al., 2013c		
THB 09TB32	S.E. Lha	29.2°N 94°E	W. Nyingchi, on Yarlung Tsangpo	Milin intrusive suite	0.512784	12	2.8	Ma et al., 2013c		
THB 09TB41-2	S.E. Lha	29.2°N 94°E	W. Nyingchi, on Yarlung Tsangpo	Milin intrusive suite	0.512775	13	2.7	Ma et al., 2013c		
THB 09TB44-5	S.E. Lha	29.2°N 94°E	W. Nyingchi, on Yarlung Tsangpo	Milin intrusive suite	0.512802	15	3.2	Ma et al., 2013c		
THB 09TB49-2	S.E. Lha	29.2°N 94°E	W. Nyingchi, on Yarlung Tsangpo	Milin intrusive suite	0.512768	6	2.5	Ma et al., 2013c		
THB 09TB30-2	S.E. Lha	29.2°N 94°E	W. Nyingchi, on Yarlung Tsangpo	Milin intrusive suite	0.51279	9	3.0	Ma et al., 2013c		
THB 09TB35-3	S.E. Lha	29.2°N 94°E	W. Nyingchi, on Yarlung Tsangpo	Milin intrusive suite	0.512797	10	3.1	Ma et al., 2013c		
THB 09TB42-2	S.E. Lha	29.2°N 94°E	W. Nyingchi, on Yarlung Tsangpo	Milin intrusive suite	0.512781	12	2.8	Ma et al., 2013c		
THB 09TB43-1	S.E. Lha	29.2°N 94°E	W. Nyingchi, on Yarlung Tsangpo	Milin intrusive suite	0.512798	6	3.1	Ma et al., 2013c		
THB 09TB43-2	S.E. Lha	29.2°N 94°E	W. Nyingchi, on Yarlung Tsangpo	Milin intrusive suite	0.512782	9	2.8	Ma et al., 2013c		
THB 09TB44-3	S.E. Lha	29.2°N 94°E	W. Nyingchi, on Yarlung Tsangpo	Milin intrusive suite	0.512823	8	3.6	Ma et al., 2013c		
THB 09TB61	S.E. Lhasa			Quguosha gabbros	0.512451	3	-3.6	Ma et al., 2017		Ma, L., Wang, Q., Li, Z.-X., Wyman, D.A., Yang, J.-H., Jiang, Z.-Q., Liu, Y., Gou, G.-N., Guo, H.-F., 2017. Subduction of Indian continent beneath southern Tibet in the latest Eocene (~35Ma): Insights from the Quguosha gabbros in southern Lhasa block. Gondwana Research, Tectonic evolution and dynamics of the Tibetan Plateau 41, 77–92. https://doi.org/10.1016/j.gr.2016.02.005
THB 11SR10-6	S.E. Lhasa			Quguosha gabbros	0.512436	3	-3.9	Ma et al., 2017		
THB 11SR10-7	S.E. Lhasa			Quguosha gabbros						
THB 09TB63	S.E. Lhasa			Quguosha gabbros	0.512476	4	-3.2	Ma et al., 2017		
THB 09TB64	S.E. Lhasa			Quguosha gabbros	0.512504	3	-2.6	Ma et al., 2017		
THB 11SR10-1	S.E. Lhasa			Quguosha gabbros	0.512493	3	-2.8	Ma et al., 2017		
THB 11SR10-4	S.E. Lhasa			Quguosha gabbros	0.512492	3	-2.8	Ma et al., 2017		

Table SII-2 (…/…)

Ech.#	Region	River	Locality	Formation	144Nd/142Nd	2s.d.	eNd(0)	Reference	Commer	Full reference
										Wang, Y.-F., Zeng, L., Gao, J., Zhao, L., Gao, L.-E., Shang, Z., 2019. Along-arc variations in isotope and trace element compositions of Paleogene gabbroic rocks in the Gangdese batholith, southern Tibet. Lithos 324–325, 877–892. https://doi.org/10.1016/j.lithos.2018.11.036
THB T0548	Nyingchi			E. Gangdese batholith	0.512472	7E-06	-3.2	Wang et al., 2019		
THB T0878-1	Nyingchi			E. Gangdese batholith	0.512444	6E-06	-3.8	Wang et al., 2019		
THB T0878-2	Nyingchi			E. Gangdese batholith	0.512453	1E-05	-3.6	Wang et al., 2019		
THB T0878-3	Nyingchi			E. Gangdese batholith	0.512467	7E-06	-3.3	Wang et al., 2019		
THB T0878-4	Nyingchi			E. Gangdese batholith	0.512441	7E-06	-3.8	Wang et al., 2019		
THB T0878-5	Nyingchi			E. Gangdese batholith	0.512431	9E-06	-4.0	Wang et al., 2019		
THB T0878-6	Nyingchi			E. Gangdese batholith	0.512438	1E-05	-3.9	Wang et al., 2019		
THB T0289	N.E. Lhasa			E. Gangdese batholith	0.512674	5E-06	0.7	Wang et al., 2019		
THB T0580-D2-	Nyingchi			E. Gangdese batholith	0.512406	8E-06	-4.5	Wang et al., 2019		
THB T0580-D2-	Nyingchi			E. Gangdese batholith	0.512418	1E-05	-4.3	Wang et al., 2019		
THB T0580-D2-	Nyingchi			E. Gangdese batholith	0.512486	7E-06	-3.0	Wang et al., 2019		
THB T0580-D1-	Nyingchi			E. Gangdese batholith	0.512593	5E-06	-0.9	Wang et al., 2019		
THB T0580-D1-	Nyingchi			E. Gangdese batholith	0.512651	7E-06	0.3	Wang et al., 2019		
THB T0580-D1-	Nyingchi			E. Gangdese batholith	0.512581	6E-06	-1.1	Wang et al., 2019		
THB T0580-14-	Nyingchi			E. Gangdese batholith	0.512449	6E-06	-3.7	Wang et al., 2019		
THB T0580-14-	Nyingchi			E. Gangdese batholith	0.512526	5E-06	-2.2	Wang et al., 2019		
THB T0580-14-(	Nyingchi			E. Gangdese batholith	0.51252	1E-05	-2.3	Wang et al., 2019		
THB T0580-14-(	Nyingchi			E. Gangdese batholith	0.512575	5E-06	-1.2	Wang et al., 2019		
THB T0580-14-(	Nyingchi			E. Gangdese batholith	0.512525	1E-05	-2.2	Wang et al., 2019		
THB T0580-14-(	Nyingchi			E. Gangdese batholith	0.512504	5E-06	-2.6	Wang et al., 2019		
THB T0934-13	Nyingchi			E. Gangdese batholith	0.512398	1E-05	-4.7	Wang et al., 2019		
THB T0934-14-	Nyingchi			E. Gangdese batholith	0.512555	1E-05	-1.6	Wang et al., 2019		
THB T0594-B1	Lhasa			C. Gangdese batholith	0.512896	9E-06	5.0	Wang et al., 2019		
THB T0594-B2	Lhasa			C. Gangdese batholith	0.512903	1E-05	5.2	Wang et al., 2019		
THB T0594-B3	Lhasa			C. Gangdese batholith	0.512918	2E-05	5.5	Wang et al., 2019		
THB T0594-B4	Lhasa			C. Gangdese batholith	0.512895	1E-05	5.0	Wang et al., 2019		
THB T0594-B5	Lhasa			C. Gangdese batholith	0.512933	6E-06	5.8	Wang et al., 2019		
THB T1031-NR	S.W. Lhasa			C. Gangdese batholith	0.512884	1E-05	4.8	Wang et al., 2019		
THB T1031-NR:	S.W. Lhasa			C. Gangdese batholith	0.512852	7E-06	4.2	Wang et al., 2019		
THB T1031-NR:	S.W. Lhasa			C. Gangdese batholith	0.512871	4E-06	4.5	Wang et al., 2019		
THB T1031-NR-	S.W. Lhasa			C. Gangdese batholith	0.512925	2E-05	5.6	Wang et al., 2019		
THB T1031-NR!	S.W. Lhasa			C. Gangdese batholith	0.512857	5E-06	4.3	Wang et al., 2019		
THB T1033-NR	S.W. Lhasa			C. Gangdese batholith	0.512865	7E-06	4.4	Wang et al., 2019		
THB T1033-NR:	S.W. Lhasa			C. Gangdese batholith	0.512891	6E-06	4.9	Wang et al., 2019		
THB T1034-GR	S.W. Lhasa			C. Gangdese batholith	0.512898	1E-05	5.1	Wang et al., 2019		
THB T1034-GR	S.W. Lhasa			C. Gangdese batholith	0.512805	7E-06	3.3	Wang et al., 2019		
THB T1034-GR	S.W. Lhasa			C. Gangdese batholith	0.512868	5E-06	4.5	Wang et al., 2019		
THB T1034-GR	S.W. Lhasa			C. Gangdese batholith	0.512795	1E-05	3.1	Wang et al., 2019		
THB T1034-GR	S.W. Lhasa			C. Gangdese batholith	0.512903	8E-06	5.2	Wang et al., 2019		
										Harrison, T.M., Grove, M., Lovera, O.M., Catlos, E.J., 1999. A unified model for the origin of Himalayan anatexis and inverted metamorphism, Main Central Thrust, Nepal Himalaya. Journal of Geophysical Research.
HHC DK89	C. Nepal		Larkya phase	Manaslu granite				Harrison et al., 1999		
HHC U315	C. Nepal		Larkya phase	Manaslu granite	0.511952		-13.4	Harrison et al., 1999		
HHC XG43	C. Nepal		Larkya phase	Manaslu granite				Harrison et al., 1999		
HHC XG46	C. Nepal		Larkya phase	Manaslu granite				Harrison et al., 1999		
HHC XG56	C. Nepal		Larkya phase	Manaslu granite	0.511952		-13.4	Harrison et al., 1999		
HHC XG102	C. Nepal		Larkya phase	Manaslu granite	0.511911		-14.2	Harrison et al., 1999		
HHC XG270	C. Nepal		Larkya phase	Manaslu granite				Harrison et al., 1999		
HHC XP130	C. Nepal		Larkya phase	Manaslu granite	0.511912		-14.2	Harrison et al., 1999		
HHC DK203	C. Nepal		Bimtang phase	Manaslu granite				Harrison et al., 1999		
HHC DK208	C. Nepal		Bimtang phase	Manaslu granite	0.511894		-14.5	Harrison et al., 1999		
HHC XG162	C. Nepal		Bimtang phase	Manaslu granite				Harrison et al., 1999		
HHC XL24	C. Nepal		Bimtang phase	Manaslu granite				Harrison et al., 1999		
										Inger, S., Harris, N., 1993. Geochemical Constraints on Leucogranite Magmatism in the Langtang Valley, Nepal Himalaya. Journal of Petrology 34, 345–368. https://doi.org/10.1093/petrology/34.2.345
HHC SKG8	E. Nepal			Langtang granite				Inger and Harris, 1993		
HHC SKG9	E. Nepal			Langtang granite				Inger and Harris, 1993		
HHC SKG12	E. Nepal			Langtang granite	0.5119		-14.4	Inger and Harris, 1993		
HHC SKG13	E. Nepal			Langtang granite				Inger and Harris, 1993		
HHC SKG15	E. Nepal			Langtang granite	0.51205		-11.5	Inger and Harris, 1993		
HHC SKG3	E. Nepal			Langtang granite				Inger and Harris, 1993		
HHC SKG4	E. Nepal			Langtang granite				Inger and Harris, 1993		
HHC KG211	E. Nepal			Langtang granite				Inger and Harris, 1993		
HHC KG208	E. Nepal			Langtang granite	0.51174		-17.5	Inger and Harris, 1993		
HHC KG210	E. Nepal			Langtang granite				Inger and Harris, 1993		
HHC KG214	E. Nepal			Langtang granite	0.51183		-15.8	Inger and Harris, 1993		
HHC KG215	E. Nepal			Langtang granite				Inger and Harris, 1993		

Table SII-2 (…/…)

Ech.#	Region	River	Locality	Formation	144Nd/142Nd	2s.d.	eNd(0)	Reference	Commer	Full reference
HHCSLM1	E. Nepal			Langtang metamorphic				Inger and Harris, 1993		
HHCLM201	E. Nepal			Langtang metamorphic				Inger and Harris, 1993		
HHCSKM2	E. Nepal			Langtang metamorphic				Inger and Harris, 1993		
HHCSKM3	E. Nepal			Langtang metamorphic				Inger and Harris, 1993		
HHCLM207	E. Nepal			Langtang metamorphic	0.51187		-15.0	Inger and Harris, 1993		
HHCLM209	E. Nepal			Langtang metamorphic				Inger and Harris, 1993		
HHCLM211	E. Nepal			Langtang metamorphic				Inger and Harris, 1993		
HHCSM201	E. Nepal			Langtang metamorphic				Inger and Harris, 1993		
HHCSM203	E. Nepal			Langtang metamorphic				Inger and Harris, 1993		
HHCSM202	E. Nepal			Langtang metamorphic	0.51252		-2.3	Inger and Harris, 1993		
HHCSM206	E. Nepal			Langtang metamorphic	0.51192		-14.0	Inger and Harris, 1993		
HHCSSM6	E. Nepal			Langtang metamorphic	0.51195		-13.4	Inger and Harris, 1993		
HHCRM201	E. Nepal			Langtang metamorphic				Inger and Harris, 1993		
HHCSNM2	E. Nepal			Langtang metamorphic				Inger and Harris, 1993		
HHCNM203	E. Nepal			Langtang metamorphic				Inger and Harris, 1993		
										Gao, Y., Wei, R., Hou, Z., Tian, S., Zhao, R., 2008. Eocene high-MgO volcanism in southern Tibet: New constraints for mantle source characteristics and deep processes. Lithos 105, 63–72. https://doi.org/10.1016/j.lithos.2008.02.008
THB LKA-01	Lhasa			Dazi volcanics	0.512883	13	4.8	Gao et al., 2008		
THB LKA-02	Lhasa			Dazi volcanics				Gao et al., 2008		
THB LKA-03	Lhasa			Dazi volcanics				Gao et al., 2008		
THB LKA-04	Lhasa			Dazi volcanics	0.512826	13	3.7	Gao et al., 2008		
THB LKA-05	Lhasa			Dazi volcanics	0.512886	11	4.8	Gao et al., 2008		
THB LKA-06	Lhasa			Dazi volcanics				Gao et al., 2008		
THB LKA-07	Lhasa			Dazi volcanics	0.512911	13	5.3	Gao et al., 2008		
THB LKA-08	Lhasa			Dazi volcanics				Gao et al., 2008		
THB LKA-09	Lhasa			Dazi volcanics				Gao et al., 2008		
THB LKA-11	Lhasa			Dazi volcanics	0.512871	13	4.5	Gao et al., 2008		
THB LKA-12	Lhasa			Dazi volcanics	0.512854	12	4.2	Gao et al., 2008		
THB LKA-13	Lhasa			Dazi volcanics	0.512856	13	4.3	Gao et al., 2008		
THB LKA-14	Lhasa			Dazi volcanics	0.512854	11	4.2	Gao et al., 2008		
THB LKA-15	Lhasa			Dazi volcanics	0.512892	12	5.0	Gao et al., 2008		
THB LKA-16	Lhasa			Dazi volcanics	0.512887	11	4.9	Gao et al., 2008		
THB LKA-17	Lhasa			Dazi volcanics	0.512886	12	4.8	Gao et al., 2008		
THB LKA-19	Lhasa			Dazi volcanics				Gao et al., 2008		
THB L012	Lhasa			Dazi volcanics	0.512885	10	4.8	Gao et al., 2008		
THB L014	Lhasa			Dazi volcanics	0.512884	10	4.8	Gao et al., 2008		
										Pan, F.-B., Zhang, H.-F., Xu, W.-C., Guo, L., Luo, B.-J., Wang, S., 2016. U–Pb zircon dating, geochemical and Sr–Nd–Hf isotopic compositions of Motuo quartz–monzonite: Implication for the genesis and diversity of the high Ba–Sr granitoids in orogenic belt. Tectonophysics 668–669, 52–64. https://doi.org/10.1016/j.tecto.2015.12.007
THB T993	E. syntax	S.E. Namche	on Siang	Motuo	0.512677	9E-06	0.8	Pan et al., 2016		
THB T998	E. syntax	S.E. Namche	on Siang	Motuo				Pan et al., 2016		
THB T1000	E. syntax	S.E. Namche	on Siang	Motuo	0.512466	6E-06	-3.4	Pan et al., 2016		
THB T1008	E. syntax	S.E. Namche	on Siang	Motuo	0.512477	3E-06	-3.1	Pan et al., 2016		
THB T1009	E. syntax	S.E. Namche	on Siang	Motuo				Pan et al., 2016		
THB T1016	E. syntax	S.E. Namche	on Siang	Motuo	0.512456	4E-06	-3.6	Pan et al., 2016		
THB T1017	E. syntax	S.E. Namche	on Siang	Motuo	0.512497	5E-06	-2.8	Pan et al., 2016		
THB T1220	E. syntax	N.E. Namche	barwa, close Dibang	52K	0.512431	3E-06	-4.0	Pan et al., 2016		
THB T1222	E. syntax	N.E. Namche	barwa, close Dibang	52K				Pan et al., 2016		
THB T1224	E. syntax	N.E. Namche	barwa, close Dibang	52K	0.512437	2E-06	-3.9	Pan et al., 2016		
										Pan, F.-B., Zhang, H.-F., Xu, W.-C., Guo, L., Luo, B.-J., Wang, S., 2016. U–Pb zircon dating, geochemical and Sr–Nd–Hf isotopic compositions of mafic intrusive rocks in the Motuo, SE Tibet constrain on their petrogenesis and tectonic implication. Lithos, Recent advances on the tectonic and magmatic evolution of the Greater Tibetan Plateau: A Special Issue in Honor of Prof. Guitang Pan 245, 133–146. https://doi.org/10.1016/j.lithos.2015.05.011
THB T699	E. syntax	S.E. Namche	on Siang	Damu	0.512391	3E-06	-4.8	Pan et al., 2016b		
THB T700	E. syntax	S.E. Namche	on Siang	Damu	0.512431	3E-06	-4.0	Pan et al., 2016b		
THB T1019	E. syntax	S.E. Namche	on Siang	Damu				Pan et al., 2016b		
THB T1020	E. syntax	S.E. Namche	on Siang	Damu				Pan et al., 2016b		
THB T829	E. syntax	N.E. Namche	barwa, close Dibang	52 K	0.512404	2E-06	-4.6	Pan et al., 2016b		
THB T836	E. syntax	N.E. Namche	barwa, close Dibang	52 K	0.512389	4E-06	-4.9	Pan et al., 2016b		
THB T1223	E. syntax	N.E. Namche	barwa, close Dibang	52 K				Pan et al., 2016b		
THB T1225	E. syntax	N.E. Namche	barwa, close Dibang	52 K				Pan et al., 2016b		
THB T1226	E. syntax	N.E. Namche	barwa, close Dibang	52 K				Pan et al., 2016b		
										Zhu, D.-C., Pan, G.-T., Chung, S.-L., Liao, Z.-L., Wang, L.-Q., Li, G.-M., 2008. SHRIMP Zircon Age and Geochemical Constraints on the Origin of Lower Jurassic Volcanic Rocks from the Yeba Formation, Southern Gangdese, South Tibet. International Geology Review 50, 442–471. https://doi.org/10.2747/0020-6814.50.5.442
THB BD01	E. Lhasa		S. Gangdese	Yeba fm	0.512699	10	1.2	Zhu et al., 2008		
THB BD21	E. Lhasa		S. Gangdese	Yeba fm	0.512718	12	1.6	Zhu et al., 2008		

Table SII-2 (…/…)

Ech.#	Region	River	Locality	Formation	144Nd/142Nd	2s.d.	eNd(0)	Reference	Commer	Full reference
THB DZ13-1	E. Lhasa		S. Gangdese	Yeba fm	0.512748	13	2.1	Zhu et al., 2008		
THB DZ07-2	E. Lhasa		S. Gangdese	Yeba fm	0.512767	10	2.5	Zhu et al., 2008		
THB BD04	E. Lhasa		S. Gangdese	Yeba fm	0.512723	12	1.7	Zhu et al., 2008		
THB BD13	E. Lhasa		S. Gangdese	Yeba fm	0.512789	11	2.9	Zhu et al., 2008		
THB BD16	E. Lhasa		S. Gangdese	Yeba fm	0.512708	13	1.4	Zhu et al., 2008		
THB YB5-2	E. Lhasa		S. Gangdese	Yeba fm	0.512767	12	2.5	Zhu et al., 2008		
THB YB5-3	E. Lhasa		S. Gangdese	Yeba fm	0.512773	11	2.6	Zhu et al., 2008		
THB DZ09-1	E. Lhasa		S. Gangdese	Yeba fm	0.512719	11	1.6	Zhu et al., 2008		
THB DZ11-1	E. Lhasa		S. Gangdese	Yeba fm	0.512707	12	1.3	Zhu et al., 2008		
THB BD19	E. Lhasa		S. Gangdese	Yeba fm	0.512687	11	1.0	Zhu et al., 2008		
THB YB5-1	E. Lhasa		S. Gangdese	Yeba fm	0.5128	12	3.2	Zhu et al., 2008		
THB DZ01-2	E. Lhasa		S. Gangdese	Yeba fm	0.512693	13	1.1	Zhu et al., 2008		
THB DZ02-1	E. Lhasa		S. Gangdese	Yeba fm						
THB DZ03-1	E. Lhasa		S. Gangdese	Yeba fm	0.51272	12	1.6	Zhu et al., 2008		
THB DZ03-2	E. Lhasa		S. Gangdese	Yeba fm	0.512643	10	0.1	Zhu et al., 2008		
THB DZ05-1	E. Lhasa		S. Gangdese	Yeba fm	0.512627	11	-0.2	Zhu et al., 2008		
THB DZ07-4	E. Lhasa		S. Gangdese	Yeba fm	0.512566	12	-1.4	Zhu et al., 2008		
										Zhang, H., Harris, N., Guo, L., Xu, W., 2010. The significance of Cenozoic magmatism from the western margin of the eastern syntaxis, southeast Tibet. Contrib Mineral Petrol 160, 83–98. https://doi.org/10.1007/s00410-009-0467-5
THB T519	E. Synta	W. Namche	Nyingchi	Bayi granite	0.512416	2E-06	-4.3	Zhang et al., 2010		
THB T520	E. Synta	W. Namche	Nyingchi	Bayi granite	0.512416	4E-06	-4.3	Zhang et al., 2010		
THB T521	E. Synta	W. Namche	Nyingchi	Bayi granite	0.512426	3E-06	-4.1	Zhang et al., 2010		
THB T522	E. Synta	W. Namche	Nyingchi	Bayi granite	0.512415	6E-06	-4.4	Zhang et al., 2010		
THB T523	E. Synta	W. Namche	Nyingchi	Bayi granite	0.512412	3E-06	-4.4	Zhang et al., 2010		
THB T524	E. Synta	W. Namche	Nyingchi	Bayi granite	0.512412	3E-06	-4.4	Zhang et al., 2010		
THB T634	E. Synta	W. Namche	Nyingchi	Lunan granodiorite	0.512459	1E-06	-3.5	Zhang et al., 2010		
THB T636	E. Synta	W. Namche	Nyingchi	Lunan granodiorite	0.512375	1E-06	-5.1	Zhang et al., 2010		
THB T637	E. Synta	W. Namche	Nyingchi	Lunan granodiorite	0.512484	3E-06	-3.0	Zhang et al., 2010		
THB T638	E. Synta	W. Namche	Nyingchi	Lunan granodiorite	0.512456	2E-06	-3.6	Zhang et al., 2010		
THB T529	E. Synta	W. Namche	Nyingchi	Confluence granite	0.512405	3E-06	-4.5	Zhang et al., 2010		
THB T525	E. Synta	W. Namche	Nyingchi	Nyingchi gneiss	0.51193	4E-06	-13.8	Zhang et al., 2010		
THB T527	E. Synta	W. Namche	Nyingchi	Nyingchi gneiss	0.512033	4E-06	-11.8	Zhang et al., 2010		
THB T528	E. Synta	W. Namche	Nyingchi	Nyingchi gneiss	0.511851	5E-06	-15.4	Zhang et al., 2010		
HHC T600	E. Synta	W. Namche	Nyingchi	Zhibai gneiss	0.512102	2E-06	-10.5	Zhang et al., 2010		
HHC T602	E. Synta	W. Namche	Nyingchi	Zhibai gneiss	0.511958	2E-06	-13.3	Zhang et al., 2010		
HHC T603	E. Synta	W. Namche	Nyingchi	Zhibai gneiss	0.511822	1E-06	-15.9	Zhang et al., 2010		
HHC T617	E. Synta	W. Namche	Nyingchi	Zhibai gneiss	0.511701	2E-06	-18.3	Zhang et al., 2010		
HHC T618	E. Synta	W. Namche	Nyingchi	Zhibai gneiss	0.511926	2E-06	-13.9	Zhang et al., 2010		
HHC T611	E. Synta	W. Namche	Nyingchi	Duoxiongla migmatite	0.511729	1E-06	-17.7	Zhang et al., 2010		
HHC T612	E. Synta	W. Namche	Nyingchi	Duoxiongla migmatite	0.511731	5E-06	-17.7	Zhang et al., 2010		
HHC T613	E. Synta	W. Namche	Nyingchi	Duoxiongla migmatite	0.511805	1E-06	-16.2	Zhang et al., 2010		
HHC T614	E. Synta	W. Namche	Nyingchi	Duoxiongla migmatite	0.511599	1E-06	-20.3	Zhang et al., 2010		
HHC T616	E. Synta	W. Namche	Nyingchi	Duoxiongla migmatite	0.511755	1E-06	-17.2	Zhang et al., 2010		
THB T684	E. Synta	S.E. Namche	Barwa	Beibeng granite	0.512425	3E-06	-4.2	Pan et al., 2012		
THB T686	E. Synta	S.E. Namche	Barwa	Beibeng granite	0.512412	1E-05	-4.4	Pan et al., 2012		
THB T690	E. Synta	S.E. Namche	Barwa	Beibeng granite	0.512506	4E-06	-2.6	Pan et al., 2012		
THB T692	E. Synta	S.E. Namche	Barwa	Beibeng granite	0.512517	3E-06	-2.4	Pan et al., 2012		
THB T697	E. Synta	S.E. Namche	Barwa	Damu granite	0.512313	2E-06	-6.3	Pan et al., 2012		
THB T698	E. Synta	S.E. Namche	Barwa	Damu granite	0.512205	4E-06	-8.4	Pan et al., 2012		
THB T1018	E. Synta	S.E. Namche	Barwa	Damu granite	0.512159	4E-06	-9.3	Pan et al., 2012		
THB T866	E. Synta	N.E. Namche	Barwa	Bomi granite	0.512018	3E-06	-12.1	Pan et al., 2012		
THB T1037	E. Synta	E. Namche	Barwa	Bolonggong granite	0.512467	7E-06	-3.3	Pan et al., 2012		
THB T1038	E. Synta	E. Namche	Barwa	Bolonggong granite	0.512697	6E-06	1.2	Pan et al., 2012		
THB T1041	E. Synta	E. Namche	Barwa	Bolonggong granite	0.512582	6E-06	-1.1	Pan et al., 2012		
THB T1043	E. Synta	E. Namche	Barwa	Bolonggong granite	0.51251	4E-06	-2.5	Pan et al., 2012		
THB T1059	E. Synta	E. Namche	Barwa	Bolonggong granite	0.512544	6E-06	-1.8	Pan et al., 2012		
THB T1061	E. Synta	E. Namche	Barwa	Bolonggong granite	0.512397	7E-06	-4.7	Pan et al., 2012		
TSS/ T856	E. Syntaxis			Bomi Group (metam)	0.511879	2E-06	-14.8	Pan et al., 2012		
TSS/ T865	E. Syntaxis			Bomi Group (metam)	0.511714	1E-06	-18.0	Pan et al., 2012		
TSS/ T867	E. Syntaxis			Bomi Group (metam)	0.511705	2E-06	-18.2	Pan et al., 2012		
TSS/ T837	E. Syntaxis			Bomi Group (metam)	0.512102	4E-06	-10.5	Pan et al., 2012		
										Liu, Y., Siebel, W., Theye, T., Massonne, H.-J., 2011. Isotopic and structural constraints on the late Miocene to Pliocene evolution of the Namche Barwa area, eastern Himalayan syntaxis, SE Tibet. Gondwana Research 19, 894–909. https://doi.org/10.1016/j.gr.2010.11.005
HHC 111920	E. Synta	W. Namche	Qiangna	Dongjiu S.	0.511741	10	-17.5	Liu et al., 20	concentr	
HHC 112101	E. Synta	W. Namche	Laiguo	Laiguo S.	0.51234	8	-5.8	Liu et al., 2011		
HHC 112102	E. Synta	W. Namche	Barwa, on Yarlung Tsangbo	Laiguo S.	0.511642	7	-19.4	Liu et al., 2011		
HHC 112104	E. Synta	W. Namche	Barwa, on Yarlung Tsangbo	Laiguo S.	0.511826	7	-15.8	Liu et al., 2011		

Table SII-2 (…/…)

	Ech.#	Region	River	Locality	Formation	144Nd/142Nd	2s.d.	eNd(0)	Reference	Commer	Full reference
HHC	112107	E. Synta	W. Namche	Laiguo section	Laiguo S.	0.511766	10	-17.0	Liu et al., 2011		
HHC	112108	E. Synta	W. Namche	Barwa, on Yarlung Tsangbo	Laiguo S.	0.511701	10	-18.3	Liu et al., 2011		
HHC	112113	E. Synta	W. Namche	Barwa, on Yarlung Tsangbo	Pei S.	0.511822	10	-15.9	Liu et al., 2011		
HHC	112115	E. Synta	W. Namche	Barwa, on Yarlung Tsangbo	Pei S.	0.511835	9	-15.7	Liu et al., 2011		
HHC	112120	E. Synta	W. Namche	Barwa, on Yarlung Tsangbo	Pei S.	0.511747	10	-17.4	Liu et al., 2011		
HHC	112125	E. Synta	W. Namche	Barwa, on Yarlung Tsangbo	Namche Barwa S.	0.511654	8	-19.2	Liu et al., 2011		
HHC	112201	E. Synta	W. Namche	Baga	Namche Barwa S.	0.511817	9	-16.0	Liu et al., 2011		
HHC	112202	E. Synta	W. Namche	Barwa, on Yarlung Tsangbo	Namche Barwa S.	0.51185	9	-15.4	Liu et al., 2011		
HHC	112203	E. Synta	W. Namche	Barwa, on Yarlung Tsangbo	Namche Barwa S.	0.511986	10	-12.7	Liu et al., 2011		
HHC	112204	E. Synta	W. Namche	Barwa, on Yarlung Tsangbo	Namche Barwa S.	0.511806	8	-16.2	Liu et al., 2011		
HHC	112301	E. Synta	W. Namche	S. Baga	Pei S.	0.511741	10	-17.5	Liu et al., 2011		
HHC	112302	E. Synta	W. Namche	Barwa, on Yarlung Tsangbo	Pei S.	0.511718	10	-17.9	Liu et al., 2011		
HHC	112303	E. Synta	W. Namche	Barwa, on Yarlung Tsangbo	Pei S.	0.51245	9	-3.7	Liu et al., 2011		
HHC	112402	E. Synta	W. Namche	W. Luxia	Dongjiu S.	0.511588	10	-20.5	Liu et al., 2011		
HHC	112404	E. Synta	W. Namche	E. Deyiang	Pei S.	0.511707	10	-18.2	Liu et al., 2011		
HHC	112601	E. Synta	W. Namche	S. Layue	Namche Barwa S.	0.511812	9	-16.1	Liu et al., 2011		
LH	KR38	Garhwal	Chandpur	30.2°N 79-80°E	Outer LH	0.511713	8E-06	-18.0	Ahmad et al., 2000		Ahmad, T., Harris, N., Bickle, M., Chapman, H., Bunbury, J., Prince, C., 2000. Isotopic constraints on the structural relationships between the Lesser Himalayan Series and the High Himalayan Crystalline Series, Garhwal Himalaya. Geological Society of America Bulletin 112, 467–477. https://doi.org/10.1130/0016-7606(2000)112<467:ICOTSR>2.0.CO;2
LH	KR40	Garhwal	Chandpur	30.2°N 79-80°E	Outer LH	0.511709	6E-06	-18.1	Ahmad et al., 2000		
LH	KR41	Garhwal	Chandpur	30.2°N 79-80°E	Outer LH	0.511723	1E-05	-17.8	Ahmad et al., 2000		
LH	KR44	Garhwal	Chandpur	30.2°N 79-80°E	Outer LH	0.511713	2E-05	-18.0	Ahmad et al., 2000		
LH	KR50	Garhwal	Chandpur	30.2°N 79-80°E	Outer LH	0.511768	9E-06	-17.0	Ahmad et al., 2000		
LH	KR146	Garhwal	Chandpur	30.2°N 79-80°E	Outer LH	0.511702	9E-06	-18.3	Ahmad et al., 2000		
LH	KR1	Garhwal	Deoban	30.2°N 79-80°E	Inner LH	0.511378	9E-06	-24.6	Ahmad et al., 2000		
LH	KR4	Garhwal	Deoban	30.2°N 79-80°E	Inner LH	0.511357	6E-06	-25.0	Ahmad et al., 2000		
LH	KR85	Garhwal	Berinag	30.2°N 79-80°E	Inner LH	0.511575	1E-05	-20.7	Ahmad et al., 2000		
LH	KR102	Garhwal	Deoban	30.2°N 79-80°E	Inner LH	0.511563	2E-05	-21.0	Ahmad et al., 2000		
LH	KR106	Garhwal	Berinag	30.2°N 79-80°E	Inner LH	0.511342	6E-06	-25.3	Ahmad et al., 2000		
LH	KR132	Garhwal	Berinag	30.2°N 79-80°E	Inner LH	0.511676	2E-05	-18.8	Ahmad et al., 2000		
LH?	KR52	Garhwal	Ramgarh	30.2°N 79-80°E	Ramgarh group	0.511382	8E-06	-24.5	Ahmad et al., 2000		
LH?	KR57	Garhwal	Ramgarh	30.2°N 79-80°E	Ramgarh group	0.511394	2E-05	-24.3	Ahmad et al., 2000		
LH?	KR82	Garhwal	Munsiari	30.2°N 79-80°E	Munsiari goup	0.511466	6E-06	-22.9	Ahmad et al., 2000		
LH?	KR113	Garhwal	Munsiari	30.2°N 79-80°E	Munsiari goup	0.511367	1E-05	-24.8	Ahmad et al., 2000		
LH?	KR122	Garhwal	Munsiari	30.2°N 79-80°E	Munsiari goup	0.511218	8E-06	-27.7	Ahmad et al., 2000		
LH?	KR124	Garhwal	Munsiari	30.2°N 79-80°E	Munsiari goup	0.511319	1E-05	-25.7	Ahmad et al., 2000		
LH?	KR126	Garhwal	Munsiari	30.2°N 79-80°E	Munsiari goup	0.511328	1E-05	-25.6	Ahmad et al., 2000		
LH?	KR128	Garhwal	Munsiari	30.2°N 79-80°E	Munsiari goup	0.511392	1E-05	-24.3	Ahmad et al., 2000		
LH?	KR130	Garhwal	Munsiari	30.2°N 79-80°E	Munsiari goup	0.511444	8E-06	-23.3	Ahmad et al., 2000		
LH?	KR134	Garhwal	Munsiari	30.2°N 79-80°E	Munsiari goup	0.511402	1E-05	-24.1	Ahmad et al., 2000		
HHC	C42/97	Garhwal	uncertain	30.2°N 79-80°E	Vaikrita thrust	0.512066	8E-06	-11.2	Ahmad et al., 2000		
HHC	C4B	Garhwal	Vaikrita	30.2°N 79-80°E	Vaikrita group	0.51186	5E-06	-15.2	Ahmad et al., 2000		
HHC	C7	Garhwal	Vaikrita	30.2°N 79-80°E	Vaikrita group	0.511754	8E-06	-17.2	Ahmad et al., 2000		
HHC	C200	Garhwal	Vaikrita	30.2°N 79-80°E	Vaikrita group	0.511675	8E-06	-18.8	Ahmad et al., 2000		
HHC	C230	Garhwal	Vaikrita	30.2°N 79-80°E	Vaikrita group	0.511924	9E-06	-13.9	Ahmad et al., 2000		
HHC	C235	Garhwal	Vaikrita	30.2°N 79-80°E	Vaikrita group	0.511702	1E-05	-18.3	Ahmad et al., 2000		
HHC	C34/97	Garhwal	Vaikrita	30.2°N 79-80°E	Vaikrita group	0.5117	8E-06	-18.3	Ahmad et al., 2000		
HHC	KR116	Garhwal	Vaikrita	30.2°N 79-80°E	Vaikrita group	0.511892	1E-05	-14.6	Ahmad et al., 2000		
HHC	KR118	Garhwal	Vaikrita	30.2°N 79-80°E	Vaikrita group	0.511857	1E-05	-15.2	Ahmad et al., 2000		
HHC	KR120	Garhwal	Vaikrita	30.2°N 79-80°E	Vaikrita group	0.511884	1E-05	-14.7	Ahmad et al., 2000		
HHC	KR143	Garhwal	Vaikrita	30.2°N 79-80°E	Vaikrita group	0.51167	1E-05	-18.9	Ahmad et al., 2000		
TSS	C29/97	Garhwal	TSS	30.2°N 79-80°E	TSS	0.511944	8E-06	-13.5	Ahmad et al., 2000		

Table SII-3. Compilation of accumulation rate and sedimentary budgets.
Not
exhaustive
Table SII-3 (…/…)

Latitudes	Location		Catchment	Type of basin	Start of acceleration	Amplitude of acceleration	Impact of glaciations	Tectonic deformation	Comments	References
Mid-latitudes	New Zealand	Bounty fan	Southern Alps	Active margin	ca. 3 Ma	massive	Major	Active tectonics. Debated impact	Negligible accumulation before 3 Ma Erosion / uplift steady state (discussion in Molnar and England, 1990) Acceleration in the relative tectonic plate movements since 4 Ma (Lamb, 2011, Fig. 20) See further comments in Jiao et al., 2017	Adams, 1980; Carter and Carter, 1996
High-latitudes	Norway	extended Vøring margin	Scandinavia	Passive margin	ca. 2.7 Ma	massive	Major	Isostatic deformation and flexure due to sediment mass	3-fold increase of rates since 0.6 Ma Regular drainage reorganisation during the last glacial periods with eastward migration of the drainage divide for the Scandinavian ice-sheet	e.g. Hjelstuen et al. ,1999; Rise et al., 2005; Dowdeswell et al., 2010
Mid-latitudes	South US	NW Gulf of Mexico	Mississipi	Passive margin	ca. 2 Ma	x 3	Potentially important	Debated	Most of sediments non glacial (Hay et al., 1989) Monsoonal climate since 4-5 Ma (e.g. Galloway et al., 2011) Basin and Range active tectonics in the Miocene Regular drainage reorganisation (Galloway et al., 2011), with northward migration of the North American divide during the last glacial periods, with the connection of the Mississipi to the Laurentide ice-sheet partly 3-D sedimentary budgets.	Hay et al., 1989; Galloway et al., 2011
Mid-latitudes	North Sea		Northern Europe	Passive margin	ca. 2.6 Ma	x 10	Major	Isostatic deformation Flexure caused by weight of sediments	Pulse of sedimentation probably controlled by accomodation. Crustal movements at 4.5-6.5 Ma with acceleration of subsidence in the Central part of the basin and deceleration at the edges (e.g. Joy, 1992; discussion in Overeem et al., 2001). Scandinavian component since the early Miocene. Regular variations of provenance, probably linked to the increase and decrease of the Scandinavian ice-sheet (Sm/Nd isotopes, Kuhlmann et al., 2004). Increase followed by x2 decrease from 1.8 Ma onwards (Anell et al., 2010), and limited accumulation since 1 Ma, because of lack of accomodation (Ottesen et al., 2018)	Overeem et al., 2001; Huuse, 2003; Anell et al., 2010

Table SII-3 (…/…)

Latitudes	Location		Catchment	Type of basin	Start of acceleration	Amplitude of acceleration	Impact of glaciations	Tectonic deformation	Comments	References
Low-latitudes	Amazon	Amazon fan	Amazon basin and Andes	Passive margin	ca. 2.4 Ma	x 4	None	Undiscussed	Onset of the fan at 12-7 Ma (Figueiredo et al., 2009) 6-fold increase of accumulation rates between 7 and 2.4 Ma Accumulation rates computed from public and non-public data Holes dominantly drilled at the fan periphery	Dobson et al., 2001; Harris and Mix, 2002; Figueiredo et al., 2009
Low-latitudes	Bengal bay	Bengal fan	Himalaya, India	Passive margin	ca. 5 Ma	x 1.8	None	Deformation linked to mass of sediments (REF) Active thrusting along the Sunda trench and Indo-Burman range since 2 Ma (Maurin and Rangin, 2009)	Acceleration not demonstrated by other workers (Curray, 1994; Einsele et al., 1996; discussion in Zhang et al., 2001; Molnar, 2004) No inclusion of the Nicobar fan sedimentary record, originating from the same area, which shows a rapid deceleration of accumulation rates since 2 Ma (McNeill et al., 2017)	Métivier et al., 1999
Mid-latitudes	Central Asia, Tibet	Tianshan, Junggar and Tarim basin		Endorrheic foreland basins	ca. 5-3 Ma	x 4 - > 10	Negligible?	Active tectonics Impact debated (e.g. Charreau et al., 2008, 2009)	Unaffected by sea-level. Almost all records show very low accumulation rates at 5-40 Ma Start of acceleration coeval with a prograding gravel wedge, which as been shown to be diachronous across the region (starts at ca. 15 to ca. 0.7 Ma, Xiyu formation, Charreau et al., 2009, Lu et al., 2010). In addition, magnetic studies show constant accumulation rates since ca 10 Ma (Charreau et al., 2005, 2006, 2009) Other magnetic studies show local decrease of accumulation rates, caused by tectonics (e.g. Chang et al., 2014) A study limited to the last 300 kyrs showed very low accumulation rates, which only fluctuate with shift of drainage linked to glacial/interglacial periods (Guerit et al., 2016)	Métivier and Gaudemer, 1997; compilation of Zhang et al., 2001
Mid-latitudes	Southern Europe		E. Alps	Foreland basins and passive margins	ca. 3-4 Ma	x 2 - 2.5	Major	Debated	Acceleration in the Black Sea, Po basin and Rhine and North Sea. Deceleration in the Pannonian basin	Kuhlemann et al., 2001, 2002
Mid-latitudes	Southern Europe		W. Alps	Foreland basins and passive margins	ca. 5-6 Ma	x 3	Major	Debated	Acceleration in the Rhône fan, Adriatic sea and North Sea. Stable accumulation at 14-5 Ma Note the Messinian crisis at 7.2 - 5.3 Ma Absence of convergence between Adriatic and European plates in modern times (Calais et al., 2002)	Kuhlemann et al., 2002

Table SII-3 (…/…)

Latitudes	Location		Catchment	Type of basin	Start of acceleration	Amplitude of acceleration	Impact of glaciations	Tectonic deformation	Comments	References
Low-latitudes	South Bolivia	Subandean foothills	Central Andes	Foreland basins	ca. 2 Ma	x 2	Potentially not negligible	Active tectonics	Unaffected by sea-level. Low accumulation rates at 6-2 Ma. Aridity?	Uba et al., 2007
Low-latitudes	SE Africa	Zambezi delta	Zambezi	Passive margin	ca. 3 Ma	x 1.5 - 2	Negligible	Debated	Sedimentation yield stay steady. Hypothesis of a subcatchment capture	Walford et al., 2005
Low-latitudes	W. Africa	Zaire	Congo-Zaire	Passive margin	ca. 2 Ma	x 2	None		Shift of depocenters along the Angola-Congo margin	Lavier et al., 2001; Ferry et al., 2004; review in Savoye et al., 2009
Low-latitudes	S. China	Red river delta	S. China	Passive margin	ca. 5.5 Ma	x 2	Possible?	Yes	This acceleration follows a 2-fold deceleration of accumulation at 12.5 Ma and an increase of subsidence caused by tectonics at 5.5 Ma	Clift, 2006; Lei et al., 2015
Low-latitudes	S. China	Pearl river delta	S. China	Passive margin	ca. 5 Ma	x 1.4	Negligible?	None	This acceleration follow a 2.5-fold deceleration of accumulation at 12-5 Ma. Provenance of sediments at one site was later defined as Taiwaneses from 3 Ma onwards (Wan et al., 2010)	Clift, 2006
Low-latitudes	India/Pakistan	Indus fan	W. Himalaya	Passive margin	ca. 2 Ma	x 2	Potentially not negligible	Active tectonics	This acceleration follow a 2-fold deceleration of accumulation at 15-2 Ma	Clift and Gaedicke, 2002; Clift et al., 2002; Clift, 2006
Latitudes	Location			Type of basin					Comments	References
Low-latitudes	North Borneo	South China sea margin	North Borneo	Passive margin		None	None	Active tectonics	Tectonic, climatic and accumulation steady-state since the middle Miocene (ca. 14 Ma) Very high erosion and weathering rates Island surrounded by deep basins, no foreland basin No thin skinned thrusting	Hall and Nichols, 2002; Morley and Back, 2008

Table SII-3 (…/…)

Latitudes	Location		Catchment	Type of basin	Start of acceleration	Amplitude of acceleration	Impact of glaciations	Tectonic deformation	Comments	References
Low-latitudes	West Africa	Niger delta	Niger	Passive margin		None	None	None	Potential deceleration at ca. 1.8 Ma, after an acceleration at 15-1.8 Ma. Very low denudation rates 0.007 mm/yr Source to sink budgets Limited resolution Use of non public data.	Grimaud et al., 2018
Low-latitudes	India	Ganga basin	Central Himalaya	Foreland basin		None	None	Active tectonics	Burbank et al., 1992 hypothesizes a bypass of sedimentation caused by a reduction of accommodation space linked to the flexure on the Indian plate	Métivier et al., 1999
Low-latitudes	SE Asia	Gulf of Thailand	Thailand	Passive margin?		None	None	Active tectonics	Deceleration at ca. 12 Ma linked to potential decrease of accomodation space and shrinking of catchment	Métivier et al., 1999; Clift, 2006
Low-latitudes	SE Asia	Mekong delta	Thailand and Laos, with part of Tibet	Passive margin		Possible	Negligible?	Active tectonics	Potential deceleration at ca. 4 Ma and re-acceleration at 2 Ma. Taking into account uncertainties, rather steady accumulation since 8 Ma	Métivier et al., 1999; Clift, 2006

Table SII-3 (…/…)

Latitudes	Location		Full References
Mid-latitudes	New Zealand	Bounty fan	Carter, R.M., Carter, L., 1996. The abyssal bounty fan and lower Bounty Channel: evolution of a rifted-margin sedimentary system. Marine Geology 130, 181–202. https://doi.org/10.1016/0025-3227(95)00139-5 Adams, J., 1980. Contemporary uplift and erosion of the Southern Alps, New Zealand. Geological Society of America Bulletin 91, 1–114. https://doi.org/10.1130/gsab-p2-91-1 Dowdeswell, J.A., Ottesen, D., Rise, L., 2010. Rates of sediment delivery from the Fennoscandian Ice Sheet through an ice age. Geology 38, 3–6. https://doi.org/10.1130/G25523.1 Rise, L., Ottesen, D., Berg, K., Lundin, E., 2005. Large-scale development of the mid-Norwegian margin during the last 3 million years. Marine and Petroleum Geology 22, 33–44. https://doi.org/10.1016/j.marpetgeo.2004.10.010
High-latitudes	Norway	extended Vøring margin	Hjelstuen, B.O., Eldholm, O., Skogseid, J., 1999. Cenozoic evolution of the northern Vøring margin. Geological Society of America Bulletin 111, 1792–1807. https://doi.org/10.1130/0016-7606(1999)111<1792:CEOTNV>2.3.CO;2
Mid-latitudes	South US	NW Gulf of Mexico	Galloway, W.E., Whiteaker, T.L., Ganey-Curry, P., 2011. History of Cenozoic North American drainage basin evolution, sediment yield, and accumulation in the Gulf of Mexico basin. Geosphere 7, 938–973. https://doi.org/10.1130/GES00647.1 Hay, W.W., Shaw, C.A., Wold, C.N., 1989. Mass-balanced paleogeographic reconstructions. Geologische Rundschau 78, 207–242. https://doi.org/10.1007/BF01988362
Mid-latitudes	North Sea		Anell, I., Thybo, H., Stratford, W., 2010. Relating Cenozoic North Sea sediments to topography in southern Norway: The interplay between tectonics and climate. Earth and Planetary Science Letters 300, 19–32. https://doi.org/10.1016/j.epsl.2010.09.009 Huuse, M., 2003. Late Cenozoic palaeogeography of the eastern North Sea Basin: climatic vs tectonic forcing of basin margin uplift and deltaic progradation. Aarhus Universitet. Overeem, I., Weltje, G.J., Bishop-Kay, C., Kroonenberg, S.B., 2001. The Late Cenozoic Eridanos delta system in the Southern North Sea Basin: a climate signal in sediment supply? Basin Research 13, 293–312. https://doi.org/10.1046/j.1365-2117.2001.00151.x

Table SII-3 (…/…)

Latitudes	Location		Full References
Low-latitudes	Amazon	Amazon fan	Figueiredo, J., Hoorn, C., Van der Ven, P., Soares, E., 2009. Late Miocene onset of the Amazon River and the Amazon deep-sea fan: Evidence from the Foz do Amazonas Basin. Geology 37, 619–622. https://doi.org/10.1130/G25567A.1 Harris, S.E., Mix, A.C., 2002. Climate and tectonic influences on continental erosion of tropical South America, 0–13 Ma. Geology 30, 447–450. https://doi.org/10.1130/0091-7613(2002)030<0447:catioc>2.0.co;2 Dobson, D.M., Dickens, G.R., Rea, D.K., 2001. Terrigenous sediment on Ceara Rise: a Cenozoic record of South American orogeny and erosion. Palaeogeography, Palaeoclimatology, Palaeoecology 165, 215–229. https://doi.org/10.1016/s0031-0182(00)00161-9 Métivier, F., Gaudemer, Y., Tapponnier, P., Klein, M., 1999. Mass accumulation rates in Asia during the Cenozoic. Geophys. J. Int. 137, 280–318. https://doi.org/10.1046/j.1365-246X.1999.00802.x
Low-latitudes	Bengal bay	Bengal fan	
Mid-latitudes	Central Asia, Tibet	Tianshan, Junggar and Tarim basin	Zhang, P.Z., Molnar, P., Downs, W.R., 2001. Increased sedimentation rates and grain sizes 2–4 Myr ago due to the influence of climate change on erosion rates. Nature 410, 891–897. https://doi.org/10.1038/35073504 Métivier, F., Gaudemer, Y., 1997. Mass transfer between eastern Tien Shan and adjacent basins (central Asia): constraints on regional tectonics and topography. Geophysical Journal International 128, 1–17. https://doi.org/10.1111/j.1365-246X.1997.tb04068.x Kuhlemann, J., Frisch, W., Székely, B., Dunkl, I., Kázmér, M., 2002. Post-collisional sediment budget history of the Alps: tectonic versus climatic control. International Journal of Earth Sciences 91, 818–837. https://doi.org/10.1007/s00531-002-0266-y
Mid-latitudes	Southern Europe		Kuhlemann, J., Frisch, W., Dunkl, I., Székely, B., 2001. Quantifying tectonic versus erosive denudation by the sediment budget: The Miocene core complexes of the Alps. Tectonophysics 330, 1–23.
Mid-latitudes	Southern Europe		Kuhlemann, J., Frisch, W., Székely, B., Dunkl, I., Kázmér, M., 2002. Post-collisional sediment budget history of the Alps: tectonic versus climatic control. International Journal of Earth Sciences 91, 818–837. https://doi.org/10.1007/s00531-002-0266-y

Table SII-3 (…/…)

Latitudes	Location		Full References
Low-latitudes	South Bolivia	Subandean foothills	Uba, C.E., Strecker, M.R., Schmitt, A.K., 2007. Increased sediment accumulation rates and climatic forcing in the central Andes during the late Miocene. Geology 35, 979. https://doi.org/10.1130/G224025A.1
Low-latitudes	SE Africa	Zambezi delta	Walford, H.L., White, N.J., Sydow, J.C., 2005. Solid sediment load history of the Zambezi Delta. Earth and Planetary Science Letters 238, 49–63. https://doi.org/10.1016/j.epsl.2005.07.014
Low-latitudes	W. Africa	Zaire	Savoye, B., Babonneau, N., Dennielou, B., Bez, M., 2009. Geological overview of the Angola–Congo margin, the Congo deep-sea fan and its submarine valleys. Deep Sea Research Part II: Topical Studies in Oceanography 56, 2169–2182. https://doi.org/10.1016/j.dsr2.2009.04.001 Ferry, J.-N., Babonneau, N., Mulder, T., Parize, O., Raillard, S., 2004. Morphogenesis of Congo submarine canyon and valley: implications about the theories of the canyons formation. Geodinamica Acta 17, 241–251. https://doi.org/10.3166/ga.17.241-251 Lavier, L.L., Steckler, M.S., Brigaud, F., 2001. Climatic and tectonic control on the Cenozoic evolution of the West African margin. Marine Geology 178, 63–80. https://doi.org/10.1016/S0025-3227(01)00175-X
Low-latitudes	S. China	Red river delta	Lei, C., Ren, J., Sternai, P., Fox, M., Willett, S., Xie, X., Clift, P.D., Liao, J., Wang, Z., 2015. Structure and sediment budget of Yinggehai–Song Hong basin, South China Sea: Implications for Cenozoic tectonics and river basin reorganization in Southeast Asia. Tectonophysics 655, 177–190. Clift, P.D., 2006. Controls on the erosion of Cenozoic Asia and the flux of clastic sediment to the ocean. Earth and Planetary Science Letters 241, 571–580. https://doi.org/10.1016/j.epsl.2005.11.028
Low-latitudes	S. China	Pearl river delta	Clift, P.D., 2006. Controls on the erosion of Cenozoic Asia and the flux of clastic sediment to the ocean. Earth and Planetary Science Letters 241, 571–580. https://doi.org/10.1016/j.epsl.2005.11.028
Low-latitudes	India/Pakistan	Indus fan	Clift, P.D., 2006. Controls on the erosion of Cenozoic Asia and the flux of clastic sediment to the ocean. Earth and Planetary Science Letters 241, 571–580. https://doi.org/10.1016/j.epsl.2005.11.028 Clift, P., Gaedicke, C., 2002. Accelerated mass flux to the Arabian Sea during the middle to late Miocene. Geology 30, 207. https://doi.org/10.1130/0091-7613(2002)030<0207:AMFTTA>2.0.CO;2 Clift, P.D., Lee, J.I., Hildebrand, P., Shimizu, N., Layne, G.D., Blusztajn, J., Blum, J.D., Garzanti, E., Khan, A.A., 2002. Nd and Pb isotope variability in the Indus River System: implications for sediment provenance and crustal heterogeneity in the Western Himalaya. Earth and Planetary Science Letters 200, 91–106. https://doi.org/10.1016/S0012-821X(02)00620-9

Latitudes	Location		
			Morley, C.K., Back, S., 2008. Estimating hinterland exhumation from late orogenic basin volume, NW Borneo. Journal of the Geological Society 165, 353–366. https://doi.org/10.1144/0016-76492007-067
Low-latitudes	North Borneo	South China sea margin	Hall, R., Nichols, G., 2002. Cenozoic sedimentation and tectonics in Borneo: climatic influences on orogenesis, in: Jones, S. J., Frostick, L. (Eds.), Sediment Flux to Basins: Causes, Controls and Consequences. Geological Society, London, Special Publications, 191, pp. 5–22. https://doi.org/10.1144/gsl.sp.2002.191.01.02

Table SII-3 (…/…)

Latitudes	Location		Full References
Low-latitudes	West Africa	Niger delta	Grimaud, J.-L., Rouby, D., Chardon, D., Beauvais, A., 2018. Cenozoic sediment budget of West Africa and the Niger delta. Basin Research 30, 169–186. https://doi.org/10.1111/bre.12248
Low-latitudes	India	Ganga basin	Métivier, F., Gaudemer, Y., Tapponnier, P., Klein, M., 1999. Mass accumulation rates in Asia during the Cenozoic. Geophys. J. Int. 137, 280–318. https://doi.org/10.1046/j.1365-246X.1999.00802.x Métivier, F., Gaudemer, Y., Tapponnier, P., Klein, M., 1999. Mass accumulation rates in Asia during the Cenozoic. Geophys. J. Int. 137, 280–318. https://doi.org/10.1046/j.1365-246X.1999.00802.x
Low-latitudes	SE Asia	Gulf of Thailand	Clift, P.D., 2006. Controls on the erosion of Cenozoic Asia and the flux of clastic sediment to the ocean. Earth and Planetary Science Letters 241, 571–580. https://doi.org/10.1016/j.epsl.2005.11.028 Métivier, F., Gaudemer, Y., Tapponnier, P., Klein, M., 1999. Mass accumulation rates in Asia during the Cenozoic. Geophys. J. Int. 137, 280–318. https://doi.org/10.1046/j.1365-246X.1999.00802.x
Low-latitudes	SE Asia	Mekong delta	Clift, P.D., 2006. Controls on the erosion of Cenozoic Asia and the flux of clastic sediment to the ocean. Earth and Planetary Science Letters 241, 571–580. https://doi.org/10.1016/j.epsl.2005.11.028

Table SII-4. Compilation of detrital thermochronometry studies.
Not exhaustive.
Table SII-4 (…/…)

Region			Basin	Type of basin	Catchment	Thermochronometers	Peak denudation	Comments	Reference
S. Asia	Himalaya	Western Nepal	Karnali Section	Foreland	Karnali	AFT	steady at 1-1.5 mm/yr since ca. 7 Ma	High denudation rates in the High Himalaya	van der Beek et al., 2006; reinterp. In Naylor et al., 2015
S. Asia	Himalaya	Central Nepal	Surai and Tinau Sections	Foreland	Rapti	AFT	steady at 1.8 mm/yr since ca. 7 Ma	High denudation rates in the High Himalaya	van der Beek et al., 2006
S. Asia	Himalaya	Western Nepal	Karnali Section	Foreland	Karnali	ZFT	steady at 1.4±0.2 mm/yr since ca. 16 Ma	High denudation rates in the High Himalaya	Bernet et al., 2006
S. Asia	Himalaya	Central Nepal	Surai and Tinau Sections	Foreland	Rapti	ZFT	steady at 1.4±0.2 mm/yr since ca. 16 Ma	High denudation rates in the High Himalaya	Bernet et al., 2006
S. Asia	Eastern Himalaya	Arunashal Pradesh	Kameng section	Foreland		ZFT	steady at 1.8 mm/yr since ca. 13 Ma	7-3 Ma : possibly paleo-Brahmaputra, and < 2.6 Ma himalayan river inc. thermal model using Pecube (Braun, 2003; Braun et al., 2012)	Chirouze et al., 2013
S. Asia	Eastern Himalaya	Arunashal Pradesh	Siji Section	Foreland		ZFT, muscovite 40Ar/39Ar	5-10-fold acceleration to > 5 mm/yr at ca. 5-7 Ma (max age not well constrained)	Linked to Namche Barwa denudation	Lang et al., 2016
S. Asia	Eastern Himalaya		Surma basin	Foreland and delta	Brahmaputra?	Rutile U-Pb	Acceleration to > 4mm/yr at 3 - 7 Ma	Limited number of grains (1 for the Pleistocene) Linked to Namche Barwa denudation	Bracciali et al., 2016
S. Asia	Himalaya		Bengal fan 8°N	Turbiditic fan	Ganga - Brahmaputra	Rutile U-Pb, ZFT	Acceleration at 5.59-3.47 Ma	Not sustained by muscovite 40Ar/39Ar and apatite U-Pb	Najman et al., 2019
W. Europe	Alps	W. Alps	Chambaran basin	Foreland		AFT	Deceleration at 13-10 Ma and steady afterwards		Glotzbach et al., 2011
S. Asia	New Zealand	S. Alps				ZFT	Acceleration at 7-4 Ma and steady afterwards	EGU communication	Lang et al., 2018
S. Asia	Himalaya	Kashmir		Foreland		Ahe, ZHe		reset of AHe + no conclusion possible for Zhe	Gavillot et al., 2018
S. Asia	SE Tibet			modern River sediment		AFT, Ahe	Acceleration at 11-4 Ma	no use of lag-time. Appearant overinterpretation ?	Duvall et al., 2012

Table SII-4 (…/…)

Region			Basin	Type of basin	Catchment	Thermochronometers	Peak denudation	Comments	Reference
W. Europe	Alps	W. and C. Alps		Foreland		ZFT	steady at 0.4-0.7 mm/yr since at least 15 Ma	Only one sample < 6 Ma (modern sample)	Bernet et al., 2001, 2009
S. Asia	Himalaya		Bengal fan 8°N	Turbiditic fan	Ganga - Brahmaputra	AFT, ZFT	steady at 4 mm/yr since at least 9-12 Ma	EGU communication	Huyghe et al., 2019
Antarctica			Pryds bay			AFT	acceleration at 30-35 mm/yr and steady afterwards		Tochilin et al., 2012

Table SII-4. Compilation of detrital thermochronometry studies.
Not exhaustive.
Table SII-4 (…/…)

Region			Basin	Type of basin	Catchment	Thermochronometers	Full reference
S. Asia	Himalaya	Western Nepal	Karnali Section	Foreland	Karnali	AFT	van der Beek, P., Robert, X., Mugnier, J.-L., Bernet, M., Huyghe, P., Labrin, E., 2006. Late Miocene–recent exhumation of the central Himalaya and recycling in the foreland basin assessed by apatite fission-track thermochronology of Siwalik sediments, Nepal. Basin Research 18, 413–434. https://doi.org/10.1111/j.1365-2117.2006.00305.x Naylor, M., Sinclair, H.D., Bernet, M., van der Beek, P., Kirstein, L.A., 2015. Bias in detrital fission track grain-age populations: Implications for reconstructing changing erosion rates. Earth and Planetary Science Letters 422, 94–104. https://doi.org/10.1016/j.epsl.2015.04.020
S. Asia	Himalaya	Central Nepal	Surai and Tinau Sections	Foreland	Rapti	AFT	van der Beek, P., Robert, X., Mugnier, J.-L., Bernet, M., Huyghe, P., Labrin, E., 2006. Late Miocene–recent exhumation of the central Himalaya and recycling in the foreland basin assessed by apatite fission-track thermochronology of Siwalik sediments, Nepal. Basin Research 18, 413–434. https://doi.org/10.1111/j.1365-2117.2006.00305.x
S. Asia	Himalaya	Western Nepal	Karnali Section	Foreland	Karnali	ZFT	Bernet, M., van der Beek, P., Pik, R., Huyghe, P., Mugnier, J.-L., Labrin, E., Szulc, A., 2006. Miocene to Recent exhumation of the central Himalaya determined from combined detrital zircon fission-track and U/Pb analysis of Siwalik sediments, western Nepal. Basin Research 18, 393–412. https://doi.org/10.1111/j.1365-2117.2006.00303.x
S. Asia	Himalaya	Central Nepal	Surai and Tinau Sections	Foreland	Rapti	ZFT	Bernet, M., van der Beek, P., Pik, R., Huyghe, P., Mugnier, J.-L., Labrin, E., Szulc, A., 2006. Miocene to Recent exhumation of the central Himalaya determined from combined detrital zircon fission-track and U/Pb analysis of Siwalik sediments, western Nepal. Basin Research 18, 393–412. https://doi.org/10.1111/j.1365-2117.2006.00303.x
S. Asia	Eastern Himalaya	Arunashal Pradesh	Kameng section	Foreland		ZFT	Chirouze, F., Huyghe, P., van der Beek, P., Chauvel, C., Chakraborty, T., Dupont-Nivet, G., Bernet, M., 2013. Tectonics, exhumation, and drainage evolution of the eastern Himalaya since 13 Ma from detrital geochemistry and thermochronology, Kameng River Section, Arunachal Pradesh. Geological Society of America Bulletin 125, 523–538. https://doi.org/10.1130/B30697.1
S. Asia	Eastern Himalaya	Arunashal Pradesh	Siji Section	Foreland		ZFT, muscovite 40Ar/39Ar	Lang, K.A., Huntington, K.W., Burmester, R., Housen, B., 2016. Rapid exhumation of the eastern Himalayan syntaxis since the late Miocene. Geological Society of America Bulletin 128, 1403–1422. https://doi.org/10.1130/B31419.1
S. Asia	Eastern Himalaya		Surma basin	Foreland and delta	Brahmaputra?	Rutile U-Pb	Bracciali, L., Parrish, R.R., Najman, Y., Smye, A., Carter, A., Wijbrans, J.R., 2016. Plio-Pleistocene exhumation of the eastern Himalayan syntaxis and its domal 'pop-up.' Earth-Science Reviews 160, 350–385. https://doi.org/10.1016/j.earscirev.2016.07.010
S. Asia	Himalaya		Bengal fan 8°N	Turbiditic fan	Ganga - Brahmaputra	Rutile U-Pb, ZFT	Najman, Y., Mark, C., Barfod, D.N., Carter, A., Parrish, R., Chew, D., Gemignani, L., 2019. Spatial and temporal trends in exhumation of the Eastern Himalaya and syntaxis as determined from a multitechnique detrital thermochronological study of the Bengal Fan. Geological Society of America Bulletin. https://doi.org/10.1130/B35031.1
W. Europe	Alps	W. Alps	Chambaran basin	Foreland		AFT	Glotzbach, C., Bernet, M., Van Der Beek, P., 2011. Detrital thermochronology records changing source areas and steady exhumation in the Western European Alps. Geology 39, 239–242. https://doi.org/10.1130/G31757.1
S. Asia	New Zealand	S. Alps				ZFT	
S. Asia	Himalaya	Kashmir		Foreland		Ahe, ZHe	Gavillot, Y., Meigs, A.J., Sousa, F.J., Stockli, D., Yule, D., Malik, M., 2018. Late Cenozoic Foreland-to-Hinterland Low-Temperature Exhumation History of the Kashmir Himalaya. Tectonics 37, 3041–3068. https://doi.org/10.1029/2017TC004668
S. Asia	SE Tibet			modern River sediment		AFT, Ahe	Duvall, A.R., Clark, M.K., Avdeev, B., Farley, K.A., Chen, Z., 2012. Widespread late Cenozoic increase in erosion rates across the interior of eastern Tibet constrained by detrital low-temperature thermochronometry. Tectonics 31, n/a-n/a. https://doi.org/10.1029/2011TC002969

Table SII-4 (…/…)

Region			Basin	Type of basin	Catchment	Thermochronometers	Full reference
W. Europe	Alps	W. and C. Alps		Foreland		ZFT	Bernet, M., Brandon, M., Garver, J., Balestieri, M.L., Ventura, B., Zattin, M., 2009. Exhuming the Alps through time: clues fromdetrital zircon fission-track thermochronology. Basin Research 21, 781–798. Bernet, M., Zattin, M., Garver, J.I., Brandon, M.T., Vance, J.A., 2001. Steady-state exhumation of the European Alps. Geology 29, 35–38. https://doi.org/10.1130/0091-7613(2001)029<0035:sseote>2.0.co;2
S. Asia	Himalaya		Bengal fan 8°N	Turbiditic fan	Ganga - Brahmaputra	AFT, ZFT	
Antarctica			Pryds bay			AFT	Tochilin, C.J., Reiners, P.W., Thomson, S.N., Gehrels, G.E., Hemming, S.R., Pierce, E.L., 2012. Erosional history of the Prydz Bay sector of East Antarctica from detrital apatite and zircon geo- and thermochronology multidating. Geochemistry, Geophysics, Geosystems 13, Q11015. https://doi.org/10.1029/2012GC004364

Table SII-5. Compilation of 10Be paleoerosion studies.
Table SII-5 (…/…)

Reference	Region	Area	Period (Ma)	Dating	Type	Catchment size (km2)	Sample Nb	Method to determine erosion rates	26Al/10Be sample Nb	Method to deal with recent exposure	Method to detect recycling	Provenance study	rates (mm/yr)
Anthony and Granger, 2007, reinterpreted by Granger and Schaller, 2014	North America	Cumberland plateau, North Apalaches, US	0.02 - 5.7	26Al/10Be	Cave sediments	Catchment not represented (small ?)	16	10Be	All	Not applicable	26Al/10Be	None	0.01 - 0.04
Amidon et al., 2017	South America	Huaco & Toro Negro Section, Eastern Andes, North Argentina	2.33 - 6.41	Paleomagnetostratigraphy (Huaco section)) Zircon U-Pb dating (Toro Negro section)	Fluvial sediments, river sections	Unclear	35	10Be	36Cl, 4 samples	36Cl	36Cl ?	Zircon U-Pb	
Balco and Stone, 2005	North America	Fisher Valley, Utah	0.6 - 0.7	Various	Buried/subaerial alluvial sediments	<100	4	10Be		4 26Al/10Be	26Al/10Be	Petrography	0.1 - 0.2
Bekadour et al., 2014	South America	Pisco valley, Central Peru	0.007 - 0.05	OSL	Cut-and-fill terraces	4.30E+03	12	10Be		0 Not applicable	None	Petrography	0.03 - 0.4
Bierman et al., 2016	Greenland	East Greenland, ODP Site 987, 918	0.001 - 7.5 Ma	Paleomagnetostratigraphy, biostratigraphy δ18O benthic foraminifera	Marine ice raft debris sand	ODP 987: > 1E+5 ODP 918: 1.5E+5 ?	46	26Al + 10Be	20 (only ODP 918)	Not applicable	26Al/10Be	Modern petrography for site ODP 918	
Cyr and Granger, 2008	W. Europe	North and Central Appenines, Adriatic side, Italy	0.8 - 0.9	26Al/10Be + interpretation	Cave and terrace sediments	Unclear	7	10Be	1/7	None	None	None	0.2 - 0.3
Davis et al., 2012	Africa	Coastal plain, Israel potential source : Nile	0.5 - 3	26Al/10Be	Dunes and eolianites	3.40E+06	9	10Be	All	26Al/10Be	26Al/10Be	Heavy mineral assemblages	0.01
Fuller et al., 2009	North America	Eel river, California	0.006 - 0.03	OSL	Strath terrace sediments	17	9	10Be		0 Not applicable	None	None	0.1 - 0.3
Garcin et al., 2017	Africa	Suguta Valley, North Kenya rift	0.009 - 0.012 (BP)	14C	fluviolacustrine sediments,	2100	3	10Be		0 None	None	None	0.02 - 0.09
Granger et al., 2001	North America	Mammoth cave, Green river, Kentucky, US	0 - 3.4	26Al/10Be	Cave sediments	Catchment not represented (small ?)	29	10Be	All	Not applicable	26Al/10Be	None	1.6 - 6.5
Grischott et al., 2016	W. Europe	Fedoz valley, Swiss Alps	0.002 - 0.005 (BP)	14C	Alluvial fan delta, cores	17	18	10Be		0 Not applicable	None	None	0.5 - 1.4
Grischott et al., 2017	W. Europe	Sebaz Valley, Lake Stappiz, Hohe Tauern, Austrian Alps	0 - > 0.015 (BP)	14C, pollens	Lake deposits, cores	34	28	10Be		0 Not applicable	None	Not strictly	0.3 - 7

Table SII-5 (…/…)

Reference	Region	Area	Period (Ma)	Dating	Type	Catchment size (km2)	Sample Nb	Method to determine erosion rates	26Al/10Be sample Nb	Method to deal with recent exposure	Method to detect recycling	Provenance study	rates (mm/yr)
Haeuselmann et al., 2007	W. Europe	SiebenHensgte - Hohgant, Aare Valley, Swiss Alps	0.07 - 4.3	U-Th, 26Al/10Be	Cave sediment	?	20 10Be		Not applicable	26Al/10Be	None	0.03 - 0.5
Hidy et al., 2014	North America	Trinity, Brazos, Colorado, Interior Texas	0.08 - 0.6	14C, OSL, Thermolumine scence, 10Be depth profile	Terraces	Colorado: 1.1E+5 Trinity: 4.5E+4	10 26Al + 10Be		9 26Al/10Be	26Al/10Be	None	0.01 - 0.03
Madella et al., 2018	S. America	Francia section, Camiña, Andean plateau, North Chile	10 - 13	Paleomagnet ostratigraphy	Fluvial deposits, river section	~3.2E+3	9 10Be		0 None	None	None	0.0005 - 0.01
Marshall et al., 2015, 2017	North America	Little lake, Oregon, US	0.001 - 0.05	14C, OSL	Paleolake drilled cores	6 27+3	10Be		Not 0 applicable	None	Not applicable	0.1 - 0.4
Mason and Romans, 2018	North America	Panamint Valley, California	0.3 - 1.5	26Al/10Be	Fan complex consisting of alluvial and lacustrine deposits	33	13 10Be	All	26Al/10Be	26Al/10Be	None (Unclear)	0.02 - 0.05
McPhillips et al., 2013	South America	Quebrada velada, Western Peru	0.016 - 0.024	IRSL	Terraces	315	7 10Be		0 None	None	Not strictly	0.03 - 0.1
Oskin et al., 2017	North America	Fish Creek - Vallecito, California	1.1 - 4	Paleomagnet ostratigraphy	Fluviodeltaic sediments, river sections	? (catchment not represented)	43 10Be		0 None	None	None	0.02 - 0.2
Puchol et al., 2017; Charreau et al., 2011	Central Asia	Yaha, Kuitun and Jingu sections, Ebi Lake core, Tianshan	0.1, 1.6 - 8.5	Paleomagnet ostratigraphy 26Al/10Be	Fluvial sediments (river sections) Lake sediments (lake drilled cores)	Yaha: ~0.8E+3 Jingu: ~2E+3 Kuitun: ~2.8E+3 Ebi lake: ~1.5E+4	75 10Be		31 26Al/10Be	26Al/10Be	Heavy mineral assemblages	0.01 - 2
Puchol, 2013	South Asia	Surai section, Siwaliks, Central Nepal	0.5 - 6.5	Paleomagnet ostratigraphy	Fluvial and lake sediments, river section	~5.5E+3	14 10Be	3/14	26Al/10Be	26Al/10Be	None	0.2 - 1.3
Refsnider, 2010	North America	Marble mountain cave, Sangre de Cristo Range, Southern Rocky mountains	1.1 - 5	26Al/10Be	Cave sediment	0.25	3 10Be		Not 0 applicable	None	None	0.005 - 0.05
Schaller et al., 2002	W. Europe	Meuse, Netherlands Allier and Dore, France	0 - 0.03 (Ma BP)	14C, U-Th, Ar-Ar	Terraces	Allier: 1.4E+4 Dore: 1.5E+3 Meuse:3.5E+4	14 10Be		0 None	None	None	0.03 - 0.08

Table SII-5 (…/…)

Reference	Region	Area	Period (Ma)	Dating	Type	Catchment size (km2)	Sample Nb	Method to determine erosion rates	26Al/10Be sample Nb	Method to deal with recent exposure	Method to detect recycling	Provenance study	rates (mm/yr)
Schaller et al., 2004	W. Europe	Meuse, Netherlands	0.1 - 1.7	Paleomagnetostratigraphy Pollen, thermoluminescence, 14C 26Al/10Be	Terraces	1.00E+04	28	26Al + 10Be	12	26Al/10Be	26Al/10Be	None	0.02 - 0.05
Schaller et al., 2016	W. Europe	Vtlava, Czech republic; Allier, France; Esla, NW Spain; Guadalquivir, SW Spain	0.08 - 2	26Al/10Be, 10Be depth profile	Terraces	Allier: 1.4E+4 Esla: 1.6E+4 Vtlava: 2.8E+4 Guadalquivir: 5.7E+4	13	10Be	0	None	None	None	0.008 - 0.06
Scherler et al., 2015	Asia	Yamuna, Garhwal Himalaya, North India	0.005 - 0.05 (Ma BP)	14C, OSL, IRSL, 10Be	Terraces	depending basin: 6E+3 to 5E+4	7	10Be	0	None	None	None	0.6 - 2.5
Stock et al., 2004, 2005	North America	Sierra Nevada, Central California	0.03 - 2.7	26Al/10Be	Cave sediment and interfluve surface	?	19	10Be	All	26Al/10Be	26Al/10Be	None	0.02 - 0.5
Val et al., 2016, reinterpreted in Amidon et al., 2017	S. America	Rio Jachal, Andes, North Argentina	1.7 - 8.8	Paleomagnetostratigraphy	Fluvial, river sections	1.00E+04	17	10Be	3/17	26Al/10Be	26Al/10Be	Detrital zircon (2 samples)	0.03 - 2.4
Pingel et al., 2019	S. America	NW Argentina, Central Andes	2 - 6	Tuff dating	Fluvial, river sections	3000	14	10Be	0	None	None	Paleocurrents	0.01 - 0.1 - 1

Table SII-5 (…/…)

Reference	Region	Area	Comments	Temporal trend of erosion rates	Offshore	Full reference
						Granger, D.E., Schaller, M., 2014. Cosmogenic Nuclides and Erosion at the Watershed Scale. Elements 10, 369–373. https://doi.org/10.2113/gselements.10.5.369
Anthony and Granger, 2007, reinterpreted by Granger and Schaller, 2014	North America	Cumberland plateau, North Apalaches, US	Provenance, Recycling and recent/modern exposure not discussed	increase		Anthony, D.M., Granger, D.E., 2007. A new chronology for the age of Appalachian erosional surfaces determined by cosmogenic nuclides in cave sediments. Earth Surface Processes and Landforms 32, 874–887. https://doi.org/10.1002/esp.1446
Amidon et al., 2017	South America	Huaco & Toro Negro Section, Eastern Andes, North Argentina	A few words about recent exposure but No discussion about recycling			Amidon, W.H., Fisher, G.B., Burbank, D.W., Ciccioli, P.L., Alonso, R.N., Gorin, A.L., Silverhart, P.H., Kylander-Clark, A.R.C., Christoffersen, M.S., 2017. Mio-Pliocene aridity in the south-central Andes associated with Southern Hemisphere cold periods. Proceedings of the National Academy of Sciences 114, 6474–6479. https://doi.org/10.1073/pnas.1700327114
Balco and Stone, 2005	North America	Fisher Valley, Utah	No discussion about recent exposure a few words about recycling			Balco, G., Stone, J.O.H., 2005. Measuring middle Pleistocene erosion rates with cosmic-ray-produced nuclides in buried alluvial sediment, Fisher Valley, southeastern Utah. Earth Surface Processes and Landforms 30, 1051–1067. https://doi.org/10.1002/esp.1262
Bekadour et al., 2014	South America	Pisco valley, Central Peru	Recycling discussed			Bekaddour, T., Schlunegger, F., Vogel, H., Delunel, R., Norton, K.P., Akçar, N., Kubik, P., 2014. Paleo erosion rates and climate shifts recorded by Quaternary cut-and-fill sequences in the Pisco valley, central Peru. Earth and Planetary Science Letters 390, 103–115. https://doi.org/10.1016/j.epsl.2013.12.048
Bierman et al., 2016	Greenland	East Greenland, ODP Site 987, 918	Provenance discussed. Recycling not discussed. Paleoconcentrations only, except one erosion rate at 0.135 Ma of 0.02 mm/yr (in their Methods). Potential variation of the source (IRD)	Increase + no impact on variability	x	Bierman, P.R., Shakun, J.D., Corbett, L.B., Zimmerman, S.R., Rood, D.H., 2016. A persistent and dynamic East Greenland Ice Sheet over the past 7.5 million years. Nature 540, 256–260. https://doi.org/10.1038/nature20147
Cyr and Granger, 2008	W. Europe	North and Central Appenines, Adriatic side, Italy	Uncertain age model			Cyr, A.J., Granger, D.E., 2008. Dynamic equilibrium among erosion, river incision, and coastal uplift in the northern and central Apennines, Italy. Geology 36, 103. https://doi.org/10.1130/G24003A.1
Davis et al., 2012	Africa	Coastal plain, Israel potential source : Nile	No discussion about recent exposure	Steady		Davis, M., Matmon, A., Rood, D.H., Avnaim-Katav, S., 2012. Constant cosmogenic nuclide concentrations in sand supplied from the Nile River over the past 2.5 m.y. Geology 40, 359–362. https://doi.org/10.1130/G32574.1
Fuller et al., 2009	North America	Eel river, California				Fuller, T.K., Perg, L.A., Willenbring, J.K., Lepper, K., 2009. Field evidence for climate-driven changes in sediment supply leading to strath terrace formation. Geology 37, 467–470. https://doi.org/10.1130/G25487A.1
Garcin et al., 2017	Africa	Suguta Valley, North Kenya rift	Recent exposure discussed			Garcin, Y., Schildgen, T.F., Torres Acosta, V., Melnick, D., Guillemoteau, J., Willenbring, J., Strecker, M.R., 2017. Short-lived increase in erosion during the African Humid Period: Evidence from the northern Kenya Rift. Earth and Planetary Science Letters 459, 58–69. https://doi.org/10.1016/j.epsl.2016.11.017
Granger et al., 2001	North America	Mammoth cave, Green river, Kentucky, US	Recycling not discussed	steady or possible decrease		Granger, D.E., Fabel, D., Palmer, A.N., 2001. Pliocene-Pleistocene incision of the Green River, Kentucky, determined from radioactive decay of cosmogenic 26Al and 10Be in Mammoth Cave sediments. Geological Society of America Bulletin 113, 825–836. https://doi.org/10.1130/0016-7606(2001)113<0825:PPIOTG>2.0.CO;2

Table SII-5 (…/…)

Reference	Region	Area	Comments	Temporal trend of erosion rates	Offshore	Full reference
Grischott et al., 2016	W. Europe	Fedoz valley, Swiss Alps				Grischott, R., Kober, F., Lupker, M., Hippe, K., Ivy-Ochs, S., Hajdas, I., Salcher, B., Christl, M., 2016. Constant denudation rates in a high alpine catchment for the last 6 kyrs: Alpine 10Be denudation rates over 6 kyr. Earth Surface Processes and Landforms 42, 1065–1077. https://doi.org/10.1002/esp.4070
Grischott et al., 2017	W. Europe	Sebaz Valley, Lake Stappiz, Hohe Tauern, Austrian Alps	Provenance discussed Variability of erosion rates			Grischott, R., Kober, F., Lupker, M., Reitner, J.M., Drescher-Schneider, R., Hajdas, I., Christl, M., Willett, S.D., 2017. Millennial scale variability of denudation rates for the last 15 kyr inferred from the detrital 10Be record of Lake Stappitz in the Hohe Tauern massif, Austrian Alps. The Holocene 27, 1914–1927. https://doi.org/10.1177/0959683617708451
Haeuselmann et al., 2007	W. Europe	SiebenHensgte - Hohgant, Aare Valley, Swiss Alps	Recycling not discussed	increase + increased variability		Haeuselmann, P., Granger, D.E., Jeannin, P.-Y., Lauritzen, S.-E., 2007. Abrupt glacial valley incision at 0.8 Ma dated from cave deposits in Switzerland. Geology 35, 143. https://doi.org/10.1130/G23094A
Hidy et al., 2014	North America	Trinity, Brazos, Colorado, Interior Texas	Provenance discussed No discussion about recent exposure			Hidy, A.J., Gosse, J.C., Blum, M.D., Gibling, M.R., 2014. Glacial–interglacial variation in denudation rates from interior Texas, USA, established with cosmogenic nuclides. Earth and Planetary Science Letters 390, 209–221. https://doi.org/10.1016/j.epsl.2014.01.011
Madella et al., 2018	S. America	Francia section, Camiña, Andean plateau, North Chile	No discussion about recent exposure, recycling or provenance			Madella, A., Delunel, R., Akçar, N., Schlunegger, F., Christl, M., 2018. 10Be-inferred paleo-denudation rates imply that the mid-Miocene western central Andes eroded as slowly as today. Scientific Reports 8. https://doi.org/10.1038/s41598-018-20681-x
Marshall et al., 2015, 2017	North America	Little lake, Oregon, US	No obs. landslides (LIDAR), but possible			Marshall, J.A., Roering, J.J., Gavin, D.G., Granger, D.E., 2017. Late Quaternary climatic controls on erosion rates and geomorphic processes in western Oregon, USA. Geological Society of America Bulletin 129, 715–731. https://doi.org/10.1130/B31509.1 Marshall, J.A., Roering, J.J., Bartlein, P.J., Gavin, D.G., Granger, D.E., Rempel, A.W., Praskievicz, S.J., Hales, T.C., 2015. Frost for the trees: Did climate increase erosion in unglaciated landscapes during the late Pleistocene? Science Advances 1, e1500715. https://doi.org/10.1126/sciadv.1500715
Mason and Romans, 2018	North America	Panamint Valley, California	Recent exposure and provenance not discussed	steady + increased variability		Mason, C.C., Romans, B.W., 2018. Climate-driven unsteady denudation and sediment flux in a high-relief unglaciated catchment–fan using 26 Al and 10 Be: Panamint Valley, California. Earth and Planetary Science Letters 492, 130–143. https://doi.org/10.1016/j.epsl.2018.03.056
McPhillips et al., 2013	South America	Quebrada velada, Western Peru				McPhillips, D., Bierman, P.R., Crocker, T., Rood, D.H., 2013. Landscape response to Pleistocene-Holocene precipitation change in the Western Cordillera, Peru: 10Be concentrations in modern sediments and terrace fills. Journal of Geophysical Research: Earth Surface 118, 2488–2499. https://doi.org/10.1002/2013JF002837
Oskin et al., 2017	North America	Fish Creek - Vallecito, California	Recent exposure and recycling not discussed. Change of provenance at 2.8 Ma?	possibly steady		Oskin, M.E., Longinotti, N.E., Peryam, T.C., Dorsey, R.J., DeBoer, C.J., Housen, B.A., Blisniuk, K.D., 2017. Steady 10Be-derived paleoerosion rates across the Plio-Pleistocene climate transition, Fish Creek-Vallecito basin, California. Journal of Geophysical Research: Earth Surface 122, 1653–1677. https://doi.org/10.1002/2016JF004113
Puchol et al., 2017; Charreau et al., 2011	Central Asia	Yaha, Kuitun and Jingu sections, Ebi Lake core, Tianshan	Provenance: potential change for the Yaha Discussion about 10Be exposure during transport for the Ebi lake Discussion about recente exposure but No discussion about recycling	increase or steadiness + increase of variability		Puchol, N., Charreau, J., Blard, P.-H., Lavé, J., Dominguez, S., Pik, R., Saint-Carlier, D., ASTER Team, 2017. Limited impact of Quaternary glaciations on denudation rates in Central Asia. Geological Society of America Bulletin 129 (3–4), 479–499. https://doi.org/10.1130/B31475.1 Charreau, J., Blard, P.-H., Puchol, N., Avouac, J.-P., Lallier-Vergès, E., Bourlès, D., Braucher, R., Gallaud, A., Finkel, R., Jolivet, M., Chen, Y., Roy, P., 2011. Paleo-erosion rates in Central Asia since 9 Ma: A transient increase at the onset of Quaternary glaciations? Earth and Planetary Science Letters 304, 85–92. https://doi.org/10.1016/j.epsl.2011.01.018

Table SII-5 (…/…)

Reference	Region	Area	Comments	Temporal trend of erosion rates	Offshore	Full reference
Puchol, 2013	South Asia	Surai section, Siwaliks, Central Nepal	Recycling and recent exposure discussed Change of provenance at 3-4 Ma?	possible increase		Puchol, N., 2013. Détermination des paléo-taux d'érosion par l'utilisation des isotopes cosmogéniques. Cas de la transition Pliocène-Pleistocène. Université de Nancy, INPL, Lorraine, Nancy.
Refsnider, 2010	North America	Marble mountain cave, Sangre de Cristo Range, Southern Rocky mountains		increase		Refsnider, K.A., 2010. Dramatic increase in late Cenozoic alpine erosion rates recorded by cave sediment in the southern Rocky Mountains. Earth and Planetary Science Letters 297, 505–511. https://doi.org/10.1016/j.epsl.2010.07.002
Schaller et al., 2002	W. Europe	Meuse, Netherlands Allier and Dore, France	No discussion about recent exposure nor recycling			Schaller, M., Von Blanckenburg, F., Veldkamp, A., Tebbens, L.A., Hovius, N., Kubik, P.W., 2002. A 30 000 yr record of erosion rates from cosmogenic 10 Be in Middle European river terraces. Earth and Planetary Science Letters 204, 307–320. https://doi.org/10.1016/s0012-821x(02)00951-2
Schaller et al., 2004	W. Europe	Meuse, Netherlands	No discussion about recent exposure nor recycling	increase + increased variability		Schaller, M., Blanckenburg, F. von, Hovius, N., Veldkamp, A., van den Berg, M.W., Kubik, P.W., 2004. Paleoerosion Rates from Cosmogenic 10Be in a 1.3 Ma Terrace Sequence: Response of the River Meuse to Changes in Climate and Rock Uplift. The Journal of Geology 112, 127–144. https://doi.org/10.1086/381654
Schaller et al., 2016	W. Europe	Vtlava, Czech republic; Allier, France; Esla, NW Spain; Guadalquivir, SW Spain	No discussion about provenance, neither recycling nor recent exposure	Possible increase		Schaller, M., Ehlers, T.A., Stor, T., Torrent, J., Lobato, L., Christl, M., Vockenhuber, C., 2016. Spatial and temporal variations in denudation rates derived from cosmogenic nuclides in four European fluvial terrace sequences. Geomorphology 274, 180–192. https://doi.org/10.1016/j.geomorph.2016.08.018
Scherler et al., 2015	Asia	Yamuna, Garhwal Himalaya, North India				Scherler, D., Bookhagen, B., Wulf, H., Preusser, F., Strecker, M.R., 2015. Increased late Pleistocene erosion rates during fluvial aggradation in the Garhwal Himalaya, northern India. Earth and Planetary Science Letters 428, 255–266. https://doi.org/10.1016/j.epsl.2015.06.034
Stock et al., 2004, 2005	North America	Sierra Nevada, Central California	Recent exposure and Recycling not discussed	decrease + increased variability		Stock, G.M., Anderson, R.S., Finkel, R.C., 2005. Rates of erosion and topographic evolution of the Sierra Nevada, California, inferred from cosmogenic26Al and10Be concentrations. Earth Surface Processes and Landforms 30, 985–1006. https://doi.org/10.1002/esp.1258 Stock, G.M., Anderson, R.S., Finkel, R.C., 2004. Pace of landscape evolution in the Sierra Nevada, California, revealed by cosmogenic dating of cave sediments. Geology 32, 193. https://doi.org/10.1130/G20197.1
Val et al., 2016, reinterpreted in Amidon et al., 2017	S. America	Rio Jachal, Andes, North Argentina	Change of provenance at 2 Ma	undetermined		Val, P., Hoke, G.D., Fosdick, J.C., Wittmann, H., 2016. Reconciling tectonic shortening, sedimentation and spatial patterns of erosion from 10Be paleo-erosion rates in the Argentine Precordillera. Earth and Planetary Science Letters 450, 173–185. https://doi.org/10.1016/j.epsl.2016.06.015
Pingel et al., 2019	S. America	NW Argentina, Central Andes	Change of provenance at 4.2 Ma	Abrupt decrease		Pingel, H., Schildgen, T., Strecker, M.R., Wittmann, H., 2019. Pliocene–Pleistocene orographic control on denudation in northwest Argentina. Geology 47, 359–362. https://doi.org/10.1130/G45800.1

Table SV-1. Biostratigraphy of samples from Site 1450A: From left to right, depth in m, samples by core, Martini zone, Okada and Bukry zone, age assigned from Gradstein et al 2012 and ABX (Denne et al., 2005), marker species.

Top Depth (m)	Samples	Zone Martini	Zone Okada & Bukry	age Gradstein (Ma) >	ABX	Markers Top/Within
218.44	46F-1, 4-5 cm	NN19	CN13b	1.03	ABX	Within S. pulcherrima
246.94	52F-1, 4-5 cm	NN19	CN13b	1.60		Top C. macintyrei
256.7	54F-1, 37-38 cm	NN19/NN18	CN13a/CN12d	1.93		Top D. brouweri
351.91	74F-1, 51-52 cm	NN18	CN12d	1.95		Top D. triradiatus
390.28	82F-1, 98-99 cm	NN18/NN17	CN12d/CN12c	2.39		Top D. pentaradiatus
392.16	82F-CC, 1-2 cm	NN17/NN16	CN12c/CN12b	2.49		Top D. surculus
427.21	90F-1, 1-2 cm	NN16b	CN12b	2.65	ABX	Top D. asymmetricus
436.83	92F-1, 13-14 cm	NN16a	CN12a	2.78	ABX	Top D. tamalis
437.94	92F-1, 124-125 cm	NN16a	CN12a	3.09	ABX	Top D. variabilis
446.21	94F-1, 1-2 cm	NN16a	CN12a	3.55	ABX	Top S. abies
523	110F-CC, 1-2 cm	NN16/NN15	CN12a/CN11b	3.70		Top R. pseudoumbilicus
550.92	117F-1, 2-3 cm	NN15	CN11	3.75	ABX	Top S. verensis
553.31	117F-3, 34-35 cm	NN13	CN11a/CN10c	4.50		Top A. primus
560.48	119F-1, 18-19 cm	NN13	CN10c	4.65	ABX	Top A. delicatus
570.05	121F-CC, 15-16 cm	NN13	CN10c	5.04		Top C. acutus
628.86	130F-1, 66-67 cm	NN12/NN11	CN10a/CN9d	5.59		Top D. quinqueramus
658.4	134X-2, 9-10 cm	NN11	CN9d/CN9c	5.94		Top N. amplificus
676.82	136X-1, 12-13 cm	NN11	CN9c	6.10	ABX	Top R. rotaria

Table SV-2. Published age datums considered for the age model of the site U1450. Published datums (France-Lanord et al. 2016b; Blum et al. 2018) that are outdated by the new datums of this study are not included.

CSF-A : core depth below sea-floor
LCO: last common occurrence, LO: last occurrence, FO: first occurrence, FCO: first common occurrence
GTS 2012: Gradstein et al., 2012 timescale

Core	Section	Depth CSF-A (m)	Zone	Marker event	GTS 2012 age (Ma)	Reference	Comment
Magnetostratigraphy							
hole U1450A							
36F	CC 25 cm	175.9		middle Matuyama (C1r.3r) polarity zo	1.185	France-Lanord et al. 2016	
Planktonic foraminifer datums							
hole U1450A							
62F	CC	299.33	PL6	FO Globorotalia tosaensis	3.35	Blum et al. 2018	Corrected age vs age in Blum et al. 2018
92F	CC	441.69	PL5-PL4	LO Dentoglobigerina altispira	3.47	Blum et al. 2018	Corrected depth vs depth in Blum et al. 2018
98F	1W 15-20 cm	465.35	PL4-PL3	LCO Sphaeroidinellopsis seminulina	3.59	France-Lanord et al. 2016	
hole U1450B							
7R	CC	660.45	M14	LO Globoquadrina dehiscens	5.92	France-Lanord et al. 2016	
Calcareous nannofossil datums							
Hole U1450A							
54F	CC	261.13	NN19-NN18	LO Discoaster brouweri	1.93	France-Lanord et al. 2016	
81F	CC	385.34	NN18-NN17	LO Discoaster pentaradiatus	2.39	France-Lanord et al. 2016	
Hole U1450B							
11R	CC	700.5	CN9c/CN9b	FO Nicklithus amplificus	6.91	France-Lanord et al. 2016	
19R	CC	782.91	CN9b/CN9a	FO Amaurolithus primus	7.42	France-Lanord et al. 2016	
21R	CC	795.07	CN9a	FCO Discoaster surculus	7.79	France-Lanord et al. 201	Corrected FCO vs "LCO" in France-Lanord et al. 2016

Table SV-3. List of observed samples.

Sample	Depth center
354-U1450A-46F-1W, 4-5 cm	218.4
354-U1450A-46F-1W, 23-24 cm	218.6
354-U1450A-46F-1W, 96-97 cm	219.4
354-U1450A-48F-1W, 615-62 cm	228.5
354-U1450A-50F-1W, 5-6 cm	237.5
354-U1450A-52F-1W, 4-5 cm	246.9
354-U1450A-52F-1W, 41-42 cm	247.3
354-U1450A-52F-1W, 111-112 cm	248.0
354-U1450A-52F-2W, 5-6 cm	248.4
354-U1450A-52F-2W, 49-50 cm	248.8
354-U1450A-52F-3W, 4-5 cm	249.2
354-U1450A-54F-1W, 37-38 cm	256.8
354-U1450A-56F-1W, 40-41 cm	266.3
354-U1450A-56F-2W, 70-71 cm	268.1
354-U1450A-58F-1W, 21-22 cm	275.6
354-U1450A-58F-2W, 79-80 cm	276.9
354-U1450A-60F-1W, 945-95 cm	285.8
354-U1450A-62F-1W, 78-785 cm	295.2
354-U1450A-62F-1W, 1375-138 cm	295.8
354-U1450A-62F-3W, 535-54 cm	297.8
354-U1450A-64F-1W, 535-54 cm	304.4
354-U1450A-68F-1W, 99-100 cm	323.9
354-U1450A-70F-1W, 20-205 cm	332.6
354-U1450A-72F-1W, 2-3 cm	341.9
354-U1450A-74F-1W, 3-4 cm	351.4
354-U1450A-74F-1W, 51-52 cm	351.9
354-U1450A-74F-1W, 84-85 cm	352.2
354-U1450A-74F-2W, 445-45 cm	353.3
354-U1450A-76F-1W, 255-26 cm	361.2
354-U1450A-82F-1W, 26-27 cm	389.6
354-U1450A-82F-1W, 98-99 cm	390.3
354-U1450A-82F-1W, 143-144 cm	390.7
354-U1450A-82F-2W, 6-7 cm	390.8
354-U1450A-82F-2W, 54-55 cm	391.3
354-U1450A-82F-2W, 78-79 cm	391.5
354-U1450A-82F-3W, 74-75 cm	393.0
354-U1450A-82F-4W, 28-29 cm	393.7
354-U1450A-84F-1W, 585-59 cm	399.3
354-U1450A-90F-1W, 1-2 cm	427.2
354-U1450A-90F-1W, 8-9 cm	427.3
354-U1450A-92F-1W, 13-14 cm	436.8
354-U1450A-92F-1W, 44-45 cm	437.1
354-U1450A-92F-1W, 124-125 cm	437.9
354-U1450A-92F-2W, 1-2 cm	438.2
354-U1450A-92F-2W, 57-58 cm	438.8
354-U1450A-92F-2W, 130-131 cm	439.5
354-U1450A-92F-2W, 145-146 cm	439.7
354-U1450A-92F-3W, 84-85 cm	440.5
354-U1450A-94F-1W, 1-2 cm	446.2
354-U1450A-94F-1W, 50-505 cm	446.7
354-U1450A-96F-1W, 395-40 cm	456.1
354-U1450A-98F-1W, 215-22 cm	465.4
354-U1450A-104F-1W, 1-2 cm	493.7
354-U1450A-104F-2W, 44-45 cm	495.6
354-U1450A-110F-1W, 2-3 cm	522.2
354-U1450A-110F-1W, 9-10 cm	522.3
354-U1450A-114F-CCW, 2-3 cm	541.2
354-U1450A-115F-1W, 3-4 cm	541.4
354-U1450A-115F-1W, 25-26 cm	541.7
354-U1450A-115F-1W, 49-50 cm	541.9
354-U1450A-115F-CCW, 1-2 cm	541.9
354-U1450A-115F-CCW, 11-12 cm	542.0
354-U1450A-117F-1W, 2-3 cm	550.9
354-U1450A-117F-1W, 36-37 cm	551.3
354-U1450A-117F-1W, 68-69 cm	551.6
354-U1450A-117F-1W, 83-86 cm	551.7
354-U1450A-117F-2W, 58-68 cm	552.8
354-U1450A-117F-3W, 34-54 cm	553.3
354-U1450A-117F-4W, 21-22 cm	554.5
354-U1450A-118F-1W, 10-11 cm	555.7
354-U1450A-118F-1W, 52-53 cm	556.1
354-U1450A-118F-1W, 110-111 cm	556.7
354-U1450A-119F-1W, 18-19 cm	560.5
354-U1450A-119F-1W, 50-51 cm	560.8
354-U1450A-119F-1W, 73-83 cm	561.1
354-U1450A-120X-1W, 19-20 cm	561.5
354-U1450A-120X-2W, 75-8 cm	562.4
354-U1450A-120X-2W, 25-28 cm	562.6
354-U1450A-120X-2W, 1065-107 cm	563.4
354-U1450A-120X-2W, 113-121 cm	563.5
354-U1450A-120X-3W, 32-33 cm	563.9
354-U1450A-120X-3W, 75-76 cm	564.3
354-U1450A-120X-3W, 94-95 cm	564.5
354-U1450A-120X-3W, 121-122 cm	564.7
354-U1450A-120X-CCW, 12-13 cm	565.0
354-U1450A-120X-CCW, 31-32 cm	565.2
354-U1450A-121X-CCW, 15-16 cm	570.1
354-U1450A-121X-CCW, 54-55 cm	570.4
354-U1450A-122X-1W, 8-9 cm	579.7
354-U1450A-122X-1W, 62-80 cm	580.3
354-U1450A-122X-1W, 142-150 cm	581.1
354-U1450A-122X-2W, 9-19 cm	581.2
354-U1450A-122X-2W, 15-16 cm	581.3
354-U1450A-123X-1W, 145-15 cm	589.5
354-U1450A-123X-1W, 10-20 cm	589.6
354-U1450A-123X-CCW, 30-40 cm	590.5
354-U1450A-124F-1W, 3-4 cm	599.0
354-U1450A-124F-1W, 37-38 cm	599.4
354-U1450A-126F-1W, 3-4 cm	608.5
354-U1450A-128F-1W, 28-29 cm	618.3
354-U1450A-128F-1W, 65-66 cm	618.7
354-U1450A-128F-1W, 86-87 cm	618.9
354-U1450A-128F-2W, 5-6 cm	619.0
354-U1450A-128F-2W, 27-28 cm	619.2
354-U1450A-128F-CCW, 8-9 cm	619.6
354-U1450A-129X-CCW, 10-11 cm	619.9
354-U1450A-130F-1W, 1-2 cm	628.2
354-U1450A-130F-1W, 18-19 cm	628.4
354-U1450A-130F-1W, 66-67 cm	628.9
354-U1450A-132X-1W, 8-9 cm	637.8
354-U1450A-133X-CCW, 15-155 cm	648.0
354-U1450A-134X-1W, 11-12 cm	657.3
354-U1450A-134X-1W, 58-59 cm	657.8
354-U1450A-134X-1W, 90-91 cm	658.1
354-U1450A-134X-2W, 9-10 cm	658.4
354-U1450A-134X-2W, 30-31 cm	658.6
354-U1450A-134X-2W, 48-49 cm	658.8
354-U1450A-134X-CCW, 11-115 cm	659.1
354-U1450A-136X-1W, 12-13 cm	676.8
354-U1450A-136X-1W, 47-48 cm	677.2
354-U1450A-136X-1W, 104-105 cm	677.7
354-U1450A-136X-2W, 19-195 cm	678.2
354-U1450A-137F-1W, 10-11 cm	686.4
354-U1450A-137F-1W, 32-33 cm	686.6
354-U1450A-137F-1W, 81-82 cm	687.1

Table SV-4. Predicted age model of the site U1450. The median ages and median accumulation rates are presented with their uncertainties. 0-175.9 m CSF-A is from Reilly, 2018. Lithology is from France-Lanord et al., 2016.

Table SV-4 (…/…)

Hole	Core	Bottom of core depth CSF-A (m)	Lithology	Median age (Ma)	Median - 2 sigma age (Ma)	Median - 1 sigma age (Ma)	Median + 1 sigma age (Ma)	Median + 2 sigma age	Median accumulation rate (cm/kyr)	Median - 2 sigma acc. rate (Ma)	Median - 1 sigma acc. rate (Ma)	Median + 1 sigma acc. rate (Ma)	Median + 2 sigma acc. Rate	Reference
A	1H	8.5	hemipelagic clay	0.254	0.251	0.252	0.256	0.257	-	-	-	-	-	Reilly 2018
A	2H	11.7	clay	0.257	0.253	0.255	0.258	0.260	-	-	-	-	-	Reilly 2018
A	3H	20.2	sand	0.269	0.261	0.264	0.274	0.280	-	-	-	-	-	Reilly 2018
A	4F	24.9	sand	0.296	0.291	0.293	0.300	0.303	-	-	-	-	-	Reilly 2018
A	5F	29.6	sand	0.299	0.293	0.295	0.302	0.306	-	-	-	-	-	Reilly 2018
A	6F	34.3	sand	0.299	0.294	0.296	0.303	0.307	-	-	-	-	-	Reilly 2018
A	7F	39.0	sand	0.301	0.294	0.297	0.305	0.308	-	-	-	-	-	Reilly 2018
A	8F	43.7	sand	0.305	0.298	0.301	0.310	0.314	-	-	-	-	-	Reilly 2018
A	91	48.5	sand	0.306	0.299	0.302	0.311	0.315	-	-	-	-	-	Reilly 2018
A	10F	53.2	sand	0.310	0.302	0.306	0.316	0.321	-	-	-	-	-	Reilly 2018
A	11F	57.9	sand	0.312	0.303	0.307	0.318	0.323	-	-	-	-	-	Reilly 2018
A	12F	62.6	sand	0.322	0.311	0.316	0.328	0.335	-	-	-	-	-	Reilly 2018
A	131	67.4	sand	0.324	0.314	0.318	0.330	0.337	-	-	-	-	-	Reilly 2018
A	14F	72.1	sand	0.348	0.338	0.343	0.353	0.359	-	-	-	-	-	Reilly 2018
A	151	76.9	hemipelagic clay	0.378	0.367	0.373	0.383	0.388	-	-	-	-	-	Reilly 2018
A	16F	81.6	sand	0.384	0.373	0.379	0.389	0.394	-	-	-	-	-	Reilly 2018
A	17F	86.3	clay	0.388	0.377	0.383	0.393	0.397	-	-	-	-	-	Reilly 2018
A	18F	91.0	sand	0.393	0.381	0.387	0.398	0.402	-	-	-	-	-	Reilly 2018
A	191	95.8	sand	0.397	0.385	0.392	0.402	0.406	-	-	-	-	-	Reilly 2018
A	20F	99.8	clay	0.417	0.403	0.410	0.425	0.430	-	-	-	-	-	Reilly 2018
A	21F	104.5	sand	0.440	0.420	0.430	0.449	0.457	-	-	-	-	-	Reilly 2018
A	22H	106.5	sand	0.464	0.446	0.455	0.473	0.481	-	-	-	-	-	Reilly 2018
A	231	109.2	sand	0.478	0.458	0.469	0.485	0.492	-	-	-	-	-	Reilly 2018
A	24H	118.7	sand	0.486	0.468	0.478	0.493	0.500	-	-	-	-	-	Reilly 2018
A	25F	123.4	sand	0.571	0.555	0.564	0.576	0.581	-	-	-	-	-	Reilly 2018
A	261	128.2	silt	0.593	0.574	0.586	0.599	0.605	-	-	-	-	-	Reilly 2018
A	27F	132.9	silt	0.600	0.581	0.592	0.609	0.620	-	-	-	-	-	Reilly 2018
A	28F	137.6	silt	0.608	0.592	0.600	0.645	0.662	-	-	-	-	-	Reilly 2018
A	291	142.4	sand	0.671	0.614	0.630	0.680	0.688	-	-	-	-	-	Reilly 2018
A	30F	147.1	sand	0.694	0.624	0.643	0.704	0.712	-	-	-	-	-	Reilly 2018
A	311	151.9	sand	0.702	0.629	0.653	0.712	0.720	-	-	-	-	-	Reilly 2018
A	32F	156.6	sand	0.729	0.659	0.692	0.740	0.749	-	-	-	-	-	Reilly 2018
A	331	161.4	sand	0.738	0.668	0.701	0.750	0.760	-	-	-	-	-	Reilly 2018
A	34F	166.1	hemipelagic clay	0.833	0.817	0.825	0.841	0.849	-	-	-	-	-	Reilly 2018
A	351	170.9	hemipelagic clay	0.913	0.905	0.909	0.918	0.923	-	-	-	-	-	Reilly 2018
A	36F	175.6	hemipelagic clay	1.201	1.195	1.198	1.204	1.206	-	-	-	-	-	Reilly 2018
A	36F	175.9	hemipelagic clay	1.196	1.192	1.193	1.205	1.215	2.8	1.0	1.5	4.0	4.5	This study

Table SV-4 (…/…)

Hole	Core	Bottom of core depth CSF-A (m)	Lithology	Median age (Ma)	Median - 2 sigma age (Ma)	Median - 1 sigma age (Ma)	Median + 1 sigma age (Ma)	Median + 2 sigma age	Median accumulation rate (cm/kyr)	Median - 2 sigma acc. rate (Ma)	Median - 1 sigma acc. rate (Ma)	Median + 1 sigma acc. rate (Ma)	Median + 2 sigma acc. Rate	Reference
A	371	180.4	hemipelagic clay	1.449	1.299	1.330	1.609	1.677	1.8	0.9	1.1	3.4	4.4	This study
A	38F	185.1	clay	1.456	1.304	1.338	1.615	1.684	115.8	13.9	41.4	190.4	220.0	This study
A	391	189.9	clay	1.463	1.310	1.346	1.622	1.692	114.5	13.8	40.2	189.3	220.1	This study
A	40F	194.6	sand	1.471	1.316	1.353	1.629	1.700	113.1	14.1	41.1	188.8	220.1	This study
A	411	199.4	sand	1.479	1.322	1.361	1.637	1.708	112.5	14.0	40.3	188.1	219.4	This study
A	42F	204.1	clay	1.486	1.328	1.368	1.644	1.716	114.7	14.0	41.2	189.7	219.2	This study
A	431	208.9	sand	1.494	1.334	1.375	1.651	1.725	115.9	13.5	40.6	190.5	218.5	This study
A	44F	213.6	sand	1.500	1.340	1.382	1.658	1.732	112.5	14.2	40.9	188.0	218.5	This study
A	451	218.4	hemipelagic clay	1.816	1.527	1.655	1.969	2.143	1.7	0.9	1.1	3.1	4.2	This study
A	46F	223.1	sand	1.824	1.533	1.662	1.975	2.150	113.1	13.6	39.4	188.8	218.8	This study
A	471	227.9	sand	1.831	1.542	1.669	1.983	2.159	114.2	13.5	39.9	187.6	218.0	This study
A	48F	232.6	sand	1.837	1.548	1.677	1.989	2.166	114.4	13.8	41.8	188.3	218.2	This study
A	491	237.4	sand	1.844	1.556	1.684	1.997	2.174	112.7	14.2	40.5	187.0	217.7	This study
A	50F	242.1	sand	1.852	1.562	1.691	2.004	2.180	111.7	14.3	42.8	186.9	217.7	This study
A	511	246.9	hemipelagic clay	2.143	1.921	2.001	2.323	2.509	1.6	0.9	1.0	3.1	4.1	This study
A	52F	251.6	clay	2.150	1.929	2.008	2.329	2.516	111.8	13.9	41.0	186.8	217.0	This study
A	531	256.4	clay	2.157	1.937	2.016	2.338	2.524	112.3	13.8	40.5	185.2	216.5	This study
A	54F	256.7	clay	2.157	1.937	2.016	2.338	2.524	114.5	14.3	43.5	187.3	217.0	This study
A	54F	261.1	clay	2.165	1.943	2.023	2.345	2.532	113.4	13.7	40.3	186.7	217.1	This study
A	551	265.9	silt	2.172	1.949	2.030	2.352	2.538	114.8	13.9	41.6	186.9	216.4	This study
A	56F	270.6	silt	2.179	1.956	2.038	2.359	2.550	111.5	13.9	40.2	185.7	216.6	This study
A	571	275.4	silt	2.186	1.962	2.045	2.368	2.556	114.8	13.9	40.5	185.8	215.9	This study
A	58F	280.1	silt	2.194	1.970	2.052	2.374	2.564	112.8	13.6	42.2	186.6	215.8	This study
A	591	284.9	clay	2.201	1.978	2.059	2.382	2.569	111.5	13.7	40.9	186.3	215.3	This study
A	60F	289.6	clay	2.208	1.983	2.067	2.390	2.577	112.4	13.6	40.8	186.7	215.6	This study
A	611	294.4	clay	2.216	1.991	2.074	2.397	2.585	111.6	13.8	40.0	185.0	214.8	This study
A	62F	299.1	clay	2.223	1.998	2.082	2.406	2.593	113.0	13.4	39.9	185.8	214.9	This study
A	631	303.9	silt	2.231	2.005	2.090	2.413	2.602	112.8	13.5	40.8	183.9	214.5	This study
A	64F	308.6	silt	2.239	2.012	2.097	2.420	2.608	112.5	14.5	42.7	185.2	214.1	This study
A	651	313.4	sand	2.245	2.019	2.105	2.428	2.614	111.0	13.0	39.3	182.8	213.7	This study
A	66F	318.1	sand	2.253	2.025	2.112	2.435	2.623	112.4	13.8	41.0	183.7	213.9	This study
A	671	322.9	sand	2.260	2.032	2.119	2.442	2.633	111.6	14.2	41.2	184.3	213.3	This study
A	68F	327.6	sand	2.267	2.040	2.127	2.448	2.640	112.7	14.2	40.0	184.8	213.2	This study
A	691	332.4	sand	2.275	2.047	2.134	2.457	2.648	111.2	13.1	39.6	183.2	212.7	This study
A	70F	337.1	sand	2.283	2.052	2.142	2.464	2.655	110.6	13.8	42.0	182.5	212.8	This study
A	711	341.9	sand	2.290	2.060	2.149	2.471	2.664	111.0	13.4	40.0	181.9	212.8	This study
A	72F	346.6	sand	2.298	2.067	2.157	2.479	2.670	112.7	13.5	40.5	183.3	212.7	This study
A	731	351.4	hemipelagic clay	2.609	2.322	2.433	2.803	3.016	1.7	0.9	1.0	3.1	3.9	This study
A	74F	351.9	sand	2.610	2.323	2.433	2.804	3.017	112.6	13.8	43.0	183.3	211.5	This study
A	74F	356.1	sand	2.616	2.328	2.440	2.810	3.024	111.5	14.0	40.3	182.8	212.3	This study
A	751	360.9	silt	2.624	2.336	2.448	2.817	3.033	111.5	13.2	39.7	183.1	211.7	This study
A	76F	365.6	silt	2.631	2.345	2.455	2.825	3.041	108.8	13.4	39.3	182.2	211.5	This study

Table SV-4 (…/…)

Hole	Core	Bottom of core depth CSF-A (m)	Lithology	Median age (Ma)	Median - 2 sigma age (Ma)	Median - 1 sigma age (Ma)	Median + 1 sigma age (Ma)	Median + 2 sigma age	Median accumulation rate (cm/kyr)	Median - 2 sigma acc. rate (Ma)	Median - 1 sigma acc. rate (Ma)	Median + 1 sigma acc. rate (Ma)	Median + 2 sigma acc. Rate	Reference
A	771	370.4	sand	2.639	2.354	2.462	2.834	3.048	109.9	13.1	41.3	182.7	211.0	This study
A	78F	375.1	sand	2.646	2.361	2.469	2.842	3.058	109.9	13.6	40.2	184.0	211.6	This study
A	791	379.9	sand	2.654	2.369	2.477	2.849	3.065	109.1	13.1	38.6	183.1	211.0	This study
A	80F	384.6	sand	2.662	2.377	2.484	2.856	3.072	109.1	13.7	40.5	182.2	210.9	This study
A	81F	385.3	hemipelagic clay	2.698	2.414	2.522	2.898	3.110	2.3	0.9	1.2	3.5	4.0	This study
A	81F	389.3	hemipelagic clay	2.938	2.600	2.753	3.142	3.365	1.9	0.8	1.1	3.2	3.9	This study
A	82F	390.3	hemipelagic clay	2.990	2.654	2.805	3.196	3.416	2.3	0.9	1.2	3.5	4.0	This study
A	82F	392.2	hemipelagic clay	3.094	2.752	2.909	3.298	3.521	2.2	0.9	1.2	3.4	4.0	This study
A	82F	394.0	hemipelagic clay	3.191	2.842	3.009	3.401	3.628	2.2	0.9	1.2	3.4	3.9	This study
A	83F	398.7	sand	3.199	2.852	3.017	3.408	3.634	108.9	13.5	39.3	180.0	209.8	This study
A	84F	403.4	clay	3.207	2.858	3.025	3.416	3.640	109.7	13.8	40.6	181.1	209.6	This study
A	851	408.2	sand	3.215	2.865	3.032	3.423	3.649	109.9	13.6	39.6	180.7	209.9	This study
A	86F	412.9	sand	3.222	2.872	3.039	3.430	3.654	109.1	13.4	40.0	180.9	209.5	This study
A	871	417.7	sand	3.230	2.880	3.046	3.437	3.662	110.7	13.3	39.9	181.8	209.1	This study
A	88F	422.4	sand	3.238	2.886	3.054	3.444	3.668	111.6	14.2	40.3	181.0	209.0	This study
A	891	427.2	sand	3.245	2.893	3.061	3.452	3.676	110.6	13.6	39.9	180.2	208.8	This study
A	90F	431.9	sand	3.254	2.899	3.069	3.459	3.685	110.7	13.2	39.5	180.7	208.8	This study
A	911	436.7	hemipelagic clay	3.551	3.225	3.380	3.772	4.011	1.7	0.8	1.0	3.0	3.8	This study
A	92F	436.8	hemipelagic clay	3.559	3.232	3.387	3.778	4.019	2.4	0.9	1.3	3.4	3.9	This study
A	92F	438.0	hemipelagic clay	3.619	3.293	3.446	3.841	4.083	2.3	0.8	1.2	3.4	3.9	This study
A	92F	441.4	hemipelagic clay	3.822	3.560	3.645	4.044	4.290	1.9	0.8	1.1	3.2	3.9	This study
A	931	446.2	silt	3.829	3.569	3.652	4.052	4.299	108.7	13.2	38.1	178.9	208.0	This study
A	94F	450.9	silt	3.837	3.576	3.660	4.060	4.308	109.9	12.9	39.5	180.0	208.2	This study
A	951	455.7	clay	3.844	3.584	3.667	4.067	4.314	109.6	13.2	39.2	179.5	207.4	This study
A	96F	460.4	clay	3.851	3.591	3.675	4.074	4.322	109.6	13.2	40.3	179.0	207.3	This study
A	971	465.2	sand	3.858	3.597	3.683	4.081	4.327	110.4	13.5	39.4	179.7	207.2	This study
A	98F	469.9	sand	3.866	3.605	3.690	4.089	4.334	111.1	13.7	41.5	179.4	207.5	This study
A	991	474.7	sand	3.874	3.612	3.698	4.097	4.339	110.6	13.5	40.7	179.7	206.8	This study
A	100F	479.4	sand	3.889	3.624	3.713	4.113	4.356	62.4	6.3	15.7	165.1	205.4	This study
A	1011	484.2	sand	3.906	3.638	3.730	4.130	4.371	60.9	6.3	15.7	163.7	203.8	This study
A	102F	488.9	sand	3.922	3.650	3.746	4.146	4.388	63.9	6.4	16.0	165.9	204.9	This study
A	1031	493.7	sand	3.938	3.664	3.763	4.162	4.410	62.8	6.3	15.4	164.4	203.8	This study
A	104F	498.4	sand	3.954	3.680	3.778	4.179	4.424	63.0	6.3	15.9	163.5	204.2	This study
A	1051	503.2	silt	3.971	3.691	3.794	4.196	4.443	61.6	6.4	15.7	164.0	203.2	This study
A	106F	507.9	silt	3.987	3.705	3.809	4.211	4.460	62.8	6.4	15.8	163.6	203.4	This study
A	1071	512.7	sand	4.004	3.721	3.825	4.228	4.473	59.9	6.3	15.7	164.0	204.0	This study
A	108F	517.4	sand	4.022	3.735	3.842	4.245	4.489	58.7	6.2	15.5	161.6	202.7	This study

Table SV-4 (…/…)

Hole	Core	Bottom of core depth CSF-A (m)	Lithology	Median age (Ma)	Median - 2 sigma age (Ma)	Median - 1 sigma age (Ma)	Median + 1 sigma age (Ma)	Median + 2 sigma age	Median accumulation rate (cm/kyr)	Median - 2 sigma acc. rate (Ma)	Median - 1 sigma acc. rate (Ma)	Median + 1 sigma acc. rate (Ma)	Median + 2 sigma acc. Rate	Reference
A	1091	522.2	sand	4.038	3.748	3.858	4.262	4.505	61.6	6.3	15.6	162.4	203.4	This study
A	110F	523.0	sand	4.040	3.751	3.861	4.265	4.507	66.4	6.7	16.4	162.3	203.1	This study
A	110F	526.9	sand	4.053	3.763	3.874	4.277	4.520	63.0	6.5	15.8	162.0	202.5	This study
A	1111	531.7	sand	4.069	3.775	3.891	4.295	4.535	62.3	6.3	15.9	162.1	203.1	This study
A	112F	536.4	sand	4.086	3.790	3.905	4.309	4.557	62.5	6.3	16.0	160.8	201.1	This study
A	1131	541.2	hemipelagic clay	4.332	3.939	4.118	4.576	4.831	2.3	0.8	1.2	7.6	28.3	This study
A	114F	541.4	hemipelagic clay	4.340	3.948	4.126	4.583	4.839	3.0	0.9	1.5	17.5	29.7	This study
A	115F	546.1	hemipelagic clay	4.578	4.151	4.352	4.830	5.088	2.3	0.8	1.2	7.7	28.2	This study
A	1161	550.9	hemipelagic clay	4.820	4.424	4.586	5.072	5.324	2.3	0.8	1.1	7.0	28.3	This study
A	117F	553.3	hemipelagic clay	4.927	4.559	4.694	5.180	5.423	2.6	0.8	1.3	13.7	28.9	This study
A	117F	555.6	hemipelagic clay	5.027	4.659	4.794	5.276	5.521	2.7	0.8	1.3	13.9	29.0	This study
A	118F	560.3	sand	5.044	4.675	4.808	5.292	5.539	61.6	6.2	15.5	160.9	201.9	This study
A	119F	561.3	sand	5.047	4.679	4.811	5.296	5.543	65.5	6.6	16.6	162.0	201.4	This study
A	120X	569.9	hemipelagic clay	5.493	5.108	5.293	5.686	5.900	2.2	0.9	1.2	3.6	25.9	This study
A	121X	579.6	silt	5.527	5.141	5.330	5.717	5.927	59.7	6.2	15.2	160.1	200.8	This study
A	122X	589.4	clay	5.561	5.180	5.366	5.749	5.955	60.3	6.2	15.4	159.4	200.4	This study
A	123X	599.0	sand	5.594	5.211	5.405	5.778	5.984	60.4	6.3	15.7	158.5	199.6	This study
A	124F	603.7	sand	5.610	5.227	5.420	5.794	5.998	61.3	6.2	15.3	157.5	199.3	This study
A	1251	608.5	silt	5.626	5.245	5.438	5.809	6.018	64.3	6.3	16.0	159.9	199.1	This study
A	126F	613.2	silt	5.641	5.262	5.456	5.822	6.030	64.9	6.2	15.9	160.2	199.7	This study
A	1271	618.0	hemipelagic clay	5.841	5.684	5.747	5.989	6.194	2.5	0.8	1.2	11.0	28.4	This study
A	128F	619.8	sand	5.847	5.690	5.753	5.995	6.201	60.8	6.4	16.1	158.3	198.4	This study
A	129X	628.2	sand	5.873	5.746	5.780	6.023	6.221	60.7	6.2	15.8	158.5	198.6	This study
A	129X	628.2	sand	5.873	5.746	5.780	6.023	6.221	67.1	7.0	16.7	161.3	198.8	This study
A	130F	632.9	sand	5.888	5.755	5.796	6.039	6.236	67.4	6.7	16.9	162.7	198.7	This study
A	1311	637.7	clay	5.904	5.766	5.812	6.055	6.250	67.6	6.9	16.8	161.2	198.6	This study
A	132X	647.4	clay	5.931	5.782	5.840	6.082	6.280	74.5	8.0	18.4	164.4	198.0	This study
A	133X	657.2	hemipelagic clay	6.110	5.883	5.952	6.297	6.488	11.0	2.0	3.0	24.7	30.2	This study
A	134X	658.4	hemipelagic clay	6.154	5.940	5.997	6.341	6.534	3.0	0.9	1.6	17.6	29.1	This study
A	134X	660.5	hemipelagic clay	6.223	5.978	6.064	6.414	6.600	3.2	1.0	1.7	19.8	29.5	This study
A	134X	667.0	hemipelagic clay	6.367	6.052	6.186	6.556	6.724	8.9	1.6	2.6	24.3	30.0	This study
A	135X	676.7	hemipelagic clay	6.521	6.158	6.328	6.704	6.821	14.0	2.1	3.2	25.6	30.2	This study
A	136X	686.3	silt	6.548	6.185	6.355	6.733	6.839	75.6	7.8	18.9	163.2	197.2	This study

Table SV-4 (…/…)

Hole	Core	Bottom of core depth CSF-A (m)	Lithology	Median age (Ma)	Median - 2 sigma age (Ma)	Median - 1 sigma age (Ma)	Median + 1 sigma age (Ma)	Median + 2 sigma age	Median accumulation rate (cm/kyr)	Median - 2 sigma acc. rate (Ma)	Median - 1 sigma acc. rate (Ma)	Median + 1 sigma acc. rate (Ma)	Median + 2 sigma acc. Rate	Reference
A	137F	687.4	silt	6.552	6.188	6.359	6.736	6.843	66.5	6.4	16.4	159.7	196.5	This study
B	10R	695.4	limestone	6.710	6.309	6.514	6.843	6.901	12.2	1.8	2.9	25.0	30.0	This study
B	11R	700.5	clay	6.727	6.326	6.529	6.858	6.910	74.3	7.4	18.3	162.9	196.4	This study
B	11R	705.1	clay	6.742	6.341	6.543	6.873	6.926	66.8	6.7	16.5	158.6	196.2	This study
B	12R	714.8	clay	6.771	6.371	6.571	6.900	6.980	71.7	7.2	17.6	160.4	196.2	This study
B	13R	724.5	clay	6.799	6.401	6.600	6.929	7.029	70.6	7.0	17.3	160.6	196.2	This study
B	14R	734.2	silt	6.828	6.423	6.629	6.959	7.073	69.3	7.2	17.5	160.0	195.5	This study
B	15R	743.9	silt	6.857	6.445	6.658	6.993	7.115	71.3	7.0	17.7	160.0	194.4	This study
B	16R	753.6	silt	6.885	6.477	6.687	7.025	7.157	67.4	6.9	16.8	158.5	194.0	This study
B	17R	763.3	clay	6.913	6.508	6.717	7.055	7.195	73.4	7.1	17.6	160.3	194.3	This study
B	18R	773.0	clay	6.943	6.536	6.745	7.084	7.237	68.3	7.1	17.2	156.6	193.9	This study
B	19R	782.7	limestone	7.166	6.710	6.950	7.344	7.417	3.6	1.7	2.5	22.1	29.1	This study
B	20R	792.4	clay	7.198	6.740	6.979	7.376	7.464	63.9	6.4	15.9	156.5	193.4	This study
B	21R	802.1	clay	7.231	6.770	7.010	7.411	7.518	60.7	6.4	15.6	153.6	192.8	This study
B	22R	811.9	clay	7.262	6.800	7.038	7.445	7.570	64.7	6.4	16.2	156.2	192.8	This study

Table SVI-1. Sample information, dating, 10Be and Sr-Nd isotopic results.

The table includes all measured Bengal Fan and Lower Meghna samples. Sample information (col. A to L) includes the geographic coordinates, the drilling core depth below sea-floor (CSF-A) and the ages determined with distinct previous models. ^{10}Be data (col. N to AI) presents the fractions selected for measurement (col. N-O), the mass of quartz decontaminated from the atmospheric contribution, the measurements of ^{9}Be (carrier + potential native ^{9}Be) by SARM (col. P to V), the measurements of ^{10}Be/^{9}Be at ASTER (col. W to AA), the 10Be paleoconcentrations computed with the ages (col. AB-AF) and the apparent Himalayan erosion rates (AH-AI). The nominal concentration of the carrier is [^{9}Be] = 2020±83 ppm. The measured ^{9}Be concentrations are on average 15% lower than the predicted concentrations, because of the potential loss of Be after addition of the ^{9}Be carrier, during dissolution and evaporation. The ^{10}Be/^{9}Be results were corrected from the average blank (Table S3). The 1-σ uncertainty for 10Be results include a correction obtained with the average difference between the results presented in Table S1 and the duplicate measurements presented in Table S2. Apparent Himalayan erosion rates were computed with the production rates of the Himalayan part of the Lower Meghna basin and by removing the Indian cratonic contribution. Sr-Nd isotopic measurement and f_G computing results are presented col. AK to AR. ^{143}Nd/^{144}Nd are reported as εNd(0), using CHUR(0) = 0.512638 (Goldstein et al., 1984). For the Lower Meghna sand, Sr-Nd data are unpublished data from France-Lanord and Galy and measured similarly than our data, except for the sample BR 446, which is from Lupker and France-Lanord and was prepared with HCl leaching. The computing results for the test of the climate forcing hypothesis are in col. AT to AW.

Table SVI-1. (…/…)

Sample information

		Localisation				Age		
Site	#	Latitude °N	Longitude °E	Center Depth CSF-A (m)	Date Type	Age (Ma)	1σ	Age model reference
Bengal fan sands								
DSF: Drilling depth below sea-floor								
Exp. 353, 14°N								
U1444	353-U1444A-6H-1W, 100-150 cm.	14.00	84.83	46.4	Sand	0.19	0.025	Clemens et al., 2016
	353-U1444A-7H-5W, 100-150 cm.			61.9	Sand	0.20	0.025	Clemens et al., 2016
	353-U1444A-9H-5W, 75-130 cm.			79.6	Sand	0.26	0.025	Clemens et al., 2016
	353-U1444A-11H-6W, 87-150 cm.			93.9	Sand	0.31	0.025	Clemens et al., 2016
	353-U1444A-24F-3W, 0-56, 65-110 cm.			208.5	Sand	3.71	0.125	Clemens et al., 2016
Exp. 354, 8°N								
U1450	354-U1450A-3H-4W, 50-120 cm.	8.01	87.67	16.0	Sand	0.26	0.003	Reilly, 2018; Weber and Reilly, 2018
	354-U1450A-8F-2W, 1-60 cm.			40.8	Sand	0.30	0.004	Reilly, 2018; Weber and Reilly, 2018
	354-U1450A-14F-2W, 90-150 cm.			70.1	Sand	0.33	0.006	Reilly, 2018; Weber and Reilly, 2018
	354-U1450A-25F-1W, 50-100 cm.			119.5	Sand	0.49	0.007	Reilly, 2018; Weber and Reilly, 2018
	354-U1450A-32F-3W, 24-84 cm.			155.4	Sand	0.71	0.026	Reilly, 2018; Weber and Reilly, 2018
	354-U1450A-40F-2W, 0-30 cm.			191.6	Sand	1.49	0.138	Lenard et al., submitted
	354-U1450A-44F-3W, 40-100 cm.			212.6	Sand	1.52	0.138	Lenard et al., submitted
	354-U1450A-50F-2W, 86-116 cm.			239.9	Sand	1.84	0.157	Lenard et al., submitted
	354-U1450A-83F-3W, 113-147 cm.			398.2	Sand	3.21	0.196	Lenard et al., submitted
	354-U1450A-90F-3W, 106-136 cm.			431.0	Sand	3.26	0.195	Lenard et al., submitted
	354-U1450A-100F-3W, 28-88 cm.			477.9	Sand	3.91	0.200	Lenard et al., submitted
	354-U1450A-110F-1W, 79-84 cm.			523.0	Sand	4.06	0.202	Lenard et al., submitted
	354-U1450A-124F-3W, 20-80 cm.			602.2	Sand	5.60	0.187	Lenard et al., submitted

Table SVI-1. (…/…)

Sample information

		Localisation				Age		
Site	#	Latitude °N	Longitude °E	Center Depth CSF-A (m)	Date	Type	Age (Ma)	1σ	Age model reference
	354-U1450A-130F-3W, 0-51 cm.			630.8		Sand	5.91	0.122	Lenard et al., submitted
U1451	354-U1451A-9H-2W, 120-145 cm.	8.01	88.74	55.1		Sand	0.32	0.003	Reilly, 2018; Weber and Reilly, 2018
	354-U1451A-12F-3W, 90-121 cm.			69.0		Sand	0.64	0.001	Reilly, 2018; Weber and Reilly, 2018
	354-U1451A-22H-5W, 92-126 cm.			118.1		Sand	2.39	0.025	France-Lanord et al., 2016
	354-U1451A-31F-2W, 44-116 cm.			199.8		Sand	6.21	0.100	Blum et al., 2018
	354-U1451A-39F-3W, 81-111 cm.			239.5		Sand	6.63	0.100	Blum et al., 2018
U1454	354-U1454B-4H-4W, 0-60 cm.	8.01	85.85	29.2		Sand	0.07	0.010	Reilly, 2018; Weber and Reilly, 2018
	354-U1454B-6F-3W, 5-65 cm.			37.6		Sand	0.13	0.010	Reilly, 2018; Weber and Reilly, 2018
	354-U1454B-25F-2W, 54-114 cm.			126.4		Sand	0.30	0.004	Reilly, 2018; Weber and Reilly, 2018
	354-U1454B-32F-2W, 80-130 cm.			159.4		Sand	1.80	0.250	France-Lanord et al., 2016
Lower Meghna									
Bedload									
Lower Meghna, Chor Fasson	BGP 34	22.19	90.83			Bedload			
Lower Meghna, Bhola	BR219	22.82	90.72		18/07/2002	Bedload			
Lower Meghna, Bhola	BR446	22.82	90.72		18/07/2004	Bedload			
Lower Meghna, Daulatkhan	BR8230	22.59	90.76		03/09/2008	Bedload			
Padma, Mawa	BR529	23.46	90.24		24/07/2005	Bedload			
Padma, Mawa	BR724	23.46	90.24		19/08/2007	Bedload			

Table SVI-1. (…/…)

^{10}Be data

#	Mass of decontaminated quartz				^{9}Be data					^{10}Be/^{9}Be measurements				
	75-125 µm fraction (g)	125-250 µm fraction (g)	Total mass (g)	1 σ (g)	Carrier mass added (mg)	^{9}Be added before dissolution (atom)	1 σ (atom)	^{9}Be measured after evaporation (atom)	1 σ (atom)	Hit count	^{10}Be/^{9}Be	1 σ	^{10}Be/^{9}Be (blank corrected)	1 σ
Bengal fan sands														
DSF: Drilling depth below sea-floor														
Exp. 353, 14°N														
353-U1444A-6H-1W, 100-150 cm.	-	34.9	34.9	0.5	101.65	1.372E+19	2.82E+17	1.096E+19	1.37E+18	121	6.951E-14	7.121E-15	6.424E-14	7.306E-15
353-U1444A-7H-5W, 100-150 cm.	-	36.7	36.7	0.6	101.99	1.376E+19	2.83E+17	1.114E+19	1.39E+18	144	9.038E-14	8.201E-15	8.512E-14	8.362E-15
353-U1444A-9H-5W, 75-130 cm.	-	32.5	32.5	0.5	101.82	1.374E+19	2.82E+17	8.913E+18	1.11E+18	98	7.301E-14	1.008E-14	6.775E-14	1.021E-14
353-U1444A-11H-6W, 87-150 cm.	-	38.3	38.3	0.6	102.08	1.377E+19	2.83E+17	1.135E+19	1.42E+18	95	7.923E-14	8.634E-15	7.397E-14	8.787E-15
353-U1444A-24F-3W, 0-56, 65-110 cm.	-	135.2	135.2	2.0	101.36	1.368E+19	2.81E+17	1.265E+19	1.58E+18	27	4.835E-14	9.678E-15	4.308E-14	9.815E-15
Exp. 354, 8°N														
354-U1450A-3H-4W, 50-120 cm.	-	45.0	45.0	0.7	101.90	1.375E+19	2.82E+17	1.162E+19	1.45E+18	64	6.987E-14	9.086E-15	6.461E-14	9.232E-15
354-U1450A-8F-2W, 1-60 cm.	-	42.6	42.6	0.6	103.15	1.392E+19	2.86E+17	1.238E+19	1.55E+18	105	7.656E-14	7.538E-15	7.129E-14	7.713E-15
354-U1450A-14F-2W, 90-150 cm.	-	37.9	37.9	0.6	102.72	1.386E+19	2.85E+17	1.202E+19	1.50E+18	240	7.227E-14	4.814E-15	6.701E-14	5.083E-15
354-U1450A-25F-1W, 50-100 cm.	-	45.3	45.3	0.7	102.55	1.384E+19	2.84E+17	9.685E+18	1.21E+18	61	5.236E-14	6.739E-15	4.710E-14	6.934E-15
354-U1450A-32F-3W, 24-84 cm.	-	22.5	22.5	0.3	102.43	1.382E+19	2.84E+17	1.139E+19	1.42E+18	45	3.153E-14	4.716E-15	2.627E-14	4.991E-15
354-U1450A-40F-2W, 0-30 cm.	-	31.8	31.8	0.5	102.49	1.383E+19	2.84E+17	1.312E+19	1.64E+18	211	3.152E-14	2.209E-15	2.626E-14	2.747E-15
354-U1450A-44F-3W, 40-100 cm.	-	-	-	-	-	-	-	-	-	-	-	-	-	-
354-U1450A-50F-2W, 86-116 cm.	6.11	25.0	31.1	0.5	101.68	1.372E+19	2.82E+17	1.132E+19	1.41E+18	23	2.568E-14	5.813E-15	2.042E-14	6.038E-15
354-U1450A-83F-3W, 113-147 cm.	40.18	50.4	90.6	1.4	102.44	1.382E+19	2.84E+17	1.234E+19	1.54E+18	25	7.149E-14	1.53E-14	6.623E-14	1.539E-14
354-U1450A-90F-3W, 106-136 cm.	-	70.5	70.5	1.1	99.87	1.348E+19	2.77E+17	1.149E+19	1.44E+18	35	7.002E-14	1.187E-14	6.476E-14	1.198E-14
354-U1450A-100F-3W, 28-88 cm.	42.88	76.7	119.5	1.8	102.18	1.379E+19	2.83E+17	1.295E+19	1.62E+18	25	2.372E-14	4.814E-15	1.846E-14	5.083E-15
354-U1450A-110F-1W, 79-84 cm.	-	156.5	156.5	2.3	101.08	1.364E+19	2.80E+17	1.358E+19	1.70E+18	18	7.746E-14	1.828E-14	7.220E-14	1.835E-14
354-U1450A-124F-3W, 20-80 cm.	30.06	132.8	162.9	2.4	102.39	1.382E+19	2.84E+17	1.31E+19	1.64E+18	16	2.984E-14	8.238E-15	2.457E-14	8.399E-15
354-U1450A-130F-3W, 0-51 cm.	-	-	-	-	-	-	-	-	-	-	-	-	-	-
354-U1451A-9H-2W, 120-145 cm.	-	66.6	66.6	1.0	102.44	1.382E+19	2.84E+17	1.249E+19	1.56E+18	32	1.332E-13	2.54E-14	1.280E-13	2.546E-14
354-U1451A-12F-3W, 90-121 cm.	-	65.1	65.1	1.0	102.01	1.376E+19	2.83E+17	1.204E+19	1.51E+18	37	1.078E-13	1.778E-14	1.025E-13	1.785E-14
354-U1451A-22H-5W, 92-126 cm.	-	60.7	60.7	0.9	100.90	1.362E+19	2.80E+17	1.169E+19	1.46E+18	15	2.073E-14	5.358E-15	1.547E-14	5.601E-15
354-U1451A-31F-2W, 44-116 cm.	-	358.4	358.4	5.4	100.97	1.362E+19	2.80E+17	1.492E+19	1.86E+18	15	4.212E-14	1.096E-14	3.686E-14	1.108E-14
354-U1451A-39F-3W, 81-111 cm.	-	-	-	-	-	-	-	-	-	-	-	-	-	-
354-U1454B-4H-4W, 0-60 cm.	-	41.6	41.6	0.6	101.95	1.376E+19	2.83E+17	1.064E+19	1.33E+18	268	1.071E-13	7.627E-15	1.018E-13	7.800E-15
354-U1454B-6F-3W, 5-65 cm.	-	41.5	41.5	0.6	102.35	1.381E+19	2.84E+17	1.001E+19	1.25E+18	272	9.655E-14	5.995E-15	9.129E-14	6.213E-15
354-U1454B-25F-2W, 54-114 cm.	-	42.0	42.0	0.6	102.44	1.382E+19	2.84E+17	1.114E+19	1.39E+18	409	9.584E-14	4.903E-15	9.058E-14	5.168E-15
354-U1454B-32F-2W, 80-130 cm.	-	52.6	52.6	0.8	101.73	1.373E+19	2.82E+17	1.143E+19	1.43E+18	42	5.052E-14	7.821E-15	4.526E-14	7.990E-15

Table SVI-1. (…/…)

^{10}Be data

#	Mass of decontaminated quartz				^{9}Be data					^{10}Be/^{9}Be measurements				
	75-125 µm fraction (g)	125-250 µm fraction (g)	Total mass (g)	1 σ (g)	Carrier mass added (mg)	^{9}Be added before dissolution (atom)	1 σ (atom)	^{9}Be measured after evaporation (atom)	1 σ (atom)	Hit count	^{10}Be/^{9}Be	1 σ	^{10}Be/^{9}Be (blank corrected)	1 σ
Lower Meghna Bedload														
BGP 34	-	-	-	-	-	-	-	-	-	-	-	-	-	-
BR219	-	30.0	30.0	0.5	102.02	1.377E+19	2.83E+17	1.357E+19	1.70E+18	258	7.747E-14	5.487E-15	7.221E-14	5.725E-15
BR446	-	46.1	46.1	0.7	102.73	1.386E+19	2.85E+17	1.136E+19	1.42E+18	133	1.698E-13	1.487E-14	1.645E-13	1.496E-14
BR8230	-	33.8	33.8	0.5	102.25	1.380E+19	2.83E+17	1.037E+19	1.30E+18	62	9.74E-14	1.494E-14	9.214E-14	1.503E-14
BR529	-	45.7	45.7	0.7	100.53	1.357E+19	2.79E+17	1.185E+19	1.48E+18	115	1.02E-13	9.593E-15	9.673E-14	9.731E-15
BR724	-	48.3	48.3	0.7	98.46	1.329E+19	2.73E+17	1.269E+19	1.59E+18	251	1.628E-13	1.205E-14	1.576E-13	1.216E-14

Table SVI-1. (…/…)

#	^{10}Be data							Sr-Nd isotopic data					
	^{10}Be results							Sr-Nd isotopic measurements					
	^{10}Be concentration (atom/g)	1 σ (atom/g)	% 1 σ uncertainty	^{10}Be paleoconcentration (atom/g)	1 σ (atom/g)	Theoretical Himalayan erosion rate (mm/y)	1 σ (mm/y)	87Sr/86Sr	2σ	144Nd/143Nd	2σ	εNd	2σ
Bengal fan sands													
DSF: Drilling depth below sea-floor													
Exp. 353, 14°N													
353-U1444A-6H-1W, 100-150 cm.	2.53E+04	2.96E+03	0.12	2.77E+04	3.27E+03	0.9	0.2	0.730860	0.000008	0.51188080	0.00001378	-14.8	0.3
353-U1444A-7H-5W, 100-150 cm.	3.19E+04	3.26E+03	0.10	3.54E+04	3.67E+03	0.7	0.1	0.733182	0.000011	0.51187341	0.00001381	-14.9	0.3
353-U1444A-9H-5W, 75-130 cm.	2.86E+04	4.44E+03	0.16	3.26E+04	5.01E+03	0.8	0.2	0.732093	0.000008	0.51188285	0.00001648	-14.7	0.3
353-U1444A-11H-6W, 87-150 cm.	2.66E+04	3.24E+03	0.12	3.11E+04	3.84E+03	0.8	0.2	0.731406	0.000196	0.51189629	0.00001320	-14.5	0.3
353-U1444A-24F-3W, 0-56, 65-110 cm.	4.37E+03	1.01E+03	0.23	2.89E+04	6.85E+03	0.9	0.3	-	-	-	-	-	-
Exp. 354, 8°N													
354-U1450A-3H-4W, 50-120 cm.	1.97E+04	2.86E+03	0.15	2.25E+04	3.24E+03	1.2	0.3	0.722046	0.000007	0.51196081	0.00001341	-13.2	0.3
354-U1450A-8F-2W, 1-60 cm.	2.33E+04	2.57E+03	0.11	2.71E+04	3.06E+03	1.0	0.2	0.727607	0.000010	0.51192570	0.00001085	-13.9	0.2
354-U1450A-14F-2W, 90-150 cm.	2.45E+04	1.95E+03	0.08	2.90E+04	2.36E+03	0.9	0.2	0.727955	0.000017	0.51191881	0.00001770	-14.0	0.3
354-U1450A-25F-1W, 50-100 cm.	1.44E+04	2.13E+03	0.15	1.84E+04	2.78E+03	1.4	0.3	0.736566	0.000012	0.51184443	0.00001065	-15.5	0.2
354-U1450A-32F-3W, 24-84 cm.	1.62E+04	3.09E+03	0.19	2.31E+04	4.51E+03	1.1	0.3	0.741857	0.000013	0.51185613	0.00001584	-15.3	0.3
354-U1450A-40F-2W, 0-30 cm.	1.14E+04	1.25E+03	0.11	2.44E+04	3.17E+03	1.1	0.2	0.744630	0.000019	0.51181702	0.00001156	-16.0	0.2
354-U1450A-44F-3W, 40-100 cm.	-	-	-	-	-	-	-	0.749003	0.000010	0.51185731	0.00002264	-15.2	0.4
354-U1450A-50F-2W, 86-116 cm.	9.01E+03	2.69E+03	0.30	2.30E+04	6.98E+03	1.2	0.4	0.726254	0.000016	0.51194153	0.00002268	-13.6	0.4
354-U1450A-83F-3W, 113-147 cm.	1.01E+04	2.38E+03	0.24	5.24E+04	1.31E+04	0.5	0.2	0.728461	0.000014	0.51192582	0.00001708	-13.9	0.3
354-U1450A-90F-3W, 106-136 cm.	1.24E+04	2.29E+03	0.18	6.56E+04	1.38E+04	0.4	0.1	0.735363	0.000012	0.51189125	0.00001115	-14.6	0.2
354-U1450A-100F-3W, 28-88 cm.	2.12E+03	5.93E+02	0.28	1.56E+04	4.61E+03	1.8	0.6	0.740776	0.000024	0.51186754	0.00002277	-15.0	0.4
354-U1450A-110F-1W, 79-84 cm.	6.30E+03	1.60E+03	0.25	5.02E+04	1.40E+04	0.6	0.2	0.737901	0.000019	0.51185873	0.00000592	-15.2	0.1
354-U1450A-124F-3W, 20-80 cm.	2.10E+03	7.17E+02	0.34	3.63E+04	1.28E+04	0.8	0.3	0.755746	0.000014	0.51181134	0.00001549	-16.1	0.3
354-U1450A-130F-3W, 0-51 cm.	-	-	-	-	-	-	-	0.754803	0.000020	0.51179634	0.00002017	-16.4	0.4
354-U1451A-9H-2W, 120-145 cm.	2.65E+04	5.32E+03	0.20	3.12E+04	6.16E+03	0.9	0.2	0.733096	0.000008	0.51189807	0.00002534	-14.4	0.5
354-U1451A-12F-3W, 90-121 cm.	2.15E+04	3.81E+03	0.18	3.00E+04	5.40E+03	0.9	0.2	0.748522	0.000008	0.51181096	0.00001410	-16.1	0.3
354-U1451A-22H-5W, 92-126 cm.	3.49E+03	1.26E+03	0.36	1.17E+04	4.20E+03	2.3	0.7	0.738964	0.000014	0.51186660	0.00002273	-15.0	0.4
354-U1451A-31F-2W, 44-116 cm.	1.40E+03	4.24E+02	0.30	3.32E+04	1.02E+04	0.9	0.3	0.754530	0.000008	0.51181482	0.00001707	-16.1	0.3
354-U1451A-39F-3W, 81-111 cm.	-	-	-	-	-	-	-	0.738004	0.000010	0.51187960	0.00001376	-14.8	0.3
354-U1454B-4H-4W, 0-60 cm.	3.37E+04	2.73E+03	0.08	3.49E+04	2.92E+03	0.7	0.1	0.722882	0.000010	0.51196610	0.00002343	-13.1	0.5
354-U1454B-6F-3W, 5-65 cm.	3.04E+04	2.20E+03	0.07	3.23E+04	2.43E+03	0.8	0.1	0.721672	0.000014	0.51198965	0.00001289	-12.6	0.3
354-U1454B-25F-2W, 54-114 cm.	2.98E+04	1.87E+03	0.06	3.48E+04	2.22E+03	0.7	0.1	0.727170	0.000018	0.51194582	0.00001797	-13.5	0.4
354-U1454B-32F-2W, 80-130 cm.	1.18E+04	2.10E+03	0.18	2.98E+04	6.47E+03	0.9	0.2	-	-	-	-	-	-

Table SVI-1. (…/…)

#	^{10}Be data							Sr-Nd isotopic data					
	^{10}Be results							Sr-Nd isotopic measurements					
	^{10}Be concentration (atom/g)	1 σ (atom/g)	% 1 σ uncertainty	^{10}Be paleoconcentration (atom/g)	1 σ (atom/g)	Theoretical Himalayan erosion rate (mm/y)	1 σ (mm/y)	87Sr/86Sr	2σ	144Nd/143Nd	2σ	εNd	2σ
Lower Meghna Bedload													
BGP 34	-	-	-	-	-	-	-	0.739911	0.000010	0.51186083	0.000007	-15.2	0.1
BR219	3.30E+04	2.80E+03	0.08	-	-	0.8	0.1	0.719928	0.000010	0.51192874	0.000003	-13.8	0.1
BR446	4.94E+04	4.65E+03	0.09	-	-	0.5	0.0	0.724126	-	0.51193600	-	-13.7	1.0
BR8230	3.76E+04	6.25E+03	0.17	-	-	0.6	0.0	0.723006	0.000012	0.51193117	0.000003	-13.8	0.1
BR529	2.86E+04	2.98E+03	0.10	-	-	0.9	0.1	-	-	-	-	-	-
BR724	4.32E+04	3.52E+03	0.08	-	-	0.7	0.1	-	-	-	-	-	-

Table SVI-1. (…/…)

#	f_G Mix: Relative fraction f_G	1σ	Test of the climatic forcing hypothesis: Factor K(t)	1σ	Himalayan erosion rate (mm/y)	1σ (mm/y)
Bengal fan sands						
DSF: Drilling depth below sea-floor						
Exp. 353, 14°N						
353-U1444A-6H-1W, 100-150 cm.	0.11	0.20	1.1	0.1	1.1	0.1
353-U1444A-7H-5W, 100-150 cm.	0.20	0.19	0.8	0.1	0.8	0.1
353-U1444A-9H-5W, 75-130 cm.	0.14	0.20	0.9	0.2	0.9	0.2
353-U1444A-11H-6W, 87-150 cm.	0.10	0.20	1.0	0.1	1.0	0.1
353-U1444A-24F-3W, 0-56, 65-110 cm.	0.65	0.29	0.9	0.3	0.9	0.3
Exp. 354, 8°N						
354-U1450A-3H-4W, 50-120 cm.	-0.34	0.26	1.4	0.2	1.4	0.2
354-U1450A-8F-2W, 1-60 cm.	-0.10	0.24	1.1	0.1	1.1	0.1
354-U1450A-14F-2W, 90-150 cm.	-0.06	0.23	1.1	0.1	1.1	0.1
354-U1450A-25F-1W, 50-100 cm.	0.34	0.16	1.5	0.3	1.5	0.3
354-U1450A-32F-3W, 24-84 cm.	0.44	0.15	1.2	0.3	1.2	0.3
354-U1450A-40F-2W, 0-30 cm.	0.56	0.13	1.1	0.2	1.1	0.2
354-U1450A-44F-3W, 40-100 cm.	0.59	0.13	-	-	-	-
354-U1450A-50F-2W, 86-116 cm.	-0.17	0.24	1.5	0.9	1.5	0.9
354-U1450A-83F-3W, 113-147 cm.	-0.07	0.24	0.6	0.3	0.6	0.3
354-U1450A-90F-3W, 106-136 cm.	0.20	0.18	0.5	0.1	0.5	0.1
354-U1450A-100F-3W, 28-88 cm.	0.39	0.15	2.0	1.0	2.0	1.0
354-U1450A-110F-1W, 79-84 cm.	0.35	0.16	0.6	0.4	0.6	0.4
354-U1450A-124F-3W, 20-80 cm.	0.78	0.10	0.8	0.8	0.8	0.8
354-U1450A-130F-3W, 0-51 cm.	0.77	0.10	-	-	-	-
354-U1451A-9H-2W, 120-145 cm.	0.14	0.20	1.0	0.2	1.0	0.2
354-U1451A-12F-3W, 90-121 cm.	0.64	0.12	0.9	0.2	0.9	0.2
354-U1451A-22H-5W, 92-126 cm.	0.36	0.16	2.9	1.8	2.9	1.8
354-U1451A-31F-2W, 44-116 cm.	0.75	0.11	0.8	0.6	0.8	0.6
354-U1451A-39F-3W, 81-111 cm.	0.30	0.17	-	-	-	-
354-U1454B-4H-4W, 0-60 cm.	-0.33	0.26	0.9	0.1	0.9	0.1
354-U1454B-6F-3W, 5-65 cm.	-0.42	0.25	1.0	0.1	1.0	0.1
354-U1454B-25F-2W, 54-114 cm.	-0.16	0.24	0.9	0.1	0.9	0.1
354-U1454B-32F-2W, 80-130 cm.	0.30	0.34	1.0	0.3	1.0	0.3

Table SVI-1. (…/…)

	f_G		Test of the climatic forcing hypothesis			
	Mix					
#	Relative fraction f_G	1σ	Factor K(t)	1σ	Himalayan erosion rate (mm/y)	1σ (mm/y)
Lower Meghna Bedload						
BGP 34	-	-	-	-	-	-
BR219	-0.31	0.26	0.9	0.1	0.9	0.1
BR446	-0.22	0.25	0.6	0.1	0.6	0.1
BR8230	-0.07	0.24	0.8	0.2	0.8	0.2
BR529	0.38	0.32	1.0	0.1	1.0	0.1
BR724	0.25	0.35	0.7	0.1	0.7	0.1

Table SVI-2. ^{10}Be duplicate results.

Six duplicates of various granulometric fractions (col. E-F) for the Bengal Fan samples and one for the Lower Meghna were measured for ^{10}Be. The results are presented in a similar way than for Table S1. The col. W presents the relative difference with the results of the same samples presented Table SVI-1.

		Mass of decontaminated quartz					^{9}Be data			
Site	#	75-125 µm fraction (g)	125-250 µm fraction (g)	Total mass (g)	1 σ (g)	Carrier mass added (mg)	^{9}Be added before dissolution (atom)	1 σ (atom)	^{9}Be measured after evaporation (atom)	1 σ (atom)
RESULTS										
Bengal fan sand										
Exp. 353, 14°N										
U1444	353-U1444A-6H-1W, 100-150 cm.	20.7	33.0	53.7	0.8	101.83	1.374E+19	3.50E+17	1.24E+19	1.55E+18
	353-U1444A-7H-5W, 100-150 cm.	33.7	-	33.7	0.5	102.02	1.377E+19	3.50E+17	1.17E+19	1.47E+18
		-	-	-	-	-	-	-	-	-
		-	-	-	-	-	-	-	-	-
		-	-	-	-	-	-	-	-	-
Exp. 354, 8°N										
	354-U1450A-3H-4W, 50-120 cm.	40.0	-	40.0	0.6	102.05	1.377E+19	3.50E+17	1.13E+19	1.42E+18
	354-U1450A-8F-2W, 1-60 cm.	34.0	30.8	64.7	1.0	102.06	1.377E+19	3.50E+17	1.15E+19	1.44E+18
	354-U1450A-14F-2W, 90-150 cm.	-	-	-	-	-	-	-	-	-
	354-U1450A-25F-1W, 50-100 cm.	17.9	16.4	34.3	0.5	102.30	1.380E+19	3.51E+17	1.05E+19	1.31E+18
Lower Meghna Bedload										
Padma, Mawa	BR529	21.4	-	21.4	0.3	101.49	1.369E+19	3.48E+17	1.30E+19	1.63E+18

Table SVI-2. (…/…)

		$^{10}Be/^{9}Be$ measurements							
Site	**#**	**Hit count**	**$^{10}Be/^{9}Be$**	**1 σ**	**$^{10}Be/^{9}Be$ (blank corrected)**	**1 σ**	**^{10}Be concentration (atom/g)**	**1 σ (atom/g)**	**Difference with 125-250 µm fraction**
RESULTS									
Bengal fan sand									
Exp. 353, 14°N									
U1444	353-U1444A-6H-1W, 100-150 cm.	48	8.61E-14	1.25E-14	8.089E-14	1.259E-14	2.07E+04	3.28E+03	0.18
	353-U1444A-7H-5W, 100-150 cm.	50	5.98E-14	9.10E-15	5.454E-14	9.247E-15	2.23E+04	3.83E+03	0.30
		-	-	-	-	-	-	-	-
		-	-	-	-	-	-	-	-
		-	-	-	-	-	-	-	-
Exp. 354, 8°N									
	354-U1450A-3H-4W, 50-120 cm.	26	6.72E-14	1.35E-14	6.190E-14	1.358E-14	2.13E+04	4.71E+03	0.08
	354-U1450A-8F-2W, 1-60 cm.	52	1.24E-13	1.88E-14	1.188E-13	1.884E-14	2.53E+04	4.08E+03	0.09
	354-U1450A-14F-2W, 90-150 cm.	-	-	-	-	-	-	-	-
	354-U1450A-25F-1W, 50-100 cm.	11	3.27E-14	9.88E-15	2.749E-14	1.002E-14	1.11E+04	4.05E+03	0.23
Lower Meghna Bedload									
Padma, Mawa	BR529	199	5.62E-14	4.04E-15	5.090E-14	4.358E-15	3.25E+04	2.95E+03	0.14
		Average difference							**0.17**

Table SVI-3. ^{10}Be blanks.
Five analytical blanks were prepared synchronously with the samples of Tables SVI-1-SVI-2.

	^{9}Be data					^{10}Be/^{9}Be measurements			
#	Carrier mass added (mg)	^{9}Be added before dissolution (atom)	1 σ (atom) 0.015	^{9}Be measured after evaporation (atom)	1 σ (atom) 0.125	Hit count	^{10}Be/^{9}Be	1 σ	
PHE30	101.85	1.374E+19	3.50E+17	1.27E+19	1.58E+18	7	4.62E-15	1.78E-15	6.35E+04
PHE31	101.85	1.374E+19	3.50E+17	1.32E+19	1.65E+18	33	6.29E-15	1.44E-15	8.64E+04
PHE40	101.90	1.375E+19	3.50E+17	1.12E+19	1.40E+18	16	4.56E-15	1.14E-15	6.27E+04
PHE41	102.23	1.379E+19	3.51E+17	1.22E+19	1.53E+18	10	6.39E-15	2.69E-15	8.82E+04
PHE42	102.24	1.380E+19	3.51E+17	1.13E+19	1.42E+18	18	4.45E-15	1.11E-15	6.14E+04
Average blank							**5.26E-15**	**1.63E-15**	**7.24E+04**

Table SVI-4. Major and trace element results.

For the Bengal Fan samples, the measurements of major and trace elements were performed at SARM (Nancy, France), following (Carignan et al., 2001) procedure and using ICP-OES iCap6500 for major element and Sc concentrations, and ICP-MS iCapQ for trace elements. For the Lower Meghna sand, data for major elements are from Lupker et al. (2013) and data for trace elements are unpublished data from France-Lanord and Galy and measured similarly than our data.

Table SVI-4 (…/…)

Site	Hole	Core #	No CRPG	As (ppm)	Ba (ppm)	Be (ppm)	Bi (ppm)	Cd (ppm)	Ce (ppm)	Co (ppm)	Cr (ppm)	Cs (ppm)	Cu (ppm)	Dy (ppm)	Er (ppm)	Eu (ppm)
			Uncertainties (%) (depending on content)													
Bengal fan sands				<20%	<5%	<20%	<20%	<20%	<5%	<20%	<5%	<15%	<20%	<10%	<5%	<5%
< D.L. : below detection limit			Detection limit	0.50	5.5	0.05	0.045	0.02	0.03	0.08	0.50	0.02	2.0	0.004	0.002	0.002
Exp. 353, 14°N																
U1444	A	6H 1444-006H	1512025	3.882	371.700	2.288	0.255	0.194	71.940	8.778	56.140	5.062	15.360	4.642	2.583	1.093
U1444	A	7H 1444-007H	1512026	2.495	370.300	2.517	0.303	0.205	82.810	8.668	52.920	5.070	10.060	5.202	2.889	1.153
U1444	A	9H 1444-009H	1512027	2.111	364.700	2.555	0.327	0.206	72.750	7.275	44.680	4.890	9.930	4.673	2.615	1.049
U1444	A	11H 1444-011H	1512028	2.456	333.700	2.408	0.267	0.309	125.300	8.256	56.810	4.532	9.657	7.135	4.049	1.429
U1444	B	24F 1444-024F	1806024	1.693	306.082	3.133	0.252	0.144	132.351	7.690	54.443	5.379	9.602	8.064	4.542	1.490
Exp. 354, 8°N																
U1450	A	3H 1450-003H	1512029	2.209	409.000	2.285	0.302	0.225	67.950	9.861	52.980	5.232	11.870	4.306	2.366	1.095
U1450	A	8F 1450-008F	1512030	2.976	386.300	2.338	0.285	0.182	72.990	8.662	52.520	5.531	10.530	4.641	2.601	1.112
U1450	A	14F 1450-014F	1512031	3.355	409.600	2.618	0.434	0.142	69.130	10.170	61.740	6.986	17.580	4.680	2.624	1.113
U1450	A	25F 1450-025F	1512032	1.882	370.300	2.066	0.236	0.191	68.110	8.737	53.210	5.299	10.880	4.438	2.437	1.074
U1450	A	32F 1450-032F	1512033	6.681	478.500	2.364	0.420	0.185	74.600	14.570	77.130	7.493	39.680	5.178	2.896	1.199
U1450	A	40F 1450-040F	1512034	4.269	427.100	2.397	0.388	< D.L.	63.810	10.840	59.590	7.512	18.670	4.126	2.245	1.018
U1450	A	44F 1450-044F	1512035	8.610	538.400	3.364	1.062	0.123	74.920	16.560	95.930	12.190	43.060	5.161	2.890	1.279
U1450	A	50F 1450-050F	1512036	7.380	489.900	2.894	0.625	< D.L.	63.500	12.950	65.810	8.789	26.630	4.390	2.415	1.087
U1450	A	83F 1450-083F	1512037	2.813	430.700	2.730	0.348	0.155	63.770	9.712	46.630	7.947	13.150	4.220	2.331	1.048
U1450	A	90F 1450-090F	1512038	< D.L.	400.200	2.332	0.260	< D.L.	50.450	7.294	37.320	6.299	8.775	3.400	1.872	0.884
U1450	A	100F 1450-100F	1512039	3.348	402.600	2.509	0.246	0.128	58.360	10.970	48.130	8.245	12.450	4.093	2.222	0.991
U1450	A	110F 1450-110F		2.509	436.697	2.699	0.295	0.101	83.351	36.058	54.815	7.522	12.695	5.308	2.907	1.226
U1450	A	124F 1450-124F	1512040	2.378	345.100	2.136	0.258	0.288	108.500	6.447	39.630	5.044	8.662	6.598	3.638	1.384
U1450	A	130F 1450-130F	1512041	2.648	387.700	2.831	0.318	0.153	67.790	9.081	42.960	8.497	12.210	4.328	2.353	0.990
U1451	A	9H 1451-009H	1512042	1.819	370.900	2.373	0.255	0.109	56.300	7.664	43.170	5.307	11.970	3.808	2.097	0.959
U1451	A	12F 1451-012F	1512043	2.062	354.800	2.454	0.241	0.124	65.150	8.543	44.680	6.280	9.477	4.423	2.357	1.028
U1451	A	22H 1451-022H	1512044	2.415	387.000	2.550	0.305		69.650	9.579	54.730	6.778	13.330	4.716	2.600	1.113
U1451	A	31F 1451-031F	1512045	2.999	325.800	2.092	0.244	0.171	69.180	7.418	43.530	6.032	9.559	4.303	2.303	1.035
U1451	A	39F 1451-039F	1512046	2.195	331.400	2.049	0.215	0.116	54.770	8.402	47.410	5.244	10.610	3.545	1.928	0.941
U1454	B	4H 1454-004H	1512047	2.723	361.600	2.555	0.296	0.256	85.630	8.383	60.510	4.772	10.850	5.198	2.825	1.222
U1454	B	6F 1454-006F	1512048	2.780	303.100	2.216	0.331	0.492	180.000	9.815	113.000	3.798	13.380	9.852	5.562	1.808
U1454	B	25F 1454-025F	1512049	3.250	321.900	2.153	0.375	0.315	132.500	8.264	66.140	4.294	18.740	7.953	4.486	1.441
U1454	B	32F 1454-032F	1806025	11.517	497.425	2.858	0.564	0.125	75.222	13.520	63.828	7.940	29.121	5.176	2.871	1.181

Table SVI-4 (…/…)

Site	Hole Core #	No CRPG	As (ppm)	Ba (ppm)	Be (ppm)	Bi (ppm)	Cd (ppm)	Ce (ppm)	Co (ppm)	Cr (ppm)	Cs (ppm)	Cu (ppm)	Dy (ppm)	Er (ppm)	Eu (ppm)
Lower Meghna Bedload															
Lower Meghna, Chor Fa	BGP 34		7.501	532.427	2.891	0.602	0.054	97.715	17.182	110.653	9.408	38.948	6.634	3.466	1.647
Lower Meghna, Bhola	BR219		1.802	215.600	1.580	0.381	1.111	415.800	12.080	224.300	1.953	6.833	24.140	13.000	4.465
Lower Meghna, Bhola	BR446		2.081	307.900	2.096	< D.L.	< D.L.	141.600	8.015	98.990	2.563	3.747	7.497	4.225	1.490
Lower Meghna, Daulatkl	BR8230		2.722	384.700	1.936	0.874	0.412	203.000	10.410	119.100	2.932	6.499	11.310	6.155	2.291
Padma, Mawa	BR529		2.247	342.600	1.815	1.302	0.355	73.860	7.215	51.750	4.321	3.729	4.086	2.145	1.038
Padma, Mawa	BR724		< D.L.	215.300	< D.L.	0.318	0.657	298.800	8.897	113.300	1.824	< D.L.	16.490	9.192	2.501

Table SVI-4 (…/…)

Site	#	Ga (ppm)	Gd (ppm)	Ge (ppm)	Hf (ppm)	Ho (ppm)	In (ppm)	La (ppm)	Lu (ppm)	Mo (ppm)	Nb (ppm)	Nd (ppm)	Ni (ppm)	Pb (ppm)	Pr (ppm)
															>10ppm: <10% > 0.1 ppm:
Bengal fan sands		<5%	<10%	<10%	<10%	<10%	<20%	<5%	<20%	>25%	<10%	<15%	<5%	<20%	<20%
< D.L. : below detection limit		0.02	0.005	0.04	0.03	0.001	0.03	0.02	0.001	0.50	0.015	0.016	2.0	0.45	0.004
Exp. 353, 14°N															
U1444	1444-006H	14.650	4.998	1.660	6.415	0.959	< D.L.	35.340	0.391	< D.L.	8.687	30.240	22.950	20.390	8.254
U1444	1444-007H	14.430	5.645	1.751	7.624	1.063	< D.L.	40.810	0.428	< D.L.	9.732	34.180	24.600	19.983	9.351
U1444	1444-009H	13.730	4.955	1.660	6.910	0.958	< D.L.	36.520	0.398	< D.L.	8.634	30.080	18.490	19.759	8.309
U1444	1444-011H	14.360	7.895	1.808	11.170	1.479	< D.L.	62.100	0.630	< D.L.	12.240	50.360	20.800	18.270	13.970
U1444	1444-024F	13.395	8.527	1.994	13.237	1.682	0.038	66.110	0.677	< D.L.	11.937	53.638	18.442	30.276	14.812
Exp. 354, 8°N															
U1450	1450-003H	15.490	4.753	1.571	6.249	0.883	< D.L.	34.440	0.361	< D.L.	10.070	28.810	24.690	20.637	7.840
U1450	1450-008F	14.830	5.018	1.668	6.690	0.956	< D.L.	37.170	0.401	< D.L.	9.853	30.500	24.210	20.984	8.356
U1450	1450-014F	16.680	4.903	1.642	5.381	0.960	< D.L.	35.100	0.391	< D.L.	10.650	28.990	28.440	21.882	7.937
U1450	1450-025F	14.180	4.792	1.580	6.495	0.903	< D.L.	34.460	0.370	< D.L.	9.477	28.760	22.390	18.371	7.846
U1450	1450-032F	17.800	5.534	1.688	5.899	1.083	< D.L.	37.950	0.436	< D.L.	11.890	32.260	56.410	20.430	8.680
U1450	1450-040F	15.730	4.481	1.629	5.091	0.856	< D.L.	32.350	0.341	< D.L.	10.160	27.050	28.770	20.209	7.334
U1450	1450-044F	23.320	5.513	2.007	4.111	1.096	< D.L.	37.810	0.437	0.517	14.420	32.020	45.780	28.548	8.635
U1450	1450-050F	19.060	4.690	1.768	4.252	0.907	< D.L.	32.280	0.360	0.525	12.170	26.920	34.410	27.404	7.284
U1450	1450-083F	15.690	4.576	1.641	5.858	0.880	< D.L.	32.380	0.350	< D.L.	10.080	27.280	22.170	22.163	7.388
U1450	1450-090F	13.450	3.642	1.586	4.172	0.723	< D.L.	25.620	0.284	< D.L.	7.998	21.450	16.920	20.184	5.807
U1450	1450-100F	14.850	4.310	1.717	5.581	0.847	< D.L.	28.990	0.329	< D.L.	9.823	24.840	25.350	19.726	6.742
U1450	1450-110F	14.096	5.812	1.636	8.652	1.086	0.043	43.436	0.435		10.729	34.906	23.481	21.110	9.472
U1450	1450-124F	11.890	7.160	1.931	11.680	1.372	< D.L.	52.420	0.562	< D.L.	11.490	44.870	15.780	17.914	12.250
U1450	1450-130F	13.740	4.725	1.690	6.661	0.900	< D.L.	33.510	0.360	< D.L.	10.420	28.660	20.710	19.819	7.807
U1451	1451-009H	13.730	4.091	1.676	5.174	0.811	< D.L.	27.500	0.321	< D.L.	8.087	23.490	24.420	21.850	6.464
U1451	1451-012F	13.740	4.723	1.699	6.268	0.913	< D.L.	31.640	0.352	< D.L.	9.238	27.640	20.630	19.768	7.511
U1451	1451-022H	15.260	5.058	1.806	6.765	0.988	< D.L.	33.870	0.392	< D.L.	10.680	29.530	23.630	20.072	7.988
U1451	1451-031F	12.080	4.704	1.746	6.817	0.879	< D.L.	33.710	0.348	< D.L.	9.412	29.150	18.950	18.238	7.961
U1451	1451-039F	12.680	3.865	1.639	5.101	0.729	< D.L.	26.890	0.293	< D.L.	8.556	23.350	21.380	16.947	6.297
U1454	1454-004H	15.150	5.702	1.625	7.911	1.061	< D.L.	43.130	0.433	< D.L.	10.170	35.560	25.460	21.254	9.743
U1454	1454-006F	15.520	10.720	1.917	19.330	2.051	< D.L.	94.270	0.883	0.507	15.870	70.730	28.650	22.918	19.770
U1454	1454-025F	14.160	8.333	1.861	12.580	1.664	< D.L.	65.870	0.678	< D.L.	12.690	52.890	19.150	18.587	14.690
U1454	1454-032F	16.639	5.377	2.168	5.741	1.070	0.049	36.636	0.410	< D.L.	11.080	30.883	37.873	26.422	8.394

Table SVI-4 (…/…)

Site	#	Ga (ppm)	Gd (ppm)	Ge (ppm)	Hf (ppm)	Ho (ppm)	In (ppm)	La (ppm)	Lu (ppm)	Mo (ppm)	Nb (ppm)	Nd (ppm)	Ni (ppm)	Pb (ppm)	Pr (ppm)
Lower Meghna Bedload															
Lower Meghna, Chor Fasson	BGP 34	24.566	6.984	1.762	6.705	1.408	0.056	47.880	0.521	0.317	16.976	42.275	55.849	26.075	11.224
Lower Meghna, Bhola	BR219	18.900	25.780	2.946	36.060	4.657	0.139	215.400	2.112	0.533	36.710	173.200	22.820	17.511	48.690
Lower Meghna, Bhola	BR446	13.850	8.290	1.921	12.250	1.452	< D.L.	71.370	0.684	< D.L.	13.730	55.370	17.910	16.992	15.500
Lower Meghna, Daulatkhan	BR8230	15.350	12.760	2.051	18.320	2.167	0.225	101.100	0.955	< D.L.	17.340	83.100	30.520	19.753	24.100
Padma, Mawa	BR529	12.480	4.673	1.563	5.870	0.747	0.162	36.770	0.329	< D.L.	7.631	30.140	19.450	19.242	8.320
Padma, Mawa	BR724	13.920	18.630	2.199	38.820	3.157	< D.L.	146.900	1.501	< D.L.	19.120	121.100	18.200	14.904	33.320

Table SVI-4 (…/…)

Site	#	Rb (ppm)	Sc (ppm)	Sb (ppm)	Sm (ppm)	Sn (ppm)	Sr (ppm)	Ta (ppm)	Tb (ppm)	Th (ppm)	Tm (ppm)	U (ppm)	V (ppm)	W (ppm)	Y (ppm)
													>50 ppm: < 15% >10ppm:		
Bengal fan sands		<5%	<15%	<20%	<15%	<20%	<5%	<10%	<20%	<10%	<20%	<15%	<10%	<20%	<15%
< D.L. : below detection limit		0.15	0.6	0.06	0.005	0.30	0.70	0.004	0.001	0.015	0.001	0.01	0.85	0.80	0.02
Exp. 353, 14°N															
U1444	1444-006H	122.100	9.110	0.231	6.061	4.308	175.800	0.957	0.768	15.950	0.381	2.530	56.550	2.524	26.240
U1444	1444-007H	120.900	8.980	0.255	6.666	4.188	177.400	1.467	0.872	18.750	0.423	3.281	56.370	2.447	29.310
U1444	1444-009H	118.000	8.570	0.228	5.958	3.867	173.600	0.992	0.776	17.250	0.388	2.811	50.580	2.306	26.190
U1444	1444-011H	107.100	11.140	0.244	9.662	5.404	174.300	1.484	1.200	27.950	0.595	4.140	62.850	3.721	40.100
U1444	1444-024F	102.750	9.940	0.393	10.400	8.112	113.536	1.597	1.321	31.463	0.686	5.177	57.388	3.437	44.317
Exp. 354, 8°N															
U1450	1450-003H	128.200	9.620	0.195	5.791	3.893	219.000	1.099	0.712	15.540	0.348	2.430	63.810	2.533	23.910
U1450	1450-008F	126.800	9.100	0.237	6.097	4.099	187.000	1.103	0.765	16.090	0.385	2.980	57.640	3.361	26.110
U1450	1450-014F	140.500	10.930	0.286	5.787	4.864	178.300	1.185	0.760	15.780	0.376	2.579	67.080	3.005	26.130
U1450	1450-025F	122.900	9.320	0.250	5.749	4.126	151.400	1.126	0.727	17.070	0.355	2.928	55.210	2.623	24.510
U1450	1450-032F	148.400	13.080	0.603	6.383	5.429	160.000	1.203	0.853	16.200	0.413	3.020	81.610	3.167	29.280
U1450	1450-040F	142.500	10.310	0.402	5.406	4.868	127.200	1.088	0.692	13.930	0.329	2.427	64.850	3.381	22.960
U1450	1450-044F	195.400	16.370	0.703	6.491	7.104	118.800	1.482	0.863	18.260	0.417	3.143	108.200	4.510	29.260
U1450	1450-050F	173.100	11.700	0.363	5.419	5.543	203.600	1.285	0.724	15.060	0.355	2.662	80.360	2.699	24.380
U1450	1450-083F	143.300	9.310	0.305	5.475	4.934	174.500	1.141	0.698	14.360	0.341	2.561	57.720	2.333	23.500
U1450	1450-090F	127.700	7.400	0.286	4.321	3.976	143.200	0.863	0.565	11.670	0.273	1.952	44.680	1.973	19.140
U1450	1450-100F	140.500	8.950	0.358	5.025	5.117	132.700	1.080	0.669	12.680	0.319	2.312	57.320	2.507	22.930
U1450	1450-110F	121.338	9.560	0.368	6.976	6.300	138.389	1.534	0.883	17.516	0.417	3.223	55.949	276.709	28.210
U1450	1450-124F	101.800	8.130	0.471	8.809	5.086	92.770	1.483	1.087	23.040	0.536	3.949	46.420	2.723	37.000
U1450	1450-130F	132.300	8.540	0.532	5.616	5.005	119.500	1.286	0.721	14.430	0.348	2.626	51.660	2.673	24.400
U1451	1451-009H	121.500	8.030	0.231	4.776	3.694	162.500	0.892	0.640	12.480	0.310	2.168	49.360	1.965	21.820
U1451	1451-012F	124.100	8.440	0.305	5.565	4.474	129.000	1.009	0.731	14.310	0.347	2.529	52.840	2.064	24.390
U1451	1451-022H	136.600	9.420	0.347	5.933	4.586	149.100	1.147	0.782	15.180	0.383	2.691	61.180	2.391	26.560
U1451	1451-031F	108.700	7.740	0.421	5.803	3.892	99.430	1.046	0.717	14.520	0.341	2.515	47.940	2.202	23.490
U1451	1451-039F	105.400	8.050	0.420	4.616	3.543	124.500	0.899	0.596	11.020	0.287	1.822	52.060	2.003	19.710
U1454	1454-004H	118.300	9.860	0.189	6.874	4.112	206.200	1.130	0.876	19.570	0.417	2.924	61.470	2.461	28.730
U1454	1454-006F	96.180	14.400	0.243	13.290	5.247	199.700	1.964	1.640	41.910	0.836	6.190	87.530	3.145	55.790
U1454	1454-025F	101.100	11.740	0.239	10.070	4.929	171.700	1.553	1.291	31.750	0.667	4.788	67.060	2.401	45.300
U1454	1454-032F	142.561	11.050	0.522	6.240	5.347	146.373	1.241	0.850	16.115	0.424	3.143	76.542	2.685	28.454

Table SVI-4 (…/…)

Site	#	Rb (ppm)	Sc (ppm)	Sb (ppm)	Sm (ppm)	Sn (ppm)	Sr (ppm)	Ta (ppm)	Tb (ppm)	Th (ppm)	Tm (ppm)	U (ppm)	V (ppm)	W (ppm)	Y (ppm)
Lower Meghna Bedload															
Lower Meghna, Chor Fasson	BGP 34	181.217		0.547	8.648	5.096	139.430	1.636	1.117	19.505	0.543	3.277	121.479	2.903	36.857
Lower Meghna, Bhola	BR219	51.560		0.441	32.240	6.130	210.800	4.372	4.111	89.170	2.000	12.830	151.900	4.482	133.900
Lower Meghna, Bhola	BR446	76.740		0.235	10.130	2.937	164.300	1.635	1.271	28.790	0.645	4.279	78.520	1.452	44.050
Lower Meghna, Daulatkhan	BR8230	72.380		1.074	15.670	6.544	186.400	1.970	1.957	45.960	0.921	6.773	98.320	2.022	62.710
Padma, Mawa	BR529	95.800		0.355	5.803	3.089	138.800	0.857	0.722	15.620	0.315	2.374	50.560	1.488	21.650
Padma, Mawa	BR724	52.630		0.608	22.860	7.759	151.000	2.541	2.854	80.310	1.404	12.160	99.140	4.774	91.150

Table SVI-4 (…/…)

Site	#	Yb (ppm)	Zn (ppm)	Zr (ppm)	SiO2 (%)	Al2O3 (%)	Fe2O3 (%)	MnO (%)	MgO (%)	CaO (%)	Na2O (%)	K2O (%)	TiO2 (%)	P2O5 (%)	Loss on Ignition LOI (%)
Bengal fan sands		<15%	> 50ppm: <10% >10ppm: <20%	<5%	<2%	>10%: <2% >5%: <10%	<10%	<20%	<10%	<15%	<10%	<10%	<20%	>25%	
< D.L. : below detection limit		0.002	7.0	1.50	0.05	0.04	0.015	0.015	0.03	0.03	0.02	0.03	0.02	0.10	
Exp. 353, 14°N															
U1444	1444-006H	2.544	50.330	238.500	73.770	11.210	3.578	0.059	1.564	2.525	2.060	2.518	0.485	< D.L.	2.220
U1444	1444-007H	2.797	46.350	282.600	73.220	10.825	3.471	0.062	1.579	3.124	2.066	2.424	0.489	< D.L.	2.520
U1444	1444-009H	2.571	46.530	255.800	74.180	10.945	3.325	0.057	1.449	2.854	2.132	2.510	0.455	< D.L.	2.150
U1444	1444-011H	4.054	49.360	428.200	71.980	11.018	4.161	0.086	1.740	3.535	2.066	2.299	0.621	< D.L.	2.430
U1444	1444-024F	4.472	47.095	496.828	74.890	9.564	4.119	0.088	1.492	2.784	1.485	2.063	0.668	0.150	2.630
Exp. 354, 8°N															
U1450	1450-003H	2.337	58.690	235.400	70.320	12.040	3.972	0.067	1.952	3.437	2.263	2.749	0.552	< D.L.	2.520
U1450	1450-008F	2.579	53.420	248.100	72.620	11.345	3.500	0.058	1.628	2.885	2.125	2.580	0.505	< D.L.	2.360
U1450	1450-014F	2.553	61.600	188.900	69.150	12.544	4.259	0.075	2.017	2.978	2.081	2.820	0.583	< D.L.	3.370
U1450	1450-025F	2.381	51.710	238.600	73.140	11.098	3.622	0.058	1.724	2.495	1.953	2.553	0.528	< D.L.	2.470
U1450	1450-032F	2.862	79.820	216.000	65.550	13.010	5.148	0.158	2.327	3.107	1.661	2.894	0.656	< D.L.	5.220
U1450	1450-040F	2.223	61.170	177.500	69.000	11.870	4.256	0.064	2.049	2.613	1.737	2.791	0.570	< D.L.	3.860
U1450	1450-044F	2.896	99.470	140.800	57.580	15.910	7.062	0.110	3.109	2.467	1.433	3.641	0.769	< D.L.	7.330
U1450	1450-050F	2.391	80.710	145.500	63.550	13.750	5.080	0.081	2.491	3.726	2.139	3.264	0.631	< D.L.	4.780
U1450	1450-083F	2.322	58.490	212.800	71.960	12.014	3.873	0.066	1.669	2.432	2.145	2.835	0.532	< D.L.	2.740
U1450	1450-090F	1.881	44.150	142.200	75.550	10.628	3.213	0.055	1.364	2.009	1.935	2.663	0.424	< D.L.	2.440
U1450	1450-100F	2.166	66.920	209.400	74.090	10.758	4.137	0.062	1.702	2.071	1.765	2.574	0.524	< D.L.	2.970
U1450	1450-110F	2.850	56.914	322.537	74.830	10.473	3.959	0.065	1.598	2.222	1.716	2.425	0.569	0.120	2.430
U1450	1450-124F	3.650	41.750	450.700	79.110	8.652	3.254	0.062	1.114	1.583	1.391	1.990	0.592	< D.L.	2.040
U1450	1450-130F	2.365	55.420	251.200	69.980	10.140	3.667	0.064	1.771	4.081	1.502	2.553	0.530	< D.L.	5.490
U1451	1451-009H	2.066	44.640	180.300	74.590	10.990	3.117	0.049	1.378	2.219	2.059	2.567	0.435	< D.L.	2.230
U1451	1451-012F	2.284	46.880	234.000	74.470	10.260	3.278	0.053	1.499	2.447	1.774	2.387	0.488	< D.L.	2.740
U1451	1451-022H	2.605	54.800	253.000	72.640	11.123	3.851	0.067	1.837	2.591	1.755	2.590	0.556	< D.L.	3.250
U1451	1451-031F	2.275	45.250	253.000	76.220	9.263	3.170	0.051	1.468	2.881	1.386	2.184	0.506	< D.L.	3.780
U1451	1451-039F	1.874	46.200	179.400	75.370	9.695	3.418	0.054	1.510	2.686	1.523	2.232	0.482	< D.L.	3.740
U1454	1454-004H	2.792	52.210	297.000	73.080	11.910	3.864	0.069	1.687	3.026	2.275	2.540	0.541	< D.L.	1.870
U1454	1454-006F	5.694	57.140	664.300	70.490	11.718	5.640	0.124	1.955	3.668	2.059	2.187	0.875	0.200	1.640
U1454	1454-025F	4.513	52.280	478.800	73.730	11.030	4.453	0.100	1.583	2.966	1.947	2.214	0.676	< D.L.	1.690
U1454	1454-032F	2.720	70.036	205.975	65.310	12.112	4.631	0.073	2.383	3.420	1.706	2.747	0.628	0.130	6.780

Table SVI-4 (…/…)

Site	#	Yb (ppm)	Zn (ppm)	Zr (ppm)	SiO2 (%)	Al2O3 (%)	Fe2O3 (%)	MnO (%)	MgO (%)	CaO (%)	Na2O (%)	K2O (%)	TiO2 (%)	P2O5 (%)	LOI (%)
Lower Meghna Bedload															
Lower Meghna, Chor Fasson	BGP 34	3.540	87.222	248.558	63.230	15.470	6.390	0.090	2.590	1.750	1.480	3.020	0.810	0.140	4.500
Lower Meghna, Bhola	BR219	13.910	77.880	1345.000	65.190	11.250	9.110	0.260	2.130	5.510	1.400	1.350	2.250	0.470	0.720
Lower Meghna, Bhola	BR446	4.380	45.290	493.900	76.015	10.126	4.575	0.108	1.342	2.802	1.795	1.910	0.775	0.150	0.740
Lower Meghna, Daulatkhan	BR8230	6.357	68.910	625.700	71.682	10.397	5.631	0.124	1.711	3.675	1.729	1.739	1.041	0.282	1.292
Padma, Mawa	BR529	2.151	38.780	217.800	76.878	10.011	3.075	0.056	1.195	2.214	1.827	2.148	0.419	0.102	1.240
Padma, Mawa	BR724	9.731	48.940	1431.000	72.674	9.313	6.438	0.153	1.710	3.585	1.490	1.342	1.139	0.245	0.897

Table SVI-4 (…/…)

Site	#	Total (%)
Bengal fan sands		
< D.L. : below detection limit		
Exp. 353, 14°N		
U1444	1444-006H	99.989
U1444	1444-007H	99.780
U1444	1444-009H	100.057
U1444	1444-011H	99.936
U1444	1444-024F	99.920
Exp. 354, 8°N		
U1450	1450-003H	99.872
U1450	1450-008F	99.606
U1450	1450-014F	99.877
U1450	1450-025F	99.641
U1450	1450-032F	99.731
U1450	1450-040F	98.810
U1450	1450-044F	99.411
U1450	1450-050F	99.492
U1450	1450-083F	100.266
U1450	1450-090F	100.281
U1450	1450-100F	100.653
U1450	1450-110F	100.410
U1450	1450-124F	99.788
U1450	1450-130F	99.778
U1451	1451-009H	99.634
U1451	1451-012F	99.396
U1451	1451-022H	100.260
U1451	1451-031F	100.909
U1451	1451-039F	100.710
U1454	1454-004H	100.862
U1454	1454-006F	100.560
U1454	1454-025F	100.389
U1454	1454-032F	99.910

Table SVI-4 (…/…)

Site	#	Total (%)
Lower Meghna		
Bedload		
Lower Meghna, Chor Fasson	BGP 34	99.470
Lower Meghna, Bhola	BR219	99.640
Lower Meghna, Bhola	BR446	100.338
Lower Meghna, Daulatkhan	BR8230	99.302
Padma, Mawa	BR529	99.163
Padma, Mawa	BR724	98.986

Table SVI-5. Chemical analyses of river sediment.

Ganga, Brahmaputra and Lower Meghna sample data are presented. Al/Si and Fe/Si ratios are from Lupker et al. (2013) and Sr concentrations, measured similarly than for the samples presented in Table S4, from this study. Type: SL: Suspended load; BL: Bed load; Bank: Bank sediments

Table SVI-5 (…/…)

Sample#	River	Locality	Lat	Long	Type	Depth (m)	Load (g/L)	Date	Al/Si mol:mol	Fe/Si mol:mol	Sr
Ganga in Bangladesh											
BR 212	Ganga	Harding bridge	24.0529	89.02465	SL	1	0.6	15-juil-98	0.39	0.09	78
BR 211	Ganga	Harding bridge	24.0529	89.02465	SL	3.5	0.8	15-juil-98	0.35	0.08	79
BR 209	Ganga	Harding bridge	24.0529	89.02465	SL	5	0.7	15-juil-98	0.36	0.09	77
BR 208	Ganga	Harding bridge	24.0529	89.02465	SL	10	0.7	15-juil-98	0.35	0.08	85
BR 210	Ganga	Harding bridge	24.0529	89.02465	SL	17	1.2	15-juil-98	0.29	0.07	87
BR 214	Ganga	Harding bridge	24.0529	89.02465	BL	22		15-juil-98	0.15	0.03	96
BR 417	Ganga	Harding bridge	24.0529	89.02465	SL	0		12-juil-00	0.39	0.09	86
BR 415	Ganga	Harding bridge	24.0529	89.02465	SL	0	0.8	12-juil-00	0.38	0.09	84
BR 414	Ganga	Harding bridge	24.0529	89.02465	SL	2	1.0	12-juil-00	0.34	0.08	90
BR 413	Ganga	Harding bridge	24.0529	89.02465	SL	4	1.3	12-juil-00	0.30	0.07	
BR 412	Ganga	Harding bridge	24.0529	89.02465	SL	6.5	1.5	12-juil-00	0.28	0.07	92
BR 411	Ganga	Harding bridge	24.0529	89.02465	SL	9	2.9	12-juil-00	0.21	0.05	97
BR 418	Ganga	Harding bridge	24.0529	89.02465	BL	10		12-juil-00	0.14	0.05	93
BR 419	Ganga	Harding bridge	24.0529	89.02465	Bank			12-juil-00	0.19	0.04	115
BR 420	Ganga	Harding bridge	24.0529	89.02465	Bank			12-juil-00	0.27	0.06	110
BR 421	Ganga	Harding bridge	24.0529	89.02465	Bank			12-juil-00	0.22	0.05	111
BR 422	Ganga	Harding bridge	24.0529	89.02465	Bank			12-juil-00	0.22	0.05	111
BR 515	Ganga	Harding bridge	24.0529	89.02465	SL	0	0.9	22-juil-01	0.37	0.10	99
BR 514	Ganga	Harding bridge	24.0529	89.02465	SL	2.5	1.4	22-juil-01	0.32	0.09	104
BR 513	Ganga	Harding bridge	24.0529	89.02465	SL	5	1.7	22-juil-01	0.28	0.07	109
BR 512	Ganga	Harding bridge	24.0529	89.02465	SL	7	1.8	22-juil-01	0.27	0.07	108
BR 511	Ganga	Harding bridge	24.0529	89.02465	SL	10	2.4	22-juil-01	0.24	0.06	107
BR 516	Ganga	Harding bridge	24.0529	89.02465	BL	11		22-juil-01	0.13	0.02	99
BR 519	Ganga	Harding bridge	24.0529	89.02465	SL	0	0.7	22-juil-01	0.42	0.12	95
BR 518	Ganga	Harding bridge	24.0529	89.02465	SL	5	1.5	22-juil-01	0.31	0.08	106
BR 517	Ganga	Harding bridge	24.0529	89.02465	SL	9.8	1.8	22-juil-01	0.28	0.07	107
BR 520	Ganga	Harding bridge	24.0529	89.02465	BL	10		22-juil-01	0.17	0.04	109
BR 522	Ganga	Harding bridge	24.0529	89.02465	SL	0		12-juil-00	0.40	0.11	96
BR 716	Ganga	Harding bridge	24.0529	89.02465	SL	0	0.7	16-août-03	0.34	0.09	93
BR 715	Ganga	Harding bridge	24.0529	89.02465	SL	3	1.4	16-août-03	0.25	0.06	98
BR 714	Ganga	Harding bridge	24.0529	89.02465	SL	8	2.2	16-août-03	0.20	0.05	100
BR 713	Ganga	Harding bridge	24.0529	89.02465	SL	10	3.1	16-août-03	0.18	0.04	101
BR 717	Ganga	Harding bridge	24.0529	89.02465	BL	11		16-août-03	0.13	0.05	92
BR 718 A	Ganga	Harding bridge	24.0529	89.02465	triSL	9.8	2.4	16-août-03	0.20	0.05	99
BR 718 B	Ganga	Harding bridge	24.0529	89.02465	triSL	10.3	3.1	16-août-03	0.18	0.04	100
BR 718 C	Ganga	Harding bridge	24.0529	89.02465	triSL	10.8	6.5	16-août-03	0.16	0.05	95
BR 8218	Ganga	Harding bridge	24.0529	89.02465	SL	2	1.4	31-août-04	0.27	0.07	103
BR 8217	Ganga	Harding bridge	24.0529	89.02465	SL	4	1.6	31-août-04	0.25	0.06	102
BR 8216	Ganga	Harding bridge	24.0529	89.02465	SL	7	1.6	31-août-04	0.25	0.06	101
BR 8215	Ganga	Harding bridge	24.0529	89.02465	SL	12	3.3	31-août-04	0.18	0.04	96
BR 8219a	Ganga	Harding bridge	24.0529	89.02465	triSL	10.5	1.5	31-août-04	0.22	0.05	103
BR 8219b	Ganga	Harding bridge	24.0529	89.02465	triSL	11	1.8	31-août-04	0.22	0.06	107
BR 8219c	Ganga	Harding bridge	24.0529	89.02465	triSL	11.5	1.4	31-août-04	0.21	0.05	105
BR 8221	Ganga	Harding bridge	24.0529	89.02465	BL	12		31-août-04	0.13	0.03	95
BR 8222	Ganga	Harding bridge	24.0529	89.02465	SL	0	0.9	31-août-04	0.33	0.08	104
BR 8250	Ganga	Harding bridge	24.0529	89.02465	SL	10	1.1	09-sept-04	0.26	0.07	102

Table SVI-5 (…/…)

Sample#	River	Locality	Lat	Long	Type	Depth (m)	Load (g/L)	Date	Al/Si mol:mol	Fe/Si mol:mol	Sr
BR 8251	Ganga	Harding bridge	24.0529	89.02465	SL	5	1.2	09-sept-04	0.26	0.07	100
BR 8252	Ganga	Harding bridge	24.0529	89.02465	BL	15		09-sept-04	0.11	0.02	90
BR 8253	Ganga	Harding bridge	24.0529	89.02465	SL	0	0.6	09-sept-04	0.33	0.08	100
BR 8255a	Ganga	Harding bridge	24.0529	89.02465	triSL	5	1.2	09-sept-04	0.26	0.07	106
BR 8255b	Ganga	Harding bridge	24.0529	89.02465	triSL	5.5	1.2	09-sept-04	0.25	0.06	104
BR 8255c	Ganga	Harding bridge	24.0529	89.02465	triSL	6	1.3	09-sept-04	0.24	0.06	112
BR 8256a	Ganga	Harding bridge	24.0529	89.02465	triSL	5.4	1.4	09-sept-04	0.22	0.05	100
BR 8256b	Ganga	Harding bridge	24.0529	89.02465	triSL	5.9	1.2	09-sept-04	0.24	0.06	98
BR 8256c	Ganga	Harding bridge	24.0529	89.02465	triSL	6.4	1.5	09-sept-04	0.21	0.05	99
BR 8279	Ganga	Harding bridge	24.0529	89.02465	SL	12	0.6	21-sept-04	0.28	0.07	102
BR 8280	Ganga	Harding bridge	24.0529	89.02465	SL	6	0.6	21-sept-04	0.30	0.08	108
BR 8281	Ganga	Harding bridge	24.0529	89.02465	SL	0	0.4	21-sept-04	0.37	0.09	87
BR 8283	Ganga	Harding bridge	24.0529	89.02465	BL	12.5		21-sept-04	0.13	0.02	85
BR 8286	Ganga	Harding bridge	24.0529	89.02465	Bank			21-sept-04	0.32	0.08	107
BR 1024	Ganga	Harding bridge	24.0529	89.02465	SL	9	0.6	07-juil-06	0.39	0.09	91
BR 1025	Ganga	Harding bridge	24.0529	89.02465	SL	5	0.6	07-juil-06	0.40	0.10	91
BR 1026	Ganga	Harding bridge	24.0529	89.02465	SL	0.3	0.5	07-juil-06	0.45	0.11	84
BR 1027	Ganga	Harding bridge	24.0529	89.02465	BL			07-juil-06	0.25	0.06	
BR 1028	Ganga	Harding bridge	24.0529	89.02465	SL	11	0.6	07-juil-06	0.38	0.09	91
BR 1030	Ganga	Harding bridge	24.0529	89.02465	SL	0	1.0	07-juil-06	0.45	0.11	85
BR 1031	Ganga	Harding bridge	24.0529	89.02465	SL	3	1.0	07-juil-06	0.43	0.10	85
BR 1032	Ganga	Harding bridge	24.0529	89.02465	SL	6	1.1	07-juil-06	0.39	0.09	91
Brahmaputra in Bangladesh											
BR 401	Brahmaputra	Sirajganj	24.47233	89.72574	SL	6.5	4.3	10-juil-00	0.23		155
BR 405	Brahmaputra	Sirajganj	24.47233	89.72574	SL	5	6.0	10-juil-00	0.22		152
BR 406	Brahmaputra	Sirajganj	24.47233	89.72574	SL	3	3.1	10-juil-00	0.25		138
BR 407	Brahmaputra	Sirajganj	24.47233	89.72574	SL	11	6.4	10-juil-00	0.23		149
BR 408	Brahmaputra	Sirajganj	24.47233	89.72574	SL	1.5	1.8	10-juil-00	0.29		124
BR 409	Brahmaputra	Sirajganj	24.47233	89.72574	SL	0	1.3	10-juil-00	0.32		114
BR 402	Brahmaputra	Sirajganj	24.47233	89.72574	SL	0		10-juil-00	0.33		108
BR 459	Brahmaputra	Sirajganj	24.47233	89.72574	SL			22-juil-00	0.38		154
BR 457	Brahmaputra	Sirajganj	24.47233	89.72574	SL	0	1.3	22-juil-00	0.36		160
BR 456	Brahmaputra	Sirajganj	24.47233	89.72574	SL	3	2.9	22-juil-00	0.29		160
BR 455	Brahmaputra	Sirajganj	24.47233	89.72574	SL	6	2.4	22-juil-00	0.30		153
BR 454	Brahmaputra	Sirajganj	24.47233	89.72574	SL	9	6.2	22-juil-00	0.23		163
BR 460	Brahmaputra	Sirajganj	24.47233	89.72574	BL	10		22-juil-00	0.17		184
BR 450	Brahmaputra	Sirajganj	24.47233	89.72574	BL			22-juil-00	0.32		166
BR 451	Brahmaputra	Sirajganj	24.47233	89.72574	BL			22-juil-00	0.40		197
BR 453	Brahmaputra	Sirajganj	24.47233	89.72574	BL			22-juil-00	0.22		147
BR 500	Brahmaputra	Sirajganj	24.47233	89.72574	SL	0		21-juil-01	0.32		133
BR 501	Brahmaputra	Sirajganj	24.47233	89.72574	SL	6.5	2.0	21-juil-01	0.29		137
BR 502	Brahmaputra	Sirajganj	24.47233	89.72574	SL	2.5	0.8	21-juil-01	0.34		113
BR 503	Brahmaputra	Sirajganj	24.47233	89.72574	BL	7.5		21-juil-01	0.19		169
BR 508	Brahmaputra	Sirajganj	24.47233	89.72574	SL	0	0.8	21-juil-01	0.36		111
BR 507	Brahmaputra	Sirajganj	24.47233	89.72574	SL	2.8	1.4	21-juil-01	0.32		118
BR 506	Brahmaputra	Sirajganj	24.47233	89.72574	SL	5	1.6	21-juil-01	0.29		133
BR 505	Brahmaputra	Sirajganj	24.47233	89.72574	SL	7	2.1	21-juil-01	0.28		135
BR 504	Brahmaputra	Sirajganj	24.47233	89.72574	SL	9.8	2.3	21-juil-01	0.25		148
BR 509	Brahmaputra	Sirajganj	24.47233	89.72574	BL	10		21-juil-01	0.15		148
BR 800	Brahmaputra	Sirajganj	24.47233	89.72574	Bank			07-janv-04	0.25		167

Table SVI-5 (…/…)

Sample#	River	Locality	Lat	Long	Type	Depth (m)	Load (g/L)	Date	Al/Si mol:mol	Fe/Si mol:mol	Sr
BR 801	Brahmaputra	Sirajganj	24.47233	89.72574	Bank			07-janv-04	0.27		149
BR 802	Brahmaputra	Sirajganj	24.47233	89.72574	Bank			07-janv-04	0.16		171
BR 205	Brahmaputra	Jamuna bg.	24.38557	89.7969	SL	0.5	1.2	14-juil-98	0.31		165
BR 204	Brahmaputra	Jamuna bg.	24.38557	89.7969	SL	2		14-juil-98	0.27		170
BR 201	Brahmaputra	Jamuna bg.	24.38557	89.7969	SL	6		14-juil-98	0.26		165
BR 202	Brahmaputra	Jamuna bg.	24.38557	89.7969	SL	9.5	1.4	14-juil-98	0.22		170
BR 203	Brahmaputra	Jamuna bg.	24.38557	89.7969	SL	11.5	5.9	14-juil-98	0.19		170
BR 206	Brahmaputra	Jamuna bg.	24.38557	89.7969	BL	12		14-juil-98	0.20		175
BR 207	Brahmaputra	Jamuna bg.	24.38557	89.7969	SL	1		14-juil-98	0.23		180
BR 705	Brahmaputra	Jamuna bg.	24.38557	89.7969	SL	1	0.5	15-août-03	0.32		176
BR 704	Brahmaputra	Jamuna bg.	24.38557	89.7969	SL	5.5	0.9	15-août-03	0.28		185
BR 703	Brahmaputra	Jamuna bg.	24.38557	89.7969	SL	11	0.7	15-août-03	0.30		177
BR 702	Brahmaputra	Jamuna bg.	24.38557	89.7969	SL	17	0.6	15-août-03	0.31		168
BR 701	Brahmaputra	Jamuna bg.	24.38557	89.7969	SL	23	0.8	15-août-03	0.28		179
BR 706	Brahmaputra	Jamuna bg.	24.38557	89.7969	Bank			15-août-03	0.19		206
BR 707 A	Brahmaputra	Jamuna bg.	24.38557	89.7969	triSL	23	2.1	15-août-03	0.22		175
BR 707 B	Brahmaputra	Jamuna bg.	24.38557	89.7969	triSL	23.5	1.4	15-août-03	0.25		173
BR 707 C	Brahmaputra	Jamuna bg.	24.38557	89.7969	triSL	24	1.3	15-août-03	0.25		173
BR 708 A	Brahmaputra	Jamuna bg.	24.38557	89.7969	triSL	4	1.1	15-août-03	0.26		168
BR 708 B	Brahmaputra	Jamuna bg.	24.38557	89.7969	triSL	4.5	1.5	15-août-03	0.23		167
BR 708 C	Brahmaputra	Jamuna bg.	24.38557	89.7969	triSL	5	2.8	15-août-03	0.21		171
BR 709	Brahmaputra	Jamuna bg.	24.38557	89.7969	SL	0		15-août-03	0.57		126
BR 8203	Brahmaputra	Jamuna bg.	24.38557	89.7969	SL	5	1.5	30-août-04	0.25		128
BR 8204	Brahmaputra	Jamuna bg.	24.38557	89.7969	SL	1	1.0	30-août-04	0.29		116
BR 8206	Brahmaputra	Jamuna bg.	24.38557	89.7969	BL	10		30-août-04	0.17		188
BR 8210	Brahmaputra	Jamuna bg.	24.38557	89.7969	SL	0	1.0	30-août-04	0.33		159
BR 8211	Brahmaputra	Jamuna bg.	24.38557	89.7969	SL	2.5	1.4	30-août-04	0.27		165
BR 8208	Brahmaputra	Jamuna bg.	24.38557	89.7969	SL	5	1.7	30-août-04	0.25		162
BR 8207	Brahmaputra	Jamuna bg.	24.38557	89.7969	SL	10	3.6	30-août-04	0.20		166
BR 8212a	Brahmaputra	Jamuna bg.	24.38557	89.7969	triSL	9	3.4	30-août-04	0.23		170
BR 8212b	Brahmaputra	Jamuna bg.	24.38557	89.7969	triSL	9.5	4.5	30-août-04	0.22		178
BR 8212c	Brahmaputra	Jamuna bg.	24.38557	89.7969	triSL	10	4.6	30-août-04	0.21		154
BR 8213	Brahmaputra	Jamuna bg.	24.38557	89.7969	BL	10		30-août-04	0.18		157
BR 8261	Brahmaputra	Jamuna bg.	24.38557	89.7969	SL	0	0.7	11-sept-04	0.29		159
BR 8260	Brahmaputra	Jamuna bg.	24.38557	89.7969	SL	6	1.3	11-sept-04	0.25		167
BR 8259	Brahmaputra	Jamuna bg.	24.38557	89.7969	SL	12	1.7	11-sept-04	0.22		152
BR 8262	Brahmaputra	Jamuna bg.	24.38557	89.7969	BL	12.8		11-sept-04	0.14		150
BR 8264a	Brahmaputra	Jamuna bg.	24.38557	89.7969	triSL	7.6	1.5	11-sept-04	0.26		173
BR 8264b	Brahmaputra	Jamuna bg.	24.38557	89.7969	triSL	8.1	1.8	11-sept-04	0.26		169
BR 8264c	Brahmaputra	Jamuna bg.	24.38557	89.7969	triSL	8.6	2.7	11-sept-04	0.25		172
BR 8265a	Brahmaputra	Jamuna bg.	24.38557	89.7969	triSL	11.9	1.4	11-sept-04	0.26		164
BR 8265b	Brahmaputra	Jamuna bg.	24.38557	89.7969	triSL	12.4	1.7	11-sept-04	0.24		168
BR 8265c	Brahmaputra	Jamuna bg.	24.38557	89.7969	triSL	12.9	2.3	11-sept-04	0.23		162
BR 8266a	Brahmaputra	Jamuna bg.	24.38557	89.7969	triSL	9.8	0.9	11-sept-04	0.27		150
BR 8266b	Brahmaputra	Jamuna bg.	24.38557	89.7969	triSL	10.3	1.4	11-sept-04	0.25		158
BR 8266c	Brahmaputra	Jamuna bg.	24.38557	89.7969	triSL	10.8	1.5	11-sept-04	0.25		156
BR 8267a	Brahmaputra	Jamuna bg.	24.38557	89.7969	triSL	14.7	1.7	11-sept-04	0.22		178
BR 8267b	Brahmaputra	Jamuna bg.	24.38557	89.7969	triSL	15.2	1.9	11-sept-04	0.22		174
BR 8267c	Brahmaputra	Jamuna bg.	24.38557	89.7969	triSL	15.7	2.0	11-sept-04	0.21		168
BR 8288	Brahmaputra	Jamuna bg.	24.38557	89.7969	SL	9	1.3	22-sept-04	0.23		169
BR 8289	Brahmaputra	Jamuna bg.	24.38557	89.7969	SL	5	0.9	22-sept-04	0.26		180

Table SVI-5 (…/…)

Sample#	River	Locality	Lat	Long	Type	Depth (m)	Load (g/L)	Date	Al/Si mol:mol	Fe/Si mol:mol	Sr
BR 8290	Brahmaputra	Jamuna bg.	24.38557	89.7969	SL	0	0.3	22-sept-04	0.33		160
BR 8292	Brahmaputra	Jamuna bg.	24.38557	89.7969	BL	11.4		22-sept-04	0.15		161
BR 1010	Brahmaputra	Jamuna bg.	24.38557	89.7969	SL	11	2.2	06-juil-06	0.25		167
BR 1011	Brahmaputra	Jamuna bg.	24.38557	89.7969	SL	8	1.9	06-juil-06	0.26		165
BR 1012	Brahmaputra	Jamuna bg.	24.38557	89.7969	SL	6	1.3	06-juil-06	0.29		160
BR 1013	Brahmaputra	Jamuna bg.	24.38557	89.7969	SL	3	1.3	06-juil-06	0.28		161
BR 1014	Brahmaputra	Jamuna bg.	24.38557	89.7969	SL	0.2	0.8	06-juil-06	0.33		166
BR 1015	Brahmaputra	Jamuna bg.	24.38557	89.7969	BL	12		06-juil-06	0.22		183
BR 1016	Brahmaputra	Jamuna bg.	24.38557	89.7969	Bank			06-juil-06	0.36		179
BR 1017	Brahmaputra	Jamuna bg.	24.38557	89.7969	BL	8		06-juil-06	0.23		212
BR 1019	Brahmaputra	Jamuna bg.	24.38557	89.7969	SL	0	1.5	06-juil-06	0.31		183
BR 1020	Brahmaputra	Jamuna bg.	24.38557	89.7969	SL	3	2.3	06-juil-06	0.27		178
BR 1021	Brahmaputra	Jamuna bg.	24.38557	89.7969	SL	6	3.1	06-juil-06	0.24		168
BR 1033	Brahmaputra	Jamuna bg.	24.38557	89.7969	SL	11.5	4.1	08-juil-06	0.21		159
BR 1034	Brahmaputra	Jamuna bg.	24.38557	89.7969	SL	8	2.2	08-juil-06	0.24		142
BR 1035	Brahmaputra	Jamuna bg.	24.38557	89.7969	SL	5	1.2	08-juil-06	0.27		142
BR 1036	Brahmaputra	Jamuna bg.	24.38557	89.7969	SL	2.7	1.2	08-juil-06	0.28		143
BR 1037	Brahmaputra	Jamuna bg.	24.38557	89.7969	SL	0.2	0.8	08-juil-06	0.32		139
BR 1038	Brahmaputra	Jamuna bg.	24.38557	89.7969	BL			08-juil-06	0.26		154
BR 1039	Brahmaputra	Jamuna bg.	24.38557	89.7969	SL	6	3.5	08-juil-06	0.23		169
BR 1040	Brahmaputra	Jamuna bg.	24.38557	89.7969	SL	6	1.9	08-juil-06	0.27		165
BR 1041	Brahmaputra	Jamuna bg.	24.38557	89.7969	SL	6	2.5	08-juil-06	0.26		182
BR 1042	Brahmaputra	Jamuna bg.	24.38557	89.7969	SL	3	1.5	08-juil-06	0.28		179
BR 1043	Brahmaputra	Jamuna bg.	24.38557	89.7969	SL	3	1.4	08-juil-06	0.29		175
BR 1044	Brahmaputra	Jamuna bg.	24.38557	89.7969	SL	3	2.1	08-juil-06	0.28		181
BR 1045	Brahmaputra	Jamuna bg.	24.38557	89.7969	SL	0	0.9	08-juil-06	0.31		172
BR 1046	Brahmaputra	Jamuna bg.	24.38557	89.7969	SL	11	2.5	08-juil-06	0.24		161
BR 1047	Brahmaputra	Jamuna bg.	24.38557	89.7969	BL			08-juil-06	0.23		206
Lower Meghna in Bangladesh											
BR 528	Lower Meghna	Mawa	23.45643	90.24388	SL	0	1.0	23-juil-01	0.35		100
BR 527	Lower Meghna	Mawa	23.45643	90.24388	SL	2.3	1.3	23-juil-01	0.32		114
BR 526	Lower Meghna	Mawa	23.45643	90.24388	SL	5	1.4	23-juil-01	0.29		121
BR 524	Lower Meghna	Mawa	23.45643	90.24388	SL	7.5	2.3	23-juil-01	0.25		136
BR 525	Lower Meghna	Mawa	23.45643	90.24388	SL	9.5	2.6	23-juil-01	0.24		127
BR 529	Lower Meghna	Mawa	23.45643	90.24388	BL	11		23-juil-01	0.16		139
BR 721	Lower Meghna	Mawa	23.45643	90.24388	SL	10	1.7	18-août-03	0.24		117
BR 722	Lower Meghna	Mawa	23.45643	90.24388	SL	4	1.1	18-août-03	0.28		117
BR 723	Lower Meghna	Mawa	23.45643	90.24388	SL	0	0.6	18-août-03	0.37		93
BR 724	Lower Meghna	Mawa	23.45643	90.24388	BL	11		18-août-03	0.15		151
BR 725 A	Lower Meghna	Mawa	23.45643	90.24388	triSL	9.8	1.9	18-août-03	0.24		117
BR 725 C	Lower Meghna	Mawa	23.45643	90.24388	triSL	10.8	10.5	18-août-03	0.17		141
BR 817	Lower Meghna	Mawa	23.45643	90.24388	Bank			13-janv-04	0.28		120
BR 819	Lower Meghna	Mawa	23.45643	90.24388	Bank			13-janv-04	0.17		138
BR 820	Lower Meghna	Mawa	23.45643	90.24388	Bank			13-janv-04	0.19		166
BR 8201	Lower Meghna	Mawa	23.45643	90.24388	SL	5	2.6	28-août-04	0.23		128
BR 8202	Lower Meghna	Mawa	23.45643	90.24388	SL	1	1.2	28-août-04	0.30		111
BR 1001	Lower Meghna	Mawa	23.45643	90.24388	SL	17.5	2.5	04-juil-06	0.23		145
BR 1002	Lower Meghna	Mawa	23.45643	90.24388	SL	13	1.6	04-juil-06	0.27		141
BR 1003	Lower Meghna	Mawa	23.45643	90.24388	SL	8	1.7	04-juil-06	0.27		146
BR 1004	Lower Meghna	Mawa	23.45643	90.24388	SL	4	1.1	04-juil-06	0.30		157

Table SVI-5 (…/…)

Sample#	River	Locality	Lat	Long	Type	Depth (m)	Load (g/L)	Date	Al/Si mol:mol	Fe/Si mol:mol	Sr
BR 1005	Lower Meghna	Mawa	23.45643	90.24388	SL	0.2	0.9	04-juil-06	0.34		145
BR 1006	Lower Meghna	Mawa	23.45643	90.24388	SL	shallow	1.7	04-juil-06	0.29		154
BR 1007	Lower Meghna	Mawa	23.45643	90.24388	SL	deep	1.9	04-juil-06	0.27		155
BR 1057	Lower Meghna	Mawa	23.45643	90.24388	SL	0	1.1	10-juil-06	0.35		131
BR 1058	Lower Meghna	Mawa	23.45643	90.24388	SL	3	1.2	10-juil-06	0.33		142
BR 1059	Lower Meghna	Mawa	23.45643	90.24388	SL	6	1.8	10-juil-06	0.30		147
BGP 21	Lower Meghna	Bhola	22.8248	90.7223	SL	0			0.41		119
BR 218	Lower Meghna	Bhola	22.8248	90.7223	SL	1.5	0.4	17-juil-98	0.37		115
BR 220	Lower Meghna	Bhola	22.8248	90.7223	SL	3	0.8	17-juil-98	0.28		124
BR 217	Lower Meghna	Bhola	22.8248	90.7223	SL	5	0.5	17-juil-98	0.31		121
BR 216	Lower Meghna	Bhola	22.8248	90.7223	SL	10	1.7	17-juil-98	0.21		134
BR 219	Lower Meghna	Bhola	22.8248	90.7223	BL	12		17-juil-98	0.21		211
BR 222	Lower Meghna	Bhola	22.8248	90.7223	Bank			17-juil-98	0.25		127
BR 448	Lower Meghna	Bhola	22.8248	90.7223	SL	0		17-juil-00	0.34		133
BR 441	Lower Meghna	Bhola	22.8248	90.7223	SL	0	0.3	17-juil-00	0.40		121
BR 444	Lower Meghna	Bhola	22.8248	90.7223	SL	2	0.6	17-juil-00	0.35		130
BR 442	Lower Meghna	Bhola	22.8248	90.7223	SL	4	0.7	17-juil-00	0.33		133
BR 440	Lower Meghna	Bhola	22.8248	90.7223	SL	6	1.8	17-juil-00	0.27		143
BR 439	Lower Meghna	Bhola	22.8248	90.7223	SL	8	3.0	17-juil-00	0.23		146
BR 445	Lower Meghna	Bhola	22.8248	90.7223	SL	10	3.9	17-juil-00	0.26		142
BR 446	Lower Meghna	Bhola	22.8248	90.7223	BL	11		17-juil-00	0.16		164
BR 8226	Lower Meghna	Daulatkhan	22.5874	90.76179	SL	16	4.9	02-sept-04	0.22		138
BR 8227	Lower Meghna	Daulatkhan	22.5874	90.76179	SL	10	5.1	02-sept-04	0.30		125
BR 8228	Lower Meghna	Daulatkhan	22.5874	90.76179	SL	5	5.0	02-sept-04	0.32		115
BR 8229	Lower Meghna	Daulatkhan	22.5874	90.76179	SL	0	9.6	02-sept-04	0.37		112
BR 8230	Lower Meghna	Daulatkhan	22.5874	90.76179	BL	17		02-sept-04	0.17		186
BR 1049	Lower Meghna	Daulatkhan	22.5874	90.76179	SL	11	0.8	11-juil-06	0.31		141
BR 1050	Lower Meghna	Daulatkhan	22.5874	90.76179	SL	0	0.6	11-juil-06	0.37		133
BR 1051	Lower Meghna	Daulatkhan	22.5874	90.76179	BL			11-juil-06	0.15		170
BR 1052	Lower Meghna	Daulatkhan	22.5874	90.76179	BL			11-juil-06	0.16		164
BR 1053	Lower Meghna	Daulatkhan	22.5874	90.76179	BL			11-juil-06	0.17		181
BGP 23	Lower Meghna	Chorfasson	22.19098	90.8257	SL	0			0.42		99
BGP 34	Lower Meghna	Chorfasson	22.19098	90.8257	BL				0.29		139
BR 8232	Lower Meghna	Chorfasson	22.19098	90.8257	SL	14	1.2	03-sept-04	0.30		120
BR 8233	Lower Meghna	Chorfasson	22.19098	90.8257	SL	7	1.0	03-sept-04	0.52		93
BR 8234	Lower Meghna	Chorfasson	22.19098	90.8257	SL	0	0.7	03-sept-04	0.40		100
BR 8235	Lower Meghna	Chorfasson	22.19098	90.8257	BL			03-sept-04	0.37		104
BR 8269	Lower Meghna	Chor Mankia	21.99301	90.67603	SL	5	1.6	16-sept-04	0.30		124
BR 8270	Lower Meghna	Chor Mankia	21.99301	90.67603	SL	0	0.7	16-sept-04	0.36		119

Table SVI-6. Sr-Nd and ^{10}Be data from river sediment used for the fG and K(t) computation.

Bulk silicate Sr-Nd data, extracted from bank and bedload, are from Galy and France-Lanord (2001), Singh and France-Lanord (2002), Singh et al. (2008). ^{10}Be data are averaged from Lupker et al. (2012, 2017). The production rates were computed using Basinga (Charreau et al., 2019) with the Lal-Stone / ERA40 atmosphere configuration using a sea-level high latitude production rate of 4.18 atom/g/y (Martin et al., 2017), factors for different particle production rates of 0.9886 for spallation, 0.0027 for slow muons, 0.0087 for fast muons and attenuation lengths of 260 g/cm2 for slow muons and 510 g/cm2 for fast muons (Braucher et al., 2011), and the basins defined in the Extended Methods.

		Sr-Nd								Approximate areas (km^2)				
		mean εNd	1σ	mean [Nd]	1σ	mean ^{87}Sr/^{86}Sr	1σ	mean [Sr]	1σ	Full basin	Plains	Basalts	Himalayan	Glacial cover
Ganga	Harding Bridge	-17.3	0.5	45	10	0.767	0.005	87	11	9.5E+05	3.7E+05	7.7E+04	2.3E+05	1.2E+04
Brahmaputra	Sirajgang / Jamuna Bridge	-14.5	0.7	45	10	0.726	0.004	175	20	5.2E+05	8.7E+04	-	4.0E+05	1.5E+04
Brahmaputra	Dibrugarh	-12.6	0.5	42	12	0.720	0.003	235	40					
Ganga + Brahmaputra										1.5E+06	4.6E+05	7.7E+04	6.3E+05	2.7E+04
Lower Meghna										1.7E+06	5.7E+05	7.7E+04	6.3E+05	2.7E+04

Table SVI-6. (…/…)

	^{10}Be Production rate (atom/g/y)			^{10}Be Production rate (atom/g/y)			Himalayan erosion			
	Including Craton, Shillong Plateau, In			Himalayan part only						
	neutron	slow muon	fast muon	neutron	slow muon	fast muon	mean ^{10}Be (atom/g)	1σ (atom/g)	mean erosion rate (mm/y)	1σ (mm/y)
Ganga	14.5	2.27E-02	4.77E-02	28.6	3.38E-02	5.87E-02	2.23E+04	2.28E+03	1.1	0.2
Brahmaputra	42.4	4.60E-02	7.01E-02	48.3	4.94E-02	7.34E-02	3.44E+04	8.09E+03	0.9	0.2
									1.0	0.3
Lower Meghna				41.2	4.37E-02	6.80E-02				

Table SVII-1. Paleomagnetism results.

The declination, inclination and polarity (N: normal, R: reverse, Int: intermediate) are presented for the silty/clayey samples having interpretable measurements. The depth of the samples is available in Table SVII-2. Note that samples with an even number (e.g. T506) have been sampled at the same location as samples with an odd number (e.g. T505).
Table SVII-1 (…/…)

Sample	Declination (°)	Inclination (°)	Polarity
Patalaia Section			
T501	377	64	N
T505	372	58	N
T506	125	38	Int
T511	354	83	N
T513	391	56	N
T514	360	56	N
T522	384	55	N
T529	405	39	N
T530	423	42	N
T531	276	32	Int
T536	344	40	N
T539	261	82	N
T542	418	9	N
T544	396	76	N
T545	308	73	N
T547	338	68	N
T549	343	53	N
Ganguli Section			
G06a	388	72	N
G08	330	25	N
G10	361	71	N
G13	341	70	N
G17	307	82	N
G21	362	36	N
G24	428	67	N
G26	415	31	N
G36	325	65	N
G39	367	22	N
G50	212	-37	R
G54	170	-22	R
G58	142	-10	R
G59	170	-19	R
G62	184	-36	R
Dwarda section			
D102	349	20	N
D107	190	-1	R
D109	179	-28	R
D113	161	-42	R
D117	222	-66	R
D121	173	-33	R
D137	179	-27	R
D150	207	-17	R
D170	297	26	Int
D178	348	56	N
D180	202	-17	R
D181	153	-28	R
D185	125	8	Int
D188	179	-2	R
D189	401	67	N
D202	389	47	N
D204	379	25	N
D210	355	75	N
D218	327	12	N
D227	139	-8	R
D236	186	5	Int
D240	153	-13	R
D247	204	-17	R
D258	156	-9	R
D263	213	-56	R
283b	346	75	N
291	336	38	N
293	349	6	N
295	330	17	N
297	368	45	N
302	385	56	N
304	361	24	N
305	384	36	N
309	344	18	N
307B	419	9	N
309	363	32	N
311	363	32	N
313	152	-20	R

Table SVII-1 (…/…)

Sample	Declination (°)	Inclination (°)	Polarity
324	211	-40	R
326	345	25	N
328	374	20	N
341	311	45	N
344	200	-13	R
356	329	22	N
366	159	-31	R
370	144	-55	R
376	182	-22	R
382	176	-5	R
391	172	-26	R
392	159	-24	R
402	192	-1	R
408	433	43	N
429	351	43	N
431	378	29	N
446	134	-10	R
448	137	-12	R
455	376	22	N
457	379	29	N
466	326	67	N
470	348	39	N
472	324	49	N
473	321	49	N
602	180	-44	R
603	182	-29	R
606	182	-7	R
610	185	-32	R
615	395	38	N
622	134	-9	R
626	165	-6	R
631	173	-36	R
635	151	-11	R
642	154	-4	R
660	183	-52	R
662	182	-36	R
668	265	-65	R
675	373	38	N
677	323	48	N
679	338	50	N
684	359	49	N
690	337	60	N
692	387	40	N
694	346	33	N
696	350	51	N
700	181	-12	R
705	343	31	N
708	381	42	N
709	350	27	N
711	340	45	N
717	351	35	N
719	357	28	N
721	305	23	N
723	381	31	N
725	144	-4	R
734	157	-22	R
737	168	-38	R
740	178	-34	R
741	171	-40	R
743	149	-24	R
746	156	-14	R
747	170	-28	R
755	166	-29	R
757	178	-51	R
759	196	-23	R
764	366	47	N
767	350	26	N
771	344	21	N
774	375	43	N
776	186	-34	R
778	199	-37	R
779	343	38	N
781	401	29	N
783	156	-48	R?
786	172	-45	R
787	165	-20	R
789	165	-20	R
794	172	-37	R
796	148	-33	R
803	205	-40	R
805	113	-50	R
807	180	-71	R

Table SVII-1 (…/…)

Sample	Declination (°)	Inclination (°)	Polarity
809	336	30	N
816	352	42	N
818	336	12	N
820	336	39	N
821	349	52	N
823	212	-54	R
825	166	-61	R
827	323	-77	Int
830	362	-52	Int
831	352	52	N
834	342	11	N
836	351	50	N
837	350	63	N
843	365	58	N
846	408	68	N
847	341	30	N
850	318	61	N
858	351	48	N
859	324	17	N
861	330	57	N
864	339	54	N
866	325	45	N
868	302	57	N
869	307	36	N
871	336	52	N
873	337	51	GC-R?
876	185	-51	R
881	150	-28	R
887	143	4	R
904	151	-41	R
906	178	-60	R
908	145	-55	R
910	196	-75	R

Table SVII-2. Clayey to fine sand sample information, magnetostratigraphic correlation results.

Field observations at the location of silty/clayey samples are indicated. The samples with an even number (e.g. T554), having the same location than the samples with an odd number (e.g. T553) are not represented. The sample depth considered for interpretation is the tape-meter computed depth, obtained from tape-meter length, dips and GPS coordinates. The results of the magnetostratigraphic correlation (Lallier et al., 2013) is indicated in columns J-K. Timescale of Gradstein et al., 2012. Arbitrary 1-σ age uncertainty of 0.1 Ma.

Table SVII-2. (…/…)

	Sample information								Magnetostratigraphic correlation results	
Sample	Tape-meter length (m)	Azimuth (°)	Strike (°)	Dip (°)	Latitude (°N)	Longitude (°E)	Estimated depth in sedimentary logs (m)	Tape-meter computed depth (m)	Age (Ma) (Ma)	1-σ (Ma)
Patalaia Section										
STARTT	-	-	-	-	-	-	0	0	-	-
T553	-	70	-	-	27.321777	84.412451	100	0	-	-
T551	19.7	155	85	45.5	27.321837	84.412558	107.5	12.593764	0.26	0.1
T549	14.5	145	-	-	27.321934	84.412575	114.5	21.036921	0.28	0.1
T547	25.3	160	-	-	27.322005	84.412405	122	38.072568	0.32	0.1
T545	7.5	40	-	-	27.322181	84.412368	129	42.219322	0.33	0.1
T543	9.0	20	90	40	27.322108	84.412490	134.5	48.357205	0.35	0.1
T541	7.6	195	90	45	27.322260	84.412324	141	53.71891	0.36	0.1
T539	10.3	160	85	-	27.322302	84.412327	147	60.828409	0.37	0.1
T537	20.0	160	90	52	27.322436	84.412436	154.5	74.728704	0.41	0.1
T535	10.0	175	90	48	27.322486	84.412350	173	82.215548	0.42	0.1
T533	10.3	30	-	-	27.322628	84.412305	182.5	88.971095	0.44	0.1
T531	10.0	50	-	-	27.322689	84.412334	187.5	93.858265	0.45	0.1
T529	17.5	150	80	52	27.322677	84.412404	193.5	105.43384	0.48	0.1
T527	14.0	130	-	-	27.322787	84.412353	202.5	112.35278	0.49	0.1
T525	17.5	170	90	56.5	27.323046	84.412296	214.5	125.71479	0.53	0.1
T523	7.7	65	-	-	27.323124	84.412328	218.5	128.24459	0.53	0.1
T521	20.4	65	-	-	27.323150	84.412260	233	135.00954	0.55	0.1
T519	15.0	30	-	-	27.323231	84.412359	243.5	145.26735	0.57	0.1
T517	7.0	155	90	51	27.323372	84.412304	250	150.29581	0.58	0.1
T515	9.7	175	90	50	27.323441	84.412292	257.5	157.98692	0.60	0.1
T513	9.6	60	-	-	27.323497	84.412207	268.5	161.82972	0.61	0.1
T511	11.5	50	70		27.323546	84.412335	274.5	167.7657	0.62	0.1
T509	9.0	30	90		27.323630	84.412349	283.5	174.05212	0.64	0.1
T507	6.2	185	-	-	27.323695	84.412398	294	179.05788	0.65	0.1
T505	9.0	0	-	-	27.323755	84.412385	302	186.37769	0.67	0.1
T503	1.0	190	-	-	27.323773	84.412227	304.5	187.1795	0.67	0.1
T501	13.0	-	-	-	27.323847	84.412265	314.5	197.80731	0.69	0.1
ENDT	-	-	-	-	-	-	324.5	207.80731	0.72	0.1
Ganguli Section										
startG0	-	-	-	-	-	-	0	0	-	-
STARTG	-	-	-	-	-	-	179.4	179.4	0.42	0.1
G01	-	-	90	47	27.322079	84.396908	182.2	179.4	0.42	0.1
G03	14.3	190	90	47	27.322245	84.396939	190.9	190.04258	0.45	0.1
G05	11.2	190	-	-	27.322290	84.396946	198.4	198.50679	0.47	0.1
GGCOS1	-	-	95	40	27.322353	84.396896	203.4	204.74549	0.48	0.1
G07	16.2	190	90	55	27.322418	84.396977	208.4	210.98419	0.50	0.1
G09	21.0	185	90	50	27.322609	84.396963	223.4	227.76977	0.54	0.1
G11	10.2	195	-	-	27.322687	84.396958	237.4	235.84359	0.56	0.1
G13	11.5	180	105	64	27.322780	84.397004	246.4	245.38394	0.58	0.1
G15	8.6	180	90	55	27.322881	84.396996	253.4	252.58229	0.60	0.1
G17	16.1	180	95	60	27.323049	84.397018	266.4	266.26405	0.63	0.1
G19	13.9	185	90	55	27.323180	84.397044	278.4	278.17951	0.65	0.1
GGCOS2	-	-	-	-	27.323301	84.397127	286.4	283.14403	0.67	0.1
G21	12.1	200	-	-	27.323386	84.397177	294.4	288.10856	0.68	0.1
G23	18.3	195	-	-	27.323483	84.397150	302.4	303.64624	0.71	0.1
G25	12.3	190	-	-	27.323567	84.397150	306.9	314.3309	0.74	0.1
G27	-	-	-	-	27.324128	84.396980	361.4	368.8309	0.87	0.1
GGCOS3	-	-	-	-	27.324147	84.396931	362.4	370.05924	0.87	0.1
G29	4.7	125	-	-	27.324194	84.396957	363.4	371.28759	0.87	0.1
G31	19.0	125	100	62	27.324252	84.396788	365.4	381.22704	0.89	0.1
G33	7.3	150	-	-	27.324298	84.396760	373.4	387.01093	0.91	0.1
G35	-	-	90	68	27.324649	84.398692	399	412.61093	0.97	0.1
G37	5.8	-	-	-	27.324724	84.398745	404	416.39308	0.98	0.1
G39	7.6		90	70	27.324822	84.398795	410	421.349	0.99	0.1
G40B	15.0	-	-	-	27.324858	84.398896	419	431.13042	1.01	0.1
GGCOS4	-	-	-	-	27.324883	84.398741	422.5	436.34717	1.02	0.1
G41	16.0	-	-	-	27.324900	84.398700	426	441.56393	1.04	0.1
G43	13.0	-	-	-	27.325104	84.399003	436	450.04116	1.06	0.1
G45	28.0	-	-	-	27.325339	84.399076	459	468.29981	1.09	0.1
G47	10.6	-	-	-	27.325412	84.399107	466.2	475.21201	1.10	0.1
G49	15.0	-	-	-	27.325567	84.399108	477	484.99343	1.12	0.1
G51	20.2	-	-	-	27.325729	84.399124	500	498.16574	1.14	0.1
G53	18.7	-	-	-	27.325888	84.399136	518	510.35991	1.16	0.1
G55	9.2	-	-	-	27.325955	84.399117	528	516.35918	1.17	0.1

Table SVII-2. (…/…)

	Sample information								Magnetostratigraphic correlation results	
Sample	Tape-meter length (m)	Azimuth (°)	Strike (°)	Dip (°)	Latitude (°N)	Longitude (°E)	Estimated depth in sedimentary logs (m)	Tape-meter computed depth (m)	Age (Ma) (Ma)	1-σ (Ma)
G57	21.0	-	-	-	27.326132	84.399131	547	530.05316	1.20	0.1
G59	15.3	-	-	-	27.326322	84.399132	561	540.03021	1.21	0.1
G61	11.4	-	-	-	27.326382	84.399060	571	547.46409	1.23	0.1
G63	12.1	-	-	-	27.326504	84.399065	580	555.35443	1.24	0.1
ENDG		-	-	-	-	-	584	559.35443	1.25	0.1
Dwarda Section										
startd	-	-	-	-	-	-	0	0	-	-
beg1201	-	-	-	-	-	-	430	430	1.00	0.1
DWCOS42 (	-	-	80	56	27.327183	84.366867	441.5	430	1.03	0.1
D101	-	-	110	58	27.327261	84.366979	453	430	1.06	0.1
D103	4.3	170	85	60	27.327319	84.367043	458	433.7215	1.06	0.1
D105	5.5	170	95	60	27.327414	84.36714	464.5	438.48157	1.07	0.1
D107	6.3	170	90	63	27.327422	84.36701	470	443.934	1.08	0.1
D109	12.0	185	-	-	27.327549	84.366949	479	454.43968	1.10	0.1
D111	9.6	180	-	-	27.327595	84.366843	486	462.87632	1.12	0.1
D113	13.0	180	-	-	27.32767	84.367108	496	474.30094	1.14	0.1
D115	11.1	15	85	59	27.327877	84.367045	507	483.72342	1.15	0.1
D117	6.6	15	-	-	27.327841	84.367094	513	489.32598	1.16	0.1
DWCOS1	-	-	-	-	27.327893	84.367141	520	495.66696	1.17	0.1
DWCOS50	-	-	-	-	27.32795	84.367233	521	496.57281	1.17	0.1
DWCOS51	-	-	-	-	27.32795	84.367233	522	497.47867	1.18	0.1
D119	15.7	10	-	-	27.327963	84.367213	528	502.91379	1.19	0.1
D121	4.6	20	85	62.5	27.328033	84.367158	532	506.71256	1.19	0.1
DWCOS49	-	-	-	-	27.3281	84.367183	535	511.34898	1.20	0.1
D123	12.5	190	90	53	27.328212	84.36713	539	517.53088	1.21	0.1
D125	13.0	185	-	-	27.328273	84.367211	548.5	528.91203	1.23	0.1
D127	20.0	175	-	-	27.328422	84.367183	569	546.42149	1.26	0.1
D129	14.2	160	-	-	27.328523	84.367114	594	558.1481	1.28	0.1
DWCOS2	-	-	-	-	27.3286	84.367141	600	562.77268	1.29	0.1
D131	11.2	160	-	-	27.328658	84.367051	606	567.39726	1.30	0.1
D133	12.8	165	-	-	27.328712	84.366968	620.5	578.26283	1.32	0.1
DWCOS48	-	-	-	-	27.328867	84.366883	624.75	583.45562	1.32	0.1
D135	12.0	170	-	-	27.328862	84.366979	629	588.64842	1.33	0.1
D137	5.0	340	-	-	27.328916	84.366959	635	592.77751	1.34	0.1
D139	11.5	190	80	66	27.329006	84.366932	645	602.73037	1.36	0.1
D141	14.7	170	-	-	27.32912	84.366632	655	615.45272	1.38	0.1
D143	13.0	350	88		27.329218	84.366553	665	626.70377	1.40	0.1
F143	-	0	-	-	27.329218	84.366553	665.01	626.71305	1.40	0.1
DWCOS47	-	-	-	-	-	-	668	629.48778	1.40	0.1
DWCOS3					27.329187	84.366413	670	631.34378	1.41	0.1
D145	10.6	5	85	62	27.329314	84.366493	675	635.98379	1.41	0.1
D147	11.0	160	-	-	27.329439	84.366394	686	645.06778	1.43	0.1
D149	4.5	170	-	-	27.329496	84.36641	692	648.96238	1.44	0.1
DWCOS4	-	-	-	-	27.329532	84.366415	696	653.42729	1.44	0.1
D151	10.2	175	87	59.5	27.329572	84.366381	700	657.8922	1.45	0.1
D153	9.3	170	-	-	27.329651	84.366347	709.5	665.94104	1.47	0.1
D155	26.4	270	-	-	27.329887	84.366328	730	665.94104	1.47	0.1
D157	15.0	170	-	-	27.330006	84.366301	742	678.92303	1.49	0.1
D159	15.0	170	-	-	27.330136	84.366304	752	691.90501	1.51	0.1
D161	9.1	170	-	-	27.330212	84.366278	761	699.78075	1.52	0.1
D163	11.5	170	87	65	27.330312	84.366281	770	709.73361	1.54	0.1
D165	5.7	170	-	-	27.330359	84.366271	775	714.66677	1.55	0.1
DWCOS5	-	-	-	-	27.330359	84.366218	779.5	718.04208	1.56	0.1
D167	7.8	170	95	62	27.330416	84.366279	784	721.4174	1.56	0.1
D169	12.6	180	-	-	27.330589	84.366297	803	732.4905	1.58	0.1
D171	18.3	5	-	-	27.330742	84.366227	816	748.51165	1.61	0.1
DWCOS46	-	-	-	-	27.330777	84.366326	822.5	755.41037	1.62	0.1
D173	15.7	180	-	-	27.330861	84.36627	829	762.30908	1.63	0.1
D175	10.5	180	-	-	27.330943	84.366252	835.5	771.53666	1.65	0.1
D177	9.7	180	87	65	27.331038	84.366249	845	780.06119	1.66	0.1
D179	16.2	5	65	61	27.331174	84.366288	855	794.24385	1.69	0.1
D181	16.9	5	-	-	27.331335	84.366328	869	809.03934	1.71	0.1
D183	9.6	5	-	-	27.331394	84.366323	879	817.44388	1.73	0.1
DWCOS6	-	-	-	-	27.331426	84.366394	885	824.7501	1.74	0.1
D185	15.3	5	-	-	27.331407	84.366337	890	830.83862	1.75	0.1
D187	13.3	5	-	-	27.331692	84.366435	900	842.48241	1.77	0.1
DWCOS45	-	-	-	-	27.33176	84.366381	905	847.06632	1.78	0.1
D189	10.8	165	85	58	27.331773	84.366215	910	851.65023	1.78	0.1
D191	11.0	165	90	62	27.331868	84.366285	920	860.98782	1.80	0.1
F191	-	0	77	64	27.331868	84.366285	920.01	860.99678	1.80	0.1
D193	5.1	178	-	-	27.33193	84.366194	925	865.46706	1.80	0.1

Table SVII-2. (…/…)

Sample information									Magnetostratigraphic correlation results	
Sample	Tape-meter length (m)	Azimuth (°)	Strike (°)	Dip (°)	Latitude (°N)	Longitude (°E)	Estimated depth in sedimentary logs (m)	Tape-meter computed depth (m)	Age (Ma) (Ma)	1-σ (Ma)
D195	17.0	140	-	-	27.332022	84.366147	934	876.91168	1.82	0.1
D197	3.8	135	-	-	27.332053	84.366084	936	879.27306	1.82	0.1
D199	15.0	160	85	58.5	27.332154	84.366071	949	891.66033	1.84	0.1
D201	6.7	215	-	-	27.332246	84.366047	955	896.48356	1.85	0.1
D203	5.0	25	-	-	27.332308	84.366086	961	900.46596	1.85	0.1
DWCOS7	-	-	-	-	27.332292	84.36614	965.5	903.97568	1.86	0.1
D205	8.5	20	92	-	27.332298	84.366197	970	907.48541	1.86	0.1
F205		0	95	60	27.332298	84.366197	970.01	907.49679	1.86	0.1
D207	15.0	25	-	-	27.332429	84.366267	980.5	919.43259	1.88	0.1
D209	5.6	10	-	-	27.332453	84.366385	983	924.2792	1.88	0.1
D211	4.0	10	90	62.5	27.33251	84.366378	985.5	927.74106	1.89	0.1
D213	-	-	90	54	27.332519	84.366781	987	928.619	1.89	0.1
D215	-	-	80	62	27.332559	84.366819	989.5	931.119	1.89	0.1
D217	14.6	165	-	-	27.332696	84.366959	996	943.51253	1.91	0.1
DWCOS44	-	-	-	-	27.33276	84.367133	1002	948.32764	1.92	0.1
D219	11.0	175	88	58	27.332798	84.367133	1008	953.14274	1.92	0.1
DWCOS8	-	-	-	-	27.332831	84.367148	1015	958.17596	1.93	0.1
D221	9.0	0	82	-	27.332819	84.367184	1019	961.05209	1.93	0.1
F221	-	0	86	59	27.332819	84.367184	1019.01	961.06224	1.93	0.1
D223	24.0	210	-	-	27.333078	84.367275	1037	979.31796	1.96	0.1
D225	13.7	210	-	-	27.333236	84.367387	1045	989.74473	1.99	0.1
D227	8.8	195	-	-	27.333343	84.367365	1051	997.2148	2.00	0.1
D229	44.0	140	-	-	27.333554	84.367171	1086	1026.8362	2.06	0.1
D231	11.0	190	-	-	27.333617	84.367118	1098	1036.3563	2.08	0.1
D233	12.2	190	-	-	27.333753	84.367223	1114	1046.915	2.11	0.1
DWCOS9	-	-	-	-	27.333776	84.367298	1119.75	1052.5405	2.12	0.1
D235	13.0	170	90	65	27.333866	84.367275	1125.5	1058.166	2.13	0.1
F235	-	0	100	61	27.333866	84.367275	1125.51	1058.1744	2.13	0.1
D237	18.5	130	-	-	27.333945	84.367277	1138	1068.6166	2.15	0.1
D239	19.7	160	88	62	27.334054	84.367064	1155	1084.8852	2.19	0.1
F239	-	0	90	56	27.334054	84.367064	1155.01	1084.8964	2.19	0.1
D241	22.0	190	90	60	27.334299	84.3673	1172	1103.9254	2.23	0.1
D243	12.5	190	-	-	27.334318	84.367179	1184	1114.7437	2.25	0.1
D245	11.7	190	-	-	27.334404	84.367158	1196	1124.8697	2.27	0.1
D247	12.4	157	-	-	27.334555	84.367286	1205	1134.9007	2.29	0.1
DWCOS10	-	-	-	-	27.334623	84.367279	1210	1140.0779	2.30	0.1
D249	13.0	155	-	-	27.334696	84.367261	1215	1145.255	2.31	0.1
D253	8.1	153	90	59.5	27.334862	84.367317	1222	1151.5975	2.33	0.1
D255	6.1	165	-	-	27.334903	84.36731	1227	1156.7756	2.34	0.1
D257	6.7	154	90	59.5	27.334949	84.367016	1231	1162.0678	2.35	0.1
F257	-	0	84	52	27.334949	84.367016	1231.01	1162.0782	2.35	0.1
D259	8.4	148	-	-	27.33501	84.367149	1237	1168.3282	2.36	0.1
D261	-	-	90	60	27.334833	84.365009	1283	1214.3282	2.46	0.1
F261	-	0	78	59	27.334833	84.365009	1283.01	1214.3387	2.46	0.1
D263	8.5	170	-	-	27.334995	84.364925	1290	1221.6846	2.48	0.1
D265	13.3	160	-	-	27.335113	84.364867	1300	1232.668	2.50	0.1
D267	24.0	56	-	-	27.335285	84.364882	1307	1244.4623	2.52	0.1
D269	12.2	170	94	55	-	-	1319	1255.021	2.55	0.1
D271	9.3	173	-	-	27.335417	84.364814	1329	1263.133	2.56	0.1
D273	9.4	170	-	-	27.335475	84.364668	1338	1271.2684	2.58	0.1
DWCOS11	-	-	-	-	27.335497	84.364676	1343	1276.2832	2.59	0.1
D275	12.0	162	90	50	27.33561	84.364788	1348	1281.2981	2.60	0.1
D277	13.2	165	-	-	27.335718	84.364785	1360	1292.5032	2.63	0.1
D279	12.9	153	80	49	27.33582	84.364691	1370	1302.6043	2.65	0.1
D281	11.0	183	86	58	27.335927	84.364784	1382	1312.258	2.67	0.1
D283	12.0	170	75	64	-	-	1395	1322.6436	2.69	0.1
D285	8.8	175	-	-	27.336093	84.364714	1401	1330.3478	2.71	0.1
D287	8.5	15	-	-	27.336117	84.364688	1410	1337.5632	2.72	0.1
D289	16.0	20	-	-	27.336309	84.364778	1421	1350.7763	2.75	0.1
D291	15.0	180	88	62	27.336497	84.364844	1434	1363.9585	2.78	0.1
D293	13.6	170	-	-	-	-	1444	1375.7289	2.81	0.1
DWCOS12	-	-	-	-	27.336714	84.364878	1447	1379.7681	2.82	0.1
D295	13.0	135	-	-	27.336651	84.364388	1450	1383.8073	2.82	0.1
D297	9.3	180	87	62	27.336695	84.364292	1470	1391.9803	2.84	0.1
D299	16.0	320	90	63	27.336865	84.364183	1477	1402.7425	2.87	0.1
D301	10.1	0	-	-	27.33689	84.364247	1486	1411.61	2.89	0.1
D303	10.0	350	-	-	27.336973	84.364056	1494	1420.2555	2.90	0.1
D305	13.7	0	-	-	27.337155	84.364051	1507	1432.2804	2.93	0.1
D307	19.0	140	-	-	27.337278	84.363758	1519	1445.0535	2.96	0.1
D309	15.0	180	95	65	27.337416	84.363567	1535	1458.2138	2.99	0.1
D311	21.0	165	95	65	27.337602	84.363516	1551	1476.0055	3.03	0.1
DWCOS13	-	-	-	-	27.337616	84.364555	1554.5	1478.9873	3.03	0.1

Table SVII-2. (…/…)

Sample information									Magnetostratigraphic correlation results	
Sample	Tape-meter length (m)	Azimuth (°)	Strike (°)	Dip (°)	Latitude (°N)	Longitude (°E)	Estimated depth in sedimentary logs (m)	Tape-meter computed depth (m)	Age (Ma) (Ma)	1-σ (Ma)
D313	6.8	180	-	-	27.337659	84.363458	1558	1481.9691	3.04	0.1
beg1202	-	-	-	-	-	-	1565	1484.9286	3.04	0.1
D315	7.1	10	-	-	27.337675	84.364639	1572.5	1488.0995	3.05	0.1
D317	8.1	10	-	-	27.337755	84.364782	1582	1495.0919	3.06	0.1
D319	9.0	350	-	-	27.337798	84.364972	1591	1502.8598	3.07	0.1
D321	7.0	180	-	-	27.337865	84.364911	1598	1508.9938	3.08	0.1
D323	11.5	180	87	64	27.337949	84.365039	1604	1519.0696	3.10	0.1
D325	21.0	30	-	-	27.338056	84.365399	1610	1535.0018	3.12	0.1
D327	31.0	180	-	-	27.338306	84.365547	1621	1562.1518	3.14	0.1
D329	34.5	250	88	57	27.33838	84.365861	1630	1572.4838	3.15	0.1
DWCOS37	-	-	-	-	27.338433	84.36605	1633.5	1576.5636	3.15	0.1
D331	14.5	230	-	-	27.338516	84.365921	1637	1580.6434	3.15	0.1
DWCOS14	-	-	-	-	27.33849	84.366074	1640	1586.5511	3.16	0.1
D333	21.0	230	-	-	27.338556	84.366071	1643	1592.4589	3.16	0.1
beg1203	-	-	-	-	-	-	1645	1594.4589	3.16	0.1
D335	-	-	-	-	27.339022	84.365403	1647.5	1596.9589	3.16	0.1
D337	-	-	-	-	27.339394	84.364786	1652	1601.4589	3.17	0.1
D339	6.4	150	90	57	27.339364	84.364841	1656.5	1606.3086	3.17	0.1
D341	18.5	170	-	-	27.339371	84.364657	1664	1622.2467	3.18	0.1
D343	9.0	175	85	50	27.339419	84.364618	1673	1630.088	3.19	0.1
DWCOS15	-	-	-	-	27.339216	84.369267	1678.5	1638.6109	3.19	0.1
D345	20.5	162	90	58	27.339585	84.364519	1684	1647.1339	3.20	0.1
D347B	25.0	217	-	-			1691	1664.5862	3.28	0.1
D347	-	-	-	-	27.339777	84.364678	1693	1666.5862	3.31	0.1
D349	8.8	185	-	-	27.339883	84.36467	1697	1674.2476	3.36	0.1
D351	14.7	180	-	-	27.339983	84.364677	1704	1687.0917	3.42	0.1
D353	-	-	-	-	27.339978	84.364486	1707.5	1690.5917	3.44	0.1
D355	17.5	0	-	-	27.340144	84.364531	1714	1705.8773	3.51	0.1
D357	7.3	0	-	-	27.340207	84.364623	1720.5	1712.2522	3.54	0.1
D359	7.5	0	-	-	27.340276	84.364543	1727	1718.8003	3.57	0.1
D361	4.0	0	-	-	27.340484	84.364788	1732.5	1722.2919	3.58	0.1
D363	16.0	0	-	-	27.340515	84.364554	1742.5	1736.2535	3.63	0.1
beg1204	-	-	-	-			1742.51	1736.2717	3.63	0.1
DWCOS16	-	-	-	-	27.340524	84.364583	1744.51	1739.9143	3.64	0.1
D365	8.5	10	-	-	27.340523	84.364624	1746.51	1743.5569	3.65	0.1
D367	8.3	0	-	-	27.340684	84.364573	1753.51	1750.7965	3.67	0.1
D369	7.3	0	-	-	27.340717	84.364635	1760.51	1757.1623	3.69	0.1
D371	8.5	10	-	-	27.340824	84.364753	1770.51	1764.4591	3.72	0.1
D373	14.0	20	90	57	27.340842	84.364746	1789.51	1775.9181	3.75	0.1
D375	8.5	0	-	-	27.340881	84.364927	1802.51	1783.3179	3.77	0.1
DWCOS17	-	-	-	-	27.34103	84.364967	1807.51	1791.6734	3.80	0.1
D377	19.5	10	-	-	27.341102	84.364854	1812.51	1800.0288	3.82	0.1
D379	21.0	40	-	-	27.341239	84.365051	1821.51	1814.0221	3.87	0.1
D381	13.6	35	98	62	27.341261	84.365133	1832.51	1823.708	3.90	0.1
D383	7.3	40	-	-	27.341328	84.365194	1840.01	1828.5683	3.91	0.1
beg1205	-	-	-	-	-	-	1842.5	1829.6275	3.91	0.1
D385	12.8	55	-	-	27.34138	84.365392	1855	1834.9448	3.93	0.1
D387	17.7	0	-	-	27.341576	84.365599	1868.5	1850.3078	3.98	0.1
D389	18.0	35	93	63	27.341675	84.365664	1876.5	1863.1008	4.02	0.1
D391	14.6	30	90	64	27.341797	84.365643	1889.5	1874.0639	4.05	0.1
D393	6.6	170	95	67	27.341839	84.365619	1896.5	1879.6975	4.07	0.1
D395	5.0	0			27.34189	84.365625	1900.5	1884.0304	4.08	0.1
D397	4.3	170	90	59	27.341889	84.365622	1905.5	1887.6991	4.09	0.1
D399	18.3	170	-	-	27.342071	84.365454	1918.5	1903.3015	4.14	0.1
DWCOS18	-	-	-	-	27.342087	84.365531	1919.5	1905.7254	4.15	0.1
D401	5.6	0	90	62	27.34212	84.365453	1920.5	1908.1492	4.15	0.1
D403	13.0	0	-	-	27.342337	84.364906	1928.5	1919.3978	4.19	0.1
D405	-	-	97	59	27.342847	84.361641	1935	1925.8978	4.20	0.1
beg1206	-	-	-	-	-	-	1942.5	1929.0565	4.21	0.1
D407	7.2	50	-	-	27.342957	84.361845	1944.5	1929.8988	4.21	0.1
D409	17.5	210	-	-	27.34328	84.361451	1952.5	1942.9947	4.24	0.1
D411	8.2	195	-	-	27.343266	84.361493	1960.5	1949.8358	4.26	0.1
D413	40.0	220	95	60	27.343658	84.361892	1969.5	1976.2874	4.32	0.1
D415	8.5	192	-	-	27.343731	84.361849	1979.5	1983.4604	4.34	0.1
DWCOS19	-	-	-	-	27.343753	84.362056	1984	1988.6522	4.35	0.1
D417	14.2	212	-	-	27.343831	84.362	1988.5	1993.844	4.37	0.1
D419	8.2	200	-	-	27.343917	84.362046	1995.5	2000.4852	4.38	0.1
D421	11.5	212	-	-	27.343961	84.362118	2003.5	2008.8866	4.40	0.1
D423	4.4	206	-	-	27.344006	84.362117	2009.5	2012.2921	4.41	0.1
D425	5.5	213	-	-	27.344067	84.362188	2014.5	2016.2629	4.42	0.1
D427	21.0	183	-	-	27.344193	84.362261	2030.5	2034.2972	4.46	0.1
D429	8.2	235	-	-	27.344226	84.362362	2036.5	2038.3402	4.47	0.1

Table SVII-2. (…/…)

Sample information									Magnetostratigraphic correlation results	
Sample	Tape-meter length (m)	Azimuth (°)	Strike (°)	Dip (°)	Latitude (°N)	Longitude (°E)	Estimated depth in sedimentary logs (m)	Tape-meter computed depth (m)	Age (Ma) (Ma)	1-σ (Ma)
beg1207	-	-	-	-	-	-	2042.5	2048.4672	4.50	0.1
D431	29.5	210	-	-	27.344262	84.363183	2049.5	2060.282	4.53	0.1
D433	23.0	177	-	-	27.34445	84.363219	2060	2079.9943	4.57	0.1
D435	10.5	170	98	55	27.344491	84.363146	2067.5	2088.8642	4.59	0.1
D437	14.0	0	103	58	27.344735	84.363093	2084	2100.859	4.62	0.1
D439	12.0	5	-	-	27.344852	84.363279	2104	2111.0861	4.64	0.1
D441	16.0	20	-	-	27.345005	84.363248	2110	2123.943	4.67	0.1
D443	12.7	20	100	56	27.345111	84.363308	2115.5	2134.1439	4.69	0.1
DWCOS20	-	-	-	-	27.345131	84.363274	2122.75	2140.8706	4.70	0.1
D445	16.0	10	90	60	27.345259	84.363243	2130	2147.5974	4.71	0.1
D447	16.0	5	-	-	27.345416	84.363217	2140.5	2161.1952	4.74	0.1
beg1208	-	-	-	-	-	-	2142.5	2164.3626	4.75	0.1
D449	23.6	30	-	-	27.345537	84.363408	2151.5	2178.616	4.77	0.1
D451	20.0	155	85	62	27.34563	84.363583	2160.5	2194.0547	4.80	0.1
D453	-	-	-	-	27.345831	84.364969	2195.5	2213.4235	4.82	0.1
D455	12.4	180	-	-	27.346006	84.365255	2210.5	2223.9403	4.83	0.1
D457	6.0	25	-	-	27.346054	84.365222	2215.5	2228.5503	4.83	0.1
D459	4.0	20	-	-	27.346127	84.365128	2221.5	2231.7351	4.83	0.1
DWCOS21	-	-	-	-	27.346109	84.365245	2225.5	2235.7351	4.84	0.1
beg1601	-	-	-	-	-	-	2229.5	2239.7351	4.84	0.1
D461	-	-	-	-	27.346475	84.365759	2234.5	2244.7351	4.84	0.1
D463	-	-	-	-	27.346667	84.365762	2240.75	2250.9851	4.85	0.1
D465	-	-	-	-	27.346802	84.365278	2247	2257.2351	4.86	0.1
D467	17.5	180	-	-	27.346937	84.36524	2253.5	2272.0195	4.87	0.1
D469	8.0	180	-	-	27.34695	84.365153	2257.5	2278.7755	4.87	0.1
D471	11.5	20	-	-	27.347152	84.365228	2261	2287.8986	4.88	0.1
D473	15.5	165	-	-	27.347282	84.365175	2265.5	2300.5329	4.89	0.1
D601	-	-	-	-	27.347467	84.3651	2273.5	2308.5329	4.90	0.1
F601	-	-	93	60	-	-	2275.5	2311.0322	4.91	0.1
D603	13.4	316	-	-	27.347617	84.365067	2280	2316.6556	4.92	0.1
D605	-	-	-	-	27.3477	84.3642	2293	2324.5277	4.93	0.1
D607	11.5	0	-	-	-	-	2299.5	2334.2	4.95	0.1
D609	16.0	0	-	-	27.348033	84.364	2305.5	2347.6489	4.97	0.1
DWCOS33	-	-	-	-	27.347955	84.36428	2310	2351.6034	4.98	0.1
D611	6.8	0	-	-	27.34795	84.364	2312	2353.361	4.98	0.1
D613	7.8	0	90	57.5	27.348067	84.364017	2317.5	2359.9093	4.99	0.1
F613	-	-	88	59	-	-	2319.5	2361.9093	4.99	0.1
beg1602	-	-	-	-	-	-	2329.5	2371.9093	5.05	0.1
D615	-	-	-	-	27.348933	84.364467	2339.5	2381.9093	5.11	0.1
D617	14.0	15	-	-	27.348967	84.364567	2349.5	2393.2243	5.19	0.1
D619	14.8	20	90	58	27.34915	84.364667	2357.5	2404.8509	5.25	0.1
D621	15.8	20	-	-	27.349317	84.364733	2367.5	2417.2495	5.27	0.1
F621	-	-	95	55	-	-	2374.5	2425.2206	5.29	0.1
D623	13.8	340	-	-	27.34936	84.36463	2377	2428.0674	5.30	0.1
F623	-	-	90	70	-	-	2392.5	2442.733	5.33	0.1
C625	20.0	15	-	-	-	-	2394	2444.1523	5.33	0.1
D625	33.8	55	-	-	27.349783	84.36495	2395.5	2460.2914	5.37	0.1
F625	-	-	85	59	-	-	2402	2466.9199	5.39	0.1
D627	13.7	350	-	-	27.349783	84.364717	2406.5	2471.5088	5.40	0.1
D629	10.5	0	-	-	27.349967	84.364833	2414.5	2480.2306	5.41	0.1
beg1603	-	-	-	-	-	-	2429.5	2495.4646	5.45	0.1
D631	35.4	30	95	61	27.350167	84.364867	2439.5	2505.6205	5.47	0.1
D633	21.5	330	88	55	27.3503	84.36475	2454.5	2521.0128	5.51	0.1
D635	-	-	-	-	27.350383	84.363467	2463.5	2528.6186	5.52	0.1
C637	20.0	108	-	-	-	-	2467.25	2533.7196	5.53	0.1
D637	9.2	111	-	-	27.350333	84.3632	2471	2536.4395	5.54	0.1
D639	13.1	340	-	-	27.350517	84.363217	2480.5	2546.5827	5.56	0.1
D641	9.0	340	-	-	27.35055	84.363083	2490.5	2553.5424	5.58	0.1
D643	25.1	30	-	-	27.350567	84.36325	2513	2571.378	5.62	0.1
D645	11.8	50	-	-	27.350917	84.363133	2527	2577.5898	5.63	0.1
beg1604	-	-	-	-	-	-	2528	2578.2979	5.63	0.1
D647	18.0	27	104	60	27.350783	84.3634	2545.5	2590.6913	5.66	0.1
DWCOS22	-	-	-	-	27.350791	84.363702	2553.25	2593.585	5.67	0.1
D649	14.2	60	-	-	27.350817	84.363617	2561	2596.4787	5.67	0.1
C651-1	20.0	128	-	-	-	-	2561.01	2606.5157	5.70	0.1
C651-2	20.0	102	-	-	-	-	2561.02	2609.9052	5.70	0.1
D651	13.6	96	-	-	27.35085	84.36405	2584	2611.0601	5.71	0.1
D653	9.7	56	-	-	27.35085	84.3642	2595.5	2615.4596	5.72	0.1
D655	-	-	-	-	27.351067	84.364867	2610	2629.9596	5.75	0.1
F655	-	-	90	51	-	-	2625.5	2645.4596	5.78	0.1
D657	-	-	90	51	27.351367	84.3657	2627	2646.9596	5.79	0.1
beg1605	-	-	-	-	-	-	2628	2670.6409	5.84	0.1

Table SVII-2. (…/…)

Sample information									Magnetostratigraphic correlation results	
Sample	Tape-meter length (m)	Azimuth (°)	Strike (°)	Dip (°)	Latitude (°N)	Longitude (°E)	Estimated depth in sedimentary logs (m)	Tape-meter computed depth (m)	Age (Ma) (Ma)	1-σ (Ma)
C659-1	20.1	25	-	-	-	-	2627	2661.6654	5.82	0.1
C659-2	20.0	58	-	-	-	-	2627.01	2670.2212	5.84	0.1
D659	29.3	65	-	-	27.351717	84.366317	2650.5	2680.1809	5.86	0.1
D661	26.0	0	-	-	27.351883	84.366567	2670	2701.0286	5.91	0.1
D663	25.9	42	-	-	27.351967	84.366867	2678	2716.4418	5.94	0.1
D665	12.8	322	-	-	27.351867	84.3665	2687	2724.5072	5.96	0.1
D667	11.8	352	-	-	27.35195	84.366517	2697	2733.8354	5.98	0.1
D669	28.3	110	-	-	27.352267	84.3663	2709	2741.5467	6.00	0.1
C671	20.0	40	-	-	-	-	2715.5	2753.7392	6.02	0.1
D671	5.3	343	-	-	27.352633	84.36625	2722	2757.7682	6.03	0.1
beg1606	-	-	-	-	-	-	2728	2763.1473	6.04	0.1
D673	20.0	328	-	-	27.352583	84.366433	2737	2771.216	6.05	0.1
D675	14.6	350	-	-	27.352683	84.366483	2749	2782.5919	6.06	0.1
D677	2.4	5	-	-	27.352683	84.366483	2751	2784.4828	6.06	0.1
D679	9.8	16	-	-	27.352733	84.366517	2760.5	2791.9209	6.07	0.1
D681	13.0	15	-	-	27.352817	84.366583	2770.5	2801.8177	6.08	0.1
D683	14.5	55	-	-	27.352867	84.366733	2783.5	2808.357	6.09	0.1
DW685	-	-	-	-	-	-	2792.5	2810.4749	6.09	0.1
D685	10.8	40	90	50	27.35295	84.366833	2811	2814.8285	6.10	0.1
D687	51.6	80	-	-	27.353133	84.367267	2824	2821.82	6.11	0.1
beg1607	-	-	-	-	-	-	2828	2825.8731	6.11	0.1
D689	24.8	3	-	-	27.35335	84.367483	2843	2841.0725	6.13	0.1
F689	-	-	85	48	-	-	2858	2853.5248	6.14	0.1
D691	22.2	15	-	-	27.353433	84.367617	2863	2857.6756	6.15	0.1
C693	20.0	24	-	-	-	-	2868.05	2871.8076	6.16	0.1
D693	8.3	6	-	-	27.353617	84.367633	2873.1	2878.1857	6.17	0.1
C695-1	-20.0	24	-	-	-	-	2873.11	2892.3032	6.19	0.1
C695-2	-8.3	6	-	-	-	-	2873.12	2898.6812	6.20	0.1
C695-3	20.0	24	-	-	-	-	2873.13	2912.7986	6.21	0.1
D695	23.7	6	-	-	27.353783	84.367717	2889	2930.9509	6.23	0.1
D697	14.8	348	-	-	27.353933	84.367633	2899	2942.0765	6.25	0.1
D699	29.8	350	-	-	27.354167	84.367667	2923	2964.5148	6.32	0.1
D701	14.6	0	-	-	27.35435	84.36765	2946	2975.6212	6.37	0.1
DWCOS23	-	-	85	50	27.354441	84.367785	2950	2988.7261	6.43	0.1
C703	19.4	333	-	-	-	-	2950.01	2988.7588	6.43	0.1
D703	10.1	92	-	-	27.35455	84.367517	2952	2989.0266	6.43	0.1
DWCOS30	-	-	-	-	-	-	2954	2990.8514	6.44	0.1
F703	-	-	98	52	-	-	2963	2999.0627	6.45	0.1
C705	20.0	6	-	-	-	-	2968.5	3004.0808	6.46	0.1
D705	41.5	70	82	47	27.3546	84.368167	2974	3014.8099	6.49	0.1
D707	-	-	85	48.5	27.35495	84.368883	2988	3028.8099	6.51	0.1
DW707	-	-	-	-	-	-	3000	3043.4956	6.54	0.1
C709	20.0	12	-	-	-	-	3000.01	3043.5079	6.54	0.1
D709	12.5	16	-	-	27.35515	84.369017	3009	3052.5162	6.56	0.1
DWCOS34			-	-	-	-	3021	3064.5162	6.58	0.1
D711	21.0	10	-	-	27.3555	84.36915	3023	3079.9683	6.61	0.1
beg1608			-	-	-	-	3028	3083.1584	6.62	0.1
D713	20.0	50	90	46	27.355433	84.369133	3038	3089.5384	6.63	0.1
D715	20.8	350	96	60	27.355717	84.369067	3050	3104.7414	6.66	0.1
D717	17.9	282	85	46	27.35575	84.369	3053	3107.5015	6.67	0.1
C719	19.6	324	-	-	-	-	3061	3119.2374	6.69	0.1
D719	10.7	278	-	-	27.355833	84.368767	3069	3120.3373	6.69	0.1
D721	17.6	298	-	-	27.3559	84.368517	3079	3126.4245	6.71	0.1
D723	28.2	69	-	-	27.356017	84.36875	3089	3133.8502	6.72	0.1
D725	-	-	90	48	27.356167	84.367109	3107	3146.2366	6.75	0.1
D727	19.8	298	-	-	27.356249	84.367083	3120	3152.8013	6.77	0.1
C729	19.8	298	-	-	-	-	3124.5	3159.351	6.78	0.1
D729	12.0	298	-	-	27.356366	84.366949	3129	3163.3119	6.79	0.1
D731	6.2	334	-	-	-	-	3137	3167.3174	6.80	0.1
DWCOS24	-	-	-	-	27.356564	84.366841	3142	3175.4126	6.82	0.1
C733	12.0	340	-	-	-	-	3142.01	3175.4288	6.82	0.1
D733	30.0	288	-	-	27.356633	84.366667	3148.1	3181.7453	6.84	0.1
D735	9.8	2	-	-	27.356667	84.366717	3158.5	3188.8095	6.85	0.1
DWCOS31	-	-	-	-	-	-	3165	3193.7679	6.87	0.1
D737	17.6	54	-	-	27.356833	84.366767	3168.5	3196.4377	6.87	0.1
DW737	-	-	-	-	-	-	3168.51	3196.4448	6.87	0.1
D739	15.6	385	-	-	27.356983	84.366733	3183	3206.6427	6.90	0.1
D741	19.0	348	-	-	-	-	3198	3219.8386	6.93	0.1
D743	3.9	356	-	-	27.356983	84.36665	3202	3222.6044	6.94	0.1
D745	-	-	88	50	27.35715	84.366783	3212	3232.6044	6.96	0.1
C747	20.0	250	-	-	-	-	3219.5	3237.628	6.98	0.1
D747	14.2	232	-	-	27.357417	84.366933	3227	3243.8993	6.99	0.1

Table SVII-2. (…/…)

Sample information									Magnetostratigraphic correlation results	
Sample	Tape-meter length (m)	Azimuth (°)	Strike (°)	Dip (°)	Latitude (°N)	Longitude (°E)	Estimated depth in sedimentary logs (m)	Tape-meter computed depth (m)	Age (Ma) (Ma)	1-σ (Ma)
beg1609	-	-	-	-	-	-	3225.5	3242.645	6.99	0.1
D749	15.0	220	-	-	27.357483	84.36725	3234.5	3252.0687	7.01	0.1
C751	20.0	112	-	-	-	-	3244.5	3257.228	7.02	0.1
D751	20.0	114	-	-	27.3577	84.366683	3254.5	3262.8581	7.04	0.1
D753	20.0	104	-	-	27.357783	84.366667	3265.5	3266.2099	7.05	0.1
D755	17.3	162	-	-	27.357933	84.366483	3276.5	3277.6593	7.08	0.1
D757	21.5	186	88	45	27.35815	84.366517	3287.5	3292.466	7.11	0.1
DW757	-	-	-	-	-	-	3293.6	3298.566	7.12	0.1
D759	-	-	-	-	27.35835	84.367217	3299.5	3304.466	7.13	0.1
D763	18.5	238	-	-	27.3583	84.3674	3309.5	3311.0411	7.14	0.1
DWCOS43			-	-	27.358411	84.367124	3315	3315.3151	7.15	0.1
D765	17.7	224	-	-	27.35845	84.3676	3320.5	3319.589	7.16	0.1
beg1610	-	-	-	-	-	-	3325.5	3324.135	7.17	0.1
D767	13.4	172	-	-	-	-	3330.5	3328.681	7.18	0.1
D769	10.5	174	-	-	27.3587	84.367283	3338.5	3335.8119	7.19	0.1
D771	12.8	220	-	-	-	-	3347.5	3342.2666	7.20	0.1
D773	7.8	148	75	42	27.358833	84.367233	3356.5	3346.8529	7.21	0.1
D775	10.8	192	-	-	27.35885	84.3674	3364.5	3353.9042	7.22	0.1
D777	16.5	164	-	-	27.358983	84.367167	3374.5	3364.7125	7.25	0.1
F777	-	-	80	50	-	-	3377.5	3367.7376	7.25	0.1
D779	8.3	182	-	-	27.35905	84.3673	3380	3370.2584	7.26	0.1
D781	15.3	198	-	-	27.359317	84.36735	3390	3379.7674	7.28	0.1
D783	11.6	184	-	-	27.359467	84.367283	3398.5	3387.4226	7.30	0.1
D785	16.2	176	-	-	27.359617	84.3673	3407.5	3398.1806	7.33	0.1
D787	12.7	176	-	-	27.3597	84.367283	3418.5	3406.5782	7.35	0.1
beg1611	-	-	-	-	-	-	3425.5	3411.4585	7.37	0.1
DWCOS32	-	-	-	-	-	-	3433	3416.6873	7.38	0.1
DWCOS25	-	-	70	47	27.359843	84.367921	3434.25	3417.5587	7.39	0.1
D789	18.3	184	82	46	27.359867	84.367383	3435.5	3418.4302	7.39	0.1
D793	-	-	-	-	27.360017	84.368017	3441.5	3423.5569	7.39	0.1
DW793	-	-	-	-	-	-	3443	3424.7491	7.40	0.1
D795	-	-	82	38	27.36015	84.36845	3448.5	3429.1204	7.40	0.1
D797	-	-	92	49	27.3601	84.368783	3455.5	3436.1204	7.43	0.1
D799	-	-	86	37	27.3603	84.369917	3460.5	3438.9159	7.44	0.1
D801	-	-	-	-	27.360667	84.369967	3468	3446.4159	7.46	0.1
DWCOS36	-	-	-	-	27.360767	84.369783	3471.75	3447.3133	7.46	0.1
D803	-	-	-	-	27.3608	84.369833	3475.5	3448.2108	7.47	0.1
D805	19.2	186	-	-	27.3609	84.369483	3497	3460.0931	7.50	0.1
D807	9.7	154	85.5	39	27.36105	84.36945	3505.5	3466.0315	7.52	0.1
D809	18.7	124	-	-	27.361317	84.369367	3518	3474.3263	7.54	0.1
D811	-	-	76	35	27.361417	84.368833	3525.5	3481.8263	7.55	0.1
beg1612	-	-	-	-	-	-	3525.51	3481.8358	7.55	0.1
F811	-	-	-	-	-	-	3533.51	3489.4465	7.57	0.1
D813	20.0	206	-	-	27.361583	84.368967	3536.01	3491.8248	7.57	0.1
D815	16.0	226	-	-	27.361633	84.369083	3540.51	3497.1872	7.58	0.1
D817	24.0	206	-	-	27.361783	84.369383	3553.01	3508.9065	7.60	0.1
DW817	-	-	-	-	-	-	3554.01	3510.0285	7.60	0.1
DWTH42	-	-	-	-	27.361909	84.369383	3557.26	3513.675	7.61	0.1
D819	13.6	160	-	-	27.361933	84.369383	3560.51	3517.3215	7.62	0.1
D821	14.7	218	-	-	27.362117	84.3695	3569.51	3522.959	7.63	0.1
D823	20.6	168	-	-	27.362333	84.369517	3581.51	3535.6581	7.65	0.1
D825	18.8	132	-	-	27.362383	84.36935	3594.51	3545.4071	7.67	0.1
D827	18.8	132	80	36	27.362567	84.369367	3604.51	3555.1927	7.69	0.1
D829	19.6	224	-	-	27.362717	84.369467	3616.31	3560.8798	7.71	0.1
D831	7.6	140	-	-	27.362767	84.369467	3622.31	3565.1428	7.71	0.1
beg1613	-	-	-	-	-	-	3625.5	3568.0829	7.72	0.1
D833	30.0	150	-	-	27.363033	84.3694	3641.5	3582.83	7.75	0.1
D835	9.5	166	66	36	27.363133	84.369333	3648	3588.4745	7.76	0.1
D837	14.6	174	-	-	27.363217	84.369267	3658	3596.8592	7.78	0.1
D839	-	-	-	-	27.363533	84.369417	3677	3613.316	7.82	0.1
D841	20.0	200	-	-	27.363667	84.369533	3685.5	3621.8184	7.83	0.1
D843	13.0	120	-	-	27.363733	84.369483	3692	3627.97	7.85	0.1
D845	13.0	140	-	-	27.363883	84.3694	3698.1	3635.2697	7.86	0.1
F845	-	-	-	-	-	-	3708.1	3643.2678	7.88	0.1
D847	20.0	176	60	32	27.36405	84.369433	3711.5	3645.9871	7.89	0.1
D849	20.5	140	-	-	27.364317	84.369483	3723.5	3657.4642	7.91	0.1
beg1614	-	-	-	-			3725.5	3659.7111	7.91	0.1
D853	27.5	166	60	33	27.364417	84.369183	3737	3672.6307	7.94	0.1
D855	16.0	204	-	-	27.364567	84.369467	3748	3677.9935	7.95	0.1
D857	12.7	110	-	-	27.3645	84.369333	3757	3683.5268	7.96	0.1
F857	-	-	66	34			3762.5	3686.1766	7.97	0.1
D859	9.6	180	55	40	27.364717	84.3693	3766.5	3688.1038	7.97	0.1

Table SVII-2. (…/…)

Sample information									Magnetostratigraphic correlation results	
Sample	Tape-meter length (m)	Azimuth (°)	Strike (°)	Dip (°)	Latitude (°N)	Longitude (°E)	Estimated depth in sedimentary logs (m)	Tape-meter computed depth (m)	Age (Ma) (Ma)	1-σ (Ma)
D861	-	-	-	-	27.365317	84.369717	3796	3708.8132	8.02	0.1
D863	15.0	180			27.365433	84.369733	3805.5	3715.4518	8.03	0.1
D865	12.0	140	-	-	27.365583	84.369683	3813.5	3721.9775	8.05	0.1
D867	17.0	156	-	-	27.365733	84.369733	3827	3730.8629	8.07	0.1
beg1615	-	-	-	-	-	-	3827.01	3730.8659	8.07	0.1
D869	-	-	62	30	27.36595	84.37005	3832.51	3732.5114	8.07	0.1
D871	16.6	134	-	-	27.36605	84.369983	3838.51	3741.3599	8.09	0.1
DWTH41	-	-	-	-	27.3662	84.3684	3844.01	3746.1046	8.10	0.1
D873	28.5	190	-	-	27.36635	84.370017	3849.51	3750.8493	8.11	0.1
D875	17.0	142	65	30	27.3665	84.369917	3860.01	3759.8066	8.12	0.1
beg1616	-	-	-	-	-	-	3867	3766.3328	8.13	0.1
D877	-	-	-	-	27.366683	84.369667	3877	3775.6692	8.14	0.1
D879	36.0	210	-	-	27.366967	84.369833	3886.5	3780.208	8.15	0.1
D881	23.3	172	-	-	27.36715	84.369833	3897	3789.5006	8.16	0.1
F881	-	-	40	31	-	-	3904.5	3796.5758	8.17	0.1
D883	22.0	154	-	-	27.367383	84.369767	3908	3799.8775	8.17	0.1
D885	22.5	140	-	-	27.367567	84.3695	3918	3811.1288	8.18	0.1
D887	17.0	140	-	-	27.367733	84.3695	3926	3819.5509	8.19	0.1
D901	17.7	138	-	-	27.367917	84.36945	3931	3828.3255	8.20	0.1
D903	17.7	138	-	-	27.36805	84.36935	3937	3837.0389	8.22	0.1
DWTH40	-	-	-	-	27.3683	84.3691	3941.5	3841.2681	8.22	0.1
D905	21.0	162	40	29	27.36885	84.369833	3946	3845.4973	8.23	0.1
D907	20.0	172	33	25	27.369133	84.36975	3952	3852.2785	8.23	0.1
D909	21.0	162	-	-	27.369233	84.369733	3959.5	3860.4446	8.24	0.1
F909-1	-	-	30	27	27.369667	84.370283	3967	3867.9446	8.25	0.1
DWCOS35	-	-	-	-	-	-	3992	3892.9446	-	-
F909-2	-	-	15	27	-	-	4017	3917.9446	-	-
F909-3	-	-	5	26	-	-	4037	3937.9446	-	-
END	-	-	-	-	-	-	4037.01	3937.9546	-	-

Table SVII-3. Medium to coarse sandy samples information, oxygen-carbon isotope, major and trace elements results.

Columns A-G indicate sandy sample information, columns H-J: oxygen-carbon isotopic results, columns K-BC: trace element results, columns BD-BO: major element results. Measurements below the detection limit are indicated by < D.L. Samples are split in several series, according their collection and processing. The depth (m) was obtained with the GPS coordinates. Arbitrary 1-σ age uncertainty of 0.1 Ma.

Table SVII-3. (…/…)

Sample information							oxygen-carbon isotopic measurements		
Site	**#**	**Latitude °N**	**Longitude °E**	**Depth (m)**	**Age (Ma)**	**1σ**	**%$CaCO_3$ (%)**	**$\delta^{18}O$ cor (‰ PDB)**	**$\delta^{13}C$ cor (‰ PDB)**
Dwarda section									
Serie #1									
Dwarda	Dwcos9	27.3338	84.3673	1,076	2.119	0	-	-	-
Dwarda	Dwcos13	27.3376	84.3646	1,502	3.032	0	-	-	-
Dwarda	Dwcos17	27.3410	84.3650	1,815	3.799	0	-	-	-
Dwarda	Dwcos20	27.3451	84.3633	2,164	4.701	0	-	-	-
Serie #2									
Dwarda	Dwcos2	27.3286	84.3671	586	1.289	0	0.0	-7.8	-3.8
Dwarda	Dwcos3	27.3292	84.3664	654	1.407	0	0.0	-11.6	-8.5
Dwarda	Dwcos4	27.3295	84.3664	676	1.445	0	0.0	-10.1	-9.3
Dwarda	Dwcos5	27.3304	84.3662	741	1.556	0	0.1	-10.6	-11.7
Dwarda	Dwcos7	27.3323	84.3661	927	1.855	0			
Dwarda	Dwcos8	27.3328	84.3671	981	1.929	0	4.7	-11.6	-5.5
Dwarda	Dwcos10	27.3346	84.3673	1,163	2.303	0	5.0	-13.9	-1.3
Dwarda	Dwcos12	27.3367	84.3649	1,403	2.816	0	3.6	-12.7	-1.5
Serie #3									
Dwarda	Dwcos11	27.3355	84.3647	1,299	2.590	0	5.9	-13.0	-1.5
Dwarda	Dwcos14	27.3385	84.3661	1,610	3.157	0	0.3	-12.2	-4.0
Dwarda	Dwcos15	27.3392	84.3693	1,662	3.192	0	0.0	-10.8	-8.2
Dwarda	Dwcos16	27.3405	84.3646	1,763	3.641	0	3.2	-15.2	-1.4
Dwarda	Dwcos18	27.3421	84.3655	1,929	4.147	0	5.5	-14.1	-1.3
Dwarda	Dwcos19	27.3438	84.3621	2,012	4.354	0	4.4	-13.7	-2.1
Dwarda	Dwcos21	27.3461	84.3652	2,258	4.836	0	0.1	-5.2	-3.5
Dwarda	Dwcos22	27.3508	84.3637	2,616	5.667	0	2.8	-14.8	-1.8
Dwarda	Dwcos24	27.3566	84.3668	3,198	6.822	0	3.9	-13.7	-1.9
Dwarda	Dwcos25	27.3598	84.3679	3,435	7.386	0	13.0	-11.0	-2.9
Serie #4									
Dwarda	Dwcos30	27.3546	84.3675	3,013	6.438	0	-	-	-
Dwarda	Dwcos31	27.3567	84.3667	3,216	6.867	0	-	-	-
Dwarda	Dwcos32	27.3597	84.3673	3,435	7.383	0	-	-	-
Dwarda	Dwcos33	27.3480	84.3643	2,374	4.975	0	-	-	-
Dwarda	Dwcos34	27.3552	84.3690	3,087	6.584	0	-	-	-
Dwarda	Dwcos37	27.3384	84.3661	1,600	3.150	0	-	-	-
Dwarda	Dwcos43	27.3584	84.3671	3,333	7.152	0	-	-	-
Dwarda	Dwcos44	27.3328	84.3671	971	1.916	0	-	-	-
Dwarda	Dwcos45	27.3318	84.3664	870	1.778	0	-	-	-
Dwarda	Dwcos46	27.3308	84.3663	778	1.620	0	-	-	-
Dwarda	Dwcos47	27.3292	84.3666	652	1.403	0	-	-	-
Dwarda	Dwcos48	27.3289	84.3670	606	1.324	0	-	-	-
Dwarda	Dwcos49	27.3281	84.3672	534	1.200	0	-	-	-
Dwarda	Dwcos50	27.3280	84.3672	520	1.175	0	-	-	-
Dwarda	Dwcos51	27.3280	84.3672	520	1.176	0	-	-	-
Dwarda	Dwcos52	27.3272	84.3669	442	1.029	0	-	-	-
Ganguli section									
Serie #1									
Ganguli	Ggcos1	27.3224	84.3969	208	0.484	0	-	-	-
Ganguli	Ggcos3	27.3241	84.3969	373	0.869	0	-	-	-
Serie #2									
Ganguli	Ggcos2	27.3233	84.3971	286	0.666	0	-	-	-
Ganguli	Ggcos4	27.3249	84.3987	439	1.023	0	-	-	-
Gonauli section									
Gonauli	Go60	27.3625	83.9980	635	1.373	0	-	-	-
Maloni Naha section									
Maloni Naha	Ca17i01	27.3796	83.9706	658	1.413	0	-	-	-
Maloni Naha	Ca17i03	27.3771	83.9710	461	1.064	0	-	-	-
Maloni Naha	Ca17i04	27.3771	83.9710	474	1.092	0	-	-	-
Maloni Naha	Ca17i08	27.3709	83.9759	200	0.465	0	-	-	-

Table SVII-3. (…/…)

S

Site	#	Site	#	No CRPG	As ppm	Ba ppm	Be ppm	Bi ppm	Cd ppm	Ce ppm	Co ppm	Cr ppm	Cs ppm	Cu ppm	Dy ppm
				Uncertainties	<20%	<5%	<20%	<20%	<20%	<5%	<20%	<5%	<15%	<20%	<10%
				Detection limit	0.50	5.5	0.05	0.045	0.02	0.03	0.08	0.50	0.02	2.0	0.004
Dwarda section		**Dwarda section**													
Serie #1		**Serie #1**													
Dwarda	Dwcos9	Dwarda	Dwcos9	-	-	-	-	-	-	-	-	-	-	-	-
Dwarda	Dwcos13	Dwarda	Dwcos13	-	-	-	-	-	-	-	-	-	-	-	-
Dwarda	Dwcos17	Dwarda	Dwcos17	-	-	-	-	-	-	-	-	-	-	-	-
Dwarda	Dwcos20	Dwarda	Dwcos20	-	-	-	-	-	-	-	-	-	-	-	-
Serie #2		**Serie #2**													
Dwarda	Dwcos2	Dwarda	Dwcos2	1512006	< L.D.	432.300	3.657	0.428	0.197	72.860	8.242	50.020	9.445	11.370	4.778
Dwarda	Dwcos3	Dwarda	Dwcos3	1512007	< L.D.	433.500	3.138	0.294	< L.D.	34.900	7.961	43.750	7.959	8.140	2.488
Dwarda	Dwcos4	Dwarda	Dwcos4	1512008	< L.D.	317.300	4.312	0.179	0.118	50.750	4.521	32.090	4.351	5.047	3.654
Dwarda	Dwcos5	Dwarda	Dwcos5	1512009	< L.D.	286.300	5.527	1.111	< L.D.	31.580	3.238	17.730	12.340	5.029	2.602
Dwarda	Dwcos7	Dwarda	Dwcos7	-	-	-	-	-	-	-	-	-	-	-	-
Dwarda	Dwcos8	Dwarda	Dwcos8	1512010	1.529	345.700	3.405	0.381	0.141	63.450	4.881	37.800	5.195	5.848	3.859
Dwarda	Dwcos10	Dwarda	Dwcos10	1512011	4.207	364.000	3.866	0.427	0.135	57.070	7.434	41.180	7.561	12.260	3.699
Dwarda	Dwcos12	Dwarda	Dwcos12	1512013	2.427	261.200	4.674	0.349	0.125	50.340	4.918	32.480	5.809	8.158	3.970
Serie #3		**Serie #3**													
Dwarda	Dwcos11	Dwarda	Dwcos11	1512012	3.200	287.300	2.555	0.181	0.121	40.570	4.602	35.810	5.475	6.098	2.834
Dwarda	Dwcos14	Dwarda	Dwcos14	1512014	< L.D.	279.700	2.636	0.258	< L.D.	35.680	3.778	29.850	6.701	< L.D.	2.101
Dwarda	Dwcos15	Dwarda	Dwcos15	1512015	< L.D.	355.000	4.052	0.321	0.128	44.900	4.313	36.380	5.612	10.670	3.057
Dwarda	Dwcos16	Dwarda	Dwcos16	1512016	2.670	326.300	3.239	0.281	0.135	61.420	5.914	35.520	5.423	9.459	4.484
Dwarda	Dwcos18	Dwarda	Dwcos18	1512017	4.706	400.200	3.790	0.239	0.151	70.680	7.538	50.520	7.757	8.155	4.653
Dwarda	Dwcos19	Dwarda	Dwcos19	1512018	2.065	288.500	2.497	0.159	0.155	65.910	5.144	43.600	3.922	5.934	5.840
Dwarda	Dwcos21	Dwarda	Dwcos21	1512019	< L.D.	317.100	2.431	0.174	0.105	47.810	5.573	41.050	5.153	5.491	3.123
Dwarda	Dwcos22	Dwarda	Dwcos22	1512020	1.206	340.700	4.160	0.277	0.114	52.320	6.930	42.090	7.223	7.212	4.034
Dwarda	Dwcos24	Dwarda	Dwcos24	1512021	1.949	400.000	2.896	0.226	0.150	56.930	8.069	49.010	7.598	8.543	3.615
Dwarda	Dwcos25	Dwarda	Dwcos25	1512022	6.466	310.900	2.356	0.225	0.131	54.180	7.024	41.650	5.336	8.967	3.753
Serie #4		**Serie #4**													
Dwarda	Dwcos30	Dwarda	Dwcos30	1704029	0.891	434.595	3.334	0.428	0.047	94.802	6.858	39.500	8.564	6.984	6.422
Dwarda	Dwcos31	Dwarda	Dwcos31	1704030	3.046	347.099	3.360	0.299	0.066	62.680	5.849	34.393	6.220	7.160	4.417
Dwarda	Dwcos32	Dwarda	Dwcos32	1704031	7.354	327.526	2.259	0.288	0.074	65.053	8.960	42.108	5.753	14.591	4.189
Dwarda	Dwcos33	Dwarda	Dwcos33	1704032	1.227	340.488	3.958	0.255	0.038	47.740	6.696	40.952	7.545	6.447	3.043
Dwarda	Dwcos34	Dwarda	Dwcos34	1704033	0.975	344.596	3.291	0.302	0.066	61.471	6.404	38.504	7.315	6.780	4.293
Dwarda	Dwcos37	Dwarda	Dwcos37	1704034	3.990	298.470	3.550	0.337	0.060	50.168	4.699	30.954	6.213	6.519	3.300
Dwarda	Dwcos43	Dwarda	Dwcos43	1704035	2.047	359.312	2.422	0.387	0.067	72.884	7.205	37.063	6.322	11.627	4.789
Dwarda	Dwcos44	Dwarda	Dwcos44	1704036	1.089	290.400	4.332	0.354	0.067	57.906	5.042	38.982	5.213	5.422	5.362
Dwarda	Dwcos45	Dwarda	Dwcos45	1704037	4.446	360.583	2.798	0.404	0.046	46.053	5.453	36.103	7.391	7.668	2.950
Dwarda	Dwcos46	Dwarda	Dwcos46	1704038	1.911	332.543	4.487	0.811	0.139	158.619	6.516	35.135	6.401	10.432	9.794
Dwarda	Dwcos47	Dwarda	Dwcos47	1704039	1.298	310.307	3.786	0.387	0.034	56.670	4.403	37.520	6.504	7.940	3.862
Dwarda	Dwcos48	Dwarda	Dwcos48	1704040	2.038	365.889	4.390	0.480	0.062	57.013	6.942	46.916	8.147	12.731	4.025
Dwarda	Dwcos49	Dwarda	Dwcos49	1704041	2.123	230.500	2.365	0.213	0.030	47.141	2.264	22.385	3.939	4.015	2.968
Dwarda	Dwcos50	Dwarda	Dwcos50	1704042	1.396	466.691	3.513	0.737	0.055	68.218	8.043	59.587	11.273	19.114	5.610
Dwarda	Dwcos51	Dwarda	Dwcos51	1704043	3.007	297.209	2.766	0.138	0.021	32.014	2.010	21.157	3.761	3.962	2.132
Dwarda	Dwcos52	Dwarda	Dwcos52	1704044	4.872	225.628	3.730	0.183	0.037	52.644	2.373	22.935	3.983	4.311	3.103
Ganguli section		**Ganguli section**													
Serie #1		**Serie #1**													
Ganguli	Ggcos1	Ganguli	Ggcos1	-	-	-	-	-	-	-	-	-	-	-	-
Ganguli	Ggcos3	Ganguli	Ggcos3	-	-	-	-	-	-	-	-	-	-	-	-
Serie #2		**Serie #2**													
Ganguli	Ggcos2	Ganguli	Ggcos2	1512023	5.136	276.900	2.990	0.151	< L.D.	42.030	3.799	33.660	5.249	7.131	2.976
Ganguli	Ggcos4	Ganguli	Ggcos4	1512024	2.367	245.900	2.796	0.214	0.108	42.000	3.538	35.440	4.215	5.744	2.750
Gonauli section		**Gonauli section**													
Gonauli	Go60	Gonauli	Go60	1704045	0.654	321.881	2.336	0.270	0.058	52.317	4.761	34.554	4.700	5.468	4.988
Maloni Naha section		**Maloni Naha section**													
Maloni Naha	Ca17i01	Maloni Naha	Ca17i01	1708139	0.898	328.214	2.056	0.246	0.049	41.114	4.916	35.805	5.505	5.853	2.601
Maloni Naha	Ca17i03	Maloni Naha	Ca17i03	1708140	0.704	199.931	1.308	0.155	0.029	45.540	3.169	22.027	3.328	3.465	2.345
Maloni Naha	Ca17i04	Maloni Naha	Ca17i04	1708141	0.690	130.570	2.121	0.128	0.027	27.298	1.197	19.570	2.140	2.798	1.957
Maloni Naha	Ca17i08	Maloni Naha	Ca17i08	1708142	2.308	233.125	2.659	0.192	0.035	42.266	2.588	21.225	4.410	3.395	2.477

Table SVII-3. (…/…)

		S								Trace elements							
Site	#	Er ppm	Eu ppm	Ga ppm	Gd ppm	Ge ppm	Hf ppm	Ho ppm	In ppm	La ppm	Lu ppm	Mo ppm	Nb ppm	Nd ppm	Ni ppm	Pb ppm	Pr ppm
		<5% 0.002	<5% 0.002	<5% 0.02	<10% 0.005	<10% 0.04	<10% 0.03	<10% 0.001	<20% 0.03	<5% 0.02	<20% 0.001	>25% 0.50	<10% 0.015	<15% 0.016	<5% 2.0	<20% 0.45	>10ppm: 0.004
Dwarda section																	
Serie #1																	
Dwarda	Dwcos9	-	-	-	-	-	-	-	-	-	-	-	-	-	-	-	-
Dwarda	Dwcos13	-	-	-	-	-	-	-	-	-	-	-	-	-	-	-	-
Dwarda	Dwcos17	-	-	-	-	-	-	-	-	-	-	-	-	-	-	-	-
Dwarda	Dwcos20	-	-	-	-	-	-	-	-	-	-	-	-	-	-	-	-
Serie #2																	
Dwarda	Dwcos2	2.741	1.138	18.680	4.909	2.017	7.308	1.013	< L.D.	34.690	0.441	< L.D.	11.270	30.300	24.050	25.482	8.389
Dwarda	Dwcos3	1.384	0.741	16.020	2.477	1.847	3.910	0.518	< L.D.	16.610	0.215	< L.D.	7.732	14.430	18.980	26.895	4.082
Dwarda	Dwcos4	2.044	0.831	10.970	3.584	1.915	4.150	0.757	< L.D.	24.600	0.328	< L.D.	5.872	21.360	10.260	17.374	5.898
Dwarda	Dwcos5	1.339	0.622	17.460	2.497	1.978	2.999	0.515	< L.D.	14.540	0.211	< L.D.	6.695	12.800	< L.D.	38.411	3.533
Dwarda	Dwcos7	-	-	-	-	-	-	-	-	-	-	-	-	-	-	-	-
Dwarda	Dwcos8	2.343	0.915	14.280	3.756	2.061	4.302	0.839	< L.D.	31.080	0.403	< L.D.	7.213	25.570	13.660	15.291	7.304
Dwarda	Dwcos10	2.064	0.888	14.770	3.921	1.834	4.963	0.767	< L.D.	27.110	0.316	0.417	8.447	23.690	18.080	21.179	6.512
Dwarda	Dwcos12	2.531	0.794	11.560	3.519	2.107	3.572	0.892	< L.D.	23.930	0.406	< L.D.	6.557	21.110	12.270	21.398	5.804
Serie #3																	
Dwarda	Dwcos11	1.782	0.666	11.910	2.752	1.863	3.127	0.631	< L.D.	19.370	0.295	0.404	6.278	16.800	13.650	15.858	4.681
Dwarda	Dwcos14	1.128	0.591	11.440	2.309	1.677	3.066	0.423	< L.D.	17.010	0.175	< L.D.	5.394	14.510	12.570	17.150	4.044
Dwarda	Dwcos15	1.814	0.747	12.900	2.897	1.986	3.743	0.666	< L.D.	21.930	0.276	< L.D.	6.302	18.580	14.030	17.873	5.062
Dwarda	Dwcos16	2.750	0.936	11.820	4.315	1.759	4.710	0.980	< L.D.	29.760	0.410	< L.D.	6.844	25.950	13.650	19.350	7.041
Dwarda	Dwcos18	2.693	1.055	14.570	4.826	1.809	5.744	0.987	< L.D.	34.980	0.408	0.458	8.893	29.300	19.360	19.987	8.029
Dwarda	Dwcos19	3.922	1.008	11.460	4.705	2.161	4.046	1.364	< L.D.	32.630	0.635	0.414	6.880	27.570	14.970	14.339	7.602
Dwarda	Dwcos21	1.856	0.716	11.800	3.218	1.809	3.930	0.670	< L.D.	23.860	0.280	< L.D.	6.636	20.070	15.480	12.563	5.468
Dwarda	Dwcos22	2.496	0.826	14.060	3.757	1.847	4.226	0.908	< L.D.	26.020	0.396	< L.D.	8.214	21.880	18.230	18.343	6.071
Dwarda	Dwcos24	2.049	0.876	15.130	3.821	1.927	4.593	0.760	< L.D.	29.310	0.321	0.587	8.685	23.990	22.820	17.930	6.542
Dwarda	Dwcos25	2.210	0.841	12.030	3.765	1.962	3.794	0.811	< L.D.	27.770	0.367	0.447	7.419	22.510	19.520	15.032	6.171
Serie #4																	
Dwarda	Dwcos30	3.536	1.291	16.107	6.794	1.572	6.977	1.336	0.045	46.704	0.499	< L.D.	10.841	39.367	16.137	21.215	10.723
Dwarda	Dwcos31	2.622	0.935	12.254	4.422	1.556	4.679	0.953	0.037	30.683	0.396	< L.D.	7.907	25.872	14.940	18.450	7.062
Dwarda	Dwcos32	2.484	0.947	12.576	4.442	1.627	4.754	0.892	0.044	32.285	0.377	< L.D.	8.837	26.983	18.818	13.572	7.323
Dwarda	Dwcos33	1.722	0.749	13.188	3.193	1.518	4.159	0.635	0.041	23.694	0.253	< L.D.	8.099	19.673	17.101	17.024	5.397
Dwarda	Dwcos34	2.617	0.856	13.442	4.302	1.581	5.131	0.936	0.041	30.333	0.406	< L.D.	9.254	25.524	14.902	14.635	7.012
Dwarda	Dwcos37	1.985	0.779	11.384	3.406	1.604	4.243	0.717	0.035	24.959	0.302	< L.D.	6.628	20.745	11.811	16.562	5.701
Dwarda	Dwcos43	2.759	1.073	13.163	5.025	1.529	6.202	1.008	0.041	36.173	0.407	< L.D.	9.106	30.296	15.944	16.580	8.315
Dwarda	Dwcos44	3.546	0.985	13.871	4.524	1.977	4.662	1.231	0.048	28.627	0.554	< L.D.	7.335	24.288	11.971	16.946	6.558
Dwarda	Dwcos45	1.679	0.790	14.145	3.143	1.553	4.207	0.614	0.042	22.671	0.251	< L.D.	7.419	19.069	14.009	22.226	5.168
Dwarda	Dwcos46	5.443	1.615	14.411	10.805	2.280	13.060	2.029	0.045	77.474	0.828	< L.D.	10.838	65.982	13.571	23.314	17.922
Dwarda	Dwcos47	2.285	0.856	12.945	3.819	1.707	5.039	0.830	0.038	28.431	0.353	< L.D.	7.871	22.850	13.476	19.533	6.243
Dwarda	Dwcos48	2.389	0.902	15.378	3.855	1.762	4.907	0.863	0.049	27.215	0.367	< L.D.	8.847	22.560	19.293	22.108	6.168
Dwarda	Dwcos49	1.667	0.642	7.972	3.084	1.514	3.813	0.613	< L.D.	22.819	0.249	< L.D.	5.190	18.969	6.530	12.306	5.214
Dwarda	Dwcos50	3.415	1.235	21.665	5.185	2.001	6.357	1.223	0.074	36.190	0.529	< L.D.	12.096	29.678	20.105	22.078	8.198
Dwarda	Dwcos51	1.265	0.470	6.999	2.115	1.464	3.217	0.449	< L.D.	16.339	0.197	< L.D.	3.540	13.241	5.981	12.556	3.670
Dwarda	Dwcos52	1.778	0.662	7.874	3.285	1.556	4.827	0.646	< L.D.	26.076	0.280	< L.D.	5.100	21.452	7.738	11.979	5.895
Ganguli section																	
Serie #1																	
Ganguli	Ggcos1	-	-	-	-	-	-	-	-	-	-	-	-	-	-	-	-
Ganguli	Ggcos3	-	-	-	-	-	-	-	-	-	-	-	-	-	-	-	-
Serie #2																	
Ganguli	Ggcos2	1.802	0.630	9.819	2.855	1.954	3.214	0.654	< L.D.	21.270	0.296	< L.D.	5.704	17.830	13.510	13.550	4.822
Ganguli	Ggcos4	1.642	0.584	9.232	2.745	1.804	3.563	0.598	< L.D.	21.450	0.264	< L.D.	5.060	17.410	11.970	13.890	4.786
Gonauli section																	
Gonauli	Go60	3.277	0.874	13.093	3.831	1.970	3.895	1.142	0.041	25.676	0.509	< L.D.	6.343	21.123	11.111	17.573	5.807
Maloni Naha section																	
Maloni Naha	Ca17i01	1.467	0.682	12.164	2.754	1.609	3.626	0.547	0.031	20.627	0.218	< L.D.	6.487	16.728	13.755	13.185	4.505
Maloni Naha	Ca17i03	1.382	0.461	7.170	2.443	1.591	4.072	0.501	< L.D.	19.585	0.216	< L.D.	4.577	15.870	10.165	13.444	4.388
Maloni Naha	Ca17i04	1.180	0.390	5.223	1.957	1.464	3.155	0.418	< L.D.	15.101	0.172	< L.D.	3.883	12.284	5.782	6.413	3.348
Maloni Naha	Ca17i08	1.447	0.528	8.464	2.507	1.468	4.220	0.517	< L.D.	18.581	0.220	< L.D.	4.679	15.113	7.519	16.252	4.138

Table SVII-3. (…/…)

S

Site	#	Rb ppm	Sc ppm	Sb ppm	Sm ppm	Sn ppm	Sr ppm	Ta ppm	Tb ppm	Th ppm	Tm ppm	U ppm	V ppm	W ppm	Y ppm	Yb ppm	Zn ppm
		<5%	<15%	<20%	<15%	<20%	<5%	<10%	<20%	<10%	<20%	<15%	>50 ppm:	<20%	<15%	<15%	> 50ppm:
		0.15	0.6	0.06	0.005	0.30	0.70	0.004	0.001	0.015	0.001	0.01	0.85	0.80	0.02	0.002	7.0
Dwarda section																	
Serie #1																	
Dwarda	Dwcos9	-	-	-	-	-	-	-	-	-	-	-	-	-	-	-	-
Dwarda	Dwcos13	-	-	-	-	-	-	-	-	-	-	-	-	-	-	-	-
Dwarda	Dwcos17	-	-	-	-	-	-	-	-	-	-	-	-	-	-	-	-
Dwarda	Dwcos20	-	-	-	-	-	-	-	-	-	-	-	-	-	-	-	-
Serie #2																	
Dwarda	Dwcos2	163.900	10.300	0.696	5.805	9.412	73.740	1.369	0.774	15.660	0.423	3.576	60.360	3.324	27.780	2.826	58.220
Dwarda	Dwcos3	161.400	7.190	0.430	2.883	5.825	100.700	1.031	0.392	8.304	0.204	3.380	46.530	2.465	14.130	1.411	45.390
Dwarda	Dwcos4	93.580	6.000	0.290	4.296	3.392	59.170	0.744	0.575	11.330	0.312	2.237	32.670	1.953	20.250	2.113	25.740
Dwarda	Dwcos5	199.900	5.040	0.234	2.846	11.300	69.660	1.145	0.406	7.135	0.198	2.165	18.360	2.299	14.010	1.350	35.830
Dwarda	Dwcos7	-	-	-	-	-	-	-	-	-	-	-	-	-	-	-	-
Dwarda	Dwcos8	116.700	7.220	0.703	4.779	4.370	107.300	0.857	0.599	11.440	0.373	2.483	41.390	1.803	22.780	2.559	28.500
Dwarda	Dwcos10	133.300	8.260	0.481	4.742	5.924	88.240	1.158	0.595	12.690	0.304	4.416	51.740	2.603	20.360	2.066	44.570
Dwarda	Dwcos12	100.900	7.490	0.410	4.206	6.975	66.770	1.512	0.593	10.370	0.393	3.305	35.870	1.846	24.240	2.661	33.910
Serie #3																	
Dwarda	Dwcos11	100.900	7.100	0.368	3.262	4.556	65.240	0.765	0.439	8.526	0.277	2.101	44.880	2.111	17.080	1.889	35.300
Dwarda	Dwcos14	128.600	5.220	0.287	2.832	4.272	53.310	0.661	0.343	7.881	0.168	2.564	36.960	1.753	11.540	1.166	30.310
Dwarda	Dwcos15	121.000	7.550	0.411	3.645	3.991	54.870	0.780	0.483	10.120	0.267	2.817	45.550	2.211	17.670	1.816	36.190
Dwarda	Dwcos16	100.500	7.150	0.451	5.148	4.208	81.060	0.916	0.690	13.440	0.409	3.416	39.290	1.797	26.560	2.771	36.550
Dwarda	Dwcos18	129.400	8.840	0.613	5.779	7.027	89.480	1.328	0.748	16.560	0.401	3.373	52.430	2.168	26.540	2.692	45.330
Dwarda	Dwcos19	91.300	9.740	0.479	5.423	3.730	82.280	0.936	0.824	12.570	0.619	2.927	55.930	1.911	37.040	4.100	35.450
Dwarda	Dwcos21	124.000	7.510	0.418	3.864	4.054	48.470	0.779	0.507	10.640	0.271	2.242	50.430	2.435	17.930	1.832	34.040
Dwarda	Dwcos22	130.600	8.590	0.668	4.393	5.622	72.250	1.202	0.620	12.440	0.380	3.675	53.660	2.583	24.300	2.567	42.820
Dwarda	Dwcos24	152.800	8.920	0.777	4.616	5.601	71.780	1.016	0.589	12.370	0.307	2.798	60.610	2.579	20.580	2.031	52.180
Dwarda	Dwcos25	121.300	7.590	0.834	4.364	3.674	65.390	0.885	0.602	11.110	0.345	2.533	60.740	2.229	22.330	2.271	44.850
Serie #4																	
Dwarda	Dwcos30	156.241	9.420	0.443	7.880	4.930	162.895	1.316	1.067	24.107	0.502	3.544	49.565	2.389	35.040	3.418	43.218
Dwarda	Dwcos31	125.154	7.410	0.692	5.135	3.839	68.363	1.068	0.715	13.852	0.383	2.695	39.623	2.010	25.399	2.630	40.245
Dwarda	Dwcos32	114.445	8.320	1.020	5.269	3.638	56.562	1.070	0.697	13.505	0.358	3.884	63.526	2.014	23.903	2.507	44.197
Dwarda	Dwcos33	131.779	7.820	0.520	3.877	4.443	56.835	0.965	0.499	10.423	0.243	3.052	47.330	2.202	16.716	1.714	41.271
Dwarda	Dwcos34	129.172	8.100	0.698	5.071	5.118	63.713	1.263	0.688	14.467	0.384	3.185	45.936	2.633	24.646	2.684	38.255
Dwarda	Dwcos37	104.536	6.470	0.445	4.091	4.426	60.585	0.870	0.538	10.425	0.288	5.263	36.413	1.728	19.109	2.013	33.168
Dwarda	Dwcos43	122.020	7.650	0.685	5.949	3.907	85.375	1.107	0.789	15.021	0.396	3.128	44.325	2.050	26.340	2.741	40.341
Dwarda	Dwcos44	100.007	9.300	0.387	4.987	4.241	90.933	1.056	0.796	11.803	0.535	2.668	36.905	2.404	32.172	3.747	34.514
Dwarda	Dwcos45	124.154	6.690	0.404	3.731	4.957	86.685	0.884	0.489	10.054	0.240	1.973	44.579	2.024	16.253	1.667	41.175
Dwarda	Dwcos46	108.373	10.670	0.479	13.186	6.306	79.941	1.671	1.656	35.760	0.787	6.631	40.811	2.482	52.251	5.474	43.135
Dwarda	Dwcos47	108.699	7.120	0.529	4.492	4.269	45.076	1.014	0.606	11.213	0.334	2.679	40.517	2.440	23.083	2.324	36.293
Dwarda	Dwcos48	132.920	9.420	0.587	4.489	4.976	47.018	1.091	0.631	11.563	0.352	2.468	49.930	2.508	22.586	2.433	50.464
Dwarda	Dwcos49	76.648	3.910	0.316	3.763	2.662	31.489	0.776	0.475	9.690	0.246	2.057	20.699	1.439	16.217	1.665	19.359
Dwarda	Dwcos50	162.970	13.940	0.709	6.066	7.590	40.319	1.455	0.865	14.866	0.502	3.206	67.171	3.604	32.472	3.505	65.309
Dwarda	Dwcos51	74.038	3.250	0.344	2.596	2.111	26.478	0.493	0.343	7.127	0.182	1.567	18.773	1.136	12.011	1.299	20.543
Dwarda	Dwcos52	78.679	4.430	0.458	4.125	10.415	27.554	0.763	0.509	11.054	0.267	2.404	24.011	1.516	16.408	1.874	22.106
Ganguli section																	
Serie #1																	
Ganguli	Ggcos1	-	-	-	-	-	-	-	-	-	-	-	-	-	-	-	-
Ganguli	Ggcos3	-	-	-	-	-	-	-	-	-	-	-	-	-	-	-	-
Serie #2																	
Ganguli	Ggcos2	114.100	6.300	0.518	3.427	3.632	29.660	0.738	0.457	7.823	0.280	1.740	35.920	1.647	17.670	1.912	34.130
Ganguli	Ggcos4	87.490	5.220	0.366	3.314	3.161	30.500	0.988	0.438	8.761	0.246	1.928	32.300	1.779	16.070	1.701	27.240
Gonauli section																	
Gonauli	Go60	90.953	8.980	0.291	4.217	3.189	65.484	0.753	0.695	10.014	0.488	2.396	34.670	1.888	30.333	3.454	37.749
Maloni Naha section																	
Maloni Naha	Ca17i01	102.086	6.140	0.471	3.318	3.604	62.641	0.935	0.424	8.184	0.211	1.954	44.236	1.831	14.539	1.453	41.646
Maloni Naha	Ca17i03	70.342	3.010	0.293	3.086	2.411	18.107	0.631	0.381	8.293	0.209	1.804	19.752	1.347	13.498	1.460	19.446
Maloni Naha	Ca17i04	47.027	2.330	0.294	2.423	2.547	13.056	0.536	0.315	6.223	0.170	1.322	15.170	0.970	11.297	1.166	17.834
Maloni Naha	Ca17i08	79.396	3.410	0.348	3.039	2.771	25.102	0.582	0.402	8.572	0.216	2.074	21.938	1.360	13.911	1.496	20.336

Table SVII-3. (…/…)

Site	#	S	Major elements										
		Zr	SiO2	Al2O3	Fe2O3	MnO	MgO	CaO	Na2O	K2O	TiO2	P2O5	LOI	Total
		ppm	%	%	%	%	%	%	%	%	%	%	%	%
													Loss on Ignition	
		<5%	<2%	>10%: <2%	<10%	<20%	<10%	<15%	<10%	<10%	<20%	>25%		
		1.50	0.05	0.04	0.015	0.015	0.03	0.03	0.02	0.03	0.02	0.10		
Dwarda section														
Serie #1														
Dwarda	Dwcos9	-	-	-	-	-	-	-	-	-	-	-	-	-
Dwarda	Dwcos13	-	-	-	-	-	-	-	-	-	-	-	-	-
Dwarda	Dwcos17	-	-	-	-	-	-	-	-	-	-	-	-	-
Dwarda	Dwcos20	-	-	-	-	-	-	-	-	-	-	-	-	-
Serie #2														
Dwarda	Dwcos2	271.700	73.280	13.180	3.046	0.027	1.163	0.679	1.207	2.915	0.527	< L.D.	4.010	100.034
Dwarda	Dwcos3	136.800	75.880	11.025	3.167	0.023	1.042	0.861	1.651	2.837	0.371	< L.D.	2.680	99.537
Dwarda	Dwcos4	140.400	81.850	8.756	1.939	0.035	0.532	0.583	0.991	2.036	0.280	< L.D.	2.120	99.122
Dwarda	Dwcos5	100.900	76.260	11.855	1.640	0.029	0.507	0.814	2.222	3.465	0.213	< L.D.	1.980	98.985
Dwarda	Dwcos7	-	-	-	-	-	-	-	-	-	-	-	-	-
Dwarda	Dwcos8	155.100	72.580	10.478	2.745	0.039	0.912	3.668	2.074	2.362	0.336	< L.D.	3.990	99.184
Dwarda	Dwcos10	181.300	71.860	10.283	3.417	0.051	1.734	3.113	1.396	2.587	0.413	< L.D.	4.480	99.334
Dwarda	Dwcos12	121.200	76.780	9.036	2.968	0.076	1.125	2.308	1.312	1.889	0.295	< L.D.	3.110	98.899
Serie #3														
Dwarda	Dwcos11	108.300	75.650	8.721	2.647	0.049	1.758	2.858	1.100	2.017	0.292	< L.D.	4.230	99.322
Dwarda	Dwcos14	104.900	80.830	8.593	2.134	0.017	1.073	0.548	1.034	2.329	0.249	< L.D.	2.500	99.307
Dwarda	Dwcos15	128.100	79.110	10.128	2.244	0.019	0.990	0.378	0.997	2.467	0.313	< L.D.	2.760	99.406
Dwarda	Dwcos16	167.100	76.760	9.256	2.737	0.064	1.196	2.433	1.214	2.000	0.345	< L.D.	3.290	99.295
Dwarda	Dwcos18	207.900	71.330	10.390	3.439	0.053	1.602	3.278	1.211	2.487	0.441	< L.D.	4.640	98.871
Dwarda	Dwcos19	140.000	74.590	9.665	3.461	0.100	1.352	2.891	1.074	1.944	0.341	< L.D.	3.650	99.068
Dwarda	Dwcos21	136.700	80.330	8.994	2.396	0.027	1.036	0.427	1.003	2.291	0.322	< L.D.	2.200	99.026
Dwarda	Dwcos22	144.500	74.100	10.110	3.399	0.051	1.264	2.162	1.256	2.575	0.399	< L.D.	3.410	98.726
Dwarda	Dwcos24	167.800	72.010	10.708	3.436	0.038	1.822	2.169	1.125	3.023	0.418	< L.D.	4.380	99.128
Dwarda	Dwcos25	130.700	66.980	8.505	3.238	0.063	2.611	5.885	0.804	2.402	0.363	< L.D.	8.040	98.891
Serie #4														
Dwarda	Dwcos30	249.823	71.580	11.818	3.133	0.029	1.819	1.049	0.732	2.845	0.478	0.130	5.590	99.190
Dwarda	Dwcos31	169.529	74.530	9.980	2.925	0.040	1.497	2.823	1.386	2.701	0.375	0.120	3.860	100.230
Dwarda	Dwcos32	174.333	71.840	9.472	4.214	0.052	1.942	3.009	1.321	2.357	0.456	0.100	4.600	99.350
Dwarda	Dwcos33	149.549	76.840	9.943	3.049	0.024	1.254	1.195	1.114	2.567	0.377	< L.D.	2.920	99.283
Dwarda	Dwcos34	180.704	76.310	10.203	3.367	0.036	1.204	0.748	1.066	2.491	0.418	0.100	3.100	99.040
Dwarda	Dwcos37	156.438	78.770	8.883	2.430	0.039	1.186	1.784	1.179	2.169	0.307	< L.D.	2.990	99.737
Dwarda	Dwcos43	217.446	72.220	10.022	3.089	0.033	1.587	2.754	1.587	2.463	0.448	0.110	4.350	98.660
Dwarda	Dwcos44	163.264	75.280	11.593	3.075	0.063	0.930	1.451	2.180	1.844	0.315	0.120	2.100	98.940
Dwarda	Dwcos45	149.940	71.740	10.298	2.924	0.027	0.902	3.471	1.396	2.490	0.342	< L.D.	5.160	98.750
Dwarda	Dwcos46	478.350	73.550	10.620	4.575	0.136	0.797	1.301	1.415	2.182	0.455	0.170	3.830	99.030
Dwarda	Dwcos47	179.642	79.170	10.143	3.279	< L.D.	0.590	0.410	0.640	2.183	0.376	< L.D.	3.090	99.881
Dwarda	Dwcos48	174.782	75.310	11.850	3.600	0.026	0.778	0.512	0.635	2.560	0.425	< L.D.	4.490	100.186
Dwarda	Dwcos49	140.995	86.470	6.866	1.134	< L.D.	0.299	0.228	0.402	1.684	0.227	< L.D.	1.620	98.930
Dwarda	Dwcos50	227.100	65.620	15.948	4.064	0.033	1.318	0.549	0.335	3.292	0.600	< L.D.	7.210	98.969
Dwarda	Dwcos51	116.115	87.720	6.041	1.078	< L.D.	0.279	0.184	0.364	1.564	0.162	< L.D.	1.500	98.892
Dwarda	Dwcos52	172.886	86.980	6.592	1.668	< L.D.	0.343	0.238	0.365	1.626	0.229	< L.D.	1.540	99.581
Ganguli section														
Serie #1														
Ganguli	Ggcos1	-	-	-	-	-	-	-	-	-	-	-	-	-
Ganguli	Ggcos3	-	-	-	-	-	-	-	-	-	-	-	-	-
Serie #2														
Ganguli	Ggcos2	109.800	84.430	7.057	2.290	0.015	0.647	0.163	0.255	2.053	0.292	< L.D.	2.240	99.442
Ganguli	Ggcos4	122.400	85.150	7.173	1.855	0.036	0.440	0.224	0.375	1.751	0.248	< L.D.	2.000	99.252
Gonauli section														
Gonauli	Go60	139.616	78.400	10.588	2.880	0.071	0.790	0.661	1.198	2.012	0.292	< L.D.	2.230	99.122
Maloni Naha section														
Maloni Naha	Ca17i01	129.894	77.690	9.138	2.293	0.025	1.334	2.704	0.971	2.153	0.291	< L.D.	4.430	101.029
Maloni Naha	Ca17i03	151.775	90.410	5.539	0.798	0.021	0.227	0.049	0.081	1.289	0.203	< L.D.	1.430	100.047
Maloni Naha	Ca17i04	115.766	93.820	4.350	0.598	< L.D.	0.152	0.036	0.060	0.929	0.168	< L.D.	0.950	101.063
Maloni Naha	Ca17i08	154.894	87.920	6.494	1.412	0.016	0.223	0.049	0.144	1.552	0.204	< L.D.	2.090	100.104

Table SVII-4. Clayey to fine sand bulk carbonate oxygen - carbon isotopic results.

Measurements on the bulk carbonate fraction. Results for the (coarser) sandy samples are presented in Table SVII-3. All samples except the G55 are from the Dwarda, the samples from the Ganguli did not lead to results. Age uncertainty of 0.1 Ma. For interpretations, only the samples having an average area (a proxy for the precision of the measurement) > 5% and $CaCO_3 \geq 20\%$ (i.e. larger than the detrital carbonate fraction in the modern Narayani sand) have been considered.

Table SVII-4. (…/…)

Analysis #	Identifier 1	Identifier 2	Sample #	Depth (m)	Age (Ma)	Average Area	$CaCO_3$ (%)	$\delta^{18}O$ (‰ PDB)	$\delta^{13}C$ (‰ PDB)
35430	DW 102	20663	D101	453.0	1.06	3	0	-10.32	-6.85
19016	G 056	2118	G55	519.2	1.17	70	25	-10.87	-8.75
35432	DW 120	19367	D119	525.9	1.19	2	0	-12.04	-8.06
17922	D 121	2116	D121	529.7	1.19	107	36	-10.49	-3.21
35433	DW 121	20459	D121	529.7	1.19	2	0	-13.32	-8.70
18463	D 123	103020	D123	540.5	1.21	8	0	-9.39	-6.49
18228	D 125	69028	D125	551.9	1.23	11	0	-9.37	-4.94
35434	DW 135	19509	D135	611.6	1.33	2	0	-11.66	-9.37
35435	DW 137	21552	D137	615.8	1.34	2	0	-12.38	-6.60
18458	D 144	10009	D143	649.7	1.40	35	2	-2.19	-1.15
35438	DW 144	20132	D143	649.7	1.40	60	2	-2.31	-1.26
18644	D 188	2046	D187	865.5	1.77	103	37	-6.30	-7.63
19359	D188	1859	D187	865.5	1.77	67	33	-5.70	-7.29
19343	D196	1786	D195	899.9	1.82	62	32	-4.07	-7.11
18252	D 199	2052	D199	914.7	1.84	96	33	-7.67	-7.26
18459	D 199b	2093	D199	914.7	1.84	98	33	-8.19	-7.36
18621	D 202	2115	D199	914.7	1.84	86	30	-6.70	-8.38
19356	D202	2142	D201	919.5	1.85	67	29	-4.62	-7.40
18619	D 210	2024	D209	947.3	1.88	43	16	-13.90	-2.31
19335	D216	1974	D215	954.1	1.89	56	26	-5.82	-5.17
18639	D 224	1990	D223	1002.3	1.96	88	33	-6.59	-10.32
19339	D241	1831	D241	1126.9	2.23	62	31	-5.26	-7.88
19125	D 244	1873	D243	1137.7	2.25	17	14	-7.47	-7.46
19351	D249	2099	D249	1168.3	2.31	8	4	-11.65	-0.85
35443	DW 253	21153	D253	1174.6	2.33	3	0	-9.60	-4.37
18245	D 255	2026	D255	1179.8	2.34	88	31	-8.12	-5.56
19336	D258	1870	D257	1185.1	2.35	74	37	-5.04	-3.29
18628	D 262	2030	D261	1237.3	2.46	177	65	-13.43	-9.70
19598	D262	275	D261	1237.3	2.46	22	64	-12.82	-1.59
19338	D269	2049	D269	1278.0	2.55	85	39	-4.91	-6.79
18646	D 274	1930	D273	1294.3	2.58	83	32	-6.36	-5.09
19358	D274	1864	D273	1294.3	2.58	83	41	-4.78	-3.83
18626	D 276	1952	D275	1304.3	2.60	70	27	-8.19	-6.51
19362	D276	1847	D275	1304.3	2.60	51	26	-6.52	-5.56
18240	D 283	2055	D283	1345.6	2.69	99	34	-9.64	-4.74
35447	DW 283	967	D283	1345.6	2.69	44	31	-8.72	-4.25
19328	D288	2099	D287	1360.6	2.72	63	28	-6.99	-3.97
18249	D 295	2049	D295	1406.8	2.82	77	27	-6.79	-8.75
18238	D 305	1957	D305	1455.3	2.93	103	37	-8.43	-4.16
35448	DW 305	1065	D305	1455.3	2.93	49	32	-7.56	-3.59
18636	D 308	2037	D307	1468.1	2.96	127	46	-19.17	-6.85
19360	D308	2108	D307	1468.1	2.96	106	47	-5.84	-1.67
19031	D 309	2072	D309	1481.2	2.99	23	9	-14.21	-1.65
35449	DW 311	24980	D311	1499.0	3.03	5	0	-9.40	-12.46
19127	D 313	2185	D313	1505.0	3.04	9	6	-13.99	-1.34
18247	D 324	2111	D323	1542.1	3.10	116	39	-11.03	-1.83
19344	D328	2028	D327	1585.2	3.14	62	28	-5.71	-1.64
19342	D329	2301	D329	1595.5	3.15	63	25	-5.98	-1.53
18465	D 339	144390	D339	1629.3	3.17	15	0	-9.03	-4.75
19032	D 347	2020	D347	1689.6	3.31	3	1	-8.31	-3.05
19034	D 357	1879	D357	1735.3	3.54	15	6	-12.28	-1.06
18449	D 362	47757	D361	1745.3	3.58	28	0	-5.39	0.77
18235	D362	1960	D361	1745.3	3.58	1	1	-7.93	-0.35
35455	DW 362	20083	D361	1745.3	3.58	13	0	-8.07	0.44
19329	D364	2087	D363	1759.3	3.63	63	28	-8.35	-3.63
18231	D 369	31027	D369	1780.2	3.69	30	1	-11.69	-1.37
35456	DW 369	26820	D369	1780.2	3.69	23	1	-12.54	-1.36
18457	D 377	10266	D377	1823.0	3.82	37	3	-13.61	-2.09
35457	DW 377	21829	D377	1823.0	3.82	69	2	-13.43	-2.00
18635	D 381	1839	D381	1846.7	3.90	132	53	-22.44	-1.68
19353	D381	1718	D381	1846.7	3.90	101	54	-5.24	-1.22
19331	D384	2173	D383	1851.6	3.91	63	27	-7.82	-3.11
18625	D 385	1980	D385	1857.9	3.93	62	23	-9.91	-3.56
19364	D385	2048	D385	1857.9	3.93	50	23	-8.59	-2.55
19334	D388	2146	D387	1873.3	3.98	62	27	-8.02	-4.96
18462	D 392	93919	D391	1897.1	4.05	1	0	-11.65	-7.20
19010	D 400	2126	D399	1926.3	4.14	64	23	-12.19	-0.11
18638	D 409	2171	D409	1966.0	4.24	94	32	-9.23	-4.54
19341	D409	1973	D409	1966.0	4.24	81	38	-8.09	-5.07
18448	D 414	1887	D413	1999.3	4.32	91	34	-11.12	-3.37
19345	D416	2036	D415	2006.5	4.34	84	38	-6.66	-2.15
18233	D 417	2095	D417	2016.8	4.37	38	13	-8.87	-3.78
18250	D 421	2074	D421	2031.9	4.40	53	18	-10.56	-2.90

Table SVII-4. (…/…)

Analysis #	Identifier 1	Identifier 2	Sample #	Depth (m)	Age (Ma)	Average Area	$CaCO_3$ (%)	$\delta^{18}O$ (‰ PDB)	$\delta^{13}C$ (‰ PDB)
18466	D 424	2014	D423	2035.3	4.41	58	20	-10.89	-3.11
19363	D424	1831	D423	2035.3	4.41	41	21	-9.84	-2.67
17920	D 425	1964	D425	2039.3	4.42	60	22	-10.37	-3.10
19011	D 442	2037	D441	2146.9	4.67	62	23	-9.19	-3.90
18643	D 446	1958	D445	2170.6	4.71	108	41	-10.74	-3.23
19355	D446	1901	D445	2170.6	4.71	95	46	-8.67	-2.49
35465	DW 446	1141	D445	2170.6	4.71	49	29	-11.24	-3.65
35466	DW 461	23159	D461	2267.3	4.84	3	0	-9.67	-9.16
18242	D 464	2129	D463	2273.5	4.85	75	25	-12.92	-3.42
19330	D466	2135	D465	2279.8	4.86	39	17	-10.06	-4.13
19337	D469	2070?	D469	2301.3	4.87	20		-14.56	-0.93
35470	DW 473	20806	D473	2323.1	4.89	1	0	-10.90	-10.08
35225	DW 601	942	D601	2331.1	4.90	30	27	-11.95	-2.11
35226	DW 603	1022	D603	2339.2	4.92	23	19	-10.75	-3.09
35227	DW 606	959	D605	2346.9	4.93	50	45	-10.07	-3.89
35230	DW 610	1115	D609	2370.0	4.97	46	36	-10.08	-3.29
35231	DW 611	1078	D611	2375.7	4.98	59	47	-10.45	1.63
35232	DW 613	1032	D613	2382.3	4.99	36	30	-12.33	-3.30
35233	DW 615	1086	D615	2404.3	5.11	34	27	-13.24	-2.55
35234	DW 618	994	D617	2415.6	5.19	31	27	-12.57	-2.84
35235	DW 620	1003	D619	2427.2	5.25	28	24	-12.42	-2.08
35238	DW 622	796	D621	2439.6	5.27	34	37	-10.75	-4.23
35239	DW 624	1035	D623	2450.4	5.30	52	43	-10.41	-4.40
35240	DW 626	1030	D625	2482.7	5.37	48	40	-10.62	-1.52
35241	DW 628	944	D627	2493.9	5.40	28	25	-12.79	-2.12
35242	DW 630	1151	D629	2502.6	5.41	28	21	-11.90	-2.85
35472	DW 631	19723	D631	2528.0	5.47	2	0	-12.42	-6.40
35244	DW 633	876	D633	2543.4	5.51	34	34	-9.77	-3.79
35473	DW 635	18844	D635	2550.7	5.52	3	0	-11.46	-9.53
35248	DW 637	894	D637	2558.6	5.54	33	32	-10.69	-4.56
35249	DW 638	1051	D637	2558.6	5.54	39	32	-11.32	-4.82
34774	DW 640	923	D639	2568.7	5.56	41	36	-8.54	-3.79
34775	DW 642	917	D641	2575.7	5.58	12	11	-11.85	-4.35
34776	DW 644	811	D643	2593.5	5.62	26	26	-12.35	-3.86
34777	DW 647	876	D647	2612.8	5.66	22	21	-13.37	-2.84
34778	DW 650	968	D649	2618.6	5.67	25	21	-13.28	-2.50
35257	DW 652	29860	D651	2633.2	5.71	7	0	-7.23	-9.37
34782	DW 653	831	D653	2637.6	5.72	22	22	-13.77	-2.46
34783	DW 658	913	D657	2669.1	5.79	32	29	-14.28	-2.75
35252	DW 660	5865	D659	2702.3	5.86	159	23	-6.39	-2.27
34785	DW 662	858	D661	2723.2	5.91	21	20	-12.09	-3.38
34786	DW 664	884	D663	2738.6	5.94	13	12	-13.20	-2.16
34787	DW 666	874	D665	2746.6	5.96	14	13	-13.87	-2.84
35478	DW 668	27748	D667	2756.0	5.98	7	0	-9.34	-10.81
34791	DW 669	909	D669	2763.7	6.00	21	19	-14.61	-3.06
34792	DW 672	845	D671	2779.9	6.03	3	3	-13.32	-3.95
34793	DW 674	863	D673	2793.3	6.05	12	12	-13.19	-2.21
35259	DW 676	29387	D675	2804.7	6.06	6	0	-9.94	-9.12
34795	DW 677	834	D677	2806.6	6.06	38	38	-10.09	-4.45
34798	DW 684	921	D683	2830.5	6.09	26	24	-12.81	-3.03
34799	DW 685	777	D685	2837.0	6.10	29	31	-13.15	-2.87
34800	DW 687	903	D687	2843.9	6.11	26	23	-14.43	-2.16
34801	DW 690	943	D689	2863.2	6.13	33	29	-12.84	-2.44
34802	DW 692	990	D691	2879.8	6.15	20	17	-13.70	-3.42
34803	DW 694	877	D693	2900.3	6.17	43	41	-11.42	-3.93
34806	DW 696	760	D695	2953.1	6.23	27	30	-12.47	-4.10
34807	DW 698	1091	D697	2964.2	6.25	24	18	-13.25	-4.06
34808	DW 702	764	D701	2997.7	6.37	20	21	-14.31	-3.40
35480	DW 704	21828	D703	3011.2	6.43	2	0	-11.96	-8.03
34810	DW 705	888	D705	3036.9	6.49	19	18	-8.04	-6.03
34811	DW 708	992	D707	3050.9	6.51	60	50	-12.06	-2.73
35481	DW 711	17992	D711	3102.1	6.61	4	0	-12.54	-5.71
35482	DW 712	27933	D711	3102.1	6.61	2	0	-12.48	-7.65
34816	DW 714	854	D713	3111.7	6.63	32	31	-13.78	-4.82
34817	DW 715	924	D715	3126.9	6.66	23	21	-13.93	-3.63
35255	DW 717	1058	D717	3129.6	6.67	28	23	-13.91	-3.87
34819	DW 719	932	D719	3142.5	6.69	26	23	-13.91	-4.04
34822	DW 721	950	D721	3148.5	6.71	24	21	-14.55	-3.69
34823	DW 723	924	D723	3156.0	6.72	31	28	-14.86	-3.87
35483	DW 725	23717	D725	3168.5	6.75	6	0	-9.80	-6.31
35250	DW 731	1020	D731	3189.6	6.80	26	22	-15.45	-3.61
35486	DW 734	16020	D733	3204.1	6.84	1	0	-11.23	-10.87
34826	DW 735	973	D735	3211.1	6.85	30	25	-14.29	-3.88
34827	DW 740	1005	D739	3229.0	6.90	24	19	-14.68	-6.73
34830	DW 741	831	D741	3242.2	6.93	25	25	-14.23	-5.01
34831	DW 743	932	D743	3244.9	6.94	9	8	-11.49	-3.27
34832	DW 746	888	D745	3254.9	6.96	34	31	-15.60	-6.49
34833	DW 748	963	D747	3266.2	6.99	51	43	-11.56	-9.31
34834	DW 749	828	D749	3274.4	7.01	20	19	-13.81	-4.43

Table SVII-4. (…/…)

Analysis #	Identifier 1	Identifier 2	Sample #	Depth (m)	Age (Ma)	Average Area	$CaCO_3$ (%)	$\delta^{18}O$ (‰ PDB)	$\delta^{13}C$ (‰ PDB)
34835	DW 751	1007	D751	3285.2	7.04	26	21	-14.65	-7.39
35487	DW 753	22853	D753	3288.5	7.05	3	0	-11.98	-8.79
34839	DW 755	842	D755	3300.0	7.08	20	20	-13.48	-3.99
34840	DW 757	930	D757	3314.8	7.11	29	26	-15.49	-5.53
34841	DW 759	1103	D759	3322.3	7.13	19	14	-14.01	-4.09
34843	DW 765	804	D765	3337.4	7.16	29	30	-14.64	-5.14
34844	DW 767	913	D767	3346.5	7.18	19	17	-15.21	-4.48
35488	DW 769	24343	D769	3353.6	7.19	7	0	-9.95	-8.39
34848	DW 771	1035	D771	3360.1	7.20	72	57	-11.46	-10.34
34849	DW 774	977	D773	3364.7	7.21	9	7	-12.48	-1.95
34850	DW 776	921	D775	3371.7	7.22	10	9	-13.14	-1.73
35489	DW 777	21883	D777	3382.5	7.25	4	0	-8.76	-5.80
34852	DW 779	821	D779	3388.1	7.26	25	25	-14.44	-6.20
34855	DW 781	973	D781	3397.6	7.28	0	0	-12.08	-13.02
35512	DW 785	491	D785	3416.0	7.33	18	25	-18.09	-5.78
34856	DW 786	941	D785	3416.0	7.33	32	28	-14.81	-5.19
35490	DW 787	17922	D787	3424.4	7.35	1	0	-12.40	-9.68
34858	DW 794	868	D793	3437.9	7.39	28	26	-14.62	-3.37
35514	DW 799	4298	D799	3453.0	7.44	130	21	-13.69	-1.59
35175	DW 804	806	D803	3462.5	7.47	28	30	-16.01	-6.08
35176	DW 805	898	D805	3474.4	7.50	40	39	-17.17	-8.22
35177	DW 807	825	D807	3480.3	7.52	3	3	-13.69	-3.22
35178	DW 813	827	D813	3506.1	7.57	63	65	-10.36	-9.24
35494	DW 816	17684	D815	3511.5	7.58	5	0	-10.51	-8.77
35182	DW 818	794	D817	3523.2	7.60	8	8	-13.28	-2.45
35183	DW 820	1006	D819	3531.6	7.62	28	24	-14.91	-4.33
35184	DW 821	876	D821	3537.2	7.63	26	26	-14.83	-5.96
35185	DW 823	888	D823	3549.9	7.65	24	24	-15.93	-5.60
35186	DW 825	890	D825	3559.7	7.67	42	41	-15.21	-8.36
35187	DW 827	1026	D827	3569.5	7.69	45	38	-13.30	-6.99
35190	DW830	959	D829	3575.2	7.71	22	20	-16.08	-6.67
35191	DW 831	945	D831	3579.4	7.71	9	8	-14.75	-7.25
35192	DW 834	890	D833	3597.1	7.75	12	12	-15.61	-5.95
35193	DW 835	822	D835	3602.7	7.76	13	13	-15.40	-5.80
35194	DW 837	874	D837	3611.1	7.78	17	16	-15.86	-5.67
35195	DW 839	901	D839	3627.8	7.82	42	40	-14.35	-8.11
35198	DW 842	928	D841	3636.3	7.83	24	23	-15.51	-3.42
35199	DW 843	920	D843	3642.5	7.85	63	59	-9.94	-9.55
35200	DW 846	916	D845	3649.8	7.86	25	23	-12.99	-1.07
35201	DW 847	878	D847	3660.5	7.89	0	0	-14.48	-11.87
35202	DW 850	886	D849	3672.0	7.91	32	32	-15.14	-8.48
35203	DW 854	962	D853	3687.1	7.94	30	27	-16.65	-6.66
35206	DW 855	1095	D855	3692.5	7.95	15	12	-16.79	-7.34
35207	DW 858	1071	D857	3698.0	7.96	30	24	-15.00	-8.14
35208	DW 859	851	D859	3702.6	7.97	13	13	-15.37	-2.20
35209	DW 861	994	D861	3724.0	8.02	61	53	-12.91	-9.71
35210	DW 864	992	D863	3730.7	8.03	4	4	-13.25	-1.86
35498	DW 868	18214	D867	3746.1	8.07	2	0	-12.58	-10.77
35214	DW 873	932	D873	3766.6	8.11	44	40	-13.86	-4.34
35215	DW 876	941	D875	3775.5	8.12	14	13	-14.31	-2.37
35216	DW 877	875	D877	3791.5	8.14	19	18	-16.00	-5.73
35217	DW 881	1081	D881	3805.3	8.16	18	14	-16.12	-7.33
35218	DW 885	910	D885	3826.9	8.18	30	28	-18.13	-5.73
35219	DW 887	1021	D887	3835.4	8.19	27	23	-17.50	-5.40
35222	DW 889	980	D889	3835.4	8.19	18	16	-15.59	-4.52
35223	DW 901	1062	D901	3844.1	8.20	50	40	-15.89	-6.73
35439	DW 906	908	D905	3861.3	8.23	12	9	-15.15	-5.72
35462	DW 910	1055	D909	3876.2	8.24	78	51	-10.63	-8.50
34842	DW 761	1007	D761			7	6	-13.84	-2.77

Table SVIII-1. Sample information, dating, ^{10}Be, Sr-Nd isotopic results.

The table includes all measured Valmiki samples. Sample information (col. A to H) includes the geographic coordinates, the stratigraphic depth and the ages determined with magnetostratigraphy (this thesis, Chapter VII). ^{10}Be data (col. J to AU) presents the fractions selected for measurement (col. J-L), the mass of quartz decontaminated from the atmospheric contribution, the measurements of ^{9}Be (carrier + potential native 9Be) by SARM (col. M-R), the measurements of 10Be/9Be at ASTER (col. S-Z), the raw ^{10}Be concentrations (col. 11-AD), the ^{10}Be corrections (col. AE-AN) and the corrected concentrations and paleoconcentrations computed with the ages (col. AO-AR) and the apparent Himalayan erosion rates (AS-AU). The nominal concentration of the carrier is indicated in column M. The measured 9Be concentrations are distinct from the predicted concentrations, because of the potential enriched Be content due to the large mass of dissolved quartz. The ^{10}Be/^{9}Be results were corrected from the average blank (Table S3). The ^{10}Be concentration was computed using the maximum value , between the predicted and measured values of of ^{9}Be. Two samples have duplicates (Table SVIII-2) and only the average values are presented in Table SVIII-1. Apparent Himalayan erosion rates were computed with the production rates of the Narayani basin, excluding the area covered by Siwalik formations. Sr-Nd isotopic measurement and lithological fraction computing results are presented col. AW-BH. ^{143}Nd/^{144}Nd are reported as εNd(0), using CHUR(0) = 0.512638 (Goldstein et al., 1984). The lithological fractions do not take into account for ~40% of the TSS contribution originating from carbonates.

Table SVIII-1. (…/…)

Sample information								^{10}Be measurements and computations									
								Mass of decontaminated quartz			^{9}Be carrier measurements						
Site	#	Latitude °N	Longitude °E	Depth (m)	Age (Ma)	Duplicate 1σ	samples	Fraction (µm)	Total mass (g)	1 σ (g)	^{9}Be carrier concentration (ppm)	Carrier mass added (mg)	^{9}Be added before dissolution (atom)	1 σ (atom)	^{9}Be measured after evaporation (atom)	1 σ (atom)	
Dwarda section																	
Serie #1																	
Dwarda	Dwcos9	27.3338	84.3673	1,076	2.119	0.1	-	125-250	65.8	1.0	3025	101.77	2.056E+19	6.00E+17	-	-	
Dwarda	Dwcos13	27.3376	84.3646	1,502	3.032	0.1	-	125-250	46.0	0.7	3025	101.83	2.058E+19	6.00E+17	-	-	
Dwarda	Dwcos17	27.3410	84.3650	1,815	3.799	0.1	-	125-250	52.7	0.8	3025	101.60	2.053E+19	5.99E+17	-	-	
Dwarda	Dwcos20	27.3451	84.3633	2,164	4.701	0.1	-	125-250	62.4	0.9	3025	101.03	2.042E+19	5.95E+17	-	-	
Serie #2																	
Dwarda	Dwcos2	27.3286	84.3671	586	1.289	0.1	-	125-250	76.1	1.1	1000	100.96	6.744E+18	1.97E+17	7.111E+18	8.89E+17	
Dwarda	Dwcos3*	27.3292	84.3664	654	1.407	0.1	2 samples	-	-	-	-	-	-	-	-	-	
Dwarda	Dwcos4*	27.3295	84.3664	676	1.445	0.1	2 samples	-	-	-	-	-	-	-	-	-	
Dwarda	Dwcos5	27.3304	84.3662	741	1.556	0.1	-	125-250	75.0	1.1	1000	100.59	6.719E+18	1.96E+17	6.702E+18	8.38E+17	
Dwarda	Dwcos7	27.3323	84.3661	927	1.855	0.1	-	125-250	104.4	1.6	1000	101.26	6.764E+18	1.97E+17	9.716E+18	1.21E+18	
Dwarda	Dwcos8	27.3328	84.3671	981	1.929	0.1	-	125-250	41.2	0.6	1000	101.37	6.771E+18	1.97E+17	6.684E+18	8.36E+17	
Dwarda	Dwcos10	27.3346	84.3673	1,163	2.303	0.1	-	125-250	151.7	2.3	1000	100.78	6.732E+18	1.96E+17	6.75E+18	8.44E+17	
Dwarda	Dwcos12	27.3367	84.3649	1,403	2.816	0.1	-	125-250	151.1	2.3	1000	101.12	6.755E+18	1.97E+17	4.824E+18	6.03E+17	
Serie #3																	
Dwarda	Dwcos11	27.3355	84.3647	1,299	2.590	0.1	-	250-500	187.5	2.8	2020	102.19	1.379E+19	4.02E+17	2.144E+19	2.68E+18	
Dwarda	Dwcos14	27.3385	84.3661	1,610	3.157	0.1	-	125-250	113.9	1.7	2020	102.48	1.383E+19	4.03E+17	1.277E+19	1.60E+18	
Dwarda	Dwcos15	27.3392	84.3693	1,662	3.192	0.1	-	125-250	212.7	3.2	2020	100.80	1.360E+19	3.97E+17	1.492E+19	1.86E+18	
Dwarda	Dwcos16	27.3405	84.3646	1,763	3.641	0.1	-	-	-	-	-	-	-	-	-	-	
Dwarda	Dwcos18	27.3421	84.3655	1,929	4.147	0.1	-	125-250	309.8	4.6	2020	101.43	1.369E+19	3.99E+17	9.561E+18	1.20E+18	
Dwarda	Dwcos19	27.3438	84.3621	2,012	4.354	0.1	-	-	-	-	-	-	-	-	-	-	
Dwarda	Dwcos21	27.3461	84.3652	2,258	4.836	0.1	-	125-250	193.6	2.9	2020	102.01	1.376E+19	4.01E+17	7.18E+18	8.98E+17	
Dwarda	Dwcos22	27.3508	84.3637	2,616	5.667	0.1	-	250-500	526.7	7.9	2020	102.16	1.379E+19	4.02E+17	3.262E+19	4.08E+18	
Dwarda	Dwcos24	27.3566	84.3668	3,198	6.822	0.1	-	125-250	229.1	3.4	2020	101.63	1.371E+19	4.00E+17	9.24E+18	1.15E+18	
Dwarda	Dwcos25	27.3598	84.3679	3,435	7.386	0.1	-	-	-	-	-	-	-	-	-	-	

Table SVIII-1. (…/…)

Sample information

^{10}Be measurements and computations

Site	#	Latitude °N	Longitude °E	Depth (m)	Age (Ma)	Duplicate 1σ samples		Mass of decontaminated quartz: Fraction (µm)	Total mass (g)	1 σ (g)	^{9}Be carrier measurements: ^{9}Be carrier concentration (ppm)	Carrier mass added (mg)	^{9}Be added before dissolution (atom)	1 σ (atom)	^{9}Be measured after evaporation (atom)	1 σ (atom)
Serie #4																
Dwarda	Dwcos30	27.3546	84.3675	3,013	6.438	0.1	-	140-280	798.6	12.0	2020	103.02	1.390E+19	4.05E+17	2.181E+19	2.73E+18
Dwarda	Dwcos31	27.3567	84.3667	3,216	6.867	0.1	-	140-280	741.9	11.1	2020	102.72	1.386E+19	4.04E+17	2.518E+19	3.15E+18
Dwarda	Dwcos32	27.3597	84.3673	3,435	7.383	0.1	-	140-280	877.6	13.2	2020	102.19	1.379E+19	4.02E+17	1.277E+19	1.60E+18
Dwarda	Dwcos33	27.3480	84.3643	2,374	4.975	0.1	-	140-280	446.1	6.7	2020	102.90	1.388E+19	4.05E+17	3.173E+19	3.97E+18
Dwarda	Dwcos34	27.3552	84.3690	3,087	6.584	0.1	-	125-250	676.7	10.2	2020	102.44	1.382E+19	4.03E+17	3.722E+19	4.65E+18
Dwarda	Dwcos37	27.3384	84.3661	1,600	3.150	0.1	-	140-280	231.5	3.5	2020	102.77	1.387E+19	4.04E+17	2.141E+19	2.68E+18
Dwarda	Dwcos43	27.3584	84.3671	3,333	7.152	0.1	-	-	-	-	-	-	-	-	-	-
Dwarda	Dwcos44	27.3328	84.3671	971	1.916	0.1	-	140-280	158.5	2.4	2020	103.11	1.391E+19	4.06E+17	1.505E+19	1.88E+18
Dwarda	Dwcos45	27.3318	84.3664	870	1.778	0.1	-	140-280	114.6	1.7	2020	103.10	1.391E+19	4.06E+17	1.762E+19	2.20E+18
Dwarda	Dwcos46	27.3308	84.3663	778	1.620	0.1	-	140-280	111.6	1.7	2020	103.23	1.393E+19	4.06E+17	1.649E+19	2.06E+18
Dwarda	Dwcos47	27.3292	84.3666	652	1.403	0.1	-	140-280	76.5	1.1	2020	102.92	1.389E+19	4.05E+17	1.413E+19	1.77E+18
Dwarda	Dwcos48	27.3289	84.3670	606	1.324	0.1	-	140-280	75.5	1.1	2020	103.04	1.390E+19	4.05E+17	1.446E+19	1.81E+18
Dwarda	Dwcos49	27.3281	84.3672	534	1.200	0.1	-	140-280	72.7	1.1	2020	102.18	1.379E+19	4.02E+17	1.575E+19	1.97E+18
Dwarda	Dwcos50	27.3280	84.3672	520	1.175	0.1	-	140-280	47.6	0.7	2020	102.46	1.383E+19	4.03E+17	1.563E+19	1.95E+18
Dwarda	Dwcos51	27.3280	84.3672	520	1.176	0.1	-	140-280	64.5	1.0	2020	102.53	1.383E+19	4.03E+17	1.65E+19	2.06E+18
Dwarda	Dwcos52	27.3272	84.3669	442	1.029	0.1	-	-	-	-	-	-	-	-	-	-
Ganguli section																
Serie #1																
Ganguli	Ggcos1	27.3224	84.3969	208	0.484	0.1	-	125-250	33.7	0.5	3025	101.70	2.055E+19	5.99E+17	-	-
Ganguli	Ggcos3	27.3241	84.3969	373	0.869	0.1	-	125-250	57.0	0.9	3025	101.94	2.060E+19	6.01E+17	-	-
Serie #2																
Ganguli	Ggcos2	27.3233	84.3971	286	0.666	0.1	-	125-250	83.1	1.2	2020	102.44	1.382E+19	4.03E+17	1.121E+19	1.40E+18
Ganguli	Ggcos4	27.3249	84.3987	439	1.023	0.1	-	125-250	127.3	1.9	2020	102.67	1.385E+19	4.04E+17	2.075E+19	2.59E+18
Gonauli section																
Gonauli	Go60	27.3625	83.9980	635	1.373	0.1	-	140-280	64.8	1.0	2020	102.30	1.380E+19	4.02E+17	1.305E+19	1.63E+18
Maloni Naha section																
Maloni Naha	Ca17i01	27.3796	83.9706	658	1.413	0.1	-	140-280	72.7	1.1	2020	102.35	1.381E+19	4.03E+17	1.287E+19	1.61E+18
Maloni Naha	Ca17i03	27.3771	83.9710	461	1.064	0.1	-	140-280	157.8	2.4	2020	102.50	1.383E+19	4.03E+17	1.475E+19	1.84E+18
Maloni Naha	Ca17i04	27.3771	83.9710	474	1.092	0.1	-	-	-	-	-	-	-	-	-	-
Maloni Naha	Ca17i08	27.3709	83.9759	200	0.465	0.1	-	140-280	125.1	1.9	2020	102.86	1.388E+19	4.05E+17	1.433E+19	1.79E+18

Table SVIII-1. (…/…)

^{10}Be measurements and computations

		^{10}Be/^{9}Be measurements								raw ^{10}Be			
Site	#	Hit nb	^{10}Be/^{9}Be	1 σ	Blank of the series of sample	1 σ	Correction by blank	^{10}Be/^{9}Be (blank corrected)	1 σ	^{10}Be (atom)	1 σ (atom)	^{10}Be (atom/g)	1 σ (atom/g)
Dwarda section													
Serie #1													
Dwarda	Dwcos9	18	2.671E-14	6.305E-15	1.84E-15	4.51E-16	0.07	2.487E-14	6.321E-15	5.11E+05	1.31E+05	7.78E+03	1.99E+03
Dwarda	Dwcos13	26	1.045E-14	2.076E-15	1.84E-15	4.51E-16	0.18	8.610E-15	2.124E-15	1.77E+05	4.40E+04	3.85E+03	9.59E+02
Dwarda	Dwcos17	36	9.854E-15	1.647E-15	1.84E-15	4.51E-16	0.19	8.009E-15	1.707E-15	1.64E+05	3.54E+04	3.12E+03	6.73E+02
Dwarda	Dwcos20	18	9.644E-15	2.377E-15	1.84E-15	4.51E-16	0.19	7.799E-15	2.419E-15	1.59E+05	4.96E+04	2.55E+03	7.96E+02
Serie #2													
Dwarda	Dwcos2	86	8.522E-14	9.459E-15	9.57E-15	3.18E-15	0.11	7.565E-14	9.981E-15	5.38E+05	9.78E+04	7.07E+03	1.29E+03
Dwarda	Dwcos3*	-	-	-	-	-	-	-	-	-	-	7.52E+03	2.24E+03
Dwarda	Dwcos4*	-	-	-	-	-	-	-	-	-	-	4.59E+03	1.28E+03
Dwarda	Dwcos5	104	6.928E-14	6.846E-15	9.57E-15	3.18E-15	0.14	5.971E-14	7.551E-15	4.01E+05	5.21E+04	5.35E+03	6.99E+02
Dwarda	Dwcos7	33	5.113E-14	8.922E-15	9.57E-15	3.18E-15	0.19	4.156E-14	9.473E-15	4.04E+05	1.05E+05	3.87E+03	1.01E+03
Dwarda	Dwcos8	23	1.85E-14	4.155E-15	9.57E-15	3.18E-15	0.52	8.931E-15	5.235E-15	6.05E+04	3.55E+04	1.47E+03	8.62E+02
Dwarda	Dwcos10	64	9.448E-14	1.187E-14	9.57E-15	3.18E-15	0.10	8.492E-14	1.229E-14	5.73E+05	1.10E+05	3.78E+03	7.25E+02
Dwarda	Dwcos12	31	8.83E-14	1.59E-14	9.57E-15	3.18E-15	0.11	7.874E-14	1.621E-14	5.32E+05	1.11E+05	3.52E+03	7.34E+02
Serie #3													
Dwarda	Dwcos11	4	1.754E-14	8.771E-15	3.24E-15	1.69E-15	0.18	1.430E-14	8.932E-15	3.07E+05	1.95E+05	1.64E+03	1.04E+03
Dwarda	Dwcos14	26	5.993E-14	1.389E-14	3.24E-15	1.69E-15	0.05	5.669E-14	1.399E-14	7.84E+05	1.95E+05	6.88E+03	1.71E+03
Dwarda	Dwcos15	140	1.961E-14	1.677E-15	3.24E-15	1.69E-15	0.17	1.637E-14	2.377E-15	2.44E+05	4.68E+04	1.15E+03	2.21E+02
Dwarda	Dwcos16	-	-	-	-	-	-	-	-	-	-	-	-
Dwarda	Dwcos18	341	4.391E-14	2.447E-15	3.24E-15	1.69E-15	0.07	4.067E-14	2.971E-15	5.57E+05	4.38E+04	1.80E+03	1.44E+02
Dwarda	Dwcos19	-	-	-	-	-	-	-	-	-	-	-	-
Dwarda	Dwcos21	127	2.281E-14	2.356E-15	3.24E-15	1.69E-15	0.14	1.957E-14	2.897E-15	2.69E+05	4.06E+04	1.39E+03	2.11E+02
Dwarda	Dwcos22	7	2.766E-14	1.046E-14	3.24E-15	1.69E-15	0.12	2.442E-14	1.060E-14	7.97E+05	3.60E+05	1.51E+03	6.83E+02
Dwarda	Dwcos24	88	2.403E-14	2.58E-15	3.24E-15	1.69E-15	0.13	2.079E-14	3.082E-15	2.85E+05	4.31E+04	1.24E+03	1.89E+02
Dwarda	Dwcos25	-	-	-	-	-	-	-	-	-	-	-	-
Serie #4													
Dwarda	Dwcos30	10	3.483E-14	1.102E-14	3.24E-15	1.69E-15	0.09	3.159E-14	1.115E-14	6.89E+05	2.58E+05	8.63E+02	3.23E+02
Dwarda	Dwcos31	11	3.943E-14	1.19E-14	3.24E-15	1.69E-15	0.08	3.619E-14	1.202E-14	9.11E+05	3.23E+05	1.23E+03	4.36E+02
Dwarda	Dwcos32	14	8.193E-14	2.258E-14	3.24E-15	1.69E-15	0.04	7.869E-14	2.264E-14	1.08E+06	3.14E+05	1.24E+03	3.58E+02
Dwarda	Dwcos33	5	1.245E-14	5.569E-15	3.24E-15	1.69E-15	0.26	9.209E-15	5.819E-15	2.92E+05	1.88E+05	6.55E+02	4.22E+02
Dwarda	Dwcos34	6	1.768E-14	7.221E-15	3.24E-15	1.69E-15	0.18	1.444E-14	7.415E-15	5.37E+05	2.84E+05	7.94E+02	4.20E+02
Dwarda	Dwcos37	8	2.258E-14	7.987E-15	3.24E-15	1.69E-15	0.14	1.934E-14	8.163E-15	4.14E+05	1.82E+05	1.79E+03	7.88E+02
Dwarda	Dwcos43	-	-	-	-	-	-	-	-	-	-	-	-
Dwarda	Dwcos44	3	1.142E-14	6.595E-15	3.24E-15	1.69E-15	0.28	8.181E-15	6.807E-15	1.23E+05	1.04E+05	7.77E+02	6.54E+02
Dwarda	Dwcos45	29	2.967E-14	6.205E-15	3.24E-15	1.69E-15	0.11	2.643E-14	6.429E-15	4.66E+05	1.27E+05	4.06E+03	1.11E+03
Dwarda	Dwcos46	13	3.776E-14	1.048E-14	3.24E-15	1.69E-15	0.09	3.452E-14	1.062E-14	5.69E+05	1.89E+05	5.10E+03	1.70E+03
Dwarda	Dwcos47	32	5.027E-14	9.317E-15	3.24E-15	1.69E-15	0.06	4.703E-14	9.468E-15	6.64E+05	1.57E+05	8.68E+03	2.06E+03
Dwarda	Dwcos48	27	5.42E-14	1.182E-14	3.24E-15	1.69E-15	0.06	5.096E-14	1.194E-14	7.37E+05	1.96E+05	9.76E+03	2.60E+03

Table SVIII-1. (…/…)

^{10}Be measurements and computations

			^{10}Be/^{9}Be measurements							raw ^{10}Be			
Site	#	Hit nb	^{10}Be/^{9}Be	1 σ	Blank of the series of sample	1 σ	Correction by blank	^{10}Be/^{9}Be (blank corrected)	1 σ	^{10}Be (atom)	1 σ (atom)	^{10}Be (atom/g)	1 σ (atom/g)
Dwarda	Dwcos49	27	3.608E-14	6.958E-15	3.24E-15	1.69E-15	0.09	3.284E-14	7.160E-15	5.17E+05	1.30E+05	7.11E+03	1.79E+03
Dwarda	Dwcos50	24	2.048E-14	4.418E-15	3.24E-15	1.69E-15	0.16	1.724E-14	4.729E-15	2.69E+05	8.12E+04	5.66E+03	1.71E+03
Dwarda	Dwcos51	14	2.881E-14	8.395E-15	3.24E-15	1.69E-15	0.11	2.557E-14	8.563E-15	4.22E+05	1.51E+05	6.54E+03	2.34E+03
Dwarda	Dwcos52	-	-	-	-	-	-	-	-	-	-	-	-
Ganguli section													
Serie #1													
Ganguli	Ggcos1	53	1.152E-14	1.615E-15	1.84E-15	4.51E-16	0.16	9.678E-15	1.677E-15	1.99E+05	3.49E+04	5.90E+03	1.04E+03
Ganguli	Ggcos3	44	2.067E-14	3.14E-15	1.84E-15	4.51E-16	0.09	1.882E-14	3.172E-15	3.88E+05	6.63E+04	6.80E+03	1.17E+03
Serie #2													
Ganguli	Ggcos2	36	2.392E-14	4.115E-15	3.24E-15	1.69E-15	0.14	2.068E-14	4.447E-15	2.86E+05	6.20E+04	3.44E+03	7.48E+02
Ganguli	Ggcos4	14	3.457E-14	9.537E-15	3.24E-15	1.69E-15	0.09	3.133E-14	9.684E-15	6.50E+05	2.17E+05	5.11E+03	1.70E+03
Gonauli section													
Gonauli	Go60	9	4.43E-14	1.478E-14	3.24E-15	1.69E-15	0.07	4.106E-14	1.487E-14	5.67E+05	2.06E+05	8.74E+03	3.18E+03
Maloni Naha section													
Maloni Naha	Ca17i01	7	2.14E-14	8.094E-15	3.24E-15	1.69E-15	0.15	1.816E-14	8.268E-15	2.51E+05	1.14E+05	3.45E+03	1.57E+03
Maloni Naha	Ca17i03	40	1.46E-13	2.316E-14	3.24E-15	1.69E-15	0.02	1.428E-13	2.322E-14	2.11E+06	4.32E+05	1.33E+04	2.74E+03
Maloni Naha	Ca17i04	-	-	-	-	-	-	-	-	-	-	-	-
Maloni Naha	Ca17i08	18	7.999E-14	2.001E-14	3.24E-15	1.69E-15	0.04	7.675E-14	2.008E-14	1.10E+06	3.19E+05	8.79E+03	2.55E+03

Table SVIII-1. (…/…)

^{10}Be measurements and computations

Site	#	^{10}Be corrections										Corrected ^{10}Be and erosion rates						
		Porosity	Density	Recent exposure (atom/g)	-1 σ (atom/g)	+1 σ (atom/g)	Correction due to recent exposure	1 σ	Correction due to plain exposure (atom/g)	1 σ % (atom/g)		Corrected 10Be computed (atom/g)	1 σ (atom/g)	Corrected ^{10}Be paleoconcentrations (at/g)	Erosion rates 1 σ (atom/g)	(mm/y)	-1 σ (mm/y)	+1 σ
Dwarda section																		
Serie #1																		
Dwarda	Dwcos9	3.66E-01	2.08E+00	4.81E+02	2.38E+02	9.25E+02	5.81E+02	3.43E+02	4.75E+02	6.79E+01	0.07	6.72E+03	2.02E+03	2.01E+04	6.08E+03	0.9	0.3	0.4
Dwarda	Dwcos13	3.27E-01	2.14E+00	4.66E+02	2.30E+02	8.95E+02	5.63E+02	3.33E+02	3.20E+02	6.40E+01	0.15	2.97E+03	1.02E+03	1.44E+04	5.01E+03	1.2	0.4	0.7
Dwarda	Dwcos17	3.00E-01	2.19E+00	4.56E+02	2.26E+02	8.77E+02	5.51E+02	3.26E+02	2.16E+02	4.33E+01	0.18	2.35E+03	7.49E+02	1.70E+04	5.65E+03	1.1	0.3	0.5
Dwarda	Dwcos20	2.73E-01	2.24E+00	4.47E+02	2.21E+02	8.59E+02	5.40E+02	3.19E+02	1.46E+02	2.73E+01	0.21	1.87E+03	8.58E+02	2.16E+04	9.81E+03	0.8	0.3	0.7
Serie #2																		
Dwarda	Dwcos2	4.18E-01	1.99E+00	5.02E+02	2.48E+02	9.66E+02	6.07E+02	3.59E+02	6.74E+02	1.04E+02	0.09	5.79E+03	1.34E+03	1.13E+04	2.73E+03	1.6	0.4	0.6
Dwarda	Dwcos3*	4.11E-01	2.00E+00	4.99E+02	2.47E+02	9.59E+02	6.03E+02	3.56E+02	6.35E+02	9.77E+01	0.08	6.29E+03	2.27E+03	1.30E+04	4.77E+03	1.4	0.4	0.9
Dwarda	Dwcos4*	4.08E-01	2.01E+00	4.98E+02	2.46E+02	9.57E+02	6.02E+02	3.56E+02	6.23E+02	9.58E+01	0.13	3.36E+03	1.33E+03	7.22E+03	2.88E+03	2.5	0.8	1.6
Dwarda	Dwcos5	4.01E-01	2.02E+00	4.95E+02	2.45E+02	9.52E+02	5.98E+02	3.53E+02	5.88E+02	9.05E+01	0.11	4.17E+03	7.89E+02	9.39E+03	1.97E+03	1.9	0.5	0.6
Dwarda	Dwcos7	3.81E-01	2.05E+00	4.87E+02	2.41E+02	9.36E+02	5.88E+02	3.48E+02	5.05E+02	7.77E+01	0.15	2.77E+03	1.07E+03	7.41E+03	2.90E+03	2.4	0.8	1.6
Dwarda	Dwcos8	3.76E-01	2.06E+00	4.85E+02	2.40E+02	9.32E+02	5.86E+02	3.46E+02	4.86E+02	7.48E+01	0.40	3.96E+02	9.32E+02	1.32E+03	2.62E+03	4.9	0.0	11.3
Dwarda	Dwcos10	3.58E-01	2.09E+00	4.77E+02	2.36E+02	9.18E+02	5.77E+02	3.41E+02	4.33E+02	6.18E+01	0.15	2.77E+03	8.03E+02	9.22E+03	2.77E+03	1.9	0.5	0.9
Dwarda	Dwcos12	3.35E-01	2.13E+00	4.69E+02	2.32E+02	9.02E+02	5.67E+02	3.35E+02	3.33E+02	7.14E+01	0.16	2.62E+03	8.10E+02	1.14E+04	3.70E+03	1.6	0.4	0.8
Serie #3																		
Dwarda	Dwcos11	3.45E-01	2.11E+00	4.72E+02	2.34E+02	9.09E+02	5.71E+02	3.37E+02	3.74E+02	8.01E+01	0.35	6.90E+02	1.10E+03	2.99E+03	4.29E+03	3.1	0.0	6.0
Dwarda	Dwcos14	3.17E-01	2.16E+00	4.62E+02	2.29E+02	8.89E+02	5.59E+02	3.30E+02	3.00E+02	6.00E+01	0.08	6.02E+03	1.75E+03	3.04E+04	8.72E+03	0.6	0.2	0.3
Dwarda	Dwcos15	3.13E-01	2.17E+00	4.61E+02	2.28E+02	8.86E+02	5.57E+02	3.29E+02	2.95E+02	5.90E+01	0.48	2.97E+02	4.00E+02	2.04E+03	2.54E+03	5.1	0.0	9.5
Dwarda	Dwcos16	-	-	-	-	-	-	-	-	-	-	-	-	-	-	-	-	-
Dwarda	Dwcos18	2.91E-01	2.21E+00	4.53E+02	2.24E+02	8.71E+02	5.47E+02	3.23E+02	1.81E+02	3.62E+01	0.30	1.07E+03	3.56E+02	9.69E+03	3.80E+03	1.8	0.6	1.2
Dwarda	Dwcos19	-	-	-	-	-	-	-	-	-	-	-	-	-	-	-	-	-
Dwarda	Dwcos21	2.66E-01	2.25E+00	4.44E+02	2.20E+02	8.55E+02	5.37E+02	3.17E+02	1.36E+02	2.55E+01	0.39	7.18E+02	3.82E+02	9.66E+03	5.69E+03	1.7	0.7	2.0
Dwarda	Dwcos22	2.42E-01	2.29E+00	4.36E+02	2.16E+02	8.39E+02	5.27E+02	3.12E+02	9.47E+01	1.67E+01	0.35	8.90E+02	7.51E+02	1.75E+04	1.44E+04	0.8	0.4	1.2
Dwarda	Dwcos24	2.06E-01	2.35E+00	4.25E+02	2.10E+02	8.18E+02	5.14E+02	3.04E+02	5.56E+01	1.24E+01	0.41	6.75E+02	3.58E+02	2.53E+04	1.46E+04	0.7	0.3	0.7
Dwarda	Dwcos25	-	-	-	-	-	-	-	-	-	-	-	-	-	-	-	-	-
Serie #4																		
Dwarda	Dwcos30	2.17E-01	2.33E+00	4.28E+02	2.12E+02	8.24E+02	5.18E+02	3.06E+02	6.39E+01	1.50E+01	0.60	2.81E+02	4.45E+02	9.94E+03	1.37E+04	0.9	0.0	1.9
Dwarda	Dwcos31	2.05E-01	2.35E+00	4.25E+02	2.10E+02	8.17E+02	5.14E+02	3.03E+02	5.44E+01	1.21E+01	0.42	6.60E+02	5.31E+02	2.51E+04	1.95E+04	0.6	0.3	0.9
Dwarda	Dwcos32	1.94E-01	2.37E+00	4.21E+02	2.08E+02	8.10E+02	5.09E+02	3.01E+02	4.18E+01	9.29E+00	0.41	6.85E+02	4.68E+02	3.41E+04	2.32E+04	0.5	0.2	0.6
Dwarda	Dwcos33	2.58E-01	2.26E+00	4.42E+02	2.18E+02	8.49E+02	5.34E+02	3.15E+02	1.27E+02	2.38E+01	0.81	-5.53E+00	5.27E+02	1.16E+03	7.51E+03	1.4	0.0	4.4
Dwarda	Dwcos34	2.13E-01	2.34E+00	4.27E+02	2.11E+02	8.21E+02	5.16E+02	3.05E+02	6.28E+01	1.40E+01	0.65	2.15E+02	5.19E+02	9.09E+03	1.65E+04	0.8	0.0	1.8
Dwarda	Dwcos37	3.18E-01	2.16E+00	4.62E+02	2.29E+02	8.89E+02	5.59E+02	3.30E+02	3.01E+02	6.02E+01	0.31	9.28E+02	8.56E+02	5.12E+03	4.48E+03	2.6	1.4	4.2
Dwarda	Dwcos43	-	-	-	-	-	-	-	-	-	-	-	-	-	-	-	-	-
Dwarda	Dwcos44	3.77E-01	2.06E+00	4.85E+02	2.40E+02	9.33E+02	5.86E+02	3.46E+02	4.90E+02	7.53E+01	0.75	-2.99E+02	7.44E+02	4.03E+02	2.14E+03	5.2	0.0	16.1
Dwarda	Dwcos45	3.87E-01	2.04E+00	4.89E+02	2.42E+02	9.41E+02	5.91E+02	3.49E+02	5.25E+02	8.08E+01	0.15	2.95E+03	1.17E+03	7.56E+03	3.00E+03	2.4	0.8	1.6
Dwarda	Dwcos46	3.97E-01	2.03E+00	4.93E+02	2.44E+02	9.48E+02	5.96E+02	3.52E+02	5.69E+02	8.76E+01	0.12	3.94E+03	1.73E+03	9.21E+03	4.04E+03	1.9	0.6	1.5
Dwarda	Dwcos47	4.11E-01	2.00E+00	4.99E+02	2.47E+02	9.59E+02	6.03E+02	3.56E+02	6.36E+02	9.78E+01	0.07	7.45E+03	2.09E+03	1.54E+04	4.43E+03	1.2	0.3	0.5
Dwarda	Dwcos48	4.16E-01	1.99E+00	5.01E+02	2.48E+02	9.64E+02	6.06E+02	3.58E+02	6.62E+02	1.02E+02	0.06	8.50E+03	2.62E+03	1.69E+04	5.30E+03	1.1	0.3	0.5

Table SVIII-1. (…/…)

^{10}Be measurements and computations

Site	#	^{10}Be corrections										Corrected ^{10}Be and erosion rates						
		Porosity	Density	Recent exposure (atom/g)	-1 σ (atom/g)	+1 σ (atom/g)	Correction due to recent exposure	1 σ	Correction due to plain exposure (atom/g)	1 σ % (atom/g)		Corrected 10Be computed (atom/g)	1 σ (atom/g)	Corrected ^{10}Be paleoconcentrations (at/g)	Erosion rates 1 σ (atom/g)	-1 σ (mm/y)	+1 σ (mm/y)	
Dwarda	Dwcos49	4.24E-01	1.98E+00	5.05E+02	2.50E+02	9.70E+02	6.10E+02	3.60E+02	7.05E+02	1.08E+02	0.09	5.80E+03	1.83E+03	1.09E+04	3.44E+03	1.6	0.5	0.8
Dwarda	Dwcos50	4.26E-01	1.98E+00	5.05E+02	2.50E+02	9.72E+02	6.11E+02	3.61E+02	7.14E+02	1.10E+02	0.11	4.33E+03	1.75E+03	8.06E+03	3.29E+03	2.2	0.7	1.6
Dwarda	Dwcos51	4.26E-01	1.98E+00	5.05E+02	2.50E+02	9.72E+02	6.11E+02	3.61E+02	7.14E+02	1.10E+02	0.09	5.22E+03	2.37E+03	9.74E+03	4.36E+03	1.8	0.6	1.5
Dwarda	Dwcos52	-	-	-	-	-	-	-	-	-	-	-	-					
Ganguli section																		
Serie #1																		
Ganguli	Ggcos1	4.63E-01	1.91E+00	5.22E+02	2.58E+02	1.00E+03	6.31E+02	3.73E+02	9.38E+02	1.56E+02	0.11	4.33E+03	1.12E+03	5.65E+03	1.51E+03	3.1	0.8	1.3
Ganguli	Ggcos3	4.43E-01	1.95E+00	5.13E+02	2.54E+02	9.86E+02	6.20E+02	3.66E+02	8.35E+02	1.28E+02	0.09	5.35E+03	1.23E+03	8.50E+03	2.06E+03	2.1	0.5	0.8
Serie #2																		
Ganguli	Ggcos2	4.54E-01	1.93E+00	5.18E+02	2.56E+02	9.96E+02	6.26E+02	3.70E+02	9.26E+02	1.42E+02	0.18	1.89E+03	8.46E+02	2.77E+03	1.26E+03	6.2	2.2	5.0
Ganguli	Ggcos4	4.35E-01	1.96E+00	5.09E+02	2.52E+02	9.80E+02	6.16E+02	3.64E+02	7.72E+02	1.19E+02	0.12	3.72E+03	1.75E+03	6.37E+03	3.05E+03	2.7	1.0	2.3
Gonauli section																		
Gonauli	Go60	4.13E-01	2.00E+00	5.00E+02	2.47E+02	9.61E+02	6.04E+02	3.57E+02	6.46E+02	9.94E+01	0.07	7.49E+03	3.20E+03	1.57E+04	6.44E+03	1.1	0.4	0.8
Maloni Naha section																		
Maloni Naha	Ca17i01	4.10E-01	2.00E+00	4.99E+02	2.47E+02	9.59E+02	6.03E+02	3.56E+02	6.33E+02	9.74E+01	0.17	2.22E+03	1.62E+03	5.48E+03	3.25E+03	3.0	1.2	3.3
Maloni Naha	Ca17i03	4.33E-01	1.96E+00	5.08E+02	2.51E+02	9.78E+02	6.15E+02	3.63E+02	7.56E+02	1.16E+02	0.05	1.20E+04	2.77E+03	2.14E+04	4.84E+03	0.8	0.2	0.3
Maloni Naha	Ca17i04	-	-	-	-	-	-	-	-	-	-	-	-	-	-	-	-	-
Maloni Naha	Ca17i08	4.64E-01	1.91E+00	5.23E+02	2.58E+02	1.01E+03	6.32E+02	3.73E+02	9.47E+02	1.58E+02	0.07	7.21E+03	2.58E+03	9.75E+03	3.30E+03	1.8	0.5	1.0

Table SVIII-1. (…/…)

Sr-Nd isotopic measurements and computations

		Sr-Nd isotopic measurements						Computed lithological fractions					
Site	#	$^{87}Sr/^{86}Sr$	2 σ	$^{144}Nd/^{143}Nd$	2 σ	εNd	2 σ	TSS	1 σ	HHC	1 σ	LH	1 σ
Dwarda section													
Serie #1													
Dwarda	Dwcos9	-	-	-	-	-	-	-	-	-	-	-	-
Dwarda	Dwcos13	-	-	-	-	-	-	-	-	-	-	-	-
Dwarda	Dwcos17	-	-	-	-	-	-	-	-	-	-	-	-
Dwarda	Dwcos20	-	-	-	-	-	-	-	-	-	-	-	-
Serie #2													
Dwarda	Dwcos2	0.757464	0.000011	0.51174150	0.00001188	-17.5	0.2	25	5.4	52	6	23	1.9
Dwarda	Dwcos3*	0.751043	0.000015	0.51173085	0.00001158	-17.7	0.2	44	6.4	34	6.8	23	2.1
Dwarda	Dwcos4*	0.761057	0.000018	0.51174627	0.00001456	-17.4	0.3	15	5.2	61	6.4	24	2.2
Dwarda	Dwcos5	0.752650	0.000014	0.51178040	0.00001487	-16.7	0.3	24	4.2	62	5.1	14	1.8
Dwarda	Dwcos7	-	-	-	-	-	-	-	-	-	-	-	-
Dwarda	Dwcos8	0.745646	0.000022	0.51173317	0.00001166	-17.7	0.2	57	6.4	22	6.7	21	2.1
Dwarda	Dwcos10	0.760049	0.000018	0.51170371	0.00001004	-18.2	0.2	30	7.2	39	7.9	31	2.3
Dwarda	Dwcos12	0.763724	0.000019	0.51170403	0.00000998	-18.2	0.2	22	6.7	46	7.7	32	2.3
Serie #3													
Dwarda	Dwcos11	0.772719	0.000021	0.51165556	0.00001708	-19.2	0.3	20	8.7	36	10.3	45	2.9
Dwarda	Dwcos14	0.778028	0.000016	0.51168813	0.00001293	-18.5	0.3	4	3.7	55	5	41	2.4
Dwarda	Dwcos15	0.768007	0.000013	0.51166939	0.00001110	-18.9	0.2	24	8.4	35	9.6	40	2.6
Dwarda	Dwcos16	0.759612	0.000014	0.51171628	0.00002468	-18.0	0.5	28	7.7	43	9.6	29	3.2
Dwarda	Dwcos18	0.753141	0.000007	0.51176498	0.00001681	-17.0	0.3	28	4.8	56	5.6	17	2
Dwarda	Dwcos19	0.762052	0.000012	0.51165706	0.00001886	-19.1	0.4	40	8.2	20	9.6	41	3.3
Dwarda	Dwcos21	0.776149	0.000012	0.51171704	0.00002276	-18.0	0.4	3	2.7	60	4.1	37	2.4
Dwarda	Dwcos22	0.769289	0.000021	0.51169808	0.00001983	-18.3	0.4	11	6.6	54	8.2	35	2.7
Dwarda	Dwcos24	0.780705	0.000010	0.51168735	0.00002054	-18.5	0.4	3	3	54	4.4	43	2.5
Dwarda	Dwcos25	0.808748	0.000016	0.51169632	0.00002625	-18.4	0.5	-	-	-	-	-	-
Serie #4													
Dwarda	Dwcos30	0.749287	0.000013	0.51180184	0.00001428	-16.3	0.3	27	3.7	65	4.5	8	1.7
Dwarda	Dwcos31	0.772869	0.000012	0.51174613	0.00001071	-17.4	0.2	2	1.5	67	2.8	31	2.2
Dwarda	Dwcos32	0.779834	0.000016	0.51173708	0.00001134	-17.6	0.2	-	-	-	-	-	-
Dwarda	Dwcos33	0.768812	0.000013	0.51171557	0.00001660	-18.0	0.3	8	5.2	60	6.5	32	2.3
Dwarda	Dwcos34	0.768883	0.000017	0.51176618	0.00001465	-17.0	0.3	2	1.7	72	2.8	26	1.9
Dwarda	Dwcos37	0.768261	0.000015	0.51168208	0.00001214	-18.6	0.2	18	7.4	44	8.5	38	2.4
Dwarda	Dwcos43	0.769204	0.000017	0.51175890	0.00001034	-17.1	0.2	2	1.6	72	2.7	27	1.9
Dwarda	Dwcos44	0.752523	0.000011	0.51173628	0.00001113	-17.6	0.2	38	6	39	6.4	22	1.9
Dwarda	Dwcos45	0.756180	0.000016	0.51171448	0.00001301	-18.0	0.3	36	7.2	36	8.1	28	2.5
Dwarda	Dwcos46	0.749597	0.000014	0.51181569	0.00001016	-16.0	0.2	22	2.8	72	3.3	6	1.2
Dwarda	Dwcos47	-	-	-	-	-	-	-	-	-	-	-	-
Dwarda	Dwcos48	0.758575	0.000030	0.51176481	0.00000926	-17.0	0.2	15	4.1	66	5	19	1.7

Table SVIII-1. (…/…)

Sr-Nd isotopic measurements and computations

		Sr-Nd isotopic measurements						Computed lithological fractions					
Site	**#**	**$^{87}Sr/^{86}Sr$**	**2 σ**	**$^{144}Nd/^{143}Nd$**	**2 σ**	**εNd**	**2 σ**	**TSS**	**1 σ**	**HHC**	**1 σ**	**LH**	**1 σ**
Dwarda	Dwcos49	0.763075	0.000011	0.51175255	0.00001890	-17.3	0.4	9	5	67	6.6	24	2.4
Dwarda	Dwcos50	0.774374	0.000011	0.51172217	0.00001244	-17.9	0.2	3	2.4	62	3.5	35	2.1
Dwarda	Dwcos51	0.767970	0.000019	0.51175530	0.00001882	-17.2	0.4	3	2.9	70	4.2	27	2.2
Dwarda	Dwcos52	0.770261	0.000061	0.51172411	0.00001273	-17.8	0.2	5	3.5	64	4.6	32	2.1
Ganguli section													
Serie #1													
Ganguli	Ggcos1	-	-	-	-	-	-	-	-	-	-	-	-
Ganguli	Ggcos3	-	-	-	-	-	-	-	-	-	-	-	-
Serie #2													
Ganguli	Ggcos2	0.776646	0.000022	0.51170592	0.00001504	-18.2	0.3	3	3	58	4.3	38	2.3
Ganguli	Ggcos4	0.769720	0.000024	0.51171596	0.00001418	-18.0	0.3	7	4.8	60	6	33	2.3
Gonauli section													
Gonauli	Go60	0.759289	0.000013	0.51175115	0.00001085	-17.3	0.2	17	4.7	60	5.5	22	1.8

Table SVIII-2. ^{10}Be results for duplicate samples.

Two couple of duplicates of various granulometric fractions (col. C) were measured for ^{10}Be. The results are presented in a similar way than for Table SVIII-1. The average ^{10}Be concentration is reported in Table SVIII-1.

	Mass of decontaminated quartz			^{9}Be carrier measurements						^{10}Be/^{9}Be measurements							raw ^{10}Be			
Samples	Fraction (µm)	Total mass (g)	1 σ (g)	9Be carrier concentration (ppm)	Carrier mass added (mg)	9Be added before dissolution (atom)	1 σ (atom)	9Be measured after evaporation (atom)	1 σ (atom)	Hit nb	10Be/9Be	1 σ	Blank of the series of sample	1 σ	10Be/9Be (blank corrected)	1 σ	10Be (atom)	1 σ (atom)	10Be computed (atom/g)	1 σ (atom/g)
Dwarda section																				
Serie #2																				
Dwcos3	125-250	75.8	1.1	1000	101.01	6.747E+18	1.97E+17	1.015E+19	1.27E+18	114	5.391E-14	5.092E-15	9.57E-15	3.18E-15	4.434E-14	6.006E-15	4.50E+05	8.30E+04	5.94E+03	1.10E+03
Dwcos4	125-250	75.5	1.1	1000	101.06	6.751E+18	1.97E+17	5.708E+18	7.13E+17	195	7.029E-14	5.118E-15	9.57E-15	3.18E-15	6.072E-14	6.028E-15	4.10E+05	4.24E+04	5.43E+03	5.68E+02
Serie #4																				
Dwcos3	125-250	212.2	3.2	2020	101.9	1.375E+19	4.01E+17	1.66E+19	2.07E+18	28	1.20E-13	2.31E-14	3.24E-15	1.69E-15	1.166E-13	2.317E-14	1.93E+06	4.54E+05	9.11E+03	2.14E+03
Dwcos4	250-500	131.4	2.0	2020	101.8	1.373E+19	4.00E+17	1.37E+19	1.72E+18	12	3.90E-14	1.20E-14	3.24E-15	1.69E-15	3.578E-14	1.215E-14	4.91E+05	1.67E+05	3.74E+03	1.28E+03

Table SVIII-3. ^{10}Be blanks.
Ten analytical blanks were prepared synchronously with the samples of Tables SVIII-1-SVIII-2.

	#	9Be carrier 2020±83 ppm	Carrier mass added (g)	9Be added before dissolution (at)	1 σ (at)	9Be measured after evaporation (at)	1 σ (at)	10Be/9Be measured	Hit nb	10Be/9Be	1 σ
Serie #1											
	BLS	3025	101.52	2.051E+19	5.98E+17	-	-		19	**1.84E-15**	**4.51E-16**
Serie #2											
	SCHA1	1000	101.64	6.790E+18	1.98E+17	-	-		13	8.55E-15	3.37E-15
	SCHA2	1000	100.62	6.721E+18	1.96E+17	-	-		20	8.72E-15	1.97E-15
	SCHA3	1000	100.75	6.730E+18	1.96E+17	-	-		12	1.14E-14	4.22E-15
										9.57E-15	**3.18E-15**
Serie #3 and #4											
	PHE24	2020	102.22	1.379E+19	4.02E+17	1.277E+19	1.60E+18		20	3.44E-15	7.70E-16
	PHE31	2020	-	-	-	1.317E+19	1.65E+18		33	6.29E-15	1.44E-15
	PHE43	2020	102.22	1.379E+19	4.02E+17	1.250E+19	1.56E+18		9	1.73E-15	6.31E-16
	PHE44	2020	101.46	1.369E+19	3.99E+17	1.121E+19	1.40E+18		6	1.68E-15	7.44E-16
	PHE45	2020	100.84	1.361E+19	3.97E+17	1.232E+19	1.54E+18		6	2.88E-15	1.25E-15
	PHE46	2020	101.98	1.376E+19	4.01E+17	1.321E+19	1.65E+18		15	3.42E-15	9.06E-16
										3.24E-15	**1.69E-15**
Other blanks, indicative, not prepared simultaneously than the samples											
	PHE30	2020	101.85	1.374E+19	4.01E+17	1.268E+19	1.58E+18		7	4.62E-15	1.78E-15
	PHE40	2020	101.90	1.375E+19	4.01E+17	1.117E+19	1.40E+18		16	4.56E-15	1.14E-15
	PHE41	2020	102.23	1.379E+19	4.02E+17	1.223E+19	1.53E+18		10	6.39E-15	2.69E-15
	PHE42	2020	102.24	1.380E+19	4.02E+17	1.134E+19	1.42E+18		18	4.45E-15	1.11E-15
										5.00E-15	**1.68E-15**

Table SVIII-4. Parameters used for the flood plain transfer model.

These parameters were either obtained by our observations on the modern channel using satellite imagery (Google Earth©) (sinuosity including average obliquity of the river relative to a radial direction) or from published studies, 1: Lupker et al., (2012); 2: Morin et al. (2018); 3: Jain and Sinha (1987); 4: Dubille and Lavé (2015); 5: Pati etal. (2019).

Parameters	Narayani River min/max	References
Sediment density	1.9/1.9	
Floodplain width (km)	70/90	5
Bankfull channel depth (m)	06-oct	4
Fraction of sediment load in floodplain in 125-250 mm fraction	0.3/0.4	3
Fraction of sediment load in channel in 125-250 mm fraction	0.15/0.25	2
Total flux of sediment at the range outlet (Mt/yr)	100/200	1, 2
Channel lateral migration rate (m/yr)	40/100	
Sediment agradation rate in the floodplain (mm/yr)	0.4/0.8	
River sinuosity	1.2/1.7	

Table SVIII-5. ^{10}Be contribution in the flood plain calculated using the transfer flood plain model for the Narayani river.
The Lauer and Willenbring (2010)s model was applied using the parameters of Table SVIII-4.

Age (Ma)	Plain transfer exposure correction (atom/g)	1 σ (atom/g)
0.0	1200	200
0.5	1300	200
1.0	1300	200
1.5	1300	200
2.0	1400	200
2.5	1400	300
3.0	1500	300
3.5	1500	300
4.0	1500	300
4.5	1600	300
5.0	1600	300
5.5	1700	300
6.0	1700	400
6.5	1800	400
7.0	1800	400
7.5	1800	400
8.0	1900	400

Table SVIII-6. Major and trace elements results on the feldspar fraction.

Columns E-AX indicate major element results, columns AX-BI: trace element results, and columns BJ-BL: Li, Cl and Li. Measurements below the detection limit are indicated by < D.L.

Site	#	No CRPG	As	Ba	Be	Bi	Cd	Ce	Co	Cr	Cs	Cu	Dy	Er	Eu	Ga	Gd	Ge	Hf
			ppm	ppm	ppm	ppm	ppm	ppm	ppm	ppm	ppm	ppm	ppm	ppm	ppm	ppm	ppm	ppm	ppm
Valmiki sections		Uncertaintie	<20%	<5%	<20%	<20%	<20%	<5%	<20%	<5%	<15%	<20%	<10%	<5%	<5%	<5%	<10%	<10%	<10%
< D.L. : below detection limit		Detection limit	0.50	5.5	0.05	0.045	0.02	0.03	0.08	0.50	0.02	2.0	0.004	0.002	0.002	0.02	0.005	0.04	0.03
Dwarda section																			
Felsdpar																			
Dwarda	Dwcos2	1708143	1.073	667.538	3.814	< L.D.	0.028	9.000	< L.D.	5.144	8.504	< L.D.	0.545	0.332	0.644	10.935	0.564	1.423	2.264
Dwarda	Dwcos3	1708144	< L.D.	784.488	5.205	< L.D.	0.031	12.415	< L.D.	6.048	6.941	< L.D.	0.649	0.360	0.994	16.478	0.735	1.454	1.979
Dwarda	Dwcos5	1708145	0.721	560.307	7.465	0.356	0.034	10.605	< L.D.	3.192	17.359	2.035	0.988	0.521	0.751	21.365	0.898	1.832	1.774
Dwarda	Dwcos10	1708146	0.912	664.581	12.156	0.318	0.036	11.869	0.173	5.951	10.645	< L.D.	0.721	0.420	0.787	15.930	0.782	1.540	2.876
Dwarda	Dwcos18	1708147	0.658	695.675	12.934	< L.D.	0.030	18.160	0.106	8.660	10.273	< L.D.	0.987	0.560	0.667	11.303	1.126	1.448	3.570

	Ho	In	La	Lu	Mo	Nb	Nd	Ni	Pb	Pr	Rb	Sc	Sb	Sm	Sn	Sr	Ta	Tb	Th
	ppm	ppm	ppm	ppm	ppm	ppm	ppm	ppm	ppm	ppm >10ppm:	ppm	ppm	ppm	ppm	ppm	ppm	ppm	ppm	ppm
Uncertainties (%) (depending on content)	<10%	<20%	<5%	<20%	>25%	<10%	<15%	<5%	<20%	<10% > 0.1 ppm: <20%	<5%	<15%	<20%	<15%	<20%	<5%	<10%	<20%	<10%
Detection limit	0.001	0.03	0.02	0.001	0.50	0.015	0.016	2.0	0.45	0.004	0.15	0.6	0.06	0.005	0.30	0.70	0.004	0.001	0.015
Dwcos2	0.116	< L.D.	4.773	0.058	< L.D.	1.183	3.545	< L.D.	42.575	0.993	185.808	< L.D.	0.107	0.698	1.548	174.429	0.182	0.089	1.731
Dwcos3	0.132	< L.D.	6.792	0.060	< L.D.	1.046	4.713	< L.D.	59.436	1.327	207.823	< L.D.	0.087	0.921	1.578	283.549	0.163	0.112	2.304
Dwcos5	0.197	< L.D.	5.589	0.078	< L.D.	1.464	4.209	< L.D.	75.584	1.188	349.160	< L.D.	< L.D.	0.993	5.544	167.289	0.290	0.160	2.103
Dwcos10	0.151	< L.D.	6.245	0.074	0.564	1.808	4.692	3.899	63.199	1.322	217.668	< L.D.	0.147	0.953	2.411	229.227	0.266	0.122	2.278
Dwcos18	0.209	< L.D.	9.386	0.095	< L.D.	2.435	7.308	< L.D.	35.637	2.030	174.604	0.690	0.254	1.381	2.565	169.490	0.334	0.170	3.371

Table SVIII-6. (…/…)

	Tm ppm	U ppm	V ppm	W ppm	Y ppm	Yb ppm	Zn ppm	Zr ppm	SiO2 %	Al2O3 %	Fe2O3 %	MnO %	MgO %	CaO %	Na2O %	K2O %	TiO2 %	P2O5 %
Uncertainties (%) (depending on content)	<20%	<15%	>50 ppm: < 15% >10ppm: <10%	<20%	<15%	<15%	> 50ppm : <10% >10ppm: <20%	<5%	<2%	>10%: <2% >5%: <10%	<10%	<20%	<10%	<15%	<10%	<10%	<20%	>25%
Detection limit	0.001	0.01	0.85	0.80	0.02	0.002	7.0	1.50	0.05	0.04	0.015	0.015	0.03	0.03	0.02	0.03	0.02	0.10
Dwcos2	0.051	0.598	4.411	0.840	3.143	0.357	< L.D.	80.596	78.510	12.536	0.055	< L.D.	< L.D.	0.892	3.285	4.675	0.048	< L.D.
Dwcos3	0.052	0.641	4.132	< L.D.	3.502	0.358	< L.D.	71.097	69.820	17.898	0.070	< L.D.	< L.D.	1.896	5.037	5.384	0.045	< L.D.
Dwcos5	0.074	1.127	1.792	1.397	5.421	0.508	< L.D.	55.527	65.000	19.927	0.042	< L.D.	< L.D.	1.198	5.747	7.131	0.043	0.100
Dwcos10	0.063	0.913	8.774	< L.D.	4.174	0.456	< L.D.	99.783	69.840	17.413	0.072	< L.D.	0.048	1.541	5.137	4.826	0.068	< L.D.
Dwcos18	0.085	1.294	8.512	1.366	5.543	0.590	< L.D.	124.177	78.540	12.536	0.086	< L.D.	0.048	0.797	3.023	4.268	0.106	< L.D.

	LOI % Loss on Ignition	Total %	B ppm	Cl ppm	Li ppm
Dwcos2	0.790	100.791	9.3	<20	13.7
Dwcos3	0.810	100.960	10.1	45	11.4
Dwcos5	0.860	100.048	11.9	26	23.1
Dwcos10	0.550	99.495	11.4	24	15.9
Dwcos18	0.510	99.914	11.4	31	21.7

Table SVIII-7. Feldspar fraction ^{36}Cl results.

Seven samples and one blank were measured. Columns B-C indicate the mass of decontaminated feldspar, columns D-I: the data of the added Cl carrier, columns J-M: the ASTER measurements, columns N-U: the computations to obtain the Cl concentration of the sample, columns V-AE: the computations to obtain the ^{36}Cl concentration and paleoconcentration in the sample. Columns AH-AO indicate the parameters necessary for these computations (Schimmelpfenning, 2009).

			Cl carrier data						Measurements			
	Deconta minated feldspar mass (g)	1 σ (g)	Cl carrier solution mass (g)	1 σ (g)	mass of Cl (mg)	1 σ	atoms of Cl (atom)	1 σ	^{35}Cl/^{37}Cl	1 σ	^{36}Cl/^{35}Cl	1 σ
DWCOS2	58.09	0.05	0.272	0.005	1.88	0.10	3.24E+19	1.7E+18	10.14	0.10	8.99E-15	1.24E-15
DWCOS3	80.59	0.05	0.274	0.005	1.90	0.10	3.27E+19	1.7E+18	5.02	0.05	1.33E-14	1.15E-15
DWCOS4	43.90	0.05	0.278	0.005	1.93	0.10	3.32E+19	1.8E+18	11.03	0.11	9.15E-15	1.15E-15
DWCOS5	85.64	0.05	0.269	0.005	1.86	0.10	3.20E+19	1.7E+18	6.39	0.06	1.05E-14	1.15E-15
DWCOS7	50.43	0.05	0.274	0.005	1.90	0.10	3.27E+19	1.7E+18	10.96	0.11	7.90E-15	1.06E-15
DWCOS10	76.09	0.05	0.276	0.005	1.91	0.10	3.29E+19	1.7E+18	7.21	0.06	1.07E-14	1.44E-15
DWCOS18	83.74	0.05	0.274	0.005	1.90	0.10	3.27E+19	1.7E+18	5.87	0.07	1.03E-14	1.18E-15
CL01 (Blank)			0.275	0.005	1.90	0.10	3.27E+19	1.7E+18	280.15	3.97	4.25E-15	7.68E-16

	Cl concentration in sample								36Cl concentration in sample									
	raw Cl (atom)	1 σ (atom)	blank-corrected Cl (atom)	1 σ (atom)	Cl mass (mg)	1 σ (mg)	Cl concentration (ppm)	1 σ (ppm)	raw ^{36}Cl (atom)	1 σ (atom)	blank-corrected ^{36}Cl (atom)	1 σ (atom)	blank correction	^{36}Cl concentration (atom/g)	1 σ (atom/g)	relative uncertainty	^{36}Cl paleoconcentration (atom/g)	1 σ
DWCOS2	1.88E+19	1.0E+18	1.85E+19	1.0E+18	1.08938	0.0602	18.8	1.0	4.19E+05	5.84E+04	2.79E+05	6.36E+04	33%	4.80E+03	1.10E+03	23%	9.26E+03	2.59E+03
DWCOS3	7.09E+19	4.1E+18	7.05E+19	4.1E+18	4.15199	0.2435	51.5	3.0	1.15E+06	1.08E+05	1.01E+06	1.11E+05	12%	1.25E+04	1.37E+03	11%	2.57E+04	4.13E+03
DWCOS4	1.71E+19	9.3E+17	1.67E+19	9.3E+17	0.98563	0.0545	22.5	1.2	4.22E+05	5.33E+04	2.82E+05	5.90E+04	33%	6.41E+03	1.34E+03	21%	1.34E+04	3.49E+03
DWCOS5	4.02E+19	2.3E+18	3.99E+19	2.3E+18	2.34894	0.1328	27.4	1.6	6.54E+05	7.41E+04	5.14E+05	7.83E+04	21%	6.00E+03	9.14E+02	15%	1.33E+04	2.70E+03
DWCOS7	1.70E+19	9.2E+17	1.66E+19	9.2E+17	0.97988	0.0544	19.4	1.1	3.60E+05	4.85E+04	2.20E+05	5.47E+04	39%	4.35E+03	1.08E+03	25%	1.12E+04	3.37E+03
DWCOS10	3.29E+19	1.8E+18	3.26E+19	1.8E+18	1.91736	0.1061	25.2	1.4	6.20E+05	8.45E+04	4.80E+05	8.83E+04	23%	6.31E+03	1.16E+03	18%	2.04E+04	4.80E+03
DWCOS18	4.87E+19	2.8E+18	4.84E+19	2.8E+18	2.84879	0.1650	34.0	2.0	7.16E+05	8.51E+04	5.76E+05	8.88E+04	20%	6.88E+03	1.06E+03	15%	5.70E+04	1.17E+04
CL01 (Blank)	3.38E+17	1.9E+16							1.40E+05	2.53E+04								

Parameters

Natural chlorine		**MM**	**ratio**
35nat	**75.77%**	**34.969**	**3.1271**
37nat	**24.23%**	**36.966**	
Clnat	**100%**	**35.453**	

6.02E+23

avogadro number

Table SVIII-8. Recent exposure computation with ^{36}Cl results.

The feldspar samples having 36Cl (Table SVIII-7) and geochemical measurements (Table SVIII-6) were selected. Columns 1-F indicate the sample information (Table SVIII-1), columns H-N: 36Cl results (Table SVIII-7), columns P-Z: the computation of the ^{10}Be due to recent exposure (without erosion of the outcrop), and columns AB-AL: the compution taking into account the erosion of the outcrop

	sample information					^{36}Cl concentration				Cl concentration		
Sample	Depth (m)	Age (Ma)	Porosity	10Be paleoconcentration (atom/g)	1 σ (atom/g)	^{36}Cl concentration (atom/g)	1 σ (atom/g)	^{36}Cl age (ka)	1 σ (ka)	Cosmogenic Cl (atom/g)	Radiogenic Cl (atom/g)	Cl capture contribution (%)
DWCOS2	585	1.29	42%	1.22E+04	2.22E+03	4803	2.6E+03	0.0234	0.52	144	4659	10
DWCOS3	654	1.41	41%	1.12E+04	2.06E+03	12536	2.1E+03	0.305	0.32	2586	9950	22
DWCOS5	741	1.56	40%	1.13E+04	1.47E+03	6001	1.8E+03	0.182	0.24	1710	4291	11
DWCOS10	1163	2.3	36%	1.26E+04	2.41E+03	6307	2.1E+03	-0.127	0.37	-865	7172	14
DWCOS18	1930	4.15	29%	1.46E+04	1.17E+03	6881	1.9E+03	-0.608	0.41	-3858	10739	21

	^{36}Cl production rate					^{10}Be contribution due to recent exposure					
Sample	Ca spallation (atom/g/y)	K spallation (atom/g/y)	Ca muonic pathway (atom/g/y)	K muonic pathway (atom/g/y)	Cl thermal neutron (atom/g/y)	inherited ^{36}Cl concentration (atom/g)	1 σ (atom/g)	recent exposure ^{36}Cl concentration (atom/g)	1 σ (atom/g)	^{10}Be contribution due to recent exposure (atom/g)	1 σ (atom/g)
DWCOS2	0.280	4.911	0.018	0.321	0.630	1010	184	-866	3209	-535	1984
DWCOS3	0.597	5.642	0.038	0.366	1.847	967	179	1619	2723	727	1222
DWCOS5	0.377	7.471	0.024	0.485	1.019	765	100	945	2253	384	915
DWCOS10	0.482	5.044	0.031	0.328	0.946	113	22	-978	2527	-545	1410
DWCOS18	0.249	4.436	0.016	0.286	1.363	2	0	-3860	2603	-2316	1562

	^{10}Be contribution due to recent exposure (including erosion)									
	^{36}Cl production rate including erosion					Ratio of production rates				
Sample	Ca spallation (atom/g/y)	K spallation (atom/g/y)	Ca muonic pathway (atom/g/y)	K muonic pathway (atom/g/y)	Cl thermal neutron (atom/g/y)	Total ^{36}Cl production rate (atom/g/y)	^{10}Be production rate (atom/g/y)	^{10}Be/^{36}Cl production rate	^{10}Be contribution due to recent exposure (atom/g)	1 σ (atom/g)
DWCOS2	45	786	66	1174	101	2171	768	0.35	-306	1135
DWCOS3	96	903	140	1337	295	2771	768	0.28	449	755
DWCOS5	60	1195	89	1772	163	3279	768	0.23	221	528
DWCOS10	77	807	113	1198	151	2346	768	0.33	-320	827
DWCOS18	40	710	58	1043	218	2069	768	0.37	-1433	967

scaling facto	l_{36}	sm	fm	sum
	a^{-1}	0.0027	0.0087	0.0114
0.927	2.30E-06			

Table SVIII-9. Recent exposure model.
Columns E-I indicate the results of the simple model and columns M-O present its parameters.

Age (Ma)	Depth (m)	Porosity	Density (g/cm3)	^{10}Be recent exposure contribution (atom/g)	min (atom/g)	max (atom/g)	-1 σ (atom/g)	+1 σ (atom/g)
0	0	0.49	1.87	535	265	1029	270	494
1	465	0.43	1.97	508	251	977	257	469
2	929	0.38	2.05	487	241	936	246	449
3	1394	0.34	2.13	469	232	902	237	433
4	1859	0.30	2.20	455	225	875	230	420
5	2324	0.26	2.26	443	219	852	224	409
6	2788	0.23	2.31	433	214	832	219	399
7	3253	0.20	2.35	424	210	816	214	392
8	3718	0.18	2.40	417	206	802	211	385

Parameters	Incision rate (mm/y)	Shielding factor
Mean	5	0.65
Min	3	0.45
Max	7	0.75

An intense debate animates the Earth Sciences community about the impact of the Glaciations on mountain ranges. Mountains develop their relief from the interaction of tectonics with climate through erosion. Erosion breaks rocks in the highland, and rivers and submarine gravity flows (turbidites) transfer the waste material to sedimentary basins. Erosion results from the action of rainfall, rivers or glaciers. Studies suggest that changes in the rainfall amplitude or seasonality, and changes in the extent of glaciers have triggered a worldwide and considerable increase of erosion rates for the last millions of years. However, this hypothesis is debated because past erosion rates are estimated with indirect approaches.

Here, I focus on the Himalaya, the iconic mountain range at the convergence of the Indian and Eurasian plates. There, the highest summits and the deepest valleys on Earth grow. Landslides and glacial erosion supply one of the highest sedimentary fluxes to the oceans. To determine the past erosion rates, I measured the amount of the 10Be cosmogenic isotope accumulated in the quartz sediment. These isotopes are produced at Earth's surface by the interaction of cosmic rays with matter. Isotopes gradually accumulate in rocks close to the surface, depending on the elevation and the erosion rates. The isotopic concentration in sediment gives access to the average erosion rate of the source drainage basin. To determine the source of sediment and the deposition paleoenvironment, I performed supplementary measurements on Sr-Nd and C-O isotopes.

I conducted my measurements on two sites. Site A consists in sandy turbidites sedimented on the deep sea floor of the Bengal Bay and collected by Expeditions 353 and 354 of the International Ocean Discovery Program. Site B consists in molasse sediment deposited at the front of the Himalaya, in the Siwalik Hills, within the Valmiki Wildlife Sanctuary in India. Site A integrates the erosion of the Ganga and Brahmaputra drainage basins, covering Central and Eastern Himalaya. Site B integrates the erosion of the Narayani-Gandak basin, covering Central Nepal.

My results yield an unprecedented insight in the variation of erosion in a mountain range over the last seven million years. They imply that average erosion rates have been steady since at least three million years in the Himalaya, despite the variations in sediment transfer or the locus of erosion, and despite intense late Cenozoic Glaciations.

La communauté des sciences de la Terre est animée d'un intense débat sur l'impact des Glaciations sur les chaînes de montagnes. Les montagnes forment leur relief à partir des interactions entre la tectonique, le climat et l'érosion. L'érosion détruit les roches en altitude et les rivières et les écoulements gravitaires sous-marins (turbidites) en transfèrent les débris vers les bassins sédimentaires. L'érosion résulte de l'action des précipitations, des rivières ou des glaciers. Des études suggèrent que les changements dans l'amplitude ou la saisonnalité des précipitations et les changements dans l'étendue des glaciers ont provoqué une augmentation mondiale et considérable des taux d'érosion sur les derniers millions d'années. Cependant, cette hypothèse est débattue car les taux d'érosion passés sont estimés avec des approches indirectes.

Ici, je me concentre sur l'Himalaya, la chaîne de montagne par excellence située à la convergence des plaques indiennes et eurasiennes. C'est là que se développent les plus hauts sommets et les vallées les plus profondes de la Terre. Les glissements de terrain et l'érosion glaciaire fournissent l'un des flux sédimentaires les plus élevés aux océans. Pour déterminer les taux d'érosion passés, j'ai mesuré la quantité d'isotope cosmogénique ^{10}Be accumulée dans le sédiment de quartz. Ces isotopes sont produits à la surface de la Terre par l'interaction des rayons cosmiques avec la matière. Les isotopes s'accumulent progressivement dans les roches proches de la surface, en fonction de l'altitude et des taux d'érosion. La concentration isotopique du sédiment donne accès au taux d'érosion moyen du bassin versant à la source de celui-ci. Pour déterminer la source des sédiments et le paléoenvironnement de dépôt, j'ai effectué des mesures complémentaires sur les isotopes Sr-Nd et C-O.

J'ai réalisé mes mesures sur deux sites. Le site A est constitué de turbidites sableuses sédimentées dans les fonds marins de la baie du Bengale et recueillies par les expéditions 353 et 354 du programme scientifique IODP. Le site B est constitué de molasses déposées au front de l'Himalaya, dans les collines des Siwaliks, au sein du sanctuaire animalier de Valmiki en Inde. Le site A intègre l'érosion des bassins versants du Gange et du Brahmapoutre, couvrant l'Himalaya central et oriental. Le site B intègre l'érosion du bassin Narayani-Gandak, qui couvre le centre du Népal.

Mes résultats donnent un aperçu sans précédent de la variation de l'érosion dans une chaîne de montagnes au cours des sept derniers millions d'années. Ils impliquent que les taux d'érosion moyens sont stables depuis au moins trois millions d'années dans l'Himalaya, malgré les variations dans le transfert sédimentaire ou sur le lieu de l'érosion, et malgré les glaciations intenses de la fin du Cénozoïque.